


# Advances in Renewable Energies and Power Quality

*Edited by Manuel Pérez-Donsión and Gianpaolo Vitale*

Copyright © 2020 Cambridge Scholars Publishing. All rights reserved. May not be reproduced in any form without permission from the publishers, except fair uses permitted under U.S. or applicable copyright law.

EBSCO Publishing : eBook Collection (EBSCOhost) - printed on 2/14/2023 2:46 PM via
AN: 2338894 ; Manuel Prez-Donsin, Editor, Gianpaolo Vitale, Editor.; Advances in Renewable Energies and Power Quality
Account: ns335141

# Advances in Renewable Energies and Power Quality

EBSCOhost - printed on 2/14/2023 2:46 PM via . All use subject to https://www.ebsco.com/terms-of-use

EBSCOhost - printed on 2/14/2023 2:46 PM via . All use subject to https://www.ebsco.com/terms-of-use

# Advances in Renewable Energies and Power Quality

Edited by

Manuel Pérez-Donsión
and Gianpaolo Vitale

Cambridge
Scholars
Publishing



EBSCOhost - printed on 2/14/2023 2:46 PM via . All use subject to https://www.ebsco.com/terms-of-use

Advances in Renewable Energies and Power Quality

Edited by Manuel Pérez-Donsión and Gianpaolo Vitale

This book first published 2020

Cambridge Scholars Publishing

Lady Stephenson Library, Newcastle upon Tyne, NE6 2PA, UK

British Library Cataloguing in Publication Data
A catalogue record for this book is available from the British Library

Copyright © 2020 by Manuel Pérez-Donsión, Gianpaolo Vitale
and contributors

All rights for this book reserved. No part of this book may be reproduced, stored in a retrieval system, or transmitted, in any form or by any means, electronic, mechanical, photocopying, recording or otherwise, without the prior permission of the copyright owner.

ISBN (10): 1-5275-4530-X
ISBN (13): 978-1-5275-4530-4

EBSCOhost - printed on 2/14/2023 2:46 PM via . All use subject to https://www.ebsco.com/terms-of-use

*To all those people who are working for getting a better World and to all those who might benefit from it*

To my wife Alicia for her love, patience and continuous collaboration and also to our son Juan José and his wife Bea

- ***Manuel Pérez Dónsion***

To my beloved parents and to my family, for their love, endless support, encouragement and abnegation

- ***Gianpaolo Vitale***

"There are only two ways to live your life. One is as though nothing is a miracle. The other is as though everything is a miracle."

- ***A. Einstein***

EBSCOhost - printed on 2/14/2023 2:46 PM via . All use subject to https://www.ebsco.com/terms-of-use

EBSCOhost - printed on 2/14/2023 2:46 PM via . All use subject to https://www.ebsco.com/terms-of-use

# TABLE OF CONTENTS

Foreword ..... xiv

To Whom this Book is Addressed ..... xvi

Acknowledgments ..... xvii

How to Use this Book ..... xix

Biographies of the Editors ..... xx

Chapter Zero ..... 1
Salamanca Declaration
Manuel Pérez Donsión, Mircea Ion Buzdugan, Péter Kádár, Mohamed El-Sayed, Ahmad Pourmovahed, Gianpaolo Vitale.

**Part I: Photovoltaic Generation**

Chapter One ..... 8
PV Systems Way of the Future
I. Gomes, R. Melicio, V. Mendes.

Chapter Two ..... 27
Segmentation of 3D Point Cloud Data for Assessment and Ranking of Photovoltaic Potential
N. Lukač, B. Žalik, G. Štumberger.

Chapter Three ..... 37
Clustering Dalily Solar Radiation from Reunion Island Using Data Analysis Methods
J.D. Lan-Sun Luk, M. Bessaf, J.P. Chabriat, P. Jeanty, M. Delsaut, L. Trovalet, H. Ralambondrainy, P. Charton.

Chapter Four ..... 54
Modelling Solar Data: Reasons, Main Methods and Applications
M. De Simón-Martìn, M. Dìez-Mediavilla, C. Alonso-Trìstan.

EBSCOhost - printed on 2/14/2023 2:46 PM via . All use subject to https://www.ebsco.com/terms-of-use

Chapter Five ..... 67
The Importance of the Cell Temperature to Model the Energy Efficiency of PV Modules
S. Jacques.

Chapter Six ..... 81
A Cost-Effective Microcontroller Based Sensor or Dual Axis Solar Tracking
Sameer D. Meshram.

Chapter Seven..... 98
Photovoltaic Powered Water Pumping Systems Applied to Family Agriculture: A Key Tool for Developing Countries
R. J. Chilundo, U. S Mahanjane, M.M.N. Diniz, A.M.E. Bezerra, P.C.M Carvalho.

Chapter Eight..... 113
Effect of Varying the Distance Between the Double Glazing of a Solar Thermal Collector on its Functioning
N. Ihaddadene, R. Ihaddadene, F. Hadji, A. Mahdi.

**Part II: Wind Generation**

Chapter Nine..... 130
New Cost-Effective Excitation Controlled Synchronous Generator-Based Wind Turbine Scheme
A. Shamsnia, M. Parniani.

Chapter Ten ..... 153
Assessment of the Main Socio-Economic Impacts of Wind Energy in Europe (527_2016)
M. Ortega, P. Del Río, E. Montero.

Chapter Eleven ..... 170
Model to Maximize Self-Computing of Olive Mills Powered by a Mixed System of Renewable Energies (263_2015)
O. Rabaza, D. Gómez-Lorente.

Chapter Twelve ..... 186
Numerical Modeling of Resistive-Type Superconducting Faults Current Limiters (293_2016)
A. Etxegarai, I. Zamora, G. Buigues, V. Valverde, E. Torres, P. Eguia.

EBSCOhost - printed on 2/14/2023 2:46 PM via . All use subject to https://www.ebsco.com/terms-of-use

**Part III: Distributed Generation**

Chapter Thirteen ..... 206
State of the Art Distributed Generation: Value Proposition for Power Islands
B. Hartmann, I. Vokony, I. Táczi

Chapter Fourteen ..... 218
Review of Fault Protection in AC Microgrids: Challenges and Potential Solutions
G. Buigues , A. Dyśko, V. Valverde, I. Zamora, E. Fernández.

Chapter Fifteen ..... 260
Power Stabilization System with Counter-Rotating-Type Pump-Turbine to Momentarily Stabilize Fluctuating Power from Renewable Resources
J. Kim, Y. Choi, T. Kanemoto.

Chapter Sixteen ..... 279
Model Predictive Control for the Management of Electrical Energy in an Agroindustrial Microgrid
C. Hernández-Hernández, F. Rodríguez, J. C. Moreno, P. R. Da Costa Mendes, J. E. Normey-Rico.

Chapter Seventeen ..... 305
Thermal and Power Production Optimization in Microgrids with Model Predictive Control
S. Raimondi Cominesi, A. Del Corno, E. Corsetti, G. A. Guagliardi, C. Sandroni, R. Scattolini.

Chapter Eighteen ..... 320
Analysis of Solutions for the Integration of Renewable Energies in Weak Networks
J.I. San Martín, F.J. Asenzio, I. Zamora, G. Saldaña, O. Oñederra.

Chapter Nineteen ..... 341
A Prototype in Reduced Scale of a Refrigeration System Controlled with Pulse Width Modulation (PWM) Using Thermoelectric Modules by Peltier Effect for Application in Internal Environments
E. Maestrelli, A. D. Spacek, J. M. Mota, E. A. Da Silva, O. H. Ando Junior, C. F. Malfatti, L. Schaeffer.

EBSCOhost - printed on 2/14/2023 2:46 PM via . All use subject to https://www.ebsco.com/terms-of-use

**Part IV: Smart Grids**

Chapter Twenty ..... 354
New Trends in Operation, Management and Control of Future Active Distribution Networks.
H. R. Baghaee, G. B. Gharehpetian.

Chapter Twenty-One ..... 381
Simulation Model of a Protection Scheme for Active Distribution Networks
R. Chiumeo, C. Gandolfi, F. Belloni, S. Pugliese.

Chapter Twenty-Two..... 403
Using On-Line Measurements to Identify Parameters of Improved Heffron-Phillips Model Including Excitation System and Governor
B. Zaker, G. B. Gharehpetian.

Chapter Twenty-Three..... 421
WiFi Monitoring of a High Temperature Control Applied to Micro Thermoelectric Generators
S. C. S. Jucá, R. I. S. Pereira, P.C.M Carvalho.

**Part V: Power Electronics, FACTS and HVDC**

Chapter Twenty-Four ..... 448
Power Electronics in FACTS and HVDC
P. Kadar.

Chapter Twenty-Five..... 470
High Performance SiC MOSFETs for Fault Tolerant Applications
Onambele J. E. Bester, A. MPanda Mabwe.

Chapter Twenty-Six..... 491
Dynamic Behaviour of Multi-Terminal VSC-Based HVDC DC Control Strategy
F. Gonzalez-Longatt, J. M. Roldan-Fernandez, S. Arnaltes, J.L. Rodríguez-Amenedo.

EBSCOhost - printed on 2/14/2023 2:46 PM via . All use subject to https://www.ebsco.com/terms-of-use

Chapter Twenty-Seven ..... 517
Capacitorless DC/DC Regulator as a Candidate Topology
for Photovoltaic Solar
H. Martínez-García, E. García-Vílchez.

Chapter Twenty-Eight ..... 535
Low Drop-Out Voltage Regulator as a Candidate Topology
for Photovoltaic Solar Facilities
H. Martínez-García, A, Saberkari, E. García-Vílchez.

Chapter Twenty-Nine ..... 559
Comparative Aspects in Control Strategies for Hybrid DC/DC Regulators
with Variables-Switching Frequency
H. Martínez-García, A, Saberkari, E. García-Vílchez.

Chapter Thirty ..... 579
A Frequency Domain SMPS Model for Harmonic Estimation
G. Malagon-Carvajal, C. Duarte, G. Ordonez-Plata.

Chapter Thirty-One ..... 599
Review of Fault Detection and Location Techniques in VSC-HVDC
and MTDC Systems (299_2016)
G. Buigues, V. Valverde, D.M. Larruskain, P. Eguía, E. Torres.

**Part VI: Harmonics, Filters and Other Correction Devices**

Chapter Thirty-Two..... 632
EMI Mitigation Through Polyphase Drive Systems Configuration
G. Winnischofer, C. A. Franҫa Sartori.

Chapter Thirty-Three..... 648
Shunt Active Power Filter with Selective Harmonics Compensation
for LV Distribution Grid
F. Belloni, R. Chiumeo, C. Gandolfi.

Chapter Thirty-Four..... 671
A Hybrid Power Filter for Load Compensation
S. P. Litrán, P. Salmerón, A. Pérez, J. Prieto.

EBSCOhost - printed on 2/14/2023 2:46 PM via . All use subject to https://www.ebsco.com/terms-of-use

Chapter Thirty-Five ..... 692
An Optimal Location Algorithm for Estimating the Injection of Harmonics Sources in Electrical Networks
L. F. Beites, M. Alvarez, A. Díaz García.

Chapter Thirty-Six ..... 706
Harmonic Modeling of Electric Vehicle Chargers in Frequency Domain
S. Müller, J. Meyer, P. Schegner, S. Djokic.

Chapter Thirty-Seven ..... 727
Harmonic Limits in Connection Agreement for Wind Power Plants
D. Schwanz, M. Bollen.

**Part VII: Voltage Sags and Dips, Power Quality**

Chapter Thirty-Eight ..... 744
Dips/Sags in Power Quality
M. Buzdugan

Chapter Thirty-Nine ..... 765
The Influence of the Network Characteristics and Environmental Conditions on Voltage Dip Performance in MV Networks
R. Chiumeo, C. Gandolfi, L. Tenti.

Chapter Forty ..... 784
Optimal Voltage Sags Monitoring through Simultaneous Analysis of Short-Circuits and Different Loading Profiles in Distribution Systems
T. R. Kempner, F. A. Mourihno, F. B. Bottura, M. Oleskovicz, J. C. M. Vieira Junior.

Chapter Forty-One ..... 802
A Power Quality Instrument for the Smart Grid Monitoring based on Higher-Order Statistics
O. Florencias-Oliveros, J. Gonzaléz-de-la-Rosa, A. Agüera-Pérez, J. Palomares-Salas, J. Sierra-Fernández.

Chapter Forty-Two ..... 821
A Power Index-based Diagnostic for Systems with Active Power Load Conditioning
J. Prieto, P. Salmerón, A. Pérez, S. P. Litrán.

EBSCOhost - printed on 2/14/2023 2:46 PM via . All use subject to https://www.ebsco.com/terms-of-use

Chapter Forty-Three ..... 837
A Case Study on High Power Compensator of the Power Grid Irregularities for Industrial Appliances
J. Iwaskiewicz, L. Wolski, M. Peréz Donsión.

Chapter Forty-Four ..... 858
Power Quality Versus Electromagnetic Compatibility in Adjustable Speed Drives
M. Buzdugan, H. Balan.

Chapter Forty-Five ..... 877
Application of Generalized Non-Active Power Theory for Parallel Hybrid Compensation of Periodic and Non-Periodic Disturbances
Z. Muller, J. Tlustý, V. Valouch.

EBSCOhost - printed on 2/14/2023 2:46 PM via . All use subject to https://www.ebsco.com/terms-of-use

# FOREWORD




Renewable sources are expected to make a crucial contribution in meeting the energy demands of our planet and help avoid the detrimental effects we experience from the use of fossil fuels. In addition, it will increase economic growth, with an increase in jobs playing a direct role in the exploitation of renewables.

With this common objective, scientists from 20 different countries meet each year to discuss the exploitation of renewable energy and its implications—some of these scientists are leading authorities in their areas of expertise.

The International Conference on Renewable Energy and Power Quality (ICREPQ) gives us an occasion to address the various challenges of renewable energy. Particular attention is given to photovoltaic cells; wind generation; distributed generation; smart grids; power electronics; FACTS and HVDC; harmonics; filters with other correction devices; voltage sags and dips; and power quality. This book is arranged with a section devoted to each of these topics. The contents have been enriched with original contributions on state-of-the-art technology, approaches, and perspectives for the corresponding part of the book. These chapters are labelled *.

The purpose of this new book is to assess and update the knowledge about and potential advantages of renewable energy sources, distributed generation, energy storage, and other factors relevant to smart systems. It is intended to be a reference work for researchers, technicians, and engineers looking for both theoretical and practical applications.

Preceding this book, two volumes containing a selection of the best papers presented at the ICREPQ conferences between 2003 and 2012 were published in 2013 by the same editor with the titles “Renewable Energy”

EBSCOhost - printed on 2/14/2023 2:46 PM via . All use subject to https://www.ebsco.com/terms-of-use

and "Power quality." This new book titled: "Advances in renewable energy and power quality" includes a selection of the best papers presented at the ICREPQ conferences from 2013 to 2017. They have been selected with the help of voluntary reviewers. The authors of the selected papers have been required to improve and update their work before its final publication.

The ICREPQ conferences take place in Spain and each year a different city is chosen. Over the last five years, the following cities have hosted the conference: Bilbao (20–23 March 2013); Córdoba (7–10 April 2014); La Coruña (25–27 March 2015); Madrid (4–6 May 2016); and Málaga (4–6 April 2017). During the last conference in Salamanca (21–23 March 2018), the "Salamanca Declaration" was prepared, which sought to assess the contribution of the scientific community to recognizing the challenges and opportunities offered by renewables. This paper is included here.

A high level of participation has always characterized the ICREPQ conferences. They give an opportunity for academics, scientists, engineers, manufacturers, and users from all over the world to come together in a pleasant location to compare their experiences, research, and results.

All the published papers are available on the conference website: http://www.icrepq.com/ and are collected in the Renewable Energy and Power Quality Journal (RE&PQJ)—this is a free electronic journal edited in Spain by the European Association for the Development of Renewable Energies, Environment and Power Quality (EA4EPQ). The ISSN is 2172-038X; the DOI (Digital Object Identifier) is:

https://doi.org/10.24084/repqjvolume.papernumber.

All papers are indexed in Scopus.

EBSCOhost - printed on 2/14/2023 2:46 PM via . All use subject to https://www.ebsco.com/terms-of-use

# TO WHOM THIS BOOK IS ADDRESSED

This book is primarily intended to meet the demands of researchers and professional engineers dealing with the exploitation of renewable energy. It should also prove useful to postgraduate students and scientists dealing with social, economic, and environmental problems related to the growing use of renewable energy systems and new "green jobs" that play a direct role in reducing the environmental impact of traditional energy sources.

This book will also be useful as a reference book for engineers, physicists, and mathematicians who are interested in the operation, project management, design, and analysis of renewable energy equipment. Each chapter contains references that allow the treated topic to be investigate further.

EBSCOhost - printed on 2/14/2023 2:46 PM via . All use subject to https://www.ebsco.com/terms-of-use

# ACKNOWLEDGMENTS

First of all, special thanks are due to Professor Manuel Perez Donsión, of the University of Vigo (Spain), for his tireless and invaluable efforts in organizing the ICREPQ conferences since 2003.

Special thanks go to all voluntary reviewers as well. Each of them reviewed more than one hundred papers to make the publication of this book possible. They are:

- Prof. Habil. Eng. Mircea Ion Buzdugan (PhD). Dean of the Faculty of Building Engineering, Technical University of Cluj-Napoca, Romania.
- Prof. Kouzou Abdellah. Laboratory of Applied Automation and Industrial Diagnosis, Faculty of Science and Technology, Djelfa University, Algeria.
- Dr. Ali Asghar Fathollahi Fard (PhD). Lecturer in the Faculty of Engineering, Multi-Media University, CyberJaya, Malaysia.
- Asst. Prof. Dr. Ali Jafer Mahdi, PhD in Electrical Engineering (2011) from the University of Liverpool, UK, Department of Electrical & Electronic Engineering. College of Engineering, University of Karbala, Karbala, Iraq.
- Prof. Ramon Bargalló Perpiñà, PhD in Industrial Engineering. Department of Electrical Engineering, Research Group: Energy Processing and Integrated Circuits (EPIC), Barcelona East School of Engineering (EEBE) UPC
- Dr. Mihai Predescu Aeolus Energy International, Bucharest, Romania. Scientific Director and Consultant in Renewable Energies, Freelancer.
- Dr. Rui Melicio. ICT, Universidade de Évora and IDMEC, Instituto Superior Técnico, Universidade de Lisboa, Portugal
- Prof. Youssef ERRAMI, (PhD). Engineer, Laboratory: Electronics, Instrumentation and Energy (LEIE); Team: Exploitation and Processing of Renewable Energy (EPRE), Physics Department, Faculty of Sciences, Chouaïb Doukkali University, El Jadida, Morocco.

EBSCOhost - printed on 2/14/2023 2:46 PM via . All use subject to https://www.ebsco.com/terms-of-use

- Etim Ubong. Center for Fuel Cell Systems Research & Powertrain Integration, Kettering University, Flint, MI, USA.
- Prof. Dr. Gorazd Štumberger, univ. dipl. inž. el. Head of the Power Engineering Institute, University of Maribor, Faculty of Electrical Engineering and Computer Science, Koroška cesta 46, 2000 Maribor, Slovenija.
- Prof. Gianpaolo Vitale. Institute for High Performance Computing and Networking (ICAR), National Research Council of Italy (CNR), Italy.
- Prof. Hamid El Qarnia, (PhD). Fluid Mechanics and Energetics Laboratory, Physics Department, Faculty of Sciences, Cadi Ayyad University, Marrakesh, Morocco.
- Prof. Mario Mañana Canteli. Associate Professor, Department of Electrical and Energy Engineering, University of Cantabria, Spain.
- Prof. Amine Stambouli. University of Sciences and Technology of Oran, Algeria.

The Editors are grateful to the European Association for the Development of Renewable Energies, Environment and Power Quality (EA4PQ); and Vigo University for institutional support.

The Editors are grateful to ICAR-CNR (Institute for High Performance Computing and Networking, National Research Council of Italy) for institutional support.

Thanks go to Cambridge Scholars Publishing for helping publish this book, which contains the most relevant papers of the last five years presented at the ICREPQ conferences dealing with renewable energy and power quality issues.

Finally, a special thanks go to all the authors that have contributed their research with the aim of improving life on our planet.

EBSCOhost - printed on 2/14/2023 2:46 PM via . All use subject to https://www.ebsco.com/terms-of-use

# How to Use this Book

This book can be used in different ways. Each part is self-contained and the first chapter is labelled *. The reader can select a chapter of interest by using the table of contents. The references given in each paper are useful for finding out further information on a paper's topic.

EBSCOhost - printed on 2/14/2023 2:46 PM via . All use subject to https://www.ebsco.com/terms-of-use

# BIOGRAPHIES OF THE EDITORS



**Manuel Pérez-Donsión** received an MSc in Industrial Engineering from the Polytechnic University of Catalonia in 1980, and his PhD from the University of Vigo in 1986. In 1987 he was made full professor at the University of Vigo.

Among other academic positions, he was the Dean of the Escuela Técnica Superior de Ingenieros Industriales y Minas from 1995 to 2001. From 2001 to 2004 he was also the Head of the Department of Electrical Engineering. He is a member of the Scientific Committee of different conferences and journals. He is the President of the European Association for the Development of Renewable Energies, Environment and Power Quality (EA4EPQ), the European Association for the Development of Electrical Engineering (EADEE), and the Spanish Association for the Development of Electrical Engineering (AEDIE). He is also the Vice-President of the Portuguese Association for the Development of Electrical Engineering (APDEE). He was awarded the Gold Insignia of the Green Week Foundation and has received four awards from electrical engineering journals. His main research interests are related to:

- power quality;
- renewable energy, with special emphasis on small hydropower and wind energy;
- modelling, diagnostics, and control of electric machines;
- permanent magnet synchronous motors;
- transient stability of electrical power systems.

He is the author of two research books; seven other books; and over one hundred research papers, some of which have been presented at national and international conferences, while others have been published in relevant journals. He has also been involved in a number of major

EBSCOhost - printed on 2/14/2023 2:46 PM via . All use subject to https://www.ebsco.com/terms-of-use

research projects. In recent years he has taught undergraduate courses in Electrical Machines, the Quality and Utilization of Electrical Energy, and the Control of Electrical Motors; at postgraduate level, he has taught Special Electrical Motors and Renewable Energies and Power Quality.



**Gianpaolo Vitale** received an MD in Electronic Engineering from the University of Palermo (Italy) in 1988. He is senior researcher at the Institute for High Performance Computing and Networking (ICAR), an Institute of the National Research Council (CNR) that belongs to the Department of Engineering, ICT and Technologies for Energy and Transport (DIITET). He received the national scientific qualification ("Abilitazione scientifica nazionale") of full professor in electric energy engineering (cod. 09/E2) in 2013 and as full professor in electronic energy engineering (cod. 09/E3) in 2017. He teaches "Industrial Electronics" as part of the MD course in electronic engineering at the University of Palermo. He has supervised research projects on the electromagnetic compatibility of electrical drives and the intelligent management of electrical energy supplied by renewable sources. He has been a senior member of the IEEE (Institute of Electrical and Electronics Engineers) since 2012 and a member of the IEEE Industrial Electronics Society, the IEEE Power Electronics Society, and the IEEE Robotics and Automation Society. He serves as a reviewer for several journals and conferences. He has been a member of the Organizing Committee of the ICREPQ Conference since 2008. He is the co-author of two books, two edited books and over one hundred scientific articles, of which 40 have been published in international ISI journals.

His current research interests are in the fields of robotics, power electronics, and power generation from renewable sources with problems related to electromagnetic compatibility. E-mail: gianpaolo.vitale@icar.cnr.it

EBSCOhost - printed on 2/14/2023 2:46 PM via . All use subject to https://www.ebsco.com/terms-of-use

EBSCOhost - printed on 2/14/2023 2:46 PM via . All use subject to https://www.ebsco.com/terms-of-use

# CHAPTER ZERO

# SALAMANCA DECLARATION


- Prof. Manuel Pérez Donsión, Chairman of the ICREPQ Steering Committee. University of Vigo, Spain.
- Prof. Mircea Ion Buzdugan, University of Cluj-Napoca, Romania.
- Prof. Péter Kádár, Óbuda University, Hungary.
- Prof. Mohamed El-Sayed, Kuwait University, Kuwait.
- Prof. Ahmad Pourmovahed, Kettering University, USA.
- Prof. Gianpaolo Vitale, National Research Council of Italy.


This declaration was made during the International Conference on Renewable Energy and Power Quality (ICREPQ'18) XVI held at the University of Salamanca, from the 21st to the 23rd of March 2018. It presents an outline of state-of-the-art technology and approaches in the fields of renewable energy and power quality, including the latest results presented at the conference. At the end of the conference, this declaration was proposed and approved by the participants. This document aims to assess the contribution of the scientific community and to recognize the prestige of the University of Salamanca on the occasion of the commemoration of its first eight centuries in existence, a process that reached its culmination in the same year as ICREPQ'18.

The use of renewable energy sources (RES) is growing apace and offers a valid solution to the mitigation of CO2 emissions. Unfortunately, they exhibit slower growth compared to the energy demand that is still satisfied by fossil fuels. The target of satisfying 50% of the market-share (corresponding to the transition from the use of fossil sources to the use of renewable sources) is still far from being achieved. For this reason, RES need to be sustained by current technology.

There are many factors relevant to the increasing use of RES. Among them is the adoption of power conditioning devices for electrical energy conversion. These lead to increased efficiency conversion and a reduction in the need for additional investment.

The new generation of advanced power electronic devices available to the market, together with new conversion topologies, allow fast switching methods that reduce losses and a higher operating temperature. Moreover,

EBSCOhost - printed on 2/14/2023 2:46 PM via . All use subject to https://www.ebsco.com/terms-of-use

the efficiency of solar and wind generation is improving, contributing to a reduction in the time taken to achieve a return and encouraging further capital investment.

The continuous growth of RES has to be taken into account during the planning of distribution grids, which were conceived for a unidirectional power flow generated by conventional sources. Now, new techniques of analysis need to be developed to take into account bidirectional power flows in distributed generation and the presence of harmonics.

The adoption of RES reduces the inertia of conventional generation systems, leading to possible instabilities, especially for non-robust grids. Therefore, a virtual inertia must be provided, so that in the case of failure a relevant amount of power can be delivered to the grid to maintain voltage and frequency stability and avoid collapse.

The availability of energy generated by RES requires that the maximum energy is extracted to cover the demand required by the customer. This situation is very different from conventional generation by fossil fuel sources where energy can be reduced according to the demand of the customer. For efficient utilization of the available renewable energy, maximum power tracking techniques have to be considered that interface RES with the grid. As a matter of fact, the intermittency of energy produced by RES means that it is usually not enough to satisfy demand. In the case of a renewable energy deficit, fossil fuels are required. If RES generation overproduces the required energy, this excess energy is lost. The solution is to be found in the adoption of a storage system. There are a few solutions currently available on the market, but they need further study to reduce overall costs and enhance system performance. In addition, environmental aspects need to be taken into account. Storage facilities that currently exist include batteries, plug-in-hybrid electric vehicles, flywheels, supercapacitors, superconducting coils and others. All these systems store energy, but further study is needed to optimize their design and operation and fulfil customer requirements.

There are many fields for which the use of RES can be promoted. For example, the process of water desalination requires electricity, which can be produced by RES, avoiding its transmission over long distances and ensuring the production of clean water.

The tri-generation of combined cooling, heating and electrical power is able to produce chilled water for air conditioning or refrigeration using a part of the heat delivered by co-generation plants. This type of plant sees high efficiency in the production of electricity and heat, with reduced fuel and energy costs. Moreover, such plants lower peak demand during hot seasons. The management of hybrid energy generation, including the new

EBSCOhost - printed on 2/14/2023 2:46 PM via . All use subject to https://www.ebsco.com/terms-of-use

trend of producing electric vehicles, requires the availability of efficient communication facilities in smart grid operations.

Deregulation of the electrical power industry, namely its classification into generation, transmission, and distribution subsystems, has led to increased research interest into the power quality delivered. This is no longer just an issue for technical groups working with power utility's, but also requires the investigation of unusual problems of interaction between the power system and customer facilities, including their basic design, maintenance issues, and the investment required to protect the equipment within these facilities, as well as the implementation of new technologies.

Electrical power quality issues do not just have significant economic consequences for customers, but also serious economic impacts on utility companies, because of the ability of the customer to choose which power sources serve them in new and free competitive markets. In practice, these new, free markets are changing the framework in which power quality is addressed across the world, and power quality objectives are now of great importance to all power system operators.

Power quality is a complex area covering many different topics. However, simplifying the matter, it can be seen as a set of electrical boundaries allowing equipment to function in its intended manner without significant loss of performance or decrease in life expectancy.

The subject of power quality is very broad by nature, covering all aspects of power system engineering, from generation, transmission and distribution to end-user problems. Of the three primary components of the electricity infrastructure, the distribution system is often the most critical part of a unified power system in terms of its effect on reliability, quality of service, cost of electricity, and impact on society.

From this perspective, electric power quality is a major concern of utilities, end users, and manufacturers. Suppliers are interested in the quality of their service; manufacturers have to build equipment that is compliant with power quality standards and regulations; and finally, customers have requirements that need fulfilment so that they feel secure in using electrically powered products.

The term power quality may often seem ambiguous, having different meanings for different people. As such, power quality can, at the same time, be a problem to be solved and a product, depending on a person's perspective. For power quality experts, power quality is obviously a problem that must be solved, while for a power marketer for instance, power quality is an important feature of a product named electrical power.

Problems related to power quality are often difficult to solve, and may have various solutions, so the choice is not always simple. The optimal

EBSCOhost - printed on 2/14/2023 2:46 PM via . All use subject to https://www.ebsco.com/terms-of-use

solution to a power quality problem usually involves a mix of solutions for each specific situation. The evaluation of solutions is certainly a key element in solving power quality problems, for both technical and economic reasons.

There are several factors driving an increased need to prevent and solve power quality problems:

- The increased use of power quality-sensitive equipment;
- The increased use of equipment that causes power quality problems;
- The increased interconnectedness of power systems;
- The deregulation of the power industry.

The increased use of power electronic components within distribution systems and a reliance on renewable energy sources, which use converters as the interface between the source and the power system, lead to power quality problems.

The problem of voltage quality is gaining increasing importance due to the widespread use of power electronics (increasing emitted interference) on the one hand, and the reduction in the signal levels of electronic equipment (increased interference susceptibility) on the other.

Electromagnetic interference causes degradation in the performance of equipment, the transmission channel, or the system through electromagnetic disturbance—any electromagnetic phenomenon which may degrade the performance of a device, equipment or system, or adversely affect living or inert matter.

The concept of electromagnetic interference is an important part of electromagnetic compatibility, defined as the ability of equipment or a system to satisfy three criteria:

- To cause no interference with other systems;
- To not be susceptible to emissions from other systems.
- To cause no interference with itself.

The lack of electromagnetic compatibility or a precarious solution of its issues may have several consequences, such as the unforeseeable and unreliable operation of equipment, and bring high risks for the ecosystem and/or human life.

In most electromagnetic compatibility issues, there is the “aggressor” of the electromagnetic environment and one or more “victims.” The aggressor conducts or radiates a sufficient amount of electromagnetic

EBSCOhost - printed on 2/14/2023 2:46 PM via . All use subject to https://www.ebsco.com/terms-of-use

energy, that it is able to interfere with equipment, representing a victim. On the other hand, the victim misoperates due to interference with the aggressor or due to the electromagnetic fields present in its environment.

Unfortunately, “victims” are not always completely innocent and that is why poor design of electromagnetic compatibility in equipment can make them sensitive to environmental electromagnetic fields and highly susceptible to electromagnetic noise.

In recent years, there has been a considerable increase in nonlinear loads. These draw harmonic currents, which have detrimental effects including communication interference; loss of reliability; increased operating costs; overheating of equipment; machine, transformer and capacitor failures; and inaccurate power metering.

A deficient quality of electrical power supplied to equipment results in the degradation of its performance; loss of productivity; damage to equipment, injury to personnel; and in some cases, loss of life. All that is needed to prevent such consequences is a clear understanding of electrical power quality and its effects on power system performance.

Based on the above, the participants of the conference suggest that the scientific community comprehensively cooperate to achieve the future goals of energy sustainability, the protection of our planet, and the assurance of a better quality of life for future generations.

EBSCOhost - printed on 2/14/2023 2:46 PM via . All use subject to https://www.ebsco.com/terms-of-use

EBSCOhost - printed on 2/14/2023 2:46 PM via . All use subject to https://www.ebsco.com/terms-of-use

# PART I:

# PHOTOVOLTAIC GENERATION

EBSCOhost - printed on 2/14/2023 2:46 PM via . All use subject to https://www.ebsco.com/terms-of-use

# CHAPTER ONE

# PV SYSTEM WAY OF THE FUTURE

ISAIAS GOMES[1,2,3] RUI MELICIO[1,2,3]
VICTOR MENDES[2,4,5]

## Abstract

This chapter synthesizes the research on solar resources, which are an important factor in ensuring a sustainable future through the photovoltaic conversion of solar energy into electric energy. Various aspects are presented including: irradiance and irradiation on the earth; current and emerging technology in photovoltaic systems; the hot-spot effect due to shade in photovoltaic systems; job creation potential; electronic power inverters; and issues concerning the integration of photovoltaic systems into the electric grid.

**Keywords**: PV technologies, sustainable future, hot-spot, job opportunities, distributed power generation, emerging technology.

## 1. Introduction

The vision of a sustainable future has been brought to the fore through environmental concern about anthropogenic greenhouse gas emissions and social demand for measures to further mitigate damage to the Earth's

[1] ICT, Universidade de Évora, Portugal.
[2] Departamento de Física, Escola de Ciências e Tecnologia, Universidade de Évora, Évora, Portugal.
[3] IDMEC, Instituto Superior Técnico, Universidade de Lisboa, Portugal.
[4] CISE, Electromechatronic Systems Research Centre, Universidade da Beira Interior, Portugal.
[5] Department of Electrical Engineering and Automation, Instituto Superior de Engenharia de Lisboa, Lisbon, Portugal.

EBSCOhost - printed on 2/14/2023 2:46 PM via . All use subject to https://www.ebsco.com/terms-of-use

habitats. Climate change debates and political action have led to the establishment of legislative packages aimed at promoting programs for a sustainable future. Programs for the mitigation of anthropogenic emissions have promoted incentives for the deployment of clean energy. For instance, in line with its sustainability policy, the EU developed a legislative framework on energy, which was launched in December 2008. This framework promotes renewable energy exploitation and energy efficiency measures through the Renewable Energy Directive (2009/28/EC), promoting measures to mitigate climate change. Directive 2009/28/EC promotes the use of renewable energy sources within the transport sector. A legally binding target was established of 20 % of total energy usage in the EU to be obtained from renewable sources. Among renewable energy sources, solar energy and wind energy are considered to be the most important ones for mitigating not just climate change, but also foreign dependence on energy imports [1]. Use of solar energy has the advantage of not requiring equipment with moving parts. Using the photovoltaic (PV) effect, direct conversion into electric energy is obtained without noise emissions into the environment.

A new setup for the energy power system brought about by the restructuring of the electricity market has appeared. This has brought about business changes both at the level of energy conversion, i.e., for producers, and at the level of electric energy usage, i.e., for consumers [2]. These changes are motivated by environmental concerns and electricity market restructuring and have been underpinned by developments and incentives for distributed power generation systems (PGSs). Developments and incentives for the integration of renewable energy have undergone a never-seen-before expansion in the exploitation of renewable energy. Consequently, an increase of mixed conversion being plugged into the energy power system has occurred [3]. Today, distributed PGSs are a reality in electricity markets with: solar energy exploitation by PV energy conversion; concentrator solar and integrated solar combined cycle systems; onshore and offshore wind energy exploitation; and advanced energy storage systems [4]. However, the structure of the electricity market imposes constraints of scale on the feasibility of bid submissions, for instance the requirement of at least power generation of 10 MW per bid in the regulating market of Nord Pool [4, 5]. As such, planned exploitation using systems of limited scale and power can only enter the market through a company acting as an intermediary and aggregating enough exploitation of power sources for a feasible bid submission. Such a company is said to be an aggregator and must have enough functionality to enable market business between the distributed energy resource

EBSCOhost - printed on 2/14/2023 2:46 PM via . All use subject to https://www.ebsco.com/terms-of-use

participants aggregated by this company and other market agents [4, 6]. The International Energy Agency (IEA), taking into consideration that solar energy is a cornerstone of the transition to sustainable energy systems, has launched the PVPS programme. This programme promotes enhancement of the international effort to facilitate the role of energy through a distributed PGS [7]. The underlying assumption of the programme is that the market for PV systems is rapidly expanding to a significant level of penetration in electricity markets in an increasing number of countries. This expansion is both in PV system connections with the electricity distribution grid and with the power transmission grid [7-10]. PV system market expansion requires good availability of reliable information on the performance and sustainability of PV systems; solar resources; technical and design guidelines; planning methods; and costs and financing, to be shared with the various actors. Particularly important to the future of PV feeding into electric grids is the development of: smart grid technology based on IoT [11-14]; PV inverter management strategies; solar energy forecasting; electrical energy storage; and the economic and technological impact on the whole energy system [7]. An increase in the reliability and the service lifetime of PV modules is also important: statistics show degradation rates of rated power for silicon and thin-film PV modules of the order of 0.8 % per year [15]. The prices of PV system components, which comprise power electronics, trackers, and structural and electrical components, have come down significantly with recent annual reductions in the range of 5 to 7 % [16]. New developments in PV business models are needed, as the decentralized character of photovoltaics shifts responsibility for energy conversion more into the hands of distributed PGSs owned by private entities, municipalities, cities, and regions [7, 17]. PV system expansion requires the manufacturers to improve the reliability of PV module technology and also the collection, analysis, and dissemination of information on technical performance and failure rates, providing a basis for data-based assessment and the development of practical recommendations for sizing purposes [7]. This chapter deals with issues regarding PV systems and is organized as follows: Section II—solar resources; Section III—PV systems technology; Section IV—failures typically occurring in PV modules; Section V—job creation potential; Section VI—supporting power electronic devices; Section VII—integration of PV systems into the electric grid. Finally, concluding remarks are presented in Section VIII.

EBSCOhost - printed on 2/14/2023 2:46 PM via . All use subject to https://www.ebsco.com/terms-of-use

## 2. Solar Resources

The Sun is at the middle of its lifetime and is estimated to become a red giant in about 5 giga years. Its energy emissions can considered to be like those of a black body with a so-called effective or emission temperature of 5,772 K from the solar atmosphere. From the core to the photosphere the temperature decreases from about 15 MK to 4,400 K; it then increases in the chromosphere from about 4,390 K to 50 kK, before decreasing again; it then increases in the corona, the aura of plasma surrounding the Sun, from about 0.8 kK to 3 MK. The transmission of energy from the Sun involves the radiation of photons with wavelengths of the spectral irradiance of the Sun. The power of radiation from nuclear fusion, where the proton-proton chain is the most important component, is about $3.86\times10^{20}$ MW, implying a loss of $4.2\times10^{3}$ Gg/s of mass. But at the Earth, as regards direct conversion of photons into electrical energy, only some photons are of a useful wavelength [18]. A photon must have a wavelength small enough to have at least energy not less than the energy equal to the difference between the highest level of energy of the valence and the lowest level of the conduction band, i.e., the band gap energy of a semiconductor substance. An electron-hole pair is created in the substance and this is called the PV effect. The average photon energy (APE) is independent of the spectral response of the PV technology and it is common to classify solar irradiance based on the relative distribution of energy over the spectrum [19]. Pre-availability studies to estimate the energy delivery at a site are required [20-23] and are based on solar availability, wind speed, temperature, and sensitivity [24, 25]. The studies require data at the site on: solar irradiance—kW/m$^2$ of Sun power; irradiation—kWh/(day m$^2$) equal to what is called Peak Sun Hours (PSH); and ambient temperature range. For instance, the PV geographical information system (PVGIS) in [26] presents average values of irradiance, irradiation, and temperature across the Earth as a function of latitude, longitude, and elevation of site. The long-term study in [27] offers average daily solar irradiation data, as shown in Fig. 1.

Fig. 1 shows that areas near the tropics have higher values for irradiation, despite the fact that near the equator daylight hours are always about 12 h/day—the irradiation is on average 4 to 5 kWh/kWp. With a change of about 0.2 % over the last four centuries, the average of the varying value of the irradiance at null air mass (AM 0), i.e., at the top of the Earth's atmosphere, is called the constant solar value and is about 1.361 kW/m$^2$. At sea level, due to atmospheric attenuation, the maximum irradiance is about 1.000 kW/m$^2$ in practice—this is known as the value of

EBSCOhost - printed on 2/14/2023 2:46 PM via . All use subject to https://www.ebsco.com/terms-of-use

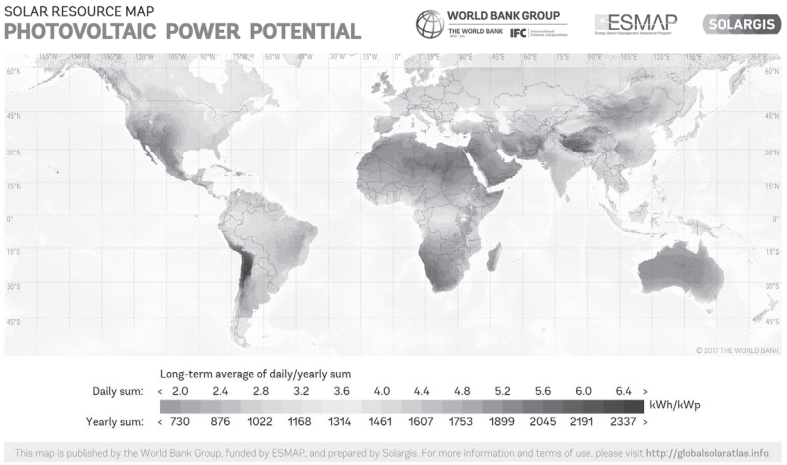



Figure 1. Solar irradiation per kWp of PV systems on the Earth [27].

irradiance at 1 Sun. The range of the temperature of a site must be identified because the higher the temperature, the lower the peak power measured in kWp in practice. Areas of the Earth having significant solar irradiation, but being deficient in other sources of energy can benefit from the exploitation of solar energy. This exploitation is significant not only as an option for capturing energy where other options are not available, but also as a source of clean energy for sustainable development. PV technology has been much enhanced through contemporary research and development. Improvements in the efficiency of PV systems and their ability to be easily included in urban areas are expected to increase. PV technology has the economic and technological potential to assist economic growth, contributing to mitigation of foreign energy dependence and energy-related environmental impacts. As such, PV technology is a technology of the future and has seen a significant decrease in price over the last decade. It is becoming an attractive option for governments, organisations, and individuals [28].

## 3. PV Technology

A PV system is based on the direct conversion of solar energy to electrical energy carried out in a PV cell. The conversion process is due to a p-n junction in a semiconductor substance and the name of the cell is typically given in association with the name of the semiconductor. Near

EBSCOhost - printed on 2/14/2023 2:46 PM via . All use subject to https://www.ebsco.com/terms-of-use

short-circuit conditions, cell behavior is almost like a dependent current source, significantly controlled by irradiance and less so by the temperature of the cell. Near open-circuit conditions, a cell's behavior is almost as a dependent voltage source, controlled by the temperature of the cell and less by irradiance. The power and output current of the cell is almost directly proportional to the irradiance. But the power declines with an increase in cell temperature. PV technology has undergone three generations: the first is conventional or wafer-based solar cells; the second is thin film-based; and the third is emerging technology [29-31]. The first generation is already mature technology and is based on: crystalline or monocrystalline silicon—c_Si or m_Si; polycrystalline or multicrystalline silicon—poly_Si or multi_Si; gallium arsenide—GaAs; or hybrid heterojunction with intrinsic thin layer technology [29-31]. C_Si cells have higher efficiencies, of about 5 % more than poly_Si, but production costs are higher. Poly_Si cells remain the dominant technology in the market with an almost 56 % share compared to 36 % for c_Si [29, 31]. Hybrid heterojunction cells with intrinsic thin layer technology are competitively priced in comparison to c_Si and poly_Si cells. They also have increased power conversion efficiency of up to 26.6 %, the highest among all silicon-based technology, and with potential for further improvement [31, 32]. Another c_Si cell type uses bifacial technology. This technology uses a cell that allows light to enter from both the front and back faces of the cell to convert the albedo, i.e., earth-reflected radiation, into electric energy [31]. Some studies favor the albedo on the back side of the module as advantageous [31, 33-35]. The second generation includes thin film technology based on amorphous silicon—a_Si; and PV cells from cadmium-tellurium and copper-indium-gallium-selenide. Thin film technology was developed to lower costs, but it has lower efficiency, by about 10 %, and suffers from light-induced degradation. As such, it has been widely used in stand-alone PV systems with cadmium-tellurium or copper-indium-gallium-selenide cells [29, 31]. Amorphous silicon (a_Si) technology is usually cheaper than cadmium-tellurium or copper-indium-gallium-selenide technology, while heterojunction with intrinsic thin layer cells are usually more expensive than standard crystalline silicon cells [31]. The third generation cells are based on novel advanced semiconductor technology, include multi-layer (tandem) cells made of amorphous silicon or gallium arsenide. Dye-sensitized, perovskite, organic and quantum dot cells are all currently under research and development [30]. An accessory feature to PV technology is encapsulation, which adds greater protection to the cell in order to ensure a longer lifetime and reliable performance [30, 31]. Encapsulation consists of the isolation of active layers from

EBSCOhost - printed on 2/14/2023 2:46 PM via . All use subject to https://www.ebsco.com/terms-of-use

atmospheric conditions, including humidity and contamination. The most common form of encapsulation uses ethylene-vinyl acetate (EVA)—a high cost but durable material [30, 31]. Coatings have also been developed to help reduce losses mainly due to the reflection of irradiance, soiling, and UV degradation. The development of coatings has followed the requirements of low cost, uniform properties, convenience, and long-term reliability [31].

## 4. PV Module Failures

Solar cells are grouped in series to form a module and modules are grouped in series or parallel to form an array. A large PV system is a set of modules connected in series or parallel with or without a tracking system. The tracking system has an angular position control that aligns the collecting plane of the PV system to the Sun's irradiance over the course of a sunny day. This setting achieves the highest level of irradiation over the plane, but even with tracking, correct consideration of the space for the PV system must be assessed to avoid the effect of shade. The performance of a PV system does not just depend on solar irradiance and cell temperature, but also on the type of connection and shading effect. The shading effect is prone to lead to a reduction in the electrical power and augmented physical degradation of the cells. The shading effect due to a passing cloud or neighbouring buildings is a cause not only for hot-spots, but also for a non-concave P-V curve [36-38]. A hot-spot on a shaded cell is prone to cause permanent damage, reducing the output power of the PV system [39]. Shadows frequently occur reducing the photo-generated electric current in the shaded area of the PV system. As this does not occur in all modules of the PV system, there is a tendency for reverse bias in modules with lower irradiance and second quadrant operation [40]. Hot-spots due to shadow are called transitory, as we expect the shadow to disappear after a while, however, in that time permanent damage can occur. Hot-spots can also occur due to internal defects in a module (IEC, 1995). Hot-spots due to internal defects are considered permanent [41]. I-V curves are strongly dependent on the irradiance and a series connection of modules is strongly affected by non-homogenous shading of PV systems, as shown in Fig. 2.

I-V curves are shown in Fig. 2 for a module at a cell temperature of 25 ºC and AM 1.5: the first quadrant behaviour at STC, i.e., having an irradiance of 1 Sun, is shown in black, as is the reflection over the I-axis of the first quadrant I-V curve graphically presenting the condition of short circuit in series connections with modules having an irradiance different to

EBSCOhost - printed on 2/14/2023 2:46 PM via . All use subject to https://www.ebsco.com/terms-of-use

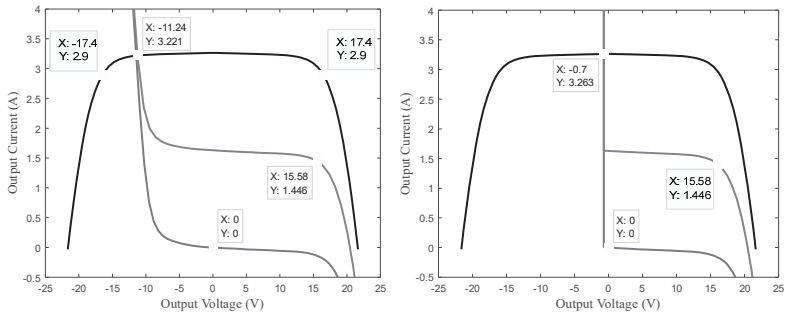



Figure 2. I-V curves at STC in black; half dark in red; fully dark in blue: a) without a bypass diode; b) with a bypass diode [38].

1 Sun; behaviour when subjected to an irradiance of 0.5 Sun, i.e., half dark in relative terms, is shown in red; behaviour at an irradiance of 0 Sun, i.e., fully dark, is shown in blue. The maximum power point (MPP) at the STC is a voltage of 17.4 V, with a current of 2.9 A and a breakdown voltage of about -10 V. The MPP at half dark is at a voltage of 15.68 V and a current of 1.446 A. So, the current and the power of the half dark module is almost half what is expected. A series connection without bypass diodes is prone to damage, as shown in the case of one module at STC conditions and the other at half or fully dark in Fig. 2 a): the short circuit condition of the series implies that the module in STC is at 11.24 V while the other module is at -11.24 V and both are at 3.221 A; the value of 3.221 A is not far-off the maximum current of the module, i.e., the short circuit current in STC, due to the fact that the I-V curve is significantly flat between 0 and 11.24 V and in view of the normal low value associated with the leakage current; the module in STC is capturing 11.24×3.221 W, i.e., first quadrant operation; the other module dissipates this power at 11.24×3.221 W, i.e., in second quadrant operation, and consequently getting hotter. This operation reaching a breakdown voltage in the module with lower irradiance is a worst case scenario where a maximum value of power to be dissipated in the module is imposed. As such, in the module with less irradiance, more internal damage is expected in a relatively short time. Considering the series with a fully dark module, while the open circuit condition overlaps the short circuit condition in this module, the module in STC is in open circuit conditions. The fully dark module is always operating in the second quadrant, while the module in STC is operating in the first quadrant. Considering the series with a half dark module, it is

EBSCOhost - printed on 2/14/2023 2:46 PM via . All use subject to https://www.ebsco.com/terms-of-use

operating between short circuit and open circuit conditions and both modules are operating in the first quadrant. Outside of that range, while the module in STC is operating in the first quadrant the half dark one is dissipating power, getting hotter, and prone to being damaged as its voltage reaches the breakdown voltage. Second quadrant operation, i.e., operation with a negative voltage, must be avoided. This is possible using a bypass diode, which starts to conduct if the voltage has a negative value: the bypass diode is in forward bias when the PV module is in reverse bias. In Fig. 2 b) the consequences of the use of a bypass diode with a built-in potential value of 0.7 V on the half dark and the fully dark I-V curves are shown. The short circuit condition of the series implies that the module in STC is at 0.7 V and 3.263 A, just a little less than the short circuit current in STC, while the other one is at -0.7 V and at a little higher current than the short-circuit current. In practice, this is equivalent to saying that the breakdown voltage is -0.7 V. The module in STC is capturing 0.7×3.263 W and the other module does not dissipate all this power. This power is slightly higher than the 0.7 V times the respective short-circuit current, which is at almost null value for the fully dark module due to the fact it has a null short-circuit current. Consequently, the half and the fully dark modules are getting hotter, but at a much slower rate, than is the case without a bypass diode, and no damage is to be expected.

The impact of hot-spots on the operational efficiency and lifetime of PV systems has been scarcely addressed. Accordingly, in the literature there is a lack of test procedures for dealing with hot-spots, as well as a lack of specific criteria referring to the acceptance or rejection of affected PV modules [41]. In terms of test procedures for dealing with hot-spots, a hot-spot resistance test is specified in IEC-61215 and in UL 1703 for crystalline silicon PV modules and in IEC-61646 for thin-film PV modules. The TÜV Rheinland Energie und Umwelt GmbH consider IEC-61215 and IEC-61646 reports about the hot spot endurance test to be one of the most critical tests [7].

Also, there are other causes that can lead to hot-spots or shading, for instance: glass breakage leading to overheating of a module; a defective bypass diode caused by a lightning strike can lead to an open-circuit bypass diode; mechanical breakage of a PV module; a junction box failure due to poor fixing; a junction box that has been opened or badly closed, leading to moisture ingress; or bad wiring [7]. The hot-spot operational behaviour of crystalline and thin-film silicon PV technology under shading is different. This is due the fact that for thin-film modules preventive measures using bypass diodes may not be possible for limiting the reverse voltage in affected cells [7].

EBSCOhost - printed on 2/14/2023 2:46 PM via . All use subject to https://www.ebsco.com/terms-of-use

## 5. Job Opportunities

Although this chapter is mainly focused on PV technology, job creation should also be taken into consideration in studying renewable technology. This is an aspect impacting labour and influencing social behaviour relating to the deployment of renewable technology—not just impacting already existing employment, but also in terms of new employment opportunities. New employment opportunities are reported as leading to significant job creation [42, 43]. The employment impacts include the types of jobs needed to give necessary support, either in the design and installation phase or in the maintenance phase to owners of PV systems. Types of jobs can be divided into direct, indirect and induced jobs. The International Renewable Energy Agency (IRENA) provides a clear and operational definition of these terms, as well as elaborating on the slight but important variations in their interpretation across studies [42]. Direct jobs, in general, are jobs related to manufacturing, construction, site development, installation, and operation and maintenance (O&M). These direct jobs are relatively easy to measure. The number of direct jobs is correlated to the rate of growth and penetration of renewable technology and the impact of direct renewable energy jobs has been reported [42, 44]. Indirect jobs are related to the supply and support of the renewable energy industry at a secondary level. Only a small fraction of available studies report explicitly on the impact of indirect jobs, concluding that effects can be expected or explicitly estimating these effects using multipliers [42, 44]. Induced jobs arise from the economic activities of direct and indirect employees, shareholders, and governments, eventually via tax on revenues from renewable technology deployment. There are few studies about the impact of induced jobs, as reported in [42, 44]. Only some studies about employment opportunities and job creation potential with fundamentally high levels of training have been performed for specific forms of exploitation of specific renewable technologies [44]. There are few studies concerning developing or emerging economies and there are reports stating that the median PV technology employment is more than two times the median value for concentrator solar technology [43, 44]. Employment intensity is expected to reduce as the technology and production techniques mature. This maturation occurs due to the growing experience and workload of the renewable energy industry, i.e., the development of economies-of-scale and learning-by-doing [44]. There are already data on O&M employment needs in the German renewable energy industry showing that employment intensity is decreasing over time. More specifically, in Germany there has been a clear decrease in O&M employment intensity

EBSCOhost - printed on 2/14/2023 2:46 PM via . All use subject to https://www.ebsco.com/terms-of-use

due to 5 %/yr and 8 %/yr average annual improvements for wind and PV from 2007 to 2011 [44]. Few studies attempt to quantify reductions in employment intensity over time resulting from scaling and learning effects. In [45], an annual decrease of 10 %/yr in the construction employment rate and 5 %/yr in the O&M employment rate are shown.

## 6. Power Electronic Converters

Power electronic converters were developed to support the integration of renewable energy sources into the electric grid [46-51]. Insulated-gate bipolar transistor (IGBTs) are the most commonly used power electronic converter devices, due to having a simple gate driver, low driving power, low switching loss, low saturation voltage, and high block voltage [52-55]. However, high manufacturing costs, high on-state voltage, and low reliability significantly reduce the appeal of IGBTs. The integrated gate-commutated thyristor (IGCT) device is currently eliciting much attention in the power electronics field, due to its lower on-state voltage, higher reliability, and lower manufacturing costs in comparison to the IGBT [55, 56]. The use of power electronic converters, namely inverters with maximum power point tracking (MPPT), are indispensable to PV systems, allowing operation at variable irradiance and enhanced power extraction. The inverter is indispensable for two reasons: to adjust the low DC voltage of the PV module to the voltage level of the electric grid using a DC-DC topology and a DC-AC topology; and to comply with the functionality of MPPT to circumvent the fact that the power delivered by the modules is very sensitive to the point of operation in the I-V curve [46, 57, 58]. Historically, low-power PV systems used single-phase inverters, but in three-phase grid connection, the use of only a single-phase inverter produces an imbalance between the phases due the injection of energy into only one phase of the grid. As reported in [46, 59], with a maximum power of 4.6 kW and a 10 % tolerance, it is possible to connect to only one phase of a three-phase grid. For power greater than 5 kW, three single-phase inverters are needed to ensure balanced energy distribution between the three phases. The inverters used in grid-connected PV systems use several circuits and there are a several options for transformer configuration. There are commercial inverters with high or low frequency transformers and even transformerless inverters. Each topology has specific characteristics and advantages and disadvantages [46, 57, 59-61]. The inverters used in grid-connected applications have functionality for MPPT, anti-islanding operation, high conversion efficiency, automatic synchronization with the grid, a low level of harmonic distortion, and a

EBSCOhost - printed on 2/14/2023 2:46 PM via . All use subject to https://www.ebsco.com/terms-of-use

power factor close to the unity value [59-63]. The performance of inverters connected to the grid depends largely on the control strategy applied [59, 64, 65].

## 7. Integration into the Electric Grid

PV power systems are best recommended for distributed PGSs. For instance, PV power systems are considered appropriate for the operation of residential appliances with or without the use of a storage battery [66, 67]. Energy storage has been highlighted as the key to larger integration of wind and PV power systems. A report by the National Renewable Energy Laboratory states that the challenges associated with meeting variation in demand while providing reliable service has motivated historical development of energy storage and that large penetration of variable generation increases the need for flexibility [68]. The integration of large scale renewable energy sources without sufficient energy storage will be a challenge for future power systems [69]. A study regarding intermittent renewable power production from wind and PV power in Europe states that significant backup generation is required to cover power demand at all times, even if wind and PV covers, on average, 100 % of the demand. Without grid connection, for example, an autonomous power system needs storage backup generation of 40 % of demand; even with an ideal grid storage backup of 20 % is needed [67, 70]. Storage technology may play a vital role in improving the overall stability and reliability of power systems and could reduce the costs of improving transmission and distribution capacity to meet the ever-growing power demand. Storage technology may also play an important role in the activity of deregulated markets, like providing arbitrage, increasing the value of renewable power in such markets [71]. In a grid-connected PV power plant, the use of an energy storage device can truly enable the power system to fully meet power demand and increase the reliability of the power system [72]. Vanadium redox flow batteries are viewed as one of the most promising storage technologies for application at power plants to compensate for fluctuations in wind and photovoltaic power generation [17, 67].

## 8. Conclusions

Despite the intermittency and volatility of solar and wind energy sources, these sources are the most important ones in mitigating climate change and dependence on energy imports. The exploitation of solar energy by PV systems has the advantage over wind energy of not needing

EBSCOhost - printed on 2/14/2023 2:46 PM via . All use subject to https://www.ebsco.com/terms-of-use

moving parts and direct conversion into electric energy. This conversion can be easily integrated into urban environments and is recommended for distributed PGSs. A literature review on PV energy conversion and market penetration shows significant progress in the technology, leading to significant decreases in the price of PV systems and, consequently, greater deployment over the last decade. Many studies have been done on issues concerned with PV systems and in the future there is expected to be even more penetration of PV technology, which is acquiring a prominent presence in the power system generation mix. Issues remain, for instance, high capacity energy storage is needed to allow PV systems to be dispatchable. A dispatchable PV system must be able to supply stored energy in an acceptable time to avoid the excessive use of expensive reserve thermal units to circumvent the intermittency and volatility of solar energy. The vanadium redox flow battery is currently viewed as one of the most promising storage technologies, allowing high capacity energy storage for application in photovoltaic power plants and compensating for fluctuations in solar energy generation. Research is also needed into preserving an acceptable margin of stability for the electrical grid. There are still many research gaps in emerging solar cell technology that need to be addressed so that this new technology can be commercialized, contributing to a decrease in prices, and encouraging PV system adoption. Historic weather data and forecasting at potential PV generation sites is also important for the purposes of design and for successful integration of PV systems.

## Acknowledgment

This work is funded by Bolsas Camões, IP / Millennium BCP Foundation and funded by: European Union through the European Regional Development Fund, included in the COMPETE 2020 (Operational Program Competitiveness and Internationalization) through the ICT project UID/GEO/04683/2019 with the reference POCI010145FEDER 007690; Portuguese Funds through the Foundation for Science and Technology-FCT under the project LAETA 2015-2020, reference UID/EMS/50022/2019; Portuguese Foundation for Science and Technology (FCT) under Project UID/EMS/00151/2019.

EBSCOhost - printed on 2/14/2023 2:46 PM via . All use subject to https://www.ebsco.com/terms-of-use

# References

[1] C. P. Castillo, F. B. Silva, C. Lavalle, “An assessment of the regional potential for solar power generation in EU-28,” Energy Policy, vol. 88, pp. 86-99, 2016.

[2] F. Cucchiella, I. D’Adamo, “Issue on supply chain of renewable energy,” Energy Conversion and Management, vol. 76, pp. 774-780, 2013.

[3] Y.-H. Liu, J.-H. Chen, J.-W. Huang, “Global maximum power point tracking algorithm for PV systems operating under partially shaded conditions using the segmentation search method,” Solar Energy, vol. 103, pp. 350-363, 2014.

[4] I. L. R. Gomes, R. Melicio, V. M. F. Mendes, H. M. I. Pousinho, “Decision making for sustainable aggregation of clean energy in day-ahead market: uncertainty and risk,” Renewable Energy, vol. 133, pp. 692-702, 2019.

[5] Q. Wang, C. Zhang, Y. Ding, G. Xydis, J. Wang, J. Ostergaard, “Review of real-time electricity markets for integrating distributed energy resources and demand response,” Applied Energy, vol. 138, pp. 695-706, 2015.

[6] J. Ikäheimo, C. Evens, S. Kärkkäinen, “Der aggregator business: the finnish case,” http://www.ece.hut.fi/enete/DER_Aggregator_Business_Finnish_Case.pdf, 2010.

[7] M. Köntges, S. Kurtz, C. Packard, K. Jahn, K. Kato, T. Friesen, H. Liu, M. V. Isenghem, “Performance and reliability of photovoltaic systems; Subtask 3.2: review of failures of photovoltaic modules,” IEA International Energy Agency, Report: IEA-PVPS T13-01:2014, 2014.

[8] S. Saraiva, R. Melicio, J. C. O. Matias, J. P. S. Catalão, C. Cabrita, “Modelling, iterative procedure and simulation results for a monocrystalline solar cell,” Renewable Energy and Power Quality Journal, vol. 1(10), pp. 541-544, 2012.

[9] S. Saraiva, R. Melicio, J. C. O. Matias, J. P. S. Catalão, C. Cabrita, “Simulation and experimental results for a photovoltaic system formed by monocrystalline solar modules,” in: Technological Innovation for Value Creation, pp. 329-336, Springer, Heidelberg, Germany, 2012.

[10] S. Saraiva, R. Melicio, J. C. O. Matias, J. P. S. Catalão, C. Cabrita, “Simulation and experimental results for a photovoltaic system formed by polycrystalline solar modules,” in: 16th IEEE Mediterranean Electrotechnical Conference, pp. 806-809, Medina Yasmine Hammamet, June 2012.

[11] I. L. R. Gomes, H. M. I. Pousinho, R. Melicio, V.M.F. Mendes, “Bidding and optimization strategies for wind-PV systems in electricity markets assisted by CPS,” Energy Procedia, vol. 106, pp. 111-121, 2016.

[12] N. C. Batista, R. Melicio, J. C. O. Matias, J. P. S. Catalão, “Photovoltaic and wind energy systems monitoring and building energy management using ZigBee devices within a smart grid,” Energy, vol. 49(1), pp. 306-315, 2013.

[13] N. C. Batista, R. Melicio, J. C. O Matias, J. P. S. Catalão, “ZigBee standard in the creation of wireless networks for advanced metering infrastructures,”

EBSCOhost - printed on 2/14/2023 2:46 PM via . All use subject to https://www.ebsco.com/terms-of-use

in: 16th IEEE Mediterranean Electrotechnical Conference, pp. 220-223, Medina Yasmine Hammamet, June 2012.
[14] N. C. Batista, R. Melicio, V. M. F. Mendes, "Services enabler architecture for smart grid and smart living services providers under industry 4.0," Energy and Buildings, vol. 141, pp. 16-27, 2017.
[15] D. C. Jordan, S. R. Kurtz, "Photovoltaic degradation rates-an analytical review," Progress in Photovoltaics: Research and Applications, vol. 21, pp. 12-29, 2013.
[16] S. Comello, S. Reichelstein, A. Sahoo, "The road ahead for solar PV power," Renewable and Sustainable Energy Reviews, vol. 92, pp. 744-756, 2018.
[17] B. N. Arribas, R. Melicio, J. G. Teixeira, V. M. F. Mendes, "Vanadium redox flow battery storage system linked to the electric grid," Renewable Energy and Power Quality Journal, vol. 1(14), pp. 1025-1030, 2016.
[18] E. M. G. Rodrigues, R. Melicio, V. M. F Mendes, J. P. S. Catalão, "Simulation of a solar cell considering single-diode equivalent circuit model," Renewable Energy and Power Quality Journal, vol. 1(9), pp. 369-373, 2011.
[19] M. Norton, A. M. Gracia Amillo, R. Galleano, "Comparison of solar spectral irradiance measurements using the average photon energy parameter," Solar Energy, vol. 120, pp. 337-344, 2015.
[20] L. A. P. Fialho, R. Melicio, V. M. F. Mendes, "PV system modeling by five parameters and in situ test," in: International Symposium on Power Electronics, Electrical Drives and Motion, pp. 573-578, Ischia, Italy, June 2014.
[21] H. X. Yang, L. Lu, J. Burnett, "Weather data and probability analysis of hybrid photovoltaic-wind power generation systems in Hong Kong," Renewable Energy, vol. 28(11), pp. 1813-1824, 2003.
[22] P. Nema, R. K. Nema, S. Rangnekar, "A current and future state of art development of hybrid energy system using wind and PV-solar: a review," Renewable and Sustainable Energy Reviews, vol. 13, pp. 2096-2103, 2009.
[23] E. F. M. Abreu, P. Canhoto, V. Prior, R. Melicio, "Solar resource assessment through long-term statistical analysis and typical data generation with different time resolutions using GHI measurements," Renewable Energy, vol. 127, pp. 398-411, 2018.
[24] M. R. Rashel, J. Rifath, T. C. F. Gonçalves, M. Tlemçani, R. Melicio, "Sensitivity analysis through error function of crystalline-Si photovoltaic cell model integrated in a smart grid," International Journal of Renewable Energy Research, vol. 7(4), pp. 1926-1933, 2017.
[25] M. R. Rashel, Md Tofael Ahmed, T. C. F. Gonçalves, M. Tlemçani, R. Melicio, "Analysis of environmental parameters sensitivity to improve modelling of a c-Si panel," Sensor Letters, vol. 16(3), pp. 176-181, 2018.
[26] PVGIS, https://ec.europa.eu/jrc/en/scientific-tool/pvgis, accessed 2018.
[27] Solargis, https://solargis.com/maps-and-gis-data/download/world, 2018.
[28] A. Ouammi, D. Zejli, H. Dagdougui, R. Benchrifa, "Artificial neural network analysis of Moroccan solar potential," Renewable and Sustainable Energy Reviews, vol. 16, pp. 4876-4889, 2012.

EBSCOhost - printed on 2/14/2023 2:46 PM via . All use subject to https://www.ebsco.com/terms-of-use

[29] J. Ramanujam, A. Verma, B. González-Díaz, R. Guerrero-Lemus, C. del Cañizo, E. García-Tabarés, I. Rey-Stolle, F. Granek, L. Korte, M. Tucci, J. Rath, U. P. Singh, T. Todorov, O. Gunawan, S. Rubio, J. L. Plaza, E. Diéguez, B. Hoffmann, S. Christiansen, G. E. Cirlin, "Inorganic photovoltaics-planar and nanostructured devices," Progress in Materials Science, vol. 82, pp. 294-404, 2016.

[30] C. S. Lai, Y. Jia, L. L. Lai, Z. Xu, M. D. McCulloch, K. P. Wong, "A comprehensive review on large-scale photovoltaic system with applications of electrical energy storage," Renewable and Sustainable Energy Reviews, vol. 78, pp. 439-451, 2017.

[31] A. Zurita, A. Castillejo-Cuberos, M. García, C. Mata-Torres, Y. Simsek, R. García, F. Antonanzas-Torres, R. A. Escobar, "State of the art and future prospects for solar PV development in Chile," Renewable and Sustainable Energy Reviews, vol. 92, pp. 701-727, 2018.

[32] K. Yoshikawa, W. Yoshida, T. Irie, H. Kawasaki, K. Konishi, H. Ishibashi, T. Asatani, D. Adachi, M. Kanematsu, H. Uzu, K. Yamamoto, "Exceeding conversion efficiency of 26% by heterojunction interdigitated back contact solar cell with thin film Si technology," Solar Energy Materials and Solar Cells, vol. 173, pp. 37-42, 2017.

[33] R. Guerrero-Lemus, R. Vega, T. Kim, A. Kimm, L. E. Shephard, "Bifacial solar photovoltaics-a technology review," Renewable and Sustainable Energy Reviews, vol. 60, pp. 1533-1549, 2016.

[34] U. A. Yusufoglu, T.M. Pletzer, L. J. Koduvelikulathu, C. Comparotto, R. Kopecek, H. Kurz, "Analysis of the annual performance of bifacial modules and optimization methods," IEEE Journal of Photovoltaics, vol. 5, pp. 320-328, 2015.

[35] S. Obara, D. Konno, Y. Utsugi, J. Morel, "Analysis of output power and capacity reduction in electrical storage facilities by peak shift control of PV system with bifacial modules," Applied Energy, vol. 128, pp. 35-48, 2015.

[36] D. Giaffreda, M. Omaña, D. Rossi, C. Metra, "Model for thermal behavior of shaded photovoltaic cells under hot-spot condition," in: IEEE International Symposium on Defect and Fault Tolerance in VLSI and Nanotechnology Systems, pp. 252-258, Vancouver, Canada, Oct. 2011.

[37] L. A. P. Fialho, R. Melicio, V. M. F. Mendes, J. G. M. Figueiredo, M. I. C. Pereira, "Effect of shading on series solar modules: simulation and experimental results," Procedia Technology, vol. 17, pp. 295-302, 2014.

[38] R. S. Anjos, R. Melicio, V. M. F. Mendes, H. M. I. Pousinho, "Crystalline silicon pv module under effect of shading simulation of the hot-spot condition," in: Technological Innovation for Smart Systems, pp. 479-487, Springer, Cham, Switzerland, 2017.

[39] D. Rossi, M. Omaña, D. Giaffreda, C. Metra, "Modeling and detection of hotspot in shaded photovoltaic cells," IEEE Transactions on Very Large Scale Integration (VLSI) Systems, vol. 23(6), pp. 1031-1039, 2015.

[40] S. Daliento, F. Di Napoli, P. Guerriero, V. d'Alessandro, "A modified bypass circuit for improved hot spot reliability of solar panels subject to partial shading," Solar Energy, vol. 134, pp. 211-218, 2016.

EBSCOhost - printed on 2/14/2023 2:46 PM via . All use subject to https://www.ebsco.com/terms-of-use

[41] R. Moretón, E. Lorenzo, L. Narvarte, “Experimental observations on hot-spots and derived acceptance/rejection criteria,” Solar Energy, vol. 118, pp. 28-40, 2015.
[42] IRENA. Renewable energy and jobs. Abu Dhabi: International Renewable Energy Agency; 2013.
[43] L. Cameron, B. van der Zwaan, “Employment factors for wind and solar energy technologies: a literature review,” Renewable and Sustainable Energy Reviews, vol. 45, pp. 160-172, 2015.
[44] E. L. Sastresa, A. A. Uson, I. Z. Bribian, S. Scarpellini, “Local impact of renewables on employment: assessment methodology and case study,” Renewable and Sustainable Energy Reviews, vol. 14, pp. 679-690, 2010.
[45] B. Heavner, S. Churchill, “Renewables work: job growth from renewable energy development in California,” in: CALPIRG Charitable Trust, Sacramento, USA, June 2002.
[46] L. A. P. Fialho, R. Melicio, V. M. F. Mendes, S. Viana, C. Rodrigues, A. Estanqueiro, “A simulation of integrated photovoltaic conversion into electric grid,” Solar Energy, vol. 110, pp. 578-594, 2014.
[47] L. A. P. Fialho, R. Melicio, V. M. F. Mendes, A. Estanqueiro, “Simulation of a-Si PV system grid connected by boost and inverter,” International Journal of Renewable Energy Research, vol. 5(2), pp. 443-451, 2015.
[48] L. A. P. Fialho, R. Melício, V. M. F. Mendes, L. Rodrigues, S. Viana, A. Estanqueiro, “Simulation of a-Si PV system linked to the grid by DC-DC boost and two-level converter,” in: 16th International Power Electronics and Motion Control Conference and Exposition, pp. 934-938, Antalya, Turkey, September 2014.
[49] L. A. P. Fialho, R. Melicio, V. M. F. Mendes, A. Estanqueiro, M.I.C. Pereira, “PV systems linked to the grid: parameter identification with a heuristic procedure,” Sustainable Energy Technologies and Assessments, vol. 10, pp. 29-31, 2015.
[50] L. A. P. Fialho, R. Melicio, V. M. F. Mendes, M. I. C. Pereira, “Simulation of a-Si PV system linked to the grid by DC boost and three-level inverter under cloud scope,” in: Technological Innovation for Cloud-based Engineering Systems, vol. IFIP AICT 450, Springer, Heidelberg, Germany, pp. 423-430, 2015.
[51] L. A. P. Fialho, R. Melício, V. M. F. Mendes, “Poly-Si PV system grid connected and fuzzy controlled,” in: 16th IEEE International Conference on Computer as a Tool, pp. 1-6, Salamanca, Spain, September 2015.
[52] O. S. Senturk, L. Helle, S. M. Nielsen, P. Rodriguez, R. Teodorescu, “Power capability investigation based on electrothermal models of press-pack IGBT three-level NPC and ANPC VSCs for multimegawatt wind turbines,” IEEE Trans. Power Electron., vol. 27(7), pp. 3195-3206, 2012.
[53] B. Zhao, Q. Song, W. Liu, “Experimental comparison of isolated bidirectional dc–dc converters based on all-Si and all-SiC power devices for next-generation power conversion application,” IEEE Trans. Ind. Electron., vol. 61(3), pp. 1389-1393, 2014.

EBSCOhost - printed on 2/14/2023 2:46 PM via . All use subject to https://www.ebsco.com/terms-of-use

[54] T. Luth, M. M. C. Merlin, T. C. Green, F. Hassan, C. D. Barker, “High-frequency operation of a dc/ac/dc system for HVdc applications,” IEEE Trans. Power Electron., vol. 29(8), pp. 4107-4115, 2014.
[55] B. Zhao, R. Zeng, Z. Yu, Q. Song, Y. Huang, Z. Chen, T. Wei, “A more prospective look at IGCT: uncovering a promising choice for dc grids,” IEEE Industrial Electronics Magazine, vol. 12(3), pp. 6-18, 2018.
[56] U. R. Vemulapati, E. Bianda, D. Torresin, M. Arnold, F. Agostini, “A method to extract the accurate junction temperature of an IGCT during conduction using gate-cathode voltage,” IEEE Trans. Power Electron., vol. 21(8), pp. 5900-5905, 2016.
[57] S. B. Kjaer, J. K. Pedersen, F. Blaabjerg, “A review of single-phase grid-connected inverters for photovoltaic modules,” IEEE Transactions Industry Applications, vol. 41, pp. 1292-1306, 2005.
[58] M. H. Moradi, S. M. R. Tousi, M. Nemati, N. S. Basir, N. Shalavi, “A robust hybrid method for maximum power point tracking in photovoltaic systems,” Solar Energy, vol. 94, pp. 266-276, 2013.
[59] G. A. Rampinelli, A. Krenzinger, F. Chenlo Romero, “Mathematical models for efficiency of inverters used in grid connected photovoltaic systems,” Renewable and Sustainable Energy Reviews, vol. 34, pp. 578-587, 2014.
[60] I. Patrao, E. Figueres, F. González-Espín, G. Garcerá, “Transformerless topologies for grid-connected single-phase photovoltaic inverters,” Renewable and Sustainable Energy Reviews, vol. 15, pp. 3423-3431, 2011.
[61] T. Khatib, A. Mohamed, K. Sopian, “A review of photovoltaic systems size optimization techniques,” Renewable and Sustainable Energy Reviews, vol. 22, pp. 454-465, 2013.
[62] D. Velasco, C. L. Trujillo, G. Garcerá, E. Figueres, “Review of anti-islanding techniques in distributed generators,” Renewable and Sustainable Energy Reviews, vol. 14, pp. 1608-1614, 2010.
[63] D. Velasco, C. L. Trujillo, G. Garcerá, E. Figueres, “Review of anti-islanding techniques in distributed generators,” Renewable and Sustainable Energy Reviews, vol. 14, pp. 1608-1614, 2010.
[64] Z. Zeng, H. Yang, R. Zao, C. Cheng, “Topologies and control strategies of multi-functional grid-connected inverters for power quality enhancement: a comprehensive review,” Renewable and Sustainable Energy Reviews, vol. 24, pp. 223-270, 2013.
[65] L. Hassaine, E. Olias, J. Quintero, V. Salas, “Overview of power inverter topologies and control structures for grid connected photovoltaic systems,” Renewable and Sustainable Energy Reviews, vol. 30, pp. 796-807, 2014.
[66] M. M. H. Bhuiyan, M. A. Asgar, “Sizing of a stand-alone photovoltaic power system at Dhaka,” Renewable Energy, vol. 28(6), pp. 929-938, 2003.
[67] I. L. R. Gomes, H. M. I. Pousinho, R. Melicio, V. M. F. Mendes, “Stochastic coordination of joint wind and photovoltaic systems with energy storage in day-ahead market,” Energy, vol. 124, pp. 310-320, 2017.
[68] P. Denholm, E. Ela, B. Kirby, M. Milligan, “The role of energy storage with renewable electricity generation,” National Renewable Energy Laboratory, Colorado, USA, 2010.

EBSCOhost - printed on 2/14/2023 2:46 PM via . All use subject to https://www.ebsco.com/terms-of-use

[69] M. Beaudin, H. Zareipour, A. Schellenberglabe, W. Rosehart, “Energy storage for mitigating the variability of renewable electricity sources: an updated review,” Energy for Sustainable Development, vol. 14(4), pp. 302-314, 2010.
[70] F. Steinke, P. Wolfrum, C. Hoffmann, “Grid vs. storage in a 100% renewable Europe,” Renewable Energy, vol. 50, pp. 826-832, 2013.
[71] K.C. Divya, J. Østergaard, “Battery energy storage technology for power systems: an overview,” Electric Power Systems Research, vol. 79(4), pp. 511-520, 2009.
[72] M. Zebarjadi, A. Askarzadeh, “Optimization of a reliable grid-connected PV-based power plant with/without energy storage system by a heuristic approach,” Solar Energy, vol. 125, pp. 12-21, 2016.

EBSCOhost - printed on 2/14/2023 2:46 PM via . All use subject to https://www.ebsco.com/terms-of-use

# CHAPTER TWO

# SEGMENTATION OF 3D POINT CLOUD DATA FOR ASSESSMENT AND RANKING OF PHOTOVOLTAIC POTENTIAL

NIKO LUKAČ[1], BORUT ŽALIK[2], GORAZD ŠTUMBERGER[3]

## Abstract

This chapter deals with segmentation of 3D point cloud data in order to estimate segmented rooftop photovoltaic (PV) potential. Point cloud data are pre-processed in order to extract the geometric details of buildings together with topographic information. A state-of-the-art shadowing algorithm is used, as well as the segmentation procedure presented here, which is based on the density-based clustering algorithm with noise (DBSCAN), in order to find geometrically suitable surfaces that are only to a certain extent in shadow. Direct irradiance and anisotropic diffuse irradiance, as well as PV potential, are estimated for each rooftop segment. Additional input data is used for this, including a given location's typical meteorological year (TMY) based on measurements of irradiance and the nonlinear characteristics of the chosen PV system. Finally, the resulting segments are ranked according to their suitability in order to find the most appropriate surfaces for the installation of PV systems.

[1] University of Maribor, Faculty of Electrical Engineering and Computer Science, Koroška cesta 46, 2000 Maribor, Slovenia. E-mail: niko.lukac@um.si
[2] University of Maribor, Faculty of Electrical Engineering and Computer Science, Koroška cesta 46, 2000 Maribor, Slovenia. E-mail: borut.zalik@um.si
[3] University of Maribor, Faculty of Electrical Engineering and Computer Science, Koroška cesta 46, 2000 Maribor, Slovenia. E-mail: gorazd.stumberger@um.si

EBSCOhost - printed on 2/14/2023 2:46 PM via . All use subject to https://www.ebsco.com/terms-of-use

**Keywords**: Photovoltaic potential, Photovoltaic systems, LiDAR data, Segmentation

## Introduction

In the next few years, it is predicted that grid parity will be achieved in developed parts of the world, with contributions mostly from wind and solar energy sources [2]. This is a direct consequence of the decreasing price of PV systems and their ever-evolving technology. A major challenge is to find the most suitable locations for PV system placement. One may argue that such surfaces should be unobstructed and oriented towards the equator. However, such a simplistic approach is insufficient and likely brings with it a number of problems. As such, there is a major requirement to consider as many influential factors as possible (e.g. shadowing from surrounding terrain and objects; surface topography; anisotropic diffuse irradiance; and direct irradiance) [3]. Over the past few years, many methods have been developed to precisely estimate the amount of solar energy a given surface receives per annum. This is usually described as the solar potential metric. Furthermore, estimation of PV potential can be performed in order to predict per-annum energy generation with a given PV system.

Over the past few years, remote sensing capabilities, as well as the availability of observational data about the Earth have both increased immensely. One such key technology is LiDAR (light detection and ranging), where an aircraft or a vehicle scans a given surface by emitting laser pulses. By estimating the duration of the paths travelled by the pulses, accurate 3D data points can be obtained, collectively forming an unstructured 3D point cloud that can then be georeferenced. Classification and further processing of the datapoints can be done in order to generate a 3D model of the terrain, buildings, and vegetation, at a given level of detail. Numerous methods have been developed in recent years dealing with solar and PV potential estimation using LiDAR or other remote sensing data [5]-[15]. The methods usually differ according to the topological structure used to generate the 3D model, either by using 2.5D grid (i.e. raster) structure, triangles (i.e. mesh), or voxels.

This chapter extends our previous work on PV potential estimation together with DBSCAN-based segmentation of rooftop surfaces in order to find the most suitable locations for PV system installation. In this chapter, we improve on the existing segmentation procedure by considering shadowing, as well as the rooftop topography (i.e. slope and aspect).

EBSCOhost - printed on 2/14/2023 2:46 PM via . All use subject to https://www.ebsco.com/terms-of-use

Furthermore, we provide analysis on how shadowing affects the segmentation of rooftops across large-scale urban areas. The geometric details of buildings are presented in a form of a 2.5D topological grid structure constructed over a classified LiDAR datapoint cloud. The grid provides an efficient means of extracting topographic details, as well as rapid estimation of shadowing. Additional inputs include long-term measurements of direct and diffuse irradiances from the given location's meteorological station. The measurements are pre-processed into typical meteorological year (TMY) values. The PV potential is then estimated by considering per-surface direct irradiance, anisotropic diffuse irradiance, shadowing from the surroundings, and the nonlinear efficiency characteristics of a given PV system. Finally, rooftop surfaces that have the same topographic properties and the amount of received shadow are then grouped together into segments using the DBSCAN algorithm.

The proposed methodology is described in the next two sections. In the first section, estimation of rooftop PV potential through LiDAR scanning is presented. Improved DBSCAN-based segmentation is described in detail in the second section. Results are presented in the third section, and the last section offers concluding remarks.

## PV potential estimation

The first stage of the proposed method involves the pre-processing of LiDAR data, which has already been classified into buildings, terrain, and vegetation. The input 3D points are denoted as $p_j$. The LiDAR point cloud is then insert into a 2.5D grid $G$ consisting of cells $c_i \in G$, where $c_i.z = \max\{p_1.z, p_2.z, \ldots p_m.z\}$, as shown in Fig. 1. The cell's slope $\beta$ and aspect $\gamma$ are estimated as:

$$\beta = \frac{\pi}{2} - \cos^{-1}\left(\frac{\mathbf{n}.z}{\sqrt{\mathbf{n}.x^2+\mathbf{n}.y^2+\mathbf{n}.z^2}}\right), \quad (1)$$

$$\gamma = \pi - \cos^{-1}\left(\frac{\mathbf{n}.y}{\sqrt{\mathbf{n}.x^2+\mathbf{n}.y^2}}\right), \quad (2)$$

where $\mathbf{n}$ is the normal vector of the given cell based on the best-fitted plane over neighbouring LiDAR points of the same classification [7].

EBSCOhost - printed on 2/14/2023 2:46 PM via . All use subject to https://www.ebsco.com/terms-of-use

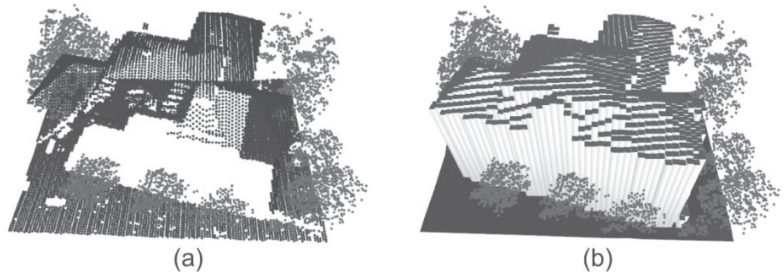



Figure 1: Example of a) classified LiDAR point cloud and b) constructed 2.5D grid. Image source: [14].

In addition to remote sensing data, nearby irradiance measurements are processed, where direct $I_b$ and diffuse $I_b$ irradiance on a horizontal surface are considered. The typical meteorological year using the Sandia [16] method is considered in this chapter. The resulting TMY-based irradiances are denoted as $\widehat{I_b}$ and $\widehat{I_d}$. These are then used in per-surface (i.e. i-th cell) irradiance estimation, as in [18]:

$$I_{b_i}(t) = S_i(t)\widehat{I_b}(t)\frac{\cos(\theta_i)}{\cos(\theta^z)}[\mathrm{Wm}^{-2}], \tag{3}$$

$$I_{d_i}(t) = \widehat{I_d}(t)R_{d_i}[\mathrm{Wm}^{-2}], \tag{4}$$

where $t$ denotes the time, $\theta_i$ the angle of incidence, and $\theta^z$ the zenith angle. $R_{d_i}$ is the anisotropic diffuse irradiance factor, based on the Perez model [19]. The shadowing coefficient $S_i$ is estimated as:

$$S_i = \begin{cases} 1 & c_i.z \leq c_j.z - d_2(c_i, c_j)(\mathrm{q}_z/\sqrt{\mathrm{q}_x^2 + \mathrm{q}_y^2}) \\ 0 & else \end{cases}, \tag{5}$$

where $d_2$ is the 2D Euclidian distance function, and $q$ denotes the directional vector from the Sun at a given time based on the sun positioning algorithm (SPA) [17]. Finally, the PV potential is estimated for a given time duration between $t_1$ and $t_2$:

$$PV_i = \int_{t_1}^{t_2} \eta(I_{b_i}(t) + I_{d_i}(t))(I_{b_i}(t) + I_{d_i}(t))\,dt\ [\mathrm{Whm}^{-2}], \tag{6}$$

where $\eta$ is a nonlinear efficiency characteristic function based on [15] for a given PV system (i.e. A-Si for amorphous silicon, P-Si for

EBSCOhost - printed on 2/14/2023 2:46 PM via . All use subject to https://www.ebsco.com/terms-of-use

polycrystalline silicon, and M-Si for monocrystalline silicon) as shown in Fig. 2.

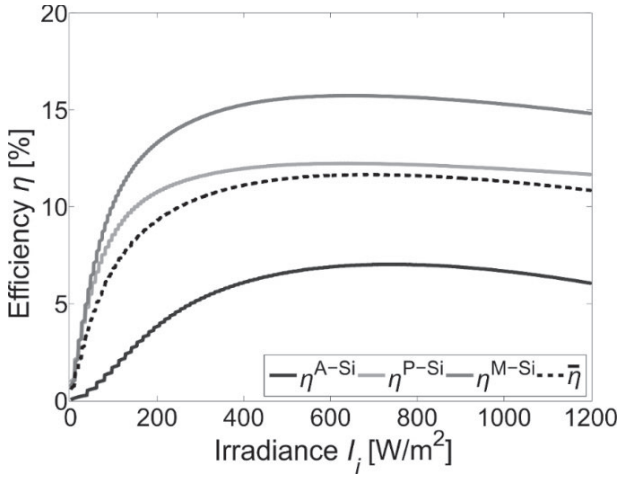



Figure 2: Estimated nonlinear efficiency characteristics of a given PV module and a solar micro inverter (with dashed line). Image source: [14].

## DBSCAN-based segmentation

The segmentation is performed by using the clustering algorithm density-based spatial clustering of applications with noise (DBSCAN) [20]. The algorithm can be described in three core steps over grid $G$:

1. Check the 8-neighbourhood of the surrounding cell of each cell within grid $G$. If the number of neighbouring cells is higher than $M$ then the cell is marked as core; otherwise it is marked as noise and disregarded.
2. For every detected core cell, find its connected component based on the 8-neighborhood over grid $G$.
3. Every non-core cell belongs to the core point (i.e. segment or cluster) if it is within the core point's neighbourhood.

The 3D positioning of the cells is not sufficient for finding neighbouring cells with similar topographic properties to form a segment. Thus, we propose the use of 5-dimensional space, defined as the set of the cells' properties $\{x, y, z, \beta, \gamma\}$. Furthermore, as an improvement of the

EBSCOhost - printed on 2/14/2023 2:46 PM via . All use subject to https://www.ebsco.com/terms-of-use

segmentation for finding more suitable surfaces for PV system placement, the cells are disregarded (marked as noise) if they are shadowed more than $T$ %. Finally, each segment is rated by $RT_s$ (7) based on its suitability for PV panel placement, relative to other segments:

$$RT_s = \begin{cases} very\ high & PV_s > 0.9 \\ high & PV_s > 0.75 \\ medium & PV_s > 0.5 \\ low & PV_s > 0.25 \\ very\ low & PV_s > 0.0 \end{cases}, \quad (7)$$

where $PV_s$ is the normalized sum of all the cells estimated PV potential for a given segment $s$:

$$PV_s = \frac{\left(\frac{1}{A_s}\sum_{i=1}^{n} PV_i\right)}{PV_{max}} \text{ [Wh]}, \quad (8)$$

where $A_s$ [m$^2$] is the segment's area and $PV_{max}$ is the segment with the maximum overall sum of its cells' PV potential.

## Results

The method presented here was tested over an urban area of Maribor City, Slovenia (46° 33' 16" N, 15° 38' 48" E). The buildings and terrain 2.5D grid model are shown in Fig. 3. The resolution of the 2.5D grid was set at 0.25 m$^2$.

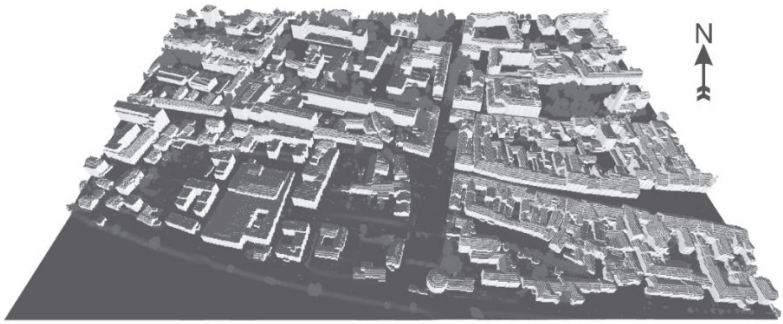



Figure 2: Constructed 2.5D grid over LiDAR point cloud of Maribor urban area. Image source: [14].

EBSCOhost - printed on 2/14/2023 2:46 PM via . All use subject to https://www.ebsco.com/terms-of-use

Direct and diffuse 10-year measurements with 15 min time-steps were taken from a nearby meteorological station at Maribor Edvard Rusjan airport (46° 28' 40" N, 15° 40' 54" E), in order to construct the TMY. The results of the segmentation are shown in Fig. 4. For the DBSCAN algorithm parameters, we used a minimal distance threshold of 4 m (i.e. minimum cluster neighbourhood), while the minimum area (i.e. minimum cluster size) of the segment was set at 5 $m^2$.

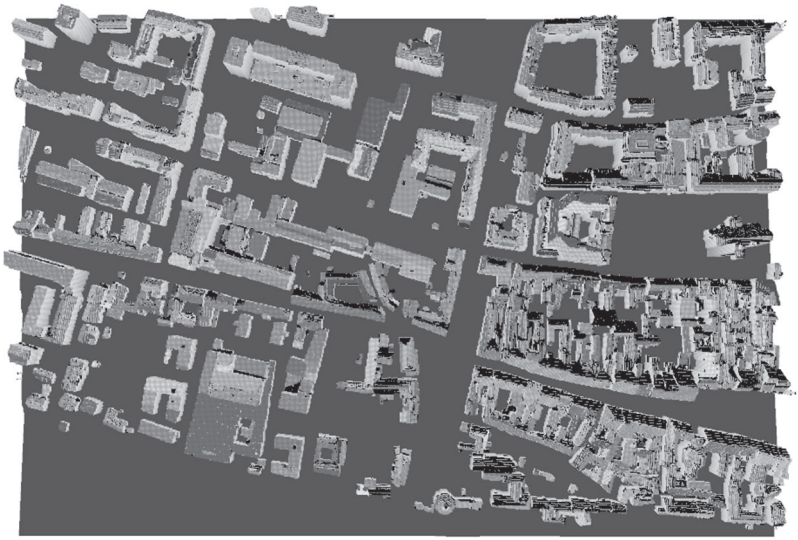


Figure 3: Results of DBSCAN-based segmentation of building rooftops in 2.5D grid consisting of terrain and buildings.

Finally, Fig. 5 shows the results of the proposed method. Each segment is ranked into one of five categories (i.e. very low, low, medium, high, and very high) based on its cumulative PV potential of all the included 2.5D cells belonging to the given segment. Hypothetical PV-systems based on M-Si and A-Si type modules together with a micro inverter were considered (based on nonlinear efficiency characteristics). The results also show how the segmentation changes and present the underlying PV potential of the obtained segments based on the amount of accepted shadowing. In this chapter we have experimented with accepted shadowing of 25%, 50%, and 75% (e.g. if a segment is shadowed for 75% or less it is considered viable, otherwise it is disregarded).

EBSCOhost - printed on 2/14/2023 2:46 PM via . All use subject to https://www.ebsco.com/terms-of-use

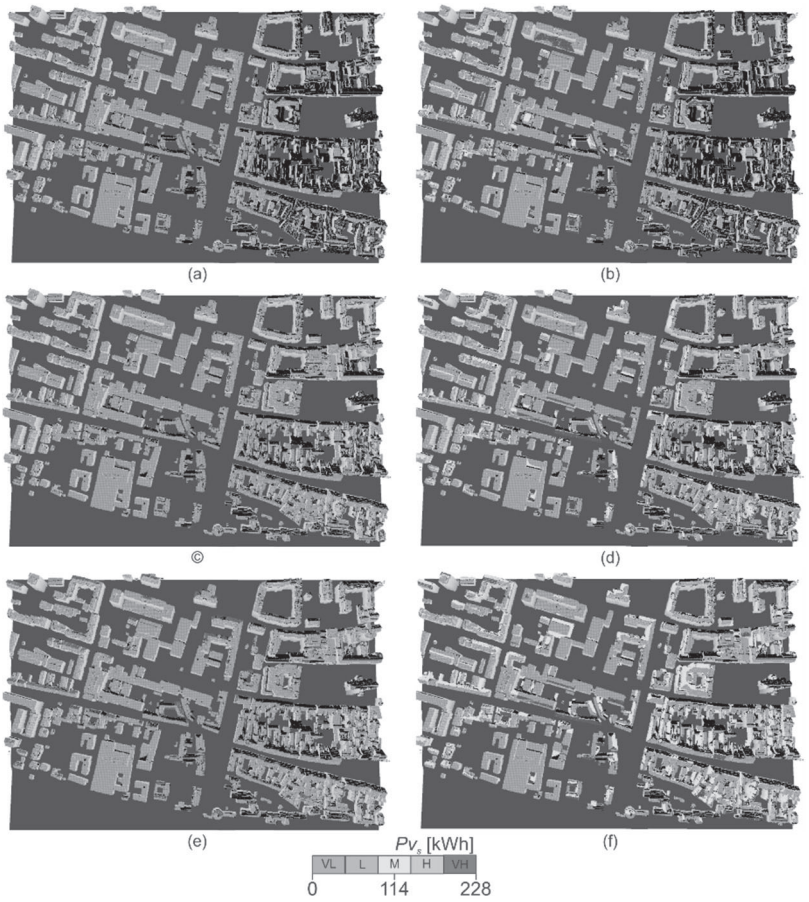



Figure 5: Rating of each segment regarding its PV potential A-Si ((a), (c) and (e)), as well as M-Si ((b), (d), and (f)) type PV modules. Legend: VL = Very Low, L = Low, M = Medium, H = High, VH = Very High. The accepted per-segment shadowing was set at 25% ((a) and (b)); 50% ((c) and (d)); and 75% ((e) and (f)).

## Conclusion

This chapter deals with the estimation of PV potential for each rooftop segment representing a continuous surface with the same topographic and shadowing characteristics. The rooftops are geometrically represented using a 2.5D topological grid structure over a classified LiDAR point

EBSCOhost - printed on 2/14/2023 2:46 PM via . All use subject to https://www.ebsco.com/terms-of-use

cloud consisting of millions of 3D datapoints. This chapter has improved on our previous work on PV estimation over rooftop segments using the DBSCAN clustering algorithm. The methodology presented here can be used on large-scale urban areas, as long the necessary remote sensing data and meteorological measurements are available in sufficient spatial and temporal resolutions.

## Acknowledgement

This work was partially supported by the Slovenian Research Agency under research programmes P2-0041 and P2-0115, and research project J2-8176.

## References

[1] N. S. Lewis, Toward Cost-Effective Solar Energy Use, Science 315 (5813), 2007, 798-801.

[2] M. A. Green, K. Emergy, Y. Hishikawa, W. Warta, E. D. Dunlop, Solar cell efficiency tables (version 45), Progress in photovoltaics: research and applications, 23(1), 2015, 1–9.

[3] D. Robinson, A. Stone, Solar radiation modelling in the urban context, Solar Energy, 77 (3), 2004, 295–309.

[4] G. Petrie, C. K. Toth, Topographic laser ranging and scanning: principles and processing. In: J. Shan, C. Toth, editors. Airborne and spaceborne laser profilers and scanners. CRC Press, 2008, 29–86.

[5] M. Šúri, J. Hofierka, A new GIS-based solar radiation model and its application to photovoltaic assessments, Transactions of GIS, 8 (2), 2004, 175-190.

[6] T. R. Tooke, N. C. Coops, A. Christen, O. Gurtuna, A. Preevot, Integrated irradiance modelling in the urban environment based on remotely sensed data, Solar Energy, 86 (10), 2012, 2923–2934.

[7] J. A. Jakubiec, C. F. Reinhart, A method for predicting city-wide electricity gains from photovoltaic panels based on LiDAR and GIS data combined with hourly Daysim simulations, Solar Energy, 93, 2013, 127–143.

[8] N. Lukač, D. Žlaus, S. Seme, G. Štumberger, B. Žalik, Buildings roofs photovoltaic potential assessment based on LiDAR (Light Detection And Ranging) data, Energy, 66, 2014, 598–609.

[9] J. M. Malof, K. Bradbury, L. M. Collins, R.G. Newell, Automatic detection of solar photovoltaic arrays in high resolution aerial imagery, Applied energy, 183, 2016, 229–240.

[10] D. Assouline, N. Mohajeri, J.L. Scartezzini, Quantifying rooftop photovoltaic solar energy potential: A machine learning approach, Solar Energy, 141, 2017, 278–296.

EBSCOhost - printed on 2/14/2023 2:46 PM via . All use subject to https://www.ebsco.com/terms-of-use

[11] S. Szabó, P. Enyedi, M. Horváth, Z. Kovács, P. Burai, T. Csoknyai, G. Szabó, Automated registration of potential locations for solar energy production with Light Detection And Ranging (LiDAR) and small format photogrammetry, Journal of Cleaner Production, 112 (part 5), 2016, 3820–3829.
[12] F. Biljecki, G.B. Heuvelink, H. Ledoux, J. Stoter, The effect of acquisition error and level of detail on the accuracy of spatial analyses, Cartography and Geographic Information Science, 45 (2), 2018, 156–176.
[13] P. Gagnon, R. Margolis, J. Melius, C. Phillips, R Elmore, Estimating rooftop solar technical potential across the US using a combination of GIS-based methods, lidar data, and statistical modeling. Environmental Research Letters, 13(2), 2018, 024–027.
[14] N. Lukač, B. Žalik, G. Štumberger, Photovoltaic potential assessment and ranking of rooftops segments based on LiDAR data, International Conference on Renewable Energies and Power Quality (ICREPQ'17), 4th to 6th April, 2017, Malaga (Spain).
[15] N. Lukač, S. Seme, K. Dežan, B. Žalik, G. Štumberger, Economic and environmental assessment of rooftops regarding suitability for photovoltaic systems installation based on remote sensing data, Energy, 107, 2016, 854–865.
[16] A. Ebrahimpour, M. Maerefat, A method for generation of typical meteorological year, Energy Conversion and Management, 51 (3), 20120, 410–417.
[17] I. Reda, A. Andreas, Solar position algorithm for solar radiation applications, Solar Energy, 76 (5), 2004, 577–89.
[18] J. A. Duffie, W. A. Beckman, Solar Engineering of Thermal Processes, Wiley-Interscience, 2006.
[19] R. Perez, R. Seals, P. Ineichen, R. Stewart, D. A. Menicucci, A new simplified version of the Perez diffuse irradiance model for tilted surfaces, Solar Energy, 39(3), 1987, 221–231.
[20] M. Ester, H. P. Kriegel, J Sander, X. Xu, A density-based algorithm for discovering clusters in large spatial databases with noise, Kdd, vol. 96, no. 34, 1996, 226–231.

EBSCOhost - printed on 2/14/2023 2:46 PM via . All use subject to https://www.ebsco.com/terms-of-use

# CHAPTER THREE

# CLUSTERING DAILY SOLAR RADIATION DATA FROM REUNION ISLAND USING DATA ANALYSIS METHODS

J. D. LAN-SUN-LUK[1], M. BESSAFI, J. P. CHABRIAT, P. JEANTY, M. DELSAUT, L. TROVALET, H. RALAMBONDRAINY, P. CHARTON

## Abstract

In this paper a method for clustering data on daily solar radiation is proposed based on the direct fraction of solar irradiance. We used measurements of diffuse and global solar radiation on a horizontal surface to compute this direct fraction. A method of hierarchical clustering on principal components was applied to data collected on Reunion (21◦S, 55◦E), a subtropical island in the Southern Hemisphere. We obtained daily data for five solar radiation classes. Interpretation of the average time series signals for each class showed that the curves produced, which describe daily weather dynamics, correlate with local meteorological phenomena. Furthermore, our data showed that the seasonal distribution of weather classes is influenced by the intensity of trade winds. The final goal of this work is to develop an approach to predict solar radiation for different time horizons and the energy potential of any given day.

[1] University of La Reunion, LE[2]P, BP 7151, 97715 St-Denis, Reunion Island. Email: lanson@univ-reunion.fr

EBSCOhost - printed on 2/14/2023 2:46 PM via . All use subject to https://www.ebsco.com/terms-of-use

**Keywords:** Diffuse and global solar radiation; subtropical weather; direct and diffuse fraction; clearness index; hierarchical clustering; principal components analysis.

## Nomenclature

| | |
|---|---|
| $k_b$ | direct fraction |
| $k_d$ | diffuse fraction |
| $f_{diff}$ | diffuse radiation, W.m$^{-2}$ |
| $f_{glo}$ | global radiation, W.m$^{-2}$ |
| $f_{dir}$ | direct radiation, W.m$^{-2}$ |
| $i$ | day index |
| $n$ | number of days |

## 1. Introduction

The development of photovoltaic systems connected to power grids has led to new research challenges. The intermittent nature of these solar production units creates a real constraint for electrical grids. This problem is critical in non-interconnected zones, such as on an isolated island. The high variability of weather encountered in such places heightens this issue. The coupling of an energy storage system to a production unit is one way of mitigating intermittency and ensuring the stability of the electricity grid. The constraints on the design and installation of such a storage system generally revolve around the response time and the amount of power needed in order to limit the impact of intermittency. Finally, the size and expected lifetime of such storage plants has a direct impact on their cost. Short-term (days) or very short-term (hours) prediction of solar irradiance as the primary energy source offers the possibility of reducing the size and cost of any storage system and of increasing the penetration of photovoltaic units into the power grid. Our work aims to better predict intra-day solar irradiance to this end. We present an original data processing model to facilitate the development of a predictive model. In doing so, we are in step with a number of recent studies [1], [2], [3], [4]. However, our work is different in two respects. Firstly, we introduce the direct fraction, $k_b$, which is defined as the ratio of the direct component to the global irradiance [5], to replace $k_t$ the clarity index usually found in this kind of study. In our method, we only deal with local measurements, which integrate all environmental factors that have an impact. The use of $k_b$ also enhances the weight of daily information.

EBSCOhost - printed on 2/14/2023 2:46 PM via . All use subject to https://www.ebsco.com/terms-of-use

Secondly, we use $k_b$ in conjunction with its time signature, which allows us to maintain information on its causal link with meteorological events. This helps us to interpret weather classes from a meteorological point of view.

In the first part of this chapter, we present the location, the instruments used, and the measurements. Then, we focus on an unsupervised method to cluster time series data. This engages a number of proven data-mining methods to identify patterns in the recorded data. We applied this methodology to the measurement of solar radiation on Reunion.

Finally, a first approach on the physical interpretation of the different classes is presented. We highlight the importance of daily cycles in our study on mean day profiles of $k_b$ for each class and their temporal statistical analysis.

This chapter is based on a revised version of a paper presented at the International Conference on Renewable Energies and Power Quality (ICREPQ'13) [16].

## 2. Data Collection and Methodologies

### *A. Diffuse and Global Solar Radiation Measurements*

Reunion, a volcanic island in the Southern Hemisphere, was the location of this study. The island has a humid tropical climate, with a large annual average solar radiation. The island combines a very rugged landscape, with large variations in altitude. The prevailing trade winds, coming from south-southeast, induce local changes in weather patterns at ground level [6]. The average temperatures oscillates from 25°C to 32°C for coastal regions and from 15°C to 22°C for regions located above 1,500 m in the interior of the island [7].

Our measurements were obtained using a SPN1 pyranometer, as described in [10], with a datalogger from Campbell Scientific for data collection and storage. The main advantage of the SPN1 sensor is its capability of simultaneously giving diffuse and global solar radiation data. Its operation requires a leveling task on installation, but no regular adjustment (it has no moving parts) or other heavy maintenance (except for calibration and interior protection against moisture), while also having a sensitivity and spectral response range compatible with our goals. This sensor is actually based on a set of seven thermopiles, symmetrically arranged below a dome-shaped cover. The specific geometry of the instrument ensures that at any time of day and in any location, there is always one sensor fully exposed to the sun and one sensor fully in shadow

EBSCOhost - printed on 2/14/2023 2:46 PM via . All use subject to https://www.ebsco.com/terms-of-use

(the World Meteorological Organization rates the SPN1 sensor as "good quality").

The measurements used for this study were sampled at 0.1 Hz, and then averaged to give one point per minute for final storage. Similar studies [1], [8] have used the same time step. Other authors have used a short time step, sampling at 1 Hz, as [3], or a longer one, such as 10 minutes in [4], [9].

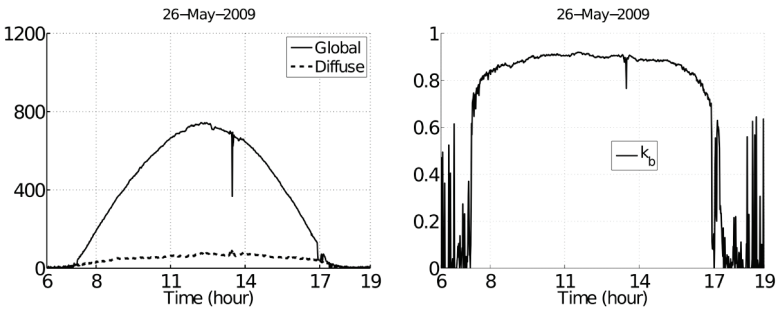
Raw measurements were collected at a location on Moufia campus (20° 54′ S, 55° 29′ E) from December 2008 to March 2012, using calibrated instruments. We constructed a database of 1,188 days. For the clustering of the data, we only retained days with no missing data, giving a final set of 959 days (80 % of the whole database).

### *B. Daily Representation of Solar Radiation*

We depict solar irradiance through use of the direct fraction $k_b$, which is related to the usual diffuse fraction, $k_d$, as follows:

$$k_b = 1 - k_d = 1 - \frac{f_{diff}}{f_{glo}} = \frac{f_{dir}}{f_{glo}} \quad (1)$$

We have defined $k_b$ as the ratio of direct radiation to global radiation. $k_b$ was directly obtained from measurements made at ground level by the SPN1 sensor of $f_{glo}$ and $f_{diff}$ as described above. When $k_b$ is close to 1, the direct radiation level is close to the global radiation level, indicating that it is a sunny day. The diffuse radiation is then very low (Fig. 1(a)). On the other hand, a value close to 0 suggests a very cloudy day—there is no direct solar radiation and the diffuse radiation is quite similar to the global radiation (Fig. 2(a)).

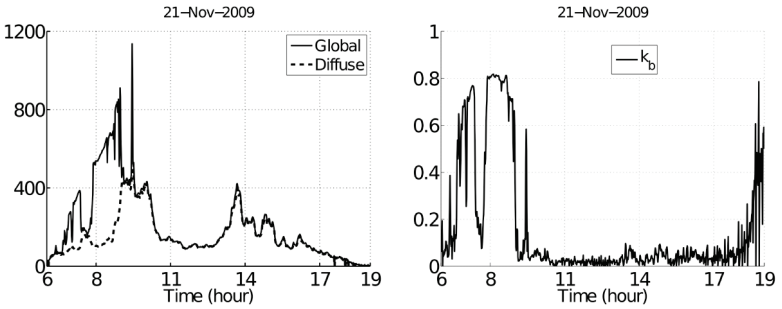



(a) Solar radiation ($W.m^{-2}$) (b) Direct fraction $k_b$

Figure 1. Example of a clear day

EBSCOhost - printed on 2/14/2023 2:46 PM via . All use subject to https://www.ebsco.com/terms-of-use

The purpose of our work was to use the direct fraction $k_b$ to identify different types of daylight conditions depending on their level of solar irradiance from among a set of known conditions, such as clear sky (Fig. 1(b)) or cloudy (Fig. 2(b)). To do so, we analyzed different samples of daily sequences of $k_b$ measured between 08:00 AM and 05:00 PM (local time, GMT+4). This restricted time slot was chosen to avoid any effect due to shadow masking the sensor at the beginning and end of the day for our station's location.




(a) Solar radiation ($W.m^{-2}$) (b) Direct fraction $k_b$

Figure 2. Example of a day with intermittent cloud

## *C. Clustering Time Series*

A time series, $s_i$, is a sequence of numbers representing the measurements of a given attribute at equal time intervals. If $I = \{1, \dots, n\}$ and $T = \{1, \dots, p\}$, a set of time series, $\{s_i \mid i \in I\}$, can be represented by a matrix $S$:

$$S = ((s_i^t)_{i \in I, t \in T}) \tag{2}$$

where $s_i^t$ is the value of the attribute for the series $s_i$ at the time $t$. In our case, a time series was used to record the different measurements of $k_b$ every minute during the test day.

Each series $s_i = (s_i^t)_{t \in T}$ is viewed as a vector in Euclidian space, $E = \mathbb{R}^p$, a weight $p_i = \frac{1}{n}$ is associated to $s_i$, and the gravity center of the set of series $\mathcal{N}(I) = \{(s_i, p_i)_{i \in I}\}$ is denoted $G$.

The methodology used to cluster a time series set involves combining three data mining methods: ***principal component analysis*** (PCA), ***Ward's***

EBSCOhost - printed on 2/14/2023 2:46 PM via . All use subject to https://www.ebsco.com/terms-of-use

***method***, and ***K-means clustering***. We used the package *FactoMineR* [11], which implements this strategy in *R*.

- *Principal component analysis* is a hierarchical clustering method used as a pre-process for reduction and de-noising. The first principal components are a set of new uncorrelated variables and extract the main information contained in the data. This is necessary for analyzing time series data when measurements are taken over a long period and when the values are correlated. The partitioning obtained by this hierarchical clustering method, when performed on a set of pertinent principal components, is more stable than that obtained from the original data.
- To determine an optimal number of clusters, the *Ward hierarchical method* [12] is applied to these principal components. The Ward method was used to organize the set of days into a sequence of nested partitions forming a hierarchical tree. The total variance is denoted *V*:

$$V = \sum_i p_i \, d^2(s_i, G) \tag{3}$$

and if we let $P = \{C_k\}_{k \in K}$ a partition of *I*. $p_{C_k}$ and $G_k$ are, respectively, the weight and the gravity center of the cluster $C_k$. To give the within-cluster variance *W*:

$$W = \sum_{k \in K} \sum_{i \in C_k} p_i \, d^2(s_i, G_k) \tag{4}$$

and the between-cluster variance *B*:

$$B = \sum_{C_k \in P} p_{C_k} \, d^2(G_k, G) \tag{5}$$

*B* characterizes the homogeneity of the clusters of partition *P*.

The Huygens theorem allows us to decompose the total variance *V* as follows: $V = B + W$. At each step, the Ward method merges two clusters to minimize the between-cluster variance. Analyzing the between-cluster variance *B* and decreasing the partitions of the hierarchical tree helps to select a good number of clusters. This number *K* of clusters is suggested when the increase of *B* between $K-1$ and *K* clusters is much greater than the one between *K* and $K+1$ clusters.

- Once a number of clusters have been selected, the quality of the partition *P* is improved by applying the *K-means* [13] algorithm. The quality of the partition *P* is measured by:

$$Q(P) = \frac{B}{V} \tag{6}$$

This gives us the percentage of variance explained by the partition.

EBSCOhost - printed on 2/14/2023 2:46 PM via . All use subject to https://www.ebsco.com/terms-of-use

### *D. Cluster Interpretation*

For a class $C_k$, the Huygens theorem is written:

$$V_k = B_k + W_k \tag{7}$$

with $V_k = \sum_{s_i \in C_k} p_i \, d^2(s_i, G)$, $B_k = p_{C_k} \, d^2(G_k, G)$ and $W_k = \sum_{i \in C_k} p_i \, d^2(s_i, G_k)$.

The quality of a class *k* is measured by:

$$Q(C_k) = \frac{B_k}{V_k} \tag{8}$$

A value close to 1 characterizes a homogeneous class.

To give meaning to clusters, we used data-mining tools developed by the University of Geneva for extracting information from sequence data. These methods have been successfully applied in various fields, including the social sciences and bioinformatics [14]. These tools were implemented in the *TraMineR* library of the *R* platform.

To apply these methods, the numerical series must first be converted into categorical data. In our case, we used normalized series where each numerical value $s_i^t \in [0,1]$ of a series $s_i$ is coded in a state or graduation $\hat{s}_i^t$ ranging from 1 to 10 according to its numerical value. A series $\hat{s}_i$ is now a vector of the space $F = [\![1; 10]\!]^P$.

$\hat{s}_i = (\hat{s}_i^t)_{i \in I}$ was the transverse state of the series at time *t* and each cluster was described by the transverse distribution of states for each time *t*. We plotted the state distribution for each class with the *TraMineR* package.

### *E. Classification Results from Reunion*

In this subsection, we present the results obtained by applying the clustering strategy to the Reunion data. Fig. 3 suggests a partition of the data into **5** classes. The percentage of variance explained by the partition is **66**%.

EBSCOhost - printed on 2/14/2023 2:46 PM via . All use subject to https://www.ebsco.com/terms-of-use

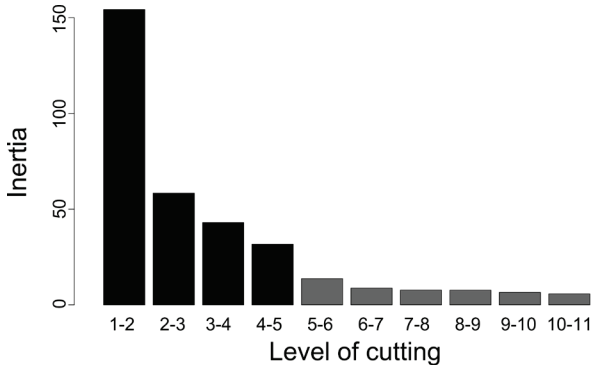



Figure 3. Bar plot of the gain in between-cluster variance

Table 1 gives the description of each class. We can see that the frequency of each class is similar except in class 3. We noticed that the variance explained ($Q(C_k)$) was important for class 1 and class 5. This means that these classes are most homogeneous and class 3 is the least homogenous.

Fig. 4 gives the state distribution of levels $k_b$ for each class. Moreover, this representation allows us to evaluate the dispersion of each state throughout the day. For classes 1, 2, 4, and 5, we can see a high frequency of the predominant state during a period of each class. In class 3, the presence of all states of $k_b$ with the same weight suggests a strong variability in days: this confirms the precedent quality results for each class.

**Table 1. Cluster Description**

| Class k | Number of observations | Frequency | $Q(C_k)$ |
|---|---|---|---|
| 1 | 178 | 18.6 % | 79.9 % |
| 2 | 191 | 20.0 % | 59.2 % |
| 3 | 130 | 13.6 % | 39.5 % |
| 4 | 223 | 23.2 % | 47.6 % |
| 5 | 237 | 24.7 % | 78.2 % |

EBSCOhost - printed on 2/14/2023 2:46 PM via . All use subject to https://www.ebsco.com/terms-of-use

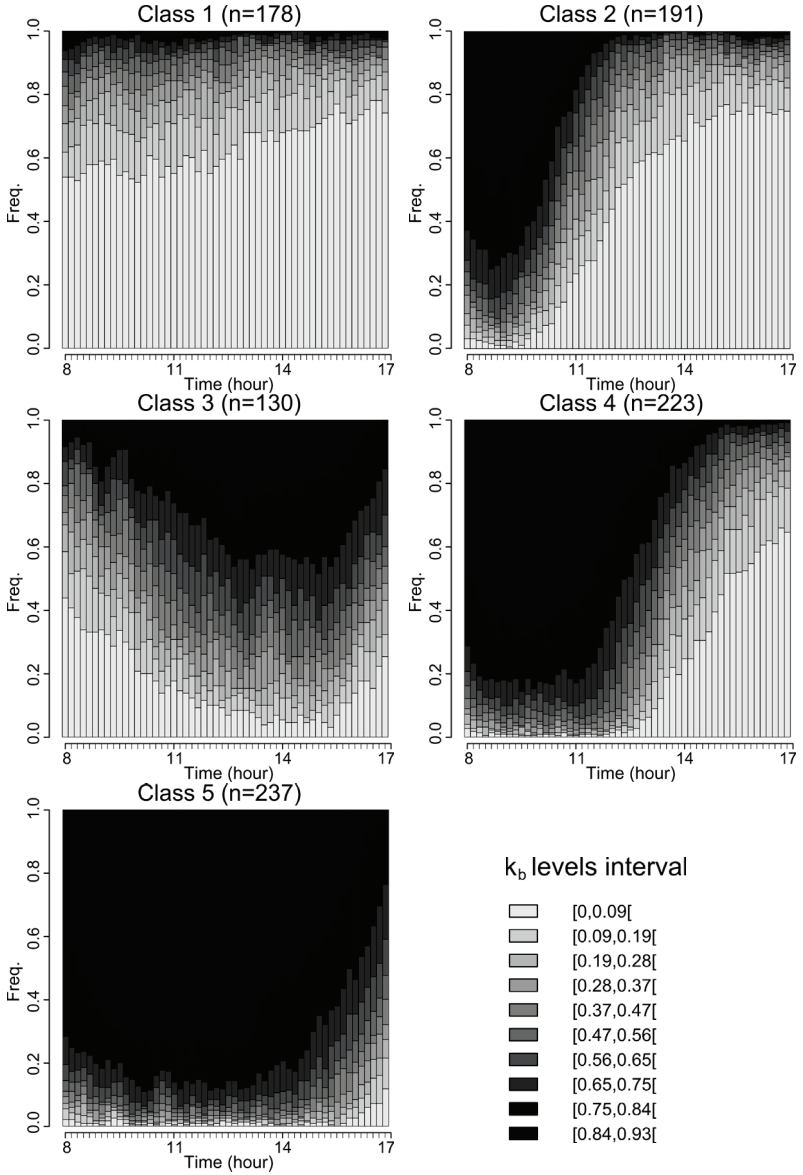



Figure 4. Transverse distribution of all states of $k_b$

EBSCOhost - printed on 2/14/2023 2:46 PM via . All use subject to https://www.ebsco.com/terms-of-use

## 3. Physical Interpretation of the Classes

The five class partitions of the direct fraction summed up the normal sunshine regimes of Reunion Island. The average trend of $k_b$ for each class of diurnal sunshine between 08:00 AM and 05:00 PM (local time) is shown in Fig. 5.

This clustering shows two types of curves:

- Type $T_1$ has a very overcast sky at the beginning of the day (classes 1 and 3), with relatively low values of $k_b$ for the whole day. For the $T_1$ type, two different situations may be identified: one giving a continued slow degradation (class 1) and the other characterized by a little improvement throughout the rest of the day (class 3).
- Type $T_2$ corresponds to an uncluttered sky giving high values for $k_b$ at the beginning of the day (classes 2, 4, and 5). Such a day begins with nice weather, but shows degradation starting at different times of the day. The atmospheric tide probably plays an important role in the variability of the semi-diurnal $k_b$ value noticed for classes 2 and 4. The different times when degradation occurred may suggest the superposition of another factor.

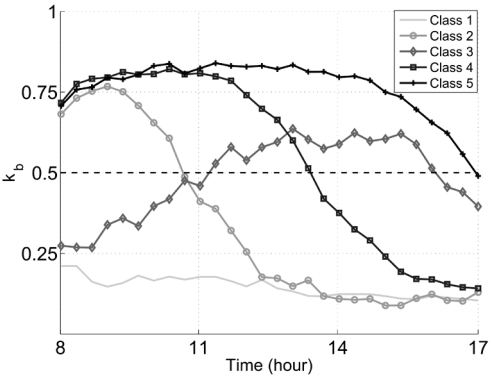



Figure 5. Average trend of direct fraction for each class

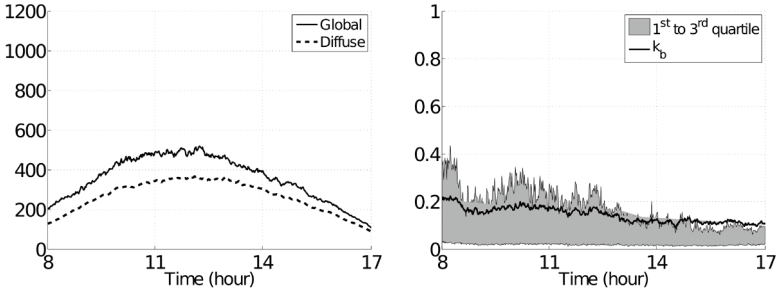
### *A. Daily Interpretation of Classes*

To illustrate the main profile of each class, we present the mean value; the first and third quartile of the direct fraction; and the mean value of the diffuse and global radiation (see Fig. 6, 7, 8, 9 and 10).

EBSCOhost - printed on 2/14/2023 2:46 PM via . All use subject to https://www.ebsco.com/terms-of-use

### *A.1. Class 1: Cloudy Days*

Class 1 corresponds to a very low level of sunshine all day. The averaged value of $k_b$ as seen in Fig. 6(b), indicates significant cloud cover. The diffuse and global radiation have almost the same shape and are relatively close to each other (Fig. 6(a)). This class suggests dominant local phenomena, which include weak trade winds accompanied by a flow of moisture leading to significant effects of orographic clouds, and a land breeze phenomenon induced by thermal contrasts.

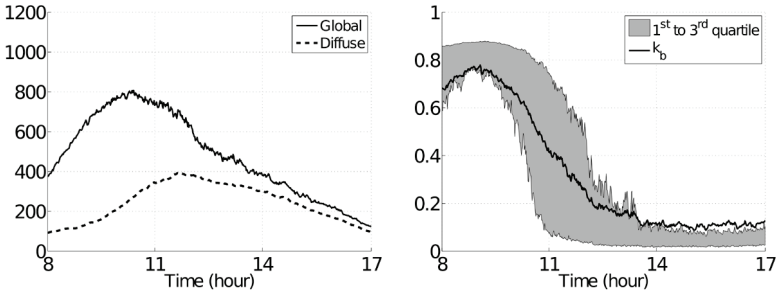



(a) Solar radiation ($W.m^{-2}$) (b) Direct fraction $k_b$

Figure 6. Class 1, mean of class

### *A.2. Class 2: Intermittent Bad Days*

Class 2 describes a sunny morning until mid-morning (around 09:00–09:30 AM) and a cloudy afternoon (Fig. 7(b)). Diffuse radiation is dominant in the afternoon while the direct component is more important at the beginning of the morning (Fig. 7(a)).



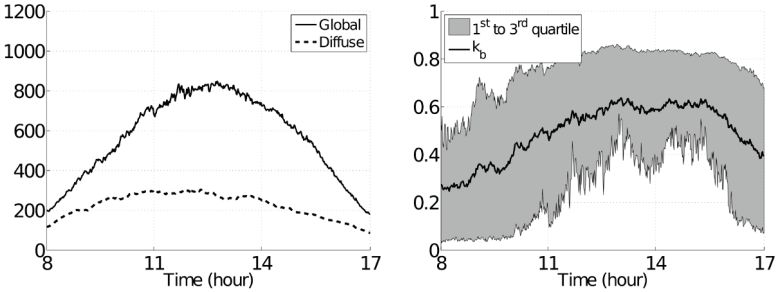

(a) Solar radiation ($W.m^{-2}$) (b) Direct fraction $k_b$

Figure 7. Class 2, mean of class

EBSCOhost - printed on 2/14/2023 2:46 PM via . All use subject to https://www.ebsco.com/terms-of-use

### *A.3. Class 3: Disturbed Days*

Class 3 corresponds to a day with variable weather and high variability in the direct fraction, with improvement in the late morning and moderate cloud cover in the afternoon. In Fig. 8(b), we can observe the maximum of $k_b$ at close to 0.6. The low value of the first quartile and the high value of the third quartile of $k_b$ illustrates the disturbed weather in this class (Fig. 8(a)).

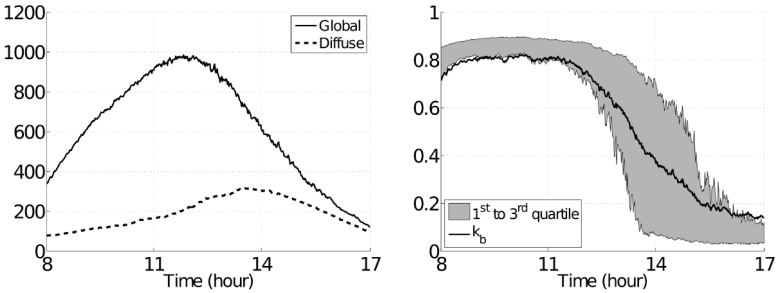



(a) Solar radiation ($W.m^{-2}$) (b) Direct fraction $k_b$

Figure 8. Class 3, mean of class

### *A.4. Class 4: Intermittent Good Days*

The behavior of class 4 (Fig. 9) is similar to class 2, but with a stronger sunny regime during all morning until early afternoon (around 00:30–01:00 PM). Later on, the diffuse radiation increases more for class 4 than for class 2.



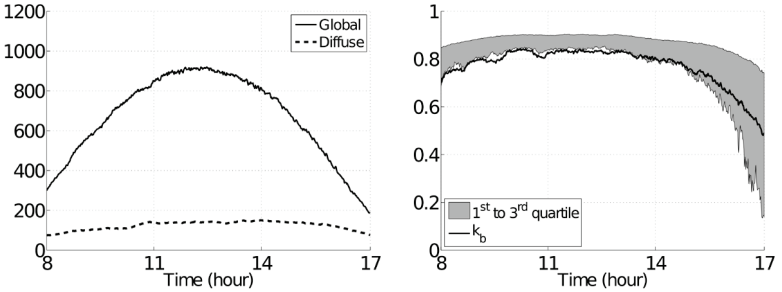

(a) Solar radiation ($W.m^{-2}$) (b) Direct fraction $k_b$

Figure 9. Class 4, mean of class

EBSCOhost - printed on 2/14/2023 2:46 PM via . All use subject to https://www.ebsco.com/terms-of-use

### *A.5. Class 5: Clear Sky Days*

Class 5 days are characterized by a $k_b$ with very little variation between the first and third quartile (Fig. 10(b)) and correspond to a regime of good weather throughout the day. Cloudy overflows affecting the site do not have a systematic character since direct radiation dominates in this class (Fig. 10(a)).




(a) Solar radiation ($W.m^{-2}$) (b) Direct fraction $k_b$

Figure 10. Class 5, mean of class

## *B. Seasonal Distribution of Classes*

Fig. 11 shows the distribution of classes from 2008 to 2012. The shaded area represents the missing days (229 days over the course of the measurement period). In order to analyze the seasonal distribution of classes, we have presented the number of occurrences for each month of the year (Fig. 12).

EBSCOhost - printed on 2/14/2023 2:46 PM via . All use subject to https://www.ebsco.com/terms-of-use

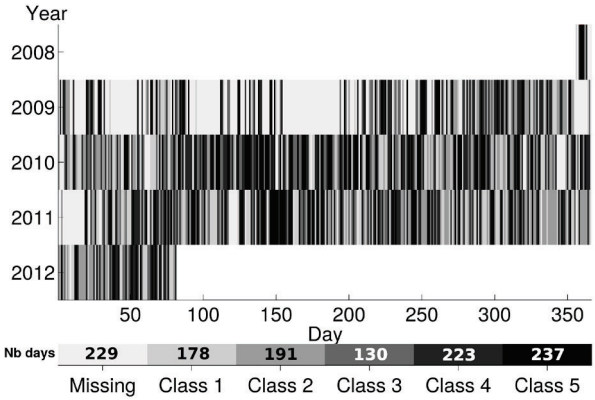



Figure 11. Time representation

We can see that classes 4 and 5 predominate in austral winter from May to October and classes 1 and 2 in austral summer from November to April [7]. Class 2 is dominant over the other classes from November to January. This could be explained by the effect of the land breeze blowing from 08:00 AM until 05:00 PM combined with trade winds, which are lighter, but potentially bring cloud induced by the mountainous nature of the landscape. Class 5 is dominant from May to October with significant primacy from May to July. On average, the trade winds are strong during the austral winter (May to October) and lighter during the austral summer (November to April). This reflects the variability of the latitudinal positioning of the Mascarene High zone of high pressure. The preponderance of clear skies (classes 4 and 5) from May to August, suggests that the intensity of trade winds is high. This consequently limits the local effect of cloud overflow induced by the land breeze observed at the site in Moufia. In addition, the austral winter trade winds are more stable and have a lower relative rate of humidity compared to those of the austral summer, which bring unstable weather.

It may be noted that classes 5 and 2 display a large amount of variability in the opposite phases of the year. However, a difference in the percentage of the occurrence of particular classes may be noticed—on average we see around 20.0 % for class 2 and 24.7 % for class 5. This implies that diurnal variability is modulated by seasonal variability, although all five classes of weather are present.

EBSCOhost - printed on 2/14/2023 2:46 PM via . All use subject to https://www.ebsco.com/terms-of-use

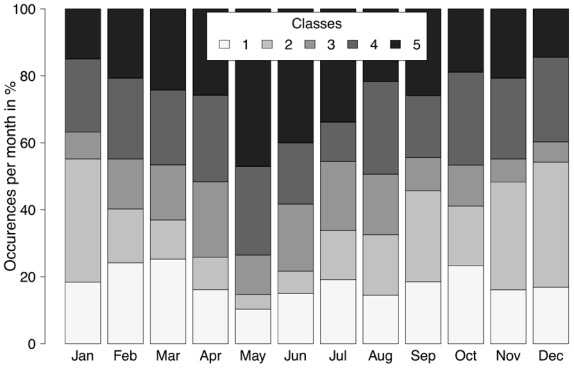



Figure 12. Histogram of the annual distribution of the classes

## *C. Classes for the Prediction of Solar Radiation*

The classification of weather conditions into five classes highlights the intrinsic characteristics of the different classes, which are distributed into two types ($T_1$, $T_2$). This classification provides a good understanding of the daily weather profile. The contribution of the type, class, and its characteristics can offer a starting point for the implementation of a tool to predict the solar radiation over the course of a day.

Observation of $k_b$ in the early morning (8 AM–10 AM) gives us a curved line and that describes the type of day. As such, the amount of solar radiation between 10 AM to 2 PM (highest energy slot time) may be predicted from information analyzed at the beginning of the day.

The class can be determined by taking into account other physical variables (humidity, pressure, wind etc.); the slope and level of $k_b$ in the morning; or by calculating the distance to the most representative model of each class for the start of the day. The estimation of the class will finally provide confidence intervals on the value of $k_b$ between 10 AM and 2 PM. For this, we need only consider the inter-quartile point of each class, which gives us the maximum and minimum boundaries for the $k_b$ level in the afternoon (Fig. 6(b), 7(b), 8(b), 9(b), 10(b)).

This process can be repeated throughout the day to adjust the choice of the class. Moreover, we may take into account the seasonality of classes to refine the confidence intervals and thus better quantify the levels of $k_b$.

EBSCOhost - printed on 2/14/2023 2:46 PM via . All use subject to https://www.ebsco.com/terms-of-use

## 4. Conclusion

This paper deals with the problem of mining daily solar radiation data. Clustering real-world data is not a trivial task as well-separated classes are rarely present in such data. We propose a cluster time series methodology, which combines three data-mining methods: *principal component analysis*, *Ward's method*, and *K-means* clustering. When applied to our data collected on Reunion, interesting patterns related to the clusters were observable. We defined five classes, with which characterize this subtropical location.

The partitioning of these temporal signals highlights the various diurnal cycles in an island environment. The weather conditions for early and mid-morning give us relevant information on the class of the day. The development of a predictive model will be based on the identification of precursors for these morning triggers.

The intra-day prediction will be our next priority. Therefore, we shall analyze the cross correlation between the direct fraction and other meteorological variables.

Finally, the possibility of interpreting these classes together with weather patterns shows that the problem of predicting solar radiation is somehow equivalent to the implementation of a very short-term meteorological model. This enables us to extend this method to other subtropical regions.

*Acknowledgement*: this work received financial support from Europe, the Regional Reunion Island Council, and the French government through the ERDF (European Regional Development Fund) and ADEME (French Environment and Energy Management Agency).

## References

[1] M. Muselli, P. Poggi, G. Notton, A. Louche, "Classification of typical meteorological days from global irradiation records and comparison between two mediterranean coastal sites in corsica island," Energy Conversion and Management 41 (Issue 10) (2000) 1043–1063.

[2] S. Harrouni, A. Guessoum, A. Maafi, "Classification of daily solar irradiation by fractional analysis of 10-min-means of solar irradiance," Theor. Appl. Climatol. 80 (2005) 27–36.

[3] T. Soubdhan, R. Emilion, R. Calif, "Classification of daily solar radiation distributions using a mixture of dirichlet distributions," Solar Energy 83 (Issue 7) (2009) 1056–1063.

[4] M. Gastòn-Romeo, T. Leon, F. Mallor, L. Ramìrez-Santigosa, "A morphological clustering method for daily solar radiation curves," Solar Energy 85 (Issue 9) (2011) 1824–1836.

EBSCOhost - printed on 2/14/2023 2:46 PM via . All use subject to https://www.ebsco.com/terms-of-use

[5] J. Ruiz-Arias, H. Alsamamra, J. Tovar-Pescador, D. Pozo-Vàzquez, "Proposal of a regressive model for the hourly diffuse solar radiation under all sky conditions," Energy Conversion and Management 51 (2010) 881–893.

[6] G. Taupin, M. Bessafi, S. Baldy, J. Bremaud, Tropospheric ozone above the southwestern indian ocean is strongly linked to dynamical conditions prevailing in the tropics," Journal of Geophysical Research 104, 7 (1999) 8057–8066.

[7] G. Jumeaux, H. Quetelard, D. Roy, "Atlas climatique de la Réunion," Météo-France, ISBN 978-2-11-128623-8, 2011.

[8] G. Notton, C. Paoli, S. Vasileva, M. L. Nivet, J. Canaletti, C. Cristofari, "Estimation of hourly global solar irradiation on tilted planes from horizontal one using artificial neural networks," Energy 39 (Issue 1) (2012) 166–179.

[9] A. Maafi, S. Harrouni, "Preliminary results of the fractal classification of daily solar irradiances," Solar Energy 75 (Issue 1) (2003) 53–61.

[10] Delta-T-Devices, SPN1 - sunshine pyranometer (May 2012).
URL http://www.delta-t.co.uk

[11] S. Lê, J. Josse, F. Husson, *Factominer*: "An R package for multivariate analysis," Journal of Statistical Software 25 (1) (2008) 1–18. URL http://www.jstatsoft.org/v25/i01

[12] F. Murtagh, P. Legendre, "Ward's hierarchical clustering method: Clustering criterion and agglomerative algorithm," ArXiv eprintsar Xiv:1111.6285. URL http://adsabs.harvard.edu/abs/2011arXiv1111.6285M

[13] F. Husson, J. Josse, J. Pagès, "Principal component methods - hierarchical clustering - partitional clustering: why would we need to choose for visualizing data," Technical Report Agrocampus.
URL http://www.agrocampus-ouest.fr/math/

[14] A. Gabadinho, G. Ritschard, N. Müller, M. Studer, "Analyzing and visualizing state sequences in R with *TraMineR*," Journal of Statistical Software 40, 4 (2011) 1–37.
URL http://www.jstatsoft.org/v40/i04/

[15] R. E. Frank, W. F. Massy, D. G. Morrison, "Bias in multiple discriminant analysis," Journal of Marketing Research 2 (1965) 250–258.

[16] P. Jeanty, et al. ICREPQ'13, Bilbao, Spain.

EBSCOhost - printed on 2/14/2023 2:46 PM via . All use subject to https://www.ebsco.com/terms-of-use

# CHAPTER FOUR

# MODELLING SOLAR DATA: REASONS, MAIN METHODS AND APPLICATIONS

M. DE SIMÓN-MARTÍN[1]
M. DÍEZ-MEDIAVILLA[2]
C. ALONSO-TRISTÁN[2]

## Abstract

The main aim of this research work is to analyse the importance of modelling solar data. Should engineers and scientists spend time modelling solar data from other variables or is it simply a waste of time? Which applications truly need a precise forecast of the solar variables? Which spatial and time resolution is needed? In this work, we propose analysing these questions and giving a brief description of the currently existing methods and the targets demanded by industrial and scientific applications in this field.

There are many methods and techniques in the field of modelling solar data, which cannot be completely described here. The authors only wish to analyse the relevance of improving these methods for the development of solar energy.

**Keywords:** solar radiation, measuring methods, modelling, solar irradiance transposition, models performance

[1] Escuela de Ingenieros de Energía y Minas. Universidad de León, Dept. Area of Electrical Engineering, Campus de Vegazana s/n, 24071 León (Spain).
[2] Escuela Politécnica Superior. Universidad de Burgos, Dept. of Electromechanical Engineering. Campus de Río Vena s/n, 09001, Burgos (Spain).

EBSCOhost - printed on 2/14/2023 2:46 PM via . All use subject to https://www.ebsco.com/terms-of-use

## Introduction

Since ancient Greece, and even before, mankind has found innovative ways to use the power of the Sun. The number of applications have increased since the last century due to the development of efficient technologies that allow the conversion of solar power into electricity or hot water. These solar energy technologies have changed the way that many businesses, industries and even houses produce heat, light, hot water, electricity or cooling [1]. Active solar techniques include the use of photovoltaic panels and solar thermal collectors to harness energy. Passive solar techniques include the orientation of a building to the Sun, the selection of materials with favourable thermal mass or light dispersing properties and the design of spaces that naturally circulate air [2]. Its impact is such that it is highly present on the political agenda in many countries. So, we can conclude that a deep analysis of the solar resource is mandatory for the development of these kinds of technologies.

The design, dimensioning and calculation of solar-energy-based systems requires precise knowledge of the amount of global irradiance and especially the direct, diffuse and reflected components that fall on surfaces that are horizontal or inclined in any direction. This latter case is of interest in the analysis of a building's efficiency or solar energy generators performance. The fruit of studies in this field allows the development and implementation of many different systems; for example, photovoltaic technology, the calculation of thermal loads and cooling in buildings, the design of efficient solar collectors, and a huge number of other technological applications that have the objective of increasing human well-being and comfort.

Since the Maastricht Treaty in 1992, the European Union's energy and environmental target has been to promote sustainable and environmentally-friendly growth in its member countries. Having set the goal of a 12.5% contribution from renewable energies with respect to total consumption for the year 2010, the 2004 Berlin Conference recommended that the percentage of renewable energies for the year 2020 should reach 20% of the total consumption of energy. This was established through the Horizon 2020 plan. Prescriptions were also made in the Kyoto Protocol on climate change, which many European countries, including Spain, signed up to. As is well known, the protocol created an obligation to lower emissions of greenhouse gases such as $CO_2$, which are produced mainly by transportation and by current systems for generating thermal and electrical energy. Within this framework, one of the paths to the achievement of the

EBSCOhost - printed on 2/14/2023 2:46 PM via . All use subject to https://www.ebsco.com/terms-of-use

stated objectives is the development of new energy strategies within urban environments.

A significant level of energy is consumed in urban environments. Policies focused on distributed generation, net energy balance or the construction of "nearly Zero Energy Buildings" (nZEBs) have been supported by both photovoltaic and thermal solar technology through their modularity and easy adaptability to any structure.

The integration of photovoltaic generators in building envelopes, giving rise to BIPV systems, offers immense potential. In Germany, for example, the integration of photovoltaic systems in buildings may allow up to 50% of demand for electricity to be covered. Other studies indicate that there could be electrical energy savings of between 30% and 50%. In any case, there would be a significant advance towards energy sustainability and self-sufficiency and, therefore, this development would seem to be unstoppable in the coming years.

Furthermore, the harnessing of solar energy via building façades can be achieved in many ways, and especially through the incorporation of thermal and photovoltaic modules.

Solar irradiation on the Earth's surface also has implications for hydrology, climatology, agriculture and many other human activities.

The solar irradiation that arrives to the external part of the Earth's atmosphere has an average value of 1 373 $W/m^2$ and it is almost constant (except when sun storms occur). However, on the Earth's surface, that value decreases to an average of 1 000 $W/m^2$ approximately and this is subject to a huge degree of uncertainty due to geographical coordinates, meteorological conditions, pollution (which causes diffraction in the atmosphere), and shadows from nearby obstacles among others. It is therefore not an easy task to model irradiation behaviour at ground level.

## Measuring solar irradiation

Global solar irradiance that reaches the Earth's surface is the sum of three components: beam, diffuse and reflected or albedo irradiance. The first component refers to the amount of energy that arrives directly in a line – the measured region, called the circumsolar region, is a solid angle of 1 steradian – from the Sun.

Diffuse irradiance is the part of solar energy that has been reflected and scattered in the atmosphere. Part of the irradiance returns to outer space and another part reaches the ground, the proportion of which depends on the size, density and characteristics of the chemical and aerosol particles present in the atmosphere.

EBSCOhost - printed on 2/14/2023 2:46 PM via . All use subject to https://www.ebsco.com/terms-of-use

The final component is irradiance that is reflected from other elements on the horizon; diffuse irradiance, the measurement and estimation of which has yet to be properly developed.

Some irradiation values can be measured with specific equipment in some ground stations, but we only have available data from very specific places and for a specific period of time [3]. Depending on the solar component we are interested in measuring, we can use the following equipment:

- For measuring global irradiance, we need to measure the complete electromagnetic broadband range using a pyranometer (see Figure 1 (a)), which can be either thermoelectric (if it is based on a thermal battery) or bimetallic (if it is based on the deflection of the free extreme of two different metals joined at the other extreme).
- For measuring beam irradiance, a pirhelyometer is needed, which is equipped with shutter devices which allow the measurement of a narrow part of the irradiance from the sky (semi-solid angle of 2.5 sr). These systems must be mounted on tracking systems to follow the Sun.
- For measuring diffuse irradiance, the most extensive method is by use of a pyranometer with a shadowing device for the beam irradiance, which can be a solar disc or ball, or a shadowing ring (see Figure 1 (c)). Currently, there also exist other devices like the rotating shadowband, skyscanners or computer generated shadowing masks for multiple irradiance sensors (Delta-T).
- For the measurement of reflected irradiance the use of an albedometer is advised, which is basically a pyranometer specially calibrated for reflected irradiance (see Figure 1(c)).

These devices can offer very high time resolution (typically one minute) so they give the best results for specific places [4].

Other systems use data collected from meteorological satellites, avoiding in this case problems with the measurement instruments being covered with frost, snow or dirt, pollution, and failure of the measurement device itself among others. Satellites are used to measure the radiation coming from the Earth's surface reflected from the ground or clouds, so the radiation absorbed and reflected by the atmosphere also needs to be taken into account.

Geostationary satellites take pictures of the Earth's surface every 15 or 30 minutes and in each pixel in the picture (which usually represents a few square kilometres) the solar radiation reaching the area can be estimated.

EBSCOhost - printed on 2/14/2023 2:46 PM via . All use subject to https://www.ebsco.com/terms-of-use

The spatial resolution can be increased with polar-orbiting satellites (which fly closer to the Earth's surface) but they can only take a few pictures a day of a particular area (so they have worse time resolution) [5]. Depending on the case study, one kind of satellite or the other would be desirable.

Furthermore, satellite methods also have special problems with snow on the ground looking like clouds in satellite images, areas with strongly varying altitude, like mountains, and places located at high latitudes.

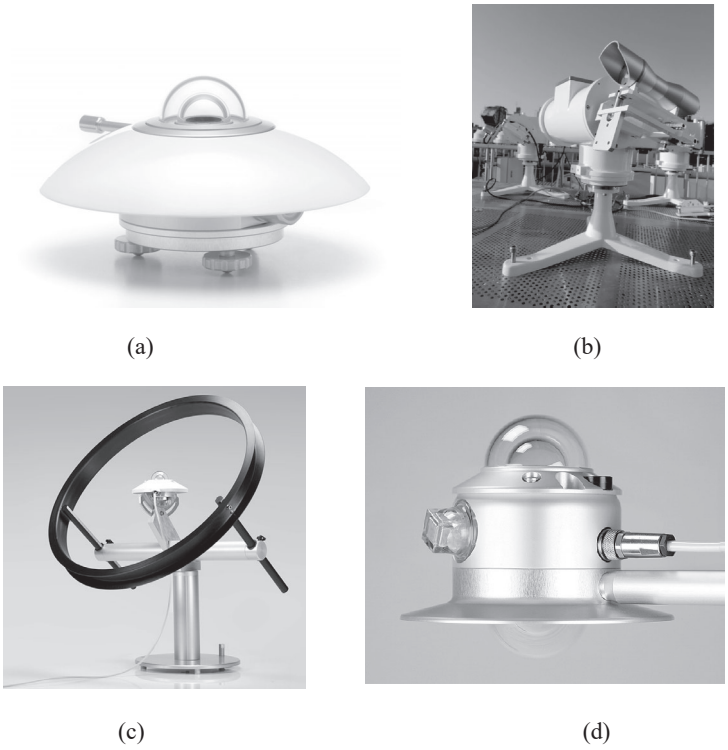
Obtaining systematic and reliable measures of solar potential at the surface is fundamentally important and not a trivial matter. Also, despite the increase over the last decade in climatological stations with the capacity to measure variables related to the magnitudes of solar irradiance in developed countries, the density of these stations is still very low due to the extent of the Earth's surface. To give an example, on average, ground stations in the United States in 2008 covered approximately 1% of the territory. The world average is estimated at 5%. Moreover, databases that record ground measures are not always complete, especially with regard to the measuring of the components of irradiance, due to the cost and difficulties of calibrating, operating and maintaining the equipment.

This leads directly to the need to develop and validate models or theories that allow us to estimate irradiance values from the available set of data, in the simplest and most precise way possible.

Whatever the measuring method it can be concluded that we do not dispose of direct measurements in every place at any time and we need to estimate irradiation values from measurements made nearby, using both spatial and time interpolations. Accurate solar models are mandatory for many applications including forecasting.

Furthermore, measuring solar irradiation is complex, requires expensive specific devices and there are a large number of areas, particularly in developing countries, where measurements are not available or are only available for short periods of time. In these cases, calculating monthly average daily radiation from other meteorological variables (such as temperature or humidity) has a particular interest.

EBSCOhost - printed on 2/14/2023 2:46 PM via . All use subject to https://www.ebsco.com/terms-of-use



(a) (b)

(c) (d)

Fig. 1. Commercial solar radiation measurement devices: (a) pyranometer, (b) pyrheliometer, (c) pyranometer with shadowband, and (d) albedometer.

## Modelling solar data

Many different models have been suggested to predict solar radiation [6], [7]. We can classify these models in four main groups, according to their main research purpose:

1. Models for irradiation forecasting from other climate variables.
2. Models for spatial interpolation.
3. Models for time interpolation. They can estimate the irradiance value of a shorter period of time from an aggregated measurement, e.g. hourly estimations from daily values.

EBSCOhost - printed on 2/14/2023 2:46 PM via . All use subject to https://www.ebsco.com/terms-of-use

4. Transposition models. These models allow the estimation of the irradiance components on a tilted and oriented surface from data from other surfaces (typically the horizontal).

The above-mentioned models can be more or less complex and use different sorts of input variables (see Table 1) [8]. The adaptation and reliability of these inputs to the case study help to achieve better or worse predictions.

**Table 1. Input parameters in solar models*.**

| Input type | Parameters |
|---|---|
| Astronomical factors | Year, month, day, UTC hour, declination, zenith, solar constant, extra-terrestrial irradiation, air mass. |
| Geographical factors | Latitude, longitude, height above sea level, albedo. |
| Meteorological surface factors | Air pressure, air temperature (dry bulb), relative humidity, wind speed. |
| Non-integral column meteorological factors | Ozone level, $NO_2$ level, precipitated water. |
| Atmospheric turbidity | Angstrom wavelength exponent, Angstrom turbidity, aerosol single-scattering albedo, Linke's turbidity, aerosol optic depth, visibility. |

* Not all the models use all the input parameters.

As can be seen in Figure 2, modelling solar irradiance on tilted (including vertical) surfaces requires several transformations and chains of models depending on the available model input data. Direct beam irradiance $B(n)$ can be estimated from the extraterrestrial irradiance value $B_{ext}(n)$, through the $\tau$ models which calculate the atmosphere's transmittance values on the horizontal surface. On the other hand, *kt* models correlate the extraterrestrial irradiance with the horizontal global irradiance and *kd* and *kb* models allow the evaluation of the diffuse and beam fractions respectively. Reflected irradiance on a given surface, $R(\theta,\gamma)$ is proportional to the albedo's reflectance $\rho$ and the horizontal global irradiance. The so-called "transposition models" transform global horizontal and diffuse horizontal irradiances into reflected and diffuse irradiances on any given plane (*Rd* and *Rr* values) tilted a zenith angle $\theta_{zp}$ and oriented an azimuth angle $\gamma_p$.

EBSCOhost - printed on 2/14/2023 2:46 PM via . All use subject to https://www.ebsco.com/terms-of-use

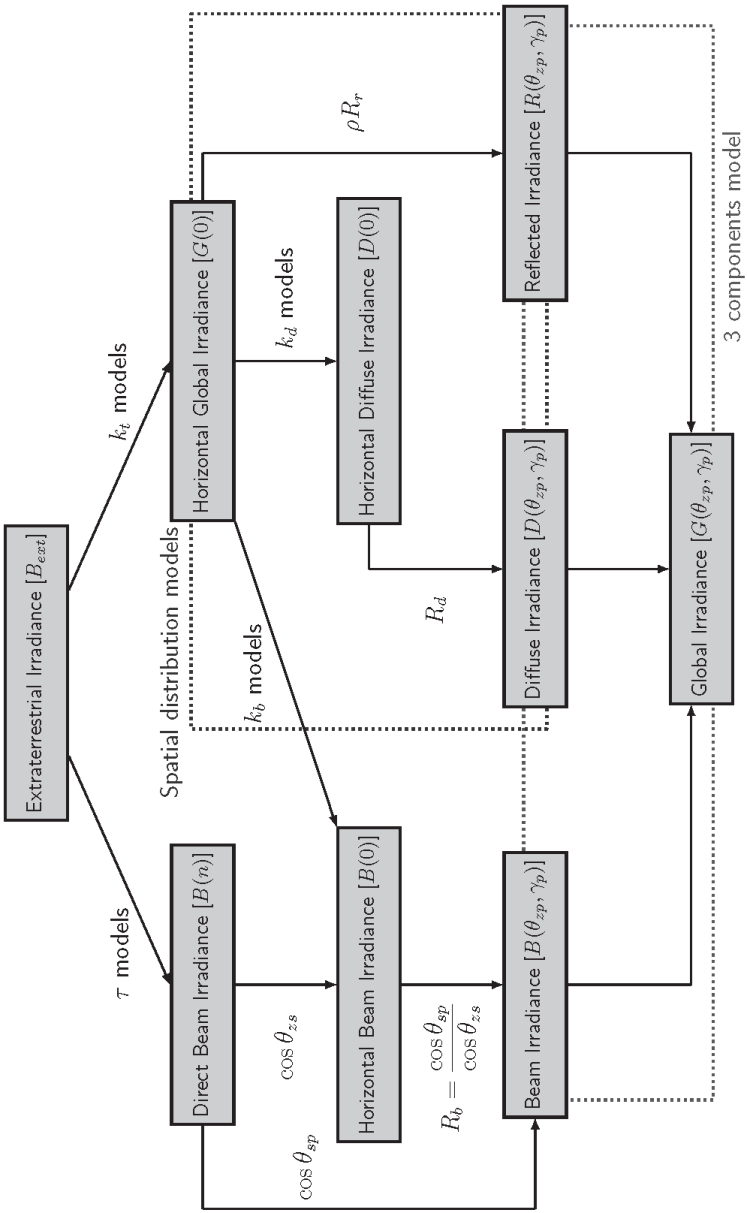



Fig. 2. Solar irradiance transposition modelling.

EBSCOhost - printed on 2/14/2023 2:46 PM via . All use subject to https://www.ebsco.com/terms-of-use

## Errors, uncertainties and problems

Many indicators can be used for calculating the accuracy of each model to compare predicted values with measured values in the case study, but two of them stand out among the others, the Mean Bias Error and the Root Mean Square Error [8]:

1. Mean Bias Error (MBE). It is defined as:

$$MBE = \frac{1}{\overline{m}}\left(\frac{1}{n}\sum_{i=1}^{n} e_i\right). \tag{1}$$

2. Root Mean Square Error (RMSE). It can be defined as:

$$RMSE = \frac{1}{\overline{m}}\sqrt{\frac{1}{n}\sum_{i=1}^{n} e_i^2}, \tag{2}$$

where:

$$\overline{m} = \frac{1}{n}\sum_{i=1}^{n} m_i, \tag{3}$$

$$e_i = c_i - m_i, \tag{4}$$

where $n$ is the number of compared elements, $c_i$ is the computed value (result from the model) and $m_i$ is the measured value.

The lower the MBE and the RMSE values the better the analysed model is. In general, it is accepted that a model has an accurate behaviour when:

$$abs(MBE) \le 10\% \quad or/and \quad RMSE \le 20\% \tag{5}$$

The RMSE value points to the short-term behaviour of the model, while the MBE value describes its long-term performance. We should highlight that a few differences of a high magnitude with regard to the reference values will significantly increase the RMSE. Conversely, overestimations can be cancelled out by underestimations in the MBE.

EBSCOhost - printed on 2/14/2023 2:46 PM via . All use subject to https://www.ebsco.com/terms-of-use

Moreover, neither the RMSE nor the MBE can provide a confidence interval to give significance to the model's predictions. Thus, in Eq. (6) the *t*-statistic is presented. It combines both statistical estimators and offers a confidence interval with a statistical significance of $\alpha$. However, this estimator is based on a very restrictive hypothesis contrast where the mean difference between the estimated and the reference values is assumed to be zero ($\mu = 0$). This estimator (see Eq. (7)) was redefined in terms of the value of such a difference, in order to avoid such a limiting restriction, and is now called $\mu_{1-\alpha}$. In this case, we took $\alpha = 0.01$. This estimator includes the sign of the MBE value, in order to analyse whether the proposed model tended either to overestimate (positive sign) or underestimate (negative sign).

$$t = \sqrt{\frac{(n-1)MBE^2}{RMSE^2 - MBE^2}}. \tag{6}$$

$$\mu_{1-\alpha} = sign(MBE)\left(|MBE| - t_{\alpha/2}\sqrt{\frac{RMSE^2 - MBE^2}{n-1}}\right). \tag{7}$$

Other common accuracy parameters are the coefficient of determination, and Willmott's index of agreement.

It should also be noted that most of the models use specific coefficients for a place and/or related to a particular average period. This fact makes the model only able to be applied in certain locations of similar climate and for a specific period. Otherwise, results cannot be compared. Some authors, like Hay, have developed global models with no dependence coefficients by studying multiple-reflection influence, but those methods require cloud albedo and surface data [9].

Furthermore, other authors, like Suehrcke, claim that global radiation and sunshine duration has an approximately quadratic relationship, and thus linear models are not appropriate for precise estimations [10].

## Main applications

Nowadays, climate change, the security of energy supply for industrial process, dependence on electronic devices and the economic recession have turned the energy sector into one of the most critical ones. In this particular case, renewable energy systems not depending on fossil fuels

EBSCOhost - printed on 2/14/2023 2:46 PM via . All use subject to https://www.ebsco.com/terms-of-use

can mean the difference between a successful society and an unsuccessful one. Therefore, studying solar potential as a renewable resource has become a key area of interest within energy planning.

Furthermore, the current implementation of Smart Grids and Smart Cities as a future trend of energy generation, distribution and model of consumption has made the prediction of energy production mandatory. An example of a Smart Grid scheme is shown in Figure 3.

In non-energy related fields, solar forecasting is also crucial, such as for example for planning crop campaigns, bioclimatic architecture designs [12], wind predictions in certain areas (sunshine heats the air mass heterogeneously), optimal electrical consumption in commercial buildings [13], among others.

## Conclusions

The relevance and need for accurate solar modelling in many fields, focusing on energy planning, has been widely observed. There is no doubt that an accurate model for solar prediction allows us to improve our design of energy systems.

Solar data can be modelled in order to estimate solar radiation from other climate variables and time prediction or, on the other hand, it can be modelled for spatial interpolation. Many models exist within different input parameters and accuracy values.

EBSCOhost - printed on 2/14/2023 2:46 PM via . All use subject to https://www.ebsco.com/terms-of-use

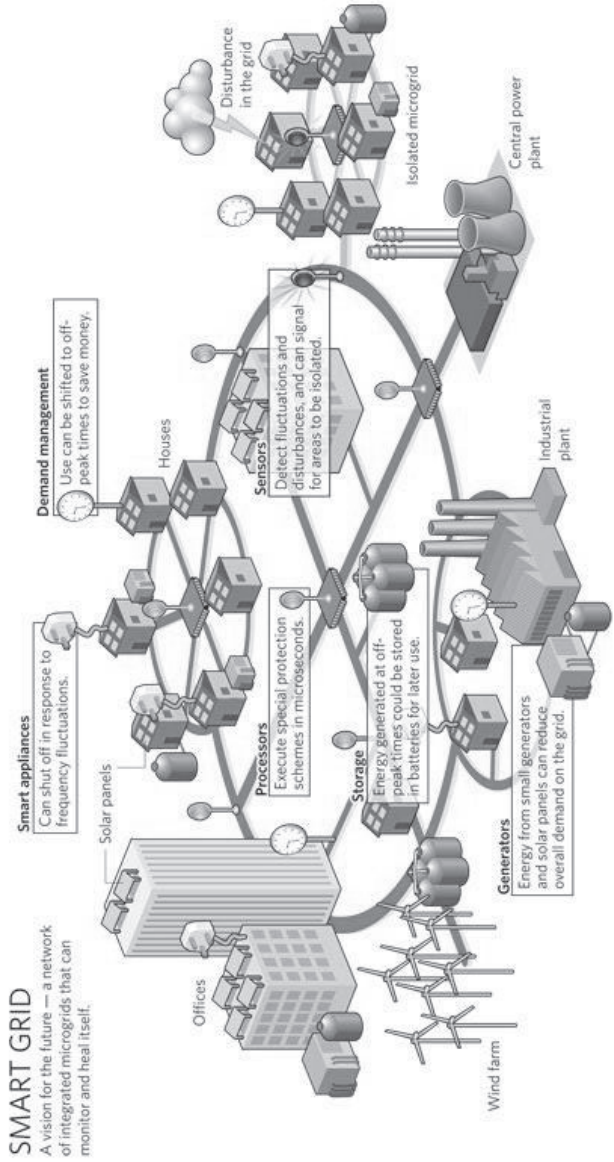



Fig. 3. Example of a Smart Grid scheme [11].

EBSCOhost - printed on 2/14/2023 2:46 PM via . All use subject to https://www.ebsco.com/terms-of-use

## Acknowledgements

This research received economic support from the Spanish Government (grant ENE2011-27511) and the Department of Culture and Education of the Regional Government of Castile and León (grant BU358A12-2).

## References

[1] M. De Carli and M. Tonon, "Effect of modelling solar radiation on the cooling performance of radiant floors," Solar Energy, vol. 85, pp. 689–712, 2011.
[2] C. Demain, M. Journée, and C. Bertrand, "Evaluation of different models to estimate the global solar radiation on inclined surfaces," Renewable Energy, vol. 50, pp. 710–721, 2013.
[3] "PVGIS solar radiation databases." [Online]. Available: http://re.jrc.ec.europa.eu/pvgis/apps4/databasehelp_en.html. [Accessed: 29-Oct-2012].
[4] "Pyranometer," Wikipedia, the free encyclopaedia. 22-Oct-2012.
[5] T. Huld, R. Müller, and A. Gambardella, "A new solar radiation database for estimating PV performance in Europe and Africa," Solar Energy, vol. 86, pp. 1803–1815, 2012.
[6] T. Khatib, A. Mohamed, and K. Sopian, "A review of solar energy modeling techniques," Renewable and Sustainable Energy Reviews, vol. 16, pp. 2864–2869, 2012.
[7] R. Yacef, M. Benghanem, and A. Mellit, "Prediction of daily global solar irradiation data using Bayesian neural network: A comparative study," Renewable Energy, vol. 48, pp. 146–154, 2012.
[8] V. Badescu, C. A. Gueymard, S. Cheval, C. Oprea, M. Baciu, A. Dumitrescu, F. Iacobescu, I. Milos, and C. Rada, "Computing global and diffuse solar hourly irradiation on clear sky. Review and testing of 54 models," Renewable and Sustainable Energy Reviews, vol. 16, no. 3, pp. 1636–1656, 2012.
[9] J. E. Hay, "Calculation of monthly mean solar radiation for horizontal and inclined surfaces," Solar Energy, vol. 23, no. 4, pp. 301–307, 1979.
[10] H. Suehrcke, "On the relationship between duration of sunshine and solar radiation on the earth's surface: Angstrom's equation revisited," Solar Energy, vol. 68, no. 5, pp. 417–425, 2000.
[11] "What is the Smart Grid? - Energy Informative," Energy Informative. [Online]. Available: http://energyinformative.org/what-is-the-smart-grid/. [Accessed: 30-Oct-2012].
[12] E. Giancola, C. Sanjuan, E. Blanco, and M. R. Heras, "Experimental assessment and modelling of the performance of an open joint ventilated façade during actual operating conditions in Mediterranean climate," Energy and Buildings, vol. 54, no. 0, pp. 363–375, Nov. 2012.
[13] C. Tíba and S. S. Leal, "Measuring and modelling illuminance in the semi-arid Northeast of Brazil," Renewable Energy, vol. 48, pp. 464–472, 2012.

EBSCOhost - printed on 2/14/2023 2:46 PM via . All use subject to https://www.ebsco.com/terms-of-use

# CHAPTER FIVE

# THE IMPORTANCE OF CELL TEMPERATURE IN MODELLING THE ENERGY EFFICIENCY OF PV MODULES

SÉBASTIEN JACQUES[1]

## Abstract

This chapter deals with a simplified, meaningful thermal model to calculate photovoltaic (PV) cell temperature, which is of utmost importance in determining the electrical energy efficiency of PV modules. This model, which has been applied to standard PV modules (or Glass/Backsheet solar panels), takes into consideration ambient temperature, incident irradiance, and wind speed. A complete experimental database was built to calibrate this model. The results of the thermal modelling provide a heat transfer coefficient law, which may be implemented in a PV simulation tool. Two key elements of this approach can be highlighted. The results enable better calculation of the electrical energy production of PV modules and help to predict the energy efficiency of PV units.

**Keywords**: Cell temperature; thermal modelling; PV module; energy efficiency prediction.

## Introduction

Photovoltaic (PV) power plants currently offer ground-breaking solutions to the challenges of energy transition. PV systems may be designed in many configurations, including: standalone or grid-connected;

[1] University of Tours, GREMAN CNRS INSA Centre Val-de-Loire UMR 7347, 7 avenue Marcel Dassault, 37200 Tours, France. Email: sebastien.jacques@univ-tours.fr

EBSCOhost - printed on 2/14/2023 2:46 PM via . All use subject to https://www.ebsco.com/terms-of-use

fixed or tracking; and flat plate or concentrator operation [1]. At the moment, many simulation tools, market orientated and academic, such as PVsyst, can be used to define a baseline for sizing a PV unit [2], [3]. The main objective is to evaluate the technical performance of a PV unit through estimation of its annual energy yield, array yield, reference yield, and system losses [4].

The PV module is one of the key elements in sizing a PV power plant. In particular, it is of utmost importance to minimize the losses caused by its operating cell temperature ($T_{cell}$). The energy efficiency of the crystalline silicon cell technology used (i.e., monocrystalline or polycrystalline), which is one of the most popular silicon solar cell families, strongly depends on the $T_{cell}$-parameter. S. Chander et al. recently reported that the relative change in PV parameters with temperature can be found between –0.0025/°C and –0.0022/°C for open circuit voltage, and 0.002/°C, –0.0013/°C, and –0.002/°C for short circuit current, fill factor, and maximum output power, respectively [5].

The $T_{cell}$-parameter is not only dependent on total irradiance, but is also related to weather conditions to an extent that has yet to be fully assessed. In particular, the influence of ambient temperature, relative humidity, wind direction, and wind speed need to be more thoroughly studied [6]. Gaglia et al. have recently provided some initial responses. In particular, they have highlighted that PV temperature mainly depends on air temperature and solar irradiance, and less so on wind speed [7]. However, wind speed, which is often neglected because of a lack of detailed data, may especially have an impact on large scale PV systems (higher than 100 kWp) in so far as the modules are exposed to convective heat transfer on both sides [8].

This chapter discusses the relevance of a simplified thermal model used to analyse the influence of the $T_{cell}$-parameter on the energy efficiency of a PV module. The study is particularly focused on silicon cells assembled in a Glass/Backsheet solar panel. This kind of assembly is also known as a standard PV module. The results of cell temperature modelling may be input into PV simulation tools to better predict the overall performance, in terms of energy efficiency, of a PV power plant.

This chapter, which is a revised version of an article presented at the International Conference on Renewable Energies and Power Quality (ICREPQ 2013), is divided into 3 sections [9]. The first one explains the methodology used in calculating the cell temperature through thermal modelling of a standard PV module. The second one describes the experimental procedure to calibrate the model. The final section discusses the relevance of such an approach with reference to the simulation results of 2 PV units (i.e., 2.6 kWp and 7.9 kWp). An in-house PV simulation tool

EBSCOhost - printed on 2/14/2023 2:46 PM via . All use subject to https://www.ebsco.com/terms-of-use

based on the MATLAB development environment was used. The results are compared to those given by commercial software to highlight the robustness of this thermal model.

## Simplified Modelling of Cell Temperature

### *Standard PV Module Thermal Modelling*

Standard PV modules, also called Glass/Backsheet PV modules, are still widely used in contemporary solar applications [10], [11]. As can be seen in Figure 1, this kind of module is composed of several materials. A tempered sheet of glass is used at the front (with a thickness of between 2 to 4 mm). This material must have low reflective properties. Monocrystalline or polycrystalline PV cells are wired up in series and/or in parallel depending on the electrical ratings of the solar panel. EVA (ethylene vinyl acetate) is the polymer most often used to encapsulate these PV cells to ensure good insulation and durability. The EVA layer on top of the solar cell, must have excellent transmittance (higher than 90%). On the backside of the PV cells, a high transparency EVA layer (with a thickness of about 0.45 mm) is used. This kind of material allows a significant amount of sunlight to pass through. It also creates more aesthetically pleasing solar panels for mass-market applications, such as greenhouses and carports. A fluoropolymer backsheet is then used. The backing plate is generally composed of a Tedlar® PVF (polyvinyl fluoride) film (with a typical thickness of between 0,025 mm and 0,050 mm) because of its optimal balance of properties in terms of weather resilience, adhesion, and mechanical strength warranting a long PV module lifetime. All these materials are assembled within an aluminium supporting structure.

It is important to note that frameless double-glass PV modules have recently emerged, mainly to achieve a significant cost reduction [12]. This kind of solar panel is composed of a layer of glass, an encapsulating material at the topside of the PV cells, the solar cells, an encapsulating material at the backside of the PV cells, and another layer of glass. The methodology described in this chapter to model cell temperature can be adapted to this PV module technology.

EBSCOhost - printed on 2/14/2023 2:46 PM via . All use subject to https://www.ebsco.com/terms-of-use

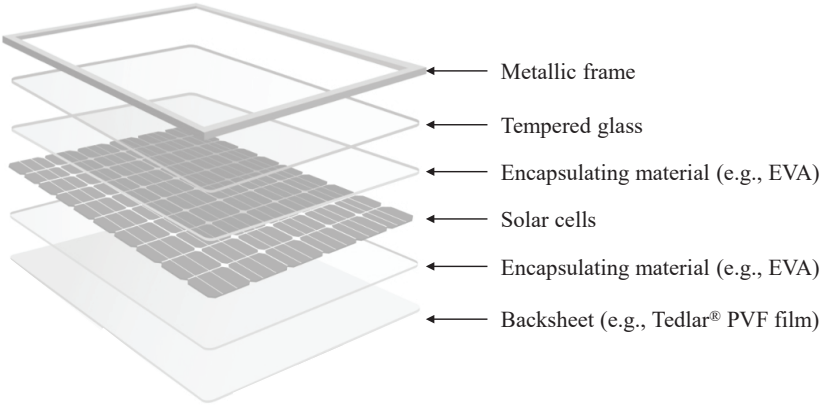



Figure 1. Cross-sectional view of a Glass/Backsheet PV module

A simplified approach for modelling the thermal behaviour of the Glass/Backsheet module (i.e., its cell temperature) in a steady-state is described here. It should be noted that the time to reach an equilibrium is not taken into consideration. In the case of transient modelling, the temperature behaviour must be simulated using several thermal resistance-thermal capacitance networks where each network corresponds to one material of the PV module assembly.

As can be seen in Figure 2, the thermal model of a Glass/Backsheet PV module is assumed to be symmetrical with the encapsulated solar cells [13]. Heat flow (Φ) is generated by thermal conduction. As a consequence, each material of the assembly has a conductive thermal resistance ($R_{th}$), which can be calculated from its physical properties (i.e., length [$l$] of the material through which heat must travel; area [$S$] of the surface conducting heat; thermal conductivity [$k$] of the material). The front side and back side of the solar panel are subjected to air-flow. Therefore, a convective thermal resistance ($R_h$) can be determined to complete the $T_{cell}$-parameter modelling. The $R_h$-parameter depends on the heat transfer coefficient ($h$), which is a key parameter to be determined. To sum up, as described in Equation (1), the cell temperature can readily be expressed as a function of: the ambient temperature ($T_a$); the conductive and convective thermal resistances (i.e., $R_{th}$ and $R_h$); the area ($A$) of contact between the PV module and ambient air; and heat flow (Φ).

$$T_{cell} = T_a + \left(R_{th} + R_h\right) \cdot \Phi \qquad (1)$$

EBSCOhost - printed on 2/14/2023 2:46 PM via . All use subject to https://www.ebsco.com/terms-of-use

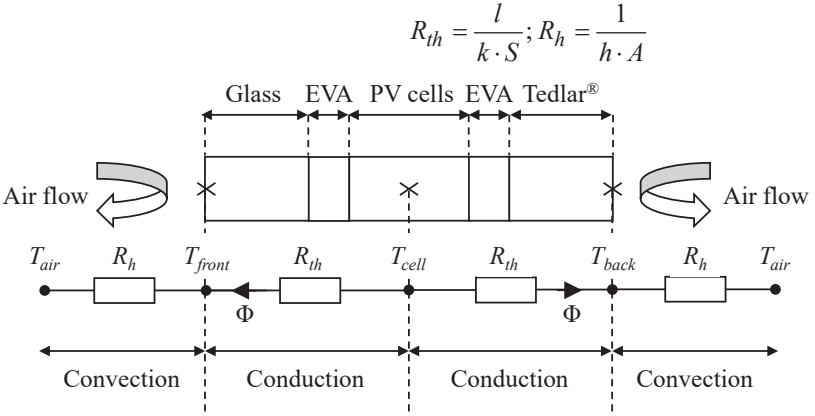



Figure 2. Simplified one-dimensional thermal modelling of a Glass/Backsheet PV module

## *Methodology to Calculate Cell Temperature*

The calculation of the $T_{cell}$-parameter is based on the NOCT (nominal operating cell temperature) coefficient. This value is often used by PV module manufacturers to compare the performance of various solar panel designs in the same conditions (i.e., incident solar radiation of 800 W/m$^2$; ambient temperature of 20 °C; wind speed of 1 m/s on both front and back surfaces of the solar panel; tilt angle of the PV module of 45°) [14], [15].

Equation (2) gives the heat balance in open-circuit conditions for both the NOCT and operating conditions. From Equation (1) and Equation (2), it is now possible to write the heat balance according to the thermal modelling of the PV module (see Equation (3)). In this equation, the cell temperature depends particularly on the heat transfer coefficient ($h$). This parameter can be determined as a function of real conditions i.e., such as the wind speed ($w$). It is a matter of both experimentally extracting the $h(w)$ relationship and comparing the values with the ones in the literature.

$$T_{cell} = T_a + \left( \frac{NOCT - 20}{800} \right) \cdot G_{inc} \tag{2}$$

where $G_{inc}$ is the in-plane tilted irradiance.

EBSCOhost - printed on 2/14/2023 2:46 PM via . All use subject to https://www.ebsco.com/terms-of-use

$$T_{cell} = T_a + \left( \frac{NOCT - 20}{800} \right) \cdot G_{inc} \cdot \frac{R_{th} + R_{h(w)}}{R_{th} + R_{h_{NOCT}}} \quad (3)$$

where: $R_{th}$ is the thermal resistance of the solar panel in conduction mode; $R_{h(w)}$ and $R_{hNOCT}$ are the convective thermal resistances of the PV module depending on the wind speed and under the NOCT conditions, respectively

## Model Validation using an Experimental Calibration

### *Experimental Environment*

Figure 3 shows the experimental environment. A monocrystalline PV module (Schüco MPE 175 MS 05) with a rated peak power of 175 Wp was used for the measurements. A data acquisition system (Expert Key 100L, Delphin Technology) was optimally networked by Ethernet. Many reference temperatures were monitored and stored using the ProfiSignal software tool. Several T-type thermocouples were used. 6 thermocouples were fixed on the front and back sides of the PV module. Two other thermocouples were placed in direct contact with the PV cells to measure the $T_{cell}$-parameter. Finally, 2 thermocouples were used to measure the ambient temperature. A pyranometer (with its tilt angle equal to 35°) was directly mounted on the solar panel. This equipment was used to measure the global incident solar radiation on the surface of the PV module. It is important to note that this pyranometer was previously calibrated with a standard pyranometer in line with the measurements specified by the manufacturer (7 μV/(kW.m$^2$)). The relative wind speed was measured using an anemometer (rotary magnet), which was fitted with a wind vane to check the wind direction. A reed switch was arranged in the plane of the magnet. Its role was to emit an electrical pulse every time the magnet passed over. The signals (frequency and voltage proportional to the rotation angle) from the wind vane were analysed by the data acquisition system. A wind tunnel was used to set a constant wind speed (the maximum speed value was equal to 40 km/h). An airy screen was also set up to protect the PV module against moderate breezes. It is important to note that all the real experimental tests were done on sunny days with a particular focus on the evolution of the ambient temperature. Indeed, this had to be as stable as possible so as not to interfere with data acquisition.

From the equations previously described, the *h*-parameter can be deduced from the measurements.

EBSCOhost - printed on 2/14/2023 2:46 PM via . All use subject to https://www.ebsco.com/terms-of-use

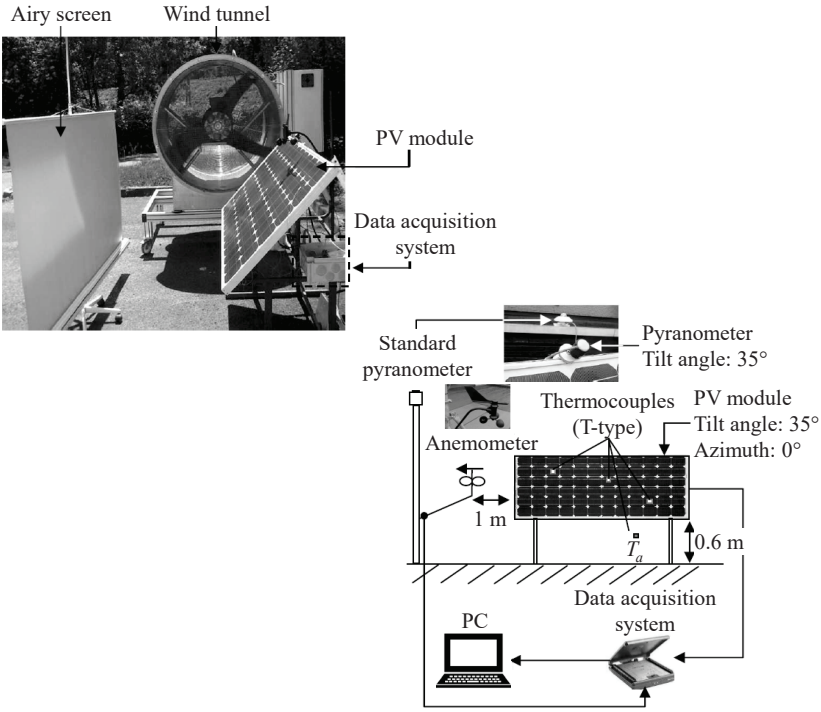



Figure 3. Experimental environment

## *Extraction of the Heat Transfer Coefficient*

A number of sets of measurements were performed over many weeks thanks to favourable weather conditions (i.e., incident solar radiation of 800 W/m$^2$; ambient temperature higher than 20 °C; negligible breezes). The speed of the wind tunnel was adjusted from 1 km/h to 30 km/h.

Fig. 4 shows the evolution of the *h*-parameter as a function of wind speed. The results highlight a linear change. The confidence boundaries are visible on the graph. In particular, the median value of the $h_{NOCT}$-parameter at 3.6 km/h, i.e. under the NOCT conditions (wind speed of 1 m/s), is about 16.7 W/(m$^2$.K). This value is close to what can be found in the literature (between 15 W/(m$^2$.K) and 20 W/(m$^2$.K)) [16], [17].

EBSCOhost - printed on 2/14/2023 2:46 PM via . All use subject to https://www.ebsco.com/terms-of-use

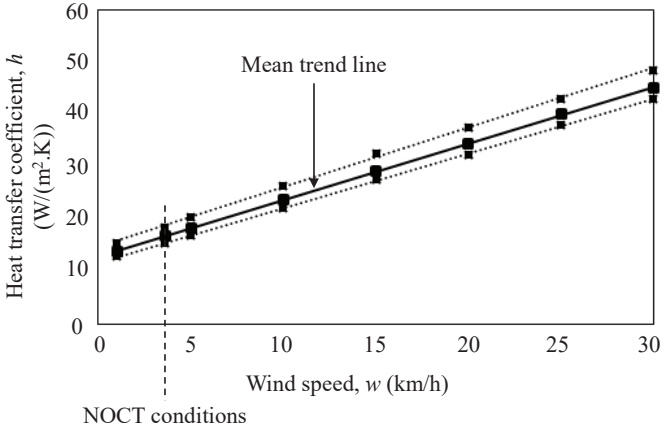



Figure 4. Heat transfer coefficient evolution in relation to wind speed

## Main Results and Discussion

### *Model Implementation in a PV Software Tool*

The previous results of the thermal modelling were directly implemented in the PVLab software tool. This tool has been developed recently to offer users a highly flexible PV simulator [2]. As can be seen in Figure 5, PVLab, which is based on the MATLAB development environment, allows users to personalize various models (i.e., optical, electrical, and thermal) and databases (i.e., the PV components such as inverters, solar panels, and, above all, meteorological databases). Therefore, many parameters can be changed—this is especially relevant for wind speed. It undeniably has added value, because existing marketed or free PV simulators cannot provide such capabilities (those simulation tools are most often distributed in the form of executable programs). To sum up, the main purpose of the PVLab simulator is to gain a better understanding of the impact of the various models and databases both on the production of electrical energy and the efficiency of PV power plants.

Hay's equations are used to calculate the global and diffuse solar irradiance on tilted planes like solar panels [18].

The electrical modelling of a PV module (see Fig. 6 and Equation (4)) is commonly described as a single-diode equivalent circuit including the influence of the serial and shunt resistances [19].

For the thermal modelling, the evolution of the *h*-parameter in relation to wind speed (see Figure 4) was used as a key input for the simulator.

EBSCOhost - printed on 2/14/2023 2:46 PM via . All use subject to https://www.ebsco.com/terms-of-use

This is a big improvement on commercial or free PV simulators, such as PVsyst. The latter, in particular, uses the global heat balance approach to calculate cell temperature. Such an approach considers the heat transfer coefficient to be constant. As such, the NOCT method described in this chapter allows for a more thorough analysis of the energy efficiency of PV modules.

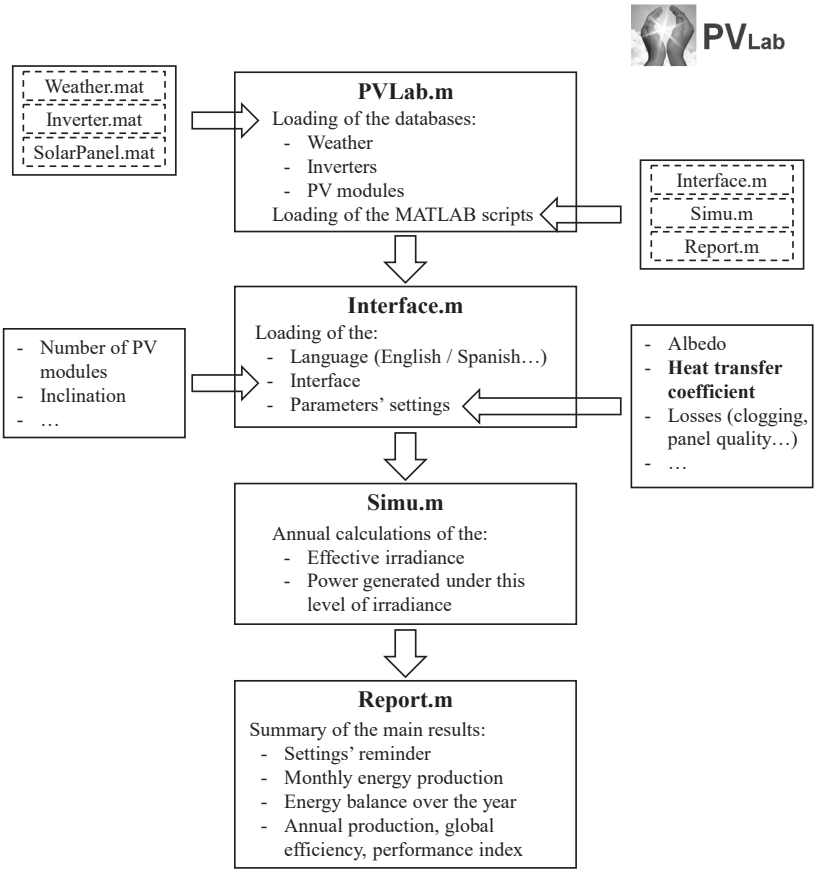



Figure 5. Global architecture of the PVLab simulation tool

EBSCOhost - printed on 2/14/2023 2:46 PM via . All use subject to https://www.ebsco.com/terms-of-use

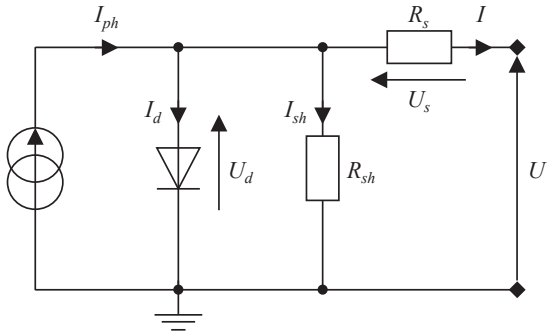



Figure 6. Single-diode equivalent circuit modelling

$$I = N_p I_{ph} - N_p I_0 \cdot \left( e^{\frac{\alpha}{N_s} \cdot \left( U + \frac{N_s}{N_p} R_s I \right)} - 1 \right) - \frac{U + \frac{N_s}{N_p} R_s I}{\frac{N_s}{N_p} R_{sh}} \quad (4)$$

where: $N_p$ and $N_s$ are the number of PV cells connected in parallel and in series, respectively; $I_{ph}$ is the photocurrent; $I_0$ is the saturation current; α is the absorption coefficient

## *Case Studies, Main Results, and Discussion*

The yearly electrical energy production of 2 medium PV plant configurations (i.e., 2.6 kWp and 7.9 kWp) was computed using PVLab. First of all, the results produced by PVLab were compared with those produced by PVsyst, using the same input data. The aim was to confirm the utility of PVLab. The influence of wind speed on solar energy production for one PV unit (i.e., 2.6 kWp) and using PVLab, is discussed.

For the simulation settings, the meteorological data (from the Meteonorm database), recorded in Tours (47°23'38" N; 0°41'48" E), France, were used. Polycrystalline PV modules (Solar World SW220; peak rated power of 220 Wp) were used. The tilt angle of each solar panel was equal to 30°. Each grid-connected system used an inverter: the SMA Sunny Boy SB3300 (nominal AC output of 3.3 kW), and the SMA Sunny Mini Central 9000TL (nominal AC output of 9 kW), for the 2.6 kWp and 7.9 kWp PV installations, respectively. It is important to note that PVLab and PVsyst were run using the same mechanical and electrical databases to characterize the PV modules and inverters.

EBSCOhost - printed on 2/14/2023 2:46 PM via . All use subject to https://www.ebsco.com/terms-of-use

Table I summarizes the simulation results for the first case study (i.e., the comparison between PVLab and PVsyst). The data show that the 2 PV simulation tools give approximately the same results (with a relative difference of about 1%), whatever the nominal power of the medium PV plant. For instance, for the PV unit with a nominal power of 2.6 kWp, the values of the yearly electrical energy production predicted by PVLab and PVsyst equalled 3,202 kWh and 3,239 kWh, respectively. All these simulation results confirm the relevance of PVLab in comparison to PVsyst, which is still a top simulator in the photovoltaic sector.

**Table I: Simulation results for the first case study. Comparison between PVLab and PVsyst**

| Nominal power (kWp) of the PV unit | Yearly electrical energy production (kWh) predicted by PVLab | Yearly electrical energy production (kWh) predicted by PVsyst | Relative difference (%)– PVLab vs. PVsyst |
|---|---|---|---|
| 2.6 | 3,202 | 3,239 | – 1.1 |
| 7.9 | 9,516 | 9,658 | – 1.2 |

In the preceding data, the wind speed (i.e., 1 m/s) was constant as described in the standard operating conditions [15]. This value is fixed in the PVsyst software tool without the ability to change it. As such, when using PVsyst it is not possible to study the influence of wind speed on the energy efficiency of PV modules. The versatility of the PVLab simulator was intended to provide partial answers to resolve this issue.

In a second case study, the influence of wind speed was taken into consideration through analysis of the *h*-parameter, as described in the previous sections. The study was performed on the PV unit with a nominal power of 2.6 kWp. Table II sums up the main results. The yearly electrical energy production predicted by PVLab slightly increases when the wind speed increases. For example, this increase is about 4% when the wind velocity rises from 1 m/s to 10 m/s. Even if those results confirm that wind speed is not the primary factor in electrical energy production, this parameter might have a greater impact on large scale PV plants.

EBSCOhost - printed on 2/14/2023 2:46 PM via . All use subject to https://www.ebsco.com/terms-of-use

**Table II: Simulation results for the second case study. Impact of wind speed on the yearly electricity production of a PV unit (2.6 kWp)**

| Wind speed (m/s) | Yearly electrical energy production (kWh) predicted by PVLab | Relative difference (%) vs. wind speed of 1 m/s |
|---|---|---|
| 1.0 | 3,202 | 0.0 |
| 2.0 | 3,250 | + 1.5 |
| 5.0 | 3,298 | + 3.0 |
| 10.0 | 3,330 | + 4.0 |
| 15.0 | 3,346 | + 4.5 |

## Conclusions

This chapter has highlighted the relevance of a simplified thermal model for a PV module to calculate its cell temperature from irradiance, ambient temperature, and wind speed. This thermal model has been applied to Glass/Backsheet solar panels, which are still widely used in modern PV units. Several measurements in real operating conditions were performed to calibrate the model.

The results of the experimental procedure show that the heat transfer coefficient increases linearly with wind speed. More specifically, these results include the value specified in the standard operating conditions (i.e., between 15 W/($m^2$.K) and 20 W/($m^2$.K)) at a wind speed of 1 m/s. Most importantly, the heat transfer coefficient is not constant, unlike that which is currently implemented in commercial or free PV software tools, such as PVsyst.

All these results were input into an in-house PV simulation tool, named PVLab, which is based on the MATLAB development environment. PVLab is a powerful, adaptable PV simulator that allows the user to modify its internal models (i.e., optical, electrical, and thermal models) and databases (i.e., meteorological data, and PV components such as PV modules and inverters).

Two case studies were simulated using PVLab and PVsyst.

EBSCOhost - printed on 2/14/2023 2:46 PM via . All use subject to https://www.ebsco.com/terms-of-use

The first one consisted of estimating the yearly electrical energy production of 2 medium PV plant configurations (i.e., 2.6 kWp and 7.9 kWp). In the same configurations, PVLab and PVsyst give approximately the same results. As such, the utility of PVLab as a simulator has been proven.

The second one consisted in obtaining a better understanding of the influence of wind speed on the yearly electrical energy production of a medium PV unit (i.e., 2.6 kWp). PVLab had to be used here because PVsyst does not offer the possibility of changing this parameter. The simulation results showed that the yearly electrical energy production predicted by PVLab does not increase significantly when the wind speed increases. Even if those results confirmed that wind speed is not the primary factor in electrical energy production, this parameter might be of significant interest in large scale PV plants.

## References

[1] Pearsall, N. M. "Introduction to photovoltaic system performance." In *The Performance of Photovoltaic (PV) Systems–Modelling, Measurement and Assessment*, edited by Nicola Pearsall. Elsevier, Amsterdam: Woodhead Publishing, 2017.

[2] Jacques, S. et al. "PVLab, a Powerful, Innovative Software Package for the Simulation of Photovoltaic Systems." *Journal of Energy and Power Engineering* 8 (October 31, 2014): 1712. Accessed June 5, 2018. doi: 10.17265/1934-8975/2014.10.008

[3] Kumar, N. M. et al. "Performance analysis of 100 kWp grid connected Si-poly photovoltaic system using PVsyst simulation tool." *Energy Procedia* 117 (June 2017): 180. Accessed June 5, 2018. doi: 10.1016/j.egypro.2017.05.121

[4] Kumar, B. S.; Sudhakar, K. "Performance evaluation of 10 MW grid connected solar photovoltaic power plant in India." *Energy Reports* 1 (November 2015): 184. Accessed June 5, 2018. doi: 10.1016/j.egyr.2015.10.001

[5] Chander, S. et al. "A study on photovoltaic parameters of mono-crystalline silicon solar cell with cell temperature." *Energy Reports* 1 (April 2015): 184. Accessed June 5, 2018. doi: 10.1016/j.egyr.2015.03.004

[6] Kaushik, S. C.; Rawat, R.; Manikandan S. "An innovative thermodynamic model for performance evaluation of photovoltaic systems: Effect of wind speed and cell temperature." *Energy Conversion and Management* 136 (March 15, 2017): 152. Accessed June 5, 2018. doi: 10.1016/j.enconman.2017.01.011

[7] Gaglia, A. G. et al. "Energy efficiency of PV panels under real outdoor conditions–An experimental assessment in Athens, Greece." *Renewable Energy* 101 (February 2017): 236. Accessed June 5, 2018. doi:

EBSCOhost - printed on 2/14/2023 2:46 PM via . All use subject to https://www.ebsco.com/terms-of-use

10.1016/j.renene.2016.08.051
[8] Messenger, Roger A.; Abtahi, Amir. *Photovoltaic Systems Engineering*, Fourth Edition. Boca Raton: CRC Press, 2017.
[9] Jacques, S. et al. "Impact of the cell temperature on the energy efficiency of a single glass PV module: thermal modelling in steady-state and validation by experimental data." In: Proceedings of the International Conference on Renewable Energies and Power Quality (ICREPQ 2013), Bilbao, Spain, March 20-22, 2013. doi: 10.24084/repqj11.281
[10] Quansah, D. A. et al. "Reliability and Degradation of Solar PV Modules–Case Study of 19-Year-Old Polycrystalline Modules in Ghana." *Technologies* 5 (May 2017): 22. Accessed June 6, 2018. doi: 10.3390/technologies5020022
[11] Luo, W. et al. "A comparative life-cycle assessment of photovoltaic electricity generation in Singapore by multicrystalline silicon technologies." *Solar Energy Materials and Solar Cells* 174 (January 2018): 157. Accessed June 6, 2018. doi: 10.1016/j.solmat.2017.08.040
[12] Tang, J. et al. "The Performance of Double Glass Photovoltaic Modules under Composite Test Conditions." *Energy Procedia* 130 (September 2017): 87. Accessed June 6, 2018. doi: 10.1016/j.egypro.2017.09.400
[13] Romary, F. et al. "Thermal Modelling to Analyze the Effect of Cell Temperature on PV Modules Energy Efficiency." In: Proceedings of the 2011 14th European Conference on Power Electronics and Applications (EPE 2011), Birmingham, UK, August 30-September 1, 2011.
[14] Bharti, R.; Kuitche, J.; TamizhMani, M. G. "Nominal Operating Cell Temperature (NOCT): Effects of module size, loading and solar spectrum." In: Proceedings of the 34th IEEE Photovoltaic Specialists Conference (PVSC 2009), Philadelphia, PA, USA, June 07-12, 2009. doi: 10.1109/PVSC.2009.5411408
[15] Lasnier, France. *Photovoltaic Engineering Handbook*. New-York: IOP Publishing Ltd 1990, 2017.
[16] Armstrong, S.; Hurley, W. G. "A thermal model for photovoltaic panels under varying atmospheric conditions." *Applied Thermal Engineering* 30 (August 2010): 1488. Accessed June 11, 2018. doi: 10.1016/j.applthermaleng.2010.03.012
[17] Kaplani, E.; Kaplanis, S. "Thermal modelling and experimental assessment of the dependence of PV module temperature on wind velocity and direction, module orientation and inclination." *Solar Energy* 107 (September 2014): 443. Accessed June 11, 2018. doi: 10.1016/j.solener.2014.05.037
[18] Mubarak, R. et al. "Comparison of Modelled and Measured Tilted Solar Irradiance for Photovoltaic Applications." *Energies* 10 (October 2017): 1688. Accessed June 12, 2018. doi: 10.3390/en10111688
[19] Rhouma, M. B. H. et al. "A simple method for extracting the parameters of the PV cell single-diode model." *Renewable Energy* 113 (December 2017): 885. Accessed June 12, 2018. doi: 10.1016/j.renene.2017.06.064

EBSCOhost - printed on 2/14/2023 2:46 PM via . All use subject to https://www.ebsco.com/terms-of-use

# CHAPTER SIX

# A COST-EFFECTIVE MICROCONTROLLER-BASED SENSOR FOR DUAL AXIS SOLAR TRACKING

SAMEER D. MESHRAM[1]

## Abstract

The energy crisis is one of the most important issues in today's world. Conventional energy resources are limited and are one of the primary drivers of pollution and global warming. As a result, the use of renewable energy is becoming increasingly popular. Solar energy is rapidly gaining ground as an important means of expanding renewable energy use. Solar tracking is employed to maximize the solar radiation collection capacity of a photovoltaic panel. In this article, we present the design, fabrication, and testing of an active dual axis closed loop solar tracking sensor. The compactness of the design facilitates its easy mounting and use on any surface or place exposed to solar irradiance. The solar irradiance is detected by an organic photovoltaic cell (OPV), which scans the sky for the maximum power point. The tracker stops operation at night and has provisions for nocturnal return of the panel(s) too. This system is independent with respect to the geographical location of the solar panel(s); diurnal and seasonal variations; and it is also scalable. The operation of the system is independent with respect to the initial configuration and the starting conditions. Experimental testing of the set-up agrees with true sun coordinates with a satisfactory degree of accuracy. This work can be extended to reduce the scanning time of the sensor.

**Keywords**: Solar sensor; dual axis; closed loop tracking; microprocessor-based; cost effective; organic photovoltaic cell (OPV).

---

[1] University of Washington—Seattle, Department of Mechanical Engineering, WA 98195, USA. Email: meshrams@uw.edu.

EBSCOhost - printed on 2/14/2023 2:46 PM via . All use subject to https://www.ebsco.com/terms-of-use

## Nomenclature

| | |
|---|---|
| $\alpha$ | Altitude angle, ° |
| $\beta$ | Inclination angle, ° |
| $\gamma_c$ | Surface azimuth angle, ° |
| $\gamma_s$ | Solar azimuth angle, ° |
| $\delta$ | Solar declination angle, ° |
| $\theta$ | Incidence angle, ° |
| $\varphi$ | Local latitude, ° |
| $\omega$ | Local hour angle, ° |
| *FF* | Fill factor |
| *PCE* | Power conversion efficiency |
| $V_{OC}$ | Open circuit voltage, V |
| $I_{SC}$ | Short circuit current, A |
| *OPV* | Organic photovoltaic |
| *LDR* | Light dependent resistor |
| *CCD* | Charge-coupled device |
| *IDE* | Integrated development environment |
| *MPP* | Maximum power point |

## Introduction

Energy is a primary factor in the socio-economic development of any nation. About 82% of the total energy consumption of the world comes from fossil fuels [1, 2]. Solar energy harvesting is becoming increasingly important as the cost and environmental impact of our non-renewable energy sources has become ever more apparent. Solar radiation is one of the most important renewable sources of energy (others include waterpower, wind, biomass, and geothermal energy). The source of solar radiation is the ongoing nuclear fusion reactions in the Sun's core and is practically inexhaustible—the Sun has a predicted life span of 5 billion more years [3]. The annual energy input of solar irradiation on the earth (5% ultraviolet, 43% visible, and 52% infrared) exceeds the world's yearly consumption by a factor of several thousand [4]. As such, photovoltaic (PV) cells are one of the most promising devices for converting solar energy into electricity.

Solar photovoltaic systems have been in development since the late 1800s when Charles Fritts built a 30 $cm^2$ cell from Selenium and Gold (1883) [5]. In 1954, Chaplin et al. demonstrated solar cells based on P-N junctions with an efficiency of 5-6 %. Recent research has reported a peak

EBSCOhost - printed on 2/14/2023 2:46 PM via . All use subject to https://www.ebsco.com/terms-of-use

efficiency of around 46% under standard testing conditions[2] [6] with an average efficiency of around 10-25%.

The power output of a given photovoltaic cell depends on its operating temperature, irradiance, and the incident angle of solar radiation [7]. Not much control can be achieved over the first two parameters for a given cell, as they are primarily a function of geographical location. On the other hand, the output of a PV cell can be substantially increased by a solar tracker, which ensures that the angle of incidence of sunlight is normalized (perpendicular) to the PV cell. Although not essential, a solar tracker can boost collected energy by 10-100% depending on the time of day time and geographical location [8]. Another study has reported that single axis trackers improve efficiency by up to 40% [9]. Furthermore, tests have shown that dual axis trackers improve efficiency by almost 50% (35 to 42% by east-west trackers and 5 to 8% by north-south trackers) [10].

An ideal solar tracker should compensate for both changes in altitude (seasonal changes) and the azimuth angle of the Sun—as pointed out by Clifford et al [6]. Additionally, there must be provision for nocturnal return of the solar panel to align with the next day's sunrise and help reduce energy losses during the early hours of sunshine.

Initial work on solar tracking was presented by Zerlaut et al [11] and Haywood et al [12] in 1976. More recent work has employed hybrid tracking strategies that use algorithms to suit different illuminative and geographical conditions, as can be seen in [13, 14]. Tracking accuracy as high as 0.1° can be obtained through picture processing techniques as shown in [15]. A new approach based on computer vision, low cost hardware, and deep learning can be found in [16].

Poulek et al. designed a single axis solar tracker based on an arrangement of solar cells connected directly to a reversible DC motor. In their work, solar cells both sense and provide energy for tracking. Sensing/driving solar cells are balanced against each other and a differential signal is used to overcome friction and aerodynamic drag. The area of the auxiliary solar panel of the tracker is about 2% of the area of the moved solar collectors, while collectable energy surplus is up to 40%. With slight modifications, this system can be used for space panel tracking in addition to terrestrial applications, but this would require a set of bifacial solar cells per panel to be tracked [17, 18].

Roth et al. designed and constructed a two-axis (one axis from east to west and the other for elevation) sun-following device with the use of a

[2]1000 W/m$^2$ solar intensity, 25 °C ambient temperature and an air mass of 1.5 (ASTM G-173-03)

EBSCOhost - printed on 2/14/2023 2:46 PM via . All use subject to https://www.ebsco.com/terms-of-use

pyrheliometer as a measuring instrument. The device works in two modes: clock mode and sun mode. In clock mode, the tracker computes the position of the Sun based on date/time information in its internal clock. Panel position errors are measured during the day and stored for later analysis and improvement. The data gathered during the day is analyzed, and a new improved set of parameters for installation errors is computed. This data is used the next day to more accurately compute the position of the Sun. In sun mode, the tracker uses theoretical data on the Sun's position to control the panel position. If the intensity drops below a certain level, it temporarily reverts back to clock mode [14, 19].

Rizk et al. designed a solar tracker that employed a new principle by using small solar cells to function as self-adjusting light sensors. The set-up provided an indication of their relative angle to the Sun by detecting the voltage output. A power increase of 30% was obtained by using this strategy [20].

Based on their functioning principle, sun trackers can be classified into three types: passive, microprocessor-based, and electro-optically controlled units [21].

Passive trackers rely on the differential expansion of substances exposed to different amounts of irradiance. They are based on thermo-sensitive substances that adjust the position of the receiving panel in accordance with the position of the Sun. Freon and bimetallic strips are the most commonly used substances in passive trackers. These systems are simple and do not need any electronic controls or motors. Some of the drawbacks of these systems are the possible use of toxic substances, slow responses, and the absence of a nocturnal return mechanism. A novel passive tracker can be found in [7]; some other interesting passive tracker designs can be found in [22-24].

Microprocessor-based trackers rely on calculating the Sun's position through mathematical calculations such as:

$$\alpha = \sin^{-1}(\cos\varphi \times cos\ \delta \times cos\ \omega + sin\ \varphi \times sin\ \delta) \quad (1)$$

$$\gamma = \cos^{-1}\left(\frac{sin\ \alpha \times sin\ \varphi - sin\ \delta}{cos\ \alpha \times \sin\varphi}\right) \quad (2)$$

The latest type of trackers are those that use both microprocessors and electro-optical sensors (LDRs and CCDs) for their operation [10-12, 17-19, 25-34].

EBSCOhost - printed on 2/14/2023 2:46 PM via . All use subject to https://www.ebsco.com/terms-of-use

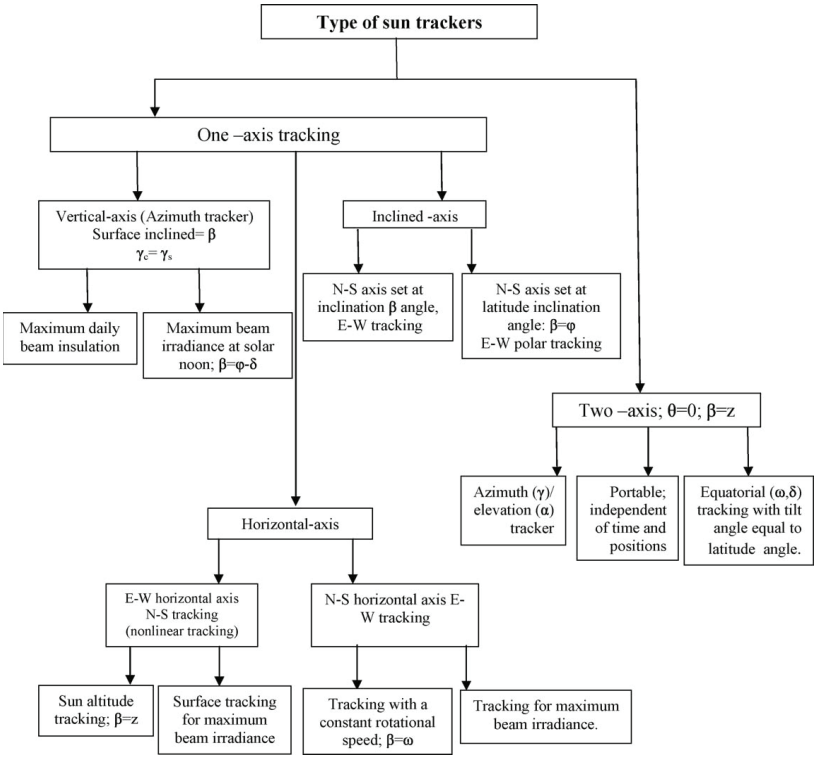



Figure 1. Types of solar tracker [8].

A more general classification divides trackers into one-axis and two-axis devices, as illustrated in Figure 1. A detailed account of different solar tracking systems can be found in the reviews [8, 35].

This article describes how a novel optical-electronic closed-loop dual-axis solar tracking sensor was designed with the help of an OPV cell. This can be readily implemented in a wide range of sun tracking scenarios. The design especially suits its use in developing and under-developed countries with limited access to technology. A prototype sensor was constructed and evaluated according to various performance parameters. The subsequent sections of this article describe the objectives of this study, the solar tracking system, the algorithm used, and the experimental results of testing. Concluding remarks are presented at the end of this article.

EBSCOhost - printed on 2/14/2023 2:46 PM via . All use subject to https://www.ebsco.com/terms-of-use

## Objectives

Keeping in mind the increase in efficiency that can be obtained and the known characteristics of an ideal tracker, this solar tracking sensor was designed as a low cost and effective alternative to currently available complex, expensive, patented, and proprietary systems. It is intended to serve as an additional incentive for the adoption of solar harvesting techniques, especially when access to technology and capital is limited.

## Description of the Solar Tracking Sensor

The sensor can be broadly divided into mechanical and electrical components, which are combined to form the solar tracking system. The mechanical structure is comprised of the frame and the electrical system consists of the motors, OPV cell, and microcontroller. The block diagram shown in Figure 2 gives an operational overview of the various components used.

The schematic of the solar sensor is shown in Figure 3. The setup consists of two servo motors (b) and (c), one of which, (b), is mounted on the frame (a) to facilitate east-west movement of the organic photovoltaic (OPV) cell (d). The cell acts as a primary sensing device for the tracker. A servo motor (c) is mounted at the base to facilitate the north-south movement of the OPV cell. The cell is connected to the fork shaped frame (a) such that it can rotate about the horizontal axis when moved by the servo (b) and vertical axis when moved by the servo (c). The tracking algorithm of the sensor is controlled by a microcontroller (e).

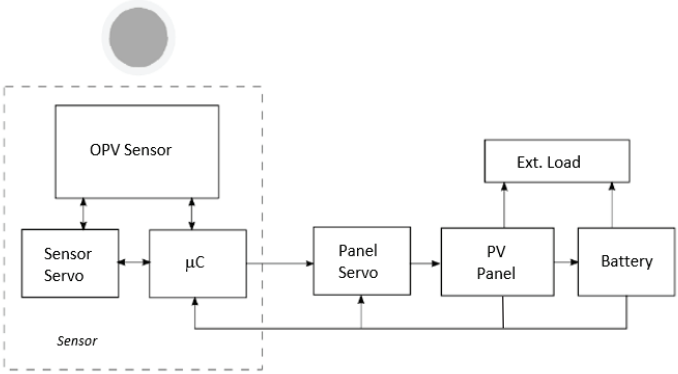



Figure 2. Schematic of the tracking system.

EBSCOhost - printed on 2/14/2023 2:46 PM via . All use subject to https://www.ebsco.com/terms-of-use

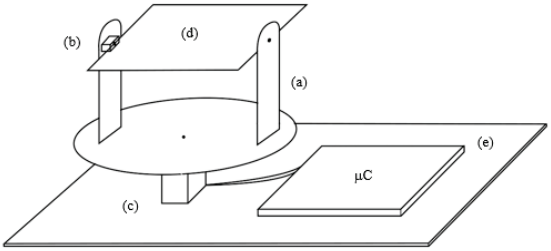



Figure 3. Construction of the sensor.

## *Mechanical Structure*

The solar tracking sensor weighs around 200 g and has overall dimensions of 200 × 200 × 200 mm. The compactness of the system enables it to be mounted conveniently with minimal use of space. The prototype was fabricated from acrylic sheets of 3 mm thickness that were bonded with a general-purpose adhesive. The frame is designed so that free 180° and 360° rotational movement of the OPV cell (120 × 80 mm) is allowed with respect to both horizontal and vertical axes, respectively, when operated by the servo motors. The tracking sensor is designed to pinpoint both the azimuth and elevation angles. Figure 4 shows the actual working model (prototype) of the sensor constructed using the above-mentioned materials.

EBSCOhost - printed on 2/14/2023 2:46 PM via . All use subject to https://www.ebsco.com/terms-of-use

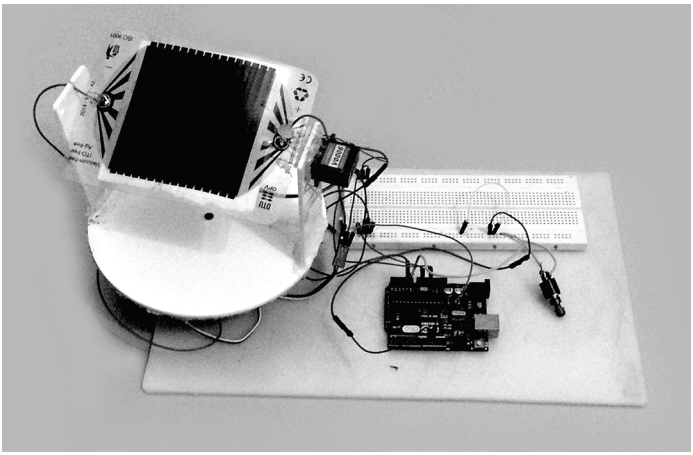


Figure 4. Prototype of the sensor.

## *Electrical System*

Abundance, fast manufacture, and low cost are what ideally epitomize organic and polymer photovoltaics and therefore inform the choice of sensor in this tracking device. These cells are indium tin oxide (ITO) free and have been shown to exceed 10 000 hours of lifetime use under standard outdoor exposure conditions. The normal operating temperature range is from –80 °C to 120 °C and the sensor used in the prototype weighs around 5 g. The I-V response of the OPV cell is shown in Figure 5 and Figure 6 shows an actual photograph of the cell used in the prototype (Figure 4) [36].

The driving mechanism of the OPV for executing its tracking cycle includes two servo motors. A smaller servo (TowerPro SG90) is used to rotate the sensor for east-west tracking, while a bigger motor (Futaba S3003) is used to turn the fork frame. PWM (pulse width modulation) is used to drive the servo motor at a controlled speed with a corresponding maximum voltage of 6 V. The duration or width of the pulse determines the angle of the shaft's rotation.

EBSCOhost - printed on 2/14/2023 2:46 PM via . All use subject to https://www.ebsco.com/terms-of-use

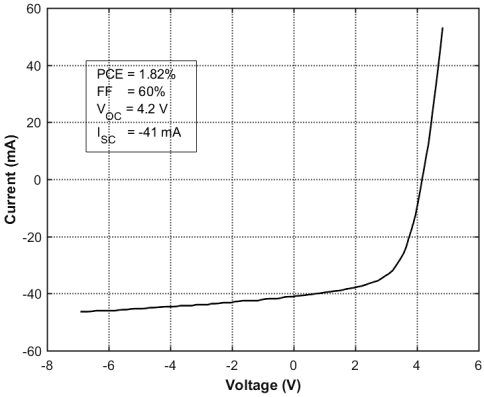



Figure 5. I-V curve of the OPV.

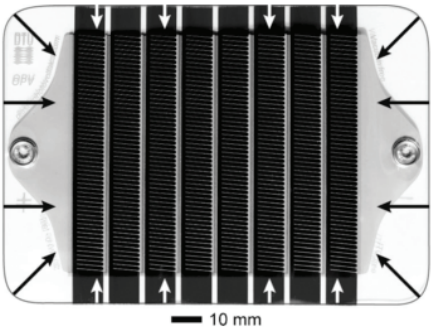



Figure 6. OPV module used as sensor.

An open source microcontroller board, Arduino Uno (Figure 7), was used as the primary controller for the servo motors and to analyze the OPV cell output. The Uno is a microcontroller board based on the ATmega328P. The analog voltage provided by the OPV cell is converted into a digital signal for processing. As the input-output pins of the microcontroller can only operate between 0 and 5 V, a simple voltage divider circuit was constructed to input the voltage from the cell (0 to 10 V) into the microcontroller. The Arduino IDE was used to program the microcontroller. The C++ program can be written and compiled in the IDE before uploading into the Arduino Uno board.

EBSCOhost - printed on 2/14/2023 2:46 PM via . All use subject to https://www.ebsco.com/terms-of-use

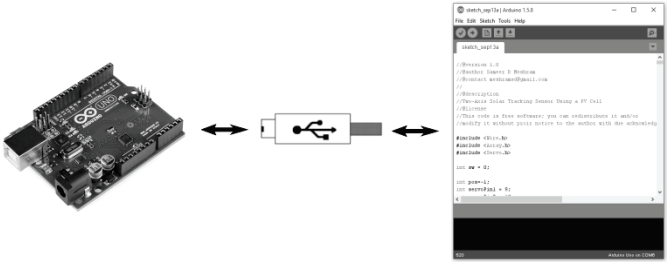


Figure 7. Process of programming the microcontroller.

The power required to drive the two servo motors and the microcontroller was taken from the USB port of a personal computer. It can also be taken from the solar energy produced by the panels to which the sensor caters, or any other external direct voltage source.

## Algorithm

The sensor first scans for the local maximum power point (MPP) across the horizon, i.e. rotating the OPV cell about the vertical axis (Figure 8), and achieves the azimuth angle corresponding to the local MPP. The local MPP is calculated at the highest magnitude of voltage across the cell for any given scan.

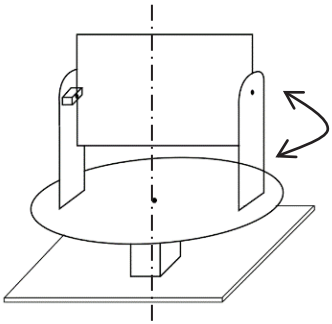


Figure 8. Scan for MPP in north-south direction.

EBSCOhost - printed on 2/14/2023 2:46 PM via . All use subject to https://www.ebsco.com/terms-of-use

Similarly, it scans for the local MPP in the east-west direction, rotating the OPV cell about the horizontal axis (Figure 9) and sets the altitude angle corresponding to the local MPP.

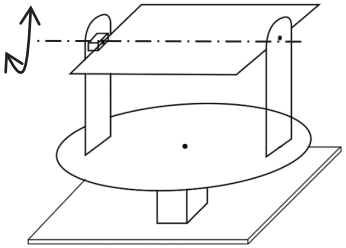


Figure 9. Scan for MPP in east-west direction.

Next, the global (overall) MPP is obtained by taking into consideration both the local east-west and north-south MPPs. Once the final position of the sensor corresponding to the global MPP is calculated, the sensor sets the panels it is connected to at the calculated positions until the next scan or search cycle begins. Each scan cycle takes around 20 seconds duration and is performed at an interval of 30 minutes. It should be noted that while the duration of a scan in the current design is constant at 20 seconds, the user has total control over the interval of the scan.

## Performance Testing and Experimental Results

In order to validate the accuracy of the sensor it was necessary to compare the experimental results with those obtained through mathematical formulae (1, 2) and sun position/angle calculators [37, 38]. To obtain this data, tests were conducted with the setup as shown in Figure 10 during the month of January 2016. Tests were made at latitude 18.9803578, longitude 72.8148362, and at an altitude of 52 meters above sea level with an average temperature of 34 °C at Mahalaxmi-Mumbai, India.

The tracking accuracy of the sensor throughout the day was determined in terms of azimuth and altitude angles and was plotted against solar time (Figure 11, 12, 13). A comparative analysis of true and observed values versus solar time showed a maximum deviation of ± 4°. The sensor output was also fed to a test panel to visually validate tracking.

EBSCOhost - printed on 2/14/2023 2:46 PM via . All use subject to https://www.ebsco.com/terms-of-use

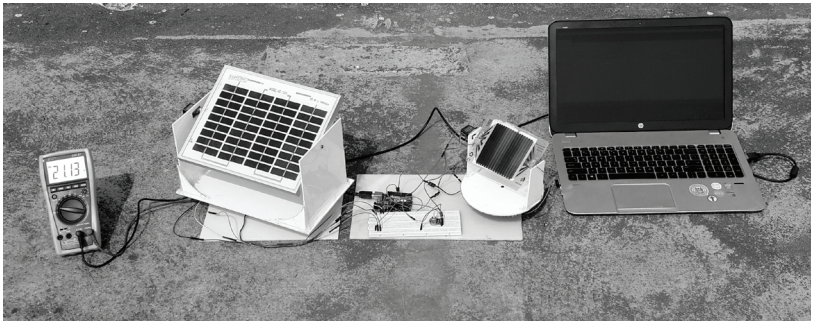


Figure 10. Experimental setup for testing.

Furthermore, the sensor was tested under three different illumination conditions—a sunny day, a cloudy day and an overcast day—to establish performance consistency in different climatic conditions (Figure 14). No variation was observed in the location of the MPP under these conditions due to the relative nature of the algorithm.

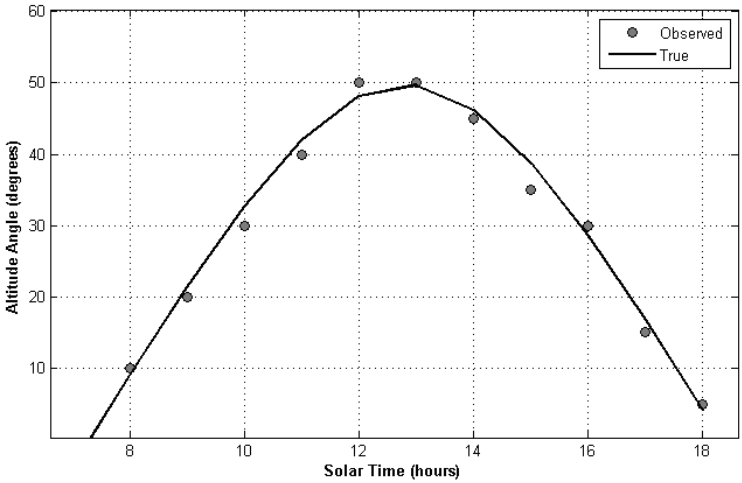



Figure 11. Comparison of altitude angle (observed and true) v. solar time.

EBSCOhost - printed on 2/14/2023 2:46 PM via . All use subject to https://www.ebsco.com/terms-of-use

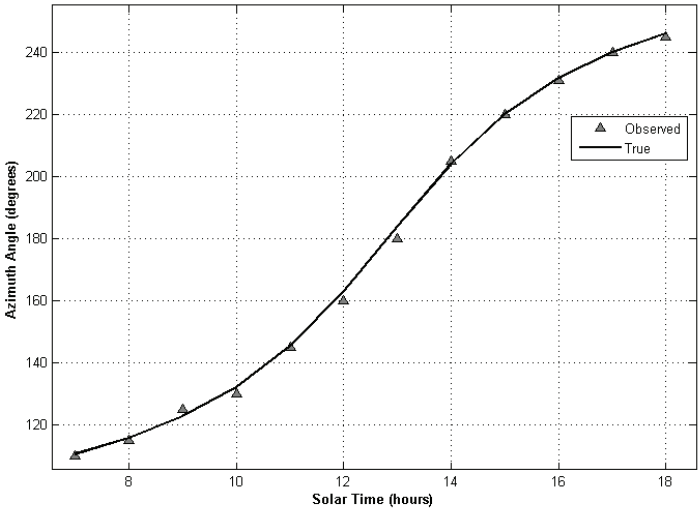



Figure 12. Comparison of azimuth angle (observed and true) v. solar time.

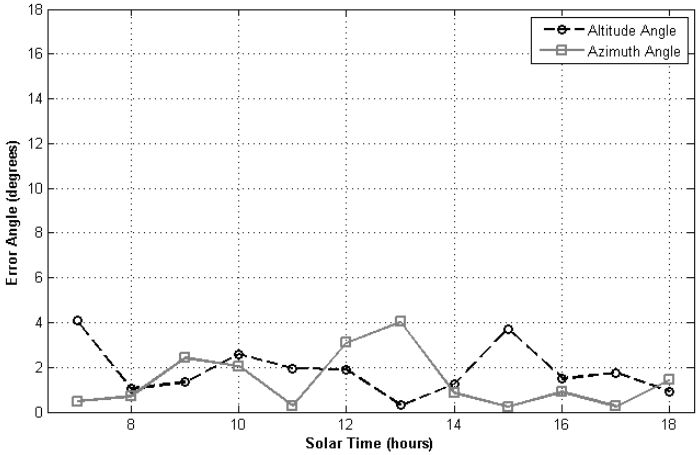



Figure 13. Mean error in azimuth and altitude angles.

EBSCOhost - printed on 2/14/2023 2:46 PM via . All use subject to https://www.ebsco.com/terms-of-use

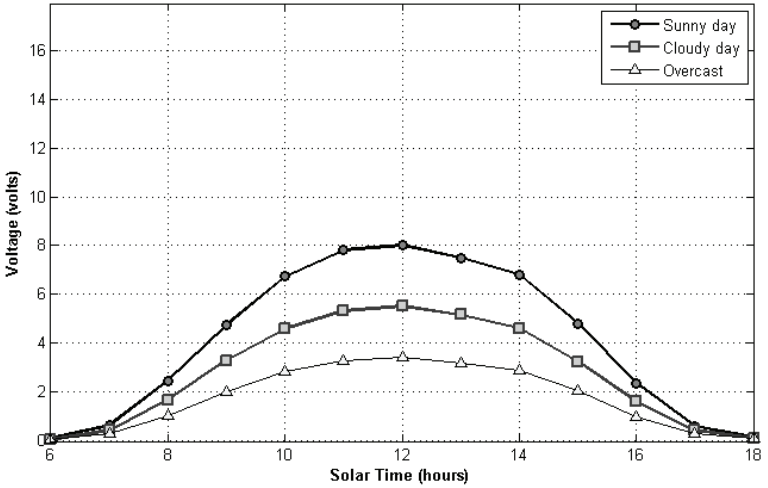



Figure 14. Performance in different climatic conditions.

## Conclusion

The proposed solar tracker design was demonstrated to be low cost (~$ 30) and simple to construct, use, and maintain. This system was designed with the aim that it could be fabricated, assembled, and made operational by anyone with a basic understanding of electrical circuits. It also employed commonly available materials and used easy fabrication techniques. The sensor implemented an organic photovoltaic cell, which is indium tin oxide (ITO) free and is environmentally friendly when compared to a number of its silicon counterparts. With a large tracking angle, it can be deployed in any geographical location, including regions above the Arctic Circle (Russia, Canada, Alaska, Scandinavia, etc.). Experiments conducted showed maximum deviation of ± 4° from the true values of the observed azimuth and altitude angles of the Sun. In addition, the system was found to be independent of the illumination conditions due to the relative nature of the algorithm.

Future work may include testing a set-up with a higher level of technological readiness and accounting for service life and environmental conditions. Improvements could be made by reducing the scan cycle time and performing a life cycle assessment (LCA) and a life cycle cost assessment (LCC).

EBSCOhost - printed on 2/14/2023 2:46 PM via . All use subject to https://www.ebsco.com/terms-of-use

## Acknowledgement

The author acknowledges reception of a free OPV cell sample from the Technical University of Denmark (DTU) and the funding and support provided by Sardar Patel College of Engineering (SPCE), Mumbai in fulfilment of this work.

## References

[1] "Key World Energy Statistics 2018," [Online] Available: http://www.iea.org/statistics/ [Accessed May. 31, 2019].
[2] "Electricity Net Generation: Total (All Sectors)," [Online] Available: http://www.eia.gov/totalenergy/data/monthly/pdf/sec7_5.pdf [Accessed Sept. 19, 2018].
[3] S. Lawrence, "Some Interesting Facts about the Sun." [Online]. Available: http://www-istp.gsfc.nasa.gov/istp/outreach/workshop/thompson/facts.html. [Accessed Sept. 19, 2018].
[4] D. Wohrle and D. Meissner, "Organic Solar Cells," *Adv. Mater.*, vol. 3, no. 3, pp. 129–138, Mar. 1991.
[5] Luque A, Hegedus S. Handbook of photovoltaic science and engineering. Hoboken (NJ): Wiley; 2003.
[6] Green MA, Hishikawa Y, Warta W, et al. Solar cell efficiency tables (version 50). Prog Photovolt Res Appl. 2017; 25:668–676. https://doi.org/10.1002/pip.2909.
[7] M. J. Clifford and D. Eastwood, "Design of a novel passive solar tracker," *Sol. Energy*, vol. 77, no. 3, pp. 269–280, Sep. 2004.
[8] H. Mousazadeh, A. Keyhani, A. Javadi, H. Mobli, K. Abrinia, and A. Sharifi, "A review of principle and sun-tracking methods for maximizing solar systems output," *Renew. Sustain. Energy Rev.*, vol. 13, no. 8, pp. 1800–1818, Oct. 2009.
[9] E. Lorenzo, M. Pérez, A. Ezpeleta, and J. Acedo, "Design of tracking photovoltaic systems with a single vertical axis," *Prog. Photovoltaics Res. Appl.*, vol. 10, no. 8, pp. 533–543, 2002.
[10] A. Argeseanu, E. Ritchie, and K. Leban, "New low cost structure for dual axis mount solar tracking system using adaptive solar sensor," in *2010 12th International Conference on Optimization of Electrical and Electronic Equipment*, 2010, pp. 1109–1114.
[11] Zerlaut, Gene A., and Robert F. Heiskell. "Solar tracking device." U.S. Patent No. 4,031,385. 21 Jun. 1977.
[12] Haywood, George Lewis, and Wesley Joseph Haywood. "Solar collector and drive circuitry control means." U.S. Patent No. 4,082,947. 4 Apr. 1978.
[13] F. R. Rubio, M. G. Ortega, F. Gordillo, and M. López-Martínez, "Application of new control strategy for sun tracking," *Energy Convers. Manag.*, vol. 48, no. 7, pp. 2174–2184, Jul. 2007.
[14] P. Roth, a. Georgiev, and H. Boudinov, "Cheap two axis sun following

EBSCOhost - printed on 2/14/2023 2:46 PM via . All use subject to https://www.ebsco.com/terms-of-use

device," *Energy Convers. Manag.*, vol. 46, no. 7–8, pp. 1179–1192, 2005.
[15] G. P. A. Minor M. Arturo, "High–Precision Solar Tracking System," 2010. [Online]. Available: http://www.iaeng.org/publication/WCE2010/WCE2010_pp844-846.pdf. [Accessed Sept. 19, 2018].
[16] J.A. Carballo, et al., New approach for solar tracking systems based on computer vision, low cost hardware and deep learning, Renewable Energy (2018), https://doi.org/10.1016/j.renene.2018.08.101.
[17] V. Poulek and M. Libra, "A very simple solar tracker for space and terrestrial applications," *Sol. Energy Mater. Sol. Cells*, vol. 60, no. 2, pp. 99–103, Jan. 2000.
[18] V. Poulek and M. Libra, "New solar tracker," *Sol. Energy Mater. Sol. Cells*, vol. 51, no. 2, pp. 113–120, Feb. 1998.
[19] P. Roth, A. Georgiev, and H. Boudinov, "Design and construction of a system for sun-tracking," *Renew. Energy*, vol. 29, no. 3, pp. 393–402, 2004.
[20] J. Rizk and Y. Chaiko, "Solar Tracking System: More Efficient Use of Solar Panels," *World Acad. Sci. Eng. Technol.*, vol. 41, pp. 313–315, 2008.
[21] H. Bentaher, H. Kaich, N. Ayadi, M. Ben Hmouda, A. Maalej, and U. Lemmer, "A simple tracking system to monitor solar PV panels," *Energy Convers. Manag.*, vol. 78, pp. 872–875, 2014.
[22] Zomeworks Corporation, Passive solar TRACK RACK, Albuquerque, NM, US Pat. No. 4275712. Oct. 1979.
[23] Berger, Alexander. "Sun tracker system for a solar assembly." U.S. Patent No. 5,798,517. Aug. 1998.
[24] M. Comsit and I. Visa, "Design of the linkages type tracking mechanisms of the solar energy conversion systems by using Multi Body Systems Method Transilvania University of Brasov Transilvania University of Brasov," in *12th IFToMM World Congress, Besançon (France)*, 2007, no. 12, pp. 1–6.
[25] C. Alippi and C. Galperti, "An Adaptive System for Optimal Solar Energy Harvesting in Wireless Sensor Network Nodes," *IEEE Trans. Circuits Syst. I Regul. Pap.*, vol. 55, no. 6, pp. 1742–1750, Jul. 2008.
[26] A. Al-Mohamad, "Efficiency improvements of photo-voltaic panels using a Sun-tracking system," *Appl. Energy*, vol. 79, no. 3, pp. 345–354, 2004.
[27] H. Arbab, B. Jazi, and M. Rezagholizadeh, "A computer tracking system of solar dish with two-axis degree freedoms based on picture processing of bar shadow," *Renew. Energy*, vol. 34, no. 4, pp. 1114–1118, 2009.
[28] J. Beltran A., J. L. Gonzalez Rubio S., and C. D. Garcia-Beltran, "Design, Manufacturing and Performance Test of a Solar Tracker Made by a Embedded Control," in *Electronics, Robotics and Automotive Mechanics Conference (CERMA 2007)*, 2007, pp. 129–134.
[29] C. S. Chin, A. Babu, and W. McBride, "Design, modeling and testing of a standalone single axis active solar tracker using MATLAB/Simulink," *Renew. Energy*, vol. 36, no. 11, pp. 3075–3090, Nov. 2011.
[30] P. K. Das, M. A. Habib, and M. Mynuddin, "Microcontroller Based Automatic Solar Tracking System with Mirror Booster," vol. 4, no. 4, pp. 125–136, 2015.

EBSCOhost - printed on 2/14/2023 2:46 PM via . All use subject to https://www.ebsco.com/terms-of-use

[31] N. Dasgupta, A. Pandey, and A. Mukerjee, "Voltage-sensing-based photovoltaic MPPT with improved tracking and drift avoidance capabilities," *Sol. Energy Mater. Sol. Cells*, vol. 92, no. 12, pp. 1552–1558, Dec. 2008.

[32] A. Kassem and M. Hamad, "A microcontroller-based multi-function solar tracking system," in *2011 IEEE International Systems Conference*, 2011, pp. 13–16.

[33] M. T. A. Khan, S. M. S. Tanzil, R. Rahman, and S. M. S. Alam, "Design and construction of an automatic solar tracking system," in *International Conference on Electrical & Computer Engineering (ICECE 2010)*, 2010, pp. 326–329.

[34] Yazidi, F. Betin, G. Notton, and G. Capolino, "Low cost two-axis solar tracker with high precision positioning," *2006 1st Int. Symp. Environ. Identities Mediterr. Area, ISEIM*, pp. 211–216, 2006.

[35] H. J. Loschi, Y. Iano, J. León, A. Moretti, F. D. Conte, and H. Braga, "A Review on Photovoltaic Systems: Mechanisms and Methods for Irradiation Tracking and Prediction," *Smart Grid Renew. Energy*, vol. 06, no. 07, pp. 187–208, 2015.

[36] F. C. Krebs, M. Hösel, M. Corazza, B. Roth, M. V. Madsen, S. A. Gevorgyan, R. R. Søndergaard, D. Karg, and M. Jørgensen, "Freely available OPV-The fast way to progress," *Energy Technol.*, vol. 1, no. 7, pp. 378–381, 2013.

[37] "Sun Position Calculator," [Online], Available: https://pveducation.org/pvcdrom/properties-of-sunlight/sun-position-calculator. [Accessed May. 31, 2019].

[38] "Sun Earth Tools," [Online], Available: https://www.sunearthtools.com/dp/tools/pos_sun.php [Accessed May. 31, 2019].

EBSCOhost - printed on 2/14/2023 2:46 PM via . All use subject to https://www.ebsco.com/terms-of-use

# CHAPTER SEVEN

# PHOTOVOLTAIC-POWERED WATER PUMPING SYSTEMS APPLIED TO FAMILY AGRICULTURE: A KEY TOOL FOR DEVELOPING COUNTRIES

CHILUNDO, R. J.[1], MAHANJANE, U. S.[1], DINIZ, M. M. N.[2], BEZERRA, A. M. E.[3], CARVALHO, P. C. M[4]

## Abstract

Solar photovoltaic (PV) technology for water pumping systems (WPS) has been one of the most popular forms of solar energy application in recent decades. Many water pumping projects for irrigation have been implemented around the world over the course of previous centuries, making it reasonable to assert that the technology is technically mature. Despite this, it still faces multiple challenges in its implementation. This chapter aims to analyze the technical and financial feasibility of a stand-alone PV-powered irrigation system to be use by a family production unit. Environmental and socio-economic aspects are also indirectly analyzed. The unit occupies a floor area of 134m$^2$, with a water reservoir that simulates a pond, lake, or well and has a capacity of 3,534 liters.

[1] Pedagogic University. Engineering Department. Av. do Trabalho, 223, Office A 2.16, Lhanguene Campus, Maputo, Mozambique. Email: rosychil@yahoo.com.br & us.mahanja@gmail.com

[2] Instituto Joazeiro de Desenvolvimento Sustentável. St. Barão do Rio Branco, 1071, sl. 1021, 60025-061, Fortaleza/CE (Brasil): Email: magilce@hotmail.com

[3] Federal University of Ceará. Fitotechny Department. Pici Campus, 60440 – 560, Fortaleza/CE (Brasil). Email: esmeraldobezerra@yahoo.com.br

[4] Federal University of Ceará. Electrical Engineering Department. Pici Campus, 60455 – 760, Fortaleza/CE (Brasil). Email: carvalho@dee.ufc.br

EBSCOhost - printed on 2/14/2023 2:46 PM via . All use subject to https://www.ebsco.com/terms-of-use

Additionally, a 12V DC pump motor and a 135Wp PV module are used. The efficiencies of the PV module, pump, and overall set were 8.4%, 42%, and 3.5%, respectively. The assumed service life is 25 years and the capital is returned after 9.3 years with an internal rate of return of 12.5%. Different applications have led us to conclude that PV-powered WPS should be considered a key tool for developing countries for securing food production and electricity supply.

**Keywords:** Photovoltaic water pumping system; irrigation; family agriculture.

## Introduction

In a world facing environmental questions, such as those related to climate change, renewable sources of electricity are an important response for both developed and developing countries. In most of the developing world, a significant part of the population has no access to the conventional electricity grid and no reliable drinking water supply for human consumption [1]. Rapid world population growth of 1.10% per year [2] adds to these challenges. Stable energy production is crucial for continuous and stable food production.

Vann Koppen et al. [3] argue that agriculture has been the engine of all economic growth and, as a consequence, the reduction of poverty throughout history. 30% of the 7.6 billion people in the world are employed in the agricultural sector [4]. The irrigation process in modern agriculture, however, is still reliant on the exploitation of fossil fuels [5]. In this context, the adoption of self-sustaining agricultural production practices using renewable and endogenous energy resources has become essential for the development of communities, both economically and socially [6].

The use of PV-powered WPS has been one of the most popular forms of solar energy application in recent decades in remote and desert areas, as well as in some urban areas too [7]. This chapter aims to analyze, experimentally, the technical and financial feasibility of a PV-powered irrigation system. This may be considered a key element in increasing the sustainability of developing countries and in disseminating knowledge related to technological innovations for the eradication of poverty and hunger and PV electricity production. Additionally, it should enable the generation of employment and secure income and environmental preservation.

EBSCOhost - printed on 2/14/2023 2:46 PM via . All use subject to https://www.ebsco.com/terms-of-use

The chapter is organized as follows: Section 1 introduces the context; Section 2 presents basic concepts regarding energy and agriculture, including an overview of PV-powered WPS; Section 3 explores the materials and methods used; Section 4 reports the results and discusses them; final conclusions are given in Section 5. This chapter is a revised version of a paper presented at the International Conference on Renewable Energies and Power Quality (ICREPQ'15) [8].

## Energy and agriculture

The productive use of energy consists in the exploitation of energy for activities that improve the income and well-being of people [9]. As such, the success of agricultural practices is strictly dependent on the availability of energy. Agricultural activity is centered on energy transformation processes, as a fundamental variable that provides integrity in agronomic growth. Energy is used for irrigation; machinery; product processing; the conservation of agricultural products; and other forms of resource exploitation in agricultural production [10].

In the19th Century, both Japan and the United States adopted practical policies to support features and technologies that improved agricultural production. This strategy encouraged the rapid development of cultivated and irrigated areas in these countries bringing the standard of agricultural activity up to a high level [11]. As a contemporary example, the government of Bangladesh has given a 50% subsidy and arranged a 35% soft loan with the aid of donor agencies so that owners or individual investors are only required to invest 15% of the total cost needed to participate in a solar irrigation program [12].

The first recorded use of a PV system in a stand-alone application in Brazil dates back to the 1980s. Since then, the most relevant program of rural electrification in the country using renewable energy systems has been the Program of Energetic Development of States and Municipalities (PRODEEM), which started operation in 1994. The aim of this project was to supply electricity to 3.72 million people living in rural and remote communities, who were not connected to the electrical grid. The program was carried out over a period of four years. PV systems were used for three community applications: school systems; water pumping systems; and public illumination. Over the course of this period, ca. 9,000 systems were installed, with a total power of 5 MWP (500 WP being the standard power per system), and at a cost of US$ 70 million. 67% of this amount went to healthcare centers and schools; 30% went to water pumping systems; and 3% went to public illumination [13].

EBSCOhost - printed on 2/14/2023 2:46 PM via . All use subject to https://www.ebsco.com/terms-of-use

In the Mozambican context, by 2021 more than 900 PV-powered WPS for irrigation will have been installed all over the country by the government through the National Irrigation Institute, representing the first major government project in this area [NII, personal interview, February 2018].

Agriculture is the set of human actions that serve to transform the natural environment to make it suitable for the growing of crops. Agriculture can classified into two principal groups[14]:

- subsistence agriculture;
- market agriculture.

Subsistence agriculture is practiced in areas smaller than 2 hectares and the most commonly applied irrigation techniques include surface, aspersion or sprinklers—these tend to be very localized [15]. Generally, PV-powered WPS offers a simple and reliable technology for small-scale irrigation use, mainly in areas of approximately 1 ha.

According to the Brazilian Institute of Geography and Statistics, 82.9% of the Northeast Region of Brazil's agricultural labor is constituted of family farmers. Similarly, 80% of the Mozambican population depends on agriculture for its subsistence [16]. According to the World Bank, globally, 3.3 people billion people live in rural areas and 2.5 billion of these are involved in agricultural activities [17].

### *Coriander (*Coriandrum sativum)

Coriander is an annual herb in the family Apiaceae that is used all over the world. All parts of the plant are edible, but the fresh leaves and dried seeds are the parts most traditionally used in cooking. Coriander leaves are particularly rich in vitamin A, vitamin C, and vitamin K. They have a moderate content of dietary minerals. Although seeds generally have a lower vitamin content, they provide significant amounts of dietary fiber, calcium, selenium, iron, magnesium, and manganese. Harvesting of the coriander crop can be done at 40 to 180 days after planting.

## Photovoltaic-powered water pumping systems

WPS can be classified according to the applied energy source and the technical characteristics of the system. There are five primary types of pumping system for crop irrigation:

EBSCOhost - printed on 2/14/2023 2:46 PM via . All use subject to https://www.ebsco.com/terms-of-use

a) PV-powered pumping systems;
b) Wind-powered pumping systems;
c) Pumping systems connected to the conventional power grid;
d) Pumping systems powered by internal combustion engines;
e) Manual pumping systems.

A PV-powered WPS generally consists of: some PV modules; a motorized pumping unit; a power conditioning system (drive, pump controller); and a storage system (optional). These systems are specially designed for pumping water from wells, ponds, rivers, and reservoirs. They are similar to conventional systems with the basic difference that the motorized pump is powered by PV modules.

Another common use of PV-powered WPS is in the desalination sector. Looking at state-of-the-art of renewable energy powered desalination plants worldwide, it can be seen that PV and wind energy converter powered reverse osmosis plants are the most attractive technological combinations for desalination [18].

The following parameters, at a minimum, should be defined as parameters for sizing a PV-powered WPS [19]:

- Water and energy demand;
- Solar irradiation data;
- Water resource characteristics;
- Hydrological cycle seasonality;
- Pumping regime.

Hydraulic power depends on the daily water flow and total head [20]:

$$P_h = 2.725 * Q_d * H_{MT} \quad (1)$$

- $Q_d$ – Daily flow designed ($m^3/h$)
- $H_{MT}$ – Total manometric height (m)
- $P_h$ – Hydraulic power [W]

The power of the electric motor is given by:

$$P = \frac{P_h}{\eta_{MP}} \quad (2)$$

EBSCOhost - printed on 2/14/2023 2:46 PM via . All use subject to https://www.ebsco.com/terms-of-use

- P – Electric motor power [W]
- $\eta_{MP}$ – Pump efficiency [%]

Solar power over the PV module area is found through:

$$H = G * A_M [W] \quad (3)$$

- H – Solar power [W]
- G – Global solar irradiance [W/m$^2$]
- $A_M$ – PV module useful area [m$^2$]

The overall efficiency of a PV-powered WPS is calculated in 3 steps:

*1) PV Module Efficiency ($\eta_{PV}$)*

$$\eta_{PV} = \frac{P}{G * A_M} = \frac{V * I}{G * A_M} * 100 \quad (4)$$

- V – Voltage [V]
- I – Current [A]

*2) Motorized pump Efficiency ($\eta_{MP}$)*

$$\eta_{MP} = \frac{P_h}{P} * 100 \quad (5)$$

*3) Overall efficiency ($\eta_G$)*

$$\eta_G = \frac{P_h}{G * A_M} * 100 \quad (6)$$

To meet the water demand of the unit production, a minimum irradiance is required for the PV module [21]. The minimum irradiance required ($G_{min}$) is calculated using:

EBSCOhost - printed on 2/14/2023 2:46 PM via . All use subject to https://www.ebsco.com/terms-of-use

$$G_{\min} = \frac{P_{\min} * G_{st}}{P_M} \quad (7)$$

$P_{min}$ – Minimum system power to operate in the desired conditions
$G_{st}$ – Standard global solar irradiance (1000W/m$^2$)
$P_M$ – Maximum PV power output

## Materials and methods

For the PV-powered WPS under study, an analytical method of mathematical calculation was adopted alongside an experimental method. For the financial analysis, the internal rate of return (IRR) and cash flow analysis were used. Cash flow analysis seeks to assess the investment time of return using the computational tool RETScreen [22].

The PV-powered WPS occupies a floor area of 134m$^2$. It has a water reservoir simulating a pond, lake, or well with a capacity of 3,534 liters. It uses a 12V DC positive displacement motor-pump and a 135Wp PV module. As shown in Fig. 1, measurements included: water flow; water pressure; PV voltage and current; and solar irradiance. Nominal motor power is 55W and pump output pressure is 14psi.

For data acquisition, an RTF pyranometer/82-05, an SU7000 flow sensor, a PN2024 pressure sensor, and current and voltage sensors were used. Control and data acquisition were made through a SanUSB system and data transmission used a Wi-Fi unit [23]. SanUSB is a computational tool for data acquisition using microcontrollers—the tool has low-cost components, can be found on local markets, and has free access. It is shown in Fig. 2.

The water distribution system for irrigation consisted of 24 micro-sprinklers with a working pressure of between 10 to 20 feet of the water column, distributed uniformly along circular beds. 12 micro-sprinklers installed along the sidelines were operated simultaneously, each at a pressure of 14psi, with an average flow of 0.9l/min for sunny days; for cloudy days 3 micro-sprinklers were operated simultaneously with a pressure of 15.3psi and a flow of 1.1l/min. The choice of circular beds offers some advantages, including more efficient use of the cultivation area, efficient use of water in irrigation, and the creation of green and harmonious environments in rural and urban areas.

EBSCOhost - printed on 2/14/2023 2:46 PM via . All use subject to https://www.ebsco.com/terms-of-use

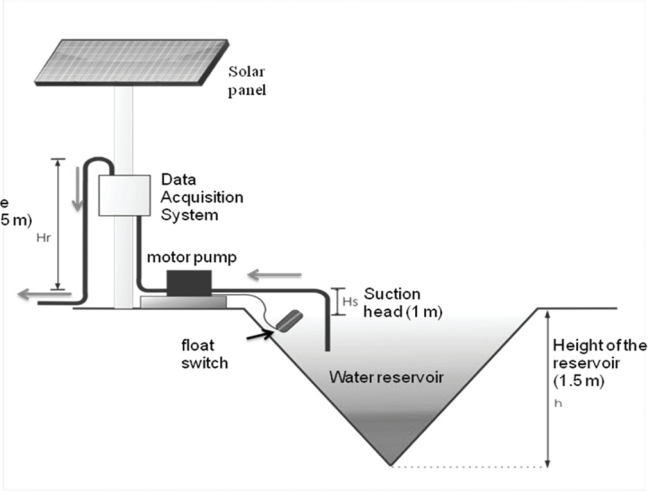



Figure 1. PV-powered WPS diagram

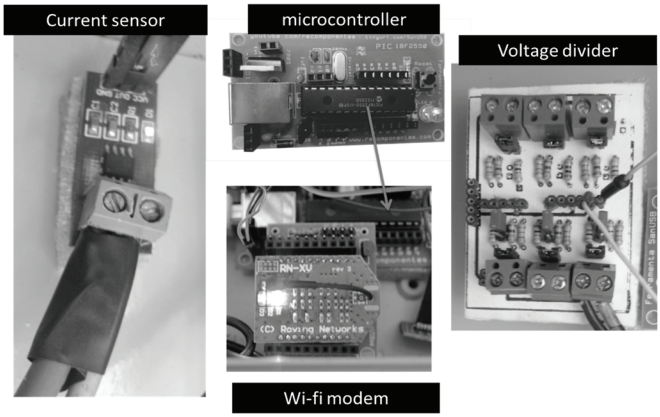



Figure 2. SanUSB system for data acquisition and transmission

Fig. 3 gives an overview of the PV-powered irrigation system as applied to familial agriculture.

EBSCOhost - printed on 2/14/2023 2:46 PM via . All use subject to https://www.ebsco.com/terms-of-use



Figure 3. PV-powered irrigation system applied to family agriculture

## Results and discussion

Water flow and solar irradiance curves are illustrated in Fig. 4. The pump operated from 7:40 a.m. to 8:35 a.m. and from 3:05 p.m. to 4:00 p.m.; the water volume pumped on the particular day shown was 709 liters, corresponding to an average flow rate of 6.4 l/min for an available solar irradiation of 6.7 kWh/m$^2$. A period of only 110 minutes was needed to achieve the water demand for irrigation of the coriander in the chosen area.

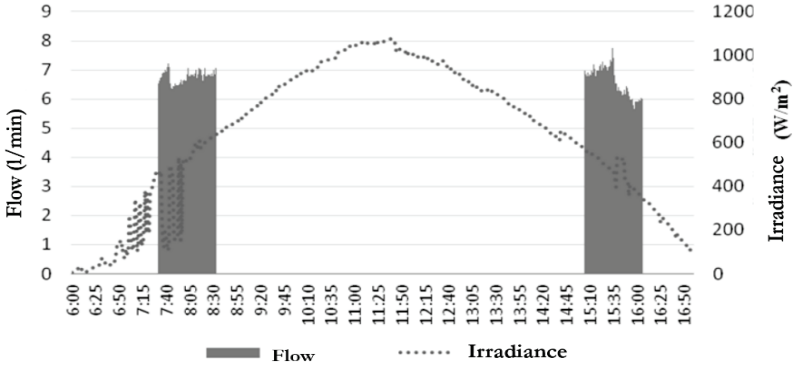



Figure 4. Flow and irradiance curves

Table I shows the daily averages and total values obtained for coriander cultivation.

EBSCOhost - printed on 2/14/2023 2:46 PM via . All use subject to https://www.ebsco.com/terms-of-use

**Table I: Daily averages and total values for coriander cultivation**

| | Daily averages | Total |
|---|---|---|
| Water consumption [liters] | 718 | 31,592 |
| Available solar irradiation [kWh/m$^2$] | 6.6 | - |
| Electricity consumption [kWh] | 0.12 | 5.3 |
| Operating time [minutes] | 110 | 4,484 |
| Coriander production [kg] | 23 | |

During the 44 days of coriander cultivation, an average daily consumption of 718 liters of water was observed, corresponding to an approximate total volume of 31,592 liters of water for irrigation. The daily electricity demand was around 0.12kWh. For the total water volume, a demand of 5.3kWh was measured. Daily average irradiation in the time period of 7:00 a.m. to 5:00 p.m. during the 44 days of cultivation was 6.6kWh/m$^2$.

The efficiencies achieved are summarized in Table II.

**Table II: PV-powered WPS efficiencies**

| | Efficiency (%) |
|---|---|
| PV module | 8.4 |
| Motor-pump | 42 |
| Overall | 3.5 |

In this study, PV module efficiency was 8.4% and motor-pump efficiency was 42%. This gives an overall efficiency of 3.5%. According to Hamidat et al. [24] and Hamza & Tiha [25], PV and overall system efficiencies do not usually exceed 10% and 5%, respectively. In turn, recent developments in PV-powered WPS with positive displacement pumps that have modern electronic control systems have increased hydraulic efficiencies by up to 70% [26].

The PV system studied has the capacity to pump water during the sunshine hours throughout the day. Due to the variation in irradiation during the productive cycle of the coriander, this analysis considers sunny and cloudy days separately. Figs. 5 and 6 show irradiance, flow and pressure values for a cloudy and a sunny day, respectively, over the course of the coriander production cycle.

EBSCOhost - printed on 2/14/2023 2:46 PM via . All use subject to https://www.ebsco.com/terms-of-use

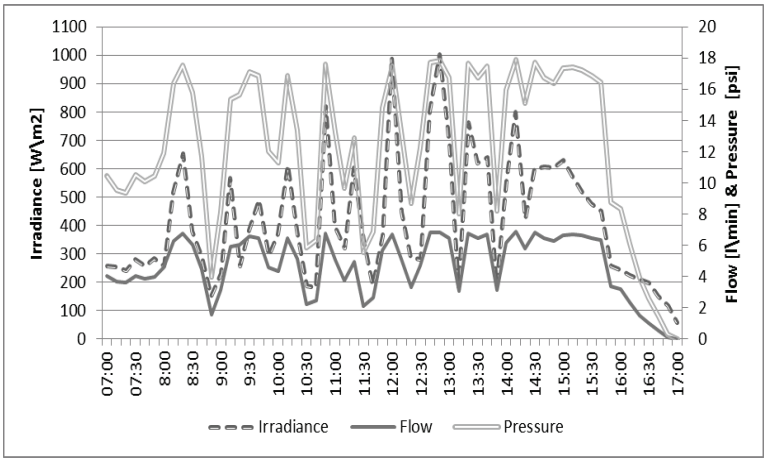



Figure 5. Irradiance, flow, and pressure values on a cloudy day

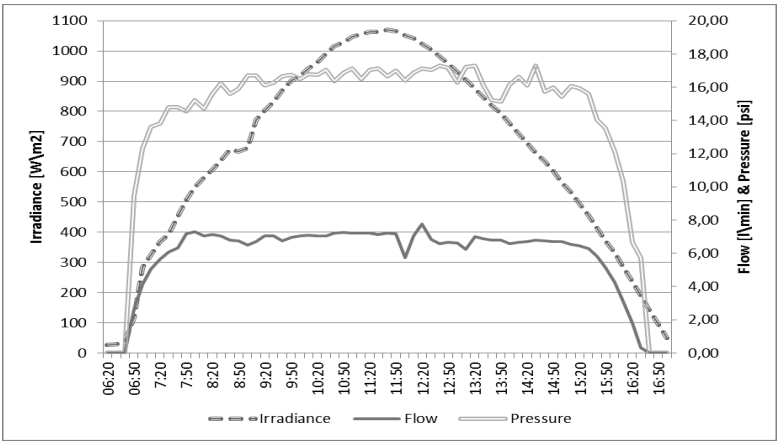



Figure 6. Irradiance, flow, and pressure values on a sunny day

For a cloudy day: solar irradiation was 4.3kW/m$^2$/day and 2,850 liters of water was supplied with an average flow of 4.75l/min and an average output pressure of 12.2psi. For a sunny day: solar irradiation was 7.04kWh/m$^2$, a volume of 3973 liters was pumped and the average flow was 6.5l/min with an average pressure of 15.4psi.

For the irrigation of the coriander, daily water demand was 800 liters for an area of 134m$^2$. Taking into account average flows, ca. 2.5 hours of

EBSCOhost - printed on 2/14/2023 2:46 PM via . All use subject to https://www.ebsco.com/terms-of-use

pumping was enough to satisfy the daily irrigation demand for the coriander. This means that for about 6 hours in the day the WPS was underutilized. Additionally, there was variation in the irrigation water volume during the growing period due to variation in solar irradiance and the soil moisture level.

Unused solar energy can be utilized to supply other energy needs, such as for powered grain dryer systems, or food processing and preservation systems. Currently, farmers and retailers face significant difficulties in preserving crops and, as a result, there is a deterioration of freshness and weight loss in vegetables. Generally, financial losses are often up to 20–30% [12]. The possibilities for optimizing the use of PV-powered WPS for irrigation offer a sustainable alternative for developing countries, which can be characterized by their weak food and electricity supply infrastructure.

## *Financial analysis and cash flow*

The cost of PV modules and accessories and the lack of perceived benefits provided by PV generation in most developing countries, which often have a high level of solar irradiation, are still barriers to significant use of the technology. Advances have been recorded in incentives for micro-generation, distributed mini-generation, and power compensation systems (Normative Resolution 482, April 17, 2012, of the Brazilian National Electric Energy Agency - ANEEL).

In this study, the input variables included: the monthly mean irradiation values over a year; PV module tilt angle; electricity price [$/MWh] defined by ANEEL; and the initial costs of the motor-pump and PV modules. Cash flow becomes positive after 9.3 years of plant operation, with an expected lifetime of 25 years considered, and an internal rate of return of 12.5%, as shown in Fig. 7.

EBSCOhost - printed on 2/14/2023 2:46 PM via . All use subject to https://www.ebsco.com/terms-of-use

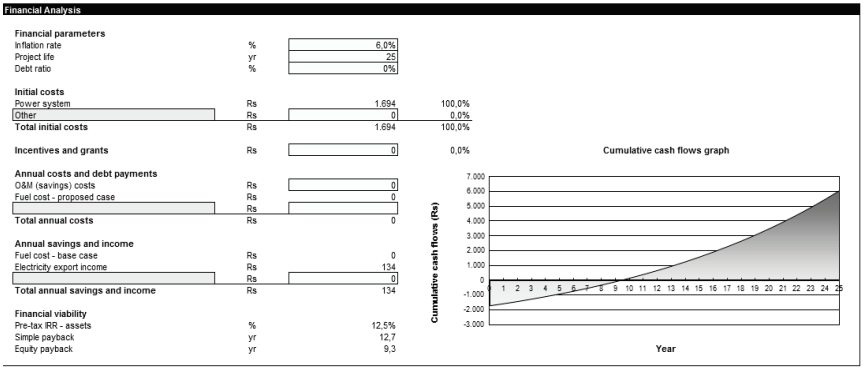



Figure 7. Cash flow considering an internal rate of return of 12.5%

## Conclusions

In terms of technical issues, some operational conditions of PV-powered WPS need to be guaranteed to adequately meet unit demand, such as electric power and pump pressure. The results of this study show that using a 135Wp PV module, a solar irradiance of 407W/m$^2$ is necessary to ensure an electric power of 55W and a pressure of 14psi. The use of circular beds allows the saving of 3,608 liters of water during the cultivation of 23kg of coriander—equivalent to an economy of 0.6kWh of electrical energy compared to a cultivation system with conventional beds.

In this study, invested capital returns after 10 years, if an internal rate of return of 10.2% is considered. PV-powered WPS for irrigation has the potential to become an increasingly economically advantageous source of electricity over expanding geographical regions—in many areas of developing countries there is no access to electricity and these systems can be adopted as a part of broader solutions to increase food production; to achieve social and economic improvement; and to contribute to a green economy. We suggest that that PV-powered WPS can be a key technology for developing countries.

## Acknowledgment

PETROBRAS for financial support.

EBSCOhost - printed on 2/14/2023 2:46 PM via . All use subject to https://www.ebsco.com/terms-of-use

# Bibliography

[1] Chilundo, R. J., Carvalho P. C. M., and Mahanjane U. S. "Potencial da Tecnologia Fotovoltaica para Irrigação de Unidades Produção Familiar: Estudo de caso para Moçambique," ABENS, Ed. Brasil: 2014, pp. 1-8.

[2] United Nations. "World Populations Prospects: The 2017 Revision," https://esa.un.org/unpd/wpp/publications/Files/WPP2017_KeyFindings.pdf last accessed: 14.03.2018," New York: 2017.

[3] B. Van Koppen, R. Namara, and R. C. Safilios. "Reducing poverty through investments in agricultural water management. Part 1. Poverty and gender issues. Part 2. Synthesis of Sub-Saharan Africa case study reports," International Water Management Institute, Colombo, Sri-Lanka, xii, 71p, 2005.

[4] UNESCO. "Relatório Mundial das Nações Unidas sobre Desenvolvimento dos Recursos Hídricos 2016," 2016.

[5] P. E. Campana, H. Li, and J. Yan. "Dynamic modeling of a PV pumping system with special consideration on water demand," *Applied Energy*, vol. 30 2013.

[6] UNESCO. "Ano Internacional da Energia Sustentável para Todos; Escolas de Associação da UNESCO," 2012.

[7] A. M. Zaki and M. N. Eskander. "Matching of photovoltaic motor-pump systems for maximum efficiency operation," *Renewable Energy*, vol. 7, no. 3, pp. 279-288, Mar.1996.

[8] R. J. Chilundo, P. C. M. Carvalho, M. M. N. Diniz, and A. M. E. Bezerra. "Photovoltaic powered irrigation system applied to familiar agriculture," International Conference on Renewable Energies and Power Quality (ICREPQ'14). La Coruña (Spain), 25th to 27th March 2015.

[9] K. Kapadia. "Productive Uses of Renewable Energy: A Review of Four Bank - GEF Projects," 2004, pp. 1-33.

[10] K. K. Tanji and B. Yaron. "Managment of water use in agriculture," Advanced series in agricultural sciences ed 1994, pp. 1-320.

[11] G. Stanhill. *Energy and agriculture*. Berlin: Spring Heidelberg New York Tokyo, 1984, pp. 1-189.

[12] Rd. M. Islam, P. C. Sarker, and S. K. Ghosh. "Prospect and advancement of solar irrigation in Bangladesh: A review," 77 ed. 2017, pp. 406-422.

[13] M. R. Borges Neto, P. C. M. Carvalho, J. O. B. Carioca, and F. J. F. Canafístula. "Biogas/photovoltaic hybrid power system for the decentralized energy supply of rural areas," *Energy Policy*, vol. 38, pp. 4497-4506, 2010.

[14] L. R. Valer, M. C. Fedrizzi, T. A. Melendez, and R. Zilles. "Sistemas Fotovoltaicos de Bombeamento para Uso na Agricultura," Universidade de São Paulo: AGRENER, 2010, pp. 1-11.

[15] Instituto Brasileiro de Geografia e Estatística. "Censo Agropecário 2006. Resultados Preliminares," IBGE, Ed. Rio de Janeiro: Instituto Brasileiro de Geografia e Estatística, 2007, pp. 1-146.

[16] INE. "Produto Interno Bruto, Optica da Produção (variação Percentual do Volume)," 2011.

EBSCOhost - printed on 2/14/2023 2:46 PM via . All use subject to https://www.ebsco.com/terms-of-use

[17] The World Bank. “World Development Report 2008: Agriculture for Development,” The World Bank, Washington DC, 2014.
[18] P. C. M. Carvalho, L. A. D. Carvalho, J. J. Hiluy Filho, and R. S. H. Oliveira. “Feasibility study of photovoltaic powered reverse osmosis and pumping plant configurations,” *IET Renew. Power Gener.*, vol. 7, no. 2, pp. 134-143, 2013.
[19] M. C. Fedrizzi. “Sistemas Fotovoltáicos de abastecimento de água para uso comunitário: Lições apreendidas e procedimentos para potencializar sua difusão.” Doutorado Programa Interunidades de Pós Graduação em Energia, Universidade de São Paulo, 2003.
[20] I. Odeh, Y. G. Yohanis, and B. Norton. “Influence of pumping head, insolation and PV array size on PV water pumping system performance,” *Solar Energy*, vol. 80, no. 1, pp. 51-64, Jan.2006.
[21] R. S. H. Oliveira. “Planta laboratorial de dessalinizaão via osmose reversa alimentada por energia solar fotovoltaica com ou sem baterias,” Mestrado Universidade Federal do Ceará, 2011.
[22] RETScreen. “http://www.nrcan.gc.ca/energy/software-tools/7465,“ Last accessed: June 2017.
[23] S. C. S. Jucá. “Desenvolvimento de Sistemas de Aquisição de Dados sem Fio Aplicados à MicrogeraçãoDescentralizada. Tese de Doutoramento,” Fortaleza, Brasil: UFC, 2014.
[24] A. Hamidat, P. Benyoucef, and T. Hartani. “Small-Scale Irrigation With Photovoltaic Water Pumping System in Sahara Regions,” *Renewable Energy*, vol. 28, pp. 1081-1096, 2003.
[25] A. A. Hamza and A. Z. Tiha. “Performance of submersible PV solar pumping systems under conditions in Sudan,” *Renewable Energy*, vol. 6, pp. 491-495, 1995.
[26] C. Protogeropoulos and S. Pearce. “Laboratory evaluation and system sizing charts for a second generation Direct PV-powered, low-cost submersible solar pump,” *Solar Energy*, vol. 68, pp. 453-474, 2000.

EBSCOhost - printed on 2/14/2023 2:46 PM via . All use subject to https://www.ebsco.com/terms-of-use

# CHAPTER EIGHT

# THE EFFECT OF VARYING THE DISTANCE BETWEEN THE DOUBLE-GLAZING OF A SOLAR THERMAL COLLECTOR ON ITS FUNCTIONING

NABILA IHADDADENE[1], RAZIKA IHADDADENE[1]
FERES HADJI[1], AZZEDDINE MAHDI[1]

## Abstract

This research deals with the effect of varying the distance between the double-glazing of a solar thermal collector on its functioning. Experiments were executed on an active solar energy demonstration system (ET 200). An ordinary 3 mm thick pane of glass, which had the same surface area as that of the experimental device, was placed above the collector at distances of 2 cm, 4 cm, and 6 cm. Tests were performed on the solar collector with single and double-glazing. To assess the performance of the solar collector with double-glazing, a heliometer was used to measure the radiation intercepted by the upper pane of glass (the added glass) instead of the lower pane of glass (the collector glass). Compared to single-glazing, double-glazing has a negative effect on the function of the solar collector (efficiency degradation). The distance between the double-glazing studied significantly decreases the efficiency of the collector; significantly increases the irradiance; and does not affect the temperature of the absorber plate.

**Keywords:** Solar energy; solar collector; double-glazing; distance between double-glazing.

[1] Department of Mechanical Engineering, M'Sila University, B.P 166 Ichbelia – M'Sila, 28000 (Algeria).

EBSCOhost - printed on 2/14/2023 2:46 PM via . All use subject to https://www.ebsco.com/terms-of-use

## Introduction

Reducing the environmental impacts of fossil fuels (i.e. warming and pollution of the atmosphere), in addition to the growing energy demand of human populations, especially in developing countries, has encouraged the development of clean and renewable energies [1]. Renewable energy is energy generated from inexhaustible sources, including wind, solar, geothermal, biomass, and hydropower. In contrast, fossil fuels (petroleum, natural gas, and coal) are non-renewable energy sources that are depleted with use.

Solar energy is the main source of renewable energy around the globe [2]-[3]-[4]. It can be converted into both heat and electricity. Producing heat is the simplest and most direct application of solar energy.

Solar thermal collectors are devices used to accomplish the conversion of solar radiation into heat for both domestic and industrial demands [5]. A solar water heater is a kind of solar collector that heats water by solar radiation.

Solar water heaters (SWH) are made of a series of pipes containing water (or water and a working fluid) that capture and convert solar radiation into heat. This is transferred to a water tank, where the newly heated water is stored (a storage system). Since 1909, most solar water heating systems used in buildings have consisted of a solar collector and a storage tank [6]. Solar collectors are the central component of solar heating systems. They collect the sun's energy and transform it into heat, which is then transmitted to the water.

Solar water heaters can use a pump to move water (forced circulation) between the collector and the storage tank, in which case the solar water heater is said to be active (most common devices). Otherwise, it is a passive system (thermosiphon system).

De Saussure built the first prototype of the SWH, called "Hotbox," which was used to produce hot water for cooking and heating in 1767. It consisted of an insulated box with two glass panels covering its top face, while its bottom was painted black [6].

The USA was the first country where the SWH was commercialized and it enjoyed wide use even before the 1900s [6]. Solar water heating technology has developed considerably since its first appearance (i.e. over the past century). Nowadays, a wide variety of SWHs exist on the market. Solar collector designs can be divided into three main types: flat plate collectors (FPC); evacuated tube collectors (ETC); and concentrating collectors (parabolic dish and parabolic trough collector). In general, an absorber plate, a thermal exchanger, insulation, and the outer box are the

EBSCOhost - printed on 2/14/2023 2:46 PM via . All use subject to https://www.ebsco.com/terms-of-use

four principal components of the FPC. Flat plate collectors are the simplest and most widely used collectors. Here, the interception area and the absorption area are equal.

The characteristics of an FPC affects the performance of the SWH. As such, most studies have been dedicated to flat plate solar collectors with the notable goal of boosting their efficiency [5]-[7]-[8]-[9]-[10] in order to improve the functioning of SWHs.

The glass in solar devices absorbs most of the infrared radiation re-emitted by the absorber, which improves the thermal efficiency of the solar collector.

This chapter constitutes a continuation of our previous work dedicated to studying the effect of the distance between double-glazing on the performance of a laboratory-based solar water heating system and presented at the International Conference on Renewable Energies and Power Quality (ICREPQ'14) [11].

This paper is organized as follows: Section 3 presents a description of the experimental setup; Section 4 shows the governing equations applied to the ET 200 solar collector; Section 5 illustrates the experimental procedure; and section 6 discusses the results obtained. The conclusion ends the paper.

## Experimental Setup

The experimental device used in this investigation is the ET200 collector, a system designed by GUNT Company (Germany) for heating domestic water (see Fig. 1).

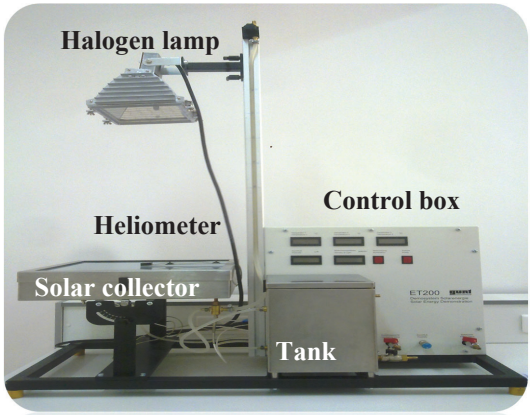



Figure 1. Experimental device.

EBSCOhost - printed on 2/14/2023 2:46 PM via . All use subject to https://www.ebsco.com/terms-of-use

This study was conducted in the laboratory under a constant incident radiation, a halogen lamp was used, instead of the sun, for this purpose (Fig. 1). In real conditions, incident solar radiation is not constant, but varies over time.

As seen in Fig. 1, the solar water heater (the experimental device) is composed of a water storage tank, a flat plate solar collector, a high-powered lamp, and a control and command box.

The solar collector is a planar collector covered with single-glazing. It turns around an axis allowing the collector to tilt from 0° to 60°.

The absorber plate is the central element of the collector. It consists of three blackened bands of 320x120 mm² each. The absorber plate is made of highly absorptive material in order to intercept the maximum incident solar energy.

The copper tubes, which act as a heat exchanger, are welded to the back of the absorber plate and connected at both ends to the water tank (in a closed loop). The heat transfer fluid used in the solar water heater is water.

Two kinds of insulators are found in the ET 200 solar collector to reduce heat loss from its front, back, and its four sides. The glass cover is used to minimize heat loss by convection from the absorber plate through the front side of the collector. Moreover, the absorber plate is not glued to the glass cover and there is a gap between them. Polystyrene is used to lower heat lost by conduction from the back and along the four sides of the solar collector. The outer metallic box seen in Fig. 1 holds the above-mentioned components.

The hot water produced through the collector is transmitted to the storage tank where it is stored. This tank is well insulated to prevent heat loss.

A volume flow control valve controls the flow rate of the pump used by the experimental device (active system). This valve is located in the control and command box.

Three PT 100 sensors were used to give temperature measurements at the inlet and outlet of the absorber ($T_1$ and $T_2$ respectively) and in the storage tank $T_3$.

A high-powered halogen lamp (Max 1000 W) was employed as a source of radiation energy. In laboratory conditions, the sun was substituted for by the halogen lamp (an artificial energy source).

The heliometer shown in Fig. 1 measures the illuminance (i.e. incident solar flux on the glass surface).

Measurements of water flow rate, temperatures, and illuminance are displayed on the digital displays of the control box (see Fig. 1).

EBSCOhost - printed on 2/14/2023 2:46 PM via . All use subject to https://www.ebsco.com/terms-of-use

The experimental device works when water is brought into contact with the absorber plate, which is exposed to the solar radiation emitted by the halogen lamp that passes through the glass cover. As a consequence, the water temperature rises (water heats up). Heated water is pumped (active system) through the collector to a helicoid heat exchanger placed in the storage tank (indirect system), heating the water in the tank.

## Governing Equations

In a steady state, the energy balance applied to the collector-intercepting surface is given by the following equation [12]:

$$E = E_u + P \tag{1}$$

Where:

$E$ : is the incident solar flux captured by the glass surface of the solar collector (W);

$E_u$ : is the useful flux, i.e. incident solar flux transmitted to water through the collector (W);

$P$ : is the heat flux lost through the back, the front, and the lateral sides of the collector.

### *Incident solar flux*

The light meter (heliometer) was placed exactly in the middle of the transparent glass surface of the collector below the radiation source (halogen lamp) to give exact results and as recommended by the manufacturer of the experimental device. [13] The heat fluxes intercepted by the glass surface were measured by the heliometer and their values were displayed (given in W/m$^2$) on the control box.

The displayed values had to be multiplied by a correction factor of 2.95 to get the true values of the incident fluxes [13]-[14]. The incident solar flux through the glass area (W/m²) of the solar collector is given by the following formula:

$$E = G \times S \tag{2}$$

Where;

$G$ : is the illuminance, i.e. incident solar flux on the glass surface (W/m²);

$S$ : is the surface area exposed to solar radiation (m²).

EBSCOhost - printed on 2/14/2023 2:46 PM via . All use subject to https://www.ebsco.com/terms-of-use

### *Useful flux*

The useful flux is the heat flux transmitted to the water and is given by the following equation:

$$E_u = \dot{m} \times C_p \times (T_2 - T_1) \tag{3}$$

where:

$\dot{m}$ : is the water mass flow rate (kg/s), which is connected to the volumetric flow rate as follows:

$$\dot{m} = \rho \times Q_v \tag{4}$$

$Q_v$ : Volumetric flow rate ($m^3/h$);

$\rho$ : Water density ($kg/m^3$);

$C_p$ : Water specific heat;

$T_2$ : Water outlet temperature of the absorber;

$T_1$ : Water inlet temperature of the absorber.

***Instantaneous Solar collector efficiency***

The instantaneous efficiency of a solar collector is defined as the ratio between the useful flux (output parameter) and the incident flux (input parameter) [12]:

$$\eta = \frac{E_u}{E} \tag{5}$$

It should be noted that the thermal analysis of the solar collector given by the above equations (steady state) is simpler than that used for the transient state, where the notion of time intervenes.

## Effect of Varying the Distance Between Double-Glazing

During the course of the experiments, to study the effect of the distance between double-glazing on the ET200 solar collector's performance, the following parameters were kept constant: the collector's intercepting surface (S = 0.13838 m², i.e. whole glass cover surface); the angle of

EBSCOhost - printed on 2/14/2023 2:46 PM via . All use subject to https://www.ebsco.com/terms-of-use

inclination of the solar collector (0°, i.e. horizontal position); the emitted power of the halogen lamp; and the water flow rate (Qv= 8 l/h).

An ordinary 3 mm thick glass pane, having the same surface area as that of the experimental device, was placed above the collector at distances of 2 cm, 4 cm, and 6 cm (see Fig. 2)

Tests were also performed on the collector without the added glass pane (single-glazing) to determine whether double-glazing enhances the performance of the solar collector.

The location of the light meter posed a problem for the double-glazed collector, as to whether it should be put on the glass of the collector or on the added pane of glass? As a result, both locations were taken into account during the experiments.

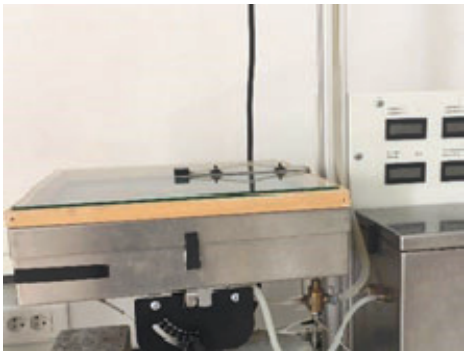


Figure 2. Solar collector with double-glazing (2 cm distance between double-glazing).

For the first location, the heliometer was placed in the middle of the collector glass surface. For the second location, it was put in the middle of the added glass (see again Fig. 2).

The duration of each experiment was set at 190 minutes and temperatures ($T_1$, $T_2$, and T3) were taken every 5 minutes, as had been done in our previous work [11]-[14]. In addition, temperature measurements were also taken at the center of the absorber plate $T_{abs}$; the collector pane $T_{gc}$; and the added pane $T_{ga}$, with the same timings (every 5 minutes).

Our experiments were conducted in the laboratory at an ambient temperature in order to work under stable conditions.

EBSCOhost - printed on 2/14/2023 2:46 PM via . All use subject to https://www.ebsco.com/terms-of-use

## Results and discussions

First of all, it should be noted that all the temperatures recorded are independent of the location of the heliometer. The incident solar radiation, on the other hand, depends on the heliometer's location.

All the temperatures recorded ($T_1$, $T_2$, $T_3$, $T_{abs}$, $T_{gc}$, and $T_{ga}$) increase with time. The curves showing the evolution of water temperatures ($T_1$, $T_2$, and $T_3$) over time for all the experiments performed describe a similar course. An illustrative example is given in Fig. 3.

Due to heat transfer occurring in the collector between water and absorber plate and inside the water tank, the temperatures at the outlet of the absorber achieved the highest values and those at the inlet of the absorber the lowest ones. More detailed explanations of this process have been given in our previous studies [11]-[14].

Fig. 4 shows the evolution over time of the temperature at the centre of the absorber plate for single and double-glazing (considering the different distances between the double-glazing).

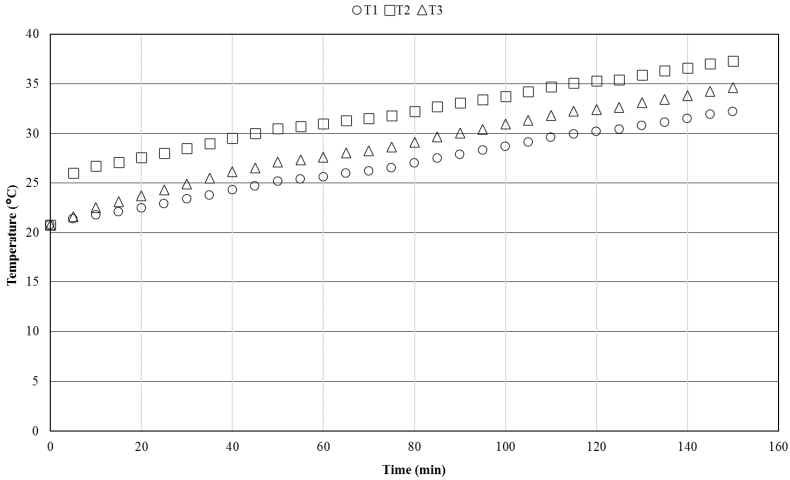



Figure 3. Temperatures $T_1$, $T_2$, and $T_3$ evolution over time for a distance of 6 cm between double-glazing.

EBSCOhost - printed on 2/14/2023 2:46 PM via . All use subject to https://www.ebsco.com/terms-of-use

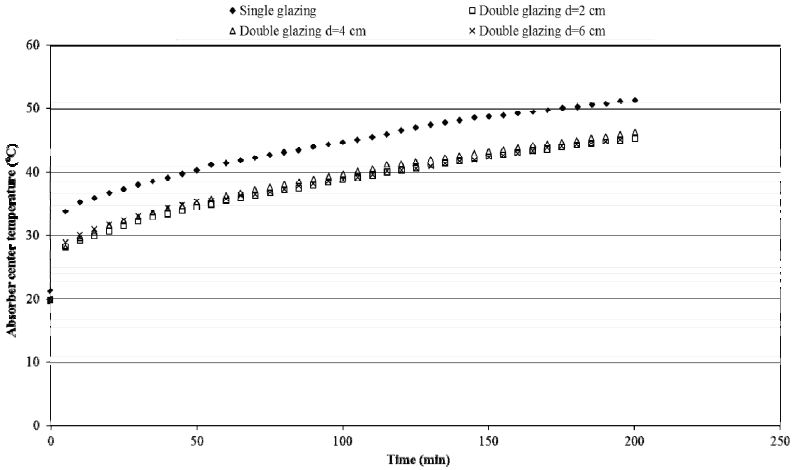



Figure 4. Absorber plate centre temperature evolution over time for single and double-glazed solar collectors.

As seen in Fig. 4, double-glazing lowers the temperature at the centre of the absorber and hence the temperature of the absorber plate. The distance between the double-glazing (from 2 cm to 6 cm) has no significant effect on the temperature of the absorber plate ($p>0.05$).

The absorber plate is a metal sheet. Since the temperatures recorded at three different points of the absorber do not show a significant difference ($p>0.05$), we can say that it acts as a medium at a uniform temperature. As such, the temperature at the center of the absorber can be considered to be the temperature of the absorber plate.

Fig. 5 shows the evolution of the temperature at the centre of the upper glass over time for single and double-glazed collectors.

The temperature at the centre of the upper glass pane of the double-glazed collector (for the different distances studied) was higher than that of the glass of the single-glazed collector. This is due to the distance separating the halogen lamp from the intercepting glass surface.

Again, there is no significant difference between the temperatures recorded at the centre of the upper glass for the different distances between the double glazing ($p>0.05$). This is due to the characteristics of the added glass (ordinary glass pane).

EBSCOhost - printed on 2/14/2023 2:46 PM via . All use subject to https://www.ebsco.com/terms-of-use

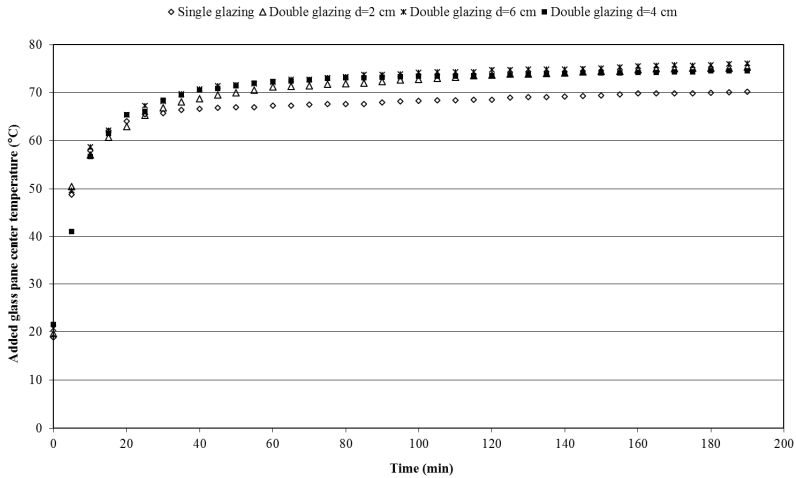



Figure 5. Upper glass temperature evolution over time for single and double-glazed collectors.

Fig. 6 displays the evolution of the tank's water temperature over time for single and double-glazed collectors (for the different distances between the double-glazing).

From Fig. 6 we can see that the double-glazed collector heats the water less than the single-glazed collector does. Moreover, varying the distance between the panes of the double-glazed collector from 2 cm to 6 cm leads to no significant variation in the tank water temperature recorded ($p > 0.05$).

This is in agreement with previous results (absorber and upper glass surface temperatures).

Quantitatively, the average temperature of the heated water using the single-glazed collector was 33.19°C, whereas an average of 30.70°C was found with the double-glazed collector.

The analysis that follows was done with the experimental device operating in a steady state (beyond 30 min.). During this regime, the energy transmitted to the water and the efficiency of the collector are both time independent.

EBSCOhost - printed on 2/14/2023 2:46 PM via . All use subject to https://www.ebsco.com/terms-of-use

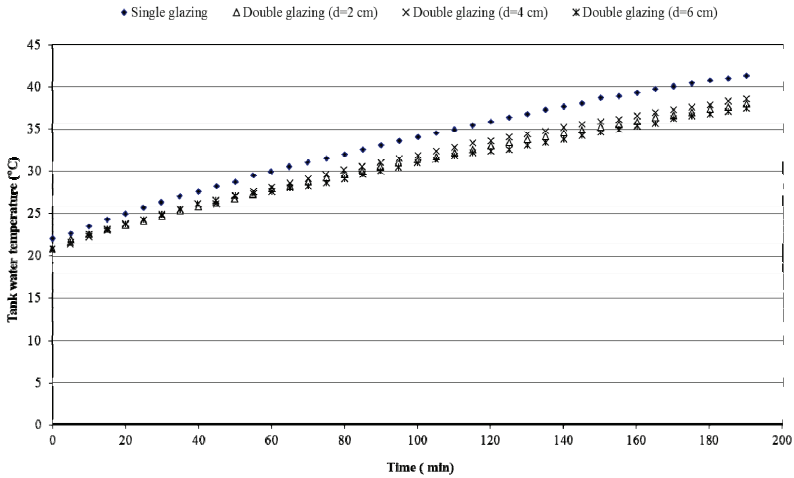



Figure 6. Tank water temperature evolution over time for single and double-glazed collectors.

As the temperature of the absorber plate is not influenced by the distance between the two panes of the double-glazed collector. It follows that the energy received by the water (useful energy) in the double-glazed collector is independent of this distance. Similarly, comparing the temperature of the absorber in the case of single and double-glazing, it follows that the energy transmitted to the water in the single-glazed collector is higher than that transmitted where double-glazing is used (see Fig. 7).

According to equation (3), the energy received by the water (useful energy) is proportional to water temperature difference. Therefore, Fig. 7 can inform us roughly (qualitatively) about the energy transmitted to the water in the single and double-glazed collectors. Moreover, double-glazing reduces useful energy by 11.3% compared to single-glazing.

In order to determine the exact location of the heliometer, two positions were studied: the middle of the upper glass pane and that of the collector glass pane. Fig. 8 shows the incident radiation for both positions of the heliometer.

EBSCOhost - printed on 2/14/2023 2:46 PM via . All use subject to https://www.ebsco.com/terms-of-use

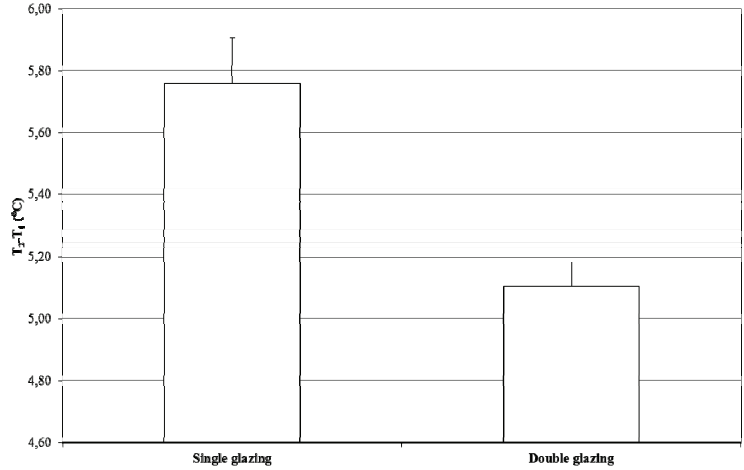



Figure 7. Water temperature difference in single and double-glazed collectors.

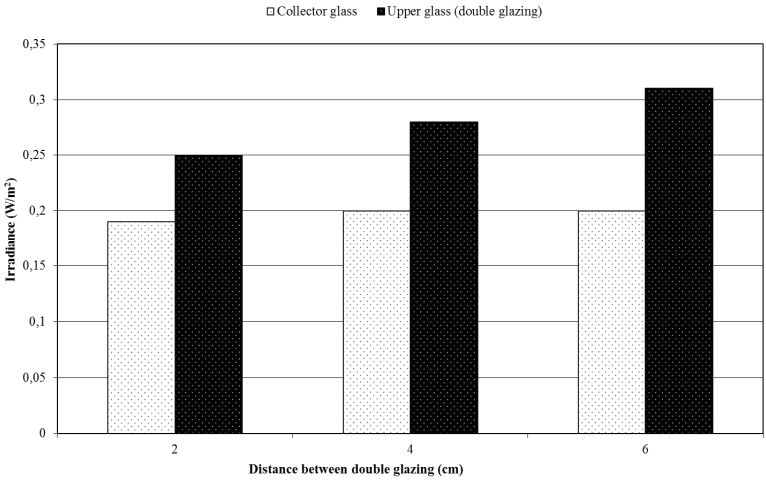



Figure 8. Effect of the position of the heliometer on the irradiance for different distances between the double-glazing.

The heliometer is the instrument that measures the incident solar flux (emitted by the halogen lamp) on the glass surface (W/m²).

As seen in Fig. 8, the location of the heliometer affects the incident solar flux. When the receiving surface is closer to the radiation source, it

EBSCOhost - printed on 2/14/2023 2:46 PM via . All use subject to https://www.ebsco.com/terms-of-use

receives more energy than when it is far away. Additionally, the distance between the double-glazing significantly influences ($p<0.05$) the energy received by the heliometer (and consequently the incident flux) when it is placed on the upper glass. It has no effect when the heliometer is placed on the collector glass (lower glass).

When the heliometer is placed on the collector glass, it receives less energy because, in addition to the distance separating the glass of the collector from the halogen lamp (as above), a part of the incident radiation is reflected by the upper pane.

According to equation (5), the efficiency of the collector with double-glazing is inversely proportional to the incident solar flux. The useful flux is constant, as previously explained. It follows that double-glazing improves the efficiency of the solar collector when the heliometer is placed on the glass collector. Inversely, it decreases the collector's efficiency when the heliometer is on the added glass. As seen above, double-glazing lowers the temperature of the tank water and the heliometer must be placed on the added glass (see Fig. 2) in order to get the right results.

Fig. 9 shows the efficiency of single and double-glazed collectors (taking in to consideration the distance between the double-glazing).

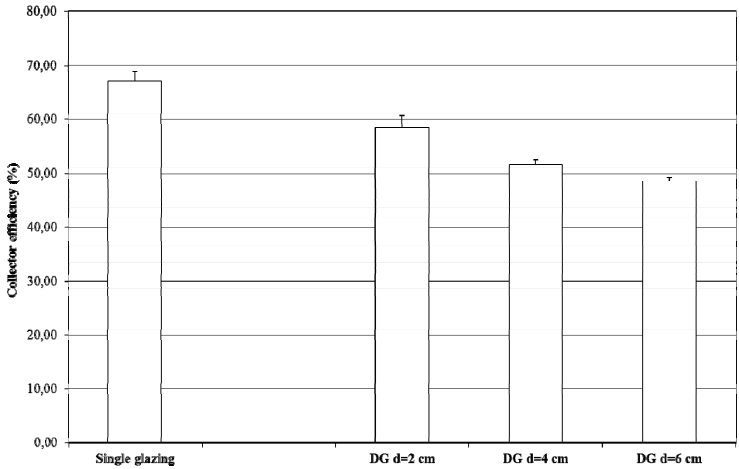



Figure 9. Efficiency of single and double-glazed collectors for different distances between the double-glazing.

As seen in Fig. 9, adding another pane of glass above the collector glass pane decreases its efficiency. This is due to the layer of air, which

EBSCOhost - printed on 2/14/2023 2:46 PM via . All use subject to https://www.ebsco.com/terms-of-use

plays the role of a thermal insulator between the two glass panes (for further explanation, please see our previous work) [11]. Lifting the upper glass of the double-glazed collector (increasing the distance between the two glass panes) decreases its performance. This decay follows a power law, according to our previous work [11].

Statistically, there is a significant difference between the efficiency of the double-glazed collector when lifting the upper glass from a distance of 2 cm to one of 6 cm ($p<0.05$).

## Conclusion

This study on the effect of varying the distance between the double-glazing of the ET 200 solar collector on its functioning has allowed us to ascertain the following points:

-The effect of adding a normal glass pane of 3 mm thickness above the collector glass lowers the temperature of the absorber plate; lowers the temperature of the tank water; increases the temperature at the center of the added glass; and decreases the efficiency of the collector.

- The right location of the heliometer for collectors with double-glazing is it in the middle of the added glass pane.

- Lifting the upper pane of glass of a double-glazed collector (increasing the distance between the two glass panes from 2 cm to 6 cm) significantly decreases its efficiency; significantly increases irradiance. This does not affect the absorber plate temperature, the tank water temperature, nor the temperature at the center of the added glass pane.

## References

[1] M. S. Adaramola. “Estimating global solar radiation using common meteorological data in Akure Nigeria,” Renewable Energy 2012, Vol. 47, pp. 38-44.

[2] J. Almorox, M. Bocco, E. Willington. “Estimation of daily global solar radiation from measured temperatures at Cãnada de Luque, Cõrdoba, Argentina,” Renewable Energy 2013, Vol. 60, pp. 382-387.

[3] K. Ka-LunLau, F. Lindberg, E. Johansson, M. I. Rasmussen, S. Thorsson. “Investigating solar energy potential in tropical urban environment: A case study of Dar es Salaam, Tanzania,” Sustainable cities and Society 2017, Vol. 30, pp. 118-127.

[4] M. Chegaar, A. Chibani. “Global solar radiation estimation in Algeria,” Energy Conversion and Management 2001, Vol. 42, pp. 967-973.

[5] M. Hazami, S. Kooli, M. Lazaar, A. Farhat, A. Belghith. “Performance of a solar storage collector,” Desalination 2005, Vol. 183, pp. 167-172.

EBSCOhost - printed on 2/14/2023 2:46 PM via . All use subject to https://www.ebsco.com/terms-of-use

[6] M. R. Islam, K. Sumathy, S. U. Khan. “Solar water heating systems and their market trends,” Renewable and Sustainable Energy Reviews 2013, Vol. 17, pp. 1-25

[7] S. Youcef-Ali. “Study and optimization of the thermal performances of the offset rectangular plate fin absorber plates, with various glazing,” Renewable Energy 2005, Vol. 30, pp. 271-280.

[8] R. Tang, Z. Sun, Z. Li, Y. Yu, H. Zhong, C. Xia. “Experimental investigation on thermal performance of flat plate collectors at night,” Energy Conversion and Management 2008, Vol. 49, pp. 2642-2646.

[9] K. Aoues; N. Moummi, M. Zellouf, A. Moummi; A. Labed; E. Achouri, A. Benchabane. “Amélioration des performances thermiques d’un capteur solaire plan à air: étude expérimentale dans la région de Biskra,” Revue des Energies Renouvelables 2009, Vol. 12, pp. 237-248.

[10] S. Jaisankar, J. Ananth, S. Thulas, S. T. Jayasuthakar, K. N. Sheeba. “A comprehensive review on solar water heaters,” Renewable and Sustainable Energy Reviews 2011, Vol.15 (6), pp. 3045-3050.

[11] N. Ihaddadene, R. Ihaddadene and A. Mahdi. “Effect of Distance between Double-glazing on the Performance of a Solar Thermal Collector,” Renewable Energy and Power Quality Journal (RE&PQJ) N° 12, 2014.

[12] R. Ben Slama. “Experimentation of a plane solar integrated collector storage water heater.” Proc. International Renewable Energy Congress, Sousse, Tunisia, November 5-7, 2010, pp. 395-403.

[13] Instrumentation manual, ET 200 Solar Energy Demonstration. GUNT, 2003.

[14] R. Ihaddadene, N. Ihaddadene, M. Bey, F. Z. Hamidibacha. “The effects of volumetric flow rate and inclination angle on the performance of a solar thermal collector, Energy Conversion and Management 2014, Vol.78, pp. 931-937.

EBSCOhost - printed on 2/14/2023 2:46 PM via . All use subject to https://www.ebsco.com/terms-of-use

EBSCOhost - printed on 2/14/2023 2:46 PM via . All use subject to https://www.ebsco.com/terms-of-use

# PART II:

# WIND GENERATION

EBSCOhost - printed on 2/14/2023 2:46 PM via . All use subject to https://www.ebsco.com/terms-of-use

# CHAPTER NINE

# A NEW COST-EFFECTIVE EXCITATION-CONTROLLED SYNCHRONOUS GENERATOR-BASED WIND TURBINE SCHEME

ALI SHAMSNIA, MOSTAFA PARNIANI[1]

## Abstract

This chapter presents a new excitation-controlled synchronous generator (ECSG) based scheme for wind turbines. The pros and cons of this scheme are analysed. The main advantages of ECSG wind turbines include cost reduction and a simplified power electronic converter. Additionally, this system maintains a level of controllability appropriate for the most advanced wind turbine schemes. The main idea behind the ECSG scheme is the employment of a synchronous generator excitation current for turbine control. This allows the generator-side converter to be simplified to a diode bridge rectifier. The main challenge facing the ECSG is the issue of torque ripple in its generator, which is discussed along with a solution. Simulation and experimental results confirm the effectiveness of the proposed wind turbine scheme.

**Keywords:** Electrically excited synchronous generator-based wind turbine; wind turbine scheme; superconductor generator; cost effective wind farm.

## Introduction

Wind turbines (WTs) are arguably the most developed sources of renewable electrical energy and have ratings of up to several MWs. Since the early days of the exploitation of wind energy for electricity generation,

[1] Center of Excellence in Power System Management and Control, Department of Electrical Engineering, Sharif University of Technology, Tehran, Iran.
Emails: shamsnia_ali@ee.sharif.edu; parniani@sharif.edu

EBSCOhost - printed on 2/14/2023 2:46 PM via . All use subject to https://www.ebsco.com/terms-of-use

different types of WT scheme have been developed. Early schemes were constant speed types, i.e. the WT generator speed was relatively constant, regardless of wind speed. With the need for higher efficiency, a requirement for the generator speed of a WT to vary in accordance with wind speed arose. This led to the development of variable speed WT schemes. Another major advantage of such WTs is the reduced mechanical stress placed on the WT blades and tower. In recent decades, different power conversion techniques have been developed for the variable speed operation of WTs. The doubly fed induction generator (DFIG) WT—a major WT system—was first developed in the late 1990s. The back-to-back voltage source converter (VSC) that is needed for the variable speed operation of this scheme has a capacity of approximately 20~30% of the WT power rating. This partially rated power converter results in the advantage of reduced cost for DFIG schemes. However, the limited range of speed control and the necessity for a strong grid to connect to during startup remain major drawbacks. Moreover, DFIG-based WTs contribute to short-circuit currents during grid faults, because the stator is directly coupled to the grid. Finally, DFIG schemes always require a multi-stage gearbox between the turbine and the generator [1], [2], [3], [4], [5].

Due to the high torque requirements, the feasible limit for an industrial three-stage gearbox (the usual choice in DFIG-based WTs) is about 5 MW. Moreover, gearboxes reduce the reliability of WTs considerably. According to a reliability study done on 6,000 onshore WTs over 11 years, while gearboxes do not have the highest failure rate, their failures result in the greatest downtime periods (an average of 340 h/failure). Obviously, gearbox failure downtime in offshore WT systems is much higher, which adds extra costs on top of maintenance costs [6]. According to [7], for an offshore DFIG-based wind farm, the downtime cost of a gearbox is the most dominant component of total downtime cost. Furthermore, replacing a faulty gearbox in a WT may cost as much as 10% of the initial construction cost. Finally, the brushes of the DFIG slip ring system have an average lifespan of 6~12 months and require regular maintenance. As such, it seems likely that the problems associated with DFIG WTs will limit their use in the future [8], [9].

An alternative scheme that overcomes the disadvantages of DFIG WTs is the variable speed full converter synchronous generator (SG) based WT. For example, this scheme makes the simplification, or even the elimination, of the WT gearbox possible. It does this by employment of high pole number, medium speed or low speed SGs. In contrast, a high pole number DFIG is technically not feasible because the bigger air gap needed, which reduces considerably the efficiency of DFIGs [8]. The dominant form of

EBSCOhost - printed on 2/14/2023 2:46 PM via . All use subject to https://www.ebsco.com/terms-of-use

SG-based WTs use back-to-back VSCs as power converters, which interfaces the stator terminal with the AC grid. A major disadvantage of this topology is that the converter must process all of the SG power, while the DFIG requires only about 30% of the WT power to be processed by the converter. The requirement for two full-rated VSCs results in a significant economic burden for this scheme [5], [9]. As such, an alternative low-cost converter for variable speed SG-based WTs has been an object of study for some time. The employment of a diode bridge rectifier (DBR) as a SG side converter has been found to be an attractive solution.

In the following section, DBR-SG-based WTs are reviewed along with their drawbacks. In Section III, a new WT scheme, called an excitation-controlled SG (ECSG) WT, is proposed, which uses an electrically excited SG (EESG) system. The ECSG WT solves the major problems of the DBR-SG WT, while maintaining its advantage of cost reduction. Section IV reviews current and future trends of EESGs in WT technology to show the potential for practical application of ECSG-based WTs. Section V elaborates the design issues of the machine-side and grid-side converters of the proposed scheme. Finally, Section VI presents simulation and experimental results and verification to clarify the performance of this scheme.

## Diode Bridge Rectifier-SG-Based WTs

In current full converter SG-based WTs, the generator-side converter is not responsible for the excitation current. As such, it is possible to use a simple DBR, while the grid-side converter is maintained by a VSC, which serves two main functions: tracking the maximum power point of the WT and regulating the output reactive power or terminal voltage. The DC link in this WT scheme consists of a current smoothing inductor, connected in series with a DBR, and a capacitor. The addition of a constant excitation generator (either PMSG or EESG) to this scheme provided the first generation of DBR-SG-based WTs to significantly reduce WT converter costs. Furthermore, the replacement of generator-side switching devices with diode rectifiers improves converter reliability [3], [5], [9], [10]. However, reduced controllability of the SG, along with the other problems described in the following, served to impede the application of this scheme.

### *Torque ripple problem in the generator*

Use of a DBR at the SG terminal results in a 6-pulse operation, and, therefore, the stator currents contain non-triplen odd harmonics. These harmonic currents create corresponding magnetic fields in the air gap that

EBSCOhost - printed on 2/14/2023 2:46 PM via . All use subject to https://www.ebsco.com/terms-of-use

rotate at different speeds from the main field. Interaction of these harmonic fields with the main field results in torque ripples, causing vibration, torsional resonance, and fatigue stress on the mechanical structure of WTs, if they are of sufficient magnitude. For example, in a 6-pulse system, the $5^{th}$ and $7^{th}$ harmonics are the major distorting currents at magnitudes of about 14% and 7%, and the corresponding torque ripple will have a harmonic component of the $6^{th}$ order with an approximate magnitude of 10% [8], [9], [11].

### *Lower generator efficiency*

The harmonic currents injected into the stator of a DBR-SG WT and the harmonic rotating magnetic fields created in the SG air gap increase its ohmic and core losses. However, according to an efficiency analysis done on DBR-SG WTs and back-to-back converter equipped SG WTs, the efficiency reduction of the DBR-SG WT generator is not particularly significant. Instead, its converter efficiency improvement (because of low loss DBR employment) is such that in comparison to back-to-back converter SG WTs, its overall efficiency is improved by at least 2% across the entire operation range [12].

### *Problem of the unity power factor*

In a SG-based WT with DBR, the passive rectifier's inability to exchange reactive power forces the SG terminal to operate according to the unity power factor. In this situation, if the synchronous reactance of the SG is low, then the terminal and air-gap power factors are close to each other. But, SGs typically have a significant synchronous reactance, resulting in a low air-gap power factor at heavy loads, which in turn limits the electric power generated. The unity power factor problem can also be studied from a SG terminal point of view. Under full load conditions, although the fundamental components of terminal voltage and current are in phase and the stator emf and current are near to rated value, a considerable voltage drop of stator synchronous reactance reduces the terminal voltage and limits SG active power to below the rated value. Thus, the rated terminal power cannot be absorbed at the rated current, and increased operating current is needed. In a SG-based WT equipped with a back-to-back converter, this problem is easily solved by the injection of reactive power into the SG terminal. The remedy used for this problem in industrial DBR-SG WTs is redesign of the SG to reduce its synchronous reactance. In addition, the SG and converter chosen need a higher rating. These corrections result in a more

EBSCOhost - printed on 2/14/2023 2:46 PM via . All use subject to https://www.ebsco.com/terms-of-use

expensive system that absorbs a part of the DBR's cost saving [11], [12].

### *Limited operational wind speed range of WT*

In a variable speed SG-based WT, generator speed changes in accordance with the wind speed. Conversely, in a constant excitation SG, the stator emf is directly proportional to the generator speed, and the stator terminal voltage depends on this emf S so that, in a SG WT with a DBR-VSC converter, the generator terminal voltage and its rectified voltage on a DC link are dependent on the wind speed. In low wind speed conditions, the DC link voltage drops to such an extent that the needed voltage for the grid-side VSC to operate properly cannot be achieved. This limits the cut-in wind speed of the WT and reduces its captured energy [9], [12]. Another adverse effect of variable DC link voltage is that the grid-side VSC must employ a wide range of modulation ratios to complete its duties. This deviates from its optimal point of operation and reduces its efficiency [3], [10].

To overcome this problem, a DC/DC boost converter is added to the DC link of second generation DBR-SG WTs (as shown in Fig.1). This converter has two main functions: boosting the DC link voltage to an appropriate level suitable for a grid-side VSC; and tracking the maximum power point of the WT. Since only one switching device is employed in the boost converter, this solution has a reasonable cost, while ensuring a full range of wind speed operation of the WT and improving its controllability [3], [9], [12], [11].

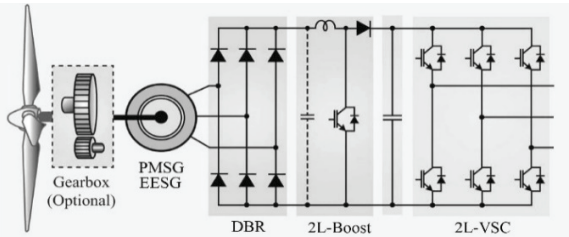



Figure 1. DBR-Boost-VSC-SG WT scheme [9]

The DBR-VSC-SG WT scheme has not been particularly successful due to the problems it has faced, especially its limited wind speed range of operation, and few industrial applications have been reported for it. For example, the Clipper Liberty 2.5 MW WT used this scheme with an over-rated voltage generator [9], [11]. Rather, it is likely that the DBR-Boost-VSC-SG WT scheme will gain widespread popularity in the WT industry [11], [13]. This scheme was first developed by the Spanish company MADE

EBSCOhost - printed on 2/14/2023 2:46 PM via . All use subject to https://www.ebsco.com/terms-of-use

[14]. Later, other manufacturers employed it in their WTs. For example, Enercon used this scheme for some of its products, like the 2MW E66/E70/E82 WT and the 3MW E82-E3 WT. Other examples that use this scheme include Vensys V70/77/82/87 WTs and Gold Wind GW70/77 WTs [8], [9], [11]. Finally, the 10 MW Britannia WT developed by Clipper is an forthcoming example of a DBR-equipped SG WT that will be used in "Round Three" wind farms as part of the UK's offshore wind power projects [8].

It is evident from the above that in spite of the aforementioned problems, the use of DBR-SG technology is well justified in the WT industry. On the other hand, although a number of problems have been resolved or improved using a DC-DC boost converter, there are still issues remaining. The new scheme proposed in the next section aims to make further improvements in this regard.

## Introduction of ECSG Topology

The main idea behind the ECSG WT scheme is that in an EESG WT, unlike a PMSG, an excitation current can be used as a means of WT control. Therefore, instead of the usual pattern of a constant excitation current for the EESG, and WT control through stator currents, variable excitation can be employed for this purpose. Of course, in an EESG directly coupled to an AC grid, adjusting the excitation current will lead to output reactive power control. But in WT applications, direct control of active power is required. The use of a DBR at the generator terminal will limit the operation of the SG to the unity power factor and varying the excitation current will lead to active power control. In fact, since the internal emf induced at the stator windings is proportional to the excitation current, any change in the excitation current will vary the stator emf and its current magnitude. As the SG terminal is operating at the unity power factor, the output active power is governed through control of the excitation current. Such a WT can be connected to an AC grid (through a VSC) or DC grid (directly or through a DC/DC converter). The electrical layout of a basic ECSG WT is shown in Fig. 2.

EBSCOhost - printed on 2/14/2023 2:46 PM via . All use subject to https://www.ebsco.com/terms-of-use

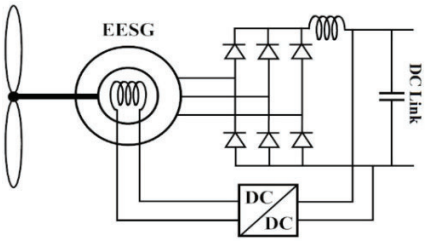



Figure 2. A basic ECSG WT scheme

## *Advantages of the ECSG scheme*

The ECSG scheme offers some advantages in comparison to conventional EESG-based WTs with back-to-back converters, some of which are found in common with other DBR SG WTs, while others are unique:

*A simpler and more reliable converter*

In comparison to a back-to-back converter EESG WT, the ECSG scheme simplifies the SG-side converter by replacing the costly VSC with a much simpler DBR that does not need any gate drive control system and is inherently more reliable. This converter simplification does not affect the turbine's controllability, since the DC/DC excitation converter of the EESG provides active power control capability. Thus, by optimal use of the existing excitation converter, the ECSG scheme offers a simplified converter WT with higher reliability. Furthermore, as the rating of SG excitation is about 5% of generator output, control of the WT through a much smaller excitation current, rather than SG armature currents, is easier and more logical.

*More economic*

According to a detailed study in [12], in a PMSG WT equipped with a back-to-back converter, replacement of the SG-side VSC with a DBR would lead to a 24% cost reduction of the WT converter. Note that the cost of adding a DC bus inductor was included in this study. Also, because of the DBR-SG WT's unity power factor problem, a 30% higher current rating was allocated for the WT converter unit in [12], and the resulting extra cost is also considered in the above evaluation. In contrast, as will be shown later, the ECSG scheme does not suffer from the unity power factor problem. Thus, an even greater cost reduction in its converter unit is expected when a back-to-back converter EESG WT is converted to an ECSG scheme. According to the price details given in [12], and without current rating improvements applied to the DBR-SG WT in this study, it

EBSCOhost - printed on 2/14/2023 2:46 PM via . All use subject to https://www.ebsco.com/terms-of-use

can be seen that the cost reduction of an ECSG WT converter can reach up to 29%. On the other hand, [9] estimates that the power converter of an onshore variable speed SG WT constitutes about 12% of the WT's overall cost. As such, the replacement of a back-to-back converter EESG WT with an ECSG scheme can lead to a 12%×29%=3.5% cost reduction of overall cost. According to [9], even a small cost reduction in WT converter system is important since this leads to huge cost savings in large wind farm projects that have hundreds of WTs, and the converter cost saving of 29% achieved by a single ECSG is a considerable amount.

Another useful economic comparison can be made between ECSG and DBR-Boost-VSC-SG WT schemes. As discussed earlier, although the addition of a boost converter and raising of the generator current rating (due to the unity power factor problem) restricts DBR-Boost-VSC-SG schemes' cost saving in comparison to what was hoped for, this scheme could still be successful in practice. The ECSG scheme, by eliminating the requirement for a boost converter and an increased current rating, acquires the entire cost saving potential of DBR-SG based WTs and displays even better economic characteristics.

*Faster inherent dynamic response*

The ECSG scheme offers faster dynamic response over the back-to-back converter EESG WT scheme. This is explained by considering two main aspects. Firstly, with a back-to-back converter, the step change of the SG-side VSC control signal causes a rapid change in SG stator current magnitude, but its emf only changes slowly as a function of generator speed (which varies slowly due to its inertia). By way of comparison, in an ECSG WT, a step change in the generator controlling signal (SG excitation voltage) changes the excitation current and generator emf rapidly (emf is a function of both the SG speed and the excitation current) and accordingly, the stator current magnitude is changed. In fact, the ECSG scheme control signal manages both effective variables on the SG terminal power. Thus, the ECSG has a faster reaction to its control signal. The other aspect of faster controllability in the ECSG is that its excitation converter provides a high current forcing capability over the field circuit through its high level input (ECSG DC link) voltage. This advantage will be more evident for superconductor excitation SGs because of zero field resistance.

## *Problems of the ECSG scheme and solutions*

The ECSG scheme shares some disadvantages in common with other DBR-SG-based WTs, which are discussed here along with their solutions.

EBSCOhost - printed on 2/14/2023 2:46 PM via . All use subject to https://www.ebsco.com/terms-of-use

*Torque ripple problem*

A suitable solution for the torque ripple problem of the ECSG scheme is through the employment of 12-pulse, 24-pulse, or higher order rectification systems. Of course, instead of a multi-winding transformer, here the EESG chosen will itself be multi-phase. This system will operate just like a multi-winding transformer-DBR system; but, instead of the cancellation of lower order harmonic currents at the primary transformer, the corresponding magnetic field harmonics will be cancelled out at the SG air gap, and the lower order torque ripples (the dominant ones) will vanish. The remaining major torque ripples in this case are of the $12^{th}$ and/or the $24^{th}$ order, with much smaller magnitudes [15].

This solution has been employed in DBR-Boost-VSC SG WTs like the Vensys V77 and Goldwind GW77 through the use of 6-phase SGs with a 30° phase shift between their 3-phase segments [9]. Overall, employment of multi-phase SGs for large WTs is common and these modifications can easily be found among current products of WT manufacturers [9], [11], [13], [15]. A multi-phase modular structure offers greater reliability, fault tolerance, and improved efficiency than a 3-phase system. In this structure, the output power is divided between a higher number of phases, allowing for a reduction in the converter module's rating, which is particularly helpful in high power WTs [13], [15].

*The unity power factor problem*

The unity power factor problem for the ECSG scheme can be easily solved without any need for redesign of the SG or improvement in the system current rating. This can be achieved through the ECSG's capacity for variable excitation. To clarify the discussion on the unity power factor problem of the ECSG, a simplified equivalent circuit of a SG equipped with a DBR is shown in Fig.3. Since only the fundamental component of the stator current is of concern, the DBR and the other parts behind the DC link are modeled as resistance (R), simulating the unity power factor operation of the SG. In addition, it is supposed that the SG is rotating at a rated speed and its internal emf is 1 pu; synchronous reactance has been assumed to be a typical value of 0.5 pu. In this situation, to deliver 1 pu of active power at the terminal, the resistance R must be 0.5 pu, which results in a 1.4 pu stator current and a 0.7 pu terminal voltage, showing 40% over current at full load.

EBSCOhost - printed on 2/14/2023 2:46 PM via . All use subject to https://www.ebsco.com/terms-of-use

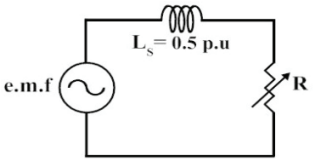



Figure 3. Simplified equivalent circuit of SG-based WT with diode rectifier

If we were to consider an ECSG with the same parameters. In this case, for example, by raising the excitation current to yield 1.1 pu emf, the over-current at rated power would reduce to just 3% (R=0.94 pu, $V_t$=0.97 pu). Thus, the ECSG scheme can reduce the over-current associated with the unity power factor problem at heavy loads to such an extent that there is no need for redesign of the SG or improvement of the system current rating.

*Limited operational wind speed range*

In the ECSG scheme, excitation control is used for the purpose of WT maximum power point tracking and DBR DC link voltage preservation at an appropriate level grid-side in the entire operational range. Thus, there is no need for a boost converter in the ECSG scheme, resulting in reduced cost and complexity, as opposed to the DBR-Boost-VSC-SG scheme.

## Current and Future Trends of EESGs in WT Technology

Since the ECSG scheme is based on EESGs, it is necessary to investigate current and future trends of EESG-equipped WTs in the wind industry to determine how useful the ECSG WT scheme may be.

### *EESGs in current WT technology*

In the nineties, SG-based WTs used electrical excitation, because permanent magnets (PMs) were too expensive. Later, when the price of PMs decreased, the focus shifted toward PMSGs, and they became commonly used in the 6 MW range. For example, Siemens moved from a DFIG to a low speed direct drive (DD)-PMSG at 6 MW SWT-6.0-120. This strategy was also adopted by other manufacturers, including GE, Hyundai, Mitsubishi, Alstom, Nordex, and AMSC. As another example, Bard Co. shifted from use of the DFIG to a medium speed simplified gearbox PMSG in the Bard 6.5. Areva, Gamesa, and Vestas have also used similar technology [3], [4], [16]. However, the main drawback of the DD-PMSG is its large size. This problem appears to become more serious as the technology pushes WTs to higher capacities. The other issue is the higher

EBSCOhost - printed on 2/14/2023 2:46 PM via . All use subject to https://www.ebsco.com/terms-of-use

cost of the SG due to the use of PM materials [3], [5], [16]. The amount of PMs used in a PMSG depends heavily on the generator speed. If we were to consider a 3-MW PMSG, the quantity of magnets required would be 650 kg/MW for a DD generator; some 160-200 kg/MW for a medium speed generator; and about 80 kg/MW for a high speed one [17]. The vast quantities of PM materials used in low speed PMSGs has led to a considerable increase in their demand. In recent decade, prices of PM materials have increased greatly. In 2011, the price of PM materials reached a point 100 times greater than prices in 2002, alarming the industry. Thankfully, one year later the prices started to reduce until they have finally stabilized at a range of four to eight times earlier values [7], [17]. Another serious concern with PM materials is the risk associated with the high geographical concentration of their supply (about 97% of them being extracted in China), resulting in supply uncertainty [17].

Since 2011, the high price of PMs have raised interest in alternatives for PMSGs. One WT manufacturer that has applied an alternative solution successfully is Enercon, which uses annular EESGs for its products [8]. Enercon has been a large and successful DD-WT manufacturer for a long time and has been one of five top WT manufacturers over the last decade [4], [7], [18]. Other manufacturers using EESGs in their WTs include M Torres, e.n.o. Energy, Global Wind Power, Kenersys, and Wikov [8].

### *Challenges associated with next generation WTs*

It is estimated that 10 MW offshore WTs will be in demand by 2020—this will be a challenge to achieve with existing generator systems [5]. As discussed earlier, geared systems have considerable reliability issues and the mass of the gearbox increases enormously with any increase in torque requirements. DD-SGs also suffer from high mass and large size problems. To increase the power rating of WTs, it is necessary to increase the blade radius, but noise and load concerns impose an upper limit on the tip speed of blades, reducing the rotational speed of the turbine ($\omega_s$) as the blade radius increases. Therefore, as the turbine shaft torque relationship $T_S = P/\omega_s$ indicates, very high torques are required for high-powered DD WTs [18]. On the other hand, the electrical torque of a SG is proportional to air gap flux density, machine volume, and the armature winding current. The peak flux density of a conventional SG is limited by saturation of steel laminates and cannot be exceeded without excessive Joule heating of the field windings. For PMSGs too, the peak air gap flux density is limited by the flux density produced by PM materials. Besides, electrical loading of the armature winding is limited by its copper loss and available cooling [19].

EBSCOhost - printed on 2/14/2023 2:46 PM via . All use subject to https://www.ebsco.com/terms-of-use

Thus, the only way to obtain higher torque is to increase the volume and weight of the SG. An upscaling of current SG technology for future large scale offshore WTs will result in an excessive rise in the drive train mass. For SG-WTs rated higher than 8 MW, the dimensions and weight increase exponentially. Accordingly, the tower, foundation, and all other supporting structures must be strengthened, resulting in a much heavier WT [6], [10], [20]. Detailed studies of future increases in the mass of WTs is reported in [21], which concludes that the supporting structure (inactive) mass of conventional SGs increases faster than active mass, as capacity grows. Finally, inactive mass becomes dominant for SGs of higher than 7MW and the cost of inactive mass comes to dominate SGs of higher than 10 MW, resulting in uneconomic SGs for large WTs. Thus, conventional technology cannot be used for next generation DD WTs and the requirement for a higher power density technology is clear [18], [20], [21], [22].

## *EESGs in next generation superconductor WTs*

Superconductors (SCs) are made of conductive materials whose resistance plunges to zero below their critical temperature. Superconducting SGs offer a promising solution for low and medium speed WTs with power ratings of above 10 MW, since employment of SC technology in SGs offers a significant reduction in the mass and size of a generator, as well as superior performance and reliability and potentially competitive costs [3], [5], [6], [10], [21], [22].

In fact, because of the zero resistance of SCs, they can carry current densities much higher than copper (40 times) with negligible losses. As such, using an SC as a DC field winding in a SG allows for considerable increase in the air gag flux density, and a much higher torque density SG can be designed. For example, increasing the air gap flux density from the conventional value of 1 T to 2~3 T in a SC-SG, offers the potential for increasing generator size and reducing weight by more than 50%, making it a potentially important component in next generation WTs [3], [4], [18], [19].

In general, DD-SC-SGs become lighter than DD-PMSGs for applications demanding more torque than 3,000 kN.m (e.g. a 5 MW, 13 rpm WT). Another distinct advantage of SC-SGs is their partial-load efficiency. The full load efficiency of SC-SGs is approximately the same as PMSGs, reaching over 96%; but at partial loads, efficiency in SC-SGs is higher than in conventional ones. This difference is more significant when loading decreases below 50%, differing by 1~2% for 50~60% loading and reaching up to 15% for loadings of 10%. This feature is advantageous for WT applications, since WTs mostly operate at partial-load conditions [3].

EBSCOhost - printed on 2/14/2023 2:46 PM via . All use subject to https://www.ebsco.com/terms-of-use

Finally, from an economic point of view it is estimated that the cost of an SC-SG will be competitive with that of 6.5 MW geared and 8 MW DD-PMSGs, and will be lower for higher ratings [6], [10], [20].

There are several industrial projects currently examining the use of SC-SGs for WTs. The DD-WT of Converteam; the 10 MW Sea Titan WT developed by AMSC; and the SuperPower 10 MW WT are just a few examples [6], [10], [20]. It is noteworthy that most of the SC designs proposed for WTs consist of a conventional stator and a SC rotor SG. The reason is that existing SCs are prone to high losses under AC operation [3], [4], [10], [18], [20], [21]. According to [17], by 2020 SC-SG WTs will be commercially available, forming up to 1% of WT annual installations worldwide; this share is predicted to grow to 18% by 2030.

It can be seen that EESGs are not just important to today's WT industry, but they are also likely to play a major role in the future of this industry. Therefore, investigating new schemes based on the potential of EESGs is important in making next generation WTs both usable and economic.

## ECSG Wind Turbine Converter Design Issues

Having examined the concept of the ECSG WT and investigated its features, in this section the choice between 12-pulse and 24-pulse rectifier ECSG structures is analyzed. Then, a suitable configuration is introduced for the grid-side converter of the WT for AC-grid wind farm applications.

### *Selection between 12-Pulse and 24-Pulse structures*

As mentioned earlier, in order to mitigate the SG torque ripple caused by the BDR, a higher than 6 pulse rectification system can be used at the SG output. Two potential candidates for this purpose are 12-pulse or 24-pulse DBRs. To choose between them, we must compare the following factors:

*Generator complexity*

Obviously a 12-phase EESG for a 24-pulse ECSG structure is more complicated to design and manufacture than a 6-phase EESG (suitable for a 12-pulse ECSG). This is why 6-phase SGs are more common in the industry today.

*Generator insulation*

For the ECSG structures studied here, it is considered that the DC links of rectifier modules are connected in series to achieve a higher voltage level

EBSCOhost - printed on 2/14/2023 2:46 PM via . All use subject to https://www.ebsco.com/terms-of-use

for grid connection. In addition, as usual for multi-phase high pole number SGs, a concentrated winding stator is assumed for ECSG structures. Under these circumstances, the stator winding insulation of an SG in a 12-pulse ECSG does not need any especial correction, since the maximum voltage between windings and the earthed stator body will reach up to the DC bus voltage of a 6-pulse module. This voltage, at worst, is equal to the corresponding 3-phase stator terminal's peak line-to-line voltage. SG insulation is normally designed to withstand this voltage. But for a 24-pulse ECSG, the maximum voltage between windings and the earthed stator is doubled, requiring SG insulation to withstand a voltage equal to two times the stator peak line-to-line voltage. This means a stronger insulation than usual is required, leading to a more costly SG.

For the remaining comparisons, a sample 6-pulse ECSG was selected as base module, and 12 and 24-pulse structures were constructed using it. Next, all the structures were simulated at different loadings to extract the relevant results.

*SG torque ripple*

Considering that restricting generator torque ripple to an appropriate level is sufficient to resolve the issue, harmonic analysis of a 6-pulse ECSG torque at 5%, 45%, and 100% loadings were done. The results shown in Fig. 4 indicate that the major ripple component of SG torque is of the 6$^{th}$ order, and this is eliminated using a 12-pulse structure. As such, a 12-pulse structure may be a suitable choice. Additionally, the total torque ripple magnitudes shown in Fig. 5 confirm the suitability of a 12-pulse structure, by alleviating torque ripple from 6.3~20% to an acceptable level of 2% across the entire operation range.

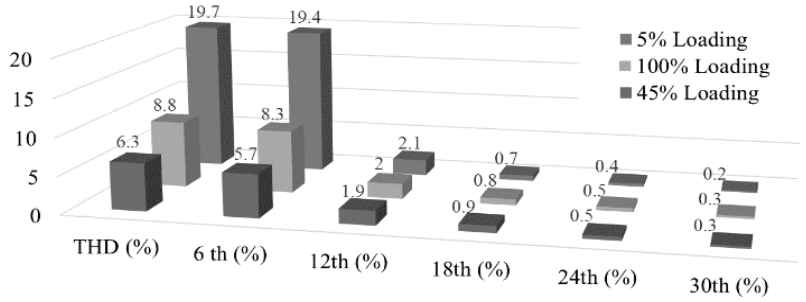



Figure 4. Harmonic analysis of 6-pulse ECSG torque ripple (results are in percentage of DC torque)

EBSCOhost - printed on 2/14/2023 2:46 PM via . All use subject to https://www.ebsco.com/terms-of-use

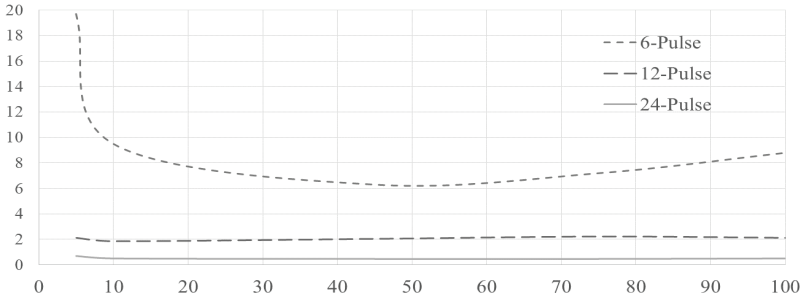



Figure 5. Total torque ripple of ECSG structures at entire operation range (in percentage of DC torque)

*DC bus voltage ripple reduction*

DC bus voltage ripples in 6, 12, and 24-pulse structures are compared in Fig. 6 at different loadings. As can be seen, replacing a 6-pulse structure with a 12-pulse one reduces the maximum DC bus voltage ripple from 5% to 2%; employment of a 24-pulse structure limits it to below 1%. Therefore, although the 24-pulse ECSG offers the best performance regarding this aspect, the 12-pulse ECSG sufficiently suppresses voltage ripple.

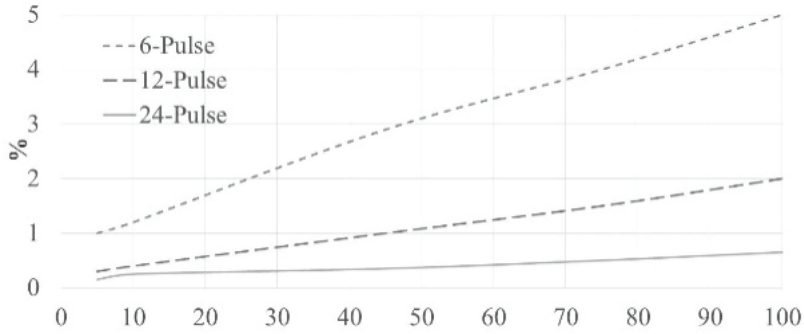



Figure 6. DC bus voltage ripple of 6, 12, and 24-pulse ECSG structures

Overall, it can be concluded that the benefits gained by upgrading a 12-pulse ECSG structure to a 24-pulse one do not justify the added complexity and cost of a 12-phase EESG. Therefore, the 12-pulse ECSG remains the better choice.

EBSCOhost - printed on 2/14/2023 2:46 PM via . All use subject to https://www.ebsco.com/terms-of-use

## *An ECSG WT scheme for an AC grid wind farm*

WT generators are often equipped with a step-up transformer to match the medium voltage of the local grid. In an onshore WT, the generator and converter are housed in a nacelle on top of the tower, while the transformer is located at ground level. Electrical power is then transmitted from the nacelle down, using droop cables, which are longer than the tower height in order to cope with excessive wind-up or twisting. The low-level output voltage of the multi-MW generator requires a high current flow in droop cables, resulting in losses [23], [24]. Alternatively, the transformer can be included in the nacelle, a choice mostly adopted offshore where estate at sea level is costly. In this situation, the bulky transformer's weight significantly increases the mechanical loading of the tower. Furthermore, its impact on O&M is important. Since a transformer cannot be made modular, large offshore cranes will be required for the eventual replacement of the transformer [5], [23], [24]. Omission of the transformer is expected to result in considerable cost saving in construction, installation, and maintenance of WTs in the future. To achieve this, multilevel converters may offer a practical solution [14], [23], [24], [25]. Apart from omission of the transformer, medium-voltage operation of WTs through multilevel grid-side converters presents other advantages, including: lower voltage stress on switching devices; improved power quality and filter size reduction; and lower switching frequency and losses [5], [13], [14], [25]. For these reasons, the wind energy industry is looking for appropriate medium-voltage multilevel topologies for large scale WTs [13]. A great number of studies have been conducted on this area. For example, [25] compared different converter topologies in terms of cost, complexity, and operation and concluded that for lower level-number topologies, an NPC (neutral point clamped) converter is the best choice; but for higher level numbers, a MMC (multilevel modular cascade) converter has more advantages.

In the case of the ECSG scheme proposed, if we suppose that a 5 MW, 4 kV, 6 phase EESG WT is utilized, the generator uses a concentrated winding stator with the 3-phase module specifications given in Table 1 [11]. The two modules are operated in a 12-pulse rectification mode.

The grid side converter is a 3-level NPC that uses two DC link capacitors in common with DBRs. Fig. 7 shows this ECSG-based WT. As mentioned, the maximum power point tracking (MPPT) in the WT is implemented by controlling the DC/DC excitation converter. The NPC converter is responsible for maintaining DC bus voltage at an appropriate level (10 kV) by adjusting the power injected into the grid. This WT, with an output voltage of 6.25 kV, is suitable for direct grid connection.

EBSCOhost - printed on 2/14/2023 2:46 PM via . All use subject to https://www.ebsco.com/terms-of-use

**Table 1. 5 MW EESG 3-phase module parameters**

| Parameter | Value | Parameter | Value |
|---|---|---|---|
| Rated Power | 2.5 MW | Stator Phase Resistance | 0.00513 p.u |
| Rated Line-to-Line Voltage | 4.0 kV | q-axis Synchronous Inductance | 0.378 p.u |
| Rated Stator Current | 485 A | d-axis Synchronous Inductance | 1.061 p.u |
| Rated Frequency | 40 Hz | Stator leakage Inductance | 0.1 p.u |

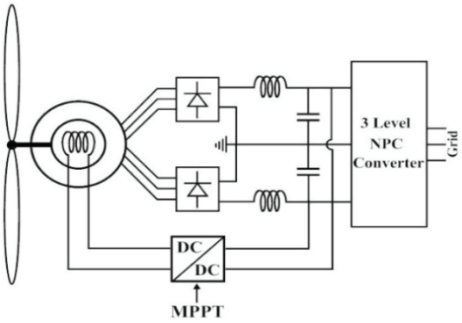



Figure 7. Electrical layout of a 12-pulse ECSG WT with AC output

## Simulation and Experimental Test Results

### *Simulation results of the sample ECSG*

The proposed ECSG WT was simulated using PSCAD software to check its MPPT capability and other expected characteristics. In the first simulation, the WT was connected to an AC grid. A popular MPPT algorithm, the hill climbing method, was used to regulate the excitation voltage of the SG. During this simulation, wind speed was decreased from an initial value of 10.3 m/s to 6 m/s by a step change at the 15$^{th}$ second of the run. Another step change was applied at the 30$^{th}$ second, which increased the wind speed to 13 m/s. The reason for using step changes, instead of a realistic wind profile, was to demonstrate the tracking capability of the proposed scheme more clearly. Shaft speed-power characteristic curves of the WT at the mentioned wind speeds are given in Fig. 8. Figure 9 shows the WT's absorbed power and shaft speed. As can be seen, the ECSG WT

EBSCOhost - printed on 2/14/2023 2:46 PM via . All use subject to https://www.ebsco.com/terms-of-use

has the level of controllability needed to fulfill MPPT.

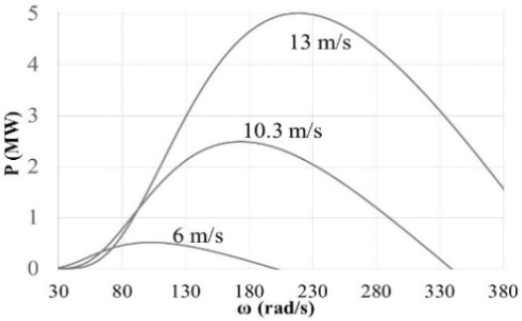



Figure 8. P-ω characteristic curves of WT

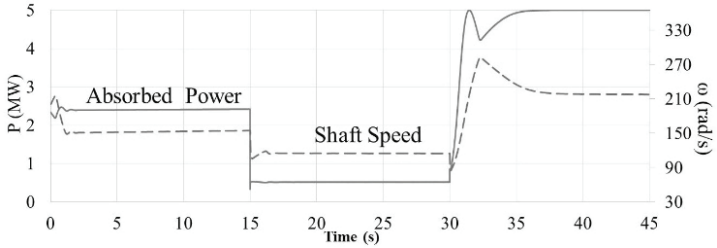



Figure 9. Results of ECSG WT for absorbed power and shaft speed

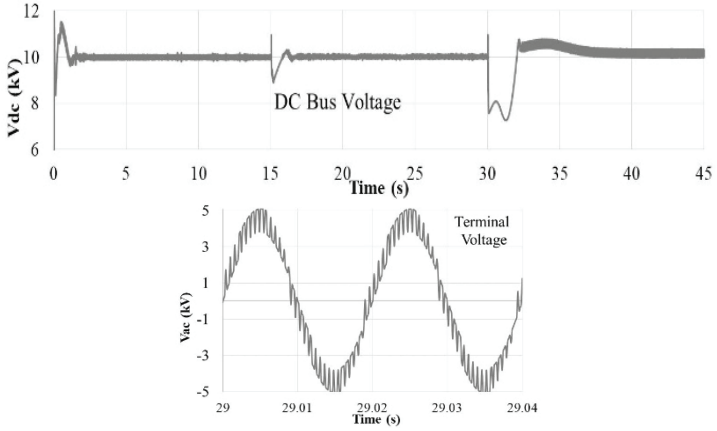



Figure 10. DC bus voltage of ECSG's converter and its terminal voltage

EBSCOhost - printed on 2/14/2023 2:46 PM via . All use subject to https://www.ebsco.com/terms-of-use

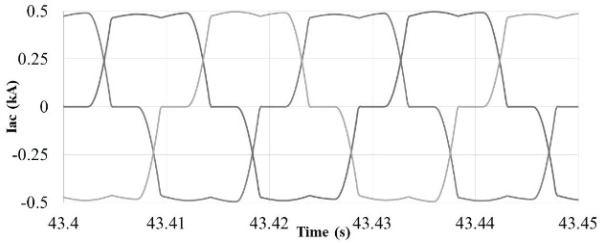



Figure 11. Current waveforms of a 3-phase EESG module at full load

Fig. 10 depicts the DC bus voltage and grid-side phase voltage and confirms the satisfactory operation of the NPC converter. Finally, Fig. 11 shows the currents of a 6-pulse SG module under full load conditions, highlighting that the unity power factor problem has been solved.

The second simulation aimed to compare the dynamic response of the proposed ECSG-based WT with that of a conventional back-to-back VSC converter WT, consisting of the same 6-phase EESG employed in the ECSG, with 1 pu excitation and 3-phase modules connected to DC links through two VSCs. Generally, the MPPT algorithm determines the current reference of these VSCs in conventional WTs. Accordingly, in this simulation, to avoid the impact of the VSCs' control loop dynamics, their current reference at each wind speed was set manually to the final value that the MPPT algorithm would choose if the control loop was active. Since both schemes benefit from the same grid-side converters, these converters were excluded from the simulations by connecting the DC bus of the WTs to DC voltage sources at the appropriate magnitude. The control loop of the proposed ECSG WT was also disabled, and, at each wind speed, the excitation voltage was set manually in the same way as a conventional WT, instead of being determined by the MPPT algorithm. These two WTs were then simulated, by changing their wind speeds from an initial value of 12 m/s to 8 m/s at the $10^{th}$ second of the run, and back to the initial value at the $20^{th}$ second. The absorbed powers of the WTs are shown in Fig. 12. As the results show, and as was predicted, the ECSG WT displays a faster inherent dynamic response than the equivalent conventional type WT.

EBSCOhost - printed on 2/14/2023 2:46 PM via . All use subject to https://www.ebsco.com/terms-of-use

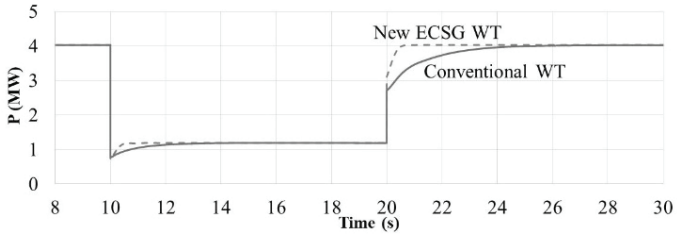



Figure 12. Dynamic response comparison of the ECSG and conventional SG-based WTs

## *Experimental Verification*

A small 4 kW prototype of the ECSG WT's electrical parts was constructed in the laboratory to verify whether excitation current control of an EESG equipped with a DBR at its terminal is an effective means of generated active power control. This setup is shown in Fig. 13.

The generator used for this purpose was a delta connected 220 V 3-phase EESG with a 3 A rated excitation current, which was connected to a 200 V DC local grid through a DBR and a smoothing inductor. The excitation current of the EESG was controlled using the hill climbing MPPT algorithm. This part of the setup represents a 6-pulse ECSG directly connected to a DC grid. To mimic the power-speed characteristics of an actual WT, a constant excitation DC motor was coupled to the ECSG shaft that was fed from the local DC grid. Variable resistance was connected in series with the armature of the motor to give different power-speed characteristics, simulating WT behavior under different wind speeds. The power-speed characteristics of this motor with four different resistance steps are shown in Fig. 14.

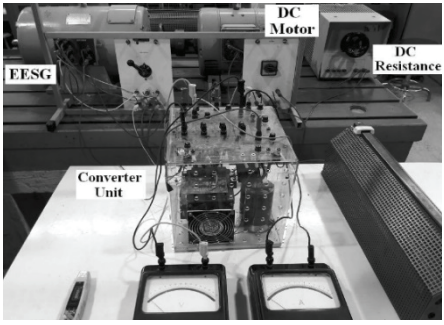



Figure 13. 6-pulse ECSG's laboratory prototype

EBSCOhost - printed on 2/14/2023 2:46 PM via . All use subject to https://www.ebsco.com/terms-of-use

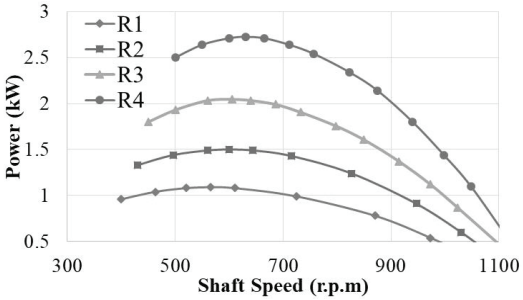



Figure 14. Power-speed characteristics of a DC motor at different series resistance steps

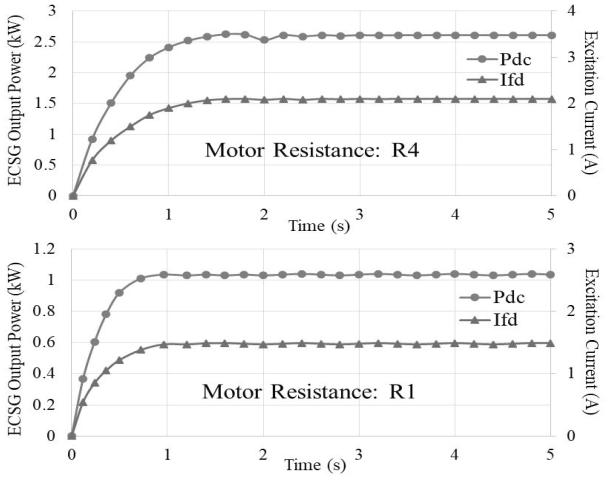



Figure 15. ECSG WT active power and its excitation current during experimental verification

This setup was run under two motor series resistances (R1 and R4) and the corresponding active powers injected by the ECSG to the DC grid, along with its excitation currents are shown in Fig. 15 for a period of 5 seconds. As the results confirm, the ECSG WT easily tracked the relevant maximum power points shown in Fig. 14. This demonstrates the level of controllability needed by a modern WT to fulfill MPPT at different wind speeds.

EBSCOhost - printed on 2/14/2023 2:46 PM via . All use subject to https://www.ebsco.com/terms-of-use

## Conclusion

An excitation-controlled synchronous generator (ECSG) based scheme is proposed here for high power WTs. This new scheme is a cost effective solution with a simplified power converter, which preserves the controllability required for high end WTs. The torque ripple problem on the turbine shaft is the main concern with the ECSG-based WT, as it can cause vibrations, torsional resonances, and fatigue stress on the mechanical structure. This problem is solved by the employment of a 6-phase SG for the ECSG WT and 12-pulse operation of diode bridge rectifiers. Simulation results confirm the effectiveness of this solution. In addition, according to the simulation and experimental results, the ECSG WT could successfully track the maximum power point at different and variable wind speeds.

Furthermore, in this paper the proposed scheme was fitted for an AC grid connection of the WT, where the use of a 6-phase SG in conjunction with a multi-level NPC inverter has made the omission of the turbine's step-up transformer possible. Simulation results confirm the satisfactory operation of this WT scheme.

## References

[1] J.A. Baroudi, V. Dinavahi, et al. "A review of power converter topologies for wind generators," IEEE conf. on Electric Machines And Drives, pp. 458–465, May, 2005.

[2] H. Polinder, F. van der Pijl. "Comparison of Direct-Drive and Geared Generator Concepts for Wind Turbines," IEEE Trans. on Energy Conversion, vol. 21, pp.725-733, 2006.

[3] Al-Bahadly. "Wind Turbines," book, InTech, 2011.

[4] H. Polinder, J. A. Ferreira, et al. "Trends in Wind Turbine Generator Systems," Emerging and Selected Topics in Power Electronics, IEEE Journal of, vol. 1, pp. 174-185, 2013.

[5] Ke Ma, Lucian Tutelea, et al. "Power Electronic Drives, Controls, and Electric Generators for Large Wind Turbines-An Overview," Electric Power Components and Systems, vol. 43 (12), pp. 1406-1421, 2015.

[6] O. Keysan, M. A. Mueller. "A Homopolar HTSG Topology for Large Direct-Drive Wind Turbines," Applied Superconductivity, IEEE Trans. on, vol. 21, pp. 3523-3531 , 2011.

[7] R. L. Arántegui. "2013 JRC Wind Status Report," JRC Scientific and Policy Reports. Luxembourg, Office of the European Union, Institute for Energy and Transport.

[8] M. Liserre, et al. "Overview of Multi-MW Wind Turbines and Wind Parks," Industrial Electronics, IEEE Trans. on, vol. 58 (4), pp. 1081-1095, 2011.

[9] V. Yaramasy, B. Wu, et al. "High-Power Wind Energy Conversion Systems:

EBSCOhost - printed on 2/14/2023 2:46 PM via . All use subject to https://www.ebsco.com/terms-of-use

State-of-the-Art and Emerging Technologies," Proc. of the IEEE, vol. 103 (5), pp. 740 -788, 2015

[10] Mueller, M. and H. Polinder. "Electrical Drives for direct drive renewable energy systems," book, Woodhead Publishing, 2013.

[11] Wu, B. Lang, Y. Zargari, N. Kouro. "Power Conversion and Control of Wind Energy Systems," book, Wiley, 2011.

[12] R. Poore, T. Lettenmaier. "Alternative Design Study Report: WindPACT Advanced Wind Turbine Drive Train Designs Study," National Renewable Energy Laboratory (NREL), 2003.

[13] M. J. Duran, S. Kouro, et al. "Six-phase PMSG wind energy conversion system based on medium-voltage multilevel converter," Power Electronics and Applications, Proceedings of the 2011-14th European Conf. on.

[14] J. M. Carrasco, L. G. Franquelo. "Power-Electronic Systems for the Grid Integration of Renewable Energy Sources: A Survey," IEEE Trans. on Industrial Electronics, vol. 53, pp. 1002-1016.

[15] A. Damiano, et al. "Design of a 10 MW multi-phase PM synchronous generator for direct-drive wind turbines," Industrial Electronics Society, IECON 2013 - 39th Conf.

[16] A. Madariaga, J. Martin, et al. "Technological trends in electric topologies for offshore wind power plants" Renewable and Sustainable Energy Reviews, vol. 24, pp.32-44, 2013.

[17] T. C. Roberto Lacal Arántegui. "2012 JRC wind status report," JRC Scientific and Policy Reports. Luxembourg, Office of the European Union, Institute for Energy and Transport.

[18] A. B. Abrahamsen, N. Magnusson, et al. "Large Superconducting Wind Turbine Generators," Energy Procedia, vol. 24, pp. 60-67, 2012

[19] H. Min-Fu, et al. "Design and Analysis of High Temperature Superconducting Generator for Offshore Wind Turbines," IEEE Trans. on Magnetics, vol. 49, pp. 1881-1884, 2013.

[20] J. Lloberas, A. Sumper, et al. "A review of high temperature superconductors for offshore wind power synchronous generators," Renewable and Sustainable Energy Reviews, vol. 38, pp. 404-414, 2014.

[21] Z. Zhang, A. Chen, et al. "High-power Generators for Offshore Wind Turbines," Energy Procedia, vol. 35, pp. 52-61, 2013.

[22] Y. Terao, M. Sekino, et al. "Comparison of Conventional and Superconducting Generator Concepts for Offshore Wind Turbines," IEEE Trans. on Applied Superconductivity, vol. 23 (3), 2013.

[23] P. K. Olsen, S. Gjerde , et al. "A Transformerless Generator-Converter Concept Making Feasible a 100 kV Light Weight Offshore Wind Turbine: Part II - The Converter," IEEE Energy Conversion Congress and Exposition, 2012.

[24] Chong H. Ng, M. A. Parker, et al. "A Multilevel Modular Converter for a Large, Light Weight Wind Turbine Generator," IEEE Trans. on Power Electronics, vol. 23 (3), pp. 1062-1074, 2008.

[25] F. Deng, C. Zhe. "Operation and Control of a DC-Grid Offshore Wind Farm Under DC Transmission System Faults," IEEE Trans. on Power Delivery, vol. 28 (3), pp. 1356-1363, 2013.

EBSCOhost - printed on 2/14/2023 2:46 PM via . All use subject to https://www.ebsco.com/terms-of-use

# CHAPTER TEN

# ASSESSMENT OF THE MAIN SOCIO-ECONOMIC IMPACTS OF WIND ENERGY IN EUROPE

MARGARITA ORTEGA[1], PABLO DEL RÍO[2] AND EDUARDO MONTERO[1]

## Abstract

The high level of penetration of renewable energy sources (RES-E) in the European Union (EU) has raised some concern among policy makers, and the public generally, about the benefits and costs of their public promotion.

The commitment of the European Commission (EU COM) has been crucial to the deployment of RES-E in all member states (EU MS). Wind energy is the renewable technology with the highest contribution to the electricity mix in Europe (excluding hydro) in recent years. As such, it offers a worthwhile case for study.

An economic analysis of the contribution of wind energy should not only take into account the policy costs of deployment (i.e. public support), which are finally paid by electricity consumers, but also its economic benefits (such as climate change mitigation and reduction of fossil fuel dependence), shared among citizens.

The aim of this chapter is to close this gap and assess the policy costs and the most relevant benefits of wind energy deployment in the EU28 (28 member states) using data from 2014. An internationally validated innovative methodology has been used for this purpose.

[1] Department of Electromechanical Engineering. University of Burgos. EPS Burgos. Avd. Cantabria, s/n 09006 Burgos (Spain). e-mail: moizquierdo@ubu.es; emontero@ubu.es

[2] Institute for Public Policies and Goods. National Research Council of Spain (CSIC). C/ Albasanz 26-28, 28037 Madrid (Spain). e-mail: pablo.delrio@csic.es

EBSCOhost - printed on 2/14/2023 2:46 PM via . All use subject to https://www.ebsco.com/terms-of-use

The results show that the benefits analysed are significant and should be considered when support costs are assessed and in the future design of energy policies in Europe.

**Keywords:** Renewable energy electricity; European support schemes; $CO_2$ abatement; fossil fuel savings; import savings.

## Nomenclature

| | |
|---|---|
| *RES-E* | Renewable energy sources |
| *EU* | European Union |
| *EU COM* | European Commission |
| *MS* | Member states |
| *PV* | Photovoltaics |
| *FIT* | Feed-in tariff |
| *FIP* | Feed-in premium |
| *TGC* | Tradable green certificates |
| *QO* | Quota obligations |
| *TN* | Tendering schemes |
| *II* | Investment subsidies |
| *FI* | Financial subsidies |
| *TE* | Tax exemptions |
| *NM* | Net metering |
| *UNFCCC* | United Nations Framework Convention on Climate Change |
| *CDM* | Clean development mechanism |
| *OM* | *Operating margin factor* |
| *BM* | *Build margin factor* |
| *CM* | *Combined margin factor* |
| *SCC* | Social cost of carbon |

## Introduction

The high level of RES-E penetration in the EU has raised concern about the costs of its public promotion, especially in terms of maintaining public support. While it is true that RES-E support costs have increased significantly over the past decade, and that it is certainly desirable to deploy RES-E at the lowest possible support costs, an analysis of the social contribution of RES-E should put those costs into perspective and also take into account the benefits of RES-E deployment. Notwithstanding their relevance, a quantification of the costs and benefits for different

EBSCOhost - printed on 2/14/2023 2:46 PM via . All use subject to https://www.ebsco.com/terms-of-use

technologies and EU member states has been absent in the literature, as described by [1]. Only a few authors have analysed the costs and benefits of RES-E in the European region. For instance, [2] compares the benefits associated with the avoidance of $CO_2$ emissions to the costs of the Spanish support scheme and [3] analyses the costs avoided by a reduction in fuels imported into Europe. The policy costs of RES-E deployment and the social benefits in terms of $CO_2$ emission reduction and fossil fuel savings in Germany are compared by [4], with the conclusion that the former outweigh the later.

The main aim of this chapter is to fill this gap and quantify, in monetary terms, the support costs and benefits related to climate change mitigation and fossil fuel savings of wind energy deployment in the EU MS during 2014. The impacts analysed (costs and benefits) of wind energy deployment fall onto different actors, as shown in [1]. For this reason, in strictly economic terms, benefits and costs cannot be directly compared and, therefore, a cost-benefit analysis is not carried out.

This chapter is structured as follows. Section 2 provides a brief description of the current state of wind energy generation and support schemes in the EU. Section 3 describes the methodology for calculating the benefits and costs related to wind energy deployment. The results are provided and discussed in section 4. Final conclusion are offered in section 5.

This chapter is an updated version of a previous paper presented at the International Conference on Renewable Energies and Power Quality (ICREPQ'16) [5].

## Current situation in Europe

In 2014, the base year for this analysis, net electricity production in the EU amounted to 3,027 TWh [6] and was concentrated in a few countries: Germany, France, and United Kingdom accounted for 48% of electricity generation.

The EU has a diversified electricity generation mix. Several energy sources had significant shares in this mix in 2014, including: coal (25.9%); nuclear (27.4%); natural gas (14.1%); and renewable energy sources (30.1%). Oil has an insignificant share in electricity generation (2.5%), although it is the main fuel in Malta and Cyprus. Within RES, wind (8.3%), has developed considerably over the last few years, although hydro (13.2%) still dominates. Biomass, biogas, and waste (5.2%), solar (3.2%), and geothermal (0.2%) energy are all growing fast, but still have smaller shares in EU MS [6].

EBSCOhost - printed on 2/14/2023 2:46 PM via . All use subject to https://www.ebsco.com/terms-of-use

Net wind energy electricity generation quadrupled between 2004 and 2014. Together with photovoltaic energy (PV), it is one of the fastest developing technologies in all EU MS, and therefore increasing significantly in importance.

Due to the higher investment costs of RES-E, support schemes have been enacted in all MS and they have had a crucial role to play in RES-E deployment. Analysis of the performance of RES-E support schemes in the EU has been the focus of much research over the past decade, for example [7] and [8].

Support schemes can basically be split into three types [9]:

- *Price-base mechanisms*. Two options can be distinguished: feed-in tariffs (FITs), which guarantee a fixed price per kWh electricity, and feed-in premiums (FIPs), which are paid on top of the market price for electricity.
- *Quantity-base mechanisms*. Tradable green certificates (TGC) or renewable quota obligations (QO) require that a percentage of electricity generation comes from RES-E. Tendering schemes (TN) are bidding systems in which developers compete for supply contracts to build RES-E capacity.
- *Others:* investment subsidies (II), soft loans (FI), tax exemptions (TE), or net metering (NM)

The first two (Price-base and quantity-base mechanisms) are sometimes combined with others mechanisms—i.e. investment subsidies (II), soft loans (FI), tax exemptions (TE), or net metering (NM)—which are complementary with the aforementioned ones [10].

EBSCOhost - printed on 2/14/2023 2:46 PM via . All use subject to https://www.ebsco.com/terms-of-use

**Table I. Instruments for wind energy deployment in the EU (2014).** References: [11] and [12]

| Member State (MS) | Main support mechanism |
|---|---|
| Austria (AT) | FIT; II |
| Belgium (BE) | TGC; II (1) |
| Bulgaria (BG) | FIT |
| Cyprus (CY) | FIT |
| Czech Republic (CZ) | FIT/FIP(2) |
| Germany (DE) | FIT(3)/FIP(4) |
| Denmark (DK) | FIP/TN |
| Estonia (EE) | FIP |
| Greece (EL) | FIT |
| Spain (ES) | Other(5) |
| Finland (FI) | FIP; II |
| France (FR) | FIT/TN(6) |
| Croatia (HR) | FIT/FIP; TN |
| Hungary (HU) | FIT |
| Ireland (IE) | FIT |
| Italy (IT) | FIT(7); FIP(8); TGC; TN(9) |
| Lithuania (LT) | FIT(10); FIT/TN(11) |
| Luxembourg (LU) | FIT; II |
| Latvia (LV) | FIT |
| Malta (MT) | |
| The Netherlands (NL) | FIP |
| Poland (PL) | TGC |
| Portugal (PT) | FIT; TN |
| Romania (RO) | TGC |
| Sweden (SE) | TGC |
| Slovenia (SI) | FIT; FIP |
| Slovakia (SK) | FIP |
| United Kingdom (UK) | TGC; FIT(12);TN |

(1) Wind off-shore; (2) Installations authorized before 2014; (3) Small installations (<100kW); (4) Mandatory for new installations since 8/2014; (5) Investment return + operation return for existing plants, calculated in accordance with a reasonable internal rate of return; (6) Calls for tender are used to determine the level of support, which is conceived as FIT up to 2016; (7) Existing plants P<1MW; (8) Existing plants P>1MW and P<1MW which did not chose FIT before; (9) New plants—Large projects; (10) P<10kW; (11) P>10kW; (12) P<5MW.

EBSCOhost - printed on 2/14/2023 2:46 PM via . All use subject to https://www.ebsco.com/terms-of-use

As shown in Table I, FITs were the main support mechanism used in the EU in 2014 for wind energy, followed by FIPs and TGC. Support schemes are currently being adapted to allow for greater market integration of RES. In recent years, major changes have been made to the introduction of FIP schemes—RES producers now receive defined support in addition to their market income, and tendering procedures have been introduced.

The EU COM has claimed that their is a need to have cost-effective and market-based instruments, suggesting that FITs have been too expensive and not sufficiently effective at integrating the increasing volume of RES-E into electricity markets [13]. The trend in recent years has been the use of auctions, as recommended by the EU COM.

## Methodology

The deployment of RES-E has two relevant benefits associated with it: abatement of $CO_2$ emissions and a reduction in fossil-fuel dependence. The economic quantification of these benefits is the main aim of this chapter. Other benefits have been analyzed in the literature, including: the merit-order effect, being the reduction of the wholesale electricity price due to greater penetration of RES-E; other environmental benefits (reduction of pollutants, such as $SO_2$); and employment generation, among others. They have not been considered in this chapter, mostly due to a lack of reliable EU-wide data. Regarding the cost side, only policy support costs have been taken into account, not system generation costs, which would be needed for a cost-benefit analysis. The costs for the electricity system related to the variable character and the limited predictability of the generation of electricity from intermittent RES-E (usually called cycling costs and balancing costs) have not been included because their values compared to other impacts are negligible with low RES-E penetration levels, as argued in [4] and [14].

In order to quantify, in monetary terms, the two benefits associated with wind energy deployment, a methodology proposed by the United Nations Framework Convention on Climate Change (UNFCCC) [15] has been used. This methodology was not originally conceived for this purpose—it is normally used for the calculation of baselines in clean development mechanism (CDM) projects. The methodology adapted was adapted in [16] and applied to the Spanish case.

According to this methodology, the $CO_2$ emission factor can be obtained using three different alternatives:

EBSCOhost - printed on 2/14/2023 2:46 PM via . All use subject to https://www.ebsco.com/terms-of-use

1) *Operating margin factor (OM).* This considers existing power plants whose current electricity production would be affected by a proposed RES-E project. The so-called average OM alternative is used in order to calculate the operating margin in this paper. The average OM emission factor is calculated as the generation-weighted average $CO_2$ emissions per unit of net electricity generation of all generating power plants serving the system, including low-cost/must-run power plants[3].

According to [15], electricity imports from other countries have been treated as an additional electricity generation technology.

The calculation of the average OM emission factor is based on the following equation:

$$EF_{\text{Average OM},y} = \Sigma_m EG_{m,y} \cdot EF_{EL,m,y}) / \Sigma EG_{m,y} \qquad \text{[Eq. 1]}$$

Where $EF_{\text{Average OM},y}$ is the operative margin factor in the year *y* ($tCO_2$/MWh); $EG_{m,y}$ is the net electricity generated by the technology *m* in the year *y* (MWh); $EF_{ELm,y}$ is the $CO_2$ emission factor of technology *m* in the year *y*; *m* are the technologies serving the system (according to the average OM definition, these are all the power generation technologies in the system); and *y* is the year of reference.

2) *Build margin factor (BM).* This refers to prospective power plants whose construction would have been affected (delayed or cancelled) by an increase in RES-E penetration. Since data on the installed capacity per fuel type are not available at the European level, an intermediate scenario has been considered whereby a 50% substitution of coal and natural gas is assumed. As coal and natural gas thermal plants are not located in either Cyprus or Malta, a single scenario in which RES-E replaces fuel-oil is considered for these two countries. The BM emission factor is the emission factor of the replaced technology or technologies.

3) *Combined margin factor (CM).* This is a weighted average of the two preceding factors. In this paper, the weighted average CM has been used, where the OM and the BM factors have equal weights. Three different scenarios have been assumed, corresponding to the scenarios chosen in calculating the BM factor:

$$EF_{CM,y} = 0{,}5 \cdot EF_{\text{Average OM},y} + 0{,}5 \cdot EF_{BM,y} \qquad \text{[Eq. 2]}$$

[3] Low-cost/must-run resources are power plants with low marginal generation costs or those dispatched independently of the daily or seasonal grid load. Both nuclear and renewable energies (including hydro) belong to this category.

EBSCOhost - printed on 2/14/2023 2:46 PM via . All use subject to https://www.ebsco.com/terms-of-use

Where $EF_{CM,y}$ is the combined margin factor in the year *y*; $EF_{Average\ OM,y}$ is the operating margin factor (using the average OM alternative) in the year *y*; and $EF_{BM}$, *y* is the build margin factor in the year *y*.

This analysis takes into account the impacts of wind energy plants on existing power plants (OM) and the voided construction of new facilities (BM).

### *Benefits from $CO_2$ emissions avoided*

The original UNFCCC methodology is applied here to calculate $CO_2$ emission reductions related to wind deployment; [17] describes the emissions from fossil fuel combustion and the oxidation factors considered are those recommended by [18]. The oxidation factors for the three fuels considered are the following: coal (99%); fuel-oil (99.5%); and natural gas (99.5%). The emissions factors are: coal (97.3 $tCO_2/TJ$); fuel-oil (77 $tCO_2/TJ$); and natural gas (55.8 $tCO_2/TJ$).

In order to translate $CO_2$ emission abatement into monetary terms, the concept of the social cost of carbon (SCC) has been used. The SCC is used to reflect the external costs of greenhouse gas emissions. It measures the full global cost today of an incremental unit of carbon emitted, summing the full global cost of the damage it imposes over the whole of its time in the atmosphere. It measures the scale of externality that needs to be incorporated into decisions on policy and investment options in government [19]. According to the review made by [20], values for the SCC show significant variations depending on the study under consideration. The median of the values of the SCC in [20] has been used (32 €/$tCO_2$). This value is higher than the price of $CO_2$ allowances under the EU Emission Trade System (EU ETS) in the reference year considered (5.96 €/$tCO_2$ in 2014). However, we consider this to be a reasonable scenario for the SCC, being the central value of the range analysed by [20]. The monetary calculation of the avoided emissions would vary if the mode (14 €/$tCO_2$) or the average (49 €/$tCO_2$) were applied.

### *Benefits from fossil fuels savings*

In order to calculate fossil fuel savings as a result of wind energy deployment, final energy has been transformed into primary energy and the result has been multiplied by the price of energy. To calculate the conversion from final to primary energy and the price of energy, the original UNFCCC methodology is adapted, replacing the emission factors

EBSCOhost - printed on 2/14/2023 2:46 PM via . All use subject to https://www.ebsco.com/terms-of-use

of participant technologies by the efficiency values and prices of these technologies, respectively.

The efficiency values considered for the transformation of primary energy into final energy were obtained from [21]. It has been assumed that coal and fuel-oil plants were built before 2001 and that natural gas and biomass plants were built in 2006. For reasons of simplicity, it has been assumed that the efficiency of fossil fuel plants does not change when they are substituted by RES-E. In reality, however, a very small increase in those efficiencies could be expected [14].

The following equation is used to transform final energy into primary energy for both the OM and BM alternatives:

$$1\ \text{MWh (Primary energy)} = 1/\eta\ \text{MWh (Final energy)} \quad \text{[Eq. 3]}$$

To calculate the conversion factors of final energy into primary energy in the CM alternative, the emission factors in the OM and BM alternatives are replaced by the efficiency values of the fuels considered.

The prices of fossil fuels used in electricity generation were obtained from [22]. Electricity imports have been treated as if they were an independent technology generator and data on wholesale electricity prices from each MS for 2014 are provided by [11] or by accessing the websites of the official organs of each MS. For those countries without available data and non-EU MS the average of the electricity price when available (42.2 €/MWh in 2014) has been used. The following standard conversion factors have been applied: Coal: 1MWh = 0.21 t; Oil: 1 MWh = 0.61 barrels; Natural gas: 1 MWh = $3.44 \cdot 10^6$ Btu. [60]

According to data provided by the International Monetary Fund [23], the price of uranium in 2014 was 33.5 €/pound. Assuming the unitary fuel consumption in [24], the price of fuel for nuclear electricity generation was 0.17 €/MWh. This price is negligible compared to the price of other fossil fuels and, as such, it was not included in the study.

Finally, it has been assumed that biomass, biogas, and wastes are local energy sources and are not imported.

Table II shows the conversion factor from final to primary energy, the $CO_2$ emission factor ($tCO_2/GWhfinal$), and the price ($€/MWh_{primary}$) that is obtained when applying this methodology.

EBSCOhost - printed on 2/14/2023 2:46 PM via . All use subject to https://www.ebsco.com/terms-of-use

**Table II. Combined margin factors used: conversion factor (final energy to primary energy), emission factors, and prices. Year 2014**

| MS | $MWh_{final}/MWh_{primary}$ | $tCO_2/MWh_{final}$ | $€/MWh_{primary}$ |
|---|---|---|---|
| AT | 1,68 | 0,34 | 15,1 |
| BE | 2,10 | 0,36 | 13,9 |
| BG | 2,16 | 0,47 | 12,5 |
| CY | 2,22 | 0,60 | 44,6 |
| CZ | 2,21 | 0,48 | 12,9 |
| DE | 2,10 | 0,49 | 13,7 |
| DK | 1,86 | 0,41 | 15,0 |
| EE | 2,05 | 0,57 | 16,0 |
| EL | 1,94 | 0,52 | 18,2 |
| ES | 2,00 | 0,41 | 13,7 |
| FI | 2,10 | 0,37 | 12,6 |
| FR | 2,37 | 0,31 | 9,4 |
| HR | 1,64 | 0,34 | 18,9 |
| HU | 2,05 | 0,36 | 14,5 |
| IE | 1,93 | 0,48 | 18,1 |
| IT | 1,90 | 0,43 | 17,0 |
| LT | 1,66 | 0,33 | 24,9 |
| LU | 1,64 | 0,33 | 22,0 |
| LV | 1,70 | 0,34 | 20,6 |
| MT | 2,24 | 0,62 | 45,1 |
| NL | 1,97 | 0,47 | 18,2 |
| PL | 2,14 | 0,61 | 14,9 |
| PT | 1,82 | 0,41 | 15,0 |
| RO | 1,95 | 0,42 | 12,8 |
| SE | 2,03 | 0,31 | 9,8 |
| SI | 1,92 | 0,36 | 13,6 |
| SK | 2,05 | 0,34 | 13,3 |
| UK | 2,12 | 0,47 | 14,6 |
| **EU28** | **2,08** | **0,42** | **13,4** |

## *Support cost calculation*

Support costs were obtained from [11] and are defined as the annual cost of incentives paid to RES-E generation as the result of national support schemes.

EBSCOhost - printed on 2/14/2023 2:46 PM via . All use subject to https://www.ebsco.com/terms-of-use

## Results and discussion

### *Benefits from $CO_2$ emissions avoided*

Applying this methodology, $CO_2$ emissions avoided in 2014 due to wind energy were 109.3 $MtCO_2$ for the EU-28. These reductions substantially increased in recent years (i.e. RES-E deployment contributed to a reduction of 35 $MtCO_2$ in 2005 and 66 $MtCO_2$ in 2010.)

A country analysis reveals that almost 59% of the total reduction is concentrated in three countries (Germany, Spain, and the United Kingdom). The development of wind energy in these countries is higher than in the rest of the member states. The increase of this technology in the United Kingdom is remarkable, especially with the development of off-shore wind generation.

The emissions avoided can be translated into monetary terms by applying a range of the SCC values considered in the review in [20]. The resulting calculations show that, in monetary terms, the reductions are in the range of 1,530 M€, when considering the mode (14€/$tCO_2$), and 5,354 M€, when considering the average value (49€/$tCO_2$), with a central value, provided by calculations made with the median (32€/$tCO_2$), of 3,497 M€.

Table III shows the avoided emissions ($MtCO_2$) related to wind energy deployment.

### *Benefits from fossil fuel savings*

According to this methodology, 513 TWh of fossil fuel generation was avoided in 2014 in the EU28. The value of those savings per MS depends on its total fossil fuel electricity generation and its electricity mix. Table III shows the primary energy saved by wind energy deployment in EU MS.

An analysis by country reveals that, again, Germany (120 TWh), Spain (102 TWh), and the United Kingdom (68 TWh) are the ones experiencing the greatest (absolute) fossil fuel savings as a result of wind energy deployment.

When the aforementioned values are translated into monetary terms, the deployment of wind energy leads to fossil fuel savings of 7,150 M€. Those savings are translated into a reduction in fossil fuel imports, with associated benefits in terms of reduced external energy dependency.

Fossil fuel savings are much higher than the savings associated with $CO_2$ emission reductions in monetary terms—a result in line with [4].

EBSCOhost - printed on 2/14/2023 2:46 PM via . All use subject to https://www.ebsco.com/terms-of-use

**Table III. Avoided $CO_2$ ($MtCO_2$) emissions and energy savings (TWh) in 2014.**

| MS | Avoided emissions ($MtCO_2$) | Fossil fuel savings (TWh) | MS | Avoided emissions ($MtCO_2$) | Fossil fuel savings (TWh) |
|---|---|---|---|---|---|
| AT | 1.2 | 6.15 | IE | 2.4 | 9.90 |
| BE | 1.7 | 9.57 | IT | 6.4 | 28.72 |
| BG | 0.6 | 2.87 | LT | 0.2 | 1.05 |
| CY | 0.11 | 0.40 | LU | 0.0 | 0.13 |
| CZ | 0.2 | 1.04 | LV | 0.0 | 0.24 |
| DE | 28.2 | 120.31 | MT | - | - |
| DK | 5.4 | 24.32 | NL | 2.7 | 11.43 |
| EE | 0.3 | 1.24 | PL | 4.7 | 16.25 |
| EL | 1.9 | 7.16 | PT | 4.9 | 21.80 |
| ES | 20.8 | 102.24 | RO | 2.6 | 11.88 |
| FI | 0.4 | 2.32 | SE | 3.4 | 22.84 |
| FR | 5.4 | 40.83 | SI | 0.0 | 0.01 |
| HR | 0.3 | 1.19 | SK | 0.0 | 0.01 |
| HU | 0.2 | 1.30 | UK | 15.1 | 67.63 |
| | | | **EU28** | **109.3** | **512.85** |

### *The costs of public support.*

As explained in section 2, virtually all EU MS have implemented some type of RES-E deployment support scheme in order to develop wind energy. Data on the levels of support for wind energy are available for 24 MS in 2014 from [11], with a non-weighted average of 55.9 €/MWh for the countries being considered. Notwithstanding that support levels widely differ between countries, these differences are not always related to the potential of wind energy as a resource, which is consistent with [25].

Table IV provides an analysis of the costs of public support for wind energy and the benefits associated with $CO_2$ emission reductions and fossil-fuel savings in those countries with available data. Although benefits and costs cannot be directly compared, because the former are distributed amongst citizens while the later are assumed in the majority of MS by electricity consumers, the results show that the aforementioned benefits are relevant for the considered countries as a whole, although they are below the costs.

A country-based analysis reveals that the benefits outweigh the policy costs in eleven of the twenty four countries with available data.

EBSCOhost - printed on 2/14/2023 2:46 PM via . All use subject to https://www.ebsco.com/terms-of-use

**Table IV. Summary of the benefits and support costs of renewable energy deployment in EU MS (M€). Year 2014.**

| MS | Benefit—$CO_2$ emissions avoided (M€) | Benefit—fossil fuel savings (M€) | Support Costs (M€) |
|---|---|---|---|
| AT | 39.4 | 93.0 | 186.8 |
| BE | 52.8 | 133.5 | 420.4 |
| BG | 19.8 | 36.0 | 0.0 |
| CY | 3.5 | 18.0 | 30.4 |
| CZ | 7.2 | 13.4 | 36.5 |
| DE | 903.1 | 1,643.8 | 4,028.4 |
| DK | 171.9 | 365.7 | 521.0 |
| EE | 10.9 | 19.8 | 7.9 |
| EL | 61.0 | 130.5 | 107.6 |
| ES | 665.4 | 1,400.9 | 1,253.6 |
| FI | 12.9 | 29.2 | 51.7 |
| FR | 173.5 | 385.5 | 814.7 |
| HR | 8.0 | 22.6 | 38.2 |
| HU | 7.4 | 18.9 | 44.1 |
| IE | 78.1 | 179.1 | 46.9 |
| IT | 205.6 | 488.5 | 1,361.9 |
| LT | 6.7 | 26.2 | 19.5 |
| LU | 0.8 | 2.9 | 3.0 |
| LV | 1.5 | 4.9 | 5.0 |
| MT | 0.0 | 0.0 | 0.0 |
| NL | 88.0 | 208.0 | 0.0 |
| PL | 149.1 | 241.5 | 547.8 |
| PT | 156.5 | 327.2 | 655.7 |
| RO | 82.0 | 152.4 | 228.3 |
| SE | 109.7 | 223.7 | 236.9 |
| SI | 0.0 | 0.1 | 0.1 |
| SK | 0.1 | 0.2 | 0.0 |
| UK | 481.7 | 985.2 | 1,878.0 |
| **EU28** | **3,496.7** | **7,150.3** | **12,524.6** |

The results of this research suggest that for mature technologies, like wind energy, price-based mechanisms have been a suitable instrument to encourage the uptake of these technologies, bringing substantial social benefits as well. However, the recent recommendations of the EU COM, which are being implemented by many countries, promote auctions.

EBSCOhost - printed on 2/14/2023 2:46 PM via . All use subject to https://www.ebsco.com/terms-of-use

Although auctions may have some problems [26], these might be mitigated with an appropriate choice of design elements. In fact, if designed properly, auctions can provide as much certainty as FITs regarding remuneration costs and in providing a cost-containment mechanism.

The picture may be different with significant RES-E penetration levels, whereby the costs of grid integration may increase significantly and mechanisms without capacity or generation caps may lead to uncontrolled increases in RES-E generation, with significant concerns in that respect.

## Conclusions

This chapter has provided an analysis of the policy costs and some of the most relevant benefits of wind energy deployment in the EU and its MS using an innovative yet internationally validated methodology.

The results show that the support costs for wind energy, which are finally paid by electricity consumers in their bills, have led to reductions in $CO_2$ emissions and fossil fuel savings that are below those costs. The fossil fuel savings are higher than the savings associated with reductions in $CO_2$ emissions. These results are highly sensitive to the cost of $CO_2$. In particular, the cost of $CO_2$ used in the calculations (32 €/t$CO_2$) is a central (median) value in the range of the values of the social cost of carbon found in the literature. Had the average of those values been chosen (49€/t$CO_2$), the benefits would have clearly offset the policy costs.

These findings offer relevant policy implications. Firstly, significant social benefits are induced by each euro of wind energy support paid by consumers. Secondly, the results suggest that FITs have also brought relevant social benefits, although they certainly have had problems of their own. Despite the criticism, FITs continue to be widely recognised as a suitable instrument for policy design in supporting RES-E expansion. Most countries are now following the recommendations of the EU COM by introducing auctions, the inconveniences of which can be dealt with by a suitable design.

Some of the limitations of this work suggest further research in this field is necessary. Firstly, apart from the reduction in $CO_2$ emissions and fossil-fuel dependence, other benefits should be considered (i.e. reduction in the emission of local pollutants; employment effects or impacts on employment growth). Secondly, a full cost-benefit analysis of wind energy deployment is worth carrying out in the future. This could be done by including system costs in the analysis. Data availability may represent a challenge in this context. Finally, the (negative) impact on the

EBSCOhost - printed on 2/14/2023 2:46 PM via . All use subject to https://www.ebsco.com/terms-of-use

conventional fossil-fuel sectors has not been considered either. Further investigation that includes those factors is recommended.

## References


[1] Breitschopf B., Held A. Guidelines for assessing costs and benefits of RET deployment. Project DIA-CORE (Intelligent Energy Europe) 2014. Contract N°: IEE/12/833/SI2.645735. Available at: http://diacore.eu/images/files2/D4.1_FhISI_Cost_Benefit_Approach_DIACORE.pdf

[2] Garcia-Redondo A. J., Román-Collado R. An economic valuation of renewable electricity promoted by feed-in system in Spain. *Renewable Energy 2014*; **68**: 51-7.

[3] European Commission. Energy Economic Developments in Europe. Directorate-General for Economic and Financial Affairs. Brussels, Belgium (2014). ISBN 978-92-79-35345-1.

[4] Marcantonini C., Ellerman A. D. The Implicit Carbon Price of Renewable Energy Incentives in Germany. *The Energy Journal 2015*; **36 (4)**: 205-30.

[5] Ortega M., Del Río, P. Gamarra, C. Montero, E. Analysis of the main socio-economic impacts of wind energy in Europe. *International Conference on Renewable Energies and Power Quality (ICREPQ'16)*, At Madrid (Spain) May 2016.

[6] EUROSTAT. Eurostat Statistical Database 2018. Available at: http://appsso.eurostat.ec.europa.eu/nui/show.do?dataset=nrg_105a&lang=en. Accessed 18 Jul. 2018.

[7] Ragwitz M., Steinhilber S., Breitschopf B., Resch G., Panzer C., Ortner A. *et al*. RE-Shaping: Shaping an effective and efficient European renewable energy market. Final Report. RE-SHAPING (Intelligent Energy Europe) 2012. Contract N°: EIE/08/517/SI2. 529243. Available at: http://www.reshaping-res-policy.eu/downloads/Final%20report%20RE-Shaping_Druck_D23.pdf

[8] Haas R., Panzer C., Resch G., Ragwitz M., Reece G., Held A. A historical review of promotion strategies for electricity from renewable energy sources in EU countries. *Renewable and Sustainable Energy Reviews 2011*; **15 (2)**: 1003–34.

[9] Del Río P. Analysing the interactions between renewable energy promotion and energy efficiency support schemes: The impact of different instruments and design elements. *Energy Policy 2012*; **38 (9):** 4978-89.

[10] Mir-Artigues P., Del Río P. Combining tariffs, investment subsidies and soft loans in a renewable electricity deployment policy. *Energy Policy 2014*; **69**: 430-42.

[11] CEER. Status Review of Renewable and Energy Efficiency Support Schemes in Europe in 2014 and 2015. Council of European Energy Regulators. Brussels, Belgium (2017). Available at: www.ceer.eu


EBSCOhost - printed on 2/14/2023 2:46 PM via . All use subject to https://www.ebsco.com/terms-of-use

[12] European Commission. RES Legal Europe 2015. Available at: www.res-legal.eu.
[13] European Commission. Communication from the Commission to the European Parliament, the Council, the European Economic and Social Committee and the Committee of the regions. A policy framework for climate and energy in the period from 2020 to 2030. COM/2014/015 final, 2014.
[14] Gutiérrez-Martín F., Da Silva-Álvarez R. A., Montoro-Pintado P. Effects of wind intermittency on reduction of $CO_2$ emissions: The case of the Spanish power system. *Energy 2013*; **61**: 108-17.
[15] UNFCCC. Tool to calculate the emission factor for an electricity system. Version 04.0. Oct, 2013. United Nations Framework Convention on Climate Change. Bonn, Germany (2013).
[16] Ortega M., Del Río P., Montero E. A. Assessing the benefits and costs of renewable electricity. The Spanish case. *Renewable and Sustainable Energy Reviews 2013*; **27**: 294-304.
[17] IPCC. Guidelines for National Greenhouse Gas Inventories. Prepared by the National Greenhouse Gas Inventories Programme, Eggleston H.S., Buendia L., Miwa K., Ngara T. and Tanabe K. (eds.) IGES 2006, Japan.
[18] European Commission. Commission Decision 2004/156/EC of 29 January 2004 establishing guidelines for the monitoring and reporting of greenhouse gas emissions pursuant to Directive 2003/87/EC of the European Parliament and of the Council (notified under document number C (2004) 130).
[19] Price R., Thornton S., Nelson S. The Social Cost of Carbon and the Shadow Price of Carbon. What they are and how to use them in economic appraisal in the U.K. Department for Environment, Food and Rural Affairs. London, United Kingdom (2007). Available at: https://www.gov.uk/government/uploads/system/uploads/attachment_data/file/243825/background.pdf
[20] Tol R. S. C. A cost–benefit analysis of the EU 20/20/2020 package. *Energy Policy 2012*; **49**: 288-295.
[21] European Commission. Commission Implementing Decision 2011/877/EU of 19 December 2011 establishing harmonised efficiency reference values for separate production of electricity and heat in application of Directive 2004/8/EC of the European Parliament and of the Council and repealing Commission Decision 2007/74/EC (notified under document C (2011) 9523).
[22] BP. BP Statistical Review of World Energy 2014. Available: http://www.bp.com/content/dam/bp/pdf/statistical-review/statistical_review_of_world_energy_2014.pdf. Accessed August 8, 2018.
[23] IMF. International Monetary Fund 2015. Available at: http://www.imf.org/external/np/res/commod/index.aspx. Accessed August 8, 2018.

EBSCOhost - printed on 2/14/2023 2:46 PM via . All use subject to https://www.ebsco.com/terms-of-use

[24] MINETUR. Annual Electricity Statistics. Ministry of Industry, Energy and Tourism of Spain. Madrid, Spain (2014). Available at: http://www.minetur.gob.es/energia/balances/Publicaciones/ElectricasAnuales/Paginas/ElectricasAnuales.aspx. Accessed January 23, 2015.

[25] del Río P., Tarancón M. A., Peñasco C. The determinants of support levels for wind energy in the European Union. An econometric study. *Mitigation and Adaptation Strategies for Global Change 2014*; **19(4)**: 391-410.

[26] del Río P., Linares P. Back to the future? Rethinking auctions for renewable electricity support. *Renewable and Sustainable Energy Reviews 2014*; **35**: 42-56.

EBSCOhost - printed on 2/14/2023 2:46 PM via . All use subject to https://www.ebsco.com/terms-of-use

# CHAPTER ELEVEN

# MODEL TO MAXIMIZE SELF-CONSUMPTION OF OLIVE MILLS POWERED BY A MIXED RENEWABLE ENERGY SYSTEM

OVIDIO RABAZA[1]
AND DANIEL GÓMEZ-LORENTE[1]

## Abstract

In recent years, with the increase in petroleum prices and gas emissions, renewable energies have come to be recommended as feed sources for various types of facilities. As such, for the period 2010 to 2020, the European Commission has established three key objectives focussed on climate change and energy sustainability. These are: a reduction in CO2 emissions; an increase in the use of renewable energies; and an increase in energy efficiency.

Installations for the production of olive oil, also called "olive mills," offer a great opportunity to reduce electricity consumption and increase profits through the use of renewable energy, as well as reduce environmental harm and maintenance costs.

This paper investigates and compares the technical and environmental feasibility of olive mills powered by renewable sources, such as solar energy, wind energy, biomass energy or a combination of them, in Andalusia (southern Spain). This is a region with huge energy dependency, but also a large amount of "green" resources available to be used.

The feasibility of these systems was carried out by taking into account the cost; power generation; CO2 equivalent emissions; and the fraction of renewable energy, with the assumption of a grid connection.

**Keywords:** Olive Mills, wind turbine, PV module, Homer software

[1] Department of Civil Engineering, University of Granada, 18071 Granada, Spain.

EBSCOhost - printed on 2/14/2023 2:46 PM via . All use subject to https://www.ebsco.com/terms-of-use

## Introduction

The current energy situation in Spain, and specifically in Andalusia, requires all sectors to consider present and future strategies in terms of optimizing energy consumption. Climate change, the Kyoto protocol, and the needs of companies to reduce energy costs, make it important to have a good knowledge of energy in key sectors [1], such as the agriculture/food production (agro-food) sector.

Olive oil is a crucial industry for the agro-food sector in Europe, since the region accounts for approximately 73 % of the world's olive oil production [2]. The industry is based in the Mediterranean Basin, including Spain, Italy, Portugal, France, Cyprus, Slovenia, and Malta. According to data from 2010, 50 % of all olive fields are situated in Spain; 26 % in Italy; and 22 % in Greece [3]. 66 % of European olive oil production is sold internationally. In 2011, 45 % of the product was sold in Europe, with Spain being the main producer and Italy the main purchaser within the European Union. Between 2010 and 2011 exports to countries outside the euro zone reached 447,000 tonnes, of which Spain sold approximately 225,000 t and Italy sold 160,000 t. The USA, Brazil, Japan, Australia, Russia, and China were the countries that imported the most olive oil [3]. As can be seen from these figures, this industry is very important for countries in southern Europe and particularly for the main olive oil producer, Spain.

Taking all this into account, the optimization of energy consumption in olive mills must be a priority for their management. However, there is a common issue related to the purchase of power for such facilities, as they only operate for a period of four to five months (normally, from December to April). The facilities and electrical supply contracts are designed for these peaks of consumption, and therefore the installations are "oversized" for the rest of the year, implying unnecessary costs.

## Description of the problem

For several years now the price of the olive oil appears to have reached a ceiling. As such, it is very important for the profitability of the sector to reduce production costs. It is important to focus efforts on the reduction of energy consumption, which is a significant cost in the agro-food industry.

Despite the fact that the olive mills are simple facilities and there are perhaps only few areas easily improved, this paper demonstrates that it is possible to achieve the optimization of these facilities and obtain similar production with lower energy consumption.

EBSCOhost - printed on 2/14/2023 2:46 PM via . All use subject to https://www.ebsco.com/terms-of-use

To achieve a reduction in power consumption, energy costs, and CO2 equivalent emissions to the atmosphere, the use of renewable energy sources is the best solution; however, not all renewable sources are suitable for this purpose. Taking into account the climatic conditions of Andalusia, three types of system were analyzed; solar energy, wind power, and biomass.

Almost all Spanish olive fields and mills are located in the south of Spain, which has the highest solar radiation levels in Europe. The region has an average yearly solar value of 4.93 kWh/m2/day and about 3.22 kWh/m2/day during the period that the olive mills are working—from November to March (see Fig. 1). These climatic conditions have allowed the installation of 882 MWp of solar photovoltaic and 1,900 MW of solar thermal power in Andalusia.

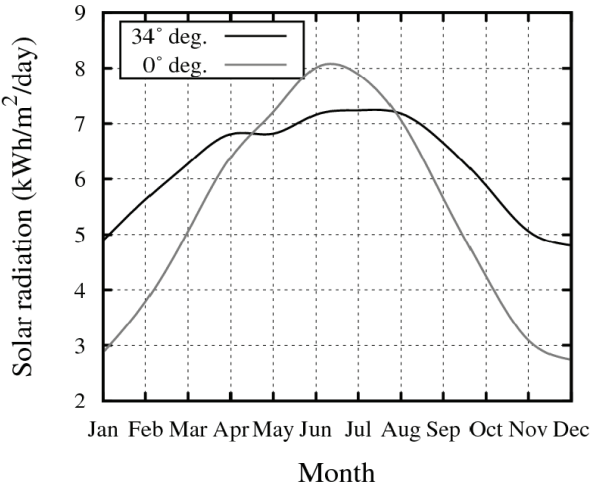



Figure 1. Monthly solar radiation in southern Spain using PVGis [4].

In terms of wind power, Andalusia has seen the installation of 3,400 MW, suggesting that conditions are suitable for the establishment of wind turbine-powered olive mills. In Fig. 2, the average wind velocity at a height of 40 m is shown.

EBSCOhost - printed on 2/14/2023 2:46 PM via . All use subject to https://www.ebsco.com/terms-of-use

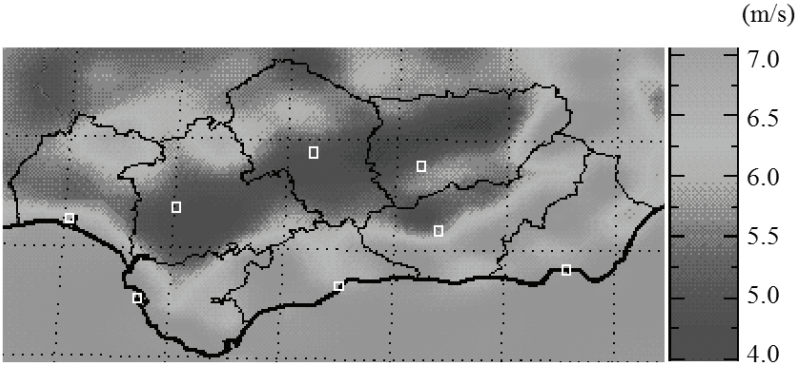



Figure 2. Wind resources in Andalusia from December to April. Height: 40 m. *Source: Andalusia Energy Agency* [5].

Finally, the amount of bio-waste from the cultivation of olive groves and oil production (prunings from olive trees and holm oak; olive-pomace oil; olive stones, etc.) is sufficient that the use of bio-fuels in boilers, stoves, and ovens, etc. may offer a potential energy source. The exploitation of biomass allows the sustainable replacement of fossil fuels and increases self-sufficiency. In this case, biomass can be used as an energy source for electricity and heating [6].

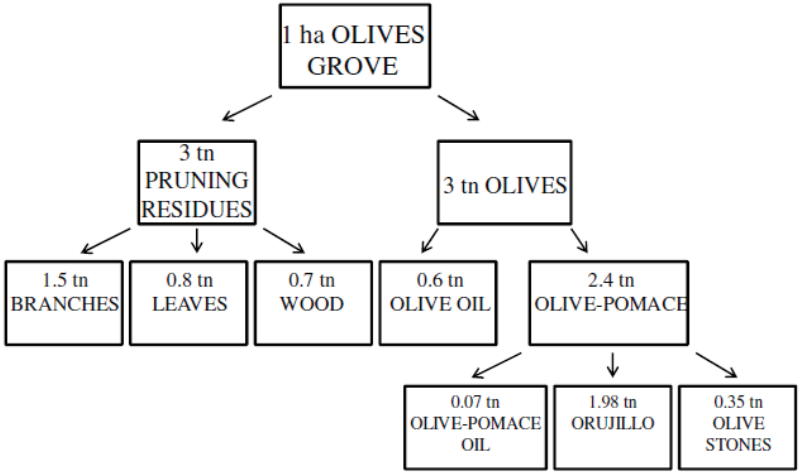



Figure 3. Biomass potential of an olive grove [6].

EBSCOhost - printed on 2/14/2023 2:46 PM via . All use subject to https://www.ebsco.com/terms-of-use

Although the resources described above are all readily available in Andalusia, the feasibility of a mixed model (with different types of renewable energy) to minimize energy consumption in olive mills has not yet been studied. Therefore, a model is developed here to show how electricity consumption can be optimized, with the aim of maximizing energy savings through the implementation of renewable energy technologies.

## Energy consumption of olive mills

The energy consumption of an olive mill can be divided into two forms: electrical energy and thermal energy.

The electricity consumed is supplied by the electrical grid and is used in the various stages of cleaning (conveyors, bar screens, washing machines, engines, etc.) and grinding the fruit (grinders and centrifugal pumps). Thermal energy is consumed through the use of hot water to maintain the temperature of the dough mixer at around 30 ºC and the ambient temperature of the cellar between 15 °C and 20 °C, as well as in the centrifuges. This water is usually heated by a boiler that uses fossil fuels, such as diesel.

In addition to energy consumption directly related to the process of olive oil production, there are other facilities that require electricity for operation, such as offices, lighting, and air conditioning.

Obviously, the level of energy consumption depends on the level of olive oil production; therefore, in this paper the size of an olive mill has been classified according to the following scheme:

**Table I: Classification of olive mills according to production [7]**

| Classification of mills | Production of Olive Oil |
|---|---|
| Small | $\leq$ 1000 tn |
| Medium | ]1000, 5000] tn |
| Large | >5000 tn |

The average power consumption of different mills according to their production is shown in Table II:

EBSCOhost - printed on 2/14/2023 2:46 PM via . All use subject to https://www.ebsco.com/terms-of-use

**Table II: Electrical consumption of olive mills according to production [7]**

| Classification of mills | Electrical Consumption |
|---|---|
| Small | 92,000 kWh |
| Medium | 435,000 kWh |
| Large | 922,500 kWh |

And finally, the consumption of thermal energy is shown in Table III:

**Table III: Consumption of thermal energy in olive mills according to production [7]**

| Classification of mills | Electrical Consumption |
|---|---|
| Small | 108,000 kWh |
| Medium | 510,650 kWh |
| Large | 1,082,900 kWh |

Using the data shown in these tables and on the available renewable resources (solar, biomass and wind), we can develop a model that will allow us to size an olive mill according to the appropriate contribution of energy from renewable sources, with the objective of maximizing the sustainability of this type of agro-food facility.

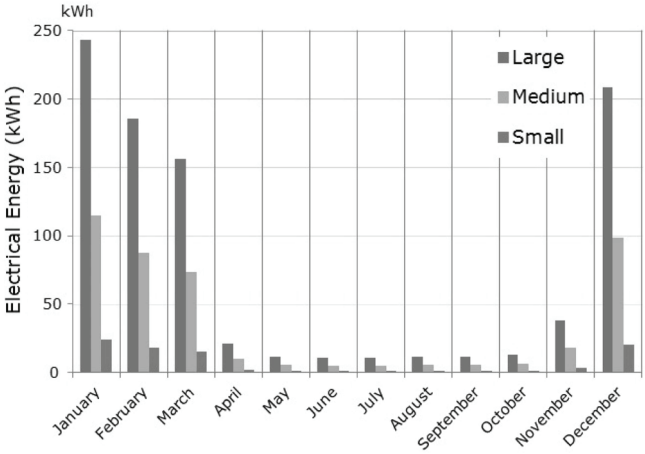



Figure 4. Monthly electrical energy consumption of olive mills depending on their classification [7].

EBSCOhost - printed on 2/14/2023 2:46 PM via . All use subject to https://www.ebsco.com/terms-of-use

### *The influence of temporary demand for energy consumption*

This part of the ago-food sector can be characterized by its temporary nature, since olive harvesting and milling depends directly on the weather. As a consequence, electrical consumption levels throughout the year are not constant. The energy consumption of oil mills audited by FAECA [8] was obtained for a time period of one year. This data is shown in Fig. 4, which clearly shows the temporariness of energy consumption.

## Materials and methods

The system was designed by calculating the monthly demand for electrical and thermal energy required by an olive mill and the power output of different combinations of solar PV, biomass, and wind turbines. The following points were taken into account in the design:

1. The energy generated as a combination of PV, biomass, and wind has to be the cheapest and lowest in terms of CO2 emissions. A biomass boiler provides power to heat the water.
2. Batteries are not used
3. AC power from the system inverter feeds into the distribution grid.
4. Maximum power from renewable systems will be 100 kW [9].

### *System model*

The proposed system is shown in Fig. 5. The system was designed using HOMER (Hybrid Optimization of Multiple Energy Resources) [10], a micro power optimization model developed and regularly improved by the American National Renewable Energy Laboratory. This application helps find the best generation system (size and number of components, costs, and environmental impacts). Furthermore, HOMER is able to evaluate the feasibility (economic and technical) of a system.

EBSCOhost - printed on 2/14/2023 2:46 PM via . All use subject to https://www.ebsco.com/terms-of-use

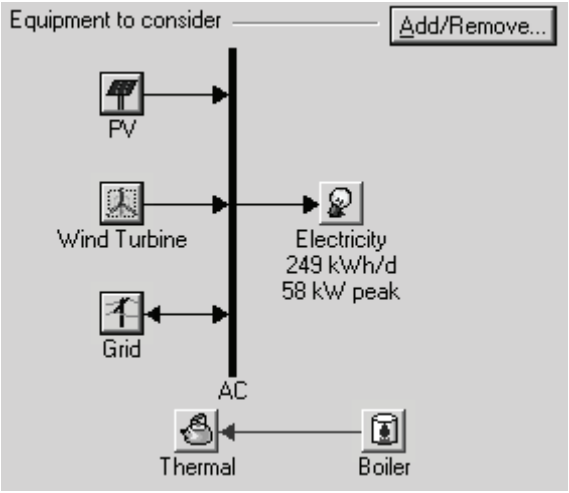



Figure 5. Basic setting of loads (small olive mills) and sources in HOMER.

In this system, PV modules and wind turbines are used to provide power to the processes in the olive mill that consume electricity and will always be connected to the grid (self-consumption). Thermal energy is supplied by biomass boilers.

In this paper, we calculate the optimum solution for the three classes of olive mill (small, medium, and large), according to the consumption of electrical and thermal energy, as shown in Tables II and III. Figs. 6 and 7 show the monthly electricity and thermal load profile of a small olive mill. Note that the busiest months are November to April. The rest of the time, there is no thermal consumption and minimal electrical consumption for powering the office facilities (lighting, air conditioning, etc.).

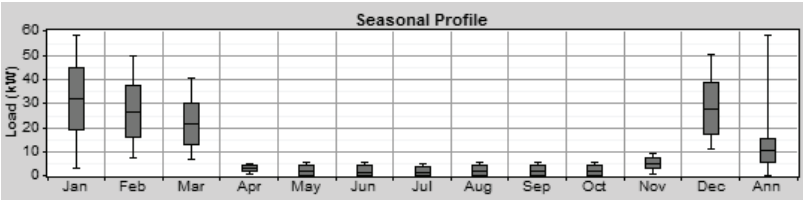



Figure 6. Monthly electricity load profile of a small olive mill.

EBSCOhost - printed on 2/14/2023 2:46 PM via . All use subject to https://www.ebsco.com/terms-of-use

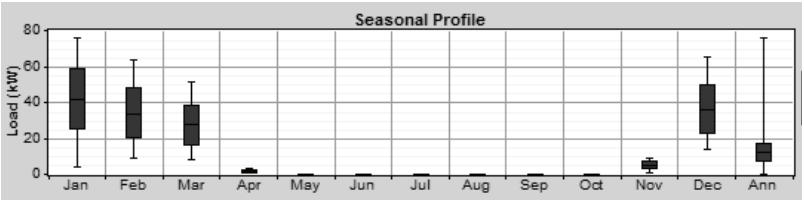



Figure 7. Monthly thermal load profile of a small olive mill.

## *PV system*

PV output primarily depends on the available solar radiation. The PV module designed in this system produces AC current. A range of 1 to 100 kW was considered and the input cost and information is shown in Table IV:

**Table IV: PV module cost and characteristics**

| Description | Cost/Information |
|---|---|
| Capital cost | 3,125 $/kW$_{AC}$ |
| Replacement cost | 2,500 $/kW$_{AC}$ |
| Life time | 25 years |
| PV tracking | No tracking |
| De-rating factor | 80 % |
| Slope (degrees) | 37.1667 |
| Ground reflectance | 20 % |

The average price shown in Table IV refers to the PV modules installed.

The main feature of the HOMER software package is that it gives the solar radiation levels once the latitude and longitude coordinates have been specified. The solar radiation is shown in Fig. 8. The proposed site is located at a latitude of 37º 10’ N and a longitude of 3º 36’ W. An annual average of 4.93 kWh/m$^2$/d of solar radiation is available.

EBSCOhost - printed on 2/14/2023 2:46 PM via . All use subject to https://www.ebsco.com/terms-of-use

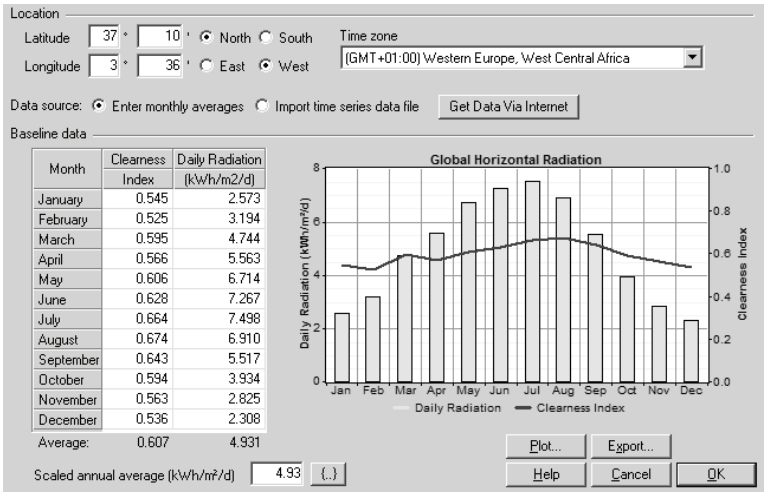



Figure 8. Monthly radiation in the south of Spain using HOMER.

## *Wind turbine*

Wind turbine output depends on the average available wind velocity. According to Fig. 2, the average velocity at a height of 40 m is 5.5 m/s$^2$. The wind turbine designed in this system produces AC current. A range of 1 to 100 kW was considered and the cost is shown in Fig. 9.

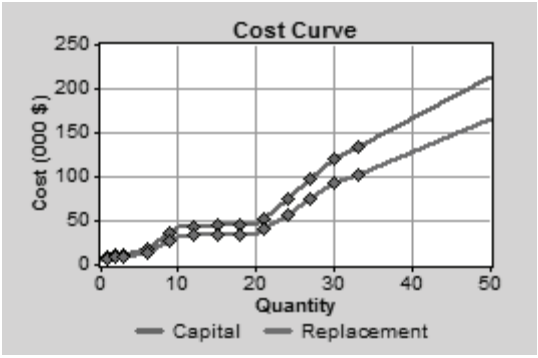



Figure 9. Cost of wind turbine as function of installed power and the cost of replacement.

EBSCOhost - printed on 2/14/2023 2:46 PM via . All use subject to https://www.ebsco.com/terms-of-use

### *Biomass boiler*

Biomass is provided by bio-waste from the cultivation of oil groves and olive oil production (prunings from olive trees and holm oak, olive pomace oil, olive stones, etc.). The waste materials obtained from cultivation have different thermal properties and densities, etc., as such, in this paper we have used an averaged value weighted with the amount of waste in production (see Fig. 3).

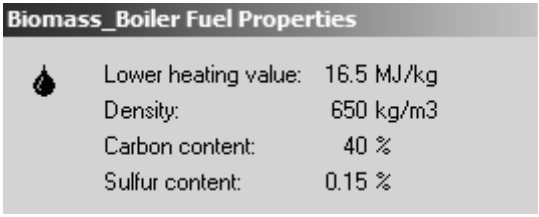



Figure 10. Biomass properties used in the model in HOMER.

The efficiency of the boiler is 85 %.

### *Grid*

The cost of electrical energy is taken to be 0.121 $/kWh off-peak rate; 0.195 $/kWh shoulder rate; 0.255 $/kWh peak rate for purchase; and 0.058 $/kWh for sale back to the grid. The monthly fee charged for the use of the electrical grid infrastructure is 3.1 $/kW/month.

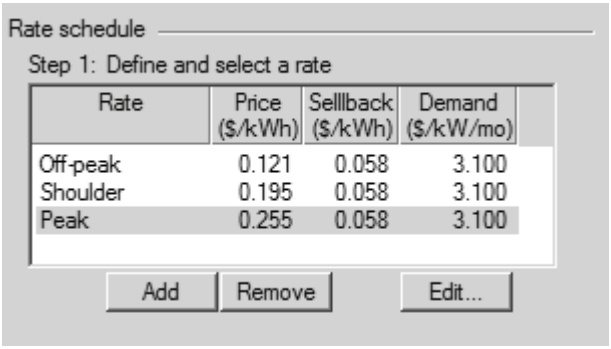



Figure 11. Cost of current tariff in electrical energy in HOMER.

EBSCOhost - printed on 2/14/2023 2:46 PM via . All use subject to https://www.ebsco.com/terms-of-use

Finally, it is necessary to take into account the time of year when each of the rates apply, in order to improve the optimization of the contribution of each system, renewable source, or network connection.

Fig. 12 shows the yearly rate schedule input in the software.

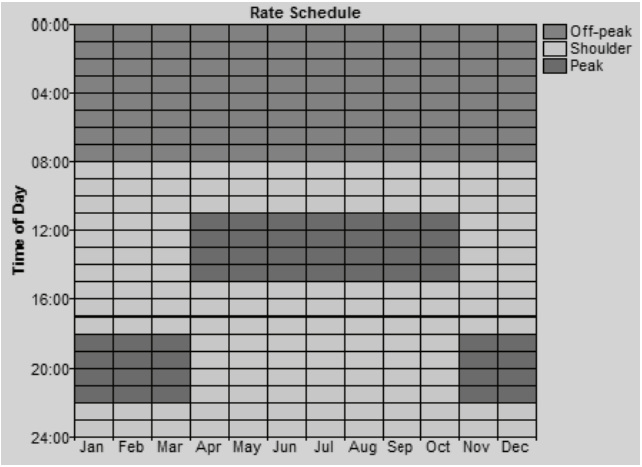



Figure 12. Rate schedule implemented in HOMER.

## Optimization result and model

The results of optimization for small olive mills indicates that the optimal system uses only PV modules connected to the grid and biomass with a 0.2 $/kWh cost of energy (COE). Beyond this optimal solution, we find another solution by using a hybrid PV-wind turbine system connected to the grid.

Sensitivity Results | Optimization Results

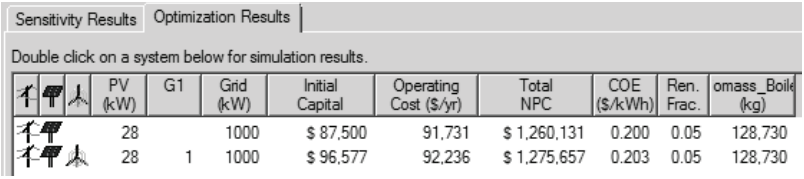
Double click on a system below for simulation results.

| | PV (kW) | G1 | Grid (kW) | Initial Captal | Operating Cost ($/yr) | Total NPC | COE ($/kWh) | Ren. Frac. | omass_Boile (kg) |
|---|---|---|---|---|---|---|---|---|---|
| | 6 | | 1000 | $ 18,750 | 19,428 | $ 267,107 | 0.200 | 0.05 | 27,170 |
| | 6 | 1 | 1000 | $ 27,827 | 19,940 | $ 282,722 | 0.213 | 0.06 | 27,170 |

Figure 13. Results of optimization for small olive mills.

EBSCOhost - printed on 2/14/2023 2:46 PM via . All use subject to https://www.ebsco.com/terms-of-use

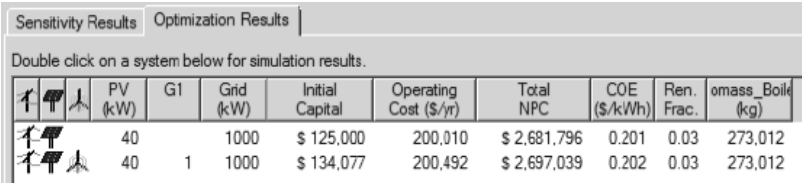
Following the same procedure for medium and large olive mills, the following results were obtained:


Sensitivity Results | Optimization Results

Double click on a system below for simulation results.

| | PV (kW) | G1 | Grid (kW) | Initial Capital | Operating Cost ($/yr) | Total NPC | COE ($/kWh) | Ren. Frac. | omass_Boile (kg) |
|---|---|---|---|---|---|---|---|---|---|
| | 28 | | 1000 | $ 87,500 | 91,731 | $ 1,260,131 | 0.200 | 0.05 | 128,730 |
| | 28 | 1 | 1000 | $ 96,577 | 92,236 | $ 1,275,657 | 0.203 | 0.05 | 128,730 |

Figure 14. Results of optimization for medium olive mills.


Sensitivity Results | Optimization Results

Double click on a system below for simulation results.

| | PV (kW) | G1 | Grid (kW) | Initial Capital | Operating Cost ($/yr) | Total NPC | COE ($/kWh) | Ren. Frac. | omass_Boile (kg) |
|---|---|---|---|---|---|---|---|---|---|
| | 40 | | 1000 | $ 125,000 | 200,010 | $ 2,681,796 | 0.201 | 0.03 | 273,012 |
| | 40 | 1 | 1000 | $ 134,077 | 200,492 | $ 2,697,039 | 0.202 | 0.03 | 273,012 |

Figure 15. Results of optimization for large olive mills.

Looking at the results shown in Figs. 13, 14 and 15, we can conclude that the optimum combination is a mixed system with PV modules connected to the grid (electrical supply) and a biomass boiler (thermal supply). The relationships between olive oil production and energy support from renewable systems is summarized in the following table:

**Table VI: Relationship between olive oil production and renewable energy support**

| Classification of mills | PV module (kW) |
|---|---|
| 1,000 tn (small) | 6 |
| 3,000 tn (medium) | 28 |
| 5,000 tn (large) | 40 |

EBSCOhost - printed on 2/14/2023 2:46 PM via . All use subject to https://www.ebsco.com/terms-of-use

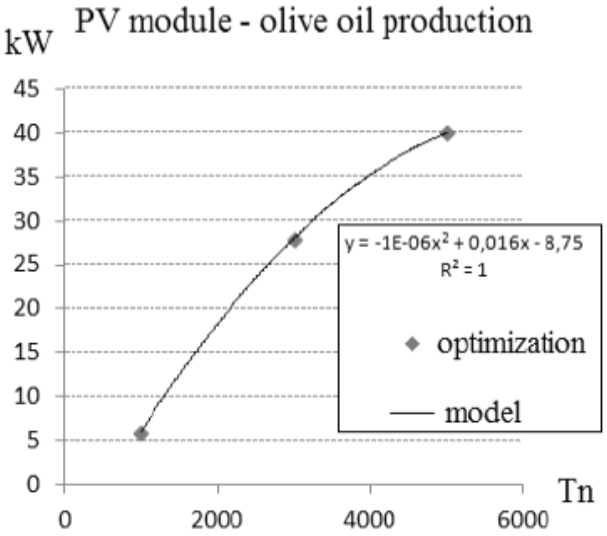



Figure 16. Polynomial fit of the optimization results.

The model, expressed as a polynomial, takes into account wind velocities of only 5.5 m/s and it is for this reason that a solution with a wind turbine is not the cheapest.

As regards biomass, in Fig. 3 we can see that for each 0.6 t of olive oil produced, almost 3.5 t of useful waste biomass (prunings; holm oak; olive-pomace oil; olive stones, etc.) is obtained. Therefore, as highlighted in Figs. 13, 14 and 15, the biomass boiler is powered by waste obtained during olive oil production.

The wind conditions in Andalusia appear less suitable for powering olive mills. As such, the authors intend to input a wide range of sampled wind velocities into the model using GIS [11, 12]. We will cross-reference this wind data with the location of olive mills in Andalusia, whose production data are already known. As a result, we will be able to assign different $a_j$ parameters (polynomial coefficients) to each olive mill, optimizing them according to their surroundings.

## Conclusions

The results obtained by using the HOMER software package have allowed us to develop a simple and realistic model to plan the energy

EBSCOhost - printed on 2/14/2023 2:46 PM via . All use subject to https://www.ebsco.com/terms-of-use

supply (electrical and thermal), based on low-carbon technologies, of olive mill operation.

The yearly quantity of energy production, consumption, and finally COE were obtained for different conditions of production to achieve an optimized system. The analysis revealed that COE is 0.2 $/kWh in the case of a grid connected system, which is lower when compared to a grid only system. This is economically advantageous.

This study of an optimized mixed system for an olive mill has shown that the proposed system can be implemented in a cost effective and environmentally friendly way.

## References

[1] M. Soshinskaya, W. H. J. Crijns-Graus, J. Van der Meer, J. M. Guerrero. "Application of a microgrid with renewables for a water treatment plant." Applied Energy. Vol 134, pp. 20–34, 2014.

[2] M. M. Pagliuca, D. Scarpato. "The olive oil sector: A comparison between consumers and experts' choices by sensory analysis." Procedia. Econ. Financ. Vol. 17, pp. 221–230, 2014.

[3] European Commission. Prospects for the Olive Oil Sector in Spain, Italy and Greece 2012–2020; European Union Press: Brussels, Belgium, 2012.

[4] The Photovoltaic Geographical Information System (PVGIS). http://re.jrc.ec.europa.eu/pvgis/.

[5] Andalusia Energy Agency. Recurso Eólico de Andalucía, Agencia Andaluza de la Energía, Sevilla (2009), pp. 63–69.

[6] A. García-Maraver, M. Zamorano, A. Ramos-Ridao, L.F. Díaz. "Analysis of olive grove residual biomass potential for electric and thermal energy generation in Andalusia (Spain)." Renewable and Sustainable Energy Reviews. Vol. 16, pp. 745–751, 2012.

[7] O. Rabaza, J. Contreras-Montes, M. J. García-Ruiz, F. Delgado-Ramos, D. Gómez-Lorente. "Techno-economic performance evaluation for olive mills powered by grid-connected photovoltaic systems." Energies. Vol. 8, pp. 11939–11954, 2015.

[8] Federación Andaluza de Empresas Cooperativas Agrarias. Manual de Ahorro y Eficiencia Energética del Sector. Almazaras. Available online: http://www.agro-alimentarias.coop/ficheros/doc/03198.pdf (accessed on 7 May 2018).

[9] Real Decreto 1699/2011. Regulación de conexiones a red de instalaciones de producción de energía eléctrica de pequeña potencia. Ministerio de Industria, Turismo y Comercio de España. 2011.

[10] The HOMER Software (HOMER Energy). http://www.homerenergy.com/software.html

EBSCOhost - printed on 2/14/2023 2:46 PM via . All use subject to https://www.ebsco.com/terms-of-use

[11] J. Arán Carrión, A. Espín Estrella, F. Aznar Dols, M. Zamorano Toro, M. Rodriguez, A. Ramos Ridao. "Environmental decision-support systems for evaluating the carrying capacity of land areas: Optimal site selection for grid-connected photovoltaic power plants." Renewable and Sustainable Energy Reviews. Vol. 12, pp. 2358–2380, 2008.

[12] J. A. Carrión, A. Espín Estrella, F. Aznar Dols, A. R. Ridao. "The electricity production capacity of photovoltaic power plants and the selection of solar energy sites in Andalusia (Spain)." Renewable Energy. Vol. 33, pp. 545–552, 2008.

EBSCOhost - printed on 2/14/2023 2:46 PM via . All use subject to https://www.ebsco.com/terms-of-use

# CHAPTER TWELVE

# NUMERICAL MODELLING OF RESISTIVE-TYPE SUPERCONDUCTING FAULT CURRENT LIMITERS

A. ETXEGARAI[1], I. ZAMORA, G. BUIGUES, V. VALVERDE, E. TORRES, AND P. EGUIA

## Abstract

This chapter introduces the main applications of superconducting materials in power systems, focusing on superconducting fault current limiters (SFCL). Recently, due to the high penetration of distributed power generation, short-circuit current values have risen. As a result, fault current limiters (FCL) based on superconducting materials have come to be considered one of the most promising solutions for limiting these fault currents. The focus of the research presented here is primarily on resistive-type SFCLs. The advantages of these are found in size, cost, and product maturity; field installation, however, is still at an early stage. Several modelling approaches for resistive type current limiters, as proposed in the literature, are reviewed here for future applications in both AC and DC systems.

**Keywords:** Superconductivity; superconducting fault current limiter (SFCL); modelling; simulation.

[1] Department of Electrical Engineering, Faculty of Engineering of Bilbao, University of the Basque Country UPV/EHU.
e-mail: agurtzane.etxegarai@ehu.eus

EBSCOhost - printed on 2/14/2023 2:46 PM via . All use subject to https://www.ebsco.com/terms-of-use

# 1. Introduction

Superconductivity is a phenomenon that occurs when materials exhibit zero electrical resistance below a specified critical temperature and are perfectly diamagnetic. Along with presenting zero electrical resistance, the Meissner effect also occurs in superconducting materials, which is the expulsion of magnetic fields. The first characteristic has applications in high performance power systems, while the second results in powerful electromagnets. This chapter focuses on the application of superconductivity in power systems. The main requirements of superconducting materials for this field include: a high critical temperature; a magnetic field; current density; stable operation; ease of manufacturing; and low cost.

Currently, a wide range of materials with superconducting characteristics are well-known. Their development and use is summarised in Section 2. Section 3 summarises the most promising applications of superconductors in power systems. This chapter presents the modelling approaches of resistive-type superconducting fault current limiters (SFCL), which are one of the most promising applications of the latest generation of superconducting materials in power systems. The classification and main characteristics of SFCLs are described in Section 4 and their practical implementation is detailed in Section 5. Sections 6 and 7 indicate the operation and modelling perspectives of resistive-type SFCLs. Finally, the main conclusions are presented in Section 8.

# 2. Evolution of superconducting materials

The development and use of materials with superconducting properties is summarised in this section, as described in [1]. The first materials to be understood to have superconducting properties were pure metals at temperatures approaching absolute zero, such as mercury at 4.2 K. Later, this group of materials included metal alloys such as niobium-tin ($Nb_3Sn$), which displayed critical temperature values near to absolute zero, although liquid helium was required as coolant. Earlier materials are now referred to as low temperature superconductors (LTS)—they have critical temperatures below 30 K.

In 1986, superconductors made from copper oxide ceramics with much higher critical temperature values were discovered by researchers at IBM—so-called high temperature superconductors (HTS). The most commonly used materials in early HTS were bismuth-based, i.e. BSCCO, most commonly Bi-2212 and Bi-2223. These materials are known today as first generation (1G) superconductors. Second generation (2G)

EBSCOhost - printed on 2/14/2023 2:46 PM via . All use subject to https://www.ebsco.com/terms-of-use

superconductors were developed more recently, including rare earth-based HTS materials ((RE)BCO).

Yttrium-based materials (YBCO) had higher critical temperatures. Many other cuprate superconductors have since been discovered and used in various applications. Among them, $MgB_2$ was proved to have a transition temperature of 39 K, putting it between LTS and HTS materials. According to the literature [2], it can currently be produced in extensive lengths and at competitive costs.

As such, it can be concluded that the increase in critical temperature has been essential to the development of superconducting materials: LTS needed to be cooled by liquid helium, while HTS ceramic compounds exhibit superconductivity at higher temperatures. As a result, those materials can be cooled by liquid nitrogen, which can be liquidized at 77 K and is far less expensive. However, ceramic materials are breakable and non-ductile, making the manufacturing of superconductor wires complex. Moreover, in order to guarantee their superconducting characteristics, conditions must be within specified critical temperature, current density, and magnetic field values.

## 3. Power system applications of superconducting materials

The most promising applications in the power system field are superconducting cables, SMES (superconducting magnetic energy storage), and SFCLs (superconducting fault current limiters). Other promising applications also mentioned in the literature include rotating machines and transformers. The main power system applications are reviewed in this section, which is based on [1].

### *A. Superconducting cables*

The earliest prototypes of superconducting cables were based on LTS using a helium cooling system. Nowadays, they have mostly been replaced by HTS cooled by liquid nitrogen—even though the manufacturing process and ductility of HTS cables is worse than in LTS cables, the final product is less expensive and the cooling system has a simpler design. Today, commercially available HTS cables are manufactured with BSCCO and YBCO. Alternatively, LTS cables are based on $MgB_2$, with a good performance/cost ratio. Initially, two designs were proposed for superconducting cables: the warm dielectric design (WD) and the cold dielectric coaxial design (CD). Today, however, commercially available cables are cold dielectric cables, where the dielectric part of the cable is

EBSCOhost - printed on 2/14/2023 2:46 PM via . All use subject to https://www.ebsco.com/terms-of-use

located inside the cryogenic cold portion of the cable structure. HTS cables have generally been applied to AC systems; HTS cables for DC systems show promising results, however, while being at an earlier stage of development.

### *B. SMES (superconducting magnetic energy storage)*

Energy storage is a key area of technological development due to the increasing penetration of renewable energy sources. SMES devices can store electric energy as a magnetic field created by the flow of direct current in a superconducting coil at a cryogenic temperature and regulated by a control system. This phenomenon occurs without resistive losses and the storage devices release their stored energy when required. In addition to a superconducting coil, an AC/DC converter is necessary for connecting an SMES to a power system. First generation systems based on LTS have now evolved into systems with HTS, such as REBCO or YBCO. Compared to other storage technologies, they show high density energy, high efficiency, and quick power response. Possible applications include: load levelling; dynamic stability; transient stability; voltage stability; frequency regulation; transmission capability enhancement; or power quality improvement.

### *C. SFCLs (superconducting fault current limiters)*

Nowadays, with the higher penetration rates of renewable energies, short-circuit currents are rising. As such, fault current limiters (FCLs) are used to rapidly limit very high currents during faults. By installing them at a bus-bar coupling or in-line, FCLs can provide an economic alternative for coping with such currents. SFCLs offer one of the most promising solutions for limiting fault currents in power grids. During fault events that breach a threshold current, the impedance increases and the short-circuit current is limited. Under normal operation, if the temperature is maintained within the critical temperature range, the device shows no resistance. Compared to other fault limiting alternatives, they have negligible impedance at normal conditions, but fast and effective current limitation within the first current rise and repetitive operation with fast and automatic recovery.

EBSCOhost - printed on 2/14/2023 2:46 PM via . All use subject to https://www.ebsco.com/terms-of-use

### *D. Other power applications: HTSG (high temperature superconducting generator)*

Superconducting materials allow high current density. Therefore, high magnetic fields can be withstood, leading to a significant reduction in the mass and size of superconducting machines. Moreover, superconducting technology achieves a significant improvement in efficiency, especially at partial loads. This aspect is particularly important for wind power generation, given that wind turbines operate mostly under part-load conditions. HTSG are also suitable candidates as off-shore wind generators, because transport and installation is eased due to a lower volume in comparison to conventional machines. However, in parallel with other power applications, manufacturing and maintenance costs and requirements are still high, which hinders their market penetration [3], [4].

## 4. Introduction to SFCLs: classification and characteristics

This chapter focuses on one of the main power applications of superconducting materials: SFCLs (superconducting fault current limiters). Four main types of SFCL are proposed in the literature, as summarised by Larruskain in [5]: resistance type; solid-state; shielded iron-core type; and saturated iron-core type.

### *A. Resistive SFCLs*

Resistive SFCLs are connected in series with the protected line and are therefore the simplest, most compact, and most economical SFCLs. Under normal operation, their impedance is almost zero. When the current, the operating temperature, or the external magnetic field surpasses a specified limit, the impedance of the superconductor increases. Additionally, a given period is necessary to cool down, which varies from seconds to minutes. The recovery time depends on the superconducting material.

### *B. Solid-state SFCLs*

Solid-state SFCLs are also called hybrid limiters, since they combine semiconductor and superconducting materials. The proposed solid-state SFCLs can be divided into two groups: bridge-type and fault current controller-type limiters. Bridge-type SFCLs are similar to bridge-type solid-state FCLs, but normal inductance is replaced by a superconducting

EBSCOhost - printed on 2/14/2023 2:46 PM via . All use subject to https://www.ebsco.com/terms-of-use

inductance. Several designs of bridge-type SFCLs can be found in the literature that have been successfully tested.

### *C. Shielded iron-core SFCLs*

Shielded iron-core SFCLs consist of a conventional primary winding around an iron core with a yoke and a superconducting cylinder. This type of limiter is similar to a transformer with the secondary side shunted by a superconducting material. During a fault, the higher current on the secondary winding causes the superconductor to be quenched, resulting in a voltage increase opposing the fault current.

### *D. Saturated iron-core SFCLs*

Saturated iron-core SFCLs, also called DC-biased core SFCLs, consist of two iron-core coils with a constant-current superconductive winding, which adds a magnetic bias. Under rated conditions, the line current is small. As a consequence, it saturates the cores with DC-bias currents. The iron has a relative permeability of 1 and acts like air for the AC coils. As such, the inductances are very small. During a fault, the line current is high enough to drive the coils out of a saturation state and into a state of high permeability. As a consequence, the total inductance increases. For this operation, there is no quenching of the superconductor. This results in the absence of a recovery period after faults.

### *E. Summary*

Whereas SFCLs add inductance, resistive SFCLs add resistance to the protected circuit during a fault event. Moreover, in the rectifier and the saturated core types, the superconductor material is not quenched. Resistive SFCLs show advantages over other types for the following reasons [1]:

- They have a simpler structure, smaller size, and lower capital cost.
- Resistive SFCLs can restrain the fault current, but also consume the electrical power of the generators during fault conditions. Thus, transient stability is enhanced.
- They are applicable to both AC and DC currents.

However, resistive SFCLs also show slow recovery times and restricted fault limitation. Those disadvantages are currently being dealt

EBSCOhost - printed on 2/14/2023 2:46 PM via . All use subject to https://www.ebsco.com/terms-of-use

with through the use of hybrid-type SFCLs. These are based on modules and can therefore limit the peak current within the half-cycle period. As a result, their coordination with conventional relays is feasible.

## 5. Practical implementation of SFCLs

Table I brings together some of the latest projects involving the installation of SFCLs in AC grids, beginning in 2010 and based on [6]. The most active countries in the development of SFCLs are Korea, China, Germany, the UK, and the USA. The main applications correspond to resistive SFCLs based on a second-generation coated conductor, such as YBCO tapes at medium voltage. YBCO presents a slower change in resistivity with respect to temperature, but faster recovery after quenching. As such, YBCO tapes show good characteristics for use in a superconducting fault current limiter operating at 77 K. Also, SFCL prototypes based on multi-strand $MgB_2$ have been cited in the literature. Their significant potential is due to low cost and a simple manufacturing process. However, superconductivity is achieved at a lower temperature and quenching resistance is smaller.

**Table I. - Latest SFCL projects**

| MANUFACTURER | DATA | TYPE | MATERIAL | FIELD TEST | PROTECTION |
|---|---|---|---|---|---|
| Innopower (China) [7] | 220 kV, 300 MVA | Saturated core | BSCCO tape | Yes (2010) | -- |
| Kepco (Korea) [8] | 22.9 kV, 3 kA | Hybrid | YBCO tape | No (2010) | Transformer |
| Nexans (Germany) [9] | 12 kV, 800 A | Resistive | BSCCO bulk | Yes (2011) | Feeder |
| RSE (Italy) [10] | 9 kV, 3.4 MVA | Resistive | BSCCO tape | Yes (2012) | Feeder |
| AMSC, Nexans, Siemens (USA) [11] | 115 kV, 1.2 kA | Resistive | YBCO tape | No (2012) | -- |
| Zenergy (USA) [12] | 138 kV, 1.3 kA | Saturated core | BSCCO tape | Yes (2012) | Transformer |
| Nexans (Spain) [13] | 24 kV, 1005 A | Resistive | YBCO tape | Yes (2013) | Bus-bar coupling |
| Nexans (UK) [14] | 12 kV, 1600/1050 A | Resistive | YBCO tape | Yes (2015) | Bus-bar coupling |
| RSE (Italy) [15] | 9 kV, 15.6 MVA | Resistive | YBCO tape | Yes (2016) | Transformer |

SFCLs are also being studied as part of the protection systems of HVDC systems, combined with fast-acting DC breakers. In fact, superconductivity is more suitable for DC systems than for AC systems as

EBSCOhost - printed on 2/14/2023 2:46 PM via . All use subject to https://www.ebsco.com/terms-of-use

superconducting materials are sensitive to magnetic fields in movement [16]. Therefore, the magnetic field distributions inside superconducting strips cause AC hysteresis losses. Resistive SFCLs are the preferred option for DC systems. However, while no prototype or real installation has been reported so far, several authors have already studied the solution from a simulation perspective in both point-to-point and multi-terminal HVDC systems. In [17], the authors present the experimental results of a DC circuit breaker (DCCB) consisting of a SFCL in series with a conventional gas circuit breaker (CB). The superconductor's limiting capacity increases the breaking capability of the DCCB—this is an emerging technology for DC current interruption. However, the application of the interrupting device is restricted to a MV DC circuit. Other authors have also worked on solutions based on the combination of mechanical CBs with SFCLs. Leon-Garcia et al. introduced a protection strategy for a three-terminal HVDC system based on the series connection of a resistive SFCL with a mechanical DCCB in [18]. In contrast to mechanical DCCBs, the use of hybrid CBs allows interruption at higher fault currents in shorter timescales [19]. Khan et al. present in [20] a modification of a hybrid DCCB, by replacing the CLR with a SFCL. This innovation allows the installation of a hybrid DCCB with a lower breaking capability; moreover, this novel device can interrupt bidirectional current flows. Its effectiveness has been validated by means of simulation for three-, four- and five-converter MTDC systems.

The modelling of superconducting limiters is important in order to analyze and design both existing and new installations in AC and DC systems.

## 6. Operation of resistive SFCLs

Within critical conditions, resistive SFCLs show no resistance to current. During this period, they are operating in a superconducting state. During short-circuits, the current increases significantly and so does the resistance of the superconductor because of the rapid rise in its temperature. This stage is commonly called the *flux-flow state*. Once the superconducting material is fully quenched, a shunt resistance is inserted into the circuit so as to reduce over-voltages. Next, the SFCL operates in a *normal conducting state*. Once the fault is cleared, resistive SFCLs may need a recovery time, during which the element is cooled until it returns to its *superconducting* state. However, SFCLs can be designed so as to operate immediately after they achieve a normal conducting state.

EBSCOhost - printed on 2/14/2023 2:46 PM via . All use subject to https://www.ebsco.com/terms-of-use

The sudden change in superconductor resistance is mainly due to the electrical properties of the superconductor material, which can be macroscopically simplified into E(J) power laws, where the electric field depends on the current density and both parameters depend on temperature. Most references are based on [21] for the E(J) characteristic of the superconductor, making use of experimental results of the first SFCL ever installed, which was made of Bi2212 materials. As shown in Fig. 1, based on [1], E(J) characteristics can be divided in three regions limited by the curves E1, E2 and E3.

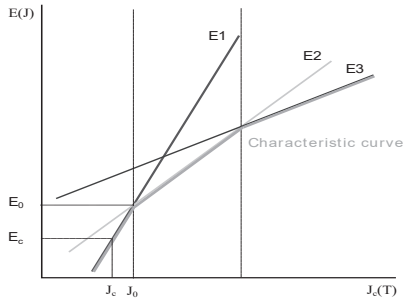



Figure 1. Characteristic E(J) curve.

Curve E1 in red represents the *superconducting region* curve; E2 in green the *flux-flow region* curve; and E3 in blue the *normal conducting region* curve. The intersection of the three curves makes up the actual characteristic curve, depicted in grey, depending on the current density at each instant. As a consequence, as current increases during a fault, the current limiter will go through those three states.

Each state is characterised by a power law (Equations (1) to (3)).

$$E_1 = E_c \cdot \left( \frac{J}{J_c(T)} \right)^{\alpha(T)} \tag{1}$$

$$E_2 = E_0 \cdot \left( \frac{E_c}{E_0} \right)^{\beta/\alpha(77K)} \cdot \left( \frac{J_c(77K)}{J_c(T)} \right) \cdot \left( \frac{J}{J_c(77K)} \right)^{\beta} \tag{2}$$

$$E_3 = \rho(T_c) \cdot \frac{T}{T_c} \cdot J \tag{3}$$

EBSCOhost - printed on 2/14/2023 2:46 PM via . All use subject to https://www.ebsco.com/terms-of-use

where $J_c$ is the critical current that must be fitted to experimental data; α and β depend on material processing conditions; ρ is normal resistivity; and $T_c$ is the critical temperature. Jc(T) and ρ(T) can be approximated as linear functions of temperature by equations (4) and (5).

$$J_c(T) \approx J_c(77K) \cdot \left( \frac{T_c - T}{T_c - 77K} \right) \tag{4}$$

$$\rho(T) \approx \rho_c(T_c) \cdot \left( \frac{T}{T_c} \right) \tag{5}$$

In order to include the effect of the magnetic field, based on experimental data, α=10 and β=3 are considered in [21]. Other values can be found in the literature dealing with several experimental results.

During the flux-flow and normal state, power is dissipated and temperature rise versus time can be calculated by (6), as indicated in [22], where c is the heat capacity per volume. Adiabatic and isotherm conditions are considered. A more complex calculation is given in (7), as introduced in [23], where $T_a$ is the ambient temperature, $Q_{sc}$ the heat dissipated in the superconductor, and $Q_{removed}$ the heat removed by the coolant.

$$\frac{dT}{dt} = E \cdot \frac{J}{c} \tag{6}$$

$$T(t) = T_a + \int_0^t \left( Q_{sc}(t) - Q_{removed}(t) \right) \cdot dt \tag{7}$$

## 7. Modelling of resistive SFCLs

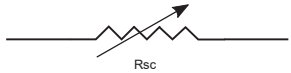
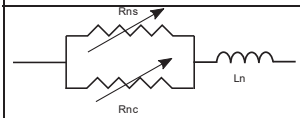
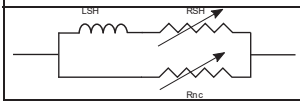
For modelling resistive-type SFCLs, several perspectives have been proposed in the literature (Table II).

A resistive SFCL is composed of a superconducting cable and a shunt resistance, which reduces over-voltages during quenching. It can also be required to divert part of the fault current after the quench in order to prevent overheating [23]. The shunt resistance can be bonded to the superconductor and/or externally. However, it is often neglected in order to simplify the analysis, as proposed by Blair et al. in [24]. Most detailed approaches include a series inductance [25]. In Sung et al. [26], a unit consists of the stabiliser resistance Rns, the superconductor resistance Rnc, and the coil inductance Ln. Its value in normal conditions, however, is

EBSCOhost - printed on 2/14/2023 2:46 PM via . All use subject to https://www.ebsco.com/terms-of-use

very small, and as a consequence, it is often neglected in modelling. Often, a SFCL is composed of several series units (n) in order to reach the specified rating.

**Table II. Modelling of resistive SFCLs.**

| Model | Reference |
|---|---|
|  | Blair et al. [24] |
|  | Sung et al. [26] |
|  | Nemdili et al. [25] |

The resistance of the superconducting tapes varies in relation to current, temperature, and magnetic field. Depending on the application, this resistance can be represented by a simple time-dependent equation (a step, linear or exponential function), or by thermo-electric models, which can also vary in complexity. On the other hand, for dealing with two and three dimensional symmetries, the numerical modelling of a SFCL can be based on finite element analysis (FEA). Finally, hardware-in-the-loop models are also mentioned in the literature. This section describes the aforementioned perspectives when modelling resistive-type SFCLs, based on [1].

### *A. Simplified models*

Simplified models consider a time-dependent perspective of the superconducting material. As a consequence, the influence of current, temperature, or magnetic field is disregarded in simplified models. Two types are indicated in the literature: binary models or a non-linear look-up table of resistance values.

Binary models show negligible resistance in the steady-state and high resistance immediately after a fault occurs. Hence, only the *superconducting*

EBSCOhost - printed on 2/14/2023 2:46 PM via . All use subject to https://www.ebsco.com/terms-of-use

and the *normal* state are considered. However, superconductor materials need a finite time to heat up and develop resistance. This aspect introduces errors, which, depending on the application, can be significant.

The non-linear look-up table method indicates SFCL resistance over time based on generic quenching equations. The exponential model in (7), as introduced in [27], is most widely accepted. However, a linear model is also presented in [28].

$$R(t) = R_{\max} \cdot \left(1 - e^{-t/\tau}\right) \tag{8}$$

where $R_{max}$ represents the maximum resistance value at the normal state, which is attained $\tau$ seconds after the initiation of a fault.

The quenching process can be triggered at a specific time in the simulation or when the instantaneous phase current exceeds a critical current Ic. Thus, the resistance of the SFCL is zero if the phase current is smaller than Ic, while it corresponds to (7) for higher fault currents.

An alternative to the exponential model in (7) is also presented in [29], all belonging to S/N (superconducting-to-normal) transition-type SFCLs. In addition, once the fault has been cleared, the transition from the *normal state* to the *superconducting state* of the SFCL is not instantaneous. There is a recovery process, as modelled in [26]. These models are called N/S (normal-to-superconducting) models.

$$R(t) = \begin{cases} 0 & \text{if } t < t_0 \\ R_{\max} \cdot \sqrt{1 - e^{-(t-t_0)/\tau}} & \text{if } t_0 \le t < t_1 \\ a_1 \cdot (t - t_1) + b_1 & \text{if } t_1 \le t < t_2 \\ a_2 \cdot (t - t_2) + b_1 & \text{if } t \ge t_2 \end{cases} \tag{9}$$

where $t_0$, $t_1$, and $t_2$ refer respectively to quenching time, first recovery starting time, and second recovery starting time. Response time $t_1$ is often considered 2 msec and recovery time $t_2$ can be adjusted under the reclosing time in the power system.

Fig. 2 compares the simplified models previously mentioned for a single fault cycle, based on [1]. According to the binary model, the superconducting material in the SFCL has negligible resistance in its steady-state; under faults, resistance increases immediately so as to limit the fault current. Regarding the S/N model, an exponential model for the flux-flow state is presented in Fig. 2. Once the fault is cleared, the superconductor is supposed to recover its superconducting state without

EBSCOhost - printed on 2/14/2023 2:46 PM via . All use subject to https://www.ebsco.com/terms-of-use

delay. Finally, the N/S model includes an exponential flux-flow state and a linear recovery.

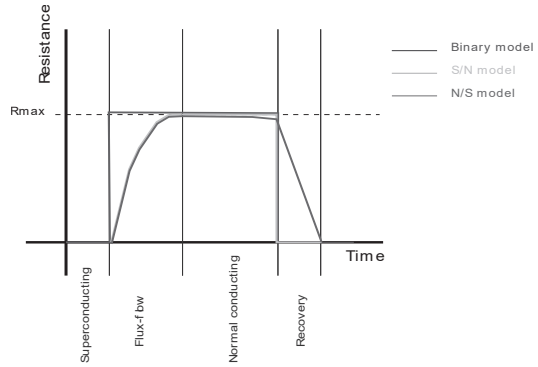



Figure 2. Comparison of resistance evolution.

### *B. Magneto-Thermal models*

The evolution of the superconductor's resistance is based on E-J power laws. Hence, a ρ(J, T) perspective is considered in thermal models, by using equations (10)-(12).

$$\rho = \begin{cases} 0 & \text{if } J < J_c, \mathrm{T} < T_c \\ \rho_c \cdot \dfrac{J}{J_c} & \text{if } J > J_c, \mathrm{T} < T_c \\ \rho_{HTS} & \text{if } T > \mathrm{T_c} \end{cases} \quad (10)$$

where:

$$\rho_c = \frac{E_c}{J_c} \quad (11)$$

$$J_c = J_c(77K) \cdot \frac{(T_c - T)}{T_c - 77K} \quad (12)$$

More detailed models include heat transfer capacity expressions of the superconducting materials. Some references include the shunt resistance. However, classic magneto-thermal models can result in complicated

EBSCOhost - printed on 2/14/2023 2:46 PM via . All use subject to https://www.ebsco.com/terms-of-use

calculations and long simulation times. Therefore, simplified magneto-thermal models, based on empirical results, have been proposed in [30], [31], and [32].

Based on the aforementioned thermal models, some references propose a R(I,T) perspective, considering a V-I characteristic, given that voltage V is related to electric field E and current I to current density J. According to [33], once the critical current is reached, resistance increases non-linearly as indicated in (13).

$$R_1 = \frac{dV}{dI} = \frac{n \cdot V_c \cdot I^{n-1}}{I_c^n} \tag{13}$$

where n is the resistive transition index, $I_c$ the critical current, and $V_c$ the critical current.

After reaching the maximum value of resistance, there is a linearly exponential decay in (14) corresponding to the *normal conducting state*.

$$R_2 = R_{\max} \cdot e^{-t_2/\tau} \tag{14}$$

where $R_{max}$ is the maximum value of resistance, $t_2$ is the start of the decay interval, and $\tau$ the time constant.

Finally, the superconducting material returns to the *superconducting state* with some slope, as indicated by (15).

$$R_3 = R_c - \frac{R_c}{m} \cdot (t_2 - t_3) \tag{15}$$

where $R_c$ is the critical value of resistance at which full power cooling is applied; m is the negative slope of the recovery; and $t_3$ is the start of the recovery interval.

### *C. Finite element analysis models*

Several models have been developed by detailed finite element analysis, mainly for inductive-type SFCLs [34], [35], [36], but also for the resistive-type [37], [38], [39]. FEA models require specialised software, such as Comsol, Magnet, or Flux2D. Model implementation can be a complicated process and simulation times are often long. Simulation results from FEA models can be used to validate other models with a high degree of accuracy [40].

EBSCOhost - printed on 2/14/2023 2:46 PM via . All use subject to https://www.ebsco.com/terms-of-use

### *D. Hardware-in-the-loop models*

Several references use real-time simulation (RTS) methodology with power-hardware-in-the-loop (PHIL) capabilities [41], [42], [23]. Power amplifiers pass the output current from a circuit simulator through the superconductor wire tested. The RTS-PHIL enables the inclusion of the actual transient reaction of the hardware being studied without any complicated numerical model, while the power system circuit can be simulated.

## 8. Conclusions

This chapter has reviewed the main applications of superconducting materials in power systems, mainly focusing on SFCLs. Additionally, several modelling approaches for SFCLs have been presented, focusing on resistive-type limiters because of their size, cost, and product maturity.

The latest projects involving resistive SFCLs have been reviewed in order to identify current implementation practices. Concurrently with the commercialization of the first SFCLs, different types of simulation model have been introduced in the literature—from simple models to more complex ones. Given that superconductors present transient states when submitted to fault currents, it can be stated that modelling is a complex challenge. As a consequence, some theoretical assumptions have to be considered in order to analyse the operation of a resistive SFCL. One dimensional models are commonly adopted for studying superconductivity, including simplified models and magneto-thermal models. Two and three dimensional models, which are based on FEA, display high accuracy, although the required simulation times are long. Hardware-in-the-loop models exhibit the real transient response of superconductor devices with no numerical model.

## Acknowledgements

The authors gratefully acknowledge the support of the Spanish Ministry of Economy, Industry, and Competitiveness (project ENE2016-79145-R AEI/FEDER, UE), the Basque Government (GISEL research group IT1083-16), as well as the University of the Basque Country UPV/EHU (research group funding PPG17/23).

EBSCOhost - printed on 2/14/2023 2:46 PM via . All use subject to https://www.ebsco.com/terms-of-use

## References


[1] A. Etxegarai, I. Zamora, G. Buigues, V. Valverde, E. Torres, and P. Eguia, «Models for Fault Current Limiters based on Superconductor Materials», in *Renewable Energy and Power Quality Journal (RE&PQJ)*, Madrid, Spain, 2016.

[2] X. Song, N. Mijatovic, B. B. Jensen, and J. Holbøll, «Design Study of Fully Superconducting Wind Turbine Generators», *IEEE Trans. Appl. Supercond.*, vol. 25, n. 3, pp. 1-5, Jun. 2015.

[3] G. Sarmiento *et al.*, «Design and Testing of Real-Scale MgB2Coils for SUPRAPOWER 10-MW Wind Generators», *IEEE Trans. Appl. Supercond.*, vol. 26, n. 3, pp. 1-6, Apr. 2016.

[4] J. Sun *et al.*, «Design and Construction of the Cryogenic Cooling System for the Rotating Magnetic Validator of the 10 MW SUPRAPOWER Offshore Superconducting Wind Turbine», *IEEE Trans. Appl. Supercond.*, vol. 28, n.º 3, pp. 1-5, Apr. 2018.

[5] D. M. Larruskain, A. Iturregi, O. Abarrategui, A. Etxegarai, and I. Zamora, «Fault Current limiting in VSC-HVDC systems with MMC converters», en *2016 International Symposium on Power Electronics, Electrical Drives, Automation and Motion (SPEEDAM)*, 2016, pp. 332-337.

[6] A. Etxegarai, A. Iturregi, M. Larruskain, I. Zamora, and P. Eguia, «Modelling and parameterization of resistive Superconducting Fault Current Limiters», en *Renewable Energy and Power Quality Journal (RE&PQJ)*, Malaga, Spain, 2017.

[7] X. Niu *et al.*, «Manufacture and test of the dc superconducting coil for a 220kV/300MVA SFCL», *Phys. Procedia*, vol. 27, pp. 388-391, 2012.

[8] O. Hyun, K. Park, J. Sim, H. Kim, S. Yim, y I. Oh, «Introduction of a Hybrid SFCL in KEPCO Grid and Local Points at Issue», *IEEE Trans. Appl. Supercond.*, vol. 19, n. 3, pp. 1946-1949, Jun. 2009.

[9] A. Hobl, S. Elschner, J. Bock, S. Krämer, C. Jänke, and J. Schramm, «Superconducting Fault Current Limiters - A new tool for the grid of the Future», presentado en CIRED Workshop, Lisbon, Portugal, 2012.

[10] L. Martini *et al.*, «The first Italian Superconducting Fault Current Limiter: Results of the field testing experience after one year operation», *J. Phys. Conf. Ser.*, vol. 507, n. 3, 2014.

[11] H.-P. Kraemer *et al.*, «Superconducting Fault Current Limiter for Transmission Voltage», *Phys. Procedia*, vol. 36, pp. 921-926, jan. 2012.

[12] F. Moriconi, F. D. L. Rosa, A. Singh, B. Chen, M. Levitskaya, and A. Nelson, «An innovative compact saturable-core HTS Fault Current Limiter - development, testing and application to transmission class networks», en *IEEE PES General Meeting*, 2010, pp. 1-8.

[13] A. Hobl, W. Goldacker, B. Dutoit, L. Martini, A. Petermann, and P. Tixador, «Design and Production of the ECCOFLOW Resistive Fault Current Limiter», *IEEE Trans. Appl. Supercond.*, vol. 23, n.º 3, pp. 5601804-5601804, Jun. 2013.


EBSCOhost - printed on 2/14/2023 2:46 PM via . All use subject to https://www.ebsco.com/terms-of-use

[14] B. West, M. Stemmle, J. Berry, and A. Hobl, «Commercial application of Superconducting Fault Current Limiters in the western power distribution network grid in the UK», presented at 23 rd International Conference on Electricity Distribution CIRED 2015, Lyon, France, 2015.

[15] G. Angeli, M. Bocchi, M. Ascade, V. Rossi, A. Valzasina, and L. Martini, «Development of Superconducting Devices for Power Grids in Italy: Update About the SFCL Project and Launching of the Research Activity on HTS Cables», *IEEE Trans. Appl. Supercond.*, vol. 27, n. 4, pp. 1-6, Jun. 2017.

[16] G. Saldaña, A. Etxegarai, D. M. Larruskain, A. Iturregi, and S. Apiñaniz, «Impact of a resistive superconductive fault current limiter in a multi-terminal HVDC grid», at *2018 19th IEEE Mediterranean Electrotechnical Conference (MELECON)*, 2018, pp. 25-29.

[17] B. Xiang, Z. Liu, Y. Geng, and S. Yanabu, «DC Circuit Breaker Using Superconductor for Current Limiting», *IEEE Trans. Appl. Supercond.*, vol. 25, n.º 2, pp. 1-7, Apr. 2015.

[18] W. R. L. Garcia, A. Bertinato, P. Tixador, B. Raison, and B. Luscan, «Full-selective protection strategy for MTDC grids based on R-type superconducting FCLs and mechanical DC circuit breakers», at *5th IET International Conference on Renewable Power Generation (RPG) 2016*, 2016, pp. 1-7.

[19] J. Häffner and B. Jacobson, «Proactive Hybrid HVDC Breakers - A key innovation for reliable HVDC grids», presented at The electric power system of the future - Integrating supergrids and microgrids International Symposium, Bologna, Italy, 2011.

[20] U. A. Khan, J. G. Lee, F. Amir, and B. W. Lee, «A Novel Model of HVDC Hybrid-Type Superconducting Circuit Breaker and Its Performance Analysis for Limiting and Breaking DC Fault Currents», *IEEE Trans. Appl. Supercond.*, vol. 25, n. 6, pp. 1-9, dic. 2015.

[21] W. Paul *et al.*, «Superconducting Fault Current Limiter Applications, technical and economical benefits, simulations and test results», presentado en Session CIGRE 2010, Paris, France.

[22] L. Ye and K.-P. Juengst, «Modeling and simulation of high temperature resistive superconducting fault current limiters», *IEEE Trans. Appl. Supercond.*, vol. 14, n. 2, pp. 839-842, Jun. 2004.

[23] J. Langston, M. Steurer, S. Woodruff, T. Baldwin, and J. Tang, «A generic real-time computer Simulation model for Superconducting fault current limiters and its application in system protection studies», *IEEE Trans. Appl. Supercond.*, vol. 15, n. 2, pp. 2090-2093, Jun. 2005.

[24] S. M. Blair, C. D. Booth, and G. M. Burt, «Current -Time Characteristics of Resistive Superconducting Fault Current Limiters», *IEEE Trans. Appl. Supercond.*, vol. 22, n. 2, Apr. 2012.

[25] S. Nemdili and S. Belkhiat, «Modeling and Simulation of Resistive Superconducting Fault-Current Limiters», *J. Supercond. Nov. Magn.*, vol. 25, n.º 7, pp. 2351-2356, Jun. 2012.

[26] B. C. Sung, D. K. Park, J.-W. Park, and T. K. Ko, «Study on a Series Resistive SFCL to Improve Power System Transient Stability: Modeling,

EBSCOhost - printed on 2/14/2023 2:46 PM via . All use subject to https://www.ebsco.com/terms-of-use

Simulation, and Experimental Verification», *IEEE Trans. Ind. Electron.*, vol. 56, n.º 7, pp. 2412-2419, Jul. 2009.

[27] I. Muta, T. Doshita, T. Nakamura, T. Egi, and T. Hoshino, «Influences of superconducting fault current limiter (SFCL) on superconducting generator in one-machine double-line system», *IEEE Trans. Appl. Supercond.*, vol. 13, n. 2, pp. 2206-2209, Jun. 2003.

[28] H. K. (Criepi) and S. Torii (Criepi), «Setting method of parameters for SN transition fault current limiter into 6.6kV distribution system», *J. Phys. Conf. Ser.*, vol. 97, n.º 1, 2008.

[29] Y. Ye, L. Xiao, H. Wang, and Z. Zhang, «Research on Resistor Type Superconducting Fault Current Limiter in Power System», en *Transmission and Distribution Conference and Exhibition: Asia and Pacific, 2005 IEEE/PES*, 2005, pp. 1-6.

[30] P. E. Sutherland, «Analytical model of superconducting to normal transition of bulk high Tc superconductor BSCCO-2212», *IEEE Trans. Appl. Supercond.*, vol. 16, n. 1, pp. 43-48, Mar. 2006.

[31] F. Roy, B. Dutoit, F. Grilli, and F. Sirois, «Magneto-Thermal Modeling of Second-Generation HTS for Resistive Fault Current Limiter Design Purposes», *IEEE Trans. Appl. Supercond.*, vol. 18, n. 1, pp. 29-35, Mar. 2008.

[32] P. J. C. Branco, M. E. Almeida, and J. A. Dente, «Proposal for an RMS thermoelectric model for a resistive-type superconducting fault current limiter (SFCL)», *Electr. Power Syst. Res.*, vol. 80, n. 10, pp. 1229-1239, oct. 2010.

[33] Elizaveta Egorova, Himanshu Bahirat, Bruce A. Mork, Warren F. Perger, and Matthew Holcomb, «EMTP-ATP Modeling of a Resistive Superconducting Fault Current Limiter», presented at International Conference on Power Systems Transients (IPST2013, Vancouver, Canada, 2013.

[34] J. Y. Zhang, Z. Q. Wei, H. Hong, W. Z. Gong, and Y. Xin, «Electromagnetic design of saturated iron core SFCL», at *2011 International Conference on Applied Superconductivity and Electromagnetic Devices (ASEMD)*, 2011, pp. 305-308.

[35] H. Heydari, A. A. Abrishami, and M. M. Bidgoli, «Comprehensive Analysis for Magnetic Shield Superconducting Fault Current Limiters», *IEEE Trans. Appl. Supercond.*, vol. 23, n. 5, Oct. 2013.

[36] M. Majka, J. Kozak, S. Kozak, G. Wojtasiewicz, and T. Janowski, «Design and Numerical Analysis of the 15 kV Class Coreless Inductive Type SFCL», *IEEE Trans. Appl. Supercond.*, vol. 25, n. 3, pp. 1-5, Jun. 2015.

[37] S. Kozak, T. Janowski, B. Kondratowicz-Kucewicz, J. Kozak, and G. Wojtasiewicz, «Experimental and numerical analysis of energy losses in resistive SFCL», *IEEE Trans. Appl. Supercond.*, vol. 15, n.º 2, Jun. 2005.

[38] J. B. Na *et al.*, «Design and Tests of Prototype Hybrid Superconducting Fault Current Limiter with Fast Switch», *IEEE Trans. Appl. Supercond.*, vol. 22, n.º 3, pp. 5602604-5602604, Jun. 2012.

EBSCOhost - printed on 2/14/2023 2:46 PM via . All use subject to https://www.ebsco.com/terms-of-use

[39] Y. J. Kim *et al.*, «Analytical Design Method of High-Tc Coated Conductor for a Resistive Superconducting Fault Current Limiter Using Finite Element Method», *IEEE Trans. Appl. Supercond.*, vol. 20, n.º 3, pp. 1172-1176, Jun. 2010.

[40] Y. Chen, S. Li, J. Sheng, Z. Jin, Z. Hong, and J. Gu, «Experimental and Numerical Study of Co-ordination of Resistive-Type Superconductor Fault Current Limiter and Relay Protection», *J. Supercond. Nov. Magn.*, vol. 26, n. 11, Apr. 2013.

[41] O. Naeckel *et al.*, «Power Hardware-in-the-Loop Testing of an Air Coil Superconducting Fault Current Limiter Demonstrator», *IEEE Trans. Appl. Supercond.*, vol. 25, n. 3, pp. 1-7, Jun. 2015.

[42] L. Graber, T. Chiocchio, J. Kvitkovic, S. Pamidi, M. Steurer, and A. Usoskin, «Finite Element Model of a Superconducting Fault Current Limiter Calibrated by Hardware-in-the-Loop Measurements», *IEEE Trans. Appl. Supercond.*, vol. 24, n. 3, pp. 1-5, Jun. 2014.

EBSCOhost - printed on 2/14/2023 2:46 PM via . All use subject to https://www.ebsco.com/terms-of-use

# PART III:

# DISTRIBUTED GENERATION

EBSCOhost - printed on 2/14/2023 2:46 PM via . All use subject to https://www.ebsco.com/terms-of-use

# CHAPTER THIRTEEN

# STATE OF THE ART DISTRIBUTED GENERATION: VALUE PROPOSITION FOR POWER ISLANDS

BÁLINT HARTMANN, ISTVÁN VOKONY, ISTVÁN TÁCZI[1]

## Abstract

The ongoing transformation of the power system has been partially started and to a great extent characterised by the development of distributed generation. From the 2000s onwards, these mostly renewable energy-based production technologies have demonstrated their ability to be an important part of the energy production portfolio. While early research and development work has focused on increasing conversion efficiencies and decreasing levelized energy costs, recent years have highlighted the need to provide technical services and thus convert distributed generation into a valuable asset of modern power systems. This paper aims to provide a comprehensive overview of this work and also to give an example of such a value proposition—island operation that is supported by distributed generators.

**Keywords**: distributed generation; island operation; photovoltaic; wind; hydro.

[1] All authors are with the BME FASTER Excellence Research Group, Department of Electric Power Engineering, Budapest University of Technology and Economics, Egry J. u. 18., 1111 Budapest. Email: hartmann.balint@vet.bme.hu, vokony.istvan@vet.bme.hu, taczi.istvan@vet.bme.hu

EBSCOhost - printed on 2/14/2023 2:46 PM via . All use subject to https://www.ebsco.com/terms-of-use

## Introduction

Currently existing electrical power systems, in most cases, have centralized generating plants with high capacity, which are usually far from areas of high load (Bhadoria et al., 2013). However, the process of market liberalization, the increasing share of renewable energy sources due to environmental policy goals, and the pursuit of energy efficiency and diversification of resources at national levels have all led to the growing importance of distributed generation (DG) (Rújula et al., 2005). Defining DG properly is not an unambiguous task: in some countries DG is considered to mean power generation source that is connected to the distribution system (or middle and low voltage networks); other approaches focus on the generation and direct connection or proximity of the load. Other classifications rely on the technology or fuel a generator uses (Pepermans et al., 2005). CIGRÉ offers a definition from a working group, which states that DG is any generation unit with a maximum capacity of 50 to 100 MW, usually connected to the distribution network and that does not have a central scheduling or dispatch availability (CIGRÉ, 1998). IEEE defines DG as generating plants that are significantly smaller than the conventional centralized ones, which are capable of connection to power systems at nearly any point (Dondi et al., 2012). The International Energy Agency refers to DG as "generating plant serving a customer on-site or providing support to a distribution network, connected to the grid at distribution-level voltages" (IEA, 2002; Gonzalez-Longatt et al., 2005).

Properly implemented distributed generation enhances reliability; reduces technical losses; postpones investment in high capacity power plants, transmission and distribution networks; and can offer ancillary services (Matei et al., 2016). Since DGs are sited near the load, their operation can have great influence on power supply reliability. Several studies have concluded that successful islanding operation can mean that the local parts of the power system can be made more resilient (Chen et al., 2017) and DG can also serve as an emergency backup (Udgave et al., 2015). If utilized properly, DG can help to reduce losses in radial networks thanks to its load proximity (Naderi et al., 2011; Chiradeja, 2015). System operators can also calculate using DG in novel and state of the art planning approaches to reduce system size and defer investment or maintenance work while keeping the security of the supply (Piccolo et al., 2009; Wang et al., 2010; Faria et al., 2018). Ancillary services, like local voltage control (Sulla et al., 2016); different levels of frequency control (containment, restoration or replacement reserve); or loss reduction services (van Thong et al., 2007; Alsokhiry et al., 2012) are also feasible.

EBSCOhost - printed on 2/14/2023 2:46 PM via . All use subject to https://www.ebsco.com/terms-of-use

The effective integration of DG is a complex process from a technical point of view. The effects on protection coordination; system stability; frequency and voltage control; and power quality issues all need to be considered (Matei et al., 2016). Regarding protection systems, overvoltage events, short-circuit behaviour changes and islanding are the most regularly mentioned effects (Arritt et al., 2015). The steady state, voltage and transient stability are also highly affected by DG (Londero et al., 2009) and it is important to develop proper analysis for the evaluation of the stability of a structurally different system (Tiutiunnyk et al., 2016). DG is also capable of participating in the control of frequency and voltage, both as part of a larger power system (Xue et al., 2008) or in the microgrid concept (Kim et al., 2016). Based on the technology, DG can affect power quality as well, e.g. in terms of the voltage profile (Quiroga et al., 2016) and sags (Ramos et al., 2018). If it utilises a power electronic converter, harmonic injection may also be challenge (Rahmani et al., 2017).

## DG requirements for islanding

In today's power systems, island operation is handled differently to normal operation, mainly due to higher technical requirements. Those requirements include, but are not limited to:

- Active and reactive power supply for selected consumers.
- Maintaining pre-defined voltage and frequency ranges.
- Adequate controllability provided by a generator, which can be operated differently than its normal characteristics (e.g. providing reactive power for motor starting).
- Load-following (shedding).
- Ability to handle certain generator outages (security reserves).
- Ensuring transient stability.
- Adequate protection and automation to handle faults and events.

In most countries around the world, operation guidelines are issued by regulators to all system operators and to provide a comprehensive framework for planning and operation of the network. Such guidelines discuss technical requirements for DGs, including both synchronous and island operation. In order to assess the possibilities of island operation based on DG units, a brief overview of the standardised requirements for Hungary is given in this section.

Grid connection of small-scale (below 500 kVA) DG units are defined by Annex 6 of the operation guidelines. The connection of such units is

EBSCOhost - printed on 2/14/2023 2:46 PM via . All use subject to https://www.ebsco.com/terms-of-use

allowed so long as the level of actual power contracted is not exceeded. If network development has to be carried out in advance of the connection, it has to be handled jointly with work on the generator. DGs with an installed capacity above 5 kVA have to be connected to three phases, while units below 2.5 kVA are allowed to be connected to a single phase. In the case of three-phase connection, power balance among the phases is desired so as to avoid asymmetry, but a maximum of 5 kVA difference is tolerated. The connection point of the DG is selected by the DSO, who is also authorised to operate the disconnector switch.

During normal operation, DGs are usually allowed to be switched on and off without the permission of the dispatcher. To avoid counter voltages, the unit can only be switched on if the voltage of the supplying network is already sensed in all phases. According to Hungarian guidelines currently in force, when DGs sense islanding (loss of mains voltage), they must be disconnected from the distribution network within 200 ms. It is possible though to create an island in which both the local generators and consumers are involved, where power quality requirements are arbitrarily defined. It is important to maintain galvanic separation from the grid so that maintenance work can be performed under de-energised conditions. If supply on the main grid has been restored, DGs must be switched off after a short delay of at least one minute (which is secured by optical section protection), and consumers have to be simultaneously reconnected to the grid. Such fast connections can be carried out using antiparallel thyristors or other power electronic devices. If multiple DGs are connected to the same network connection point, sequential reconnection is necessary, which has to be coordinated with the dispatcher. Voltage change caused by the reconnection of DGs must remain below 2 and 3% on medium and low-voltage networks, respectively.

## Fót Liveable Future Park

The potential island for our case study is located near Fót, Hungary, at the site of a Childcare Foundation and is called the Liveable Future Park. The park originally served as an equine therapy centre, but in recent years cooperation with the local DSO has allowed the installation of a significant number of DGs. The park consists of a horse-field, stables, offices and other small buildings.

The electrical network of the park (Fig. 1) is supplied by a 160 kVA transformer from the main grid, which feeds two main circuits. One of them serves the parking lot and its vicinity, two 22 kW electric car chargers and a pump, while all other significant loads are connected to the other circuit.

EBSCOhost - printed on 2/14/2023 2:46 PM via . All use subject to https://www.ebsco.com/terms-of-use

The daily pattern of electrical loads is shown in Figure 2. It can be seen that the load shows a seasonal variation with high winter consumption and lower summer needs. Peak loads are in the range of 20 kW, while the baseload of the park is approximately 3 kW. Relatively few devices consume the majority of the electricity, i.e. water pumps, the electric car charger, the heat pump, and lighting (Table I). Based on measurements of the SCADA system, annual electricity consumption of the park is approximately 73,000 kWh.

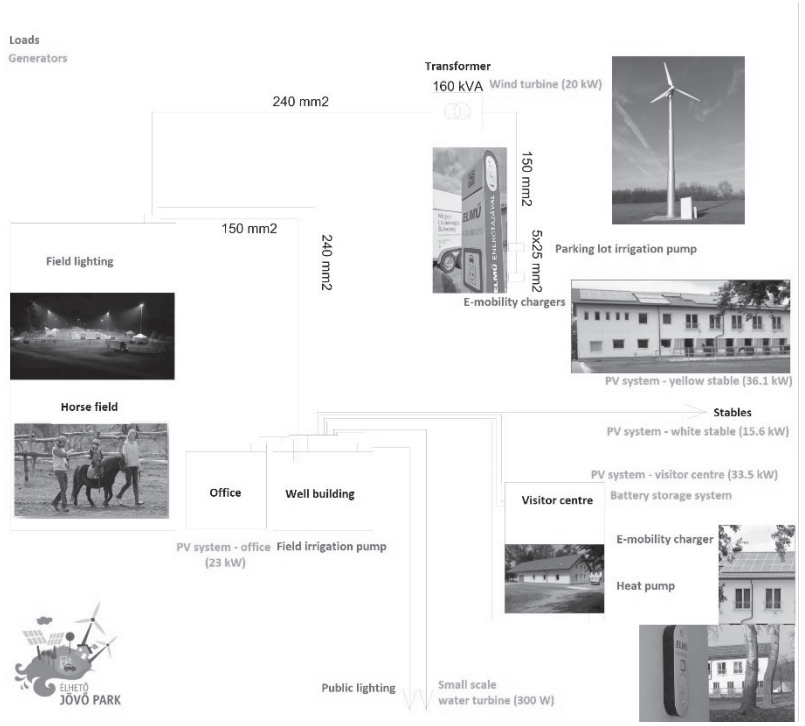



Figure 1. Electrical topology of Fót Liveable Future Park

EBSCOhost - printed on 2/14/2023 2:46 PM via . All use subject to https://www.ebsco.com/terms-of-use

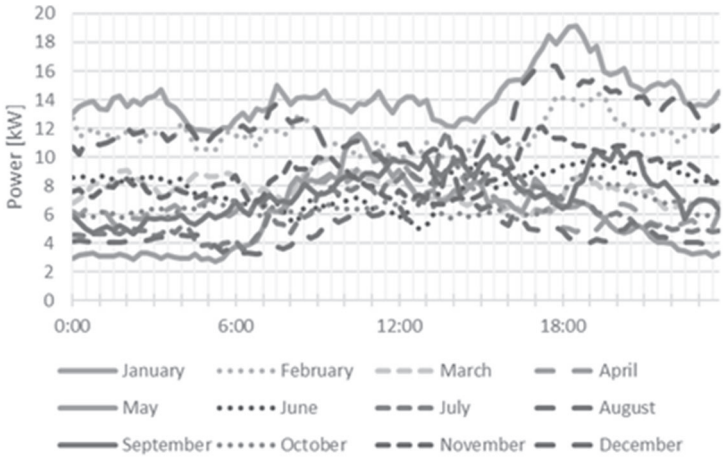



Figure 2. Consumption patterns of representative days for each month

The park is equipped with a number of DG units. Solar photovoltaic systems have been installed on the roofs of the stables, the office building, and the visitor centre. Their cumulative capacity is 108.2 kWp. The four systems are facing south east (20–35° deviation from south). Their expected specific annual electricity production is between 1,100 and 1,200 kWh/kWp. A 20 kW small-scale wind turbine (OUYAD FD-12) is directly connected to the grid transformer. Its energy production is very low and has not exceeded 60 MWh in any of the 5 years since it has been installed. It should be noted that low production levels are identified as a result of multiple technological issues (e.g. the inverter needing to be replaced) and not meteorological reasons. To utilize the potential hydro-power of the creek that is flowing through the park, a low-head turbine has been installed. The 300 W micro-unit includes a generator and a power controller and is connected directly to the battery system of the park. This latter decision is caused by the low working time of the plant—changes in the water input and sand blocks are limiting its useful operating time to approximately 250 hours annually.

EBSCOhost - printed on 2/14/2023 2:46 PM via . All use subject to https://www.ebsco.com/terms-of-use

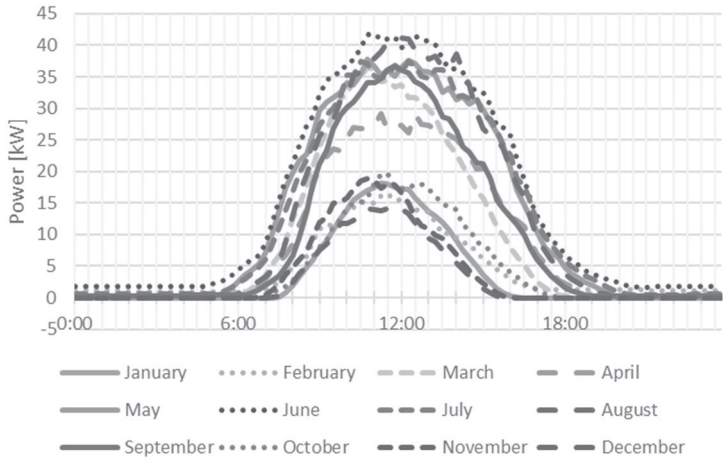



Figure 3. Production patterns of DGs in the park

## Examination of island operation supported by DGs

Early research work considering the potential island operation of the system has been carried out, focusing on forecasting of photovoltaic production using artificial intelligence and demand-side management. The results of these studies align with the above sections of the paper. Island operation of the site is feasible from a technical perspective, as the production of the photovoltaic plants exceeds annual consumption by approximately 70% (124 MWh versus 73 MWh).

**Table I: Most important electrical devices of the park**

| Generation and storage of the microgrid | Significant loads |
|---|---|
| Photovoltaic system Yellow Stable (36.1 kW) | E-mobility chargers (44 kW) |
| Photovoltaic system Visitor Centre (33.5 kW) | Field irrigation pump (37 kW) |
| Wind turbine (20 kW) | Field lighting (24 kW) |
| Photovoltaic system Office (23 kW) | E-mobility charger (Visitor Centre, 11 kW) |

EBSCOhost - printed on 2/14/2023 2:46 PM via . All use subject to https://www.ebsco.com/terms-of-use

| | |
|---|---|
| Li-ion battery storage (20 kW, 80 kWh) | Parking lot irrigation pump (11 kW) |
| Photovoltaic system White Stable (15.6 kW) | Heat pump (5.4 kW) |
| Small water turbine (300 W) | Public lighting (5 kW) |

To analyse seasonal differences of production and consumption, a time-series model with a quarter-hourly resolution was developed in MS Excel, allowing the calculation of both patterns for representative days of each month. Using the quarter-hourly net power balance data, the amount of electricity which could be stored and later used was calculated. Selecting certain technical parameters of battery energy storage (75% cycle efficiency and 60% allowed depth for a maximized lifetime), and the power and capacity values of the storage were determined, as shown in Table II. With a 36 kW/432 kWh storage system, the DGs of the park can supply electricity consumption during 7 months of the year, leaving only 5 months where electricity is drawn from the main grid. Those months are typically the ones with low production from the photovoltaic plants and higher consumption due to heating needs. As the storage system of the park is currently only capable of storing 80 kWh, either upscaling of the unit is needed or another firm backup capacity has to be provided. These options are compared in the following.

**Table II. Results of the simulation (all units are in kWh/day)**

| | Consumption | Surplus DG production | Recoverable after storage | Supply from main grid | Unsupplied consumption | Grid feedback |
|---|---|---|---|---|---|---|
| January | 342.20 | 8.42 | 6.31 | 265.37 | 259.05 | 0 |
| February | 277.39 | 15.64 | 11.73 | -185.18 | 173.45 | 0 |
| March | 184.78 | 142.73 | 107.04 | -107.76 | 0.71 | 0 |
| April | 164.46 | 120.32 | 90.24 | -77.34 | 0 | 12.89 |
| May | 138.95 | 202.84 | 152.13 | -41.44 | 0 | 110.69 |
| June | 190.40 | 248.15 | 186.11 | -77.84 | 0 | 108.26 |
| July | 152.31 | 202.97 | 152.23 | -49.09 | 0 | 103.12 |
| August | 118.57 | 223.35 | 167.51 | -19.39 | 0 | 118.12 |
| September | 181.58 | 142.70 | 107.02 | -90.59 | 0 | 16.43 |
| October | 157.46 | 51.09 | 38.32 | -104.34 | 66.02 | 0 |
| November | 208.64 | 32.86 | 24.65 | -153.89 | 129.24 | 0 |
| December | 294.93 | 7.86 | 5.89 | -236.99 | 231.09 | 0 |

Main consumers at the site need to be grouped together, helping to determine the amount of electricity that must be provided temporarily during the period of desynchronization. Critical consumption has to be fed

EBSCOhost - printed on 2/14/2023 2:46 PM via . All use subject to https://www.ebsco.com/terms-of-use

via a subsidiary branch to provide galvanic separation from the main grid, thus preventing feedback to the faulty DSO network. This subsidiary branch is also used to provide connection to the DG units, so that during island operation consumers of primary importance are served.

For the realisation of this, three options are proposed by the authors:

- By upscaling the energy storage system and connecting it to the subsidiary branch, island operation can be ensured. In this case, control tasks are the responsibilities of the storage unit and installation of a grid forming inverter is necessary to provide the requisite technical conditions.
- Volatility of renewable energy-based production can be levelled and supplemented by an extra generator unit with good ramping capabilities, such as a diesel generator. In this case the generator itself would be responsible for control tasks.
- The hybrid option would involve a combination of the previous mentioned cases, as the subsidiary circuit would host both the upscaled battery and the firm capacity provider. The main advantage of this is that the nominal capacity of both units can be reduced, while fully exploiting renewable energy sources. In this case, the generator could provide control for the island. This option is shown in Fig. X.

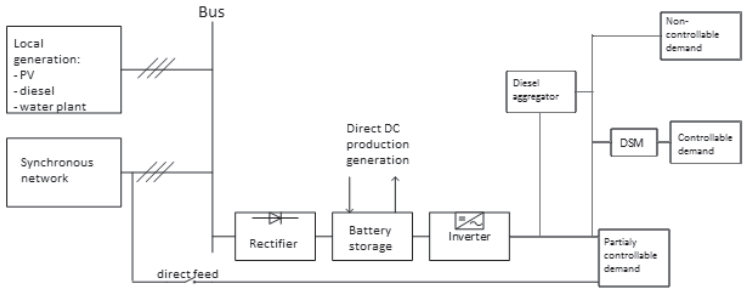



Figure 3. Hybrid topology for island operation of the park

## Conclusions

This paper has demonstrated how state-of-the-art distributed generator technology can supply island systems with considerable electricity needs. The Fót Liveable Future Park has been selected as a case study, as it offers

EBSCOhost - printed on 2/14/2023 2:46 PM via . All use subject to https://www.ebsco.com/terms-of-use

a good representation of a rural site that might occasionally require the ability to operate as an island. After analysing the historical production and consumption data for the site, it was concluded that the existing distributed generation is technically able to serve the annual electricity needs of the park. Using a time-series model of representative days for each month, surplus and deficit electricity volumes were calculated, and the size of the necessary energy storage unit was determined. Finally, three technical options were shown, the hybrid solution being the most feasible for a potential island operation, while also keeping infrastructural costs at an acceptable level.

## References

Bhadoria, V; Singh, N.; Shrivastava, V. (2013.) A Review on Distributed Generation Definitions and DG Impacts on Distribution System. International Conference on Advanced Computing and Communication Technologies.

Rújula, B. A. A.; Amada M. J.; Bernal-Agustín J. L.; Loyo Y. J. M.; Navarro D. J. (2005.) A. Definitions for Distributed Generation: a revision. Renewable Energies and Power Quality Journal. Vol. 1. No. 3. pp. 340–343.

Pepermans, G.; Driesen J.; Haeseldonckx, D.; Belmans, R.; D'haeseleer, W. (2005.) Distributed Generation: definition, benefits and issues. Energy Policy.

CIGRÉ SC #37. (1998.) Impact of increasing contribution of dispersed generation on the Power System

Dondi, P.; Bayoumi, D.; Haederli, C.; Julian, D.; Suter, M. (2002.) Network integration of distributed power generation. Journal of Power Sources. Volume 106, Issue 1. p. 1–9.

International Energy Agency (2002.) Distributed Generation in Liberalised Electricity Markets.

Gonzalez-Longatt, F.; Fortoul, C. (2005.) Review of the Distributed Generation Concept: Attempt of Unification. Renewable Energy and Power Quality Journal. Vol 1. No. 3. pp. 281–284.

Matei, G. G.; Gavrilaş M. (2016.) Voltage regulation in distribution networks with distributed generation—A review. Proceedings of International Conference and Exposition on Electrical and Power Engineering (EPE). pp. 728–732.

Chen, G.; Zhang, F.; You, D.; Wang, Y.; Lu, G.; Zou, Q.; Liu, H.; Qian, J.; Xu, H. (2017.) Reliability Evaliation of Distribution System with Distributed Generation. 4th International Conference on Mechanics and Mechatronics Research.

Udgave, A. D.; Jadhav, H. T. (2015.) A review on Distribution Network protection with penetration of Distributed Generation. IEEE 9th International Conference on Intelligent Systems and Control (ISCO), Coimbatore. pp. 1–4.

Chiradeja, P. (2005.) Benefit of Distributed Generation: A Line Loss Reduction Analysis. IEEE/PES Transmission & Distribution Conference & Exposition: Asia and Pacific. Dalian. pp. 1–5.

EBSCOhost - printed on 2/14/2023 2:46 PM via . All use subject to https://www.ebsco.com/terms-of-use

Naderi, Me. S.; Naderi, Mo. S; Rahmani, K; Gharehpetian, G. B.; Zahedi, L. (2011.) Quantitative Assesment of Distributed Generation Benefints to Improve Power System Indices. International Conference on Renewable Energies and Power Quality. Canary Islands. pp. 1–6.

Piccolo, A.; Siano, P. (2009.) Evaluating the Impact of Network Investment Deferral on Distributed Generation Expansion. IEEE Transactions on Power Systems. Vol. 24, no. 3. pp. 1559–1567

Faria, W. R.; De Oliveira, M. E.; Rocha, H. X.; Da Silva, L. G. W. (2018.) Electrical Distribution System's Reconfiguration Considering Distributed Generation: Implementation and Comparison of Metaheuristic Tools. R enewable Energy and Power Quality Journal. Vol. 1. No. 16. pp. 362–367.

Wang, D. T.; Ochoa L.; Harrison, G. (2010.) DG impact on investment deferral: Network planning and security of supply. IEEE PES General Meeting. Providence, RI. pp. 1–1.

Sulla, F.; Björnsted, J.; Samuelsson, O. (2016.) Voltage Control Capability of Distributed Generation in Low Voltage Network. Renewable Energy: Selected Issues Volume I. Cambridge Scholars Publishing. pp. 117–131.

Alsokhiry, F.; Adam, G. P.; Lo, K. L. (2012.) Contribution of distributed generation to ancillary services. 47th International Universities Power Engineering Conference. London. pp. 1–5.

Van Thong, V.; Driesen, J.; Belmans, R. (2007.) Using Distributed Generation to Support and Provide Ancillary Services for the Power System. International Conference on Clean Electrical Power. Capri. pp. 159–163.

Arritt, R. F.; Dugan, R. C. (2015.) Review of the Impacts of Distributed Generation on Distribution Protection. 2015 IEEE Rural Electric Power Conference. Asheville, NC. pp. 69–74.

Londero, R. R.; Affonso, C. M.; Nunes, M. V. A. (2009.) Impact of distributed generation in steady state, voltage and transient stability—Real case. IEEE Bucharest PowerTech. Bucharest. pp. 1–6.

Tiutiunnyk, F.; Prystupa, A.; Bodunov, V. (2016.) Improving methods for evaluating the stability of electrical systems with distributed generation. 2nd International Young Scientists Forum on Applied Physics and Engineering (YSF). Kharkiv. pp. 37–40.

Xue, Y.; Chang, L.; Venkatesh, B. (2008.) Energy management and control of aggregated distributed generations. Canadian Conference on Electrical and Computer Engineering. Niagara Falls, ON. pp. 1151–1154.

Kim, Y.; Kim, E.; Moon, S. (2016.) Frequency and Voltage Control Strategy of Standalone Microgrids with High Penetration of Intermittent Renewable Generation Systems. IEEE Transactions on Power Systems. Vol. 31, No. 1. pp. 718–728.

Quiroga, G. A.; Kagan, H.; Amasifen, J. C. C.; Almeida, C. F. M.; Kagan, N.; Vicentini, E. (2016.) Study of the Distributed Generation impact on distributed networks, focused on quality of power. 17th International Conference on Harmonics and Quality of Power (ICHQP). Belo Horizonte. pp. 855–860.

Ramos, A. C. L.; Batista, A. J.; Leborgne, R. C.; Domingues, E. G.; Calixto, W. P. (2018.) A First Approach on the Impact of Distributed Generation and

EBSCOhost - printed on 2/14/2023 2:46 PM via . All use subject to https://www.ebsco.com/terms-of-use

Network Topology on Studies of Voltage Sags. Renewable Energy and Power Quality Journal. Vol. 1. No. 16. pp. 114–120.

Rahmani, R.; Aghaee, S. S.; Hosseinian, S. H.; Sadeghi, S. H. H. (2017.) Determining maximum penetration level of distributed generation sources in distribution network considering harmonic limits and maintain protection coordination scheme. Conference on Electrical Power Distribution Networks Conference (EPDC). Semnan. pp. 196–199.

EBSCOhost - printed on 2/14/2023 2:46 PM via . All use subject to https://www.ebsco.com/terms-of-use

# CHAPTER FOURTEEN

# REVIEW OF FAULT PROTECTION IN AC MICROGRIDS: CHALLENGES AND POTENTIAL SOLUTIONS

G. BUIGUES[1], A. DYŚKO[2], V. VALVERDE[1], I. ZAMORA[1], E. FERNÁNDEZ[1]

## Abstract

The design of protection systems associated with medium and low voltage networks has traditionally been based on an assumption of unidirectional power flows, making use of time-coordinated overcurrent relays, which is an efficient and reliable way of protecting against network faults. The changes that these systems have undergone over recent decades, particularly regarding the growing population of distributed generation (DG) systems, along with the fact that many of these sources can be connected to form independent microgrids, have challenged this perspective.

A number of alternative solutions have recently appeared in the technical literature and this chapter aims to provide a comprehensive overview of the existing proposals for protection design in microgrids. Apart from describing and classifying the most relevant protection methods, the key benefits and drawbacks of each approach are presented,

[1] Department of Electrical Engineering, Faculty of Engineering of Bilbao, University of the Basque Country (UPV/EHU), Plaza Ingenieros Torres Quevedo 1, 48013 Bilbao (Spain).
E-mail: garikoitz.buigues@ehu.eus, victor.valverde@ehu.eus, inmaculada.zamora@ehu.eus, elvira.fernandezh@ehu.eus
[2] Department of Electronic and Electrical Engineering, University of Strathclyde, 204 George, Glasgow G1 1XW (United Kingdom). E-mail: a.dysko@strath.ac.uk

EBSCOhost - printed on 2/14/2023 2:46 PM via . All use subject to https://www.ebsco.com/terms-of-use

followed by a number of concluding remarks and practical recommendations.

**Keywords:** Microgrid protection; inverter-interfaced microgrids; islanded microgrid; grid-connected microgrid.

# 1. Introduction

Over the past decade, the concept of the "microgrid" has emerged as an enhanced way of integrating sustainable energy sources into electricity networks. Its main benefits lie in ways that it supplies power locally; reduces grid investment due to lower network capacity requirements; reduces operational costs and power losses; reduces peak load; and increases continuity of supply [1]. However, since operation and control methods in microgrids differ significantly from those used in conventional power systems, along with these benefits, use of microgrids also raises a number of challenges, one of which is the issue of protection [2].

The aim of this review is to provide a broad analysis with respect to the technical literature that deals with issues of microgrid protection. An attempt has been made to group these proposals in terms of their specific protection approach, but the scope of this chapter is limited to those publications that specifically consider the concept of an AC microgrid with inverter-interfaced microsources, as well as dealing with protection coordination when changing the operation mode from one that is grid-connected to one that is islanded.

# 2. General aspects in microgrid protection

## *2.1. Introduction to microgrids*

The concept of the microgrid was initially regarded as being an aggregation of distributed energy resources (DER), energy storage systems, and controllable loads located in a low voltage (LV) system of less than 10 MVA [3], which was designed to work either connected to a medium voltage (MV) grid at a point of common coupling (PCC) or islanded in a controlled way. However, with recent developments in technology, there are now microgrid systems with larger capacities [4] and ones that incorporate both LV and MV networks. This is not to suggest that the simple addition of DER to an electrical system creates a microgrid. For a microgrid to be viable, the DER should have enough

EBSCOhost - printed on 2/14/2023 2:46 PM via . All use subject to https://www.ebsco.com/terms-of-use

capacity to feed all (or at least, most) of the loads connected to that portion of the electrical system [5].

These microgrids may be divided into three different categories [6]: utility microgrids; industrial/commercial microgrids; and remote microgrids. Whereas the first two categories are thought to be able to work in both grid-connected and islanded operation systems, it is expected that the last one only works in an islanded mode. With regard to the intentional islanding and microgrid experience around the world, there are various microgrid implementations (or active experiments) that can help us better understand and design microgrid operation [4, 7-12]. While some of the experiments undertaken have been purely for R&D purposes, others have been deployed on islands or isolated/distant grids.

Some of the most important advantages that microgrids may provide to both utilities and end-consumers (and society in general) include the following aspects [13]:

- Improved efficiency in energy distribution.
- Minimised global energy consumption, therefore reducing emissions in energy generation.
- Higher service quality and improved continuity of supply.
- Cost efficient electricity infrastructure replacement.

For this purpose, since 2003 the IEEE Standards Coordinating Committee 21 (SCC21) has supported the development of the standard IEEE 1547 Standard for Interconnecting Distributed Resources with Electric Power Systems, which establishes criteria and requirements for the interconnection of DER with electrical power systems [14-18]. These documents cover microgrids and intentional islands that contain DER connected to utility electricity power systems [9, 19]. IEEE Std. 1547.4-2011 (IEEE Guide for Design, Operation, and Integration of Distributed Resource Island Systems with Electric Power Systems) states that:

> "*Operationally, when establishing the island, there may be protection system changes that have been designed that require implementation. Examples of such include distance relays for clearing of ground faults, reclosing changes, reconfiguring DR to non-IEEE-1547 settings, and relay settings changes.*"

## *2.2. Microgrid protection*

The microgrid concept faces a number of challenges in several fields—not only from a protection point of view, but also from a control and

EBSCOhost - printed on 2/14/2023 2:46 PM via . All use subject to https://www.ebsco.com/terms-of-use

dispatch perspective [20]. It could be argued that the control of microgrid islanding and its subsequent resynchronisation, along with the possible requirement of dispatching the microgrid as a single entity may be of the utmost importance.

As far as protection systems are concerned, the concept of the microgrid offers two potential benefits:

- In the case of a fault in the main network, the microgrid should be disconnected from it and operate in an islanded mode.
- In the case of a fault within the microgrid, the smallest part of the microgrid should be disconnected so that the rest of it can continue working.

Due to their specific characteristics and operation, microgrid protection systems have to deal with new technical challenges [20, 21], including:

- Generation systems connected to both MV and LV systems, making power flow bidirectional;
- Two operational modes: grid connected and islanded/stand-alone;
- Continual topological changes in a LV network due to the connection/disconnection of generators, storage systems, and loads;
- Intermittence in the generation of several microsources connected to a microgrid;
- In some cases, the increasing penetration of rotating machines may cause fault currents to exceed equipment ratings.
- Insufficient level of short-circuit current in islanding operation mode, in microgrids dominated by power-electronics interfaced DG;
- Reduction in the permissible tripping times when faults occur in MV and LV systems, in order to maintain the stability of the microgrid;
- Nuisance tripping of protection due to faults on adjacent feeders.

The protection of a microgrid has a close relationship to a number of operation and control issues [22]. As such, the protection strategy should be consistent with operation and control requirements [23]. In this way, plug-and-play and peer-to-peer are basic principles of microgrid operation [24, 25], which should be used for each component of a microgrid [26]:

- The peer-to-peer concept guarantees that a single component of a microgrid is not critical for its correct operation and it is able to

EBSCOhost - printed on 2/14/2023 2:46 PM via . All use subject to https://www.ebsco.com/terms-of-use

continue operating with the loss of any single component or source. This also implies that there should not be critical components for microgrid protection.
– The plug-and-play concept requires that a unit can be placed at any point of the microgrid without the need for reengineering, therefore reducing the possibility of error. This also affects the protection system, since it should not need to be reengineered when a new unit is placed in the microgrid.

### *2.2.1. Inverter-dominated microgrids*

Considering the type of interface used in connecting to a microgrid, there are two main types of DG sources [23]:

– Directly connected, rotating machine-based DG sources, including synchronous and induction generators, which are able to provide high short circuit fault currents for a short period of time (a few cycles), approximately 5-10 times the load current.
– Inverter-based DG sources, which have limited thermal overload capability, and therefore, much reduced contribution to the fault current (typically 2-3 times the rated current).

However, despite their limited fault current generation capability many microsources are typically connected to a microgrid by means of a power electronic inverter, either because their output is not compatible with the grid voltage (e.g. photovoltaic panels and microturbines) or due to other flexibility benefits provided by power electronics in energy extraction and management (wind turbines, etc.) [27]. Due to the low thermal inertia of semiconductor switches, inverters are actively current limited and, because of their small fault current contribution, they unavoidably cause other problems that have to be considered when designing the protection system [3, 27]:

– Characteristics of inverters under fault conditions may not be consistent with the existing protection devices;
– Throughout the whole microgrid, there may be different inverters with different characteristics;
– Even in the case of an individual inverter, its basic characteristics may differ depending on its design or application;
– There may be difficulties in characterising inverter behaviour for short-circuit studies, since this depends on the control strategy;

EBSCOhost - printed on 2/14/2023 2:46 PM via . All use subject to https://www.ebsco.com/terms-of-use

– There may be a significantly reduced fault current level when the change is made from a grid-connected to an islanded mode of operation.

The last point in particularly is a key issue and has been the subject of much research in recent years. The characteristics of most protective devices used in microgrids are usually similar to those used in distribution networks [3] and the protection of traditional distribution networks are based on large fault currents. However, under islanded-operation, the utility grid cannot contribute to the fault and, therefore, its magnitude is limited to what the microsources can provide. Consequently, traditional overcurrent protection schemes may no longer be applicable due to the current limitations of most inverters [28, 29].

### *2.2.2. Microgrid islanding*

As stated previously, in the case of a fault in the main network, the microgrid should be disconnected rapidly and efficiently from the rest of the grid, leading to an islanded or stand-alone form of operation in order to protect the loads connected to the microgrid. This disconnection presents two major issues for guaranteeing stable operation of the microgrid [3]:

– How to determine the exact moment at which the microgrid has to be disconnected from the grid;
– How to sectionalise the microgrid and adequately coordinate protection devices throughout the microgrid.

During islanded operation of the microgrid, it is also important that the earthing system is properly studied and arranged [22], especially in LV systems for single-phase earth faults. As a starting point, the protection guidelines for a microgrid state that the microgrid should be disconnected from the main grid only by opening the circuit breaker upstream of the MV/LV transformer, having therefore a source earth present for any event that may happen in the microgrid [30].

In this regard, and considering the results of several simulation studies that have been conducted in grid-connected and islanded operation, the main conclusion seems to be that a TN system with a multi-grounded neutral is the most suitable option [20, 30-33]. Not only would it be a preferable option from a safety perspective (reduced touch and step voltages; smaller transient ground potential rise in the event of lightning

EBSCOhost - printed on 2/14/2023 2:46 PM via . All use subject to https://www.ebsco.com/terms-of-use

strike), but it can also be operated with simple overcurrent devices due to its higher fault current levels.

Notwithstanding this, the choice of a TN earthing system may pose several problems:

- TT is the most common system found in LV installations [30];
- The change of fault current levels from grid-connected to islanded operation is more radical in TN systems [30];
- Faults at a higher voltage level (MV) may more easily migrate into the LV grid [20] in TN systems;
- Because of the variety of microsources and energy storage devices, their installation sites may be so dispersed that it would be very difficult or expensive to apply a TN system. Some authors recommend the use of a combined earthing mode using TN and TT—TN for electrical equipment in buildings and TT for DG or distributed electrical equipment outside buildings [34].

#### *2.2.2. Protection coordination*

Another major problem that has to be dealt with in microgrid protection is that of selectivity [35], which requires that only the protection device closest to the fault is triggered [36]. If it takes too much time, a higher-level protection system will take over.

In a distribution system with the power flowing in one direction (without DG sources), this can be achieved by applying an adequate time grading to overcurrent relays. However, when DG sources are spread throughout the microgrid, this is no longer possible, since contributions to the fault may come from any direction. As such, one possible scenario is that a healthy feeder is disconnected by its own protection device because of its contribution to the fault in a neighbouring feeder [36]. At the same time, when the microgrid is connected to the distribution network, the contribution from the DG may reduce the fault current that flows through the protection system, therefore reducing its sensitivity [37].

## 3. Protection systems

### *3.1. General scope*

One of the main benefits of DG is the possibility of improving the reliability and continuity of an energy supply by making the autonomous operation of a part of the network possible, in an islanded or stand-alone

EBSCOhost - printed on 2/14/2023 2:46 PM via . All use subject to https://www.ebsco.com/terms-of-use

mode, during a power outage of the main grid. However, many challenges have yet to be addressed and many problems have to be solved before this possibility becomes real and practicable [38]. Over the last few decades, DG sources such as this have been forced to disconnect from the grid in the event of faults or significant disturbances appearing in the network [39]. For example, IEEE 929-1988 required the disconnection of the DG once it was islanded. The disconnection of these DG sources may lead to power quality reduction and stability problems.

As such, an increasing number of countries (e.g. Germany) are updating their regulations in order to ensure that DG sources supply adequate short circuit current. Also, in order to improve the reliability and stability of the system, fault-ride-through capability requirements for DG connected in high voltage (HV) and MV networks have been introduced. Similar guidelines are currently being considered for the LV level.

The main scope of this chapter is to provide an overview of the different solutions that have been proposed to address the most common issues related to microgrid protection, especially overcurrent protection problems derived from the connection of inverter-interfaced microsources, either in grid-connected mode or in islanding operation.

### *3.2. Voltage-based methodologies*

Voltage-based protection techniques make use of voltage measurements to protect microgrids under different fault scenarios.

Major work in this field was conducted by a research group at the University of Bath, led by H. Al-Nasseri and M. A. Redfern [40-44]. They explored a fast fault detection method for inverter-interfaced microgrids that was valid for different types of faults [42]. The authors proposed monitoring the microsource output voltages, using two steps to convert the measured signals from the abc operating frame to DC quantities in the dq frame. In order to differentiate between in-zone and out-of-zone faults, some thresholds are applied to the voltage drop, which have different values depending on the type of fault. This scheme is aimed at complementing traditional types of protection that respond to high current faults.

This methodology [41] was updated by replacing the thresholds used for zone discrimination with a communication link between the relays. This communication link allows a comparison of the mean average values sensed in the output voltages (DC dq frame) and, consequently, allows for the isolation of the appropriate zone in the event of a fault. Later [40], this technique was completed by developing a decision-making procedure for

EBSCOhost - printed on 2/14/2023 2:46 PM via . All use subject to https://www.ebsco.com/terms-of-use

the comparison of the average voltage values in each relay. Finally [43], the decision-making procedure was improved again by adding some weighting factors based on the impedances of the converters.

Using the harmonic content to improve the protection system in microgrids with inverter-interfaced microsources [44] was also proposed for ground faults. Firstly, the type of fault is identified by monitoring the variation of the fundamental frequency (50 Hz). Next, the voltage THD of the different feeder relays is analysed in order to determine the fault zone. At this point, the communication link between the relays will play an important role. Al-Nasseri and Redfearn considered that this approach could be used as a backup for the main protection devices.

In order to avoid the difficulty of the previous methods associated with detecting the oscillation waveform of the voltage variation, C. Hou and X. Hu [45] used a very similar approach (abc frame to DC dq frame), but, instead of using voltage magnitude, they proposed using its positive sequence only. Additionally, they concluded that due to the different processes that have to be implemented (positive sequence component extraction; dq reference frame transformation and filtering), the total detection time might eventually be affected.

T. Loix et al. [46] summarise the impact of different fault types in a microgrid on direct, inverse, and homopolar voltage components. The authors claim that a distinction among the three fault types can be made by considering the direct and inverse voltage components only, without using the homopolar information. They suggest that in this way a very efficient fault detection method based on properly transformed voltage measurements can be developed. Consequently, they propose a microgrid protection strategy based on voltage and current measurements of the fault.

However, they also highlight the importance of the inverter control scheme, which ultimately controls the magnitudes of the voltage components. This may result in different behaviour when compared to other control strategies. In this regard, M. Brucoli and T. C. Green [47] had shown previously how the control of an inverter can influence the response of an islanded microgrid in the event of a fault. After analysing two possible multi-loop controls of a stand-alone source inverter (dq0 coordinate and phase coordinates), the authors concluded that voltage sequence components offer a good approach for fault detection in an islanded microgrid under dq0-type control.

Finally, X-p. Wang et al. [48] has proposed a very similar approach that determines the fault occurrence and the faulted zone based on a voltage measurement in the busbar, and its subsequent transformation

EBSCOhost - printed on 2/14/2023 2:46 PM via . All use subject to https://www.ebsco.com/terms-of-use

from abc coordinates to dq coordinates. The authors also provide its hardware and software structure.

In general, the main problems that may be faced when dealing with these kinds of voltage-based methodologies are:

- Minor differences in voltage drop among the relays located at both ends of short lines lead to protection operation failures, due to a reduction in the voltage gradient [49];
- A relatively high calculation complexity when it comes to Park's transformation application [49];
- Problems in detection of high impedance faults (HIF) [50];
- Problems with the practical application of some of these methodologies, as well as with communication infrastructure, when a high number of DG units are present [51];
- Methods may be strongly dependent on the network architecture and on the definition of the "protection zone" of the relay associated with each generator [51];
- Reduced sensitivity when the microgrid is connected to the main grid.

Accordingly, voltage-based protection schemes are usually considered inadequate for primary microgrid protection.

### *3.3. Differential protection*

The main principle of differential protection relies on comparing currents (or other magnitudes, such as energy, frequency, etc.) at the ends of a specific zone, so that it operates when a predetermined threshold is exceeded.

H. Nikkhajoei and R. H. Lasseter [24] proposed a combined methodology for microgrid protection based on differential protection and the analysis of symmetrical components. Considering studies conducted over the AEP CERTS microgrid, similar to those previously, the authors use a network zoning approach. In this way, the relay dividing each zone uses differential protection to detect single line-to-ground (SLG) faults that occur in its up-stream zone; a zero-sequence current component analysis also has to be added in the event of a down-stream SLG fault. In the case of a line-to-line (LL) fault, the negative-sequence current is used by the relay to detect the fault. However, in order to be able to distinguish between faults and unbalanced operating conditions, the authors propose the application of several thresholds to the analysis of the current sequence components.

EBSCOhost - printed on 2/14/2023 2:46 PM via . All use subject to https://www.ebsco.com/terms-of-use

In the same year, H. H. Zeineldin et al. [52] addressed two main challenges of future microgrids: voltage/frequency control and protection. Besides designing a DG interface control strategy applicable to both grid-connected and islanded operation, they also proposed a protection scheme based on differential relays in order to achieve a good level of protection and coordination in both situations. By equipping each line with two current transformers (CT)—one at each end of the line—once a previously specified threshold has been exceeded, the differential relays are designed to operate in 50 ms, coordinated with the islanded detection algorithm. The authors consider faults in both islanded and grid-connected situations.

On the basis of some of the conclusions obtained through different simulations conducted over a realistically possible MV microgrid [53], S. Conti et al. [51] present different protection philosophies/schemes for three fault cases: phase-to-ground faults in isolated neutral micro-grids; three-phase faults in micro-grids with synchronous-based generators; and multi-phase faults in micro-grids with inverter-interfaced generators.

- In the first two fault cases, three protection schemes are presented. The first one is an adaptation of an off-line fault location procedure designed by the same author for distribution systems with DG [54], which is then part of an integrated protection scheme [55]. The second one is based on direct communication between neighbouring protections.
- The third relies on comparison of the current differential between two directional relays placed in each branch, considering both the amplitude and direction of the measured currents.

E. Sortomme et al. [50] proposed a protection scheme based on relays with a communication overlay, considering both radial and loop structures in the microgrid, and also addressing the problem of HIF. The authors proposed the creation of a differential relaying scheme by using commonly used relays at the end of each line segment. In the event of a communication failure in one of the relays, there would be a backup protection system, so that the relays would rely on comparative voltage protection until the system was restored. It is also possible to reduce the cost that such a system would require, by installing only sensor units at the buses with a communication link to the substation, where a central controller can apply the same protection scheme. Some years later, in order to reduce the number of relays minimising customer outages, the authors improved their methodology developing a relay and sensor placement optimisation algorithm based on genetic algorithms [56].

EBSCOhost - printed on 2/14/2023 2:46 PM via . All use subject to https://www.ebsco.com/terms-of-use

Inspired by the previous methodology, A. Prasai et al. [57] provided a PLC communication-based methodology aimed at meshed microgrids, whose protection is substantially different to radially configured ones. Besides analysing the differential protection in all the elements involved in the microgrid (loads, buses, sources, etc.), in order to protect lines from both low and high impedance faults of all types (SLG, LL, LLG, …), the authors proposed three different levels of protection:

- Primary protection: differential current protection (in magnitude and direction) with a fully operational communication in every line.
- Secondary protection: in the event of communication loss in a specific line before or during a fault, this line is immediately tripped.
- Tertiary backup/protection: if both primary and secondary protection systems fail to isolate the fault, after a specified length of time has passed, then all the lines that are experiencing high current due to the fault will trip.

Based on communication methods, X. Li et al. [49] compared, through simulation (on a Real Time Digital Simulator), the performance of two of the most common solutions in this field when the microgrid is operating in an islanded mode: coordinated differential relays and the previously mentioned abc-dq transformed voltage measurements. They concluded that differential-based methods are more accurate, but have a higher cost. At the same time, after reviewing some commonly proposed methodologies for microgrid protection, J.Wei et al. [58] stated that the differential current protection scheme is possibly the most effective solution for both network and microgrid protection.

Similarly to [57], M. Dewadasa et al. [59] proposed a new differential approach to improve protection in meshed inverter-interfaced microgrids, as well as in those with a radial configuration. They did not solely focus on feeder protection, but also offered solutions to protect other subgroups (buses, DG sources, etc.). With regard to feeder primary protection, apart from considering three-phase current elements for each phase, they also added a further two elements for negative and zero-sequence currents. Whereas the phase differential elements provide protection against high-current faults, the negative and zero-sequence currents aim to protect against lower-current unbalanced faults. In the event of failure of the primary protection's communication system, they proposed a backup scheme based on an overcurrent and undervoltage approach [60, 61].

EBSCOhost - printed on 2/14/2023 2:46 PM via . All use subject to https://www.ebsco.com/terms-of-use

M. P. Nthontho et al. [62] discussed the use of a differential current protection scheme in a photovoltaic-based meshed microgrid. In order to avoid the uncertainty in the relay settings as a consequence of frequent DG connection and disconnection, the authors proposed using a knowledge-based differential current protection. By having IEDs and digital differential relays throughout the network, the IEDs would implement grid control algorithms on programmable logic circuits and send communication-based control actions to digital relays. The authors also proposed the use of wireless network technology for wide-area differential current protection of meshed microgrids [63].

Another approach to differential protection for microgrids is presented by S. R. Samantaray et al. [64, 65]. The authors proposed a differential energy-based protection scheme, which is supposed to be less sensitive to synchronisation errors than time-domain data (differential currents). In their method fault currents are measured at both ends of a line and processed through a modified Stockwell transform (S-transform) to obtain the spectral energy content, the difference of which is the key indicator of fault patterns in the microgrid according to a set threshold.

Similarly, A. Gururani et al. [66] presented a time-frequency-based differential energy-based protection scheme for non-stationary analysis. In order to overcome the limitation of other methodologies, they use the Hilbert-Huang transform to process the information, comparing the results with those obtained using the S-transform. Different thresholds are applied for grid-connected mode, islanded mode, and HIF, which have to be studied for each system configuration.

Differential current-based methodologies are one of the most commonly treated approaches for microgrid protection. One of the main benefits of these differential protection approaches is that they are not affected by the bidirectional power flow and the reduced fault current level of islanded microgrids. However, as with other techniques, they also have some problems or difficulties that may appear and that the abovementioned methodologies try to overcome in some way. In this regard it is worth mentioning:

- The need for communication infrastructure that may fail at some point, leaving the microgrid unprotected. For this reason, some authors provide different levels of backup protection;
- The need for synchronised measurements;
- Problems due to transients when connecting and disconnecting DG sources;
- Problems due to unbalanced systems or loads;

EBSCOhost - printed on 2/14/2023 2:46 PM via . All use subject to https://www.ebsco.com/terms-of-use

– Relatively high cost.

### *3.4. Distance protection*

Considering that the impedance of a line is proportional to its length, distance protection systems are based on measuring the impedance between the impedance relay and the selected reach point. They are designed to operate only for faults occurring between the relay location and the selected reach point.

The main methodology that uses this approach is based on research conducted by M. Dewadasa et al. [61, 67-73]. Here the authors firstly analysed [67] the suitability of applying distance relays with mho characteristics to protect microgrids during faults, in both grid-connected and islanded operational modes. Their results demonstrated that this kind of scheme may cause unacceptable operations when no directional feature is added to the distance protection. Building on this previous study, the authors proposed a new admittance relay with inverse time tripping characteristics (ITA), capable of detecting faults in both grid-connected and islanded microgrids [68, 69]. Besides adding inverse time characteristics to each zone of protection, it also has the ability to isolate the faults occurring at either side of it, since it can also operate for reverse faults. However, the reach settings should be different for forward and reverse faults.

In order to be able to operate under fault resistances different to zero, the authors proposed adding an extra relay characteristic zone, the settings of which depend on the maximum equivalent admittance of loads under normal operation. This is because this method will not work for high resistive faults, where fault currents may have comparable magnitudes to load currents. Whereas this proposal was firstly evaluated for a simple radial distribution network for permanent resistive faults, its study was extended to the detection of arc faults, to more complicated radial distribution networks (IEEE 34 node test feeder) [71], and to meshed networks [72].

P. Sankarakumar et al. [74] have also considered differential or distance protection to be an appropriate approach in microgrid protection, due to low fault current levels. H. Lin et al. [75, 76] used a mho-based distance protection system for a MV microgrid in Denmark, using three zones of protection and taking into account the infeed current effect. The authors also proposed using this approach to change the setting groups of the relays when the microgrid topology is reconfigured.

EBSCOhost - printed on 2/14/2023 2:46 PM via . All use subject to https://www.ebsco.com/terms-of-use

The main problems and challenges when it comes to the accurate performance of distance relays are listed below [72, 73, 77]:

- Limited fault resistance that can be reliably detected;
- Errors in the measured admittance because of fault resistance;
- Increased tripping time because of the down-stream source in-feed;
- Loss of accuracy due to problems in fundamental extraction, caused by harmonics, current transients, decaying DC magnitude, and time constant.

### *3.5. Overcurrent protection and symmetrical components*

A number of proposals have sought to enhance the performance of traditional overcurrent protection, sometimes resorting to measurement and calculations with symmetrical components.

H. Nikkhajoei and R.H. Lasseter [25] presented a possible solution for fault detection in islanded microgrids based on the measurement of symmetrical components of the currents. To be precise, they proposed the use of zero-sequence current detection for SLG faults (coordinated with unbalanced loads) and negative sequence current for LL faults.

B. Li et al. [78] briefly described a novel pilot instantaneous overcurrent protection scheme, based on two routines, which can perform instantaneous protection for local line and remote busbar regardless of the DGs location. R. J. Best et al. [21] proposed a communication assisted protection selectivity strategy with three structural levels to be applied in order with voltage-restrained directional overcurrent protections:

- Level 1 provides fault detection and protection based on local voltage and current measurements.
- Level 2 involves a transfer of minimal data (trip signals, blocking signals, etc.) between relays immediately upstream and downstream from one another.
- Level 3 adapts relay settings by communicating with a supervisory controller.

Continuing their previous work on coordinating protection devices in conventional distribution networks [79], Zamani et al. proposed a strategy to protect LV microgrids based on microprocessor-based overcurrent relays and directional elements [80]. Adequate for both modes of operation (grid-connected and islanded), it does not require communications and is independent of the fault current magnitude. They also presented the

EBSCOhost - printed on 2/14/2023 2:46 PM via . All use subject to https://www.ebsco.com/terms-of-use

concept and structure of a new relay that allows for this strategy. In the case of the islanded mode of operation, the authors proposed the replacement of some protective devices and the use of overcurrent devices for fault detection, with the help of measurements of zero- and negative-sequence components of the currents, along with some old methodologies for HIF detection [81]. In order to achieve proper coordination, they suggested the use of a definite time grading technique with a directional characteristic. Additionally, when a microgrid is grid-connected, conventional overcurrent protection can still be employed. In general, the proposed protection strategy enables single-phase tripping in order to increase security of supply.

M. R. Miveh et al. [82] also considered the use of symmetrical components for all kinds of fault location (asymmetrical and symmetrical) in microgrids, along with a communication channel with a narrow bandwidth (solely to exchange information on status, not electrical measurements). By installing digital relays between two terminals in the same line, negative- and positive- sequence measurements of currents and voltages can be used in order to detect faults, with different settings in their forward and reverse regions.

L. M. Pintos et al. [83], building on previous work on current-only directional overcurrent relays [84, 85], proposed a protection system that identifies the direction of faults in microgrids without the need for a voltage reference. They used recursive phasor estimation with a sliding window based on the discrete Fourier transform (DFT), implementing directional overcurrent protection with only current measurements and using protection relays at both ends of the same line.

H. H. Zeineldin et al. [86] initially presented a protection coordination scheme for meshed distribution systems with DG, using dual setting relays and trying to minimise the overall time of operation of the relays during primary and backup operation. However, a significant problem with this application is found during operation in backup protection, where communication failures may occur. In order to improve the methodology for microgrids, the same authors [87] proposed a communication assisted dual setting relay, using low bandwidth communication for backup operation.

It needs to be noted that the main problem with these kinds of protection system is usually related to the necessity of an extensive deployment of communication systems. In such cases, in the event of communication system failure, overcurrent protection and coordination may be jeopardised.

EBSCOhost - printed on 2/14/2023 2:46 PM via . All use subject to https://www.ebsco.com/terms-of-use

### *3.6. Adaptive protection systems*

One interesting possibility in solving the main problems associated with fault protection in microgrids (low-current fault detection and protection coordination under network reconfigurations [88]) may be found in the application of an adaptive solution. This is defined in [89] as follows:

- Adaptive Protection: an on-line activity that modifies the preferred protective response to a change in system conditions or requirements. It is usually automatic, but can include timely human intervention.
- Adaptive Relay: a relay that can have its settings, characteristics, or logic functions changed on-line in a timely manner by means of externally generated signals or control action.

However, these kinds of solutions require a cost-efficient technological update in the protection devices to be installed in the microgrid [13, 20], namely:

- Use of numerical relays (Intelligent Electronic Devices, IEDs) instead of other kinds of protection that do not allow their settings to be changed (e.g. fuses), although overcurrent protection devices with directional sensitivity may be enough in some cases;
- These IEDs should be able to work with different settings or tripping characteristics, which can be locally or remotely changed;
- A communication infrastructure among the IEDs should exist, in any accepted protocol (Modbus, IEC 61850, etc.), so that they can share and exchange information, either in a centralised or decentralised system.

One of the first papers that proposed the application of adaptive protection techniques in microgrids was written by R. M. Tumilty et al. [88]. After analysing the use of voltage drop methodologies in order to detect faults in islanded microgrids, the authors described the possibility of adaptively applying one of these methodologies to adjust the settings in overcurrent protections. They proposed using the differential voltage drop response that would appear in short circuits and overloads, taking into account its magnitude, so as to clearly differentiate these two events and, accordingly, move the time-current characteristic of the protection without the need for communication.

EBSCOhost - printed on 2/14/2023 2:46 PM via . All use subject to https://www.ebsco.com/terms-of-use

Some years later, Oudalov and Fidigatti [13] presented a protection system using digital relaying and advanced communications based on a central architecture. Although in this system each circuit breaker (CB) takes its own tripping decision using directional overcurrent protection, this adaptive protection system is aimed at maintaining the settings of each relay, which are updated with regard to the current state of the microgrid. This is achieved in two main steps:

- Off-line analysis, where all possible scenarios are simulated (registering the situation of each CB) and the fault currents passing each CB are estimated (this may be applied to every kind of fault). After processing, the most suitable settings for each CB and situation are calculated. All this information is finally saved in a specific data structure.
- On-line operation, where the microgrid central controller (MCC) is periodically checking or triggered by an event (tripping of a CB, alarm, etc.) so as to identify a new situation that may have occurred. Once this new situation is identified with a registered entry in the structure table, it uploads the new settings to each CB.

N. Schaefer et al. [20, 39] proposed an adaptive protection system for distribution networks with DER. The authors described an algorithm for the adaptive protection relay, which comprises:

- A real-time block, responsible for analysing the actual state of the grid and based mainly on modules of conventional protection techniques.
- A non-real-time block, which uses predictive data on the availability of DG, in order to review existing tripping characteristics, provided that the boundary conditions are not broken with the operation predicted by the decentralised energy management system (DEMS).

Another adaptive method for microgrids dominated by inverter-based distributed generators was presented by Y. Han et al. [90, 91]. Using the fault component method, the authors proposed obtaining the impedance of the system by calculating the voltage and current fault components. By comparing the system's impedance and the microgrid's impedance instantaneous overcurrent protections can be automatically adjusted to new situations.

K. Dang et al. [23] proposed an adaptive methodology to solve the earth-fault protection problems that so frequently occur in microgrids. To

EBSCOhost - printed on 2/14/2023 2:46 PM via . All use subject to https://www.ebsco.com/terms-of-use

this end they used a procedure comparing the zero-sequence current and a threshold. K-H. Zheng and M-C. Xia [37] and M. Khederzadeh [92] have supported the idea of using adaptive protection systems for microgrid protection. The latter provides an algorithm to coordinate different relays over a specific microgrid, although it is difficult to generalise its procedure for any other microgrid configuration.

T. S. Ustun et al. [93-95] presented an adaptive protection system based on an extensive communication system that monitors the microgrid by means of a central protection unit (CPU). This CPU, using extensive communication with every single relay and DG in the microgrid, along with a data map that stores the relevant control variables of each component, can respond to dynamic changes in the system (such as connection/disconnection of DG). In their methodology, two elements are essential to adequate protection:

- Firstly, in defining protective thresholds it is important to appropriately calculate the fault impact factor of every DG resource on the fault current seen by any relay [96, 97].
- Secondly, considering the importance of the communication systems in their approach, the authors analysed the use of advanced communication systems according to IEC 61850, as well as the extension IEC 61850-7-420 [98-101].

In order to preserve dynamic security in microgrids, S. Teimourzadeh et al. [102] presented a three-stage adaptive protection approach:

- Stage 1 consists of offline analyses to devise the dynamic security models of microgrids (including synchronous generator-based and inverter-based DER). The required data and settings are also determined at this stage.
- Stage 2 uses these models and the online microgrid data to calculate equilibrium points, regions of attraction and protection zones for DER operations.
- Stage 3 monitors the microgrid variables in real time, in order to decide if the protection zone boundary has been violated.

As a result of the different proposals, it can be concluded that the main problems with regard to the possible implementation of an adaptive protection system may be:

EBSCOhost - printed on 2/14/2023 2:46 PM via . All use subject to https://www.ebsco.com/terms-of-use

- The need for prior knowledge of all possible microgrid configurations;
- The requirement of running extensive power flows or short circuit calculations when a topology change is detected;
- The need for communication infrastructure may be high;
- The necessity of updating or upgrading many protection devices (fuses, etc.) that are currently used in existing power systems.

### *3.7. Use of external devices to ensure high protection performance*

In situations when fault current levels drastically differ between grid-connected and islanded operation (typically with inverter-interfaced DG), the design of an adequate protection system, which performs properly in both situations, can be a real challenge. In the case of overcurrent relays or residual current devices (RCD), the most frequent approach is to try to adapt their settings (adaptive systems, etc.) to the new fault current level, as soon as the microgrid changes its operation state.

In this regard, it may be possible to apply a different approach that actively modifies the fault current level when the microgrid changes from grid-connected to islanded operation and vice versa, by means of certain externally installed devices. These devices can either increase or decrease the fault level. The main options are as follows:

- By reducing the aggregated contribution of many DG sources, which can alter the fault current level sufficiently to exceed the design limit of various equipment components [20], as well as to guarantee adequate coordination despite the feeding effect of DG to fault current, fault current limiters (FCL) can be used [103]. This effect is particularly evident with synchronous machine-based DG.
- By equalising the fault current level in both grid-connected and islanded operation, due to the reduced fault contribution by inverter-interfaced DG sources. This can be achieved in two different ways:
  1) By incorporating energy storage devices (flywheels, batteries, etc.) into the microgrid in order to increase the fault current to a desired level [104], allowing overcurrent protection to operate in a traditional way [49]. In low voltage circuits, clearing faults with overcurrent devices would require an available fault current of at least three times the maximum load current of the circuit [5, 105];

EBSCOhost - printed on 2/14/2023 2:46 PM via . All use subject to https://www.ebsco.com/terms-of-use

2) By installing certain devices between the main grid and the microgrid, to alleviate the contribution of fault current from the utility grid and preserve the integrity of the overcurrent relays' settings in both operation modes [106].

However, the main problems associated with the use of these types of devices embedded in the microgrid are as follows:

- Storage devices require large investment and need to match the main grid's short circuit level so as to guarantee that faults are cleared in a timely manner [107];
- The application of schemes based on FCL technology is only possible up to a certain number of connected DGs. For very high levels of DGs, it can be difficult to determine the impedance value of the FCL due to the mutual influence of the DG [103];
- Sources with high short circuit capability (flywheels, etc.) require significant investment and their safe operation depends on correct maintenance of the unit [46];
- Methods based on an additional current source are highly dependent on the technology of islanding detection and the correct operation of the current source [49].

### *3.7.1. Fault current limiters*

A. Oudalov et al. [20] analysed the existing technologies in fault current limitation and highlighted the most important requirements for an ideal FCL in microgrids. Additionally, they provided details of two promising current limiting methods—one of them already available ($I_s$-limiter) and the other one under development (liquid metal FCL).

U. A. Khan et al. [108] analysed the results of positioning a superconducting FCL (SFCL) in a microgrid and its impact on fault current reduction. The authors considered two different kinds of microgrids (an AC MV microgrid with a wind farm and a DC LV microgrid with a photovoltaic farm) connected to a conventional power system, with different arrangements for the SFCL placement. The authors concluded that the SFCL should not be installed directly at the substation or branch networks, since higher fault current reduction is achieved when the SFCL is located at the point of connection to the DG.

Y. Zhang and A. Dougal [109] provided an overview of different FCL technologies at or near field test status. According to their capabilities and characteristics, the authors assigned each type to its most appropriate

EBSCOhost - printed on 2/14/2023 2:46 PM via . All use subject to https://www.ebsco.com/terms-of-use

location: at microgrid site (solid-state FCL—SSFCL); at DG source site (SSFCL); at distribution network (resistive or saturated iron-core superconducting FCL—SFCL, and dynamic FCL—DFCL); or in the transmission network (resistive or saturated iron-core superconducting FCL).

### *3.7.2. Energy storage devices*

Although N. Jayawarna et al. [30, 110] initially focussed their attention on microgrid grounding systems and their behaviour during fault situations, they also proposed the use of a flywheel energy storage system to increase the fault current level in an islanded microgrid as the use of one central device that supplies fault current would be less expensive than overrating all the converters in the microgrid. Continuing this line of research, some of these authors have provided more details about such a storage system, showing how it should be implemented and controlled in order to act as the main fault current source in the islanded mode of operation [105, 111, 112]. The objective of this control system is to encompass the four operating modes of the microgrid: two steady states of operation (grid-connected and islanded) and two transient modes of operation (islanding and resynchronising).

F. van Overbeeke [113] described an alternative to the use of flywheel storage systems so as to provide the required fault current when required. Since the flywheel's inverter should sustain a factor 3 overload for several seconds, potentially posing a problem when trying to purchase it on the open market, the author describes a new network component specifically intended to provide an additional fault level to an islanded microgrid: fault current source (FCS). This system consists of four subsystems (electricity storage device, power electronic converter, triggering circuit and charging module)—a prototype was built in order to demonstrate its concept and properties in a practical configuration.

### *3.7.3. Other devices*

One of the first proposals considering the application of a current limitation approach to microgrids was presented by D. M. Vilathgamuwa et al. [114]. Although the intention was different (to protect the microgrid against the large line currents that can flow along the interconnection distribution feeder during utility voltage sags), the authors proposed using a voltage-source inverter between the microgrid and the utility grid, along with two current-limiting algorithms. These algorithms work as a virtual

EBSCOhost - printed on 2/14/2023 2:46 PM via . All use subject to https://www.ebsco.com/terms-of-use

RL or L impedance in series with the distribution feeder in order to limit current flow during utility voltage sags.

R. M. Kamel et al. [32] recommended the installation of some kind of current limiter in series with the main grid, when the microgrid is operated in grid-connected mode, in order to reduce touch voltages at the faulted bus and to reduce the rating of overcurrent protection devices.

M. Khederzadeh has addressed the protection problem of a variable fault current in microgrids by trying to reduce the main grid's contribution to the fault [106]. The author proposed the use of a static series compensator (SSC) in the PCC in order to preserve the integrity of the overcurrent relays' settings in both operation modes: grid-connected and islanded. Increasing the line impedance during the faults, it would perform as a FCL alleviating the contribution to the fault current by the utility grid. In fact, it could be used with two distinct applications:

- As a capacitive compensator, decreasing the line impedance to increase the power flow.
- As an inductive compensator, increasing the line impedance to decrease the fault current level.

## *3.8. Other techniques*

Apart from the methodologies described in the previous sections, there are also other approaches that have been less frequently proposed. These have been divided into three groups.

### *3.8.1. High frequency treatment or transient information*

The proposals in this field are mainly based on wavelet transforms (WT)—using different wavelet functions applied to high frequency measurements or travelling waves. WT decomposes a function using basis functions that, unlike the Fourier transform, have finite extent in both frequency and time.

S. Shi et al. [115] proposed an algorithm for microgrids that identifies a disturbance as a fault or a switch operation, in order to subsequently identify the faulted zone. The proposed scheme uses the busbar voltages to determine the existence of the fault and wavelet treatment of the current travelling waves to identify the faulty feeder. To be precise, they use a derivative of the cubic B-spline function as the mother wavelet and four level wavelet transforms are processed. The authors claim that this

EBSCOhost - printed on 2/14/2023 2:46 PM via . All use subject to https://www.ebsco.com/terms-of-use

protection system is independent of grid-connected or stand-alone operation of the microgrid.

In the same year, H. Yi et al. [116] introduced the use of wavelet analysis into the filter algorithm in microgrid protection systems, in which the Fourier algorithm is currently the most widely used. Since the latter has unsatisfactory filtering effects when it comes to non-integer harmonics or non-stationary signals, the authors proposed the use of an improved recursive wavelet method based on the Chaari complex wavelet as a filter algorithm. Aimed at analysing the fault characteristics of a microgrid dominated by an inverter-interfaced DG in islanding mode, the authors claimed that this methodology could effectively filter the decaying DC and non-integer harmonics. Apparently, this algorithm may also be able to offer more information in fault detection.

S. A. Saleh et al. [117] also highlighted the advantages of using a wavelet approach instead of Fourier analysis for non-periodic and non-stationary disturbances. They proposed using a novel method for detecting and classifying transient disturbances into faults and non-faults in microgrid systems. Based on extracting the high-frequency components of the current present in the dq axis, the signatures of the wavelet packet transform (WPT) coefficients in the high-frequency sub-band are evaluated. They have achieved good results in differentiating fault transients (single-phase and three-phase faults) from non-fault ones (grid connection and step changes in wind speed).

### *3.8.2. Use of artificial intelligence*

Artificial intelligence (AI) is a collection of techniques modelled on the thought and behaviour of human beings and animals. AI systems help to take rational decisions, much like a human expert, by including missing data, considering evolving situations, and extrapolating from experience accumulated over long time horizons.

Within this group, the particle swarm optimisation (PSO) algorithm is a heuristic technique aimed at solving constrained optimisation problems. Initialised with a population of random solutions, it was originally developed based on observation of the social behavior of animals.

H. H. Zeineldin et al. [118, 119] proposed a heuristic methodology in order to solve the directional overcurrent relay coordination problem in microgrids when changing from grid-connected operation to islanded operation. The authors used mixed integer nonlinear programming (MINP) to formulate the problem, which was subsequently solved using the PSO algorithm. The position of the particles in the PSO algorithm is updated

EBSCOhost - printed on 2/14/2023 2:46 PM via . All use subject to https://www.ebsco.com/terms-of-use

according to feasibility, fitness value, and an acceptance ratio. However, they only considered two possible operating situations (grid-connected and stand-alone), obtaining two possible settings for each relay (in each case, both pickup current and time dial setting), but topology changes were not analysed. Moreover, only synchronous machines were analysed as DG and, in the case of stand-alone operation, non-critical loads were expected to be disconnected. Some years later, a modified protection scheme based on [118] was presented by H. Qu et al. [120]. The authors claimed that the strength of their algorithm was its reliance on two main stages: a particle's position initialisation and a particle's position and velocity update. Y. Damchi et al. [121] used a hybrid algorithm based on modified PSO and linear programming to coordinate directional overcurrent relays. In the last two cases [120, 121], the network used to simulate the case study and to obtain results had almost the same layout as [118].

While having a totally different objective to previous work with PSO, W. Prommee et al. [122] proposed the use of improved binary PSO (IBPSO) to understand the optimal placement and number of protective devices (switches, reclosers and fuses) in microgrids, in order to minimise reliability indexes (SAIDI, SAIFI) and total cost. After analysing five different scenarios over a specific network, the authors concluded that IBPSO results were a better research direction than binary PSO and ant colony optimisation (ACO). H. S. Pandya et al. [123] used PSO to develop a protection approach for parallel feeders with directional elements in a microgrid, in order to optimise the selection of the time setting multiplier (TSM) and plug setting multiplier (PSM). S. T. P. Srnivas et al. [124] presented a new approach for microgrid relay coordination based on a hybrid technique of interval linear programming (ILP) and modified PSO. In this case, grid connected and isolated modes were considered with different fault current scenarios.

Another approach for AI is data mining (DM), which is the process of discovering patterns by analysing large data sets to develop models that are used to predict and describe system outputs [125]. Models in predictive data mining can be used for classification, estimation, and prediction, etc., whereas those in descriptive data mining are used to discover patterns and relationships in large data sets. There are different methods for data mining, such as decision trees (DT) and random forests (RF), etc.

In 2007, G. Joós and K. El-Arroudi [126] presented three research projects based on DM technology that were being developed at that time at McGill University. The first two were related to islanding detection, but one of the main objectives of the third project was to develop an automated technique for protection coordination studies, including

EBSCOhost - printed on 2/14/2023 2:46 PM via . All use subject to https://www.ebsco.com/terms-of-use

selectivity and sensitivity analyses. E. Casagrande et al. [127] undertook a DM-based study to protect isolated inverter-based microgrids. Their study was mainly focused on the feature extraction-selection component, which is an important pre-processing stage in reducing the amount of data used as an input in a statistical classifier. The authors concluded that symmetrical components were among the best features for fault detection tasks. This conclusion led the authors to use DM in designing a differential protection scheme [128] that relied on symmetrical components, where the statistical classifier was implemented using the RF algorithm.

S. Kar et al. [129-131] also proposed the use of a DM-based differential intelligent protection scheme for microgrid protection, considering the high computational burden of applying the S-transform in their previous differential methodology [64, 65], which may result in a slower response time. Using the voltage and current information at both ends of each feeder and adjacent ones, several features (ROCOV, ROCOF, ROCPAD, etc.) are obtained through DFT pre-processing. This can be used to build a DM model based on a DT, which will provide information about the existence of a fault. These authors also proposed using a combination of the maximal overlapping discrete wavelet transform (DWT) and DT for HIF detection on microgrids [132]. D. P. Mishra et al. [125] presented a microgrid protection scheme that combined the use of DWT for feature extraction and DM models for decision making. The authors analysed the use of DT compared to RF and concluded that, despite their similar performance, DT had fewer implementation difficulties.

An important form of AI is the artificial neural network (ANN). This is a powerful problem-solving tool that emulates how biological nervous systems process information. It shows a remarkable ability to derive a solution from complicated or imprecise data related to real-world problems. The distributed, parallel, and adaptive processing of ANNs makes them an appropriate tool when it comes to dealing with massive, distorted, repetitive, and vague information. ANN techniques are relatively easy to implement and do not require any prior knowledge of the system model being studied.

One of the first to suggest using an ANN for microgrid protection purposes was S. Balantrapu [133]. The author stated that ANNs are suitable for designing an efficient microgrid protection scheme, because, amongst other reasons, they are perfect for pattern recognition problems (like distance protection) and for handling corrupt data. P. P. K. Chan et al. [134] compared and analysed the performance of four well-known classification methods applicable to fault detection in microgrids: radial

EBSCOhost - printed on 2/14/2023 2:46 PM via . All use subject to https://www.ebsco.com/terms-of-use

basis function neural networks (RBFNN); decision trees (DT), k nearest neighbours (KNN); and naïve Bayes (NB). These were compared in terms of their accuracy in noise and noise-free conditions.

Developing on their previous work for adaptive protection [75, 76], H. Lin et al. [135] proposed the use of two ANN models with real-time measurements to detect and locate faults in a microgrid. The fault location result of the ANN can be redundantly compared to the least squares estimation (LSE) results obtained from field recordings. J. J. Q. Yu et al. [136] used DWT and deep neural networks (DNN) to devise a fault detection scheme for microgrids. DWT was used as a pre-processing tool for branch current measurements and then a DNN (a special type of ANN with multiple hidden layers) was then used to obtain fault information (fault type, faulted phase, fault detection, and location).

Finally, fuzzy logic (FL) is a form of many-valued logic that uses human-like reasoning in its approach to ambiguous data (fuzzy data). The basic concept underlying FL is that of a linguistic variable—a variable whose values are words rather than numbers. FL is a rule-based approach where a set of rules are used to make a relevant decision. The first stage is fuzzification, followed by application of the rule base, and, finally, defuzzification.

A. H. Abdulwahid et al. presented three different applications of FL to microgrid protection. Firstly, they describe a combined use of fuzzy decision processes and Hilbert space-based power theory to improve differential protection performance, avoiding dependency on the selection of threshold values [137]. Secondly, they proposed the protection of busbars in microgrids using a fuzzy reasoning system along with Rogowski coil current sensors, so as to avoid the saturation that may appear in current transformers [138]. Finally, another protection approach for microgrids was described that was based on a combination of symmetrical components (criterion function and phase selection) and an adaptive neuro-fuzzy inference system (ANFIS) [139].

Similar to other techniques that they had proposed, O. V. Gnana Swathika et al. [140] used a central protection center (CPC) to identify faults in the microgrid, by means of FL and graph algorithms (including Boruvka's-aided Dijkstra algorithm). S. B. A. Bukhari et al. [141] proposed using an interval type-2 FL system (IT2FLS) to detect, classify, and locate faults in microgrids. The first FL subsystem (IT2FLS-1) was designed to detect and classify different types of faults using the fundamental components of current and voltage signals. The second FL subsystem (IT2FLS-2) used the phase relationship between superimposed modal voltages and currents to obtain the direction of faults. The outputs

EBSCOhost - printed on 2/14/2023 2:46 PM via . All use subject to https://www.ebsco.com/terms-of-use

of both subsystems were then processed to determine the faulted zone and to generate the trip signals.

### *3.8.2. Use of advanced mathematical methods and tools*

Dijkstra's algorithm is a graph search algorithm that is used to find the shortest path from an initial node to all the other nodes of a graph. It can be used in combination with Prim's algorithm (Prim's-aided Dijkstra), which identifies a minimum spanning tree for a connected weighted undirected graph. T. S. Ustun et al. [142] proposed the use of Dijkstra's algorithm in order to obtain the relay hierarchy of the network, regardless of changes in dynamic structure that this network may have undergone. Since this can be done automatically, it may be used in a plug-and-play fashion. Assisted by this, the selectivity of the protection system can be properly updated by changing the relay's settings according to their current position as determined by this algorithm. It may also help to detect the direction of fault currents and thus isolate the fault. The implementation of this system requires a communication system between the microgrid components, which can be set up by means of IEC 61850. O. V. Gnana Swathika et al. [143], incorporating a CPC, presented a Prim's-aided Dijkstra algorithm to identify the current topology of the network and the shortest route from the faulted point to the nearest operating source. The CPC is responsible for monitoring the feeder currents, as well as identifying the fault occurrence and the faulted feeder.

Mathematical morphology (MM) is a theory and technique used for the analysis and processing of geometrical structures based on set theory, lattice theory, topology, and random functions. It is based on the shape of a time-domain waveform [144]. X. Li et al. [145] presented a double-end protection strategy using the transient fault information (time and polarity features) included in the initial current travelling waves, based on two principles: modified MM technology and a backup solution based on the rate of change of the current. This method would be applicable in radial or meshed grids and the inherent problem associated with the fault inception angle has also been addressed. Some years later, these authors modified their technique [146] to improve its applicability in meshed networks and networks where single-ended measurements are used. This was done by the introduction of additional protection elements and by using the apparent features of erosion and dilation waveforms. T. Gush et al. [144] proposed the of use MM along with recursive least-squares methods to detect, classify, and locate faults in microgrids by using single-ended

EBSCOhost - printed on 2/14/2023 2:46 PM via . All use subject to https://www.ebsco.com/terms-of-use

current and voltage measurements, and considering both grid-connected and islanded modes of operation.

There are also a variety of different mathematical tools that may be used with the same purpose. G. Huo et al. [147] examined the concept of brittleness entropy of a complex system in microgrid protection. They proposed using the negentropy concept for faults in the main grid (system level protection) and the brittle link entropy concept for faults within the microgrid (unit level protection). M. Esreraig et al. [148] presented a new technique that used a state observer as a fault detector. Dividing the microgrid into different zones, three observers per phase were used in each zone (voltage measurement at the beginning and the end, along with current measurement at the end of the line) in order to detect the faulted zone and phase. This technique also distinguishes between fault and loading/contribution currents. The authors proposed two ways of accomplishing this distinction: using an observer's residual and using the current direction. J. Shi et al. [149] proposed using time-coloured Petri nets (T-CPN) for fault diagnosis in microgrids. A T-CPN gathers information (protection information, breaker information, and electrical components information) in corresponding database tables and divides the reasoning process into three different levels: transient fault diagnosis; removing redundant information; and delay fault diagnosis and alarm. M. Manohar et al. [150-152] presented a microgrid protection scheme based on a DWT pre-processor and a space vector machine (SVM) based ensemble classifier, in order to perform mode detection, fault detection/classification, and section identification and location.

## 4. Conclusions

Based on an analysis of the wide range of technical publications presented in the previous sections, the main conclusions and recommendations regarding the protection of microgrids can be summarised as follows:

- Although microgrid protection has raised increasing interest over recent years, there are still relatively few references that address the microgrid protection problem properly, let alone give enough information to fully understand and choose the best approach.
- Although the authors that are most closely related to protection manufacturing companies seem to favour adaptive protection systems, a general trend in this direction has not been observed.

EBSCOhost - printed on 2/14/2023 2:46 PM via . All use subject to https://www.ebsco.com/terms-of-use

- It seems to be clear that there is an increasing need to upgrade many protection devices (including fuses) currently used in power systems (mainly in LV systems), in order to facilitate the application of new and unconventional protection system solutions in microgrids.
- Regardless of the protection methodology, it seems that some kind of communication system is necessary—either centrally operated or distributed.
- In order to deal satisfactorily with the protection problems associated with bidirectional power flows, the need for a directional feature is clear. This would imply different settings for each fault direction and, in some cases, the use of different protective methods for each fault direction may be necessary.
- Many references divide the microgid into a number of smaller zones and subsequently apply the proposed methodology separately to each one of them—a divide-and-conquer-type approach.
- The number of references using artificial intelligence techniques in order to improve microgrid protection is not particularly high, especially those using ANNs.
- There are certain specific problems that have rarely been analysed in the cited references, such as high impedance faults and the protection of meshed networks.
- Similar to other research areas in power system protection, it is likely that, in order to develop an optimal protection system for microgrids, a combination of different protection techniques will be necessary.
- Communication infrastructure, monitoring technology, available measurements, and the availability of physical models may determine the best approach in each case.
- To support the acceleration of future deployment of practical microgrids, an effort should be made to develop international standards and engineering recommendations related to fault protection in typical microgrids.

## Acknowledgement

The authors gratefully acknowledge support from the Spanish Ministry of Economy, Industry and Competitiveness (project ENE2016-79145-R AEI/FEDER, UE), the Basque Government (GISEL research group IT1083-16), as well as from the University of the Basque Country UPV/EHU (research group funding PPG17/23).

EBSCOhost - printed on 2/14/2023 2:46 PM via . All use subject to https://www.ebsco.com/terms-of-use

## References

[1] D. Ming, Z. Yingyuan, and M. Meiqin, "Key technologies for microgrids-a review", in *Sustainable Power Generation and Supply, 2009. SUPERGEN '09. International Conference on*, 2009, pp. 1-5.
[2] Z. Bo. (2011) The challenge of protecting microgrids. *Alstom Grid*.
[3] S. Chowdhury, S. P. Chowdhury, and P. Crossley, *Microgrids and Active Distribution Networks*: Institution of Engineering and Technology, 2009.
[4] T. S. Ustun, C. Ozansoy, and A. Zayegh, "Recent developments in microgrids and example cases around the world—A review", *Renewable and Sustainable Energy Reviews,* vol. 15, pp. 4030-4041, 2011.
[5] W. E. Feero, D. C. Dawson, and J. Stevens, "White paper on protection issues of the microgrid concept", 2002.
[6] J. Driesen and F. Katiraei, "Design for distributed energy resources", *Power and Energy Magazine, IEEE,* vol. 6, pp. 30-40, 2008.
[7] M. Agrawal and A. Mittal, "Micro grid technological activities across the globe: a review", *International Journal of Research and Reviews in Applied Sciences,* vol. 7, pp. 147-152, 2011.
[8] M. Barnes, J. Kondoh, H. Asano, J. Oyarzabal, G. Ventakaramanan, R. Lasseter, N. Hatziargyriou, and T. Green, "Real-World MicroGrids-An Overview", in *System of Systems Engineering, 2007. SoSE '07. IEEE International Conference on*, 2007, pp. 1-8.
[9] T. E. Del Carpio Huayllas, D. S. Ramos, and R. L. Vasquez-Arnez, "Microgrid systems: Current status and challenges", in *Transmission and Distribution Conference and Exposition: Latin America (T&D-LA), 2010 IEEE/PES*, 2010, pp. 7-12.
[10] P. Ji, X. Zhou Xiao, and S. Wu, "Review on sustainable development of island microgrid", in *Advanced Power System Automation and Protection (APAP), 2011 International Conference on*, 2011, pp. 1806-1813.
[11] N. W. A. Lidula and A. D. Rajapakse, "Microgrids research: A review of experimental microgrids and test systems", *Renewable and Sustainable Energy Reviews,* vol. 15, pp. 186-202, 2011.
[12] I. Mitra, T. Degner, and M. Braun, "Distributed Generation and Microgrids for Small Island Electrification in Developing Countries: A Review", *Solar Energy Society of India (SESI) Journal,* vol. 18, pp. 6-20, 2008.
[13] A. Oudalov and A. Fidigatti, "Adaptive Network Protection in Microgrids", *International Journal of Distributed Energy Resources,* vol. 5, pp. 201-225, 2009.
[14] IEEE, "IEEE Recommended Practice for Interconnecting Distributed Resources with Electric Power Systems Distribution Secondary Networks", in *IEEE Std 1547.6-2011*, ed, 2011, pp. 1-38.
[15] IEEE, "IEEE Guide for Design, Operation, and Integration of Distributed Resource Island Systems with Electric Power Systems", in *IEEE Std 1547.4-2011*, ed, 2011, pp. 1-54.

EBSCOhost - printed on 2/14/2023 2:46 PM via . All use subject to https://www.ebsco.com/terms-of-use

[16] IEEE, "IEEE Application Guide for IEEE Std 1547, IEEE Standard for Interconnecting Distributed Resources with Electric Power Systems", in *IEEE Std 1547.2-2008*, ed, 2009, pp. 1-207.
[17] IEEE, "IEEE Guide for Monitoring, Information Exchange, and Control of Distributed Resources Interconnected With Electric Power Systems", in *IEEE Std 1547.3-2007*, ed, 2007, pp. 1-158.
[18] IEEE, "IEEE Standard Conformance Test Procedures for Equipment Interconnecting Distributed Resources With Electric Power Systems", in *IEEE Std 1547.1-2005*, ed, 2005, pp. 0_1-54.
[19] B. Kroposki, T. Basso, and R. DeBlasio, "Microgrid standards and technologies", in *Power and Energy Society General Meeting - Conversion and Delivery of Electrical Energy in the 21st Century, 2008 IEEE*, 2008, pp. 1-4.
[20] A. Oudalov, A. Fidigatti, T. Degner, B. Valov, C. Hardt, J. M. Yarza, R. Li, N. Jenkins, B. Awad, F. v. Overbeeke, N. Hatziargyriou, and M. Lorentzou, "Novel Protection Systems for Microgrids", 2009.
[21] R. J. Best, D. J. Morrow, and P. A. Crossley, "Communication assisted protection selectivity for reconfigurable and islanded power networks", in *Universities Power Engineering Conference (UPEC), 2009 Proceedings of the 44th International*, 2009, pp. 1-5.
[22] H. J. Laaksonen, "Protection Principles for Future Microgrids", *Power Electronics, IEEE Transactions on,* vol. 25, pp. 2910-2918, 2010.
[23] D. Ke, H. Xin, B. Daqiang, and F. Cunliang, "An adaptive protection method for the inverter dominated microgrid", in *Electrical Machines and Systems (ICEMS), 2011 International Conference on*, 2011, pp. 1-5.
[24] H. Nikkhajoei and R. H. Lasseter, "Microgrid fault protection based on symmetrical and differential current components", 2006.
[25] H. Nikkhajoei and R. H. Lasseter, "Microgrid Protection", in *Power Engineering Society General Meeting, 2007. IEEE*, 2007, pp. 1-6.
[26] R. H. Lasseter and P. Piagi, "Control and Design of Microgrid Components", 2006.
[27] C. A. Plet, M. Graovac, T. C. Green, and R. Iravani, "Fault response of grid-connected inverter dominated networks", in *Power and Energy Society General Meeting, 2010 IEEE*, 2010, pp. 1-8.
[28] M. Brucoli, T. C. Green, and J. D. F. McDonald, "Modelling and Analysis of Fault Behaviour of Inverter Microgrids to Aid Future Fault Detection", in *System of Systems Engineering, 2007. SoSE '07. IEEE International Conference on*, 2007, pp. 1-6.
[29] E. Sortomme, G. J. Mapes, B. A. Foster, and S. S. Venkata, "Fault analysis and protection of a microgrid", in *Power Symposium, 2008. NAPS '08. 40th North American*, 2008, pp. 1-6.
[30] N. Jayawarna, N. Jenkins, M. Barnes, M. Lorentzou, S. Papthanassiou, and N. Hatziagyriou, "Safety analysis of a microgrid", in *Future Power Systems, 2005 International Conference on*, 2005, pp. 7 pp.-7.

EBSCOhost - printed on 2/14/2023 2:46 PM via . All use subject to https://www.ebsco.com/terms-of-use

[31] R. M. Kamel, A. Chaouachi, and K. Nagasaka, “Design and Testing of Three Earthing Systems for Micro-Grid Protection during the Islanding Mode”, *Smart Grid and Renewable Energy,* vol. 1, pp. 132-142, 2010.
[32] R. M. Kamel, A. Chaouachi, and K. Nagasaka, “Comparison the Performances of Three Earthing Systems for Micro-Grid Protection during the Grid Connected Mode”, *Smart Grid and Renewable Energy,* vol. 2, pp. 206-215, 2011.
[33] M. Lorentzou, N. D. Hatziargyriou, and S. A. Papathanassiou, “Investigation of the effect of grounding practices in a Microgrid installation”, in *4th European PV-Hybrid and Mini-Grid Conference*, Athens (Greece), 2008.
[34] B. Li, Y. Li, and T. Ma, “Research on earthing schemes in LV microgrids”, in *Advanced Power System Automation and Protection (APAP), 2011 International Conference on*, 2011, pp. 1003-1007.
[35] C. X. Wu, F. S. Wen, and Y. L. Lou, “The existed problems and possible solutions of micro-grid based on distributed generation”, in *Electric Utility Deregulation and Restructuring and Power Technologies, 2008. DRPT 2008. Third International Conference on*, 2008, pp. 2763-2768.
[36] J. Driesen, P. Vermeyen, and R. Belmans, “Protection Issues in Microgrids with Multiple Distributed Generation Units”, in *Power Conversion Conference - Nagoya, 2007. PCC '07*, 2007, pp. 646-653.
[37] Z. Kai-Hui and X. Ming-Chao, “Impacts of microgrid on protection of distribution networks and protection strategy of microgrid”, in *Advanced Power System Automation and Protection (APAP), 2011 International Conference on*, 2011, pp. 356-359.
[38] P. Mahat, Z. Chen, and B. Bak-Jensen, “Islanding Operation of Distribution System with Distributed Generations”, in *Proceedings of the Danish PhD Seminar on detailed Modelling and Validation of Electrical Components and Systems*, 2010, pp. 23-26.
[39] N. Schaefer, T. Degner, A. Shustov, T. Keil, and J. Jaeger, “Adaptive protection system for distribution networks with distributed energy resources”, in *Developments in Power System Protection (DPSP 2010). Managing the Change, 10th IET International Conference on*, 2010, pp. 1-5.
[40] H. Al-Nasseri and M. A. Redfern, “A new voltage based relay scheme to protect micro-grids dominated by embedded generation using solid state converters”, in *19th International Conference on Electricity Distributio (CIRED 2007)*, Vienna (Austria), 2007, pp. 1-4.
[41] H. Al-Nasseri, M. A. Redfern, and F. Li, “A voltage based protection for micro-grids containing power electronic converters”, in *Power Engineering Society General Meeting, 2006. IEEE*, 2006, p. 7 pp.
[42] H. Al-Nasseri, M. A. Redfern, and R. O'Gorman, “Protecting micro-grid systems containing solid-state converter generation”, in *Future Power Systems, 2005 International Conference on*, 2005, pp. 5 pp.-5.
[43] M. A. Redfern and H. Al-Nasseri, “Protection of micro-grids dominated by distributed generation using solid state converters”, in *Developments in Power System Protection, 2008. DPSP 2008. IET 9th International Conference on*, 2008, pp. 670-674.

EBSCOhost - printed on 2/14/2023 2:46 PM via . All use subject to https://www.ebsco.com/terms-of-use

[44] H. Al-Nasseri and M. A. Redfern, "Harmonics content based protection scheme for Micro-grids dominated by solid state converters", in *Power System Conference, 2008. MEPCON 2008. 12th International Middle-East*, 2008, pp. 50-56.

[45] C. Hou and X. Hu, "A study of voltage detection based fault judgement method in micro-grid with inverter interfaced power source", in *The International Conference on Electrical Engineering*, Shenyang (China), 2009, pp. 1-5.

[46] T. Loix, T. Wijnhoven, and G. Deconinck, "Protection of microgrids with a high penetration of inverter-coupled energy sources", in *Integration of Wide-Scale Renewable Resources Into the Power Delivery System, 2009 CIGRE/IEEE PES Joint Symposium*, 2009, pp. 1-6.

[47] M. Brucoli and T. C. Green, "Fault behaviour in islanded microgrids", in *19th International Conference on Electricity Distributio (CIRED 2007)*, Vienna (Austria), 2007, pp. 1-4.

[48] W. Xiao-ping, L. Yang, and Y. Yong-yang, "Research on the relay protection system for a small laboratory-scale microgrid system", in *Industrial Electronics and Applications (ICIEA), 2011 6th IEEE Conference on*, 2011, pp. 2712-2716.

[49] L. Xinyao, A. Dysko, and G. M. Burt, "Application of communication based distribution protection schemes in islanded systems", in *Universities Power Engineering Conference (UPEC), 2010 45th International*, 2010, pp. 1-6.

[50] E. Sortomme, S. S. Venkata, and J. Mitra, "Microgrid Protection Using Communication-Assisted Digital Relays", *Power Delivery, IEEE Transactions on,* vol. 25, pp. 2789-2796, 2010.

[51] S. Conti, L. Raffa, and U. Vagliasindi, "Innovative solutions for protection schemes in autonomous MV micro-grids", in *Clean Electrical Power, 2009 International Conference on*, 2009, pp. 647-654.

[52] H. H. Zeineldin, E. F. El-Saadany, and M. M. A. Salama, "Distributed Generation Micro-Grid Operation: Control and Protection", in *Power Systems Conference: Advanced Metering, Protection, Control, Communication, and Distributed Resources, 2006. PS '06*, 2006, pp. 105-111.

[53] S. Conti, L. Raffa, and U. Vagliasindi, "Analysis of protection issues in autonomous MV micro-grids", in *20th International Conference on Electricity Distributio (CIRED 2009)*, Prague (Czech Republic), 2009, pp. 1-5.

[54] S. Conti and S. Nicotra, "Procedures for fault location and isolation to solve protection selectivity problems in MV distribution networks with dispersed generation", *Electric Power Systems Research,* vol. 79, pp. 57-64, 2009.

[55] S. Conti and S. Raiti, "Integrated protection scheme to coordinate MV distribution network devices, DG interface protections and micro-grids operation", in *Clean Electrical Power, 2009 International Conference on*, 2009, pp. 640-646.

[56] E. Sortomme, J. Ren, and S. S. Venkata, "A differential zone protection scheme for microgrids", in *2013 IEEE Power & Energy Society General Meeting*, 2013, pp. 1-5.

EBSCOhost - printed on 2/14/2023 2:46 PM via . All use subject to https://www.ebsco.com/terms-of-use

[57] A. Prasai, D. Yi, A. Paquette, E. Buck, R. Harley, and D. Divan, "Protection of meshed microgrids with communication overlay", in *Energy Conversion Congress and Exposition (ECCE), 2010 IEEE*, 2010, pp. 64-71.
[58] W. Jiang, Z.-y. He, and Z.-q. Bo, "The Overview of Research on Microgrid Protection Development", in *Intelligent System Design and Engineering Application (ISDEA), 2010 International Conference on*, 2010, pp. 692-697.
[59] M. Dewadasa, A. Ghosh, and G. Ledwich, "Protection of microgrids using differential relays", in *Universities Power Engineering Conference (AUPEC), 2011 21st Australasian*, 2011, pp. 1-6.
[60] M. Dewadasa and A. Ghosh, "Protection of meshed microgrids", 2011.
[61] A. Ghosh and M. Dewadasa, "Operation Control and Energy Management of Distributed Generation", 2011.
[62] M. P. Nthontho, S. P. Chowdhury, S. Winberg, and S. Chowdhury, "Protection of domestic solar photovoltaic based microgrid", in *Developments in Power Systems Protection, 2012. DPSP 2012. 11th International Conference on*, 2012, pp. 1-6.
[63] M. P. Nthontho, S. P. Chowdhury, S. Winberg, and S. Chowdhury, "Communication networks for domestic photovoltaic based microgrid protection", in *Developments in Power Systems Protection, 2012. DPSP 2012. 11th International Conference on*, 2012, pp. 1-6.
[64] S. R. Samantaray, G. Joos, and I. Kamwa, "Differential energy based microgrid protection against fault conditions", in *Innovative Smart Grid Technologies (ISGT), 2012 IEEE PES*, 2012, pp. 1-7.
[65] S. Kar and S. R. Samantaray, "Time-frequency transform-based differential scheme for microgrid protection", *IET Generation, Transmission & Distribution,* vol. 8, pp. 310-320, 2014.
[66] A. Gururani, S. R. Mohanty, and J. C. Mohanta, "Microgrid protection using Hilbert-Huang transform based-differential scheme", *IET Generation, Transmission & Distribution,* vol. 10, pp. 3707-3716, 2016.
[67] M. Dewadasa, A. Ghosh, and G. Ledwich, "Distance protection solution for a converter controlled microgrid", in *15th National Power Systems Conference (NPSC)*, Bombay (India), 2008, pp. 586-591.
[68] M. Dewadasa, R. Majumder, A. Ghosh, and G. Ledwich, "Control and protection of a microgrid with converter interfaced micro sources", in *Power Systems, 2009. ICPS '09. International Conference on*, 2009, pp. 1-6.
[69] M. Dewadasa, A. Ghosh, and G. Ledwich, "An inverse time admittance relay for fault detection in distribution networks containing DGs", in *TENCON 2009 - 2009 IEEE Region 10 Conference*, 2009, pp. 1-6.
[70] R. Majumder, M. Dewadasa, A. Ghosh, G. Ledwich, and F. Zare, "Control and protection of a microgrid connected to utility through back-to-back converters", *Electric Power Systems Research,* vol. 81, pp. 1424-1435, 2011.
[71] M. Dewadasa, A. Ghosh, and G. Ledwich, "Fold back current control and admittance protection scheme for a distribution network containing distributed generators", *Generation, Transmission & Distribution, IET,* vol. 4, pp. 952-962, 2010.

EBSCOhost - printed on 2/14/2023 2:46 PM via . All use subject to https://www.ebsco.com/terms-of-use

[72] M. Dewadasa, A. Ghosh, G. Ledwich, and M. Wishart, "Fault isolation in distributed generation connected distribution networks", *Generation, Transmission & Distribution, IET,* vol. 5, pp. 1053-1061, 2011.
[73] M. Dewadasa, "Protection for distributed generation interfaced networks", Electrical Engineering, Faculty of Built Environment and Engineering, Queensland University of Technology, Queensland (Australia), 2010.
[74] P. Sankarakumar and K. Venkataraman, "Use of transmission protection technology in distribution relays", in *Developments in Power Systems Protection, 2012. DPSP 2012. 11th International Conference on*, 2012, pp. 1-5.
[75] H. Lin, C. Liu, J. M. Guerrero, and J. C. Vásquez, "Distance protection for microgrids in distribution system", in *IECON 2015 - 41st Annual Conference of the IEEE Industrial Electronics Society*, 2015, pp. 000731-000736.
[76] H. Lin, J. M. Guerrero, J. C. Vásquez, and C. Liu, "Adaptive distance protection for microgrids", in *IECON 2015 - 41st Annual Conference of the IEEE Industrial Electronics Society*, 2015, pp. 000725-000730.
[77] R. M. Kamel, M. A. Alsaffar, and M. K. Habib, "Novel and simple scheme for Micro-Grid protection by connecting its loads neutral points: A review on Micro-Grid protection techniques", *Renewable and Sustainable Energy Reviews,* vol. 58, pp. 931-942, 2016/05/01/ 2016.
[78] L. Bin, L. Yongli, B. Zhiqian, and A. Klimek, "Design of protection and control scheme for microgrid systems", in *Universities Power Engineering Conference (UPEC), 2009 Proceedings of the 44th International*, 2009, pp. 1-5.
[79] A. Zamani, T. Sidhu, and A. Yazdani, "A strategy for protection coordination in radial distribution networks with distributed generators", in *Power and Energy Society General Meeting, 2010 IEEE*, 2010, pp. 1-8.
[80] M. A. Zamani, T. S. Sidhu, and A. Yazdani, "A Protection Strategy and Microprocessor-Based Relay for Low-Voltage Microgrids", *Power Delivery, IEEE Transactions on,* vol. 26, pp. 1873-1883, 2011.
[81] R. D. Christie, H. Zadehgol, and M. M. Habib, "High impedance fault detection in low voltage networks", *Power Delivery, IEEE Transactions on,* vol. 8, pp. 1829-1836, 1993.
[82] M. R. Miveh, M. Gandomkar, S. Mirsaeidi, and H. Nasiban, "Micro-Grid Protection by Designing a Communication-Assisted Digital Relay", *American Journal of Scientific Research,* pp. 62-68, 2012.
[83] L. d. M. Pintos, M. Moreto, and J. G. Rolim, "Applicability Analysis of Directional Overcurrent Relay without Voltage Reference in Microgrids", *IEEE Latin America Transactions,* vol. 14, pp. 687-693, 2016.
[84] A. Ukil, B. Deck, and V. H. Shah, "Smart distribution protection using current-only directional overcurrent relay", in *2010 IEEE PES Innovative Smart Grid Technologies Conference Europe (ISGT Europe)*, 2010, pp. 1-7.
[85] A. Ukil, B. Deck, and V. H. Shah, "Current-Only Directional Overcurrent Relay", *IEEE Sensors Journal,* vol. 11, pp. 1403-1404, 2011.
[86] H. H. Zeineldin, H. M. Sharaf, D. K. Ibrahim, and E. E. D. A. El-Zahab, "Optimal Protection Coordination for Meshed Distribution Systems With

EBSCOhost - printed on 2/14/2023 2:46 PM via . All use subject to https://www.ebsco.com/terms-of-use

DG Using Dual Setting Directional Over-Current Relays", *IEEE Transactions on Smart Grid,* vol. 6, pp. 115-123, 2015.

[87] H. M. Sharaf, H. H. Zeineldin, and E. El-Saadany, "Protection Coordination for Microgrids With Grid-Connected and Islanded Capabilities Using Communication Assisted Dual Setting Directional Overcurrent Relays", *IEEE Transactions on Smart Grid,* vol. 9, pp. 143-151, 2018.

[88] R. M. Tumilty, M. Brucoli, G. M. Burt, and T. C. Green, "Approaches to Network Protection for Inverter Dominated Electrical Distribution Systems", in *Power Electronics, Machines and Drives, 2006. The 3rd IET International Conference on*, 2006, pp. 622-626.

[89] G. D. Rockefeller, C. L. Wagner, J. R. Linders, K. L. Hicks, and D. T. Rizy, "Adaptive transmission relaying concepts for improved performance", *Power Delivery, IEEE Transactions on,* vol. 3, pp. 1446-1458, 1988.

[90] Y. Han, X. Hu, and D. Zhang, "Study of adaptive fault current algorithm for microgrid dominated by inverter based distributed generators", in *Power Electronics for Distributed Generation Systems (PEDG), 2010 2nd IEEE International Symposium on*, 2010, pp. 852-854.

[91] Y. Han, X. Hu, and D. Zhang, "A new adaptive current protection scheme of distribution networks with distributed generation", in *Sustainable Power Generation and Supply, 2009. SUPERGEN '09. International Conference on*, 2009, pp. 1-5.

[92] M. Khederzadeh, "Adaptive setting of protective relays in microgrids in grid-connected and autonomous operation", *IET Conference Publications,* vol. 2012, pp. P14-P14, 2012.

[93] T. S. Ustun, C. Ozansoy, and A. Zayegh, "A central microgrid protection system for networks with fault current limiters", in *Environment and Electrical Engineering (EEEIC), 2011 10th International Conference on*, 2011, pp. 1-4.

[94] T. S. Ustun, C. Ozansoy, and A. Zayegh, "A microgrid protection system with central protection unit and extensive communication", in *Environment and Electrical Engineering (EEEIC), 2011 10th International Conference on*, 2011, pp. 1-4.

[95] T. S. Ustun, C. Ozansoy, and A. Zayegh, "Modeling and simulation of a microgrid protection system with central protection unit", in *IEEE 2013 Tencon - Spring*, 2013, pp. 5-9.

[96] C. Ozansoy, "A methodology for determining fault current impact coefficients of distributed energy resources in an adaptive protection scheme", in *2015 9th International Conference on Electrical and Electronics Engineering (ELECO)*, 2015, pp. 479-483.

[97] T. S. Ustun, C. Ozansoy, and A. Ustun, "Fault current coefficient and time delay assignment for microgrid protection system with central protection unit", *IEEE Transactions on Power Systems,* vol. 28, pp. 598-606, 2013.

[98] T. S. Ustun, R. H. Khan, A. Hadbah, and A. Kalam, "An adaptive microgrid protection scheme based on a wide-area smart grid communications network", in *2013 IEEE Latin-America Conference on Communications*, 2013, pp. 1-5.

EBSCOhost - printed on 2/14/2023 2:46 PM via . All use subject to https://www.ebsco.com/terms-of-use

[99] T. S. Ustun, C. Ozansoy, and A. Zayegh, "Simulation of communication infrastructure of a centralized microgrid protection system based on IEC 61850-7-420", in *2012 IEEE Third International Conference on Smart Grid Communications (SmartGridComm)*, 2012, pp. 492-497.

[100] C. Ozansoy, "Design of an adaptive protection system for microgrids with distributed energy resources in accordance with IEC 61850-7-420", in *2015 9th International Conference on Electrical and Electronics Engineering (ELECO)*, 2015, pp. 474-478.

[101] T. S. Ustun, C. Ozansoy, and A. Zayegh, "Modeling of a Centralized Microgrid Protection System and Distributed Energy Resources According to IEC 61850-7-420", *IEEE Transactions on Power Systems,* vol. 27, pp. 1560-1567, 2012.

[102] S. Teimourzadeh, F. Aminifar, M. Davarpanah, and M. Shahidehpour, "Adaptive Protection for Preserving Microgrid Security", *IEEE Transactions on Smart Grid,* pp. 1-1, 2017.

[103] J. Chen, Z.-y. He, and W. Jiang, "The Overview of Protection Schemes for Distribution Systems Containing Micro-Grid", in *Power and Energy Engineering Conference (APPEEC), 2011 Asia-Pacific*, 2011, pp. 1-4.

[104] B. Hussain, S. M. Sharkh, S. Hussain, and M. A. Abusara, "Integration of distributed generation into the grid: Protection challenges and solutions", in *Developments in Power System Protection (DPSP 2010). Managing the Change, 10th IET International Conference on*, 2010, pp. 1-5.

[105] N. Jayawarna, M. Barnes, C. Jones, and N. Jenkins, "Operating MicroGrid Energy Storage Control during Network Faults", in *System of Systems Engineering, 2007. SoSE '07. IEEE International Conference on*, 2007, pp. 1-7.

[106] M. Khederzadeh, "Preservation of overcurrent relays coordination in microgrids by application of static series compensators", in *Developments in Power Systems Protection, 2012. DPSP 2012. 11th International Conference on*, 2012, pp. 1-5.

[107] P. Mahat, C. Zhe, B. Bak-Jensen, and C. L. Bak, "A Simple Adaptive Overcurrent Protection of Distribution Systems With Distributed Generation", *Smart Grid, IEEE Transactions on,* vol. 2, pp. 428-437, 2011.

[108] U. A. Khan, H. Jae-Sang, S. Jae-Kyu, and L. Bang-Wook, "Application and positioning analysis of a resistive type Superconducting Fault Current Limiter in AC and DC microgrids using Simulink and SimPowerSystem", in *Electric Power Equipment - Switching Technology (ICEPE-ST), 2011 1st International Conference on*, 2011, pp. 348-351.

[109] Y. Zhang and R. Dougal, "State of the Art of Fault Current Limiters and Their Applications in Smart Grid", in *2012 IEEE PES General Meeting*, San Diego (USA), 2012, pp. 1-6.

[110] N. Jayawarna, N. Jenkins, M. Barnes, M. Lorentzou, S. Papathanassiou, and N. Hatziargyriou, "Safety analysys of a microgrid", *International Journal of Distributed Energy Resources,* vol. 2, pp. 261-278, 2006.

EBSCOhost - printed on 2/14/2023 2:46 PM via . All use subject to https://www.ebsco.com/terms-of-use

[111] N. Jayawarna and M. Barnes, “Central storage unit response requirement in 'Good Citizen' Microgrid”, in *Power Electronics and Applications, 2009. EPE '09. 13th European Conference on*, 2009, pp. 1-10.

[112] C. Jones, C. Fitzer, and M. Barnes, “Unified control and operation of a 20 kVA laboratory microgrid incorporating flywheel energy storage”, *International Journal of Distributed Energy Resources,* vol. 3, pp. 313-337, 2007.

[113] F. van Overbeeke, “Fault current source to ensure the fault level in inverter-dominated networks”, in *Electricity Distribution - Part 1, 2009. CIRED 2009. 20th International Conference and Exhibition on*, 2009, pp. 1-4.

[114] D. M. Vilathgamuwa, L. Poh Chiang, and Y. Li, “Protection of Microgrids During Utility Voltage Sags”, *Industrial Electronics, IEEE Transactions on,* vol. 53, pp. 1427-1436, 2006.

[115] S. Shi, B. Jiang, X. Dong, and Z. Bo, “Protection of microgrid”, in *Developments in Power System Protection (DPSP 2010). Managing the Change, 10th IET International Conference on*, 2010, pp. 1-4.

[116] Y. Han, X. Hu, and D. Zhang, “Study on applying wavelet transform to the protection algorithm of microgrid dominated by inverter -interfaced DGs”, in *Power System Technology (POWERCON), 2010 International Conference on*, 2010, pp. 1-6.

[117] S. A. Saleh, R. Ahshan, M. A. Rahman, M. S. A. Khaizaran, and B. Alsayed, “Implementing and testing d-q WPT-based digital protection for micro-grid systems”, in *Industry Applications Society Annual Meeting (IAS), 2011 IEEE*, 2011, pp. 1-8.

[118] H. H. Zeineldin, E. F. El-Saadany, and M. M. A. Salama, “Protective Relay Coordination for Micro-grid Operation Using Particle Swarm Optimization”, in *Power Engineering, 2006 Large Engineering Systems Conference on*, 2006, pp. 152-157.

[119] H. H. Zeineldin, E. F. El-Saadany, and M. M. A. Salama, “Optimal coordination of overcurrent relays using a modified particle swarm optimization”, *Electric Power Systems Research,* vol. 76, pp. 988-995, 2006.

[120] H. Qu, Q. Jia, and Z. Bo, “MPSO based protective relay coordination for Micro-grid”, in *Developments in Power System Protection (DPSP 2010). Managing the Change, 10th IET International Conference on*, 2010, pp. 1-5.

[121] Y. Damchi, H. R. Mashhadi, J. Sadeh, and M. Bashir, “Optimal coordination of directional overcurrent relays in a microgrid system using a hybrid particle swarm optimization”, in *Advanced Power System Automation and Protection (APAP), 2011 International Conference on*, 2011, pp. 1135-1138.

[122] W. Prommee, N. Pongprapunt, and W. Ongsakul, “Improved reliability model and optimal protective device placement in Micro Grid by Improved Binary Particle Swarm Optimization”, in *Power Electronics and ECCE Asia (ICPE & ECCE), 2011 IEEE 8th International Conference on*, 2011, pp. 1514-1519.

[123] H. S. Pandya, D. M. Pandeji, R. K. Iyer, and P. M. Purohit, “Digital protection strategy of microgrid with relay time grading using particle swarm

EBSCOhost - printed on 2/14/2023 2:46 PM via . All use subject to https://www.ebsco.com/terms-of-use

optimization", in *2015 5th Nirma University International Conference on Engineering (NUiCONE)*, 2015, pp. 1-6.

[124] S. T. P. Srinivas and K. S. Swarup, "Optimal relay coordination for microgrids using hybrid modified particle swarm optimization - Interval linear programming approach", in *2017 North American Power Symposium (NAPS)*, 2017, pp. 1-6.

[125] D. P. Mishra, S. R. Samantaray, and G. Joos, "A Combined Wavelet and Data-Mining Based Intelligent Protection Scheme for Microgrid", *IEEE Transactions on Smart Grid,* vol. 7, pp. 2295-2304, 2016.

[126] G. Joós and K. El-Arroudi, "Modeling Protection for DGs and Microgrids Using Data Mining", in *Nagoya Microgrid Symposium*, Nagoya (Japan), 2007.

[127] E. Casagrande, W. L. Woon, H. H. Zeineldin, and N. H. Kan'an, "Data mining approach to fault detection for isolated inverter-based microgrids", *IET Generation, Transmission & Distribution,* vol. 7, pp. 745-754, 2013.

[128] E. Casagrande, W. L. Woon, H. H. Zeineldin, and D. Svetinovic, "A Differential Sequence Component Protection Scheme for Microgrids With Inverter-Based Distributed Generators", *IEEE Transactions on Smart Grid,* vol. 5, pp. 29-37, 2014.

[129] S. Kar and S. R. Samantaray, "Combined S-transform and data-mining based intelligent micro-grid protection scheme", in *2014 Students Conference on Engineering and Systems*, 2014, pp. 1-5.

[130] S. Kar, S. R. Samantaray, and M. D. Zadeh, "Data-Mining Model Based Intelligent Differential Microgrid Protection Scheme", *IEEE Systems Journal,* vol. 11, pp. 1161-1169, 2017.

[131] S. Kar and S. R. Samantaray, "Data-mining based comprehensive primary and backup protection scheme for micro-grid", in *2015 IEEE Power, Communication and Information Technology Conference (PCITC)*, 2015, pp. 505-510.

[132] S. Kar and S. R. Samantaray, "High impedance fault detection in microgrid using maximal overlapping discrete wavelet transform and decision tree", in *2016 International Conference on Electrical Power and Energy Systems (ICEPES)*, 2016, pp. 258-263.

[133] S. Balantrapu. (2010) Role of artificial neural networks in microgrid. *Energy Pulse*. Available: http://www.energypulse.net/centers/article/article_display.cfm?a_id=2355

[134] P. P. K. Chan, Z. Jing, Q. Zhi-Wei, W. W. Y. Ng, and D. S. Yeung, "Comparision of different classifiers in fault detection in microgrid", in *Machine Learning and Cybernetics (ICMLC), 2011 International Conference on*, 2011, pp. 1210-1213.

[135] L. Hengwei, J. M. Guerrero, J. Chenxi, T. Zheng-hua, J. C. Vasquez, and L. Chengxi, "Adaptive overcurrent protection for microgrids in extensive distribution systems", in *IECON 2016 - 42nd Annual Conference of the IEEE Industrial Electronics Society*, 2016, pp. 4042-4047.

EBSCOhost - printed on 2/14/2023 2:46 PM via . All use subject to https://www.ebsco.com/terms-of-use

[136] J. J. Q. Yu, Y. Hou, A. Y. S. Lam, and V. O. K. Li, "Intelligent Fault Detection Scheme for Microgrids with Wavelet-based Deep Neural Networks", *IEEE Transactions on Smart Grid,* pp. 1-1, 2017.

[137] A. H. Abdulwahid and S. Wang, "A new differential protection scheme for microgrid using Hilbert space based power setting and fuzzy decision processes", in *2016 IEEE 11th Conference on Industrial Electronics and Applications (ICIEA)*, 2016, pp. 6-11.

[138] A. H. Abdulwahid and W. Shaorong, "A busbar differential protection based on fuzzy reasoning system and Rogowski-coil current sensor for microgrid", in *2016 IEEE PES Asia-Pacific Power and Energy Engineering Conference (APPEEC)*, 2016, pp. 194-199.

[139] A. H. Abdulwahid and W. Shaorong, "A new protection approach for microgrid based upon combined ANFIS with Symmetrical Components", in *2016 IEEE PES Asia-Pacific Power and Energy Engineering Conference (APPEEC)*, 2016, pp. 1984-1989.

[140] O. V. G. Swathika, S. Angalaeswari, V. A. Krishnan, K. Jamuna, and J. L. F. Daya, "Fuzzy Decision and Graph Algorithms Aided Adaptive Protection of Microgrid", *Energy Procedia,* vol. 117, pp. 1078-1084, 2017/06/01/ 2017.

[141] S. B. A. Bukhari, R. Haider, M. Saeed Uz Zaman, Y.-S. Oh, G.-J. Cho, and C.-H. Kim, "An interval type-2 fuzzy logic based strategy for microgrid protection", *International Journal of Electrical Power & Energy Systems,* vol. 98, pp. 209-218, 2018/06/01/ 2018.

[142] T. S. Ustun, C. Ozansoy, and A. Zayegh, "Implementation of Dijkstra's algorithm in a dynamic microgrid for relay hierarchy detection", in *Smart Grid Communications (SmartGridComm), 2011 IEEE International Conference on*, 2011, pp. 481-486.

[143] O. V. G. Swathika and S. Hemamalini, "Prims-Aided Dijkstra Algorithm for Adaptive Protection in Microgrids", *IEEE Journal of Emerging and Selected Topics in Power Electronics,* vol. 4, pp. 1279-1286, 2016.

[144] T. Gush, S. B. A. Bukhari, R. Haider, S. Admasie, Y.-S. Oh, G.-J. Cho, and C.-H. Kim, "Fault detection and location in a microgrid using mathematical morphology and recursive least square methods", *International Journal of Electrical Power & Energy Systems,* vol. 102, pp. 324-331, 2018/11/01/ 2018.

[145] X. Li, A. Dysko, and G. Burt, "Enhanced protection for inverter dominated microgrid using transient fault information", in *Developments in Power Systems Protection, 2012. DPSP 2012. 11th International Conference on*, 2012, pp. 1-5.

[146] X. Li, A. Dyśko, and G. M. Burt, "Traveling Wave-Based Protection Scheme for Inverter-Dominated Microgrid Using Mathematical Morphology", *IEEE Transactions on Smart Grid,* vol. 5, pp. 2211-2218, 2014.

[147] H. Guang, W. Qi, R. Panxiang, and J. Delin, "Brittleness entropy of complex system based protection of microgrid", in *Strategic Technology (IFOST), 2011 6th International Forum on*, 2011, pp. 433-436.

EBSCOhost - printed on 2/14/2023 2:46 PM via . All use subject to https://www.ebsco.com/terms-of-use

[148] M. Esreraig and J. Mitra, "An observer-based protection system for microgrids", in *Power and Energy Society General Meeting, 2011 IEEE*, 2011, pp. 1-7.

[149] J. Shi, W. Sun, and C. Li, "Fault Diagnosis of Micro-Grid Based on Advanced Petri Net", *Applied Mechanics and Materials,* vol. 130-134, pp. 3015-3019, 2012.

[150] M. Manohar, E. Koley, and S. Ghosh, "A reliable fault detection and classification scheme based on wavelet transform and ensemble of SVM for microgrid protection", in *2017 3rd International Conference on Applied and Theoretical Computing and Communication Technology (iCATccT)*, 2017, pp. 24-28.

[151] M. Manohar and E. Koley, "SVM based protection scheme for microgrid", in *2017 International Conference on Intelligent Computing, Instrumentation and Control Technologies (ICICICT)*, 2017, pp. 429-432.

[152] M. Manohar, E. Koley, and S. Ghosh, "Reliable protection scheme for PV integrated microgrid using an ensemble classifier approach with real-time validation", *IET Science, Measurement & Technology,* vol. 12, pp. 200-208, 2018.

EBSCOhost - printed on 2/14/2023 2:46 PM via . All use subject to https://www.ebsco.com/terms-of-use

# CHAPTER FIFTEEN

# POWER STABILISATION SYSTEM WITH COUNTER-ROTATING-TYPE PUMP-TURBINE TO MOMENTARILY STABILISE FLUCTUATING POWER FROM RENEWABLE RESOURCES

JIN-HYUK KIM[1], YOUNG-SEOK CHOI[2], TOSHIAKI KANEMOTO[3]

## Abstract

This chapter presents a hybrid power stabilisation system with a counter-rotating-type pump-turbine unit that aims to momentarily stabilise fluctuating power from renewable energy resources. It has been experimentally verified that this unit is reasonably effective in momentarily/instantaneously stabilising unstable fluctuating power generation. In addition, systematic optimisation has been carried out to improve the hydrodynamic performance of this pump-turbine unit using three-dimensional Reynolds-averaged Navier-Stokes equations. At highest efficiency, the optimal design yields a maximum increase in hydraulic efficiency of 2.68 % over a reference design. The detailed internal flow

[1] Korea Institute of Industrial Technology, Thermal & Fluid System R&D Group, 89 Yangdaegiro-gil, Ipjang-myeon, Seobuk-gu, Cheonan-si, Chungcheongnam-do 31056, Republic of Korea. Email: jinhyuk@kitech.re.kr

[2] Korea Institute of Industrial Technology, Thermal & Fluid System R&D Group, 89 Yangdaegiro-gil, Ipjang-myeon, Seobuk-gu, Cheonan-si, Chungcheongnam-do 31056, Republic of Korea. Email: yschoi@kitech.re.kr

[3] Daijin Precision Co., Ltd. (Daijin Pump), 127 Gongdan 1-daero 260beon-gil, Siheung-si, Gyeonggi-do 15112 Republic of Korea. Email: kanemoto.toshiaki886@mail.kyutech.jp

EBSCOhost - printed on 2/14/2023 2:46 PM via . All use subject to https://www.ebsco.com/terms-of-use

fields between the reference and optimal designs are analysed and discussed here.

**Keywords:** Power stabilisation system; counter-rotating-type pump-turbine unit; wind turbine unit; turbine mode; optimisation.

## Nomenclature

| | |
|---|---|
| AC | Alternating current |
| ANOVA | Analysis of variance |
| $C$ | Regression analysis coefficients |
| $D$ | Diameter, m |
| EXP | Experiment |
| F | Objective function value |
| $g$ | Acceleration of gravity, m/s$^2$ |
| $H$ | Head, m |
| INV | Inverter |
| LE | Leading edge |
| LHS | Latin hypercube sampling |
| $N$ | Number of design variables |
| $N_T$ | Total rotational speed, rpm |
| $P$ | Power, kW |
| $P_G$ | Constant power, MW |
| $P_{11}$ | Turbine output, m-kW |
| $Q$ | Volume flow rate, m$^3$/s |
| $R^2$ | Correlation coefficient in least-squares surface fitting |
| $R^2_{adj}$ | Adjusted correlation coefficient |
| RANS | Reynolds-averaged Navier-Stokes |
| RMS | Root mean square |
| RMSE | Root-mean-square error |
| RSA | Response surface approximation |
| SST | Shear stress transport |
| TE | Trailing edge |
| V | Velocity, m/s |
| $x$ | Set of design variables |
| β | Runner blade angle, degree |
| $\eta$ | Efficiency |
| $\rho$ | Density, kg/m$^3$ |

EBSCOhost - printed on 2/14/2023 2:46 PM via . All use subject to https://www.ebsco.com/terms-of-use

| Subscripts | |
|---|---|
| 1 | First |
| 2 | Second |
| F | Front |
| R | Rear |

## Introduction

In recent years, researchers have increasingly focused on developing advanced technologies and high-performance design of renewable turbomachines to extract renewable energy from natural resources, such as water, wind, sunlight, and waves. However, it is difficult to supply stable power from such resources owing to abrupt changes in the weather. Hence, power stabilisation systems need to be developed to solve this problem by employing different designs. Kanemoto and colleagues [1] [2] have proposed a hybrid power stabilisation system with a counter-rotating-type pump-turbine unit as a unique form of pumped storage. They have demonstrated that this system can instantaneously stabilise the fluctuating power output from a wind power station with the help of the counter-rotating-type pump-turbine unit. This advanced technology is not only applicable to wind power, but to all other forms of renewable energy as well.

A lot of research has been conducted into improving the hydrodynamic performance of counter-rotating-type pump units or pump-turbine units, using a range of experimental and computational methods. The advantages of this counter-rotating technique have already been demonstrated by a number researchers. Kanemoto et al. [3] invented unique double rotational armatures coupled with counter-rotating-type impellers or runners to suppress unstable performance and cavitation in an entire operational region. They termed these features ‘smart control’ [4]. Kim and colleagues [5] [6] have also attempted to optimise counter-rotating blades using various design techniques to improve the hydraulic performance of the counter-rotating-type pump-turbine unit. They successfully improved the efficiency of the counter-rotating-type pump-turbine unit in both its pump and turbine modes [7]. Momosaki et al. [8] performed numerical analysis and experimental testing to understand the internal flow structure in counter-rotating-type axial flow pump rotors—especially for the rear rotor. Moreover, they performed transient analysis by studying the interaction between the front and rear rotors to obtain realistic solutions. Kasahara et al. [9] analysed the internal flow characteristics of a counter-rotating-type axial flow pump-turbine unit in pump and turbine modes by performing

EBSCOhost - printed on 2/14/2023 2:46 PM via . All use subject to https://www.ebsco.com/terms-of-use

detailed numerical analysis. They also analysed the reasons for performance loss and found that reverse flow and separation occurred near the hub and shroud tips of both the front and rear impellers/runners.

With the aim of momentarily stabilising fluctuating power from renewable energy resources, this work presents a hybrid power stabilisation system with a counter-rotating-type pump-turbine unit and experimentally verifies the effective performance of such a unit in both pumping and turbine modes. Moreover, this work presents an optimisation procedure for the high-performance design of a counter-rotating-type pump-turbine unit in the turbine mode using analysis based on three-dimensional Reynolds-averaged Navier-Stokes (RANS). This chapter is a revised version of a paper presented at the International Conference on Renewable Energies and Power Quality (ICREPQ'14) [10].

## Power stabilisation system with unique pumped storage

Among renewable energy resources, wind power is the most problematic in terms of instability and fluctuation. As such, wind power has been chosen as the example for the power stabilisation system. Fig. 1 shows the output from an intelligent wind power unit used for domestic purposes. The output was averaged every minute, as shown in Fig. 2, where the average output was, arbitrarily, 16,000 times as high as the output shown in Fig. 1. For convenience, it was assumed here that the wind power station would provide a constant power $P_G$ of 1 MW to the grid system. When the wind velocity is faster than that necessary to produce the constant $P_G$, the output from the wind power unit provides both $P_G$ to the grid system and surplus power for the pump-turbine unit in pumping mode. In contrast, when the wind velocity is slower than that necessary to produce $P_G$, the hydroelectric power, namely, the power produced in the turbine mode of this unit, compensates for $P_G$ by uniting with the output from the wind power unit. The decision of whether to select pumping mode or turbine mode is made once per minute (Fig. 2) by judging the output from the wind power unit, considering that the final objective is to make the average time as short as possible.

Fig. 3 shows a schematic diagram of the power stabilisation system with the counter-rotating-type pump-turbine unit. The system is primarily composed of an electric accumulator with minimal capacity, a power control device, and a counter-rotating-type pump-turbine unit. The output from the wind turbine is directly connected to the electric accumulator, and the power control device detects whether the output is higher or lower than $P_G$. The power control device requires the electric accumulator to

EBSCOhost - printed on 2/14/2023 2:46 PM via . All use subject to https://www.ebsco.com/terms-of-use

provide constant power $P_G$ to the grid system and also operate the pump-turbine unit in pumping mode using surplus power when the wind velocity is faster than needed to produce $P_G$, as shown in Fig. 3. As such, the surplus output is stored as potential energy in the pumping mode. In contrast, as shown in Fig. 3, the power control device requires the pump-turbine unit to operate in turbine mode, where the stored potential energy is converted into hydroelectric power, so as to use $P_G$ to overcome the output deficit from the wind power unit.

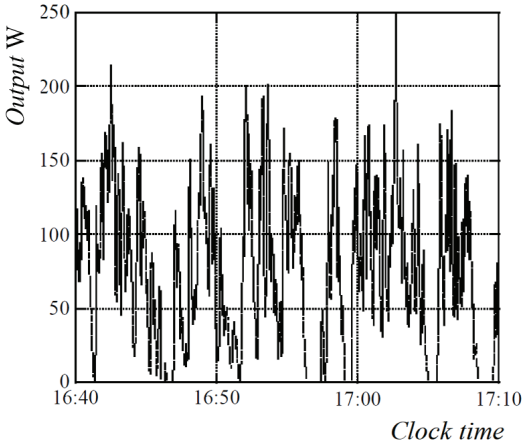



Figure 1. Output from an intelligent wind power unit used for domestic purposes.

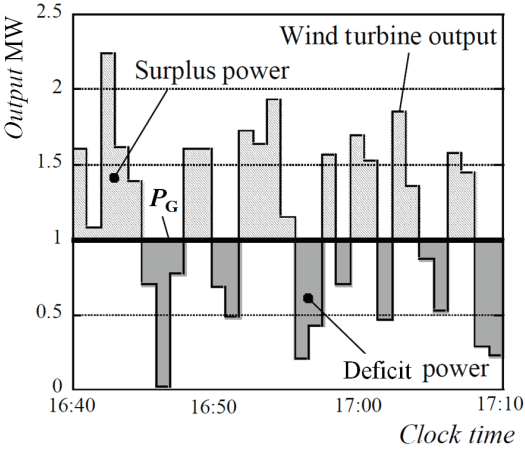



Figure 2. Output averaged per minute.

EBSCOhost - printed on 2/14/2023 2:46 PM via . All use subject to https://www.ebsco.com/terms-of-use

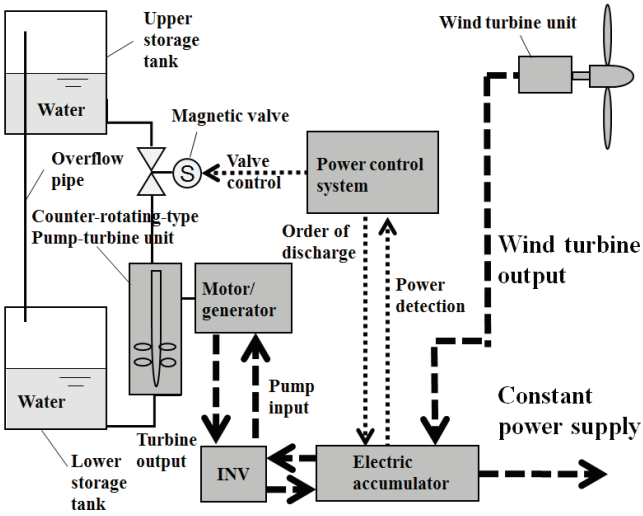
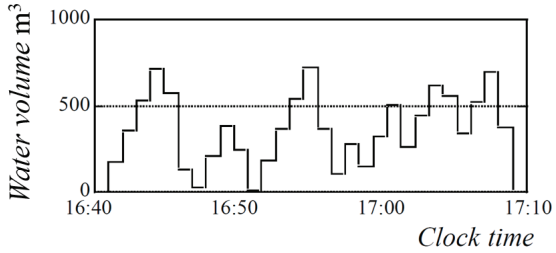
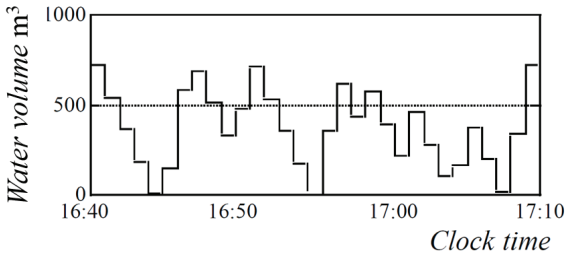



Figure 3. Power stabilisation system.



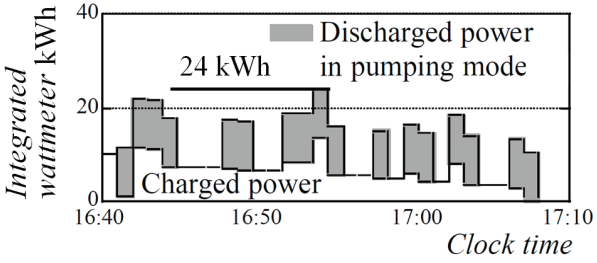

(a) Upper storage tank



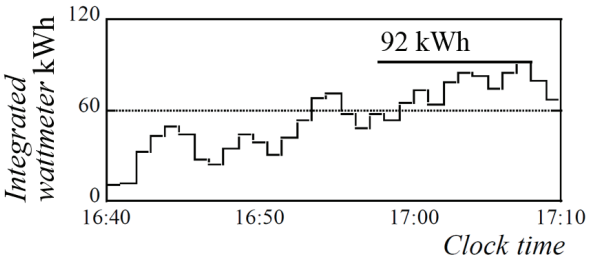

(b) Lower storage tank

Figure 4. Water volume in storage tanks.

EBSCOhost - printed on 2/14/2023 2:46 PM via . All use subject to https://www.ebsco.com/terms-of-use




(a) With power stabilisation system




(b) Without power stabilisation system

Figure 5. Capacity in electric accumulator.

Fig. 4 shows the water volume of the upper and lower storage tanks in the power stabilisation system. Fig. 5 shows the integrated watt-meter in the accumulator: the pumping/turbine head is 15 m; the input is 625 kW in the pumping mode; and the hydroelectric output is adjusted to guarantee the generation of $P_G$ in response to the output of the wind power unit. The electrical accumulator requires a capacity of up to 24 kWh as shown in Fig. 5(a), whereas the power stabilisation system operates according to the graphs in Fig. 4. The capacity of 24 kWh is 1/8th of the capacity of the electrical accumulator installed in a traditional wind power station without the proposed stabilisation system, as confirmed in Fig. 5. To put the above stabilisation system into practical use, a pump-turbine unit suitable for the above operations needs to be developed.

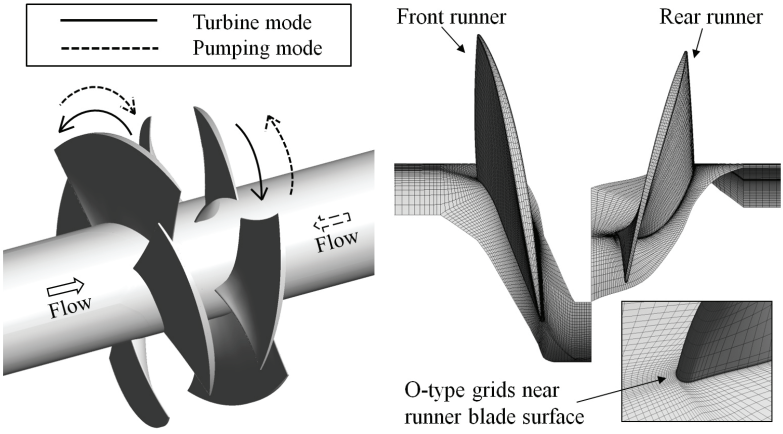
## Counter-rotating-type pump-turbine unit

In this work, a counter-rotating-type pump-turbine unit designed in a previous work [4] was considered for optimisation in turbine mode. The unit in this paper (Fig. 6) consists of a front impeller (rear runner) with

EBSCOhost - printed on 2/14/2023 2:46 PM via . All use subject to https://www.ebsco.com/terms-of-use

five blades, and a rear impeller (front runner) with four blades. It operates at a total speed of 1,800 rpm, i.e., the relative rotational speed between the front and rear runners is kept constant at $n_T$ = 1,800 rpm. The blade sections were defined according to the design of the NACA4409 hydrofoil with a single arc camber; thereafter, the sections were redesigned using a commercial computational fluid dynamics code to improve pump performance [11]. The volumetric flow rate and unit output at the point of highest efficiency were 0.025 $m^3/s$ and 5.94 kW, respectively, with an efficiency of 81.26 %.

In this unit, the traditional motor has been replaced with a new type of alternating current (AC) induction motor with double rotational armatures. The inner and outer armatures drive the front and rear impellers, respectively. The relative rotational speed between both the armatures is kept constant, and the rotational torque is counter-balanced between both the impellers/armatures. Any change in the angular momentum through the front impeller must be the same as that through the rear impeller. Such operating conditions play an important role in automatically adjusting the front and rear impeller operations in response to the discharge; successfully suppressing unstable operation at low discharge; and suppressing cavitation at high discharge. Furthermore, the authors have invented a counter-rotating-type hydroelectric unit,




(a) Counter-rotating-type pump-turbine unit

(b) Computational grids

Fig. 6. Counter-rotating-type pump-turbine unit and computational grids.

EBSCOhost - printed on 2/14/2023 2:46 PM via . All use subject to https://www.ebsco.com/terms-of-use

which is composed of tandem runners and a special generator with double rotational armatures [12]. The unit has important advantages: the induced voltage is sufficiently high without the use of supplementary equipment such as a gearbox and the rotational moment hardly acts on the mounting bed because the rotational torque is counter-balanced between the armatures/runners.

## Numerical simulation method

The flow through the counter-rotating-type pump-turbine unit was analysed by solving three-dimensional incompressible RANS equations with a k–ω-based shear stress transport (SST) turbulence model using a finite volume solver, i.e. the commercial code ANSYS CFX-12.1.

Figure 6(b) shows the computational domain for numerical analysis. The domain consists of a single passage for each of the rotational runners of the counter-rotating-type pump-turbine unit. The flow between two adjacent runner blades was assumed to be periodic in the direction of rotation. The designed normal velocity and averaged static pressure were set at the inlet and outlet of the computational domain, respectively. Water was considered to be the working fluid. The solid surfaces in the computational domain were considered to be hydraulically smooth with adiabatic and no-slip conditions. The stage method [13], which involves the circumferential averaging of the fluxes through bands on the interface, was used to establish the connection between the front and rear runners.

A hexahedral grid system was constructed in the computational domain with O-type grids near the blade surfaces and H/J/C/L-type grids in other regions, as shown in Fig. 6(b). The grid systems for the front and rear runner domains were constructed using approximately 510,000 and 420,000 grid points, respectively. Here, to benefit from the k-ω-based SST model, the near-wall grid resolution was adjusted such that $y+ \leq 2$; this adjustment allowed the wall shear stress to be accurately captured and the low-Reynolds-number SST model to be implemented [14]. Consequentially, the total grid system had approximately 930,000 grid points for the numerical analysis.

Convergence criteria were established by setting the root-mean-square (RMS) values of the residuals of the governing equations to less than $10^{-5}$ for all equations. The computations were performed using an Intel Xeon CPU with a clock speed of 3.47 GHz. The converged solutions were obtained after 500 iterations, and the computational time was approximately 4 h.

EBSCOhost - printed on 2/14/2023 2:46 PM via . All use subject to https://www.ebsco.com/terms-of-use

## Optimisation results for counter-rotating-type runner in turbine mode

To verify the accuracy of the numerical analysis, the results of the flow analysis were compared with experimental data obtained in previous research [1]. The counter-rotating-type pump-turbine unit used for this validation was considered as the reference model. Figure 7 shows the validation results in relation to the performance characteristic curves for turbine output ($P_{11} = P/D^2/H^{3/2}$, where $D$ is the turbine diameter) and efficiency in the turbine mode of the unit. As shown in the figure, the computed unit output and efficiency values are in reasonable agreement with the experimental data across the entire range of the volume flow rates. Thus, it can be seen that the numerical method proposed in this work is valid and reliable.

The aim of this optimisation was to maximise the efficiency ($\eta = P/\rho gQH$, where $P$, $\rho$, $g$, $Q$, and $H$ denote the output power, density, acceleration of gravity, volume flow rate, and head, respectively) in the turbine mode of the counter-rotating-type pump-turbine unit. In previous work [9], through analysis of the internal flow field at the best efficiency point of the reference model, some losses caused by reverse flows were observed in the near-hub region of both the runners. These losses have an adverse effect on the overall turbine performance of the unit. Hence, to reduce these losses, two design variables related to the hub profiles of both the runners were employed. Namely, the distribution of angle β at the hub span of both the runners was changed, as shown in Fig. 8. Angle β is defined as the angle between the axis of rotation and a tangent of the camber line at the hub span. The entire β distribution was changed equally along a runner hub with a fixed meridional geometry. Here, when the β distribution at each hub was changed equally, the runner blade profiles at other locations were interpolated using a B-spline curve from the hub to the tip, whereas the vane profiles at the mid-span and tip were fixed.

To determine the feasible design space formed by ranges of design variables, sensitivity tests were individually performed and the ranges of the design variables were decided (Table I). As a design-of-experiment approach, 12 design points were generated within the design space with the help of Latin hypercube sampling (LHS) [15]. The objective functions for these design points were evaluated to construct the response surface for optimisation.

The response surface approximation (RSA) [16] model was employed as a surrogate to predict the objective function values in the

EBSCOhost - printed on 2/14/2023 2:46 PM via . All use subject to https://www.ebsco.com/terms-of-use

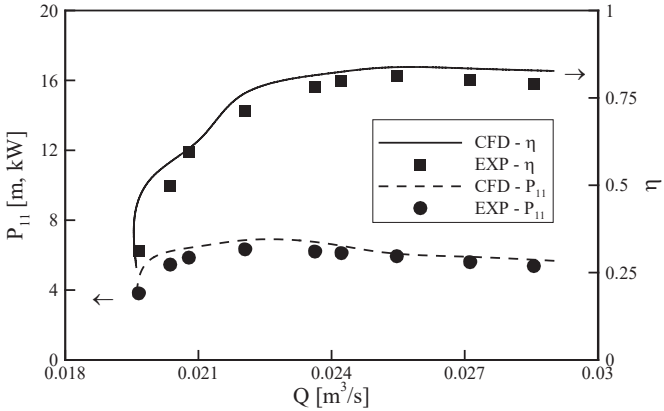



Fig. 7. Validation of numerical results.

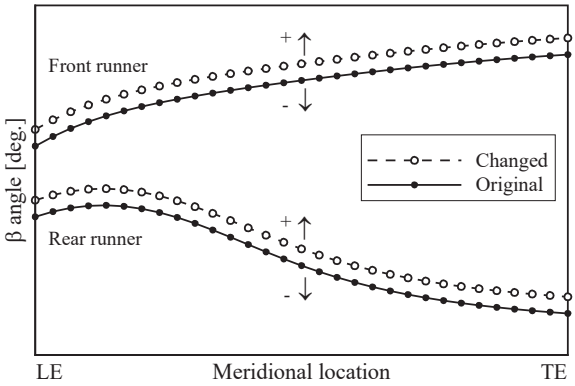



Fig. 8. β distribution at hub span of both runner blades.

**Table I: Ranges of design variables.**

| Variable | Lower | Reference | Upper |
|---|---|---|---|
| $\beta_F$ | -6 | 0 | 2 |
| $\beta_R$ | -2 | 0 | 8 |

EBSCOhost - printed on 2/14/2023 2:46 PM via . All use subject to https://www.ebsco.com/terms-of-use

design space determined by sensitivity tests. The RSA model, which provides a methodology for fitting a polynomial function to discrete responses obtained from numerical calculations, represents the association between design variables and response functions. The constructed response of a second-order polynomial RSA can be expressed as follows:

$$F(x) = C_0 + \sum_{j=1}^{N} C_j x_j + \sum_{j=1}^{N} C_{jj} x_{jj}^2 + \sum \sum_{i \neq j}^{N} C_{ij} x_i x_j \tag{1}$$

where $C$, $N$, and $x$ represent the regression analysis coefficients, the number of design variables, and a set of design variables, respectively; and the number of regression analysis coefficients ($C_0$, $C_j$, etc.) is $(N + 1) \times (N + 2)/2$. After constructing the RSA model, the optimum point was sought using sequential quadratic programming [17], which is a gradient-based optimisation technique and a generalisation of Newton's method.

In the optimisation, the RSA model for the objective function was obtained by using the numerical results at the 12 design points sampled by LHS. To measure the uncertainty in the set of coefficients of the polynomial for the RSA model, an analysis of variance (ANOVA) and a regression analysis with t-statistics [16] were carried out. The values of $R^2$ and $R^2_{adj}$ for second-order curve fitting and the RMS error (RMSE) of the RSA model are listed in Table II. Here, $R^2$ and $R^2_{adj}$ represent the correlation coefficient in the least-squares surface fitting and the adjusted correlation coefficient, respectively. The value of $R^2_{adj}$ for the objective function was 0.983, which is reliable according to the $0.9 < R^2_{adj} < 1.0$ range for the accurate prediction of the RSA model [18]. Accordingly, the constructed final RSA model can be expressed in terms of normalised design variables as follows:

$$\begin{aligned} \eta = {} & 0.8589 + 0.0109x_1 + 0.00156x_2 \\ & + 0.0088x_1x_2 - 0.0142x_1^2 - 0.0151x_2^2 \end{aligned} \tag{2}$$

where $x_1$ and $x_2$ represent $\beta_F$ and $\beta_R$, respectively.

The design variables for the optimised pump-turbine unit predicted by the RSA model are listed in Table III. In comparison to the reference design, the optimum design has smaller and bigger angles for the front and rear runners, respectively. The efficiency of the reference design obtained through the RANS analysis was 84.09 %, as listed in Table III(b). On the other hand, the efficiency of the optimum design was predicted to be 86.76 % based on the optimisation and was calculated to be 86.77 % by

EBSCOhost - printed on 2/14/2023 2:46 PM via . All use subject to https://www.ebsco.com/terms-of-use

the RANS analysis. The RSA model provided a good prediction with a relative error of 0.01 %. The efficiency of the optimum design represented a 2.68 % improvement over that of the reference design at the best efficiency point.

A three-dimensional mesh plot of the constructed final RSA model is shown in Fig. 9. The optimum point located at (-2.41l; 5.53) on the surface is clearly seen in this figure. The sensitivity of the objective function to each design variable was tested, as shown in Fig. 10. The variation in each design variable was restricted to ±10 % of its optimum value. $F_{opt}$ represents the objective function's value at the optimum point, and the results show that the objective function was more sensitive to $\beta_R$ than to $\beta_F$ near the optimum point.

**Table II: Results of ANOVA and regression analysis.**

| Objective function | $R^2$ | $R^2_{adj}$ | RMSE |
|---|---|---|---|
| $\eta$ | 0.991 | 0.983 | 0.0003 |

**Table III: Results of design optimisation.**

(a) Design variables

| Design | $\beta_F$ (deg.) | $\beta_R$ (deg.) |
|---|---|---|
| Reference design | 0 | 0 |
| Optimum design | -2.41 | 5.53 |

(b) Objective function values

| Design | Prediction (%) | RANS (%) | Error (%) | Increment (%) |
|---|---|---|---|---|
| Reference design | - | 84.09 | - | - |
| Optimum design | 86.76 | 86.77 | 0.01 | 2.68 |

EBSCOhost - printed on 2/14/2023 2:46 PM via . All use subject to https://www.ebsco.com/terms-of-use

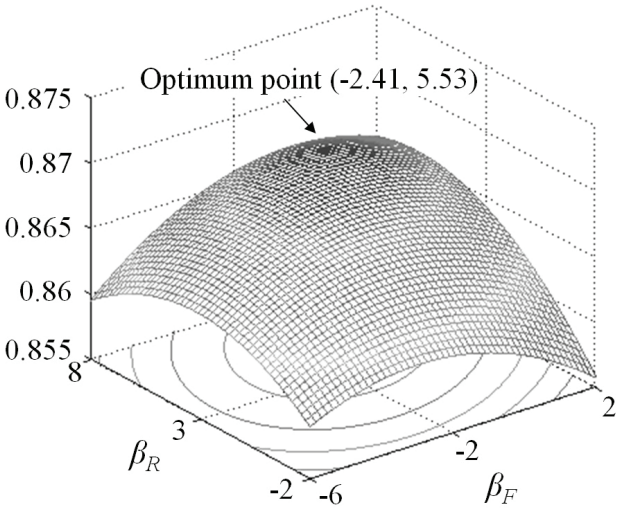



Fig. 9. Three-dimensional plot for RSA model.

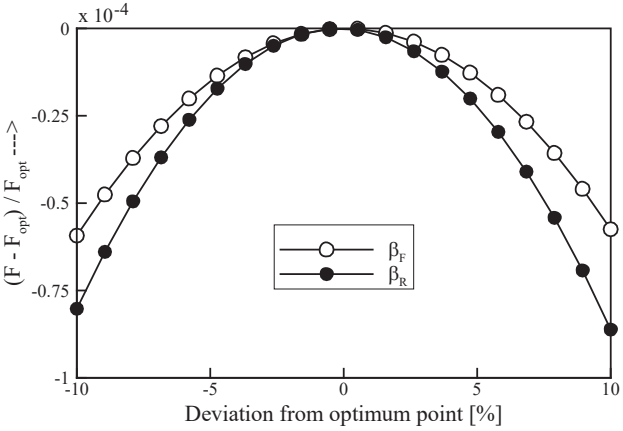



Fig. 10. Results of sensitivity test.

To assess the performance characteristics of the optimised pump-turbine unit, flow analysis was carried out for several volume flow rates for the reference and optimum designs. Fig. 11 shows the performance characteristic curves for the turbine output and efficiency in the turbine mode for the reference and optimum designs. Considerable improvements were observed in both the output and efficiency curves through

EBSCOhost - printed on 2/14/2023 2:46 PM via . All use subject to https://www.ebsco.com/terms-of-use

optimisation for volume flow rates higher than approximately 0.022 $m^3/s$. It should be noted that the optimum design gave the highest value, especially in the region of high volume flow rates. Accordingly, using this optimisation, the output curve, as well as the efficiency curve, was significantly improved in the high-volume flow rate region.

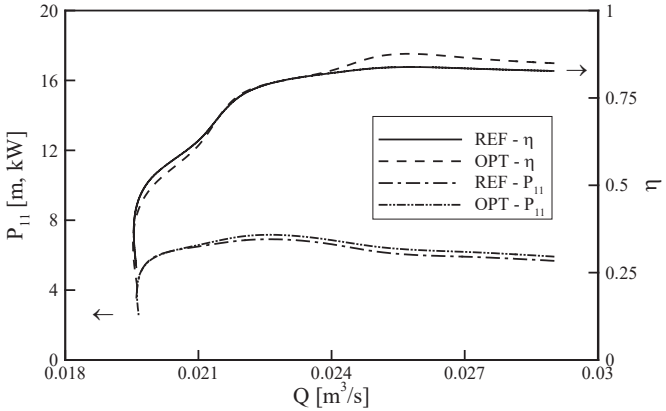



Fig. 11. Performance characteristic curves.

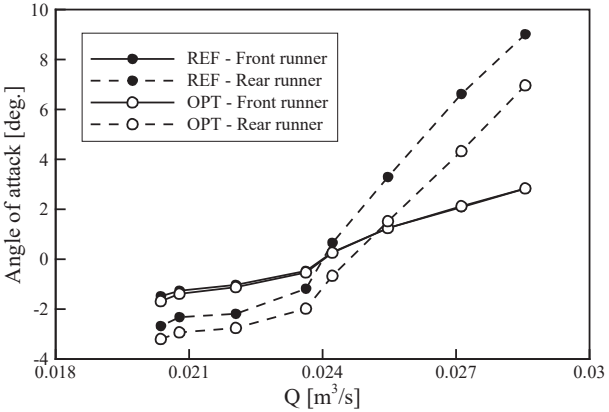
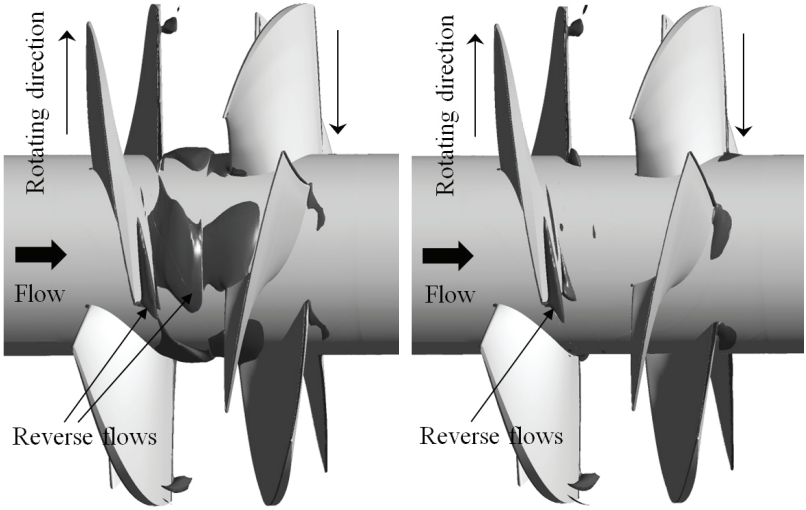



Fig. 12. Distribution of angle of attack at RMS radius.

EBSCOhost - printed on 2/14/2023 2:46 PM via . All use subject to https://www.ebsco.com/terms-of-use

Fig. 12 shows the distribution of the angle of attack at the RMS radius, where the angle of attack was predicted using the averaged flow angle at 5 mm upstream and downstream sections of the runners, respectively. As shown in Fig. 12, the angles of attack for the front runners of the reference and optimum designs were almost the same in the region covering the entire range of the volume flow rates, whereas remarkable decrements were seen in the angles of attack in the rear runner of the optimum design for the flow rate region higher than approximately 0.023 $m^3/s$. The reverse flow zone near the hub in the rear runner of the optimum design reduced clearly, and accordingly, these results illustrate the enhancement of the pump-turbine unit's turbine performance as a result of optimisation.

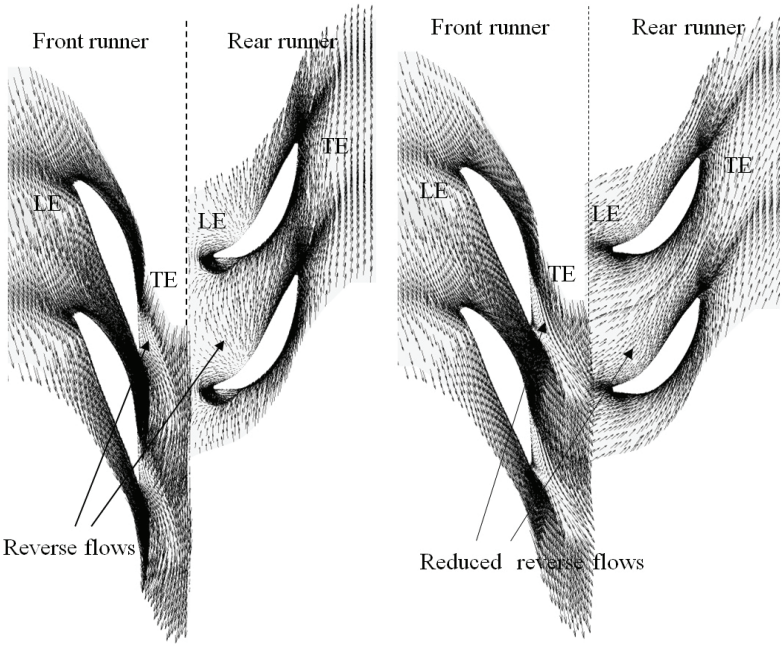
Fig. 13 shows the isosurfaces with a reverse flow of 0.1 m/s. As mentioned previously, this reverse flow, which produces a negative velocity, has an adverse effect on the overall performance of the counter-rotating-type pump-turbine unit. As shown in Fig. 13, an extensive reverse flow region was formed on the hub between both the runners of the reference design, whereas a similar reverse flow isosurface disappeared in the optimum design. On the other hand, small reverse flow components still occurred near the downstream region where the span was 90 % in the front runners of both the designs.




(a) Reference design (b) Optimum design

Figure 13. Isosurfaces with reverse flow of 0.1 m/s.

EBSCOhost - printed on 2/14/2023 2:46 PM via . All use subject to https://www.ebsco.com/terms-of-use




(a) Reference design (b) Optimum design

Figure 14. Velocity vectors near hub span (unit: m/s).

The velocity vectors near the hub span for the reference and optimum designs are plotted in Fig. 14. In the reference design, the reverse flow zone occurred on the suction side downstream of the front runner. In particular, an extensive reverse flow occupying the entire blade-to-blade passage occurred in the upstream region of the reference rear runner. In contrast, reverse flows were generally reduced in the optimum design, and most importantly, the main flow was stabilised substantially near the upstream region of the rear runner. Therefore, the optimum design produced mostly stable flows in both the runner passages.

## Conclusion

In this study, a unique power stabilisation system with a counter-rotating-type pump-turbine unit was developed to provide high-quality constant power for the grid system. The operation of the system was demonstrated in response to the fluctuating output from a wind turbine,

EBSCOhost - printed on 2/14/2023 2:46 PM via . All use subject to https://www.ebsco.com/terms-of-use

and the counter-rotating-type pump-turbine unit was proposed for pumped storage. To enhance the turbine efficiency of the pump-turbine unit, the unit was optimised in the turbine mode using two design variables related to the hub profiles for both the runners. The design optimisation results showed that in comparison with the efficiency of the reference design, the efficiency of the optimum design improved by 2.68 % at the best efficiency point and the efficiency curve was significantly enhanced in the region of high volume flow rates along with the turbine's output. On the basis of these results, multi-objective optimisation work to enhance performance in both turbine and pumping modes will be performed in the near future.

## Acknowledgements

This work was supported by the SEED Research Project Grant at the Korea Institute of Industrial Technology (KITECH) (No. ER150004), that was funded by the Ministry of Science, ICT and Future Planning (MSIP). The authors gratefully acknowledge this support.

## References

[1] Murakami, T., and Kanemoto, T., 2013, "Counter-Rotating Type Pump-Turbine Unit Cooperating with Wind Power Unit," Journal of Thermal Science, Vol. 22, No. 1, pp.7–12.

[2] Kanemoto, T., Kasahara, R., Honda, H., Miyaji, T., and Kim, J. H., 2013, "Counter-Rotating Type Pump-Turbine Unit Stabilizing Momentarily Fluctuating Power From Renewable Energy Resources," Proceedings of ASME 2013 International Mechanical Engineering Congress & Exposition, San Diego, California, USA, IMECE2013-66000.

[3] Kanemoto, T., and Oba, S., 2004, "Proposition of Unique Pumping System with Counter-Rotating Mechanism," International Journal of Rotating Machinery, Vol. 10, No. 4, pp.233–240.

[4] Kanemoto, T., Kimura, S., Oba, S., and Sato, M., 2000, "Smart Control of Axial Flow Pump Performances by Means of Counter-Rotating Type (1st Report, Counter-Rotating Type and Performances), Transaction of the JSME Series B, Vol. 66, No. 651, pp.2927–2933.

[5] Kim, J. H., Kasahara, R., Kanemoto, T., Miyaji, T., Choi, Y. S., Kim, J. H., Lee, K. Y., and Galal, A. M., 2014, "Multiobjective Optimization of a Counterrotating Type Pump-Turbine Unit Operated at Turbine Mode," Advances in Mechanical Engineering, Vol. 2014, Article ID 467235, 11 pages.

[6] Kim, J. H., Cho, B. M., Kim, S., Kim, J. W., Suh, K. W., Choi, Y. S., Kanemoto, T., and Kim, J. H., 2017, "Design Technique to Improve the

EBSCOhost - printed on 2/14/2023 2:46 PM via . All use subject to https://www.ebsco.com/terms-of-use

Energy Efficiency of a Counter-Rotating Type Pump-Turbine," Renewable Energy, Vol. 101, pp.647–659.

[7] Kim, J. W., Suh, K. W., Choi, Y. S., Lee, K. Y., Kim, J. H., Kanemoto, T., and Kim, J. H., 2016, "Simultaneous Efficiency Improvement of Pump and Turbine Modes for a Counter-Rotating Type Pump-Turbine," Advances in Mechanical Engineering, Vol. 8, No. 11, pp.2813–2826.

[8] Momosaki, T., Usami, S., Watanabe, S., and Furukawa, A., 2010, "Numerical Simulation of Internal Flow in a Contra-Rotating Axial Flow Pump," IOP Conference Series: Earth and Environmental Science, Vol. 12, No. 1, Paper No. 012046.

[9] Kasahara, R., Takano, G., Murakami, T., Kanemoto, T., and Komaki, K, 2012, "Counter-Rotating Type Axial Flow Pump Unit in Turbine Mode for Micro Grid System," IOP Conference Series: Earth and Environmental Science, Vol. 15, No. 4, Paper No. 042026.

[10] Kim, J. H., Kasahara, R., Miyaji, T., Kanemoto, T., and Choi, Y. S., 2014, "Power Stabilization System with Unique Pumped Storage to Stabilize Momentarily Fluctuating Power from Renewable Resources (Counter-Rotating Type Pump-Turbine Unit Operated at Turbine Mode)," International Conference on Renewable Energies and Power Quality (ICREPQ'14), Cordoba, Spain, Paper No. 274.

[11] Oba, S., and Kanemoto, T., 2004, "Design of Counter-Rotating Impellers by Inverse Method to Improve Pump Performances," 22th IAHR Symposium on Hydraulic Machinery and Systems, Stockholm, Sweden, Paper No. B9-1.

[12] Tanaka, D., and Kanemoto, T., 2006, "Development of Counter-Rotational Type Machine for Hydroelectric Power generation (3rd Report, Design Materials for Solidity of Axial Flow Runners)," Transaction of the JSME Series B, Vol. 72, No. 715, pp.686–692 (in Japanese).

[13] ANSYS CFX-11.0, 2006, ANSYS CFX-Solver Theory Guide, ANSYS Inc.

[14] Menter, F.R., 1994, "Two-Equation Eddy-Viscosity Turbulence Models for Engineering Application," AIAA Journal, Vol. 32, No. 8, pp.1598–1605.

[15] Sacks, J., Welch, W. J., Mitchell, T. J., and Wynn, H. P., 1989, "Design and Analysis of Computer Experiments," Statistical Science, Vol. 4, No. 4, pp.409–435.

[16] Myers, R. H., and Montgomery, D. C., 1995, Response Surface Methodology: Process and Product Optimization Using Designed Experiments, (Wiley, New York, USA).

[17] MATLAB®, 2004, The Language of Technical Computing, Release 14, (The MathWorks Inc.).

[18] Giunta, A. A., 1997, "Aircraft Multidisciplinary Design Optimization using Design of Experimental Theory and Response Surface Modeling Methods," Ph.D. thesis, Department of Aerospace Engineering, Virginia Polytechnic Institute and State University, Blacksburg, VA.

EBSCOhost - printed on 2/14/2023 2:46 PM via . All use subject to https://www.ebsco.com/terms-of-use

# CHAPTER SIXTEEN

# MODEL PREDICTIVE CONTROL FOR THE MANAGEMENT OF ELECTRICAL ENERGY IN AN AGROINDUSTRIAL MICROGRID

CÉSAR HERNÁNDEZ-HERNÁNDEZ[1],
FRANCISCO RODRÍGUEZ[1],
JOSÉ CARLOS MORENO[1],
PAULO RENATO DA COSTA MENDES[2]
AND JULIO ELÍAS NORMEY-RICO[2]

## Abstract

Microgrids allow for the integration of renewable sources of energy, such as solar and wind; distributed energy resources, such as combined heat and power; energy storage; and demand response. In addition, the use of local sources of energy to serve local loads helps reduce energy losses in transmission and distribution, further increasing the efficiency of the electricity delivery system. In this chapter, the problem of energy optimization in an agroindustrial microgrid (MG) located in south-eastern Spain is examined. An energy storage system (ESS), which exchanges energy with the utility grid, was developed using model predictive control (MPC) techniques. System modelling was undertaken using energy hub methodology. The results were obtained under different solar conditions.

[1] Department of Informatics, Agrifood Campus of International Excellence ceiA3, CIESOL Research Center on Solar Energy, University of Almeria, 04120 Almeria (Spain). E-mail: chdezh@ual.es, frrodrig@ual.es, jcmoreno@ual.es
[2] Department of Systems and Automation, Federal University of Santa Catarina, Brazil. E-mail: paulocrm@hotmail.com, julio.normey@ufsc.br

EBSCOhost - printed on 2/14/2023 2:46 PM via . All use subject to https://www.ebsco.com/terms-of-use

MPC techniques allow for the maximization of the economic benefit of microgrids and minimization of the degradation of the storage system.

**Keywords:** Microgrid; energy hubs; model predictive control.

## Introduction

Today, and in the future, electricity generation and distribution systems need to be intelligent, renewable, and adaptable. Such requirements will direct the evolution of conventional electricity grids towards smart grids. Efficient energy generation and consumption are essential for achieving ambitious goals of sustainable development and the mitigation of air pollution and climate change [1]–[3]. Efficient and safe power distribution, together with minimized and balanced power consumption, are now an integral part of the economic activity of most developed countries. One of the biggest issues faced is how distribution networks can supply energy according to greatly varying demands. In the coming years, clean and renewable energy generation will come to the fore [4].

Conventional energy sources are limited and rapidly depleting, while the generation of electricity has risen substantially in the last few decades. This has, in turn, caused a significant increase in carbon dioxide emissions, as reported by British Petroleum in its 2017 annual report [5]. The quantity of coal, gas, and oil reserves buried deep underground or below the ocean floor remains unknown. Consequently, identifying and extracting new sources of traditional fuels is becoming ever more difficult and expensive. Furthermore, their exploitation is very dangerous with difficulties drilling below the ocean floor, or because large amounts of natural gas need to be burnt when refining oil sands. Moreover, global warming and energy crises are beginning to have a negative impact on the quality of human life [6].

In this context, the growing political consensus regarding the seriousness of the threat posed by climate change (CC) has made the transition to a low-carbon economy in Europe by 2050 an important priority for European member states. An essential step along this road is reaching the three key objectives for 2020, namely: to reduce greenhouse gas emissions (GGE) by 20%; to obtain 20% of final energy from renewable sources; and to reduce total energy consumption by 20% [7], [8]. An estimated 19.1% of global final energy consumption was sourced from renewables in 2013. This recent growth in the electricity sector has been driven primarily by wind and solar PV [5].

One of the main problems associated with these kinds of renewable energy system is their reliability and the quality of the power supply they

EBSCOhost - printed on 2/14/2023 2:46 PM via . All use subject to https://www.ebsco.com/terms-of-use

provide. As renewable sources are intermittent, unpredictable fluctuations may appear in their power output [9]. Furthermore, electrical generation from renewable sources is not subject to demand, which creates an imbalance in the system. One way to overcome this problem is to include intermediate storage, such as batteries, water pumping systems, super-capacitors, compressed air systems, fly wheels, and superconducting magnetic energy storage units, etc. [10]. This buffering capability can help reduce the idea that renewable energy is an undispatchable source, due to its inherent unpredictability and variability. The use of storage systems enables the optimization of the microgrid operating point in both islanded and connected-to-the-grid modes, making it possible to properly manage the exchange of energy with the external network.

A structural solution that has been studied in recent years involves the splitting of the electrical network into smaller self-generation units based on renewable energy, where the use of energy storage compensates for fluctuations in generation and the randomness of consumer behaviour, as is shown in [11]–[15]. The concept of the microgrid, introduced by [16], has the potential to become a powerful tool in improving the quality and reliability of the electrical system. A microgrid is defined as a hybrid system that includes several sources and storage devices to fulfil local loads [17]. According to [18], a microgrid can be seen as a set of loads, generators, and storage units whose management can be done independently, or who can be connected to the external network in a coordinated way to contribute to the stability of the whole system.

Regarding modelling, most of the algorithms proposed in the literature use very simplified models of power systems, vehicle motion, and load characteristics. In particular, the modelling framework called energy hubs [19] allows for the integration of different forms of production and storage using microgrids, vehicle to grid (V2G) systems, and the interconnection of different microgrids or a microgrid connected to an electric network.

With increasing demands placed on improving productivity and efficiency, the operational requirements of energy systems are becoming tighter. This makes it necessary to invest in the automatic operation and control of the electricity subsystems to achieve enhanced efficiency of the whole plant. It is already known that optimal operation of each subsystem in an energy plant does not necessarily lead to optimal operation of the whole system, and may possibly lead to contradictory behaviour in the system. This makes coordination between the various elements of the whole plant necessary. This is typically carried out by a supervised automatic system, which lies at an upper level in the control hierarchy of the plant. As such, the targets of each subsystem are provided by this upper level so that

EBSCOhost - printed on 2/14/2023 2:46 PM via . All use subject to https://www.ebsco.com/terms-of-use

the quality of the service is ensured and, if possible, operation close to the optimal operating point is achieved. From an efficiency point of view, the best control technique should take into account the efficient operation of each subsystem while simultaneously ensuring quality requirements are fulfilled.

In [20], the authors review the latest documents related to the use of hybrid energy storage systems (HESS), which facilitate the introduction of renewable energy sources (RES) in MGs. In [21] a summary of the approaches that are available and currently being investigated (system configuration; unit size; control and energy management) for optimal design of RES hybrid systems is presented. In general, microgrid energy management is carried out through heuristic algorithms [22], [23], although there are applications that use MPC strategies, such as those presented in [24] and [25]. Optimal control of distributed energy resources using model predictive control with a battery storage system is examined in [26]. In the case of hybrid storage systems, MPC appears to be a good solution, as shown in [27], [28] and [21].

Recent work has brought to light MPC-based control structures used to master microgrids with renewable sources: [29] describes a hydrogen-based domestic microgrid controlled by a MPC-based structure; [30] considers plug-in hybrid electric vehicles based on multi-carrier systems; and [31] proposes a MPC for energy management of a microgrid connected to an electric vehicle charging station. In terms of renewable source applications, [32] analyses wind balancing capabilities using heuristics and MPC, whereas [13] focuses on a renewable microgrid in an isolated load area. The optimization of a hybrid energy producer based on a sugar cane power plant, considering biomass, biogas, solar, and wind power as primary energy sources is discussed in [33], [34], and [35]. Comparisons of different prediction methods based on time series and neural networks to predict energy demand and production and different optimum energy distribution scenarios are provided in [36]; these can assist us in determining when short-term energy prediction models combined with model predictive control should be used. Generic MPC-based structures are seen in [37] and [38], and economic optimization is examined in [39], [40] and [41].

The objective of this chapter is to present a simulation of a case study using MPC strategies and the methodology of energy hubs to optimize the energy distribution in an agroindustrial microgrid, consisting of agricultural, processing, and input supply companies located around a particular territory. The algorithm used manages the use of renewable energy sources, storage, and the purchase and sale of electric power to the external network. The simulation was performed using real data, as well as mixed integer

EBSCOhost - printed on 2/14/2023 2:46 PM via . All use subject to https://www.ebsco.com/terms-of-use

linear programming (MILP) and mixed integer quadratic programming (MIQP). This chapter highlights the benefits of using MPC techniques in MGs, to make use of renewable energy resources and energy storage systems more efficiently. In addition, the real price of energy (€/kWh) available on the electricity market is considered.

This chapter is organized as follows. In the following section, the microgrid and the implemented methodology are presented. The next section deals with system modelling and the control algorithm; the model of the microgrid and the control formulation are presented. The results and discussions are then presented, and finally, the conclusions are outlined.

## An Agroindustrial Microgrid Case Study

The MG is integrated by a PV system—an electric vehicle in which the batteries serve as an energy storage system—and two load systems (a building and a greenhouse). Fig. 1 gives a schematic of the microgrid. Additionally, the microgrid has a connection to the utility grid allowing the purchase and sale of energy when necessary.

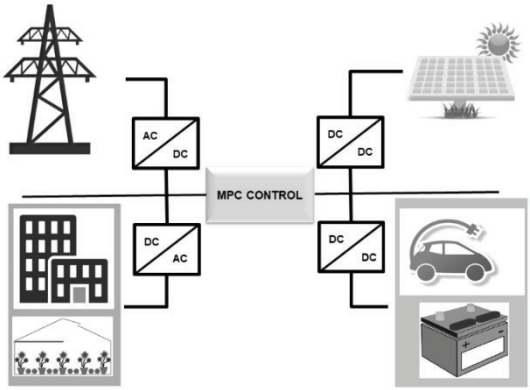



Fig. 1. Microgrid schematic.

### *Microgrid Components*

*CIESOL building*. The CDdI-CIESOL-ARFRISOL building (Fig. 2a) is a solar energy research centre located on the campus of the UAL (University of Almeria) in the southeast of Spain. It has two floors and a total surface area of 1071.92 $m^2$. It is composed of six offices, all of them with an easterly

EBSCOhost - printed on 2/14/2023 2:46 PM via . All use subject to https://www.ebsco.com/terms-of-use

orientation and located on the ground floor, with the exception of the main office which is on the upper floor; additionally, there are eight laboratories that face north (four located on the ground floor and devoted to Solar Chemistry; four are found on the upper floor, two for the Modelling and Automatic Control unit and two for the Evaluation of Solar Resources unit). There is also a plant where a high efficiency boiler and an absorption machine are located, and finally, rooms for the employees of the centre, such as the kitchen and the toilets [42].

*PV system.* The University of Almeria has installed various photovoltaic systems on its site. These can be found in the car parks, on the roofs of buildings, and around recreational/entertainment areas. The total system can generate 110 kWp, approximately ten times the output of CIESOL's photovoltaic system. The PV system placed on CIESOL's sloping roof (see Fig. 2b) has a total of four modules linked in three sets of 14 panels/series and with each having a unit capacity of 222 Wp/panel. The electrical energy produced is direct current at low voltage, which is converted to alternating current via a 230 V inverter, creating a photovoltaic field of 9.324 kWp. The inverters feed into the national grid, as is required under legislation for renewable energy source utilization in Spain. The PV system is mounted on a south-facing stainless-steel support structure and is tilted at 22º. This tilt angle maximizes yearly energy production [43].

The energy produced by all of these sets is used to supply the CIESOL building's energy demands, along with that of the greenhouses; any surplus energy can be stored in the batteries or sold to the utility grid when appropriate.

*The greenhouse.* The greenhouse studied is a greenhouse multi-span Parral-type (see Fig. 2c), with a surface area of 877 $m^2$, oriented north to south. The facilities are located on the experimental station of the Cajamar Foundation, 'Las Palmerillas,' in the municipality of El Ejido, Almeria, in the southeast of Spain [15]. Conditions in the greenhouse are controlled by lateral and overhead ventilation systems, which are powered through independent AC motors; aerothermo; a heating system with hot water pipes fed with biomass; a $CO_2$ enrichment system created by the burning of biomass; shade nets; and feeding systems for water and nutrients. It is equipped with measuring equipment that covers 52 variables and is designed to develop identification tests and to develop strategies for climate control, fertigation, and electrical power management. Furthermore, the greenhouse has programmable energy demand sensors (SINEAX M 561)

EBSCOhost - printed on 2/14/2023 2:46 PM via . All use subject to https://www.ebsco.com/terms-of-use

with RS-232 interfaces that connect to a computer with appropriate software [44]–[46].

*The electric vehicle and its batteries.* The electric vehicle's battery bank, which is utilized by the MG, consists of eight Greensaver SP210-6 batteries with lead-acid silicone technology connected in series. Figure 2d shows the electric vehicle and the batteries, while Table I shows the batteries' characteristics [47].

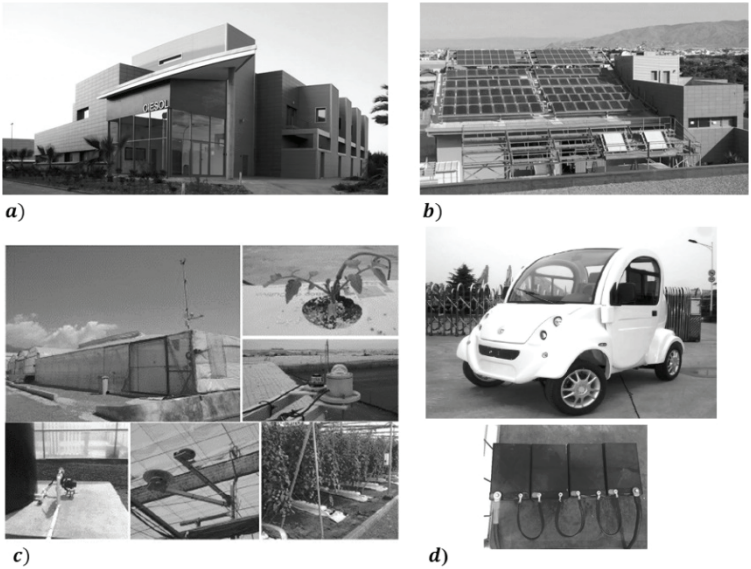



Fig. 2. a) CIESOL building, b) PV system, c) the greenhouse, and d) the electric vehicle and the batteries.

**Table I. Main characteristics of the SP210-6 battery.**

| Characteristics | Value |
|---|---|
| Height | 255 mm |
| Width | 179 mm |
| Length | 626 mm |
| Voltage | 6 V |
| Capacity | 210 Ah |

*Microgrid controller.* The MG uses a centralized controller [48] unit, which is responsible for correct process operation. The main goal of the MG

EBSCOhost - printed on 2/14/2023 2:46 PM via . All use subject to https://www.ebsco.com/terms-of-use

controller is to attend to the demand of the greenhouse and the CIESOL building, buying as little energy as possible from the main grid. The controller uses car batteries as energy storage units to optimize energy use during the day.

## *Microgrid Modelling Framework*

The methodology of energy hubs examined in this chapter has previously been described in [20] and [49]. An energy hub is defined as an interface between energy production, consumers, and the transmission line [49]. From the point of view of the energy system, a hub can be identified as a unit that provides the following features: (1) power input and output; (2) energy conversion; (3) and energy storage. Some of the main features of a hub are:

- Within energy hubs, losses occur only in converter and storage elements.
- If not mentioned explicitly, unidirectional power flow from the inputs to the outputs of the converters should be assumed.
- Power flow through converter devices is characterized by power and energy efficiency only, no other quantities are used.

This methodology is summarized as follows: a single converter converts, at time instant $k$, a generic $r$ input flow $u_r^L(k)$ of a generic hub in a $p$ output flow $y_p(k)$, where superscript $L$ is associated with converter input flows. Input-output conversion is defined through the so-called coupling factors $\gamma_{p,r}^L$ which correspond to a converter's steady-state conversion efficiency between input and output flows:

$$\mathrm{y_p(k)} = \gamma_{\mathrm{p,r}}^{\mathrm{L}} \mathrm{u_r^L(k)} \tag{1}$$

With several converters, (1) can be written as follows:

$$\underbrace{\begin{bmatrix} \mathrm{y_1(k)} \\ \vdots \\ \mathrm{y_{n_p}(k)} \end{bmatrix}}_{\mathrm{y_i(k)}} = \underbrace{\begin{bmatrix} \gamma_{1,1}^{\mathrm{L}} & \cdots & \gamma_{1,n_r}^{\mathrm{L}} \\ \vdots & \ddots & \vdots \\ \gamma_{n_p,1}^{\mathrm{L}} & \cdots & \gamma_{n_p,n_r}^{\mathrm{L}} \end{bmatrix}}_{\Gamma_{\mathrm{i}}^{\mathrm{L}}} \underbrace{\begin{bmatrix} \mathrm{u_1(k)} \\ \vdots \\ \mathrm{u_{n_r}(k)} \end{bmatrix}}_{\mathrm{u_i^L}} \tag{2}$$

where $\Gamma_i^L$ is the converter coupling matrix.

EBSCOhost - printed on 2/14/2023 2:46 PM via . All use subject to https://www.ebsco.com/terms-of-use

Following this formulation, and from a discrete-time point of view, internal storage state $x_{i,s}$ at sampling time $k+1$ depends on the state at previous sample $k$ and on the total exchanged flow $\breve{u}_{i,s}^{E}(k)$ during the period $\Delta T$ ranging between $k$ and $k+1$, where the values of the input-output flow steady state are described by the relation:

$$\breve{U}_{I,S}^{E}(k) = e_{I,S}(k)u_{I,S}^{E}(k) \tag{3}$$

where $\boldsymbol{e_{i,s}(k)}$ is the efficiency of the $(\boldsymbol{i,s})$ interface charging/discharging hub, which describes the energy exchange between the system and the storage. This factor depends on the direction of flow exchanged as follows:

$$\boldsymbol{e_{i,s}} = \begin{cases} \boldsymbol{e_{i,s}^{+},\ if\ u_{i,s}^{E} \geq 0\ (charging)} \\ \boldsymbol{e_{i,s}^{-},\ othercase\ (discharging)} \end{cases} \tag{4}$$

where $\boldsymbol{e_{i,s}^{+}}$ and $\boldsymbol{e_{i,s}^{-}}$ are the charging and discharging efficiency, respectively ([21], [50]). Assuming $\boldsymbol{\breve{u}_{i,s}^{E}(k)}$ to remain constant during $\boldsymbol{\Delta T}$:

$$x_{i,s}(k+1) = x_{i,s}(k) + \int_{k}^{k+1} \breve{u}_{i,s}^{E}(t)dt = x_{i,s}(k) + \breve{u}_{i,s}^{E}(k)^{k}\Delta T \tag{5}$$

If several storage systems are considered:

$$\underbrace{\begin{bmatrix} x_{i,1}(k+1) \\ \vdots \\ x_{i,n_s}(k+1) \end{bmatrix}}_{x_i(k+1)} = \underbrace{\begin{bmatrix} x_{i,1}(k) \\ \vdots \\ x_{i,n_s}(k) \end{bmatrix}}_{x_i(k)} + \underbrace{\begin{bmatrix} e_{i,1}(k) & & \\ & \ddots & \\ & & e_{i,n_s}(k) \end{bmatrix}}_{\Lambda_i^E(k)} \underbrace{\begin{bmatrix} \breve{u}_{i,1}^{E}(k) \\ \vdots \\ \breve{u}_{i,n_s}^{E}(k) \end{bmatrix}}_{\breve{u}_i^E(k)} \tag{6}$$

Then, a simple hub can be represented by the following condensed form:

$$\begin{aligned} x_i(k+1) &= x_i(k) + \Lambda_i^E(k)u_i^E(k) \\ y_i(k) &= \Gamma_i^L u_i^L(k) \end{aligned} \tag{7}$$

## System modelling and control algorithm

This section describes the modelling of the plant and the controller used.

EBSCOhost - printed on 2/14/2023 2:46 PM via . All use subject to https://www.ebsco.com/terms-of-use

### *Microgrid Model*

The plant model consists of two parts: following equation (5), the evolution of the variable state ($SOC_{BAT}$) of the microgrid is described by the linear model:

$$SOC_{BAT}(k+1) = SOC_{BAT}(k) + \frac{(\eta_{BAT_{CH}} \cdot P_{BAT_{CH}}(k) + \eta_{BAT_{DISCH}} \cdot P_{BAT_{DISCH}}(k))\, T_s}{C_{BAT}} \quad (8)$$

where $\eta_{BAT_{CH}}$ and $\eta_{BAT_{DISCH}}$ are the efficiency of charge and discharge of the battery, respectively, and $T_s$ is the sample time; $C_{BAT}$ is the battery capacity; $P_{BAT_{CH}}(k)$ and $P_{BAT_{DISCH}}(k)$ are the charge and discharge power of batteries at time $t = k$ and $SOC_{BAT}$ is the state of charge of the batteries.

Moreover, remaining power at time $t = k$ of subsystems that integrate MGs as follows:

$$P_{rem}(k) = P_{pv}(k) - (P_{CIE}(k) + P_{gh}(k)) \quad (9)$$

where $P_{pv}(k)$, $P_{CIE}(k)$, and $P_{gh}(k)$ are the energy production of the PV system and the energy demand of the CIESOL building and the greenhouses, which comprise a hectare of land. The input vector to the MG is defined according to:

$$u = [P_{solar} \quad P_{GridPurch} \quad P_{GridSale} \quad P_{BAT_{CH}} \quad P_{BAT_{DISCH}}]^T \quad (10)$$

where $P_{solar}$ is the generated solar power, $P_{GridPurch}$ and $P_{GridSale}$ are the purchase and sale of energy to the utility grid. Fig. 3 shows the proposed control diagram.

Therefore, the MG can be modeled in a condensed form as a single hub:

$$\begin{aligned} x(k+1) &= Ax(k) + \Lambda u(k) \\ y(k) &= \Gamma u(k) \end{aligned} \quad (11)$$

EBSCOhost - printed on 2/14/2023 2:46 PM via . All use subject to https://www.ebsco.com/terms-of-use

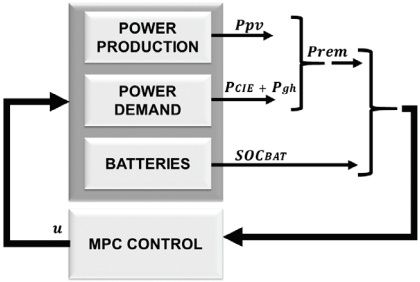



Fig. 3. Proposed control diagram.

where:

$$A = [1] \tag{12}$$

$$\Lambda = \begin{bmatrix} 0 & 0 & 0 & \frac{\eta_{BAT_{CH}}}{C_{BAT}} & \frac{\eta_{BAT_{DISCH}}}{C_{BAT}} \end{bmatrix} \tag{13}$$

$$\Gamma = [\eta_{solar} \quad 1 \quad -1 \quad -1 \quad -1] \tag{14}$$

and $\eta_{solar}$ is the conversion efficiency of solar energy.

## *Controller*

The controller is designed for economic optimization of the microgrid and to sensibly manage battery usage by determining the exact loading time. The MPC cost function is given by:

$$J = \sum_{l=0}^{N_p-1}\left(\tilde{u}(k+l)^T Q_u \tilde{u}(k+l) + f^T \tilde{u}(k+l)\right) + \sum_{l=0}^{N_p-1}\left(\tilde{x}(k+l) - \tilde{x}_{ref}(k+l)\right)^T Q_x \left(\tilde{x}(k+l) - \tilde{x}_{ref}(k+l)\right) \tag{15}$$

s.t.

$$\underline{x} \leq \tilde{x}(k+l+1) \leq \overline{x} \tag{16}$$

$$\underline{u} \leq \tilde{u}(k+l+1) \leq \overline{u} \tag{17}$$

$$\tilde{y}(k+l) = P_{CIE}(k) + P_{gh}(k) \tag{18}$$

$$\widetilde{u(1)}(k+l) = P_{solar}(k) \tag{19}$$

$$x(k) = \check{x}(k) \tag{20}$$

for $l = 0, \ldots, N_p - 1$. Where $Q_u$ and $Q_u$ are positive definite weighting matrices, $f$ is a linear function, and $N_p$ is the prediction horizon. Regarding notation, "$\tilde{a}$" over variables is used to denote variables over the prediction horizon, while $\underline{a_i}$ and $\overline{a_i}$ denote the minimum and maximum allowed values, respectively. $\check{a}_i$ refers to variables the values of which are supposed to be

EBSCOhost - printed on 2/14/2023 2:46 PM via . All use subject to https://www.ebsco.com/terms-of-use

known, for example, initial conditions, as can be seen in equation (20) where the initial state of charge of the batteries is assumed. Equation (19) means that the controller is forced to use all the energy that the PV system provides.

Binary variables are introduced to the formula as constraints to ensure the proper use of the renewable energy sources, to manage electricity purchase and sale from and to the external network, and to utilize the storage to minimize oscillations between production and demand. The binary variables are:

$$\delta_{GridPurch}(k) = \begin{cases} 1 & P_{GridPurch}(k) > 0 \\ 0 & P_{GridPurch}(k) = 0 \end{cases} \tag{21}$$

$$\delta_{GridSale}(k) = \begin{cases} 1 & P_{GridSale}(k) > 0 \\ 0 & P_{GridSale}(k) = 0 \end{cases} \tag{22}$$

$$\delta_{GridPurch}(k) + \delta_{GridSale}(k) = 1 \tag{23}$$

$$\delta_{BAT_{CH}}(k) = \begin{cases} 1 & P_{BAT_{CH}}(k) > 0 \\ 0 & P_{BAT_{CH}}(k) = 0 \end{cases} \tag{24}$$

$$\delta_{BAT_{DISCH}}(k) = \begin{cases} 1 & P_{BAT_{DISCH}}(k) < 0 \\ 0 & P_{BAT_{DISCH}}(k) = 0 \end{cases} \tag{25}$$

$$\delta_{BAT_{CH}}(k) + \delta_{BAT_{DISCH}}(k) = 1 \tag{26}$$

The state space formulation of a hub has been transformed into the mixed logical dynamic (MLD) formulation, considering the concepts of propositional calculus and integer linear programming, as shown in [51]. This formulation makes it possible to include binary variables introduced in a discrete-time dynamic system in order to describe, in a unified model, the evolution of the continuous and logic signals of the system. The conditions $P_{GridPurch}(k) > 0$; $P_{GridSale}(k) > 0$; and $P_{BAT_{CH}}(k) > 0$ in equations (21), (22), and (24); and the condition $P_{BAT_{DISCH}} < 0$ in equation (25) can be associated to the binary variables $\delta_{GridPurch}$; $\delta_{GridSale}$; $\delta_{BAT_{CH}}$; and $\delta_{BAT_{DISCH}}$, respectively, so that:

$$\begin{gathered} [P_{GridPurch}(k) > 0] \rightarrow [\delta_{GridPurch}(k) = 1] \\ [P_{GridSale}(k) > 0] \rightarrow [\delta_{GridSale}(k) = 1] \\ \left[P_{BAT_{CH}}(k) > 0\right] \rightarrow \left[\delta_{BAT_{CH}}(k) = 1\right] \\ \left[P_{BAT_{DISCH}}(k) < 0\right] \rightarrow \left[\delta_{BAT_{DISCH}}(k) = 1\right] \end{gathered} \tag{27}$$

Relations (27) can be expressed by the inequalities:

EBSCOhost - printed on 2/14/2023 2:46 PM via . All use subject to https://www.ebsco.com/terms-of-use

$$\begin{gathered}(M_1+\epsilon)\delta_{GridPurch}(k)-P_{GridPurch}\delta_{GridPurch}(k)>0\\(M_2+\epsilon)\delta_{GridSale}(k)-P_{GridSale}\delta_{GridSale}(k)>0\\(M_3+\epsilon)\delta_{BAT_{CH}}(k)-P_{BAT_{DISCH}}\delta_{BAT_{CH}}(k)>0\\(m+\epsilon)\delta_{BAT_{DISCH}}(k)-P_{BAT_{DISCH}}\delta_{BAT_{DISCH}}(k)<0\end{gathered} \tag{28}$$

where:

$$\begin{gathered}M_1=\max_{k\in\mathbb{R}}P_{GridPurch}(k)\\M_2=\max_{k\in\mathbb{R}}P_{GridSale}(k)\\M_3=\max_{k\in\mathbb{R}}P_{BAT_{CH}}(k)\\m=\min_{k\in\mathbb{R}}P_{BAT_{DISCH}}(k)\end{gathered} \tag{29}$$

and $\epsilon$ is a small tolerance (typically the machine precision).

In equation (21), if $P_{GridPurch}(k)>0$ then $\delta_{GridPurch}(k)=1$, meaning that the energy is purchased from the grid and so the weight is used on the purchased value. In (22), if $P_{GridSale}(k)>0$ this implies $\delta_{GridSale}(k)=1$, which means that it is used on the value of sale. Analogous analysis is performed for equations (24) and (25). Furthermore, equations (23) and (26) are associated to the exclusive sum (exclusive or), such that

$$\begin{gathered}[P_{GridPurch}(k)\oplus P_{GridSale}(k)]\\\left[P_{BAT_{CH}}(k)\oplus P_{BAT_{DISCH}}(k)\right]\end{gathered} \tag{30}$$

This means only one action can be performed at any one time—purchasing or selling energy and charging or discharging battery energy—furthermore, doing neither is not possible.

Additionally, the economic aspects of buying and selling energy have been considered in the objective function (15). The cost of energy exchange with the utility grid is given by the price of energy in the daily market, which is different for purchase and sale. The sale of power to the utility grid and the purchase of power from the utility grid are defined by the variables $P_{GridSale}$ and $P_{GridPurch}$ respectively. Thus, the proposed cost function is given by:

$$\begin{aligned}J=\sum_{l=0}^{N_p-1}\big(&-\Upsilon_{sale}(k+l)\cdot P_{GridSale}(k+l)+\Upsilon_{Purch}(k+l)\cdot\\&P_{GridPurch}(k+l)\big)\cdot T_s\end{aligned} \tag{31}$$

EBSCOhost - printed on 2/14/2023 2:46 PM via . All use subject to https://www.ebsco.com/terms-of-use

for $l = 0, \ldots, N_p - 1$. Where $\Upsilon_{sale}$ and $\Upsilon_{Purch}$ are the purchase and sale price of energy, respectively.

## Results and Discussion

In order to illustrate the benefits of using renewable energies and storage systems, as well as MPC for optimal economic dispatch energy distribution, two different cases using MILP-MPC and MIQP-MPC were studied.

1. Case 1. A 2-day economic analysis was carried out. One sunny day and one day that had clouds in the morning and part of the afternoon were evaluated. The initial state of charge of the batteries was assumed to be 60%, with 50% being the desirable setpoint, allowing for fluctuations.
2. Case 2. To perform the second analysis, the same days as in case 1 were considered. For this analysis, an initial state of charge for the batteries of 80% was considered. An attempt was made to maintain the batteries at 50% throughout the day, allowing for fluctuations, as well as trying to reach an end of day battery charge state of 80%.

The rest of the conditions considered are described in each case.

*Case 1. A simulation for a sunny day and a day with passing clouds with an initial $SOC_{BAT}$ of 60%.*

The results presented below were simulated in accordance with the following conditions:

- The simulation used real data collected for a sunny day and a day with passing clouds.
- Two similar sets of batteries and 10 similar greenhouses, such as those presented in the "Agroindustrial Microgrid Case Study" section, were considered.
- The battery degradation cost and the maintenance cost of the photovoltaic system were not considered.
- The cost function weights in equation (15) were adjusted using simulations.
- The first term in equation (15) was used for renewable sources management and for the purchase/sale of energy from the grid. The matrix of weights $Q_u$ and the function $f$ were tuned according to the price of energy to minimize storage system use. The second term of

EBSCOhost - printed on 2/14/2023 2:46 PM via . All use subject to https://www.ebsco.com/terms-of-use

the objective function in equation (15), $Q_x$, was tuned to keep the storage load at around 50% allowing deviations from this value when there was a need to store more energy or use the stored energy; the minimum charge state allowed in the batteries was 30%. An initial state of charge in the batteries of 60% was considered.

- The controller was implemented in MATLAB [52] using the YALMIP [53] toolbox and the CPLEX solver [54].
- The quadratic term of the cost function in equation (15) was taken as zero in order to perform the MILP optimization.

Figures 4 and 5 show the results for the sunny day. The amount of solar energy available, as well as the amount of energy used to charge the batteries and the amount of energy obtained from their discharge, was observed (see Fig. 4a and 5a). In addition, the energy flow between the microgrid and the utility grid is shown for the sunny day using MIQP-MPC and MILP-MPC, respectively. These figures show that energy was allowed to be sold for between 10 and 15 hours; this was due to a surplus of energy and because the batteries were charged to around the reference level.

Furthermore, Figs. 4b and 5b show the SOC of the batteries—the controller tended to maintain the amount of stored energy at 50% allowing fluctuations at times when there was not enough renewable energy to meet demand. Moreover, it can be seen that for the optimal distribution of energy using MILP-MPC, the changes in battery charging and discharging were more abrupt and more frequent than those made using MIQP-MPC. These sudden changes lead to increased wear on the batteries.

Regarding the day with passing clouds (see Fig. 6 and 7), it can be observed that during the periods 11:00-13:00 and 14:00-15:00, an energy sale was made using MIQP-MPC (Fig. 6a); this occurred because of an excess of energy during those hours. For the periods 11:00-12:00 and 14:00-15:00 using MILP-MPC (Fig. 7a) there was also an energy sale due to a surplus of energy. The state of charge of the batteries is shown in Fig. 6b and 7b for MIQP-MPC and MILP-MPC, respectively. As with the sunny day case study, changes in battery charging and discharging were more sudden when using MILP-MPC.

Table II presents a comparison between the rule-based controllers, MILP-MPC, and MIQP-MPC, considering the sunny and cloudy day scenarios. The rule-based controller does not use the batteries and all differences between the demand and the energy generated by the PV system is supplied or absorbed by the utility grid. When using both MPCs, the battery was also taken into account.

EBSCOhost - printed on 2/14/2023 2:46 PM via . All use subject to https://www.ebsco.com/terms-of-use

Table II shows the total energy exchange with the utility grid, as well as the cost and profit of the purchase and sale. The MIQP-MPC algorithm made the lowest energy purchase for both days (approximately 40 kWh lower on a completely sunny and 50 kWh lower on a cloudy day).

The total gross cost (total cost of purchase - benefit of sale) for the sunny day using MIQP-MPC was 125.62 €; using MILP-MPC it was 127.02 €. This compares well with the 129.46 € of the rule-based controller.

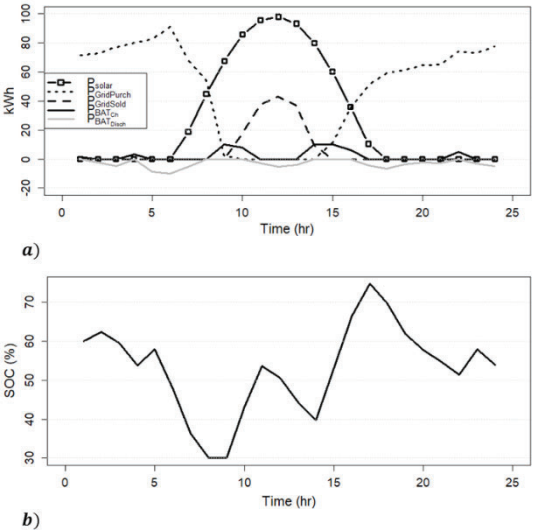
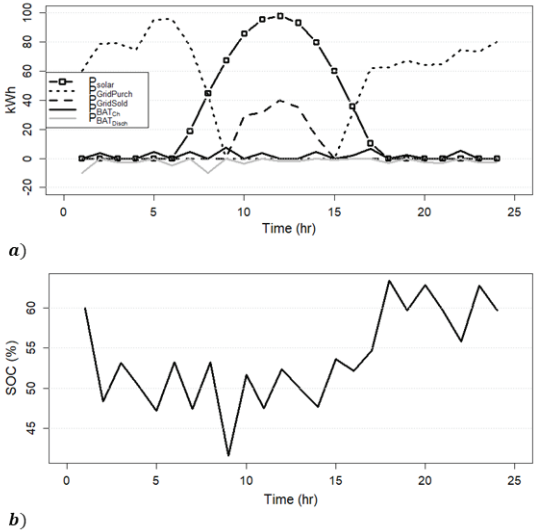



Fig. 4. Sunny day for case 1 using MIQP-MPC. a) Economical dispatch. b) State of charge of the batteries.

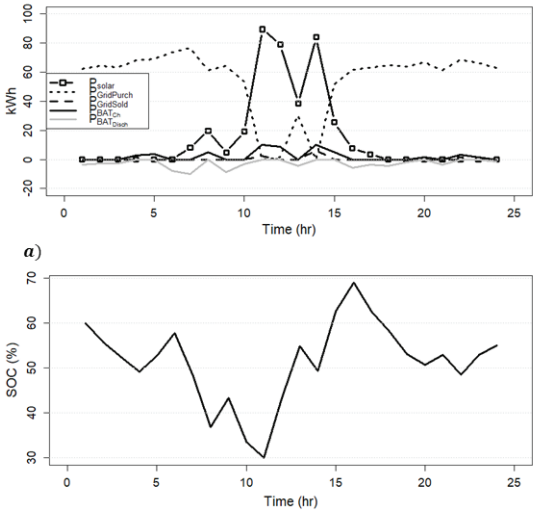
EBSCOhost - printed on 2/14/2023 2:46 PM via . All use subject to https://www.ebsco.com/terms-of-use




***a***)

***b***)

Fig. 5. Sunny day for case 1 using MILP-MPC. a) Economical dispatch. b) State of charge of the batteries.




***a***)

***b***)

Fig. 6. Day with passing clouds for case 1 using MIQP-MPC. a) Economical dispatch. b) State of charge of the batteries.

EBSCOhost - printed on 2/14/2023 2:46 PM via . All use subject to https://www.ebsco.com/terms-of-use

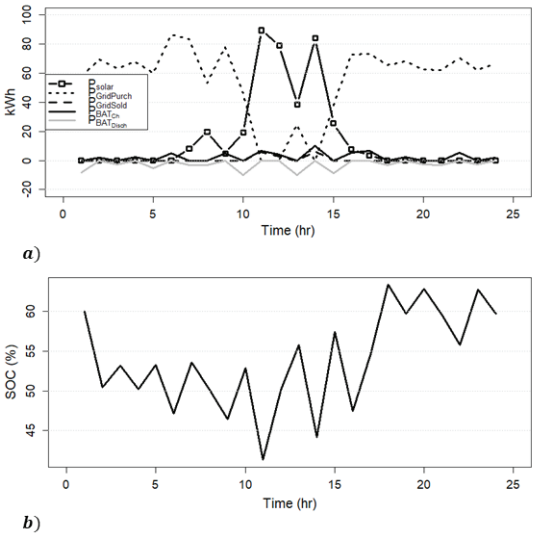



Fig. 7. Day with passing clouds for case 1 using MILP-MPC. a) Economical dispatch. b) State of charge of the batteries.

**Table II. Power energy (kWh) exchanged with the utility grid for case 1.**

| Scenario | Controller | Total kWh Purchased | Total Cost (€) of Purchase | Total kWh Sold | Benefit (€) of Sale |
|---|---|---|---|---|---|
| Sunny day | Rule-based | 1201.80 | 138.43 | 158.32 | 8.97 |
| | MILP-MPC | 1176.16 | 135.51 | 150.26 | 8.49 |
| | MIQP-MPC | 1163.15 | 133.79 | 144.68 | 8.17 |
| Cloudy day | Rule-based | 1357.34 | 157.04 | 35.49 | 1.99 |
| | MILP-MPC | 1322.16 | 153.08 | 14.62 | 0.82 |
| | MIQP-MPC | 1308.38 | 151.25 | 8.28 | 0.46 |

Moreover, for the cloudy day the gross cost was 150.79 € for the MIQP-MPC; 152.26 € for the MILP-MPC; and 155.05 € for the rule-based controller. There were savings of approximately 3.9 € and 4.3 € using MIQP-MPC on a sunny day and a cloudy day, respectively. Under the simulated conditions, this generates savings of 2.96% using MIQP-MPC, and 1.88% using MILP-MPC for the sunny day. For the cloudy day, savings of 2.74% and 1.74% for the MIQP-MPC and the MILP-MPC, respectively, were seen.

EBSCOhost - printed on 2/14/2023 2:46 PM via . All use subject to https://www.ebsco.com/terms-of-use

*Case 2. A simulation for a sunny day and a day with passing clouds and an initial $SOC_{BAT}$ of 80%.*

Figures 8a and 9a show the evolution of the PV, batteries, and utility grid energy during both scenarios. In the case of the sunny day, Fig. 8a, it can be seen that energy was allowed to be sold for between 10 and 15 hours using MIQP-MPC and MILP-MPC. In addition, Figs. 8b (for MIQP-MPC) and 9b (for MILP-MPC) show the SOC of the batteries. It can be seen that during the day, the SOC stayed at around 50%, allowing for fluctuations. In the final hours of the day, the state of charge increased towards 80%. Furthermore, it was possible to observe that for the optimal distribution of energy using MILP-MPC, the changes in the batteries' charge and discharge were more abrupt and more frequent than those obtained with the MIQP-MPC.

For the day with passing clouds, during the periods 11:00-12:00 and 14:00-15:00 using MIQP-MPC (Fig. 10a) there was a sale of energy because of a surplus. In Fig. 11a, we can see that while using MILP-MPC, in the periods 11:00-13:00 and 14:00-15:00, a sale of energy was made.

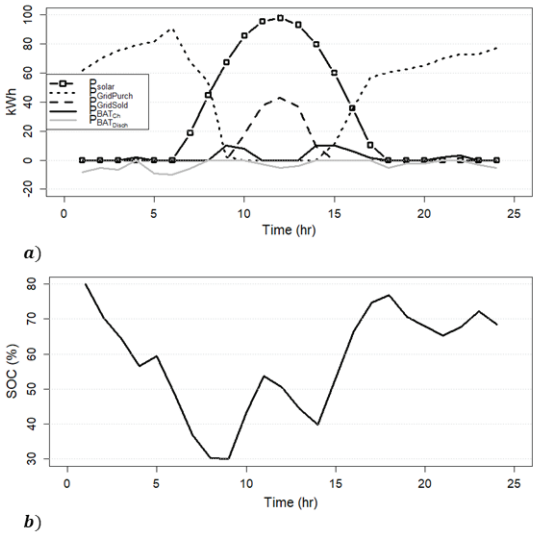



Fig. 8. Sunny day for case 2 using MIQP-MPC. a) Economical dispatch. b) State of charge of the batteries.

EBSCOhost - printed on 2/14/2023 2:46 PM via . All use subject to https://www.ebsco.com/terms-of-use

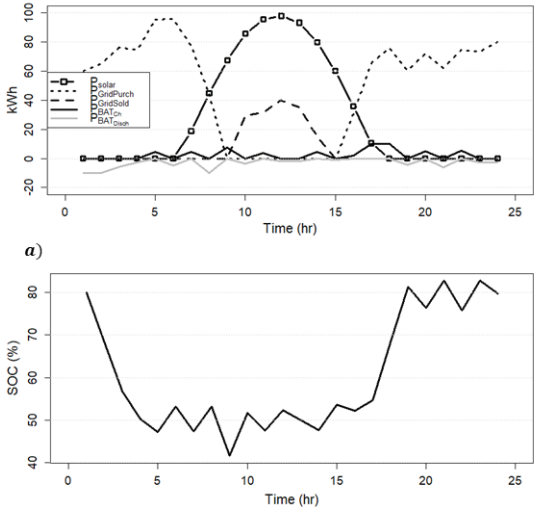



Fig. 9. Sunny day for case 2 using MILP-MPC. a) Economical dispatch. b) State of charge of the batteries.

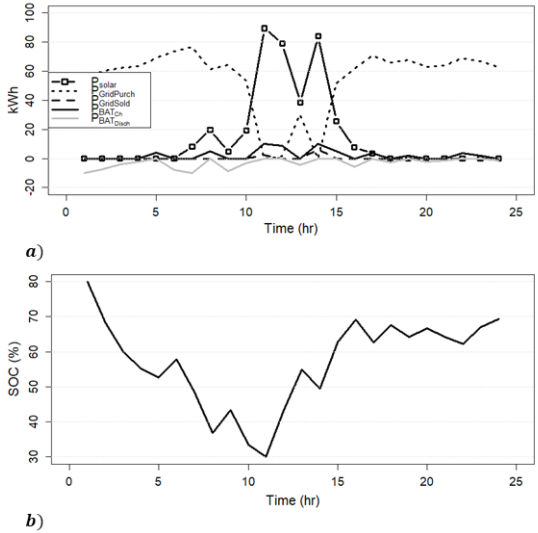



Fig. 10. Day with passing clouds for case 2 using MIQP-MPC. a) Economical dispatch. b) State of charge of the batteries.

EBSCOhost - printed on 2/14/2023 2:46 PM via . All use subject to https://www.ebsco.com/terms-of-use

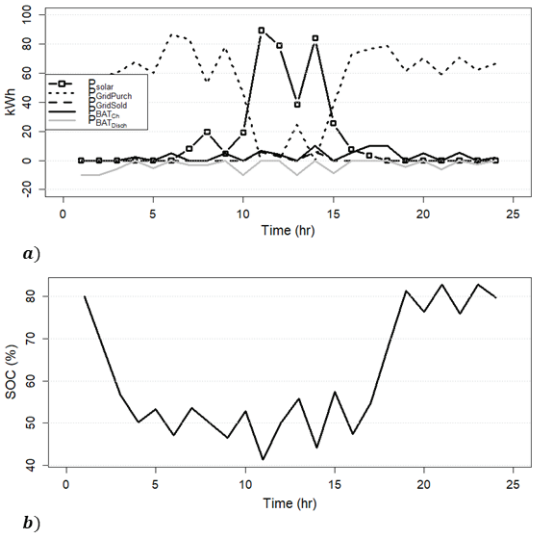



Fig. 11. Day with passing clouds for case 2 using MILP-MPC. a) Economical dispatch. b) State of charge of the batteries.

The state of charge of the batteries on the sunny day is shown in Fig. 10b and 11b for MIQP-MPC and MILP-MPC, respectively. It can be seen that during the day, maintenance of the battery charge at 50% was attempted, allowing for fluctuations. In the final hours of the day, the state of charge tended towards 80%.

A comparison between the rule-based controller, MILP-MPC, and MIQP-MPC, considering the sunny and the cloudy day scenarios, is presented in Table III. The total energy exchanged with the utility grid, and the cost and profit of the purchase and sale are shown in Table III. As in case 1, the MIQP-MPC algorithm is the one that saw the lowest purchase of energy for both days. Compared to the rule-based controller, the MIQP-MPC purchased 36.23 kWh and 45.43 kWh less, for the sunny and cloudy days respectively.

The differences compared to case 1 were minimal. In this case, using MIQP-MPC on the sunny day generated a saving in the total gross cost of 3.26 €; this was 1.34 € using MILP-MPC. Consequently, MIQP-MPC saw a saving of 2.51% and MILP-MPC one of 1.03%. The total saving for the cloudy day was 3.54 € for MIQP-MPC and 1.72 € for MILP-MPC. This was a saving of 2.28% using MIQP-MPC and 1.10% using MILP-MPC.

EBSCOhost - printed on 2/14/2023 2:46 PM via . All use subject to https://www.ebsco.com/terms-of-use

**Table III. Power energy (kWh) exchanged with the utility grid for case 2.**

| Scenario | Controller | Total kWh Purchased | Total Cost (€) of Purchase | Total kWh Sold | Benefit (€) of Sale |
|---|---|---|---|---|---|
| Sunny day | Rule-based | 1201.80 | 138.43 | 158.32 | 8.97 |
| | MILP-MPC | 1182.71 | 136.61 | 150.26 | 8.49 |
| | MIQP-MPC | 1165.57 | 134.37 | 144.86 | 8.17 |
| Cloudy day | Rule-based | 1357.34 | 157.04 | 35.49 | 1.99 |
| | MILP-MPC | 1328.48 | 154.15 | 14.62 | 0.82 |
| | MIQP-MPC | 1311.91 | 151.97 | 8.28 | 0.46 |

## Conclusions and future work

The control strategy performed its stated goal of economic optimization satisfactorily in terms of aspects such as the purchase and sale of kWh that were considered, along with various optimization strategies (MILP-MPC and MIQP-MPC) related to the behavior of the storage system, the cost benefit (in €), and the distribution of energy. Two different cases were studied. In case 1, observations were made on a sunny day and a day with passing clouds—the initial state of the batteries was assumed to be 60% and they were maintained throughout the day at 50%, allowing for fluctuations. In case 2, the same days were considered as in case 1, but with an initial state of charge of the batteries of 80%. A load state of 50% was maintained throughout the day and in the final hours of the day an attempt was made to increase this to 80%. For both cases, the best results were obtained using MIQP-MPC, which achieved savings of approximately 3%. It also made better use of the batteries displaying smooth changes between charging and discharging.

In the future, research on using alternative energies, such as the thermal energy produced from the burning of biomass in the greenhouse, and adding storage systems, such as thermal energy storage, will be carried out. This will increase the complexity of the operation and energy distribution of the MG. With respect to the energy management strategy, demand response techniques and stochastic programming can be utilized in order to give

EBSCOhost - printed on 2/14/2023 2:46 PM via . All use subject to https://www.ebsco.com/terms-of-use

greater freedom to the energy management system and to deal with the fluctuations of renewable energy sources.

## Acknowledgement

This work has been funded by the National R+D+I Plan Project DPI2017-85007-R of the Spanish Ministry of Economy and Competitiveness and the ERDF.

Julio E. Normey-Rico thanks CNPq Brazil, projects 401126/2014-5 and 305785/2015-0.

## References

[1] T. B. Johansson and L. Burnham, *Renewable energy: sources for fuels and electricity*. Island Press, 1993.

[2] S. Shafiee and E. Topal, "A long-term view of worldwide fossil fuel prices," *Appl. Energy*, vol. 87, no. 3, pp. 988–1000, Mar. 2010.

[3] S. Shafiee and E. Topal, "When will fossil fuel reserves be diminished?" *Energy Policy*, vol. 37, no. 1, pp. 181–189, Jan. 2009.

[4] H. Jiayi, J. Chuanwen, and X. Rong, "A review on distributed energy resources and MicroGrid," *Renew. Sustain. Energy Rev.*, vol. 12, no. 9, pp. 2472–2483, 2008.

[5] BP, "BP Statistical Review of World Energy," 2017.

[6] M. Pacesila, S. G. Burcea, and S. E. Colesca, "Analysis of renewable energies in European Union," *Renew. Sustain. Energy Rev.*, vol. 56, pp. 156–170, 2016.

[7] "Reducción de los gases de efecto invernadero: hoja de ruta en 2050." [Online]. Available: http://eur-lex.europa.eu/legal-content/ES/TXT/?uri=URISERV:em0045. [Accessed: 26-Jul-2017].

[8] EU, "Directive 2009/29/EC of the European Parliament and of the Council of 23 April 2009 amending Directive 2003/87/EC so as to improve and extend the greenhouse gas emission allowance trading scheme of the Community."

[9] D. Anderson and M. Leach, "Harvesting and redistributing renewable energy: on the role of gas and electricity grids to overcome intermittency through the generation and storage of hydrogen," *Energy Policy*, vol. 32, no. 14, pp. 1603–1614, Sep. 2004.

[10] R. Dell and D. A. Rand, "Energy storage — a key technology for global energy sustainability," *J. Power Sources*, vol. 100, no. 1–2, pp. 2–17, Nov. 2001.

[11] A. Karabiber, C. Keles, A. Kaygusuz, and B. B. Alagoz, "An approach for the integration of renewable distributed generation in hybrid DC/AC microgrids," *Renew. Energy*, vol. 52, pp. 251–259, 2013.

[12] M. S. Carmeli, F. Castelli-Dezza, M. Mauri, G. Marchegiani, and D. Rosati, "Control strategies and configurations of hybrid distributed generation systems," *Renew. Energy*, vol. 41, pp. 294–305, May 2012.

[13] H. Morais, P. Kádár, P. Faria, Z. A. Vale, and H. M. Khodr, "Optimal

EBSCOhost - printed on 2/14/2023 2:46 PM via . All use subject to https://www.ebsco.com/terms-of-use

scheduling of a renewable micro-grid in an isolated load area using mixed-integer linear programming," *Renew. Energy*, vol. 35, no. 1, pp. 151–156, Jan. 2010.

[14] E. Dursun and O. Kilic, "Comparative evaluation of different power management strategies of a stand-alone PV/Wind/PEMFC hybrid power system," *Int. J. Electr. Power Energy Syst.*, vol. 34, no. 1, pp. 81–89, Jan. 2012.

[15] B. Indu Rani, G. Saravana Ilango, and C. Nagamani, "Power flow management algorithm for photovoltaic systems feeding DC/AC loads," *Renew. Energy*, vol. 43, pp. 267–275, Jul. 2012.

[16] R. H. Lasseter, "Microgrids," in *Power Engineering Society Winter Meeting, 2002. IEEE*, 2002, vol. 1, pp. 305–308.

[17] Q. Fu, A. Hamidi, A. Nasiri, V. Bhavaraju, S. B. Krstic, and P. Theisen, "The Role of Energy Storage in a Microgrid Concept: Examining the opportunities and promise of microgrids," *IEEE Electrif. Mag.*, vol. 1, no. 2, pp. 21–29, Dec. 2013.

[18] D. E. Olivares *et al.*, "Trends in Microgrid Control," *IEEE Trans. Smart Grid*, vol. 5, no. 4, pp. 1905–1919, Jul. 2014.

[19] M. Geidl, G. Koeppel, P. Favre-Perrod, B. Klockl, G. Andersson, and K. Frohlich, "Energy hubs for the future," *IEEE Power Energy Mag.*, vol. 5, no. 1, pp. 24–30, 2007.

[20] M. Geidl and G. Andersson, "A modeling and optimization approach for multiple energy carrier power flow," in *2005 IEEE Russia Power Tech*, 2005, pp. 1–7.

[21] P. R. da C. Mendes, J. E. Normey-Rico, and C. B. Alba, "Economic energy management of a microgrid including electric vehicles," in *2015 IEEE PES Innovative Smart Grid Technologies Latin America (ISGT LATAM)*, 2015, pp. 869–874.

[22] M. H. Nehrir *et al.*, "A Review of Hybrid Renewable/Alternative Energy Systems for Electric Power Generation: Configurations, Control, and Applications," *IEEE Trans. Sustain. Energy*, vol. 2, no. 4, pp. 392–403, Oct. 2011.

[23] W. Gu, Z. Wu, and X. Yuan, "Microgrid economic optimal operation of the combined heat and power system with renewable energy," in *IEEE PES General Meeting*, 2010, pp. 1–6.

[24] G. Ferrari-Trecate, E. Gallestey, P. Letizia, M. Spedicato, M. Morari, and M. Antoine, "Modeling and Control of Co-Generation Power Plants: A Hybrid System Approach," *IEEE Trans. Control Syst. Technol.*, vol. 12, no. 5, pp. 694–705, Sep. 2004.

[25] L. Valverde, C. Bordons, and F. Rosa, "Power management using model predictive control in a hydrogen-based microgrid," in *IECON 2012 - 38th Annual Conference on IEEE Industrial Electronics Society*, 2012, pp. 5669–5676.

[26] R. R. Negenborn, M. Houwing, B. De Schutter, and J. Hellendoorn, "Model predictive control for residential energy resources using a mixed-logical dynamic model," in *2009 International Conference on Networking, Sensing*

EBSCOhost - printed on 2/14/2023 2:46 PM via . All use subject to https://www.ebsco.com/terms-of-use

*and Control*, 2009, pp. 702–707.

[27] A. J. del Real, A. Arce, and C. Bordons, "Hybrid model predictive control of a two-generator power plant integrating photovoltaic panels and a fuel cell," in *2007 46th IEEE Conference on Decision and Control*, 2007, pp. 5447–5452.

[28] L. Valverde, C. Bordons, and F. Rosa, "Integration of fuel cell technologies in renewable-energy-based microgrids optimizing operational costs and durability," *IEEE Trans. Ind. Electron.*, vol. 63, no. 1, pp. 167–177, 2016.

[29] L. Valverde, F. Rosa, and C. Bordons, "Design, Planning and Management of a Hydrogen-Based Microgrid," *IEEE Trans. Ind. Informatics*, vol. 9, no. 3, pp. 1398–1404, Aug. 2013.

[30] M. D. Galus and G. Andersson, "Power system considerations of plug-in hybrid electric vehicles based on a multi energy carrier model," in *2009 IEEE Power & Energy Society General Meeting*, 2009, pp. 1–8.

[31] P. R. C. Mendes, L. V. Isorna, C. Bordons, and J. E. Normey-Rico, "Energy management of an experimental microgrid coupled to a V2G system," *J. Power Sources*, vol. 327, pp. 702–713, Sep. 2016.

[32] M. D. Galus, R. La Fauci, and G. Andersson, "Investigating PHEV wind balancing capabilities using heuristics and model predictive control," in *IEEE PES General Meeting*, 2010, pp. 1–8.

[33] M. M. Morato, P. R. da Costa Mendes, A. A. Cani, J. E. Normey-Rico, and C. Bordons, "Future Hybrid Local Energy Generation Paradigm for the Brazilian Sugarcane Industry Scenario," *Int. J. Electr. Power Energy Syst.*, vol. 101, pp. 139–150, Oct. 2018.

[34] M. Menezes Morato, P. R. da Costa Mendes, J. E. Normey-Rico, and C. Bordons, "Optimal operation of hybrid power systems including renewable sources in the sugar cane industry," *IET Renew. Power Gener.*, vol. 11, no. 8, pp. 1237–1245, Jun. 2017.

[35] J. D. Vergara-Dietrich, M. M. Morato, P. R. C. Mendes, A. A. Cani, J. E. Normey-Rico, and C. Bordons, "Advanced chance-constrained predictive control for the efficient energy management of renewable power systems," *J. Process Control*, Dec. 2017.

[36] C. Hernández-Hernández, F. Rodríguez, J. C. Moreno, P. R. da Costa Mendes, J. E. Normey-Rico, and J. L. Guzmán, "The Comparison Study of Short-Term Prediction Methods to Enhance the Model Predictive Controller Applied to Microgrid Energy Management," *Energies*, vol. 10, no. 7, p. 884, 2017.

[37] M. Arnold, R. R. Negenborn, G. Andersson, and B. De Schutter, "Model-based predictive control applied to multi-carrier energy systems," in *2009 IEEE Power & Energy Society General Meeting*, 2009, pp. 1–8.

[38] A. Parisio, E. Rikos, and L. Glielmo, "A Model Predictive Control Approach to Microgrid Operation Optimization," *IEEE Trans. Control Syst. Technol.*, vol. 22, no. 5, pp. 1813–1827, Sep. 2014.

[39] M. C. Bozchalui, S. A. Hashmi, H. Hassen, C. A. Canizares, and K. Bhattacharya, "Optimal Operation of Residential Energy Hubs in Smart Grids," *IEEE Trans. Smart Grid*, vol. 3, no. 4, pp. 1755–1766, Dec. 2012.

EBSCOhost - printed on 2/14/2023 2:46 PM via . All use subject to https://www.ebsco.com/terms-of-use

[40] A. Parisio and L. Glielmo, "A mixed integer linear formulation for microgrid economic scheduling," in *2011 IEEE International Conference on Smart Grid Communications (SmartGridComm)*, 2011, pp. 505–510.
[41] C. Hernández-Hernández, F. Rodríguez, J. C. Moreno, P. R. da Costa Mendes, and J. E. Normey-Rico, "The use of Model Predictive Control (MPC) in the optimal distribution of electrical energy in a microgrid located in southeastern of Spain: A case study simulation," in *International Conference on Renewable Energy and Power Quality*, 2017.
[42] S. Rosiek and F. J. Batlles, "Integration of the solar thermal energy in the construction: Analysis of the solar-assisted air-conditioning system installed in CIESOL building," *Renew. Energy*, vol. 34, no. 6, pp. 1423–1431, 2009.
[43] S. Rosiek and F. J. Batlles, "Renewable energy solutions for building cooling, heating and power system installed in an institutional building: Case study in southern Spain," *Renew. Sustain. Energy Rev.*, vol. 26, pp. 147–168, 2013.
[44] F. Rodríguez, M. Berenguel, J. L. Guzmán, and A. Ramírez-Arias, *Modeling and Control of Greenhouse Crop Growth*. Springer International Publishing, 2015.
[45] J. A. Sánchez-Molina, J. V. Reinoso, F. G. Acién, F. Rodríguez, and J. C. López, "Development of a biomass-based system for nocturnal temperature and diurnal CO2 concentration control in greenhouses," *Biomass and Bioenergy*, vol. 67, pp. 60–71, Aug. 2014.
[46] C. Hernández, J. del Sagrado, F. Rodríguez, J. C. Moreno, and J. A. Sanchez, "Modeling of energy demand of a High-Tech greenhouse in warm climate based on Bayesian networks," *Math. Probl. Eng.*, vol. 2015, p. 11, 2015.
[47] J. L. Torres, R. Gonzalez, A. Gimenez, and J. Lopez, "Energy management strategy for plug-in hybrid electric vehicles. A comparative study," *Appl. Energy*, vol. 113, pp. 816–824, 2014.
[48] E. F. Camacho, C. B. Alba, and C. Bordons, *Model predictive control*, vol. 2. Springer Science & Business Media, 2004.
[49] M. Geidl, G. Koeppel, P. Favre-Perrod, B. Klockl, G. Andersson, and K. Frohlich, "Energy hubs for the future," *IEEE Power Energy Mag.*, vol. 5, no. 1, pp. 24–30, Jan. 2007.
[50] P. R. C. Mendes, L. V. Isorna, C. Bordons, and J. E. Normey-Rico, "Energy management of an experimental microgrid coupled to a V2G system," *J. Power Sources*, vol. 327, pp. 702–713, Sep. 2016.
[51] A. Bemporad and M. Morari, "Control of systems integrating logic, dynamics, and constraints," *Automatica*, vol. 35, no. 3, pp. 407–427, Mar. 1999.
[52] MATLAB, *R2014a*. The MathWorks Inc., 2014.
[53] J. Lofberg, "YALMIP : A Toolbox for Modeling and Optimization in MATLAB.," in *CACSD Conference, Taipei, Taiwan.*, 2004.
[54] IBM ILOG CPLEX Optimization Studio, "CPLEX," 2017. [Online]. Available: https://www.ibm.com/analytics/cplex-optimizer.

EBSCOhost - printed on 2/14/2023 2:46 PM via . All use subject to https://www.ebsco.com/terms-of-use

# CHAPTER SEVENTEEN

# THERMAL AND POWER PRODUCTION OPTIMIZATION IN MICROGRIDS WITH MODEL PREDICTIVE CONTROL

S. RAIMONDI COMINESI, A. DEL CORNO, E. CORSETTI, G. A. GUAGLIARDI, C. SANDRONI, R. SCATTOLINI[1]

**Keywords**: Model Predictive Control, Mixed-Integer Linear Programming, Microgrids Energy Management

## I. Introduction

Energy management is a key factor in optimizing the integration of power and thermal needs, as well as dispatchable and non-dispatchable sources (see e.g. [1], [2]). This has been testified to by experimentation (e.g. [3], [4] and references) on microgrids. The aim is to maximize, as far as possible, the efficiency of distributed electricity generation devices. This integration is also an important requirement in meeting local needs and the decarbonisation of energy production. The integration of dispatchable and non-dispatchable renewable devices ensures greater compensation for uncertainty in local management, mitigating, as far as possible, their influence on bigger voltage networks. The advantages of an optimal overarching management policy in microgrids are large and

[1] E. Corsetti (*corresponding author*), A. Del Corno, G. A. Guagliardi and C. Sandroni are with RSE S.p.A., (email: edoardo.corsetti@rse-web.it; ada.delcorno@rse-web.it; giuseppe.guagliardi@rse-web.it; carlo.sandroni@rse-web.it). S. Raimondi Cominesi and R. Scattolini are with the Dipartimento di Elettronica, Informazione e Bioingegneria, Politecnico di Milano, 20133 Milan, (e-mail: riccardo.scattolini@polimi.it)

EBSCOhost - printed on 2/14/2023 2:46 PM via . All use subject to https://www.ebsco.com/terms-of-use

varied. These range from simple economic savings to global reductions in CO2 emissions. Although some work has already been done on this topic (see [4]), the issue remains unresolved. In this paper, we present an algorithm to manage energy resources, which takes as its input an estimated load request profile (electrical and thermal), together with non-dispatchable renewable production forecasts and temperature forecasts. The output of the algorithm consists of a day-ahead optimal energy exchange with the network and the optimal dispatching of microgrid controllable devices. In the course of a daily production operation plan, potential forecast errors represent a threat to the ability to comply with the computed optimal exchange profile of the utility grid. In order to cope with such errors, we developed a method capable of adapting the production plan. A simulation of a case study is shown in order to illustrate the possible results of this approach.

The proposed approach is highly generalizable and adaptable to similar microgrids. Preliminary results concerning this research have been presented in [5]. However, only electrical energy production was considered, while thermal energy management was neglected. This paper is organized as follows: Section II contains the descriptive model of the microgrid used as an example to test the algorithm. The optimization problems are then formalized in Section III and the simulation results are presented in Section IV. Finally, conclusions are drawn in Section V.

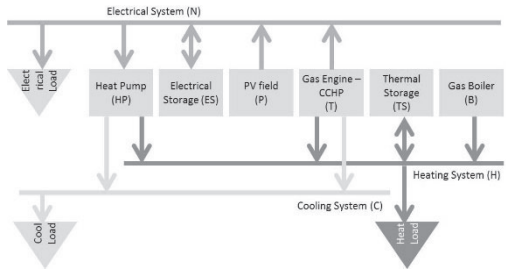



Figure 1. The description of the microgrid system

## II. Description of the System

The case study microgrid (MG) considered in this work included several devices that needed to be efficiently coordinated in order to satisfy the electrical power request $y_L^{elt}$ and both the hot $y_L^h$ and cold $y_L^c$ thermal power requests. As shown in Figure 1, the microgrid was equipped with: a dispatchable generator (a gas engine, denoted by the letter T); an electrical

EBSCOhost - printed on 2/14/2023 2:46 PM via . All use subject to https://www.ebsco.com/terms-of-use

storage device (a battery, denoted by ES); and a photovoltaic non-dispatchable field (identified by the letter P). Combined with the power exchanged with the distribution network (hereafter denoted with the letter N), these components constituted the electrical power request. In the chosen setup, the gas engine could also be used to help cope with either the hot or cold thermal power request. This also held for the heat pump (identified by the letter H), which acted as a converter from electrical to thermal power. A gas boiler (B) and a thermal storage unit (TS) contributed to satisfying the hot thermal power request. The dispatchable units of the MG used embedded controllers and the dynamics of the devices modeled were constituted by the I/O relationship between the desired set-points, control variables of the system, and the actual power output. The photovoltaic panels were not adjustable and all the power they produced, $y_P$, flowed through the MG. The electrical loads were not controllable and were considered to be satisfied. Daily predictions of both PV power production and power requests were assumed to be available. The connection to N was bidirectional and allowed for both the purchase and sale of electric power on the energy market. The net power exchanged between the MG and N (positive if power is absorbed) is denoted by $y_N$. The purchase cost and the sale price were forecast (subject to market fluctuations). For the definition of the discrete-time models of the MG components, we adopted the sampling period $\tau = 15$ minutes.

- *Model of the electrical storage system*

The storage device was modeled as an integrator, with the internal state $x_{ES}$ representing the normalized state of charge (SOC). Since the charge efficiency $\eta_{CH}$ is generally different from the discharge efficiency $\eta_{DCH}$, we considered two inputs for this model: $u_{ES}^{CH}(k)$ and $u_{ES}^{DCH}(k)$. These represented the absolute value of the power absorbed and released, respectively, from the battery. The SOC dynamics are described by the following system:

$$\begin{aligned} x_{ES}(k+1) &= x_{ES}(k) + \frac{\tau}{C_{ES}^{max}}\left(\eta_{CH} u_{ES}^{CH}(k) \right. \\ &\qquad \left. - \eta_{DCH}^{-1} u_{ES}^{DCH}(k)\right) \\ y_{ES}(k) &= u_{ES}^{DCH}(k) - u_{ES}^{CH}(k) \end{aligned} \tag{1}$$

where $C_{ES}^{max}$ is the nominal capacity of the storage system. We considered a battery with $C_{ES}^{max} = 32$ kWh. The output of the system $y_{ES}(k)$ represents the power exchanged between the battery and the microgrid—positive if

EBSCOhost - printed on 2/14/2023 2:46 PM via . All use subject to https://www.ebsco.com/terms-of-use

flowing out from the storage device. To complete the description, the following operational constraint was included:

$$u_{ES}^{DCH}(k) \cdot u_{ES}^{CH}(k) = 0, \forall k \in \mathrm{N} \quad (2)$$

Notice that under condition (2), model (1) is equivalent to a piecewise linear system. The charge and discharge processes are symmetrical and the power set-points are upper-bounded accordingly so that $\forall\ k\ \in T$. The constraints:

$$0 \leq u_{ES}^{CH}(k) \leq u_{ES}^{max}$$
$$0 \leq u_{ES}^{DCH}(k) \leq u_{ES}^{max}$$

are enforced. For the ES we used $u_{ES}^{max} = 30\ kW$. Finally, in order to increase the useful life of the electrical storage system, the state of charge was bounded between $x_{ES}^{min}$ = 0.15 and $x_{ES}^{max}$ = 0.9.

- *Model of the gas engine (CCHP)*

The model of the gas engine (combined cooling and heating production) was based on a device at the RSE test facility in Milan. The controller governing the engine distinguishes four operating states: *starting*, *running*, *stopping*, and *stopped*. When the system is in running mode, the relationship between the machine set point $u_T(k)$ and the actual output $y_T^{elt}(k)$ is expressed by means of the following transfer function:

$$G_T(s) = \frac{(1 + 4.6 * 10^{-8}s)}{(1 + 54.74s)^2} e^{-110.8s} \quad (3)$$

As reasonably expected, the settling time of this system (approximately 1 minute in length) motivates the adoption of a zero order model. In other words, in *running* mode:

$$y_T(k) = u_T(k) \quad (4)$$

The steady-state power output of T, $y_T^{elt}$, was bounded between the values $u_T^{min}$ = 25 kW and $u_T^{max}$ = 50 kW, and the set-point $u_T$ was constrained accordingly. The consumption of the auxiliary actuators (i.e., the fuel pump and the internal cooling system) was computed as an extra electrical load and its value was about 4 kW. The contribution of the gas engine to the power balance during the identified transient phases, strongly depends on the time grain adopted (τ).

EBSCOhost - printed on 2/14/2023 2:46 PM via . All use subject to https://www.ebsco.com/terms-of-use

The *stopping* and the *starting* states last an amount of time neglected with respect to τ. The ramp rate constraint limits the output power variation to model the physical limits of the device:

$$\left|y_T^{elt}(k+1) - y_T^{elt}(k)\right| \leq \Delta_T^{elt}\ t = 1,2,..,T-1$$

The gas engine produces heating ($y_T^h$) and cooling ($y_T^c$) thermal energy. In both cases, its production can be expressed through an affine function of the electrical power output. Consistent with these properties, the following equations were introduced in the model:

$$\begin{aligned} y_T^h(k) &= (a^h y_T^{elt}(k) + \beta^h) \\ y_T^c(k) &= (a^c y_T^{elt}(k) + \beta^c) \end{aligned} \tag{5}$$

The terms $\alpha$ and $\beta$ were the affine function parameters.

- *Model of the gas boiler*

For the purpose of this project, the boiler device was a generic dispatchable hot thermal power gas-supplied generator. Considering the sampling period adopted for the model, we reasonably assumed that the device was constantly in a steady state. To represent the dynamics of such a generator, the following algebraic equation was adopted:

$$y_B(k) = u_B(k) \tag{6}$$

The operational bounds were fixed as $u_B^{min} = 0\ kWt$ and $u_B^{max} = 150\ kWt$ and the operating range was set as:

$$u_B^{min} \leq u_B(k) \leq u_B^{max} \tag{7}$$

- *Model of the heat pump*

The electrical heat pump was a device that could absorb electrical power in order to produce either heating or cooling thermal power. In *heating* mode, the heat pump drains heat from the outside environment and conveys it inside the building. The transferred heat over the absorbed electrical energy ratio, known as COP (*coefficient of performance*) is the standard parameter used by manufacturers to define the efficiency of a process. In *cooling* mode, the heat flow direction is reversed. In this case the process efficiency is commonly represented by the absorbed heat over absorbed electrical energy ratio, known as EER (*energy efficiency ratio*). The values assumed by both the COP and EER parameters are strictly

EBSCOhost - printed on 2/14/2023 2:46 PM via . All use subject to https://www.ebsco.com/terms-of-use

dependent on the conditions under which the device operates. Consistent with [6], we focused our attention on the dependence on the environmental temperature. In particular, assuming available temperature (*temp*) forecasts, we considered the time-varying efficiency parameters, *COP(temp)* and *EER(temp)*, obtained through identified non-linear mapping functions. The model we used for taking into account the contribution of the heat pump to the MG had two input variables: $u_H$ the absolute value of the power request; and $\delta_H$ a boolean variable that makes explicit the operating mode of the heat pump. $\delta_H = 0$ if the device is working in cooling mode and $\delta_H = 1$ in the opposite case. The output of the model was the absorbed electrical power $y_H^{elt}$, and the two thermal power outputs—$y_H^h$, $y_H^c$ (where the use of the superscript letter is analogous to the one in the gas engine model). Consistent with this, the heat pump was defined by the following equations:

$$\begin{aligned} y_H^h(k) &= \delta_H u_H(k) \\ y_H^c(k) &= (1-\delta_H) u_H(k) \\ y_H^{elt}(k) &= \frac{y_H^h(k)}{COP(temp)} + \frac{y_H^c(k)}{EER(temp)} \end{aligned} \tag{8}$$

The output variables of the heat pump were bounded by the values $y_H^{min} = 0\ kWt$ and $y_H^{max} = 80\ kWt$, so that:

$$\begin{aligned} y_H^{h-min} \le\ y_H^h \le\ y_H^{h-max} \\ y_H^{c-min} \le\ y_H^c \le\ y_H^{c-max} \end{aligned} \tag{9}$$

- *Model of the thermal storage*

The model of the thermal storage device was similar to the electrical one. We considered a system that used a 5,000 liter water (5 $m^3$) tank exchanging thermal power with the asymmetric efficiency coefficients $\theta_{IN}$ and $\theta_{OUT}$. The temperature range of the system was between 60°C and 80°C. Its normalized value is represented by the state variable $x_{TS}$. Similar to the system in (1), the input was split into two different input variables according to the direction of the thermal power flow ($u_{TS}^{OUT}$ and $u_{TS}^{IN}$). The model was defined as:

$$\begin{aligned} x_{TS}(k+1) &= \lambda \cdot x_{TS}(k) \\ &\quad + \frac{\tau}{C_{TS}}\left(\theta_{IN} u_{TS}^{IN}(k) + \theta_{OUT}^{-1} u_{TS}^{OUT}(k)\right) \\ y_{TS}(k) &= u_{TS}^{OUT}(k) - u_{TS}^{IN}(k) \text{ and} \\ u_{TS}^{OUT}(k) &\cdot u_{TS}^{IN}(k) = 0 \end{aligned} \tag{10}$$

EBSCOhost - printed on 2/14/2023 2:46 PM via . All use subject to https://www.ebsco.com/terms-of-use

where $C_{TS}$ represents the heat capacity of the water tank and λ represents the stored thermal energy saved between contiguous time-steps, expressed in *pu*. The temperature of the heating source ($T_H$) and the temperature at which the heat was drained ($T_D$) are assumed to be constant. The limitation of the thermal power exchange imposed by the maximum mass flow rate of the storage pump ($\rho_{max}$), the heat capacity ($c_{TS}$), and the temperature gap ($\Delta T$) is expressed by the following constraint:

$$\begin{aligned} &u_{TS}^{OUT} \leq \delta_{TS}^{MAX}(\rho_{max} x_{TS}, T_H) \text{ and} \\ &u_{TS}^{IN} \leq \delta_{TS}^{MAX}(\rho_{max} x_{TS}, T_H) \end{aligned} \tag{11}$$

- *The overall microgrid model*

The models of the devices presented above were combined to give an overall microgrid model, which was defined by the use of Mixed Logical Dynamical (MLD) system formalism [7]. This reformulation was based on the definition of a set of auxiliary variables (continuous or binary) included in a vector $w_{\text{MLD}}$, which allowed the conversion of all the previously introduced logic relations to a set of linear inequalities with binary variables. The process was completed through the use of the freely available software tool HYSDEL [8]. As such:

$$\begin{aligned} &x_{MLD}(k) = [x_{ES}(k)\ t_{on}(k) t_{off}(k)\ x_{TS}(k)]^T \\ &u_{MLD}(k) = \\ &[u_{ES}(k)\ \delta_T^{-t}(k)\ u_T(k)\ \delta_T^{-elt}(k)\ \delta_H(k)\ u_H(k)\ u_{TS}(k)]^T \end{aligned}$$

denoting the state and input vectors, respectively. It was intended that $u_{ES}(k) = [u_{ES}^{CH}(k)\ u_{ES}^{DCH}(k)]^{\mathsf{T}}$ and $u_{TS}(k) = [u_{TS}^{IN}(k)\ u_{TS}^{OUT}(k)]^{\mathsf{T}}$. Thus, the overall MLD model takes the form:

$$\begin{aligned} x_{MLD}(k+1) &= A x_{MLD}(k) + B_u u_{MLD}(k) + B_{aux} w_{MLD}(k) \\ y_{MLD}(k) &= C x_{MLD}(k) + C_u u_{MLD}(k) + D_{aux} w_{MLD}(k) \\ E_{aff} &\geq E_x x_{MLD}(k) + E_u u_{MLD}(k) + E_{aux} w_{MLD}(k) \end{aligned} \tag{12}$$

Notice that the output $y_{MLD}$ of the system is a vector composed as follows:

$$y_{MLD}(k) = \begin{bmatrix} y_{MLD}^{elt}(k) \\ y_{MLD}^{h}(k) \\ y_{MLD}^{c}(k) \end{bmatrix}$$

EBSCOhost - printed on 2/14/2023 2:46 PM via . All use subject to https://www.ebsco.com/terms-of-use

As already noted, the system has to satisfy three different load requests altogether. From the electrical point of view, due to the connection with the distribution network, the following constraints hold:

$$y_{MLD}^{elt}(k) + y_p(k) + y_N(k) = y_L(k) \tag{13}$$

$$\begin{matrix} y_{MLD}^{h}(k) \geq y_L^h(k) \\ y_{MLD}^{c}(k) \geq y_L^c(k) \end{matrix} \tag{14}$$

## III. The Optimization Problem

The purpose of the algorithm was to optimize the cost of electric and thermal production during daily operation, while satisfying the three load request profiles, in accordance with the dynamics and the operational constraints of the devices. Taking into account the non-dispatchable production forecast and load predictions, the algorithm computes the initial operation plan of each MG element for the whole day ahead. Planned energy exchanges with the utility grid, corresponding to the network power profile, are denoted as:

$$y_N^{ref}(k), with\ k = 0, 1, \dots, 95$$

In a real-world applications, this would be shared with the distribution network manager and would act as a reference plan for the day's operation. When the estimated variables show unexpected behavior, or in presence of more reliable forecasts, the system is able to update the production profiles of the devices. A new plan can be devised, but the resulting component $y_N$ should be as close as possible to the reference plan, in order to avoid penalties from the network manager. As illustrated in Section III-B, this requirement necessarily modifies the cost function resulting in a different optimization problem.

- *Initial optimization problem*

The objective function to be minimized accounts for:

- The operational cost of the gas engine (denoted by $c_T$) and its start-up cost ($c_T^{st}$).
- The trade prices with the network: the cost of the energy absorbed ($c_N^a$) and the price of the energy sold ($c_N^s$).
- The operational cost of the boiler (denoted by $c_B$).

The objective function can be defined by:

EBSCOhost - printed on 2/14/2023 2:46 PM via . All use subject to https://www.ebsco.com/terms-of-use

$$J^{ref} = \sum_{k=0}^{95} c_Y(k) y_T(k) + c_T^{st}(k) \max\{\delta_T(k) - \delta_T(k-1), 0\} + \\ + c_N^a(k) \max\{y_N(k), 0\} + c_N^s \min\{y_N(k), 0\} + c_B(k) y_B(k) \quad (15)$$

and the optimization problem to be solved is:

$$\min_{u_{MLD}(0:95)} J^{ref} \quad (16)$$

where $u_{MLD}(0:95)$ stands for the sequence $u_{MLD}(0)$, $u_{MLD}(1), .., u_{MLD}(95)$, subject to the dynamics (12), the load satisfaction constraints (13), (14), and the operational constraints of the devices. For all *k = 0,.., 95*:

$$u_{ES}^{CH}(k) \in [u_{CH}^{min}, u_{CH}^{max}] \qquad x_{ES}(k) \in [0.15, 0.9]$$
$$u_{ES}^{DCH}(k) \in [u_{DCH}^{min}, u_{DCH}^{max}] \qquad u_{ES}^{CH}(k) = 0 \vee u_{ES}^{DCH}(k) = 0$$
$$u_T(k) \in [u_T^{min}, u_T^{max}]$$
$$u_B(k) \in [0, u_B^{max}]$$
$$u_H^h(k) \in [0, u_H^{h,max}] \qquad u_H^c(k) \in [0, u_H^{c,max}]$$
$$u_{TS}^{IN}(k) \in [u_{TS}^{IN,min}, u_{TS}^{IN,max}] \qquad x_{TS}(k) \in [0,1]$$
$$u_{TS}^{OUT}(k) \in [u_{TS}^{OUT,min}, u_{TS}^{OUT,max}] \qquad u_{TS}^{IN}(k) = 0 \vee u_{TS}^{OUT}(k) = 0$$

(16) results in a mixed-integer linear program (MILP), which can be readily solved by using suitable software code (for instance IBM-ILOG-Cplex©).

- *Plan updating*

As will be further illustrated in section IV, during system operation the forecast input data may deviate greatly from general trends. In these cases, it may be helpful to provide more reliable forecasts. In this case the algorithm is run with updated input data, taking into account specific constraints, to fix the grid exchange according to the original daily production plan. In general, the updated plan allows a better fit of the error due to incorrect forecast data and tries to limit, as much as possible, increasing costs $J^{ref}$. In order to accomplish this task, a new optimization problem is implemented.

EBSCOhost - printed on 2/14/2023 2:46 PM via . All use subject to https://www.ebsco.com/terms-of-use

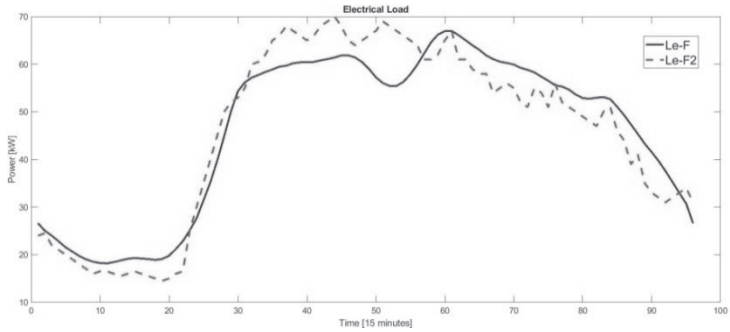



Figure 2. (a) Electrical load: day-ahead and current-day forecasts (solid blue and dashed red, respectively).

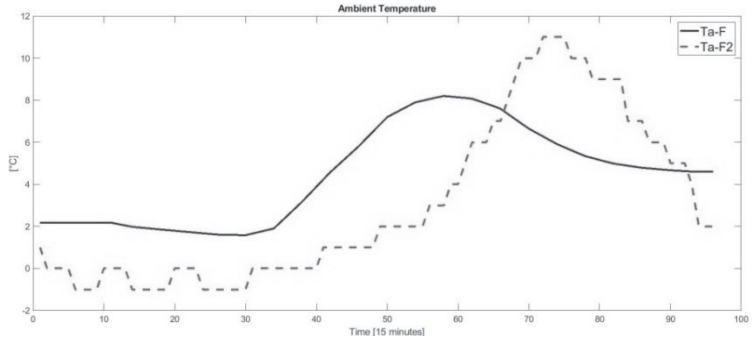



Figure 2. (b) Ambient temperature: day-ahead and current-day forecasts (solid blue and dashed red, respectively).

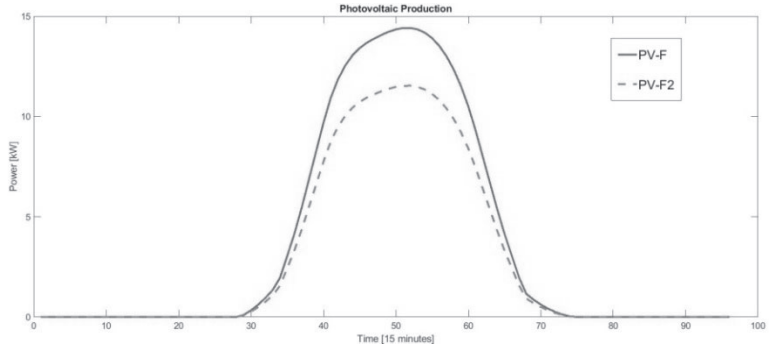



Figure 2. (b) Ambient temperature: day-ahead and current-day forecasts (solid blue and dashed red, respectively).

EBSCOhost - printed on 2/14/2023 2:46 PM via . All use subject to https://www.ebsco.com/terms-of-use

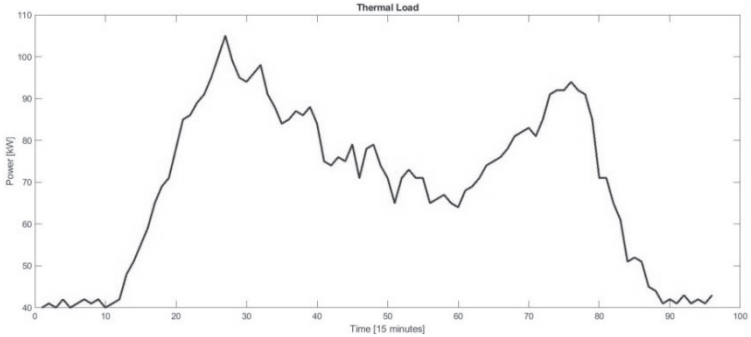



Figure 2. (d) Hot thermal power request.

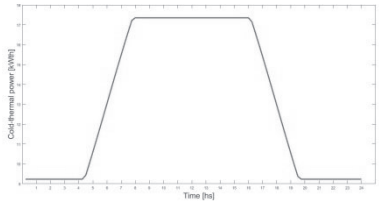



Figure 2. (e) Cold thermal power request.

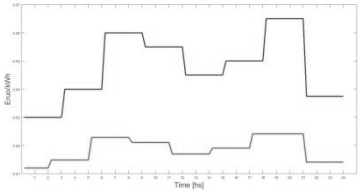



Figure 2. (f) Production and trade energy prices: $c_N^a$ (blue), and $c_N^s$ (red).

The objective function associated with this updating optimization problem is defined by:

$$J^{upd} = \sum_{k=0}^{95} c_Y(k)y_T(k) + c_T^{st}(k)\max\{\delta_T(k) - \delta_T(k-1), 0\} + \\ +c_N(k)\cdot|y_N^{ref} - y_N(k)| + c_B(k)y_B(k) \quad (17)$$

where the terms quantifying the cost/price for the energy exchanged with the network in (15), are replaced by a term penalizing the discrepancy from the reference plan. The resulting optimization problem is therefore,

$$\min_{u_{MLD}(0:95)} J^{upd} \quad (18)$$

subject to: the dynamics (12); the load balances (13), (14); and the same operational constraints of the devices in (16).

EBSCOhost - printed on 2/14/2023 2:46 PM via . All use subject to https://www.ebsco.com/terms-of-use

## IV. The Simulation Study

Regarding the simulation test, we considered the input data in Figure 2. The solid lines in (a), (d), and (e) illustrate, respectively, the prediction for the electrical power load, together with the expected hot and cold thermal power requests. These are the requests that need to be satisfied by the microgrid. The forecasts of environmental temperature and photovoltaic panel production are shown by the solid lines in (b) and (c). Finally, (f) analyzes the unitary trade energy prices.

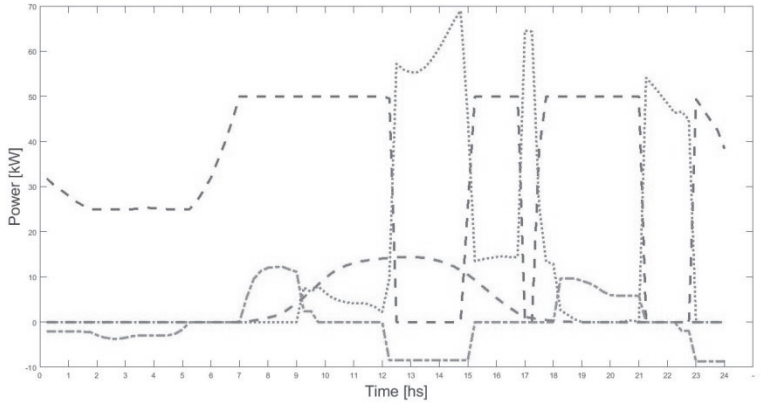



Figure 3. Electrical production plan: $y_T^{elt}$(dashed blue line), $y_N$ (dotted red line), $y_{ES}$ (dash-dot green line), $y_P$ (dashed magenta line).

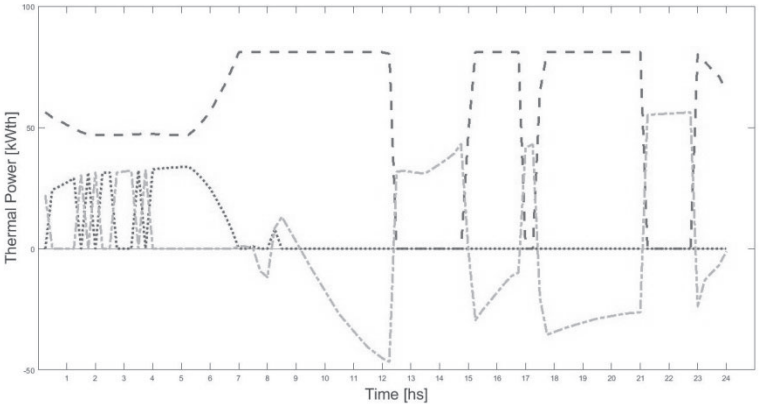



Figure 4a. Hot thermal production plan: $y_T^h$ (dashed blue line), $y_B$ (dotted red line), $y_{TS}$ (green dash-dot line).

EBSCOhost - printed on 2/14/2023 2:46 PM via . All use subject to https://www.ebsco.com/terms-of-use

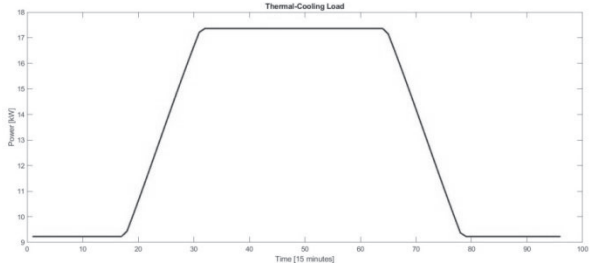



Figure 4b. Cold thermal production plan, supplied by heat pump

According to the day-ahead forecast input data and the trade energy prices, the algorithm allows us to define the optimal daily production plan. Figure 3 shows how the electric power production is distributed among the different devices that compose the microgrid. The optimal power exchange profile is represented by the dotted red line while the other curves define the device set-points that allow compliance with such a profile. In figures 4(a) and 4(b) the thermal power production profiles of the components that should be adopted in order to satisfy the predicted requests are reported. It is clear that any open-loop application of the production plan is subject to possible errors, due to the uncertain knowledge of the forecast input values. In order to partially cope with this issue, whenever corrections of the forecast profiles may be accessible during the daily execution of the plan, it is possible use the update policy presented in III-B. Considering for example that the actual electrical load consumption, the photovoltaic production, and the outside temperature are more consistent with the dashed lines than with the solid lines in figures 2 (a), (d), and (e), respectively, the initial plan would be bound to commit an error concerning the energy exchange with the network. Such an error might be corrected by revising the optimization plan in accordance with more reliable data. Figure 5 shows the profiles of the power exchange in different cases. The dashed red line, representing the power actually exchanged with the network without any correction of the initial plan, drifts away from the agreed profile $y_N^{ref}$. For example, assuming that more reliable forecasts are available around 10 a.m., the production plan can be revised accordingly in order to compensate for the initially erroneous inputs (as the dotted blue line shows). It should be noted that, even without considering any variation of the thermal request in the example, the electrical and thermal power balances are still correlated because of the heat pump.

EBSCOhost - printed on 2/14/2023 2:46 PM via . All use subject to https://www.ebsco.com/terms-of-use

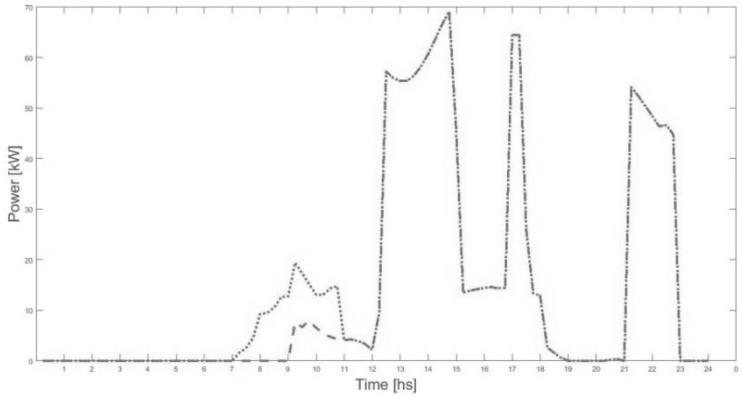



Figure 5. The effect of the update policy on the power exchange with the electrical network: agreed $y_N^{ref}$ (dashed blue line) and $y_N$ with update of the input variables (dotted red line).

In particular, the error in the temperature forecast may cause an erroneous dispatch value of the devices. Consequently, these devices require a different amount of electrical power in order to satisfy the new thermal request. In order to reduce the economic damage due to incorrect device dispatching, the algorithm is run again with the new forecasts as inputs. The computation performed with respect to these inputs, which is now closer to the real situation, corrects the device dispatch ensuring a cost reduction.

## Conclusions

This paper has presented a method for optimal energy management of a microgrid subject to electric and thermal power requests and connected to the utility grid. The algorithm presented allows us to define the optimal energy exchange profile with the network in a day-ahead scenario. Furthermore, taking into account the possibility of obtaining more reliable information on forecast data throughout the day, the method we have presented allows a revision of the daily-plan to maintain grid exchange as close as possible to the plan originally set (most likely agreed with the market operator). Even if the introduction of a lower-level controller is most likely to be needed to compensate for higher-frequency fluctuations, the effect of an update policy is clearly beneficial and allows for better coordination of the devices that compose the microgrid. The results of the

EBSCOhost - printed on 2/14/2023 2:46 PM via . All use subject to https://www.ebsco.com/terms-of-use

simulation highlight the potential of the approach and suggest further research on the topic.

## Acknowledgement

This work has been financed by the Research Fund for the Italian Electrical System under the Contract Agreement between RSE S.p.A. and the Ministry of Economic Development, General Directorate for Nuclear Energy, Renewable Energy and Energy Efficiency, in compliance with the Decree of March 8, 2006.

## References

[1] US Department of Energy, "The smart grid: an introduction," in Technical Report, 2009.

[2] R. Lasseter and P. Paigi, "Microgrid: a conceptual solution," in IEEE 35th Annual Power Electronics Specialists Conf., vol. 6, 2004, pp. 4285–4290.

[3] A. Parisio, E. Rikos, and L. Glielmo, "A model predictive control approach to microgrid operation optimization," IEEE Trans. on Control Systems Technology, vol. 22, no. 5, pp. 1813–1827, 2014.

[4] S. Bracco, F. Delfino, F. Pampararo, M. Robba, and M. Rossi, "A mathematical model for the optimal operation of the University of Genoa Smart Polygeneration Microgrid. Evaluation of technical, economic and environmental performance indicators," Energy, vol. 64, pp. 912–922, 2014.

[5] S. Cominesi, M. Farina, L. Giulioni, B. Picasso, and R. Scattolini, "Two-layer predictive control of a micro-grid including stochastic energy sources," in American Control Conference (ACC), 2015, pp. 918–923.

[6] RSE S.p.A., La pompa di calore per un comfort sostenibile. Editrice Alkes, 2013.

[7] A. Bemporad and M. Morari, "Control of systems integrating logic, dynamics, and constraints," Automatica, vol. 35(3), pp. 407–427, 1999.

[8] F. Torrisi and A. Bemporad, "HYSDEL—A tool for generating computational hybrid models for analysis and synthesis problems," IEEE Transactions on Control Systems Technology, vol. 12, pp. 235–249, Mar. 2004. [Online]. Available: http://control.ee.ethz.ch/index.cgi?page= publications;action=details;id=2223

EBSCOhost - printed on 2/14/2023 2:46 PM via . All use subject to https://www.ebsco.com/terms-of-use

# CHAPTER EIGHTEEN

# ANALYSIS OF SOLUTIONS FOR THE INTEGRATION OF RENEWABLE ENERGY IN WEAK NETWORKS

J. I. SAN MARTÍN[1], F. J. ASENSIO, I. ZAMORA, G. SALDAÑA, O. OÑEDERRA AND M. GONZÁLEZ-PÉREZ

## Abstract

This chapter deals with a number of issues related to the integration of renewable generation in weak power grids. The term "weak network" is currently used, without rigorous definition, for power grids, in opposition to the concept of a "strong" electrical network. A strong network is one where voltage and frequency variables are kept constant and independent of changes in load, as well as of structural modifications, i.e. variation of any part of the electrical system. In this context, the definition of a weak network can be established by considering those networks in which higher variations are tolerated in both voltage and frequency than those admitted for other networks. As such, this chapter presents previously published considerations regarding these networks. Initially, the main parameters that characterize these types of networks are reviewed, in terms of short circuit power, system inertia, and frequency and voltage characteristics. Afterwards, improvement measures in the structure of weak power grids are proposed, analysing different storage technologies in order to guarantee high efficiency and reliability of the power system. Finally, the chapter reviews the most prominent projects developed worldwide, including the integration of renewable energy in weak grids

[1] Engineering School of Gipuzkoa (Section of Eibar), Otaola av. 29, 20600 Eibar (Spain), Email: joseignacio.sanmartin@ehu.eus

EBSCOhost - printed on 2/14/2023 2:46 PM via . All use subject to https://www.ebsco.com/terms-of-use

**Keywords:** renewable distributed generation; weak power grids; wind energy; photovoltaic generation; storage technologies; hydrogen.

## Introduction

This chapter deals with issues associated with the integration of renewable generation into weak power grids with two main areas of focus. First, the number of publications dealing with weak networks is very limited when compared to papers studying the integration of renewable generation into strong networks and for which the network problems are well understood. The second reason is related to the characteristics of weak networks where, for events that are known to occur in strong networks the generators are subjected to greater demands. Additionally, in weak networks, there are additional problems that do not occur in strong networks. As such the study of network events needs to be comprehensive [1].

According to [2], a power grid can be considered weak when the source impedance is large, the short-circuit power is low and the mechanical inertia is small. The strength of a system is defined in terms of the amount of generation loss necessary to reduce to 1 Hz the frequency of the system without shedding loads. The strength of a weak network, for which the power flow from neighbouring areas is not significant, will depend on the power-frequency characteristics of the connected load. As such, a weak network is one in which the capacity of the network is small with respect to the loads on the system [3]. Other possible definitions are based on the weakest bus of a power system. A weak point in a network is one where changes in the active or reactive power flows to or from the network cause voltage changes at that point and neighbouring points of the network [4]. The weakest bus of a system is the one that is closest to a voltage collapse [5].

In turn, there are several ways to measure the strength of a network or identify weak networks in relation to the above definitions, such as the inertia constant, ie, the ability of an AC system to maintain voltage and frequency depends on the rotational inertia of the system: the lower the inertia constant, the weaker the system. In networks with renewable generation, the inertia constant is usually low, since the connection of such generators to the network is performed by power electronic converters.

Regarding short-circuit power [6], it should be noted that transmission lines in weak power grids are normally operated at lower voltage levels than in strong networks. In addition, power is supplied by a few generating groups of small unit power. Therefore, weak grids show low short-circuit

EBSCOhost - printed on 2/14/2023 2:46 PM via . All use subject to https://www.ebsco.com/terms-of-use

power values. In general, the short-circuit power at a given point of common coupling (PCC) is higher when the grid is meshed near to the PCC. Weak and isolated grids mainly consist of radial feeders and as such their short-circuit power values are still lower.

When integrating renewable generation in one location, one must consider the source impedance before and after connecting the generator to the grid, or the short circuit power available at the connection point [7]. This is usually measured using the short circuit ratio (SCR), defined as the relation of the short-circuit power at the PCC to the capacity of the generation plant. SCR values lower than 20 are considered to be indicative of a weak network [8].

Finally, some authors measure the strength of a grid in terms of the voltage stability of a bus or an area of the grid [9]. Also, the R/X relation in the PCC can give an indication of a grid's 'stiffness'—it has a large value in weak grids, because these grids tend to be resistive distribution networks [10].

## Improvements in the structure of weak power grids

Keeping the definition of a weak power grid in mind, an island electricity grid, or island network, is the most common form of this kind of network. In order to minimize the technical problems associated with integrating renewable energy generation into weak grids, it is advisable to reduce the impedance of the equivalent circuit in the PCC of power plants, selecting locations with "strong" network connections. However, this is not always possible in islanded networks, considering that energy generation sources are often in remote areas. Therefore, the following improvements are proposed [11]:

1. Development of interconnections between islanded grids, such as the proposed interconnection between the grid of Gran Canaria Island and the grid of the Lanzarote-Fuerteventura islands, in the Canary Island archipelago of Spain. Depending on the length and rated power, the interconnection can be done using HVDC technology. Upgrades to existing power networks may also be necessary.
2. Large scale deployment of energy storage and regulation systems, including pumped hydropower where available, as discussed in Section 3.
3. Repowering of existing generation plants, normally older wind plants, to take advantage of improvements in technology [12].

EBSCOhost - printed on 2/14/2023 2:46 PM via . All use subject to https://www.ebsco.com/terms-of-use

4. Development of advanced grid codes with stringent voltage and frequency fault ride through requirements [13], so that generation assets based on renewable energy sources actively contribute to active and reactive power control strategies.
5. Improved energy efficiency and energy management systems, strongly related to improving capacity forecasting techniques.
6. Reduction of electricity generation costs.

## Characteristics of storage technologies

In the context of distributed generation, new sources of energy are based on taking direct advantage of natural resources whose power production peaks cannot usually be adjusted to energy demand. They can see large fluctuations in their daily, seasonal, annual or even multi-year cycles of energy production. Demand, on the other hand, can vary throughout the day, the week, or the year. Consequently, a reserve of energy is required, i.e., there is a need to store energy when there is a surplus and to release it when energy demand increases beyond production.

In general, the reliability of the electricity supply is achieved through a combination of base-load, cyclical and peaking power plants.

A significant resource in efficient energy management systems is energy storage. This storage can allow the design of plants for practically constant load operation below peak demand, a process known as peak levelling, which significantly reduces the high capital costs of power plants. There are many storage techniques, based on all kinds of energy, including mechanical, chemical and thermal.

Storage technologies have different technical and economic characteristics and fulfil different criteria. These vary considerably depending on needs and applications [14]. These technologies can be divided into four categories, depending on their application [15]:

1. *Low power applications in remote areas*, mainly to supply transducers and emergency terminals.
2. *Medium power applications in remote areas*, such as individual electrical systems and village power supplies.
3. *Network connection application with peak levelling.*
4. *Power-quality applications*.

For the first two categories, small-scale systems are suitable and energy can be stored as kinetic energy; chemical energy; compressed air; hydrogen; and using supercapacitors and superconductors.

EBSCOhost - printed on 2/14/2023 2:46 PM via . All use subject to https://www.ebsco.com/terms-of-use

For the third and fourth categories, large-scale systems are suitable and energy can be stored as gravitational energy in hydraulic systems; thermal energy in the form of latent and sensible heat; chemical energy in accumulators and batteries; and compressed air.

The *storage capacity* of these different technologies is defined as the amount of energy available in the storage system after completing the load cycle. Discharge is often incomplete and for this reason it is defined according to total energy stored, $W_{st}$ (Wh), which is higher than the usable energy at a certain point of operation, $W_{ut}$.

*Available energy*, in some of these storage technologies, is determined by the constitution and dimensions of the generator-motor system used in the stored energy conversion chain. The available power, generally, is expressed as a mean value and, frequently, to represent the maximum power of charge or discharge, a peak value $P_{max}$ (W) is used.

The energy supplied in the discharge of the different technologies, or depth of discharge, is the ratio of energy discharged in relation to the amount of energy that can be stored; this is usually given as a percentage. This energy must be available for supply during peak hours.

Regarding discharge time, its duration from maximum power is determined by the expression in (1), [16].

$$\tau(s) = \frac{W_{st}}{P_{\max}} \tag{1}$$

where: $\tau(s)$ is the discharging time [s]; $W_{st}$ is the total energy stored [W·s]; and $P_{max}$ is the maximum or peak power [W].

To evaluate the efficiency of storage technologies, the ratio between the energy released and the energy stored is used; its value is obtained by means of expression (2), [3].

$$\eta = \frac{W_{ut}}{W_{st}} \tag{2}$$

where $\eta$ is the efficiency of the storage technology and $W_{ut}$ is the useful or recoverable energy for a specific point of operation [W·s].

The *durability* of these storage technologies is given by the number of times that the storage unit can release energy from the level for which it was designed after each recharge. It is expressed as the maximum number of cycles, *N*, with each cycle corresponding to a charge and discharge.

EBSCOhost - printed on 2/14/2023 2:46 PM via . All use subject to https://www.ebsco.com/terms-of-use

The *autonomy* of these technologies refers to the maximum time that the system can release energy continuously. It is defined by equation (3).

$$a = \frac{W_{ut}}{P_{dt}} \tag{3}$$

where $a$ is the autonomy [s] and $P_d$ is the maximum discharge power [W].

## Energy storage systems

Novel energy storage systems offer a promising solution to the problem of integrating renewable energy generation into weak power grids, allowing greater availability of renewable sources in island grids. In addition, energy storage allows for greater efficiency of the electrical system, reducing the need for backup power generation. It increases the reliability of the system too, avoiding the costs of supply disruption. Moreover, storage technologies are important for levelling the load curve and reducing the difference between peak and valley hours.

Fig.1 shows different applications of energy storage technologies. In terms of their application in electric power systems, two types of storage are considered [13]:

1. Electricity/electricity: batteries, flywheels, hydropower and compressed air.
2. Electricity/fuel: hydrogen storage.

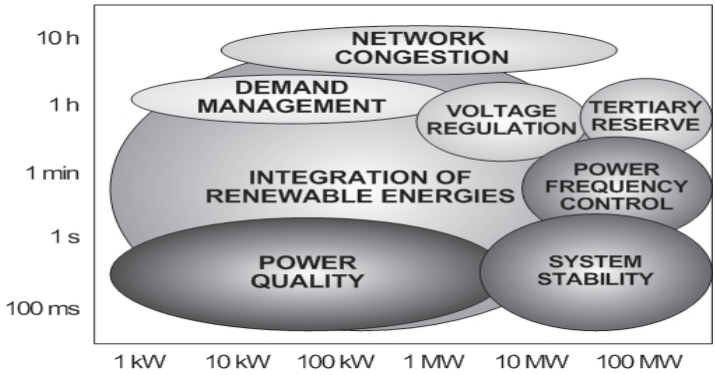



Figure 1. Applications of storage systems.

EBSCOhost - printed on 2/14/2023 2:46 PM via . All use subject to https://www.ebsco.com/terms-of-use

## *Hydropower storage*

Hydropower storage systems, consisting of turbine/pump units, are a good way of integrating variable power generation in weak power grids in islands with the requisite topography. A good example of this is the wind-hydro-pumped station at El Hierro, in the Canary Islands, which integrates an 11.5 MW wind power plant and a hydropower storage plant with 11.32 MW of turbine capacity and 6 MW of pumping capacity.

This technology allows the use of electric power in off-peak hours to pump water from a lower reservoir to a higher altitude one. When the water stored in the upper reservoir passes through a hydraulic turbine, it produces electrical energy, which can be injected into the network at peak times. The main advantages of this system include the low cost of the energy and the possibility of frequency regulation.

These pumping systems are based on reversible electric and hydraulic machines—a generator-motor and a turbine-pump. The transition time from the generation to the accumulation state must be short to respond to sudden changes in the power needs of the electrical network.

In hydropower storage technology, the ratio of energy supplied to the network and the energy consumed while pumping must be considered when evaluating the overall efficiency of the energy storage system. The energy used to pump a water volume, $V$, to a height, $h$, with a specific pumping efficiency, $\eta_p$, is given by equation (4). Additionally, the energy supplied to the electrical network by a generator of efficiency, $\eta_g$, can be obtained using equation (5).

$$E_{pumping} = \frac{\rho \cdot g \cdot h \cdot V}{\eta_p} \tag{4}$$

$$E_{generator} = \rho \cdot g \cdot h \cdot V \cdot \eta_g \tag{5}$$

## *Batteries*

Batteries are devices that convert chemical energy into electrical energy through the oxidation and reduction of their component materials. They consist of a base unit, which is combined with other units, in series or parallel, to obtain the required levels of capacity or voltage.

Many types of electrochemical batteries have been developed to be used in electric power systems, including: lead acid; flooded-type; valve-

EBSCOhost - printed on 2/14/2023 2:46 PM via . All use subject to https://www.ebsco.com/terms-of-use

regulated; sodium sulfur; lithium ion; metal air; flow batteries; vanadium redox; zinc bromine; and nickel cadmium, etc.

These batteries have specific parameters that characterize them. The following can be pointed to:

1. *The open circuit voltage*. This is measured when the battery is not working.
2. *Capacity in Ah*. This is the amount of current that can be supplied in a specified discharge.
3. *State of charge (SOC)*. Specifies the percentage of battery capacity available with respect to its nominal value.
4. *Maximum discharge current* of the battery.
5. *State of health (SOH)*. Reflects the general condition of a battery and its ability to deliver the specified performance in comparison to a fresh battery.
6. *State of performance (SOF)*. Indicates the battery capacity to perform some specific parts of the working cycle.
7. *Depth of discharge (DOD)*. This parameter represents the amount of energy that can be extracted from a battery. It is expressed as a percentage of the total battery capacity.

A good example of using batteries to integrate renewable energy is that of the STORE (Storage Technologies of Reliable Energy) project, launched by Endesa in the Canary Islands. With a budget of over 14 million euros, financed by European funding, STORE allows energy storage in batteries 4 feet high by 8 wide, which serve as an energy reservoir and are available for possible eventualities, as well as storing surplus energy, such as when there are strong winds. The medium-term objective is to replace all existing backup generation setups on the archipelago of the Canary Islands, as well as to improve the economy and security of supply and achieve greater integration of renewable energy [17].

## *Flywheels*

Flywheels store energy in kinetic form. The amount of energy stored is given by expression (6).

$$E = \frac{1}{2} I \cdot \omega^2 \tag{6}$$

EBSCOhost - printed on 2/14/2023 2:46 PM via . All use subject to https://www.ebsco.com/terms-of-use

where $I$ is the moment of inertia of the flywheel [kg·m$^2$] and $\omega$ is the angular velocity [rad/s].

The maximum energy stored is ultimately limited by the tensile strength of the material of the flywheel. The maximum specific energy density $E_{sp}$ that can be stored in a flywheel is given by expression (7).

$$E_{sp} = k_s \frac{\sigma_m}{\rho} \tag{7}$$

where: $\sigma_m$ is the maximum tensile strength of the flywheel material [N/m$^2$]; $k_s$ is the shape factor; and $\rho$ is the density of the flywheel material [kg/m$^3$].

Based on the rotor material, there are two types of flywheels:

1. *Advanced composite rotor*, such as graphite or carbon-fiber. These materials provide high specific energy.
2. *Steel rotor*. This type of flywheel is used in traditional designs (with large diameters, low speed and low power and energy densities) and new high performance flywheels.

In the context of distributed generation, flywheels allow a levelling of the load, storing energy in off-peak hours and returning energy to the network at peak times. As a result, losses in transport and distribution are reduced and the use of existing substations is optimized since lower consumption peaks are obtained.

Flywheels can provide a desired amount of energy with a relatively short time interval, so they can play an important role in primary frequency regulation.

The main advantages of flywheels in comparison to batteries include their very high efficiency (the reduction of variable cost, mainly losses, produces considerable savings in facilities working 24 hours a day); long lifetime (about three times the life of batteries); and reduced time to load (flywheels are fully loaded in 4 minutes unlike batteries that need several hours to load).

REE, the Spanish system operator, has installed a flywheel on Lanzarote Island connected to a 66 kV substation that can supply 18 MW instantaneously and respond to sudden frequency drops due to the loss of a

EBSCOhost - printed on 2/14/2023 2:46 PM via . All use subject to https://www.ebsco.com/terms-of-use

diesel generator, arresting frequency variation and avoiding the tripping of renewable generation plants and load shedding.

## *Hydrogen storage*

The objective of merging the technology of hydrogen production with wind energy is to produce a coupling between the production of energy and its final consumption. One of the main objectives of hydrogen technology is that this element can serve as an energy storage system. The inclusion of hydrogen production in wind farms (for large-scale production) or in a wind turbine (isolated production) forms an integrated wind-hydrogen system. Hybrid systems for hydrogen production by wind energy are primarily composed of the following elements:

- A wind turbine, or a set of wind turbines forming a wind farm that functions as the primary energy source of the system.
- An electrolyser, in which hydrogen is produced from the electrolysis of water. As a by-product of the chemical reaction that takes place, oxygen is obtained, which can be harnessed.
- A hydrogen storage system, which will store the hydrogen produced in the electrolyser.

When the electric power produced by a wind farm is greater than the network demand, or greater than the prediction made for the electric power, the surplus electric power is diverted to an electrolyser in which water electrolysis occurs (an electrochemical reaction in which hydrogen and oxygen are formed). The hydrogen is stored and the oxygen is usually released into the environment. When the power demand of the electrical network is greater than the power generation, or the predicted power to be produced is lower than that given at any moment, hydrogen is consumed to adjust predicted power generation to real demand. There are several ways to carry out this transformation including the combustion of hydrogen in alternative internal combustion engines connected to electric generators, or through its electrochemical reaction in fuel cells.

The use of the energy generated by wind turbines to carry out the electrolysis of water is considered the most promising option to produce hydrogen without pollution, especially in distributed systems. One of the challenges of this technology is to reduce the cost of wind turbines and electrolysers. Another important challenge is the optimization of integrated turbine-electrolyser-storage systems.

EBSCOhost - printed on 2/14/2023 2:46 PM via . All use subject to https://www.ebsco.com/terms-of-use

[18] proposes the combination of wind energy with storage systems based on hydrogen. This system would absorb untapped wind power in valley hours, as well as operating as a load to smooth the daily load curve. Possible locations of hydrogen storage systems on islands include onshore and offshore wind farms or distribution substations. This alternative system is given in Fig.2

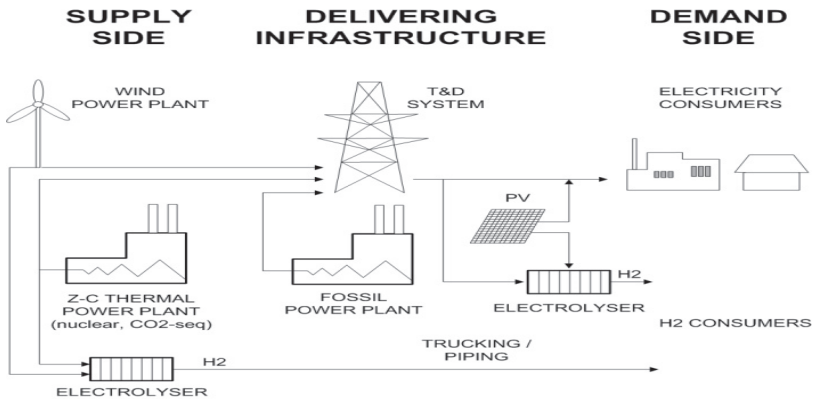



Figure 2. Hydrogen storage system application [15].

## *Comparison of characteristics of storage technologies*

The use of storage technologies can facilitate the connection of microgenerators to the network, allowing smoothing of energy production from intermittent energy sources. Flywheels, batteries, supercapacitors, fuel cells, etc, are all devices currently being developed to store energy [19]. The main characteristics of these storage devices are shown in Table I [20]. In Fig. 3, the applications of storage systems are presented as a function of discharge duration and energy rating [21].

EBSCOhost - printed on 2/14/2023 2:46 PM via . All use subject to https://www.ebsco.com/terms-of-use

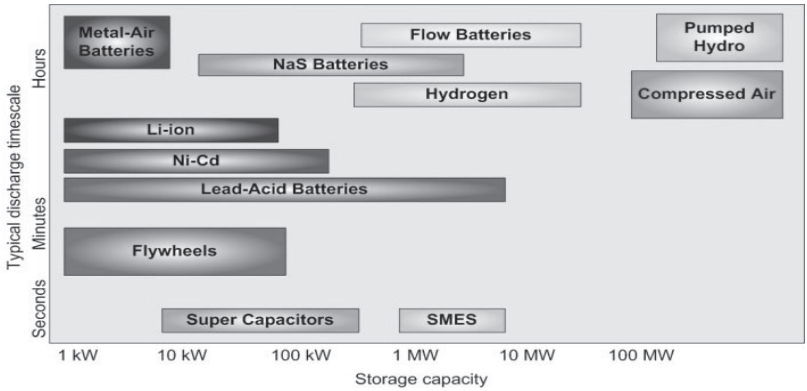



Figure 3. Characteristics of energy storage [18].

## Relevant Projects

In this section, a number of projects related to the integration of renewable generation in weak power grids are presented. In general, these projects are big European projects with multiple participants and funded by the European Commission within the framework of various research programs.

The projects are presented in chronological order. The main objectives of these projects are described and additional information sources are provided.

The described projects are: DISPOWER; RES project for El Hierro; RENEWISLANDS; UPWIND; IS POWER; STORIES; TRES; and MORE MICROGRIDS.

### *DISPOWER*

The aim of the "Distributed Generation with High Penetration of Renewable Energy Sources" (DISPOWER) project is to help the transition from an actual centralized system to a market-oriented decentralized system. For this purpose, the project deals with the integration of renewable and distributed energy generation, while considering technical, legal, economic and social factors.

EBSCOhost - printed on 2/14/2023 2:46 PM via . All use subject to https://www.ebsco.com/terms-of-use

**Table I: Technical characteristics of energy storage systems**

| | Efficiency (%) | Capacity (MW) | Energy density (Wh/kg) | Capital ($/kW) | Capital ($/kWh) | Response time | Lifetime (years) | Maturity | Enviromental impact |
|---|---|---|---|---|---|---|---|---|---|
| TES | 30-60 | 0-300 | 80-250 | 200-300 | 3-50 | - | 5-40 | Developed | Small |
| PHS | 75-85 | 100-5000 | 0.5-1.5 | 600-2000 | 5-100 | Fast (ms) | 40-60 | Mature | Negative |
| CAES | 50-89 | 3-400 | 30-60 | 400-2000 | 2-100 | Fast | 20-60 | Developed | Negative |
| Flywheel | 93-95 | 0.25 | 10-30 | 350 | 5000 | Very fast (<ms) | ~ 15 | Demonstration | Almost |
| Pb-acid battery | 70-90 | 0-40 | 30-50 | 300 | 400 | Fast | 5-15 | Mature | Negative |
| Ni-Cd battery | 60-65 | 0-40 | 50-75 | 500-1500 | 800-1500 | Fast | 10-20 | Commercial | Negative |
| Na-S battery | 80-90 | 0.05-8 | 150-240 | 1000- | 300-500 | Fast | 10-15 | Commercial | Negative |
| Li-ion battery | 85-90 | 0.1 | 75-200 | 3000 | 2500 | Fast | 5-15 | Demonstration | Negative |
| Fuel cells | 20-50 | 0-50 | 800-10000 | 4000 | 10-20 | Goog (< 1s) | 5-15 | Developing | Small |
| Flow battery | 75-85 | 0.3-15 | 10-50 | 600-1500 | 150-1000 | Very fast | 5-15 | Developing | Negative |
| Capacitors | 60-65 | 0.05 | 0.05-5 | 400 | 1000 | Very fast | ~5 | Developed | Small |
| Supercapacitors | 90-95 | 0.3 | 2.5-15 | 300 | 2000 | Very fast | 20+ | Developed | Small |
| SMES | 95-98 | 0.1-10 | 0.5-5 | 300 | 10000 | Very fast | 20+ | Demonstration | Benign |

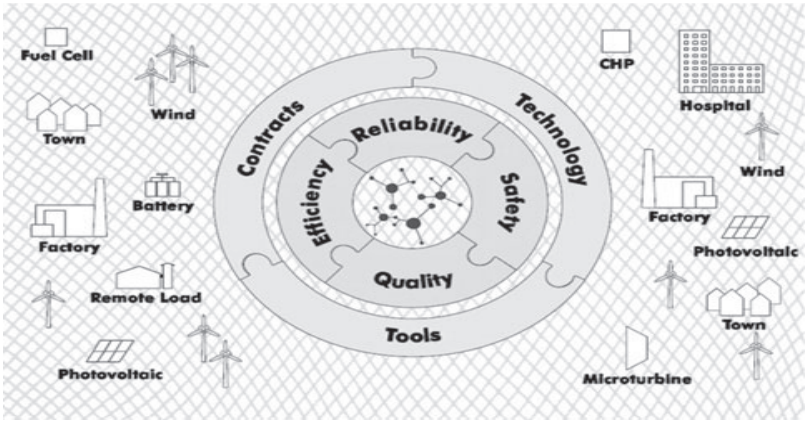



Figure 4. DISPOWER project.

The objective of this project is to design a plan for the connection of distributed generation both to the European synchronous network and to isolated networks. A major goal of the project is that important structural changes and factors, such as network control, network stability, quality of supply and security of supply, are all considered.

EBSCOhost - printed on 2/14/2023 2:46 PM via . All use subject to https://www.ebsco.com/terms-of-use

These are the tasks of the project:

- Develop control concepts and strategies in networks with distributed generation.
- Develop quality and security standards in networks with distributed generation.
- Development of planning and design tools to achieve the integration of distributed generation.
- Information technology system development for online energy management using the Internet.
- Research into energy market contracts and prices.

A full description of the tasks carried out in this project are given in [22]. The project also analysed in detail the integration of distributed generation in islands and weak grids. In [23], related tasks are described and a detailed report with results is given in [24].

### *RES project for El Hierro*

The name of the project is "Implementation of 100% Res Project for El Hierro Island Canary Island, 1st phase." The objective of the project is to have an autonomous energy system based on renewable energy on El Hierro Island (Canarias). Among the proposed generation systems, a wind power generation system with hydropower storage was considered.

The initial commissioning date of the project was 2005. However, the project was delayed and developed as the Gorona del Viento project with a combined wind and hydropower station. The power station is composed of a wind farm, a water pumping system and a hydropower station. The wind farm supplies power directly to the grid and simultaneously supplies a water pumping system with a reservoir. The hydropower station generates power using the stored water, increasing the security of supply and network stability [25].

EBSCOhost - printed on 2/14/2023 2:46 PM via . All use subject to https://www.ebsco.com/terms-of-use

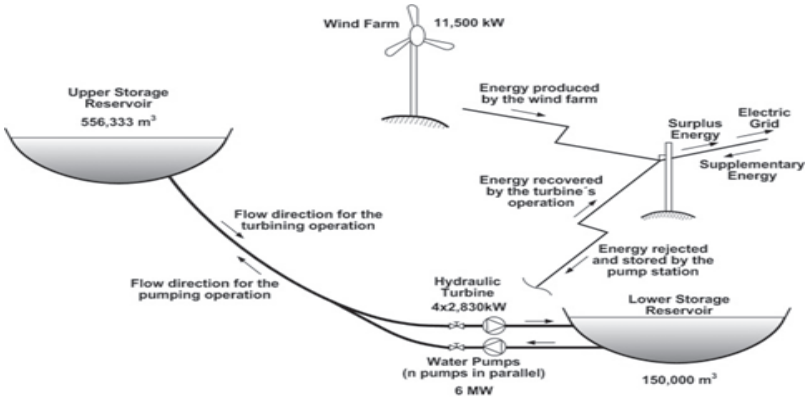



Figure 5. Combined wind and hydropower station in El Hierro.

The combination of wind and a hydropower station transforms an intermittent power supply into a controlled constant supply, maximizing the utilization efficiency of wind power. The thermal plant works as a reserve for low wind periods, minimizing fossil fuel consumption.

The forecast demand was 48 GWh in 2015, based on Canarias energy planning PECAN 2006; however, the design of the water installation, which is not modular, has been set for completion by 2030. Furthermore, the capacity of the reservoir takes into account the water needed for public use on the island.

## *RENEWISLANDS*

The objective of the "Renewable Energy Solutions for Islands" project is the integration of renewable generation, fuel cells and hydrogen infrastructure in the power network of islands [26].

Goals of the project include the analysis of the integration of intermittent renewable generation in isolated systems and the development of a generation system based on renewable energy and fuel cells on the island of Porto Santo, Madeira. In [27], the first two parts of the project are described, while [28] describes the other two parts. The project is based on an isolated network model with renewable energy and storage using the software HYDROGEMS. In Fig. 6, the configuration used by the renewable energy sources to generate hydrogen for the fuel cell supply is shown.

EBSCOhost - printed on 2/14/2023 2:46 PM via . All use subject to https://www.ebsco.com/terms-of-use

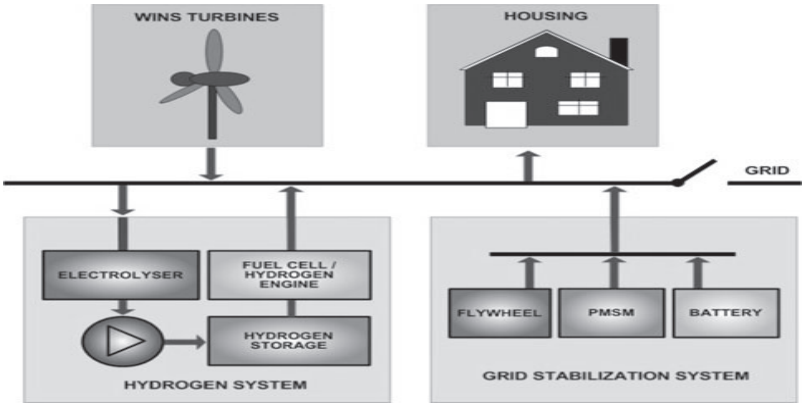



Figure 6. Renewable energies and fuel cell.

## *UPWIND*

UpWind is Europe's largest R&D wind energy project. It aims to substantially develop and verify improved models of the principal wind turbine components, which the industry needs for the design and manufacture of wind turbines in very large-scale future applications, e.g. offshore wind farms of several hundred MW. In this sense, the purpose of the "Very large wind turbines for onshore and offshore applications" project is to analyse the future direction of wind energy. More precisely, the design of 8–10 MW wind turbines for offshore and onshore applications is analysed [29]. The wind turbines needed will be very large (>8–10 MW) with rotor diameters of over 120 m. Current design methods and available components and materials do not yet allow such up-scaling.

Weak grids were analysed as part of task 9 "WP9: Electrical grid." The design requirements of wind turbines were analysed in terms of the reliability requirements of the power grid, and design improvements were developed. Part 3 of this task was related to small isolated systems.

The design and control of the electrical system of wind farms was analysed, in relation to the grid code and the use of automatic frequency and voltage control. System inertia; the parameters of protection relays; voltage and frequency stability; and combined droop and inertia control, were all addressed.

EBSCOhost - printed on 2/14/2023 2:46 PM via . All use subject to https://www.ebsco.com/terms-of-use

## *IS POWER*

The name of the project is: "Isolated power systems, knowledge and technology sharing: distributed generation, grid and demand management." The objective of the IS Power project is the analysis of sustainable development in an island system economy, managing available natural resources and integrating them efficiently into the power grid. The aim is to develop technical and regulatory frameworks to improve the operation of these energy systems and facilitate greater integration of renewable energy and distributed generation [30].

The project has been divided between four working groups that deal with the following subjects:

1. Network management in isolated systems and methods of distributed generation integration.
2. Distributed generation technologies: characteristics and impact of power in isolated systems.
3. Demand side management; procedures and tools; and impacts in isolated systems.
4. Regulatory frameworks to facilitate the integration of distributed generation in isolated systems.

## *STORIES*

The name of the project is "Addressing barriers to STORage technologies for increasing the penetration of Intermittent Energy Sources." The aim of the project is to facilitate the integration of renewable generation in islands by including the changes needed for storage technologies into regulatory frameworks. One particular objective is to analyse the aspects of grid connection and stability when renewable generation penetration in an island is low [31].

## *TRES*

The name of the project is "Transition to a sustainable energy model in Madeira, Azores and Canarias." The objective of the project is to find technical solutions to maximize renewable energy generation in the Canary Islands. The results can then be extrapolated to Madeira and Azores. The five particular objectives defined are: develop meteorological models for photovoltaic and wind power forecasting; analyse the dynamic stability of grids with renewable generation; identify feasible storage

EBSCOhost - printed on 2/14/2023 2:46 PM via . All use subject to https://www.ebsco.com/terms-of-use

capacity to compensate for the variability and intermittency of renewable generation; and analyse the use of biomass in the production of biofuels and measures for greater energy efficiency [32].

The project is divided into five parts. The second part deals with the dynamic stability of island grids, taking into account the effect of renewable energy generation in the grid.

### *MORE MICROGRIDS*

The MORE MICROGRIDS project aims to increase the penetration of microgeneration in electrical networks through the exploitation and extension of the microgrid concept. This involves the investigation of alternative microgenerator control strategies and alternative network designs; the development of new tools for multi-microgrid management operation; and the standardisation of technical and commercial protocols.

Microgrids are novel distribution network structures offering a number of important advantages. From the customer's point of view, microgrids provide both thermal and electricity needs; enhance local reliability; reduce emissions; improve power quality through voltage support; reduce voltage drops; and potentially lower the costs of energy supply. From a utility provider's point of view, the application of distributed energy sources can potentially reduce the demand for distribution and transmission facilities. In addition, microgrids can be operated in isolation or inter-connectedly, allowing greater access to electric and thermal energy for populations in remote areas [33].

## Conclusions

This chapter has presented the state of development experienced by weak networks, addressing its definition and the improvements that can be introduced for more efficient operation of the electricity system. We then reviewed some of the proposed solutions in terms of storage technologies to optimize the integration of renewable energy in weak grids. Finally, the most relevant projects that have been completed or are being carried out in the integration of renewable energy into weak grids have been described.

## Acknowledgement

The authors acknowledge the financial support of the Gipuzkoa Provincial Council (project Etorkizuna Eraikiz 2019 DGE19/03), the Basque Government (GISEL research group IT1191-19 and PIBA_2019_

EBSCOhost - printed on 2/14/2023 2:46 PM via . All use subject to https://www.ebsco.com/terms-of-use

1_0098), as well as from the University of the Basque Country UPV/EHU (PES16/31 and GIU18/181).

## References

[1] J. I. San Martin[1], P. Eguia, A. Etxegarai, E. Torres, I. Albizu. « A Survey on Innovative Solutions and Projects for the Integration of Renewable Generation in Weak Power Grids», International Conference on Renewable Energies and Power Quality (ICREPQ'15, La Coruña (Spain), 25th to 27th, March, 2015.

[2] P. Kundur, N. J. Balu, & M. G. Lauby, Power system stability and control. McGraw-Hill, 1994.

[3] «Introducing Nuclear Power Plants into Electrical Power Systems of Limited Capacity: Problems and Remedial Measures», International Atomic Energy Agency, Vienna, Technical Reports 271, 1987.

[4] J. O. G. Tande, «Exploitation of wind-energy resources in proximity to weak electric grids», Applied Energy, vol. 65, no. 1–4, pp.395–401, abr. 2000.

[5] A. Sode-Yome & N. Mithulananthan, «Voltage stability assessment and enhancement of the Thailand power system». Power Plants and Power Systems Control, Kananaskis, Canada, 2006.

[6] Massimo Valentini, Vladislav Akhmatov, Florin Iov, & Jan Thosted, «Fault Current Contribution from VSC-based Wind Turbines to the Grid», 2008.

[7 A. Y. Nair & T. T. Lie, «Integration of wind power into power systems—voltage stability studies», in Advances in Power System Control, Operation and Management (APSCOM 2009), 8th International Conference on, 2009, pp.1–6.

[8] Akarin Suwannarat, «Wind Farms in Weak Grids Compensated with STATCOM», Aalborg University, Denmark, 2005.

[9] H. Hashim, Y. R. Omar, I. Z. Abidin, R. A. Zahidi, N. Ahmad, & A. M. Ali, «Weak area analysis based on the apparent impedance and voltage indices», in Energy and Environment, 2009. ICEE 2009. 3rd International Conference, 2009, pp.251–255.

[10] E. Twining & D. G. Holmes, «Voltage compensation in weak distribution networks using multiple shunt connected voltage source inverters», in Power Tech Conference Proceedings, 2003 IEEE Bologna, 2003, vol. 4, p.8, vol. 4.

[11] Santiago Marin, «Características estructurales de los sistemas insulares de Canarias», Las Palmas de Gran Canaria, nov-2010.

[12] Manuel Ortega Monserrat, «La importancia de la repotenciación de los parques para mejorar la integración en la red de la energía eólica y mejorar la producción de los emplazamientos», Las Palmas de Gran Canaria, nov-2010.

[13] A. Etxegarai, P. Eguia, E. Torres A. Iturregi, V. Valverde, «Review of grid connection requirements for generation assets in weak power grids, Renewable and Sustainable Energy Reviews», vol. 41, pp.1501–1514, January 2015.

EBSCOhost - printed on 2/14/2023 2:46 PM via . All use subject to https://www.ebsco.com/terms-of-use

[14] J. I. San Martín, I. Zamora, J. J., V. Aperribay, P. Eguía, «Hybrid fuel cells technologies for electrical microgrids»,Electric Power Systems Research, vol. 80, pp.993–1005, 2010.
[15] H. Ibrahim, A. Ilinca, J. Perron, «Energy Storage Systems. Characteristics and Comparisons», Renewable and Sustainable Energy Reviews, vol. 12, pp.1221–1250, 2008.
[16] G. Robin, M. Ruellan, B. Multon, H. Ben Ahmed, P. Y. Glorennec, «Solutions de stockage de l'énergie pour les systèmes de production intermittente d'électricité renouvelable», Systèmes et applications des technologies de l'information et de l'énergie, (UMR 8029 CNRS), ENS Cachan (France), 2004.
[17] M. Milosevic, G. Andersson «Generation control in Small Isolated Power Systems», 37th Annual North American Power Symposium, pp.524–529, 2005.
[18] Marcus Newborough, «Wind Hydrogen Systems», Las Palmas de Gran Canaria, nov-2010.
[19] J. I. San Martín, I. Zamora, J. J. San Martín, V. Aperribay, P. Eguía, « Energy Storage Technologies for Electric Applications», International Conference on Renewable Energies and Power Quality (ICREPQ'11), Las Palmas de Gran Canaria (Spain), 13th to 15th April, 2011
[20] T. Kousksou, P. Bruel, A. Jamil, T. El Rhafiki, Y. Zeraouli, « Energy storage: Applications and challenges», Solar Energy Materials & Solar Cells, vol. 120, pp.59–80, 2014.
[21] D. O. Akinyele, R. K. Rayudu, « Review of energy storage technologies for sustainable power networks», Sustainable Energy Technologies and Assessments, vol. 8, pp.74–91 2014.
[22] T. Degner, J. Schmid, P. Strauss, «DISPOWER. Distributed Generation with High Penetration of Renewable Energy Sources. Final Public Report», 2006. http://www.iset.unikassel.de/dispower_static/documents/fpr
[23] R. Belhomme, «Distributed generation on European islands and weak grids: case studies. Project Highlight No. 33», http://www.iset.unikassel.de/dispower_static/documents/highlight033.pdf.
[24] R. Belhomme, «Deliverable D7.3-Distributed generation on European islands and weak grids-Public Report», DISPOWER European project, del_2005_0079.
[25] http://ec.europa.eu/energy/idae_site/deploy/prj042/prj042_2.html
[26] http://www.islenet.net/?secid=3&pid=19&spid=45&
[27] «Renewislands. Renewable Energy Solutions for Islands. Newsletter No.1», jun 2004 http://www.islenet.net/docs/RENEWISLANDS_Newsletter_no1_final.pdf.
[28] «Renewislands. Renewable Energy Solutions for Islands. Newsletter No.2», feb-2005. http://www.islenet.net/docs/RENEWISLANDS_Newsletter_no2_Final.pdf.
[29] http://www.upwind.eu/
[30] http://www.ispower.eu/
[31] http://www.storiesproject.eu

EBSCOhost - printed on 2/14/2023 2:46 PM via . All use subject to https://www.ebsco.com/terms-of-use

[32] http://proyectotres.itccanarias.org
[33] http://www.microgrids.eu/index.php

EBSCOhost - printed on 2/14/2023 2:46 PM via . All use subject to https://www.ebsco.com/terms-of-use

# CHAPTER NINETEEN

# A PROTOTYPE AT REDUCED SCALE OF A REFRIGERATION SYSTEM CONTROLLED THROUGH PULSE WIDTH MODULATION (PWM) USING THERMOELECTRIC MODULES AND THE PELTIER EFFECT FOR APPLICATION IN INTERNAL ENVIRONMENTS

MAESTRELLI, E.[1], SPACEK, A. D.[1], MOTA, J. M.[1], DA SILVA, E. A.[1], ANDO JUNIOR, O. H.[2], MALFATTI, C. F.[3], SCHAEFFER, L.[3]

## Abstract

This paper presents the design and construction of a prototype at a reduced scale for a refrigeration system to replace air conditioners that use compressors. The operation of the proposed system differs from current

[1] Department of Automation. SATC, Beneficent Association of Santa Catarina Coal Industry, Street Pascoal Meller, 73. Criciúma - SC (Brazil)
Phone/Fax number: +55 48 3431-75.50, E-mail everlise.maestrelli@satc.edu.br, anderson.spacek@satc.edu.br, joao.neto@satc.edu.br, eder.silva@satc.edu.br
[2] Department of Renewable Energies. UNILA, Federal University of Latin American Integration Av. Sílvio Américo Sasdelli, 1842. Foz do Iguaçu-PR (Brazil).
Phone/Fax number: +55 45 3576-73.07,
E-mail oswaldo.junior@unila.edu.br
[3] School of Engineering UFRGS, Federal University of Rio Grande do Sul. Av. Osvaldo Aranha, 103. Porto Alegre - RS (Brazil)
Phone/Fax number: +55 51 3308-31.29, E-mail celia.malfatti@ufrgs.br, schaefer@ufrgs.br

EBSCOhost - printed on 2/14/2023 2:46 PM via . All use subject to https://www.ebsco.com/terms-of-use

systems that use a compressor in that it uses the Peltier effect (thermoelectric modules), controlled by PWM, to ensure maximum efficiency and precise control of the desired temperature. The prototype removes air from the external environment, creating a circular channel where the temperature is reduced through thermal exchange with the cool surface of the thermoelectric modules. After this thermal exchange, the refrigerated air is directed to the desired location. The system is controlled through PWM modulation for an electronic system that includes: one temperature sensor LM35; a development kit Arduino UNO; and LabVIEW 2014 software.

The experimental development and validation of the prototype is presented in this paper. The success of the prototype confirms the technical feasibility of constructing an air conditioner using thermoelectric modules.

**Keywords:** Peltier effect; thermoelectric modules; PWM; air conditioner; Arduino Uno; LabVIEW.

## Introduction

Over the course of the air conditioner's existence, the focus has always been on achieving a high yield. The aim has been to generate maximum thermal exchange with the lowest possible power consumption, i.e. with maximum energy efficiency [1]. Recent research has sought to verify the potential of some applications of thermoelectric phenomena in the development of devices for refrigerating air using the Peltier effect [2]. However, the coefficients of performance shown in thermoelectric materials have been inferior to the coefficients when compared to the Carnot cycle, which is most commonly used in refrigeration. The efficiencies of these different processes can be compared on the basis of the maximum efficiency reached at operating temperatures. Fig. 1 graphically displays the difference between the performances of the two systems being discussed.

EBSCOhost - printed on 2/14/2023 2:46 PM via . All use subject to https://www.ebsco.com/terms-of-use

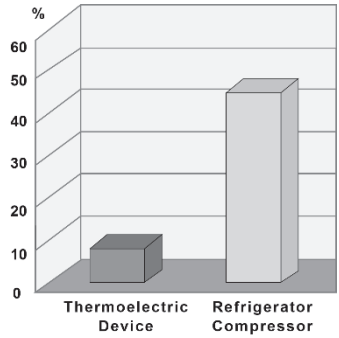



Figure 1. Comparative of coefficient performance [3]

According to Souza, the differences are considerable—thermoelectric materials have an efficiency of 5 to 10%, while compressor refrigerators have an average maximum efficiency of 45% [3]. This paper aims to contribute to the debate by proposing a cooling system with thermoelectric modules that utilize the Peltier effect, a focus on electronic control to optimize power consumption, and by highlighting the feasibility of its transformation into a commercial product.

## Thermoelectric Effect

Thermoelectric materials are semiconductors—when subjected to temperature differences they can generate energy in the form of electrical voltage and when subjected to electric energy they generate a temperature gradient that varies between faces [4]. Thermoelectric modules are typically constructed from semiconductor materials, with a structure formed to increase current density and output power. They are manufactured from materials such as tellurium, antimony, germanium, and silver, which are subjected to a high level of doping to create semiconductors [5]. These in turn are welded into a sandwich of two ceramic plates, ensuring both heat transfer and sufficient mechanical strength. Fig. 2 shows the formation of such a module with PN junctions connected in series.

EBSCOhost - printed on 2/14/2023 2:46 PM via . All use subject to https://www.ebsco.com/terms-of-use

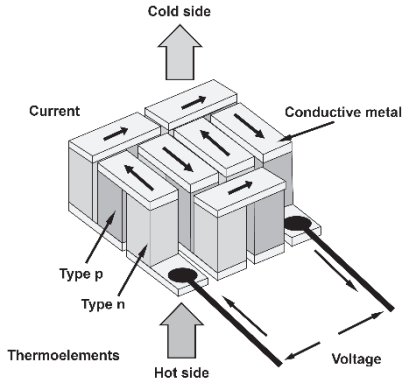



Figure 2. Formation of the thermoelectric module [6]

By applying a greater temperature to one side, a constant current flows over the semiconductor material, with a voltage formed by the association of several elements. All commercial thermoelectric modules are based on this principle; these modules are manufactured for different values of temperature, size, and power. Fig. 3 shows a commercial module.



Figure 3. Commercial thermoelectric module [6]

The advantages of thermoelectric materials include: high reliability; low maintenance; versatility; low size and weight; silent operation; and secure performance [7]. Recent research has shown that new techniques in the development of thermoelectric materials offer efficiencies higher than 20% [8, 9]. With the evolution of thermoelectric materials, it is now possible to apply them in various areas and operating conditions. For example, they can be used for power generation in industries where heat loss is present (thermoelectric power plants, foundries), or even in the exhaust of a car. In these two cases, there may be a considerable increase in overall system

EBSCOhost - printed on 2/14/2023 2:46 PM via . All use subject to https://www.ebsco.com/terms-of-use

efficiency [10]. In other cases, their use can be applied to the cooling of foodstuffs, electronics, and air conditioning systems (although their cooling efficiency is still low compared to existing devices such as compressors). [11]

The Peltier effect removes the rate of heat Qc, which is absorbed in the environment to be cooled, and which may be at any temperature. The heat that will be dissipated at the hot side of the material is defined as the sum of the heat absorbed at the cold side where electric power is applied. The coefficient of performance (COP) of cooling systems using thermoelectric materials does not yet achieve satisfactory performance—this is calculated by dividing the liquid heat absorbed at the cold side by the electrical potency applied [2]:

$$COP = \frac{Qc}{Pin} \tag{1}$$

COP: Coefficient of Performance
Qc [W]: Liquid heat absorbed
Pin [W]: Electrical potency to be applied

The input power dissipated is the heat subtracted from the liquid heat that has been absorbed [2]:

$$Pin = Qh - Qc \tag{2}$$

Pin [W]: Electrical potency to be applied
Qh [W]: Dissipated heat
Qc [W]: Liquid heat absorbed

Thus, the coefficient of performance can be expressed as: [3]

$$COP = \frac{Qc}{Qh - Qc} \tag{3}$$

The temperature coefficient can be summarized by a combination of dissipated heat and absorbed heat.

EBSCOhost - printed on 2/14/2023 2:46 PM via . All use subject to https://www.ebsco.com/terms-of-use

## Prototype of the Cooling System

The prototype refrigeration system using thermoelectric modules and the Peltier effect, which is controlled by a PWM to optimize the energy consumed by the modules and ensure precise temperature control, is composed of distinct units, as shown in Fig. 4.

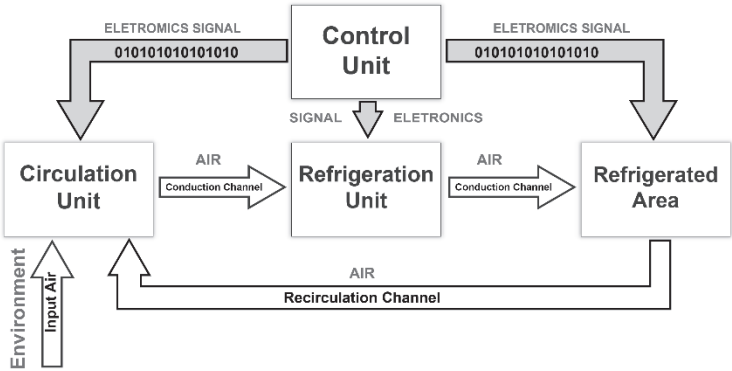



Figure 4. Schematic of the proposed system

The circulation unit is responsible for moving the air in the system. This unit draws air from both the external and internal environments by forcing it to circulate until it finally arrives at the cooling area. The refrigeration unit is responsible for a decrease in air temperature through aluminum thermal sinks connected to the cool face of the thermoelectric modules. This contact between the air and the cool face of the aluminum sinks ensure that thermal exchange and refrigeration of the air take place; the cooled air is then conducted to the desired area. Fig. 5 shows the prototype assembly.

EBSCOhost - printed on 2/14/2023 2:46 PM via . All use subject to https://www.ebsco.com/terms-of-use

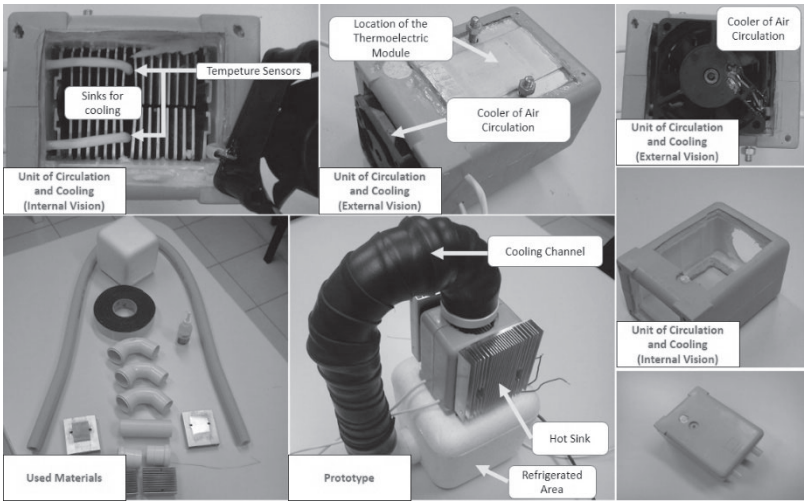



Figure 5. Prototype construction

The control unit uses the prototyping platform ARDUINO UNO V3 and LABVIEW 2014 software. These can be seen in Figure 6 and are used to read the signals from the temperature sensors. Using an algorithm developed to condition the signal, they process the data and act on a potency PWM drive to ensure the efficiency of the system and precise temperature control.

To measure the cooling capacity and the correct functioning of the unit, sensors were located both inside and outside the refrigerated area to obtain the temperature gradient, as well as on the sinks for measuring the thermal power generated in the thermoelectric modules. Fig. 6 shows the workbench for realization of the validations tests.

EBSCOhost - printed on 2/14/2023 2:46 PM via . All use subject to https://www.ebsco.com/terms-of-use

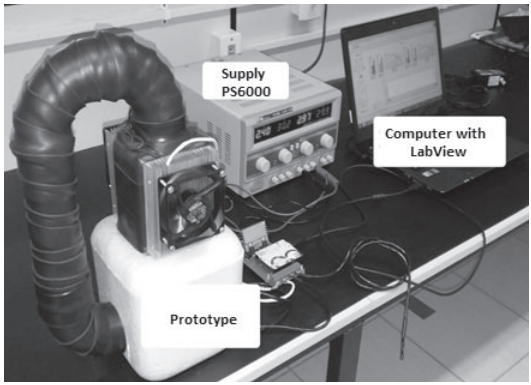



Figure 6. Proposed refrigeration system

## Validation

The prototype was subjected to validation tests to verify its air cooling capacity from heat exchange with the thermoelectric modules. During the tests, internal and external temperature data were collected so as to confirm the reduction of temperature inside the refrigerated environment. As part of this validation process, temperatures at the internal and external sinks were also collected so as to check their behaviour during the process. In addition, electrical voltage and current data were also collected in order to assess the unit's true performance and assess its feasibility for wider implementation.

The validation methodology presented in Figure 7, is based on experimental operation within an air conditioned room, which had a temperature of about 21°C to 22°C throughout the period of testing. The waiting time for stabilization of temperatures was five minutes after initialization. After this time, the system was powered up for a forty minute period, with records made every second, totalling 2,400 data points. The choice of time validation was decided on after pre-tests demonstrated that the prototype does not suffer large variations after this time period.

EBSCOhost - printed on 2/14/2023 2:46 PM via . All use subject to https://www.ebsco.com/terms-of-use

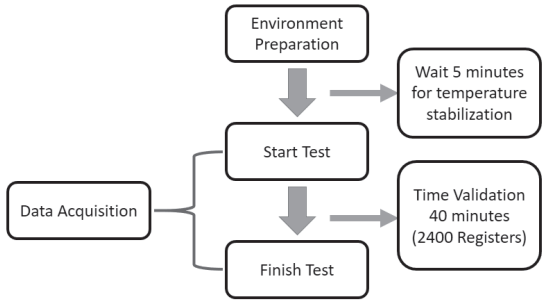



Figure 7. Validation diagram

Figure 8 shows all the temperature measurements made during the of forty minute test period.

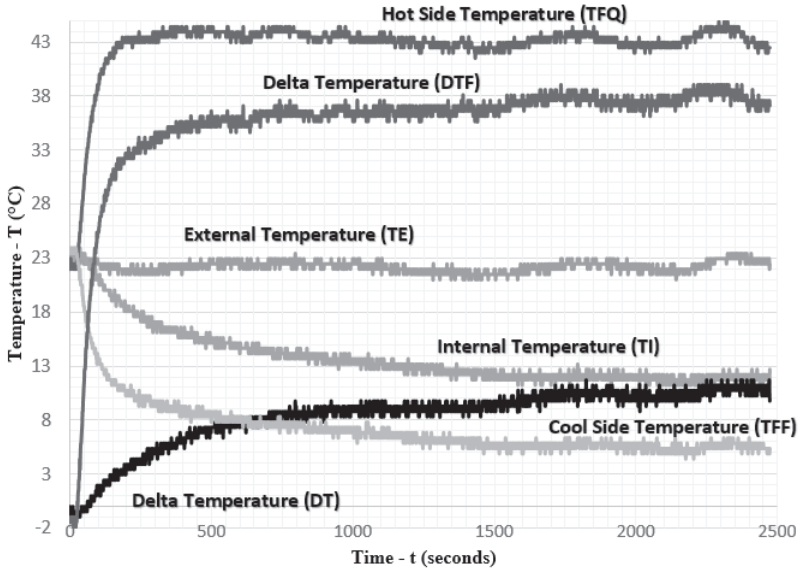



Figure 8. Graph of the results (all temperatures)

For better viewing and discussion of the results, Figure 9 shows only the values for the internal temperature, external temperature, and delta temperature of the prototype.

EBSCOhost - printed on 2/14/2023 2:46 PM via . All use subject to https://www.ebsco.com/terms-of-use

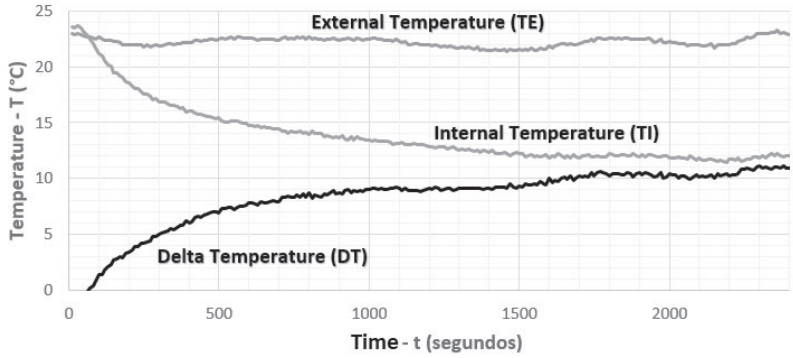



Figure 9. Graph of the results (Internal and External Temperature)

As can easily be observed from the chart, the external temperature (TE) varied very little throughout the validation period. This is because conditions in the environment where the tests were conducted were already stable. The internal temperature (TI) in the environment to be cooled had a slightly higher onset temperature than the external temperature (TE). This is partly because the sensor was enclosed and was not impacted by the air conditioning of the room where the tests were conducted. After the start, the internal temperature (TI) decreased and in 500 seconds (approximately eight minutes) the temperature had already decreased to 15°C. This is a decrease of approximately 8°C, when compared to the initial temperature of 23°C. In evaluating the curve of the internal temperature (TI), it can be observed that there is a higher initial variation. After 500 seconds the temperature change slowed down until it reached its minimum of 11°C near the end of the test period. The delta curve presented on the chart clearly shows how the difference between the internal temperature and external temperature increases over time and clearly shows the success of the proposed system regarding this aspect of functionality. It is necessary to further assess the issue of efficiency.

Table 1 summarizes the validation data obtained.

**Table 1. Summary of validation data**

| Data | Value | Data | Value |
|---|---|---|---|
| Acquisition time | 2,400 s | Number of records | 2,400 |
| Initial external temperature | 22°C | Final external temperature | 21°C |
| Initial internal temperature | 23°C | Final internal temperature | 11°C |
| Voltage | 30Vdc | Current | 5,37A |

EBSCOhost - printed on 2/14/2023 2:46 PM via . All use subject to https://www.ebsco.com/terms-of-use

## Final Considerations

The results of the prototype confirmed a real decrease of the test environment's internal temperature when using thermoelectric modules. This confirmation opens up the possibility of scaling up this application with the ultimate goal of replacing existing air conditioning that use compressors. Advantages of the proposed system include a reduction in the vibration and noise generated by the compressor and the development of devices with variable geometry that can be adapted to diverse environments.

From a technical point of view, this study confirms the feasibility of the proposal, since the monitored test environment achieved a temperature of 11°C, as shown in the recorded data. However, it is necessary to expand on this study to determine the proposed system's economic feasibility—the efficiency of current thermoelectric modules is limited meaning that they have much greater energy consumption.

## References

[1] GONÇALVES, L. *Condicionamento de Ar e sua Evolução Tecnológica***.** 100 f. Trabalho de conclusão de curso para obtenção do grau de Bacharel em construção civil com ênfase ambiental. Universidade Anhembi Morumbi, São Paulo, 2005.

[2] STRYHALSKI, J. Um Pouco de Física do Estado Sólido**.** Centro de Ciências tecnológicas – CCT, Joinville, 2010.

[3] SOUZA D. H., Otimização do Uso de Refrigeradores Termoelétricos em Processos de Refrigeração. 59f. Monografia (Engenharia Mecânica) Universidade de Brasília, Brasília, 2007.

[4] O. H. Ando Jr, C. L. Izidoro, J. M. Gomes, J. H. Correia, J. P. Carmo, L. Schaffer. "Acquisition and Monitoring System for TEG Characterization." International Journal of Distributed Sensor Networks: Hindawi Publishing Corporation, (Invited). ISI indexed with impact factor. ISSN 1550-1329.

[5] ANDO JUNIOR, O. H., FERRO, J. L., SCHAEFFER, L. "Design and Sizing Electric Micro Generator Using Thermoelectric Modules." Journal of Energy and Power Engineering, v. 1, p. 2373-2380, 2013.

[6] CAMPOS, D. N.; OLIVEIRA, T. C. Controlador de Temperatura Microprocessado Utilizando Célula Peltier. 84 f. Monografias (Engenharia Elétrica). Universidade Gama Filho. Rio de Janeiro, 2011.

[7] FARIAS, Sandro Ricardo Alves. "Protótipo de um microgerador termoelétrico de estado sólido: cogeração a gás." 2009. 98 f. Dissertação (Mestrado) – Universidade Federal do Rio Grande do Norte. Natal, 2009.

[8] Peter M. Attia, Matthew R. Lewis, Cory C. Bomberger, Ajay K. Prasad, Jushua M. O. Zide. "Experimental studies of thermoelectric power generation in dynamic temperature environments." Energy: Elsevier Science, pp. 453-456, August 2013.

EBSCOhost - printed on 2/14/2023 2:46 PM via . All use subject to https://www.ebsco.com/terms-of-use

[9] Gomez, Miguel; Reid, Rachel; Ohara Brandon; Lee, Hohyun, “Influence of electrical current variance and thermal resistances on optimum working conditions and geometry for thermoelectric energy harvesting.” Journal of Applied Physics vol.113, pp.174909, 174908-8, May 2013. Doi: 10.1063/1.4802668

[10] ANDO JUNIOR, O. H.; FERRO, J. L.; IZIDORO, C. L.; MAESTRELLI, E.; SPACEK, A. D.; NETO, J. M.; MALFATTI, C. F.; SCHAEFFER, L. Proposal of a Thermoelectric Microgenerator based on Seebeck Effect to Energy Harvesting in Industrial Processes. Renewable Energy & Power Quality Journal (RE&PQJ), v. 1, p. 227, 2014.

[11] RIFFAT, S.B.; MA, Xiaoli. “Thermoelectrics: a review of present and potential applications.” School of the Built environment, The University of Nottingham. Dez. 2002.

EBSCOhost - printed on 2/14/2023 2:46 PM via . All use subject to https://www.ebsco.com/terms-of-use

# PART IV:

# SMART GRIDS

EBSCOhost - printed on 2/14/2023 2:46 PM via . All use subject to https://www.ebsco.com/terms-of-use

# CHAPTER TWENTY

# NEW TRENDS IN OPERATION, MANAGEMENT, AND CONTROL OF FUTURE ACTIVE DISTRIBUTION NETWORKS[1]

HAMID REZA BAGHAEE
AND GEVORK B. GHAREHPETIAN

## Abstract

The environmental and economic benefits of the microgrid, along with its acceptability and the degree of proliferation in the utility power industry, are primarily determined by the envisioned controller capabilities and the operational features. The required control and operational strategies of a microgrid can differ significantly and even conceptually from those of the conventional power systems relying on the type and depth of the penetration of distributed energy resource units, load characteristics and power quality constraints, and market participation strategies. The present chapter provided the basic definitions and requirements for control structure and power, along with the power management system/energy management systems (PMS/EMS) of the microgrid. In addition, it introduced the basic infrastructures of EMS/PMS and different possible control schemes, and finally reviewed the current challenges and future trends for the operation, management, and control of future active distribution networks.

**Keywords:** Active distribution network, centralized control, decentralized control, distributed control, energy management system, hierarchical control, microgrid, power management system.

[1] Electrical Engineering Department, Amirkabir University of Technology, Tehran, 159163-4311, Iran, e-mail: hrbaghaee@aut.ac.ir, grptian@aut.ac.ir ).

EBSCOhost - printed on 2/14/2023 2:46 PM via . All use subject to https://www.ebsco.com/terms-of-use

# 1. Introduction

The increased depth of the penetration of distributed generation (DG) units, distributed energy resources/renewable energy resources (DERs/RERs), energy storage systems, and technological advancements in power electronics in the distribution grids leads to the emergence of different concepts. These concepts include active distribution networks (ADNs) [1], microgrids [2][4], and virtual power plants [5], along with the movement of the energy sector to the era of electric vehicles and DERs such as wind generation, photovoltaic, fuel-cells, and micro-turbines [6],[7]. The integration of DERs/RERs into low-voltage DNs may have different benefits including improving reliability and power quality [8][10]. In addition, other inherent benefits of DERs/RERs encompass increased voltage stability and the reduced emissions of harmful gases and other negative environmental impacts. Further, the RERs lead to the need for solutions regarding new problems such as the co-ordination of protection in both directions, protection from islanding, energy quality based distribution, and the management of the energy deficit and excess. The performance of DG units and microgrids relies on DG operational conditions and the protection systems [11][13].

The present chapter introduces the basic architecture and discusses the challenges and trends in the operation, management, and control of future ADNs toward modern smart microgrids.

# 2. Active Distribution Networks (ADNs) and Microgrids

## *2.1. Distributed Generation*

The conventional power system is globally facing several problems such as the gradual depletion of fossil fuel resources, poor energy efficiency, and environmental pollutions. These problems have led to a new trend of generating power locally at the distribution voltage level by using non-conventional/renewable energy sources. These energy sources include natural gas, biogas, wind generation, solar photovoltaic cells, fuel cells, combined heat and power (CHP) systems, microturbines, as well as Stirling engines and their integration into the utility distribution network. This type of power generation is termed as distributed generation (DG) and the energy sources are called distributed energy resources (DERs). The term ‘Distributed Generation’ was devised to distinguish this concept of generation from centralised conventional generation. The distribution network becomes active by integrating DG and thus it is termed as ADN.

EBSCOhost - printed on 2/14/2023 2:46 PM via . All use subject to https://www.ebsco.com/terms-of-use

In the late 1990s, the major issues related to DG were extensively evaluated by the working groups of the International Council on Large Electric Systems and the International Conference and Exhibition on Electricity Distribution in their review reports.

Several country-specific strict definitions are available for DG worldwide relying on plant rating, generation voltage level, and the like. However, the impact of DG on the power system is normally identical irrespective of these different definitions. According to several research studies, some universally accepted common attributes of DG are as follows:

- It is not centrally planned by the power utility nor is it centrally dispatchable.
- It is normally smaller than 50 MW.
- The power sources or distributed generators are normally connected to the distribution system, which are typically of voltages 230/415 V-145 kV.

### *2.2. Integration of DG Units into Distribution Networks*

The following technical, economic, and environmental benefits in addition to several advantages provided by conventional power systems led to the gradual development and integration of DG systems:

- The need for the augmentation of the conventional generation leads to the continuous depletion of fossil fuel reserves due to the rapid load growth. Therefore, most countries are looking for non-conventional/renewable energy resources as an alternative.
- The reduction of environmental pollutions and global warming acts as a key factor in preferring renewable resources over fossil fuels. As part of the Kyoto Protocol, the EU, the UK and various other countries are planning to cut down greenhouse gas (i.e., carbon and nitrogenous by-products) emissions in order to counter the climate change and global warming. Therefore, they are working on new energy generation and utilisation policies to support the proper utilisation of these energy sources. Furthermore, the exploitation of DERs is expected to help generate eco-friendly clean power with extremely less environmental impacts.
- DG provides a better scope for setting up co-generation, tri-generation, or CHP plants regarding utilising the waste heat for industrial/domestic/commercial applications. This increases the

EBSCOhost - printed on 2/14/2023 2:46 PM via . All use subject to https://www.ebsco.com/terms-of-use

overall energy efficiency of the plant and thus reduces the thermal pollution of the environment.

- DERs are generally considered as the modular units of small capacity due to lower energy density and reliance on the geographical conditions of a region. Additionally, these units are geographically widespread and typically located close to the loads, which is required for the technical and economic viability of the plants. For example, CHP plants should be placed highly close to their heat loads since transporting waste heat over long distances is not economical. This facilitates to find the sites for these plants and helps to decrease the construction time and capital investment. In addition, the physical proximity of load and source reduces the transmission and distribution (T&D) losses. The separate connection of a DER to the utility distribution network is possible since power is generated at a low voltage (LV) or it may be interconnected as microgrids. Then, the microgrid can be connected to the utility as a separate semi-autonomous entity as well.
- The stand-alone and grid-connected operations of DERs help in augmenting generation and improving the overall power quality and reliability. Further, a deregulated environment and open access to the distribution network provide greater opportunities for DG integration. In some countries, the fuel diversity offered by DG is considered valuable while in some developing countries, the shortage of power is such acute that any form of generation is encouraged to meet the load demand.

### *2.3. Active Distribution Network*

Electricity networks are in the era of the major transition from stable passive distribution networks with unidirectional electricity transportation to ADNs with bidirectional electricity transportation. Furthermore, distribution networks are considered passive without any DG units since the electrical power is supplied by the national grid system to the customers embedded in the distribution networks. However, they become active when DG units are added to the distribution system leading to bidirectional power flows in the networks. Thus, developing countries should emphasize the development of sustainable electricity infrastructure in order to affect this transition while developed countries should adopt the technical and economic challenges in order to transform distribution networks. The UK industry regulator, the Office of Gas and Electricity Markets (Ofgem), named this challenge as ‘Rewiring Britain’. ADNs need

EBSCOhost - printed on 2/14/2023 2:46 PM via . All use subject to https://www.ebsco.com/terms-of-use

to incorporate flexible and intelligent controls with distributed intelligent systems. To harness the clean energy from renewable DERs, ADNs should further employ future network technologies that lead to smartgrid or microgrid networks.

The present 'fit-and-forget' strategy of DG employment needs to be changed in active network management. In other words, it should incorporate the integration of DGs in distribution networks and demand-side management. The UK-based Centre for Distributed Generation and Sustainable Electrical Energy[2] demonstrated that the application of active network management methods can greatly support more DG connections as compared to networks with no active management.

Several Departments of Trade and Industry and Ofgem reports indicate that intelligent ADNs have become widespread. The following factors support the evolution of ADNs:

- Pressing the customer expectations of high-quality reliable power distribution
- Increasing the desire of policymakers for accommodating renewable DERs with energy storage devices
- Focusing on carbon commitment to reduce emissions by 50% by 2050
- Motivating the distribution network operators toward better asset utilisation and management by deferring the replacement of age-old assets, and the like

Extensive research is necessary for implementing evolutionary ADNs regarding flexible and intelligent operation and control. The study should mainly focus on different areas as follows:

- Wide area active control
- Adaptive protection and control
- Network management devices
- Real-time network simulation
- Advanced sensors and measurements
- Distributed pervasive communication
- Knowledge extraction by intelligent methods
- Novel design of transmission and distribution systems

[2] (www.sedg.ac.uk)

EBSCOhost - printed on 2/14/2023 2:46 PM via . All use subject to https://www.ebsco.com/terms-of-use

### *2.4. Concept of Microgrid*

Microgrids are small-scale, LV CHP supply networks which are designed to supply electrical and heat loads for a small community (e.g., a housing estate or a suburban locality) or an academic or public community (e.g., a university or school, a commercial area, an industrial site, a trading estate, or a municipal region). Fig. 1 displays the scheme of a microgrid with its control and communication systems. The microgrid is essentially an ADN since it is the conglomerate of DG systems and different loads at distribution voltage level. The generators or microsources employed in a microgrid are normally renewable/non-conventional DERs which are integrated to generate power at distribution voltage. From the operational viewpoint, the microsources should be equipped with power electronic interfaces and controls in order to provide the required flexibility. This is to ensure operation as a single aggregated system and to maintain the specified power quality and energy output. Additionally, this control flexibility allows the microgrid to present itself to the main utility power system as a single controlled unit which meets the local energy needs for reliability and security.

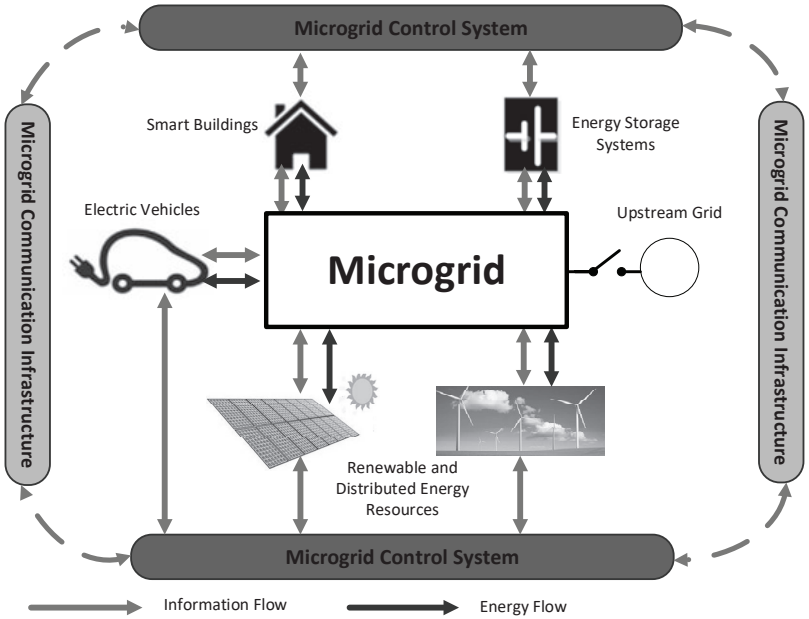



Fig. 1. Simplified scheme of a microgrid with its control and communication systems [18]

EBSCOhost - printed on 2/14/2023 2:46 PM via . All use subject to https://www.ebsco.com/terms-of-use

The key differences between a microgrid and a conventional power plant are as follows:

- Microsources have an extremely smaller capacity with respect to large generators in conventional power plants.
- Power generated at the distribution voltage can be directly fed to the utility distribution network.
- Microsources are normally installed close to the customer premises so that the electrical/heat loads can be efficiently supplied with satisfactory voltage and frequency profile, as well as negligible line losses. In addition, the technical features of a microgrid make it suitable for supplying power to remote areas of a country. In these areas, the supply from the national grid system is either difficult to avail due to the topology or frequently disrupted related to severe climatic conditions or man-made disturbances. From the grid viewpoint, a microgrid is treated as a controlled entity within the power system, which is considered as its main advantage. Further, the microgrid can be operated as a single aggregated load, which ascertains its easy controllability and compliance with grid rules and regulations without hampering the reliability and security of the power utility. From the customers' point of view, microgrids are beneficial for locally meeting their electrical/heat requirements. Furthermore, they can supply uninterruptible power, improve local reliability, reduce feeder losses, and provide local voltage support. From the environmental point of view, microgrids reduce environmental pollution and global warming through utilizing low-carbon technology. However, a number of technical, regulatory, and economic issues should be resolved before microgrids can become commonplace in order to achieve a stable and secure operation. Some problem areas requiring due attention include the intermittent and climate-dependent nature of the generation of the DERs, the low energy content of the fuels, and the lack of standards and regulations for operating the microgrids in synchronism with the power utility. The study of such issues requires extensive real-time and off-line research, which can receive support from the leading engineering and research institutes worldwide.

EBSCOhost - printed on 2/14/2023 2:46 PM via . All use subject to https://www.ebsco.com/terms-of-use

## 3. Basic Infrastructures for Control and Management of Microgrids

Fig. 2 illustrates a typical multi-layer block diagram representation for the general structure of a microgrid control system [14][17]. The field layer integrates all the physical components such as distributed energy resources (DERs), power converters acting as the interface between the DER and the grid, grid components (e.g., transformer, switchgears, transmission lines, and the like), and power consumers (loads).

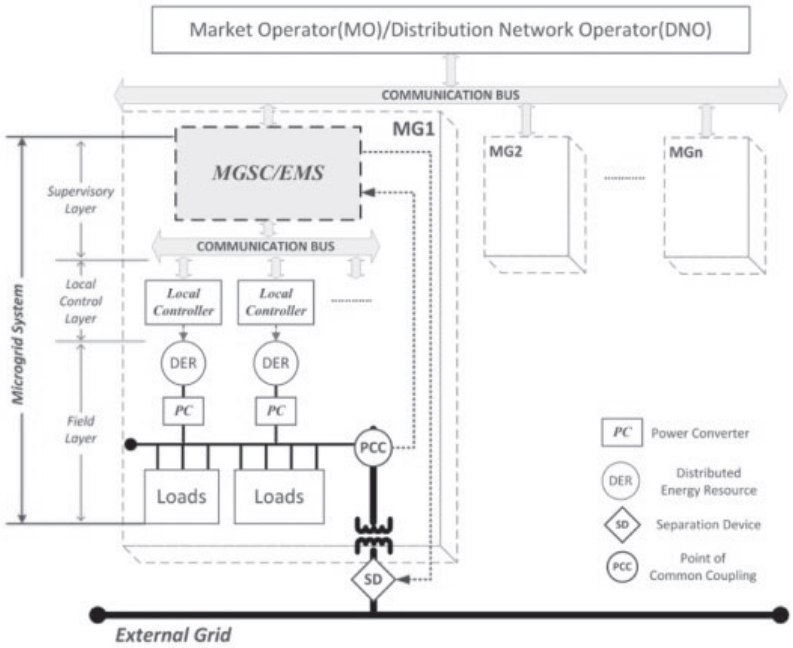



Fig. 2. General structure of a microgrid control system [18]

The local control layer includes basic functions such as local generation/consumption control and energy storage system management and normally follows the instructions from upper-level controllers. Additionally, the top level of the microgrid control system performs the functions of supervisory control and data acquisition. In addition, this layer is occasionally called the energy management system (EMS), microgrid supervisory controller (MGSC), or microgrid central controller. The MGSC/EMS aims to provide necessary functions like power quality

EBSCOhost - printed on 2/14/2023 2:46 PM via . All use subject to https://www.ebsco.com/terms-of-use

control, ancillary services, energy market participation, and system operation optimization by enhancing its intelligence level [14]. The influence from a higher level operator such as distribution network operator and a market operator may be considered as well. The availability of information and communication technology is naturally of utmost importance for realizing these functions. The ever increasing demands on desirable characteristics for future microgrids lead to more challenges to MGSC/EMS [14],[15]. For instance, it should be possible to achieve a smooth transition between islanded and grid-connected modes under either intentional or unintentional conditions, integrate the demand-side strategies, and handle the increasing penetration of renewable energy by developing advanced scheduling and dispatching strategies considering prediction errors.

## 4. Microgrid Control Schemes

Distributed generation (DG) units can be classified into grid-forming (voltage-controlled), grid-feeding (voltage-controlled), or grid-supporting (voltage/current-controlled) units [20]. The mainly used control strategies for grid-feeding inverters are discussed in [21]. This section focuses on the control strategies for grid-forming and grid-supporting converters which participate in microgrid power sharing and balancing. Grid-feeding and grid-supporting converters can be presented, along with these grid-forming converters as well.

A further classification of grid-forming control strategies can be based on communication requirements. Communication-based controllers include master/slave [22][24],[25], centralized [27],[28], decentralized [29],[30], distributed [29],[30], and hierarchical [6],[9],[16],[31] controls. Controllers without communication are generally based on the droop concept.

Four basic communication-assisted schemes are available for controlling large-scale systems (LSSs). These systems nearly include different coupled sub-systems which have some interactions together. Based on the theory of large-scale systems [26], the LSSs can be controlled based on centralized, decentralized, distributed, and hierarchical control structures. These control schemes are illustrated in Figs. 6a-d and their main salient features are summarized as follows.

EBSCOhost - printed on 2/14/2023 2:46 PM via . All use subject to https://www.ebsco.com/terms-of-use

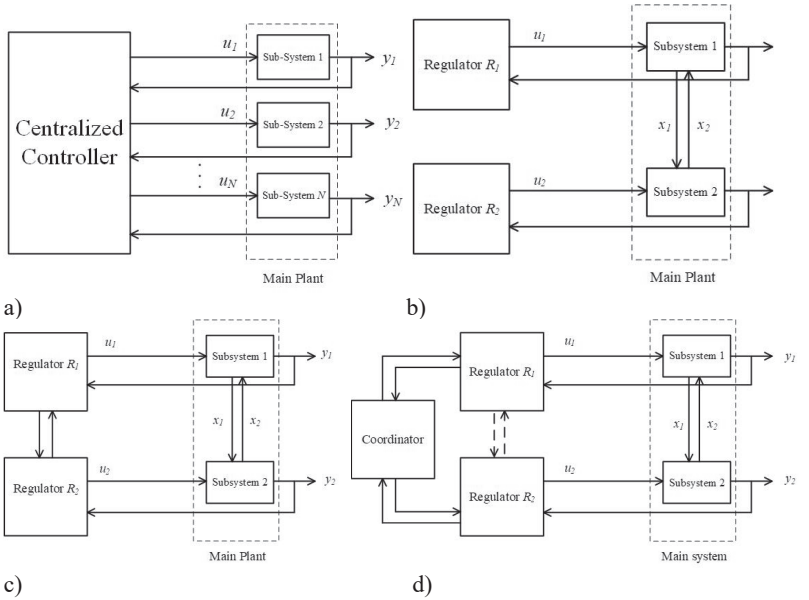



Fig. 3. Basic block diagram representation of control architectures based on the theory of large-scale systems

*Note.* (a) Centralized control, (b) decentralized control, (c) distributed control, and (d) hierarchical control which were obtained from [26].

## *4.1. Centralized Control*

The design of centralized controllers for LSSs is complicated due to their intrinsic computational complexities, reliability constraints, and the limitations of the communication bandwidth. As shown in Fig. 3a, all computations are performed in a centralized controller (which have all system information) and the necessary commands are transmitted to the actuators. The amount of computations in the centralized controller increases extensively when the system (microgrid in this chapter) becomes extremely larger. Thus, the required computation time increases and the controller demonstrates slow and inefficient performance which is unacceptable in real-time applications. Further, the communication between subsystems and centralized controllers demand fast two-way high-bandwidth communication (HBC) which results in increasing the investment costs. More importantly, the centralized control strategy has low reliability since a failure in the controller stops the operation of the entire plant. Considering the above-mentioned disadvantages, the

EBSCOhost - printed on 2/14/2023 2:46 PM via . All use subject to https://www.ebsco.com/terms-of-use

centralized controller should be re-designed or at least essential changes are required if a controllable agent (e.g., DG/energy storage system unit or plug-in hybrid electric vehicle charging station) is added to the microgrid. Table 1 presents the benefits and disadvantages of the centralized control structure.

Based on the same hierarchy in Fig. 2, the functions of MGSC/EMS can be implemented in a centralized or decentralized method. The level of decentralization is defined by the intelligence of Local Controllers (LCs), which can be used only for executing the commands from the upper level or making their own decisions. As shown in Fig. 4, general comparison is made concerning different aspects and levels of MGSC/EMS decentralization. Either way has its advantages and disadvantages, which determine its appropriateness of application on the specific MG type (e.g., residential, commercial, or military) and the legal and physical features (e.g., location, ownership, size, topology, and the like).

EBSCOhost - printed on 2/14/2023 2:46 PM via . All use subject to https://www.ebsco.com/terms-of-use

EBSCOhost - printed on 2/14/2023 2:46 PM via . All use subject to https://www.ebsco.com/terms-of-use



**Table 1. Comparison between the characteristics of different control strategies of microgrids**

| Control Structure | References | Communication | Implementation | Reliability | Advantages | Disadvantages |
|---|---|---|---|---|---|---|
| **Centralized** | [27],[28] | Fast, two-way, HBC | High | Low | Guarantee of stability Optimality | Inefficiency and no applicability in large-scale systems, needs fast two-way HBC, low reliability and slow performance |
| **Decentralized** | [29],[30] | LBC | Reasonable | High | High reliability, reasonable Implementation cost, the only need for LBC | Stability, operation in case of strong interaction between the subsystems |
| **Distributed** | [54],[57],[58] | LBC | Low | High | High reliability, the need for LBC, global optimality, low computation burden | Concerns for stability and robustness |
| **Hierarchical** | [6],[9],[16],[31] | LBC | Reasonable | High | Easy implementation, simple and easy operation and maintenance, fast data transmission between all layers, low computation burden | Concerns for stability and robustness |

*Note.* HBC: High-bandwidth communication; LBC: Low-bandwidth communication

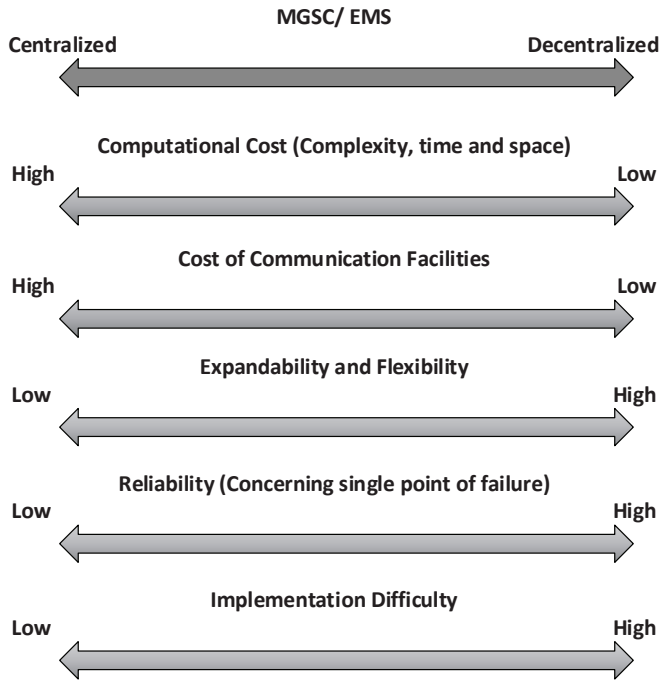



Fig. 4. Characteristics of microgrid control system in different levels of decentralization [18]

Centralized control and management systems typically require data collection from MG components and the external grid. Based on the gathered information, scheduling and optimization procedures can be conducted to achieve an economic and efficient operation. The advantages of centralized MGSC/EMS include the real-time observability of the entire system and straightforward implementation. If designed properly, it provides strong supervision and wide control over the entire system. Furthermore, confidential and private information can be protected within the central unit. However, from another point of view, those features indicate that the MGCC needs to be highly powerful in order to process considerable amounts of data and make proper decisions. Additionally, HBC is required for exchanging the information timely. In addition, the centralized management entails a single point of failure, and the central unit fault collapses the entire system. Further, low flexibility/expandability is considered as another critical limit of centralized management.

EBSCOhost - printed on 2/14/2023 2:46 PM via . All use subject to https://www.ebsco.com/terms-of-use

Considering the above-mentioned discussion, centralized MGSC/EMS is normally more suitable for the following MG cases [18]:

- Small scale MGs where centralized information gathering and decision making (DM) can be realized with low communication and computation cost
- All the properties within the MG have a common goal so that the MGSC/EMS can operate the MG as a unity
- Military MGs where high privacy/confidence is necessary
- System configuration is approximately fixed which requires no high flexibility/expandability

For example, [32] offered a new hybrid distributed network-based power control scheme. This scheme contains distributed power regulators which are mounted on each DG unit to ensure the precise tracking of the optimized set-points assigned by the central energy management unit (EMU). The measured average power is transferred to the EMU in order to calculate the share of each unit based on the real-time optimization criteria and thus using a low bandwidth communication link. The proposed structure has a good tolerance to communication delays. Furthermore, some other approaches are proposed in the literature, including master-slave [33], centralized load sharing [34], average load sharing [35][37], current limitation control [38], and circulating chain control [39]. These methods offer good voltage regulation and power sharing accuracy [39],[40] while, unlike droop methods (which follows), the output voltage is closer to the nominal value [41]. However, these techniques are only applicable to DG systems connected to a common bus or adjacent to each other since the distribution of the sharing signals of the dynamic power, whose transmission in long distances requires high bandwidth connections, is impractical or at least costly in the case of the dispersion of DGs. Additionally, centralized control approaches reduce the system reliability compared to the inherent increasing reliability characteristics of microgrid implementation.

### *4.2. Decentralized Control*

All the sub-systems of the plant are controlled separately by their LCs in the decentralized control structure. Additionally, some interactions probably exist between the subsystems so that less interactions may be closer to the suboptimal condition (Fig. 3b). In the decentralized scheme, all controllable agents and their LCs play an identically important role. In

EBSCOhost - printed on 2/14/2023 2:46 PM via . All use subject to https://www.ebsco.com/terms-of-use

addition, this scheme has higher reliability compared to centralized control since it has no centralized controller with excessive communication. On the other hand, the decentralized scheme provides the highest independence for a controllable agent so that each agent has its own LC which operates based on its local measurements. Thus, there is no need for a fast two-way HBC and a centralized controller which were vital in the previously explained control scheme. This means that a failure in each of the controllable agents or LCs cannot collapse the operation of the entire plant. When a failure occurs, one (or more) controllable agent(s) and the related LC(s) can be added to or removed from the plant without re-designing the controller. Therefore, decentralized control systems were utilized [14],[42],[43] to achieve a more flexible operation while avoiding a single point of failure. According to [44] and [45-48], recent progress in alternative communication technologies (e.g., WiFi, Zigbee, and the like) and information exchange algorithms (e.g., PeerTo-Peer, Gossip, Consensus, and the like) enables the possibility of decentralized control and management in practical applications. In that sense, functions provided by the conventional centralized control mechanism (e.g., frequency and voltage regulation, distributed energy resource coordination, and energy management) can be realized in a decentralized method as well. However, the level of decentralization can range from centralized to completely decentralized [49]. Multiagent System-based MGSC/EMS has become a prominent research direction since it provides the possibility to actualize decentralized management functions. It can have the same hierarchy and functions like the centralized ones while transferring the DM authority to the local side by increasing the intelligence level of the LCs. Further, Information and Communication Technology (ICT) plays a decisive role since the local decisions are made based on necessary information from the environment and neighborhood. In general, decentralized control and energy management can somehow reduce the computational burden since the DM is processed locally and MGSC/EMS only needs to perform information sharing/coordination. Furthermore, the system can keep a normal operation even after losing MGSC/EMS functions, which avoid the single point of the failure. Another advantage is that the realization of plug-and-play functionality is highly easier, which considerably enhances MG flexibility/expandability. However, the decentralized operation requires well synchronization among the units and the communication system begins to play a pivotal role in system safety and stability, which requires extensive study and analysis. Additionally, information security is considered as another critical issue. Generally, decentralized tertiary

EBSCOhost - printed on 2/14/2023 2:46 PM via . All use subject to https://www.ebsco.com/terms-of-use

control and energy management can be more desirable by the following considerations [50][52]:

- The size of the MG is large or the generation, consumption, and storage are widely dispersed which makes centralized data acquisition difficult or costly
- The resources are owned by different entities who have their own operation goals and require local DM schemes
- Periodical fast reconfigurations of the systems like adding or removing the existing units are necessary. The second method is decentralized, including the agent-based decentralized control method [53],[54], sliding-mode voltage control [55],[56], and droop control [57][64] which is more common. In the droop method, the microsources have the plug-and-play capability. Using the droop curves of voltage and frequency, all resources can share power among them without requiring any communication links. Accordingly, the voltage and frequency of microgrid buses can be controlled for communication systems at no cost [65][67]. Although the droop method guarantees no constant amplitude and frequency for microgrids, eliminating the communication link makes this method more attractive [59]. In the decentralized control method, each distributed energy source (i.e., generation or storage) operates independently using the measured local signals. Thus, no source is considered as the reference and all sources are at a single control level. Therefore, deleting or adding a source creates no disturbance in the other source operations. On the other hand, this method requires all resources in order to be dispatchable. In addition, non-dispatchable resources can be changed to dispatchable ones by adding an energy storage element. There is no need for the communication system and the lack of a reference source increases the reliability of the system. These techniques regulate the output voltage and frequency based on the active and reactive powers which are delivered by the inverter. Accordingly, better reliability and flexibility can be achieved in the physical location of the DG units [16],[39],[58]. Previous evidence suggests that applying the droop method is the best way to control the DGs in the microgrid [69]. Further, nearly all experimentally implemented microgrids use droop methods [70].

EBSCOhost - printed on 2/14/2023 2:46 PM via . All use subject to https://www.ebsco.com/terms-of-use

### *4.3. Distributed Control*

The distributed control is a subset of the decentralized control in which the information can be exchanged among the LCs of the subsystems and thus it has higher reliability compared to the decentralized control scheme (Fig. 3c). Furthermore, this scheme is discriminated from the decentralized one based on communication, cooperation, and coordination features. Communication means a weak interaction between the LCs. In other words, the LCs only exchange the information of the subsystems although these exchanges not generally and necessarily lead to the optimality, stability, and robustness of the entire system. Additionally, coordination is close to cooperation while the only difference is that the sub-problems are coordinated by an observer for the sake of achieving the global optimality in coordination.

### *4.4. Hierarchical Control*

The hierarchical control of the LSSs is basically a controller which includes centralized and distributed control strategies. In such strategies, the upstream control layers produce the required set points of the inner control levels that are closer to the physical layer and have faster dynamics but less operation time. Fig. 3d illustrates the basic block diagram of the hierarchical control system. The upper layers have slower dynamics and the control variables are calculated in the upper layers and then transmitted to the lower layers as the reference signal (Fig. 3d). Considering the difference between the dynamics and operation time of different layers, the hierarchical scheme needs a stable and robust platform for stabilizing the plant. This scheme has an easy implementation, as well as simple and easy operation and maintenance and fast data transmission between all layers. It can be quickly modified/fixed in case of any change or failure as well. In addition, considering its distributed computation, this scheme demands no massive computations. In general, the MG management is a complex multi-objective control system, which deals with issues from different technical areas, time scales, and physical levels. The domains of the interest include load power sharing, voltage/frequency and power quality regulation, market participation, short-/long-term scheduling, and the like. To properly handle these issues, a hierarchical control scheme is proposed and widely accepted as a standardized solution for efficient MG management [3],[14],[16],[17]. It should be noted that the intended terminology differs from the one used in some recent studies. For instance, [62] places energy management functions into secondary control while

EBSCOhost - printed on 2/14/2023 2:46 PM via . All use subject to https://www.ebsco.com/terms-of-use

tertiary control is defined for multiple MG coordination. This chapter focuses the standardized definition introduced in [14], [16], and [17] and obtained from conventional power systems. It comprises three principal levels as follows:

- ***Primary level****:* Primary control performs the control of local power, voltage, and current. Further, it normally follows the setting points given by upper level controllers and performs control actions over the interface PCs. The details and descriptions of control functions in the different layers of hierarchical control structure are depicted in Fig. 5.
- ***Secondary level***: In the existing hierarchy, secondary control appears on top of the primary control and it deals with power quality control such as voltage/frequency restoration, as well as voltage unbalance and harmonic compensation. Furthermore, it is in charge of synchronization and power exchange with the main grid or the other MGs.
- ***Tertiary level***: The tertiary control aims to introduce intelligence in the entire system. To this end, it attempts to optimize the MG operation based on the merits of interests, mainly including efficiency and economics. The knowledge from both the MG side and the external grid is essential for performing the optimization functions and ICT is a key enabling technology in this regard. The DM algorithms are employed to process the obtained information and take proper actions.

In this conventional control structure, both tertiary and secondary controls are implemented in the MGSC/EMS. The bandwidths of different control levels are normally separated by at least an order of magnitude, implying the decoupling of the dynamics at different levels. This feature simplifies the modeling and analysis of microgrid systems. The regulation speed becomes slower when moving toward higher control levels. For example, the droop control in the primary level has typically the response within 1-10 msec. and the secondary control speed can reach up to 100 msec.-1 sec. based on the speed limit of the underlying communication technology. However, the tertiary control performs the DM in discrete time steps ranging from seconds to hours.

EBSCOhost - printed on 2/14/2023 2:46 PM via . All use subject to https://www.ebsco.com/terms-of-use

## 5. Current Challenges and Future Trends in the Control and Management of Microgrids

In an islanded microgrid, the control system aims to control the voltage and frequency subject to the active/reactive power sharing [16], [19],[71]-[74]. In the grid-connected mode, the control system controls the active/reactive power and voltage and the frequency is specified by the upstream network. In both modes of the operation, the microgrid is subjected to

- Different small-signal and large-signal disturbances
- Different nonlinearities from the nonlinear dynamics of distributed energy/renewable energy resources (DERs/RERs) and nonlinear loads
- Various topological, parametric, and communication uncertainties

A resilient microgrid should have robust performance against all the above-mentioned disturbances, nonlinearities, and uncertainties [75]-[76]. Different studies well addressed the robust stability of the microgrids for small and large-signal disturbances [4],[6],[9],[12],[19],[22]-[24]. Then, new solutions were presented for nonlinearities from the nonlinear/unbalanced loads and nonlinear dynamics of DERs/RERs in [6], [12], [71]-[73], [77], and [78], respectively. Additionally, other studies discussed the solutions for the robust power flow and control of microgrid under parametric, topological, and communication system uncertainties and the time delay [2],[9],[72]-[74],[79]-[85].

The current challenges and future trends of microgrids include, but not limited to the following items:

- Considering operation and power quality
- Designing the protection system considering the effect of the control system
- Improving fault ride-through capability
- Improving the power/current sharing of DER units considering stability
- Analysing robust power flow
- Applying techniques for uncertainty handling
- Considering the effect of communication latencies such as noise, time-delay, and the like
- Integrating the huge number of charging stations of electric vehicles

EBSCOhost - printed on 2/14/2023 2:46 PM via . All use subject to https://www.ebsco.com/terms-of-use

- Addressing the demand response
- Improving measurement systems
- Improving resiliency, security, and reliability

## 6. Conclusion

The present chapter reviewed the basic concepts and the necessary requirements for control structure and power management system/energy management systems (PMS/EMS) of the microgrid. In addition, the basic infrastructures of EMS/PMS and different possible control schemes were introduced, followed by discussing the current challenges and future trends for operation, management and control of future active distribution networks. Finally, although different research reports are available in this area, various available issues pave the way for the experts and academic researchers to conduct different studies in a wide range of areas in the future.

## References

[1] C. Li, X. Liu, K. Sun, Y. Cao, F. Ma, and B. Zhou, "A hybrid control strategy to support voltage in industrial active distribution networks," *IEEE Trans. on Power Delivery*, vol. PP, no. 99, pp. 1–11, Jul. 2018.

[2] H. R. Baghaee, M. Mirsalim, G. B. Gharehpetian, and H. A. Talebi, "Eigenvalue, robustness and time delay analysis of hierarchical control scheme in multi-DER microgrid to enhance small/large-signal stability using complementary loop and fuzzy logic controller," *Journal of Circuits, Systems and Computers*, vol. 26, no. 06, pp. 1–26, Jun. 2017.

[3] D. E. Olivares, A. Mehrizi-Sani, A. H. Etemadi, C. A. Canizares, R. Iravani, M. Kazerani, A. H. Hajimiragha, O. Gomis-Bellmunt, M. Saeedifard, R. Palma-Behnke, G. A. Jimenez-Estevez, and N. D. Hatziargyriou, "Trends in microgrid control," *IEEE Trans. on Smart Grid*, vol. 5, no. 4, pp. 1905–1919, Jul. 2014.

[4] H. Karimi, E. J. Davison, and R. Iravani, "Multivariable servomechanism controller for autonomous operation of a distributed generation unit: Design and performance evaluation," *IEEE Trans. on Power Sy*stems, vol. 25, no. 2, pp. 853–865, may 2010.

[5] P. Moutis and N. D. Hatziargyriou, "Decision trees-aided active power reduction of a virtual power plant for power system over-frequency mitigation," *IEEE Trans. on Industrial Informatics*, vol. 11, no. 1, pp. 251–261, feb 2015.

[6] H. R. Baghaee, M. Mirsalim, G. B. Gharehpetian, and H. A. Talebi, "Decentralized sliding mode control of WG/PV/FC microgrids under

EBSCOhost - printed on 2/14/2023 2:46 PM via . All use subject to https://www.ebsco.com/terms-of-use

unbalanced and nonlinear load conditions for on- and off-grid modes," *IEEE Systems Journal*, vol. 12, no. 4, pp. 3108–3119, Dec. 2018.

[7] H. R. Baghaee, M. Mirsalim, G. B. Gharehpetian, and H. A. Talebi, "Fuzzy unscented transform for uncertainty quantification of correlated wind/PV microgrids: possibilistic–probabilistic power flow based on RBFNNs," *IET Renewable Power Generation*, vol. 11, no. 6, pp. 867–877, may 2017.

[8] H. R. Baghaee, M. Mirsalim, G. B. Gharehpetian, and H. A. Talebi, "Reliability/cost-based multi-objective Pareto optimal design of stand-alone wind/PV/FC generation microgrid system," *Energy*, vol. 115, pp. 1022–1041, nov 2016.

[9] H. R. Baghaee, M. Mirsalim, G. B. Gharehpetian, and H. A. Talebi, "A generalized descriptor-system robust h1 control of autonomous microgrids to improve small and large signal stability considering communication delays and load nonlinearities," *International Journal of Electrical Power & Energy Systems*, vol. 92, pp. 63–82, Nov. 2017.

[10] M. B. Delghavi and A. Yazdani, "Sliding-mode control of AC voltages and currents of dispatchable distributed energy resources in master-slave-organized inverter-based microgrids," *IEEE Trans. on Smart Grid*, vol. PP, no. 99, pp. 1–12, Sep. 2017.

[11] H. R. Baghaee, M. Mirsalim, G. B. Gharehpetian, and H. A. Talebi, "A new current limiting strategy and fault model to improve fault ridethrough capability of inverter interfaced DERs in autonomous microgrids," *Sustainable Energy Technologies and Assessments*, vol. 24, pp. 71–81, Dec. 2017.

[12] A. H. Etemadi and R. Iravani, "Overcurrent and overload protection of directly voltage-controlled distributed resources in a microgrid," *IEEE Trans. on Industrial Electronics*, vol. 60, no. 12, pp. 5629–5638, Dec. 2013.

[13] S. Kar, S. R. Samantaray, and M. D. Zadeh, "Data-mining model based intelligent differential microgrid protection scheme," *IEEE Systems Journal*, vol. 11, no. 2, pp. 1161–1169, Jun. 2017.

[14] F. Katiraei, R. Iravani, N. Hatziargyriou, and A. Dimeas, "Microgrids management," *IEEE Power and Energy Magazine*, vol. 6, no. 3, pp. 54–65, May 2008.

[15] P. Piagi and R. Lasseter, "Autonomous control of microgrids," in IEEE Power Engineering Society General Meeting. Montreal, Que., Canada: IEEE, Jun. 2006, pp. 1–8.

[16] J. M. Guerrero, J. C. Vasquez, J. Matas, L. G. de Vicuna, and M. Castilla, "Hierarchical control of droop-controlled AC and DC microgrids—a general approach toward standardization," *IEEE Trans. on Industrial Electronics*, vol. 58, no. 1, pp. 158–172, jan 2011.

[17] A. Bidram and A. Davoudi, "Hierarchical structure of microgrids control system," *IEEE Trans. on Smart Grid*, vol. 3, no. 4, pp. 1963–1976, dec 2012.

[18] L. Meng, E. R. Sanseverino, A. Luna, T. Dragicevic, J. C. Vasquez, and J. M. Guerrero, "Microgrid supervisory controllers and energy management systems: A literature review," *Renewable and Sustainable Energy Reviews*, vol. 60, pp. 1263–1273, jul 2016.

EBSCOhost - printed on 2/14/2023 2:46 PM via . All use subject to https://www.ebsco.com/terms-of-use

[19] H. R. Baghaee, M. Mirsalim, and G. B. Gharehpetian, "Real-time verification of new controller to improve small/large-signal stability and fault ride-through capability of multi-DER microgrids," *IET Gen. Trans. Dist*., vol. 10, no. 12, pp. 3068–3084, Sept. 2016

[20] J. Rocabert, A. Luna, F. Blaabjerg, and P. Rodr´ıguez, "Control of power converters in AC microgrids," *IEEE Trans. on Power Electronics*, vol. 27, no. 11, pp. 4734–4749, nov 2012.

[21] F. Blaabjerg, R. Teodorescu, M. Liserre, and A. Timbus, "Overview of control and grid synchronization for distributed power generation systems," *IEEE Trans. on Industrial Electronics*, vol. 53, no. 5, pp. 1398–1409, oct 2006.

[22] H. Karimi, E. J. Davison, and R. Iravani, "Multivariable servomechanism controller for autonomous operation of a distributed generation unit: Design and performance evaluation," *IEEE Trans. on Power Systems*, vol. 25, no. 2, pp. 853–865, may 2010.

[23] M. Babazadeh and H. Karimi, "A robust two-degree-of-freedom control strategy for an islanded microgrid," *IEEE Trans. on Power Delivery*, vol. 28, no. 3, pp. 1339–1347, jul 2013.

[24] M. B. Delghavi and A. Yazdani, "Sliding-mode control of AC voltages and currents of dispatchable distributed energy resources in master-slave-organized inverter-based microgrids," *IEEE Trans. on Smart Grid*, vol. PP, no. 99, pp. 1–12, Sep. 2017.

[25] H. Han, X. Hou, J. Yang, J. Wu, M. Su, and J. M. Guerrero, "Review of power sharing control strategies for islanding operation of AC microgrids," *IEEE Trans. on Smart Grid*, vol. 7, no. 1, pp. 200–215, Jan. 2016.

[26] M. Jamshidi, Ed., *Large-Scale Systems: Modeling, Control and Fuzzy Logic*, 1st ed. Upper Saddle River, New Jersey 07458, USA: Prentice Hall PTR, 2001.

[27] A. G. Tsikalakis and N. D. Hatziargyriou, "Centralized control for optimizing microgrids operation," *IEEE Trans. Energy Convers*., vol. 23, no. 1, pp. 241–248, Mar. 2008.

[28] N. Pogaku, M. Prodanovic, and T. C. Green, "Modeling, analysis and testing of autonomous operation of an inverter-based microgrid," *IEEE Trans. on Power Electronics*, vol. 22, no. 2, pp. 613–625, mar 2007.

[29] Y. Mohamed and E. El-Saadany, "Adaptive decentralized droop controller to preserve power sharing stability of paralleled inverters in distributed generation microgrids," *IEEE Trans. on Power Electronics*, vol. 23, no. 6, pp. 2806–2816, nov 2008.

[30] Y.-R. Mohamed and E. El-Saadany, "A control method of gridconnected PWM voltage source inverters to mitigate fast voltage disturbances," *IEEE Trans. on Power Systems*, vol. 24, no. 1, pp. 489–491, feb 2009.

[31] J. M. Guerrero, M. Chandorkar, T.-L. Lee, and P. C. Loh, "Advanced control architectures for intelligent microgrids—part I: Decentralized and hierarchical control," *IEEE Trans. on Industrial Electronics*, vol. 60, no. 4, pp. 1254–1262, apr 2013.

EBSCOhost - printed on 2/14/2023 2:46 PM via . All use subject to https://www.ebsco.com/terms-of-use

[32] A. Kahrobaeian and Y. A.-R. I. Mohamed, "Networked-based hybrid distributed power sharing and control for islanded microgrid systems," *IEEE Trans. on Power Electronics*, vol. 30, no. 2, pp. 603–617, feb 2015.

[33] B. Zhao, X. Zhang, and J. Chen, "Integrated microgrid laboratory system," in 2013 *IEEE Power & Energy Society General Meeting*. IEEE, 2013.

[34] T. Iwade, S. Komiyama, Y. Tanimura, M. Yamanaka, M. Sakane, and K. Hirachi, "A novel small-scale ups using a parallel redundant operation system," in 25th *International Telecommunications Energy Conference*, 2003. INTELEC '03., Yokohama, Japan, Oct. 2003, pp. 480–483.

[35] X. Sun, L.-K. Wong, Y.-S. Lee, and D. Xu, "Design and analysis of an optimal controller for parallel multi-inverter systems," *IEEE Trans. on Circuits and Systems II: Express Briefs*, vol. 53, no. 1, pp. 56–61, jan 2006.

[36] Z. He, Y. Xing, and Y. Hu, "Low cost compound current sharing control for inverters in parallel operation," in *IEEE 35th Annual Power Electronics Specialists Conference (IEEE Cat. No.04CH37551)*. Aachen, Germany: IEEE, Jun. 2004, pp. 222–227.

[37] H.-M. Hsieh, T.-F. Wu, Y.-E. Wu, H.-S. Nien, Y.-E. Wu, and Y.-K. Chen, "A compensation strategy for parallel inverters to achieve precise weighting current distribution," in *Fourteenth IAS Annual Meeting. Conference Record of the 2005 Industry Applications Conference*, vol. 2. Kowloon, Hong Kong, China: IEEE, Oct. 2005, pp. 945–960.

[38] S. Chiang, C. Lin, and C. Yen, "Current limitation control technique for parallel operation of UPS inverters," in *35th Annual Power Electronics Specialists Conference (IEEE Cat. No.04CH37551)*, vol. 3. Aachen, Germany: IEEE, Jun., pp. 1922–1926.

[39] J. M. Guerrero, L. Hang, and J. Uceda, "Control of distributed uninterruptible power supply systems," *IEEE Trans. on Industrial Electronics*, vol. 55, no. 8, pp. 2845–2859, Aug. 2008.

[40] A. Tuladhar, H. Jin, T. Unger, and K. Mauch, "Control of parallel inverters in distributed AC power systems with consideration of line impedance effect," *IEEE Trans. on Industry Applications*, vol. 36, no. 1, pp. 131–138, Jan. 2000.

[41] T. Vandoorn, J. D. Kooning, B. Meersman, and L. Vandevelde, "Review of primary control strategies for islanded microgrids with power electronic interfaces," *Renewable and Sustainable Energy Reviews*, vol. 19, no. 1, pp. 613–628, mar 2013.

[42] S. D. J. McArthur, E. M. Davidson, V. M. Catterson, A. L. Dimeas, N. D. Hatziargyriou, F. Ponci, and T. Funabashi, "Multi-agent systems for power engineering applications—part I: Concepts, approaches, and technical challenges," *IEEE Trans. on Power Systems*, vol. 22, no. 4, pp. 1743–1752, Nov. 2007.

[43] S. D. J. McArthur, E. M. Davidson, V. M. Catterson, A. L. Dimeas, N. D. Hatziargyriou, F. Ponci, and T. Funabashi, "Multi-agent systems for power engineering applications—part II: Technologies, standards, and tools for building multi-agent systems," *IEEE Trans. on Power Systems*, vol. 22, no. 4, pp. 1753–1759, Nov. 2007.

EBSCOhost - printed on 2/14/2023 2:46 PM via . All use subject to https://www.ebsco.com/terms-of-use

[44] D. Niyato, L. Xiao, and P. Wang, "Machine-to-machine communications for home energy management system in smart grid," *IEEE Communications Magazine*, vol. 49, no. 4, pp. 53–59, Apr. 2011.

[45] R. C. Qiu, Z. Hu, Z. Chen, N. Guo, R. Ranganathan, S. Hou, and G. Zheng, "Cognitive radio network for the smart grid: Experimental system architecture, control algorithms, security, and microgrid testbed," *IEEE Trans. on Smart Gri*d, vol. 2, no. 4, pp. 724–740, dec 2011.

[46] Z. Fan, P. Kulkarni, S. Gormus, C. Efthymiou, G. Kalogridis, M. Sooriyabandara, Z. Zhu, S. Lambotharan, and W. H. Chin, "Smart grid communications: Overview of research challenges, solutions, and standardization activities," *IEEE Communications Surveys & Tutorials*, vol. 15, no. 1, pp. 21–38, 2013.

[47] K. Iniewski, Smart Grid Infrastructure & Networking, 1st ed. New York, NY, USA: Mc Graw Hill, 2013.

[48] V. C. Gungor, D. Sahin, T. Kocak, S. Ergut, C. Buccella, C. Cecati, and G. P. Hancke, "Smart grid technologies: Communication technologies and standards," *IEEE Trans. on Industrial Informatics*, vol. 7, no. 4, pp. 529–539, nov 2011.

[49] A. Dimeas and N. Hatziargyriou, "Operation of a multiagent system for microgrid control," *IEEE Trans. on Power Systems*, vol. 20, no. 3, pp. 1447–1455, aug 2005.

[50] W. Liu, W. Gu, W. Sheng, X. Meng, Z. Wu, and W. Chen, "Decentralized multi-agent system-based cooperative frequency control for autonomous microgrids with communication constraints," *IEEE Trans. on Sustainable Energy*, vol. 5, no. 2, pp. 446–456, apr. 2014.

[51] Y. Xu and W. Liu, "Novel multiagent based load restoration algorithm for microgrids," *IEEE Trans. on Smart Grid*, vol. 2, no. 1, pp. 152–161, mar 2011.

[52] J. He and Y. W. Li, "An enhanced microgrid load demand sharing strategy," *IEEE Trans. on Power Electronics*, vol. 27, no. 9, pp. 3984–3995, sep 2012.

[53] Q. Li, F. Chen, M. Chen, J. M. Guerrero, and D. Abbott, "Agent-based decentralized control method for islanded microgrids," *IEEE Trans. on Smart Grid*, pp. 1–1, 2015.

[54] H. Cai, G. Hu, F. L. Lewis, and A. Davoudi, "A distributed feedforward approach to cooperative control of AC microgrids," *IEEE Trans. on Power Systems*, vol. 31, no. 5, pp. 4057–4067, sep 2016.

[55] Z. Chen, A. Luo, H. Wang, Y. Chen, M. Li, and Y. Huang, "Adaptive sliding-mode voltage control for inverter operating in islanded mode in microgrid," *International Journal of Electrical Power & Energy Systems*, vol. 66, pp. 133–143, mar 2015.

[56] N. M. Dehkordi, N. Sadati, and M. Hamzeh, "A back-stepping high-order sliding mode voltage control strategy for an islanded microgrid with harmonic/interharmonic loads," *Control Engineering Practice*, vol. 58, pp. 150–160, Jan. 2017.

[57] J. Guerrero, J. Matas, L. G. D. V. D. Vicuna, M. Castilla, and J. Miret, "Wireless-control strategy for parallel operation of distributed generation

EBSCOhost - printed on 2/14/2023 2:46 PM via . All use subject to https://www.ebsco.com/terms-of-use

inverters," *IEEE Trans. on Industrial Electronics*, vol. 53, no. 5, pp. 1461–1470, oct 2006.

[58] J. M. Guerrero, J. Matas, L. G. de Vicuna, M. Castilla, and J. Miret, "Decentralized control for parallel operation of distributed generation inverters using resistive output impedance," *IEEE Trans. on Industrial Electronics*, vol. 54, no. 2, pp. 994–1004, apr 2007.

[59] J. Guerrero, J. Vasquez, J. Matas, M. Castilla, and L. de Vicuna, "Control strategy for flexible microgrid based on parallel line-interactive UPS systems," *IEEE Trans. on Industrial Electronics*, vol. 56, no. 3, pp. 726–736, mar 2009.

[60] E. Barklund, N. Pogaku, M. Prodanovic, C. Hernandez-Aramburo, and T. Green, "Energy management in autonomous microgrid using stability-constrained droop control of inverters," *IEEE Trans. on Power Electronics*, vol. 23, no. 5, pp. 2346–2352, sep 2008.

[61] N. Pogaku, M. Prodanovic, and T. C. Green, "Modeling, analysis and testing of autonomous operation of an inverter-based microgrid," *IEEE Trans. on Power Electronics*, vol. 22, no. 2, pp. 613–625, mar 2007.

[62] M. B. Delghavi and A. Yazdani, "A unified control strategy for electronically interfaced distributed energy resources," *IEEE Trans. on Power Delivery*, vol. 27, no. 2, pp. 803–812, apr 2012.

[63] Z. Zhang, X. Huang, J. Jiang, and B. Wu, "A load-sharing control scheme for a microgrid with a fixed frequency inverter," *Electric Power Systems Research*, vol. 80, no. 3, pp. 311–317, mar 2010.

[64] T. L. Vandoorn, B. Meersman, J. D. M. D. Kooning, and L. Vandevelde, "Analogy between conventional grid control and islanded microgrid control based on a global DC-link voltage droop," *IEEE Trans. on Power Delivery*, vol. 27, no. 3, pp. 1405–1414, jul 2012.

[65] T. L. Vandoorn, B. Renders, L. Degroote, B. Meersman, and L. Vandevelde, "Active load control in islanded microgrids based on the grid voltage," *IEEE Trans. on Smart Grid*, vol. 2, no. 1, pp. 139–151, mar 2011.

[66] T. L. Vandoorn, B. Meersman, L. Degroote, B. Renders, and L. Vandevelde, "A control strategy for islanded microgrids with DC-link voltage control," *IEEE Trans. on Power Delivery*, vol. 26, no. 2, pp. 703–713, apr 2011.

[67] X. Huang, X. Jin, T. Ma, and Y. Tong, "A voltage and frequency droop control method for microsources," in *2011 International Conference on Electrical Machines and Systems. Beijing, China: IEEE*, Aug. 2011, pp. 1–5.

[68] P. H. Divshali, A. Alimardani, S. H. Hosseinian, and M. Abedi, "Decentralized cooperative control strategy of microsources for stabilizing autonomous VSC-based microgrids," *IEEE Trans. on Power Systems*, vol. 27, no. 4, pp. 1949–1959, nov 2012.

[69] R. Zamora and A. K. Srivastava, "Controls for microgrids with storage: Review, challenges, and research needs," *Renewable and Sustainable Energy Reviews*, vol. 14, no. 7, pp. 2009–2018, sep 2010.

[70] N. Lidula and A. Rajapakse, "Microgrids research: A review of experimental microgrids and test systems," *Renewable and Sustainable Energy Reviews*, vol. 15, no. 1, pp. 186–202, jan 2011.

EBSCOhost - printed on 2/14/2023 2:46 PM via . All use subject to https://www.ebsco.com/terms-of-use

[71] H.R. Baghaee, M. Mirsalim, G.B. Gharehpetian, H.A. Talebi, "A Decentralized Robust Mixed $H_2/H_\infty$ Voltage Control Scheme to Improve Small/Large-Signal Stability and FRT capability of Islanded Multi-DER Microgrid Considering Load Disturbances", *IEEE Systems Journal*, vol. 12, no. 3, pp. 2610-2621, April 2017.

[72] H.R. Baghaee, M. Mirsalim, G.B. Gharehpetian, H.A. Talebi, "Nonlinear load sharing and voltage compensation of microgrids based on harmonic power-flow calculations using radial basis function neural networks", *IEEE Systems Journal*, vol. 12 no. 3, pp. 2749-2759, September 2018, DOI: 10.1109/JSYST.2016.2645165.

[73] H.R. Baghaee, M. Mirsalim, G.B. Gharehpetian, H.A. Talebi, "Unbalanced harmonic power sharing and voltage compensation of microgrids using radial basis function neural network-based harmonic power-flow calculations for distributed and decentralized control structures", *IET Gen., Trans. Dist*., vol. 12, no. 7, pp. 1518–1530, April 2018, DOI: 10.1049/iet-gtd.2016.1277.

[74] H.R. Baghaee, M. Mirsalim, G.B. Gharehpetian, "Power calculation using RBF neural networks to improve power sharing of hierarchical control scheme in multi-DER microgrids", *IEEE Journal of Emerging and Selected Topics in Power Electronics*, vol. 4, no. 4, pp. 1217-1225, December 2016, DOI: 10.1109/JESTPE.2016.2581762.

[75] Z. Li, M. Shahidehpour, F. Aminifar, A. Alabdulwahab, Y. Al-Turki, "Networked Microgrids for Enhancing the Power System Resilience", *Proceedings of the IEEE*, vol. 105, no. 7, pp. 1289-13010, July 2017.

[76] H.R. Baghaee, "Control of Microgrids to Respond to Large-Signal Disturbances and Nonlinearities and its Real-time Implementation", PhD. Dissertation Department of Electrical and Computer Engineering, Amirkabir University of Technology, Tehran, Iran, 2017.

[77] H.R. Baghaee, M. Mirsalim, G.B. Gharehpetian, "Performance improvement of Multi-DER microgrid for small and large-signal disturbances and nonlinear loads: novel complementary control loop and fuzzy controller in a hierarchical droop-based control scheme", *IEEE Systems Journal*, vol. 12, no. 1, pp. 444-451, March 2018, DOI: 10.1109/JSYST.2016.2580617.

[78] H.R. Baghaee, M. Mirsalim, G.B. Gharehpetian, H.A. Talebi "A decentralized power management and sliding mode control strategy for hybrid AC/DC microgrids including renewable energy resources", *IEEE Trans. on Industrial Informatics*, vol. PP, no. 99, pp. 1-10, March 2017, DOI: 10.1109/TII.2017.2677943.

[79] H.R. Baghaee, M. Mirsalim, G.B. Gharehpetian, H.A. Talebi, "Three phase AC/DC power-flow for balanced/unbalanced microgrids including wind/solar, droop-controlled and electronically-coupled distributed energy resources using RBF neural networks", *IET Power Electronics*, vol. 10, no. 3, pp. 313-328, March 2017, DOI: 10.1049/iet-pel.2016.0010.

[80] H.R. Baghaee, M. Mirsalim, G.B. Gharehpetian, H. Talebi, "Generalized three phase robust load-flow for radial and meshed power systems with and without uncertainty in energy resources using dynamic radial basis functions

EBSCOhost - printed on 2/14/2023 2:46 PM via . All use subject to https://www.ebsco.com/terms-of-use

neural networks", Journal of Cleaner Production, vol 174, part C, pp. 96-113, February 2018, DOI: 10.1016/j.jclepro.2017.10.316.

[81] A.H. Etemadi, E.J. Davison, R. Iravani, "A Generalized Decentralized Robust Control of Islanded Microgrids", *IEEE Trans. on Power Sys*., vol. 29, no. 6, pp. 3102-3113, Oct.2014/

[82] M. S. Sadabadi, A. Karimi, H. Karimi, "Fixed-order decentralized/distributed control of islanded inverter-interfaced microgrids," *Control Engineering Practice*, vol. 45, pp. 174–193, December 2015.

[83] X. Lu, X. Yu, J. Lai, J.M. Guerrero, H. Zhou, "Distributed Secondary Voltage and Frequency Control for Islanded Microgrids with Uncertain Communication Links", *IEEE Trans. on Ind. informatics*, vol. PP, no. 99, pp. 1-13, August 2016.

[84] N. Mahdian-Dehkordi, H. R. Baghaee, N. Sadati, J. M. Guerrero, "Distributed Noise-resilient Secondary Voltage and Frequency Control for Islanded Microgrids", *IEEE Trans. on Smart Grid*, vol. PP, no. 99, pp. 1-11, DOI: 10.1109/TSG.2018.2834951.

[85] J. Lai, H. Zhou, X. Lu, X. Yu, W. Hu, "Droop-Based Distributed Cooperative Control for Microgrids with Time-varying Delays", *IEEE Trans. Smart Grid*, vol. 7, no. 4, pp. 1775-1789, July 2016.

EBSCOhost - printed on 2/14/2023 2:46 PM via . All use subject to https://www.ebsco.com/terms-of-use

# CHAPTER TWENTY-ONE

# SIMULATION MODEL OF A PROTECTION SCHEME FOR ACTIVE DISTRIBUTION NETWORKS

R. CHIUMEO[1], C. GANDOLFI[1], F. BELLONI[2], S. PUGLIESE[2]

## Abstract

The growing trend of installed power coming from Distributed Generators (DG) in distribution networks is causing new issues in grid operation. In particular, the interaction between DG and grid protections can cause nuisance trips, unwanted island operations and, in general, a worsening in power quality. This chapter discusses a possible protection scheme suited for active networks, both radial and meshed, implementing logic selectivity. The proposed approach is based on directional protections coordinated through communications. Simulation models of an urban Medium Voltage (MV) distribution grid, distributed generators and the types of protections employed were developed in the DIgSILENT Power Factory environment. Digital simulations confirmed the effectiveness of the proposed approach.

**Keywords:** Active networks, grid protections, logic selectivity, MV distribution grid, radial/meshed grid.

[1] Ricerca sul Sistema Energetico—RSE S.p.A. Via Rubattino 54, 20134, Milano, Italy, e-mail: chiara.gandolfi@rse-web.it.
[2] Unareti S.p.A.

EBSCOhost - printed on 2/14/2023 2:46 PM via . All use subject to https://www.ebsco.com/terms-of-use

## Introduction

A number of different factors, including improvements in power electronics; a reduction in transmission and distribution costs; environmental issues; and the need to diversify power sources, is driving a rapid increase in Distributed Generators (DG) connected to Medium Voltage (MV) distribution grids. The presence of large amounts of DG can interact with the grid and can have major impacts on power quality. Some of these primary interactions between DG and distribution grids are:

- Reversal of power flow;
- Harmonic pollution;
- Voltage increases;
- Voltage variations;
- Flicker;
- Nuisance trips/failures of grid protections;
- Unwanted island operations [1, 2].

This chapter, focusing on the last two phenomena, proposes a possible protection scheme suited to active distribution grids [3]. Such a scheme makes use of directional line overcurrent relays and directional earth relays and introduces communication between the grid protections and interface protections of DG [4]. The main goals of the proposed solution are: management of bidirectional power flows; logic selectivity; faulty line segment selection; and reduced risk of unwanted islands.

This chapter deals with the implementation of the proposed protection scheme for radial and meshed distribution grids in the DIgSILENT[3] Power Factory digital simulation environment. To this end, models of a typical urban MV distribution grid, grid protections, DG interface protections and the communication systems needed were developed.

The impact of delays in signal communication transmission was also considered to evaluate the impact of these time delays on grid performance. Digital simulations were performed to show the effectiveness of the proposed solution.

## Operational principles of the protection scheme

The protection scheme typically employed in a MV distribution feeder is based on a main protection, including an overcurrent relay (non-

[3] DIgSILENT Power Factory, version 14.1.4.

EBSCOhost - printed on 2/14/2023 2:46 PM via . All use subject to https://www.ebsco.com/terms-of-use

directional) and a directional earth relay, installed at the Primary Substation (PS) level together with a circuit breaker [5]. In the case of a fault on the line, the protection trips, disconnecting the whole feeder from the main grid. In order to reduce the risk of unwanted island operations, each generator is equipped with an interface protection, which trips in the case of an under/over-voltage or frequency variation larger than a dead band around the nominal value.

The main drawbacks of this protection scheme are:

- Disconnection of the entire feeder in the case of a fault;
- Possible disconnection of generators in non-faulted lines;
- Possible unwanted island operation (the interface protection does not recognize the loss of the main);
- Reclosure procedures affecting the whole feeder.

In the proposed protection scheme, the distribution feeder is subdivided into two or more segments. A line protection and a circuit breaker are installed at both ends of each line segment. Each protection is composed of a directional line overcurrent relay and a directional earth relay. Line protections can exchange messages, and, in particular, two different logic commands can be sent/received:

- BLOCK: the receiving protection is disabled, so that it cannot trip;
- TRIP: the receiving protection is forced to trip, independently of its settings.

Also, DG interface protections need to be modified and adapted. In particular, they need to accept TRIP commands and they need to provide two different dead bands around the nominal frequency value, as shown in Figure 1.

The wider dead band is employed in standard conditions, while the narrower one is automatically activated only in cases where the fault is located near the generator [6].

The operational principles of the proposed protection scheme are illustrated in Figure 2. Two directional protections, one for each possible direction, are installed at the primary substation level and at the secondary substations, as shown in Figure 2. In the example, a fault occurs in the second line segment.

EBSCOhost - printed on 2/14/2023 2:46 PM via . All use subject to https://www.ebsco.com/terms-of-use

Protections P0 and P1B are started by fault currents supplied by the primary substation; P2A (and P3A, if the line has more segments than in Figure 2) may be started by a fault current supplied by DG2.




Figure 1. Narrow and wide frequency bands of the DG interface protections.

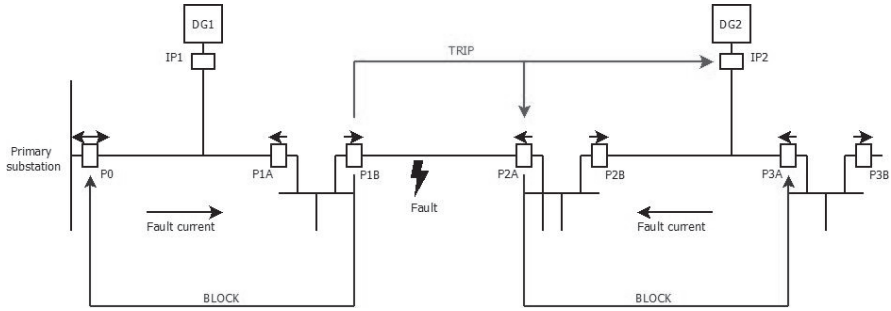



Figure 2. Illustration of the operational principles of the protection scheme.

In the proposed scheme, for both radial and meshed grid configurations:

1. P1B sends a BLOCK message to P0, i.e. in the opposite direction to the fault current; the same holds for P2A and P3A.
2. P0 and P3A, being blocked, do not trip, while P1B and P2A can trip.
3. If P1B is the first protection that trips, it sends a TRIP signal to P2A which is forced to trip too.
4. A TRIP signal is sent to all DGs connected downstream of P1B, forcing disconnections.

EBSCOhost - printed on 2/14/2023 2:46 PM via . All use subject to https://www.ebsco.com/terms-of-use

In this a way, the fault is unsupplied and the faulted line segment is detected by the tripping of P1B and P2A. The line segments upstream of the faulted one remain supplied and the relevant DGs remain connected if they have a Fault Ride Through (FRT) capability. In the case of a communication failure, the protection P0 does not receive the BLOCK signal and trips, disconnecting the whole distribution feeder. In this way, the protection scheme is still functional, even though it has reduced performance.[4]

The proposed protection scheme has two main drawbacks:

- The protection setup must take into account communication time delays, such as an intentional delay in the maximum current protection relays to avoid instantaneous tripping before receiving the block signal. Due to this delay some PQ indices may show worse performance or the lines can be overloaded for a period of time not compatible with their thermal limits, as discussed at the end of this chapter.
- Protections and circuit breakers need to be duplicated along the line to reduce load disconnection (Figure 2).

## Simulation models

For the study presented here, the following DIgSILENT Power Factory simulation models were developed:

- MV distribution grid (radial and meshed configurations);
- Distributed generators;
- Directional line protections and directional earth protections;
- DG interface protections;
- Communication channels with adjustable delays.

### *Distribution grid*

A model based on a radial urban MV distribution network of the Italian DSO Unareti S.p.A. was considered. Even though quite general, the selected network had some peculiarities, such as the presence of a 23 kV level and a 9 kV level and the connection of two 23 kV busbars with eight parallel lines. The network scheme with three different voltage levels (9, 23, and 220 kV) is represented in Figure 3. The new type of directional protections were installed in the two zones circled, while typical line

[4] In this case, performances are the same as those of the current protection system.

EBSCOhost - printed on 2/14/2023 2:46 PM via . All use subject to https://www.ebsco.com/terms-of-use

protections were installed at the beginning of all the other distribution feeders. Maximum current protections were installed at the secondary side of each transformer. The neutral point of the MV network was not connected to earth.

The scheme for the meshed grid configuration is reported in Figure 15.

### *Distributed generators*

Photovoltaic distributed generation was considered in the study. DIgSILENT native models of PV generators were employed, with custom controls. In particular, during steady-state conditions, PV generators supplied their rated power, while during a voltage dip they supplied reactive current $\Delta I_q$ proportional to the voltage drop $\Delta V$, according to the formula:

$$\frac{\Delta I_q}{I_N} = k \frac{\Delta V}{V_N} \tag{1}$$

where $I_N$ is the rated current; VN is the rated voltage; and k≥2 [7–10]. The model employed does not take into account the presence of power electronic switches.

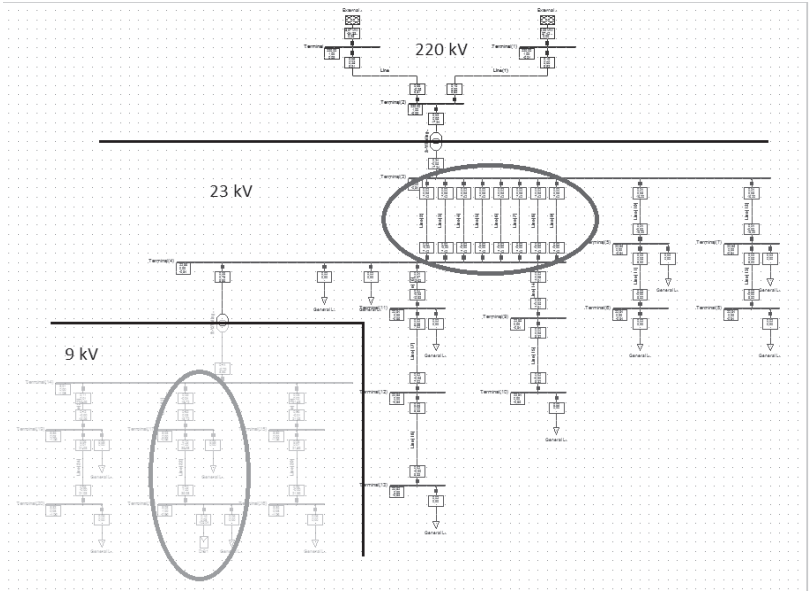



Figure 3. DIgSILENT MV network model.

EBSCOhost - printed on 2/14/2023 2:46 PM via . All use subject to https://www.ebsco.com/terms-of-use

### *Directional protections*

Line protections were implemented as multifunction protections, which incorporate both directional overcurrent and directional earth protections. The model, implemented within the DIgSILENT Power Factory environment, also allowed the dispatch and reception of BLOCK and TRIP signals.

The directional overcurrent relay can be set up with three different current threshold levels, each one with a different time delay. The directional earth relay has a current and voltage threshold with a configurable angular sector and time delay.

The BLOCK signal is dispatched when the protection starts, while the TRIP signal is dispatched when the protection actually trips.

Circuit breakers were modelled too. In particular, a mechanical time delay of 80 ms between reception of the opening command and the actual opening was considered.

### *Interface protections*

The block scheme of the interface protection model is represented in Figure 4.

In line with the latest Italian standards [6], the model integrates three different protection functions:

- Over/under-voltage;
- Over/under-frequency (wide band)—always active;
- Over/under frequency (narrow band)—activated only if the grid voltage negative or zero sequences exceed a threshold value or the positive sequence decreases below a given limit.[5]

[5] This allows the identification of a MV fault by a frequency variation generated in the HV transmission network.

EBSCOhost - printed on 2/14/2023 2:46 PM via . All use subject to https://www.ebsco.com/terms-of-use

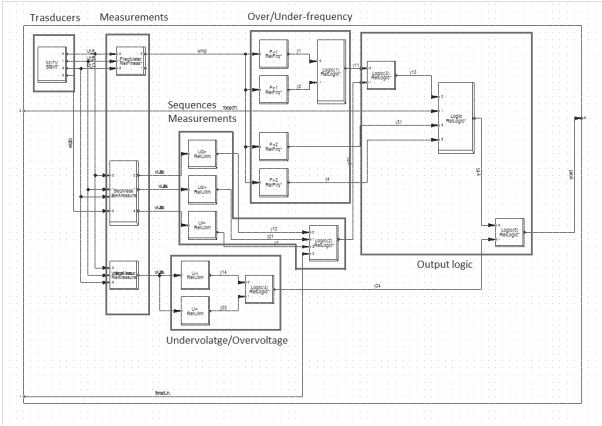



Figure 4. DIgSILENT implementation of interface protection.

An additional overvoltage protection needs to be present according to Italian standards, but it is not included in the model since it considers very slow voltage variations.

## *Communication channel*

Communication exchanges between protections are represented in the DIgSILENT block scheme reported in Figure 5, where an adjustable time delay is inserted along each signal path to simulate communication lags.

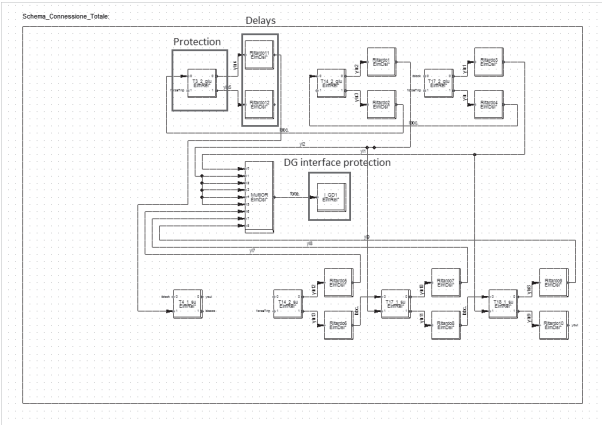



Figure 5. Communication channel model.

EBSCOhost - printed on 2/14/2023 2:46 PM via . All use subject to https://www.ebsco.com/terms-of-use

### *Protection settings*

Traditional line protections and DG interface protections were set according to typical Italian thresholds, as reported in Table 1.

**Table I. Protections settings.**

| Protection | Threshold | Intentional delay |
|---|---|---|
| *Line overcurrent @9 kV* | | |
| 51.S1 | 1.5 $I_{nom}$ | 1 s |
| 51.S2 | 1 kA | 0.25 s |
| 51.S3 | 2 kA | 0 s |
| *Line overcurrent @23 kV* | | |
| 51.S1 | 1.5 $I_{nom}$ | 1 s |
| 51.S2 | 0.8 kA | 0.25 s |
| 51.S3 | 1.4 kA | 0 s |
| *Transformer secondary side overcurrent* | | |
| 51 | 1.6 $I_{nom,2}$ | 1.5 s |
| *Directional earth @9 kV** | | |
| 67N | 12 mA | 0.4 s |
| 59N | 0.4 V | 0.4 s |
| *Directional earth @23 kV** | | |
| 67N | 12 mA | 0.4 s |
| 59N | 0.8 V | 0.4 s |
| *Interface protection* | | |
| 59 | 1.15 $V_N$ | 0.2 s |
| 27 | 0.4 $V_N$ | 0.2 s |
| 81>.S1 | 50.3 Hz | 0.1 s |
| 81>.S2 | 51.5 Hz | 0.1 s |
| 81<.S1 | 49.7 Hz | 0.1 s |
| 81<.S2 | 47.5 Hz | 0.1 s |

*Settings also valid for the directional earth relays of the new protection models.

The directional line relays were set in a similar fashion to the traditional line overcurrent relay, but adding an intentional delay to the 51.S3 protection in order to take into account possible communication time-lags. In this chapter, a typical communication time-lag of 20 ms was supposed, and as such an intentional time delay of 30 ms was added to the overcurrent protection. This time-lag is typical of fibre optic-based communications.

EBSCOhost - printed on 2/14/2023 2:46 PM via . All use subject to https://www.ebsco.com/terms-of-use

## Simulation results

The proposed protection scheme was tested through digital simulations in the DIgSILENT environment. Different case studies were considered, in order to assess both the logic selectivity of the new type of protections and the interactions with typical protection schemes considering radial (Figure 3) and meshed grid configurations (Figure 15).

### *Radial grid configuration*

*Polyphase fault on the line equipped with the proposed protection scheme*

A three-phase short-circuit was simulated on the 9 kV line with about 2 MVA of connected DG. It was located in the second line segment, at 3 km from the 23 kV/9 kV transformer. The simulation time began at t = -100 ms and the fault occurred at t = 0 s. The time-overcurrent plots of the directional line protections are reported in Figure 6 together with relevant short-circuit current values.

According to the plots in Figure 6, if no logic selectivity is applied, both the protections installed on the faulted line would trip, since the short-circuit current, shown as vertical lines, intersects the protection characteristics at the same time value (reported on the y-axes).

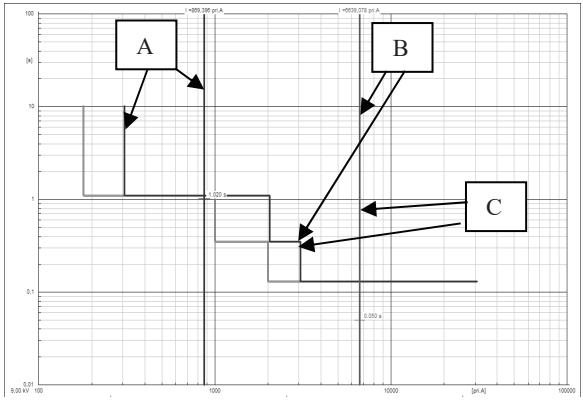



Figure 6. Directional line protection time-overcurrent plots: protections installed at the PS (A), at the beginning of the faulted line (B) and along the same line (C). B and C curves overlap.

With the proposed approach, the protection closer to the fault is the only one left active, minimizing the number of disconnected users. In this

EBSCOhost - printed on 2/14/2023 2:46 PM via . All use subject to https://www.ebsco.com/terms-of-use

example, DGs are also disconnected from the feeder, since they are located downstream of the fault. Figure 7 reports the following simulation results:

8a) starting status of the protection at the PS (220/23 kV);
8b) starting status of the protection at the beginning of the MV line (9 kV);
8c) starting status of the protection closer to the fault;
8d) blocking signal (high) and tripping status (low) of the protection at the PS;
8e) blocking signal (high) and tripping status (low) of the protection at the beginning of the MV line;
8f) blocking signal (low) and tripping status (high) of the protection closer to the fault.

Only the protection closest to the fault actually trips, forcing the tripping of both the DG interface protection and the directional line protection installed downstream of the feeder. The final status of the three 9 kV feeders is shown in Figure 8, where the open breakers are highlighted with red circles.

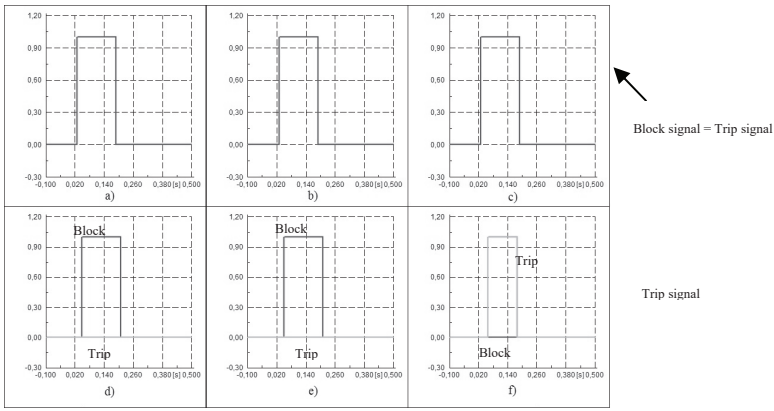



Figure 7. Simulation results: protections starting; blocking signal exchange; and protections tripping.

The resulting voltage waveforms at different 23 kV and 9 kV busbars are reported in Figure 9, where it is shown that only the line segments

EBSCOhost - printed on 2/14/2023 2:46 PM via . All use subject to https://www.ebsco.com/terms-of-use

downstream of the fault are disconnected from the main grid. The case of a single-phase fault is similar to this one and as such it is not reported.

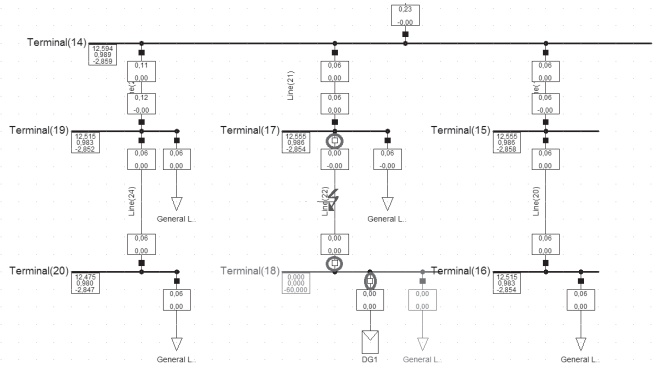



Figure 8. Grid configuration after protection intervention. Open breakers after protection trips are highlighted with red circles.

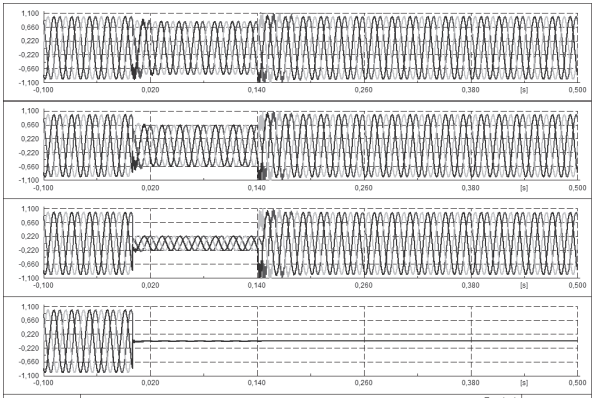



Figure 9. Line-to-line voltages at different points of the MV distribution grid. a) 23 kV primary substation busbar; b) 9 kV busbar; c) 9 kV line (2 km); d) 9 kV line (4 km).

EBSCOhost - printed on 2/14/2023 2:46 PM via . All use subject to https://www.ebsco.com/terms-of-use

## *Radial grid configuration*

*Polyphase fault on a 23 kV line equipped with the proposed protection scheme*

A three-phase short-circuit occurring on one of the eight parallel 23 kV lines outgoing from the primary substation MV busbar was simulated. The faulted line was selected by the trip of the protection installed at the feeder starting point, which also forced the protection at the end of the line to trip. The forced trip of this second protection avoids the fault being supplied from the primary substation through the healthy lines. Figure 10 shows the trip signal dispatched by the "upper" protection and received by the "lower" one, with a 20 ms delay, and the fault currents.

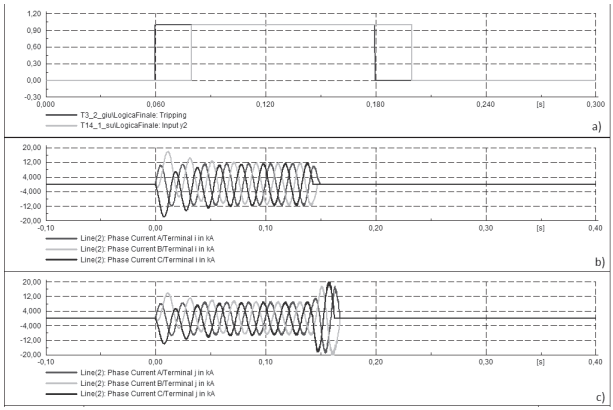



Figure 10. Line protections coordination: a) time delay between dispatched and received TRIP signals; b) fault currents from the primary substation; c) fault currents through healthy lines.

## *Radial grid configuration*

*Polyphase fault on a line equipped with a traditional protection scheme*

A three-phase short-circuit was simulated on one of the 9 kV distribution lines. The fault occurred at t = 0 s and at 1.5 km from the 9 kV busbar. In this case, the typical protection setup ensured that the protection installed at the primary substation level did not trip, as shown in the time-overcurrent plot in Figure 11.

The configuration of the 9 kV portion of the grid after the trip of protections is shown in Figure 12.

EBSCOhost - printed on 2/14/2023 2:46 PM via . All use subject to https://www.ebsco.com/terms-of-use

The faulted feeder was disconnected from the main grid, as also shown by the voltages of different MV busbars, reported in Figure 13.

In this case, DG interface protections were not forced to trip by any external signal. The generator was equipped with FRT capabilities and it was controlled to supply reactive current during the voltage dip, according to (1). Figure 14 reports the grid frequency and voltage measured by the interface protections. Even if the DG current is sufficient to make the relevant line protection start, logic selectivity and communication avoid nuisance trips.

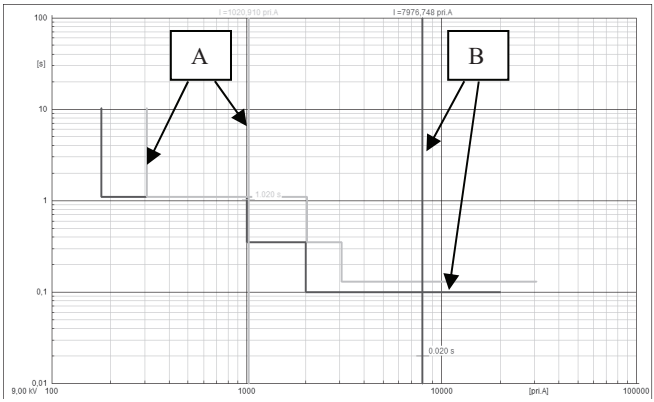



Figure 11. Time-overcurrent plot. The primary substation protection characteristic is represented in A, while the 9 kV line protection characteristic is in B.

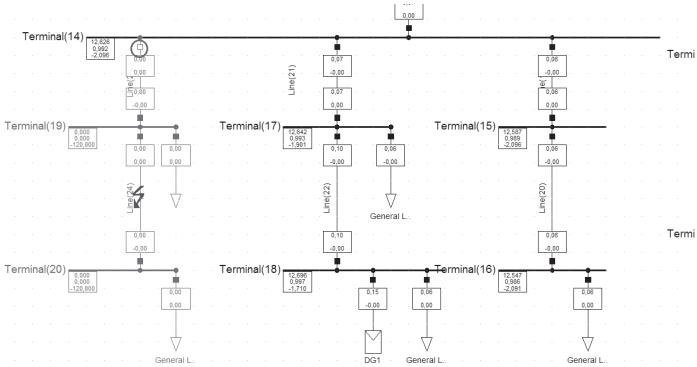



Figure 12. Final grid configuration. Open breaker is highlighted with a circle.

EBSCOhost - printed on 2/14/2023 2:46 PM via . All use subject to https://www.ebsco.com/terms-of-use

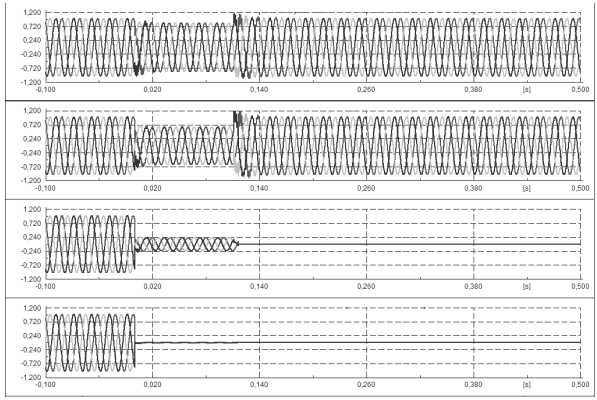



Figure 13. Line-to-line voltages at different points of the MV network: a) 23 kV primary substation busbar; b) 9 kV busbar; c) 9 kV line (2 km); d) 9 kV line (4 km).

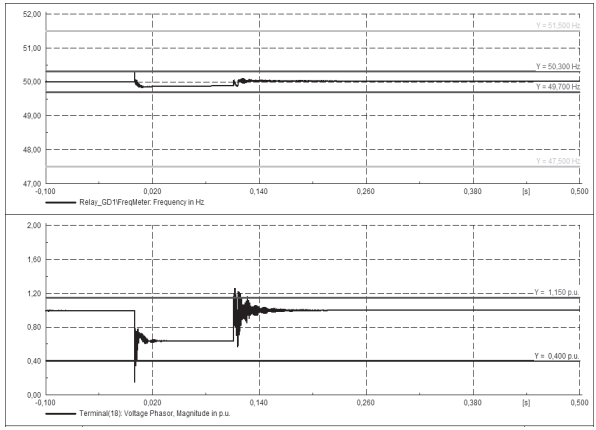



Figure 14. Grid frequency and voltage measured by the DG interface protection, compared to relevant threshold values.

## *Meshed grid configuration: double polyphase fault*

The application of protection logic to a meshed distribution grid configuration was evaluated, in particular considering a ring scheme as shown in Figure 15. The directional protections were installed at the PS

EBSCOhost - printed on 2/14/2023 2:46 PM via . All use subject to https://www.ebsco.com/terms-of-use

and the Secondary Substation (SS) as indicated. Two radial lines with traditional protections were considered too.

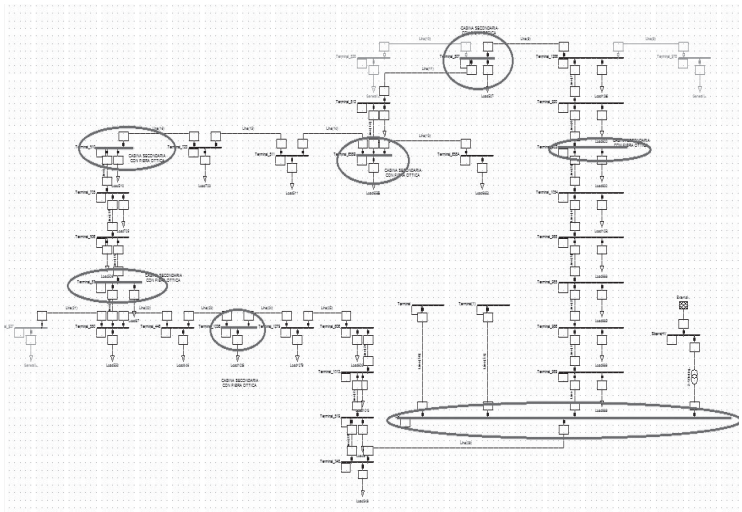


Figure 15. Meshed grid structure.

The simulation results refer to two consecutive polyphase faults at different points of the ring line (Figure 16). The first one (1) occurred at t = 0 s and the second one (2) at t = 0.5 s. After fault (1), all the protections installed on the ring line were started for the maximum current threshold: the blocking signal inhibited all the protections except for the two placed directly upstream and downstream of the fault point that could trip, selecting the faulty feeder.[6] Thereafter, the grid operated in a radial configuration.

When the second fault occurred (2) the protection logic acted in the same way as for a radial grid. The main voltage waveforms, referring to the nodes in Figure 16, are reported in Figure 17 and the final grid configuration is shown in Figure 18.

[6] To activate the protections blocked during the elimination of the first fault, it is necessary to provide a timing mechanism to reset the blocking state.

EBSCOhost - printed on 2/14/2023 2:46 PM via . All use subject to https://www.ebsco.com/terms-of-use

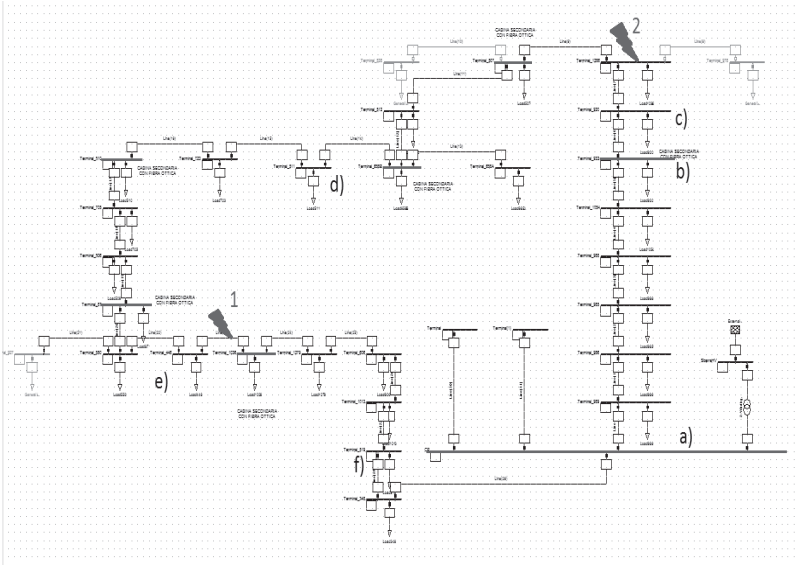



Figure 16. Fault position in the ring line.

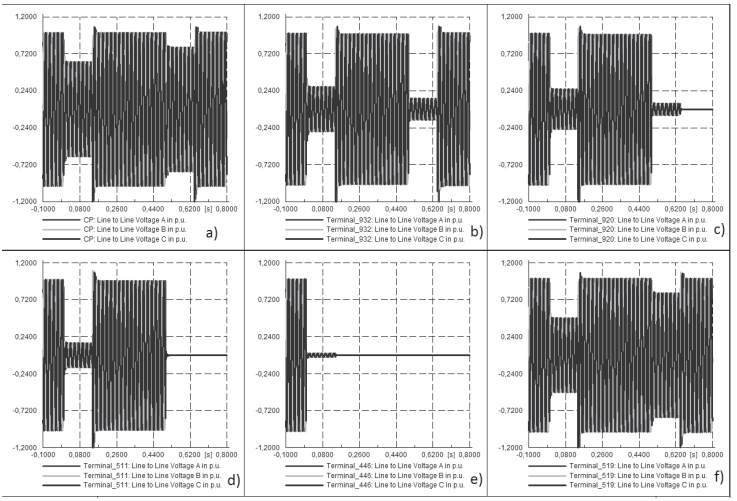



Figure 17. Voltage waveform at the different points of the grid shown in Figure 16.

EBSCOhost - printed on 2/14/2023 2:46 PM via . All use subject to https://www.ebsco.com/terms-of-use

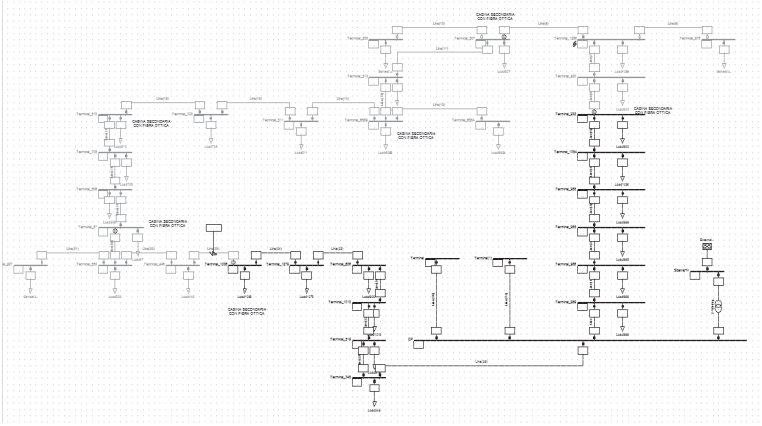


Figure 18. Grid configuration after second fault selection.

### *Line circuit breaker malfunction*

To characterized the behavior of the system, a trip failure of a line Circuit Breaker (CB) was simulated considering the ring configuration in case of the fault in (1) (Figure 16). It was assumed that the failed CB was installed immediately upstream of the fault, covering the ring anti-clockwise starting from the primary substation.

In this case, the block signal is sent from the protection of the failed CB ($P_1$) to the one upstream, in the direction of the fault currents ($P_2$). After the reset of the block condition,[7] since no single CB has cleared the fault, the $P_2$ protection trips. In Figure 19, the signals involved are shown; in Figure 20 the MV primary substation voltages are reported.

In conclusion, in the case of a circuit breaker malfunction the following issues are pertinent:

- the protection scheme can work properly even though it displays lower performance;
- the grid protection can be used as a back-up;
- the time to select the fault is double that in a properly operating system.

[7] In the simulation, the block reset time was fixed to 150 ms after its start.

EBSCOhost - printed on 2/14/2023 2:46 PM via . All use subject to https://www.ebsco.com/terms-of-use

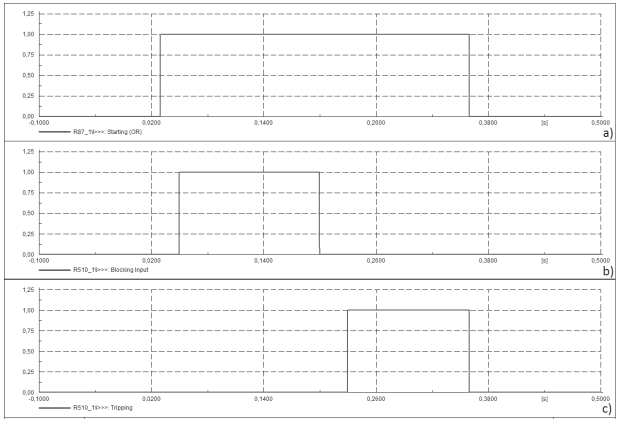



Figure 19. Protection signal exchange: a) CB failure start; b) block recived by protection $P_2$ (reset signal after 150 ms); c) protection $P_2$ trip.

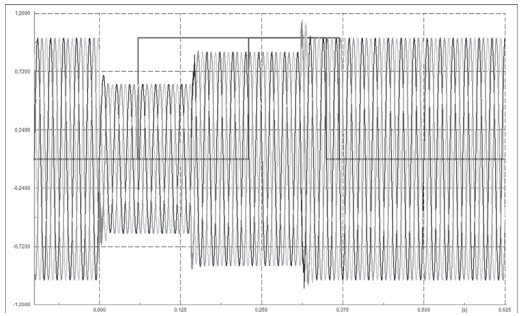


Figure 20. Primary substation voltages in pu and trip signals; the time between protection start and the CB trip explains the delay in voltage restoration.

## *Communication channel time delay impact on PQ indices*

As noted previously, the use of a communication channel between the protections implies the introduction of an intentional delay; this means that the faulty currents flow in the feeder for a longer time in the grid. The result of this includes:

- higher thermal stress on the line ($I^2t$ index grows linearly during the time of persistent fault currents);
- the relevant voltage dip duration is higher.

EBSCOhost - printed on 2/14/2023 2:46 PM via . All use subject to https://www.ebsco.com/terms-of-use

This second effect has to be taken into consideration because of its impact on grid PQ level.

In accordance with the standard EN 50160 [11], voltage dips are classified with voltage depth (u) and duration as show in Table II. The "A" cells correspond to the immunity area for class 2 apparatuses, which are supposed to be connected to the public distribution network (IEC 61000-4-11 [12]); while the "A" + "B" cells represent the immunity area for class 3 equipment, which operate in industrial environments (IEC 61000-4-34 [13]).

**Table II. Voltage dips classification EN 50160.**

| Residual voltage [%] | 20-200 [ms] | 200-500 [ms] | 0,5-1 [s] | 1,0-5 [s] | 5,0-60 [s] |
|---|---|---|---|---|---|
| **90 > u ≥ 80** | A | A | B | B | |
| **80 > u ≥ 70** | A | A | | | |
| **70 > u ≥ 40** | B | | | | |
| **40 > u ≥ 5** | | | | | |
| **5 > u ≥ 1** | | | | | |

Another way to classify grid performance is to use a synthetic index as:

- N3b—number of voltage dips under the class 3 immunity curve;
- R-DFI (Regulated Dip Frequency Index), calculated considering weight 1 for the voltage dips under the class 3 immunity area; weight 0 for the ones in the "A" cells; and weight 0.5 for events in the "B" cells.

The values of these indices can be affected by the proposed protection scheme: in Figure 21 the index trends are shown considering different time delays in the protection communication channel. The values were calculated beginning with the voltage dip data collected from the QuEEN monitoring system[8] in Italy for the year 2011.

As shown, the index N3b is strongly influenced by the communication delay, particularly when considering a delay of over 60 ms.

[8] http://queen.erse-web.it/eng/home.aspx.

EBSCOhost - printed on 2/14/2023 2:46 PM via . All use subject to https://www.ebsco.com/terms-of-use

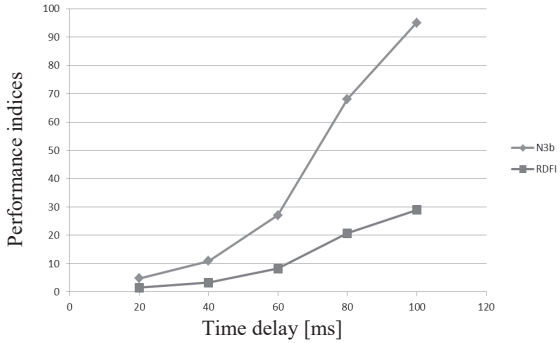



Figure 21. N3b and R-DFI index for different values of the protection communication channel time delay.

## Conclusions

A possible protection scheme suited for mixed passive and active distribution networks, considering radial and meshed configuration, is presented in this chapter. This logic makes use of directional line over current relays, directional earth relays and distributed generator interface protections, coordinated through a communication system. The proposed scheme offers certain advantages in terms of: logic selectivity; dealing with bidirectional power flows; optimal management of DG disconnections; faulted line segment selection; and integration with pre-existing protection schemes. The proposed solution also has some drawbacks due to communication time-lags and the need for redundancy.

Digital simulations, performed with DIgSILENT Power Factory, showed the effectiveness of the proposed approach for different types of faults and different grid configurations (radial and meshed). In the simulations, a grid model including protections and distributed generators, was developed.

Finally, an analysis of the possible effect on some power quality indices arising from the application of the proposed system was carried out, highlighting the need for fast communication channels to guarantee a high PQ level in the grid.

## Acknowledgement

This work has been financed by the Research Fund for the Italian Electrical System under the Contract Agreement between RSE S.p.A. and the Ministry of Economic Development—General Directorate for Nuclear

EBSCOhost - printed on 2/14/2023 2:46 PM via . All use subject to https://www.ebsco.com/terms-of-use

Energy, Renewable Energy and Energy Efficiency in compliance with the Decree of March 8, 2006.

## References


[1] F. J. Pazos, "Operational experience and field tests on islanding event caused by large photovoltaic plants," 21th International Conference on Electricity Distribution, CIRED2011, 6–9 June, Frankfurt, Germany.

[2] Z. Ye, A. Kolwalkar, Y. Zhang, P. Du, R. Walling, "Evaluation of anti-islanding schemes based on non-detection zone concept," IEEE 34th Annual Power Electronics Specialist Conference, PESC'03, 15-19 June 2003, Niskayuna, NY, USA, Vol. 4, pp.1735–1741.

[3] F. Belloni, R. Chiumeo, C. Gandolfi, A. Villa, "A protection coordination scheme for active distribution networks," 47th International Universities' Power Engineering Conference, UPEC 2012, 4–7 September 2012, London, UK, pp.1–6.

[4] R. Calone, A. Cerretti, A. Fatica, "Evolution of fault locator on MV distribution networks: from simple stand-alone device, to a sophisticated strategic component of the SMART GRID control system," 21th International Conference on Electricity Distribution, CIRED2011, 6–9 June, Frankfurt, Germany.

[5] A. Cerretti, G. Scrosati, L. Consiglio, "Upgrade of ENEL MV network automation to improve performances in presence of faults and to deal DG," 21th International Conference on Electricity Distribution, CIRED2011, 6–9 June, Frankfurt, Germany.

[6] A. A. V. V., "Codice di trasmissione, dispacciamento, sviluppo e sicurezza della rete," web: http://www.terna.it/—in Italian language.

[7] R. Chiumeo, C. Gandolfi, "A Three Phase Photovoltaic Power System Connected to the MV Network: Behaviour during Voltage Dips," ICREPQ 2011, 13–15 April, Las Palmas di Gran Canaria, Spain, pp.1–6.

[8] A. A. V. V., "Transmission Code 2007," web: http://www.vde.com/.

[9] F. J. Pazos, "Power frequency overvoltages generated by solar plants," 20th International Conference on Electricity Distribution, CIRED2009, 8–11 June 2009, Prague, Czech Republic, pp. 1-4.

[10] F. Belloni, C. Chiappa, R. Chiumeo, P. Groppelli, A. Villa, "Sistemi elettronici di potenza per la connessione della generazione distribuita alla rete elettrica: analisi del comportamento a fronte dei disturbi di rete", final report "Ricerca di Sistema", web: http://www.rse-web.it - in Italian language.

[11] EN 50160, "Voltage characteristics in public distribution system," Ed. 2010.

[12] IEC 61000-4-11: Electromagnetic Compatibility (EMC)—Part 4–11: Voltage dips, short Interruptions and voltage variations immunity test (on a.c. input power port).

[13] IEC 61000-4-34: Electromagnetic compatibility (EMC)—Part 4–34: Testing and measurement techniques—Voltage dips, short interruptions and voltage variations immunity tests for equipment with input current more than 16 A per phase, 10-2005.


EBSCOhost - printed on 2/14/2023 2:46 PM via . All use subject to https://www.ebsco.com/terms-of-use

# CHAPTER TWENTY-TWO

# USING ON-LINE MEASUREMENTS TO IDENTIFY PARAMETERS OF IMPROVED HEFFRON-PHILLIPS MODEL INCLUDING EXCITATION SYSTEM AND GOVERNOR

B. ZAKER[1], G. B. GHAREHPETIAN[2]

## Abstract

The Heffron-Phillips (HP) model of synchronous generator is a fourth order linear model including a third order synchronous machine and a first order automatic voltage regulator (AVR) model. In the present study, a more detailed model of excitation and turbine-governor systems are added to the model as an improved HP model. The classic HP model just includes a simple gain and time constant for AVR model without including governor model. Further, the proposed improved HP model includes PID-based controllers for both excitation and turbine-governor systems. In this paper, a genetic algorithm-based method is proposed to identify the parameters of the proposed model using on-line measurements data. In the proposed method, the reference signals of the voltage and active power are considered as the input signals of excitation and turbine-governor systems, respectively, while the terminal voltage and output active power of the synchronous machine are regarded as output signals in order to identify the parameters of the system by means of matching the

[1] School of Electrical and Computer Engineering, Shiraz University, Shiraz, Iran. (b.zaker@shirazu.ac.ir)
[2] Electrical Engineering Department, Amirkabir University of Technology, Tehran, Iran. (grptian@aut.ac.ir)

EBSCOhost - printed on 2/14/2023 2:46 PM via . All use subject to https://www.ebsco.com/terms-of-use

estimated output signals of the simulated system and measured signals of the real system using genetic algorithm. The proposed method is applied to a single machine which connects an infinite bus system.

**Keywords:** Genetic algorithm, Heffron-Phillips model, parameter estimation, Synchronous generator.

## 1. Introduction

An accurate analysis of the power system is essential for understanding and predicting the behaviour of a power system such as security assessment. The first requirement of these analyses is to identify the parameters of different elements in the network including synchronous generators, power transformers, transmission lines, loads, and the like. Thus, modelling and identifying their parameters have attracted a lot of attention due to the major role of the synchronous generators in power systems.

Generally, the parameters related to the synchronous generator are identified based on off-line and on-line approach. The machine is not in service in off-line identification methods. The traditional methods of identifying the parameters related to the synchronous generator have been specified in IEEE standard [1] although they include some drawbacks. In this regard, some other off-line methods have been proposed such as using suddenly shorted circuit results and applying least squares method [2], exciting the stator windings with DC signal, while the rotor is in standstill [3], using stand still frequency response (SSFR), and an inverter-based voltage source [4]. [5-10]. However, these kinds of tests are usually difficult and time-consuming. In addition, the temperature effect and load changes have not been considered by these methods. However, the main drawback of these methods is related to the fact that the generator should be off-grid. In other words, the generator should be stopped for using, which is not economic. Accordingly, on-line identification methods were proposed to overcome the aforementioned issues [11-17]. The use of a small disturbance to the nominal value of the input signal is regarded as the basis for on-line identification methods. This signal should be applied to the system so that no interference can occur in the normal operation of the system. Generally, on-line parameter identification methods of synchronous generator can be classified into black-box and grey-box modelling methods. The black-box modelling approach [18-20] is related

EBSCOhost - printed on 2/14/2023 2:46 PM via . All use subject to https://www.ebsco.com/terms-of-use

to the input and output datasets of the synchronous generator in order to map these sets, where the structure of the system is arbitrary. These methods use wavelet transform, neural networks, and the like [18-20]. However, in grey-box modelling methods [11-14], the identification procedure is based on real physical structure of the synchronous machine such as third order model called Heffron-Phillips model. These methods use Kalman filter, Prony approach, transfer function estimation, etc. [11-14]. Usually, the excitation system is not considered in aforementioned methods and the parameters of the excitation system have been separately identified [21-24]. However, few studies have been conducted on identifying synchronous generator in the presence of controllers such as excitation system and turbine-governor system [16, 25, 26]. In this study, the excitation and turbine-governor systems were considered in the identification procedure.

In the present study, the synchronous generator, excitation, and turbine-governor parameters were simultaneously identified based on an improved Heffron-Phillips (HP) model. The classic HP model just includes a simple gain and time constant for automatic voltage regulator (AVR) model without including governor model. Further, the proposed improved HP model includes PID-based controllers for both excitation and turbine-governor systems.

Optimization is conducted by using genetic algorithm and on-line measurement data provided by Phasor Measurement Units (PMUs). Monitoring is considered as one of the most important objectives of the smart grids. The PMUs are the primary source of measurements, which is widely used in smart power grids. In the proposed method, the reference signals of the voltage and active power were considered as the input signals of excitation and turbine-governor systems, respectively, while the terminal voltage and output active power of the synchronous machine are regarded as output signals in order to identify the parameters of the system by means of matching the estimated output signals of the simulated system and measured signals of the real system using genetic algorithm. The proposed method is applied to a single machine which connects an infinite bus system.

This chapter is organized as follows. A brief description of classic and improved HP models is presented in Section 2. The identification procedure is explained in Section 3. Section 4 describes the case study and simulation results. Finally, the conclusion is discussed in Section 5.

EBSCOhost - printed on 2/14/2023 2:46 PM via . All use subject to https://www.ebsco.com/terms-of-use

## 2. Heffron-Phillips Model

A synchronous machine is connected to an infinite bus, which is considered as the case study in the present study, as shown in Fig. 1. This system includes a power transformer and two parallel transmission lines. Generally, the classic HP model of the synchronous generator is a fourth order linear model including a third order synchronous machine and a first order AVR. This model is suitable for small signal analysis, where linear approximation is useful. Therefore, all the input and output signals of this model such as $x$ have variations within a small domain around their nominal value shown by delta ($\Delta x$). The nonlinear equations of the synchronous machine and details of linearization procedure were discussed in [27]. Fig. 2 displays the block diagram of the linear model, where $\omega$ represents the rotor angular speed, $\delta$ indicates the rotor angle, $e'_q$ means the transient internal voltage of the armature, and $E_{FD}$ is considered as the field voltage. The input signals encompass $V_{ref}$ and $T_m$, which are the reference voltage of the AVR and input torque, respectively. In addition, the mechanical parameters are $D$ and $H$, which indicate the damping factor and rotor inertia, respectively. $T'_{do}$ is considered as the direct axis open circuit time constant. Finally, $K_A$ and $T_A$ indicate the DC gain and time constant of the AVR.

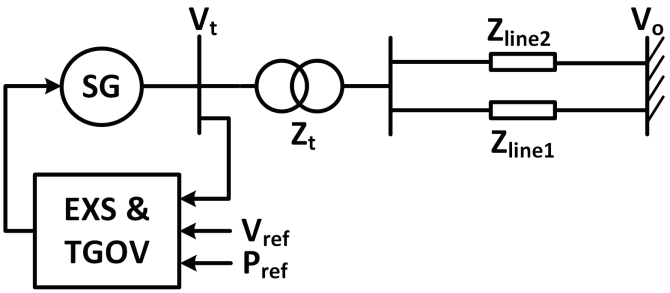



Fig. 1. Single machine infinite bus system.

EBSCOhost - printed on 2/14/2023 2:46 PM via . All use subject to https://www.ebsco.com/terms-of-use

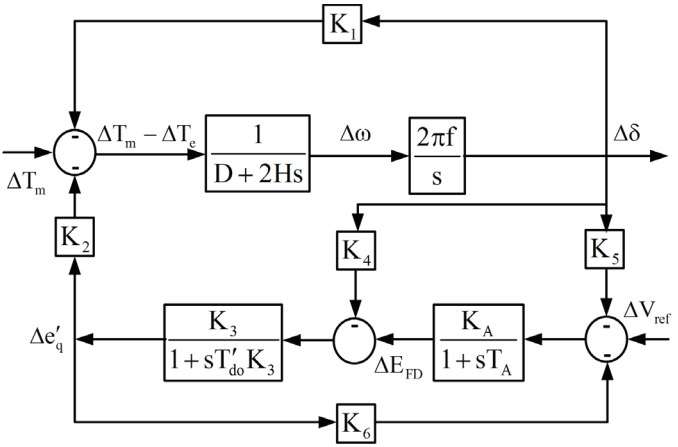



Fig. 2. Block diagram of classic HP model.

As illustrated in Fig. 2, this model contains six coefficients $K_1$-$K_6$ called HP model coefficients. The values of these coefficients are the functions of the operating point and reactances of the synchronous generator. These reactances include the steady state and transient reactance of the direct and quadratic axis (i.e., $X_d$, $X_q$, and $X'_d$). The operating point involves the terminal voltage ($V_{t0}$), and active and reactive power of the synchronous machine (i.e., $P_{e0}$, and $Q_{e0}$). Further, the calculation method of these coefficients is explained in [27].

The state-space variables and equations of this model are as follows:

$$\begin{aligned} x &= \left[\Delta\omega \quad \Delta\delta \quad \Delta e'_q \quad \Delta E_{FD}\right]^T \\ u &= \left[\Delta U_E \quad \Delta T_M\right]^T \\ y &= \left[\Delta V_t \quad \Delta P_e\right]^T \end{aligned} \tag{1}$$

$$\begin{aligned} \dot{x} &= Ax + Bu \\ y &= Cx \end{aligned} \tag{2}$$

where we have:

EBSCOhost - printed on 2/14/2023 2:46 PM via . All use subject to https://www.ebsco.com/terms-of-use

$$A=\begin{bmatrix} -D/2H & -K_1/2H & -K_2/2H & 0 \\ \omega_b & 0 & 0 & 0 \\ 0 & -K_4/T'_{do} & -1/(T'_{do}K_3) & 1/T'_{do} \\ 0 & -K_A K_5/T_A & -K_A K_6/T_A & -1/T_A \end{bmatrix}$$

$$B=\begin{bmatrix} 0 & 1/2H \\ 0 & 0 \\ 0 & 0 \\ K_A/T_A & 0 \end{bmatrix} \qquad C=\begin{bmatrix} 0 & K_5 & K_6 & 0 \\ 0 & K_1 & K_2 & 0 \end{bmatrix} \tag{3}$$

As mentioned in Introduction section, the improved HP model is proposed to model the excitation and turbine-governor systems. For this purpose, the standard static type of IEEE-ST6B and load control loop of standard GGOV1 (gas turbine) is considered for excitation and turbine-governor systems models, respectively. Considering these models, the block diagram of the proposed improved HP model is presented in Fig. 3.

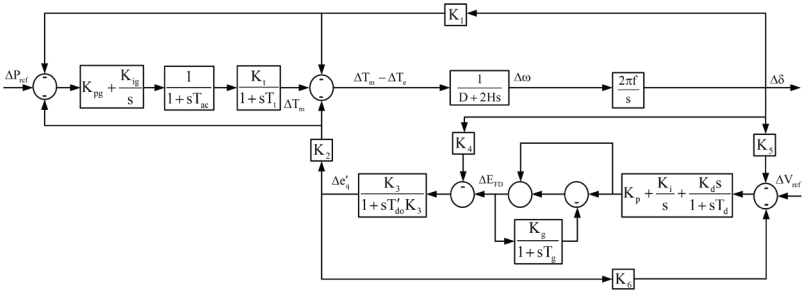



Fig. 3. Block diagram of the proposed improved HP model.

As illustrated in Fig. 3, $K_p$, $K_i$, $K_d$ and $T_d$ are proportional, integral, derivative gains, and time constant of excitation system, respectively. $K_g$ and $T_g$ indicate the regulator feedback parameters of excitation system. $K_{pg}$, $K_{ig}$, $K_t$, $T_t$ and $T_{ac}$ represent proportional, integral and turbine gains, turbine and valve actuator time constants of turbine-governor system, respectively.

EBSCOhost - printed on 2/14/2023 2:46 PM via . All use subject to https://www.ebsco.com/terms-of-use

## 3. Identification method

The present study aimed to identify the third order synchronous generator parameters including reactances, direct axis open circuit time constant, mechanical parameters, excitation and turbine-governor parameters. The identification is performed as follows:

Step 1: An operating point is considered to initialize the detailed nonlinear model. Then, the steady state values of the terminal voltage, active power, and reactive power of the synchronous generator are measured.

Step 2: A step signal with 1% magnitude of the nominal value is applied to the reference of excitation system in the detailed nonlinear model. The magnitude of this disturbance should be small to have a good linear approximation. Then, the oscillation of the terminal voltage is measured.

Step 3: The improved HP model is simulated, along with its ten unknown parameters. Based on sensitivity analysis results of [16], these parameters have the most important effect on the terminal voltage. During this step, other mechanical and turbine-governor parameters are set to their average values according to the typical values provided by standards. The genetic algorithm optimization procedure is used to minimize the error among measured outputs of the nonlinear system and estimated outputs of the simulated HP model by using the following objective function:

$$O.F._1 = \sqrt{\sum_i \left( \underline{V}_{ti} - \hat{\underline{V}}_{ti} \right)^2} \tag{4}$$

where $\underline{V}_t$ and $\hat{\underline{V}}_t$ are sampled vectors of measured and simulated outputs, respectively.

Step 4: A step signal with small magnitude is implemented to the reference of the turbine-governor. In addition, the magnitude of this disturbance should be small to have a good linear approximation. Then, the oscillation of the output active power is measured.

Step 5: The improved HP model with seven unknown parameters is simulated. According to the results of sensitivity analysis [16], these parameters have the most important effect on the output active power. During this step, other electrical and excitation system parameters are set to their estimated values in Step 3. The genetic algorithm optimization is

EBSCOhost - printed on 2/14/2023 2:46 PM via . All use subject to https://www.ebsco.com/terms-of-use

used to minimize the error among measured outputs of the system and estimated outputs of the simulated system using following objective function:

$$O.F._{2} = \sqrt{\sum_{i} \left( \underline{P}_{ei} - \underline{\hat{P}}_{ei} \right)^{2}} \tag{5}$$

where $\underline{P}_{e}$ and $\underline{\hat{P}}_{e}$ are sampled vectors of measured and simulated outputs, respectively.

Although the reactances are not directly used in the HP block diagram, the coefficients depend on them as explained in [27] as follows:

$$\begin{aligned} K_1 &= f_1\left(X_d, X_q, X'_d, V_{t0}, P_{e0}, Q_{e0}\right) \\ K_2 &= f_2\left(X_d, X_q, X'_d, V_{t0}, P_{e0}, Q_{e0}\right) \\ &\vdots \\ K_6 &= f_6\left(X_d, X_q, X'_d, V_{t0}, P_{e0}, Q_{e0}\right) \end{aligned} \tag{6}$$

## 4. Case study and simulation results

The case study is a single machine infinite bus system as shown in Fig. 1. This system represents a gas power plant unit which is connected to an infinite bus through a transformer and transmission lines. The nonlinear detailed system is simulated in DIgSILENT software. The improved HP model and identification procedure are conducted in MATLAB. The specifications of the synchronous machine, its operating point, excitation and turbine-governor systems, power transformer, and transmission line are given in Tables 1 and 2.

As mentioned in Section 3, two small steps are separately applied to the references of the voltage and active power to measure the required signals for identification. These two references, which are used in steps 3 and 5 of identification procedure, are shown in Figs. 4 and 5. It is worth noting that all the signals shown in all figures are variation around the operating point (delta values).

EBSCOhost - printed on 2/14/2023 2:46 PM via . All use subject to https://www.ebsco.com/terms-of-use

**Table 1. Synchronous generator data.**

| Parameter | Value | Parameter | Value |
|---|---|---|---|
| Nominal Power | 210 MVA | $D$ | 0.1200 pu |
| Nominal Freq. | 50 Hz | $V_{t0}$ | 1.0023 pu |
| Nominal Vol. | 15.75 kV | $P_{e0}$ | 0.65 pu |
| $X_d$ | 2.642 pu | $Q_{e0}$ | 0.02 pu |
| $X_q$ | 2.346 pu | $Z_t$ | 0.16 pu |
| $X'_d$ | 0.337 pu | $X_{L1}=X_{L2}$ | 0.453 Ω/km |
| $T'_{do}$ | 5.800 s | $R_{L1}=R_{L2}$ | 0.075 Ω/km |
| $H$ | 5.344 s | Line length | 101 km |

**Table 2. Excitation and turbine-governor systems data.**

| Parameter | Value | Parameter | Value |
|---|---|---|---|
| $K_p$ | 25 | $K_{pg}$ | 2 |
| $K_i$ | 40 | $K_{ig}$ | 0.8 |
| $K_d$ | 0.10 | $T_{ac}$ | 0.4 s |
| $T_d$ | 0.01 s | $K_t$ | 1 |
| $K_g$ | 0.01 | $T_t$ | 3 s |
| $T_g$ | 0.25 s | - | - |

In order to make the parameter estimation more practical, additive white Gaussian noise with signal-to-noise ratio value of 10 is added to the output signals of the detailed nonlinear model as follows:

$$\tilde{S} = S + N_{WG} \tag{7}$$

where $S$ and $\tilde{S}$ represent pure and noisy signals, respectively.

First, the step change is applied to voltage reference as described in step 3. Then, the genetic algorithm is used to minimize the objective function, which is described by Eq. (4). The initial population is set to 20 for each parameter. The search space of each parameter is presented in Table 3. The estimated parameters of this step are given in the first column of Table 4. As mentioned in Section 3, turbine-governor and mechanical parameters of synchronous generator are set to average values during this step. These values are also given in the first column of Table 4.

EBSCOhost - printed on 2/14/2023 2:46 PM via . All use subject to https://www.ebsco.com/terms-of-use

Accordingly, step change is applied to load reference as described in step 5.

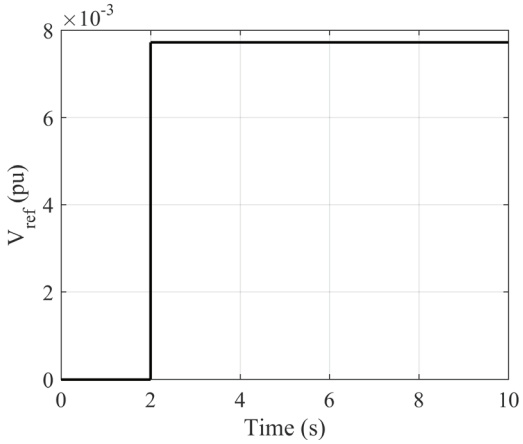



Fig. 4. Step signal of voltage reference.

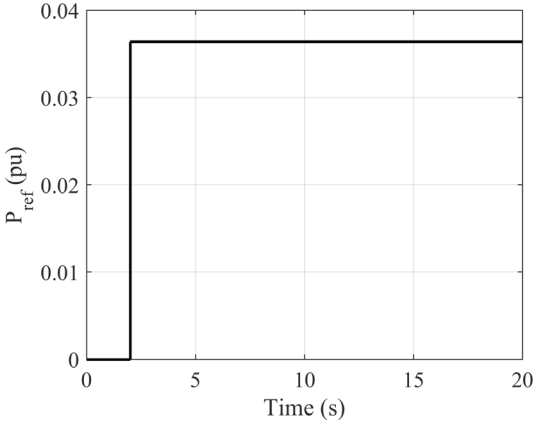



Fig. 5. Step signal of load reference.

During this step, the estimated parameters of step 3 are constant and genetic algorithm is used to minimize the objective function of Eq. (5) in

EBSCOhost - printed on 2/14/2023 2:46 PM via . All use subject to https://www.ebsco.com/terms-of-use

order to estimate mechanical parameters of synchronous generator and turbine-governor parameters. The estimated parameters of this step are given in the second column of Table 4. In addition, the second column of Table 4 presents the final estimated values of all parameters.

**Table 3. The search space of parameters.**

| Parameter | Range | Parameter | Range | Parameter | Range |
|---|---|---|---|---|---|
| $X_d$ | [1.5~3] | $K_i$ | [1~100] | $K_{ig}$ | [0.1~10] |
| $X_q$ | [1.5~3] | $K_p$ | [1~50] | $K_{pg}$ | [0.1~10] |
| $X'_d$ | [0.1~0.5] | $K_d$ | [0~0.5] | $K_t$ | [0.1~1] |
| $T'_{do}$ | [5~7] | $T_d$ | [0~1.0] | $T_t$ | [0.1~5] |
| $H$ | [2~7] | $K_g$ | [0~1.0] | $T_{ac}$ | [0.1~1] |
| $D$ | [0.01~0.15] | $T_g$ | [0~1.0] | - | - |

**Table 4. Estimated values of parameters.**

| Parameter | O.F.$_1$ | O.F.$_2$ |
|---|---|---|
| $X_d$ | **2.707** | 2.707 |
| $X_q$ | **2.421** | 2.421 |
| $X'_d$ | **0.350** | 0.350 |
| $T'_{do}$ | **5.102** | 5.102 |
| $K_i$ | **43.95** | 43.95 |
| $K_p$ | **21.10** | 21.10 |
| $K_d$ | **0.089** | 0.089 |
| $T_d$ | **0.291** | 0.291 |
| $K_g$ | **0.015** | 0.015 |
| $T_g$ | **0.182** | 0.182 |
| $D$ | 0.050 | **0.132** |
| $H$ | 4.000 | **5.200** |
| $K_{ig}$ | 0.100 | **0.954** |
| $K_{pg}$ | 0.500 | **2.934** |
| $K_t$ | 0.500 | **0.843** |
| $T_t$ | 2.000 | **3.625** |
| $T_{ac}$ | 0.500 | **0.446** |

Further, the corresponding parameter is estimated in this step, as shown in the bold value in each column of Table 4. Compared to the real values of parameters, the estimation results have good accuracy. However,

EBSCOhost - printed on 2/14/2023 2:46 PM via . All use subject to https://www.ebsco.com/terms-of-use

some parameters may have estimated the values which are a little far from their real ones in order to compensate for these structural differences because of some simplifications in the proposed HP model compared to the detailed nonlinear model of synchronous generator.

In order to demonstrate the effectiveness and precision of this identification procedure, the simulated output signals are compared with the outputs of the detailed nonlinear model using the estimated parameters of the improved HP model. The results are shown in Figs. 6 and 7.

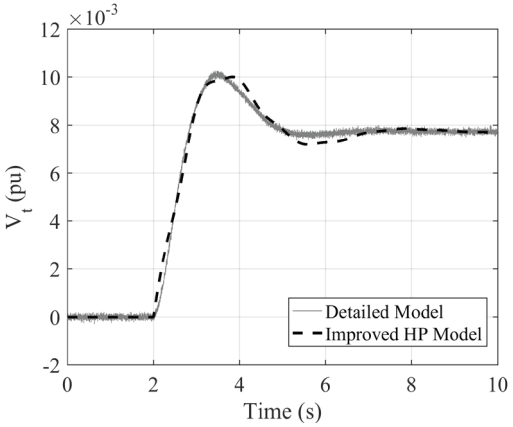



Fig. 6. Comparison of terminal voltage.

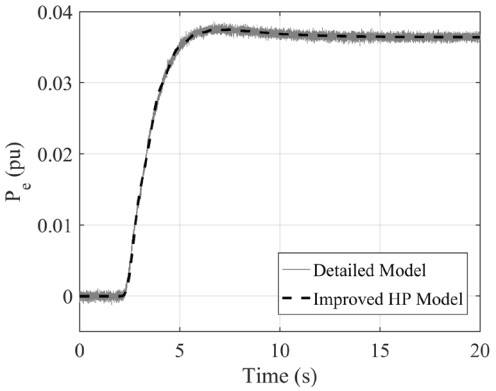



Fig. 7. Comparison of output active power.

EBSCOhost - printed on 2/14/2023 2:46 PM via . All use subject to https://www.ebsco.com/terms-of-use

As illustrated in Figs. 6 and 7, the outputs of the proposed HP model are appropriately fit to the outputs of the detailed model. Regarding validation, the obtained model and parameters are tested under two new operating points rather than the one used in identification procedure. The first new operating point (OP1) is $V_{t0}$=1.0418 pu, $P_{e0}$=0.75 pu and $Q_{e0}$=0.30 pu, and the second (OP2) is $V_{t0}$=1.0210 pu, $P_{e0}$=0.67 pu and $Q_{e0}$=0.15 pu. Figs.8-11 display the results of comparing the proposed HP model and detailed model at these new operating points. The consistency of the results at different operating points represents the accuracy of the modelling and estimation of the parameter.

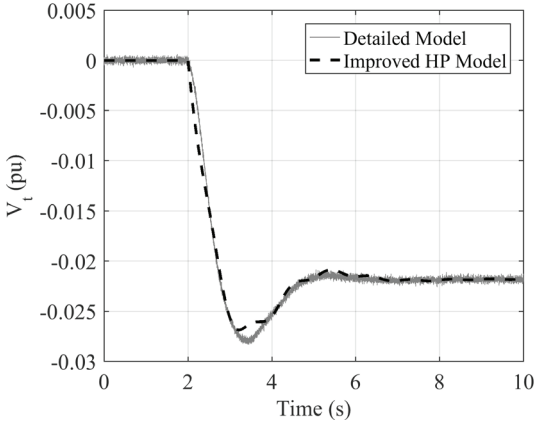



Fig. 8. Comparison of terminal voltage at OP1.

EBSCOhost - printed on 2/14/2023 2:46 PM via . All use subject to https://www.ebsco.com/terms-of-use

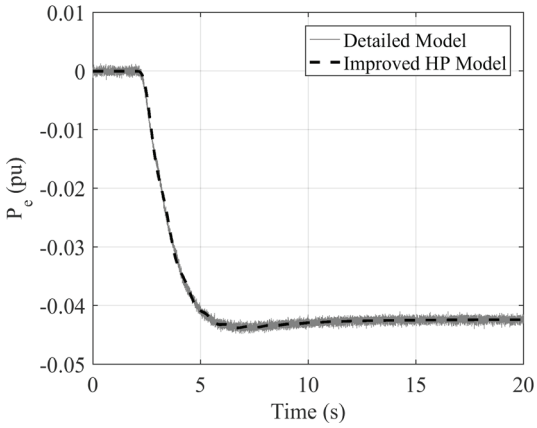



Fig. 9. Comparison of output active power at OP1.

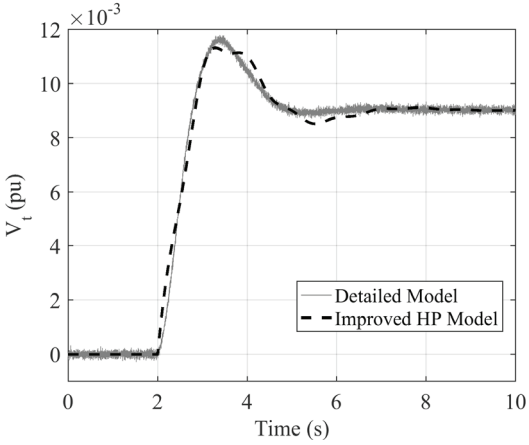



Fig. 10. Comparison of terminal voltage at OP2.

EBSCOhost - printed on 2/14/2023 2:46 PM via . All use subject to https://www.ebsco.com/terms-of-use

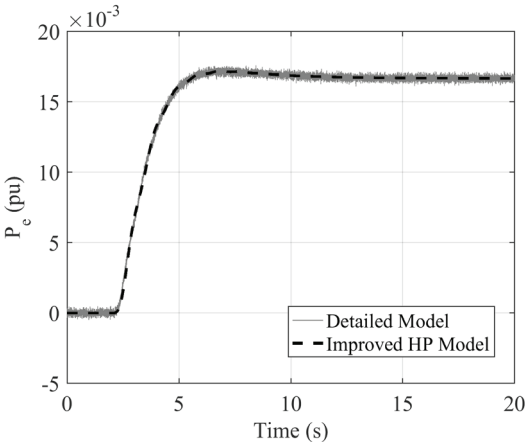



Fig. 11. Comparison of output active power at OP2

## 5. Conclusion

In the present study, the identification of synchronous generator parameters in the presence of excitation and turbine-governor systems in the frame of an improved HP model was proposed using on-line measurements data and optimization based on genetic algorithm. PMUs is widely used in these grids by providing on-line measurements since the smart grid concept is based on monitoring and communication infrastructures. These parameters are essential for analyzing power systems, designing the controllers such as power system stabilizer (PSS), and assessing the security of the network. In the proposed method, the references of the voltage and load are considered as the input signals while the terminal voltage and output active power of the synchronous machine are regarded as output signals. Further, the proposed method was applied to a single machine infinite bus system. The simulation results indicated the accuracy of the identification procedure and the validation test confirmed the precision of the estimated parameters at different operating points.

EBSCOhost - printed on 2/14/2023 2:46 PM via . All use subject to https://www.ebsco.com/terms-of-use

## References

[1] ANSI/IEEE Standard 115-1983, *IEEE Guide: Test Procedured for Synchronous Machines.*

[2] E. Mouni, S. Tnani and G. Champenois; "Synchronous generator modeling and parameter estimation using least square method", *Journal of Simulation Modeling Practice and Theory*, Vol. 16, pp. 678-689, 2008.

[3] M. Hasni, O. Touhami, R. Ibtiouen, M. Fadel, and S. Caux; "Estimation of synchronous machine parameters by standstill tests", *Mathematics and Computers in Simulation*, No. 81, pp. 277-289, 2010.

[4] T. L. Vandoorn, F. M. De Belie, T. J. Vyncke, J. A. Melkebeek, and P. Lataire; "Generation of Multisinusoidal Test Signals for the Identification of Synchronous-Machine Parameters by Using a Voltage-Source Inverter", *IEEE Trans. Industrial Electronics*, Vol. 57, No.1, pp. 430-439, 2010.

[5] M. A. Arjona, M. Cisneros-Gonzales, and C. Hernandez; "Parameter Estimation of a Synchronous Generator Using a Sine Cardinal Perturbation and Mixed Stochastic-Deterministics Algorithms", *IEEE Trans. Industrial Electronics*, Vol. 58, No.2, pp.486-493, 2011.

[6] J. Lidenholm, and U. Lundin; "Estimation of Hydropower Generator Parameters Through Field Simulations of Standard Tests", *IEEE Trans. Energy Conversion*, Vol. 25, No. 4, pp.931-939, 2010.

[7] G. Shackshaft, and A. T. Poray; "Implementation of New Approach to Determination of Synchronous Machine Parameters from Tests", *Proc. IEE (London)*, Vol. 124, No. 12, pp. 1 170- 1 178, 1977.

[8] F. P. deMello and J. R. Ribeiro; "Derivation of Synchronous Machine Parameters from Tests", *IEEE Trans*., Vol. PAS-96, pp. 1211-1218, 1977.

[9] F. P. deMello and L. N. Hannett; "Validation of Synchronous Machine Modelsand Determination of Model Parameters from Tests", *IEEE Trans*., Vol. PAS-100, pp. 662-672, 1981.

[10] R. Wamkeue, C. Jolette, A. B. Mpanda Mabwe, and I. Kamwa; "Cross-Identification of Synchronous Generator Parameters From RTDT Test Time-Domain Analytical Responses", *IEEE Trans. Energy Conversion*, Vol. 26, No. 3, pp. 776-786, 2011.

[11] M. Huang, W. Li, and W. Yan; "Estimation parameters of synchronous generators using square-root unscented Kalman filter", *Electric Power System Research*, Vol. 80, pp. 1137-1144, 2010.

[12] M. Dehghani, and S. K. Y. Nikravesh; "Nonlinear state space model identification of synchronous generators", *Electric Power System Research*, Vol. 78, pp. 926-940, 2008.

[13] M. Karrari, and O. P. Malik; "Identification of Physical Parameters of a Synchronous Generator From Online Measurments", *IEEE Trans. Energy Conversion*, Vol. 19, No. 2, pp. 407-415, 2004.

EBSCOhost - printed on 2/14/2023 2:46 PM via . All use subject to https://www.ebsco.com/terms-of-use

[14] M. Soliman, D. Westwik, and O. P. Malik; "Identification of Heffron-Phillips model parameters for synchronous generators operating in closed loop", *IET Gener., Transm. and Distrib.*, Vol. 2, No. 4, pp. 530-541, 2008.

[15] B. Zaker, G. B. Gharehpetian, and N. Moaddabi, "Parameter Identification of Heffron-Phillips Model Considering AVR Using On-Line Measurements Data," in *International Conference on Renewable Energies and Power Quality (ICREPQ'14)*, 2014.

[16] B. Zaker, G. B. Gharehpetian, M. Karrari, and N. Moaddabi, "Simultaneous Parameter Identification of Synchronous Generator and Excitation System Using Online Measurements," *IEEE Trans. Smart Grid*, vol. 7, no. 3, pp. 1230–1238, May 2016.

[17] B. Zaker, G. B. Gharehpetian, and M. Karrari, "Improving Synchronous Generator Parameters Estimation Using d-q Axes Tests and Considering Saturation Effect," *IEEE Trans. Ind. Informatics*, pp. 1–1, 2017.

[18] M. Karrari, and M. B. Menhaj, "Application of different neural networks for identification of power systems," *Presented at Int. Conf. Control*, U.K., 2000.

[19] B. Zaker, M. Karrari, M. Mirsalim, G. B. Gharehpetian, and N. Moaddabi, "PMU-Based Matching Pursuit Method for Black-Box Modeling of Synchronous Generator," *J. Iran. Assoc. Electr. Electron. Eng.*, vol. 12, no. 3, pp. 33–39, 2015.

[20] B. Zaker, G. B. Gharehpetian, M. Mirsalim, and N. Moaddabi, "PMU-based linear and nonlinear black-box modelling of power systems," in *21st Iranian Conference on Electrical Engineering (ICEE)*, 2013, pp. 1–6.

[21] A. J. Saaverda-Montes, J. M. Ramirez-Scarpetta, and O. P. Malik; "Methodology to estimate parameters of an excitation system based on experimental conditions", *Electric Power System Research*, Vol. 81, pp. 170-176, 2011.

[22] D. C. Aliprantis, S. D. Sudhoff, and B. T. Kuhn; "Genetic Algorithm-Base Parameter Identification of a Hysteretic Brushless Exciter Model", *IEEE Trans. Energy Conversion*, Vol. 21, No. 1, pp. 148-154, 2006.

[23] T. Bi, A. Xue, G. Xu, X. Guo, F. Ge, and Z. Wang; "On-line Parameter Identification for Excitation System based on PMU Data", *4th International Conference on Critical Infrastructures*, pp. 1-4, 2009.

[24] M. Rasouli, and M. Karrari; "Nonlinear Identification of a Brushless Excitation System Via Field Tests", *IEEE Trans. Energy Conversion*, Vol. 19, No. 4, pp. 733-740, 2004.

[25] A. Khodadadi, B. Zaker, R. Khalili, S. M. Hosseini, Sh. Karrari and M. Karrari, "Dynamical Modelling and Parameters Identification of Real Power Plant Synchronous Generator and Excitation System," *9th International Conference on Mathematical Modeling*, Viena, 21-23 Feb. 2018.

[26] R. Khalili, H. Rabieyan, A. Khodadadi, B. Zaker, M. Karrari and Sh. Karrari, "Mathematical Modelling and Parameter Estimation of an Industrial Steam

EBSCOhost - printed on 2/14/2023 2:46 PM via . All use subject to https://www.ebsco.com/terms-of-use

Turbine-Generator Based on Operational Data," *9th International Conference on Mathematical Modeling*, Viena, 21-23 Feb. 2018.
[27] Y. Yu; *Electric Power System Dynamics*, Academic Press Inc., 1983.

EBSCOhost - printed on 2/14/2023 2:46 PM via . All use subject to https://www.ebsco.com/terms-of-use

# CHAPTER TWENTY-THREE

# WIFI MONITORING OF A HIGH TEMPERATURE CONTROL APPLIED TO MICRO THERMOELECTRIC GENERATORS

JUCÁ, S. C. S.[1], PEREIRA, R. I. S.[2], CARVALHO, P. C. M[2]

## Abstract

This paper describes the design and implementation of a high temperature control monitor (HTCM) for investigating the characteristics of new thermoelectric generator (TEG) materials. The characteristics of TEGs include: small size; zero-carbon emissions; no moving parts or noise; and the ability to produce electricity using waste heat. New materials are expected to be able to work with a temperature difference of up to 400 K; most common TEGs, which use tellurium, operate with temperature differences of up to 200 K and cannot withstand temperatures higher than 473 K. In the initial phase of the study, we implemented a mathematical model of a digitalized linear AC voltage phase switch to perform exact temperature control of the HTCM's thermal power and to regulate the TEG's temperature difference. This model achieves high accuracy temperature control through digital control of AC voltage phase switching. During measurement of the TEG's performance, the HTCM keeps the hot side of the TEG at a specified temperature, while the cold side is held at a temperature of approximately 293 K. This HTCM embedded system was developed to test new TEG materials in specified

[1] Federal Institute of Ceará. Computing Department. 61939-140, Maracanaú-CE, Brazil. E-mail: sandrojuca@ifce.edu.br

[2] Federal University of Ceará. Electrical Engineering Department. Pici Campus, 60455-760, Fortaleza-CE, Brazil. E-mail: renata@dee.ufc.br, carvalho@dee.ufc.br

EBSCOhost - printed on 2/14/2023 2:46 PM via . All use subject to https://www.ebsco.com/terms-of-use

high temperature ranges and to acquire and transmit data to an online host PC. In the second phase, we used free hardware and software for online monitoring based on a WiFi embedded modem applied to a TEG. The main objective was to analyse plant variables through online monitoring software to allow data storage in an online database and chart generation with the possibility of remote access.

**Keywords:** Embedded system; online monitoring; thermoelectric power generation.

## Introduction

The increasing number of problems with electric energy generation from fossil fuels, such as the accumulation of carbon dioxide, air pollution, and global warming, highlight the vital importance of further development of alternative energy technologies. As an environment-friendly energy source, thermoelectric power generation has attracted considerable interest due to its small size, zero carbon emissions, absence of moving parts, low acoustic noise, and high reliability. Thermoelectric generators (TEGs) are also a good choice for producing electric power by recycling waste thermal energy [1]. TEGs can be designed for use with large energy generation systems (geothermal energy [2] for example) or for working with small heat sources, such as those used in automotive or home applications for waste heat recovery. TEGs have even been miniaturized so as to absorb body heat for powering small electronic devices like wristwatches [3]. Thermoelectric power generation is based on the Seebeck effect where electric current flows across a junction of two different metals, joined at two points, one metal heats up while the other is kept at a lower temperature. Thermoelectric energy production is one of the main processes for converting thermal energy directly into electrical energy. It ensures long, reliable operation without maintenance due to the nonexistence of moving parts [4]–[9]. Thermoelectric modules can be formed by P and N type semiconductors that are connected in series electrically, and parallel thermally, between two ceramic layers. A TEG is made by heating one side and cooling the other side of the thermoelectric module and connecting a load to the module end points. A basic schematic of a TEG is shown in Fig. 1.

EBSCOhost - printed on 2/14/2023 2:46 PM via . All use subject to https://www.ebsco.com/terms-of-use

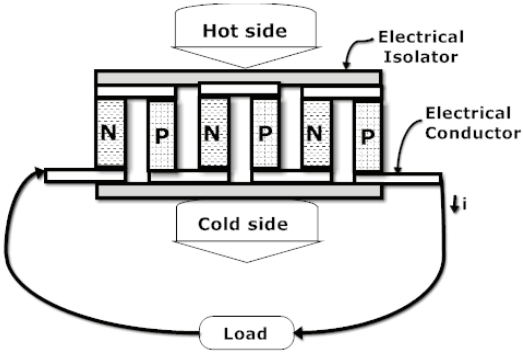



Figure 1. Basic schematic of a thermoelectric generation process

Electrons on the material's hot side become more energized than those on the cold side. These electrons will flow from the hot side to the cold side when both sides are connected with a conductor wire. These electrons produce the electrical current. By connecting many thermocouples in series, it is possible to increase the output voltage and power [1]. Micro TEGs are used by the North American Space Agency (NASA) to supply electric energy to the Curiosity robot on Mars, through heat liberated by radioisotope nuclear decay reactions [10]. They are also used as a source of renewable electric co-generation through the heat supplied by incinerated municipal solid waste, automobile engines, or industrial machinery [11]. This research project consists of two phases:

1. Phase 1 describes the development of the temperature control and data transmission equipment used to evaluate new TEG materials that operate with a higher temperature differential than usual TEGs. Due to the higher temperature difference (up to 400 K), compared to the usual 50 K, there are no available test systems on the market [4], [5], [9]. The aim of this system was to produce a constant temperature difference, controlled by the host PC, and to measure the electrical parameters of these new TEG materials [12].
2. Phase 2 involved the development of an online monitoring system, using an embedded WiFi modem, to analyse the variables of a thermoelectric micro-generation plant. Additionally, online monitoring software was developed to allow the storage of data in an online database. Additionally, users can generate graphs of the stored data on the same page with remote access through an Internet connection. In this case study, the temperature values of

EBSCOhost - printed on 2/14/2023 2:46 PM via . All use subject to https://www.ebsco.com/terms-of-use

the TEG's hot and cold sides, as well as TEG voltage, electric current, and power, were analysed for five different loads on an open circuit.

## Phase 1: Design and Construction of the HTCM for Micro-TEGs

To investigate and analyse high temperature micro-TEGs, it is necessary to measure the efficiency of thermoelectric materials at different temperatures. This section describes the design of the HTCM that was used for parameter measurement of the micro-TEG.

The HTCM needed to generate a constant temperature value of 300 K to 700 K on the TEG's hot side during measurement. Temperature settings are transmitted by an external control device (usually the host PC). Current temperature values were transmitted back from the HTCM to the control device to identify the correct point for TEG parameter measurement. The communication between the HTCM and control device allows for automatic measurement of the TEG parameters through the full temperature range.

The HCTM embedded system was designed and implemented to test new TEG materials according to specified high temperature ranges and to acquire and transmit the data to a host PC. Temperature regulation, especially at high temperatures, involves operating at high electrical power, which cannot be controlled directly by the host PC. The HTCM contains power semiconductor switches with a proper driver and protection circuits. These circuits are controlled by an embedded microcontroller, which allows for the real-time operation of the HTCM device. The host PC must have enough processing power for this task, but normal operating systems do not have the real-time capability necessary, which is very important for safe operation of the power circuit. Task sharing between the control device and the HTCM allows for stable operation even with high electromagnetic interference. As such, the following requirements for the HTCM were developed:

1) Temperature control accuracy: 3 K.
2) Temperature range: 300 K to 700 K.
3) Heating element power: 500 W.
4) USB interface for data exchange between PC and microcontroller and firmware update.

EBSCOhost - printed on 2/14/2023 2:46 PM via . All use subject to https://www.ebsco.com/terms-of-use

By increasing the power, heat increases rapidly, while the time to achieve the new temperature set-point decreases. The new output power value, different from the default value, will cause the recalculation of the PI-controller parameters. The HCTM was developed based on a microcontroller with a USB interface to ensure easy firmware upgrading via a bootloader system. Free software was used for this system, including an editor, compiler, programming environment, and a bootloader for easy firmware upgrading without an external programming device. Fig. 2 shows the functional diagram of the HTCM.

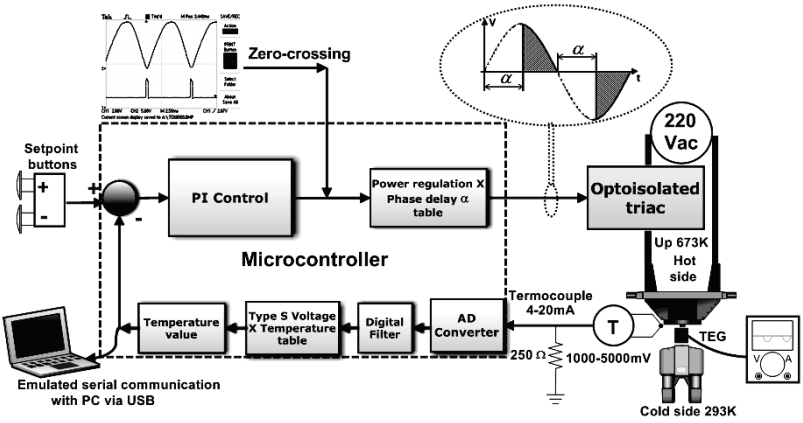



Figure 2. Functional diagram of the HTCM

A microcontroller built-in USB-interface was used for the connection to the PC and to update the microcontroller firmware. This allows for easy re-programming of the HTCM without the use of an external programming device and special programming interfaces.

To realize the micro-TEG's performance measurement, the HTCM heated the TEG's hot side. To keep the cold side at a constant temperature of approximately 293 K, regulated chiller equipment was used.

For the exact temperature measurement in the range of 300 K to 700 K, a type S thermocouple was used. The measurement amplifier used, together with the thermocouple [13], has a built-in cold-side compensation circuit and produces an output current signal of 4 to 20 mA for the thermocouple's whole temperature range. This output current signal is transformed to DC voltage (1000 to 5000 mV) using a 250 Ω precision resistor and is then converted into digital form by the built in 10-bit ADC.

EBSCOhost - printed on 2/14/2023 2:46 PM via . All use subject to https://www.ebsco.com/terms-of-use

ADC-converted values are processed by a programmed digital 1st order FIR (finite impulse response) filter contained in the firmware microcontroller to eliminate peak values and electrical noise. Because the output signal of the S-type thermocouple is not linear, the obtained digital codes must be transformed into temperature values using a coefficient table. These coefficients, for the whole thermocouple temperature range (0 to 1200 °C), are saved in the microcontroller program memory and must be applied at each temperature measurement to obtain the correct temperature values. Besides the temperature measurements, the HTCM also needs the set-point temperature settings that correspond to the desired temperature on the TEG and that are achieved by the temperature control process. These temperature settings can either be transmitted from the host PC, by an external control device via a communication interface, or they can be directly entered by the operator from the keypad.

Current temperature and temperature settings are shown on the LCD screen on HTCM's top side. This screen is also used for controlling the HTCM's actual state. The actual values of the temperature settings are shown in real time on the LCD display when the temperature settings are change by use of the control device.

The HTCM output signal is calculated from the difference between the temperature settings and the current temperature. This difference, also called temperature error, is used in the PI-regulator to calculate the output signal that is to be converted.

A power switch (optoisolated TRIAC) is used to connect the line voltage to the heating element. The temperature control is taken by switching the line voltage at pre-calculated times on each AC voltage period. Because the heating element is powered by AC voltage, the switching off the line voltage is done automatically by crossing the zero value. The desired amount of energy for the heating element is controlled by manipulating the phase delay between voltage switching moments.

These moments of a zero-crossing value by the line are established by the external circuit, called a zero-cross detector circuit. The AC voltage from the transformer, which is connected to the bridge rectifier, allows the detection of each half wave. The rectified voltage arrives at the resistance divider and goes through a low-pass filter connected to the base of the bipolar transistor. The output signal from the collector of the bipolar transistor is connected to the microcontroller interrupt pin; it is used to calculate the right moment for turning on the TRIAC. In Fig. 3 the HTCM board is shown with interface connectors, a power system, and power control components. The board was developed using SMD components,

EBSCOhost - printed on 2/14/2023 2:46 PM via . All use subject to https://www.ebsco.com/terms-of-use

which is why some discrete components, like the resistor and capacitor, are located on the bottom.

As shown in Fig. 3, the HTCM board is composed of: a power TRIAC (1); an optocoupler TRIAC driver (2); a RS-232 interface (3); a USB interface (4); an output for optional cooler connection (5); an S-type thermocouple interface (6); a liquid crystal display interface (7); a microcontroller (8); a keyboard interface (9); a programming mode push-button (10); and a zero-cross input circuit (11).

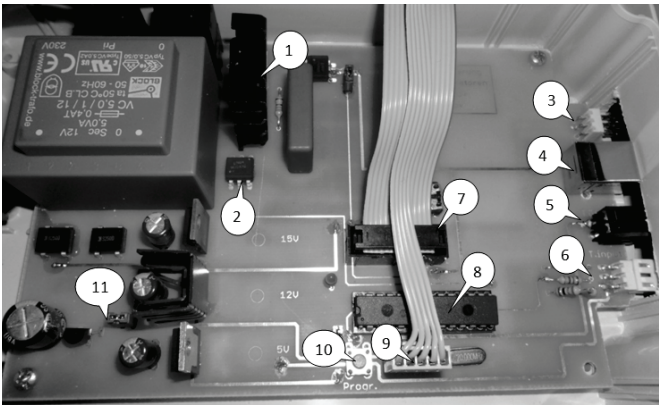



Figure 3. HTCM board

The complete system consists of: a HTCM (1); a micro-TEG (2) with a hot (3) and a cold (4) side; and a thermocouple temperature sensor (5), as shown in Fig. 4.

EBSCOhost - printed on 2/14/2023 2:46 PM via . All use subject to https://www.ebsco.com/terms-of-use

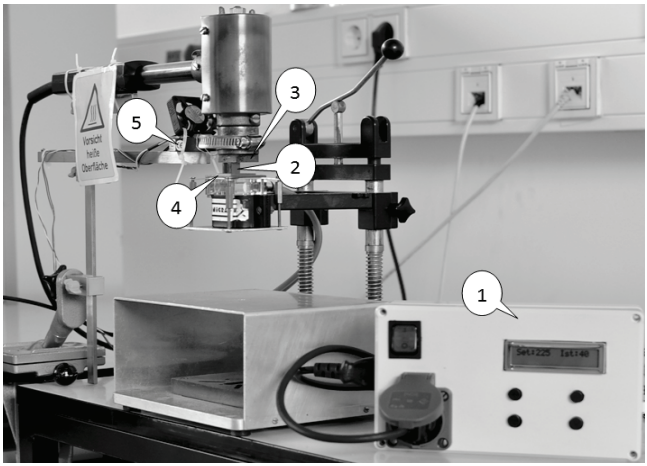



Figure 4. HTCD with heating device and micro-TEG

## *Programming and Debugging Tools*

Data acquisition and monitoring systems were used at various stages of micro-generation, such as predicting generation failures, practical verification of design data, and optimization of the generation efficiency. The setup allows for the generation parameters and operation to be modified in real time.

This paper describes an online monitoring system, programmed on free software and data acquisition systems and built with electronic components. These electronic sensing microcontroller systems were built and programmed with the ability to update the firmware wirelessly via bluetooth or ZigBee protocols. We used an embedded system based on a microcontroller with USB interface and software for the development of embedded systems, i.e., a system that manipulates data within another larger system, as is the case with monitoring systems [14], [15].

The project programming tool is called SanUSB. This tool can update the PIC microcontroller firmware via USB channel, is executable in Linux, Mac OSX, and Windows® operating systems; it is available from the archives at http://www.tinyurl.com/SanUSB [16]. Additionally, the SanUSB tool enables user-friendly programming and debugging directly through open source [17] virtual serial emulation. This can be created quickly and effectively at the very moment the microcontroller is connected directly to a PC through the USB interface. Equipment designed and built for specific applications tend to be less costly, enhance

EBSCOhost - printed on 2/14/2023 2:46 PM via . All use subject to https://www.ebsco.com/terms-of-use

performance, and provide user-friendly environments for control and communication [18]–[20].

## *HTCM Mathematical Model*

Commercially available PI or PID controllers tend to switch the output on and off once every second or less. This procedure may be appropriate for soldering stations or similar devices, but it may cause output temperature pulsing in embedded measurement systems like the HTCM. For this reason, the HTCM uses another strategy, dosing the output power in each half-wave AC period.

As the heating device supply voltage has a sinusoidal waveform, the linear phase sweep of the supply voltage will have a nonlinear power sweep on to the heating element. The mathematical model developed is used to calculate the desired values of the linear phase angle as a function of linear output power to compensate for the nonlinearity of the supply voltage. The HTCM embedded system controller works to maintain stability, as it is designed with the calculated values of the phase angle available in a microcontroller firmware table.

The TRIAC phase control is used for temperature regulation—it automatically switches off at the end of each half-wave of the supply voltage. TRIAC switching on is done by a command from the microcontroller according to the calculated phase delay. The TRIAC cannot switch on for any calculated moment, because the microcontroller is a digital device that is clocked by a defined frequency and can operate only within discrete time moments. The time interval for the phase delay is generated by a timer interrupt counter (microcontroller periphery device) and can operate with only a few hundred discrete interruptions in each sinusoidal half-wave period (10 ms). A larger interruption frequency is limited by the microcontroller CPU processing capacity, which is also used for other real-time tasks, like temperature measurement and peripheral interface control. Through practical experimentation it was established that an interruption frequency of 500 times per sinusoidal half-wave period does not noticeably affect the execution of other real-time tasks in the embedded system.

Varying the number of the interruption counter (and the phase angle $\alpha$) also changes the output power delivered to the heater ($P_{del}$) [21]. If there is no delay applied ($\alpha = 0$), the TRIAC will switch on immediately after detecting a zero-crossing event and the power delivered to the heater will be maximized, as calculated by equation (1):

EBSCOhost - printed on 2/14/2023 2:46 PM via . All use subject to https://www.ebsco.com/terms-of-use

$$Pdel = \frac{V_{rms}^2}{R} \tag{1}$$

where $V_{rms}$ is the real value of the supply voltage and R is the heating device resistance. The simplest way to control the output power is through linear change of the phase angle used for switching on the TRIAC. In this case, the digitalized model of the phase angle change, as a function of the timer interrupt counter (x) by the maximum counter value N (pro half-cycle), is expressed by equation (2):

$$real_phase(x) = \frac{\pi \cdot x}{N} \tag{2}$$

As such, the output power can be expressed by equation (3), described as 'real power':

$$real_{power}(x) = \int_{real_{phase}(x)}^{\pi} \sin(x)\,dx \tag{3}$$

The integral in (3) represents the total power from the TRIAC open moment until the end of the half-cycle. This expression is described as real power because the dependence of the output power on the variable x is not linear in this case. The ideal power is described by the linear changing (decreasing) of the maximum output power as a function of variable x, according to (4):

$$ideal_power(x) = \int_0^{\pi} \sin(x)dx - \frac{\int_0^{\pi} \sin(x)dx \cdot x}{N} \tag{4}$$

where $\int_0^{\pi} \sin(x)dx$ is the maximum output power for each half-cycle.

Practical experiments with a PI control response show that an output power division of 300 equal parts is enough to achieve the desired accuracy in temperature regulation. As such, the value of N is 300 and the value of x can be changed from 0 to N. Output power linear regulation is not possible through linear regulation of the phase angle delay. A special dependence needs to be deduced to calculate the phase delay values according to the desired part of the output power. Real and ideal power model graphs are shown in Fig. 5. The maximum power value is 2 because the integral of sin(x) over the half period equals 2.

EBSCOhost - printed on 2/14/2023 2:46 PM via . All use subject to https://www.ebsco.com/terms-of-use

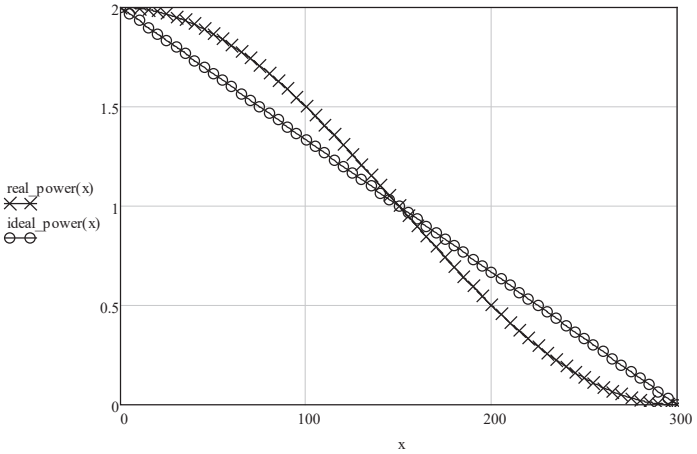



Figure 5. Real and ideal power model graphs

The relative error between the ideal and real power model (in percent) expressed in equation (5) is shown in Fig. 6. The maximum error introduced between the linear power changing model and linear phase changing model is about 10%:

$$power_error(x) = \frac{(real_power(x) - ideal_power(x)) \cdot 100}{\int_0^{\pi} \sin(x)dx} \tag{5}$$

To calculate the exact phase delay for switching on the TRIAC, the ideal phase function is presented in equations (6) and (7). It is obtained from the ideal power equation through a function analogous to equation (3).

$$ideal_{phase}(x) = a\cos(ideal_{power}(x) - 1) \tag{6}$$

$$ideal_phase(x) = a\cos\left(\int_0^{\pi} \sin(x)dx - \frac{\int_0^{\pi} \sin(x)dx \cdot x}{300} - 1\right) \tag{7}$$

EBSCOhost - printed on 2/14/2023 2:46 PM via . All use subject to https://www.ebsco.com/terms-of-use

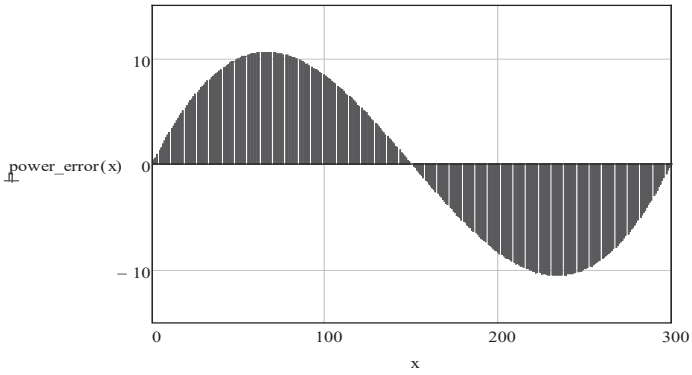



Figure 6. Relative error between ideal and real power model (in percent)

In the ideal case, there is no linearization error and the power division is optimal. The TRIAC cannot be switched by the microcontroller for any calculated time moment. The microcontroller operates only with certain predefined discrete time moments, and the calculated phase value of the equation (7) must be rounded to the next discrete time moment. It is obvious that such a rounding procedure will cause an error in the output power value. It is also obvious that more than N discrete time moments are needed to represent N rounded values of output power. When N is equal to 300 values of output power, it is rounded to T and equal to 500 possible values of the phase delay. The 500 possible values of the phase delay correspond to timer interrupts occurring at 20 μs (10 ms/500) intervals after zero-crossing identification. There are just 500 interrupts per each sine half-wave, to represent 300 values on the output power. Therefore, they are rounded to the next timer interrupt phase by the maximum interrupt value T per each half-wave expressed in equation (8):

$$dig_phase(x) = round\ \left(\frac{ideal_phase(x) \cdot T}{\pi}\right) \tag{8}$$

The resultant output power function using the rounded values of the phase delay is shown in (9). The calculated values for the function are presented as a table and saved in the microcontroller program memory. This table is used to calculate the corrected value of the output power.

$$dig_power(x) = \int_{\frac{dig_phase(x) \cdot \pi}{T}}^{\pi} \sin(x)dx \tag{9}$$

EBSCOhost - printed on 2/14/2023 2:46 PM via . All use subject to https://www.ebsco.com/terms-of-use

The resultant error between the ideal and rounded linear power model (in percent) is expressed in equation (10) and shown in Fig. 7. The maximum theoretical error between the ideal and rounded power models is less than 0.2%.

$$power_{error}(x) = \frac{(dig_{power}(x) - ideal_{power}(x)).100}{\int_0^{\pi} \sin(x)dx} \tag{10}$$

Digitalized rounded linear power model values are transformed into integer values and inserted in the microcontroller firmware as a table. The maximum error between the ideal and rounded power models is less than 0.2%. As such, the mathematical model allows us to reduce the linearization error of 10% to less than 0.2%.

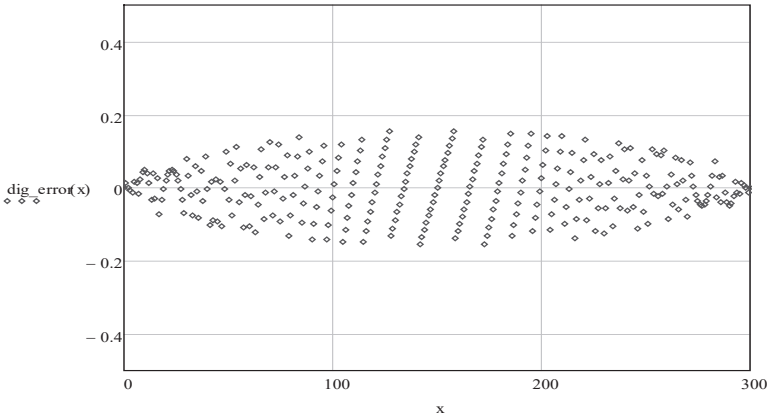



Figure 7. Resultant error between ideal and rounded linear power model (in percent)

## *HTCM Application in a High Temperature Micro-TEG*

Fig. 8 shows the implementation of the HTCM for measuring the parameters of a high-temperature TEG, using a controlled temperature differential of up to 400 K. The figure shows the typical values of internal resistance (Ω), open-circuit voltage (mV), short-circuit current (mA), TEG output power (μW), and the temperature difference parameter (K) on the TEG.

EBSCOhost - printed on 2/14/2023 2:46 PM via . All use subject to https://www.ebsco.com/terms-of-use

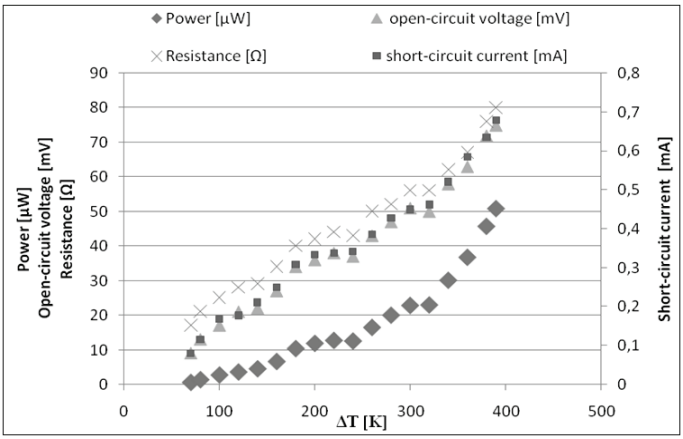



Figure 8. Values of the internal resistance (Ω), open-circuit voltage (mV), short-circuit current (mA), TEG output power (µW), and temperature difference parameter (K) on the TEG

## Phase 2: WiFi Data Acquisition System

In the second phase of this research, an embedded WiFi data acquisition system with WiFi connection was developed [22]. The embedded WiFi system programming is based on open source and free software—this is an advantage of the proposed system. The board sends the monitored data to an online server, which is also programmed using open source software. The TEG used is composed of more than one thermoelectric pair, as shown in Fig. 9.

Data acquisition and online monitoring systems are found worldwide in large power plants with complex boards and circuits. They are often very expensive, making them impractical for residential use or other microgeneration range clients (up to 75 kW). In this section, we present efficient techniques developed for online monitoring with free software, sensing, and data transmission via WiFi. We intend for this to contribute to the diffusion and installation of microgeneration systems based on renewable energy sources, such as thermoelectric microgeneration.

EBSCOhost - printed on 2/14/2023 2:46 PM via . All use subject to https://www.ebsco.com/terms-of-use

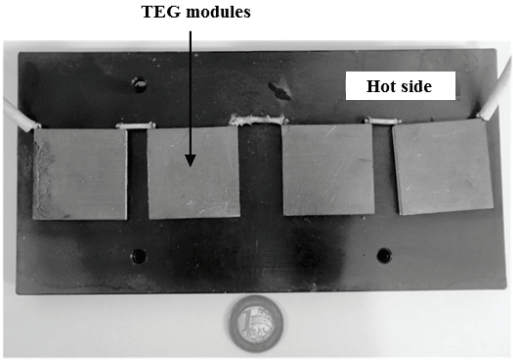



Figure 9. TEG modules (TEHP1-1264-0.8) [23]

The modulated hardware (Fig. 10) consists of a microcontroller board (a), called SanUSB, connected to a WiFi RN-XV (b) modem via an adapter circuit (c) developed for this application to adjust the connection pins between SanUSB and WiFi, as well as to convert the voltage from 5 V (SanUSB) to 3.3 V (WiFi).

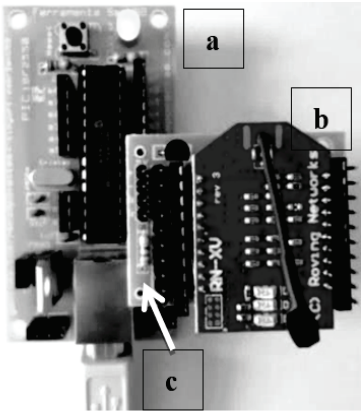



Figure 10. Data acquisition board with WiFi modem

A WiFi-based platform is presented in [24], which sends data from body-movement sensors wirelessly to a mobile device to control interactive systems, such as music applications. In [25], a Wi-Fi bio-impedance device to evaluate sarcopenia, that is, loss of muscle mass due

EBSCOhost - printed on 2/14/2023 2:46 PM via . All use subject to https://www.ebsco.com/terms-of-use

to age, was designed, developed and analyzed. The system is based on a WiFi protocol for remote control of the device and allows full Internet integration. Another wireless system developed for body temperature measurements is shown in [26]. Three other studies on wireless remote sensing are presented in [27]–[29].

In addition to the aforementioned applications, [30] proposes a wireless sensor network inside buildings to send data and control actuators via WiFi. The innovation presented by the author is SmartGate—a gateway with two transceivers integrated into a single printed circuit board. Gateway use allows the implementation of a wireless sensor network with wake-up receivers that can be accessed via the Internet from any point in the world. This generates battery energy savings, because the sensor only measures when a command is received remotely. In [31], a system based on software and hardware for data acquisition in applications with optical recognition is described.

The microcontroller circuit used in this second phase of the project is based on a computer programming tool for microcontrollers via USB. This was developed using free software and its registration in Brazil was granted by the National Institute of industrial property (INPI) with the number 088503. It is executable in the operating systems of Linux, Mac OSX, and Windows®, with files available in the SanUSB Group [16]. It has been released as free software. Equipment developed for specific applications tends to be more cost-effective and easier to understand.

Free software is developed from voluntary contributions through the Internet by a community that includes developers around the world. This software often offers better performance, encourages creativity, allows the creation of dedicated applications, and makes it possible to find and correct coding errors faster than in proprietary software [17]. It is important to emphasize that the USB port is used as the microcontroller system power supply only during the code development and programming phases of the board.

In this context, the data transmission system for monitoring the efficiency of TEG modules (Fig. 11) consists of a hot side AC power control board (a), a hot-side temperature sensor (b), a data acquisition card (c), and a WiFi modem (d).

EBSCOhost - printed on 2/14/2023 2:46 PM via . All use subject to https://www.ebsco.com/terms-of-use

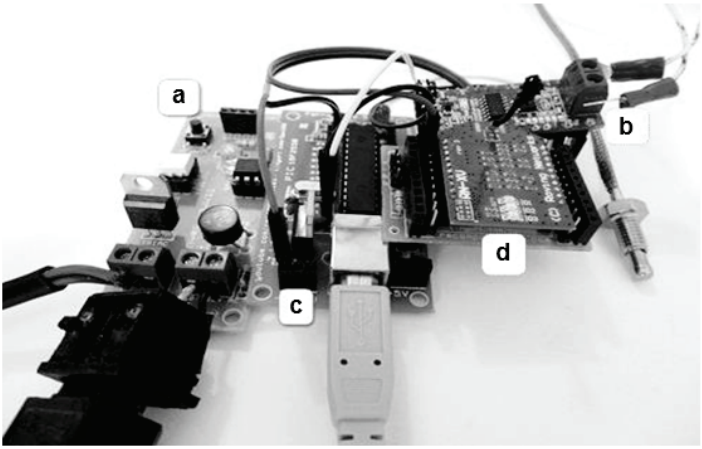



Figure 11. WiFi data acquisition system applied to TEG modules

## *TEG Monitoring*

WiFi networks use radio wave technologies with the standards set by the Institute of Electrical and Electronics Engineers (IEEE), including IEEE 802.11a, 802.11b, and 802.11g. These standards provide a secure and reliable wireless connection. WiFi networks can be used to connect between computing devices, as well as to connect them to the Internet [32]. WiFi networks operate on 2.4 GHz unlicensed radio bands in the IEEE 802.11b and IEEE 802.11g standards and at the 5 GHz frequency in the 802.11a standard [33].

The WiFi modem is based on the RN-171 module to allow connection to wireless networks. Only four pins are required for power and data transmission using this modem. This device has an independent antenna, which increases the coverage area and provides stronger transmission signals. It also supports the most common communication protocols, including Transmission Control Protocol (TCP), User Datagram Protocol (UDP), and File Transfer Protocol (FTP).

If there is more than one WiFi module or computing device connected to the Internet on a home network using a broadband router or gateway, most of the time this router only contains an Internet IP address and each device on the internal network uses a local Intranet IP address provided by the router. The local Intranet IP address is usually created dynamically through a service called Dynamic Host Configuration Protocol (DHCP) by the router itself, or statically defined by the user according to the network.

EBSCOhost - printed on 2/14/2023 2:46 PM via . All use subject to https://www.ebsco.com/terms-of-use

For example, if the router's address is 192.168.1.1, the fixed IP address of the Intranet created by the user could be 192.168.1.195, if there is no other device previously configured with this IP. In the online monitoring system that was developed, the microcontroller circuit connected to the WiFi module can operate in both modes: as a server, when a browser (speaker or client) requests the microcontroller (listener or server) to operate a load; or as a client (speaker), when the microcontroller sends analog or digital data to any server with a database.

In this case, the sending of information to the online database was configured with remote access via WiFi, without charging for data flow, unlike the applications that use the 3G/GPRS protocol from mobile operators. In the following, the development, programming, and application of the online monitoring and wireless data acquisition system using open source software is described.

Online databases can be consulted by any computer device with access to the Internet through a personal password. The query can be done at any time, with an update every minute [34]. Fig. 12 shows how the monitoring develops in two stages, 'a' and 'b':

(a) Sensing, conditioning, and data transmission;
(b) Data storage in an online database and presentation to the user.

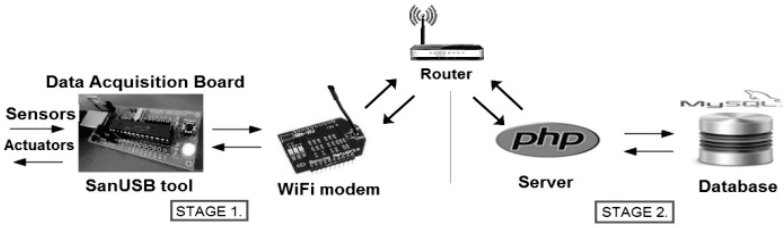



Figure 12. Steps in the monitoring system

The first stage, 'a', establishes communication between the sensors connected to the data acquisition board. The second stage, 'b', refers to the presentation layer, developed in the PHP programming language with MySQL database.

The first stage of wireless sensing, conditioning, and acquisition reads sensor data every minute, which is then saved to the microcontroller's internal memory (EEPROM). Every ten minutes, the mean value of the data measured is calculated and sent to the second stage. Actuators can be connected to the board, allowing control of WiFi loads through the server.

EBSCOhost - printed on 2/14/2023 2:46 PM via . All use subject to https://www.ebsco.com/terms-of-use

In this application, a communication interface for the acquisition system and another one working in parallel for presentation to the user were developed.

The first interface is responsible for receiving the data, storing it in the persistent database, and sending a confirmation to the microcontroller. The user interface, however, provides a user-friendly front end that enables the user to view data in the form of a spreadsheet or chart. Embedded firmware was programmed using a digital filter to identify and exclude abnormal values that differed by more than 100% from the maximum and minimum values of the variable measured every minute. The system diagram is shown in Fig. 13.

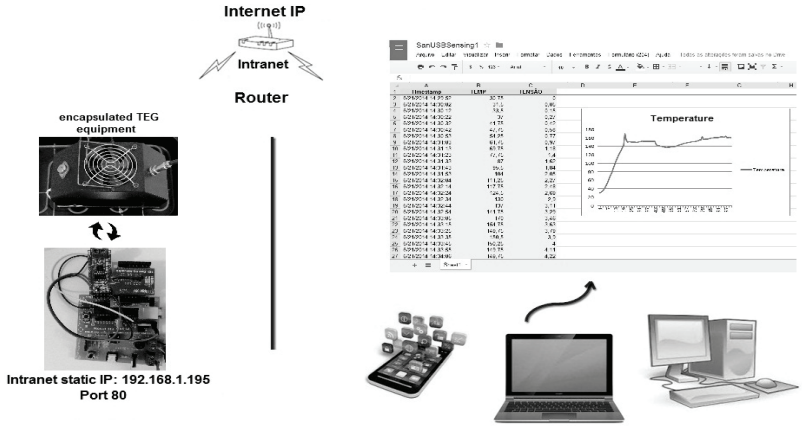



Figure 13. Online monitoring process via WiFi modem

The free monitoring software used, Web Monitor, is an application developed in an online server with the programming language PHP in conjunction with a database structured in the DBMS (database management system) to assist in visualizing the microgeneration data [35]. To access the web page, it is necessary to enter the web page link in PHP and fill in the authentication data with pre-registered username and password. As such, only pre-registered users can be redirected to the system home page.

Through the Web monitor it is possible to consult the data stored in the online database through smartphones or PCs. Considering that the ethernet standard is the most used solution in proprietary systems for network interconnectivity, using free software in a WiFi network for monitoring decreases costs [36]. The minimum sampling time for viewing the data on

EBSCOhost - printed on 2/14/2023 2:46 PM via . All use subject to https://www.ebsco.com/terms-of-use

the server is approximately three seconds after sending this request via WiFi—this is considered a limitation for real-time systems.

In the monitoring menu, the user can view the data measured in graph and log form, as shown in Fig. 14. By clicking on the Logs submenu, the user can view the data in the form of a spreadsheet, with the date and time the value was received by the database. To generate the graphs, we used the Highcharts library, written in Java Script, which is a programming language interpreted for WEB. The chart is refreshed every 30 seconds and to view the measurement for a specific day, the user must select a valid date in the calendar and confirm with the magnifying glass button. The graph will then be updated and show the representative mean of ten minutes of the selected sensor. The system also offers the option of printing or exporting graphics in PNG, JPEG, PDF, and SVG formats.




Figure 14. Expanded menu screen (in Portuguese)

To access the system remotely through a computational device, it is necessary to enter the pre-defined static IP in the microcontroller firmware—for example 192.168.1.195, followed by a bar and one of the commands programmed in the microcontroller circuit (192.168. 1,195/YT), as shown in Fig. 15, together with the confirmation screen for receiving the measurement data of the thermoelectric microgenerator from the online server.

By accessing the Logs link, the user can monitor in real time the information sent by the system via WiFi every ten seconds. The user can also generate graphs on the same page that the data is stored, as shown in Fig. 16.

EBSCOhost - printed on 2/14/2023 2:46 PM via . All use subject to https://www.ebsco.com/terms-of-use

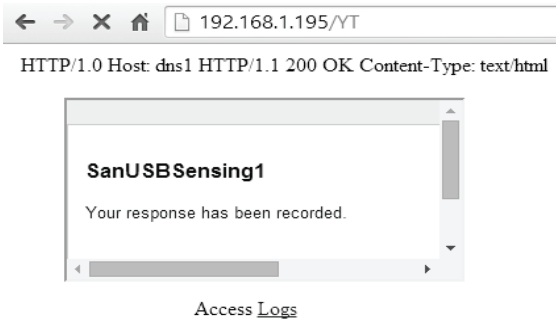



Figure 15. Confirmation response of the data receipt by the online server

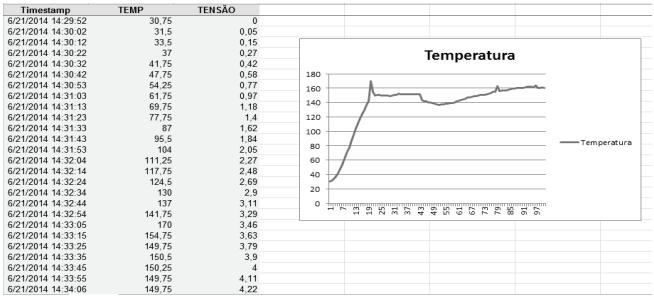



Figure 16. Recording data in the online database and graphing

## Results

The TEG hot-side temperature control, developed in the project's second stage, was graded to a reference temperature of 200ºC. In one analysis, this value was reached in approximately 16 minutes, as can be seen in Fig. 17 (a). The cold side temperature was maintained at 40ºC, resulting in a temperature difference of 160ºC. Temperature values were compared with the infrared temperature sensor VA6510 [37]. Five different loads (10 Ω, 20 Ω, 30 Ω, 40 Ω, and 50 Ω) were used.

Fig. 17 (b) shows the voltage values obtained according to the temperature stabilization time (16 minutes) on the hot side at 200ºC. The modules generated approximately 5 V for the five different loads, however, each one presents a different curve in time. The higher load of 50 Ω, generates the maximum value of 5 V after 15 minutes, and remains

EBSCOhost - printed on 2/14/2023 2:46 PM via . All use subject to https://www.ebsco.com/terms-of-use

at this point due to the implemented control, while the others reach the peak in less time, due to lower resistances.

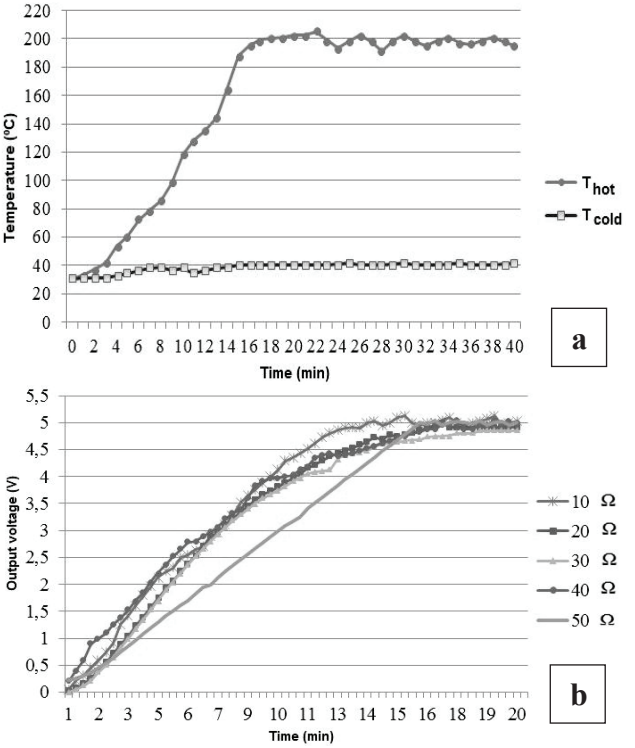



Figure 17. (a) Hot and cold side variation in temperature; (b) Output voltage for five different loads

## Conclusions

In the project's first phase, the HTCM that was developed operated with a PI temperature regulation realized by a microcontroller system with an optoisolated TRIAC output. The temperature can be set by the keypad or from an external control device through the communication interface. This communication between the HTCM and the control device allows for fully automated TEG parameter measurement through the complete temperature range.

EBSCOhost - printed on 2/14/2023 2:46 PM via . All use subject to https://www.ebsco.com/terms-of-use

To measure TEG performance, the temperature difference was obtained with the HTCM holding the TEG's hot side at a constant temperature, while the temperature of the cold side was approximately 293 K. To ensure exact balancing of the output power, a special mathematical model for the output power control was designed. Based on changing the switching on points of the TRIAC, this model takes into account the nonlinearity of the AC supply voltage. The signal from the zero-crossing detector circuit, which is connected to the microcontroller input pin, is used as a base point for phase shifting.

The mathematical model of the phase change allows for exact output power balancing versus linear phase changing of the supply voltage. As such, the HTCM shows good performance, reliability, and easy firmware updating when operating online.

In the project's second phase, the microcontrolled circuit, as well as the online monitoring software, were developed in free, multiplatform software (Linux, Windows®, and Mac OSX), with the aim of contributing to the diffusion of this computational tool.

A user can view the monitoring data through a smartphone, tablet, PC, or any other computing device with Internet access, through user profile and password access. Queries to the database can be made at any time with an update every minute. The hot-side temperature of the TEG was controlled at 200ºC, which was reached in about 16 minutes. The cold-side temperature was maintained at 40ºC, resulting in a temperature difference of 160ºC.

For this application, the system that was developed was efficient in relation to real-time monitoring of the microgeneration plant, although the data were sent to the databank at an interval of three seconds after measurement, adjusting to the temperature control with an inherently slow response. This was in accordance with the aims of the project. The use of open source tools also allows the accessibility of different user profiles. The system can be expanded to store data from other digital or analog sensors, as well as other types of data related to renewable energy plants.

## Acknowledgment

The authors would like to thank CNPq and Vale for financial support of the project through the Form-Engineering program; CAPES and DAAD (*Deutscher Akademischer Austauschdienst*) for the research grants awarded; and UFC and IFCE for the provision of laboratories and equipment.

EBSCOhost - printed on 2/14/2023 2:46 PM via . All use subject to https://www.ebsco.com/terms-of-use

## References


[1] P. H. Kao, P. J. Shih, C. L. Dai, and M. C. Liu, "Fabrication and characterization of CMOS-MEMS thermoelectric micro generators," *Sensors*, vol. 10, no. 2, pp. 1315–1325, 2010.

[2] R. Ahiska and S. Dişlitaş, "Microcontroller Based Thermoelectric Generator Application," *G.U. J. Sci.*, vol. 19, no. 2, pp. 135–141, 2006.

[3] G. J. Snyder, "Small thermoelectric generators-The Electrochemical Society," *Int. Conf. Thermoelectr. ICT, Proc.*, vol. 2002-Janua, no. 2, pp. 424–426, 2008.

[4] E. Schwyter, W. Glatz, L. Durrer, and C. Hierold, "Flexible micro thermoelectric generator based on electroplated Bi2+xTe3-x," in *Design, Test, Integration and Packaging of MEMS/MOEMS*, 2008, pp. 9–11.

[5] H. S. Han, Y. H. Kim, S. Y. Kim, S. Um, and J. M. Hyun, "Performance measurement and analysis of a thermoelectric power generator," *Therm. Thermomechanical Phenom. Electron. Syst.*, pp. 1–7, 2010.

[6] A. Kucukkomurler, "Thermoelectric powered high temperature wireless sensing and telemetry," *2009 4th IEEE Conf. Ind. Electron. Appl. ICIEA 2009*, pp. 1080–1086, 2009.

[7] B. Jang, S. Han, and J.-Y. Kim, "Optimal design for micro-thermoelectric generators using finite element analysis," *Microelectron. Eng.*, vol. 88, no. 5, pp. 775–778, 2011.

[8] R. Y. Nuwayhid, D. M. Rowe, and G. Min, "Low cost stove-top thermoelectric generator for regions with unreliable electricity supply," *Renew. Energy*, vol. 28, no. 2, pp. 205–222, 2003.

[9] W. Glatz, E. Schwyter, L. Durrer, and C. Hierold, "Bi2Te3-based flexible micro thermoelectric generator with optimized design," *J. Microelectromechanical Syst.*, vol. 18, no. 3, pp. 763–772, 2009.

[10] NASA, "Multi-Mission Radioisotope Thermoelectric Generator Heat Exchangers for the Mars Science Laboratory Rover," *NASA'S JET PROPULSION LABORATORY*, 2012. .

[11] B. Ismail and W. Ahmed, "Thermoelectric Power Generation Using Waste-Heat Energy as an Alternative Green Technology," *Recent Patents Electr. Eng.*, vol. 2, no. 1, pp. 27–39, 2009.

[12] S. C. S. Jucá, P. C. M. Carvalho, R. I. S. Pereira, D. Petrov, and U. Hilleringmann, "Design and Implementation of a High Temperature Control Monitoring Applied to Micro Thermoelectric Generators," *Int. Conf. Renew. Energies Power Qual.*, vol. 11, 2013.

[13] Beckhoff, "Analog signal transmission : Current interface 4 … 20 mA ( Live Zero principle )." .

[14] S. C. S. Jucá, P. C. M. Carvalho, and F. T. Brito, "A low cost concept for data acquisition systems applied to decentralized renewable energy plants," *Sensors*, vol. 11, no. 1, pp. 743–756, 2011.

[15] F. T. Brito, S. C. S. Jucá, and P. C. M. Carvalho, "Controllogger : A remote monitoring system for decentralized renewable energy sources," in *Renewable Energy and Power Quality Journal*, 2012, pp. 1–4.


EBSCOhost - printed on 2/14/2023 2:46 PM via . All use subject to https://www.ebsco.com/terms-of-use

[16] SanUSB Group, "SanUSB," 2018. [Online]. Available: http://sanusb.org/.
[17] J. W. Paulson, G. Succi, and A. Eberlein, "An empirical study of open-source and closed-sou software products," *IEEE Trans. Softw. Eng.*, vol. 30, no. 4, pp. 246–256, 2004.
[18] H. Belmili, S. M. Ait Cheikh, M. Haddadi, and C. Larbes, "Design and development of a data acquisition system for photovoltaic modules characterization," *Renew. Energy*, vol. 35, no. 7, pp. 1484–1492, 2010.
[19] M. C. Balan, M. Damian, and L. Jäntschi, "Preliminary Results on Design and Implementation of a Solar Radiation Monitoring System," *Direct*, pp. 963–978, 2008.
[20] S. Rosiek and F. J. Batlles, "A microcontroller-based data-acquisition system for meteorological station monitoring," *Energy Convers. Manag.*, vol. 49, no. 12, pp. 3746–3754, 2008.
[21] D. Ibrahim, *Microcontroller-Based Temperature Monitoring and Control*. Newnes, 2002.
[22] R. I. S. Pereira, S. C. S. Juca, and P. C. M. Carvalho, "Online Monitoring System for Electrical Microgeneration via Embedded WiFi Modem," *IEEE Lat. Am. Trans.*, vol. 14, no. 7, pp. 3124–3129, 2016.
[23] R. I. S. Pereira, P. C. M. Carvalho, and S. C. S. Jucá, "WiFi Data Acquisition System and online monitoring applied to thermoelectric microgeneration modules," *Renew. Energy Power Qual. J.*, no. 13, pp. 1–6, 2015.
[24] J. Torresen, Y. Hafting, and K. Nymoen, "A New Wi-Fi based Platform for Wireless Sensor Data Collection," *New Interfaces Music. Expr.*, pp. 337–340, 2013.
[25] D. Križaj, M. Baloh, R. Brajkovič, and T. Žagar, "Design and Development of a Portable WiFi enabled BIA device," *J. Phys. Conf. Ser. 434*, 2013.
[26] G. C. Martins and F. R. De Sousa, "An RF-powered temperature sensor designed for biomedical applications," *SBCCI 2013 26th Symp. Integr. Circuits Syst. Des.*, pp. 5–10, 2013.
[27] M. S. Durante and S. Mahlknecht, "An Ultra Low Power Wakeup Receiver for Wireless Sensor Nodes," *Third Int. Conf. Sens. Technol. Appl. SENSORCOMM*, pp. 167–170, 2009.
[28] H. Raisigel, G. Chabanis, I. Ressejac, and M. Trouillon, "Autonomous wireless sensor node for building climate conditioning application," *Fourth Int. Conf. Sens. Technol. Appl. SENSORCOMM*, pp. 68–73, 2010.
[29] F. P. Roque, E. V. Zaldívar, and O. A. De Fuentes, "Sistema de adquisición de datos con comunicación inalámbrica," *RIELAC Rev. Ingeriría Electrónica, Automática y Comun.*, vol. 34, no. 3, pp. 63–73, 2013.
[30] G. U. Gamm, S. Sester, and L. M. Reindl, "SmartGate – connecting wireless sensor nodes to the Internet," *J. Sensors Sens. Syst.*, vol. 2, no. 1, pp. 45–50, 2013.
[31] A. R. de Alexandria *et al.*, "An OCR System for Numerals Applied to Energy Meters," *IEEE Lat. Am. Trans.*, vol. 12, no. 6, 2014.
[32] G. S. V. Radha, K. Rao, and G. Radhamani, *WiMAX: A Wireless Technology Revolution*. New York: Auerbach Publications, 2007.
[33] IEEE802, "IEEE 802.11, The Working Group Setting the Standards for

EBSCOhost - printed on 2/14/2023 2:46 PM via . All use subject to https://www.ebsco.com/terms-of-use

Wireless LANs," 2015. .
[34] R. I. S. Pereira, I. M. Dupont, P. C. M. Carvalho, and S. C. S. Jucá, "IoT embedded linux system based on Raspberry Pi applied to real-time cloud monitoring of a decentralized photovoltaic plant," *Meas. J.*, vol. 114, pp. 286–297, 2018.
[35] I. M. Dupont, R. I. . S. Pereira, P. C. M. Carvalho, and S. C. S. Jucá, "Sistema Embarcado Linux Aplicado Ao Monitoramento Em Nuvem De Planta De Microgeração Fotovoltaica," in *VI Congresso Brasileiro de Energia Solar*, 2016, no. 2010.
[36] R. I. S. Pereira, S. C. S. Jucá, and P. C. M. Carvalho, "IoT embedded systems network and sensors signal conditioning applied to decentralized photovoltaic plants," *Measurement*, vol. 142, pp. 195–212, 2019.
[37] V&A INSTRUMENT, "Mini-infrared Thermometer," in *User Manual*, 2010.

EBSCOhost - printed on 2/14/2023 2:46 PM via . All use subject to https://www.ebsco.com/terms-of-use

# PART V:

# POWER ELECTRONICS, FACTS AND HVDC

EBSCOhost - printed on 2/14/2023 2:46 PM via . All use subject to https://www.ebsco.com/terms-of-use

# CHAPTER TWENTY-FOUR

# POWER ELECTRONICS IN FACTS AND HVDC

PETER KADAR[1]

## Abstract

The growing power transport need requires special compensators, rectifiers, inverters. In the last decades the performance of the semiconductor switching elements strongly developed, examples are the silicon IGBTs or SiCMosfet-s. 100 MVA range Flexible Alternating Current Transmission System parts as Static synchronous compensators, short-circuit current limiters or Phase shifters can be built in with these units. The new semiconductor elements have been applied not only to Back-to-back connections, but to High Voltage Direct Current power transmission lines of over 1 MVolts DC, over 10 GW power and over 3000 km distance. The age of large scale DC power grids has arrived.

**Keywords:** power electronics, FACTS, HVDC, large scale applications

## Challenges in network operation

A power system works as a pool with many feed-in points (power plants) and many load-points (substations close to customers). The flows on the passive network are evolving and are affected by power in/outputs in combination with the network topology and parameters. With appropriate conditions, the system is in balance, and the line flows and busbar voltages can be measured and exactly calculated by iterative load-flow calculation programs.

In the traditional model, the flow situation can be influenced by:

[1] Óbuda University, Power Systems Department, Budapest, HUNGARY
peter.kadar@t-online.hu

EBSCOhost - printed on 2/14/2023 2:46 PM via . All use subject to https://www.ebsco.com/terms-of-use

- generator setting;
- topology;
- change in the transformer tap position (longitudinal and cross-direction);
- dispatching active power generation;
- reactive source control;
- load adjusting.

The dispatcher has no opportunity for smooth intervention to change parallel flows. The dynamic load; weather dependent renewable generation; inter-system scheduled trade; loss minimization; dynamic voltage control; transient and dynamic stability; and power swings require new flow control methods and devices. FACTS (flexible alternating current transmission system) and HVDC (high voltage direct current transmission) are tools that can ameliorate these issues.

## Emerging role of power electronics

A hundred years ago, DC transmission was a viable option for urban distribution systems (e.g. 110 V DC). Energy conversion was performed using traditional electromechanical machines. The appearance of high-speed semiconductor switching elements gave impulse to controlled power applications, such as traction engines (urban trams, metros or high-speed trains); controlled industrial drives; rotating generator couplings (e.g. wind); and static inverters (e.g. photovoltaics). The focus is now on active power network flow control and regulator applications.

## Switching elements

The basic element of power electronic applications is the unidirectional switch, which is an electrical valve causing minimal power loss, ideally with a low transition time from close to zero resistance to infinite insulation resistance. For power system frequencies (50–60 Hz) the following switching elements were/are applied

- mechanical switches—commutators in DC machines;
- mercury vapor rectifiers (as diodes);
- semiconductor diodes;
- thyristors (as controlled diodes);
- IGBTs—high efficiency fast switching insulated-gate bipolar transistor (off-and-on switchable).

EBSCOhost - printed on 2/14/2023 2:46 PM via . All use subject to https://www.ebsco.com/terms-of-use

Nowadays, a semiconductor element can switch hundreds of amps and insulate to over 10 kV (e.g. 6.5 kV/200 A silicon IGBT; 10 kV/120 A SiCMosfet; 15 kV/20 A SiC IGBT).[2] In some power electronic devices (e.g. pulse width modulation inverters) the switching frequency is dozens of kHz. From this perspective the duration of the switching transition is crucial—it takes microseconds. Wide band-gap silicon carbide (SiC) devices offer better characteristics for high voltage, high speed, and low power loss applications than traditional silicon (Si) semiconductors.

In FACTS and HVDC applications, we control gigawatts of power with line currents and insulation voltages much larger than an individual semiconductor element can withstand. That is why diodes/thyristors or IGBTs are mounted in stacks.[3] The mechanical construction must take into account not only thermal properties, but electromagnetic dynamics and high density electrical space of these elements. Once we are above several hundred kVs at the primary voltage level, it is not easy to insulate the electrical triggering wires and it was for this purpose that light triggered thyristors were developed.[4]

## FACTS devices

First generation FACTS tools mainly applied thyristors as fast electronic switches, instead of mechanical breakers. The second generation devices are sophisticated power electronic circuits using internal inverters.

### *Series and parallel compensators*

The capacity of high voltage power lines produces a lot of reactive power and this causes an increase in voltage in free running mode (Ferranti effect). In the case of the load, the inductive power line consumes reactive power; the lack or surplus depends on the actual load situation. To keep the voltages within appropriate limits, a serial/parallel reactive power source is required along the line, e.g. in the middle of long lines. These can be in series or in shunt positions.

---

[2] https://www.nist.gov/sites/default/files/documents/pml/high_megawatt/NIST_MW_Drives_workshop_sbver9.pdf

[3] e.g. IXYS 900A 6.5kV press-pack IGBT http://www.westcode.com/publicity/press_rel/press58.pdf

[4] e.g. Short form catalog 2018 power semiconductors for industrial and consumer applications www.infineon.com/power

EBSCOhost - printed on 2/14/2023 2:46 PM via . All use subject to https://www.ebsco.com/terms-of-use

FACTS devices are formed from power electronics and static electrical elements (capacitors and reactors) that help regulate the operating parameters and raise the transmission capacity.

**Series FACTS devices:**

- *Thyristor-controlled/switched series reactor* (TCSR/TSSR). A fixed series reactor is shunted by a thyristor controlled reactor.
- *Thyristor-controlled/switched capacitor* (TCSC/TSSC). A fixed series capacitor is shunted by a thyristor controlled reactor. Possible roles of TSCS devices include:
  - increase in power transfer capability;
  - control line power flow;
  - mitigate sub-synchronous resonance;
  - damping of inter-area low frequency oscillation;
  - improve stability;
  - compensate;
  - increase stability margin.[5]
- *Static synchronous series compensator* (SSSC). Such as a thyristor controlled series capacitor and/or reactor.
  - *Static synchronous compensator* (SSSC/STATCOM). The controlled reactive power is generated by an inverter and the power is coupled to the line by a serial transformer.

The first large TSCS device was inaugurated in 1993 at the C. J. Slatt Substation, Oregon, USA (500kV; 3-phase, 60Hz).[6]

[5] Acharya, Naresh, Sode-Yome, Arthit and Mithulananthan, Nadarajah (2005). Facts about flexible AC transmission systems (FACTS) controllers: practical installations and benefits. Australian Universities Power Engineering Conference (AUPEC), Hobart, Tasmania, Australia, September 25–28, 2005. Tasmania, Australia: School of Engineering, University of Tasmania.

[6] K. R. Padiyar, Anil M. Kulkarni: Dynamics and Control of Electric Transmission and Microgrids; Wiley, 2019; p154.

EBSCOhost - printed on 2/14/2023 2:46 PM via . All use subject to https://www.ebsco.com/terms-of-use

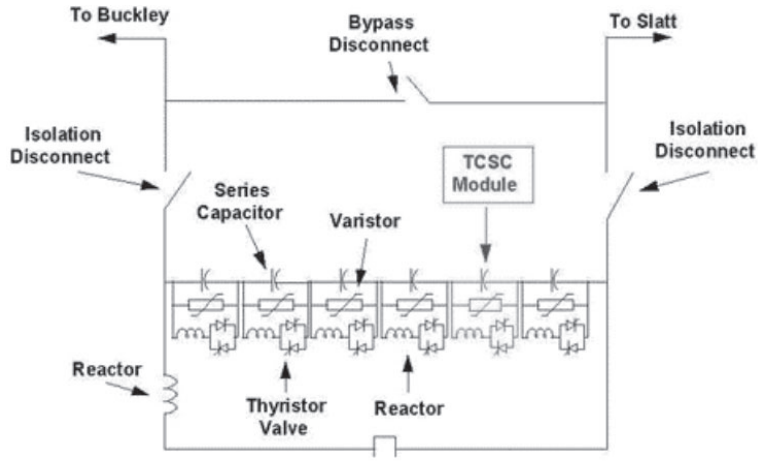



Figure 1. The C. J. Slatt, Oregon TCS application.[7]

In North America, South America and Asia, long distances limit the amount of transferable power because the electrical reactance of the lines causes overlarge phase shifts, pushing the line to the edge of its stability range. The solution is a TCS that 'rotates back' the phase angle, so that the power transmission capacity increases, as for example in the Hydro-Québec (HQ) Project Montagnais Substation, Canada North-East Network with applied capacitor rating: 30 Ω; 2,300 A; 1,500 MVAr (3 x 476 MVAr). The realized compensation degree = 40 %. Using this device, the transfer capability of the 1,200 km 765 kV power line was raised to 6,000MW.[8]

## *FACTS shunt position*

*Static VAR compensator (SVC)*

Ensuring power quality sometimes necessitates the dynamic injection of the required amount of reactive power into the network. Mechanically-switched reactors (MSR) and mechanically-switched capacitors (MSC), where the reactors or capacitors are switched by breakers (e.g. vacuum

[7] FACTS technology for open access. CIGRE JWG 14/37/38/39-24. Final Draft report. August 2000.
[8] Siemens, Flexible AC Transmission Systems Series Compensation, https://www.energy.siemens.com/nl/en/power-transmission/facts/

EBSCOhost - printed on 2/14/2023 2:46 PM via . All use subject to https://www.ebsco.com/terms-of-use

breakers), are not applicable where there are a high number of switches. For fast and variable reactive power compensation, the traditional shunt settings are supplemented by semiconductor elements:

- *Thyristor-controlled reactor* (TCR): the reactance is continuously changeable.
- *Thyristor-switched reactor* (TSR): steadily switched on/off reactors in a reactor bank.
- *Thyristor-switched capacitor* (TSC): steadily switched on/off capacitors in a capacitor bank.

*Static synchronous compensator (STATCOM).*

Controlled reactive power is generated by an inverter and the power is coupled to the line by a shunt transformer.

The following figures show STATCOM applications for 220 kV. They can inject from 65 Mvar inductive to 140 and 100 Mvar capacitive power into the network. The three-phase, closed-loop voltage controller switches IGBTs (insulated gate bipolar transistors) and PCTs (phase-controlled thyristors).9

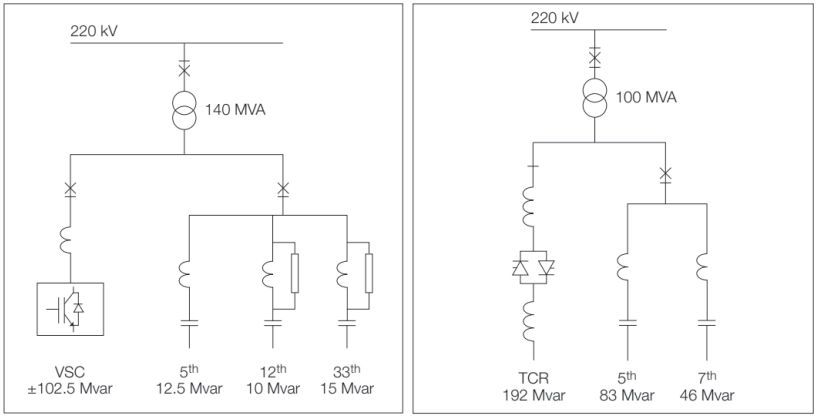



Figure 2. Single line diagram of Cerro Navia and Polpaico SVC application in Chile.[9]

In the classical model of a power system, huge amounts of mechanical power is stored in the mass of rotating machines that can span short-

[9] FACTS for grid voltage stabilization and increased power transmission capability in Chile https://library.e.abb.com/public

EBSCOhost - printed on 2/14/2023 2:46 PM via . All use subject to https://www.ebsco.com/terms-of-use

duration failures and allow for power-frequency control. With the emerging share of power electronics connected to renewable generation sources, we lose these capacities. Parallel-connected synchronous condensers help stabilize the grid, providing short-circuit power and inertia, contributing to frequency and voltage support for dynamic grid stability. Static VAR compensators (SVC), STATCOM, and synchronous condenser systems (SCS) alleviate this problem.

In 2018, a STATCOM was installed at Rourkela Station in India. It operates mechanically switched components at a 400 kV level and with dynamic ranges of 600 MVAr and 250 MVAr.[10]

## *Phase shifting*

There were only a few tools that could influence the natural flow across the passive elements in meshed power systems. Special phase shifter transformers have been developed solely with the purpose of adding additional voltage sources in the loops. They generate circulating current that can increase or decrease the flows in nearby branches. The phase shifting transformer's additive voltage vector can be in parallel, but is usually perpendicular to the phase voltage. The cost of these transformers is high and the control is realized by changing the tap position. The mechanical switches have limited speed and need maintenance. The appropriate equipment should also work under normal steady-state, dynamic, and emergency conditions.

Phase shifting can be effectuated by a serial or parallel-coupled voltage source. The unified power flow controller (UPFC) can be considered to be a STATCOM and SSSC connected to a common DC unit. It achieves continuous and fast phase shift control across a wide range.

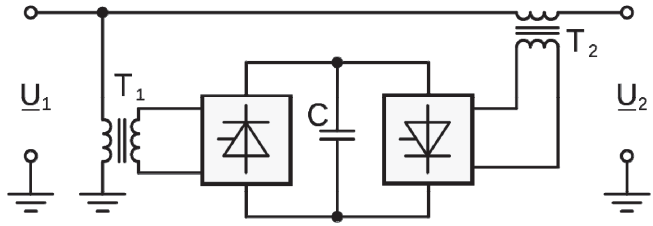



Figure 3. The idea of the Unified Power Flow Controller (UPFC).[11]

[10] http://www.siemens.co.in/en/news_press/index/siemens-commissions-worlds-largest-statcom-installation-for-pgcil.htm

EBSCOhost - printed on 2/14/2023 2:46 PM via . All use subject to https://www.ebsco.com/terms-of-use

The UPFC has an important role in the damping of sub-harmonic power swings in large power systems.[12] A form of UPFC has been tested with two 100 MVA converters connected by two 100 MVA high voltage series transformers and a 200 MVA shunt transformer to a 345 kVA system. This convertible static compensator (CSC) includes the functions of a static synchronous compensator (STATCOM), a static synchronous series compensator (SSSC), a unified power flow controller (UPFC) and an interline power flow controller (IPFC).[13]

### *Short-circuit current limiters*

In recent decades, the power capacity of the distribution network has experienced steady growth—more and thicker cables and E-mobility have sped up this process. At the same time, the short-circuit capacity has grown and has difficulty with previously installed elements of the network. Previous central short-circuit currents, which limit serial reactors, influence voltage quality, and drown-drop-transformers (e.g. by up to 18 %) also reduce power quality. The hazard of arc flash is also a growing problem as short circuit currents can now reach the 80–100 kA level.

New solutions to these problems include local resonant, high speed commutation and solid state current limiters (SSCL).[14] [15]

---

[11] http://www.wikiwand.com/de/Unified-Power-Flow-Controller - under the CC BY-SA 4.0 license

[12] Wagdy Mansour, Mohamed Mandour, Mohamed EL-Shimy, Fahmi Bendary: Damping of Power Systems Oscillations using FACTS Power Oscillation Damper: Design and Performance Analysis; in Proceedings of the 14th International Middle East Power Systems Conference (MEPCON'14), pp 015; DOI: 10.13140/RG.2.2.33170.25285

[13] B. Shperling, J. Sun, S. Bhattacharya: Power flow control on 345 kV lines with the 200 MVA convertible static compensator; 2005 IEEE Russia Power Tech DOI: 10.1109/PTC.2005.4524832

[14] Основы современной энергетики: в 2 т./под общей редакцией чл.-корр. РАН Е.В. Аметистова. 4-е изд. М.: МЭИ

[15] Damsky, Gelman, Frederick: A Solid State Current Limiter A Solid State Current Limiter https://www.epa.gov/sites/production/files/2016-02/documents/conf02_damsky_paper.pdf

EBSCOhost - printed on 2/14/2023 2:46 PM via . All use subject to https://www.ebsco.com/terms-of-use

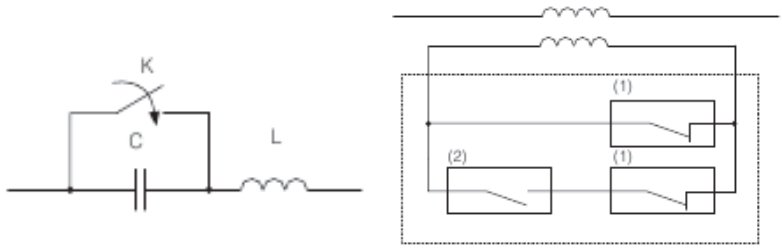



Figure 3. Resonant and high speed commutation limiters.

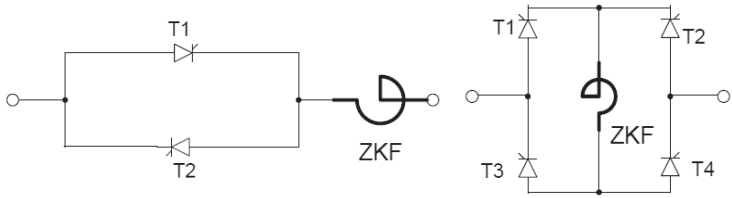



Figure 4. Solid-state short-circuit current limiters.

## *The electronic transformer*

The SST (electronic power transformer, power electronic transformer or solid-state transformer) has gained great importance nowadays. High frequency power conversion has been used for a long time in order to reduce the size of applied iron core transformers. It makes transformers lighter and cheaper, as well.

A SST typically consists of a rectifier, a DC-DC converter and an inverter.

The traditional MV/LV distribution transformers have fixed tap positions and in the case of dynamic voltage changes in solar photovoltaic, storage or wind applications cannot dump excess power. The SST's active bridge control can regulate the line voltage across a wide range using a prescribed strategy.

EBSCOhost - printed on 2/14/2023 2:46 PM via . All use subject to https://www.ebsco.com/terms-of-use

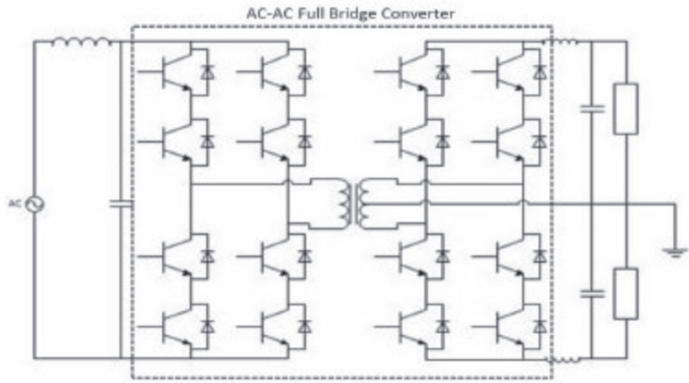



Figure 5. Single-stage SST topology.[16]

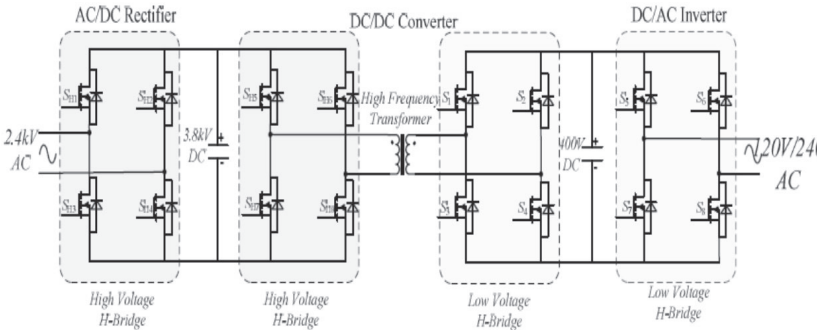



Figure 6. Two level electronic converter topology.[17]

The electronic transformer has gained importance in last years. High PV penetration into low voltage network disturbs the daily voltage profile. Up to this point, many utilities have applied central feeding point voltage controllers to counter-balance the high load caused by resistive voltage drops from changes in the tap position of HV/MV (e.g. 120/20 kV) transformers. This phenomenon was previously controlled by the

[16] Change Chen, Chengxiong Mao, Dan Wang, Jiming Lu: The research on special electronic power transformer; Istanbul University. Journal of Electrical Electronics Engineering, 2009 Volume 9 No. 1 (895–903)

[17] Ashok S.: Solid State Transformer; Short term Course on Power Electronics for Grid connected Renewable Energy Systems, National Institute of Technology Calicut, PEGCRES 2015

EBSCOhost - printed on 2/14/2023 2:46 PM via . All use subject to https://www.ebsco.com/terms-of-use

substation line-out power (current) measurement. The next figure shows the typical operation of central feeding point voltage control. In the case of a high load (midday), the voltage tap position is raised (6 times per a day); in lower load situations it is stepped back (another 6 times). The customer voltage was held within the 236.4–230.5 V range, which is less than 2.5 % away from the nominal voltage!

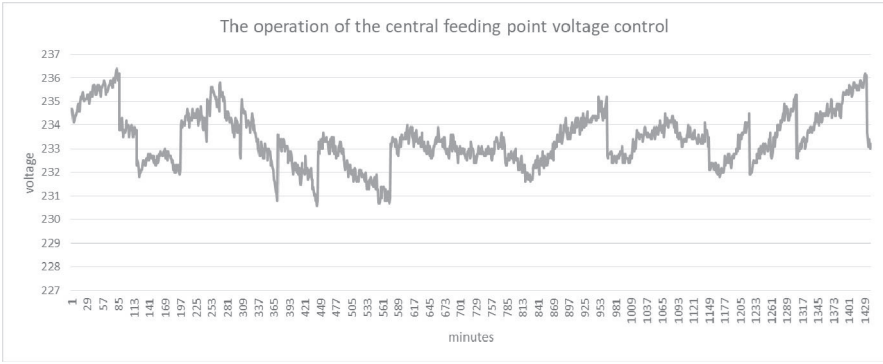



Figure 7. Daily LV voltage profile.[18]

The daytime PV generation in certain LV (0.4 kV) lines raises the voltage on specific streets (where many PV installations are). Meanwhile, in other streets, voltages remain in the normal range. The LV/LV SST can act as a street-level voltage control device. SSTs placed in the middle of the LV line can raise/drop the line voltage with approx. +/–15 %, depending on the actual load and PV generation situation. Rapid control can handle the cloud movement caused by PV generation drop-out and return.

[18] P. Kadar: Line voltage control on LV networks, script, 2018

EBSCOhost - printed on 2/14/2023 2:46 PM via . All use subject to https://www.ebsco.com/terms-of-use

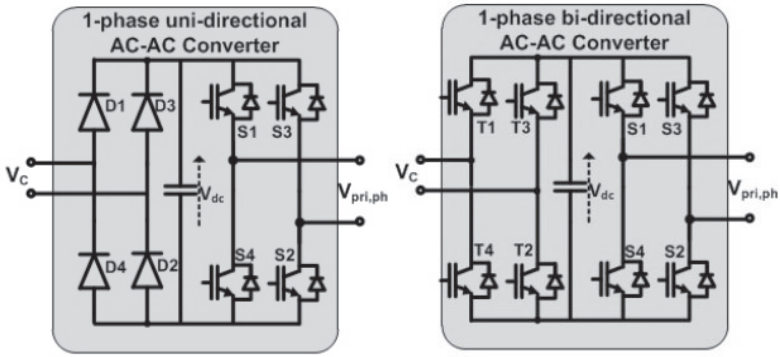



Figure 8. Uni and bidirectional AC-AC converters.[19]

In the following figure, the effect of the operation of a bidirectional LV/LV SST transformer can be seen. The high dynamics of the control are crucial to power quality. The controller can be a totally autonomous, local controller that measures the transformers current, direction and both voltages.

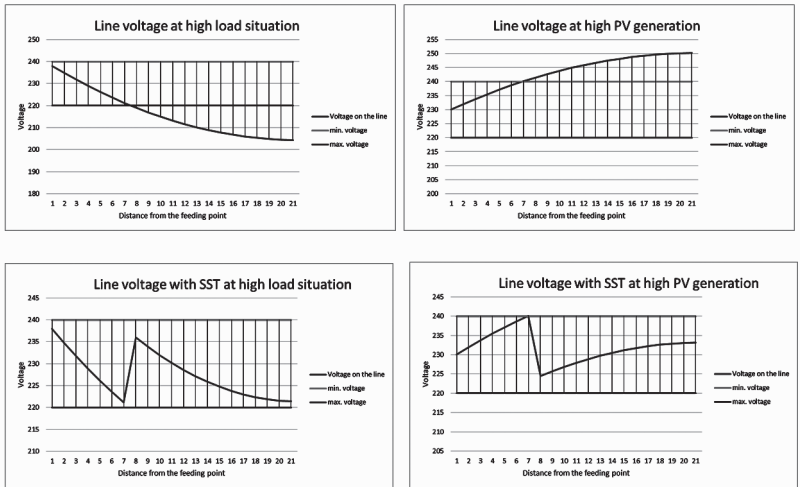



Figure 9. The (street)line voltage profile with and without LV/LV SST.18

[19] Dr. Prasad N. Enjeti: Advance Power Electronic Converters for Renewable Energy Systems; https://www.slideshare.net/enjeti/advance-power-electronic-converters-for-renewable-energy-systems

EBSCOhost - printed on 2/14/2023 2:46 PM via . All use subject to https://www.ebsco.com/terms-of-use

### *Present and future*

Today, besides traditional power system elements, high-tech power electronic solutions allow for smooth and fast control of the power flow in large extension systems. The main goal is to broaden the network and to explore the existing system capability using sophisticated control.

Local energy storage and controller devices gain more importance both for customers and the low voltage distribution network with the integration of small-scale renewable sources. The medium voltage network uses more power electronic voltage regulators and VAR compensators.

## The HVDC

### *Limits of AC transmission*

The energy of a single DC machine was capable of being transmitted for dozens of kilometer in 1882. DC energy distribution was a real competitor to AC systems a hundred years ago, but the ease of AC voltage transformation won out and now regional, national and continental power systems use AC. However, with their increasing size some difficulties have occurred. The distance of AC line transmission is limited because of stability problems.

Using DC, we have better utilization of wire and insulation and can transmit almost 50 % more energy, taking into account the RMS of the same peak voltage of AC or DC. In the case of DC transmission, we have less dielectric loss, a smaller corona effect, a lower skin effect, no reactive power problem, and a better insulation usability factor compared to AC. Furthermore, total line costs are about two-thirds those of AC lines. DC terminal costs (converters, filters) are higher, but with a length of more than 600 kms in the case of overhead lines, or 50 km of submarine cable, this type of transmission is cheaper.

EBSCOhost - printed on 2/14/2023 2:46 PM via . All use subject to https://www.ebsco.com/terms-of-use

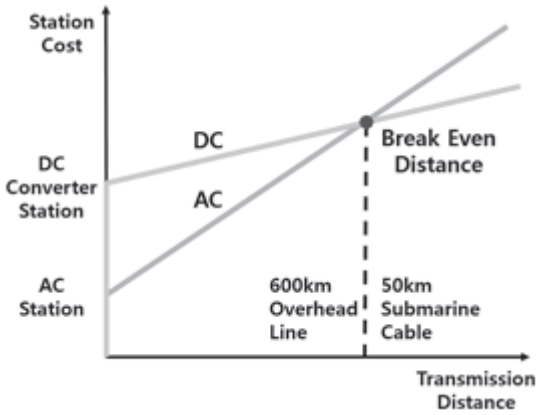



Figure 10. Comparison of AC and DC transmission costs.[20]

Positive attributes also include greater controllability and stability.

A secure and more eco-friendly solution is a bipolar arrangement where the two conductors sometimes run on different paths. Current flows through the earth only in the case of failure. The early submarine systems used monopole cable, with the return conductor being sea water itself.

The main elements of HVDC connection are: converter transformers; semiconductor stacks; harmonic filters; and the power line or cable. The typical 12 pulse HVDC converter only has harmonics of over 600 Hz, which are easy to filter. The early HVDC converters were based on thyristors with a line-commutated current-sourced (LCC) solution that had significant reactive power consumption. Nowadays, IGBTs with voltage-sourced self-commutated (VSC) circuits are more common.

[20] http://kapes.co.kr/eng/business/e_technology1.asp

EBSCOhost - printed on 2/14/2023 2:46 PM via . All use subject to https://www.ebsco.com/terms-of-use

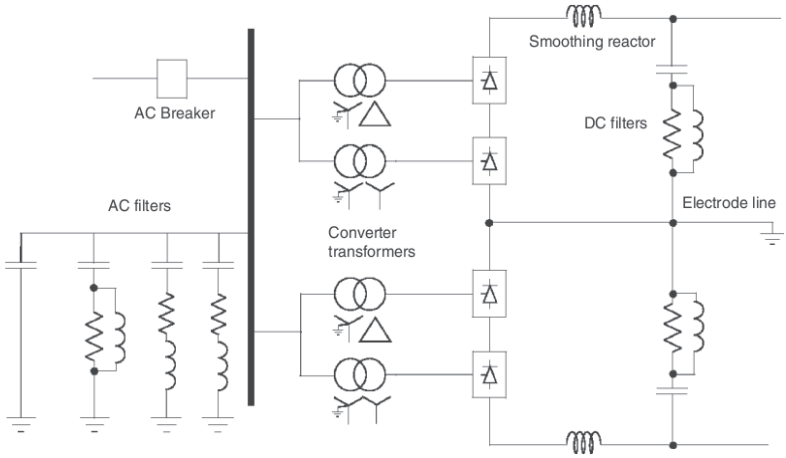



Figure 11. Typical LCC HVDC converter station.[21]

## *Role of HVDC lines*

In the middle of a large extension system (e.g. the European ENTSO-e system), or between two systems, a simple AC line will transport as much power as defined by the status of the system(s); this can be exactly calculated by load-flow calculation methods. We have no direct influence on the passive line.

Active FACTS tools do not behave like the classic passive four-pole model (e.g. a transformer or an overhead line), but have their "own rules," and operate using a control strategy.

The HVDC connection in the load-flow calculation can be modelled as a controlled line (four-pole) that can transmit controlled power in both directions (power injection), independently of the state of the large network.

## *Controlled transmission in a system*

In the northwest part of the ENTSO-e system, renewable penetration is very high. In the case of high wind conditions, the generation portfolio differs significantly from windless conditions, and the European load-flow

[21] Power electronics handbook: devices, circuits, and applications handbook/edited by Muhammad H. Rashid. 3rd ed. Copyright 2011, Elsevier Inc.

EBSCOhost - printed on 2/14/2023 2:46 PM via . All use subject to https://www.ebsco.com/terms-of-use

is in a different state. It is not easy to keep the right voltage and current values on the passive network elements. The TCSCs and other active FACTS elements help handle these situations and use the lines to their limits.

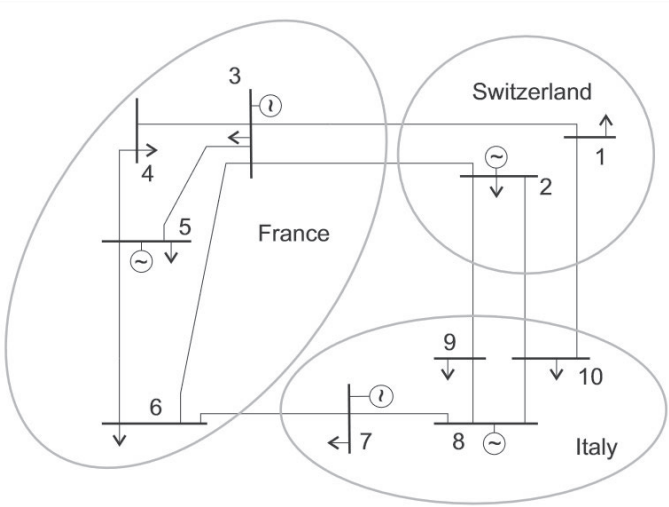



Figure 12. 10 bus model for the TCSC placement in the ENTSO-e system.[22]

The operation of power system-wide active control FACTS devices needs to be coordinated with the generator-mounted PSS (power system stabilizer).[23]

### *Connection between large systems*

In a power system, only one operational frequency exits, and it cannot be permanently connected to other system parts with asynchronous frequency. Although the trend is towards united continental systems, in Europe six synchronous areas exist. Different generation portfolios, large

[22] Chatzivasileiadis, Andersson: A Fully Controllable Power System—Concept for FACTS and HVDC Placement, https://arxiv.org/pdf/1506.08250

[23] Krum Gerasimov, Konstantin Gerasimov, Nikolay Nikolaev: Advanced Tools for Stability Improvement of Interconnected Electric Power Systems; September 2014, International Scientific Symposium Electrical Power Engineering, Varna, Bulgaria, ISBN 978-954-20-0497-4, pp.5–9

EBSCOhost - printed on 2/14/2023 2:46 PM via . All use subject to https://www.ebsco.com/terms-of-use

renewable penetration and the energy market require more and more connections between these different areas. The two frequencies and the sea between the systems suggests the use of submarine HVDC cables. Dozens of HVDC interconnectors are in operation in Europe and are planned for the near future e.g. in the North Sea Region.

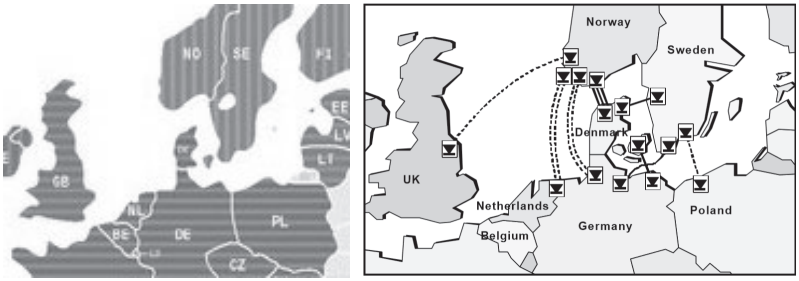



Figure 13. Different synchronous areas in North Europe[24] and HVDC cable interconnections between Nordel, British and ENTSO-e systems.7

## *Emerging HVDC grids*

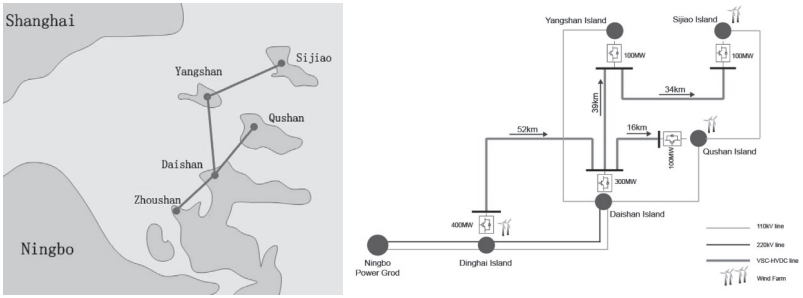



Figure 14. The Zhoushan Island and the Five Terminal VSC HVDC Network.[25]

Zhoushan Island in southeast China is a strongly developing area with 1.2 million inhabitants. The 2013 800 MW peak load was forecast to increase to 2,500 MW in 2020 and 4,700 MW in 2030. The 220 and 110

[24] ENTSO-e North Seas - regional planning https://tyndp.entsoe.eu/2016/insight-reports/north-seas/#grid-development-in-rg-ns
[25] Wang, Lori, Dianfeng, Pudney: HVT Power Systems Hierarchical control in a 5-terminal VSC-HVDC project; November 19th, 2014, Published in Energize

EBSCOhost - printed on 2/14/2023 2:46 PM via . All use subject to https://www.ebsco.com/terms-of-use

kV AC power system experienced serious problems in 2013. A decision was made to satisfy future energy needs, strengthen the island grid, enhance reliability and integrate more non-dispatchable renewable energy. The five existing substations have been strengthened by large capacity ±200 kV multi-terminal HVDC systems (400 + 300 + 3 x 100 MW). Currently, the HVDC grid serves as a secondary support for the primary AC network, but in the future it may become the primary network.

The cost was reasonable because only a few lines were necessary (2 pole conductors, instead of 3 phases) and the devices were small in size. There were additional favorable features, such as the fact that the VSC-HVDC (voltage-sourced converter HVDC) system can easily change power flow direction, can be adjusted quickly and can provide black start functionality. It can also provide its own reactive power compensation to improve power system stability and power quality. Another benefit is that no AC harmonic filter is required.

### *Back-to-back connection*

The back-to-back solution may be described as a HVDC link between two nodes of the network(s), with a length that is practically zero. This link is placed in the substation and with this element a forced and controlled power flow can be realized in both directions. It helps in cases where the natural flow needs to be changed and can be useful for energy transfer between two (semi)independent power systems.

More than fifty back-to-back (B2B) applications are in operation around the world. The largest is 500 kV with a 2,000 MW capacity and connects the Argentinean asynchronous 50 Hz system and Brazil's 60 Hz network near the Brazilian city of Garabi.[26]

[26] Graham, Jonsson, Moni: The Garabi 2000 MW interconnection back-to-back HWDC connect weak AC systems; https://library.e.abb.com

EBSCOhost - printed on 2/14/2023 2:46 PM via . All use subject to https://www.ebsco.com/terms-of-use

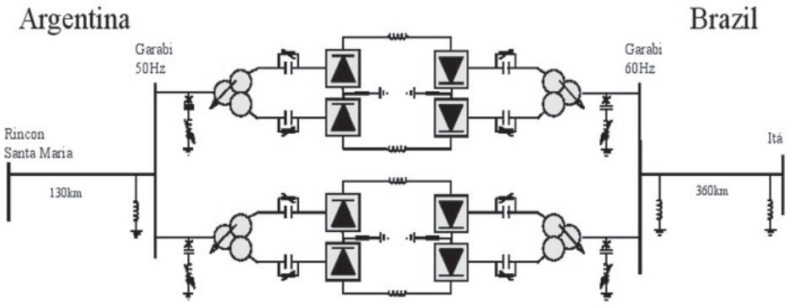



Figure 15. The Garabi B2B connection.[27]

The Itaipu hydroelectic dam's huge capacity is split between Paraguay and Brazil. The surplus power from the 50 Hz Paraguayan network is also returned to Brazil through a 700 MW DC link.[28]

There are three 600 MW B2B links between Germany (former GDR—Wolmirstedt and Etzenricht) and Austria and Hungary. Energy trade flourished between the western European UCTE system (today ENTSO-E) and the system of the former Eastern Bloc. This was made possible by direct tie lines between the Austrian system and, for example, some Hungarian units. Some generators were connected to the Austrian system through a 150 km long line. In addition to this unique generator connection, a wider range solution was built at the beginning of the nineties. The 600 MW B2B operated at 142 kV. Following the fall of the Iron Curtain some countries switched, step-by-step, from the eastern system to the western system and so today both the eastern part of Germany and Hungary belong to and operate in the same ENTSO-E system. There was no point in trading only through these points and several new lines established strong connections between the parts of the old system and these B2Bs were shut down in the mid-nineties.

## *Present and future*

HVDC solutions have increase over the last fifty years. In 2005, 70,000 MW capacity was in use in a hundred projects[29]; this number has

[27] Belmans, Hertem, Cole: Techno-economic aspects of power systems. Master in Advanced Power Electrical Engineering, Leuven

[28] Tony Sacks: Britain prepares for the French connection; New scientist, London, UK, 21 November 1985, p.31.

EBSCOhost - printed on 2/14/2023 2:46 PM via . All use subject to https://www.ebsco.com/terms-of-use

increased since then. One of the first large scale applications was developed by ABB in central Africa. Kolwezi is an important copper and cobalt mining center and uranium ore is mined in the region as well. In the Democratic Republic of Congo, there is no high density power network and the hydropower source is far away on the river Congo, near Inga. Because of stability problems, it is not possible to construct a sufficiently long single AC line. ABB constructed a +/–500 kV, 1,700 km long, 560 MW DC overhead line with the help of power electronics in 1982. In 2017, its capacity was upgraded to 1,000 MW.[30]

The following table shows the distribution of HVDC systems.

**Table I. Overview of existing HVDC systems.**

| *Continent* | *Year of first installation* | *Number of existing systems* | *Highest DC voltage level (kV)* | *Maximum transmitted power (MW)* | *Maximum length (km)* |
|---|---|---|---|---|---|
| Africa | 1979 | 4 | 533 | 2000 | 1700 |
| Asia | 1979 | 50 | 1100 | 12000 | 3300 |
| Australia & Oceania | 1965 | 5 | 400 | 700 | 611 |
| Europe | 1939 | 70 | 600 | 1000 | 580 |
| North America | 1932 | 20 | 600 | 400 | 1362 |
| South America | 1987 | 4 | 800 | 7100 | 2375 |

By the end of 2018, about 9,500 km of DC cable and overhead lines was operating In Europe. This is about 2 % of the length of the continental ENTSO-e system.[31] Counting the total number of lines in European systems, this is a little less than 1 %. 8,100 km of new DC line construction is scheduled by 2025. The largest ones are the EuroAsia Interconnector project[32] (Israel via Cyprus and Crete, 1,500 km) and the

[29] Power electronics handbook: devices, circuits, and applications handbook/edited by Muhammad H. Rashid. 3rd ed. Copyright 2011, Elsevier Inc.
[30] https://new.abb.com/systems/hvdc/references/inga-kolwezi
[31] The length of the line sin the ENTSO-e power system: AC lines—473289 km, AC cables—5055 km, DC cables—8546 km, No. of large transformers—7960. Based on the data in https://www.entsoe.eu/data/power-stats/inventory-of-transmission/
[32] https://www.euroasia-interconnector.com/

EBSCOhost - printed on 2/14/2023 2:46 PM via . All use subject to https://www.ebsco.com/terms-of-use

EuroAfrica Interconnector project[33] (Egypt via Cyprus and Crete, 1,700 km) with 500 kV DC undersea cables.

75 % of existing DC lines in Asia are in China. The world's largest ultra-HVDC line (+/–1,100 kV; 12,000 MW) started operation at the end of 2018. The Changji-to-Guquan project stretches 3,293 km.[34] It transmits renewable energy from the northwest to the southeast industrial zone. India is currently planning a 800 kV, 6,000 MW, 1,800 km line, too.

A Pan-African HVDC supergrid is planned starting from the Inga hydropower project in the direction of the Mediterranean coast of Africa and towards South Africa.

In North America, 3,500 km of new DC lines are scheduled for the next decade. There are plans to set up a Pan-American supergrid in the USA with the eastern and western parts connected by back-to-back interties.

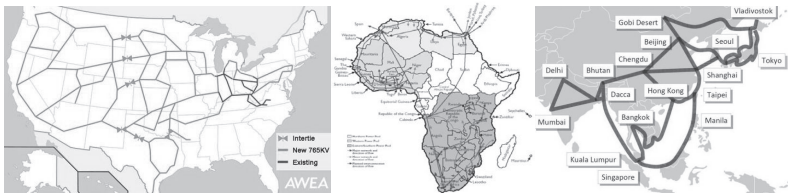



Figure 16. The Pan-American, Pan-African and Pan-Asian supergrid plans with HVDC.[35] [36]

## Conclusion

The basics of the power systems were laid a hundred years ago. The power supply will continue applying a large number of passive transformers, power lines, and switches in the future. Controllability and power quality require the use of power electronics tools that are small in number, but significant in effect. The large scale expansion of the grid can be achieved using HVDC connections. Growing power transmission needs increases in unit measures and voltage level going towards the development of ultra-HVDC. To maintain voltage quality in the high-

[33] https://www.euroafrica-interconnector.com/

[34] World's Biggest Ultra-high Voltage Line Powers Up Across China; https://www.tdworld.com/overhead-transmission/worlds-biggest-ultra-high-voltage-line-powers-across-china Jan 02, 2019

[35] American Wind Energy Association proposal.

[36] The Asian Super Grid https://apjjf.org/-John_A_-Mathews/3858

EBSCOhost - printed on 2/14/2023 2:46 PM via . All use subject to https://www.ebsco.com/terms-of-use

penetration renewable energy source environment, it is necessary to build more and more power electronic devices into the distribution network, such as static VAR compensators and solid-state transformers.

EBSCOhost - printed on 2/14/2023 2:46 PM via . All use subject to https://www.ebsco.com/terms-of-use

# CHAPTER TWENTY-FIVE

# HIGH PERFORMANCE SIC MOSFETS FOR FAULT TOLERANT APPLICATIONS

CHARLES ONAMBELE[1], JEAN ERNST BESTER[1], AUGUSTIN MPANDA MABWE[1]

## Abstract

Harsh environmental applications are characterized by significant constraints regarding temperature, volume, fault-tolerance, and efficiency. As the introduction of power electronics to such systems is constantly growing, research activities to expand knowledge on the capabilities of available technologies for such applications in the field are essential, including applications in aerospace and renewable energies. This chapter evaluates the performance of a silicon carbide (SiC) MOSFET transistor for a multiphase power converter for fault-tolerant applications. Two methods are employed in this study: the model provided by the manufacturer was used in a simulation for a fault-tolerant electric drive application, after which, under the same operating conditions, the power module was characterized and its performance evaluated. Both methods led to high system efficiencies of around 97–98% for a 1200V-400A SiC MOSFET transistor module integrated into a 120kW-100A 6-phase modular inverter. The validated parameters of the SiC power MOSFET module were also used to present its impacts on the parameters of an input electromagnetic interference (EMI) filter for aerospace applications.

**Keywords:** High efficiency; fault-tolerant applications; modular inverter; SiC power MOSFET module; switching characterization.

[1] Graduate School of Electronic and Electrical Engineering (ESIEE-Amiens). 14, Quai de la Somme, 80082 Amiens, France. Phone number: +0033 322 662 067. E-mail: mpanda@esiee-amiens.fr

EBSCOhost - printed on 2/14/2023 2:46 PM via . All use subject to https://www.ebsco.com/terms-of-use

## Introduction

The challenge of global warming is encouraging academics and industrial scientists to develop innovative and green power systems. Whether this is for isolated renewable energy power plants or electrification of road and aerospace vehicles, designers often face new and severe constraints. Indeed, in such critical applications, lightness, compactness, fault-tolerance [1], and high efficiency are all expected from the same high frequency power electronic system. The latter is made up of specific topologies based on electronic components chosen to meet differing expectations.

In order to increase the fault-tolerance capabilities of a power electronic system, redundancy is a common characteristic of power converters [2]. The characteristics of the electronic components that will be duplicated become essential when the system has to be highly efficient, light, and compact all at the same time.

The main elements of any power electronic system, semiconductor switches, have undergone constant development since the invention of the diode [3]. The longstanding bipolar junction transistor (BJT) is known to allow high-voltage operation, but has the drawback of high switching losses for both the silicon (Si) and the silicon carbide versions (SiC) [4]. Many studies show that SiC materials have more attractive characteristics than Si materials, thanks to the wider bandgap achieved [5]-[9]. SiC materials have:

- High thermal conductivity allowing for high temperature operation.
- The ability to withstand high electric fields.
- High current density.

In its Si version, the metal-oxide field effect transistor (MOSFET) features low losses in its command circuit, as opposed to the BJT, thanks to the gate-source voltage required for turn-on. However, the Si MOSFET is not suitable for high voltage operation.

The integrated gate bipolar transistor (IGBT) is very popular because it combines the advantages of both the BJT and the MOSFET. It has some limitations in applications requiring high switching frequencies for high power density and efficiency.

As such, Silicon Carbide (SiC) power MOSFET modules have become serious contenders. For switching frequencies higher than 12kHz, they have lower power losses than Si devices [10]–[13], consequently increasing

EBSCOhost - printed on 2/14/2023 2:46 PM via . All use subject to https://www.ebsco.com/terms-of-use

the efficiency of SiC MOSFET-based converters. The lower power losses that need to dissipate favour a reduction in the volume and weight of the heat sink. But, to achieve a lighter and more efficient system, some parameters can become obstacles for designers, such as load current, temperature, incomplete datasheets for new devices, etc. Characterization of power modules helps us to obtain specific data from measurements, which are then used for electrical performance analysis.

Many studies have successfully carried out characterizations of MOSFET devices [11], [12], [14], [15], although some have been limited in terms of current [11], [14], [15]. These studies based their performance analyses on electrical behaviour and high temperature operation.

In this chapter, those conditions or requirements that may severely tax power electronics applications are explained. Then, a model-based performance analysis is presented, preceding the characterization of a dual-SiC power MOSFET module for temperatures varying from 25°C to 150°C, as well as a measurements-based performance study of an H-bridge inverter. The module tested was the CREE® HT-3201 [16]. This chapter evaluates the dynamic performance and efficiency of a high power multiphase converter (120kW-100A-25kHz) based on SiC technology for fault-tolerant applications.

Based on the methodology proposed in [17], the validated parameters of the SiC power MOSFET module were used to present its impact on the parameters of an input electromagnetic compatibility (EMC) filter for aerospace applications.

## *Harsh Intrinsic Conditions*

These are probably the first constraints that designers consider, as they are directly inform the components used in a power system.

High operating voltages and/or currents (100A or more) lead to important challenges throughout the design stage and prototype manufacturing. As an example, high current MOSFETs, which are being progressively introduced in applications for aircraft, imply other constraints on power sources, measurement devices, bus bars, and power cables, etc. Some of these constraints are detailed further in this chapter.

The efficiency of the system is also a major goal for some applications. A high efficiency requirement (95% or more) may lead to the necessity of choosing technologies that are capable of maintaining high performance, despite other constraints.

For applications requiring weight savings, such as aerospace, embedded power electronics must be optimized too. In this case, the main

EBSCOhost - printed on 2/14/2023 2:46 PM via . All use subject to https://www.ebsco.com/terms-of-use

heavy components are usually passive elements, such as filters or cooling systems. When the number of active devices increases, which is the case when redundancy is used to increase the fault-tolerance of systems, the individual weight of the main redundant components becomes a significant parameter.

### *Environmental Conditions*

Ambient temperature, altitude, and vibration are all conditions that need to be considered when designing a power electronics system, as they can affect the overall performance of the system. Most electronic devices are manufactured for a specific temperature range. Power semiconductor devices, such as the CREE® HT-3201 [16], are able to maintain their performance over a specified temperature range.

However, elevated ambient temperatures reduce the chances of achieving an efficient air cooling system. Knowing that the maximum junction temperatures of power electronics transistors are around 150°C, the higher the ambient temperature, the faster these devices will reach their absolute maximum temperature values.

In the case of a forced air-cooled system with fans, altitude modifies the fan airflow curves and, as a result, the cooling performance. Vibrations are also critical, mainly from the mechanical point of view—the sensitivity of a system to vibration needs to be acceptable. Furthermore, other climatic conditions can affect system performance and reliability, as described in [18], [19].

## System Description

The schematic diagram of the system under consideration is depicted in Fig. 1. This configuration was developed for an aerospace application [20]. The high-voltage DC bus (540V) is interfaced with a hexa-phase permanent magnet synchronous machine (6-phase PMSM) by use of a multiphase DC/AC converter and a filter. This system features simplicity and redundancy to maintain a significant fault-tolerant capability.

EBSCOhost - printed on 2/14/2023 2:46 PM via . All use subject to https://www.ebsco.com/terms-of-use

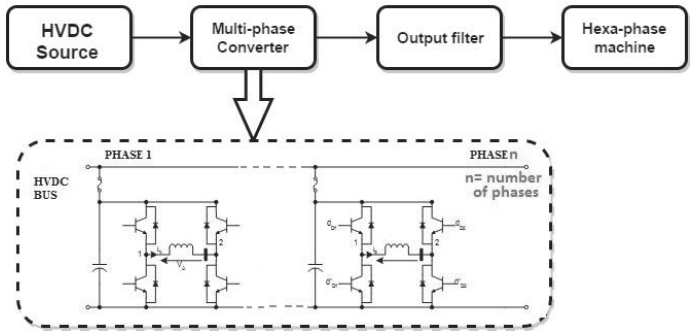



Fig. 1. System description showing only two phases of the machine.

This six-phase topology allows continuous operation in the case of loss of up to three phases. In fault operation modes, the targeted power is also degraded compared to the normal mode, but the system is not put out of service. The multiphase power converter is used for power flow control to fulfil the power requirements of the machine in different operation modes (120kW in normal operating conditions and 85kW in degraded modes) with the constraints of high efficiency, optimised power-to-weight ratio, and high power density. In this application, the power converter is composed of six H-bridge inverters based on highly integrated SiC power MOSFET modules. These semiconductor devices can achieve high performance and reliable power conversion as they offer ultra-low losses, as well as the ability to function at high operating temperatures. The modular topology of the system allows us to evaluate its efficiency by focusing on the behaviour of a single phase, considering an equal repartition of the power between phases.

## Model-based Performance Evaluation of a 120kW-100A 6-Phase Modular Inverter in an H-bridge Topology

Given the availability of the SiC MOSFET HT-3201 model in LTspice®, it is possible to assess its performance in specified applications. The model represents a half-bridge module composed of detailed models of the SiC switches, the Schottky diodes, and the parasitic inductances of the package used by the manufacturer—from the inner drain, source, and gate of each switch to the outer connections. Parasitic inductances between two switches are also included. These parasitic elements also depend on

EBSCOhost - printed on 2/14/2023 2:46 PM via . All use subject to https://www.ebsco.com/terms-of-use

the layout and may have an impact upon measurements. Hence, a full-bridge inverter was modelled in the LTspice® environment, as shown in Fig. 2, representing one phase of the modular inverter. Considering that all the switches have the same gate resistance, the appropriate value of the gate resistor has been chosen through simulations to be 2.2Ω. The module was simulated beforehand with the double pulse test scheme [13] shown in Fig. 5. The results of this first simulation show good performance concerning switching behaviour (Fig. 3). In fact, the overvoltage in turn-off operation is very low (about 5%) and the total computed switching losses are around 5mJ (turn-on and turn-off). The current overshoot at turn-on is quite high (more than the double the 100A objective and final value), but is still below the 400A rating of the device.

In order to compute the efficiency of the inverter in Fig. 2, additional spice directives were added allowing the following calculations in a steady-state regime: average input and output power; resulting losses and resulting efficiency.

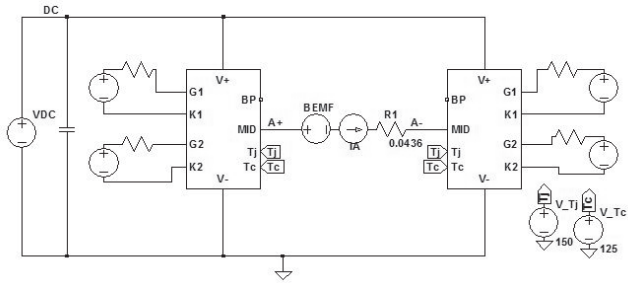



Fig. 2. Full-bridge schematic in LTspice® with one-phase equivalent circuit model of the machine.

EBSCOhost - printed on 2/14/2023 2:46 PM via . All use subject to https://www.ebsco.com/terms-of-use

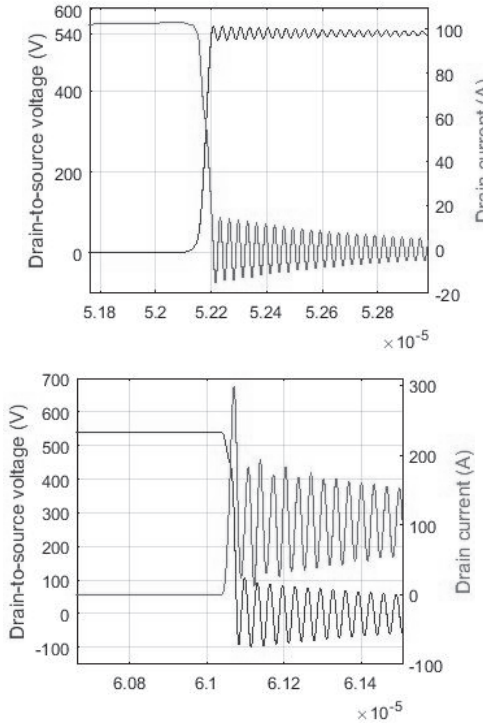



Fig. 3. Double-pulse simulation: turn-off (top), turn-on (bottom), voltage (blue) and current (red).

The simulated efficiency is expressed using (1):

$$\text{Converter}_{\text{Efficiency}} = \frac{\text{Average output power}}{\text{Average input power}} \quad (1)$$

Fig. 4 shows the results of the simulation, knowing that certain inputs have been imposed, extracted from a Simulink® control model described in [19]. The latter was constructed with a model of the 6-phase PMSM based on finite-element simulations to take into account any non-linearities of the magnetic flux of the machine. Moreover, a modular current control was implemented for each phase so as to allow magnetic independence between phases. Gate drive voltages (d1_high, d1_low, d2_high, and d2_low), BEMF (back electromotive) voltage source, and

EBSCOhost - printed on 2/14/2023 2:46 PM via . All use subject to https://www.ebsco.com/terms-of-use

phase current were therefore inputs for the LTspice® model, whereas the phase voltage was the main output.

Table I contains the post-processed results, which are still to be confirmed by later tests and measurements.

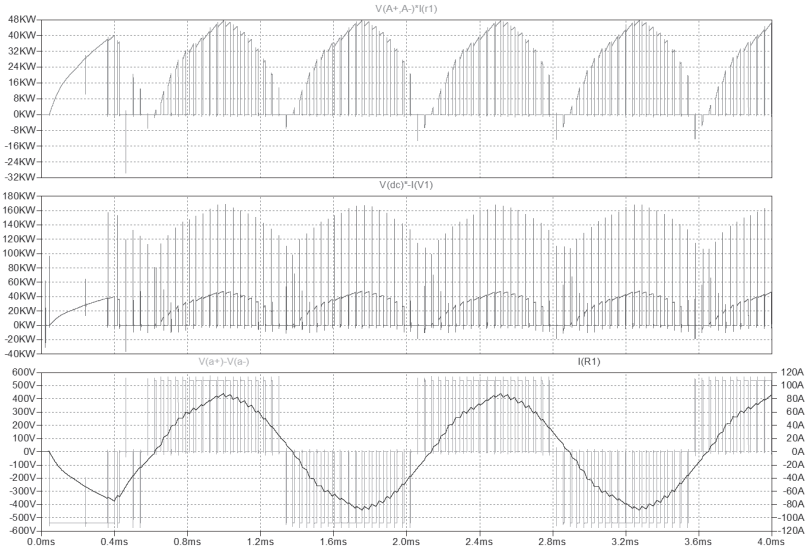



Fig. 4. Full-bridge simulation results in LTspice®, from top to bottom: output power, input power, load current (blue), and output voltage (green).

**Table I. Post-processed results using Spice directives in a steady-state regime.**

| Switching frequency (kHz) | Average input power (kW) | Average output power (kW) | Average power losses (W) | Efficiency (%) |
|---|---|---|---|---|
| **25** | 17.63 | 17.28 | 355 | 97.9 |
| **12.5** | 16.1 | 15.92 | 184 | 98.9 |

EBSCOhost - printed on 2/14/2023 2:46 PM via . All use subject to https://www.ebsco.com/terms-of-use

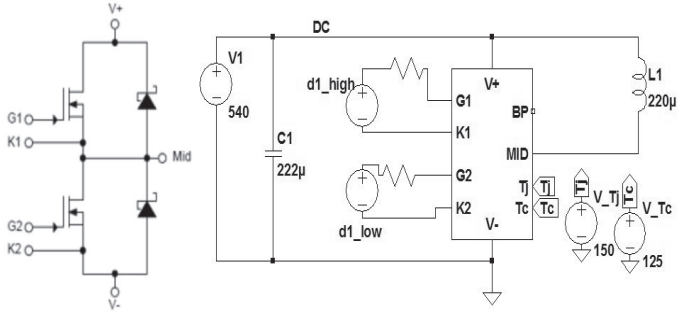



Fig. 5. SiC Module HT-3201 (left) and the double-pulse test setup (right).

## SiC MOSFET Switching Characterization

This paragraph describes the activities undertaken in order to measure the turn-on and turn-off switching energies of one MOSFET of the HT-3201 power module, with the test schematic shown in Fig. 5 [16]. Each transistor corresponds to a 4-leaded component, the kelvin source connection contributing to better system performance, which is absent in 3-leaded components [21]. The module was tested along with its ITGD2-3001 gate driver from CREE®.

### *Gate Driver ITGD2-3001 Functionality Test*

The half-bridge gate driver was configured to supply the lower MOSFET of the module. It is manufactured with a gate resistor of 5Ω for each switch driver. The goal of this functionality test was to keep the upper transistor off (d1_high = -5V) and provide appropriate command signals to the lower transistor (d1_low = -5/+20V). Here, the gate driver inputs require a pair of signals from a differential source. Because of the unavailability of such a source, the positive line input has to be connected to the logic rail and the negative line input to the midpoint of the logic rail. The test was undertaken at room temperature using a DC current source, an oscilloscope, and a frequency generator to provide the command signal (logic rail). Fig. 6 shows the gate driver output signals $V_{gs1}$ (-5V) and $V_{gs2}$ (-5/+20V), resulting from a command signal $V_{cmd}$, set to 0/+5V at 20kHz. This command signal was connected to the positive line of the differential inputs and the negative line was connected to +2.5V. The minimum high level value of the PWM signal needed to achieve -5/+20V at $V_{gs2}$ was obtained experimentally as +2.7V.

EBSCOhost - printed on 2/14/2023 2:46 PM via . All use subject to https://www.ebsco.com/terms-of-use

## *Test of the Half-bridge HT-3201 Power MOSFET Module*

### *Test Setup and Conditions*

The power module was assembled with the gate driver and placed on a hotplate. The latter was used for testing the device at temperatures varying from 25 to 150°C. The well-known double-pulse test method [13], shown in Fig. 5, was used to measure the switching characteristics of the lower MOSFET in the knowledge that the upper MOSFET would behave in the same way under similar conditions.

The method consisted of supplying the gate driver with a driving signal of two pulses of different lengths: the first pulse was the shortest and was used to measure the turn-off energy losses at the falling stage of the pulse, whereas the second one (which is generally five to ten times longer) was used to measure the turn-on energy losses at the rising stage. The actual length depended on the current that was to be achieved at the end of the first pulse. This value was found through testing and correlation with the theoretical relationship between the voltage of the inductor and the current.

These loss measurements were directly obtained through integration of the instantaneous turn-on and turn-off powers over the respective switching periods.

The layout of the setup is given in Fig. 7 and was composed of:

- An aluminium hot plate with hot oil inside, which was used to heat up the power module baseplate.
- A DC bus capacitor (black part on the left side of Fig. 7) of 120μF placed on top of the hot plate via a wooden plate to create an air gap between the hot plate and the capacitor, so as to avoid overheating.

EBSCOhost - printed on 2/14/2023 2:46 PM via . All use subject to https://www.ebsco.com/terms-of-use

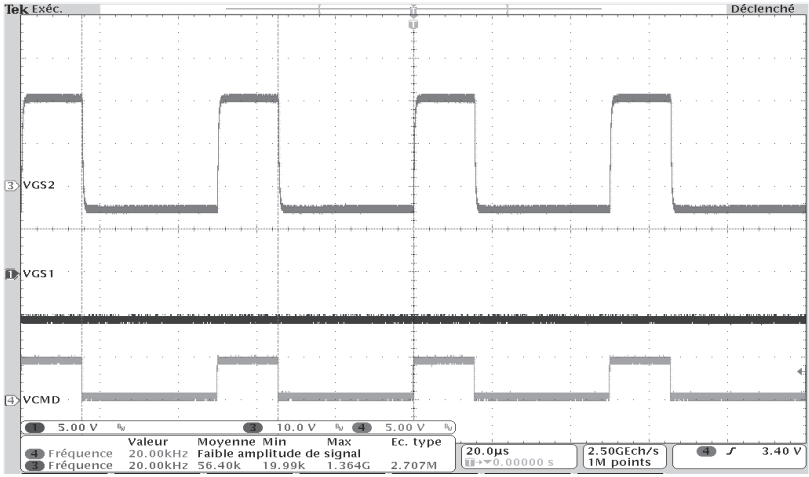



Fig. 6. Gate driver output signals—from top: $V_{gs2}$; $V_{gs1}$; $V_{cmd}$.

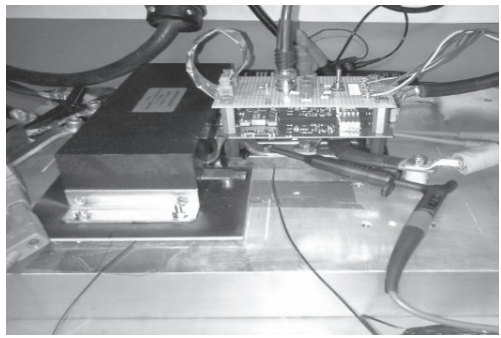


Fig. 7. Test setup for characterization of the CREE® HT-3201 module.

- The SiC power module was placed on the hot plate using thermal grease and fixation screws, close to the capacitor with copper bus bars to ensure good connections. This proximity was necessary to reduce the effect of parasitic inductances.
- The half-bridge gate driver was fixed on top of the module and was characterized by a 5Ω gate resistor per switch.
- A custom input/output board for the gate driver was used in order to have an appropriate interface between the setup and the measurement instruments:
    - for the voltage, a 1kV AC probe;

EBSCOhost - printed on 2/14/2023 2:46 PM via . All use subject to https://www.ebsco.com/terms-of-use

- for the current, a 300kA wide-bandwidth AC probe, also called a Rogowski current probe, was used to accurately measure pulsed currents that appear in the transition phases of MOSFET switching.

As can be seen, the assembly in Fig. 7 is very compact. Table II summarizes the different switching tests carried out for different case temperatures at a specific operating condition: 540VDC–100 A. The latter corresponds to the nominal operating point of the hexa-phase machine of the considered fault-tolerant power system. The maximum admissible current of the module is 400A for a case temperature of 25°C and 170A at 175°C. Therefore, the power MOSFET half-bridge module is appropriate for the targeted application.

### *Double Pulse Test Results and Comparison with Simulation*

Switching waveforms consist of turn-on and turn-off characteristics: drain current and drain-source voltage. Using some features of the Tektronix® oscilloscope, it is possible to obtain switching power waveforms and to compute the switching energies. Fig. 8 shows an example of the switching tests results obtained. The different tests gave similar waveforms compared to the simulation previously performed (Fig. 3). The different energy losses obtained for the specific operating conditions are reported in Table III.

The results show that the higher the case temperature is, the higher the energy losses will be. For example, an increase in temperature from 25°C to 100°C (tests 1 and 2, respectively), at the same voltage and current conditions, leads to an increase in total switching losses of about 27%. At temperatures very close to the maximum admissible for the module (tests 3 and 4), the behaviour was slightly different. It should also be noted that a change in temperature of 25°C in this region does not severely affect the total switching losses.

**Table II. Conditions of the switching tests of the half-bridge SiC module**

| Number of tests | Test conditions |
|---|---|
| 4 | **Test 1**: 25°C – 540VDC – 100A<br>**Test 2**: 100°C – 540VDC – 100A<br>**Test 3**: 125°C – 540VDC – 100A<br>**Test 4**: 150°C – 540VDC – 100A |

EBSCOhost - printed on 2/14/2023 2:46 PM via . All use subject to https://www.ebsco.com/terms-of-use

**Table III. Energy losses for different tests at 540VDC and 100A.**

| Test conditions | Turn-on energy losses (mJ) | Turn-off energy losses (mJ) | Total energy losses (mJ) |
|---|---|---|---|
| **Test 1: 25°C** | 4.3 | 1.9 | 6.2 |
| **Test 2: 100°C** | 5.3 | 2.6 | 7.9 |
| **Test 3: 125°C** | 5.6 | 3.7 | 9.3 |
| **Test 4: 150°C** | 5.8 | 3.1 | 8.9 |

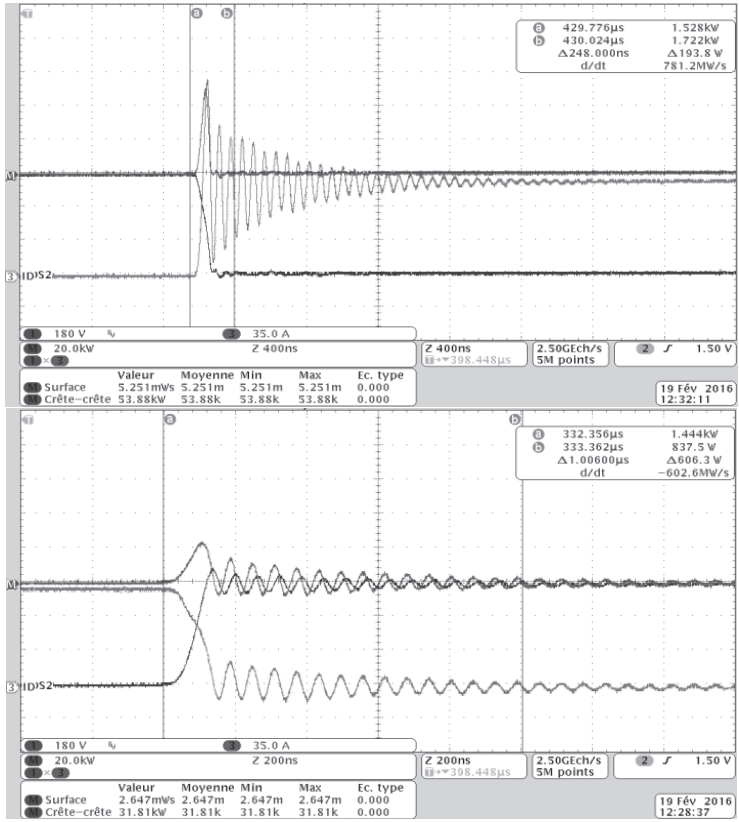



Fig. 8. Test 3—Turn-on (top), turn-off (bottom): drain-source voltage (blue); drain current (purple); power (red).

EBSCOhost - printed on 2/14/2023 2:46 PM via . All use subject to https://www.ebsco.com/terms-of-use

## Measurement-based Performance Evaluation of a 120kW-100A-25kHz 6-phase Modular Inverter in an H-bridge Topology

To evaluate the performance of the SiC module, a full-bridge inverter was modelled in the Simulink® environment, as shown in Fig. 9, corresponding to one phase of the system described above.

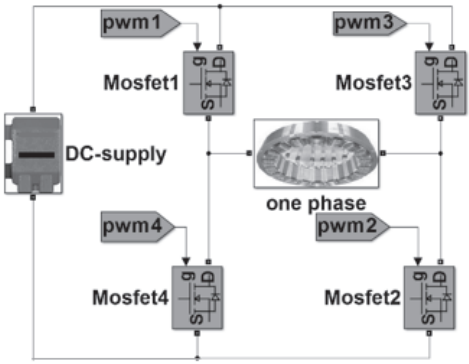



Fig. 9. Independent phase powered in H-bridge configuration simulated in MATLAB/Simulink®.

Double pulse test results were used to compute the efficiency of the converter with a one-phase model of the machine using MATLAB/Simulink® [19].

The loss calculations only consider the conduction and switching losses of the modules (MOSFETs and diodes); they neglect other losses, such as driver losses. Total energy losses were taken to be 10mJ, corresponding to the measurement results of Test 3, which was the worst case measurement result with a current of 100A. The simulation assumed a unipolar sinusoidal PWM scheme, and the following equations were used in MATLAB® to compute the power losses:

$$P_M = P_{CM} + P_{swM} \tag{2}$$

$$P_M = R_{DSon}\, I_{Drms}^2 + \left(E_{onM} + E_{offM}\right) f_{sw} \tag{3}$$

$$P_D = P_{CD} + P_{swD} \tag{4}$$

EBSCOhost - printed on 2/14/2023 2:46 PM via . All use subject to https://www.ebsco.com/terms-of-use

$$P_D = u_{D0}\, I_{Fav} + R_D\, I^2_{Frms} + E_{onD}\, f_{sw} \quad (5)$$

where $P_{CM}$ and $P_{swM}$ are MOSFET conducting and switching losses, respectively; $P_{CD}$ and $P_{swD}$ are body diode conduction and switching losses; and $P_M$ and $P_D$ are MOSFET and diode total losses. Parameters $R_{DSon}$ and $R_D$ are the MOSFET on-state resistance and the diode forward resistance. Parameter $u_{D0}$ is the forward voltage of the diode during conduction; $I_{Drms}$ is the MOSFET root-mean-square value of the drain current; $I_{Frms}$ is the forward current of the diode; and $I_{Fav}$ is the average forward current of the diode. $E_{onM} + E_{offM}$ equals the total energy losses measured and is considered to be 10mJ. $E_{onD}$ corresponds to the body diode, the losses of which are negligible when compared to MOSFET losses. To compute the efficiency of the converter, the following equations were used:

$$P_{in_{converter}} = V_{DC}\, I_{supply_{rms}} \quad (6)$$

$$P_{o_{converter}} = P_{in_{converter}} - P_{losses} \quad (7)$$

$$Efficiency = P_{o_{converter}} / P_{in_{converter}} \quad (8)$$

$P_{in_{converter}}$ and $P_{o_{converter}}$ represent the converter's input and output power, respectively; $V_{DC}$ the DC supply voltage; and $I_{supply_{rms}}$, the root-mean-square value of the supply current.

Fig. 10 shows the efficiency achieved as a function of the switching frequency. The efficiency achieved for the converter was around 97% at a switching frequency of 25kHz; and 98% at a switching frequency of 12.5kHz.

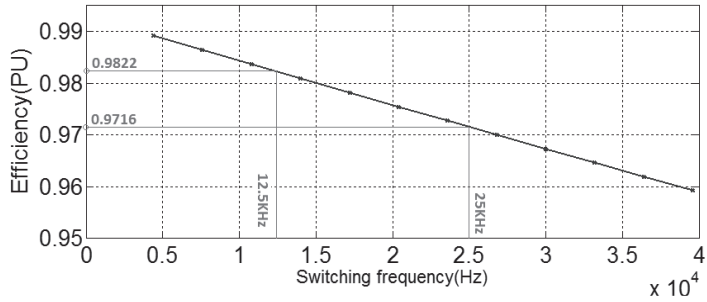



Fig. 10. Efficiency as a function of switching frequency.

EBSCOhost - printed on 2/14/2023 2:46 PM via . All use subject to https://www.ebsco.com/terms-of-use

**Table IV. Comparison between model-based and measurement-based efficiency computations.**

| Switching frequency (kHz) | Model-based efficiency (%) | Measurement-based efficiency [%] |
|---|---|---|
| **25** | 97.9 | 97.1 |
| **12.5** | 98.9 | 98.2 |

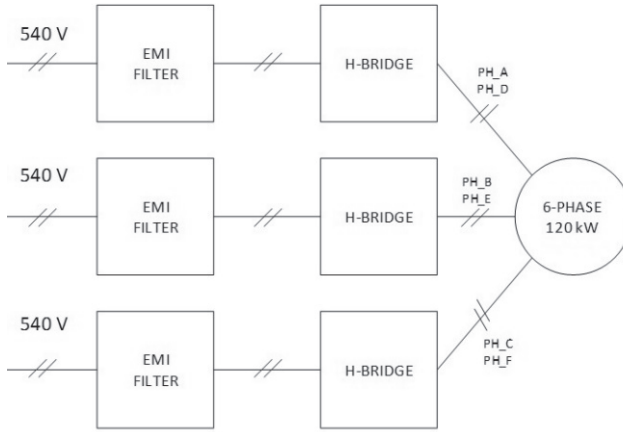



Fig. 11. Introduction of the EMI filters.

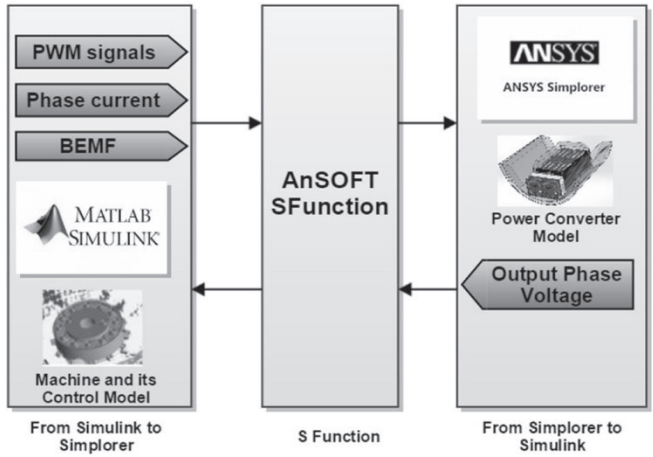



Fig. 12. Matlab/Simulink and Ansys/Simplorer co-simulation structure.

EBSCOhost - printed on 2/14/2023 2:46 PM via . All use subject to https://www.ebsco.com/terms-of-use

Using (6), (7), and (8), the efficiencies achieved were computed. The results are given in Table IV. It may be remarked that the efficiencies from the two methods are quite close to each other. The achieved results show that SiC MOSFETs can be used in applications where high efficiency is required. Evaluations of the efficiency levels, as reported in this chapter, help to determine the maximum switching frequency needed for a minimum target system efficiency.

## Impact of the Validated SiC MOSFET Model on the Parameters of an EMC Filter for Aerospace Applications

The capability of a SiC MOSFET module to operate at high switching frequencies while maintaining a high efficiency has been validated. This advantage may impact greatly upon the weight and volume of the EMI input filter, knowing that the targeted application has these constraints.

An EMC/EMI (electromagnetic interference) input filter (Fig. 11) was simulated to keep the common-mode noise of the system below the limitations of the DO-160 standard. A co-simulation model (Fig. 12) was built in the Ansys Simplorer® platform for the converter and in Matlab/Simulink® for the machine and its control [22]. This allowed us to take into consideration the non-linearities of each subsystem and the different parasitic capacitors, which draw the noise current to the ground. Figs. 13 and 14 show the results of the insertion of an LC-type common-mode filter, which consists of a choke of 133µH and a capacitor of 243nF.

EBSCOhost - printed on 2/14/2023 2:46 PM via . All use subject to https://www.ebsco.com/terms-of-use

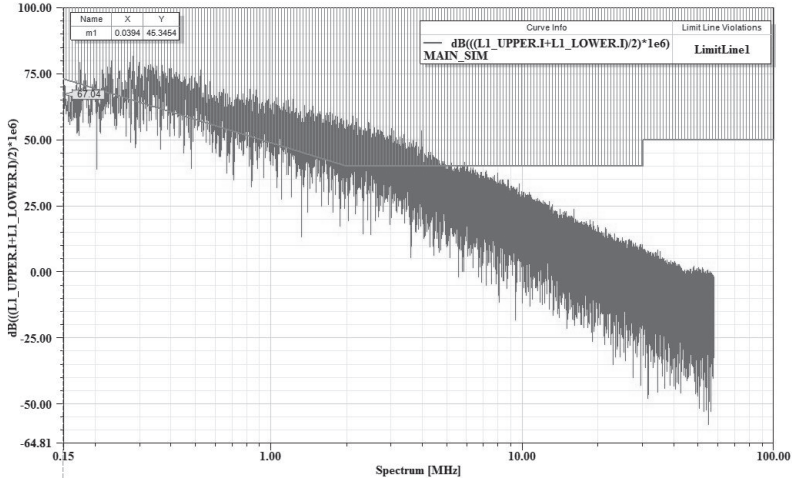



Fig. 13. Common-mode current spectrum before EMI Filter implementation.

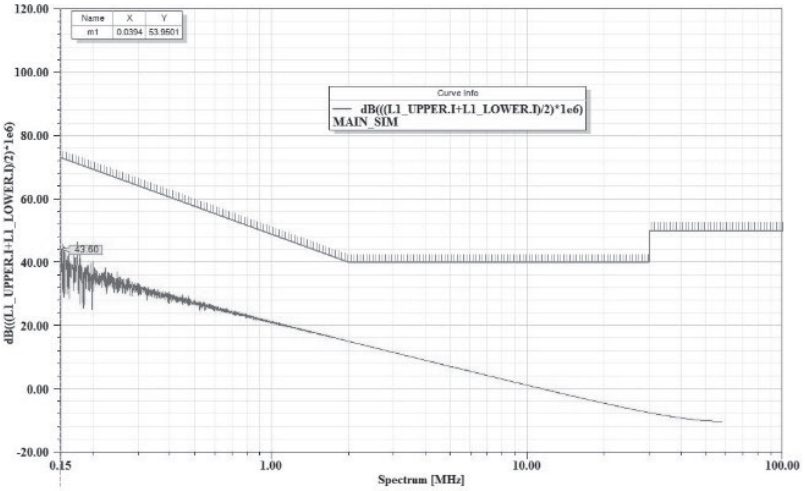



Fig. 14. Common-mode current spectrum after EMI filter implementation.

This evaluation has shown that the higher the operating switching frequency, the lower the values of the passive elements. Thus, the SiC module power MOSFET can contribute to a reduction in the volume and weight of the EMI common-mode filter.

EBSCOhost - printed on 2/14/2023 2:46 PM via . All use subject to https://www.ebsco.com/terms-of-use

## Conclusion

This chapter reports a performance evaluation of a high performance silicon carbide (SiC) MOSFET transistor for a multiphase converter for fault-tolerant applications, such as those found in the aerospace field. System efficiency was computed using an LTspice® model provided by the vendor, and measurements were undertaken with the actual power module to validate the model behaviour and its results. The power module and its gate driver were subject to testing. Using the double-pulse test method, characterization of the switches was carried out for the operating conditions of a multiphase inverter with different temperatures for the switches.

The system considered was a 120kW-100A-25kHz 6-phase modular inverter in an H-bridge topology. The converter efficiency achieved was around 97–98% for a switching frequency of around 12.5–25kHz and a current of 100A peak value. The higher the switching frequency becomes, the higher the switching losses will be.

Moreover, the passive elements of an EMI filter integrated into the design, and simulated in a co-simulation model between Matlab/Simulink® and Simplorer®, predicted lower volume and weight. In other words, the SiC-based module is a valuable candidate for fault-tolerant applications aiming for high efficiency at similar power and switching frequency levels.

## Acknowledgements

This work was undertaken in the framework of JTI Clean Sky Systems for Green Operations WP2.3.4.2 ETRD “Electrical Tail Rotor Drive” and is associated with SoW S632_AH_Hybrid Propulsion_2015. Furthermore, the authors are grateful to CREE® which provided the LTspice® model of the module and advice on its proper use of the devices.

## References

[1] M. Villani, M. Tursini, G. Fabri, and L. Castellini, ‘High Reliability Permanent Magnet Brushless Motor Drive for Aircraft Application,’ *IEEE Trans. Ind. Electron.*, vol. 59, no. 5, pp. 2073–2081, May 2012.

[2] G. Fabri, E. D. Loggia, M. Tursini, and M. Villani, ‘Fault-tolerant design of motor-drives for high reliability applications,’ in *2015 IEEE 1st International Forum on Research and Technologies for Society and Industry Leveraging a better tomorrow (RTSI), Sept.* 2015, pp. 219–225.

[3] APEC 2015 [Available online]

EBSCOhost - printed on 2/14/2023 2:46 PM via . All use subject to https://www.ebsco.com/terms-of-use

http://www.psma.com/sites/default/files/uploads/tech-forums-semiconductor/presentations/11-market-and-technology-trends-wbg-power-module-packaging.pdf

[4] H. Yu, J. Lai, X. Li, Y. Luo, L. Fursin, J. H. Zhao, P. Aleksandrov, B. Wright and M. Weiner, 'An IGBT and MOSFET gated SiC bipolar junction transistor,' in Conference Record of the 2002 IEEE Industry Applications Conference. 37th IAS Annual Meeting (Cat. No. 02CH37344), t. 4, Oct. 2002, 2609-2613 vol.4.

[5] R. Riedel, A. Kienzle, W. Dressler, L. Ruwisch, J. Bill and F. Aldinger, «A silicoboron carbonitride ceramic stable to 2,000 C», en, Nature, t. 382, no. 6594, p. 796-798, août 1996, ISSN : 0028-0836.

[6] A. Dzurak, «Quantum computing: Diamond and silicon converge», en, Nature, t. 479, no 7371, p. 47-48, Nov. 2011, ISSN: 0028-0836.

[7] E. J. Doser, «A Simple Method of Producing Extremely Pure Crystals of alpha Silicon Carbide», en, Nature, t. 211, no 5050, p. 731-732, août 1966, ISSN : 0028-0836.

[8] R. Madar, «Materials science: Silicon carbide in contention», en, Nature, t. 430, no 7003, p. 974-975, août 2004, ISSN : 0028-0836.

[9] D. Nakamura, I. Gunjishima, S. Yamaguchi, T. Ito, A. Okamoto, H. Kondo, S. Onda et K. Takatori, «Ultrahigh-quality silicon carbide single crystals», en, Nature, t. 430, no 7003, p. 1009-1012, août 2004, ISSN: 0028-0836.

[10] R. Yapa, A. J. Forsyth, and R. Todd, 'Analysis of SiC technology in two-level and three-level converters for aerospace applications,' in *Power Electronics, Machines and Drives (PEMD 2014), 7th IET International Conference on*, 2014, pp. 1–6.

[11] Z. Chen, D. Boroyevich, R. Burgos, and F. Wang, 'Characterization and modeling of 1.2 kv, 20 A SiC MOSFETs,' in *Energy Conversion Congress and Exposition, 2009. ECCE 2009. IEEE*, 2009, pp. 1480–1487.

[12] J. Fabre, P. Ladoux, and M. Piton, 'Characterization and Implementation of Dual-SiC MOSFET Modules for Future Use in Traction Converters,' *IEEE Trans. Power Electron.*, vol. 30, no. 8, pp. 4079–4090, Aug. 2015.

[13] J. Biela, M. Schweizer, S. Waffler, and J. W. Kolar, 'SiC versus Si— Evaluation of Potentials for Performance Improvement of Inverter and DC–DC Converter Systems by SiC Power Semiconductors,' *IEEE Trans. Ind. Electron.*, vol. 58, no. 7, pp. 2872–2882, Jul. 2011.

[14] F. Kato, R. Simanjorang, F. Lang, H. Nakagawa, H. Yamaguchi, and H. Sato, '250 °C-Operated sandwich-structured all-SiC power module,' *Jpn. J. Appl. Phys.*, vol. 54, no. 4S, p. 04DP06, Apr. 2015.

[15] G. Wang *et al.*, 'Static and dynamic performance characterization and comparison of 15 kV SiC MOSFET and 15 kV SiC n-IGBTs,' in *2015 IEEE 27th International Symposium on Power Semiconductor Devices IC's (ISPSD)*, 2015, pp. 229–232.

[16] [Online]. Available: http://www.apei.net/products/ht-3000.aspx

[17] X. Xinjian and Dingfei-Ge, 'Research on reliability evaluation of electronic products under environmental conditions,' in *Fifth World Congress on*

EBSCOhost - printed on 2/14/2023 2:46 PM via . All use subject to https://www.ebsco.com/terms-of-use

*Intelligent Control and Automation, 2004. WCICA 2004*, 2004, vol. 4, p. 3146–3149 Vol.4.

[17] R. L. Ozenbaugh et T. M. Pullen, EMI Filter Design, Third Edition, CRC Press. mar. 2017, ISBN : 978-1-138-07407-1.

[18] R. Ciprian and B. Lehman, 'Modeling effects of relative humidity, moisture, and extreme environmental conditions on power electronic performance,' in *IEEE Energy Conversion Congress and Exposition, 2009. ECCE 2009*, 2009, pp. 1052–1059.

[19] C. Onambele, M. Elsied, A. Mpanda Mabwe et A. El Hajjaji, 'Multi-Phase Modular Drive System: A Case Study in Electrical Aircraft Applications', en, Energies, t. 11, no 1, p. 5, Dec. 2017.

[21] V. Crisafulli, 'A new package with kelvin source connection for increasing power density in power electronics design,' in *2015 17th European Conference on Power Electronics and Applications (EPE'15 ECCE-Europe)*, 2015, pp. 1–8.

[22] C. Onambele, A. Mpanda, M. Elsied et F. Giacchetti, 'Co-simulation modeling of high performance motor-drive systems for aerospace applications,' in *2017 IEEE International Electric Machines and Drives Conference (IEMDC)*, 2017, p. 1-6.

EBSCOhost - printed on 2/14/2023 2:46 PM via . All use subject to https://www.ebsco.com/terms-of-use

# CHAPTER TWENTY-SIX

# DYNAMIC BEHAVIOUR OF MULTI-TERMINAL VSC-BASED HVDC DC CONTROL STRATEGY

FRANCISCO GONZALEZ-LONGATT[1]
JUAN M. ROLDAN-FERNANDEZ
SANTIAGO ARNALTES
J.L. RODRÍGUEZ-AMENEDO

## Abstract

The massive integration of renewable (especially deep-water offshore wind power), and the need to increase cross-border bulk power transmission are making the use of a DC transmission system an critical reality. Voltage Source Converter (VSC) High Voltage DC (HVDC) transmission systems allow the usage of more flexible and efficient configurations such as the Multi-terminal VSC-HVDC (MVSCDC) networks. This chapter aims to evaluate the effect of DC-voltage control strategy on the dynamic behaviour of multi-terminal VSC-based HVDC after a converter outage. In this paper, two dc voltage control strategies are considered: (i) standard voltage margin method (SVMM) and (ii) standard voltage-droop method (SVDM). The impact is evaluated in this paper using time-domain simulations on a simple test system using DIgSILENT® PowerFactory™ considering a sudden disconnection of a converter-station. Simulation results demonstrate how important is the DC-voltage control strategy and the location/number of DC-buses involved in the DC-voltage on the dynamic response of the MVSCDC systems. The voltage margin control is capable of surviving a converter outage just if this converter is operating in constant power mode.

[1] Wolfson School of Mechanical, Electrical and Manufacturing Engineering. Centre for Renewable Energy Systems Technology – CREST.
Loughborough University. United Kingdom. Fglongatt@fglongatt.org

EBSCOhost - printed on 2/14/2023 2:46 PM via . All use subject to https://www.ebsco.com/terms-of-use

**Keywords**: DC transmission systems, dynamic response, multi-terminal DC, voltage source converters.

## Introduction

The Paris Agreement builds upon the Convention and for the first time brings all nations into a common cause to undertake ambitious efforts to combat climate change and adapt to its effects, with enhanced support to assist developing countries to do so. The Paris Agreement central aim is to strengthen the global response to the threat of climate change by keeping a global temperature rise this century well below 2°C above pre-industrial levels and to pursue efforts to limit the temperature increase even further to 1.5 degrees Celsius[1].

Preventing dangerous climate change is an urgent priority for the European Union (EU). Europe is working hard to cut its greenhouse gas emissions substantially while encouraging other nations and regions to do likewise [2]. EU 2020 climate and energy package is pursuing three primary targets [3]: (i) 20% cut in greenhouse gas emissions (from 1990 levels), (ii) 20% of EU energy from renewables and (iii) 20% improvement in energy efficiency. To fulfil the Energy Roadmap 2050, a dramatic reduction in electricity generation sector is required, it can be done maximising the power contribution coming from the massive integration of renewable energy generation and low carbon technologies play a significant role. The integration of a significant amount of offshore wind power plants distant from the shore, especially deep-water wind farms, requires the use of long DC undersea power cables [4]. DC networks are quite attractive for the integration of this clean energy [5], [6].

*Voltage Source Converter* (VSC) *High Voltage DC* (HVDC) transmission systems allow the usage of more elaborate configurations such as the *Multi-terminal VSC-HVDC* (MVSCDC) networks [7]. It offers higher reliability, redundant and flexible technology to enable the massive integration of offshore wind power in future power systems [8]. Also, MVSCDCs are required in order to balancing and transportation of electricity in order to reach the objective of the one single European market.

Remarkable efforts on the research on MVSCDC have been developed in several areas in recent times. Quite many publications are devoted to several subjects of MVSCDC involving since the classical steady-state performance [9], [10], [11], [12], [13], classical and security-constrained optimal power flow [12] and [14], [15], [16], modelling [17], [18], [19], control and protection [20], [21], [22], [23], [24], [25], and simulation of dynamic behaviour [9], [26], [27], [28], [29]. The traditional reliability and

EBSCOhost - printed on 2/14/2023 2:46 PM via . All use subject to https://www.ebsco.com/terms-of-use

availability of the MVSCDC after contingencies like VSC outages or faults and their capacity for recovering after faults and disturbances. Cable and converter station outages create a severe risk of instability in hybrid ac/dc network because of a massive amount of power transmitted by MTDC system. DC voltage control is a vital aspect that indicates the power balance and the stability of an MVSCDC system.

This chapter aims to evaluate the impact of the DC voltage control strategies on the dynamic behaviour of multi-terminal VSC-based HVDC following a converter outage. The existing research considers two different approaches: *Standard Voltage Margin Method* (SVMM) and *Standard Voltage Droop Method* (SVDM). Section 2 presents a general introduction to the fundamentals of control systems in MVSCDC systems and gives the theoretical background of dc voltage strategies. Section 3 shows the simulations results and discussion about the behaviour of multi-terminal VSC-based HVDC following a converter outage under different control strategies. Finally, Section 4 concludes. The analysis of faults o outage events permits to predict and evaluate the performance of the control strategies and: (i) demonstrates bipolar configuration can provide minimal voltage deviation from the initial nominal voltage than monopolar network (ii) bipolar configuration (small dc voltage drops) allow the operation within the rated voltage limits.

This chapter is based on the revised version of the paper presented at the International Conference on Renewable Energies and Power Quality (ICREPQ'16) [30].

## Control Strategies for MVSCDC Network Operation

Inside an MVSCDC network, the controllers are one of the most critical components because they define the performance of the whole system and try to minimise any deviation from the desired performance. This section is dedicated to presenting a detailed explanation of the main control strategies required for the operation of MVSCDC and the modelling requirements of the control schemes.

In a general sense, the control system for an MVSCDC is composed of two different layers of controllers [31], [32], [33], [34]:

(i) *Terminal controllers* and
(ii) *Master controller*

The left-hand side of Fig. 1, shows the two main layers of control dedicated to MVSCDC: Layer 1: Master control, and Layer 2: Terminal

EBSCOhost - printed on 2/14/2023 2:46 PM via . All use subject to https://www.ebsco.com/terms-of-use

controller; details of the signal flow and intra-classification of the controllers are depicted in the right-hand side: Layer 2: Outer controller, Inner controller and Firing controller.

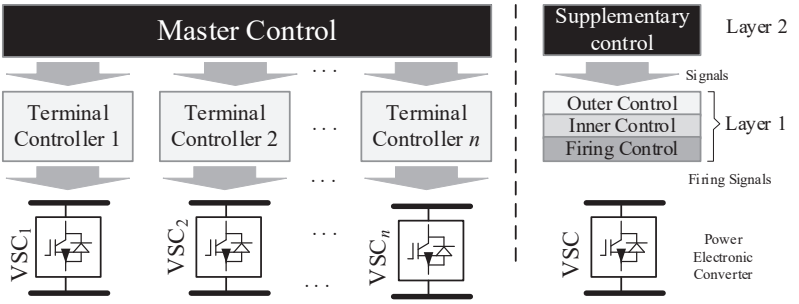



Fig. 1. Schematic representation of typical structure the MVSCDC control system hierarchy.

## Master Controller

The *master controller* is provided with the minimum set of functions necessary for the coordinated operation of the terminals in the DC circuits [32], i.e. start and stop, minimisation of losses, oscillation damping and power flow reversal, black start, ac frequency and AC voltage support.

The master controller can be used to perform a very specialised function such as optimising the overall performance of the MVSCDC by regulating the DC side voltage.

The master controllers are not necessary for the operation of the MVSCDC system but greatly enhance their functionality. Some of the functionalities that can be included in the master controller include:

- **Frequency control**: Frequency control is indispensable when a converter is located in a passive system, but it can also be used in an active power system. Frequency is regulated by modulating active power.
- **Damping control**: A converter can damp oscillations occurring in the AC power system by an additional controller. Input signals can be local, or not local, such as generator speeds, which may require communication. The output signal modulates active power so that the active power swing is counteracted.

EBSCOhost - printed on 2/14/2023 2:46 PM via . All use subject to https://www.ebsco.com/terms-of-use

– **Wide area AC voltage control**: Instead of directly controlling AC voltage in the outer controller, an additional loop can be created around the reactive power control. The reactive power setpoint is determined from the desired AC voltage.

In this chapter, no models for supplementary controllers are discussed as they are not included in this chapter. Apart from the fact that MVSCDC systems can operate normally (not necessarily optimise!) without supplementary controllers, the reason is that it is not desirable to come up with generic models of master controllers.

## Terminal Controllers

The *terminal controller* controls the specific converter by calculating the PWM (*Pulse Width Modulation*) pulses for the converter bridges. The firing controller is the fastest controller and inner control, outer control and supplementary control are used for increasingly higher-level functions and have increasingly higher cycle times.

This MVSCDC control system is implemented in a hierarchical way. It is a cascaded system, where every level accepts the input of the previous one and feeds its output signal to the next level. This is schematically represented in Fig. 1.

As aforementioned before, firing control is the lowest control level inside the terminal control system, and it acts very fast. Firing control, as known as valve control, takes the desired converter waveform as an input and determines using the valve firing logic the pulses that need to be generated [35]. The firing logic is communicated to the controllable switches (e.g. IGBTs GTO's), and pulses are generated that switch on/off the switched at the appropriate instants. The firing instances are synchronised using a *Phase-Locked Loop* (PLL).

The pattern of the pulses depends on the topology of the bridge and the switching method. As converters are considered to be a black box, the details of the converter topology are not known and modelling the firing control is impossible. However, firing control has cycle times in the few microseconds range.

The use of the *space vector* in the control design and implementation enables to make a fully decoupled linear control of active and reactive currents.

The *d*-*q* reference frame is selected in such a way that the *d*-axis is aligned to the voltage phasor of phase-*a* of point *X*. This means that the PLL should be phase-locked to phase-*a* voltage phasor of the reference point, *X*.

EBSCOhost - printed on 2/14/2023 2:46 PM via . All use subject to https://www.ebsco.com/terms-of-use

Considering the previous assumptions, the *dq*-components of the phase-*a* of point *X* results:

$$\begin{aligned} V_{q,X} &= 0 \\ V_{d,X} &= V_X \end{aligned} \tag{0.1}$$

The simplified equivalent model of VSC-HVDC in *d-q* reference is shown in Fig. 2.

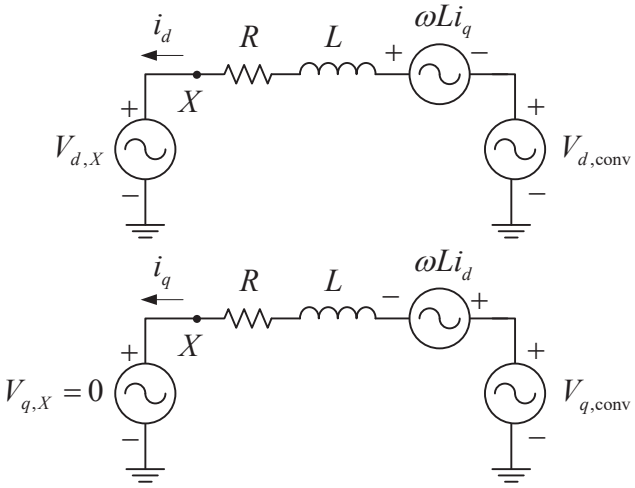



Fig. 2. Equivalent circuits in *d* and *q* axes of the VSC-HVDC, circuits are referred to *d*-axis aligned with voltage phasor of phase-*a*.

From the *d-q* equivalent circuit and observing from reference point *X*, the apparent power ($S_{conv}$) injected by the VSC converter into the AC network is given by:

$$S_{conv} = \frac{1}{2}\left(V_{d,X} + j0\right)\left(i_d - ji_q\right) = P + jQ \tag{0.2}$$

The active and reactive powers (*P, Q*) provided by the VSC-HVDC converter to the AC become:

$$P = \frac{3}{2} V_{d,X} i_d \tag{0.3}$$

$$Q = -\frac{3}{2} V_{d,X} i_q \tag{0.4}$$

The *inner control or current control loop* is designed to be much faster than the outer controllers. It is not fast enough, however, to warrant

EBSCOhost - printed on 2/14/2023 2:46 PM via . All use subject to https://www.ebsco.com/terms-of-use

neglecting its dynamics. This means current controllers and all relevant controllers higher in the hierarchy must be modelled. This control system controls the current through the phase reactor. Decoupled control is used, which means that voltages and currents are decomposed into *dq*-components, controlled independently [35]. The output of the current control is the desired converter voltage.

The inner current controller is developed based on the following equation.

$$L\frac{d}{dt}\begin{bmatrix} i_d \\ i_q \end{bmatrix} = \begin{bmatrix} V_{d,X} \\ V_{q,\mathrm{X}} \end{bmatrix} - \begin{bmatrix} V_{d,\mathrm{conv}} \\ V_{q,\mathrm{conv}} \end{bmatrix} - r\begin{bmatrix} i_d \\ i_q \end{bmatrix} - \omega L\begin{bmatrix} 0 & 1 \\ -1 & 0 \end{bmatrix}\begin{bmatrix} i_d \\ i_q \end{bmatrix} \tag{0.5}$$

An implementation of equation (16.5) is presented in Fig. 3, it shows the *d*- and *q*-components current controllers of the inner current loop.

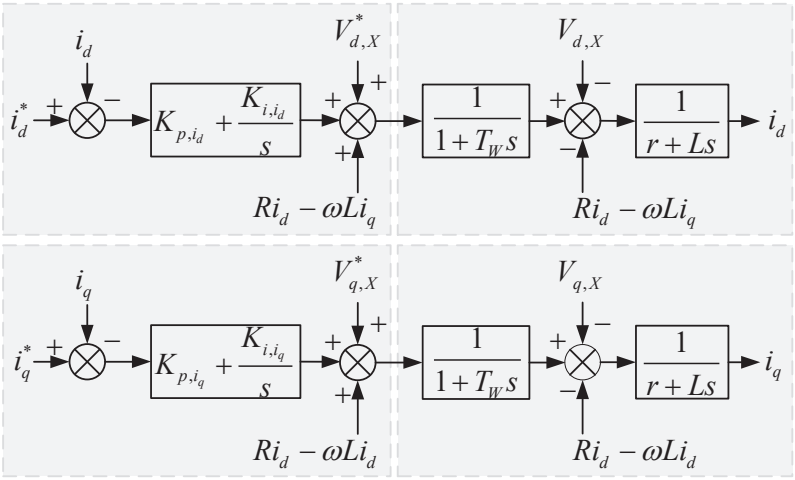



Fig. 3. Block diagram depicting the inner current controllers. Models are represented in *dq*-axis.

The power electronic converter is assumed to be real (average-phasor model) as a consequence, it has a time delay caused by the sinusoidal pulse width modulator, and it can be approximated as:

$$e^{-T_w s} \approx \frac{1}{(1+T_w s)} \tag{0.6}$$

where the time delay ($T_W$) is defined by:

EBSCOhost - printed on 2/14/2023 2:46 PM via . All use subject to https://www.ebsco.com/terms-of-use

$$T_w = \frac{1}{2f_s} \tag{0.7}$$

where $f_s$ is the switching frequency of the converter. *Proportional-integral* (PI) controllers are used for closed-loop control, and the zeroes of the PI controllers are selected to cancel the dominant pole in the external circuit [18].

The time constant $\tau = L/r$, provided by the AC reactor (series contactor to the power electronic converter), is much higher than $T_w$ for a typical VSC-HVDC, and hence will be the dominant pole to be cancelled. The cross-coupling currents in the equation (16.5) are compensated by feedforward terms in the controllers, as shown in Fig. 3.

The *outer controllers* are the ones responsible for providing the current references signals for the inner current controller. The terminal controller determines the behaviour of the converter at the system bus. Several targets can be set [36]:

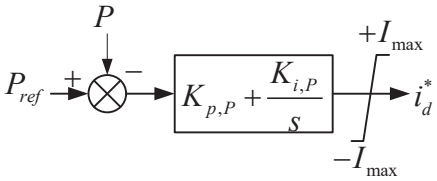
- **Active power control (*P*)**: determines the active power exchanged with the AC grid.
- **Reactive power control (*Q*)**: determines the reactive power exchanged with the AC grid.
- **AC voltage control ($V_{ac}$)** instead of controlling reactive power, AC voltage can be directly controlled, determining the voltage of the system bus.
- **DC voltage control ($U_{dc}$)**: used to keep the DC voltage control constant.

The outer controllers have in common that they provide a current set point in the *dq*-frame for the inner current controller. Their behaviour directly influences the dynamics of the AC system and are therefore of paramount importance in modelling MVSCDC systems.

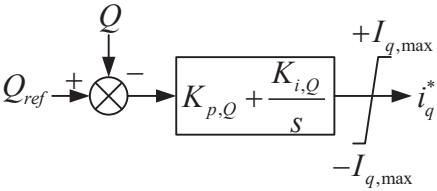
### *Active power control*

Active current ($i_d$) is used to control either of active power flow or DC voltage level. Similarly, the reactive current ($i_q$) is used to control either of reactive power flow into a stiff grid connection or AC voltage support in weak grid connection.

EBSCOhost - printed on 2/14/2023 2:46 PM via . All use subject to https://www.ebsco.com/terms-of-use




(a) Bloch diagram of PI controller for active power control.




(b) Bloch diagram of PI controller for reactive power control.

Fig. 4. General representation of Active and reactive power controllers.

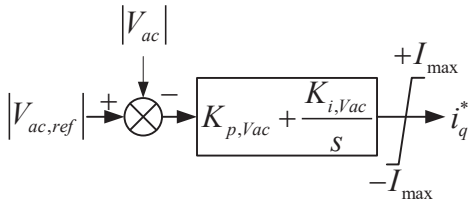



Fig. 5. General representation of AC voltage controller.

The active power flow ($P$) of the VSC-HVDC terminal is given by the following equation:

$$P_{dq} = \frac{3}{2} V_{d,X} i_d \tag{0.8}$$

where $V_x$ is the resultant voltage in $dq$-reference frame and is desired to have a constant value. Hence active power flow can be controlled by active current ($i_d$).

This controller allows excellent control of the active power exchanged with the AC grid. An implementation of the active power controller is presented in Fig. 4.a.

The output of the active power controller ($i_d^*$) provides the reference input to the $d$-axis current controller of the inner current loop in Fig. 4 a). The maximum current through the VSC-HVDC converter must be controlled in order to avoid potentially dangerous overcurrents on the commutation devices. In order to limit the magnitude of current in the VSC-

EBSCOhost - printed on 2/14/2023 2:46 PM via . All use subject to https://www.ebsco.com/terms-of-use

HVDC to a maximum limit, the output of the active power controller is followed by a limiter function of $\pm I_{\max}$ limits, where:

$$-I_{\max} \le i_d^* \le +I_{\max} \tag{0.9}$$

where the current limit is assumed to be equal to the rated current ($I_{max} = I_{rated}$)

The reactive power ($Q$) exchanged by the VSC-HVDC converter and the AC grid is given by equation (4):

$$Q = -\frac{3}{2} V_{d,X} i_q \tag{0.10}$$

The reference of reactive current ($i_q^*$) is used to control the reactive power flow provided by the VSC-HVDC converter and implementation of this controller is presented in Fig. 4.b. As in the case of active power control, $i_q$* will be the reference input for the reactive current controller of the inner current loop in Fig. 4.b.

The reference of reactive current ($i_q^*$) must be limited in order to avoid any damage on the commutation devices, as a consequence, $i_q^*$ is limited to $\pm I_{q,\max}$ in such a way that the total converter current should not exceed the rated current ($I_{max} = I_{rated}$). This takes the assumption that that priority is given to transfer of active power. Hence:

$$I_{q,\max} = \sqrt{I_{\max}^2 - \left(i_d^*\right)^2} \tag{0.11}$$

## *AC Voltage Controller*

A VSC-HVDC converter connected to a power system has the capability to control the AC voltage at the connection point; this feature is especially important or weak grid, where there are significant line resistance and inductance creating a considerable amount of voltage fluctuations with changing active power flow.

This controller is designed to regulate the amplitude of the ac voltage ($V_{ac}$) at the common bus to be equal to the given reference value by modifying $i_q$*. This implies that the controller governs the converter to generate an amount of reactive power so that the voltage at the common bus matches the given reference value ($V_{ac,ref}$). An implementation of this controller is presented in Fig. 5.

## *DC Voltage Controller*

Inside a MVSCDC network, DC control is undoubtedly one of the most important tasks given to converter stations. A well-controlled DC on a

EBSCOhost - printed on 2/14/2023 2:46 PM via . All use subject to https://www.ebsco.com/terms-of-use

MVSCDC grid requires a balanced power flow between all the interconnected nodes.

DC voltage control is undoubtedly one of the most important tasks given to the VSC-HVDC stations inside a MVSCDC network. A well-controlled DC voltage on a MVSCDC system is a guarantee of the power balance between all the interconnected nodes. Considering the operational requirements for dc voltage on MVSCDC, the literature provides two main control strategies which possibly can be applied in future transnational networks [37]: (i) Standard *Voltage Margin Method* (SVMM) and (ii) *Standard Voltage Droop Method* (SVDM). These methods enable sharing of load among two or more dc voltage regulating terminals operating in parallel and provide controls in MVSCDC. Fig. 6 shows a general scheme for VSC-HVDC system considering only two converter substations.

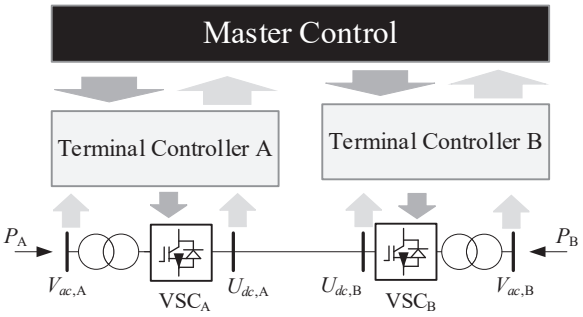



Fig. 6. General scheme for two converter stations VSC-HVDC system. VSCi operates as an inverter ($P_i$<0) or rectifier ($P_i$>0) depending on power flow direction.

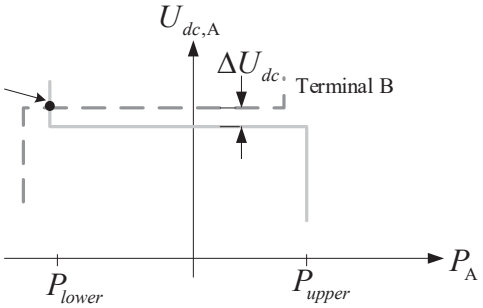



Fig. 7. $U_{dc}$-$P$ characteristic showing the operating point "a" in VMM for one terminal.

EBSCOhost - printed on 2/14/2023 2:46 PM via . All use subject to https://www.ebsco.com/terms-of-use

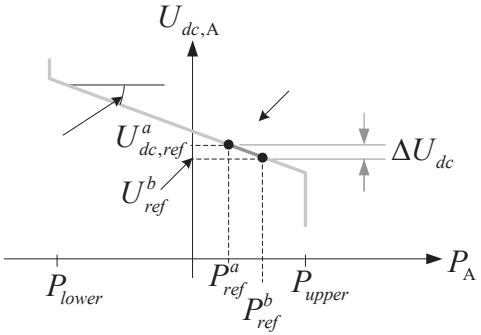



Fig. 8. $U_{dc}$-$P$ characteristic showing the operating point "a" in SVDM for one terminal.

The SVMM is defined as the difference between the dc reference voltages of the two-terminal, [38], [39], [40]. Fig. 7 shows the $U_{dc}$-$P$ characteristics of both terminals at Terminal A, the intersection $U_{dc}$-$P$ of the characteristics of each terminal is the operating point "a". The dc voltage-droop, K, indicates the degree of compensation of power unbalances in the dc network at the cost of a reduction in the dc bus voltage. This principle of SVDM control is shown in Fig. 8. When the active power is to be transmitted from Terminal B to Terminal A ($P_A<0$, $P_B>0$), the voltage margin ($\Delta U_{dc}$) is subtracted from the dc reference voltage for Terminal A. Terminal B (rectifier) determines the dc system voltage and Terminal A (inverter) controls the active power ($P_A$) determined by the lower limit of the dc voltage regulator. The dc voltage controller tries to keep the dc voltage to the reference value $U_{dc,ref}$ by adjusting $P_A$, until $P_A$ reaches the upper limit or the lower limit.

The voltage margin method gives a reliable way of controlling MVSCDC without the need for communication between terminals and is capable of keeping the steady-state voltage within pre-set limits even after load switching and disconnection of some converter terminals. However, on the other hand, this method implies allocation of only one terminal at a time for the regulation of DC voltage and the other terminals do not experience significant change during changes in the power flow of the DC network.

EBSCOhost - printed on 2/14/2023 2:46 PM via . All use subject to https://www.ebsco.com/terms-of-use

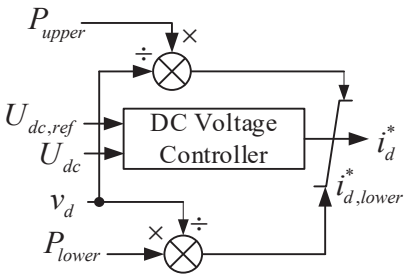



Fig. 9. Block diagram of the scheme for VMM controller with adjustable limits.

Frequency droop control is a well-established method and the basis for stable operation in all AC grids. The system's frequency is used as a global measure of the instantaneous balance between power generation and demand [40]. The DC voltage-droop method is a coordinated control to maintain a power balance and a desired power exchange in the MVSCDC. This control is a modification of the SVMM control where the horizontal line sections ($P_{lowe}r<P_A<P_{upper}$) of the $U_{dc}$-$P$ characteristic curves are replaced by a line with a small slope ($m_c$) [41]. The dc voltage-droop, $m_c$, indicates the degree of compensation of power unbalances in the DC grid at the cost of a reduction in the DC bus voltage. This principle of SVMM control is shown in Fig. 8. When $U_{dc,A}$ drops (e.g. due to significant withdrawal of power someplace else in the dc network, operation point moves from "a" to "b") the slack converter station ($VSC_A$) will increase the active power injection in the DC grid $P_A$ until a new equilibrium point ( $U^b_{dc,ref}$ , $P^b_{A,ref}$ ), at a lower DC voltage, is reached ( $U^b_{dc,ref} = U^a_{dc,ref} - \Delta U_{dc}$ ). The use of a proportional DC voltage-controller allows multiple converters to regulate the voltage at the same time and the concept of the distributed slack bus is possible.

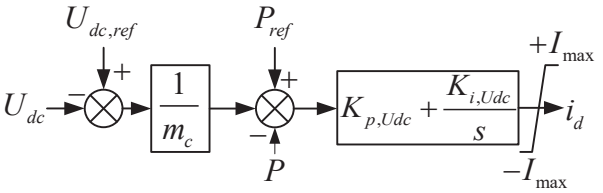


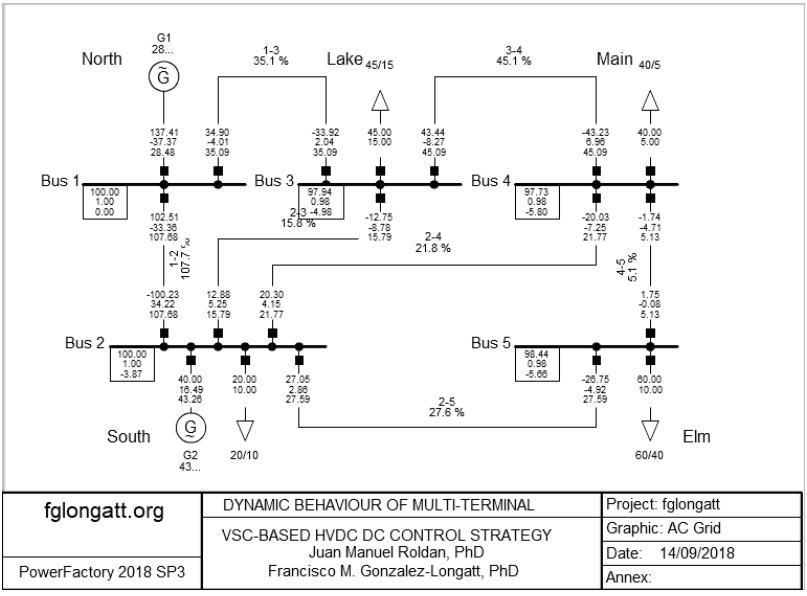

Fig. 10. Block diagram of the voltage droop controller.

EBSCOhost - printed on 2/14/2023 2:46 PM via . All use subject to https://www.ebsco.com/terms-of-use

Figure 8 shows how is implemented the droop characteristic based on the power active controller. When voltage droop control is used in the absence of a PI controller, the voltage controller's active power P will change when the value of the dc bus voltage changes.

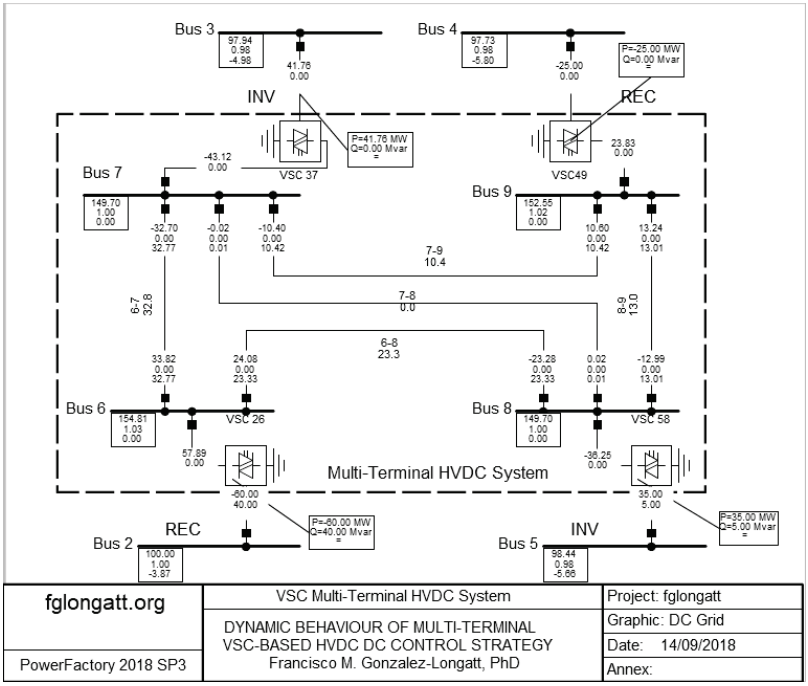
## Simulation and Results

In this paper, the dynamic behaviour of an MVSCDC system after the loss of a converter station is analysed. Time-domain simulations are based on a hybrid ac/dc system. The ac networks are based on the traditional 5-node test network taken from the book of Stagg and El-Abiad [42], for illustrative purposes the dc network is a 4-node VSC multi-terminal HVDC network. It consists of 4 VSC stations tied together by five DC submarine transmission cables rated at 150 kV describing a parallel multi-terminal HVDC. DIgSILENT PowerFactory™ [43] is used to perform the time-domain simulations; the model of all controllers are developed using *DIgSILENT Simulation Language* (DSL).




(a) 5-node AC network.

EBSCOhost - printed on 2/14/2023 2:46 PM via . All use subject to https://www.ebsco.com/terms-of-use




(a) 4-node MVSCDC network.

Fig. 11. Steady-state condition for the hybrid AC/DC test network.

Two dc network configurations are studied in this section: (i) *mono-polar network configuration* and (ii) *bipolar network configuration.* Two dc voltage control strategies are considered in this paper: (i) *Standard Voltage Margin Method* (SVMM) and (ii) *Standard Voltage Droop Method* (SVDM). Seven cases are evaluated: *Case I*: The converter station VSC37 is chosen as dc slack-bus when the VMM is used, thereby controlling the voltage on the dc network. Converter stations VSC26, VSC58, VSC49 converter stations are directly controlling their reactive power injections (constant *P*-mode). The converter station VSC37 is also used to control the voltage at bus 3 ($U_3$ = 0.98 pu). *Case II:* This case considers the use of multiple dc slack buses, in this case, all converter stations are using controller based on SDVDM considering $K$ = -1.00. *Case III:* It is similar to Case II but it considers $K$ = -3.00, *Case IV:* $K$ = -4.00, *Case V:* $K$ = -6.00, *Case VI:* $K$ = -0.50 and *Case VII:* $K$ = -0.20. A single contingency is considered where outage converter station is VSC37.

EBSCOhost - printed on 2/14/2023 2:46 PM via . All use subject to https://www.ebsco.com/terms-of-use

*A. Monopolar Network Configuration*

The plots of $U_{dc}$ versus $P_{dc}$ of the *Cases I-VII* following a sudden disconnection of VSC37 are shown in Fig. 11-Fig. 14. Results show that there is some level of control coupling between the converter terminals using SVMM and SDVDM.

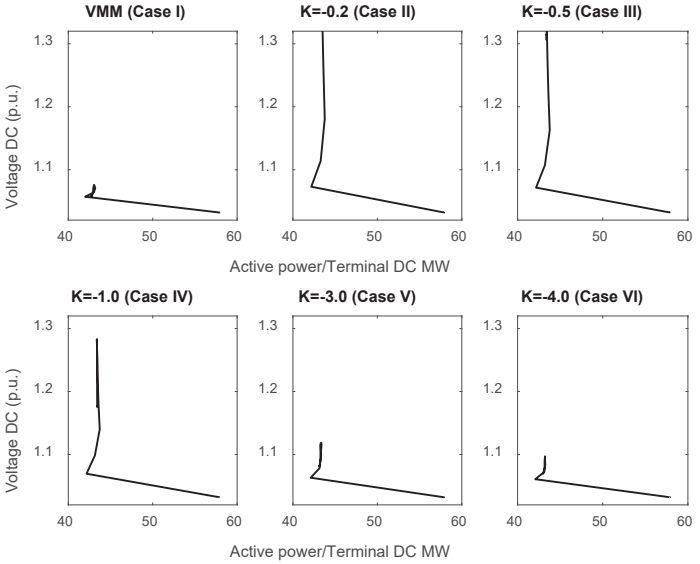



Fig. 11. Simulation results: $U_{dc}$-$P_{dc}$ VSC26. Monopolar Network.

EBSCOhost - printed on 2/14/2023 2:46 PM via . All use subject to https://www.ebsco.com/terms-of-use

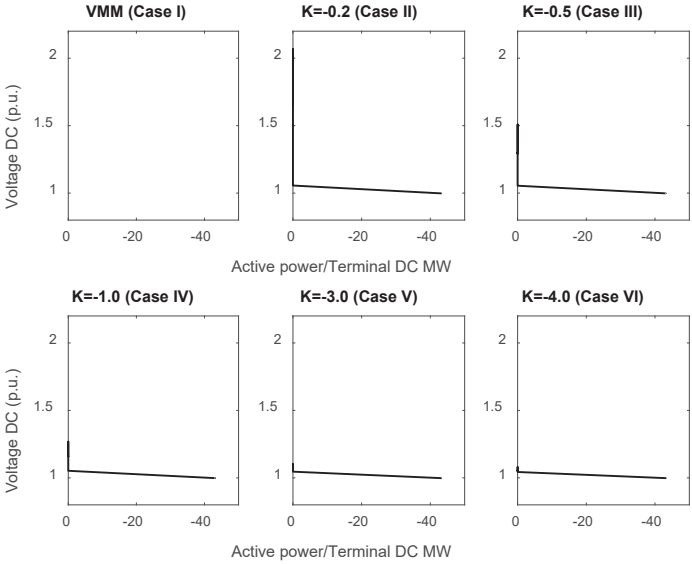



Fig. 12. Simulation results: $U_{dc}$-$P_{dc}$ VSC37. Monopolar Network.

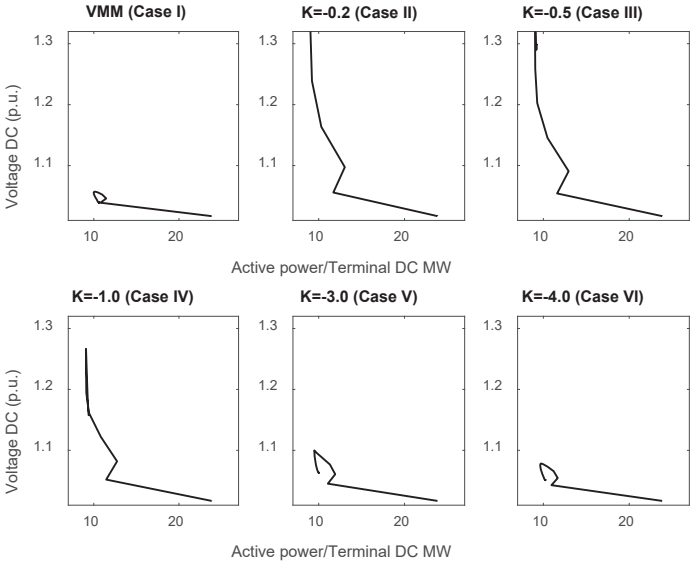



Fig. 13. Simulation results: $U_{dc}$-$P_{dc}$ VSC58. Monopolar Network.

EBSCOhost - printed on 2/14/2023 2:46 PM via . All use subject to https://www.ebsco.com/terms-of-use

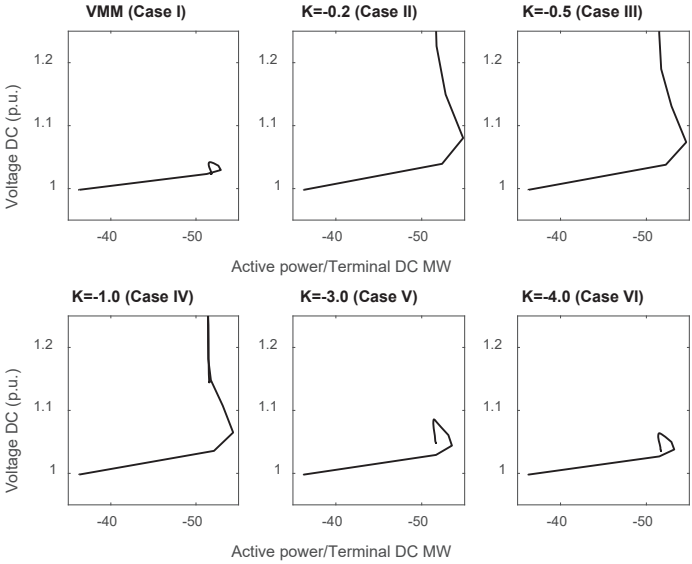



Fig. 14. Simulation results: $U_{dc}$-$P_{dc}$ VSC49. Monopolar Network.

On dc bus 6, *Case II* ($K$ = -0.2) attains the highest maximum instantaneous voltage value of 2.0761 pu at 0.30 sec taking a more extended period of time to peak. *Case VII* where $K$ = -6.00 takes the shorter time of 0.15 sec to reach the maximum instantaneous voltage on the dc buses having its lowest values 1.0759 pu on bus 6. The *Case I* shows the lowest variation of steady-state voltage at 1.0376 pu and *Case II* has the highest variation of 1.6885 pu.

It can be concluded that the slope $K$ in droop control influences the voltage response in the system such that, the smaller the slope value, the lower the peak value attained and the faster time it takes to a peak having low variation from steady-state voltage. There is a power imbalance resulting from the converter outage. However, the power produced is shared between the terminals having the same droop characteristics provided the terminals have enough capacity to compensate the power unbalance. The *Case I* using VMM shows the highest variation of steady-state power flow because only one converter is capable of controlling the dc voltage in the system at a time ($U_{dc}$-$Q$ mode) with the other converters controlling active power ($P$-$Q$).

EBSCOhost - printed on 2/14/2023 2:46 PM via . All use subject to https://www.ebsco.com/terms-of-use

Table I shows the percentage of change resulting from the converter outage on other buses. The lowest voltage change is in *Case I* and for droop controller, as the *K* values get smaller, the voltage change decreases (where *K* = -0.40 and -0.60 showed profound changes in value).

**Table I. Percentage of dc voltage change (%) after a sudden disconnection of VSC37 for Monopolar Network**

| *Bus* | *Case* | | | | | | |
|---|---|---|---|---|---|---|---|
| | *I* | *II* | *III* | *IV* | *V* | *VI* | *VII* |
| 6 | 3.21 | 6 | 3.21 | 6 | 3.21 | 6 | 3.21 |
| 7 | 0.21 | 7 | 0.21 | 7 | 0.21 | 7 | 0.21 |
| 8 | 0.21 | 8 | 0.21 | 8 | 0.21 | 8 | 0.21 |
| 9 | 1.68 | 9 | 1.68 | 9 | 1.68 | 9 | 1.68 |

From Table I, *Case II* (K = -0.2) has a very high percentage change in dc voltage, and as the slope value decreases, the percentage change also decreases. It can be deduced that a system is prone to imbalance when operating large slope constants in droop control implying that a small slope *K* value results in higher sensitivity to dc bus voltage at the expense of more significant deviations of power flow from the nominal power, however, this will allow for a stronger dc network. *Case I* maintained the lowest voltage change, voltages on buses 7 and 8 decreased to 149.6 kV, 0.21% less than controlled nominal voltage. The dc cable power flows response of the *Cases I-VII* following a sudden disconnection of VSC37 are shown in Fig. 15-Fig. 19.

**Table II. Maximum instantaneous dc power flow transfer ($P_{ij}$) in dc power cables in MW**

| *Cable* | *Case* | | | | | | |
|---|---|---|---|---|---|---|---|
| | *I* | *II* | *III* | *IV* | *V* | *VI* | *VII* |
| 6 - 7 | 21.33 | 18.32 | 18.21 | 18.13 | 18.01 | 18.35 | 18.36 |
| 6 - 8 | 31.52 | 25.49 | 25.31 | 25.27 | 25.22 | 25.48 | 25.49 |
| 7 - 8 | 22.52 | 17.59 | 17.37 | 17.30 | 17.21 | 17.66 | 17.72 |
| 7- 9 | -1.64 | 1.28 | 1.10 | 1.03 | 0.88 | 1.36 | 1.93 |
| 8 - 9 | 18.13 | 10.35 | 10.60 | 10.67 | 10.87 | 10.24 | 9.65 |

*B. Bipolar Network Configuration*

Six instances, Case II-VII, are evaluated for the bipolar network in this paper. This considers the use of multiple dc slack buses, where all converter stations are using controller based on SVDM. The following slope coefficient K for the droop control is considered *Case II-VII*: *K* = -0.20, -

EBSCOhost - printed on 2/14/2023 2:46 PM via . All use subject to https://www.ebsco.com/terms-of-use

0.50, -1.00, -3.00, -4.00, and -6.00.

**Table II. Percentage of dc voltage change after sudden disconnection of VSC37: Bi-polar Network Configuration**

| *Bus* | *Case* | | | | | |
|---|---|---|---|---|---|---|
| | *II* | *III* | *IV* | *V* | *VI* | *VIII* |
| 6 | 3.30 | 15.82 | 23.73 | 29.46 | 30.20 | 30.94 |
| 7 | 2.67 | 16.23 | 24.19 | 29.95 | 30.69 | 31.44 |
| 8 | 2.67 | 16.59 | 24.59 | 30.38 | 31.13 | 31.88 |
| 9 | 2.91 | 16.29 | 24.26 | 30.03 | 30.77 | 31.51 |

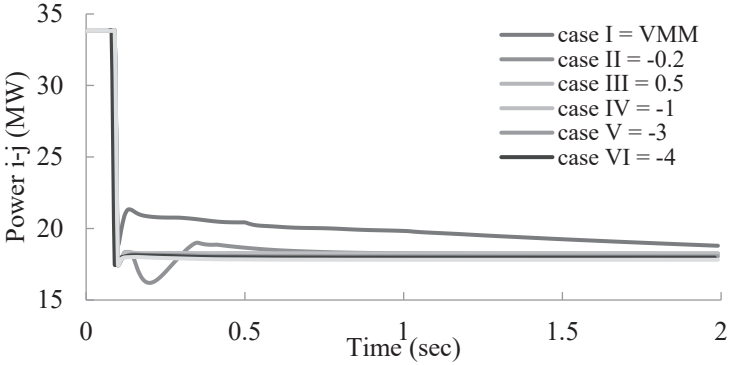



Fig. 15. Simulation results: power flows on DC submarine transmission cables for cable 6-7. Monopolar Network Configuration

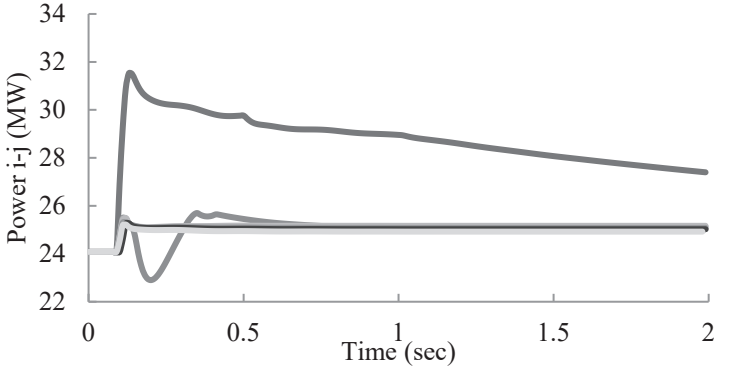



Fig. 16. Simulation results: power flows on DC submarine transmission for cable 6-8. Monopolar Network Configuration.

EBSCOhost - printed on 2/14/2023 2:46 PM via . All use subject to https://www.ebsco.com/terms-of-use

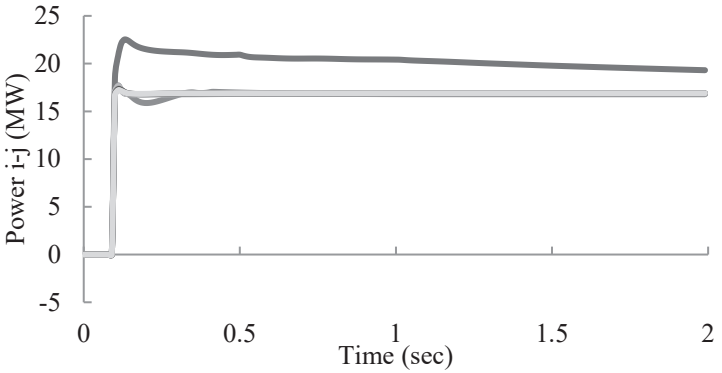



Fig. 17. Simulation results: power flows on DC submarine transmission for cable 7-8. Monopolar Network Configuration.

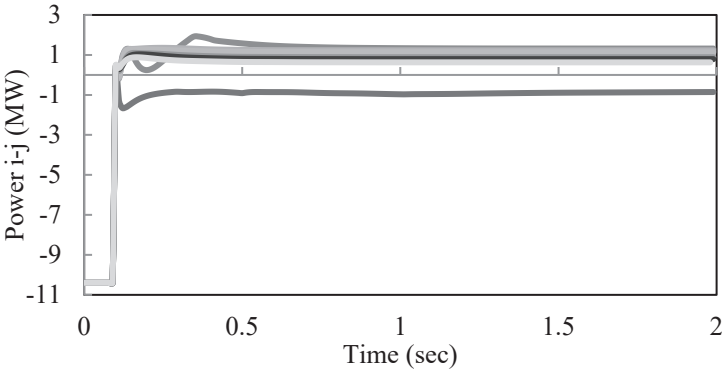



Fig. 18. Simulation results: power flows on DC submarine transmission cable 7-9. Monopolar Network Configuration.

EBSCOhost - printed on 2/14/2023 2:46 PM via . All use subject to https://www.ebsco.com/terms-of-use

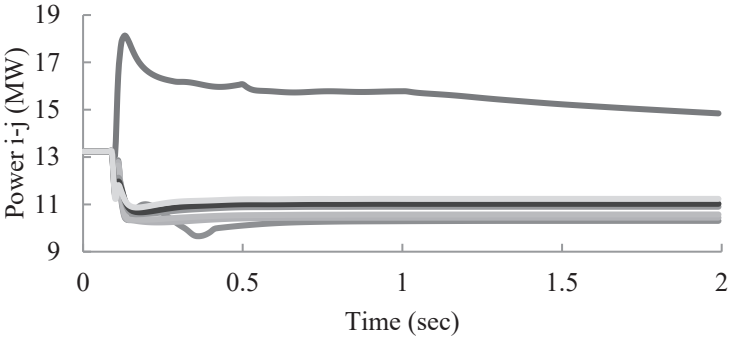



Fig. 19. Simulation results: power flows on DC submarine transmission cable 8-9. Mono-polar Network Configuration.

From Table II, *Case II* on dc bus 6 has the highest nominal voltage change of 3.30% from the rated nominal voltage. As the slope constant decreased, the voltages were seen to be within the voltage limit. This is better be understood by looking at it from the maximum instantaneous voltage attained where $K$= -0.20 reaches 1.720 pu which is 63.85 away from the rated nominal voltage. $K$ = -6.00 reached a max of 1.055 pu which is just 0.5% deviation from the rated voltage and is able to come back to steady-state voltage of 1.035 pu rapidly (recall the operation limit is max 1.050 pu). Simulation results show a level of power imbalance resulting from the converter outage, however; the excess power produced was successfully shared between the terminals having the same droop characteristics provided the terminals have enough capacity to compensate for the power unbalance.

## Conclusion

This paper evaluates the impact of the dc voltage control strategy on the dynamic behaviour of multi-terminal VSC-based HVDC following a converter outage; two strategies are analysed in this paper: SVMM and SVDM. Simulation results have shown that in the event of an outage of a converter station, there is a power imbalance in the MTDC network which is successfully distributed among the various converter terminals. The rate and efficacy of power balancing are however based on the control strategy and network configuration implemented. This was verified by the ability of converters using a smaller droop constant $K$ in SVDM to deliver a quicker response than those having a more significant droop or using SVMM

EBSCOhost - printed on 2/14/2023 2:46 PM via . All use subject to https://www.ebsco.com/terms-of-use

scheme. A comparison of the monopolar and bipolar network showed that bipolar network delivered better power stability with minimal voltage deviation from the initial nominal voltage than the mono-polar network. Bipolar using smaller droops were seen to operate within the rated voltage limit and had 3.3% overvoltage for a more considerable droop constant. Also, results showed that power oscillations in the ac side are transferable to the dc side if a converter exceeds the rated current limit.

# Appendix

**Table A. Numerical parameters of controller used at VSC stations in MTDC network.**

| *VSC Station* | *Control* | *Controller Gain [pu]* | *Time Constant [sec]* | *Min. Current on q-d axis ($I_{min}$)[pu]* | *Max. Current on q-d axis ($I_{max}$) [pu]* |
|---|---|---|---|---|---|
| *VSC26* | *Q* | $K_q$ = 3.00 | $T_q$ =0.2 | -1.03 | 1.03 |
| | *P* | $K_p$ = 1.00 | $T_p$ =0.1 | -1.03 | 1.03 |
| *VSC37* | *Q* | $K_q$ = 3.00 | $T_q$ =0.2 | -1.03 | 1.03 |
| | *P* | $K_p$ = 1.00 | $T_p$ =0.1 | -1.03 | 1.03 |
| *VSC49* | *Q* | $K_q$ = 1.00 | $T_q$ =0.1 | -1.03 | 1.03 |
| | *P* | $K_p$ = 1.00 | $T_p$ =0.1 | -1.03 | 1.03 |
| *VSC58* | *Q* | $K_q$ = 3.00 | $T_q$ =0.2 | -1.03 | 1.03 |
| | *P* | $K_p$ = 1.00 | $T_p$ =0.1 | -1.03 | 1.03 |

**Table B. Converter Set points.**

| *Converter Station* | *Control Mode* | *Active Power Set point [MW]* | *Reactive Power Set point [MVAR*MVA$_r$*]* | *Operation Mode* |
|---|---|---|---|---|
| *VSC37* | $U_{dc}$-*Q* | 41.00 | 0.00 | DC slack bus |
| *VSC26* | *P-Q* | -60.00 | 40.00 | Rectifier |
| *VSC58* | *P-Q* | 35.00 | 5.00 | Inverter |
| *VSC49* | *P-Q* | -25.00 | 0.00 | Rectifier |

# References

[1] "The Paris Agreement | UNFCCC." [Online]. Available: https://unfccc.int/process-and-meetings/the-paris-agreement/the-paris-agreement. [Accessed: 14-Sep-2018].

[2] "EU climate action | Climate Action." [Online]. Available: https://ec.europa.eu/clima/citizens/eu_en. [Accessed: 14-Sep-2018].

[3] F. Gonzalez-Longatt, J. L. Rueda, and M. A. M. M. Van Der Meijden, "Effects

EBSCOhost - printed on 2/14/2023 2:46 PM via . All use subject to https://www.ebsco.com/terms-of-use

of grounding configurations on post-contingency performance of MTDC system: A 3-Terminal example," in *Proceedings of the Universities Power Engineering Conference*, 2015, vol. 2015–Novem.

[4] F. Harold R. Chamorro, Camilo A. Ordones, Jimmy C-H. Peng and G.-L. and V. K. Sood, "Coherency Estimation in Power Systems: A Koopman Operator Approach," in *Computational Intelligence and Optimization Methods for Control Engineering*, 2018.

[5] F. Gonzalez-Longatt, "Optimal power flow in MTDC systems based on a DC-independent system operator objective," in *2015 IEEE Eindhoven PowerTech, PowerTech 2015*, 2015.

[6] F. Gonzalez-Longatt, "Optimal steady-state operation of a MTDC system based on DC-independent system operator objectives," in *IET Seminar Digest*, 2015, vol. 2015, no. CP654.

[7] F. Gonzalez-Longatt and J. Roldan, "Effects of DC Voltage control strategy on voltage response on multi-terminal HVDC following loss of a converter station," in *IEEE Power and Energy Society General Meeting*, 2013.

[8] F. Gonzalez-Longatt and J. M. Roldan, "Effects of dc voltage control strategies of voltage response on multi-terminal HVDC following a disturbance," in *2012 47th International Universities Power Engineering Conference (UPEC)*, 2012, pp. 1–6.

[9] J. Beerten, S. Cole, and R. Belmans, "Generalized Steady-State VSC MTDC Model for Sequential AC/DC Power Flow Algorithms," *Power Syst. IEEE Trans.*, vol. 27, no. 2, pp. 821–829, 2012.

[10] J. Beerten, S. Cole, and R. Belmans, "Implementation aspects of a sequential AC/DC power flow computation algorithm for Multi-terminal VSC HVDC systems," in *AC and DC Power Transmission, 2010. ACDC. 9th IET International Conference on*, 2010, pp. 1–6.

[11] M. E. El-Hawary and S. T. Ibrahim, "A new approach to AC-DC load flow analysis," *Electr. Power Syst. Res.*, vol. 33, no. 3, pp. 193–200, 1995.

[12] E. Iggland, R. Wiget, S. Chatzivasileiadis, and G. Anderson, "Multi-Area DC-OPF for HVAC and HVDC Grids," *Power Syst. IEEE Trans.*, vol. 30, no. 5, pp. 2450–2459, 2015.

[13] W. Wenyuan and M. Barnes, "Power Flow Algorithms for Multi-Terminal VSC-HVDC With Droop Control," *Power Syst. IEEE Trans.*, vol. 29, no. 4, pp. 1721–1730, 2014.

[14] I. A. Calle, P. Ledesma, and E. D. Castronuovo, "Advanced application of transient stability constrained-optimal power flow to a transmission system including an HVDC-LCC link," *Gener. Transm. Distrib. IET*, vol. 9, no. 13, pp. 1765–1772, 2015.

[15] J. Cao, W. Du, and H. F. Wang, "An Improved Corrective Security Constrained OPF for Meshed AC/DC Grids With Multi-Terminal VSC-HVDC," *Power Syst. IEEE Trans.*, vol. 31, no. 1, pp. 485–495, 2016.

[16] A. Rabiee and A. Soroudi, "Stochastic Multiperiod OPF Model of Power Systems With HVDC-Connected Intermittent Wind Power Generation," *Power Deliv. IEEE Trans.*, vol. 29, no. 1, pp. 336–344, 2014.

[17] H. Saad, T. Ould-Bachir, J. Mahseredjian, C. Dufour, S. Dennetiere, and S.

EBSCOhost - printed on 2/14/2023 2:46 PM via . All use subject to https://www.ebsco.com/terms-of-use

Nguefeu, "Real-Time Simulation of MMCs Using CPU and FPGA," *Power Electron. IEEE Trans.*, vol. 30, no. 1, pp. 259–267, 2015.

[18] N. T. Trinh, M. Zeller, K. Wuerflinger, and I. Erlich, "Generic Model of MMC-VSC-HVDC for Interaction Study With AC Power System," *Power Syst. IEEE Trans.*, vol. 31, no. 1, pp. 27–34, 2016.

[19] D. Zonetti, R. Ortega, and A. Benchaib, "Modeling and control of HVDC transmission systems from theory to practice and back," *Control Eng. Pract.*, vol. 45, pp. 133–146, 2015.

[20] F. D. Bianchi and J. L. Dominguez-Garcia, "Coordinated Frequency Control Using MT-HVDC Grids With Wind Power Plants," *Sustain. Energy, IEEE Trans.*, vol. 7, no. 1, pp. 213–220, 2016.

[21] L. Hongzhi and C. Zhe, "Contribution of VSC-HVDC to Frequency Regulation of Power Systems With Offshore Wind Generation," *Energy Conversion, IEEE Trans.*, vol. 30, no. 3, pp. 918–926, 2015.

[22] L. Luhui, Z. Jinwu, W. Chen, J. Zhuangxian, W. Jin, and C. Bo, "A Hybrid DC Vacuum Circuit Breaker for Medium Voltage: Principle and First Measurements," *Power Deliv. IEEE Trans.*, vol. 30, no. 5, pp. 2096–2101, 2015.

[23] A. Raza, X. Dianguo, L. Yuchao, S. Xunwen, B. W. Williams, and C. Cecati, "Coordinated Operation and Control of VSC Based Multiterminal High Voltage DC Transmission Systems," *Sustain. Energy, IEEE Trans.*, vol. 7, no. 1, pp. 364–373, 2016.

[24] M. Hajian, Z. Lu, and D. Jovcic, "DC Transmission Grid With Low-Speed Protection Using Mechanical DC Circuit Breakers," *Power Deliv. IEEE Trans.*, vol. 30, no. 3, pp. 1383–1391, 2015.

[25] D. Jovcic, M. Taherbaneh, J. P. Taisne, and S. Nguefeu, "Offshore DC Grids as an Interconnection of Radial Systems: Protection and Control Aspects," *Smart Grid, IEEE Trans.*, vol. 6, no. 2, pp. 903–910, 2015.

[26] R. Eriksson, "Coordinated Control of Multiterminal DC Grid Power Injections for Improved Rotor-Angle Stability Based on Lyapunov Theory," *Power Deliv. IEEE Trans.*, vol. 29, no. 4, pp. 1789–1797, 2014.

[27] Z. Jiebei, J. M. Guerrero, W. Hung, C. D. Booth, and G. P. Adam, "Generic inertia emulation controller for multi-terminal voltage-source-converter high voltage direct current systems," *Renew. Power Gener. IET*, vol. 8, no. 7, pp. 740–748, 2014.

[28] L. Sheng, X. Zheng, H. Wen, T. Geng, and X. Yinglin, "Electromechanical Transient Modeling of Modular Multilevel Converter Based Multi-Terminal HVDC Systems," *Power Syst. IEEE Trans.*, vol. 29, no. 1, pp. 72–83, 2014.

[29] W. Wenyuan, A. Beddard, M. Barnes, and O. Marjanovic, "Analysis of Active Power Control for VSC–HVDC," *Power Deliv. IEEE Trans.*, vol. 29, no. 4, pp. 1978–1988, 2014.

[30] F. Gonzalez-Longatt, S. Arnaltes, and J. Rodríguez, "Dynamic Behaviour of Multi-Terminal VSC-Based HVDC after a Converter Outage: DC Control Strategy," *International Conference on Renewable Energies and Power Quality (ICREPQ'16)*. Madrid, Spain, 2016.

EBSCOhost - printed on 2/14/2023 2:46 PM via . All use subject to https://www.ebsco.com/terms-of-use

[31] J. Zhu, “Future multi-terminal HVDC transmission systems using Voltage source converters ,” *45th International Universities Power Engineering Conference (UPEC), 2010* . Cardiff, Wales , pp. 1–6, 2010.
[32] T. Nakajima and S. Irokawa, “A control system for HVDC transmission by voltage sourced converters,” in *Power Engineering Society Summer Meeting, 1999. IEEE*, 1999, vol. 2, pp. 1113–1119 vol.2.
[33] N. Seki, “Field testing of 53 MVA three-terminal DC link between power system using GTO converters,” in *IEEE Power Engineering Society Winter Meeting, 2000* , 2000, vol. 4, pp. 2504–2508.
[34] J. Wang, X. Li, and X. Qiu, “Power system research on distributed generation penetration,” *Autom. Electr. Power Syst.*, vol. 29, pp. 97–99, 2005.
[35] S. Cole, “Steady-State and Dynamic Modelling of VSC HVDC Systems for Power Systems Simulation,” Universiteit Leuven, Belgium, 2010.
[36] FOSG, “Friends of Supergrind. Position paper on the EC Communication for a European Infrastructure Package,” 2010. [Online]. Available: http://www.friendsofthesupergrid.eu/documentation.aspx.
[37] F. Gonzalez-Longatt, J. M. Roldan, J. Rueda, C. A. Charalambous, and B. S. Rajpurohit, “Implementation of Simplified Models of Local Controller for Multi-terminal HVDC Systems in DIgSILENT PowerFactory,” in *PowerFactory Applications for Power System Analysis*, F. M. Gonzalez-Longatt and J. Luis Rueda, Eds. Springer International Publishing, 2014, pp. 447–472.
[38] F. Gonzalez-Longatt and J. M. Roldan, “Effects of dc voltage control strategies of voltage response on multi-terminal HVDC following a disturbance,” in *Proceedings of the Universities Power Engineering Conference*, 2012.
[39] T. M. Haileselassie and K. Uhlen, “Power flow analysis of multi-terminal HVDC networks,” in *PowerTech, 2011 IEEE Trondheim*, 2011, pp. 1–6.
[40] T. M. Haileselassie and K. Uhlen, “Primary frequency control of remote grids connected by multi-terminal HVDC,” in *Power and Energy Society General Meeting, 2010 IEEE*, 2010, pp. 1–6.
[41] R. L. Hendriks, G. C. Paap, and W. L. Kling, “Control of a multiterminal VSC transmission scheme for connecting offshore wind farms,” in *European Wind Energy Conference*, 2007.
[42] G. W. Stagg and A. H. El-Abiad, *Computer methods in power system analysis*. New York: McGraw-Hill, 1968.
[43] DIgSILENT, “DIgSILENT PowerFactory, Version 15.2.” Gomaringen, Germany, 2015.

EBSCOhost - printed on 2/14/2023 2:46 PM via . All use subject to https://www.ebsco.com/terms-of-use

# CHAPTER TWENTY-SEVEN

# CAPACITORLESS DC/DC REGULATOR AS A CANDIDATE TOPOLOGY FOR PHOTOVOLTAIC SOLAR

HERMINIO MARTÍNEZ-GARCÍA[1]
ENCARNA GARCÍA-VÍLCHEZ[1]

## Abstract

Linear-assisted DC/DC regulators (or linear-switching hybrid DC/DC regulators) consist of a linear voltage regulator (classic NPN/nMOS topologies or PNP/pMOS low-dropout structures) connected in parallel with a switching DC/DC converter. This chapter describes the analysis and implementation of a hybrid DC/DC power regulator. The proposed topology consists of a series linear voltage regulator in parallel with a switching step-down converter. This topology sees a small ripple in the output voltage, a fast response to load variations, and high efficiency at high load current conditions. It is a good candidate for energy processing in photovoltaic solar facilities. In order to control these hybrid structures, different strategies exist that allow the fixing of the switching frequency as a function of some parameters of the linear regulator. In hybrid structures, there is not a classical feedback loop, as found in DC/DC converters, but they are still feedback systems. Therefore, small-signal analysis is important in ensuring the stability of the implemented power supply system. From the proposed analysis, we can deduce the critical

[1] Department of Electronics Engineering, Eastern Barcelona School of Engineering (EEBE), Diagonal-Besòs Campus, Technical University of Catalonia—BarcelonaTech (UPC), Eduard Maristany Ave., nº10–14, E-08019. Barcelona, Spain. E-mail: herminio.martinez@upc.edu

EBSCOhost - printed on 2/14/2023 2:46 PM via . All use subject to https://www.ebsco.com/terms-of-use

components causing instability in the hybrid regulator and also understand how to improve the final design.

**Keywords:** DC/DC switching converters; linear voltage regulators; linear-assisted DC/DC voltage regulators.

## Introduction

In recent decades, solar photovoltaic applications have come to be seen as important sources of power production due to the negative environmental effects of fossil fuels. Solar systems provide great potential for power generation because of their modularity, low cost, and the possibility of easy and close installation to existing utilities. In general, a photovoltaic system can be considered to have three main stages: a PV module, a DC/DC converter, and a DC/AC inverter. Several types of DC/DC converter are used for this kind of application. However, they can be classified into two different groups: linear voltage regulators and switching DC/DC converters. Linear regulators and switching converters, such as step-down (buck), step-up (boost), and buck-boost converters, are both widely used in photovoltaic systems. However, they both have important drawbacks.

Series linear regulators have been widely used in power supply systems in applications with low or moderate currents and consumption [1], [2], [3]. This kind of voltage regulators has several advantages. However, in spite of these advantages, linear regulators present some serious drawbacks. For example, the efficiency of these structures hardly exceeds 50% and the series-pass transistor has to hold up to all the current demanded by the load. Thus, this component has to be dimensioned (both electrically and thermically) to dissipate a large quantity of energy, increasing its price, volume, and weight in the supply system.

The drawbacks presented above for linear voltage regulators are improved upon in DC/DC switching converters [4], [5], ]6]. The efficiency of these converters, despite not reaching 100% due to the omnipresent circuit losses, is near optimal. But the design and implementation of this sort of converter is a more complex process than for linear regulators, especially in terms of their control loops when both line and load regulation is desired. In addition, the intrinsic switching of these converters leads to the production of significant ripples in the output voltage and an incremental increase in electromagnetic interference (EMI) in neighboring electronic systems.

EBSCOhost - printed on 2/14/2023 2:46 PM via . All use subject to https://www.ebsco.com/terms-of-use

In this chapter, a linear-switching hybrid regulator (or linear-assisted regulator) is modeled and implemented. These structures make good use of the advantages of the two previously mentioned alternatives (linear regulators and switching converters). Some of the aforementioned drawbacks are minimized, such as the low efficiency and high power dissipation of linear regulators, and the design complexity in the control for switching converters. These structures have an intrinsic control loop. This loop maintains a constant output voltage and determinates the duty ratio of the switching converter—possibly inducing instabilities. The stability of the system depends on the values of the circuit components and the values of the load, as with linear regulators. Therefore, stability analysis is necessary to obtain design guidelines for this kind of DC/DC regulator.

Fig. 1 shows the simplest configuration. The linear voltage regulator guarantees the output voltage and the analog comparator ($CMP_1$) controls the conduction or cut of the transistor, $Q_1$, and fixes the switching frequency. Note that the objective of the switching converter is to provide the excess of current that the linear regulator does not, as equation (1) indicates:

$$I_{out} = i_{reg}(t) + i_L(t) \tag{1}$$

In a first approximation, we do not consider hysteresis in the comparator $CMP_1$. The sense of the linear current ($i_{reg}$) is engaged by means of $R_{lim}$ (shunt resistor). We can establish a boundary current value for the linear regulator as in (2):

$$I_\gamma = \frac{V_{ref}}{R_{\text{lim}}} \tag{2}$$

When $i_{reg}$ tends to increase $I_\gamma$ the $Q_1$ switch is ON; and when $i_{reg}$ tends to decrease $I_\gamma$ the switch $Q_1$ is OFF. The current $I_{out}$ is a constant value and $i_L$ increases or decreases in linear form. Consequently, the share of the current holds as in equation (1) and as can be seen in the waveforms in Fig. 2.

EBSCOhost - printed on 2/14/2023 2:46 PM via . All use subject to https://www.ebsco.com/terms-of-use

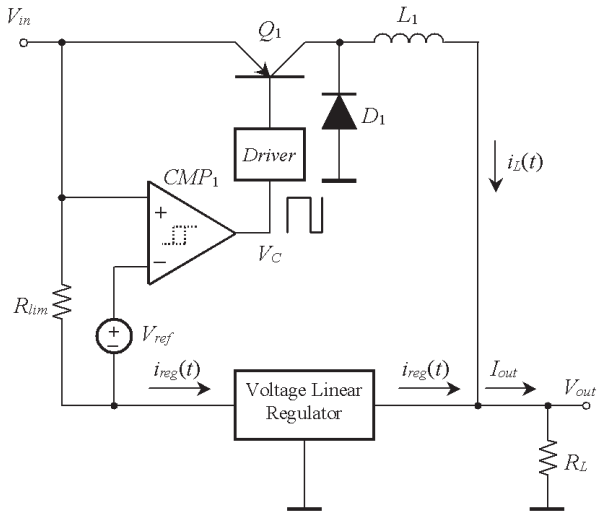



Figure 1. Basic structure of a self-switched hybrid regulator.

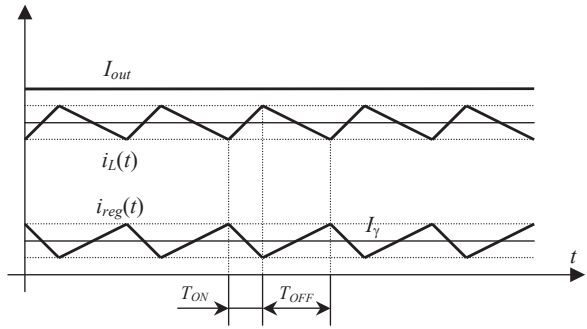



Figure 2. Currents through the load resistor ($I_{out}$), inductance $L_1$ ($i_L$), and linear regulator ($i_{reg}$) in the steady-state.

In the practical implementation of the regulator, the current $I_\gamma$ should be the minimum, necessary value to make the linear regulator work properly, without penalizing its good regulation characteristics and keeping its losses bounded. In addition, the comparator $CMP_1$ must include a hysteresis to limit the maximum value of the switching frequency and, thus, the switching losses of the converter. The switching frequency of the hybrid regulator is given by (3):

EBSCOhost - printed on 2/14/2023 2:46 PM via . All use subject to https://www.ebsco.com/terms-of-use

$$f_S = \frac{R_{\lim}}{L_1}\frac{R_1 + R_2}{R_1 V_{sat}} V_{out}\left(1 - \frac{V_{out}}{V_{in}}\right), \quad (3)$$

$V_{sat}$ is the positive saturation voltage at the output of the comparator, close to $V_{CC}$. The resistors $R_1$ and $R_2$ of the Schmitt trigger establish the upper and lower switching thresholds of the comparator.

## Implementation of the Hybrid Regulator

Fig. 3 shows the practical implementation of the self-switched hybrid regulator. The reference Zener diode $D_2$ fixes the voltage $V_{ref}$ that limits the maximum current through the linear regulator. The linear block is implemented with the operational amplifier $OA_2$, the transistor $Q_2$, and resistors $R_5$ and $R_6$. The precision voltage reference $D_3$ (or Zener diode) determines the output voltage of the whole circuit. The current $I_\gamma$ has been adjusted in this case, according to expression (2), to 50 mA.

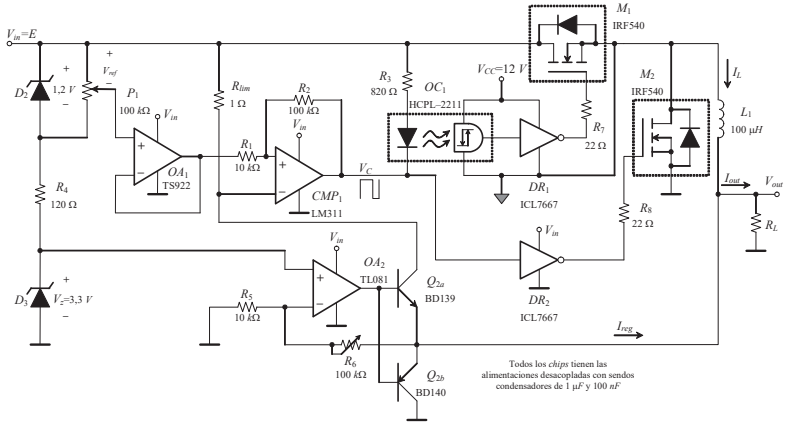



Figure 3. Schematic of the hybrid regulator prototype used to validate the proposed structure.

Fig. 4 shows the simulation of a transient of the hybrid regulator with $V_{in} = E = 10$ V. The response of the system to an input voltage step from 10 V to 13 V in the time instance $t = 20$ μs, and a step change of the load

EBSCOhost - printed on 2/14/2023 2:46 PM via . All use subject to https://www.ebsco.com/terms-of-use

resistor of 50%, from 10 Ω to 5 Ω in $t$ = 40 μs is shown. As we can see, the hybrid regulator gives an excellent response.

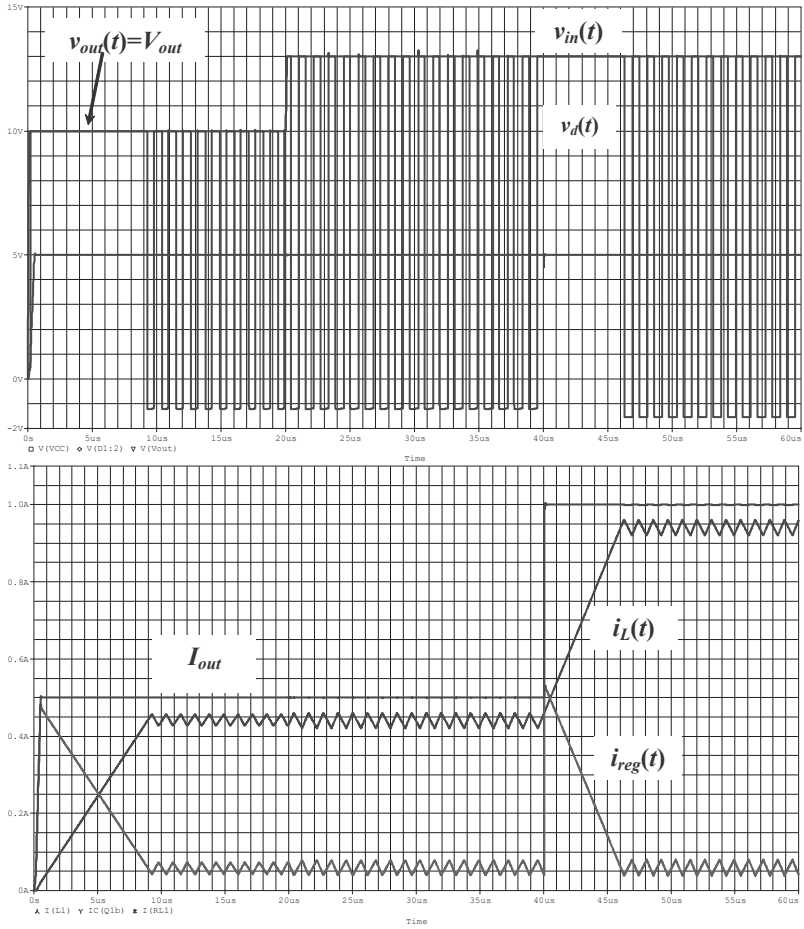



Figure 4. Transient response of the hybrid regulator to input voltage and load perturbations.

Fig. 5 shows the experimental waveforms of the output voltage $V_{out}$ (channel 1) and the cathode voltage of the diode $D_1$ (channel 2) for the hybrid regulator with $V_Z$ = 3.3 V and an output current equal to 1 A. The prototype is shown in Fig. 6.

EBSCOhost - printed on 2/14/2023 2:46 PM via . All use subject to https://www.ebsco.com/terms-of-use

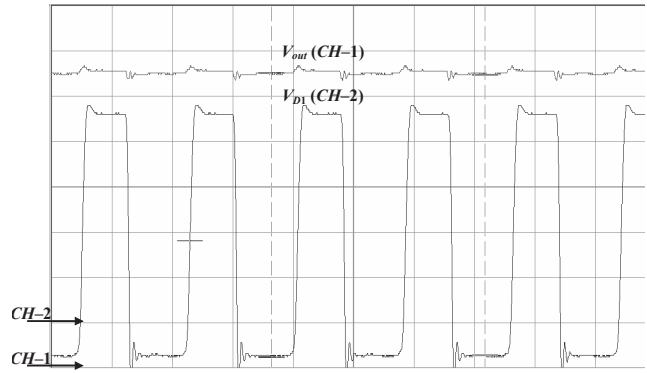



Fig. 5. Experimental waveforms of output voltage $V_{out}$ (channel 1) and cathode voltage of the diode $D_1$ (channel 2). Channel 1: 0.5 V/div. Channel 2: 1 V/div. TB: 1 μs/div.

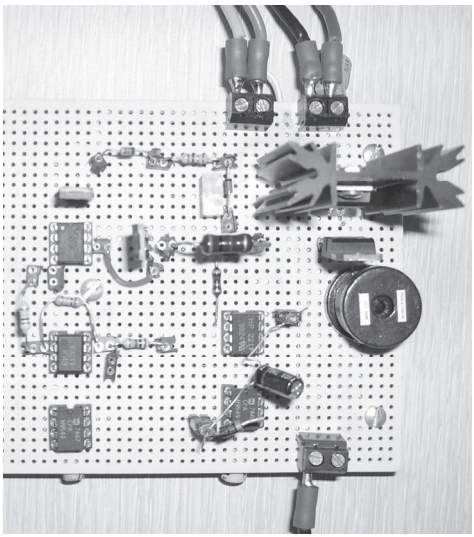


Figure 6. The linear-assisted regulator prototype used to validate the proposed structure.

Fig. 7 shows the efficiency achieved in the aforementioned hybrid regulator as a function of the load current, with a margin ranging from 0 A to 5 A. Measurements were made for the threshold current $I_\gamma$ through the linear regulator of 50 mA. Across a wide margin of load conditions,

EBSCOhost - printed on 2/14/2023 2:46 PM via . All use subject to https://www.ebsco.com/terms-of-use

efficiency rose to 85%, independently of the output current. In the case of a light load, efficiency decreased and tended towards conventional linear regulator efficiency.

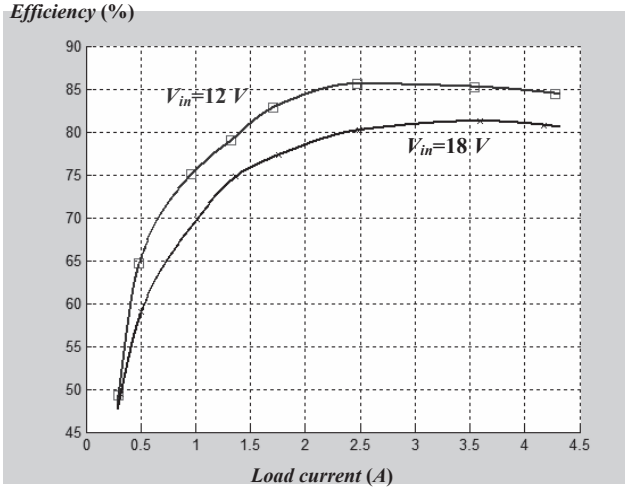



Figure 7. Efficiency of the experimental hybrid regulator versus the load current.

## Small Signal Analysis of the Hybrid Regulator

Linear-assisted regulators, as we can see in Fig. 1 and Fig. 3, do not include a classical output capacitor. The linear regulator included in the hybrid regulator ensures the output voltage value and a free ripple waveform. But it is interesting to note the effect of an output capacitor in the regulator. This component can be added in order to eliminate possible transitory peaks in the output voltage, or should be considered when load nature is capacitive.

The presence of an output capacitor or parasitic capacitance load can induce instability in the regulator. This instability is reflected as a considerable increment in the output voltage ripple around the desired average output voltage and large fluctuations of the duty cycle of the switching converter. The switching frequency experiences large variations with respect to the null output capacitance case and the frequency value does not correspond to equation (3). In addition, the current $i_{reg}$ of the linear regulator increases and the efficiency of the hybrid regulator drops significantly.

EBSCOhost - printed on 2/14/2023 2:46 PM via . All use subject to https://www.ebsco.com/terms-of-use

Fig. 8 shows the transient response of the linear-assisted regulator under the same conditions as those in Fig. 4, but with an output capacitance of $C_L$ = 100 nF and an equivalent series resistance (ESR) equal to 10 mΩ. Note that the inclusion of this $C_L$ network changes the current sharing considered in expression (1) and the ideal current waveforms presented in Fig. 2.

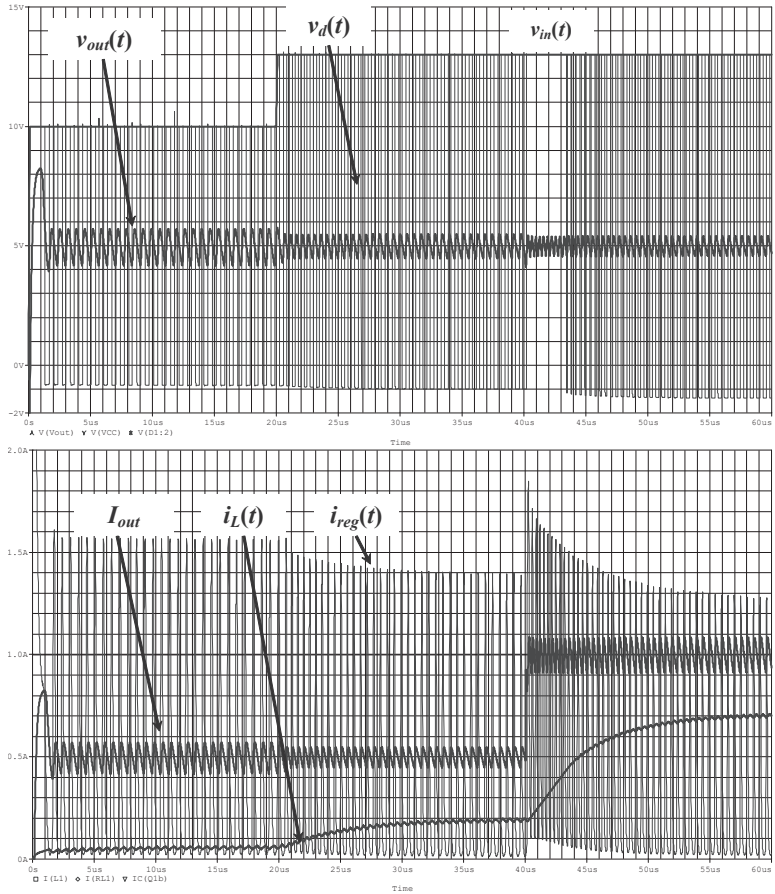



Figure 8. Transient response of the linear-assisted regulator with an output capacitance of $C_L$ = 100 nF.

Therefore, the $C_L$ has to be an agreed value. This value must be high enough to help cancel out perturbations, but guarantee stability in the

EBSCOhost - printed on 2/14/2023 2:46 PM via . All use subject to https://www.ebsco.com/terms-of-use

supply system. Experimentation with the prototype has shown that, together with the output capacitance, some others parameters affect the stability of the hybrid regulator. The most important components are the equivalent series resistance of the output capacitance $C_L$, the load resistor $R_L$, and the inductor $L_1$.

All these points make it necessary to analyze the hybrid regulator in order to design approaches that guarantee stability. A model of the linear-assisted DC/DC regulator is presented in Fig. 9.

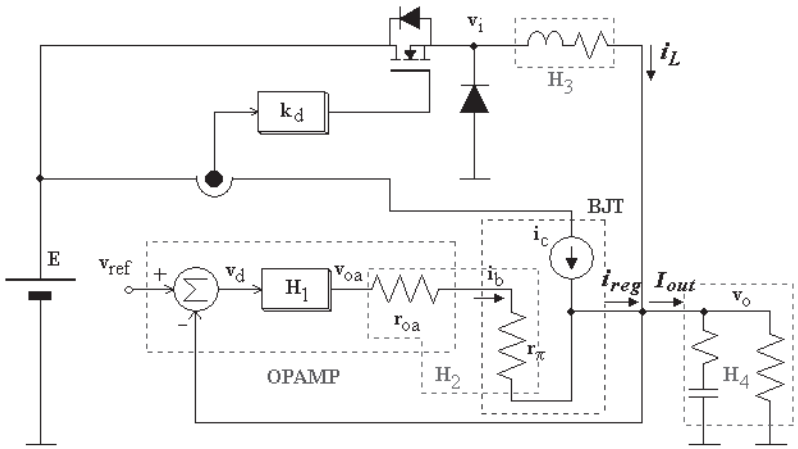



Figure 9. Proposed model of the linear-assisted DC/DC regulator.

The low-pass response of the operational amplifier is considered in block $H_1$, with a differential gain ($A_d$), a dominant pole ($\omega_o$), and its output resistance ($r_{oa}$). For the bipolar junction transistor (BJT) (working in its linear zone), the base-emitter dynamic resistance ($r_\pi$) and a current gain ($\beta$) are considered. Thus, block $H_2$ only contains the association of resistors $r_{oa}$ and $r_\pi$. The $r_\pi$ value is calculated as usual from equation (4):

$$r_\pi = \frac{dv_{be}}{di_b} = \frac{\beta}{I_{Cq}} \frac{v_T}{\lambda} \tag{4}$$

The $k_d$ block makes sense of the collector current in order to obtain the conducting ratio of the switching transistor. Its value is given by equation (5):

EBSCOhost - printed on 2/14/2023 2:46 PM via . All use subject to https://www.ebsco.com/terms-of-use

$$k_d = \frac{\Delta d}{\Delta i_c} = \frac{1}{i_{c,\max}} \tag{5}$$

The inductor small signal voltage is $v_i$ and is defined as usual:

$$v_i = \left(d \cdot E + e \cdot D\right) - v_o \tag{6}$$

The inductor current ($i_s$) is obtained thanks to the voltage $v_i$ and the block $H_3$, which models the inductor and its series resistance. Finally, with the output current ($i_o$) and block $H_4$, the output voltage ($v_o$) is obtained. In block $H_4$ the load resistance and output capacitor with its ESR is modeled.

In Fig. 10, the flow graph of the modeled linear-assisted regulator is presented.

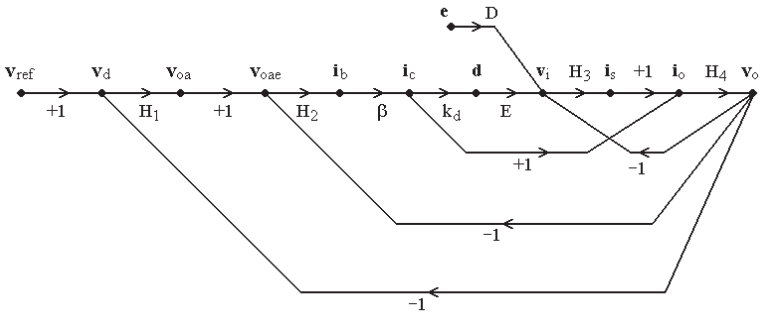



Figure 10. Flow graph of the modeled linear-assisted regulator.

Applying the Mason rule we obtain the transfer function given by:

$$G(s) = \frac{v_o(s)}{v_{ref}(s)} \tag{7}$$

In Table I the Maple® code in order to obtain the transfer function of equation (7) is presented. The result was simulated with Matlab® to obtain the pole-zero map of the system (*pzmap* function). The simulation values used are close to the experimental values of the prototype (Table II).

Using the transfer function given in (7), and applying the Routh-Hurwitz criterion, it is possible to obtain a design equation for the linear-assisted regulator that determines its stability as a function of the circuit

EBSCOhost - printed on 2/14/2023 2:46 PM via . All use subject to https://www.ebsco.com/terms-of-use

components. The denominator of the transfer function is a 3rd order polynomial in the form:

$$a_3 s^3 + a_2 s^2 + a_1 s + a_0 \tag{8}$$

The coefficients $a_0$, $a_1$, $a_2$, and $a_3$ of equation (8) consist of a considerable number of terms. The system will be stable if the condition presented in (9), which requires that all the coefficients of the characteristic equation are positives, is satisfied:

$$a_1 \, a_2 > a_3 \, a_0 \tag{9}$$

Removing negligible terms from the inequality in (9), reorganizing the most important terms in the expression, and isolating the capacitance $C_L$ gives:

$$C_L < \frac{\left(\beta R_L + r_d + r_{oa}\right)\left(k_d E + A_{oa}\omega_{oa} L_1\right)}{A_{oa}\omega_{oa} k_d R_L E \left(r_d + r_{oa}\right)} \tag{10}$$

For the design values considered in the prototype of the linear-assisted regulator, equation (10) can be simplified to equation (11):

$$C_L < \frac{2 L_1}{k_d \, R_L \, E} \tag{11}$$

where $\beta R_L \approx r_d + r_{oa}$ and $k_d E << A_{oa} \, \omega_{oa} \, L_1$.

As the experimental studies predicted, there is a strong influence on the stability of the hybrid regulator exercised by the inductor $L_1$, the load $R_L$, the input voltage $E$, and the sense of the linear current $i_{reg}$ by means of $k_d$ parameter. From equation (10), the critical value of $C_L$ for the experimental components of the linear-assisted regulator is 1 μF.

EBSCOhost - printed on 2/14/2023 2:46 PM via . All use subject to https://www.ebsco.com/terms-of-use

**Table I: The Maple® code used to obtain the transfer function given in equation (6).**

```
restart;
H1:=Aoa/(1+s/woa);
H2:=1/(roa+rd);
H3:=1/(rl+s*L);
H4:=R*(1/C/s+rc)/(R+1/C/s+rc);
P1:=H1*H2*beta*kd*E*H3*H4;
A1:=1;
P2:=H1*H2*beta*H4;
A2:=1;
L1:=-H3*H4;
L2:=-H2*beta*kd*E*H3*H4;
L3:=-H2*beta*H4;
L4:=-H1*H2*beta*kd*E*H3*H4;
L5:=-H1*H2*beta*H4;
g:=(P1*A1+P2*A2)/(1-L1+L2+L3+L4+L5));
g1:=simplify(g);
g2:=sort(g1,s);
```

**Table II: Simulation values used in the model.**

| Parameter | Value |
|---|---|
| $A_{oa}$ | $2 \cdot 10^5$ V/V |
| $\omega_{oa}$ | $2 \cdot \pi \cdot 10$ rad/s |
| $r_{oa}$ | 100 Ω |
| $E$ | 12 V |
| $R_L$ | 2 Ω |
| $L_1$ | 100 μH |
| $v_T$ | 25 mV |
| $\lambda$ | 1 |
| $I_{cq} = I_\gamma$ | 50 mA |
| $\beta$ | 100 |
| $r_d$ | $(\beta \cdot v_t)/(\lambda \cdot I_{cq})$ |
| $k_d$ | $1/100 \cdot 10^{-3}$ |

EBSCOhost - printed on 2/14/2023 2:46 PM via . All use subject to https://www.ebsco.com/terms-of-use

## Simulation and Experimental Results

From the model proposed in the previous section, some interesting simulations were carried out in order to determine the stability of the system as a function of different circuit parameters.

Fig. 11 presents a root locus diagram of the transfer function presented in (7). The figure shows three set of curves for different values of the capacitor ESR (1 mΩ, 10 mΩ, and 100 mΩ). In the three plots, the capacitor values go from $C_L$ = 100 nF to $C_L$ = $10^4$ μF. Note that when the ESR has a low value, the system easily tends towards instability when the capacitance value is higher than 1 μF. On the other hand, when the capacitor ESR is relatively high, the stability of the system is assured, even when output capacitance is high.

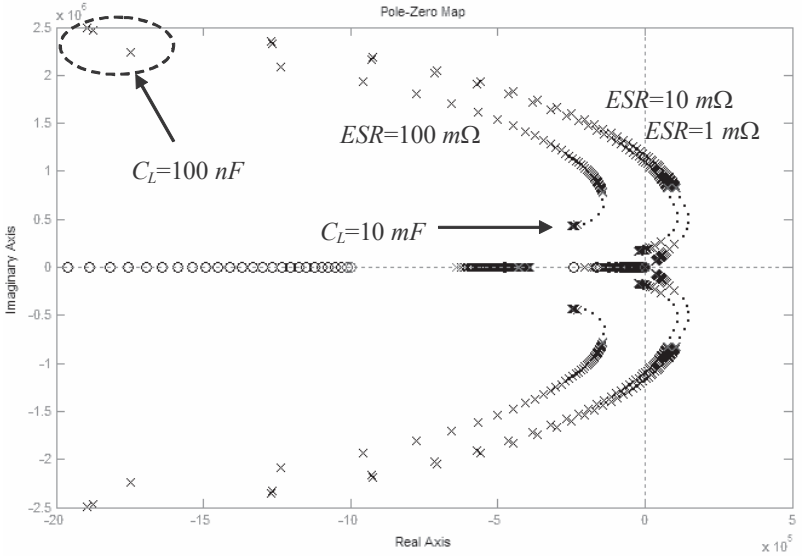



Figure 11. Root locus diagram for different values of capacitor ESR and output capacitance $C_L$.

Fig. 12 shows a root locus diagram of the transfer function given in (7) for three different values of the inductor $L_1$ (200 μH, 100 μH, and 50 μH). As in the previous figure, the three plots show results for capacitor values from 100 nF to 10 mF. When inductance $L_1$ has a small value, the linear-

EBSCOhost - printed on 2/14/2023 2:46 PM via . All use subject to https://www.ebsco.com/terms-of-use

assisted regulator tends towards instability for small values of output capacitance.

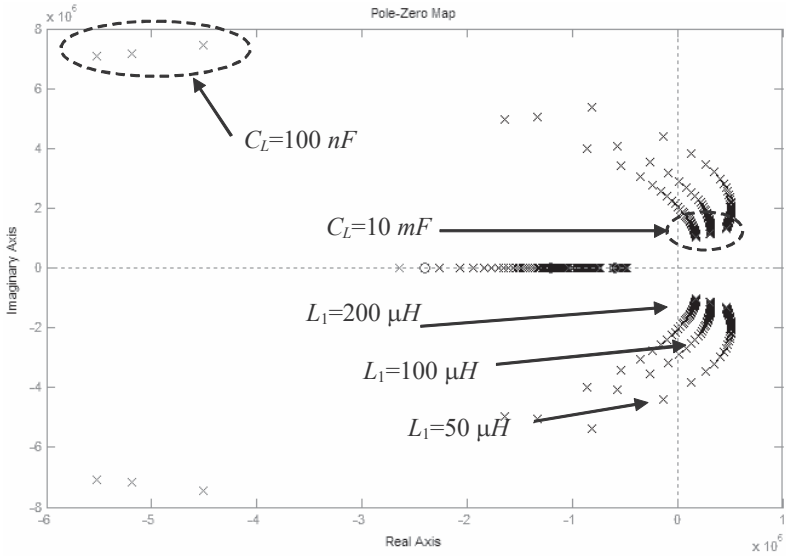



Figure 12. Root locus diagram for different values of the inductor $L_1$ and output capacitance $C_L$.

Finally, Fig. 13 presents a root locus diagram of the transfer function shown in (7) for three different values of the load $R_L$ (0.2 Ω, 2 Ω, and 20 Ω). As in the previous figures, the capacitor values go from 100 nF to 10 mF. Note that when the load resistor has a high value, the system tends towards instability when the capacitance value increases.

By varying different circuit parameters, other plots can be obtained. However, the aforementioned parameters ($C_L$, capacitor ESR, $L_1$, and load resistance) are the four most important ones in determining the stability of the linear-assisted regulator. Other parameters such as, for instance, the inductor series resistance, the open loop gain of the op-amp, and the output resistance of the op-amp, have an effect on the dynamics of the hybrid regulator, but do not actually lead to instability in the converter.

For the values given in Table II, the limit capacitor ensures that the stability of the linear-assisted regulator is equal to 1 μF. This value coincides with the experimental results obtained experimentally in the laboratory.

EBSCOhost - printed on 2/14/2023 2:46 PM via . All use subject to https://www.ebsco.com/terms-of-use

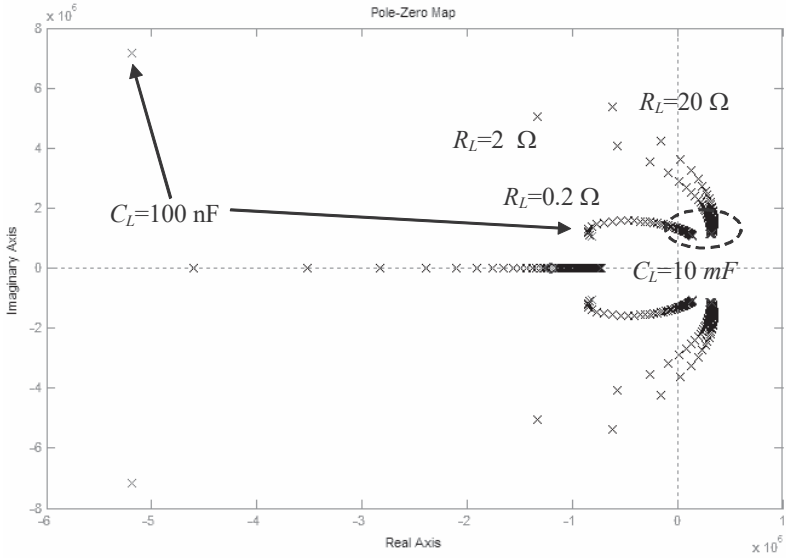



Figure 13. Root locus diagram for different values of the load resistor $R_L$ and output capacitance $C_L$.

## Conclusions and Further Research

In this chapter, the implementation and modeling of a linear-assisted regulator has been shown. The proposed hybrid regulator uses a switching-linear hybrid structure. The system has a control loop to maintain a constant output voltage. This closed loop can induce instabilities as a function of the values of the circuit components and the load (in a similar way to linear regulators).

Therefore, a stability study is necessary in order to obtain design guidelines for this kind of DC/DC regulator and ensure the stability of the implemented power supply system. From the aforementioned analysis, we can establish criteria for the selection of components and load conditions for the hybrid regulator.

The analysis shows that $C_L$, capacitor ESR, inductance $L_1$, and load resistance are the most influential circuit parameters in terms of the stability of the hybrid regulator. In addition, we note the importance of the capacitor ESR value and the nature of the load.

EBSCOhost - printed on 2/14/2023 2:46 PM via . All use subject to https://www.ebsco.com/terms-of-use

Notice that the linear-assisted regulators presented in this chapter are variable frequency structures. In this case, the switching frequency depends on the parameters of the regulator (according to expression (3)), and is not fixed by an external clock. This drawback affects the design of the hybrid regulator and the selection of its components. In addition, this feature is not desirable in some applications because variable switching frequency could insert interference into the bandwidth of neighboring electronic circuits or even of the electronic system that the hybrid regulator supplies. Thus, further research in this area may be necessary for improvements in the topology with the design of a ***constant-frequency linear-assisted DC/DC regulator***. In this new structure, it would be possible to choose the desired switching frequency independently of the component values.

With these new ***constant-frequency*** alternatives, the control loop of the system would be based on the current-mode technique. However, the main disadvantage of a hybrid regulator with current-mode control is the inherent instability of the loop when switch duty ratios are greater than 0.5. In order to make the proposed linear-assisted regulator stable, the control loop should use a technique based on slope compensation.

## Acknowledgement

This work has been partially supported by the Spanish Ministerio de Ciencia, Innovación y Universidades (MICINN) – Agencia Estatal de Investigación (AEI), and the European Regional Development Funds (FEDER), by project PGC2018-098946-B-I00.

## References

[1] R. J. Widlar: New Developments in IC Voltage Regulators. IEEE Journal of Solid-State Circuits, vol. SC-6 (nº 1): pp.2–7, February, 1971.

[2] R. K. Dokania, and G. A. Rincón-Mora: Cancellation of Load Regulation in Low Drop-Out Regulators. Electronic Letters, vol. 38 (nº 22): pp.1300–1302, 24th October, 2002.

[3] V. Grupta, G. A. Rincón-Mora, and P. Raha: Analysis and Design of Monolithic, High PSR, Linear Regulator for SoC Applications. Proceedings of the IEEE International SoC Conference: pp.311–315, 2004.

[4] R. W. Erickson and D. Maksimovic: Fundamentals of Power Electronics. 2nd edition, Ed. Kluwer Academic Publishers, 2001.

[5] J. G. Kassakian, M. F. Schlecht, and G. C. Verghese: Principles of Power Electronics. Ed. Addison-Wesley, 1991.

EBSCOhost - printed on 2/14/2023 2:46 PM via . All use subject to https://www.ebsco.com/terms-of-use

[6] N. Mohan, T. M. Underland, and W. P. Robbins: Power Electronics: Converters, Applications and Design. Ed. John Wiley & Sons, 1989.

[7] X. Zhou, P. L. Wong, P. Xu, F. C. Lee, and A. Q. Huang: Investigation of Candidate VRM Topologies for Future Microprocessors. IEEE Transactions on Power Electronics, vol. 15 (nº 6): pp.1172–1182, November 2000.

[8] B. Arbetter and D. Maksimovic: DC-DC Converter with Fast Transient Response and High Efficiency for Low-Voltage Microprocessor Loads. IEEE Applied Power Electronics Conference, pp.156-162. 1998.

[9] G. Villar, E. Alarcón, F. Guinjoan, and A. Poveda: Efficiency-Oriented Switching Frequency Tuning for a Buck Switching Power Converter. IEEE International Symposium on Circuits and Systems (ISCAS'05): 2005.

EBSCOhost - printed on 2/14/2023 2:46 PM via . All use subject to https://www.ebsco.com/terms-of-use

# CHAPTER TWENTY-EIGHT

# LOW DROP-OUT VOLTAGE REGULATOR AS A CANDIDATE TOPOLOGY FOR PHOTOVOLTAIC SOLAR FACILITIES

HERMINIO MARTÍNEZ-GARCÍA[1]
ENCARNA GARCÍA-VÍLCHEZ[1]
ALIREZA SABERKARI[2]

## Abstract

This chapter presents a design for a 4.5-*V*, 450-*mA* low drop-out (LDO) linear voltage regulator based on a two-stage cascode operational transconductance amplifier (OTA) as an error amplifier for photovoltaic solar DC-DC regulation. The aforementioned two-stage OTA is designed with a cascode current mirroring technique to boost the output impedance. The proposed OTA has a DC gain of 101 dB under no load condition.

The designed reference voltage included in the LDO regulator is provided by a band gap reference with the temperature coefficient ($T_\gamma$) of 0.025 *mV/ºC*. The proposed LDO regulator has a maximum drop-out voltage of 0.5 *V* @ 450 *mA* of load current, and has a worst case power supply rejection ratio (PSRR) of [54.5 *dB*, 34.3 *dB*] @ [100 *Hz*, 10 *kHz*] in full load conditions. All the proposed circuits were designed using CMOS technology. The design was checked in order to corroborate its

[1] Department of Electronics Engineering, Eastern Barcelona School of Engineering (EEBE), Diagonal-Besòs Campus, Technical University of Catalonia—BarcelonaTech (UPC), Eduard Maristany Ave., nº 10–14, E-08019. Barcelona (Spain). E-mail: herminio.martinez@upc.edu

[2] Microelectronics Research Laboratory, Department of Electrical Engineering, University of Guilan, Rasht, Iran. E-mail: a_saberkari@guilan.ac.ir

EBSCOhost - printed on 2/14/2023 2:46 PM via . All use subject to https://www.ebsco.com/terms-of-use

performance for a wide range of input voltages. We found that the circuit design worked well meeting all the initial specification requirements.

**Keywords:** photovoltaic solar DC-DC regulator; low drop-out (LDO) linear voltage regulator; operational transconductance amplifier (OTA; band gap reference; cascode current mirror.

## Introduction

Virtually all power supplies employ semiconductors to provide a regulated output voltage. If the supply has an AC input, it is rectified to become a DC voltage. A power DC-DC integrated circuit (IC) converter accepts a DC input and produces a DC output or controls external power output semiconductor switches to produce a suitable DC output. It is a voltage regulator when its output voltage is fed back into a circuit, causing the voltage to remain constant. In this case, if the output voltage rises or falls, the feedback causes the output to remain the same.

The power converter can operate either as a switch-mode or a linear circuit. In a linear configuration, the controlling transistor always dissipates power. This can be minimized by use of low-dropout regulators (LDOs) even when there is a relatively low voltage difference between the input and output. LDO ICs have simpler circuits than their switch-mode cousins and produce less noise (no switching), but are limited by their current-handling and power dissipation capabilities. Some LDO ICs are specified for about 200 *mA* and others can handle up to about 1 *A* [1].

## Voltage Regulator Fundamentals

As shown in Fig. 1, in general, a linear voltage regulator consists of an internal reference voltage, an error amplifier, a sensing network (normally, a feedback voltage divider), and a pass device (usually, a pass transistor). The output current is delivered via the pass element controlled by the error amplifier. Note that the design limit of the pass device defines the maximum load current the regulator can source and still maintain regulation.

The error amplifier compares both the reference and output feedback voltages. The control circuitry must monitor (sense) the output voltage, and adjust the current flowing through the pass element (as required by the load) to hold the output voltage at the desired value. If the output feedback voltage is lower than the reference, the error amplifier allows more current

EBSCOhost - printed on 2/14/2023 2:46 PM via . All use subject to https://www.ebsco.com/terms-of-use

to flow through the pass transistor. As a consequence, the output voltage increases.

On the contrary, if the feedback voltage is higher than the reference voltage, the error amplifier allows less current to flow through the pass transistor, decreasing the output voltage.

As such, the output voltage is controlled using a feedback loop, which requires some form of compensation to assure loop stability. Most linear regulators have built-in compensation, and are completely stable without external components. Although recently external-capacitorless LDOs have being receiving attention, some linear regulators (especially low-dropout types) require some form of external capacitance connected from the output lead to ground to assure regulator stability [2]-[3].

Another characteristic of any linear regulator is that it requires a finite amount of time to "correct" the output voltage after a change in load current demand. This "time lag" defines the characteristic known as transient response, which is a measure of how fast the regulator returns to a steady-state condition after a load change.

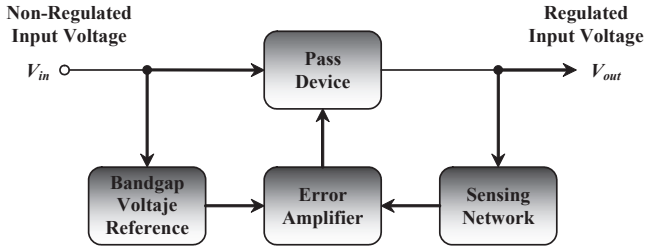



Figure 1. Block diagram of a series pass voltage regulator with feedback.

## *Different Types of Pass Element*

*NPN (quasi-LDO and Standard) Linear Regulators*

Conventional linear regulators (Fig. 2) use NPN bipolar transistors as the pass element. Usually, the pass element is composed of a PNP base current driver transistor ($Q_{1b}$) and a single NPN power transistor or, even, a Darlington pair ($Q_{1a}$). In the first case, with a single NPN transistor, the regulator is usually called a ***quasi-LDO*** and, in the second case, a ***standard*** linear regulator.

EBSCOhost - printed on 2/14/2023 2:46 PM via . All use subject to https://www.ebsco.com/terms-of-use

Therefore, in the case of a single NPN power transistor, the drop voltage, i.e. the minimum voltage difference between input and output, is equal to:

$$V_{SAT,PNP} + V_{BE,NPN}, \tag{1}$$

which, in general, is about 1.2 *V*. Moreover, in the case of a Darlington pair, this drop voltage is given by:

$$V_{SAT,PNP} + 2V_{BE,NPN}, \tag{2}$$

which, in this case, is about 2.0 *V*.

In addition, in practical implementations, functionality and integrated protection are limited and additional protection circuitry is required.

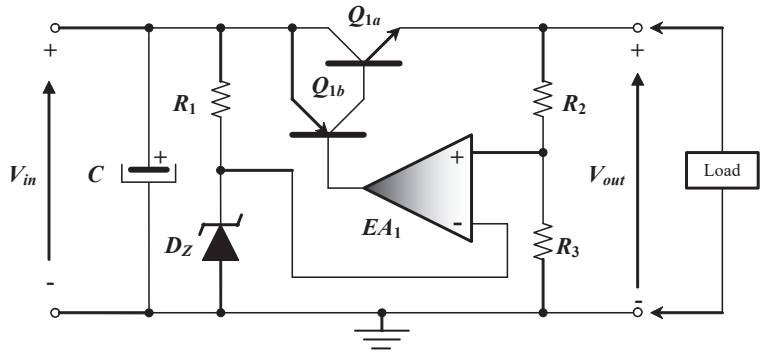



Figure 2. Series pass voltage regulator with feedback and NPN transistor as pass element.

*PNP Linear Regulators*

With only a single PNP bipolar transistor ($Q_1$ in Fig. 3) as the pass element, the drop voltage of a PNP regulator is about 0.5 *V*. For this reason, this type of regulator is called a ***low drop-out*** (LDO) regulator. This enables it to operate during a drop in battery voltage (e.g., with cranking). In addition, PNP regulators are protected against reverse polarity faults.

Standard regulators are usually the best for AC-powered applications, where their low cost and high load current make them an ideal choice. In

EBSCOhost - printed on 2/14/2023 2:46 PM via . All use subject to https://www.ebsco.com/terms-of-use

AC-powered applications, the voltage across the regulator is usually at least 3 *V* or more. Therefore, in this kind of application, dropout voltage is not critical.

Curiously, in this type of application (where the voltage drop across the regulator is > 3 *V*) standard regulators are actually more efficient than LDO types (because the standard one has much less internal power dissipation due to ground pin current).

However, a LDO regulator is the most suitable for renewable (such as photovoltaic solar facilities) and battery-powered applications, because the lower dropout voltage translates directly into cost savings by reducing the number of battery cells required to provide a regulated output voltage. If the input-output voltage difference is low (like 1 *V* to 2 *V*), the LDO is more efficient than a standard regulator because of its reduced power dissipation resulting from the load current and the input-output voltage difference [4].

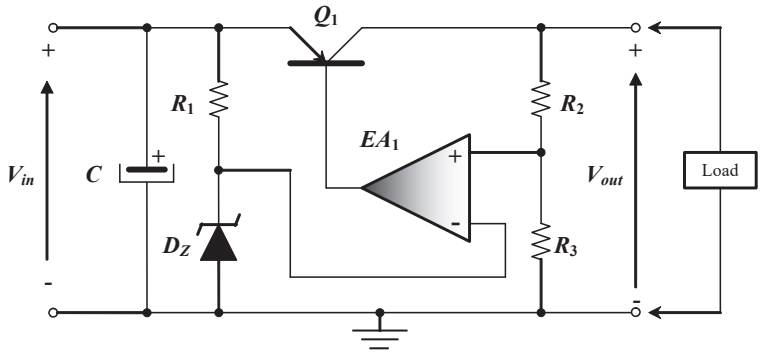



Figure 3. Series pass voltage regulator with feedback and PNP transistor as pass element.

*NMOS Linear Regulators*

NMOS pass transistors, as a pass element, provide very low drop-out voltage and minimal quiescent current. However, in this case, a charge pump is needed to achieve the low drop-out voltage, because the gate of the NMOS needs to be approximately 2 *V* higher than the voltage at source, to drive the pass element open. Taking into account this point, which is a disadvantage, the charge pump also introduces additional line noise.

EBSCOhost - printed on 2/14/2023 2:46 PM via . All use subject to https://www.ebsco.com/terms-of-use

*PMOS Linear Regulators*

Using PMOS linear regulators as the pass element provides a very low drop-out voltage and minimal quiescent current. In this case, an internal charge pump is not necessary for the PMOS pass element. In addition, new control loop concepts in PMOS linear regulators allow a faster regulation loop and better stability, requiring only a single output capacitor (in general, lower than 1 $\mu F$) for stable operation.

## LDO Voltage Regulators Fundamentals

As discussed above, LDO voltage linear regulators [5]-[6]-[7]-[8] have gained significant importance due to the increased use of battery-powered devices and photovoltaic solar DC-DC voltage regulation. The main function of the LDO regulator is to provide a reliable, stable, and constant voltage. It has come to be considered an important component in the power management of cell phones, laptops, and wireless applications, etc., where dropout voltage is an important issue [9].

Fig. 4 shows the overall topology of the proposed LDO regulator. As can be seen, it consists of three main blocks: an error amplifier, a voltage reference, and a pass transistor with external load capacitance with a small value of internal resistance (ESR) for frequency compensation. The error amplifier of the LDO regulator, in the negative feedback condition, constantly compares the output voltage with the reference voltage and maintains a constant output voltage by varying the gate to source voltage of the pass transistor, according to the error signal. Since the output of the error amplifier is used to drive the gate of the pass transistor, which is naturally a capacitive load, the best option for the error amplifier is an operational transconductance amplifier (OTA) [10]-[11] with high output impedance (Fig. 5). In addition, it is very easy to model an OTA as a single pole system because of its high output impedance, which forms a low frequency pole with small load capacitance. Therefore, OTAs are the best components to drive these capacitive loads because their output signal is current controlled by a differential input signal.

The voltage reference is an important component of voltage regulators, since it decides the nominal output voltage. The main design issue will be its temperature coefficient, which ideally has to be zero, or very near to it. There are many approaches to obtain the reference voltage. However, one method is the use of a band gap voltage reference (BGR) with a very low temperature coefficient [12]. Finally, a PMOS pass transistor, which carries a major part of the current across the whole circuit, drives the load.

EBSCOhost - printed on 2/14/2023 2:46 PM via . All use subject to https://www.ebsco.com/terms-of-use

Its dimensions are determined such that it is able to withstand the maximum rated current and to achieve the rated low dropout voltage.

The chapter is organized as follows: in the next section, the design of the two-stage cascode OTA using CMOS technology is described. Next, the design of the LDO regulator is discussed, including the design of the error amplifier based on the proposed OTA, and the design of the pass transistor using CMOS technology. Finally, the simulation results obtained for both the proposed OTA and LDO regulator are presented.

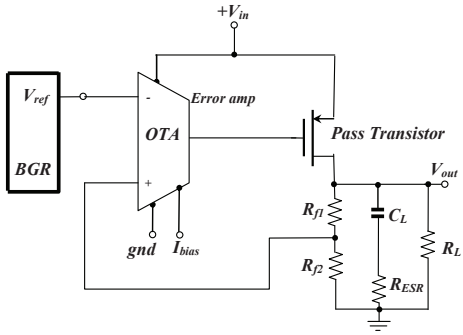



Figure 4. Topology of the proposed LDO linear voltage regulator.

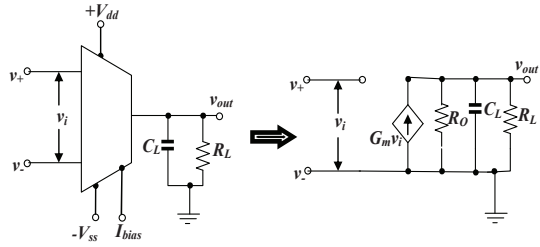



Figure 5. Small signal model of an OTA with $C_L$ and $R_L$.

## Design of the Operational Transconductance Amplifier (OTA)

Fig. 6 shows a classical two-stage OTA using CMOS technology [11], operated using a rail of $+V_{dd}$ and $-V_{ss}$ power supplies and with an external bias current $I_{bias}$ and a single ended output. The first stage is the normal *n*-channel differential input pair ($m_1$ and $m_2$) with *p*-channel current mirror

EBSCOhost - printed on 2/14/2023 2:46 PM via . All use subject to https://www.ebsco.com/terms-of-use

as its active load ($m_3$ and $m_4$). The drain currents of $m_1$ and $m_2$ are mirrored by $m_6$ and $m_5$, respectively, which is the second (gain) stage in the classical current mirroring technique with the current ratio of 1:$\alpha$. In Fig. 6, we get:

$$I_a = \left(I_{bias}/2\right) - g_{m(2)}\, v_i/2 \text{ , and } I_b = \left(I_{bias}/2\right) + g_{m(1)}\, v_i/2 \tag{3}$$

The single ended output is taken out from point $P1$, through which a current of:

$$I_o = g_{m(1,2)} \cdot \alpha \cdot v_i \tag{4}$$

flows, where $v_i = (v_+) - (v_-)$ is the differential input. Therefore, the voltage controlled current source is obtained and the transconductance of this OTA, $G_m$, is given by the expression:

$$G_m = \frac{I_O}{V_i} = \alpha \cdot g_{m(1,2)} \tag{5}$$

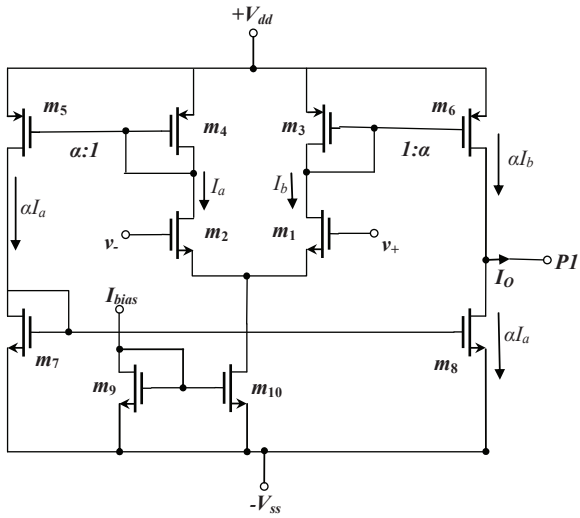



Figure 6. Classical two-stage OTA using CMOS technology.

EBSCOhost - printed on 2/14/2023 2:46 PM via . All use subject to https://www.ebsco.com/terms-of-use

It should be noted that according to equation (5), the transconductance of the OTA is dependent on the $g_m$ of the MOS transistors of the input differential pair, which is in-turn dependent on the DC current flowing through it, i.e., $\sqrt{I_{bias}/2}$. As such, it may be said to be a current-controlled gain OTA. The parameter $\alpha$ is called the gain factor and is modified by varying the ratio $W/L$ of the second stage with respect to the input stage ($W/L_{(6,5)}$:$W/L_{(3,4)}$). The equivalent small signal model representation of the OTA is shown in Fig. 5. As seen in this figure, the voltage gain ($A_v(s)$) is given by the expression:

$$\frac{V_{out}(s)}{V_i(s)} = A_v(s) = \frac{A_v}{1+\frac{s}{\omega_o}} = G_m . Z_L(s) \quad (6)$$

where $G_m$ is the transconductance of the OTA, given by equation (5), while the cut-off frequency $\omega_o$ is given by:

$$\omega_o = \frac{1}{(R_o \parallel R_L) C_L} \quad (7)$$

$Z_L$(s) is the output impedance of the OTA, which is given by:

$$Z_L(s) = \frac{R_o \parallel R_L}{1+(R_o \parallel R_L)(C_L s)} \quad (8)$$

It should be noted that the OTA has a high output impedance thanks to the common source output configuration, which gives the high output impedance $r_o(m_8)||r_o(m_6)$. The main advantage of the OTA is that, due to its high output impedance, frequency compensation is easier. The load capacitance ($C_L$) only creates the dominant pole. Hence, the unity gain bandwidth is varied by varying the load capacitance to obtain a suitable phase margin (PM) according to the application and ensuring the stability of the system.

Fig. 7 shows the improved two-stage OTA using CMOS technology, adopting the cascode technique to boost the output impedance and the DC voltage gain (no load) of the classical OTA, optimizing the proposed OTA.

EBSCOhost - printed on 2/14/2023 2:46 PM via . All use subject to https://www.ebsco.com/terms-of-use

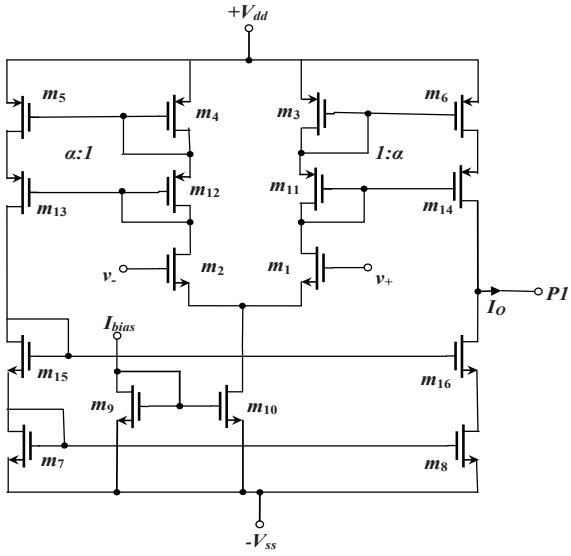



Figure 7. Proposed two-stage cascode OTA using CMOS technology.

In the proposed design ($m_{4,5}$) and ($m_{12,13}$); ($m_{3,6}$) and ($m_{11,14}$); and ($m_{15,16}$) and ($m_{7,8}$) form the cascode pairs with current mirroring. The main design criteria of the proposed OTA are the same as the classical OTA design, which depends on equations (5), (6), and (8). The output resistance is approximately equal to $g_{m(14)}r_o(m_{14})$. The main advantage is the boosting of output impedance by a factor of approximately $r_o(m_6)||g_{m(16)}r_o(m_{16})r_o(m_8)$, which is quite significant. The output impedance, $R_o$, is varied by varying the ratios $W/L_{(6,14,16,8)}$ and in-turn varying $g_m$. Regarding the other important parameters, the input impedance $R_i \approx \infty$ (since the input is at the gate of the MOSFETs), the DC voltage gain of the OTA, from equations (6) and (8), is given by:

$$A_v = G_m \left( R_o \,||\, R_L \right) \tag{9}$$

Equation (9) can be used to find $g_{m(1,2)}$ experimentally by obtaining the AC response of the proposed OTA for $R_L = \infty$, and obtaining its output impedance plot with respect to frequency. Therefore, the equation for DC gain reduces to:

EBSCOhost - printed on 2/14/2023 2:46 PM via . All use subject to https://www.ebsco.com/terms-of-use

$$A_v \approx G_m R_o \tag{10}$$

Later on, simulation results for a classical OTA are compared to the proposed OTA by considering certain parameters. In addition, different parameters of the proposed OTA, like AC response, DC gain, and output impedance, etc., are also presented.

## Design of the Low Drop-out (LDO) Linear Voltage Regulator

Fig. 4 shows the classical topology of the proposed LDO regulator. It consists of three main blocks: the *error amplifier* block; the *voltage reference* block; and the *pass transistor*—it is biased by means of an external current $I_{bias}$. In standard voltage regulators, the main difference compared to an LDO is found in the pass transistor block. Normally, in a typical voltage regulator, the pass transistor element will be an *n*MOS (or *npn*) transistor in a source follower (or emitter follower) configuration, which has a typical dropout voltage of 2 *V*. However, in a LDO regulator, the pass transistor element is a *p*MOS (or *pnp*) transistor in a common source (or common emitter in bipolar counterpart) configuration, in which its dropout voltage is nothing, but its saturation voltage has a typical value of 0.3 ~ 0.5 *V*.

Since a *p*MOS transistor is used as the pass transistor in common source output configuration (Fig. 4), one of the handicaps in a LDO regulator is that it forms a high output impedance, creating a pole within the unity gain frequency. Because there is already a low frequency pole provided by the error amplifier (OTA), an extra phase is contributed by the pole formed by the high output impedance of the LDO and its overall response in decreasing the phase margin causes a stability issue in the system. Therefore, an output capacitance with a small $R_{ESR}$ is needed to compensate the above-mentioned pole. $R_{ESR}$ together with load capacitance ($C_L$) form a zero to compensate the effect of the pole created by the high output impedance of the LDO regulator.

The resistors $R_{f1}$ and $R_{f2}$ in Fig. 4 are used to set the output voltage ($V_{out}$). The error amplifier forms a negative feedback loop, which constantly compares the error signal at the output with the reference voltage to maintain a constant $V_{out}$ by varying the gate voltage of the pass transistor, controlling the current flowing through it. As such, the output voltage is given by:

EBSCOhost - printed on 2/14/2023 2:46 PM via . All use subject to https://www.ebsco.com/terms-of-use

$$V_{out} = \left(1 + \frac{R_{f1}}{R_{f2}}\right) V_{ref} \tag{11}$$

By choosing the appropriate values for the resistors and reference voltage, the output voltage $V_{out}$ is set.

The initial design specifications given for the proposed LDO regulator are shown in Table I. Fig. 8 gives the complete schematic of the CMOS LDO linear voltage regulator in order to perform in line with these design specifications. The dimensions of the circuit transistors in the proposed LDO linear voltage regulator in Fig. 8 are depicted in Table II.

As can be seen in Fig. 8, the proposed design has three main parts: (1) the error amplifier; (2) the voltage reference circuit; and (3) the pass transistor, as well as a suitable load capacitance $C_L$.

## *Design of the Error Amplifier in the Proposed LDO Regulator*

The error amplifier in the proposed LDO regulator basically consists of the OTA previously discussed. It can be seen in Fig. 5 and its design criteria has already been discussed. The only difference is that here, it operates only at a positive voltage, i.e., without a negative voltage $-V_{ss}$, and instead that point is connected to ground. According to this design, the simulation for an open loop AC response is conducted several times with the OTA operating at $+V_{dd}$ and *GND* (Fig. 9). Since the OTA is operating at these two potentials, the input terminals must be provided with proper DC bias in order to get a good open loop AC response with high DC gain. As such, the proposed OTA is simulated with different values of offset voltage ($V_{offset}$) at the input points, while obtaining its open loop AC response.

For this particular design, after different simulations, it can be seen that to get a better response, $V_{offset} > 0.6\ V$. When this OTA is working as an error amplifier in the proposed LDO, $V_{offset}$ is set by the reference voltage ($V_{ref}$). Thus, the reference voltage has to be greater than 0.6 *V*. As a consequence, in the design specifications of the LDO regulator, $V_{ref} = 0.65\ V$. The capacitor $C_1$ (Miller capacitor) is connected to two high impedance points in the circuit, which ensures a good phase margin in the proposed design; $C_1$ is set to 40 *pF*.

EBSCOhost - printed on 2/14/2023 2:46 PM via . All use subject to https://www.ebsco.com/terms-of-use

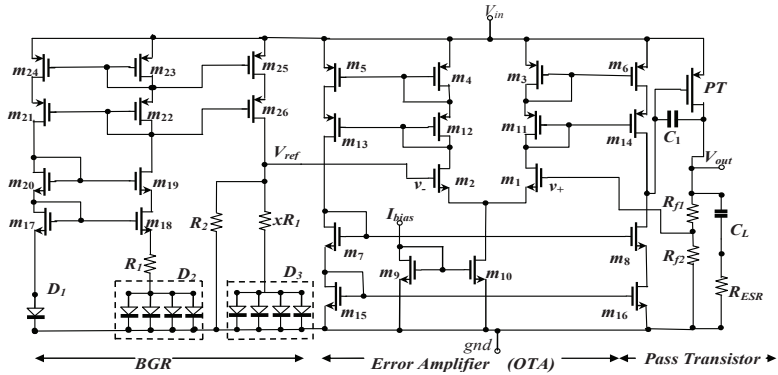



Figure 8. Proposed design of LDO linear voltage regulator.

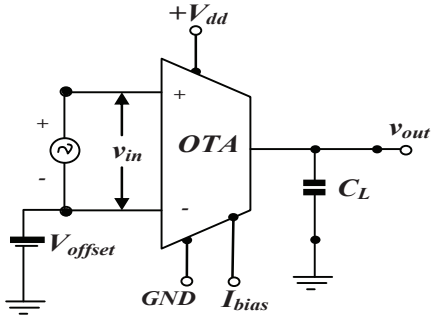



Figure 9. Proposed OTA operating in $+V_{dd}$ and GND with input offset.

**Table I: Design specifications of the proposed LDO regulator**

| *Design Specification* | *Value* |
|---|---|
| Output voltage ($V_{out}$) | 4.5 $V$ (1% allowance) |
| Max. output current ($I_{out,max}$) | 450 $mA$ |
| Reference voltage ($V_{ref}$) | 650 $mV$ |
| Maximum drop-out voltage ($V_{\text{drop}}$) at $I_{out}$ = 450 $mA$ | 500 $mV$ |

EBSCOhost - printed on 2/14/2023 2:46 PM via . All use subject to https://www.ebsco.com/terms-of-use

**Table II: Dimensions of the transistors in the proposed LDO linear voltage regulator in Fig. 8**

| *Transistor* | *Width* (*W*) *in* μm | *Length* (*L*) *in* μm |
|---|---|---|
| $m_1$ , $m_2$ | 500 | 1 |
| $m_3$ , $m_4$ , $m_{11}$ , $m_{12}$ | 40 | 1 |
| $m_5$ , $m_6$ , $m_{14}$ , $m_{13}$ | 800 | 1 |
| $m_7$ , $m_8$ , $m_{15}$ , $m_{16}$ | 800 | 1 |
| $m_9$ , $m_{10}$ | 100 | 1 |
| $m_{17}$ , $m_{18}$ , $m_{19}$ , $m_{20}$ | 100 | 1 |
| $m_{21}$ , $m_{22}$ , $m_{23}$ , $m_{24}$ | 100 | 1 |
| $m_{25}$ , $m_{26}$ | 100 | 1 |
| PT (pass transistor) | 8000 | 1 |

The error amplifier in the negative feedback condition decides the output voltage ($V_{out}$) by constantly comparing the error signal with $V_{ref}$, which is 0.65 *V*. According to equation (11), to get the desired value of $V_{out} = 4.5V$, $R_{f1} = 14.8\ k\Omega$ and $R_{f2} = 2.5\ k\Omega$ are chosen.

## Simulation Results and Observations

The proposed circuit blocks were built in Cadence Hit-Kit V3.70, using CMOS technology. Simulation was done using the Spectre software package, with the BSIM-3.3 as the MOSFET model.

### *Operational Transconductance Amplifier*

The proposed OTA, as shown in Fig. 7, was built and simulated with $+V_{dd} = 5\ V$, $-V_{ss} = 0\ V$, and with the bias current $I_{bias} = 50\ \mu A$. The circuit was simulated in order to obtain some parameters and then compared with the results from the classical OTA shown in Fig. 6. The open loop AC Response of the proposed OTA is plotted and shown in Fig. 10 for the load capacitance $C_L = 0.4\ nF$ under no-load conditions. The results showed DC gain of $A_V = 101.13\ dB$ and unity gain bandwidth of $UGB = 4.5\ MHz$ with a phase margin of $PM = 59.17^o$.

In addition, the proposed OTA circuit was simulated with $C_L = 1\ nF$. The DC gain was the same, but $UGB = 1.98\ MHz$ with $PM = 75.3^o$, whereas in the classical OTA, $UGB = 2.316\ MHz$ with $PM = 81.07^o$. This boosting of the DC gain in the proposed OTA when compared to the classical OTA configuration under no load conditions is due to the increase in the output impedance thanks to the cascode current mirrors in

EBSCOhost - printed on 2/14/2023 2:46 PM via . All use subject to https://www.ebsco.com/terms-of-use

the first configuration. The DC gain under no load condition matches equation (10).

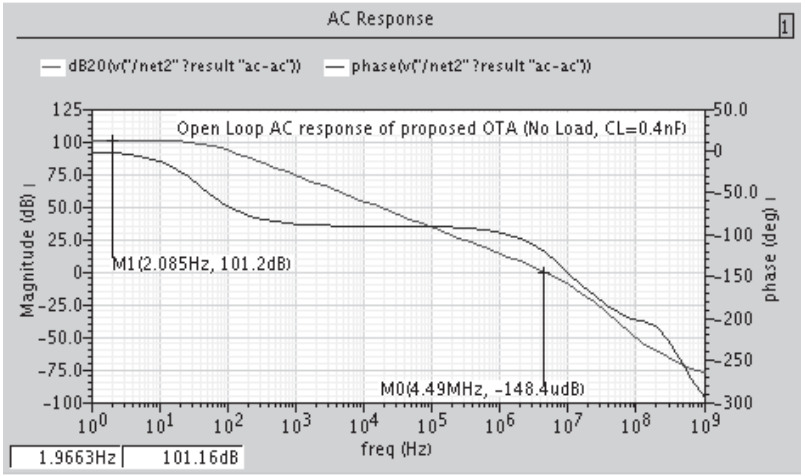



Figure 10. AC Response of the proposed OTA, with $C_L = 0.4\ nF$, $R_L = \infty$.

Another important parameter, the output impedance, was evaluated by simulating the circuit with differential inputs grounded and applying an AC voltage source at the output node, with $C_L = 1\ nF$, finding the current through that voltage source. Fig. 11 shows the output impedance $Z_L(s)$ with $R_L = \infty$, with respect to frequency change in the proposed OTA. It can be seen in this figure that the large signal output impedance ($R_O$) in the proposed OTA is 1.35 $M\Omega$, which is a high output impedance, thanks to the cascode current mirroring technique in the proposed OTA.

Another parameter that determines the gain is $g_{m(1,2)}$ of the input differential pair MOSFETs. This was found out experimentally, in Figs. 10 and 11, and using equations (5) and (10) under no load conditions. From these figures, the values of $R_O$ and DC gain $A_v$ can be obtained, with a gain factor $\alpha$ set to 20. Substituting appropriate values, it was found that $g_{m(1,2)} = 2.12\ mS$. This value fits well with the theoretical value found using the model file parameters ($k_n$, $V_{tn}$) and DC current $I_{bias}/2$, i.e., 2.204 $mS$.

EBSCOhost - printed on 2/14/2023 2:46 PM via . All use subject to https://www.ebsco.com/terms-of-use

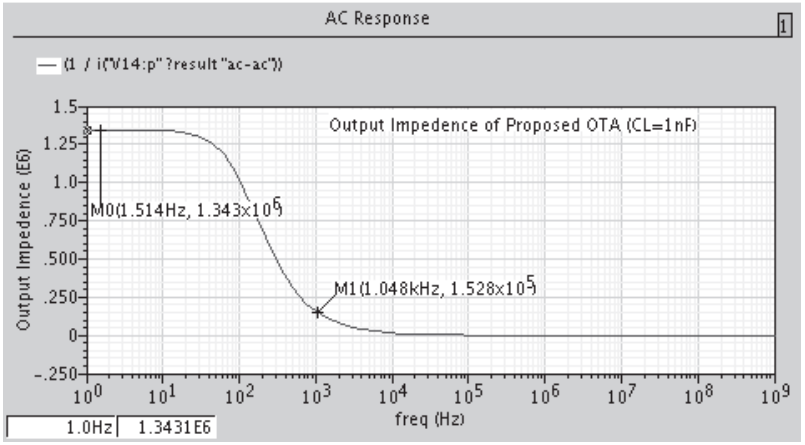



Figure 11. Output impedance vs. frequency of the proposed OTA.

## *LDO Voltage Regulator*

Fig. 8 shows the proposed LDO regulator circuit with its three parts: the error amplifier (based on the previously proposed OTA); the band-gap reference circuit; and the pass transistor. This circuit was built and simulated with $V_{in}$ ranging from 5 $V$ to 20 $V$, $I_{bias} = 50\ \mu A$, and it was found that the designed circuit fits the specifications in Table I. Tables III and IV give a summary of the simulation results obtained for the band-gap reference voltage and LDO regulator circuits, respectively.

**Table III: Simulation results of band-gap reference voltage circuit**

| *Parameters* | *Values* |
|---|---|
| $V_{ref}$ at $T = 25\ ^oC$ | 653 $mV$ |
| $T_\gamma$ | 0.025 $mV/^oC$ |
| Line Regulation | 0.44 $mV/V$ |
| Power drawn, $V_{in} = 5\ V$ | 0.54 $mW$ |

EBSCOhost - printed on 2/14/2023 2:46 PM via . All use subject to https://www.ebsco.com/terms-of-use

**Table IV: Simulation results obtained for the proposed LDO regulator**

| *Parameter* | *Value* | | |
|---|---|---|---|
| | ***For*** $R_L$ = ∞ | ***For*** $R_L$ = **10 Ω** | ***For*** $R_L$ **= 45 Ω** |
| $V_{out}$ for $V_{in}$ = 5 *V* | 4.509 *V* | 4.504 *V* | 4.507 *V* |
| $I_L$ for $V_{in}$ = 5 *V* | 0 *A* | 450.4 *mA* | 100.1 *mA* |
| $V_{drop}$ | 0.06 *V* | 0.5 *V* | 0.15 *V* |
| Line regulation | 3.2 *mV/V* | 3.4 m*V/V* | 3.2 *mV/V* |
| Load regulation | 0.012 *V/A* | | |
| $V_{out}$ settling time $I_L$ = 0 – 450 *mA* in 1 µs | 4.2 µ*s* | | |
| $V_{out}$ settling time $I_L$ = 450 *mA* – 0 in 1 µs | 40 µ*s* | | |
| PSRR (full load) | @ 100 *Hz* | 54.45 *dB* | |
| | @10 *kHz* | 34.31 *dB* | |
| $V_{out}$ settling time $V_{in}$=5 *V* – 20 *V* in 1 µ*s* | 6 µ*s* | | |
| $V_{out}$ settling time $V_{in}$=20 *V* – 5 *V* in 1 µ*s* | 4 µ*s* | | |

The proposed LDO regulator circuit (Fig. 8) was simulated to obtain its most important characteristics and parameters [13], like DC response, line regulation, load regulation, PSRR, open loop AC Response, response for load variations, settling time for load variations, and transient responses for input variations.

The DC response of the LDO circuit was obtained under different load conditions—$R_L$ = 10 Ω, 45 Ω, and ∞. The typical response for $R_L$ = 10 Ω and ∞ are shown in Fig. 12. This DC response was used to divine the drop-out voltage ($V_{drop}$) of the proposed LDO regulator by spotting the point at which the $V_{out}$ reached a constant value. Thus, by knowing the corresponding value for $V_{in}$, the dropout voltage can be found. It can be seen in the figures that for $R_L$ = ∞, $V_{drop}$ = 0.06 *V*, and for full load conditions ($R_L$ = 10 Ω), the dropout voltage was $V_{drop}$ = 0.5 *V*. This shows that there is a trade-off between the maximum load and the drop-out voltage, hence the user has to use this proposed LDO regulator according to the application requirements. From the plots of the DC response (Fig.

EBSCOhost - printed on 2/14/2023 2:46 PM via . All use subject to https://www.ebsco.com/terms-of-use

12), the line regulation for the corresponding $R_L$ can be discovered by considering $V_{out}$ for $V_{in} = 5\ V \sim 20\ V$. Using equation (12):

$$LR = \frac{\frac{\Delta V_{out}}{V_{out}}}{\frac{\Delta V_{in}}{V_{in}}} \tag{12}$$

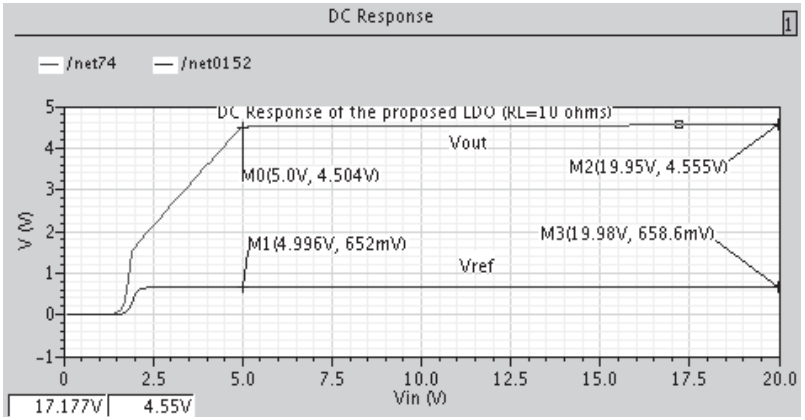



Figure 12. DC response of the proposed LDO and band-gap reference for full load condition.

we can find that the line regulation (*LR*) for $R_L = \infty$ is 3.2 *mV/V*; for $R_L =$ 10 Ω it is 3.4 *mV/V*; and for $R_L = 45$ Ω it is 3.2 *mV/V*. Load regulation was obtained by sweeping $I_L$ from 0 *A* to 450 *mA* with $V_{in} = 5\ V$. In Fig. 13, the load regulation is 0.012 *V/A*.

EBSCOhost - printed on 2/14/2023 2:46 PM via . All use subject to https://www.ebsco.com/terms-of-use

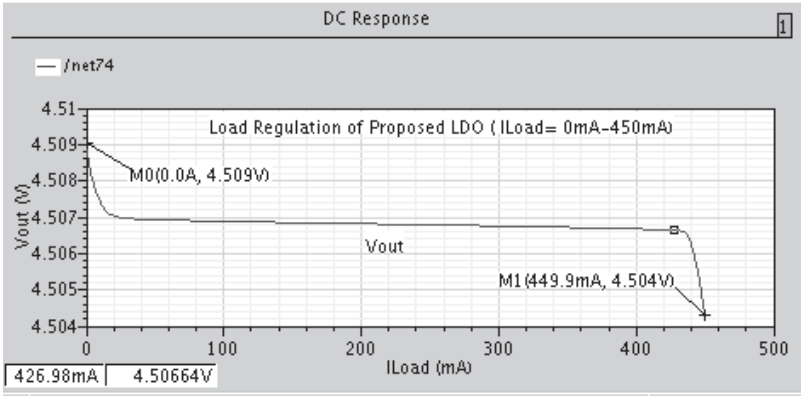



Figure 13. Load regulation of the LDO regulator, $I_L = 0\ A - 450\ mA$.

With $V_{in} = 5\ V$ and $R_L = \infty$, the current flowing through the supply had a value of 1.29 *mA*, which is usually referred to as the sum of the current needed to bias the whole circuit, with the leakage current through the feedback circuit in the error amplifier (quiescent current). This current is small compared to the maximum output rated current $I_{L(max)} = 450\ mA$, giving a power efficiency at a full load condition of 89.74%. On the other hand, $V_{out} = 4.509\ V$ for $R_L = \infty$ and $V_{out} = 4.504\ V$ for $R_L = 10\ \Omega$, while satisfying the initial design specifications in Table I.

Another important parameter to consider is the power supply rejection ratio (PSRR), which decides the ripple rejection capability of the circuit. The PSRR was found for two load conditions: no load and full load. It was found that under the no load condition at 100 *Hz*, PSRR = 56.26 *dB*; at 10 *kHz*, PSRR = 46.53 *dB*. For the full load condition at 100 *Hz*, PSRR = 54.45 *dB*; and at 10 *kHz*, PSRR = 34.31 *dB* (Fig. 14). The open loop AC Response of the LDO regulator is shown in Fig. 15. DC gain was found to be 32.56 *dB*, *UGB* = 18.68 *kHz* with a *PM* of 91.35º, ensuring the stability of the circuit.

EBSCOhost - printed on 2/14/2023 2:46 PM via . All use subject to https://www.ebsco.com/terms-of-use

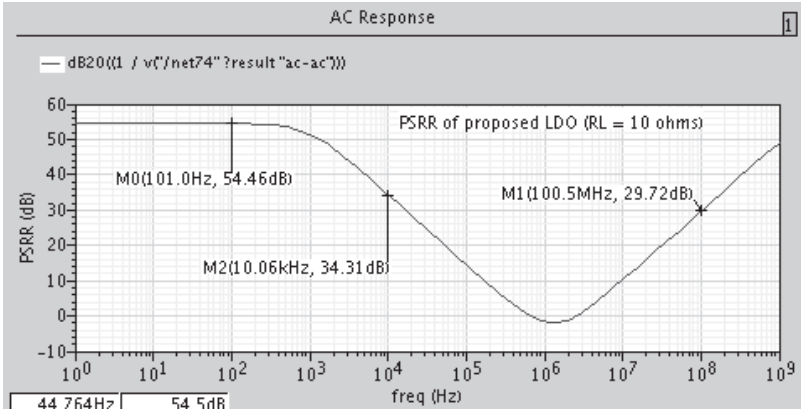



Figure 14. PSRR of the LDO regulator, $R_L = 10\ \Omega$.

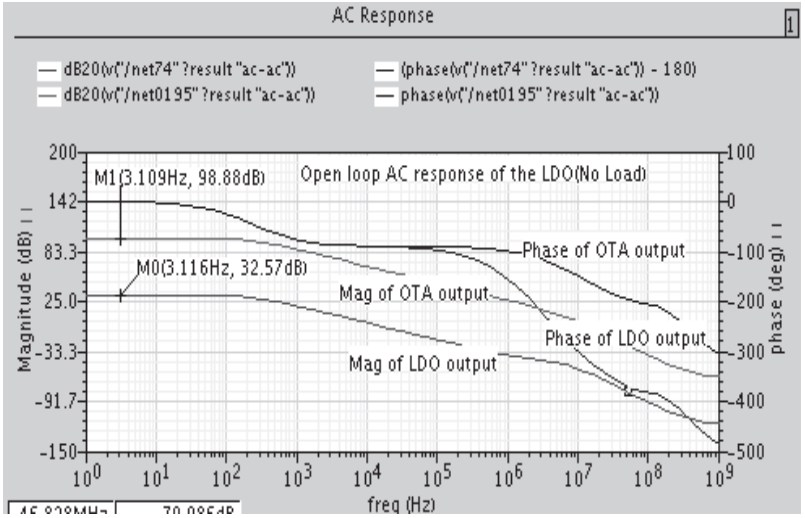



Figure 15. Open loop AC response at the LDO and error amplifier outputs.

Finally, the response for the load variations of the proposed LDO and the settling times for full load variations are depicted in Fig. 16; transient responses for input variations are given in Fig. 17.

EBSCOhost - printed on 2/14/2023 2:46 PM via . All use subject to https://www.ebsco.com/terms-of-use

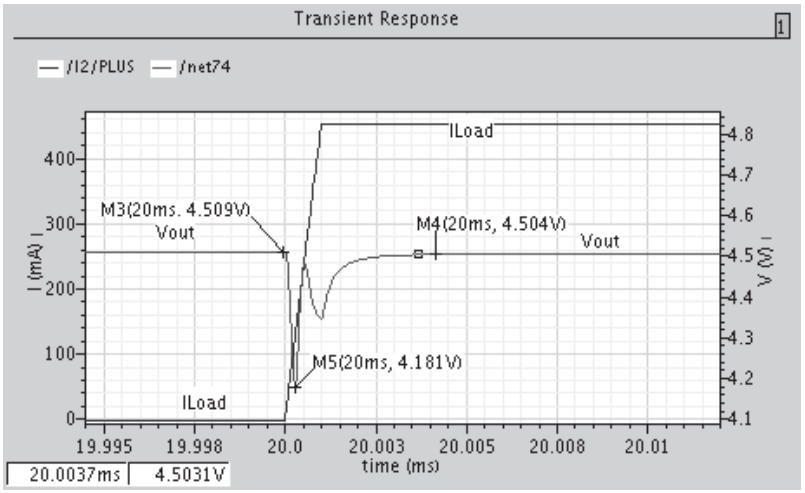



Figure 16. Settling time of $V_{out}$ for a step $I_L = 0\ A - 450$ m$A$ in 1 $\mu s$.

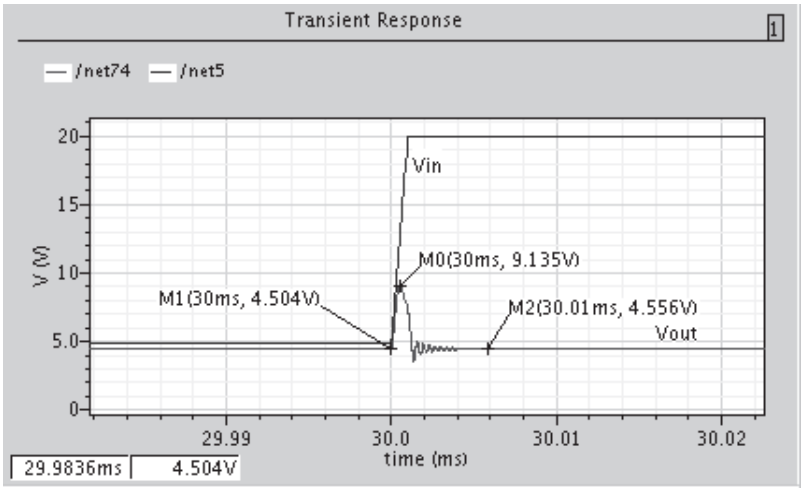



Figure 17. Response of $V_{out}$ for $V_{in} = 5\ V - 20\ V$ in 1 $\mu s$ for full load.

## Conclusions and Further Research

This chapter has offered a proposal for a low drop-out voltage regulator based on a two-stage cascode operational transconductance

EBSCOhost - printed on 2/14/2023 2:46 PM via . All use subject to https://www.ebsco.com/terms-of-use

amplifier (OTA) as an error amplifier. It was designed in 0.35 $\mu m$ CMOS technology and simulated in Cadence Spectre software with the MOSFET model BSIM-3.3.

The current measured regulated output voltage was 4.5 $V$ with a maximum current of 450 $mA$. The LDO regulator design has a dropout voltage of 0.5 $V$ under full load conditions, with good line and load regulation of 3.2 $mV/V$ and 0.012 $V/A$, respectively. The PSRR of the design was found to be 54.45 $dB$ at 100 $Hz$ and 34.31 $dB$ at 10 $kHz$ under full load conditions. The LDO linear voltage regulator includes a band gap reference circuit that provides a constant reference voltage of 0.653 $V$ with a temperature co-efficient ($T_\gamma$) of 0.025 $mV/^oC$.

A majority of LDO voltage regulators operate with very large pass transistor as the power stage, to handle heavy-load currents, resulting in a large equivalent capacitance at the gate of the pass device, which, in turn, restricts the slew-rate at this node and thereby degrades the dynamic performance. Moreover, the stability of the LDO will degrade at no-load and light-load conditions, as the poles at the gate of the pass device and at the output node are very close together. Compelling evidence continues to show that operation in standby mode is expected for most of the time, suggesting that the large pass transistor should be eliminated for no-load conditions and its utilization for maximum load currents. When the power transistor is applied at its maximum, the greatest output voltage variations are due to the load transients that occur under no-load and light-load changes (usually less than 1 $mA$) [14]. Pass transistor segmentation into smaller sizes and adaptively controlling their action according to the load demands could be an alternative solution for increasing the slew-rate at the gate of the pass device and provide a wider closed-loop bandwidth. As a result, significant advancements in the stability and dynamic performance of the LDO voltage regulator will be made. This can be successfully accomplished by employing two pass transistors, the smaller one for no-load to light-load conditions, and the larger one for light-load to full-load conditions. This would offer a proper tradeoff between circuit complexity, power dissipation of the control circuitry, and overall dynamic performance.

In previous work [15], the authors carried out a stability and transient analysis on a LDO voltage regulator with two different size-segmented pass transistors in comparison to the conventional one, which has a single large size pass device and assuming the pass transistors are in the saturation region all the time for simplicity's sake. However, this is an approximation that may not be valid for all load conditions, especially for light and heavy loads. As such, there is a significant difference between the theory and simulation results under certain load conditions. This issue

EBSCOhost - printed on 2/14/2023 2:46 PM via . All use subject to https://www.ebsco.com/terms-of-use

needs to be reconsidered and reformulated to resolve these differences. Pass transistor operation in different regions depending on the load current, in the subthreshold region under no-load condition and the triode one by increasing the load current, is applied to derive the pole-zero equations.

Consequently, better relations for ensuring the stability and a wider bandwidth are achieved. In addition, a reliable and closed form output pole was calculated considering the feedback loop from the output of the LDO voltage regulator. These findings will inform the fabrication of the next generation of LDO voltage regulators meeting the characteristics of higher stability, lower power consumption, and improved dynamic performance at the expense of adding control circuitry.

## Acknowledgement

This work has been partially supported by the Spanish Ministerio de Ciencia, Innovación y Universidades (MICINN) – Agencia Estatal de Investigación (AEI), and the European Regional Development Funds (FEDER), by project PGC2018-098946-B-I00.

## References

[1] S. Davis. *Power Management. Power Supplies, Systems, Applications, Components, Semniconductors*. Ed. Penton Media, Inc., 2016. http://pages.electronicdesign.com/power-management-series (Aug. 22th, 2018).

[2] Fathipour, R.; Saberkari, A.; Martínez-García, H.; Alarcón-Cot, E. (2014). *High Slew Rate Current Mode Transconductance Error Amplifier for Low Quiescent Current Output–Capacitorless CMOS LDO Regulator*. Integration. The VLSI Journal, 47(2), 204–212. doi: 10.1016/j.vlsi.2013.10.005.

[3] Vahideh Shirmohammadli, Alireza Saberkari; Herminio Martínez-García; Eduard Alarcón-Cot. (2017). *Low Power Output-Capacitorless Class-AB CMOS LDO Regulator*. Proceedings of the 2017 IEEE International Symposium on Circuits and Systems (ISCAS'17). doi: 10.1109/ISCAS.2017.8050958.

[4] M. Day (2006). *Understanding Low Drop Out (LDO) Regulators.* Texas Instruments, SLUP239, 9-1 – 9-6. http://www.ti.com/lit/ml/slup239/slup239.pdf (Aug. 22th, 2018).

[5] Rincón-Mora, G. A. (2009). *Analog IC Design with Low-Dropout Regulator.* New York: McGraw-Hill.

[6] Rincón-Mora, G. A. & Allen, P. E. (1998). *A Low-Voltage, Low Quiescent Current, Low Drop-Out Regulator.* IEEE Journal of Solid-State Circuits,

EBSCOhost - printed on 2/14/2023 2:46 PM via . All use subject to https://www.ebsco.com/terms-of-use

33(1), 36–44. doi: 10.1109/4.654935.

[7] Chava, C. K. & Silva-Martínez, J. (2004). *A Frequency Compensation Scheme for LDO Voltage Regulators*. IEEE Transactions on Circuits and Systems–I: Regular Papers, 51(6), 1041–1050. doi: 10.1109/TCSI.2004.829239.

[8] Milliken, R. J.; Silva-Martínez, J. & Sánchez-Sinencio, E. (2007). *Full On-Chip CMOS Low-Dropout Voltage Regulator*. IEEE Transactions on Circuits and Systems–I: Regular Papers, 54(9), 1879–1890. doi: 10.1109/TCSI.2007.902615.

[9] King, B. M. (2000). *Advantages of Using PMOS-Type Low-Dropout Linear Regulators in Battery Applications*. Texas Instruments Incorporated, Analog Applications Journal (Power Management), 16–21.

[10] Chen, H.-P. ; Liao, Y.-Z. & Lee, W.-T. (2009). *Tunable Mixed-Mode OTA-C Universal Filter*. Analog Integrated Circuits and Signal Processing, 58(2), 135–141. doi: 10.1007/s10470-008-9228-z.

[11] Kim, D. Y.; Choi, S. W.; Ahn, J. C. & Fujii, N. (1990). *The Design and Comparison of Elliptic filters with OTA-C Structure*. Proceedings of the IEEE 33rd Midwest Symposium on Circuits and Systems (MWSCAS 1990). doi: 10.1109/MWSCAS.1990.140761.

[12] Jun, C. & Guican, C. (2001). *A CMOS Bandgap Reference Circuit.* Proceedings of the 4th International Conference on ASIC. doi: 10.1109/ICASIC.2001.982550.

[13] Tantawy, R. & Brauer, E. J. (2004). *Performance Evaluation of CMOS Low Drop-Out Voltage Regulator.* Proceedings of the IEEE 47th International Midwest Symposium on Circuits and Systems (MWSCAS 2004). doi: 10.1109/MWSCAS.2004.1353917

[14] A. Saberkari, F. Qaraqanabadi, V. Shirmohammadli, H. Martinez, and E. Alarcon, “Output-capacitorless segmented low-dropout voltage regulator with controlled pass transistors,” Wiley Int. J. Circ. Theor. Appl., vol. 44, no. 2, pp. 460–475, Feb. 2016.

[15] V. Shirmohammadli, A. Saberkari, H. Martinez, and E. Alarcon, “Enhancing the performance of output-capacitorless LDO regulators by pass-transistor segmentation,” in Proc. IEEE Int. Symp. Circuits Syst. (ISCAS’16), May 2016, pp. 490–493.

EBSCOhost - printed on 2/14/2023 2:46 PM via . All use subject to https://www.ebsco.com/terms-of-use

# CHAPTER TWENTY-NINE

# COMPARATIVE ASPECTS OF CONTROL STRATEGIES FOR HYBRID DC/DC REGULATORS WITH VARIABLE-SWITCHING FREQUENCY

HERMINIO MARTÍNEZ-GARCÍA[1]
ALIREZA SABERKARI[2]
ENCARNA GARCÍA-VÍLCHEZ[1]

## Abstract

Linear-assisted DC/DC regulators (or linear-switching hybrid DC/DC regulators) consist of a linear voltage regulator (classic NPN/nMOS topologies or PNP/pMOS low-dropout structures) connected in parallel with a switching DC/DC converter. They are a good candidate for energy processing in photovoltaic solar facilities. In order to control these hybrid structures, different strategies exist that allow the switching frequency to be fixed as a function of certain parameters of the linear regulator. This chapter compares two control strategies that, although they can be applied to the same circuit structure with a linear-assisted regulator, are different. The first one, as reported in the existing literature, completely cancels out the average current through the linear regulator in a steady state to achieve a reduction in losses. Thus, the efficiency of the whole system increases

[1] Department of Electronics Engineering, Eastern Barcelona School of Engineering (EEBE), Diagonal-Besòs Campus, Technical University of Catalonia—BarcelonaTech (UPC), Eduard Maristany Ave., nº 10–14, E-08019. Barcelona, Spain. E-mail: herminio.martinez@upc.edu
[2] Microelectronics Research Laboratory, Department of Electrical Engineering, University of Guilan, Rasht, Iran. E-mail: a_saberkari@guilan.ac.ir

EBSCOhost - printed on 2/14/2023 2:46 PM via . All use subject to https://www.ebsco.com/terms-of-use

and almost equals one with a standalone switching converter. The proposed approach, in spite of a slight increment in the linear regulator's losses, reduces output ripple due to the crossover distortion of the linear regulator output stage.

**Keywords:** DC/DC switching converters; linear voltage regulators; linear-assisted DC/DC voltage regulators.

## Introduction

Two different methods have been widely used for decades to provide the necessary power supply voltage of electronic circuits and systems. These two alternatives are: (1) the use of series linear voltage regulators (standard NPN—or nMOS in MOS version—topologies and PNP/pMOS low-dropout (LDO) structures) [1]-[2]-[3]; and (2) DC/DC switching converters, with which high current and high efficiency power supply systems can be achieved [4]-[5]-[6].

However, a third alternative, with a linear-assisted DC/DC regulator (also known as a linear-switching hybrid regulators), is possible. These circuit structures are the subject of increasing interest for implementation in power supply systems that have two demanding design specifications: (1) high slew-rate of the output current; and (2) high current consumption by the output load. This is the case with systems using modern microprocessors and DSPs, where both requirements converge [7]-[8]. These linear-switching hybrid regulators are able to combine the well-known advantages of the two existing alternatives in the implementation of DC/DC voltage regulators or converters, reducing their disadvantages. Linear-assisted DC/DC regulators can be implemented using printed circuits and with discrete components. They offer an attractive alternative and can be integrated into on-chip power supply systems as part of power management systems.

The basic scheme of a linear-assisted regulator is shown in Fig. 1 [9]-[10]. This structure primarily consists of a voltage linear regulator in parallel with a step-down switching DC/DC converter. In this type of regulator, the value of the output voltage, considered to be a constant, is fixed with high precision by the voltage linear regulator. The current through this linear regulator is continuously sensed by the current sense element $R_m$. According to its value, the controller either activates or does not activate the output of the comparator $CMP_1$ that controls the switching element of the DC/DC converter. Notice that the current through the linear

EBSCOhost - printed on 2/14/2023 2:46 PM via . All use subject to https://www.ebsco.com/terms-of-use

regulator constitutes a measurement of the error of the power supply system.

At the output, the power stage (the switching converter) injects the current required to force the current through the linear regulator up to a minimum value (not necessarily zero). As a consequence, a power supply system is obtained where the switching frequency is fixed, among other parameters (such as the possible hysteresis of the analog comparator), by the value of the current passing through the linear regulator.

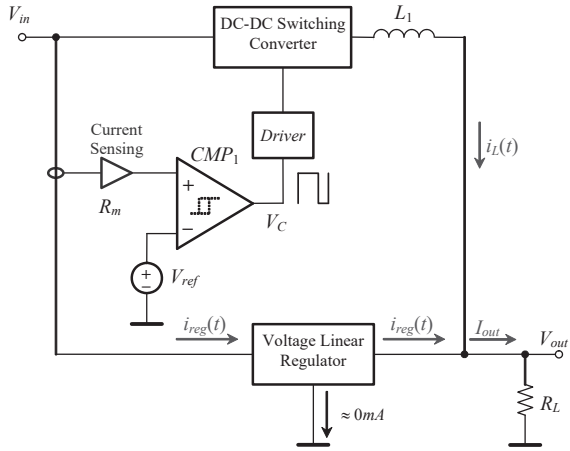



Figure 1. Block diagram of a linear-assisted regulator.

An additional advantage of the structure shown in Fig. 1, and in contrast to what happens in other hybrid structures that work in an open loop [11], is that the use of filters in the respective outputs of the linear and switching blocks (and, therefore, the possible optimization or equalization of its group propagation delays) is not, in this case, necessary. This chapter allows us to compare two control strategies that can be applied to the same circuit structure of a linear-assisted regulator. However, they are significantly different. The first one (that we will denominate *A* and has previously been reported in the literature [12]-[13]), attempts to completely cancel out the current passing through the linear regulator in a steady state in order to achieve a reduction in losses. Thus, the efficiency of the whole system increases and almost equals that of the switching converter. This system sees the switching DC/DC converter as the primary block and the linear regulator as the auxiliary module.

EBSCOhost - printed on 2/14/2023 2:46 PM via . All use subject to https://www.ebsco.com/terms-of-use

The alternative proposal (strategy *B*) allows an averaged current to flow through the linear regulator. Despite a slight increase in the linear regulator's losses, this strategy reduces output ripple due to the crossover distortion at its output stage. As such, this approach sees the linear one as the primary block and the switching one as the auxiliary module.

In Section 2, the strategy for control *A* is discussed and its advantages and drawbacks are considered. In Section 3 the strategy for control *B* is compared to *A*. In Section 4 the linear-assisted regulator is modified to improve its transient response. Finally, some conclusions are offered in Section 5.

## Control Strategy *A*

The first of the two control strategies considered in this chapter is implemented with a hybrid regulator as in Fig. 2. The linear-assisted regulator consists of a linear regulator (including transistors $Q_{2a}$ and $Q_{2b}$, which form an output complementary push-pull stage) and a switching DC/DC converter connected in parallel with the first one. In this case, the switching converter is a step-down type (buck converter) without output capacitance. In this strategy, the switching converter is considered to be the main block and the linear regulator is considered to be the auxiliary block that "assists" the first one when it is not able to provide output currents with high variations (that is to say, with a high slew rate of the load current).

This control strategy consists of sensing the current passing through the linear regulator and transforming it into a voltage (thanks to the current sensing element $R_m$), controlling the switching frequency of the DC/DC switching converter. The main objective is to provide ***all*** the load current in steady-state conditions (to obtain high efficiency across the whole system). Thus, in steady-state conditions the linear regulator does not provide current to the load, but it maintains the output voltage at an acceptable DC value.

However, when variable output loads are driven, the linear regulator enables high transitory changes in the current in order to maintain a constant output voltage for the whole structure (Fig. 3). Therefore, we can consider this type of control to be a ***control strategy with null average linear regulator current***. Resistors $R_1$ and $R_2$ of the Schmitt trigger determine the width of the hysteresis cycle and, thus, the maximum value of the switching frequency of the DC/DC converter.

EBSCOhost - printed on 2/14/2023 2:46 PM via . All use subject to https://www.ebsco.com/terms-of-use

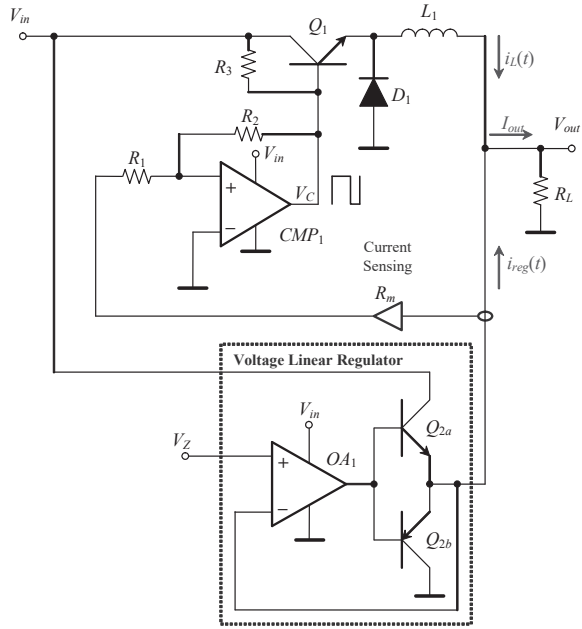



Figure 2. Basic structure of a linear-assisted regulator in control strategy *A*.

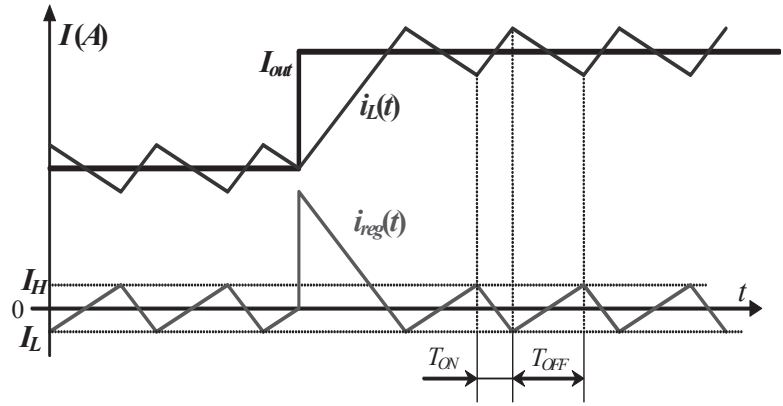



Figure 3. Principle of operation of a linear-assisted regulator with control strategy *A*.

EBSCOhost - printed on 2/14/2023 2:46 PM via . All use subject to https://www.ebsco.com/terms-of-use

## Control Strategy *B*

The strategy proposed here is analyzed using the step-down switching converter shown in Fig. 4 [14]-[15]. As in Fig. 2, the linear regulator also consists of a push-pull output stage (transistors $Q_{2a}$ and $Q_{2b}$). In this strategy, the main objective of the DC/DC switching converter is to provide most (but ***not all***) of the load current in steady-state conditions to achieve a good level of efficiency across the whole system. Thanks to the incorporation of the reference voltage $V_{ref}$ at the inverting input of the analog comparator $CMP_1$, the linear regulator provides a small part of the load current in a steady state, maintaining the output voltage at an acceptable constant value.

As a matter of fact, if the current demanded by the load is lower than the maximum value of the current, the ***switching threshold current*** $I_\gamma$, the output of the comparator $CMP_1$ will be low, disabling the DC/DC switching converter and, thus, the current through the inductor $L_1$, which will be zero. Therefore, the voltage linear regulator supplies the load $R_L$, providing all the output current ($I_{reg} = I_{out}$).

When the current demanded by the load surpasses the current limit $I_\gamma$, the output of the comparator will automatically shift to a high level, causing the current through the inductance $L_1$ to grow linearly, according to:

$$i_L(t) = \frac{V_{in} - V_{out}}{L_1} t + I_L(\tau_1) \tag{1}$$

In this expression, the conduction collector-emitter voltage of transistor $Q_1$ is ignored. $I_L(\tau_1)$ is the initial value of the current through the inductor $L_1$ at the time instant $T_{ON}$. Considering the output current to be $I_{out} = I_{reg} + I_L$, and assuming it to be constant (equal to $V_{out}/R_L$), the linear regulator current $I_{reg}$ will decrease linearly, becoming slightly smaller than $I_\gamma$. At this moment, the comparator will change its output to a lower level, cutting the transistor $Q_1$ and causing the current through the inductor to decrease according to equation (2):

$$i_L(t) = -\frac{V_{out}}{L_1} t + I_L(\tau_2) \tag{2}$$

In this expression, the diode $D_1$ is considered ideal (with zero direct voltage). $I_L(\tau_2)$ is the maximum value reached by the current flowing

EBSCOhost - printed on 2/14/2023 2:46 PM via . All use subject to https://www.ebsco.com/terms-of-use

through the inductor (just at the beginning of the interval $T_{OFF}$). When the inductor current decreases to a value in which $I_{reg}>I_{\gamma}$, the comparator changes its state to a high level, repeating the cycle.

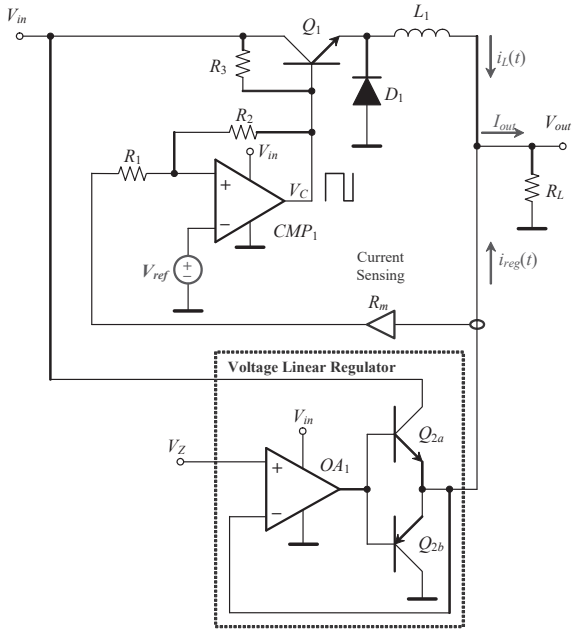



Figure 4. Basic structure of a linear-assisted regulator with control strategy *B*.

Without hysteresis in the comparator, the switching point of the DC/DC switching converter is given by the switching threshold current $I_{\gamma}$, of the linear regulator. This can be adjusted to a desired value thanks to the gain of the current sensing element $R_m$, and the reference voltage $V_{ref}$, according to the expression:

$$I_{\gamma} = \frac{V_{ref}}{R_m} \tag{3}$$

In the case of a comparator without hysteresis, intrinsic delays in the electronic circuits will determine a small hysteresis that limits the maximum value of the linear-assisted regulator's switching frequency (Fig. 5). However, with the objective of fixing this switching frequency to

EBSCOhost - printed on 2/14/2023 2:46 PM via . All use subject to https://www.ebsco.com/terms-of-use

a practical value, in order not to significantly increase losses by the switching process, it is important to add the aforementioned hysteresis to the comparator $CMP_1$.

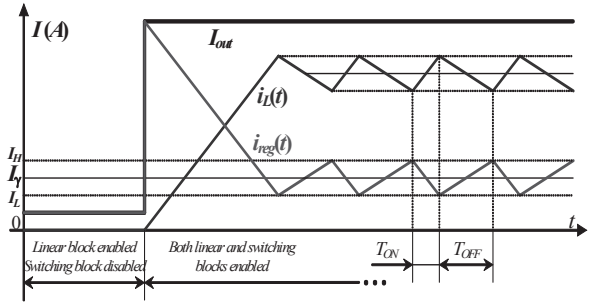



Figure 5. Principle of operation of a linear-assisted regulator with control strategy *B*.

Notice that if the load current is below $I_\gamma$, the switching block (the DC/DC converter) is disabled in order to minimize its losses. Thus, only the linear regulator provides the output current for slight load conditions. Fig. 6 shows the experimental efficiency versus the load current of the two strategies. A comparison of control strategy *A* and the one proposed by authors (strategy *B*) is shown for $V_{out} = 5\ V$. Four different $I_\gamma$ values are shown: 0 *mA* (strategy *A*); and 10 *mA*, 50 *mA*, and 100 *mA* (all for strategy *B*). Note that if $I_\gamma$ is low, efficiency is almost unaffected, reducing output ripple too.

## Improvement of the Linear-assisted Regulator with Control Strategy *B*

Studying the preceding figures, it is possible to question the necessity or not of using the transistor PNP $Q_{2b}$ in the scheme laid out in Fig. 4, since, in steady state conditions (and unlike strategy *A*), it always remains in cut. However, its inclusion is necessary to increase the response speed of the linear regulator from decremental variations of the load current. In fact, one of the objectives of the linear regulator, besides achieving excellent regulation of the output voltage, free of ripples, is to provide fast current responses to abrupt variations in the load consumption. The switching DC/DC converter cannot respond to these variations of the output current. As such, current transients must be provided (or absorbed,

EBSCOhost - printed on 2/14/2023 2:46 PM via . All use subject to https://www.ebsco.com/terms-of-use

depending on whether the variation of the load current is incremental or decremental) by the linear regulator.

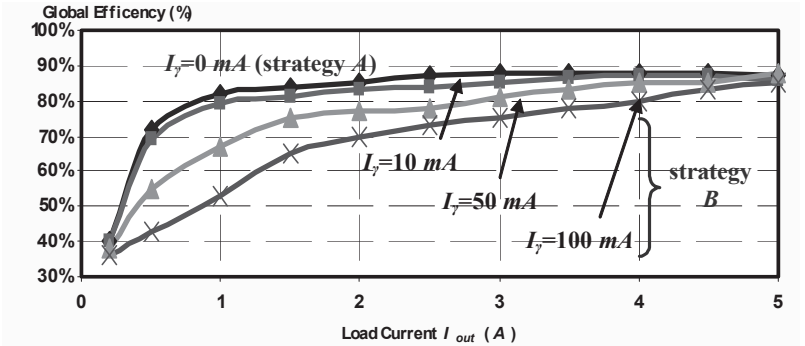



Figure 6. Experimental efficiency for control strategy *A* and for the one proposed by the authors (strategy *B*) with $V_{out}$ = 5 *V*. Four different $I_\gamma$ values are shown: 0 *mA* (strategy *A*); and 10 *mA*, 50 *mA*, and 100 *mA* (all for strategy *B*).

This is shown in the previous figures when the consumption of the load increases from an initial value (in this case 1 *A*) to an end value that is greater (equal to 2 *A*). Nevertheless, it is important to note that, if the response is to be maintained for descendent variations of the load current, the linear voltage regulator must incorporate the transistor $Q_{2b}$ (in both Fig. 2 and Fig. 4) to allow bidirectional output currents.

In Fig. 7, we can see the response of the proposed hybrid regulator in Fig. 4 without the $Q_{2b}$ transistor—with an increase in the load current at $t$ = 40 μ*s* and a decreasing variation at $t$ = 60 μ*s*. Note that the answer provided by the linear regulator for ascending variations of the load current is good enough, and allows, therefore, the output voltage to be maintained at a set constant during the transient. However, the set response is not appropriate for descendent variations, as it is the response time of the setup marked by the switching converter and loses the load regulation at that time interval.

However, for the hybrid regulator in Fig. 4, if the transistor PNP $Q_{2b}$ is added, its response improves significantly when the load current decreases. In Fig. 8 we can see that, when a decrease in the output current takes place from 2 *A* to a 1 *A* at $t$ = 60 μ*s*, the transistor $Q_{2b}$, included in the linear regulator, can absorb the excess current, provided by the inductor $L_1$, that the load no longer accepts. Thus, the linear regulator can maintain the output voltage with good regulation (free of ripples) even with decreasing transients. Finally, Fig. 9 shows experimental details of the

EBSCOhost - printed on 2/14/2023 2:46 PM via . All use subject to https://www.ebsco.com/terms-of-use

load regulation when the load current changes from 5 *A* to 1.4 *A* for the hybrid regulator, without (Fig. 9.*a*) and with (Fig. 9.*b*) the transistor $Q_{2b}$. The switching threshold current is adjusted to 50 *mA*.

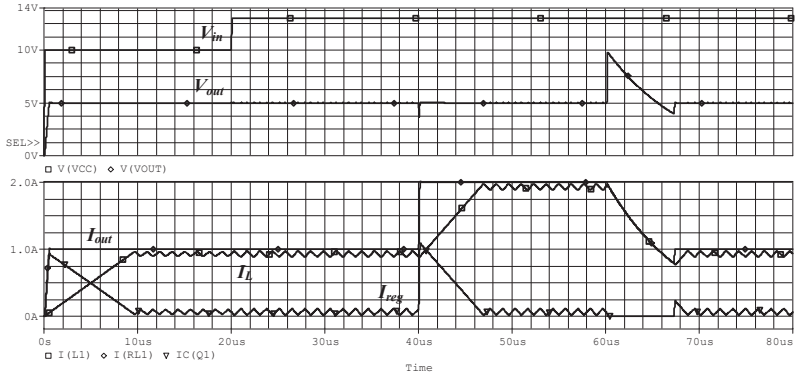



Figure 7. Detail of the lack of load regulation when the load current changes from 2 *A* to 1 *A* at $t$ = 60 μ*s* for the regulator in Fig. 4 without the transistor $Q_{2b}$ (variation in the load resistance from 2.5 Ω to 5 Ω). The switching threshold current is adjusted to 50 *mA*.

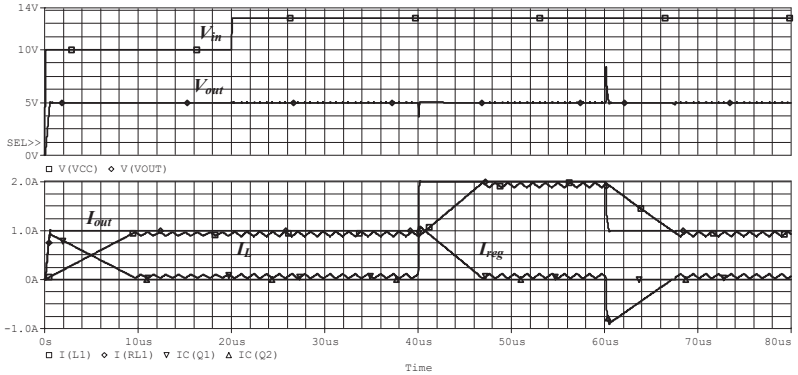



Figure 8. Details of the improvement obtained in load regulation when the load current changes from 2 *A* to 1 *A* at the time instant $t$ = 60 μ*s* for the hybrid regulator with the transistor $Q_{2b}$ (variation in the load resistance from 2.5 Ω to 5 Ω). The switching threshold current is adjusted to 50 *mA*.

EBSCOhost - printed on 2/14/2023 2:46 PM via . All use subject to https://www.ebsco.com/terms-of-use

# Further Research: Current-mode One-cycle Linear-assisted DC/DC Regulator

## *One-cycle Control Concept*

One-cycle control was proposed by Keyue M. Smedley in 1991 and realized initially with a buck PWM converter [16]-[17]-[18]. DC/DC switching converters with one-cycle control reject input perturbations in only one switching cycle and instantly follow the control reference. It has been said that one-cycle control is universal and can be applied directly to switching converters in either PWM or quasi-resonant modes [18]-[19]. Boost converters, Cûk converters, three-phase PFC converters, and three-phase boost rectifiers have all been presented with one-cycle control. A general-purpose feed-forward one-cycle controller was also advanced.

One-cycle control theory is shown in Fig. 10 and its operating waveforms are shown in Fig. 11.

## *Topology of the Current-mode One-cycle Linear-assisted DC/DC Regulator*

Based on the variable-frequency linear-assisted DC/DC regulator presented in Fig. 1, the structure of the proposed linear-assisted DC/DC regulator with a current-mode one-cycle control strategy is shown in Fig. 12. In this figure, we can see the linear regulator, the switching DC/DC converter, and the control loop that fixes the duty cycle of the switch element $Q_1$.

The basic idea of the proposed control is to achieve an average inductor current during the time interval $T_{ON}$ equal to the output current. As such, we take into account that:

$$i_L(t) + i_{reg}(t) = I_{out}, \tag{4}$$

EBSCOhost - printed on 2/14/2023 2:46 PM via . All use subject to https://www.ebsco.com/terms-of-use

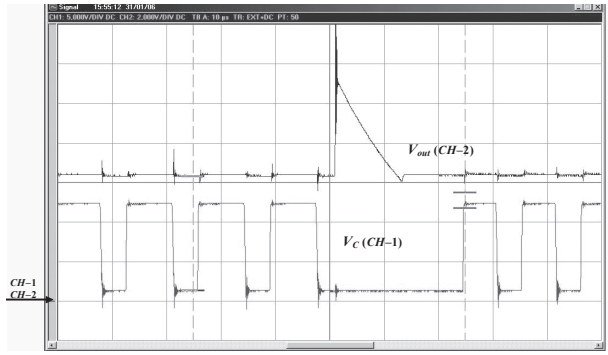



Figure 9. Experimental results of load regulation when the load current changes from 5 *A* to 1.4 *A* for the hybrid regulator: **(*a*)** without, and **(*b*)**, with the transistor $Q_{2b}$. The switching threshold current is adjusted to 50 *mA*.

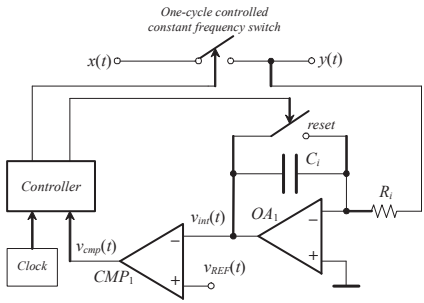



Figure 10. Basic scheme for one-cycle control.

EBSCOhost - printed on 2/14/2023 2:46 PM via . All use subject to https://www.ebsco.com/terms-of-use

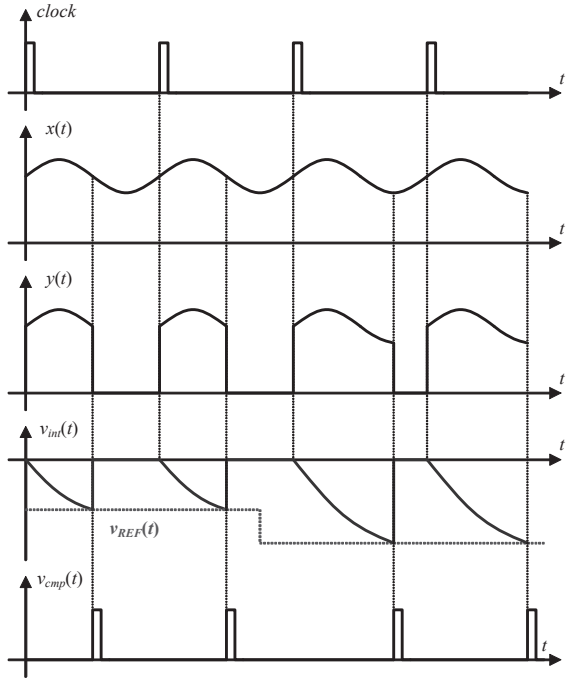



Figure 11. Typical waveforms of one-cycle control.

The average value provided by the linear regulator block will tend to be zero. In addition, note that the main difference with one-cycle control is that the linear regulator fixes the output voltage. In fact, the output voltage is given (and fixed) by the linear regulator. Therefore, according to what was described before, the new proposed technique can reject not only power disturbances, but load disturbances too.

The main idea of the proposed control is to achieve an average value for the current flowing across the inductor during the time interval $T_{ON}$ ($=\overline{d}(t)T_S$) equal to the average value of the current flowing through the load during this interval. Therefore, considering that the output current is given by $I_{out} = I_{reg} + I_L$, as mentioned above, the average current flowing through the linear regulator will tend towards zero.

EBSCOhost - printed on 2/14/2023 2:46 PM via . All use subject to https://www.ebsco.com/terms-of-use

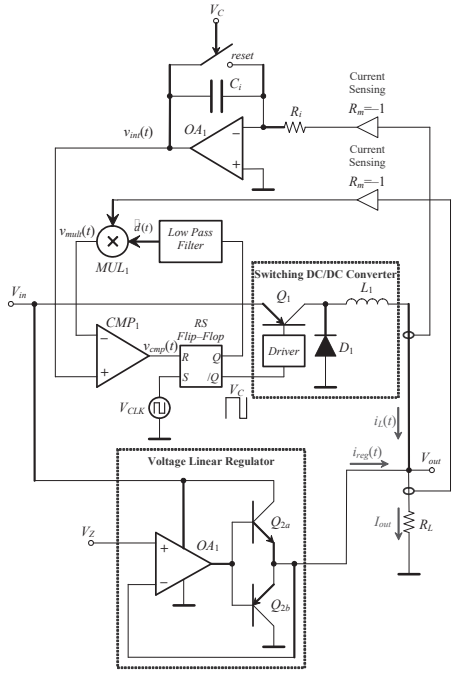



Figure 12. Basic structure of a current-mode one-cycle linear-assisted DC/DC regulator.

On the one hand, the low-pass filter extracts the average value of the duty cycle $\bar{d}(t)$, which is multiplied by the output current $I_{out}$ (considered constant), providing a measure of the average value of the current flowing through the load during the interval $T_{ON}$. Thus, considering the gain factor of the current sensing element $R_m = 1$, we have:

$$v_{mult}(t) = \bar{d}(t) I_{out} \tag{5}$$

On the other hand, the analog integrator provides a measurement of the average value of the current flowing across the inductor during the time interval $T_{ON}$, considering that the time constant is given by:

$$R_i C_i = T_S \tag{6}$$

EBSCOhost - printed on 2/14/2023 2:46 PM via . All use subject to https://www.ebsco.com/terms-of-use

Therefore:

$$v_{\text{int}}(t) = \frac{1}{R_i C_i}\int_o^t i_L(t)dt = \frac{1}{T_S}\int_o^t i_L(t)dt \quad , \tag{7}$$

where the gain factor of the current sensing element $R_m = -1$ (the negative sign compensates the additional inversion provided by the integrator).

The average value of the switched variable at the switch output is guaranteed to be:

$$\frac{1}{T_S}\int_o^{dT_S} i_L(t)dt = \bar{d}(t)I_{out} \quad , \tag{8}$$

in each cycle. Fig. 13 shows the operating waveforms of the circuit when $v_{REF}(t)$ is constant.

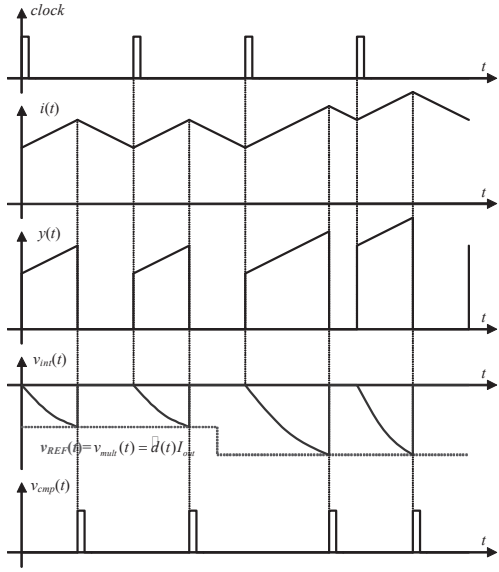



Figure 13. Typical waveforms of the proposed linear-assisted regulator with current-mode one-cycle control.

EBSCOhost - printed on 2/14/2023 2:46 PM via . All use subject to https://www.ebsco.com/terms-of-use

In order to validate the proposed structure of the current-mode one-cycle linear-assisted DC/DC regulator in Fig. 12, simulation results were obtained from a system that provides 5.0 $V$ at output $V_{out}$. The value of the inductor was $L$ = 100 $\mu H$. Fig. 14 shows the circuit and the start-up transient waveforms when the current-mode one-cycle linear-assisted DC/DC regulator provides 2 $A$ at output $V_{out}$. Note that the one-cycle control loop ensures a value of near zero for the average current flowing through the linear stage.

Fig. 15 shows the transient response of the linear-assisted DC/DC regulator when the reference voltage increases from 5 $V$ to 8 $V$ at 500 $\mu s$.

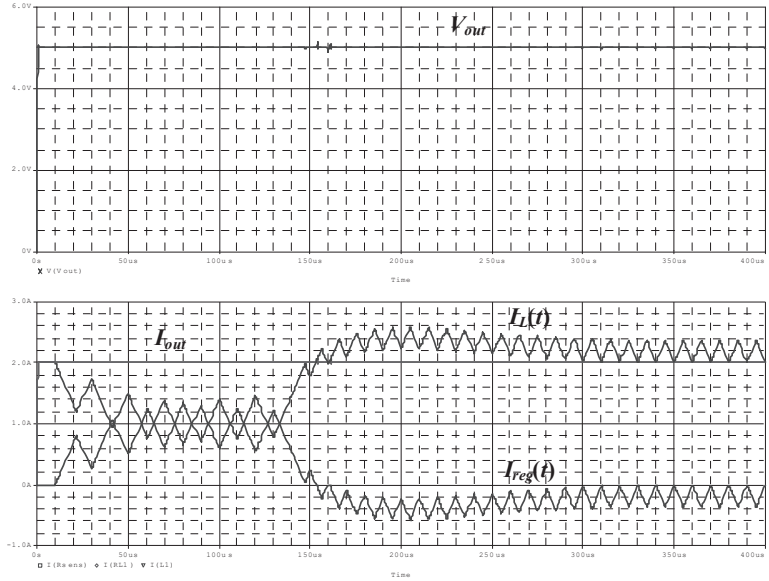



Figure 14. Start-up transient waveforms when the current-mode one-cycle linear-assisted DC/DC regulator provides 2 $A$ at output $V_{out}$. Note that the one-cycle control loop ensures a value of near zero for the average current flowing through the linear stage.

EBSCOhost - printed on 2/14/2023 2:46 PM via . All use subject to https://www.ebsco.com/terms-of-use

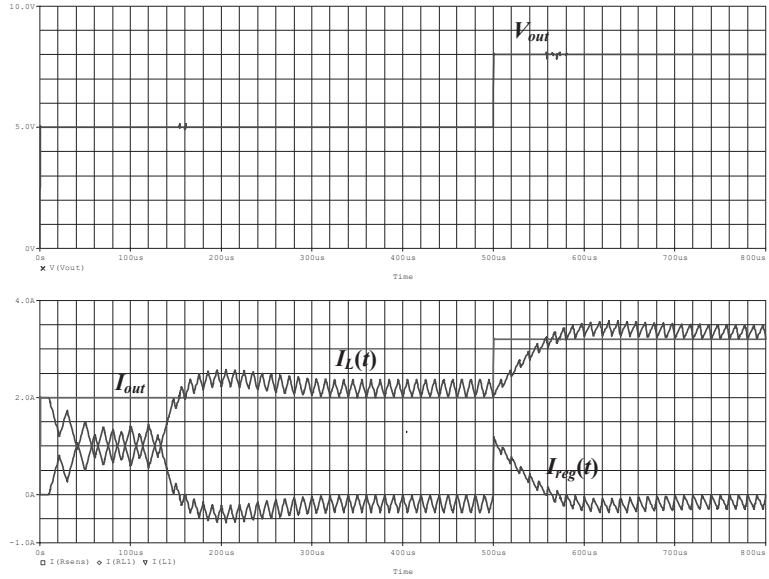



Figure 15. Transient response of the linear-assisted DC/DC regulator when the reference voltage increases from 5 *V* to 8 *V* at 500 μ*s*.

## Conclusions

This chapter has compared two different control strategies for power DC/DC linear-assisted (or hybrid) regulators based on the association of a linear regulator in parallel with a switching converter. The first of the two strategies (strategy *A* with a ***null average value in the linear regulator current***) achieves high efficiency, similar to switching converters, because, in steady state conditions, the power dissipated in the linear regulator is practically zero. However, it also sees the presence of a ripple output voltage because the pass transistor of the output linear stage is switching between the cut and the conduction in every switching period.

The proposal presented in this chapter (control strategy *B* with a ***non-null average value in the linear regulator current***), allows a little current through the linear stage, causing the efficiency of the setup to diminish slightly. However, it achieves an output voltage practically free of spurious ripples.

In addition, the design and simulation of a current-mode one-cycle control linear-assisted DC/DC regulator has been presented. The last part

EBSCOhost - printed on 2/14/2023 2:46 PM via . All use subject to https://www.ebsco.com/terms-of-use

of the chapter has shown that linear-assisted DC/DC regulators are suitable structures that utilize the advantages of the two classical alternatives when designing power supply systems (voltage linear regulators and switching DC/DC converters). Starting from this linear-assisted topology, and using the general idea of one-cycle control, a current-mode one-cycle linear-assisted DC/DC regulator has been proposed. The proposed DC/DC hybrid regulator offers good line regulation, thanks to its excellent power source disturbance rejection with a one-cycle control loop; sufficient load regulation thanks to its limited load disturbance with a linear regulator; and, finally, high efficiency with a switching converter.

Note that linear-assisted regulators presented in the first part of this chapter are variable-frequency structures. In this case, the switching frequency depends on the parameters of the regulator, and is not fixed by an external clock. This drawback affects the design of the hybrid regulator and the selection of its components. In addition, this feature is not desirable in some applications because variable switching frequencies may be inserted into the bandwidth of neighboring electronic circuits or even of the electronic system that the hybrid regulator supplies. Thus, further research in this area may see an improvement in the design topology of a ***constant-frequency linear-assisted regulator***. In this new structure, it is possible to choose the desired switching frequency independently of the component values. Note that one possibility is presented in the last part of this chapter with the description of a current-mode one-cycle linear-assisted DC/DC regulator, in which the clock generator $V_{CLK}$ (see Fig. 12) fixes this switching frequency.

However, it is also possible to have new ***constant-frequency*** alternatives where the control loop of the system uses the current-mode technique. The main disadvantage of a hybrid regulator with current-mode control is the inherent instability of the loop when switching duty ratios are greater than 0.5. In order to make the proposed linear-assisted regulator stable, the control loop should include a technique based on slope compensation.

## Acknowledgement

This work has been partially supported by the Spanish Ministerio de Ciencia, Innovación y Universidades (MICINN) – Agencia Estatal de Investigación (AEI), and the European Regional Development Funds (FEDER), by project PGC2018-098946-B-I00.

EBSCOhost - printed on 2/14/2023 2:46 PM via . All use subject to https://www.ebsco.com/terms-of-use

## References


[1] C. K. Chava, J. Silva-Martínez. "A Frequency Compensation Scheme for LDO Voltage Regulators." *IEEE Transactions on Circuits and Systems–I: Regular Papers*, vol. 51 (nº 6): pp.1041–1050, June 2004.

[2] R. J. Milliken, J. Silva-Martínez, E. Sánchez-Sinencio. "Full On-Chip CMOS Low-Dropout Voltage Regulator." *IEEE Transactions on Circuits and Systems–I: Regular Papers*, vol. 54 (nº 9): pp.1879–1890, September 2007.

[3] V. Grupta, G. A. Rincón-Mora, P. Raha. "Analysis and Design of Monolithic, High PSR, Linear Regulator for SoC Applications." *Proceedings of the IEEE International SoC Conference*: pp.311–315, 2004.

[4] R. W. Erickson, D. Maksimovic. *Fundamentals of Power Electronics*. 2nd edition, Ed. Kluwer Academic Publishers, 2001.

[5] J. G. Kassakian, M. F. Schlecht, G. C. Verghese. *Principles of Power Electronics*. Ed. Addison-Wesley, 1991.

[6] N. Mohan, T. M. Underland, W. P. Robbins. *Power Electronics: Converters, Applications and Design*. Ed. John Wiley & Sons, 1989.

[7] X. Zhou, P. L. Wong, P. Xu, F. C. Lee, A. Q. Huang. "Investigation of Candidate VRM Topologies for Future Microprocessors." *IEEE Transactions on Power Electronics*, vol. 15 (nº 6): pp.1172–1182, November 2000.

[8] B. Arbetter, D. Maksimovic. "DC–DC Converter with Fast Transient Response and High Efficiency for Low-Voltage Microprocessor Loads." *IEEE Applied Power Electronics Conference*, pp.156–162. 1998.

[9] P. Midya, F. H. Schlereth. "Dual Switched Mode Power Converter." *IECON. Industrial Electronics Society*: pp.155–158, 1989.

[10] F. H. Schlereth, P. Midya. "Modified Switched Power Convertor with Zero Ripple." *Proceedings of the 32nd IEEE Midwest Symposium on Circuits and Systems (MWSCAS'90)*: pp.517–520, 1990.

[11] V. Yousefzadeh, E. Alarcón, D. Maksimovic. "Band Separation and Efficiency Optimization in Linear-Assisted Switching Power Amplifiers." *Proceedings of the 37th IEEE Power Electronics Specialists Conference, 2006* (PESC'06), pp.1–7, 18-22 June 2006.

[12] R. Vázquez, A. Barrado, E. Olías, A. Lázaro. "Theoretical Study and Implementation of a High Dynamic Performance, High Efficiency and Low Voltage Hybrid Power Supply." *Proceedings of the IEEE 32nd Annual Power Electronics Specialists Conference, 2001* (*PESC 2001*), vol. 3: pp.1517–1522. 17-21 June 2001.

[13] A. Barrado, R. Vázquez, E. Olías, A. Lázaro, J. Pleite. "Theoretical Study and Implementation of a Fast Transient Response Hybrid Power Supply." *IEEE Transactions on Power Electronics*, vol. 19 (nº 4): pp.1003–1009, July 2004.


EBSCOhost - printed on 2/14/2023 2:46 PM via . All use subject to https://www.ebsco.com/terms-of-use

[14] H. Martínez, A. Conesa. "Modeling of Linear-Assisted DC–DC Converters." European Conference on Circuit Theory and Design 2007 (ECCTD 2007), 26th-30th August 2007.

[15] A. Conesa, H. Martínez, J. M. Huerta. "Modeling of Linear & Switching Hybrid DC-DC Converters." 12th European Conference on Power Electronics and Applications (EPE 2007), September 2007.

[16] K. M. Smedley, S. Cuk. "One-Cycle of Switching Converters." *Proceedings of the 22nd Power Electronics Specialists Conference.* (PESC'91): pp.888–896. 1991.

[17] K. M. Smedley, S. Cuk. "One-Cycle of Switching Converters". *IEEE Transactions on Power Electronics*, vol. 10 (nº 6): pp.625–633, November 1995.

[18] Z. Hu, B. Zhang, W. Deng. "Feasibility Study on One Cycle Control for PWM Switched Converters." *Proceedings of the 5th 35th Annual IEEE Power Electronics Specialists Conference*: pp.3359–3365, 2004.

[19] Y. Wang, S. Shen. "Research on One-Cycle Control for Switching Converters." *Proceedings of the 5th World Congress on Intelligent Control and Automation*: pp.74–77, June 2004.

EBSCOhost - printed on 2/14/2023 2:46 PM via . All use subject to https://www.ebsco.com/terms-of-use

# CHAPTER THIRTY

# A FREQUENCY DOMAIN SMPS MODEL FOR HARMONIC ESTIMATION

G. MALAGON-CARVAJAL, C. DUARTE, G. ORDONEZ-PLATA[1]

## Abstract

Loads using a switched-mode power supply (SMPS), e.g. home appliances or other power electronic (PE) devices, have increased in recent years. As such, harmonic analysis of these loads is useful for assessing current levels of distortion in low voltage grids. However, making an assessment that considers attenuation-amplification and diversity effects represents a challenge for harmonic modelling in the frequency domain (FD). This research presents two different methods for computing a frequency domain model (FDM) by using time domain model (TDM) simulations instead of current measurements when the magnitude and phase angle of the supply voltage harmonics change. The relevant FDM is based on the Norton equivalent model (NEM), which provides an admittance matrix suitable for assessing the impact of PE devices on harmonic current distortion, with lower computational costs than a TDM. These methods of computing the FDM are based on polar-plot fingerprints and rectangular-plots computed from TDMs. The FDM results were compared with the TDM results in terms of the magnitude relative error and the phase angle absolute error. This study demonstrates that the proposed method is appropriate for computing accurate and efficient FDMs from a set of current

[1] Universidad Industrial de Santander (UIS), Dept. of Electrical, Electronic and Telecommunications Engineering (E3T), Carrera 27 Calle 9, 680002, Bucaramanga, Colombia. Email: gabriel.malagon@correo.uis.edu.co, cedagua@uis.edu.co, gaby@uis.edu.co

EBSCOhost - printed on 2/14/2023 2:46 PM via . All use subject to https://www.ebsco.com/terms-of-use

and voltage waveforms, which may be obtained via TDM simulations or measurements.

**Keywords:** Time domain model; frequency domain models; harmonic attenuation-diversity; admittance matrix; SMPS.

## Introduction

PE devices based on SMPS have become widely adopted in the residential sector. Many users operating different home appliances connected to low voltage grids can inject a significant amount of harmonic current into the power grid, especially when operating under non-sinusoidal grid voltage conditions [1], [2]. As such, the characterization and modelling of residential loads is an important area of research [3].

For instance, the studies in [4]–[6] made use of sinusoidal, flat-top, and pointed-top distorted supply voltage waveforms in order to characterize the current drawn by home appliances. However, a small number of measurements may be insufficient to describe load harmonic behaviour under variations in the supply voltage. The studies in [7]–[9] use an extensive field-measurement-based approach to compute models for an actual range of harmonic variations of the supply voltage. Moreover, a frequency sweep process (FSP) is described in [10]–[13] using several laboratory measurements. [10] presents a study on the characterization of small photovoltaic inverters (PVIs) and [11] studies the interactions between these inverters and electric vehicle battery chargers (EVBC) using three typical waveforms. The experiments in [10] were limited to low odd-order harmonics superimposed onto the fundamental supply voltage component using three different configurations: 1) 'Single harmonics-H1'—one harmonic was superimposed at a time from the 3$^{rd}$ up to the 19$^{th}$ harmonic and 144 voltage/current waveforms were measured per harmonic order. 2) 'Combinations of harmonics-H2'—two harmonic orders were selected to be superimposed from the 3$^{rd}$, 5$^{th}$, and 7$^{th}$ harmonics; while one of the selected harmonics was kept constant, the phase angle and magnitude of the other were varied; 128 measurements were made per harmonic order. 3) 'Random combinations of harmonics-H3'—900 voltage waveforms were randomly selected from the 1,440 waveforms set in the first configuration (Single harmonics-H1). Moreover, in [12], 144 supply voltage distorted waveforms, including one harmonic at a time up to the 11$^{th}$ harmonic, were used to characterize household loads, and in [13], 3,000 supply voltage operating conditions up to the 19$^{th}$ harmonic order for an EVBC were examined. Nevertheless, a comprehensive current characterization requires

EBSCOhost - printed on 2/14/2023 2:46 PM via . All use subject to https://www.ebsco.com/terms-of-use

knowledge of load behaviour under different voltage operating conditions, a delimited operation zone, for instance, by standards for voltage regulation or distortion. Furthermore, extensive measurements without an automatic voltage control system can take a long time. In this chapter, a TDM previously proposed by the authors was modified for use as a generic SMPS, including CFLs, and several current signals for different voltage operating conditions were computed.

A TDM for a generic SMPS corresponds to a circuit-based model (CBM), which uses a circuital architecture or topology. Its main advantage is that it shows the best performance in describing the current waveform when harmonic magnitudes and phase angles of the supply voltage vary. Nonetheless, its long simulation times and the fact that model parameters are sometimes unknown make the modelling of collective harmonic distortion for multiple loads unfeasible. In an attempt to overcome this problem, two parameter estimation approaches have been proposed: a *measurement-based approach* [14]–[18] and an *optimization-based approach* [19], [20]. In [14], the model parameters were estimated from different indices, which are normally used to characterize current and voltage waveforms. The results were satisfactory, but only a few sets of measurements were used to assess performance. [15] and [16] used several measurements of electric components and manufacturer data to estimate the parameters of the model, which can be used to satisfactorily compute the current harmonic distortion of a group of home appliances [17], [18]. Using the second approach, [19] proposed *optimization of the error* between simulated and measured currents of the model presented in [20]. However, so far, model parameters using this approach have only been computed for 230 V, 50 Hz circuits.

A FDM for a generic SMPS may be computed by two different approaches: a *measurement/simulation-based approach* and an *analytical derivation-based approach*. In the *first approach*, the voltage and current measurements or time domain (TD) simulations are transformed into the FD and harmonic current source models (HCSM) or coupled/decoupled NEMs are built from them. The advantages, disadvantages, and performance assessments of these models are presented in [20]–[22]. Additionally, a number of different methods to compute the admittance matrix have been proposed in [9] and [23]–[29]. [24]–[27] present mathematical methods for computing the admittance matrix element by element or using matrix inversion procedures. In [9] and [24]–[27], mathematical methods for computing the admittance matrix element by element or using matrix inversion procedures are presented. [23], [28], and [29] further investigate the effects of supply voltage harmonic distortion on harmonic currents

EBSCOhost - printed on 2/14/2023 2:46 PM via . All use subject to https://www.ebsco.com/terms-of-use

through polar-plots of admittances or currents/voltages (fingerprints); but only [28] and [29] include the modelling of the admittance phase angles. With the *analytical derivation approach*, the FDM is computed from analytical expressions of waveforms or circuit models in the TD, which were then transformed into the FD. For instance, in [30] and [31], this approach was used to compute a harmonically-coupled admittance matrix (HCAM) based model, whose performance was assessed through modelling a three-phase diode-bridge rectifier [32], CFLs [33], and home appliances [9].

The main challenge to overcome with FDMs is the successful estimation of harmonic currents when *attenuation-amplification* and *diversity* effects are present. *Attenuation-amplification* is defined in [34] and [35] as the interaction between a distorted voltage and the system equivalent series impedance when loads are aggregated (to compute a parallel equivalent). As a result of this interaction, an attenuation or amplification of the current distortion may occur [36], [37]. *Diversity* is described as the partial cancellation of harmonic currents of different loads at the point of common coupling (PCC). This cancellation is caused by a dispersion in the harmonic current phase angles, which is related to the characteristics of the load, variations in demand, or parameters such as rated power or power factor [34], [35], [38]. In order to cope with *attenuation-amplification* and *diversity* effects, the procedure for computing a FDM must include the supply voltage harmonic magnitude and phase angle variations. Most of the methods found in the literature consider variations in the harmonic magnitude; some of them also investigate and analyse the effect of variations in the harmonic phase angle on the elements of the admittance matrix, as in [29] where the admittance is computed in the form of a larger tensor model, and [28] where the model also makes use of an admittance matrix.

This work is a revised and extended version of reference [28], which was presented at the International Conference on Renewable Energies and Power Quality (ICREPQ'17). The simulations and results have been extended to include 21,600 signals or voltage operating points obtained from: 20 step magnitude variations; 72 step phase angle variations; and 15 odd harmonic orders. Each supply voltage signal and its correspondent current signal were computed through MATLAB & Simulink® TDM simulations. These synthetic signals were used to carry out the model training process to produce the admittance matrix. Model validation was performed using 10,000 random signals. For both processes, model training and model validation, the error was computed in order to compare the results proposed in [23] and [28] to the results of the TDM in [20].

EBSCOhost - printed on 2/14/2023 2:46 PM via . All use subject to https://www.ebsco.com/terms-of-use

This chapter is organized as follows: The Generic SMPS Time Domain Model section describes the blocks and parameters of the TDM. In The SMPS Frequency Domain Model section, the structure of the FDM, the simulation-experiment framework, the polar-plot fingerprints, the rectangular-plots, and the method of computing the admittance matrix are addressed. In the Analysis and Results section, the relative and absolute errors are proposed to assess the performance of the method. Finally, the conclusions of this research are presented.

## The Generic SMPS Time Domain Model

### *SMPS circuit-based model*

The generic TDM corresponds to the circuit-based model (CBM) presented in Fig. 1 and comprises: a power supply $Vs$; a rectifier bridge composed of diodes ($D_1$, $D_2$, $D_3$, and $D_4$); an input resistance $R$; an input filter inductance $L$; a DC link capacitance $C$; and an equivalent resistance $Req$, which can be a function of DC link voltage $v(t)$, as explained in [20] for a compact fluorescent lamp (CFL).

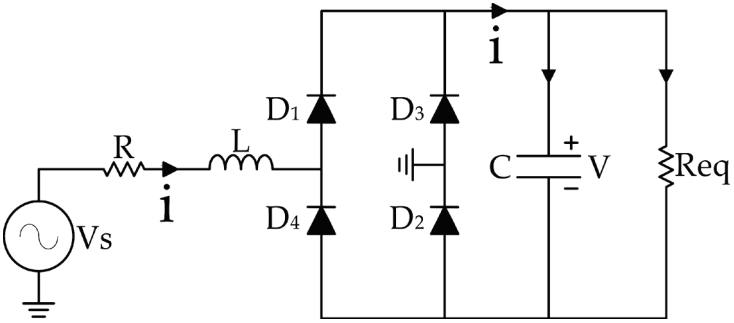



Figure 1. The generic SMPS circuit-based model (CBM)

In this generic SMPS model, two states are defined: *charging state* and *discharging state*. These states are determined by the input current, the DC capacitor, and the conduction states of the diode bridge. In this model, these diodes are modelled as ideal diodes.

EBSCOhost - printed on 2/14/2023 2:46 PM via . All use subject to https://www.ebsco.com/terms-of-use

### *Charging state*

In this state, diodes $D_1$ and $D_2$ conduct during the positive semi-cycle of $v_s(t)$ and diodes $D_3$ and $D_4$ during the negative semi-cycle. Each pair of diodes start conducting when the DC link voltage $v(t)$ is greater than the rectified supply voltage $|v_s(t)|$ and stop conducing when the input current $i(t)$ reaches the value zero with negative slope. According to Kirchhoff's Laws, the input current $i(t)$ and the DC link voltage $v(t)$ comply with:

$$v_s(t) = R\,i(t) + L\frac{di(t)}{dt} + v(t) \quad , \tag{1}$$

$$i(t) = C\frac{dv(t)}{dt} + \frac{v(t)}{Req} \quad . \tag{2}$$

Using equations (1) and (2) the generic SMPS time domain model can be represented by a continuous state space model as:

$$\begin{bmatrix} \frac{di}{dt} \\ \frac{dv}{dt} \end{bmatrix} = \begin{bmatrix} -\frac{R}{L} & -\frac{1}{L} \\ +\frac{1}{C} & -\frac{1}{Req\,C} \end{bmatrix} \begin{bmatrix} i \\ v \end{bmatrix} + \begin{bmatrix} \frac{1}{L} \\ 0 \end{bmatrix} v_s \tag{3}$$

### *Discharging state*

In this state, the diodes do not conduct and the DC link voltage $v(t)$ and the input current $i(t)$ are given by:

$$v(t) = V_{st}\,e^{-\frac{t}{Req\,C}} \quad , \tag{4}$$

$$i(t) = 0 \quad . \tag{5}$$

Where $V_{st}$ is the initial (starting) value of the DC link voltage $v(t)$. The generic SMPS TDM presented here was implemented in the MATLAB & Simulink® platform (See Fig. 2) and can be downloaded from:

EBSCOhost - printed on 2/14/2023 2:46 PM via . All use subject to https://www.ebsco.com/terms-of-use

https://www.mathworks.com/matlabcentral/fileexchange/61601-time-domain-model-for-a-smps-cfl.

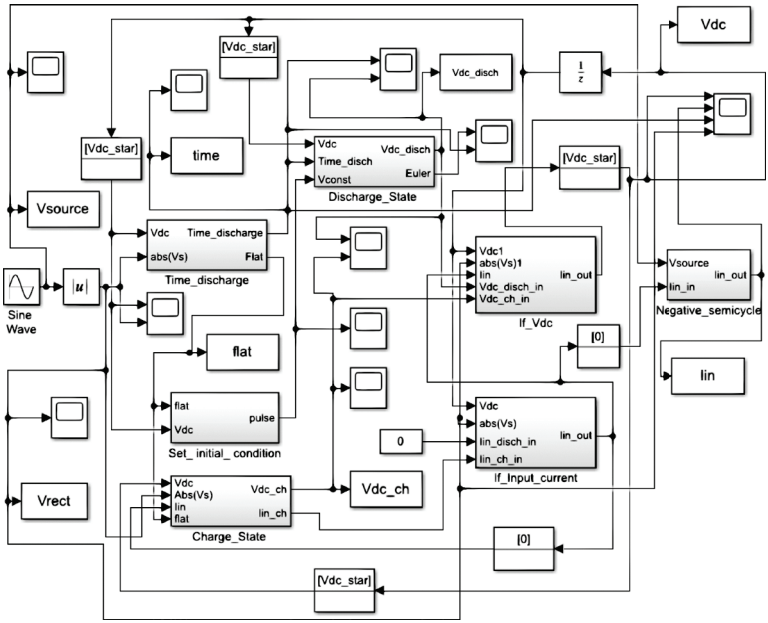



Figure 2. Generic SMPS implemented in the MATLAB & Simulink® platform

The blocks comprising this implementation are described as follows:

### *SMPS Simulink® model: Charge_Stage block*

The *Charge_State block* is formed by the subsystem blocks: *Req_ch* and *Set_initial_condition*. The first block models $R_{eq}$ during the charge stage, and the second one defines the initial conditions of the instantaneous DC link voltage $v(t)$.

EBSCOhost - printed on 2/14/2023 2:46 PM via . All use subject to https://www.ebsco.com/terms-of-use

***SMPS Simulink® model: Discharge_Stage block***

This block models $Req$ during the discharge stage, as a function of the instantaneous DC link voltage $v(t)$.

***SMPS Simulink® model: Time_Discharge block***

This Time_Discharge block determines the time of the transition between charging and discharging states.

***SMPS Simulink® model: If_Input_Current block***

This block decides the transition between charging and discharging states by comparing v and $|Vs|$ or by identifying zero crossings in the input current. It also determines the input current signal (charging or discharging) that is saved as the simulation result.

***SMPS Simulink® model: If_Vdc block***

This block has a similar function to the previous one, but determines the DC link voltage that corresponds to the simulation result.

***SMPS Simulink® model: Negative_semicycle block***

This block builds the results during the supply voltage negative semi-cycle.

## The SMPS Frequency Domain Model

### *Model structure*

The FDM is a linear model, $I_{(n)} = Y_{(n,n)} \times Vs_{(n)}$, composed of a current vector, $I_{(n)}$, an admittance matrix, $Y_{(n,n)}$, that describes the behaviour of the load, and a supply voltage operating point vector, $Vs_{(n)}$, for a given voltage and current harmonic order, $k$, as follows:

The entries in the first column of the admittance matrix were previously computed from a fundamental reference voltage, $V_{r(1)}$, as: $Y_{(k,l)} = Ir_{(k)} / Vr_{(l)}$ for k = 1, 3, 5, …, h, for h = 2n-1 and $n$ total harmonics or matrix and

EBSCOhost - printed on 2/14/2023 2:46 PM via . All use subject to https://www.ebsco.com/terms-of-use

$$\begin{bmatrix} \mathbf{I}_{(1)} \\ \mathbf{I}_{(3)} \\ \mathbf{I}_{(5)} \\ \vdots \\ \mathbf{I}_{(k)} \\ \vdots \\ \mathbf{I}_{(h)} \end{bmatrix} = \begin{bmatrix} \begin{bmatrix} \mathbf{Y}_{(1,1)} \\ \mathbf{Y}_{(3,1)} \\ \mathbf{Y}_{(5,1)} \\ \vdots \\ \mathbf{Y}_{(k,1)} \\ \vdots \\ \mathbf{Y}_{(h,1)} \end{bmatrix} & \begin{bmatrix} \mathbf{Y}_{(1,3)} & \mathbf{Y}_{(1,5)} & \cdots & \mathbf{Y}_{(1,k)} & \cdots & \mathbf{Y}_{(1,h)} \\ \mathbf{Y}_{(3,3)} & \mathbf{Y}_{(3,5)} & \cdots & \mathbf{Y}_{(3,k)} & \cdots & \mathbf{Y}_{(3,h)} \\ \mathbf{Y}_{(5,3)} & \mathbf{Y}_{(5,5)} & \cdots & \mathbf{Y}_{(5,k)} & \cdots & \mathbf{Y}_{(5,h)} \\ \vdots & \vdots & \ddots & \vdots & \ddots & \vdots \\ \mathbf{Y}_{(k,3)} & \mathbf{Y}_{(k,5)} & \cdots & \mathbf{Y}_{(k,k)} & \cdots & \mathbf{Y}_{(k,h)} \\ \vdots & \vdots & \ddots & \vdots & \ddots & \vdots \\ \mathbf{Y}_{(h,3)} & \mathbf{Y}_{(h,5)} & \cdots & \mathbf{Y}_{(h,k)} & \cdots & \mathbf{Y}_{(h,h)} \end{bmatrix} \end{bmatrix} \begin{bmatrix} \mathbf{Vs}_{(1)} \\ \mathbf{Vs}_{(3)} \\ \mathbf{Vs}_{(5)} \\ \vdots \\ \mathbf{Vs}_{(k)} \\ \vdots \\ \mathbf{Vs}_{(h)} \end{bmatrix} \tag{6}$$

vectors dimensions. Where $\mathrm{Ir}_{(n)}$ is the current vector for the reference voltage vector given by $\mathrm{Vr} = \left[\mathrm{Vr}_{(1)}, 0, 0, \ldots, 0\right]^{\mathrm{T}}$.

## *Model training*

Model training can be achieved through an FSP, which can be implemented in the laboratory or via simulation packages.

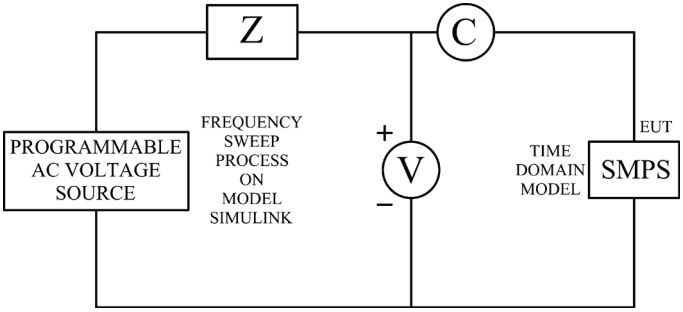



Figure 3. Simulation/experimental framework for the FSP

The simulation/experimental setup is shown in Fig. 3. It comprises: a programmable AC voltage source, which allows for the harmonic magnitude and phase angle variations of the supply voltage; an SMPS load (home appliances, power electronic devices, or lighting equipment), which corresponds to Equipment Under Test (EUT), the line and the source impedances (Z); and data acquisition equipment (V, C), which stores voltage and current waveforms.

The frequency sweep process (FSP) is introduced in [24] and corresponds to the following procedures:

EBSCOhost - printed on 2/14/2023 2:46 PM via . All use subject to https://www.ebsco.com/terms-of-use

1. Initially, a fundamental (not distorted) reference or nominal supply voltage value is set, $Vr_{(1)}$. Then, voltage regulation is gradually defined in steps. For instance, 10 voltage regulation steps, from 0% up to a limit proposed by Std ANSI C84.1.
2. The fundamental supply voltage is set to the reference value, i.e., nominal amplitude and zero phase angle. The third harmonic is added to the fundamental voltage (in this work, only odd harmonics are considered) and its magnitude and phase angle are gradually varied in steps. For example: 10 magnitude steps, from 0% up to the limit established by Std UN50160:2015 (see Table 1), and 12 phase angle steps, from 0° to 360°.
3. The previous procedure is repeated for each harmonic order ($3^{rd}$, $5^{th}$, …, h), superimposing onto the fixed fundamental component one harmonic at a time. Again, the magnitude and phase angle of the added harmonic are gradually varied in steps, following a previously determined experiment design.
4. Supply voltage and current response waveforms are stored for each procedure.
5. The recorded signals in the TD are transformed into the FD to compute the voltage and current spectra.
6. Finally, the polar-plot fingerprints and rectangular plots are created. For each harmonic order combination in the supply voltage ($1^{st}$, $1^{st}$ and $3^{rd}$, $1^{st}$ and $5^{th}$, ...), a set of polar-plot fingerprints indicating magnitude and phase angle per harmonic current response are drawn (See subsection *Polar-plot fingerprints*). The rectangular plots present the |I|-|V| relationship for each phase angle, and the variation in current harmonic caused by each supply voltage harmonic magnitude step and the corresponding current magnitude (See subsection *Rectangular- |I|-|V| plots*).

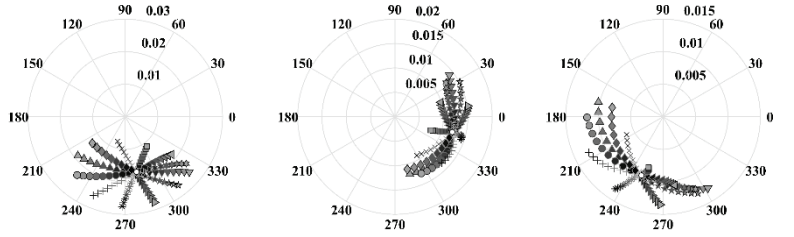
## *Polar-plot fingerprints*

A *current fingerprint* is a polar-plot representation of the load harmonic current behaviour when the magnitude and phase angle of the supply voltage varies. Each fingerprint exhibits the effect of a voltage harmonic order $\nu$, on a given current harmonic order μ. Thus, each current fingerprint is intended to be modelled by one element of the admittance matrix $Y_{(\mu,\nu)}$ (see Equation (2)), even when the harmonic supply voltage varies in magnitude and phase angle.

EBSCOhost - printed on 2/14/2023 2:46 PM via . All use subject to https://www.ebsco.com/terms-of-use

In Fig. 4 and Fig. 5 b), different *current fingerprints* are deployed. Each point with the same mark type is referred to as a *bullet* and a set of *bullets* is referred to as a *branch*.

Each *branch* is generated by the magnitude variation when the phase angle is fixed; therefore, each new *branch* corresponds to a new variation in phase angle. *Branches* can exhibit non-linear and linear behaviour, as Fig. 4 and in Fig. 5 b), respectively.




a) 9th current harmonic fingerprint for magnitude and phase angle variation of 5th harmonic supply voltage superimposed to fixed fundamental component.

b) 15th current harmonic fingerprint for magnitude and phase angle variation of 5th harmonic supply voltage superimposed to fixed fundamental component

c) 17th current harmonic fingerprint for magnitude and phase angle variation of 5th harmonic supply voltage superimposed to fixed fundamental component

Figure 4. Current (A) polar fingerprints for supply voltage with the 5th harmonic superimposed onto the fundamental component, considering 10 magnitude steps, from 0% up to the limits established by Std UN50160: 2015 (see Table 1), and 12 phase angle steps, from 0° to 360°.

## *Rectangular- |I|-|V| plots*

A rectangular- |I|-|V| plot for a pair of harmonics orders ($^{\mu,\nu}$), represents the variation of the $^{\mu th}$ harmonic current magnitude when the $^{\nu th}$ harmonic (superimposed onto a fixed fundamental component) supply voltage magnitude varies, but its phase angle is kept fixed to a $^{j th}$ value (i.e., as in the $^{j th}$ *branch* of a *current fingerprint* (see Fig. 5 c)).

For instance, for each branch in a *current fingerprint*, a branch on the rectangular-plot can be drawn. In the case of linear loads (e.g., impedances), the rectangular |I|-|V| plots are expected to be straight lines (See Fig. 5 c)),

EBSCOhost - printed on 2/14/2023 2:46 PM via . All use subject to https://www.ebsco.com/terms-of-use

and a linear regression with steepness $m_{Y(\mu,v)\,j}$, for every *j-branch* can be used to approximate the relation $\left(|I|_{\mu} = f\left(|V|_{v}\right)\right)_{j}$.

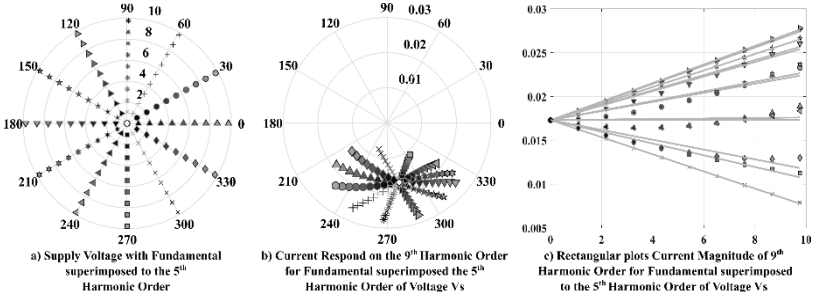



Figure 5. Examples of a voltage (V) fingerprint, a current (A) fingerprint, and a rectangular- |I|-|V| plot, considering 10 magnitude steps, from 0% up to the limit established by Std UN50160:2015 limits, (see Table 1), and 12 phase angle steps, from 0° to 360°.

**Table 1 Harmonic voltage magnitude limits proposed by Std UN50160:2015**

| Orders | 5 | 7, 11 | 13, 17 | 19, 23 | 25 |
|---|---|---|---|---|---|
| Uh [%] | 3 | 2.5 | 2 | 1.5 | 1.0 |
| Orders | > 25 | 3 | 9 | 15, 21 | > 21 |
| Uh [%] | 0.5 | 3 | 1.5 | 0.5 | 0.3 |

## *Proposed method to compute the admittance matrix*

The method proposed in this research to compute the admittance matrix is derived from the analysis of *current polar fingerprints* and the linear regression of *rectangular- |I|-|V| plots* for N *branches* (j=1, 2, 3, …, N) [28]. Equation (7) is used to compute both the magnitude and phase angle of every element in the admittance matrix. The magnitude information is obtained for the rectangular- |I|-|V| plot of every *j-branch* from the slope of the least-squares linear fit $\left(|I|_{\mu} = m_{Y(\mu,v)}\,|V|_{v}\right)_{j}$.

The phase angle information is determined from the *current* and *voltage polar fingerprints* by computing the least-squares linear fits $\left(\Im\{I\}_{\mu} = m_{V}\,\Re\{I\}_{\mu} + b_{I(\mu)}\right)_{j}$ and $\left(\Im\{V\}_{v} = m_{V}\,\Re\{V\}_{v}\right)_{j}$ for every *j-branch*. Given

EBSCOhost - printed on 2/14/2023 2:46 PM via . All use subject to https://www.ebsco.com/terms-of-use

that the supply voltage is controlled during the FSP, the linear fit of the voltage polar fingerprints is known beforehand and its computation is not needed.

$$Y_{(\mu,v)} = \frac{1}{N}\sum_{j=1}^{N}\left(m_{Y(\mu,v)}\, e^{i\theta_{Y(\mu,v)}}\right)_j \tag{7}$$

Where:

$m_{Y(\mu,v)}$ is computed from $\mathrm{Fit}\left(\left|I\right|_\mu = m_{Y(\mu,v)}\left|V\right|_v\right)_j$

$m_{I(\mu)}$ is computed from $\mathrm{Fit}\left(\Im\{I\}_\mu = m_V \Re\{I\}_\mu + b_{I(\mu)}\right)_j$

$m_{V(v)}$ is computed from $\mathrm{Fit}\left(\Im\{V\}_v = m_V \Re\{V\}_v\right)_j$

$\theta_{I(\mu)} = \tan^{-1}(m_{I(\mu)})$, $\theta_{V(v)} = \tan^{-1}(m_{V(v)})$ and $\theta_{Y(\mu,v)} = \theta_{I(\mu)} - \theta_{V(v)}$

## Analysis and Results

In order to assess the performance of the proposed method in equation (7), three models were compared: 1) the SMPS TDM proposed in [20]; 2) the FDM proposed in [23], which does not consider the harmonic phase angle in the admittance matrix; and 3) the FDM proposed in [28], which takes into account the phase angles for different harmonic orders. Both FDMs are computed from TDM simulations. In order to assess the SMPS model's performance, a 15 W CFL was used and modelled with parameters taken from [19] (see Table 2).

**Table 2 Fitted parameters fitted for a 15 W 230 V 50 Hz CFL**

| $X_{C_{CFL}}$ | $X_{L_{CFL}}$ | $R_{CFL}$ | Req,Charging | | | Req,Discharging | | |
|---|---|---|---|---|---|---|---|---|
| [μS] | [Ω] | [Ω] | Ac | Bc | Cc | Bd | Cd | f[Hz] |
| 1130.97 | 0.13 | 15.03 | 0.04 | 19.47 | 1195.93 | 24.5 | 94.29 | 50 |

The model training, as described above, was implemented for a 15 W CFL 230 V 50 Hz using fourteen odd harmonics, from the 3rd to the 29th. For every harmonic, 72 phase angles equally separated from 0° to 360° and 20 magnitude values equally separated from 0% to the limits proposed by Std UN50160:2015 were considered. For the fundamental component (230 V for the experiments in this work), twenty equally separated regulation

EBSCOhost - printed on 2/14/2023 2:46 PM via . All use subject to https://www.ebsco.com/terms-of-use

magnitudes were set from 0% to 5% of the nominal voltage in accordance with Std ANSI C84.1. In this way, 15 harmonics × 20 magnitude steps × 72 phase angle steps = 21,600 different voltage operating points were used to model the CFL.

Model validation was conducted using 10,000 randomly selected voltages and the correspondent 10,000 current signals computed from the three considered models. Voltage regulation of the fundamental component magnitude was set from 0% (230 V) up to the standard voltage regulation 5%. For harmonic components, the magnitude was randomly set using a uniformly distributed probability density function of between 0% (0 V) to the limits proposed in Std UN501160:2015, maintaining the total harmonic distortion voltage THDV = 3%. Similarly, the phase angles of the harmonic components were randomly set using a uniform distribution from 0° to 360°.

Relative and absolute error figures were used to assess the performance of the considered models. The magnitude relative error $E\|I\|(k)[\%]$ between the $k^{th}$ harmonic order estimated by the FDMs and that estimated by the TDM were defined as:

$$E\|I\|(k)[\%] = \left| \frac{\|I\|_{TDM(k)} - \|I\|_{FDM(k)}}{\|I\|_{TDM(k)}} \right| \times 100\% \quad (8)$$

Additionally, the correspondent phase angle absolute error $E\angle I(k)[^\circ]$ was defined as:

$$E\angle I(k)[^\circ] = \left| \angle I_{TDM(k)} - \angle I_{FDM(k)} \right| \quad (9)$$

Tables 3 and 4 present the statistical parameters (mean, standard deviation and median) per harmonic order of training and validation errors, respectively. Likewise, figures 6 to 9 show box-plots with the main statistical training and validation error parameters per harmonic order.
The whiskers reveal the most extreme data points, the central mark indicates the median, and the bottom and top marks display the 25th and 75th percentiles, respectively.

Fig. 6 and Fig. 7 reveal low training errors for the FDMs proposed in [28] and [23]: the magnitude error means are close to 10% for the model proposed in [28] and close to 15% for the one proposed in [23]. In addition, absolute phase angle errors do not exceed 15° and 20°, respectively. Nevertheless, in Table 4, the statistics highlight a better performance for the

EBSCOhost - printed on 2/14/2023 2:46 PM via . All use subject to https://www.ebsco.com/terms-of-use

FDM proposed in [23], with lower mean and standard deviation figures for the 3rd and higher harmonic orders.

**Table 3. Statistical parameters of training error per harmonic order ($\mu$: mean, $\sigma$ : standard deviation, $\bar{x}$ : median)**

| | | 1 | 3 | 5 | 7 | 9 | 11 | 13 | 15 | 17 | 19 | 21 | 23 | 25 | 27 | 29 |
|---|---|---|---|---|---|---|---|---|---|---|---|---|---|---|---|---|
| | | Relative error of magnitude [%] | | | | | | | | | | | | | | |
| [28] | $\mu$ | 0.6 | 1.6 | 3.8 | 7.3 | 12.7 | 15.1 | 17.0 | 19.4 | 21.8 | 22.9 | 25.1 | 27.9 | 26.2 | 24.8 | 26.6 |
| | $\sigma$ | 0.8 | 1.9 | 5.2 | 13.2 | 83.3 | 50.2 | 52.1 | 66.6 | 68.9 | 62.5 | 223.5 | 71.7 | 63.5 | 70.5 | 149.6 |
| | $\bar{x}$ | 0.4 | 0.9 | 1.9 | 2.2 | 4.2 | 4.6 | 6.2 | 6.9 | 8.9 | 10.8 | 10.0 | 12.4 | 11.8 | 13.4 | 10.6 |
| [23] | $\mu$ | 0.4 | 3.1 | 6.1 | 9.4 | 19.5 | 23.3 | 21.6 | 26.3 | 31.2 | 28.0 | 32.4 | 34.6 | 32.5 | 34.5 | 36.9 |
| | $\sigma$ | 0.5 | 4.2 | 9.4 | 16.1 | 179.6 | 86.0 | 51.4 | 95.9 | 117.7 | 78.6 | 264.5 | 96.5 | 87.5 | 115.6 | 211.1 |
| | $\bar{x}$ | 0.3 | 1.5 | 2.3 | 2.9 | 4.6 | 6.9 | 8.2 | 7.9 | 10.1 | 13.9 | 11.9 | 12.8 | 14.9 | 16.9 | 13.8 |
| | | Absolute error of phase angle [°] | | | | | | | | | | | | | | |
| [28] | $\mu$ | 0.8 | 2.2 | 3.0 | 4.2 | 7.7 | 12.3 | 13.5 | 16.2 | 18.9 | 21.9 | 24.4 | 26.3 | 26.8 | 28.3 | 28.1 |
| | $\sigma$ | 0.9 | 2.6 | 4.0 | 7.1 | 11.4 | 17.5 | 21.0 | 25.8 | 26.6 | 28.9 | 32.0 | 32.1 | 32.0 | 33.7 | 32.7 |
| | $\bar{x}$ | 0.4 | 1.2 | 1.6 | 1.3 | 3.2 | 6.4 | 5.7 | 6.1 | 9.0 | 11.5 | 11.4 | 14.5 | 14.8 | 15.1 | 15.7 |
| [23] | $\mu$ | 0.8 | 2.5 | 3.9 | 5.8 | 10.5 | 15.4 | 15.2 | 20.9 | 24.9 | 22.1 | 30.3 | 32.0 | 28.7 | 34.4 | 32.3 |
| | $\sigma$ | 0.9 | 3.5 | 5.6 | 9.2 | 18.6 | 23.8 | 23.4 | 34.4 | 36.5 | 25.9 | 41.2 | 41.3 | 33.5 | 40.2 | 39.0 |
| | $\bar{x}$ | 0.5 | 1.1 | 1.7 | 2.3 | 3.8 | 6.6 | 6.3 | 6.2 | 9.3 | 12.1 | 12.0 | 13.1 | 15.4 | 18.7 | 15.4 |

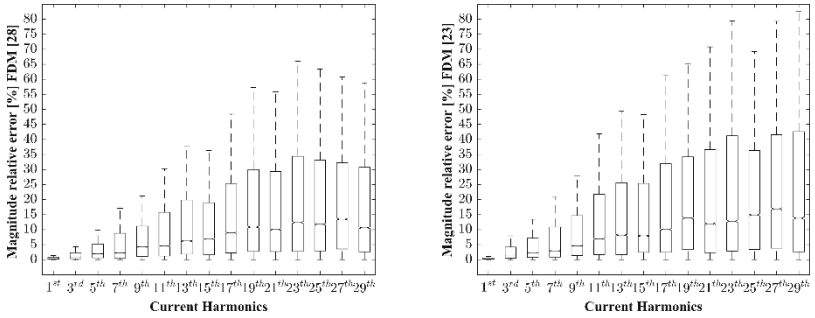



Figure 6. Magnitude relative training error of FDMs in [28] and [23].

EBSCOhost - printed on 2/14/2023 2:46 PM via . All use subject to https://www.ebsco.com/terms-of-use

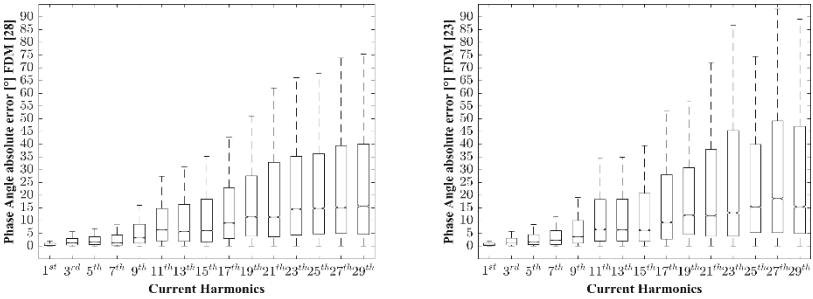



Figure 7. Phase angle absolute training error of FDMs in [28] and [23].

The magnitude and phase angle validation error boxplots presented in Fig. 8 and Fig. 9 exhibit similar median results. However, in Table 4 the FDM proposed in [28] slightly outperforms the one proposed in [23] when estimating low order harmonics (less than 15% and 12° as compared to 18% and 14°, respectively), which are the orders that contribute most to the error.

**Table 4. Statistical parameters of validation error per harmonic order ($\mu$: mean, $\sigma$ : standard deviation, $\bar{X}$ : median)**

| | | 1 | 3 | 5 | 7 | 9 | 11 | 13 | 15 | 17 | 19 | 21 | 23 | 25 | 27 | 29 |
|---|---|---|---|---|---|---|---|---|---|---|---|---|---|---|---|---|
| | | Relative error of magnitude [%] | | | | | | | | | | | | | | |
| [28] | $\mu$ | 2.3 | 6.1 | 15.0 | 32.4 | 50.2 | 55.2 | 58.3 | 60.0 | 58.9 | 61.2 | 60.0 | 65.5 | 62.6 | 63.5 | 71.8 |
| | $\sigma$ | 1.6 | 5.0 | 14.1 | 52.6 | 115.6 | 129.4 | 196.4 | 147.3 | 76.8 | 110.2 | 115.5 | 152.2 | 87.0 | 125.2 | 641.4 |
| | $\bar{X}$ | 2.0 | 4.9 | 10.7 | 19.9 | 30.3 | 37.2 | 36.5 | 44.2 | 52.4 | 52.0 | 54.4 | 56.5 | 58.1 | 56.0 | 51.6 |
| [23] | $\mu$ | 1.2 | 5.2 | 18.4 | 41.7 | 62.7 | 80.6 | 82.6 | 94.9 | 82.8 | 83.5 | 95.1 | 100.7 | 86.2 | 95.8 | 116.2 |
| | $\sigma$ | 0.8 | 4.3 | 16.5 | 55.5 | 139.0 | 183.8 | 293.5 | 301.3 | 170.0 | 254.4 | 260.3 | 341.2 | 206.7 | 253.4 | 996.6 |
| | $\bar{X}$ | 1.1 | 4.3 | 14.2 | 28.2 | 34.5 | 54.5 | 39.6 | 49.8 | 47.8 | 45.9 | 48.8 | 50.6 | 46.7 | 49.0 | 51.9 |
| | | Absolute error of phase angle [°] | | | | | | | | | | | | | | |
| [28] | $\mu$ | 2.9 | 8.3 | 12.1 | 18.1 | 29.1 | 44.4 | 48.9 | 60.5 | 65.1 | 72.9 | 79.3 | 77.4 | 83.4 | 84.3 | 85.0 |
| | $\sigma$ | 2.0 | 5.7 | 8.8 | 13.9 | 26.0 | 34.1 | 40.0 | 43.9 | 47.7 | 48.0 | 50.9 | 50.6 | 49.2 | 49.8 | 51.1 |
| | $\bar{X}$ | 2.7 | 7.6 | 10.4 | 15.2 | 22.8 | 37.5 | 38.6 | 52.0 | 54.5 | 66.6 | 74.7 | 70.8 | 80.4 | 82.0 | 82.1 |
| [23] | $\mu$ | 2.9 | 10.8 | 13.6 | 19.5 | 40.8 | 65.2 | 51.1 | 77.1 | 88.8 | 67.8 | 94.2 | 87.1 | 78.1 | 96.5 | 83.8 |
| | $\sigma$ | 1.9 | 7.4 | 10.0 | 15.6 | 31.2 | 49.1 | 42.3 | 48.4 | 52.0 | 48.4 | 50.0 | 51.0 | 49.1 | 51.1 | 51.4 |
| | $\bar{X}$ | 2.7 | 9.8 | 11.6 | 16.1 | 34.8 | 53.3 | 39.6 | 72.0 | 88.1 | 58.7 | 96.3 | 85.6 | 73.5 | 100.0 | 80.3 |

EBSCOhost - printed on 2/14/2023 2:46 PM via . All use subject to https://www.ebsco.com/terms-of-use

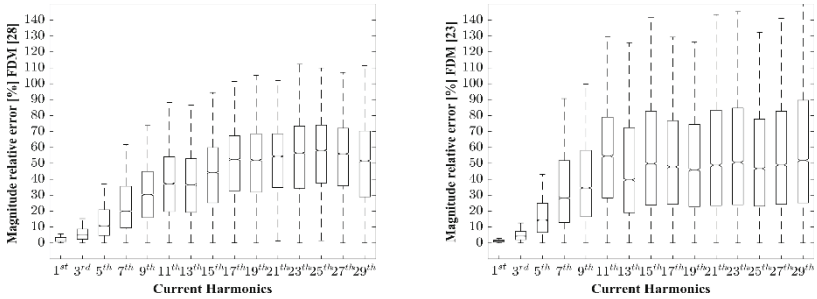



Figure 8. Magnitude relative validation error of FDMs in [28] and [23].

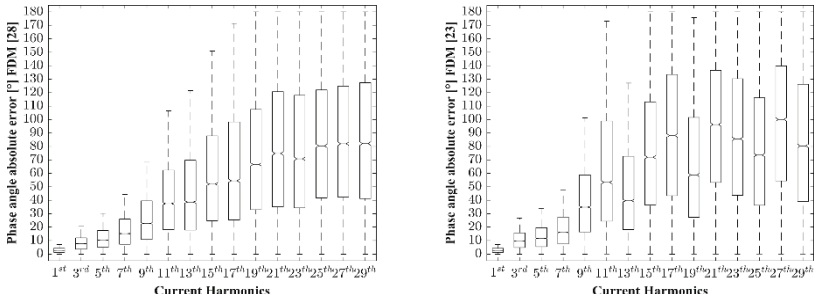



Figure 9. Phase angle absolute validation error of FDMs in [28] and [23].

## Conclusions

A generic SMPS time domain model and its implementation in MATLAB & Simulink® are described and documented in this work. Specifically, a CFL TDM was used to compute several current signals when multiple variations of the supply voltage were considered. These signals were then used to train and validate two methods to compute FDMs for SMPS-based loads. The training and validation strategies illustrated in this chapter were devised to show that the proposed FDM can cope with harmonic distortion attenuation-amplification and diversity effects. The methods for computing FDMs considered in this study, exhibit similar performance when estimating the input current harmonics under several supply voltage operating conditions complying with Std UN50160:2015. The proposed FDM outperforms the FDM previously proposed in the literature. Therefore, it is necessary to carry out further research in order to improve the performance of the FDM to deal successfully with attenuation-amplification and diversity effects. Furthermore, future research to address an error definition that

EBSCOhost - printed on 2/14/2023 2:46 PM via . All use subject to https://www.ebsco.com/terms-of-use

decomposes the total error, per harmonic and for all harmonics, into magnitude and phase angle error contributions, is recommended.

## Acknowledgments

The authors gratefully acknowledge the support provided by COLCIENCIAS through the grant *Convocatoria Nacional No. 567 para Estudios de Doctorado en Colombia*.

## References

[1] P. F. Ribeiro *et al.*, "Harmonic distortion during the 2010 FIFA World Cup," in *Power and Energy Society General Meeting, 2011 IEEE*, 2011, pp. 1–8.

[2] A. M. Blanco, S. Yanchenko, J. Meyer, and P. Schegner, "The impact of supply voltage distortion on the harmonic current emission of non-linear loads," *DYNA*, vol. 82, no. 192, 2015.

[3] D. Salles, C. Jiang, W. Xu, W. Freitas, and H. E. Mazin, "Assessing the Collective Harmonic Impact of Modern Residential Loads;Part I: Methodology," *IEEE Trans. Power Deliv.*, vol. 27, no. 4, pp. 1937–1946, Oct. 2012.

[4] A. M. Blanco, R. Stiegler, and J. Meyer, "Power quality disturbances caused by modern lighting equipment {(CFL and LED)}," in *PowerTech (POWERTECH), 2013 IEEE Grenoble*, 2013, pp. 1–6.

[5] A. B. Nassif and J. Acharya, "An investigation on the harmonic attenuation effect of modern compact fluorescent lamps," in *2008 13th International Conference on Harmonics and Quality of Power*, 2008, pp. 1–6.

[6] J. Yong, A. B. Nassif, and W. Xu, "Effect of voltage crest shape on the harmonic amplification and attenuation of diode-bridge converter-based loads," *IET Gener. Transm. Distrib.*, vol. 5, no. 10, pp. 1033–1041, 2011.

[7] V. Cuk, J. F. G. Cobben, W. L. Kling, and P. F. Ribeiro, "Analysis of harmonic current summation based on field measurements," *IET Gener. Transm. Distrib.*, vol. 7, no. 12, pp. 1391–1400, 2013.

[8] M. T. Au and J. V. Milanovic, "Development of Stochastic Aggregate Harmonic Load Model Based on Field Measurements," *Power Deliv. IEEE Trans.*, vol. 22, no. 1, pp. 323–330, 2007.

[9] A. B. N. J. Y. W. Xu, "Measurement-based approach for constructing harmonic models of electronic home appliances," *IET Gener. Transm. Distrib.*, vol. 4, no. 3, pp. 363–375, 2010.

[10] S. Müller, J. Meyer, and P. Schegner, "Characterization of small photovoltaic inverters for harmonic modeling," in *2014 16th International Conference on Harmonics and Quality of Power (ICHQP)*, 2014, pp. 659–663.

[11] S. Müller, F. Möller, J. Meyer, A. J. Collin, and S. Z. Djokic, "Characterisation of harmonic interactions between electric vehicle battery chargers and PV inverters," in *2014 16th International Conference on Harmonics and Quality of Power (ICHQP)*, 2014, pp. 645–649.

EBSCOhost - printed on 2/14/2023 2:46 PM via . All use subject to https://www.ebsco.com/terms-of-use

[12] M. F. Romero, L. Gallego, J. Meyer, and S. Müller, "Characterization of non-linear household loads for frequency domain modeling," *Ing. e Investig.*, vol. 35, no. 1Sup, pp. 65–72, 2015.
[13] S. Müller, J. Meyer, P. Schegner, and S. Djokic, "Harmonic modeling of electric vehicle chargers in frequency domain," in *International Conference on Renewable energies and Power Quality (ICREPQ)*, 2015, pp. 1–6.
[14] J. Yong, L. Chen, and S. Chen, "Modeling of home appliances for power distribution system harmonic analysis," *IEEE Trans. Power Deliv.*, vol. 25, no. 4, pp. 3147–3155, 2010.
[15] S. Z. Djokic and A. J. Collin, "Cancellation and attenuation of harmonics in low voltage networks," *Proc. Int. Conf. Harmon. Qual. Power, ICHQP*, pp. 137–141, 2014.
[16] A. J. Collin, S. Z. Djokic, C. E. Cresswell, A. M. Blanco, and J. Meyer, "Cancellation of harmonics between groups of modern compact fluorescent lamps," in *Power Electronics, Electrical Drives, Automation and Motion (SPEEDAM), 2014 International Symposium on*, 2014, pp. 1190–1194.
[17] A. J. Collin, J. L. Acosta, B. P. Hayes, and S. Z. Djokic, "Component-based aggregate load models for combined power flow and harmonic analysis," in *Power Generation, Transmission, Distribution and Energy Conversion (MedPower 2010), 7th Mediterranean Conference and Exhibition on*, 2010, pp. 1–10.
[18] S. Z. Djokic and A. J. Collin, "Cancellation and attenuation of harmonics in low voltage networks," in *Harmonics and Quality of Power (ICHQP), 2014 IEEE 16th International Conference on*, 2014, pp. 137–141.
[19] G. Malagon-Carvajal, J. Bello-Pena, G. Ordonez-Plata, and C. Duarte, "A comparison between Circuit-Based and Harmonic-Current-Source models for compact fluorescent lamps," in *Proceedings of International Conference on Harmonics and Quality of Power, ICHQP*, 2016, vol. 2016–Decem.
[20] G. Malagon-Carvajal, J. Bello-Peña, G. Ordóñez Plata, and C. Duarte Gualdrón, "Analytical and experimental discussion of a circuit-based model for compact fluorescent lamps in a 60 Hz power grid," *Ing. e Investig.*, vol. 35, no. 1, 2015.
[21] M. E. Balci, D. Ozturk, O. Karacasu, and M. H. Hocaoglu, "Experimental verification of harmonic load models," in *Universities Power Engineering Conference, 2008. UPEC 2008. 43rd International*, 2008, pp. 1–4.
[22] A. S. Koch, J. M. A. Myrzik, T. Wiesner, and L. Jendernalik, "Harmonic measurement and modeling for mass implementation of nonlinear appliances," in *2012 IEEE Power and Energy Society General Meeting*, 2012, pp. 1–6.
[23] J. Meyer, S. Müller, P. Schegner, S. Z. Djokic, A. J. Collin, and X. Xu, "Comparison of methods for modelling electric vehicle chargers for harmonic studies," in *2016 Power Systems Computation Conference (PSCC)*, 2016, pp. 1–7.
[24] M. Fauri, "Harmonie modelling of non-linear load by means of crossed frequency admittance matrix," *IEEE Trans. Power Syst.*, vol. 12, no. 4, pp. 1632–1638, 1997.
[25] A. S. Fölting, J. M. A. Myrzik, T. Wiesner, and L. Jendernalik, "Practical

EBSCOhost - printed on 2/14/2023 2:46 PM via . All use subject to https://www.ebsco.com/terms-of-use

implementation of the coupled norton approach for nonlinear harmonic models," *Proc. - 2014 Power Syst. Comput. Conf. PSCC 2014*, vol. 1, 2014.

[26] A. S. Koch, J. M. A. Myrzik, T. Wiesner, and L. Jendernalik, "Evaluation and validation of Norton approaches for nonlinear harmonic models," in *PowerTech (POWERTECH), 2013 IEEE Grenoble*, 2013, pp. 1–6.

[27] C. F. M. Almeida and N. Kagan, "Harmonic coupled norton equivalent model for modeling harmonic-producing loads," *ICHQP 2010 - 14th Int. Conf. Harmon. Qual. Power*, 2010.

[28] G. Malagon-Carvajal, J. Bello-Peña, G. Ordóñez, and C. Duarte, "Time-to-Frequency Domain SMPS Model for Harmonic Estimation: Methodology," in *International Conference on Renewable Energies and Power Quality (ICREPQ'17)*, 2017, pp. 1–7.

[29] J. E. Caicedo, A. A. Romero, and H. C. Zini, "Frequency Domain Modeling of Nonlinear Loads , considering Harmonic Interaction," 2017.

[30] J. G. Mayordomo, L. F. Beites, R. Asensi, F. Orzaez, M. Izzeddine, and L. Zabala, "A contribution for modeling controlled and uncontrolled AC/DC converters in harmonic power flows," *IEEE Trans. Power Deliv.*, vol. 13, no. 4, pp. 1501–1508, Oct. 1998.

[31] Y. Sun, G. Zhang, W. Xu, and J. G. Mayordomo, "A harmonically coupled admittance matrix model for AC/DC converters," *IEEE Trans. Power Syst.*, vol. 22, no. 4, pp. 1574–1582, 2007.

[32] C. Dai, J. Yong, Y. Sun, and J. Li, "Frequency-domain harmonic matrix model for three-phase diode-bridge rectifier," *IET Gener. Transm. Distrib.*, vol. 10, no. 7, pp. 1605–1614, 2016.

[33] J. Yong, L. Chen, A. B. Nassif, and W. Xu, "A Frequency-Domain Harmonic Model for Compact Fluorescent Lamps," *IEEE Trans. Power Deliv.*, vol. 25, no. 2, pp. 1182–1189, 2010.

[34] A. Mansoor, W. M. Grady, P. T. Staats, R. S. Thallam, M. T. Doyle, and M. J. Samotyj, "Predicting the net harmonic currents produced by large numbers of distributed single-phase computer loads," *IEEE Trans. Power Deliv.*, vol. 10, no. 4, pp. 2001–2006, Oct. 1995.

[35] A. Mansoor, W. M. Grady, A. H. Chowdhury, and M. J. Samotyi, "An investigation of harmonics attenuation and diversity among distributed single-phase power electronic loads," *Power Deliv. IEEE Trans.*, vol. 10, no. 1, pp. 467–473, 1995.

[36] H. E. Mazin, E. E. Nino, W. Xu, and J. Yong, "A Study on the Harmonic Contributions of Residential Loads," *Power Deliv. IEEE Trans.*, vol. 26, no. 3, pp. 1592–1599, 2011.

[37] G. Malagon-Carvajal, C. Duarte, G. Ordonez-Plata, C. Almeida, and N. Kagan, "Harmonic attenuation-amplification effect on lighting branch circuits," in *2017 6th International Conference on Renewable Energy Research and Applications, ICRERA 2017*, 2017, vol. 2017–Janua.

[38] T. F. on Harmonics Modeling and Simulation, "Modeling and simulation of the propagation of harmonics in electric power networks. I. Concepts, models, and simulation techniques," *Power Deliv. IEEE Trans.*, vol. 11, no. 1, pp. 452–465, 1996.

EBSCOhost - printed on 2/14/2023 2:46 PM via . All use subject to https://www.ebsco.com/terms-of-use

# CHAPTER THIRTY-ONE

# REVIEW OF FAULT DETECTION AND LOCATION TECHNIQUES IN VSC-HVDC AND MTDC SYSTEMS

G. BUIGUES[1], V. VALVERDE[1], D.M. LARRUSKAIN[1], P. EGUÍA[1], E. TORRES[1]

## Abstract

Considering the importance that HVDC systems are expected to have in the future of power networks, this chapter aims to provide a broad overview of protection against DC faults in such systems. In particular, it analyses the detection and location techniques that have been proposed, focusing on the approaches that are set to be applied in modern HVDC networks, comprising VSC-HVDC and MTDC systems.

**Keywords:** DC faults; fault detection; fault location; VSC-HVDC; MTDC.

## 1. Introduction

The integration of new renewable generation technologies into the power system has seen important challenges over recent decades. Hosting capacity for renewable generation in AC networks is often limited in order to avoid stability issues. Considering that the vast majority of these energy

[1] Department of Electrical Engineering, Faculty of Engineering of Bilbao, University of the Basque Country (UPV/EHU), Plaza Ingenieros Torres Quevedo 1, 48013 Bilbao (Spain).
E-mail: garikoitz.buigues@ehu.eus, victor.valverde@ehu.eus, marene.larruskain@ehu.eus, pablo.eguia@ehu.eus, esther.torresi@ehu.eus

EBSCOhost - printed on 2/14/2023 2:46 PM via . All use subject to https://www.ebsco.com/terms-of-use

sources are located in remote locations where possible connections to AC networks are weak or non-existent, the development of high voltage DC (HVDC) grids has emerged as an interesting solution to integrate large amounts of renewable power generation so that a future with reduced greenhouse gas emissions can be achieved. Some examples of projects in this field include the European "Supergrid" [1, 2], Medgrid, and OffshoreGrid, etc. In these kinds of initiatives, the meshed topology and application of a multi-terminal HVDC system is usually the favoured solution [3], due to its reliability. In addition, the long distances expected between new installations and the need for new technical solutions to narrow the choice of transmission technology down all have to be taken into consideration.

In this context, voltage source converter (VSC) technology and VSC-based multi-terminal DC grids (MTDC), along with modular multi-level converters (MMC), are set to be of the utmost importance in future HVDC meshed networks. VSC-based MTDC systems can provide significant benefits for transmission networks, such as decoupled control of active power and reactive power; support for weak AC systems; black start capability; and a small footprint. However, the current maximum capacity of a VSC-HVDC line is still limited, whereas the line commutated converter (LCC) based MTDC takes advantages of low cost and large capacity. As a result, the higher power rating has made LCC MTDC the main choice for bulk power/long distance applications [4]. Notwithstanding this, these well-known conventional DC systems (LCC-HVDC) are unlikely to meet the requirements of future networks [2].

Finally, despite the multiple advantages of VSC-HVDC systems compared to conventional LCC-HVDC systems, this technology is extremely vulnerable to DC faults, which makes quick detection and location of such a fault essential in order to isolate the problematic area. This chapter is intended to give a broad overview of the solutions proposed to date in this field, focusing on VSC-based and related systems.

## 2. Protection in VSC-HVDC and MTDC systems

Conventional thyristor-based HVDC systems (LCC-HVDC) are based on a well-proven technology that offers a high power transmission capacity, but has limited reactive power control. Nowadays, IGBT-based VSC technology offers numerous advantages over its predecessor (black-start capability; no need for short-circuit ratio; smaller converter station size; independent control of active and reactive power; voltage variation stabilization; mitigation of voltage fluctuation, etc.) [1, 5].

EBSCOhost - printed on 2/14/2023 2:46 PM via . All use subject to https://www.ebsco.com/terms-of-use

However, an important drawback of VSC converters is that they are vulnerable to DC faults [6, 7] and such a fault needs to be detected and cleared very quickly, therefore reducing the information and time available to protection systems [8]. In this regard, those techniques traditionally developed for fault detection and location in conventional LCC-HVDC systems or AC networks are not generally applicable in VSC-HVDC and MTDC systems, mainly because of the excessive time that is necessary to implement the techniques, or due to key components being incompatible [9]. Nonetheless, the development of a HVDC protection system should be guided by the same protection requirements that are traditionally well established in AC-systems: reliability, speed, selectivity, sensitivity, and economy [10].

Furthermore, with the rise of VSC technology, MTDC systems have started to increase in relevance and it is expected that VSC-based HVDC systems will provide the basis for future multi-terminal networks [2]. Multi-terminal DC systems have been proposed for multiple applications, including: offshore wind farms; underground urban subtransmission and distribution systems; shipboard power supplies; and as the backbone for distributed and renewable generation systems [11]. These systems can have various topologies, such as point to point, general ring, and star topologies [12].

However, MTDC systems pose new challenges and problems with respect to traditional point-to-point HVDC systems, especially when affected by a fault. In this case, the sudden change of power flow on all parts of the system, from the converter stations to the fault point, may affect both the AC system and the DC system. As such, a rapid de-energisation of the faulted zone becomes vital [13]. Although research into fault detection and location methods for conventional LCC-HVDC transmission lines has been undertaken for many years, research on protecting VSC-HVDC and MTDC systems is still in its early stages.

In this regard, the development of modern meshed HVDC grids is feasible using different types of VSC: two-level (2L-VSC); three-level (3L-VSC); and Modular Multilevel Converters (MMC). MMC is a relatively new VSC technology that has many advantages (low total harmonic distortion, reduced losses, etc.) over conventional 2-level VSC-HVDC, and it is likely that future HVDC grids will be based on this technology [10, 14, 15]. Theoretical research has primarily been focused on system modelling simulations and steady-state control strategy [16] and there are not many studies on MMC-MTDC system protection strategies under DC faults,

EBSCOhost - printed on 2/14/2023 2:46 PM via . All use subject to https://www.ebsco.com/terms-of-use

As a result, the protection of these VSC-based HVDC systems, including the detection and location of DC faults, remains of significant concern.

## 3. Fault detection and location in VSC-HVDC and MTDC systems

### *3.1. High frequency and signal processing. Travelling waves and wavelet analysis*

Currently, most fault detection and location approaches used in HVDC systems are based, in one way or another, on travelling waves and related methods. Travelling wave algorithms determine the fault location by considering the time taken by the fault-generated travelling wave to propagate along the line. Consequently, their accuracy strongly depends on precise detection of the surge arrival time. Although these methods have generally positive benefits (fast response; high accuracy; not easily affected by factors such as bus configuration, fault types, fault resistance, ground resistance, loading conditions, and system parameters, etc.), they also face important technical problems (difficult wave-head detection; strong dependence on the sampling frequency; vulnerable to interference signals; challenging fault location in combined overhead/underground systems, etc.) [17-20].

In this regard, in order to correctly detect DC fault wave fronts, many of these approaches use a wavelet transform (WT) [10]. Wavelet analysis is a powerful signal analysis tool well suited to fault generated signals, since it is very good at detecting transient changes. Wavelet analysis is based on decomposing signals into ‘scales’ using a wavelet prototype function called a ‘mother wavelet’ [21]. For WT-based techniques, a high speed processing unit is necessary due to the considerable calculations that take place in the process [20].

These methods are usually grouped into different subcategories as regards where the measurements are taken—single-ended or multi-ended. Whereas the single-ended principle bases its performance on induced transient travelling waves and associated reflected waves to determine fault location at one line terminal, the double-ended principle uses the time difference between the absolute arrival times of fault induced initial surges measured at both terminals of the line. The single-ended principle is more cost effective for realisation with a high level of accuracy, but the double ended principle is more reliable as it only makes use of the fault generated

EBSCOhost - printed on 2/14/2023 2:46 PM via . All use subject to https://www.ebsco.com/terms-of-use

initial surges. It does, however, require two sets of equipment to be installed—one at either end of the supervised line [22].

Several approaches have been proposed since 2008 that try to address the problems related to VSC-HVDC and MTDC systems. They offer different solutions that include travelling waves and/or related high-frequency techniques. One of the first techniques in this regard was proposed by Y-J Kwon et al., whose algorithm is based on travelling waves and cross correlation with a kind of simple step function [23]. It was verified for both LCC and VSC type HVDC systems.

Some years later, S. Guo Bing et al. [19, 24] presented a single-ended protection and fault location method for VSC-HVDC transmission lines that combined the fast Fourier transform (FFT) and Prony algorithms. By extracting the natural frequency, the wave speed at the dominant frequency allows the calculation of the fault distance.

Over the course of several years, O. M. K. Kasun Nanayakkara et al. developed a very thorough methodology using travelling waves and the continuous wavelet transform (CWT) [25]. Initially, they focussed on conventional two-terminal HVDC systems composed of a combination of overhead lines and cables [26-28], using only the measurements at the converter terminals. K. P. A. Nuwan Pathirana et al. (from the same research group) [29, 30], proposed a similar approach so as to apply this kind of technique to VSC-based HVDC schemes. They presented an algorithm for DC fault location in a star-connected multi-terminal VSC-HVDC system [12]. Although it was initially derived for a three-terminal network, it can also be applied to a N-terminal network. However, this topology is not a common MTDC system topology due to its low level of reliability [31].

K. De Kerf et al. proposed the use of three independent fault criteria (voltage wavelet analysis, current wavelet analysis, and voltage derivative and magnitude), along with a triple modular redundancy (TMR) technique to detect DC faults in multi-terminal VSC-HVDC systems [32]. This methodology was used some years later by B. Chang et al. [33] to study the equivalent two-level converter system response under a pole-to-pole fault in a VSC-HVDC based MTDC system.

The same year, R. K. Mallick and R. K. Patnaik described a wavelet-based detection method for DC line faults in a three terminal VSC-HVDC system [21]. Using energy thresholds and a decision tree they determined the type of fault and the faulted line. One year later, a group of researchers at Wuhan University (China) [34, 35] used a very similar approach to detect and locate faults in a MTDC system. A similar use of WT was

EBSCOhost - printed on 2/14/2023 2:46 PM via . All use subject to https://www.ebsco.com/terms-of-use

analysed by J. Descloux 3 [36] in attempting to compare its selectivity performance with a methodology based on differential analysis.

S. Azizi et al. [31, 37] presented a novel travelling wave-based methodology for fault location in VSC-HVDC based MTDC systems. Using graph theory and two mathematical lemmas, along with WT and the first arrival time of the travelling wave, an offline-online methodology was proposed to detect the faulted segment and to identify the fault distance.

H. A. A. Hassan et al. [38, 39] developed a method to locate temporary and permanent faults on a non-homogeneous VSC-HVDC system. Modelling the behaviour of travelling waves though modal domain analysis and using Rogowsky coils for voltage and current measurements, the proposed methodology relies on synchronised measurements at both ends.

Based on a previously developed methodology for AC transmission lines [40], R. Razzaghi et al. described [41] a fault location procedure for MTDC networks based on the Electromagnetic Time Reversal (EMTR). Although the faulted line and the fault type needs to be detected in advance (the authors recommended using the approach proposed by J. Descloux in [42]), this information is used to select a specific observation point at which the recorded electromagnetic transients are time-reversed and back-injected into an emulated network model for different estimated fault locations.

Y. Ming Yeap et al. focussed their research on differentiating among AC faults, DC faults, and load changes in HVDC systems. The authors proposed the use of either mere observation of the wavelet analysis [43], a novel amplitude tracking square wave methodology [44], or a short time Fourier transform (only for pole-to-pole faults) [45, 46] using a Hamming 32-point window and a standard deviation over the side lobes amplitude.

S. H. Ashrafi et al. proposed a novel approach for detecting and recognising DC faults in VSC-HVDC based offshore wind farms [47], including HVDC cable faults and unbalancing of the DC capacitor bank. In this case, transient over-voltages in the cable sheaths are analysed by means of WT, using its frequency spectrum to differentiate DC faults from AC faults and the sign of its peak to detect positive cable ground faults.

Using a technique developed for conventional LCC-HVDC systems [17], H. Zheng-You presented [48] a novel transmission line protection scheme for VSC-HVDC systems, based on the relationship between the natural frequency and the fault distance, and only using single-end current data. They applied the MUltiple SIgnal Classification (MUSIC) method to extract the dominant natural frequency, which was then used in two protection principles: one used to detect close internal faults and the other

EBSCOhost - printed on 2/14/2023 2:46 PM via . All use subject to https://www.ebsco.com/terms-of-use

to detect end line and external faults. In the same year, S. Wang et al. [14] proposed the use of a fault detection method for overhead MMC-HVDC lines based on wavelet entropy. Their approach evaluates the wavelet entropy of the current signal to detect the fault.

In considering the problems related to travelling wave head identification in VSC-HVDC systems, H. Xu et al. [49] proposed the calculation of zero-sequence capacitance so as to determine the arrival time of a travelling wave head and, consequently, detect a ground fault. Once the arrival time is detected, the fault location can be estimated. J. Wang et al. [50] proposed using the polarities of the voltage and current travelling waves to detect faults in MTDC systems based on single-end measurements. However, such a method may be very sensitive to noise and lead to false indication of faults [51].

N. Johannesson et al. devised two different approaches for fault detection in MTDC systems, both based on travelling wave related technologies. Firstly, the authors introduced a double-ended differential protection system, which is developed in the frequency dimension and then translated into the time dimension [52]. Secondly, the authors proposed a single-ended detection method using the incident travelling wave [53], which is achieved by representing the frequency dependent characteristic admittance according to a rational approximation.

R. Perveen et al. developed a fault detection and location technique [54-56] for VSC-HVDC links connecting offshore wind farms to onshore grids, using travelling waves and different signal processing techniques (WT, Stockwell transform, empirical mode decomposition (EMD), Hilbert transform), along with least-squares support vector-machines (LS-SVMs) for fault classification. Several indices are used for this purpose, such as energy, spread of the instantaneous temporal energy density, and deviation of the instantaneous temporal energy density.

G. Auran et al. [57] introduced a new pole-to-ground fault detection algorithm for VSC-based MTDC systems using half-bridge MMC-converters. The first current wave after the fault occurs, along with a current threshold, is used to determine if the fault is on the MTDC grid. Afterwards, three sequential criteria (using current thresholds, time differences between current wave arrivals, and current derivatives) are used to determine whether the fault is internal or external. X. Chuanxin et al. [58] proposed using the Stockwell transform (S-transform) to locate faults on VSC-HVDC transmission lines. The authors claim that compared to WT, the results when using the S-transform are more intuitive, accurate, and easily identified.

EBSCOhost - printed on 2/14/2023 2:46 PM via . All use subject to https://www.ebsco.com/terms-of-use

X. Chu et al. presented [59, 60] an analytical method for fault characteristics and non-unit detection, suitable for all HVDC power systems with boundary units (shunt capacitors in VSC-HVDC systems). Based on the frequency response characteristics of the boundary units, the authors used the distributed parameter model of transmission lines to calculate the transfer function (the quotient between the voltage source and the fault voltage) and the input impedance (the quotient between the voltage source and the fault current). An input impedance of high frequency for the external fault is much greater than that of low frequency, while for an internal fault, there is almost no difference between high frequency and low frequency. As a result, it is possible to distinguish between internal and external faults, as well as to determine the faulted pole.

R. E. Torres-Olguin et al. [61, 62] proposed a communication-less fault detection strategy based on travelling waves to be used in VSC-based MTDC systems that are integrated with offshore wind farms. By using inductive fault current limiters (FCL) near each protection relay and measuring currents on the DC side, the algorithm scheme is composed of two units: the travelling wave-based unit (which monitors whether the wavelet energy exceeds a predefined threshold or not) and the directional unit (which verifies the direction of the DC current). As such, a fault is detected when the wavelet energy is exceeded and the current has a positive direction.

A. E. B. Abu-Elanien et al. [63] described a non-communication based protection algorithm for VSC-based MTDC systems. Based on the idea of using the stray capacitance of busbars connecting line sections to obtain high and low frequency energies that allow the differentiation of internal and external faults, the authors proposed adding low-capacitance shunt capacitors to all busbars, since they discovered that stray capacitance alone cannot be used to realise this non-communication strategy.

Other authors that have also used or recommended the use of travelling waves and wavelets for fault detection and location in VSC-based HVDC systems include: B. Mitra et al. [64], M. Brenna et al. [65], and Z. Zhou et al. [66].

### *3.2. Current differential protection and related strategies*

Current differential protection has been widely used in AC networks for decades, but its application in HVDC systems may cause some problems that have prevent it from meeting operational speed

EBSCOhost - printed on 2/14/2023 2:46 PM via . All use subject to https://www.ebsco.com/terms-of-use

requirements. Therefore, traditional differential protection is often used as a back-up in HVDC transmission lines [67].

The basic principle that lies behind traditional differential current protection relies on the measurement of currents at both ends of the line [10], calculating the difference between them, and then comparing this to a pre-defined threshold. If the threshold is exceeded, the protection is tripped [68]. If measurements from both ends have to be taken, synchronous current data from both stations may be required, making a parallel telecommunications link necessary, along with having accurate parameters for HVDC lines, a high sampling rate, and a high communication speed [67]. In this regard, the reliability of the entire protection system would depend on the telecommunication system's availability. Such a telecommunication-based DC protection system may not be desirable due to economic (a large number of accurate and fast current and voltage sensors are required [69]) and reliability reasons, so a local detection principle may be more appropriate [10].

The main methodology in this area has been proposed by J. Descloux et al. [36, 42, 70, 71]. They developed a differential current algorithm, along with a telecommunications link for each power cable, focused on VSC-based MTDC grids. This protection plan consists of three different protection algorithms: main cable protection to selectively detect DC faults on cables; busbar protection to detect faults between a converter station and the feeder's current sensors; and backup protection to protect the grid in case of malfunction. This approach has also been applied by M. Hajian et al. [72] in VSC-HVDC based MTDC systems with mechanical DC circuit breakers. Y. Li et al. [73, 74] have also used it as a second step for fault detection in VSC-HVDC systems with hybrid circuit breakers.

However, considering the possible loss of communication, the same authors provided a solution using a non-communicative protection principle [36, 75]. This new protection algorithm is based on differential voltage measurements using inductors placed in series at each end of every conductor. This last approach has also been used by Y. Li et al. [73, 74] as a first step for fault detection in VSC-HVDC systems with hybrid circuit breakers.

G. Song et al. used fault component current to protect cable lines—this was initially developed for VSC-HVDC systems [67, 76] and then extended to LCC-HVDC systems [77]. Using only terminal currents and without the need for serious synchronization, the differences in current changes and fault component current characteristics at both ends can be used to identify internal or external faults in VSC-HVDC cable lines. Two possible variations to this methodology have also been proposed: using

EBSCOhost - printed on 2/14/2023 2:46 PM via . All use subject to https://www.ebsco.com/terms-of-use

capacitances in both terminals [78] and applying a correlation analysis of the differential current and differential voltage derivative [79].

A. Adamczyk et al. used the differential measurement between the two ends of a branch to evaluate faulty branches in MTDC grids [8]: i.e. whether the fault lies within a cable section (positive current sum) or if it is external to that branch (negative current sum). Later, some of the same authors attempted to find ways to minimise the impact of DC faults on HVDC networks [80]. In comparing inverse DC current vs. the characteristics of the rate of change of DC current ($I_{dc}$ vs. $dI_{dc}/dt$), they proposed a protection coordination method that provides a grading margin between the protection characteristics of a HVDC breaker and a converter, in order to prioritise the opening of the HVDC breaker over the converter block.

I. Dallas and C. Booth [9], using a simulation analysis over a two-level VSC-based MTDC system, concluded that the critical time is so short that it would be difficult to implement an effective differential protection system. They claim that a fast, discriminative protection scheme with no communications for MTDC systems is desirable.

A. E. B. Abu-Elanien et al. [15] conceived of a differential protection technique for MTDC transmission lines based on the electrical current data at both ends of each line section and using a discrete wavelet transform (DWT). This method depends on calculating an energy index for the de-noised versions of positive and negative pole currents at both ends of a line, in order to discriminate between internal and external faults. The authors describe a complete methodology that includes four steps: fast fault detection; internal and external fault discrimination; faulty pole classification; and fault location.

Finally, D. Tzelepis et al. [51] devised a new methodology for the quick detection of faults in VSC-based MTDC systems, using a so-called single-end differential protection system. Their approach requires distributing a series of current measuring sensors (multi-point optical current sensing devices) along each line. The protection is organised in three different stages. Stage I includes a differential current threshold comparison between adjacent sensors, which allows discrimination between internal and external faults. Once the threshold of the previous stage has been reached, Stage II ensures that the operating decision is not due to a short signal disturbance, based on the rate of change of the current. Stage III initiates a tripping signal to the circuit breaker.

EBSCOhost - printed on 2/14/2023 2:46 PM via . All use subject to https://www.ebsco.com/terms-of-use

### *3.3. Electrical measurements and parameters*

Among the numerous options that can be found within this field, the most conventional is overcurrent protection. Overcurrent schemes use the current magnitude as an indicator of a fault and give the command to trip if the current exceeds a certain threshold. However, they provide little selectivity, which makes them generally unsuitable for DC grids. In this regard, the use of a directional form of protection may increase the level of selectivity, although if the fault is established near to the protection, this may trip unnecessarily as well. Another option is the development of distance protection methods, which use the impedance between the protection and the faulted point to estimate fault distance. In DC systems, abrupt changes in frequency during fault transients may lead to inaccurate estimations of the fault location [68].

From this heterogeneous group of proposals, it is worth mentioning the so-called "handshaking method," developed by L. Tang and B. T. Ooi in 2002, which builds on a previous version of a DC fault detection methodology in multi-terminal VSC-HVDC transmission systems [81]. Using simultaneous DC voltage and current thresholds in the converter stations to detect the fault, they proposed that 10 different fault detection schemes should be applied under different fault types or protection configurations. Afterwards, using pre-fault and post-fault current measurements, they used the directions of the DC fault currents and based on the results of three independent methods selected the potential faulted line [11, 82]. This "handshaking method" was also used by Y. Xu et al. [16] as a part of their protection coordination strategy for meshed MMC-HVDC systems under DC faults.

Recent analyses agrees to some extent with the use of the direction of a fault current and the current derivative in order to identify the faulted branch and to select the faulted section [83]. A. Samir et al. proposed [20] what they call a "Relative Direction Method"—a communication-based strategy that depends on the relative directions between currents passing through each line connected to the same bus. Additionally, E. Kontos et al. [84-86] used the fault current direction method described in [81] for their research into VSC-MTDC systems, including the use of a central controller and fiber optics. They noted that the thresholds for the protective functions should be project-specific and based on network characteristics and the ratings of the grid assets.

For several years, J. Yang et al. have analysed the implications of different DC cable faults in VSC-HVDC systems [87, 88]. They

EBSCOhost - printed on 2/14/2023 2:46 PM via . All use subject to https://www.ebsco.com/terms-of-use

established a detailed protection scheme for meshed VSC-HVDC transmission systems using real-time information [87-89]. In addressing the possibility of high resistance faults, their short-circuit fault location method relies on the installation of another voltage sensor along with two voltage dividers, [90-92]. In the case of ground faults, they proposed the use of single-ended voltage and current measurements, which can also be used for offline maintenance and fault location [93].

Developing on previous research in the field of shipboard power systems, M. Shukr et al. proposed the use of an active impedance estimation technique to locate faults in VSC-HVDC transmission lines [94]. Creating a voltage disturbance in the DC line at the supply end, the resultant current transient is measured at the capacitor point of connection, which is then used to obtain the fault distance and DC resistance. The proposed method identifies the faulted line and the type of fault.

S. Fletcher et al. [95] proposed the idea of measuring the initial di/dt and rate of current rise (ROCR) to detect the existence of a DC fault, as well as to calculate the inductance to that faulted point. This protection system would operate under the assumption that, under fault conditions, the current will rise more rapidly than under normal operating conditions. As such, a distance protection scheme in order to determine the faulted zone can be implemented. Some years later, M. Ikhide et al. [96-98] applied the same idea to fault detection in MMC-based MTDC-HVDC systems, using the initial di/dt (IRRC, initial rate of rise of the current) measurement. The results of their analysis prove that the IRRC is independent of the cable resistance.

J. Suonan et al. have described a distance protection system for conventional HVDC and VSC-HVDC transmission lines [99] by taking into account the frequency-dependent nature of line parameters and the presence of harmonics during transients in order to enhance measurement accuracy. By using local sampling data (voltages and currents), the proposed algorithm can identify the fault distance.

Since 2013, J. I. Marvik et al. have studied the identification of suitable fault selection criteria for VSC-HVDC systems, based on local measurements [83, 100]. By considering four possible candidates (DC-current, DC-current derivative, DC-voltage, and DC-voltage derivative) and according to four criteria (dependability, speed, security, and selectivity), the authors conclude that derivatives are generally the best choice for primary protection, while DC-current magnitude may be more suited to reserve/back-up protection. Based on these conclusions, they proposed a new protection scheme for VSC-based MTDC systems [101, 102] that were designed to detect and clear cable-to-ground faults ranging

EBSCOhost - printed on 2/14/2023 2:46 PM via . All use subject to https://www.ebsco.com/terms-of-use

from those with very low to those with relatively high impedance. Their methodology is based on two complementary and integrated layers, and assuming that inductive FCLs and DC breakers are present at each end of the cable connection:

- The first protection layer compares the current derivative against a predefined threshold to cope with low impedance faults, using a communication-less fault detection system [103].
- The secondary protection layer implements a differential current protection system intended to cope with higher impedance faults.

Developing on a previously designed protection scheme for traditional LCC-HVDC systems [104], X. Zheng et al. proposed a harmonic current protection scheme for VSC-HVDC systems [105]. Based on the inherent characteristics of the carrier-based PWM converters, and using the fault responses of the first carrier wave frequency harmonic current, this methodology can recognise the internal and external faults in a point-to-point HVDC transmission system. Similarly, J. Sneath et al. [106-108] described a fault detection scheme for MTDC systems based on the ROCOV measured at the line side of the di/dt limiting reactors. To this end, the rate of change of voltage (ROCOV) based protection thresholds (max. ROCOV for remote faults and min. ROCOV for immediate faults) are set for each grid, once the inductor value has been properly chosen. A year later, R. E. Torres et al. [68] devised a model that combined the use of feeder inductors and an overcurrent protection scheme to locate faults in multi-terminal VSC-HVDC systems. The feeder inductors are placed near each protection relay (at the end of each DC line) and the function of the current is positive above and negative below a predetermined input current called the pickup current.

A. K. Marten and C. Troitzsch et al. presented [10, 109] a DC fault detection methodology for pole-to-pole faults, as well as for pole-to-earth faults, in VSC-HVDC-based MTDC systems. Without relying on a telecommunications system and using only local current and voltage measurements, the authors proposed three criteria in order to ensure reliable identification of fault type and fault location: the differential current criterion to determine if the fault is located on the line between the converter and DC switch yard or in the DC switch yard itself; evaluation of the DC line fault detection criteria ($\Delta I$, $\Delta U$ and $I_E$) to check whether a line fault is located on the observed line; and back-up protection by checking the operational ranges of these variables with the aid of delay tripping curves

EBSCOhost - printed on 2/14/2023 2:46 PM via . All use subject to https://www.ebsco.com/terms-of-use

Similar to other methodologies, W. Leterme et al. proposed [110, 111] a protection methodology for meshed HVDC grids using a series reactor to split the grid into different zones. This non-unit protection scheme against DC faults uses an undervoltage criterion to discriminate normal operation from faults. Next, a combination of the voltage derivative and the undervoltage criterion is used to discriminate between internal and external faults. Finally, the current derivative is used to discriminate between forward and backward faults. Furthermore, an efficient method for determining the protection thresholds is provided [112].

Considering the important problems that may arise from a possible malfunction of protections in HVDC Grids, and completing their previous studies on primary protection, W. Leterme et al. also developed a new local backup relaying algorithm for HVDC grids [111, 113], which leads to a short delay between primary and backup protective actions. The proposed backup protection algorithm consists of two separate subsystems to detect the failure of the breaker associated with the primary relay, as well as the failure of the relays on adjacent lines. In this regard, two different approaches are presented:

- Breaker failure detection using a linear threshold: in this approach, linear discriminant analysis (LDA) is used to find a threshold (or decision boundary) that divides the UI-plane into two regions associated with cleared and uncleared faults [111, 114, 115]. Originally developed for a symmetrical monopolar configuration, this methodology has been extended to bipolar systems and its robustness has been assessed against different operating conditions and system parameters [116].
- Breaker and relay failure detection using classifiers: although various classification methods can be used for the proposed backup protection algorithm, the K-nearest neighbours (KNN) classifier is used (as it was in some of their previous work) [69]. The classifier uses three features from the current and voltage measurements at the primary protection zone: the instantaneous voltage and current, and a time tag [111].

M. Habibur Rahman et al. [117-120] proposed using a rather simple combination of a single ended overcurrent and current derivative approach to detect a DC fault on a MTDC system based on a MMC—this is only a fraction of a wider protection strategy based on DC network partitions.

J. Wang et al. [50] developed a methodology that combined the voltage derivative and current derivative for single-ended enhanced

EBSCOhost - printed on 2/14/2023 2:46 PM via . All use subject to https://www.ebsco.com/terms-of-use

protection performance in MTDC systems. A negative current derivative indicates an external fault, so a positive current derivative indicates that the fault could be within the protection zone.

S. P. Azad et al. presented a rather simple current differential technique [69] for fault detection and identification in VSC-HVDC-based MTDC systems, using a simple sum of currents for fault identification (distinguishing bus faults from line faults) and a KNN classifier for faulty line identification. Some years later, the lead authors [121] extended their methodology and presented a local bus primary relaying algorithm based on measurements obtained from current sensors only, in order to detect faults and identify their locations in HVDC grids. The proposed primary relaying algorithm consists of several fault detection and identification (FDI) units. Each one is associated with one DC bus. Each FDI unit includes three types of modules: a bus fault detection module; a line fault detection module; and a breaker coordination module. This methodology has also been used by A. Mokhberdoran et al. [122-124] to develop their protection strategy for MTDC grids based on unidirectional hybrid circuit breakers.

J. Liu et al. presented two different protection schemes for VSC-based MTDC systems. In the first [125], the comparison of the currents at the DC-link capacitor branch and both ends of the DC line makes detection of an internal DC fault possible. However, the current comparison by itself has several drawbacks (especially for distant faults), so a current correlation system is used, by means of the Pearson correlation coefficient. In the second [126], which is based on a supplemental inductor placed at each end of the DC line, they propose using both a main protection (adequate for smaller fault resistances) and a backup protection system to differentiate between internal and external faults:

- A voltage derivative criterion is used as a startup element for the protection system.
- The main protection system is adequate for smaller fault resistances. In this case, the ratio of transient voltages (ROTV) at both ends of the inductor is calculated, for both ends of the DC line, and compared with a pre-set threshold.
- The backup protection system requires communication between both ends of the DC line to compare the ROTV values against another pre-set threshold.

The authors also compared its performance against other similar methodologies proposed by other authors [105, 108, 110].

EBSCOhost - printed on 2/14/2023 2:46 PM via . All use subject to https://www.ebsco.com/terms-of-use

Similar to the approach used by J. Sneath [108], R. Li et al. [103] proposed using the rate of change of DC reactor voltage to detect a DC pole-to-pole fault in a meshed multi-terminal HVDC system (with a symmetrical monopole HVDC structure) with DC reactors connected to each end of the DC cables. Using two predefined thresholds (initial threshold and protection threshold), along with a time interval and a minimum fault detection time (which gives better EMI noise immunization), the fault voltage distribution among the DC terminal inductances and the arm inductances are analysed using the parallel-series equivalent circuit, while the DC reactor voltage is continuously monitored. All the measurements are local, so communication is not required. The authors claim that their methodology has better performance than other similar approaches (such as [108] and [101]) when considering detection speed, accuracy, reliability, and robustness.

K. Jia et al. presented [127] a single-ended fault location algorithm for DC pole-to-pole faults in VSC-HVDC systems. Using analyses of the DC fault circuit and its differential equations during the "discharging phase" (where the fault is only fed by the DC link), as well as applying Prony's method to obtain some factors and coefficients, the distance to the fault can be calculated. This calculation can distinguish between close-end faults and remote-end faults and, at the same time, accuracy can be estimated by comparing a coefficient against a pre-defined threshold.

P. T. Lewis et al. [128, 129] designed a fault section identification algorithm for MMC-based HVDC systems with non-homogeneous sections (cable and overhead line). Section identification is achieved using the system characteristic voltage and current signals (peaks and oscillations, or the absence of them) observed after an AC circuit breaker operates. As such, not only is it possible to determine the faulted line and section, but also the type of fault (pole-to-ground or pole-to-pole), allowing the performance of the recloser if necessary.

Finally, P. Tünnerhoff et al. [130] proposed using the controllability of modern full bridge MMC converters to locate pole-to-ground DC faults in bipolar HVDC systems, evoking well-defined AC voltage and current components on the DC side. The authors focus was only on fault location and they suggested using transient line protection methods [131] for fault detection. Compared to other HVDC fault localization methods, smaller sampling rates for voltage and current measurements can be used without affecting the reliability of the calculated results.

EBSCOhost - printed on 2/14/2023 2:46 PM via . All use subject to https://www.ebsco.com/terms-of-use

### *3.4. Artificial intelligence*

Artificial Intelligence (AI) is a collection of techniques modelled on the thought and behaviour of human beings and animals. AI can be taught to make rational decisions, much like a human expert, by including missing data, considering evolving situations, and using accumulated experience over time. Each artificial intelligence technique has its own advantages and disadvantages.

One of the main AI models is the artificial neural network (ANN). This is a powerful problem-solving tool that emulates how biological nervous systems process information; it shows a remarkable ability to derive a solution from complicated or imprecise data related to real-world problems. Another important approach is that of fuzzy logic (FL), which is a form of many-valued logic and deals with reasoning, similar to human reasoning, that analyses ambiguous data (fuzzy data). FL is a rule-based approach where a set of rules are used to make the relevant decision.

Although they have been more frequently developed for conventional LCC-HVDC systems, AI techniques have also been proposed for DC fault detection and location techniques for VSC-based HVDC systems.

S. Xiaoyun et al. [132] proposed a method to diagnose and identify faults in VSC-HVDC systems using the fluctuation range of the amplitude in the DC voltage signal. Firstly, according to the amplitude range of the DC voltage fluctuation, the fault feature is determined. Secondly, the fault signal is pre-processed to eliminate the effect of the DC voltage setting, and the fault characteristics are extracted using wavelet analysis. Finally, faulty and healthy modes are identified by means of backpropagation (BP) ANN.

B. Paily et al [133, 134] presented a methodology some years later to identify and classify both AC and DC faults in VSC-HVDC systems with the help of FL. The current and voltage measured at a substation are used to obtain their equivalent d-q axis magnitudes (Park transformation), which form the input variables in the fuzzy inference engine.

Similarly to the methodology proposed by S. Xiaoyun, Z. Li et al. developed [135] a condition monitoring and fault diagnosis method for HVDC systems. This uses independent component analysis (ICA) to separate useful fault source components from multi-channel sensor signals (voltages and currents) in HVDC systems. After ICA processing, useful fault sources are extracted and prepared for wavelet analysis. Finally, the energy values of the wavelet sub-bands are used as the fault feature vector in an ANN.

A. A. A. Hage et al. [136] devised a fault detection, location, and classification technique for MTDC systems. Based on analytical models of

EBSCOhost - printed on 2/14/2023 2:46 PM via . All use subject to https://www.ebsco.com/terms-of-use

the DC grid, this approach uses a number of dynamic models for different fault types and fault locations. The technique involves two steps. Firstly, an on-line single-ended algorithm is used, where a bank of Kalman filters—one each for every model—is executed at all converter/switching stations. These Kalman filters help to identify the smaller distance ('residual' in the authors' terminology) between local observations and model dynamics, which indicates the best fitting model and infers the fault type and faulted line. Secondly, an off-line double-ended algorithm is used based on the same principle as the on-line version. The difference is found in the reliance on a fault model with a much finer discretization and the use of historical and synchronised measurements from both line ends.

R. C. Santos et al. [137] proposed a new algorithm for fault detection, location, and classification in VSC-based HVDC links, using a feed-forward multi-layer perceptron (MLP) ANN. Using only local signals at the rectifier substation and without any communication link, this approach is able to detect and classify a fault occurring at either the rectifier substation, on the DC line, or at the inverter substation. To develop this task, four different kinds of ANNs are considered: to detect a fault condition; to identify the fault section; to classify a fault at the rectifier substation; and to classify a fault at the inverter substation. Additionally, in order to improve the algorithm's performance concerning faults on the inverter's side, the authors proposed the use of three independent ANNs to classify faults, instead of only one ANN with three outputs—to detect single-phase faults, to detect double-phase faults, and to detect three-phase faults.

A. Hossam-Eldin et al. [138, 139] conceived of a hybrid travelling wave fuzzy logic-based wavelet decomposition technique to identify a faulty line in MTDC networks, in addition to accurately determining the fault location. Using the MTDC system of [11] for simulation and verification purposes, the proposed algorithm identifies fault location through three steps:

- Fault detection, since the wavelet detail D2 shows an abrupt change in amplitude at the instance of a fault occurrence.
- Fault type classification, where the D2 of all lines is further fed into a FL voter, which identifies the faulted line and classifies the type of fault.
- Identification of fault location, using a travelling wave developed tool, which obtains the time of the front wave and the reflected wave using wavelet coefficient peaks.

EBSCOhost - printed on 2/14/2023 2:46 PM via . All use subject to https://www.ebsco.com/terms-of-use

S. Vasanth et al. (who were also involved in [43-45]) presented a model that combined the use of WT and MLP ANNs to detect pole-to-pole faults in two-terminal VSC-HVDC links [140]. Q. Yang et al. [141] proposed a novel multi-terminal HVDC protection scheme based on ANN and high frequency components detected from fault current signals only, which is similar to the approach the authors used for DC microgrids [142]. To this end, an FFT is applied to the windowed signal to create the input data for the ANN. An ANN is then used to perform fault detection and, if a fault condition is detected, two more ANNs are used for fault classification and location purposes.

## 4. Conclusions

This chapter is intended to provide a foundation for further research in the field of protection for modern HVDC systems, including the development of suitable protection strategies for their safe and secure operation, by giving a broad and accurate review of the techniques for DC fault detection and location developed to date.

From this analysis, it can be concluded that, although the number of proposals to detect and locate DC faults in VSC-HVDC and MTDC systems has traditionally been lower than the approaches proposed for conventional LCC-HVDC systems, they are increasing at an impressive rate. This is especially so in the past 5 years.

In addition, the types of techniques proposed for fault detection and location in these systems has become increasingly heterogeneous, which confirms the difficulty of finding a main line of research that covers the specific needs of future HVDC systems. Despite the fact that traditional approaches (differential protection, distance protection, travelling waves, etc.) are among the most commonly proposed methodologies, other kinds of techniques, like artificial intelligence, are gaining more and more impetus.

## Acknowledgement

The authors gratefully acknowledge the support of the Spanish Ministry of Economy, Industry and Competitiveness (project ENE2016-79145-R AEI/FEDER, UE), the Basque Government (GISEL research group IT1083-16), and the University of the Basque Country UPV/EHU (research group funding PPG17/23).

EBSCOhost - printed on 2/14/2023 2:46 PM via . All use subject to https://www.ebsco.com/terms-of-use

## References

[1] F. Gonzalez-Longatt and J. M. Roldan, "Effects of dc voltage control strategies of voltage response on multi-terminal HVDC following a disturbance", in *Universities Power Engineering Conference (UPEC), 2012 47th International*, 2012, pp. 1-6.

[2] I. Dallas, C. Booth, and A. Dysko. 2013, *Control and Protection of Supergrids*.

[3] A. Wasserrab and G. Balzer, "Evaluation of short circuit currents in multi-terminal HVDC systems", in *Electrical and Power Engineering (EPE), 2012 International Conference and Exposition on*, 2012, pp. 213-218.

[4] Y. Xiaobo, Y. Dawei, Y. Chunming, Y. Chengyan, Y. Chao, and R. T. H. Li, "A DC fault clearance method for series multi-terminal HVDC system", in *Energy Conversion Congress and Exposition (ECCE), 2014 IEEE*, 2014, pp. 2663-2669.

[5] Z. Zhou, "Co-ordination of Converter Controls and an Analysis of Converter Operating Limits in VSC-HVdc Grids", A Thesis submitted to the Faculty of Graduate Studies in partial fulfillment of the requirements for the degree of Doctor of Philosophy, Department of Electrical and Computer Engineering, University of Manitoba, Winnipeg, Manitoba, Canada, 2013.

[6] D. Jovcic, Z. Lu, and M. Hajian, "LCL VSC Converter for High-Power Applications", *Power Delivery, IEEE Transactions on,* vol. 28, pp. 137-144, 2013.

[7] Z. Lu and D. Jovcic, "Comparison of L-VSC and LCL-VSC converter for HVDC transmission", in *Power Electronics and Motion Control Conference (EPE/PEMC), 2012 15th International*, 2012, pp. DS3b.5-1-DS3b.5-7.

[8] A. Adamczyk, C. D. Barker, and H. Ha, "Fault detection and branch identification for HVDC grids", in *Developments in Power System Protection (DPSP 2014), 12th IET International Conference on*, 2014, pp. 1-6.

[9] I. Dallas and C. Booth, "Teleprotection in multi-terminal HVDC supergrids", in *Developments in Power System Protection (DPSP 2014), 12th IET International Conference on*, 2014, pp. 1-6.

[10] A. K. Marten, C. Troitzsch, and D. Westermann, "Non-telecommunication based DC line fault detection methodology for meshed HVDC grids", in *AC and DC Power Transmission, 11th IET International Conference on*, 2015, pp. 1-8.

[11] T. Lianxiang and O. Boon-Teck, "Locating and Isolating DC Faults in Multi-Terminal DC Systems", *Power Delivery, IEEE Transactions on,* vol. 22, pp. 1877-1884, 2007.

[12] O. M. K. K. Nanayakkara, A. D. Rajapakse, and R. Wachal, "Traveling-Wave-Based Line Fault Location in Star-Connected Multi-terminal HVDC Systems", *Power Delivery, IEEE Transactions on,* vol. 27, pp. 2286-2294, 2012.

[13] S. P. Le Blond, Q. Deng, and M. Burgin, "High frequency protection scheme for multi-terminal HVDC overhead lines", in *Developments in Power System*

EBSCOhost - printed on 2/14/2023 2:46 PM via . All use subject to https://www.ebsco.com/terms-of-use

*Protection (DPSP 2014), 12th IET International Conference on*, 2014, pp. 1-5.

[14] W. Shuai, B. Tianshu, and J. Ke, "Wavelet entropy based fault detection approach for MMC-HVDC lines", in *Power & Energy Society General Meeting, 2015 IEEE*, 2015, pp. 1-5.

[15] A. E. B. Abu-Elanien, A. A. Elserougi, A. S. Abdel-Khalik, A. M. Massoud, and S. Ahmed, "A differential protection technique for multi-terminal HVDC", *Electric Power Systems Research,* vol. 130, pp. 78-88, 1// 2016.

[16] Y. Xu, D. Shi, and S. Qiu, "Protection coordination of meshed MMC-MTDC transmission systems under DC faults", in *TENCON 2013 - 2013 IEEE Region 10 Conference (31194)*, 2013, pp. 1-5.

[17] H. Zheng-you, L. Kai, L. Xiao-peng, L. Sheng, Y. Jian-wei, and M. Rui-kun, "Natural Frequency-Based Line Fault Location in HVDC Lines", *Power Delivery, IEEE Transactions on,* vol. 29, pp. 851-859, 2014.

[18] H. Livani and C. Y. Evrenosoglu, "A single-ended fault location method for segmented HVDC transmission line", *Electric Power Systems Research,* vol. 107, pp. 190-198, 2014.

[19] G. Song, X. Cai, S. Gao, J. Suonan, and G. Li, "Natural frequency based protection and fault location for VSC-HVDC transmission lines", in *Advanced Power System Automation and Protection (APAP), 2011 International Conference on*, 2011, pp. 177-182.

[20] A. Samir, A. E. B. Abu-Elanien, A. S. Abdel-Khalik, A. M. Massoud, and S. Ahmed, "A directional protection technique for MTDC networks", in *Electric Power and Energy Conversion Systems (EPECS), 2015 4th International Conference on*, 2015, pp. 1-6.

[21] R. K. Mallick and R. K. Patnaik, "Fault analysis of voltage-source converter based multi-terminal HVDC transmission links", in *Energy, Automation, and Signal (ICEAS), 2011 International Conference on*, 2011, pp. 1-7.

[22] P. Chen, B. Xu, J. Li, and Y. Ge, "Modern travelling wave based fault location techniques for HVDC transmission lines", *Transactions of Tianjin University,* vol. 14, pp. 139-143, 2008// 2008.

[23] K. Young-Jin, K. Sang-Hee, L. Dong-Gyu, and K. Hyung-Kyu, "Fault Location Algorithm Based on Cross Correlation Method for HVDC Cable Lines", in *Developments in Power System Protection, 2008. DPSP 2008. IET 9th International Conference on*, 2008, pp. 360-364.

[24] G. Song, X. Chu, X. Cai, S. Gao, and M. Ran, "A fault-location method for VSC-HVDC transmission lines based on natural frequency of current", *International Journal of Electrical Power & Energy Systems,* vol. 63, pp. 347-352, 12// 2014.

[25] O. M. K. K. Nanayakkara, "Line fault location in emerging HVDC transmission systems", Thesis for the Degree of Doctor of Philosophy, Department of Electrical and Computer Engineering, University of Manitoba, Winnipeg, Manitoba, Canada, 2014.

[26] O. M. K. K. Nanayakkara, A. D. Rajapakse, and R. Wachal, "Location of DC Line Faults in Conventional HVDC Systems With Segments of Cables and

EBSCOhost - printed on 2/14/2023 2:46 PM via . All use subject to https://www.ebsco.com/terms-of-use

Overhead Lines Using Terminal Measurements", *Power Delivery, IEEE Transactions on,* vol. 27, pp. 279-288, 2012.

[27] O. M. K. K. Nanayakkara, A. D. Rajapakse, and R. Wachal, "Fault location in extra long HVDC transmission lines using continuous wavelet transform", in *International Conference on Power Systems Transients (IPST)*, Delft, The Netherlands, 2011, p. 7.

[28] O. M. K. K. Nanayakkara, A. D. Rajapakse, and R. Wachal, "Fault Location in Extra Long HVDC Transmission Lines Using Discrete Wavelet Transform", in *Conference on Power Systems*, Vancouver, Canada, 2010, p. 9.

[29] K. P. A. N. Pathirana, "Travelling Wave Based DC Line Fault Location in VSC HVDC Systems", Thesis submitted in partial fulfilment of the requirements of the degree of Master of Science, Department of Electrical and Computer Engineering, University of Manitoba, Winnipeg, 2012.

[30] K. P. A. N. Pathirana, A. D. Rajapakse, O. M. K. K. Nanayakkara, and R. Wachal, "Detecting fault generated surges in DC line of VSC HVDC schemes for travelling wave based fault location", in *CIGRÉ Canada Conference*, Montréal, Québec, Canada, 2012, p. 7.

[31] S. Azizi, M. Sanaye-Pasand, M. Abedini, and A. Hassani, "A Traveling-Wave-Based Methodology for Wide-Area Fault Location in Multi-terminal DC Systems", *Power Delivery, IEEE Transactions on,* vol. 29, pp. 2552-2560, 2014.

[32] K. De Kerf, K. Srivastava, M. Reza, D. Bekaert, S. Cole, D. Van Hertem, and R. Belmans, "Wavelet-based protection strategy for DC faults in multi-terminal VSC HVDC systems", *Generation, Transmission & Distribution, IET,* vol. 5, pp. 496-503, 2011.

[33] B. Chang, O. Cwikowski, M. Barnes, and R. Shuttleworth, "Multi-terminal VSC-HVDC Pole-to-pole Fault Analysis and Fault Recovery Study", in *AC and DC Power Transmission, 11th IET International Conference on*, 2015, pp. 1-8.

[34] Y. Di, L. Yawen, D. Yifeng, and Z. Xuan, "Fault detection and location for MTDC combining wavelet analysis and travelling wave", in *Power Engineering and Automation Conference (PEAM), 2012 IEEE*, 2012, pp. 1-4.

[35] J. Zhai, Y. Ding, B. Xu, and Y. Li, "Wavelet and travelling wave based DC cable fault localization in MTDC", in *Environmental Electromagnetics (CEEM), 2012 6th Asia-Pacific Conference on*, 2012, pp. 206-209.

[36] J. Descloux, "Protection contre les courts-circuits des réseaux à courant continu de forte puissance", Thèse pour obtenir le grade de Docteur Génie Électrique, Laboratoire de Génie Électrique de Grenoble (G2Elab), Université de Grenoble, École Doctorale Électronique, Électrotechnique, Automatique et Traitement du Signal, 2013.

[37] S. Azizi, S. Afsharnia, and M. Sanaye-Pasand, "Fault location on multi-terminal DC systems using synchronized current measurements", *International Journal of Electrical Power & Energy Systems,* vol. 63, pp. 779-786, 2014.

EBSCOhost - printed on 2/14/2023 2:46 PM via . All use subject to https://www.ebsco.com/terms-of-use

[38] H. A. A. Hassan, B. M. Grainger, T. E. McDermott, and G. F. Reed, "Fault location identification of a hybrid HVDC-VSC system containing cable and overhead line segments using transient data", in *2016 IEEE/PES Transmission and Distribution Conference and Exposition (T&D)*, 2016, pp. 1-5.

[39] H. A. A. Hassan, "Fault location identification for a vsc-hvdc system with a long hybrid transmission medium", Thesis submitted in partial fulfillment of the requirements for the degree of Master of Science, Swanson School of Engineering (University of Pittsburgh), 2014.

[40] R. Razzaghi, G. Lugrin, H. M. Manesh, C. Romero, M. Paolone, and F. Rachidi, "An Efficient Method Based on the Electromagnetic Time Reversal to Locate Faults in Power Networks", *Power Delivery, IEEE Transactions on,* vol. 28, pp. 1663-1673, 2013.

[41] R. Razzaghi, M. Paolone, F. Rachidi, J. Descloux, B. Raison, and N. Retiere, "Fault location in multi-terminal HVDC networks based on Electromagnetic Time Reversal with limited time reversal window", in *Power Systems Computation Conference (PSCC), 2014*, 2014, pp. 1-7.

[42] J. Descloux, B. Raison, and J. B. Curis, "Protection strategy for undersea MTDC grids", in *PowerTech (POWERTECH), 2013 IEEE Grenoble*, 2013, pp. 1-6.

[43] Y. Yew Ming and A. Ukil, "Wavelet based fault analysis in HVDC system", in *Industrial Electronics Society, IECON 2014 - 40th Annual Conference of the IEEE*, 2014, pp. 2472-2478.

[44] M. Yew and A. Ukil, "Differentiation of fault and load change in HVDC system using Amplitude Tracking Square Wave", in *PowerTech, 2015 IEEE Eindhoven*, 2015, pp. 1-5.

[45] Y. M. Yeap and A. Ukil, "Fault detection in HVDC system using Short Time Fourier Transform", in *2016 IEEE Power and Energy Society General Meeting (PESGM)*, 2016, pp. 1-5.

[46] Y. M. Yeap, A. Ukil, and N. Geddada, "STFT analysis of high frequency components in transient signals in multi-terminal HVDC system", in *IECON 2016 - 42nd Annual Conference of the IEEE Industrial Electronics Society*, 2016, pp. 4008-4013.

[47] S. H. Ashrafi Niaki, H. Kazemi Karegar, and M. Ghalei Monfared, "A novel fault detection method for VSC-HVDC transmission system of offshore wind farm", *International Journal of Electrical Power & Energy Systems,* vol. 73, pp. 475-483, 2015.

[48] H. Zheng-You and L. Kai, "Natural frequency-based protection scheme for voltage source converter-based high-voltage direct current transmission lines", *Generation, Transmission & Distribution, IET,* vol. 9, pp. 1519-1525, 2015.

[49] H. Xu and G. Song, "A novel traveling wave head identification method in VSC-HVDC based on parameter identification", in *2015 5th International Conference on Electric Utility Deregulation and Restructuring and Power Technologies (DRPT)*, 2015, pp. 933-937.

EBSCOhost - printed on 2/14/2023 2:46 PM via . All use subject to https://www.ebsco.com/terms-of-use

[50] J. Wang, B. Berrgren, K. Linden, J. Pan, and R. Nuqui, "Multi-terminal DC system line protection requirement and high-speed protection solutions", in *Cigré International Symposium*, Lund (Sweden), 2015.

[51] D. Tzelepis, A. Dyśko, G. Fusiek, J. Nelson, P. Niewczas, D. Vozikis, P. Orr, N. Gordon, and C. D. Booth, "Single-Ended Differential Protection in MTDC Networks Using Optical Sensors", *IEEE Transactions on Power Delivery,* vol. 32, pp. 1605-1615, 2017.

[52] N. Johannesson and S. Norrga, "Longitudinal differential protection based on the Universal Line Model", in *IECON 2015 - 41st Annual Conference of the IEEE Industrial Electronics Society*, 2015, pp. 001091-001096.

[53] N. Johannesson, S. Norrga, and C. Wikström, "Selective wave-front based protection algorithm for MTDC systems", in *13th International Conference on Development in Power System Protection 2016 (DPSP)*, 2016, pp. 1-6.

[54] R. Perveen, N. Kishor, and S. R. Mohanty, "Fault detection for offshore wind farm connected to onshore grid via voltage source converter-high voltage direct current", *IET Generation, Transmission & Distribution,* vol. 9, pp. 2544-2554, 2015.

[55] R. Perveen, S. R. Mohanty, and N. Kishor, "Fault location in VSC-HVDC section for grid integrated offshore wind farm by EMD", in *2016 18th Mediterranean Electrotechnical Conference (MELECON)*, 2016, pp. 1-5.

[56] R. Perveen, N. Kishor, and S. R. Mohanty, "Fault detection and optimal coordination of overcurrent relay in offshore wind farm connected to onshore grid with VSC–HVDC", *International Transactions on Electrical Energy Systems,* vol. 26, pp. 841-863, 2016.

[57] G. Auran, B. Raison, J. Descloux, and S. Nguefeu, "A novel pole-to-ground fault detection algorithm for meshed HVDC grids with half-bridge MMC converters and full recourse to DC circuit breakers", in *13th International Conference on Development in Power System Protection 2016 (DPSP)*, 2016, pp. 1-6.

[58] X. Chuanxin, C. Qing, and W. Lei, "A single-terminal traveling wave fault location method for VSC-HVDC transmission lines based on S-transform", in *2016 IEEE PES Asia-Pacific Power and Energy Engineering Conference (APPEEC)*, 2016, pp. 1008-1012.

[59] X. Chu, G. Song, and J. Liang, "Analytical method of fault characteristic and non-unit protection for HVDC transmission lines", *CSEE Journal of Power and Energy Systems,* vol. 2, pp. 37-43, 2016.

[60] L. Peiyao, S. Guobing, C. Xu, and W. Ting, "One quick-action protection scheme for VSC-HVDC transmission lines with considering the frequency-dependent characteristics of cables", in *2016 IEEE PES Asia-Pacific Power and Energy Engineering Conference (APPEEC)*, 2016, pp. 2480-2484.

[61] R. E. Torres-Olguin and H. K. H×idalen, "Travelling waves-based fault detection method in multi-terminal HVDC grids connecting offshore wind farms", in *13th International Conference on Development in Power System Protection 2016 (DPSP)*, 2016, pp. 1-7.

EBSCOhost - printed on 2/14/2023 2:46 PM via . All use subject to https://www.ebsco.com/terms-of-use

[62] R. E. Torres-Olguin, "Non-unit fault detection method in multi-terminal HVDC system based on the high frequency transients on travelling waves", Norwegian University of Science and Technology 2016.
[63] A. E. B. Abu-Elanien, A. S. Abdel-Khalik, A. M. Massoud, and S. Ahmed, "A non-communication based protection algorithm for multi-terminal HVDC grids", *Electric Power Systems Research,* vol. 144, pp. 41-51, 2017.
[64] B. Mitra, B. Chowdhury, and M. Manjrekar, "Fault analysis and hybrid protection scheme for multi-terminal HVDC using Wavelet transform", in *2016 North American Power Symposium (NAPS)*, 2016, pp. 1-6.
[65] M. Brenna, F. Foiadelli, and M. Longo, "Fault detection HVDC systems applied to renewable sources", in *2016 17th International Conference on Harmonics and Quality of Power (ICHQP)*, 2016, pp. 691-696.
[66] Z. Zhou, Q. Jin, and Y. Zhang, "Discrete Wavelet Transform Based Fault Analysis and Identification in Flexible HVDC Transmission Systems", in *International Forum on Energy, Environment Science and Materials (IFEESM)*, Shenzhen (China), 2015.
[67] S. Guobing, C. Xinlei, L. Dekun, G. Shuping, and S. Jiale, "A novel pilot protection principle for VSC-HVDC cable lines based on fault component current", in *Power Engineering and Automation Conference (PEAM), 2012 IEEE*, 2012, pp. 1-4.
[68] R. E. Torres-Olguin and H. K. Hoidalen, "Inverse time overcurrent protection scheme for fault location in multi-terminal HVDC", in *PowerTech, 2015 IEEE Eindhoven*, 2015, pp. 1-6.
[69] S. P. Azad, W. Leterme, and D. Van Hertem, "A DC grid primary protection algorithm based on current measurements", in *Power Electronics and Applications (EPE'15 ECCE-Europe), 2015 17th European Conference on*, 2015, pp. 1-10.
[70] J. Descloux, C. Gandioli, B. Raison, N. Hadjsaid, and P. Tixador, "Protection system for meshed HVDC network using superconducting fault current limiters", in *PowerTech (POWERTECH), 2013 IEEE Grenoble*, 2013, pp. 1-5.
[71] J. Descloux, P. Rault, S. Nguefeu, J.-B. Curtis, X. Guillaud, F. Colas, and B. Raison, "HVDC meshed grid: Control and protection of a multi-terminal HVDC system", in *2012 CIGRÉ Session*, Paris (France), 2012, p. 10.
[72] M. Hajian, Z. Lu, and D. Jovcic, "DC Transmission Grid With Low-Speed Protection Using Mechanical DC Circuit Breakers", *Power Delivery, IEEE Transactions on,* vol. 30, pp. 1383-1391, 2015.
[73] Y. Li, X. Shi, F. Wang, L. M. Tolbert, and J. Liu, "Dc fault protection of multi-terminal VSC-HVDC system with hybrid dc circuit breaker", in *2016 IEEE Energy Conversion Congress and Exposition (ECCE)*, 2016, pp. 1-8.
[74] Y. Li, "Design, Control and Protection of Modular Multilevel Converter (MMC)-Based Multi-Terminal HVDC System", Thesis submitted in partial fulfillment of the requirements for the degree of Doctor of Philosophy, University of Tennessee, 2016.
[75] J. Descloux, B. Raison, and J. B. Curis, "Protection algorithm based on differential voltage measurement for MTDC grids", in *Developments in*

EBSCOhost - printed on 2/14/2023 2:46 PM via . All use subject to https://www.ebsco.com/terms-of-use

*Power System Protection (DPSP 2014), 12th IET International Conference on*, 2014, pp. 1-5.

[76] G. Song, X. Chu, X. Cai, and S. Gao, "A novel pilot protection principle for VSC-HVDC cable lines based on fault component current", *International Journal of Electrical Power & Energy Systems,* vol. 53, pp. 426-433, 2013.

[77] S. Gao, G. Song, Z. Ma, and X. Jin, "Novel pilot protection principle for high-voltage direct current transmission lines based on fault component current characteristics", *Generation, Transmission & Distribution, IET,* vol. 9, pp. 468-474, 2015.

[78] X. F. Jin, G. B. Song, and Z. B. Ma, "A novel pilot protection for VSC-HVDC transmission lines based on parameter identification", in *Developments in Power System Protection (DPSP 2014), 12th IET International Conference on*, 2014, pp. 1-6.

[79] X. Jin and G. Song, "A Novel Pilot Protection for VSC-HVDC Transmission Lines Based on Correlation Analysis", *Energy and Power Engineering,* vol. 5, pp. 1182-1186, 2013.

[80] R. Gupta, C. D. Barker, A. Adamczyk, R. S. Whitehouse, and K. J. Dyke, "Protection coordination in multi-terminal HVDC networks for DC fault clearance", in *13th International Conference on Development in Power System Protection 2016 (DPSP)*, 2016, pp. 1-6.

[81] T. Lianxiang and O. Boon-Teck, "Protection of VSC-multi-terminal HVDC against DC faults", in *Power Electronics Specialists Conference, 2002. pesc 02. 2002 IEEE 33rd Annual*, 2002, pp. 719-724 vol. 2.

[82] T. Lianxiang, "Control and protection of multi-terminal DC transmission systems based on voltage-source converters", Thesis submitted in partial fulfillment of the requirements for the degree of Doctor of Philosophy, Department of Electrical and Computer Engineering, McGill University, Montreal, Quebec, Canada, 2003.

[83] J. I. Marvik and H. G. Svendsen, "Analysis of Grid Faults in Offshore Wind Farm with HVDC Connection", *Energy Procedia,* vol. 35, pp. 81-90, 2013.

[84] E. Kontos, R. T. Pinto, and P. Bauer, "Fast DC fault recovery technique for H-bridge MMC-based HVDC networks", in *2015 IEEE Energy Conversion Congress and Exposition (ECCE)*, 2015, pp. 3351-3358.

[85] E. Kontos, S. Rodrigues, R. T. Pinto, and P. Bauer, "Optimization of limiting reactors design for DC fault protection of multi-terminal HVDC networks", in *2014 IEEE Energy Conversion Congress and Exposition (ECCE)*, 2014, pp. 5347-5354.

[86] E. Kontos, R. Teixeira, S. Rodrigues, and P. Bauer, "Impact of HVDC Transmission System Topology on Multi-terminal DC Network Faults", *Power Delivery, IEEE Transactions on,* vol. 30, pp. 844-852, 2015.

[87] J. Yang, "Fault Analysis and Protection for Wind Power Generation Systems", Thesis submitted in fulfilment of the requirements for the degree of Doctor of Philosophy, Electronics and Electrical Engineering, College of Science and Engineering, University of Glasgow, 2011.

[88] J. Yang and J. E. Fletcher, "Protection Schemes for Meshed VSC-HVDC Transmission Systems for Large-Scale Offshore Wind Farms", in *Large*

EBSCOhost - printed on 2/14/2023 2:46 PM via . All use subject to https://www.ebsco.com/terms-of-use

*Scale Renewable Power Generation*, J.Hossain and A. Mahmud, Eds., ed Singapore: Springer, 2014, pp. 369-393.

[89] J. Yang, J. E. Fletcher, J. O'Reilly, G. P. Adam, and S. Fan, "Protection scheme design for meshed VSC-HVDC transmission systems of large-scale wind farms", in *AC and DC Power Transmission, 2010. ACDC. 9th IET International Conference on*, 2010, pp. 1-5.

[90] Y. Jin, J. E. Fletcher, and J. O'Reilly, "Multi-terminal DC Wind Farm Collection Grid Internal Fault Analysis and Protection Design", *Power Delivery, IEEE Transactions on,* vol. 25, pp. 2308-2318, 2010.

[91] Y. Jin, J. O'Reilly, and J. E. Fletcher, "An overview of DC cable modelling for fault analysis of VSC-HVDC transmission systems", in *Universities Power Engineering Conference (AUPEC), 2010 20th Australasian*, 2010, pp. 1-5.

[92] Y. Jin, J. E. Fletcher, and J. O'Reilly, "Multi-terminal DC wind farm collection and transmission system internal fault analysis", in *Industrial Electronics (ISIE), 2010 IEEE International Symposium on*, 2010, pp. 2437-2442.

[93] Y. Jin, J. E. Fletcher, and J. O'Reilly, "Short-Circuit and Ground Fault Analyses and Location in VSC-Based DC Network Cables", *Industrial Electronics, IEEE Transactions on,* vol. 59, pp. 3827-3837, 2012.

[94] M. Shukr, D. W. P. Thomas, and P. Zanchetta, "VSC-HVDC transmission line faults location using active line impedance estimation", in *Energy Conference and Exhibition (ENERGYCON), 2012 IEEE International*, 2012, pp. 244-248.

[95] S. Fletcher, P. Norman, S. Galloway, and G. Burt, "Fault detection and location in DC systems from initial di/dt measurement", in *Euro Tech Con Conference*, Manchester (United Kingdom), 2012.

[96] M. Ikhide, "DC line protection for multi-terminal (MT)-HVDC systems", in *9th Universities High Voltage Network Colloquium*, Cardiff (United Kingdom), 2016.

[97] M. A. Ikhide, S. B. Tennakoon, A. Griffiths, S. Subramanian, H. Ha, and A. Adamczyk, "Limitations of di/dt technique in DC line protection", in *13th International Conference on Development in Power System Protection 2016 (DPSP)*, 2016, pp. 1-6.

[98] M. Ikhide, S. Tennakoon, A. Griffiths, S. Subramanian, and H. Ha, "Fault detection in Multi-Terminal Modular Multilevel Converter (MMC) based High Voltage DC (HVDC) transmission system", in *2015 50th International Universities Power Engineering Conference (UPEC)*, 2015, pp. 1-6.

[99] J. Suonan, J. Zhang, Z. Jiao, L. Yang, and G. Song, "Distance Protection for HVDC Transmission Lines Considering Frequency-Dependent Parameters", *Power Delivery, IEEE Transactions on,* vol. 28, pp. 723-732, 2013.

[100] J. I. Marvik, S. D'Arco, and J. A. Suul, "Communication-less fault detection in radial multi-terminal offshore HVDC grids", in *AC and DC Power Transmission, 11th IET International Conference on*, 2015, pp. 1-8.

EBSCOhost - printed on 2/14/2023 2:46 PM via . All use subject to https://www.ebsco.com/terms-of-use

[101] J. I. Marvik, S. D'Arco, and K. Sharifabadi, "Protection scheme for multi-terminal radial VSC HVDC system without communication between terminals", in *Cigré International Symposium*, Lund (Sweden), 2015.
[102] J. I. Marvik, S. D. Arco, and J. A. Suul, "A two-layer detection strategy for protecting multi-terminal HVDC systems against faults within a wide range of impedances", in *13th International Conference on Development in Power System Protection 2016 (DPSP)*, 2016, pp. 1-6.
[103] R. Li, L. Xu, and L. Yao, "DC Fault Detection and Location in Meshed Multi-terminal HVDC Systems Based on DC Reactor Voltage Change Rate", *IEEE Transactions on Power Delivery,* vol. PP, pp. 1-1, 2016.
[104] X.-D. Zheng, N.-L. Tai, J. S. Thorp, and G.-L. Yang, "A Transient Harmonic Current Protection Scheme for HVDC Transmission Line", *Power Delivery, IEEE Transactions on,* vol. 27, pp. 2278-2285, 2012.
[105] Z. Xiaodong, T. Nengling, W. Zhongyu, and J. Thorp, "Harmonic current protection scheme for voltage source converter-based high-voltage direct current transmission system", *Generation, Transmission & Distribution, IET,* vol. 8, pp. 1509-1515, 2014.
[106] J. Sneath and A. D. Rajapakse, "DC Fault Protection of a Nine-Terminal MMC HVDC Grid", in *AC and DC Power Transmission, 11th IET International Conference on*, 2015, pp. 1-8.
[107] J. Sneath, "Grounded HVDC Grid Line Fault Protection Using Rate of Change of Voltage and Hybrid DC Breakers", Thesis submitted in partial fulfilment of the requirements of the degree of Master of Science, Department of Electrical and Computer Engineering, University of Manitoba, Winnipeg, Manitoba, 2014.
[108] J. Sneath and A. D. Rajapakse, "Fault Detection and Interruption in an Earthed HVDC Grid Using ROCOV and Hybrid DC Breakers", *IEEE Transactions on Power Delivery,* vol. 31, pp. 973-981, 2016.
[109] C. Troitzsch, A. K. Marten, and D. Westermann, "Non-telecommunication based DC line fault detection methodology for meshed HVDC grids", *IET Generation, Transmission & Distribution,* vol. 10, pp. 4231-4239, 2016.
[110] W. Leterme, J. Beerten, and D. Van Hertem, "Non-unit protection of HVDC grids with inductive dc cable termination", *Power Delivery, IEEE Transactions on,* vol. 31, pp. 820-828, 2016.
[111] W. Leterme, "Communication-less protection algorithms for meshed VSC HVDC cable grids", Thesis submitted in partial fulfillment of the requirements for the degree of Doctor of Philosophy, Department of Electrical Engineering, University of Leuven, 2016.
[112] W. Leterme, N. Ahmed, J. Beerten, x, L. ngquist, D. Van Hertem, and S. Norrga, "A new HVDC grid test system for HVDC grid dynamics and protection studies in EMT-type software", in *AC and DC Power Transmission, 11th IET International Conference on*, 2015, pp. 1-7.
[113] W. Leterme, S. P. Azad, and D. V. Hertem, "A Local Backup Protection Algorithm for HVDC Grids", *IEEE Transactions on Power Delivery,* vol. 31, pp. 1767-1775, 2016.

EBSCOhost - printed on 2/14/2023 2:46 PM via . All use subject to https://www.ebsco.com/terms-of-use

[114] S. Pirooz Azad, W. Leterme, and D. Van Hertem, "Fast breaker failure backup protection for HVDC grids", *Electric Power Systems Research,* vol. 138, pp. 99-105, 2016.

[115] S. P. Azad, W. Leterme, and D. V. Hertem, "Fast breaker failure backup protection for HVDC grids", in *11th International Conference on Power Systems Transients (IPST)*, Cavtat (Croatia), 2015.

[116] M. Wang, W. Leterme, J. Berteen, and D. V. Hertem, "Robustness Evaluation of Fast Breaker Failure Backup Protection in Bipolar HVDC Grids", in *13th International Conference on AC and DC Power Transmission (ACDC)*, Manchester (United Kingdom), 2017.

[117] M. H. Rahman, L. Xu, and K. Bell, "DC Fault Protection of Multi-terminal HVDC Systems Using DC Network Partition and DC Circuit Breakers", in *6th Protection, Automation and Control World Conference (PAC World)*, Glasgow (United Kingdom), 2015.

[118] M. H. Rahman, L. Xu, and L. Yao, "Protection of large partitioned MTDC Networks Using DC-DC converters and circuit breakers", *Protection and Control of Modern Power Systems,* vol. 1, p. 19, 2016.

[119] Y. Liangzhong, W. Jing, X. Lie, and M. H. Rahman, "Studies of coordinated zone protection strategy for DC grid", in *2016 IEEE 8th International Power Electronics and Motion Control Conference (IPEMC-ECCE Asia)*, 2016, pp. 713-718.

[120] M. H. Rahman, L. Xu, and Y. Liangzhong, "DC fault protection strategy considering DC network partition", in *2016 IEEE Power and Energy Society General Meeting (PESGM)*, 2016, pp. 1-5.

[121] S. P. Azad and D. V. Hertem, "A Fast Local Bus Current-Based Primary Relaying Algorithm for HVDC Grids", *IEEE Transactions on Power Delivery,* vol. 32, pp. 193-202, 2017.

[122] A. Mokhberdoran, S. Pirooz Azad, D. Van Hertem, N. Silva, and A. Carvalho, "Protection of HVDC Grids Using Unidirectional DC Circuit Breakers and Fast Local Protection Algorithm", in *13th International Conference on AC and DC Power Transmission (ACDC)*, Manchester (United Kingdom), 2017.

[123] A. Mokhberdoran, N. Silva, H. Leite, and A. Carvalho, "Unidirectional Protection Strategy for Multi-terminal HVDC Grids", *Transactions on Environment and Electrical Engineering,* vol. 1, pp. 1-8, 2016.

[124] A. Mokhberdoran, N. Silva, H. Leite, and A. Carvalho, "A directional protection strategy for multi-terminal VSC-HVDC grids", in *2016 IEEE 16th International Conference on Environment and Electrical Engineering (EEEIC)*, 2016, pp. 1-6.

[125] L. Jian, T. Nengling, F. Chunju, C. Shi, and W. Pan, "A fault detection method for DC lines in VSC-HVDC system based on current correlation", in *2016 IEEE Power and Energy Society General Meeting (PESGM)*, 2016, pp. 1-5.

[126] J. Liu, N. Tai, and C. Fan, "Transient-Voltage-Based Protection Scheme for DC Line Faults in the Multi-terminal VSC-HVDC System", *IEEE Transactions on Power Delivery,* vol. 32, pp. 1483-1494, 2017.

EBSCOhost - printed on 2/14/2023 2:46 PM via . All use subject to https://www.ebsco.com/terms-of-use

[127] K. Jia, M. Li, T. Bi, and Q. Yang, "A voltage resonance-based single-ended online fault location algorithm for DC distribution networks", *Science China Technological Sciences,* vol. 59, pp. 721-729, 2016.
[128] P. T. Lewis, B. M. Grainger, H. A. A. Hassan, and G. F. Reed, "Communication-less fault section identification for hybrid HVDC transmission systems", 2016.
[129] P. T. Lewis, B. M. Grainger, H. A. A. Hassan, A. Barchowsky, and G. F. Reed, "Fault Section Identification Protection Algorithm for Modular Multilevel Converter-Based High Voltage DC With a Hybrid Transmission Corridor", *IEEE Transactions on Industrial Electronics,* vol. 63, pp. 5652-5662, 2016.
[130] P. Tünnerhoff, C. Petino, M. Battiato, and A. Schnettler, "Distance protection for HVDC transmission lines based on MMC modulation strategy", in *2016 Electric Power Quality and Supply Reliability (PQ)*, 2016, pp. 283-288.
[131] C. Karawita, D. H. R. Suriyaarachchi, and M. Mohaddes, "A Controlled DC Fault Clearance Mechanism for Full-Bridge MMC VSC Converters", in *Cigré International Symposium*, Lund (Sweden), 2015.
[132] X. Sun, X. Tong, and J. Yin, "Fault Diagnosis for VSC-HVDC Using Wavelet Transform", in *Power and Energy Engineering Conference (APPEEC), 2012 Asia-Pacific*, 2012, pp. 1-4.
[133] B. Paily, S. Kumaravel, M. Basu, and M. Conlon, "Fault analysis of VSC HVDC systems using fuzzy logic", in *Signal Processing, Informatics, Communication and Energy Systems (SPICES), 2015 IEEE International Conference on*, 2015, pp. 1-5.
[134] B. Paily, "HVDC Systems Fault Analysis Using Various Signal Processing Techniques", Thesis submitted for the Degree of Doctor of Philosophy, School of Electrical and Electronic Engineering, Dublin Institute of Technology, 2015.
[135] C. S. Zhixiong Li, Yuanjing Li, J. Xing, Benyu Su, "Efficient Fault Feature Extraction and Fault Isolation for High Voltage DC Transmissions", *Elektronika ir Elektrotechnika,* vol. 21, pp. 7-12, 2015.
[136] A. A. A. Hage, B. Piepenbreier, D. Buchstaller, and M. Engel, "A multiple model approach to fault detection and localization in multi-terminal HVDC systems", in *IECON 2015 - 41st Annual Conference of the IEEE Industrial Electronics Society*, 2015, pp. 2282-2287.
[137] R. C. Santos, S. Le Blond, D. V. Coury, and R. K. Aggarwal, "A novel and comprehensive single terminal ANN based decision support for relaying of VSC based HVDC links", *Electric Power Systems Research,* vol. 141, pp. 333-343, 2016.
[138] A. Hossam-Eldin, A. Lotfy, M. Elgamal, and M. Ebeed, "Combined traveling wave and fuzzy logic based fault location in multi-terminal HVDC systems", in *2016 IEEE 16th International Conference on Environment and Electrical Engineering (EEEIC)*, 2016, pp. 1-6.
[139] A. H. Eldin, A. Lotfy, M. Elgamal, and M. Ebeed, "Protection oriented observability in multi-terminal HVDC systems", in *2016 7th International*

EBSCOhost - printed on 2/14/2023 2:46 PM via . All use subject to https://www.ebsco.com/terms-of-use

*Conference on Information and Communication Systems (ICICS)*, 2016, pp. 102-108.

[140] S. Vasanth, Y. M. Yeap, and A. Ukil, "Fault location estimation for VSC-HVDC system using Artificial Neural Network", in *2016 IEEE Region 10 Conference (TENCON)*, 2016, pp. 501-504.

[141] Q. Yang, S. Le Blond, R. Aggarwal, Y. Wang, and J. Li, "New ANN method for multi-terminal HVDC protection relaying", *Electric Power Systems Research,* vol. 148, pp. 192-201, 2017.

[142] Q. Yang, J. Li, S. Le Blond, and C. Wang, "Artificial Neural Network Based Fault Detection and Fault Location in the DC Microgrid", *Energy Procedia,* vol. 103, pp. 129-134, 2016.

EBSCOhost - printed on 2/14/2023 2:46 PM via . All use subject to https://www.ebsco.com/terms-of-use

EBSCOhost - printed on 2/14/2023 2:46 PM via . All use subject to https://www.ebsco.com/terms-of-use

# PART VI:

# HARMONICS, FILTERS AND OTHER CORRECTION DEVICES

EBSCOhost - printed on 2/14/2023 2:46 PM via . All use subject to https://www.ebsco.com/terms-of-use

# CHAPTER THIRTY-TWO

# EMI MITIGATION THROUGH A POLYPHASE DRIVE SYSTEM CONFIGURATION

GODOFREDO WINNISCHOFER[1],
CARLOS ANTONIO FRANÇA SARTORI[2]

## Abstract

A non-conventional polyphase drive system is presented in this paper. Its topology aims to reduce conducted emissions and related electromagnetic interference (EMI) through its configuration and components. The general aspects concerning the generation of common-mode voltages, their circulating current paths, and their effects are discussed. In order to validate and evaluate the efficiency of the proposed methodology, statistical and experimental evaluations were carried out, the results of which are presented and analyzed. Finally, philosophical aspects of the proposed methodology and other approaches are discussed.

**Keywords:** Electromagnetic compatibility (EMC); conducted emission control; common-mode current; motor drive system.

## Introduction

Over the past two decades, the use of low-voltage three-phase inverters in industry has increased considerably. The reduced cost of inverters has seen their wide use for controlling induction motors in many applications. The progress of power electronics technology, especially switching

[1] Engineer Specialist at ABB Ltda, Brasil and Researcher at Laboratório de Eletromagnetismo Aplicado, Escola Politécnica da Universidade de São Paulo.
[2] Professor at Laboratório de Eletromagnetismo Aplicado, Escola Politécnica da Universidade de São Paulo and Researcher at Instituto de Pesquisas Energéticas e Nucleares/Comissão Nacional de Energia Nuclear.

EBSCOhost - printed on 2/14/2023 2:46 PM via . All use subject to https://www.ebsco.com/terms-of-use

devices such as IGBTs and MOSFETs, is one of the main reasons for this success. The high-speed commutation of these devices and the consequent reduction of switching losses has led to a reduction in inverter frame size. Moreover, this has allowed inverters to operate at higher switching frequencies, getting better dynamic response from conventional three-phase induction motors, with a reduction in their losses and an overall improvement in drive system performance. However, the same devices responsible for the success of conventional three-phase inverters, are also responsible for electromagnetic disturbances [1]. Control techniques based on PWM and the corresponding drive system topology—the most common type—produce common-mode (CM) and differential-mode (DM) noise [1]-[10]. The very fast transition of IGBTs and MOSFETs, associated with this type of switching pattern produces transients of voltage and current, and this contributes to the impacts of electromagnetic phenomena, in particular, reflected wave overvoltage [1], [11]-[18]. That is, they account for conducted and radiated electromagnetic interference (EMI). In addition to causing EMI, these events play an important role in the reliability of the drive system. Reflected wave overvoltage is responsible for motor insulation stress [11], [12], and CM currents that cause premature wear in bearings [1]-[8], [19]. Over the past 20 years, an extensive literature has developed discussing these problems. It should also be stated that many advances have been made to address them. Reinforced motor insulation and cable length limitations have become established as requirements to avoid overvoltage problems. Furthermore, isolated bearings have become common in inverter driven motors. The use of shielded cables, with an ideal phase distribution, specially developed for inverter-driven systems, should also be mentioned as a newly established engineering practice [1], [9], [10]. Some of these countermeasures have helped to minimize EMI, but, over the years, the main focus has been on aspects of functional system reliability. This means that there remains a large gap for EMI improvement in inverter-driven systems. This study focuses on this aspect, particularly on the control of emissions caused by common-mode noise.

## Drive System Configurations and EMI Control

The most common topology for a three-phase drive system is a voltage source inverter using pulse width modulation (VSI PWM) for controlling induction motors. The drive is usually composed of a single-phase (4 diodes) or a three-phase (6 diodes) rectifier bridge, a DC capacitor bank, and the three-phase inverter bridge composed of six switching devices.

EBSCOhost - printed on 2/14/2023 2:46 PM via . All use subject to https://www.ebsco.com/terms-of-use

The pulses generated by the commutation of the inverter devices produce voltage variation with high frequency oscillations and, consequently, currents of high frequency that flow through the existing stray capacitances dispersed in motor windings and cables. These currents are differential-mode (DM) and common-mode (CM) currents [1]-[8].

Differential-mode currents are those that flow back to the noise source through the same circuit as the fundamental current. For this reason, certain authors call them normal-mode currents, too [2], [3]. The resulting electrical fields created by these currents are subtracted from each other, resulting in a reduction in electric field. CM currents are those that flow back to the noise source through the ground. As a consequence, the resulting electric field has reduced compensation. Thus, CM currents produce more intensive electrical fields and have much greater potential for producing EMI due to radiated emissions than differential-mode currents. As such, the former is usually the focus of investigations into EMI [2], [20].

The most common switching devices are IGBTs, which can be used in all low-voltage inverter power and voltage ranges, and MOSFETs, used in low-power and low-voltage applications, usually equal to or below 220V. MOSFETs have faster switching transitions and, consequently, allow inverters to operate at higher switching frequencies, increasing the effects of EMI. Typically, IGBT drives operate in a switching frequency range under 25 kHz, while MOSFET drives operate at switching frequencies from 25 kHz to 100 kHz. As such, the faster the switching transition of the inverter semiconductor, the higher the contribution of DM and CM noise to the EMI. However, it is not only the switching speed that is responsible for CM currents, but also the switching pattern and, primarily, the interaction between the switches.

In three-phase drive systems, CM voltages are caused by the asymmetry of the pulses. As shown in Figure 1, the CM voltage can be obtained simply by averaging the three phase voltages [21]. In a perfect sinusoidal three-phase system, the result would be zero, meaning there was no CM voltage. However, when the motor is fed by a PWM inverter, the supply voltage is not sinusoidal, but composed of discrete pulses. [5]-[8], [10].

$$V_{CM} = \frac{V_a + V_b + V_c}{3} \tag{1}$$

EBSCOhost - printed on 2/14/2023 2:46 PM via . All use subject to https://www.ebsco.com/terms-of-use

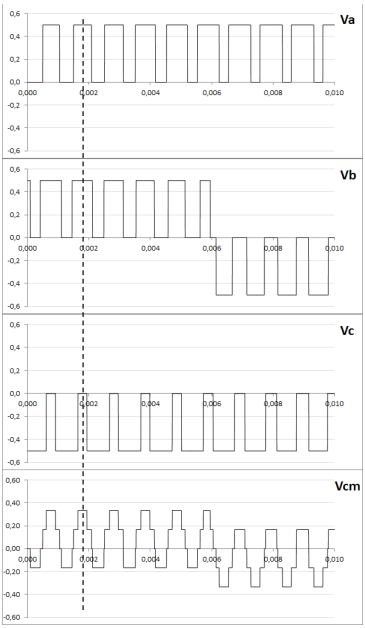



Figure 1. Pulse voltage waveforms in a three-phase motor, fed by an inverter, and the resulting CM voltage

The most common technique for controlling CM voltages is the use of passive RLC filters at the inverter output. These filters contribute to a reduction in DM and CM noise, but are not considered sufficiently efficient for all frequency ranges. Furthermore, the addition of filters results in increased losses, increased weight, and increased space consumption [1], [3], [5]. This kind of solution is based on reducing the ease with which the noise can reach the object that is its focus, which is the motor.

The literature presents many active circuits for CM voltage cancellation. A common topology is the four-leg configuration. In this topology, a fourth pair of IGBTs is added to the inverter module and a device, which can be a passive filter or a CM transformer, is wired between the inverter and the motor. This circuit captures the CM current at the output of the inverter and leads it back to the internal DC link. These circuits have the advantage of reducing CM currents in a broader range than passive filters [5], [8]. However, it should be noted that this also implies an increase in the number of power semiconductors used—these are not commonly found on the market. This kind of solution is based, unlike the previous

EBSCOhost - printed on 2/14/2023 2:46 PM via . All use subject to https://www.ebsco.com/terms-of-use

one, on facilitating the return of the noise so that it deviates from its focus, rather than making it more difficult to reach its destination. It should perhaps be stated that the adoption of these methods assumes that DM and CM voltages and currents cannot be avoided. As such, the noise is still present in the system and it is then only a question of whether it is stopped from reaching its destination, or whether it reaches it with reduced intensity.

## The Proposed Configuration

A dual-bridge configuration is discussed in this paper. This configuration has been proposed by other authors [22], [23]. The idea of the dual-bridge is to minimize common mode voltage through the addition of extra switches, as shown in Figure 2.

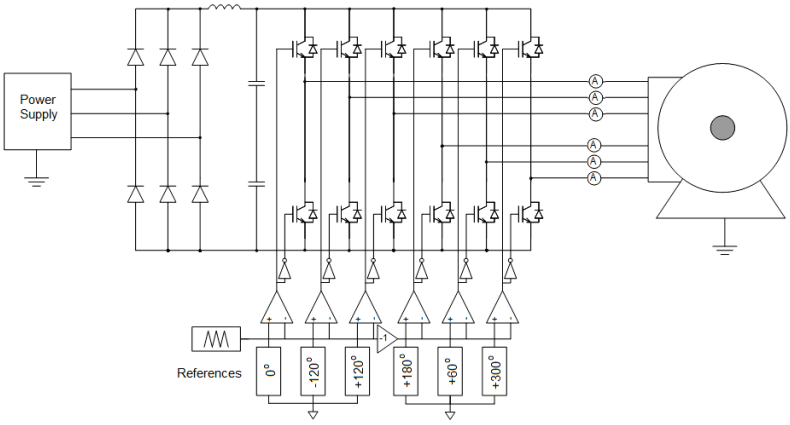



Figure 2. Proposed Dual-bridge (Six-Phase) Inverter Topology

According to [21], it can be deduced that the VCM is given by formula (2) below [22].

$$V_{CM} = \frac{V_a + V_b + V_c + V'_a + V'_b + V'_c}{6} \quad (2)$$

EBSCOhost - printed on 2/14/2023 2:46 PM via . All use subject to https://www.ebsco.com/terms-of-use

As shown graphically in Figure 3, the phase voltages Va', Vb', and Vc', in opposition to the original phases Va, Vb, and Vc, will neutralize the CM voltage.

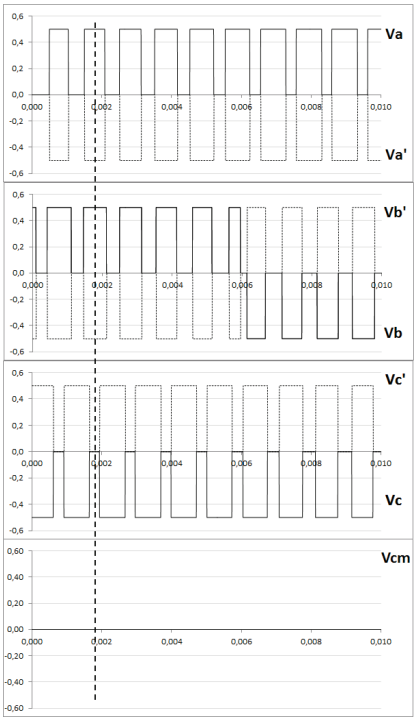



Figure 3. Voltages in dual-bridge topology used for CM emission control

This solution is considered by some authors too be an active circuit configuration and so it is natural to compare it to other ones. Such a comparison suggests that this solution seems to be less efficient, since it demands many more IGBTs. However, it should be noted that its design is different. It is distinct from active circuits that drain the common mode current generated by the CM voltage, reducing the VCM just after a passive device such as a LC filter or similar; the dual-bridge inverter aims to mitigate the CM voltage at its generation stage, reducing the CM current. This is a very different solution in that it identifies noise as something that can be avoided, rather than considering it to be something intrinsic to the process and only capable of being blocked or diverted.

EBSCOhost - printed on 2/14/2023 2:46 PM via . All use subject to https://www.ebsco.com/terms-of-use

One other point to be noted is that this solution is applied to the entire system, rather than a single component such as the drive, which is the case in an active circuit model. This makes sense, since the reason for the CM voltage in drive-systems is the asymmetry of the pulses generated through the system's configuration. The result is a system with six phases. Two alternatives are possible:

- One inverter with six legs, switching in such a way that it generates six phases, shifted by 60 degrees to each other and a six-phase motor.
- Two three-phase inverters, switching in opposition. This means one inverter with a three-phase system shifted by 180 degrees from the other three phase-system [8]. This is a dual-bridge concept—shown in Figure 3.

The following analysis shows that the two solutions present the same output waveforms and therefore have the same performance [8]. The difference is basically a matter of nomenclature. However, the dual-bridge solution is easier to implement and for this reason was the one chosen to be tested.

A dual-inverter is easily assembled from two conventional three-phase inverters, while the dual-motor is easily obtained from a motor prepared to work with 220V/380V/440V and with twelve terminals available for the voltage combinations. Such a motor has 2 windings for each phase in order to allow their connection in series or in parallel, as shown in Figure 6.

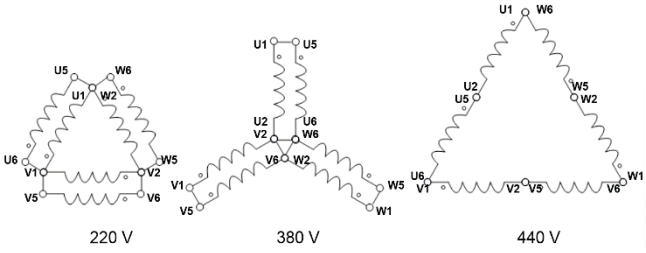



Figure 4. Connections of a twelve-terminal motor: 220V/380V/440V

To transform the twelve-terminal motor into a double three-phase motor, it is necessary to rearrange the windings as shown in Figure 5. A new winding connection, inverting the polarity of the second set of three-phases, is necessary in order to maintain the same flux.

EBSCOhost - printed on 2/14/2023 2:46 PM via . All use subject to https://www.ebsco.com/terms-of-use

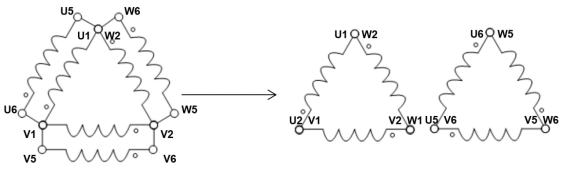



Figure 5. Connections of a double-delta motor

## Test Setup

Several simulations were conducted to analyze the viability of the proposed configuration [8]. All the combinations mentioned above were simulated with different models and gave similar results, with reductions in CM current of greater than 99%. The simulation also helped to define the dual-phase inverter test prototype. The simulations showed that a simple inversion of the IGBTs' gate signals from one inverter to the other—from the upper side IGBTs to the lower side IGBTs and vice-versa—as shown in Figure 6, allows for proper operation.

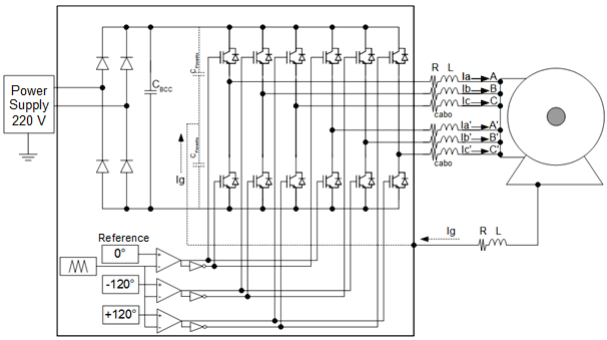



Figure 6. Configuration of dual-bridge inverter for test implementation.

Following the simulation model, an inverter model that allowed for easy IGBT gate signal crossing was acquired commercially—the ABB ACS50 inverter model was selected. When investigating the drive control board, it was noted that the IR2136 integrated circuit was used as a gate driver. One inverter had all of its functionality retained, and was thus termed the "master"; the other inverter had all control circuitry before the gate driver removed and was named "follower." The high-side reference from the master drive was used as the reference of the follower drive's low

EBSCOhost - printed on 2/14/2023 2:46 PM via . All use subject to https://www.ebsco.com/terms-of-use

side and vice-versa. This gate signal reference crossing guarantees the inversion of pulses and the result is a three-phase system shifted by 180' from the master drive. Figure 7 shows the connections between the two inverters. There was no need to implement a control algorithm. A third drive module of the same model and power range was acquired to be used as a conventional three-phase inverter module for comparison. In this way, the same control algorithm, the same components and structure, and the same electronic board layout was used in both inverter types: conventional and dual-bridge. This was done to avoid the possibility that some results were simply a matter of better implementation.

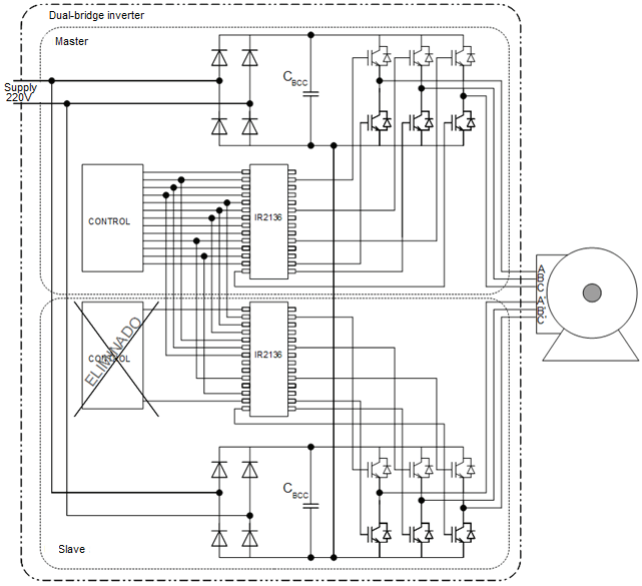



Figure 7. Interconnection scheme between two three-phase inverters to form a dual-bridge drive

The assembled dual-bridge inverter prototype is shown in Figure 8. Its main characteristics are: a scalar inverter; a single-phase input; and a three-phase IGBT-based output, 220Vac, 0.18kW, 1,4A. The switching frequency was set to 16 kHz.

EBSCOhost - printed on 2/14/2023 2:46 PM via . All use subject to https://www.ebsco.com/terms-of-use

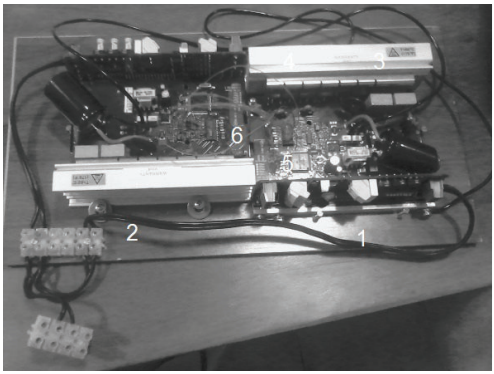



Figure 8. Photo of the test arrangement assembled with two conventional inverters

A conventional three-phase induction motor with 12 terminals, of rated power equal to 0.25 kW, was prepared for quick connection change. It was used to compose the test setup with the dual-bridge inverter. During the tests, the windings were reconnected several times from a conventional three-phase configuration to the proposed dual-bridge configuration and vice-versa. Additionally, a third inverter of the same type and size was used for testing the conventional topology. Two three-phase cables were used to connect the drive to the motor. These power cables were composed of three conductors with a 0.5 mm² cross section, twisted with 50 turns per meter.

## Results

### *A. Common Mode Voltage Reduction*

The voltage difference between the inverter earthing point and the motor earthing point were measured as an indicator of the CM voltage. This measurement was made at three different speed setpoints corresponding to frequencies equal to 60 Hz (high speed); 30 Hz (medium speed); and 5 Hz (lower speed). For this measurement, a 5:1 resistive divider, composed of 5 resistors of 270 Ω and installed between the two points, was used. The voltage was measured over the closest resistor to the drive. The measurements were made with a digital scope and the collected data were saved in *.txt files. Data from the different measurements were combined in the same files for comparison.

EBSCOhost - printed on 2/14/2023 2:46 PM via . All use subject to https://www.ebsco.com/terms-of-use

The measurements were performed, firstly, with the conventional three-phase configuration and then with the proposed configuration. The RMS values of the voltages in both configurations were calculated. The results are shown in Table 1.

**Table 1—Motor frame voltage measurements**

| configuration | conventional | | proposed | | $V_{CM}$ reduction |
|---|---|---|---|---|---|
| speed | Vrms | σ | Vrms | σ | |
| high | 5.74 V | 0.3% | 0.66 V | 0.3% | 88.5% |
| medium | 10.90 V | 0.2% | 0.71 V | 0.2% | 93.5% |
| low | 13.68 V | 0.1% | 0.70 V | 0.1% | 94.9% |

The individually measured frame voltage waveforms for the high speed condition were combined in a single graph, as shown in Figure 9.

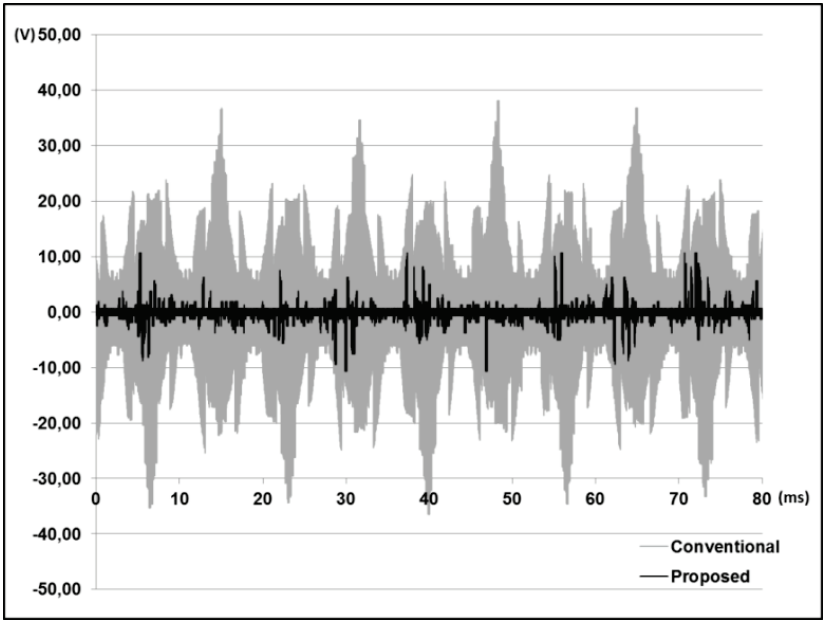



Figure 9. Motor frame voltage waveforms along an 80 ms time period

EBSCOhost - printed on 2/14/2023 2:46 PM via . All use subject to https://www.ebsco.com/terms-of-use

### *B. Common Mode Current Reduction*

For evaluation of the CM current reduction, the motor and inverter grounding points were connected with a 0.5 mm² wire. A shunt at the inverter side was adopted for current measuring.

The ground current through the motor and inverter frames was measured over the grounding cable shunt. Since the measurements were performed under the same conditions, that is, using the same grounding cable, there was no need to convert the measured voltage to current and the CM analysis was made directly, using the measured voltage.

The measurement was made at the 60 Hz speed setpoint. The CM current reduction reached 86.4%, based on the same pre-established criteria. The CM current waveforms in an 80 ms period are shown in Figure 10.

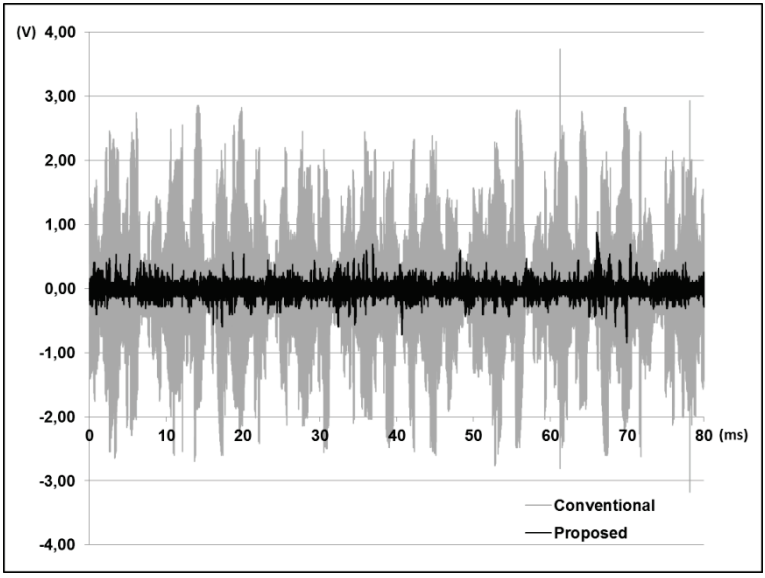



Figure 10. Common mode current waveforms across an 80 ms time period

A LISN was used to evaluate its influence on the results. The earth current between the motor and the drive frames presented variation of less than 10%, as shown in Table 2. However, variation in the earth current between the inverter frame and the general system ground, measured using the same procedure, indicated a difference of 50% for the conventional

EBSCOhost - printed on 2/14/2023 2:46 PM via . All use subject to https://www.ebsco.com/terms-of-use

configuration. This suggests that the LISN introduced a different impedance between the ground and the line phases, which had less influence on the amount of common mode current between the motor and drive. As such, considering the focus of this research and the measurements and data comparison procedures, the LISN can be concluded to not to have a significant impact on the results of this study; however, it should be considered when the earth current between the drive and system ground is evaluated.

**Table 2—Earth current measurement with and without LISN**

| Configuration | Position | Vrms with LISN mV | Vrms without LISN mV | Vrms with LISN / without LISN % |
|---|---|---|---|---|
| Conventional | Motor - Drive | 424.2 | 400.8 | 106.0 % |
| | Drive – System Ground | 40.4 | 80.1 | 50.4 % |
| Proposed | Motor - Drive | 56.3 | 60.9 | 92.4 % |
| | Drive – System Ground | 30.6 | 30.3 | 101.0 % |

## Conclusions

The theory suggests that this topology is efficient for CM voltage and current reduction, and the tests have proved this to be the case. Despite the small size of the test prototype, it may be concluded that similar results will be obtained at higher power, since the applied theory is the same. However, future tests should be conducted on higher power testing arrangements. This constitutes a potential solution to the problem of how to reduce electromagnetic interference and other well-known issues related to system reliability, such as those concerning bearing wear, etc.

It may also be inferred that this solution, as developed here, is also applicable to inverters with more sophisticated control characteristics, such as flux vectors and DTC.

Evaluating other active circuits for common mode voltage cancellation, it may be noted that they are not able to operate without generating a certain amount of noise. This is shown in Figure 1, which highlights the inability of a single switching device to generate the necessary waveform to compensate for the existing one. In this case, the cancellation of the common mode voltage is only possible through the addition of a passive filter. While guidance for installations and passive filters can restrain the

EBSCOhost - printed on 2/14/2023 2:46 PM via . All use subject to https://www.ebsco.com/terms-of-use

CM noise generated and active circuits capture it, the topology proposed is based on a reduction of the noise directly at the source. It may be stated that, conceptually, this topology is an advance on previous conducted emission controls and resulting EMI effects.

As mentioned above, the dual-bridge topology is commonly compared to that using four-leg inverters as an active circuit solution. This comparison has led to the conclusion that it is not an economically efficient solution, because it demands many more components. However, it should be observed that the motor is obtained from a conventional three-phase motor with multiple voltage connections, which means there are no extra costs for its development. Regarding the inverter, it should be noted that each semiconductor will conduct half of the current, compared to a three-phase topology, allowing the use of smaller IGBTs. For drive sizes in which the solution for increasing power is the paralleling of IGBTs, the proposed configuration will not result in a significant cost increase. Also, in low power inverters, where control corresponds to a reasonable portion of the total cost, the impact of the increase in IGBTs will not be significant. As such, the proposed topology is a viable solution for new installations. Existing installations may present a certain amount of inconvenience in terms of the need for replacement cabling. [8], [22]

The proposed topology may offer an affordable EMI control solution for transportation: the marine industry, railways, and the promising market in electrical and hybrid-electric vehicles. In those cases, size and weight reductions are important criteria for equipment design and the possibility of eliminating passive filters is an added bonus. In cases where the solution is usually customized to a final product, vehicle, train, or vessel, there is no reason not to consider a dual-bridge topology.

## Acknowledgements

The authors acknowledge ABB Ltda, Brazil, the Navy Technological Center in São Paulo (CTMSP) and the Pontifícia Universidade Católica for providing the equipment and installations required for complementing the experimental measurements.

This work was partially supported by CNPq (PQ 307867/2011-0).

EBSCOhost - printed on 2/14/2023 2:46 PM via . All use subject to https://www.ebsco.com/terms-of-use

## References

[1] Skibinski, G. L.; Kerkman, R. J.; Schlegel, D. “EMI emissions of modern PWM AC drives,” Industry Applications Magazine, IEEE , vol.5, no.6, pp.47-80, Nov/Dec 1999

[2] Ogasawara, S.; Ayano, H.; Akagi, H. “Measurement and reduction of EMI radiated by a PWM inverter-fed AC motor drive system,” Industry Applications, IEEE Transactions on, vol.33, no.4, pp.1019-1026, Jul/Aug 1997

[3] Mutoh, N.; Kanesaki, M.; Nakashima, J.; Ogata, M. “A new method to control common-mode currents focusing on common-mode current paths produced in motor drive systems,” Industry Applications Conference, 2003. 38th IAS Annual Meeting. Conference Record of the, vol.1, no., pp. 459-466 vol.1, 12-16 Oct. 2003

[4] Julian, A. L.; Oriti, G.; Lipo, T. A. “Elimination of common-mode voltage in three-phase sinusoidal power converters,” Power Electronics, IEEE Transactions on, vol.14, no.5, pp.982-989, Sep 1999

[5] Consoli, A.; Oriti, G.; Testa, A.; Julian, A. L. “Induction motor modeling for common-mode and differential mode emission evaluation,” Industry Applications Conference, 1996. Thirty-First IAS Annual Meeting, IAS '96., Conference Record of the 1996 IEEE , vol.1, no., pp.595-599 vol.1, 6-10 Oct 1996

[6] Cacciato, M.; Consoli, A.; Scarcella, G.; Testa, A. “Reduction of common-mode currents in PWM inverter motor drives,” Industry Applications, IEEE Transactions on , vol.35, no.2, pp.469-476, Mar/Apr 1999

[7] Di Piazza, M. C.; Tine, G.; Vitale, G. “An Improved Active Common-Mode Voltage Compensation Device for Induction Motor Drives,” Industrial Electronics, IEEE Transactions on, vol.55, no.4, pp.1823-1834, April 2008

[8] Winnischofer, G.; Sartori, C. A. F. “Polyphase Drive Systems Configuration aiming EMI Mitigation”, International Conference on Renewable Energies and Power Quality (ICREPQ’13), March 2013

[9] ABB, Grounding and Cabling of the Drive System - Variable Speed Drives, June 2005

[10] Hanigovszki, N.; Landkildehus, J.; Spiazzi, G.; Blaabjerg, F. “An EMC evaluation of the use of unshielded motor cables in AC adjustable speed drive applications,” Power Electronics, IEEE Transactions on, vol.21, no.1, pp. 273- 281, Jan. 2006

[11] Persson, E. “Transient effects in application of PWM inverters to induction motors,” Industry Applications, IEEE Transactions on, vol.28, no.5, pp.1095-1101, Sep/Oct 1992

[12] Melfi, M. J. “Low-Voltage PWM inverter-fed motor insulation issues,” Industry Applications, IEEE Transactions on, vol.42, no.1, pp. 128- 133, Jan.-Feb. 2006

[13] Korhonen, J.; Strom, J.-P.; Tyster, J.; Silventoinen, P.; Saren, H.; Rauma, K. “Control of an inverter output active du/dt filtering method,” Industrial

EBSCOhost - printed on 2/14/2023 2:46 PM via . All use subject to https://www.ebsco.com/terms-of-use

Electronics, 2009. IECON '09. 35th Annual Conference of IEEE, vol., no., pp.316-321, 3-5 Nov. 2009

[14] Moreira, A. F.; Lipo, T. A.; Venkataramanan, G.; Bernet, S. "High-frequency modeling for cable and induction motor overvoltage studies in long cable drives," Industry Applications, IEEE Transactions on, vol.38, no.5, pp. 1297- 1306, Sep/Oct 2002

[15] Gerster, C.; Hofer, P. Gate-controlled dv/dt- and di/dt-limitation in high power IGBT converters, EPE Journal, Vol. 5, no 3/4, January 1996, page 11-16

[16] Habetler, T. G.; Naik, R. E.; Nondahl, T. A. "Design and implementation of an inverter output LC filter used for dv/dt reduction," Applied Power Electronics Conference and Exposition, 1999. APEC '99. Fourteenth Annual , vol.2, no., pp.1279-1284 vol.2, 14-18 Mar 1999

[17] Kerkman, R. J.; Leggate, D.; Skibinski, G. L. "Interaction of drive modulation and cable parameters on AC motor transients," Industry Applications, IEEE Transactions on , vol.33, no.3, pp.722-731, May/Jun 1997

[18] Kerkman, R. J.; Skibinski, G. L.; Schlegel, D. W. "AC drives: year 2000 (Y2K) and beyond," Applied Power Electronics Conference and Exposition, 1999. APEC '99. Fourteenth Annual, vol.1, no., pp.28-39 vol.1, 14-18 Mar 1999

[19] ABB, Technical Guide No. 5 - Bearing Currents in Modern AC Drive Systems, December 1999

[20] Paul, Clayton R.; Introduction to electromagnetic compatibility; 2nd ed, John Wiley & Sons, Inc, 2006

[21] Ogasawara, S.; Akagi, H. Modeling and damping of high-frequency leakage currents in PWM inverter-fed AC motor drive systems. IEEE Transactions on Industry Applications, vol.32, no.5, pp.1105-1114, Sep/Oct 1996.

[22] Jouanne, A. v.; Zhang, H. "A Dual-Bridge Inverter Approach to Eliminating Common-Mode Voltages and Bearing and Leakage Currents," IEEE Transactions on Power Electronics, Vol. 14, N.o 1, January 1999

[23] Somasekhar, V. T.; Gopakumar, K.; Pittet, A.; Ranganathan, V. T.; "PWM inverter switching strategy for a dual two-level inverter fed open-end winding induction motor drive with a switched neutral,",# IEE Proceedings - Electric Power Applications, Vol. 149, pp. 152-160, March 2002

EBSCOhost - printed on 2/14/2023 2:46 PM via . All use subject to https://www.ebsco.com/terms-of-use

# CHAPTER THIRTY-THREE

# SHUNT ACTIVE POWER FILTER WITH SELECTIVE HARMONIC COMPENSATION FOR A LV DISTRIBUTION GRID

F. BELLONI[1], R. CHIUMEO[2], C. GANDOLFI[2]

## Abstract

A four-wire model Shunt Active Power Filter (SAPF) employable in a low voltage distribution grid is presented in this paper. This device is to help improve Power Quality (PQ) by compensating the harmonic currents, reactive power and current unbalances that come from disturbing loads. Each compensating function can be activated or disabled according to the specific requirements of the application. Selective harmonic compensation is also possible, in order to avoid possible resonances at specific frequencies. A current hysteresis modulation, with predictive calculation of threshold bands so as to achieve fixed switching frequency, is adopted for a fast dynamic response. The compensation of the proposed active power filter and the associated control scheme under steady-state and transient conditions is demonstrated through digital simulations, real-time Control Hardware in The Loop (CHIL) simulations and experimental prototype testing.

**Keywords:** Shunt Active Power Filter, Selective Harmonic Compensation, Power Quality, Predictive Hysteresis Band Current Modulation, Real-Time Control Hardware in The Loop (CHIL) simulations.

[1] Unareti S.p.A.
[2] Ricerca sul Sistema Energetico—RSE S.p.A. Via Rubattino 54, 20134, Milano, Italy, e-mail: chiara.gandolfi@rse-web.it.

EBSCOhost - printed on 2/14/2023 2:46 PM via . All use subject to https://www.ebsco.com/terms-of-use

## Introduction

The number of grid connected electronic loads has increased significantly in recent years. LED lighting systems, electric vehicles, air-conditioners and many other systems based upon power electronics are gaining in popularity. Electronic loads have particular relevance in the implementation of demand-response mechanisms [1].

Electronic loads are disturbing loads that inject harmonics, reactive power and/or flicker into the grid. Additionally, such loads are sensitive to grid disturbances, like voltage unbalances, voltage dips and interruptions. A high level of PQ is needed to ensure the proper operation of electronic/sensitive loads connected to distribution grids.

Shunt active power filters (SAPF) offer an effective solution for improving the power quality of distribution grids. They compensate the harmonics and reactive power of disturbing loads, taking advantage of the capability of power electronic converters to generate arbitrary currents.

This paper describes the implementation of a SAPF, to be connected in Low Voltage (LV) distribution grids close to a disturbing or sensitive load. The device is able to compensate the harmonic currents, reactive power and current unbalances from a disturbing load. Each compensating function can be activated or disabled according to the specific requirements of the application. Additionally, Selective Harmonic Compensation (SHC) is possible in order to avoid possible resonances at given frequencies. A current hysteresis predictive band modulation was adopted for a fast dynamic response. A predictive algorithm for the dynamic calculation of upper and lower hysteresis limits was also adopted to ensure fixed switching frequency in every condition [2]–[4].

The circuit was designed for load compensation of up to 9 kVA and a simulation model was implemented in the ATPDraw digital simulation environment.

To test the performance of the defined control logic, real-time Control Hardware in The Loop (CHIL) simulations were undertaken. As good results were obtained, a power prototype was developed and tested.

Digital and CHIL simulation results, relevant to different operating conditions and load typologies, are presented, and a final comparison to the experimental test of the prototype is made.

EBSCOhost - printed on 2/14/2023 2:46 PM via . All use subject to https://www.ebsco.com/terms-of-use

## The Shunt Active Power Filter

A schematic view of the proposed SAPF circuit topology is given in Figure 1.

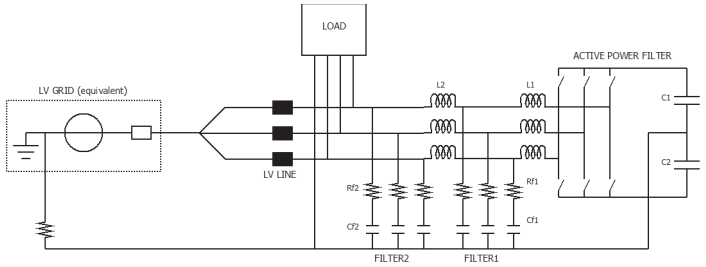



Figure 1. Schematic view of the SAPF and complete system configuration.

The circuit is based on a three-phase bridge with two capacitors on the DC side, C1 and C2, connected in series, so that their central point is available for connection to the 4th wire and to ground through a small-value resistor. In this way, a path for zero sequence currents is ensured and unbalanced loads can be compensated. The equivalent DC capacitance was chosen in order to maintain the ripple on the DC voltage of less than 1.5 % of its nominal value when a single phase load of power equal to 33 % of the SAPF's nominal power is compensated, according to the formula:

$$\Delta V_{CC\%} = \frac{4A_N}{3\pi\omega_0 V_{CCN}^2 C_{CC}} \qquad (1)$$

Output filters are designed according to the reactive power they process as a percentage of the nominal power of the SAPF. The filter's resistors are used for the damping of oscillations that may arise during transients. It was decided to use a damping factor of $\chi = 0.7$, and the resistor was designed according to the relation:

$$R_{f,i} = \frac{1}{2\chi}\sqrt{\frac{L_{eq}}{C_{f,i}}} \qquad (2)$$

where i = 1, 2 and $L_{eq}$ is the total equivalent inductance seen by the filter in relation to the grid. The design parameters adopted are reported in Table I.

EBSCOhost - printed on 2/14/2023 2:46 PM via . All use subject to https://www.ebsco.com/terms-of-use

**Table I. SAPF design parameters.**

| | | | |
|---|---|---|---|
| Nominal power | $A_N$ | 9 kVA | |
| DC voltage | $V_{DC}$ | 600 V | |
| AC voltage | $V_{AC}$ | 214 V | line-to-line |
| DC capacitors | $C_{DC}$ | 9 mF each | $C_{eq}$ 4.5 mF |
| Inductance | $L_1$ | 2.7 mH | $X_{cc}$ = 16.5 % |
| | $L_2$ | 0.48 mH | $X_{cc}$ = 3 % |
| Filter 1 capacitor | $C_{f1}$ | 3.14 μF | Q = 0.5 % $A_N$ |
| Filter 1 resistor | $R_{f1}$ | 8.7 Ω | |
| Filter 2 capacitor | $C_{f2}$ | 67.5 μF | Q = 10.3 % $A_N$ |
| Filter 2 resistor | $R_{f2}$ | 3.8 Ω | |

The disturbing/sensitive load is connected directly at the output of the SAPF. In the implemented model, a simplified Thévenin equivalent to a LV distribution grid was considered and the load and the SAPF were connected to it through a LV line 200 m in length.

## SAPF Control Scheme for Selective Harmonic Compensation

The designed closed control loop of the SAPF has three main objectives:

- maintaining the central point of the DC capacitors at ground level;
- regulating the DC voltage at a reference level;
- compensating load harmonic currents with an SHC strategy, reactive power and unbalances.

The block scheme of the control approach adopted is shown in Figure 2. The main outputs of the control are three current references, one for each phase, to be passed to the modulator for the generation of the actual SAPF current [5]. As shown in the scheme, the DC capacitor central point voltage was compared to a reference value, 0 V, and the result was processed by a Proportional-Integral (PI) regulator with anti-windup. The output regulator directly contributes to the total current reference. The measured DC voltage was compared to a reference value and the resulting error was processed through a PI regulator, whose output was used together with Clarke components of the grid voltages, to calculate two current references over axes αβ, which were added to other references coming from the control branches which compensate the harmonics.

EBSCOhost - printed on 2/14/2023 2:46 PM via . All use subject to https://www.ebsco.com/terms-of-use

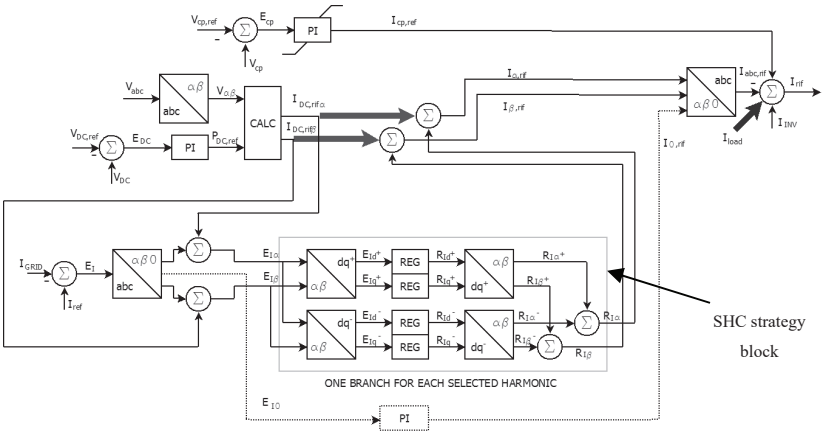



Figure 2. Block scheme of the control of the SAPF.

The SHC strategy was implemented, starting from the measurement of the grid currents and comparing the measured values with fixed references of 0 A. The resulting errors were transformed for each harmonic order over the rotating axis *dq* using a generalised Park transform, which also took into account negative sequences, according to the formula:

$$\begin{bmatrix} E_{Id}^{+} \\ E_{Iq}^{+} \\ E_{Id}^{-} \\ E_{Iq}^{-} \end{bmatrix} = \begin{bmatrix} \cos(k2\pi f_0 t) & \sin(k2\pi f_0 t) \\ -\sin(k2\pi f_0 t) & \cos(k2\pi f_0 t) \\ \cos(k2\pi f_0 t) & -\sin(k2\pi f_0 t) \\ \sin(k2\pi f_0 t) & \cos(k2\pi f_0 t) \end{bmatrix} \begin{bmatrix} E_{I\alpha} \\ E_{I\beta} \end{bmatrix} \quad (3)$$

where k is the harmonic order to be compensated. The results, four signals for each harmonic, were processed through regulators in the form:

$$H_k(s) = \frac{K_{Ik} T_k}{1 + sT_k} \quad (4)$$

where $K_{Ik} = 2.2/(n_{pk}T_s)$, $T_k = (K_{Ik}A_k)^{-1}$ and $n_{pk}T_s$ is the response time to the step change of the regulator input; $A_k$ is the desired attenuation factor for the *k*-th harmonics; and $T_k$ is employed to adjust the DC gain of the regulator.

As reported above, the outputs of regulators (4) were added together, transformed over αβ axes, and added to reference currents coming from the DC voltage regulation branch. Finally, the sum was reported in the abc

EBSCOhost - printed on 2/14/2023 2:46 PM via . All use subject to https://www.ebsco.com/terms-of-use

reference frame and contributed to the total reference current. The SAPF also compensated the reactive power of its own output filters. The load current was also added to the total reference in a feedforward (FFW) compensation scheme. The FFW path assures a fast dynamic response of the SAPF to load changes, but it does not allow the selective compensation of harmonics. For this reason, the FFW can be disabled if grid resonances arise, and the compensation of harmonics close to resonant frequency are also inhibited.

The regulators were designed to obtain the following dynamic performances:

- DC voltage regulator —> response time to step variation: 500 ms;
- harmonic compensation —> attenuation: 1/100; response time to step variation: 250 ms; DC gain: 44.

The DC voltage regulation loop had a slower dynamic than the current regulation loop, so that fast variation of load active power could also be compensated.

### *Predictive hysteresis band current modulation*

The three current references obtained are compared to the inverter currents generated, and these errors, one for each phase, are sent to a modulation stage for the determination of the turn-ON and turn-OFF command pattern of the circuit switches.

The proposed modulation is a hysteresis band modulation, where, if one of the current errors hits an upper threshold value, the upper switch of the relevant bridge leg is switched OFF, while the lower one is switched ON. In such a way, the SAPF current decreases, until the current error hits a lower threshold limit, and the switch status is then inverted.

The implemented modulation strategy adapts the calculation of the threshold limits and links commutation also to a clock signal in order to ensure fixed switching frequency and a null mean value of the current error over 20 ms (grid voltage period) [6][7]. The hysteresis band limits for the $k$-th switching period are predictively calculated during the ($k$-1)-th period, measuring the slope of the current. The evolution of the SAPF current is shown in Figure 3. The final algorithm for the modulation is as follows:

- if current error hits upper threshold limit: upper switch OFF, lower switch ON;
- if current error hits lower threshold limit: upper switch ON, lower switch OFF;

EBSCOhost - printed on 2/14/2023 2:46 PM via . All use subject to https://www.ebsco.com/terms-of-use

- clock rising edge: calculate lower threshold band for the next switching period:
    - if current error is negative: upper switch ON, lower switch OFF;
    - otherwise: upper switch OFF, lower switch ON;
- clock falling edge: calculate upper threshold band for the next switching period:
    - if current error is positive: upper switch OFF, lower switch ON;
    - otherwise: upper switch ON, lower switch OFF.

The adopted modulation strategy offers the following advantages:

- fast dynamic response to load/reference changes;
- known harmonic content of currents, due to fixed switching frequency.

In the implemented simulation model of the SAPF, the switching frequency was fixed at 12.8 kHz, equivalent to a switching period of 78.125 μs, which was also the clock frequency; the upper (lower) threshold limits were bound within the range (-)1.4 A–(-)4.6 A above (under) the current reference values.

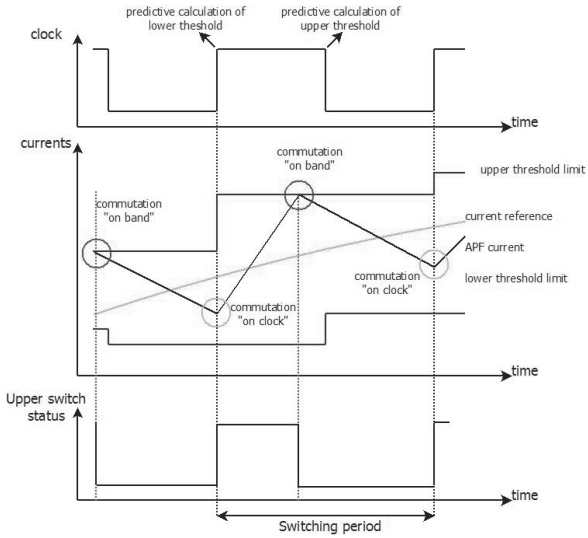



Figure 3. Visual description of the modulation algorithm and time evolution of the SAPF current.

EBSCOhost - printed on 2/14/2023 2:46 PM via . All use subject to https://www.ebsco.com/terms-of-use

The digital and CHIL simulation results are shown in the next sections. At the end, a comparison with the experimental test of the developed prototype is made. All the control strategies were evaluated (open loop; closed loop selective; closed loop not selective) in this study. In the following, the results for the closed control loop with feedforward, as reported in Figure 2, are shown.

## Digital Simulation Results

A simulation model of the 9 kVA SAPF was implemented in the ATPDraw digital simulator environment. The model included all the elements reported in Figure 1. Different type of loads were also considered, including:

- RL three-phase model;
- RL single-phase model;
- three-phase diode rectifier bridge.

The simulations performed covered steady state compensation of all kinds of load and transient behaviours; f.i. load connection and disconnection; the behaviour of the active filter in case of unbalanced supply grid voltages; and its behaviour in the presence of capacitive load and resonances.

### *Compensation of a three-phase RL load*

The load was represented as a three-phase RL circuit, connected in series. Since the load was linear, no harmonic currents needed to be compensated; the inductive component of the load requires an amount of reactive power from the grid which should be compensated by the SAPF. Load parameters were: a total apparent power of 7.742 kVA and a power factor of 0.9 (active power 6.96 kW and reactive power 3.39 kVAr). The active and reactive powers of the load, of the SAPF and that supplied by the grid are shown in

Figure **4**. In particular, the transient occurring during connection of this kind of load was evaluated (t = 0.3 s). After the initial transient, the SAPF compensates only the reactive power of the load, while the active power is supplied by the grid. The residual reactive power supplied by the grid is due to the partial compensation of the reactive power of the SAPF, since the regulators present finite DC gain. SAPF output current, for one phase only, is shown in Figure 5, together with the reference and the hysteresis bands.

EBSCOhost - printed on 2/14/2023 2:46 PM via . All use subject to https://www.ebsco.com/terms-of-use

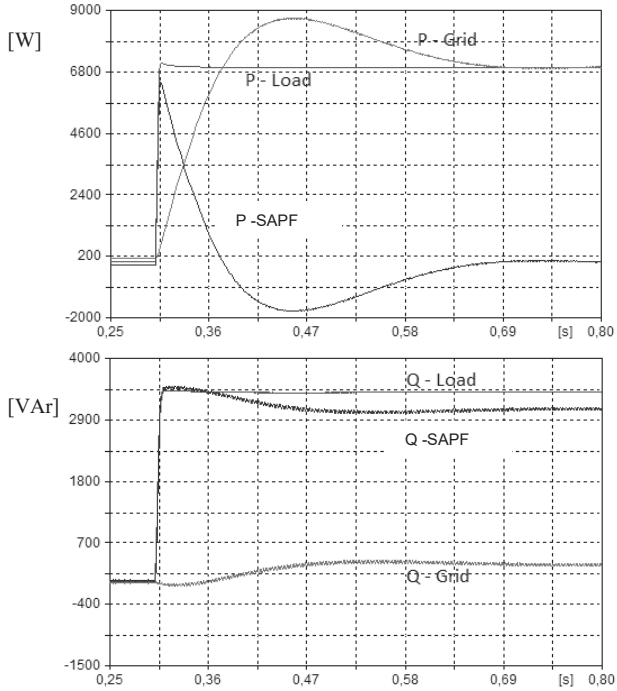



Figure 4. Linear load reactive power compensation: active and reactive power waveforms.

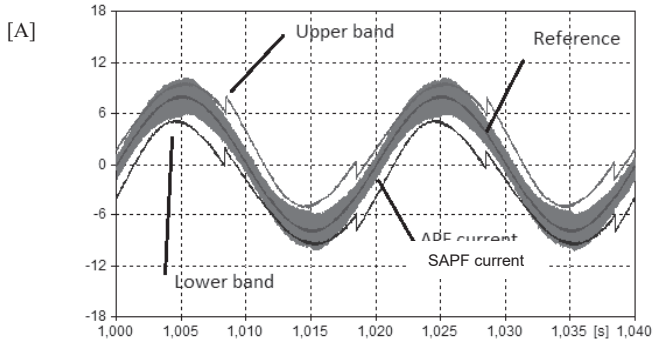



Figure 5. SAPF current, reference current and hysteresis bands.

EBSCOhost - printed on 2/14/2023 2:46 PM via . All use subject to https://www.ebsco.com/terms-of-use

### *Compensation of a single-phase RL load*

In this case, the single-phase RL load was connected to phase 'c.' Load parameters were the same as in the previous case ($R_{load}$ = 5.33 Ω; $L_{load}$ = 8.27 mH), but the SAPF had to take into account current unbalances. As such, it needed to supply both the reactive power and the oscillating component of the active power of the load. Simulation results are given in Figure 6. As explained before, part of the reactive power of the SAPF output filter is not compensated. Residual oscillations of grid supplied active power had an amplitude 1.3 % that of the load oscillations amplitude.

The DC voltage of the SAPF is shown in Figure 7a. In this case, the amplitude of the 100 Hz oscillations on the DC voltage was below 1 % of the nominal voltage level (600 V).

In Figure 7b, the grid and single-phase load currents (with an offset to see the waveforms better) are shown; thanks to the SAPF compensation, the grid currents are symmetrical.

EBSCOhost - printed on 2/14/2023 2:46 PM via . All use subject to https://www.ebsco.com/terms-of-use

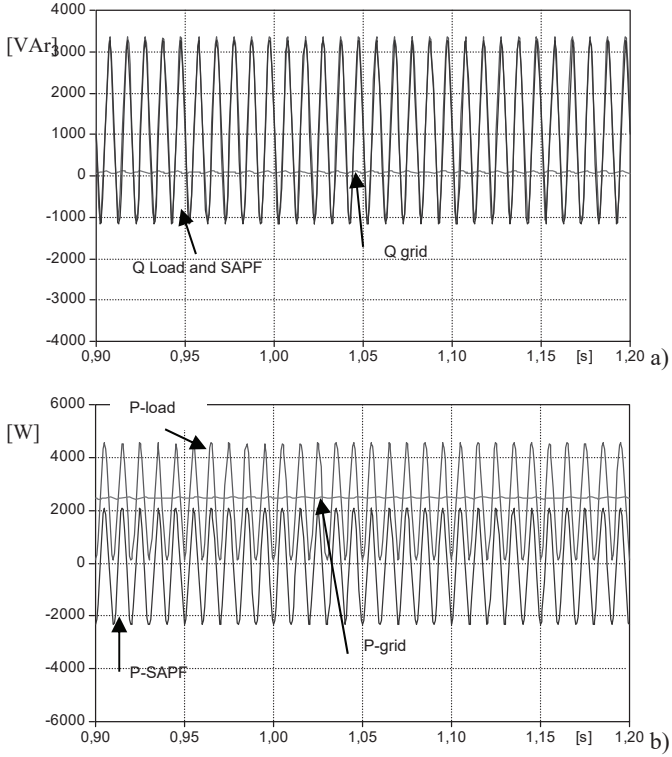



Figure 6. SAPF compensation of a single-phase RL load: a) reactive powers, b) active powers.

EBSCOhost - printed on 2/14/2023 2:46 PM via . All use subject to https://www.ebsco.com/terms-of-use

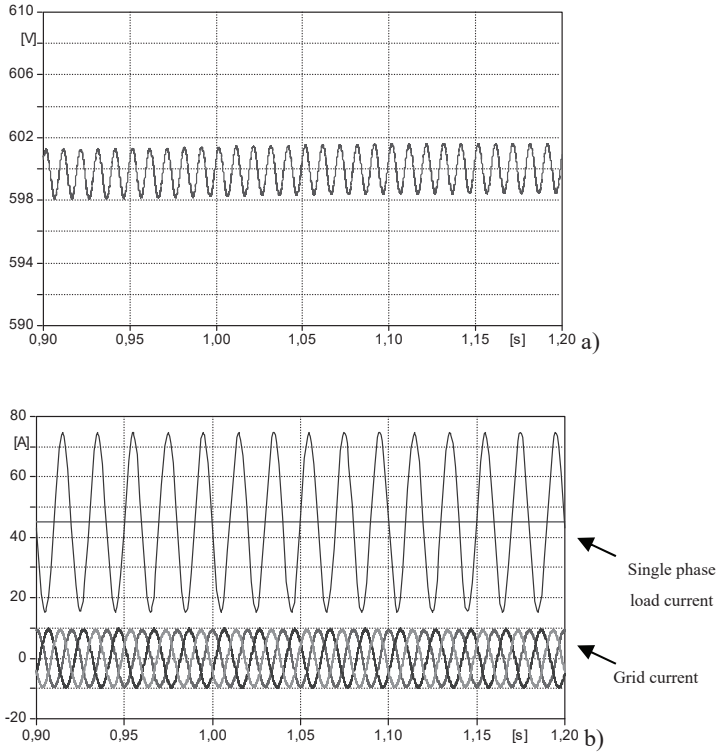



Figure 7. SAPF compensation of a single-phase RL load: a) DC voltage of SAPF; b) Grid currents and single-phase load currents with SAPF during compensation of a single-phase load.

## *Compensation of a diode bridge rectifier load*

A three-phase diode bridge rectifier was considered as a disturbing load. The rectifier also had input inductances on the AC side, so that it absorbed active and reactive power (8 kVA; 7.5 kW; 2.5 kVAr); it was characterized by currents with odd order harmonic components ($5^{th}$-$7^{th}$-$11^{th}$-$13^{th}$-$17^{th}$-$19^{th}$-…). The circuit scheme is reported in Figure 8.

The connection transient of the diode bridge rectifier started at time t = 0.32 s: the SAPF was able to fully compensate the load harmonic currents within 4 grid cycles (80 ms), as shown in Figure 9; reactive power compensation was nearly instantaneous, as shown in Figure 10.

EBSCOhost - printed on 2/14/2023 2:46 PM via . All use subject to https://www.ebsco.com/terms-of-use

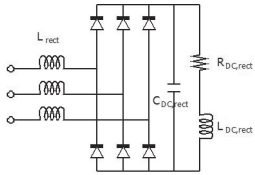



Figure 8. Non-linear load model.

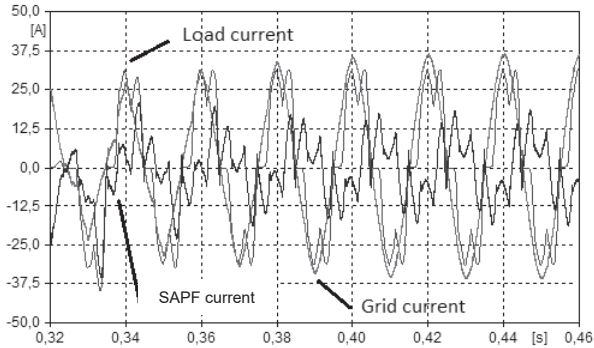



Figure 9. Compensation of load harmonic currents (phase ‘a’) during the disturbing load connection.

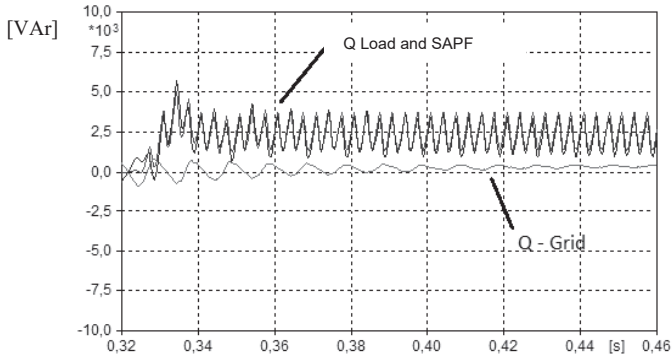



Figure 10. Compensation of reactive power during the disturbing load connection.

Load, SAPF and resulting grid currents are shown in Figure 11 (only phase ‘a’ currents are shown for simplicity). In Figure 12, the amplitude of the harmonic spectra of the load and grid currents are shown. Even though the FFW compensation of load currents tends to compensate every current

EBSCOhost - printed on 2/14/2023 2:46 PM via . All use subject to https://www.ebsco.com/terms-of-use

harmonic, only regulators for odd harmonics were activated in the control. The Total Harmonic Distortion (THD) of the load current was 26.67 %, while the grid current THD was reduced to 1 %.

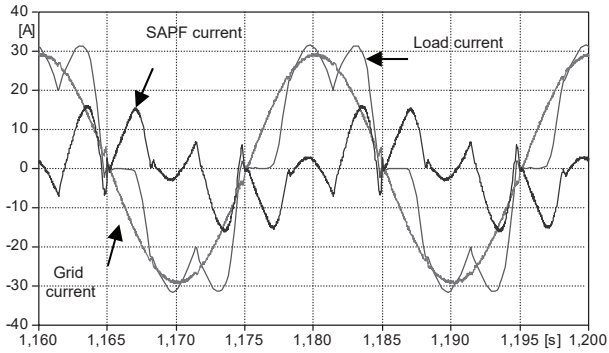



Figure 11. Compensation of harmonic currents of a distorting load (phase 'a').

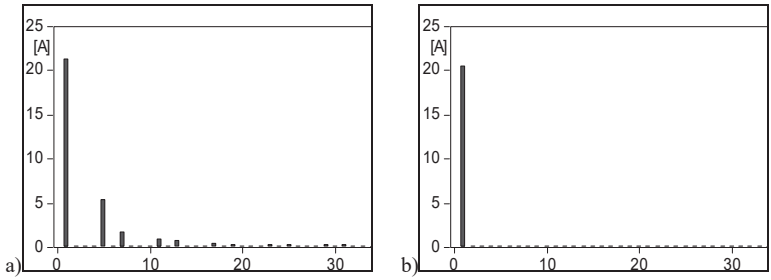



Figure 12. Spectra of load current (a) and grid current (b).

## *Behaviour in case of unbalanced supply grid voltages*

In the presence of a disturbing load, such as the one considered above, it is worthwhile to evaluate the capability of the active filter to compensate in the presence of unbalanced supply grid voltages. As the SAPF is a shunt device, it cannot compensate network voltage unbalance due to poor network quality, even if it has to ensure the mitigation of the effect of the disturbing load in the grid currents in this operational condition. The hypothetical solution is to have supply voltages with an unbalance of 2 % (Figure 13).

EBSCOhost - printed on 2/14/2023 2:46 PM via . All use subject to https://www.ebsco.com/terms-of-use

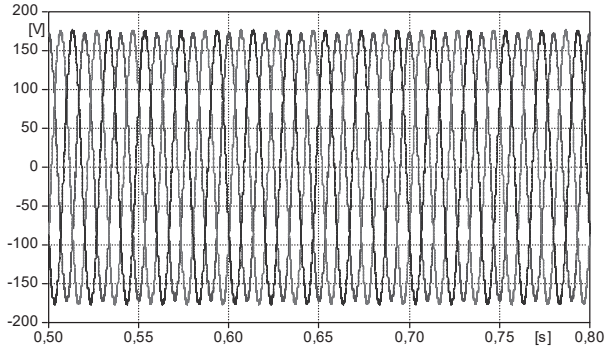



Figure 13. Grid voltages with an unbalance of 2 %.

Figure 14 shows the simulation results, which make it possible to confirm the SAPF compensation effect: the THD of the load was 26.67 %, while the residual grid current had a THD of 1.26 %.

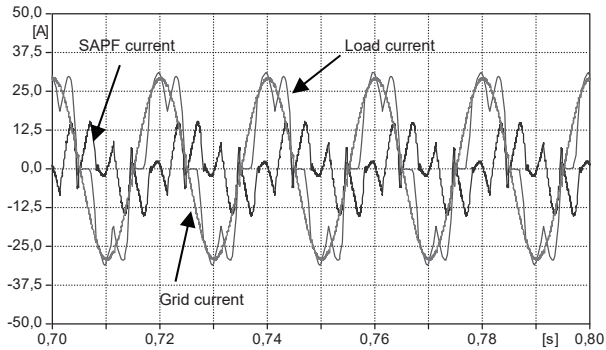



Figure 14. Load, grid and SAPF currents (phase ‘a’) with unbalanced supply grid voltages.

## Control Hardware-in-the-loop Simulations

After running digital simulations in the ATPDraw environment, the proposed control strategies were also tested using a digital microprocessor (ARM Cortex M4) in order to test their performances through CHIL real-time simulation[3]. In this method, there is no power transfer and the power

[3] The RT digital simulator used at RSE is an OPAL RT simulator (http://opal-rt.com).

EBSCOhost - printed on 2/14/2023 2:46 PM via . All use subject to https://www.ebsco.com/terms-of-use

system is modelled inside the simulator. The external controller takes signals from the simulator and processes them to produce outputs, which are sent back to the system in the simulator (I/O). Figure 15 shows the principles of the CHIL scheme.

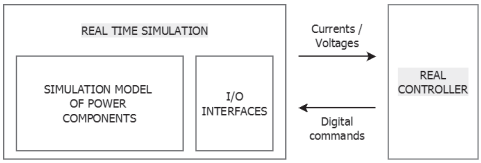



Figure 15. CHIL principle scheme.

The first phase of the study was to validate the CHIL simulation results by comparing them to the ones made in ATPDraw, which were treated as benchmarks.

The real time simulator allows the calculation of power circuit models with a fixed time step. The switching frequency of the UC was considered to be equal to 12.8 kHz and the switching period was $T_{sw}$ = 78.125 μs: the simulation time has to be an integer fraction of this period (f.i. $T_{sw}/5$) to avoid any shift between the generated waveform and the clock of the system, as well as to reduce the aliasing.

As detailed in Figure 15, in this study the 'real-world' controller was represented by the microprocessor, while the simulation model in the Matlab/Simulink environment included the distribution grid and all SAPF main components (Figure 1). Figure 16 describes the RSE laboratory implementation of the CHIL simulation.

In general, CHIL simulations require a time delay for the acquisition/generation of the signals exchanged between the simulation model and the microprocessor hardware. This delay is related to the simulation time-step. In fact, the inverter switching signals generated by the microprocessor are asynchronous with simulation time-steps. As such, their action is effective in the simulation with a time delay: Figure 17 shows this time-line. This also means that when a change occurs in simulated quantities in a given time-step they are sent to the real controller only at the following time-step. The outcome of these delays is that simulated current and voltage spectra are not precisely those theoretically expected or in purely digital simulations, as a spreading of the harmonic content of the waveforms occurs.

EBSCOhost - printed on 2/14/2023 2:46 PM via . All use subject to https://www.ebsco.com/terms-of-use

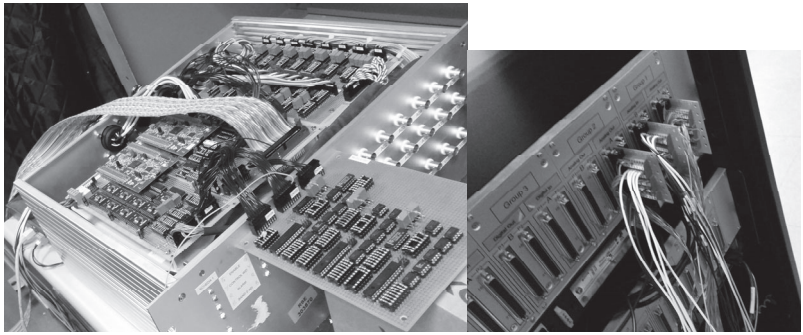


Figure 16. Details of the CHIL laboratory implementation: controller and RT simulator I/O interface.

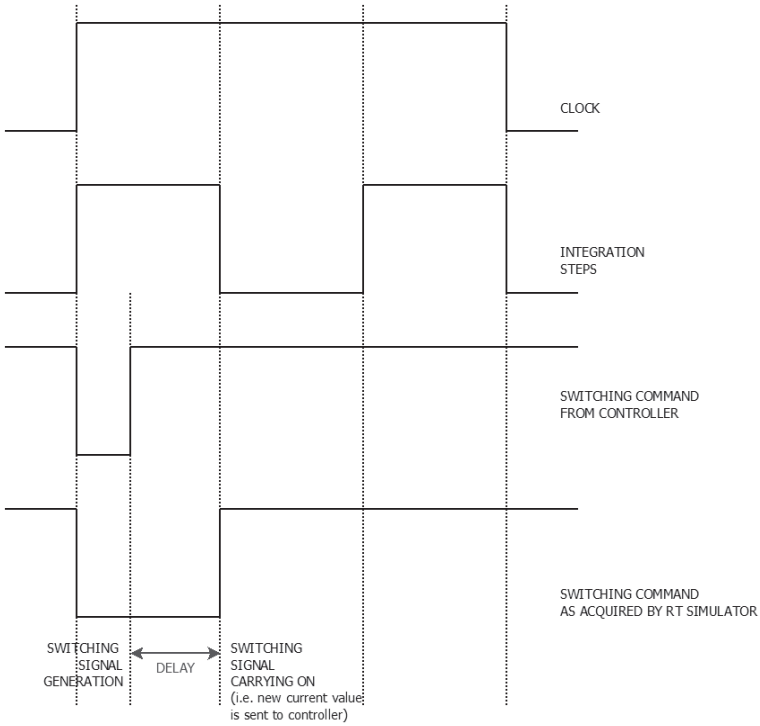



Figure 17. Switching signal time-line with time delay due to integration step of the digital real time simulator.

EBSCOhost - printed on 2/14/2023 2:46 PM via . All use subject to https://www.ebsco.com/terms-of-use

Comparison between the ATPDraw and CHIL simulation results indicates that the delay in acquisition/generation of the signals exchanged between the simulation model and the microprocessor hardware, considering a time-step of $T_{sw}/5$ (15.625 μs), has a noticeable effect on the waveforms. A possible solution to decrease the impact of this delay would be to reduce the calculation time-step of the RT simulator, but this parameter is strictly connected to the RT simulator's performance and to the complexity of the simulated model. A minimum time-step of 12 μs is achievable for the system used in the study with the RT simulator; but such a time-step is not an integer sub-multiple of the switching period $T_{sw}$ (78.125 μs). An alternative feasible solution is to model the system with a grid frequency equal to 5 Hz (instead of 50 Hz) to obtain a UC switching frequency reduced by a factor of 10 and, consequently, a switching period ten times bigger ($T_{sw}$ = 781.25 μs). In this way, maintaining a fixed simulation time-step (15.625 μs), the relevant time delay weight is reduced. If all the time constants of the system are scaled up by a factor of 10:

- the grid frequency has to be equal to 5 Hz;
- the switching frequency has to be equal to 1,280 Hz ($T_{sw}$ = 781.25 μs);
- capacitors and inductances have to be scaled up 10 times;
- control regulator time constants have to be multiplied by a factor 10.

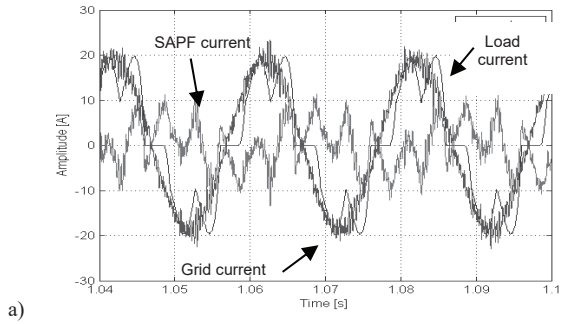
The behavior of the system during grid connection was evaluated considering different kinds of load (RL three-phase and single-phase; three-phase diode bridge rectifier) and for different control schemes and strategies (open or closed loop; total or selective harmonic compensation).

In the next section, the results of CHIL simulations with a non-linear load are presented. A three-phase diode bridge rectifier was considered as a disturbing non-linear load with the same characteristics described previously (Figure 8).

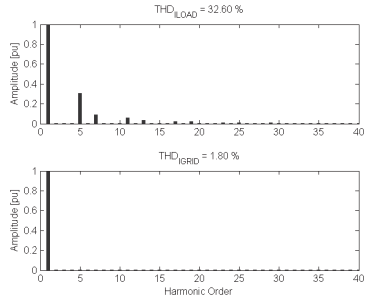
The SAPF supplies the reactive power and compensates the harmonics currents of the load. Figure 18 reports the load, compensator and grid currents during grid connected operation with a closed loop control scheme and total harmonic compensation.

As shown previously, thanks to the compensator, in the case of total harmonic compensation, the residual grid currents have a THD of less than 2 %. In general, for all the control methods considered, this upper value is guaranteed and the results are comparable to previous ones (Figure 9-12).

EBSCOhost - printed on 2/14/2023 2:46 PM via . All use subject to https://www.ebsco.com/terms-of-use




a)




b)

Figure 18. a) Load, compensator and grid currents during grid connected operation with a closed loop control scheme and total harmonic compensation; b) load and residual grid current harmonics and relevant total harmonic distortion indexes.

## Prototype Test-bed

To complete the study of the behaviour and performance of this compensator device, a prototype was developed in accordance with the scheme in Figure 1 and the parameter values reported in Table I. The test-bed of the prototype is shown in Figure 19.

In Figure 20, in line with the previous simulation results, the test results are shown for a diode bridge rectifier (Figure 8) and with a closed loop control logic with feedforward (Figure 2).

EBSCOhost - printed on 2/14/2023 2:46 PM via . All use subject to https://www.ebsco.com/terms-of-use

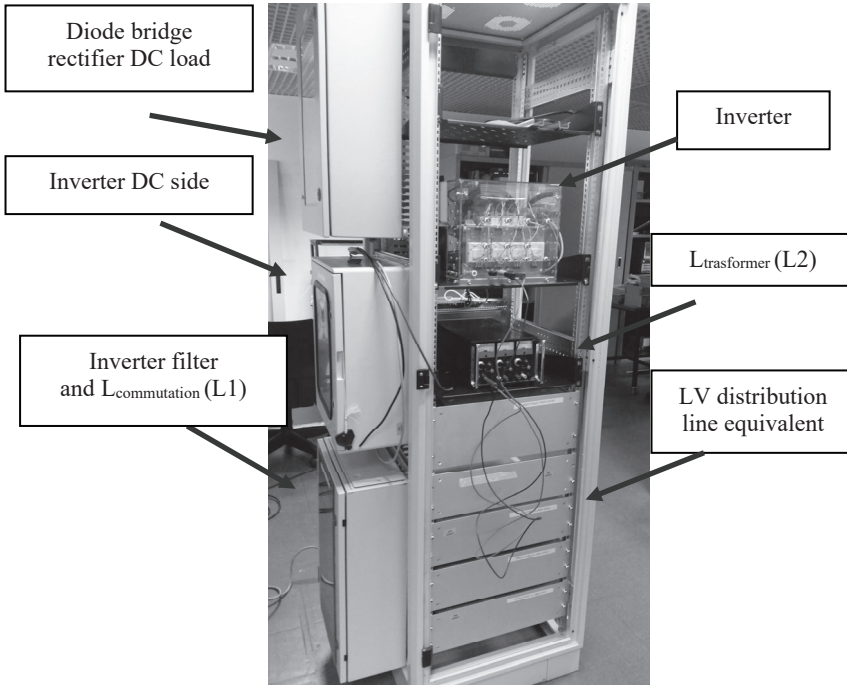



Figure 19. Test-bed prototype.

EBSCOhost - printed on 2/14/2023 2:46 PM via . All use subject to https://www.ebsco.com/terms-of-use

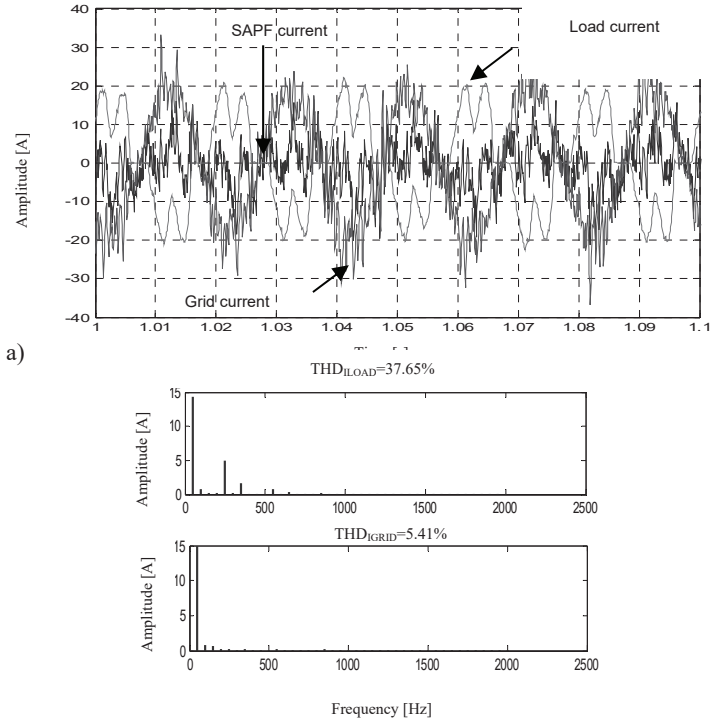



Figure 20. Experimental results during grid connected operation with a closed loop control scheme and total harmonic compensation: a) load, compensator and grid currents; b) load and residual grid current harmonics and relevant total harmonic distortion indexes.

The correspondence between the results obtained through experimentation (Figure 20) and digital simulation (the ATPDraw environment, Figures 9-12, real time environment, Figure 20) confirms the representativeness of the results obtained with the test platform.

In Table II, the performance of the SAPF in terms of residual harmonic distortion in the distribution grid are shown. As expected, the prototype test shows the worst result due to the presence of measurement errors and disturbances. In any case, the good performance of the device as an active filter are validated.

EBSCOhost - printed on 2/14/2023 2:46 PM via . All use subject to https://www.ebsco.com/terms-of-use

**Table II. Closed loop with feedforward control logic performances**

| | THD_load | THD_grid |
|---|---|---|
| **Digital simulation** | 38.65 % | <1 % |
| **CHIL simulation** | 36.62 % | <2 % |
| **Prototype test** | 37.65 % | 5.41 % |

## Conclusions

This paper presents the performance of a 9 kW shunt active power filter for the improvement of PQ and for power factor correction with disturbing or sensitive loads. The proposed SAPF acts as a controlled current generator, whose reference current is nominally equal to the disturbing components of the load currents. The adopted control approach allows fast dynamic responses to load changes, but it can be modified to obtain selective harmonic compensation, at the cost of slower dynamics. The proposed modulation strategy uses a hysteresis band current control, modified so that in each switching period the current threshold limits are predicted for the following period in order to guarantee fixed switching frequency. Such a modulation allows very fast responses to reference changes while ensuring a 'defined' harmonic spectrum of the SAPF currents. The SAPF behaviour was simulated for different kinds of load: three-phase RL balanced; single-phase RL; and three-phase diode bridge rectifier, both in steady-state and transient conditions, and in the case of unbalanced supply voltages. In each case, the SAPF achieved a good degree of compensation of the disturbing current components of the load, with fast dynamic responses to rapid load changes. The system response to possible grid and load resonances was also analysed through simulation. In this case, it emerged that a possible control strategy for the SAPF was to disable the direct compensation of load currents (FFW) and to select the harmonics to be compensated.

After the first validation, controller hardware-in-the-loop real-time simulations were done as an advanced and effective simulation technique to test the performance of the circuit in different operating conditions. The control strategies were implemented on a real digital microprocessor and tested with CHIL simulations, allowing the test of real control devices. The CHIL tests performed in the RSE laboratory confirmed the good performance of the compensator in each analysed operating condition. In general, pure digital simulations are useful to understand the behaviour of a power system during transients, but such techniques do not provide evidence about possible issues arising in the real implementation of a system. This limitation can be overcome by real time CHIL simulations,

EBSCOhost - printed on 2/14/2023 2:46 PM via . All use subject to https://www.ebsco.com/terms-of-use

which allow the testing of real controllers, before the implementation of a power prototype.

Following the good results obtained with different kinds of simulation, a power prototype was developed. This device was tested in the laboratory and the correspondence between the results obtained through experimentation and with the digital simulations (ATPDraw and real-time) confirms the representativeness of the results obtained with the test platform and the good performance of the SAPF as a power quality compensator.

## Acknowledgement

This work has been financed by the Research Fund for the Italian Electrical System under the Contract Agreement between RSE S.p.A. and the Ministry of Economic Development—General Directorate for Nuclear Energy, Renewable Energy and Energy Efficiency in compliance with the Decree of March 8, 2006.

## References

[1]. P. K. Steimer, “Enabled by high power electronics—Energy efficiency, renewables and smart grids,” Power Electronics Conference (IPEC 2010), 21–24 June 2010, Sapporo (Japan).

[2]. J. He, Yun Wei Li, F. Blaabjerg, X. Wang, “Active Harmonic Filtering Using Current-Controlled, Grid-Connected DG Units With Closed-Loop Power Control,” Power Electronics, IEEE Transactions on (Vol. 29, Issue 2), Feb. 2014.

[3]. L. Herman, I. Papic, B. Blazic, “A Proportional-Resonant Current Controller for Selective Harmonic Compensation in a Hybrid Active Power Filter,” Power Delivery, IEEE Transactions on (Vol. 29, Issue 5), Oct. 2014.

[4]. S. K. Khadem, M. Basu, M. F. Conlon, “Harmonic power compensation capacity of shunt active power filter and its relationship with design parameters,” Power Electronics, IET (Vol. 7, Issue 2), Feb. 2014.

[5]. P. Acuna, L. Moran, M. Rivera, J. Dixon, “Improved Active Power Filter Performance for Renewable Power Generation Systems,” Power Electronics, IEEE Transactions on (Vol. 29, Issue 2), Feb. 2014.

[6]. P. Karuppanan, S. R. Prusty, K. Mahapatra, “Adaptive-Hysteresis Current Controller based Active Power Filter for Power Quality Enhancement,” in Proc. Of International Conference on Sustainable Energy and Intelligent Systems (SEISCON 2011).

[7]. B. C. Babu, M. Mohapatra, S. Jena, A. Naik, “Dynamic Performance of Adaptive Hysteresis Current Controller for Mains-connected Inverter System,” International Conference on Industrial Electronics, Control and Robotics 2010.

EBSCOhost - printed on 2/14/2023 2:46 PM via . All use subject to https://www.ebsco.com/terms-of-use

# CHAPTER THIRTY-FOUR

# A HYBRID POWER FILTER FOR LOAD COMPENSATION

SALVADOR P. LITRÁN, PATRICIO SALMERÓN, ALEJANDRO PÉREZ, JAIME PRIETO [1]

## Abstract

Modern electrical systems must provide electrical power of adequate quality to meet international standards. It is described in this paper a control strategy for an active compensator based on a hybrid filter topology to ensure this. This topology is formed by use of an active power filter connected in series with the source, and a passive filter connected in parallel with the load. The proposed strategy seeks to minimize the RMS value of the voltage at the point of common coupling so that the source transfers the power demanded by the load. Thus, the determination of the reference signal is posed as a constrained optimization problem. The strategy was designed for four-wire systems and enables the compensation of current harmonics, reactive power, and neutral current. Furthermore, an experimental prototype was developed. This allowed for verification of the new strategy for different types of loads.

**Keywords**: harmonics, active filter, hybrid filter, electric power quality

[1] The authors are part of the Department of Electrical Engineering, Huelva University, Spain.

EBSCOhost - printed on 2/14/2023 2:46 PM via . All use subject to https://www.ebsco.com/terms-of-use

## Introduction

In recent decades, the concept of power quality (PQ) has gained notoriety in the field of electrical engineering. Today, it is a matter of great interest to electricity production and distribution companies, as well as to end users.

A number of different solutions for improving power quality have been proposed. Some of these rely on the use of passive filters, which can be understood as devices that change impedance as a function of frequency [1]. Others are based on active filters, which are able to compensate for network harmonics with electronic power converters [2]. These filters can be connected in parallel [3], or in series [4], [5], depending on the load type that needs to be compensated for. Furthermore, a combination of both filter kinds (active and passive) is possible, forming what is known as a hybrid filter [6], [7]. Here, the active filter contributes to improving the frequency response of the passive filter.

One of these hybrid filter topologies uses an active filter in series with the source and a passive filter in parallel with the load [8]–[10]. This configuration improves the behaviour of the passive filter, which, tuned to the appropriate frequency, achieves the elimination of source current harmonics and a consequent enhancement of signal quality.

Various control strategies have been tested using an active filter to improve the filtering characteristics of a passive filter. To this end, a common strategy has been to generate a voltage proportional to the source current harmonics in the active filter [6], [7]. The active filter presents high impedance to the load current harmonics. This improves the behaviour of the passive filter, so that it prevents possible resonances and ensures that the filtering characteristics of the passive filter are independent of the source impedance.

In another strategy, the active filter generates a voltage equal to the load voltage harmonics, but of opposite sign. However, it is unable to fully avoid the disadvantages of passive filters. More recently, a hybrid strategy combining both strategies has been proposed, which improves on both these strategies [5].

Other proposed strategies recommend that the active filter generates a voltage to compensate for the reactive power of the set load and passive filter, thus eliminating source current harmonics [11]. The calculation algorithm used was based on the formulation of the instantaneous reactive power [12], [13], in order to achieve constant power on the source side when it is applied to a balanced, three-phase, and three-wire system.

EBSCOhost - printed on 2/14/2023 2:46 PM via . All use subject to https://www.ebsco.com/terms-of-use

A similar compensation methodology was proposed in [14] with a control strategy based on a dual vectorial formulation of the instantaneous reactive power. This strategy is applicable to unbalanced, three-phase, four-wire systems and it allows the reactive power to be compensated for and the source current harmonics to be eliminated.

This paper presents a control strategy for a hybrid filter composed of an active power filter connected in series and a passive filter connected in parallel. The proposed strategy aims to minimize the effective value of the voltage at the point of common coupling (PCC) to ensure the power transference demanded by the load.

The determination of the reference signal is addressed as a constrained optimization problem in systems of four wires. This allows for the mitigation of current harmonics, the compensation of reactive power, and the elimination of neutral current.

The proposed strategy was applied to an experimental prototype hybrid filter, allowing the verification of its performance in compensating for nonlinear loads in four-wire systems.

## Control Strategy for a Hybrid Compensator

This section presents a compensation method based on an average value. The aim is to determine the minimum RMS value of the voltage at the PCC (point of common coupling) so that the system transfers the active power to the load. To develop this strategy, a polyphasic system was considered to be a special kind of multi-conductor system [15]. A four-wire, three-phase system can therefore be represented by means of a multi-conductor system, as shown in Fig. 1.

The currents $i_1$, $i_2$, $i_3$, and $i_4$ are the components of the line current vector, which is defined by:

$$\mathbf{i} = \begin{bmatrix} i_1 & i_2 & i_3 & i_4 \end{bmatrix}^T \tag{1}$$

As a consequence of Kirchhoff's current law, the current vector, **i**, is satisfied by:

$$\begin{bmatrix} 1 & 1 & 1 & 1 \end{bmatrix} \begin{bmatrix} i_1 & i_2 & i_3 & i_4 \end{bmatrix}^T = 0 \tag{2}$$

One of the components can always be expressed as a linear combination of the others. From the mathematical point of view, only 4-1 components are sufficient to describe the current vector. However, in four-

EBSCOhost - printed on 2/14/2023 2:46 PM via . All use subject to https://www.ebsco.com/terms-of-use

wire, three-phase systems the use of the four current components permits a direct description of system behaviour.

The system voltages may be defined with respect to a virtual neutral point. This neutral point is formed by four impedances of the same value, as shown in Fig. 1.

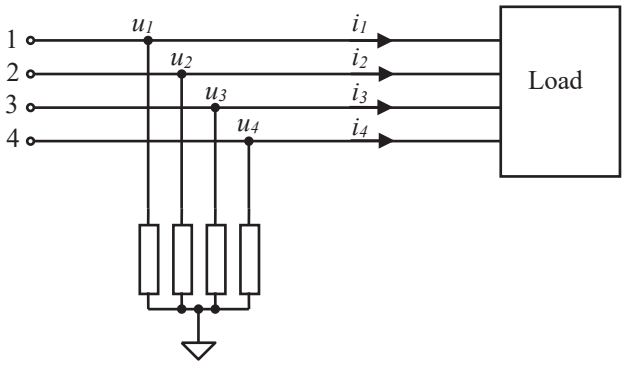



Figure 1. Four-wire system

In this way, it is possible to define the voltages, $u_1$, $u_2$, $u_3$, and $u_4$ of each wire with respect to this common point [16], [17]. These voltages are the components of the voltage vector, **u**, which is defined by means of:

$$\mathbf{u} = \begin{bmatrix} u_1 & u_2 & u_3 & u_4 \end{bmatrix}^T \tag{3}$$

The four components of the voltage vector must verify that:

$$\begin{bmatrix} 1 & 1 & 1 & 1 \end{bmatrix} \begin{bmatrix} u_1 & u_2 & u_3 & u_4 \end{bmatrix}^T = 0 \tag{4}$$

In what follows, the subscript $\sum$ is used to refer to these "collective" values, including the fourth wire.

For a four-wire system, instantaneous power is obtained from the scalar product of the voltage vector and the current vector. It is expressed by the equation:

$$p_{\Sigma} = \mathbf{u}^T \cdot \mathbf{i} \tag{5}$$

In steady state and periodic conditions, the average value of the instantaneous active power and RMS value of the voltage vector and the current vector are defined for a fundamental period, $T$. In regular

EBSCOhost - printed on 2/14/2023 2:46 PM via . All use subject to https://www.ebsco.com/terms-of-use

conditions for an observation interval, $T$, corresponding to one period or a multiple of the period, the root mean square or RMS value is given by:

$$U_{\Sigma} = \sqrt{\overline{\|\mathbf{u}\|^2}} = \sqrt{\frac{1}{T}\int_t^{t+T}\left(\sum_{j=1}^{4} u_j^2\right)dt} = \sqrt{\sum_{j=1}^{4} U_j^2} \tag{6}$$

Here, $U_j$ is the RMS value of the $j$ component of the voltage vector. In a similar manner, for the current vector given in (1) the root mean square value is defined by:

$$I_{\Sigma} = \sqrt{\overline{\|\mathbf{i}\|^2}} = \sqrt{\frac{1}{T}\int_t^{t+T}\left(\sum_{j=1}^{4} i_j^2\right)dt} = \sqrt{\sum_{j=1}^{4} I_j^2} \tag{7}$$

where $I_j$ is the RMS value of the $j$ component of the current vector.

The active power is obtained by the average value of the instantaneous power given in (5). Thus, for the fundamental period $T$, the active power is given by:

$$P_{\Sigma} = \frac{1}{T}\int_t^{t+T} p_{\Sigma}\, dt \tag{8}$$

The aim of compensation with a series APF (active power filter) is the optimization of the average power transferred from source to load. For this, the voltage vector, **u**, is determined such that its minimum RMS value permits the power transfer. To solve this optimization problem, Lagrange multipliers are used. The objective function is defined by:

$$F = \frac{1}{T}\int_t^{t+T} \mathbf{u}\cdot\mathbf{u}\, dt \tag{9}$$

subject to the constraint:

$$G = \frac{1}{T}\int_t^{t+T} \mathbf{u}\cdot\mathbf{i}\, dt = P_{\Sigma} \tag{10}$$

Once $F$ and $G$ functions are defined, as in (9) and (10), the Lagrangian equation is expressed as:

$$L = F + \lambda G \tag{11}$$

EBSCOhost - printed on 2/14/2023 2:46 PM via . All use subject to https://www.ebsco.com/terms-of-use

Applying:

$$\frac{\partial L}{\partial \mathbf{u}} = 0$$
$$\frac{\partial L}{\partial \lambda} = 0 \tag{12}$$

The result is an equation system whose solution is:

$$\mathbf{u} = R \cdot \mathbf{i} \tag{13}$$

where $R$ is given by the ratio between the average power and the RMS value of the current

$$R = \frac{P_{\Sigma}}{I_{\Sigma}^2} \tag{14}$$

Here, $R$ represents the value of a resistive three-phase load, which transfers the same active power as the load. The application of (13) enables determination of the voltage vector, **u**. Voltages applied to a symmetrical resistive load of resistance $R$ transfer the same average power that the load needs to compensate. In this way, from the point of common coupling in the system, a unity power factor is achieved.

Fig. 2 shows a system of four wires compensated by means of a series active power filter. This is represented by four controlled voltage sources with values $u_{C1}$, $u_{C2}$, $u_{C3}$, and $u_{C4}$. These four components make up the compensation voltage vector, as defined by:

$$\mathbf{u}_C = \begin{bmatrix} u_{C1} & u_{C2} & u_{C3} & u_{C4} \end{bmatrix}^T \tag{15}$$

EBSCOhost - printed on 2/14/2023 2:46 PM via . All use subject to https://www.ebsco.com/terms-of-use

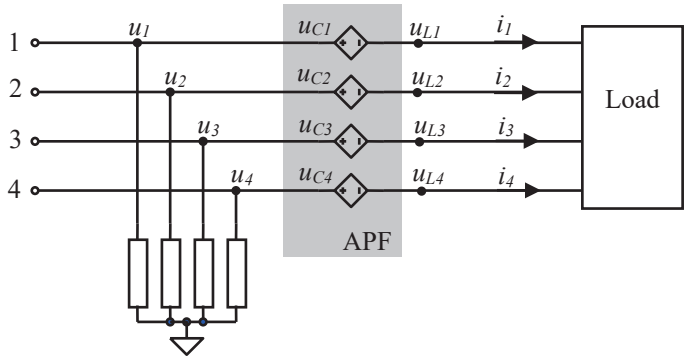



Figure 2. Four-wire system with series compensation equipment

When Kirchhoff's voltage law is applied to the circuit in Fig. 2, it provides the next relationship for the compensation voltage, $\mathbf{u}_C$:

$$\mathbf{u}_C = \mathbf{u} - \mathbf{u}_L \tag{16}$$

where $\mathbf{u}_L$ is the load voltage vector. Taking into account equations (13) and (14) gives:

$$\mathbf{u}_C = \frac{P_\Sigma}{I_\Sigma^2}\mathbf{i} - \mathbf{u}_L \tag{17}$$

Furthermore, it is possible to obtain the average power transferred by the compensator. For this purpose, the expression (17) is multiplied by the current vector. If the resulting expression is integrated over the period $T$, the system power balance is obtained:

$$\frac{1}{T}\int_t^{t+T} \mathbf{u}_C \cdot \mathbf{i}\, dt = \frac{1}{T}\int_t^{t+T} \frac{P_\Sigma}{I_\Sigma^2}\mathbf{i}\cdot\mathbf{i}\, dt - \frac{1}{T}\int_t^{t+T} \mathbf{u}_L \cdot \mathbf{i}\, dt \tag{18}$$

The first term is the average power of the compensator, so that (18) can be rewritten as:

$$P_{C\Sigma} = \frac{1}{T}\int_t^{t+T} \frac{P_\Sigma}{I_\Sigma^2}\mathbf{i}\cdot\mathbf{i}\, dt - \frac{1}{T}\int_t^{t+T} \mathbf{u}_L \cdot \mathbf{i}\, dt \tag{19}$$

The first term in (19) constitutes the active power consumed by the resistor $R$ and the second term constitutes the load average power, $P_{L\Sigma}$, which can be expressed by:

EBSCOhost - printed on 2/14/2023 2:46 PM via . All use subject to https://www.ebsco.com/terms-of-use

$$P_{C\Sigma} = \frac{P_{\Sigma}}{I_{\Sigma}^2} \frac{1}{T} \int_{t}^{t+T} \mathbf{i} \cdot \mathbf{i} \, dt - P_{L\Sigma} \tag{20}$$

Considering the expressions (7) and (14), equation (20) can be set as:

$$P_{C\Sigma} = R \, I_{\Sigma}^2 - P_{L\Sigma} = P_{\Sigma} - P_{L\Sigma} \tag{21}$$

The expression (21) represents the power balance of the compensated system. The average power transferred by the compensator must be zero:

$$P_{\Sigma} = P_{L\Sigma} \tag{22}$$

The relationship of equality (22) allows the numerator of (14) to be identified as the average power load:

$$R = \frac{P_{L\Sigma}}{I_{\Sigma}^2} \tag{23}$$

Thus, the compensation voltage vector defined in (17) must be expressed in terms of the average power of the load, this is:

$$\mathbf{u}_C = \frac{P_{L\Sigma}}{I_{\Sigma}^2} \mathbf{i} - \mathbf{u}_L \tag{24}$$

The application of equation (24) requires a four-branch inverter for four-wire systems. The use of this type of configuration has a higher cost and added complexity in the control circuit. In what follows, a simplification of the control strategy is carried out, allowing the use of a three-branch converter.

The compensation strategy defined by (24) is based on the set APF-load, which behaves as a symmetrical resistive load ($R$) as shown in Fig. 3. The set of four resistors connected in a star shape represents the optimum load. This load has the same structure and the same voltage set as the load connected in a star topology, which defines the virtual neutral point in Fig. 2.

An unbalanced nonlinear load can be represented by means of three nonlinear branches connected between the phase and neutral, as Fig. 4a shows. In this figure, according to (24), the following equations are obtained:

EBSCOhost - printed on 2/14/2023 2:46 PM via . All use subject to https://www.ebsco.com/terms-of-use

$$u_{C1} = \frac{P_{L\Sigma}}{I_{\Sigma}^2} i_1 - u_{L1}$$
$$\vdots$$
$$u_{C4} = \frac{P_{L\Sigma}}{I_{\Sigma}^2} i_4 - u_{L4} \tag{25}$$

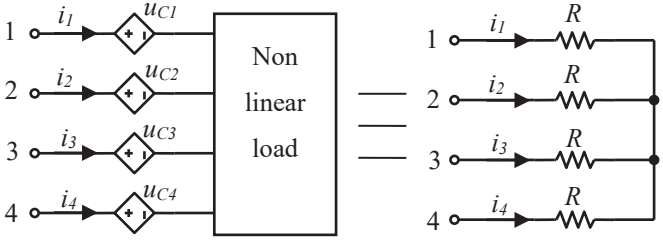



Figure 3. Resistive behaviour of series APF and load

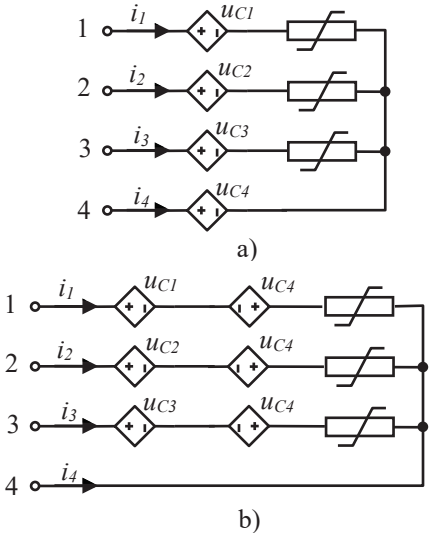



Fig. 4. Correction of the compensation voltage when $i_4 \neq 0$

EBSCOhost - printed on 2/14/2023 2:46 PM via . All use subject to https://www.ebsco.com/terms-of-use

When the source $u_{C4}$ is displaced to the branches 1, 2, and 3, the scheme shown in Fig. 4b is obtained. The set of compensation voltages is then:

$$u'_{C1} = u_{C1} - u_{C4} = \frac{P_{L\Sigma}}{I_{\Sigma}^2}\left(i_1 - i_4\right) - u_{L4}$$

$$u'_{C2} = u_{C2} - u_{C4} = \frac{P_{L\Sigma}}{I_{\Sigma}^2}\left(i_2 - i_4\right) - u_{L4}$$

$$u'_{C3} = u_{C3} - u_{C4} = \frac{P_{L\Sigma}}{I_{\Sigma}^2}\left(i_3 - i_4\right) - u_{L4} \tag{26}$$

Expressions (26) allow to determine the compensation voltages for an active power filter constituted by three branches for any permutation of supply voltage.

## Capacitor Voltage Control at the DC Side

The inverter generates a certain waveform from a constant voltage value on its DC side. This DC voltage is obtained from the charge of a capacitor, or two capacitors with intermediate tap if it is necessary to dispose of a fourth wire. For proper operation of the APF, its voltage must remain constant at the DC side. This voltage should not vary in the case of an inverter with ideal switching devices and a control strategy where the average power transferred by the compensator is zero. However, fluctuations occur in practice due to switching losses in power electronic devices, the conductance of these devices, losses in the capacitors, and delays introduced by the control circuit.

To compensate for voltage variations, it is possible to operate the APF as a controlled rectifier, transferring the necessary active power from the AC side to the DC side of the inverter [18]. This is achieved when the active filter generates a sinusoidal voltage in phase with the current whose product corresponds to the required active power. The control circuit must include some strategy that meets this objective to work. Therefore, the control system of the active power filter should have two regulation loops with clearly differentiated functions: the main control loop designed to carry out the load compensation strategy according to the reference voltage established in (26); and the secondary control loop with the objective of maintaining the average voltage around a reference value at the capacitors. This second loop modifies the reference value of the original compensation voltage by varying the mean value of the

EBSCOhost - printed on 2/14/2023 2:46 PM via . All use subject to https://www.ebsco.com/terms-of-use

instantaneous active power developed by the active filter and regulating the DC side voltage.

The input variable in the secondary control loop is the error in the voltages of the capacitors with respect to a reference value. The output variable is a set of voltage references determined from the active power value that has to be absorbed or delivered by the active filter in order to compensate for the error in the input voltage.

Generally, the coordinated action of both control loops, the primary and secondary, makes it difficult to obtain an analytical expression that reflects the instantaneous evolution of the voltage at the DC side for a variation in the active power absorbed by the load. Thus, when a variation of the load occurs, the main control loop determines the new voltage components that must be compensated. This involves a delay in the calculation of the compensation voltage determined by the dynamics of the main control loop. The detected delay in the compensation voltage references implies that the active filter transiently compensates the system according to an incorrect value of the active power, which causes a variation of the voltage on the DC side. In this situation, the secondary control loop acts to eliminate that voltage variation. This control loop presents a nonlinear behavior, so it is difficult to obtain an analytical expression of the evolution that the voltage will follow at the DC side. For this reason, the dimensions of the capacitors are decided according to steady state considerations [19]. This is the approach taken in the following.

Fig. 5 shows a power circuit with ideal switching devices for the series-APF. Two condensers have been included with a midpoint at the side, to which a fourth conductor is connected. Furthermore, at the AC side a filter has been connected to eliminate the ripple caused by high frequency switching.

EBSCOhost - printed on 2/14/2023 2:46 PM via . All use subject to https://www.ebsco.com/terms-of-use

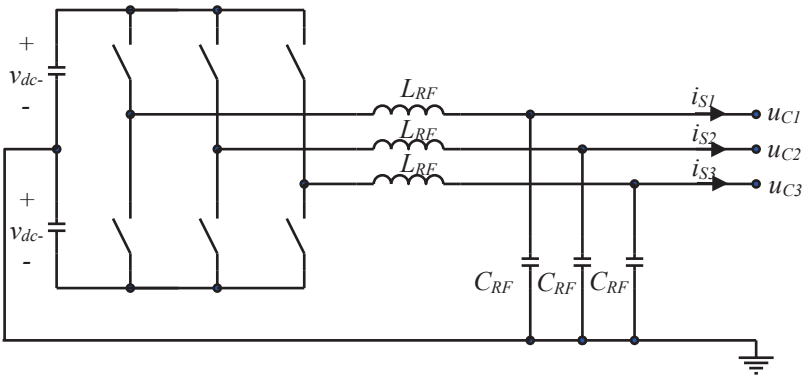



Figure 5. Series active filter scheme

The energy in the capacitors will remain constant when the power at the DC side and AC side is equal:

$$p_{dc} = p_{ac} \tag{27}$$

According to Fig. 5, when the voltages in the two capacitors are the same, the following expression can be obtained:

$$2C v_{dc} \frac{dv_{dc}}{dt} = \mathbf{u}_C \, \mathbf{i}_S^T \tag{28}$$

where $\mathbf{u}_C$ is the compensation voltage vector and $\mathbf{i}_S$ is the source current vector:

$$\mathbf{u}_C = \begin{bmatrix} u_{C1} & u_{C2} & u_{C3} \end{bmatrix}^T \tag{29}$$

$$\mathbf{i}_S = \begin{bmatrix} i_{S1} & i_{S2} & i_{S3} \end{bmatrix}^T \tag{30}$$

Taking into account the compensation voltage as given by (24), equation (28) can be expressed as:

$$2C v_{dc} \frac{dv_{dc}}{dt} = R \mathbf{i}_S \, \mathbf{i}_S^T - \mathbf{v}_L \, \mathbf{i}_S^T \tag{31}$$

EBSCOhost - printed on 2/14/2023 2:46 PM via . All use subject to https://www.ebsco.com/terms-of-use

This equation helps in designing the voltage control of the capacitors. A variation in the voltage of the capacitors means that the filter injects/absorbs energy from the system and the control must restore the energy transferred from the capacitors.

For the regulation of the voltage at the DC side, the APF must work in rectifier mode. In this situation, two control methods are generally used: current control and voltage control [20]. The first method is most commonly used for reasons of simplicity. It relies on forcing the phase current to follow a sinusoidal reference pattern. The amplitude of the reference current is obtained from the relationship in (32)

$$I_{MAX} = G_C\, e = G_C \left( V_{ref} - V_{dc} \right) \tag{32}$$

where $G_C$ represents the transfer function of the controller. A proportional integral controller is shown in Fig. 6 (PI). Finally, the reference waveform is obtained by multiplying $I_{MAX}$ by a sine function with the same frequency as the fundamental frequency and the same phase angle as the desired function. The sine function is obtained from the direct sequence fundamental component of the source current ($\mathbf{i_1}^+$ in Figure 6).

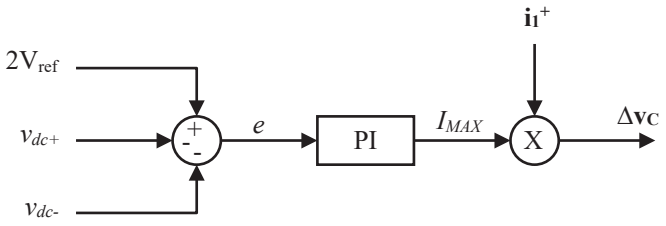



Figure 6. Voltage control at the DC side

## Hybrid Filter Prototype

This section describes each of the components of the experimental prototype that was developed. Fig. 7 shows the power circuit with the hybrid compensator.

The active filter consisted of three modules: Semikron IGBTs, model SKM50GB123, with three SKHI 22A from the same manufacturer. At the DC side, the inverter had two capacitors of 2200 μF, which worked at 100 V. At the AC side of the inverter, a ripple LC filter formed using an inductor of 0.13 mH and a capacitor of 50 μF was connected. The function

EBSCOhost - printed on 2/14/2023 2:46 PM via . All use subject to https://www.ebsco.com/terms-of-use

of this filter was to eliminate high frequency components caused by the switching of the power devices.

The set inverter and ripple filter was matched to the power system by means of three single-phase transformers of 1 kVA with a turn ratio of 1:1 to ensure galvanic isolation.

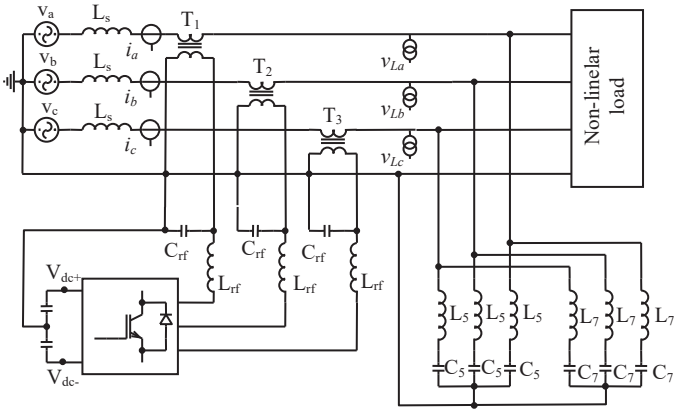



Figure 7. Experimental prototype scheme of hybrid filter

The control scheme shown in Fig. 8 was used to determine the reference voltage of the active filter. The input signals used included the phase voltage vector, which was measured at the load side, and the source current vector, whose components are the three line currents. Fig. 7 shows the position of the sensors used for measuring the voltage and current.

EBSCOhost - printed on 2/14/2023 2:46 PM via . All use subject to https://www.ebsco.com/terms-of-use

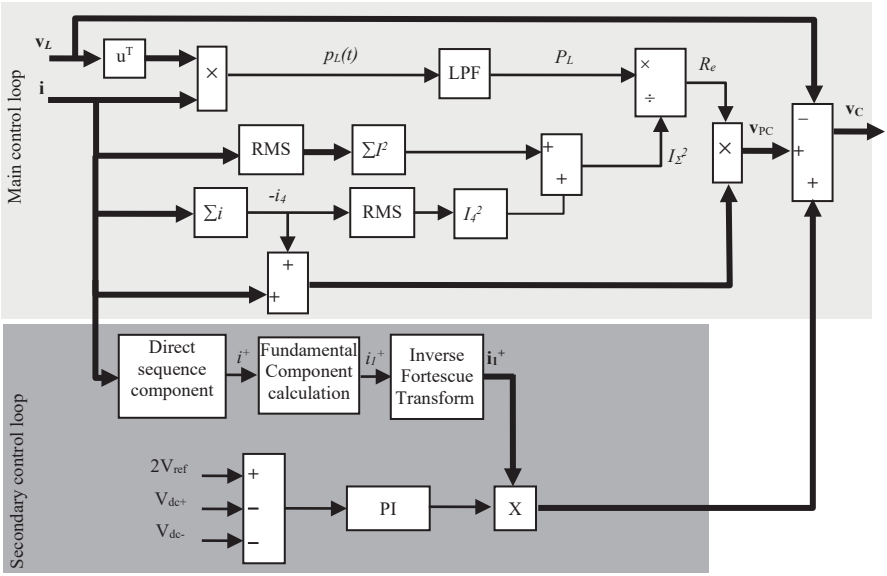



Figure 8. Block scheme to determine the compensation voltage

The control strategy was implemented with control and general application data acquisition cards compatible with MATLAB-Simulink and developed by dSPACE. dSPACE RTI together with Mathworks RTW automatically generate real-time code. This allows the processor board to be programmed and I/O boards to be selected. It is based on the DS 1005 PPC in a dSPACE expansion box. The input board used was the dSPACE DS 2004 A/D and the output board was the DS 51001 DWO. The control board used a PowerPC 750GX processor running at 1 GHz. For the experimental prototype, the sampling rate was limited to 50 μs in order to avoid overrun errors.

A hysteresis band control loop was defined. This is a PWM control technique that is adequate for applications with active power filters. The converter IGBT (insulated gate bipolar transistor) gating signals are generated by comparison of the reference signal with the inverter output voltage and the transistor switches when the error exceeds a fixed magnitude: the hysteresis band. In this control type, switching frequency is variable, although in our design this frequency was limited to 20 kHz so as not to reach the IGBTs maximum switching frequency.

EBSCOhost - printed on 2/14/2023 2:46 PM via . All use subject to https://www.ebsco.com/terms-of-use

The passive filter was constituted by two LC branches tuned to the 5th and 7th harmonics. The branch tuned to the harmonic of the fifth order consisted of an inductance of 13.5 mH and a capacitor of 30 μF. The branch tuned to the 7th harmonic was formed by an inductance of 6.75 mH and a capacitor of 30 μF.

The power circuit was supplied by a sinusoidal balanced three-phase 100 V source with a 50 Hz frequency and a source inductance of 1.8 mH, and a source resistance of 1.4 Ω.

The nonlinear load consisted of three uncontrolled single-phase rectifiers connected at the phase and neutral wire. Three GBPC2510 modules from International Rectifier were used. At their DC side, a 12.5 Ω resistance in series with a 55 mH inductance was connected.

## Experimental Results

To demonstrate the validity of the proposed control strategy, the experimental prototype was subjected to different tests. Experimental results were obtained for the system as shown in Fig. 7 and described previously.

Fig. 9 shows the waveform of the source currents and the voltages at the point of common coupling before compensation. The source current had an RMS value of 5.9 A with a THD value of 26.8 %. The system presented a slight current imbalance as shown in Fig. 9b. This was due to the tolerance in the values of the passive elements connected at the DC side of the rectifiers. With respect to the voltage at the PCC, the RMS value was 97.4 V and the THD value was 8.7 %.

When the passive filter tuned to the 5th and 7th harmonics was connected, the waveforms shown in Fig. 10 were measured. The RMS value and the THD value of the source current were 5.9 A and 31.5 %, respectively. The waveform currents presented a THD higher than without passive filter. This was due to the increase of the third order harmonic, which changed from 1.2 A to 1.7 A. The voltage measured at the PCC had an RMS value of 99.3 V and 7.4 % of the THD value.

When the active and passive filters were connected, the waveforms shown in Fig. 11 were measured. Voltages at the PCC and source currents had practically sinusoidal waveforms. The first one had an RMS value of 98.6 V and 1.3 % THD, while the second one had an RMS value of 5.5 A and a THD value of 2.7 %.

EBSCOhost - printed on 2/14/2023 2:46 PM via . All use subject to https://www.ebsco.com/terms-of-use

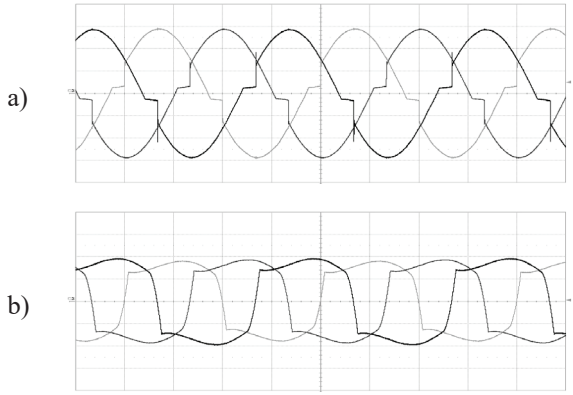



Figure 9. Load without compensation: a) voltage at the PCC; b) source currents. 48V/div; 4 A/div; 5ms/div

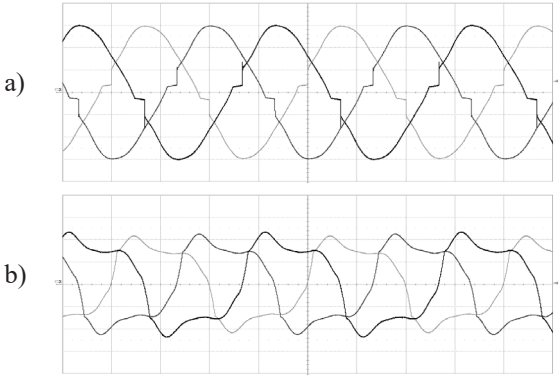



Figure 7. System with passive filter: a) voltages at the PCC; b) source currents. 48V/div; 4 A/div; 5ms/div

EBSCOhost - printed on 2/14/2023 2:46 PM via . All use subject to https://www.ebsco.com/terms-of-use

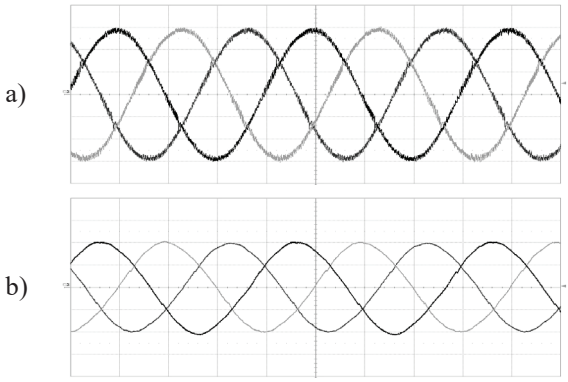



Figure 8. System with SAPPF: a) voltages at the PCC; b) source currents. 48V/div; 4 A/div; 5ms/div

Table I summarizes the most important results. Harmonics, THD, powers, and power factors are included. Only the results for phase 'a' are shown. These values were measured with the network analyser Fluke 434. The power column, P, shows how the power consumed by the set was slightly higher when the compensation equipment was connected. This is mainly due to the consumption of the passive filter. On the other hand, the apparent power of the active filter was 0.10 kVA, representing approximately 17% of the apparent power of the load.

Regarding the performance of each of the subsystems of compensation equipment—the passive filter and the APF—it is interesting to note the following. The passive filter compensated almost all the reactive power, which was reduced from 0.16 to 0.03 kvar when it was connected. However, this reduction represents an increase in the power factor from 0.91 to 0.94. This is a consequence of the worsening of the source current THD.

The active filter was able to reduce the total harmonic distortion due to an improvement in the filtering characteristic of the passive filter. As shown in Table I, the fifth order harmonic of the source current with the compensated system had an RMS value of 0.7 A; with the passive filter connected this was reduced to 0.4 A. However, the active filter was able to significantly improve the filtering characteristic of the passive filter, since it mitigates source current harmonics almost completely.

EBSCOhost - printed on 2/14/2023 2:46 PM via . All use subject to https://www.ebsco.com/terms-of-use

**Table I. Measured Results: (1) without filters, (2) with passive filter, (3) with SAPPF**

| | | THD (%) | RMS | H1 | H3 | H5 | H7 | H9 | P (kW) | Q (kvar) | S (kVA) | PF |
|---|---|---|---|---|---|---|---|---|---|---|---|---|
| (1) | V | 8.7 | 97.4 | 97.0 | 4.2 | 3.8 | 3.4 | 3 | 0.53 | 0.16 (ind) | 0.56 | 0.91 |
| | I | 26.8 | 5.9 | 5.7 | 1.2 | 0.7 | 0.5 | 0.3 | | | | |
| (2) | V | 7.4 | 99.3 | 99.0 | 5.7 | 2.0 | 0.8 | 1.6 | 0.56 | 0.03 (ind) | 0.56 | 0.94 |
| | I | 31.5 | 5.9 | 5.6 | 1.7 | 0.4 | 0.1 | 0.2 | | | | |
| (3) | V | 1.3 | 98.6 | 98.6 | 0.5 | 0.1 | 0.1 | 0.1 | 0.56 | 0.01 | 0.56 | 0.99 |
| | I | 2.7 | 5.5 | 5.5 | 0.1 | 0.0 | 0.0 | 0.0 | | | | |

## Conclusions

In this work, a control strategy for a hybrid filter constituted by a series active filter and a shunt passive filter was developed. This strategy was based on optimizing the power transference between the source and the load. By applying Lagrange multipliers, the value of the equivalent resistance of the set load-compensator was determined in order to achieve a unity power factor. The control strategy was developed for a multi-conductor system and afterwards it was particularized to an active filter of three branches. The main control loop was designed to carry out the calculation of the reference voltage in order to compensate the load, according to this strategy. A secondary control loop was proposed with the objective of maintaining the average voltage at the capacitors around a set reference value.

Finally, an experimental prototype was designed and the practical results for a nonlinear load, type HCS (harmonic current source), balanced, and four-wire system were presented. The results obtained enabled the verification of the resistive behaviour of the set load-compensator. The application of the proposed strategy led to the mitigation of the source current harmonics and the compensation of the load reactive power.

## References

[1] F. Z. Peng, “Harmonics sources and filtering approaches,” IEEE Industry Applications Magazine, Vol, 7, Issue 4, pp. 18-25, 2001.

[2] Akagi H., “Active harmonic filters,” Proceedings of the IEEE, Vol. 93, Issue 12, pp. 2128–2141, Dec. 2005.

[3] Yong Wang, Jialong Xu, Ling Feng, Chengmin Wang, “A Novel Hybrid Modular Three-Level Shunt Active Power Filter,” IEEE Transactions on Power Electronics, Vol. 33, Issue 9, pp. 7591–7600, Sept. 2018.

EBSCOhost - printed on 2/14/2023 2:46 PM via . All use subject to https://www.ebsco.com/terms-of-use

[4] Dayi Li, Meng Song, Jing Hu, Yunsong Luo, Xueli Xiao; Kai Yang, "Improved series active power filter with fundamental and harmonic magnetic flux hybrid compensation," IET Power Electronics, Vol. 11, Issue 6, pp. 1038-1045, 2018.
[5] Wang Z., Wang Q., Yao W. and Liu J., "A series active power filter adopting hybrid control approach," IEEE Trans. Power Electronics, Vol. 16, No. 3, pp. 301–310, May 2001.
[6] Peng F. Z., Akagi H., Nabae A., "A new approach to harmonic compensation in power systems-a combined system of shunt passive and series active filters," IEEE Trans. Industry Applications. Vol, 26, No. 6, pp. 983–990, Nov/Dec 1990.
[7] Rivas, D.; Moran, L.; Dixon, J.W.; Espinoza, J.R.; "Improving passive filter compensation performance with active techniques," IEEE Trans. On Industrial Electronics, Vol. 50, Issue 1, pp. 161–170, Feb 2003.
[8] An Luo; Zhikang Shuai; Wenji Zhu; Ruixiang Fan; Chunming Tu, "Development of hybrid active power filter based on the adaptive fuzzy dividing frequency-control method," IEEE Trans. on Power Delivery, Vol. 24, Issue 1, pp. 424–432, Jan. 2009.
[9] Corasaniti, V. F.; Barbieri, M. B.; Arnera, P. L.; Valla, M. I., "Hybrid Active Filter for Reactive and Harmonics Compensation in a Distribution Network," IEEE Trans. on Industrial Electronics, Vol. 56, Issue 3, pp. 670–677, March 2009.
[10] T.-L. Lee, Y.-C. Wang, J.-C. Li, and J. M. Guerrero, "Hybrid active filter with variable conductance for harmonic resonance suppression in industrial power systems," IEEE Trans. Ind. Electron., vol. 62, no. 2, pp. 746–756, Feb. 2015.
[11] Kim Y. S., Kim J. S. and Ko S. H., "Three-phase three-wire series active power filter, which compensates for harmonics and reactive power," IEE proc. Electric. Power Applications, Vol, 151, No. 3, pp. 276–282, May 2004.
[12] Herrera, R.S.; Salmerón, P.; "Instantaneous Reactive Power Theory: A Reference in the Nonlinear Loads Compensation," IEEE Trans. on Industrial Electronics, Vol. 56, Issue 6, pp. 2015–2022, June 2009.
[13] Superti-Furga, G.; Todeschini, G., "Discussion on instantaneous p–q strategies for control of active filters," IEEE Trans. on Power Electronics, Vol. 23, Issue 4, pp. 1945–1955, July 2008.
[14] Salmerón P. y Litrán S. P., "A Control Strategy for Hybrid Power Filter to Compensate Four-Wires Three_Phase Systems," IEEE Transaction on Power Electronics. Vol. 25, Isue 7, pp. 1923–1931, July 2010.
[15] Depenbrock M., "Quantities of a multiterminal circuit determined on the basis of Kirchhoff's laws," in Proc. 4th Int. Workshop Power Definitions Measurements Under Non-Sinusoidal Conditions, Italy, pp. 29–35, 1997.
[16] Salvador P. Litrán, Patricio Salmerón, Alejandro Pérez Vallés, "Control strategy to improve the power factor with a hybrid filter," International Conference on Renewable Energies and Power Quality (ICREPQ'13), March 2013.

EBSCOhost - printed on 2/14/2023 2:46 PM via . All use subject to https://www.ebsco.com/terms-of-use

[17] Salvador P. Litrán, Patricio Salmerón, “Reference Voltage Optimization of a Hybrid Filter for Nonlinear Load Compensation,” IEEE Transactions on Industrial Electronics, Vol. 61, Issue 6, pp. 2648–2654, June 2014.
[18] Yu Wang, Yun-Xiang Xie, Xiang Liu, “Analysis and Design of DC-link Voltage Controller in Shunt Active Power Filter,” Journal of Power Electronics, Vol. 15(3), pp. 763–774, May 2015.
[19] C.-S. Lam, W.-H. Choi, M.-C. Wong, and Y.-D. Han, “Adaptive dc-link voltage controlled hybrid active power filters for reactive power compensation,” IEEE Trans. Power Electron., vol. 27, no. 4, pp. 1758–1772, Apr. 2012.
[20] Muhammad H. Rashid, “Power electronics handbook,” 4th edition, Elsevier, 2018.

EBSCOhost - printed on 2/14/2023 2:46 PM via . All use subject to https://www.ebsco.com/terms-of-use

# CHAPTER THIRTY-FIVE

# AN OPTIMAL LOCATION ALGORITHM FOR ESTIMATING THE INJECTION OF HARMONIC SOURCES IN ELECTRICAL NETWORKS

LUIS F. BEITES[1], MANUEL ALVAREZ[2], AGUSTÍN DÍAZ GARCÍA[3]

## Abstract

Today, the presence of disturbing loads in low, medium, and high voltage networks is increasing harmonics and imbalances in transmission levels. Economic reasons make the installation of harmonic measurement devices in all the buses of a system difficult. To remedy this, it should be possible to install harmonic measurement equipment in a selected fraction of the buses of a network and an estimation of harmonic current injection can be made by using this selection.

In this chapter, a method to estimate the best buses at which to install harmonic voltage measurement equipment is presented. Based on the configuration of the network supplied by the TSO (by means of its impedance matrix), this method allows us to determine which are the best buses to use.

The method is currently being implemented for the Spanish TSO Red Eléctrica de España (REE), so that the presence of harmonics and imbalances in the Spanish transmission network can be monitored. Using

[1] Department of Electrical Engineering; E.T.S.I.I ; Universidad Politécnica de Madrid, José Gutierrez Abascal, 2 28006 Madrid (Spain); Phone number:+0034 913363178, e-mail: luis.fbeites@upm.es

[2] Department of mathematics; E.T.S.I.I; Universidad Politécnica de Madrid, José Gutierrez Abascal, 2 28006 Madrid (Spain); malvarez@etsii.upm.es

[3] Red Eléctrica de España, REE; Paseo del Conde de los Gaitanes 177, 28109 Alcobendas (Madrid); agustin.diaz@ree.es

EBSCOhost - printed on 2/14/2023 2:46 PM via . All use subject to https://www.ebsco.com/terms-of-use

actual equipment allows us to determine the best buses for future installation of harmonic measuring devices on transmission networks. This project is being undertaken by the electrical and mathematics departments of UPM as part of an investigatory project (GENINF) with REE funding.

**Keywords:** Harmonic distortion; harmonic source location; multiple harmonic sources; power quality.

## Introduction

Traditionally, harmonic sources examined in studies of transmission networks are those that are directly connected to the network. Alternatively, they are large power loads in distribution networks very close to the transmission network. This scenario is changing with the growing presence of a large number of low power distorting loads and with the presence of distorting generators in distribution networks.

The injection of harmonics and imbalances into transmission networks has therefore become more dispersed, and, as such, a greater number of buses in such a transmission network have become possible sources of harmonic currents. Transmission system operators (TSOs) aim to keep these buses under surveillance, in order to monitor compliance with emission limits and ensure a good standard of power quality in their networks. As such, it is important for power companies that they can identify those network buses that are sources of distorted currents.

The optimal solution to this problem would be to install appropriate measuring equipment at all suspicious buses. However, this is unfeasible from an economic point of view [1]. When measurements are taken at a large proportion of the buses of a network, state estimation techniques can then be used to identify harmonic sources [2]. However, this is not practical in a real power system, due to the huge number of buses. Only partial measurements are usually made—some of them at buses where no current source is present. In a previous paper [3], neural network methods were suggested as a means of identifying and evaluating harmonic current sources.

In the case of some TSOs, the number of measuring devices is very small when compared to the total number of network buses, resulting in a very underdetermined system. Additionally, in most cases only voltage harmonics are measured, with the measurement of currents being limited to points of connection of large loads.

The estimation of harmonic sources in a power network must necessarily be made with a limited number of measurements taken on specific buses

EBSCOhost - printed on 2/14/2023 2:46 PM via . All use subject to https://www.ebsco.com/terms-of-use

and lines in a network. In addition, measurement errors add to the limitations placed on the number of measurements that can made; this all makes harmonic detection highly problematic. An early study that aims to resolve this problem can be found in [2], which, imitating the procedure used in fundamental state estimation, proposes the use of a least squares technique. This procedure is systematized in [1].

Due to the limited number of measuring devices used, the question of where to place the sensors to obtain the best possible detection, taking into account that it is possible to restrict the number of buses that are suspected of being a source of harmonics, remains. To deal with this problem, a number of variants of the least squares technique have been proposed, [4] [5]. In [6], the problem was solved by using a combinatorial optimization procedure, but this technique seems computationally expensive for implementation in an actual network with a large number of nodes.

## Problem and Solution

The proposed solution involves the optimal selection of nodes in a network for the measurement of voltage, in order to estimate the harmonic currents injected into a subset of the buses on the network. The following paragraphs provide a mathematical formulation of this.

The model consists of a network of $n$ buses. In it, a subset of $q < n$ buses are the nodes where the injection of harmonic currents may exist (for example, buses in which a non-linear load is directly connected, or buses connected to an industrial load). In the rest of the nodes the injection of harmonic currents is considered to be zero.

As is well known, the relationship between nodal voltages and currents takes the form $\mathbf{V} = \mathbf{ZI}$, where $\mathbf{Z}$ is the sub-matrix of the impedance matrix of dimension $q \times n$ with columns corresponding to nodes in which there are harmonic current sources.

If there are $p < n$ harmonic voltage meters installed, it is possible to select from $\mathbf{Z}$ and $\mathbf{V}$ those rows corresponding to the measured voltages. Through this, a system of $p$ equations with $q$ unknowns is obtained, taking the form:

$$\mathbf{Z}_m \ \mathbf{I} = \mathbf{V}_m$$

In this equation, $\boldsymbol{Z_m}$ and $\boldsymbol{V_m}$ are the corresponding submatrices of $\mathbf{Z}$ and $\mathbf{V}$, with dimensions $p \times q$ and $p \times 1$. If $p < q$, i.e. there are fewer meters than suspicious buses, this system of equations is indeterminate, admitting multiple solutions.

EBSCOhost - printed on 2/14/2023 2:46 PM via . All use subject to https://www.ebsco.com/terms-of-use

One possible way to estimate the currents injected into the nodes is by solution of the minimum norm, which (on the assumption that the rank of the matrix $\mathbf{Z_m}$ matches the number of rows $p$) is given by the expression:

$$\mathbf{I}_{est} = \mathbf{Z}_m^{'}[\mathbf{Z}_m\mathbf{Z}_m^{'}]^{-1}\mathbf{V}_m$$

The general solution of this equation can be represented in the form:

$$\mathbf{I} = \mathbf{I}_{est} + \mathbf{Nh}$$

where $\mathbf{h}$ is a vector of ($q$-$p$) freely varying parameters and $\mathbf{N}$ is a matrix of dimensions $q \times (q-p)$ and full rank ($q$-$p$). This complies with:

$$\mathbf{Z}_m\mathbf{N} = \mathbf{O}$$

where $\mathbf{O}$ is the null matrix of dimensions $p \times (q-p)$. Eventually, in large networks, some of the rows of matrix $\mathbf{N}$ are all zero elements, which means that the corresponding currents are determined uniquely by the topology of the network. These rows are characterized by the index of the rows of a submatrix $\mathbf{U}$ of the identity matrix of order $q$, such that:

$$\mathbf{UN} = \mathbf{O}$$

Equivalently, those rows are determined because they are necessarily linear combinations of the rows of the matrix $\mathbf{Z}_m$.

A subset of nodes that may be of interest in detecting the existence of harmonic injections can be chosen. Once these nodes have been predetermined, the optimum selection of the voltages to be measured can be stated as finding the rows of the matrix $\mathbf{Z}$ that best approximate as a whole to the rows of the corresponding matrix $\mathbf{U}$.

As $\mathbf{S}$ is a submatrix of the identity matrix of order $n$, which selects $p$ rows of the impedance matrix $\mathbf{Z}$, the best approach, in the Frobenius norm of the matrix $\mathbf{U}$, is given by linear combinations of the rows of the $\mathbf{SZ}$ matrix, expressed as:

$$\mathbf{U}_S = \mathbf{U}[\mathbf{Z}'\mathbf{S}'\mathbf{S}\mathbf{Z}]^{-1}\mathbf{Z}'\mathbf{S}'$$

where $\mathbf{S}'$ and $\mathbf{Z}'$ are the transpose and conjugate transpose matrices of matrices $\mathbf{S}$ and $\mathbf{Z}$, respectively. Ideally, the optimum solution involves determining a matrix $\mathbf{S}$ that solves the following minimization problem:

$$\min_S(\text{trace}[\mathbf{U}'\mathbf{U}_S])$$

Obviously, this problem has a combinatorial complication that makes it intractable. However, it is possible to obtain a suboptimal solution by extending the procedures known as matching pursuit to the matrix case. It is possible to iteratively determine the subsystem with a determined number of vectors extracted from a predetermined set of vectors, which comes

EBSCOhost - printed on 2/14/2023 2:46 PM via . All use subject to https://www.ebsco.com/terms-of-use

closest, linearly, to a given vector. In the following, these methods are reviewed and extended.

## Greedy Subset Selection Algorithms

These algorithms are applied to a fixed set $\{\mathbf{a}_1,\ldots,\mathbf{a}_\nu\}$ of vectors in $\mathbf{C}^n$ that, for convenience, are assumed to have a unit norm. Given $p<n$ and vector $\mathbf{b}$, the solution is to select $p$ vectors in the above set so that the orthogonal projection $\hat{\mathbf{b}}$ of the vector $\mathbf{b}$ on the subspace generated by these vectors gives the best approximation of vector **b**, in the sense that the Euclidean norm $\left\|\mathbf{b}-\hat{\mathbf{b}}\right\|$ will be the minimum.

To determine the optimal solution, $\binom{\nu}{p}$ possible subsets would have to be checked and this computation quickly becomes unfeasible as the size of $\nu$ and $p$ increase. Therefore, several suboptimal methods of reasonable complexity have been developed. In the greedy algorithms, also known as forward selection, the subset is arranged sequentially, building and incorporating one vector in each iteration. The idea is to start by finding the vector $\mathbf{a}_i$ closest to $\mathbf{b}$ and then adding vectors one by one until $p$ vectors have been selected, adding the vector that gives the largest decrement of the least squares residual each time.

So-called orthogonal matching pursuit is briefly described here. The index of the first selected vector is obtained by:

$$i_1 = \operatorname{argmax}_{1\le i\le \nu} \left|\mathbf{a}_i^{'}\mathbf{b}\right|$$

Having selected the first $k$ vectors $\mathbf{a}_{i_1},\ldots,\mathbf{a}_{i_k}$, the subspace linearly generated by these vectors is the range subspace of the matrix:

$$\mathbf{A}_k = \left[\mathbf{a}_{i_1}\cdots\mathbf{a}_{i_k}\right]$$

whose columns are these vectors. The orthogonal projection of the vector $\mathbf{b}$ on this subspace is given by:

$$\hat{\mathbf{b}}_k = \mathbf{A}_k\left(\mathbf{A}_{k'}\mathbf{A}_k\right)^{-1}\mathbf{A}_k\mathbf{b}$$

and the corresponding orthogonal residual is the vector $\mathbf{b}_k^{\perp} = \mathbf{b}-\hat{\mathbf{b}}_k$. Having obtained this vector, the index of the next vector is given by:

$$i_{k+1} = \operatorname{argmax}_{i\in J_k} \left|\mathbf{a}_i^{'}\mathbf{b}_k^{\perp}\right|$$

EBSCOhost - printed on 2/14/2023 2:46 PM via . All use subject to https://www.ebsco.com/terms-of-use

where $J_k$ is the set of indexes of the $\nu - k$ remaining vectors after exclusion of the initial set of $k$ selected vectors.

The above procedure can be extended step by step to the subset selection for several vectors. If we let these vectors be the columns of the matrix, then:

$$\mathbf{B} = \begin{bmatrix} \mathbf{b}_1 & \cdots & \mathbf{b}_m \end{bmatrix}$$

and, as before, considering for each subset of $p$ vectors, the matrix:

$$\hat{\mathbf{B}} = \begin{bmatrix} \hat{\mathbf{b}}_1 & \cdots & \hat{\mathbf{b}}_m \end{bmatrix}$$

whose columns are the orthogonal projections of the columns of $\mathbf{B}$ on the subspace linearly generated by the vectors of this subset.

From here we can obtain the subset such that the Frobenius norm of the matrix difference $\mathbf{B} - \hat{\mathbf{B}}$ is:

$$\left\| \mathbf{B} - \hat{\mathbf{B}} \right\|_F^2 = \operatorname{trace}\left( \mathbf{B} - \hat{\mathbf{B}} \right)' \left( \mathbf{B} - \hat{\mathbf{B}} \right) = \left\| \mathbf{B} \right\|_F^2 - \left\| \hat{\mathbf{B}} \right\|_F^2$$

which will be minimal. In the $k$ iteration, the matrix:

$$\mathbf{B}_k^{\perp} := \mathbf{B} - \mathbf{A}_k \left( \mathbf{A}_{k'} \mathbf{A}_k \right)^{-1} \mathbf{A}_k \mathbf{B}$$

is obtained and the index of the next vector is be given by:

$$i_{k+1} = \operatorname{argmax}_{i \in J_k} \left\| \mathbf{a}_i' \mathbf{B}_k^{\perp} \right\|_1$$

## Backward Subset Selection Algorithms

All the forward selection algorithms have a limitation. If a vector is selected in one iteration, it remains forever in the selected set. Then, if, for example, the first vector is erroneously selected, it is clear that the correct set of vectors cannot be selected. For this reason, sequential backward elimination algorithms have been proposed for the subset selection problem as an alternative to forward selection. The idea is to start with all vectors present and remove one vector each time until only $p$ vectors remain.

As before, a set $\{\mathbf{a}_1, \ldots, \mathbf{a}_\nu\}$ of $\nu$ vectors in $\mathbf{C}^n$ is supposed to exist, but to simplify the exposition, we also suppose that they are linearly independent, for which $\nu \leq n$. By considering the matrix:

$$\mathbf{A} = \begin{bmatrix} \mathbf{a}_1 & \cdots & \mathbf{a}_\nu \end{bmatrix}$$

the best approximation of the vector $\mathbf{b}$ using all the columns of this matrix is given by:

EBSCOhost - printed on 2/14/2023 2:46 PM via . All use subject to https://www.ebsco.com/terms-of-use

$$\hat{\mathbf{b}} = \mathbf{A}\left[\mathbf{A}'\mathbf{A}\right]^{-1}\mathbf{A}'\mathbf{b}$$

To describe the first step of the elimination process, we consider the matrices:

$$\mathbf{A}_k = \left[\mathbf{a}_1 \ \cdots \ \mathbf{a}_{k-1} \ \mathbf{a}_{k+1} \ \cdots \ \mathbf{a}_\nu\right], \qquad k = 1,\ldots,\nu$$

Each matrix is obtained by elimination of the $k$ column in $\mathbf{A}$. For each of these matrices the best approximation is given by:

$$\hat{\mathbf{b}}_k = \mathbf{A}_k\left[\mathbf{A}_k'\mathbf{A}_k\right]^{-1}\mathbf{A}_k'\mathbf{b}$$

Clearly, for all $k$ we have:

$$\left\|\hat{\mathbf{b}}\right\| - \left\|\hat{\mathbf{b}}_k\right\| \geq 0$$

Then the column that gives the least of these differences is eliminated from the matrix $\mathbf{A}$.

This elimination procedure is repeated until only $p$ vectors remain.

The complexity of this algorithm is greater than the complexity of the forward algorithm, but frequently the subset selected is better. Using the results obtained in [8], the computational burden can be reduced with the following considerations. In introducing the matrix:

$$\mathbf{G} = \left[\mathbf{A}'\mathbf{A}\right]^{-1}$$

let $\gamma_k$ be the $k$ element of the diagonal of $\mathbf{G}$ ($\gamma_k = \mathbf{G}(k,k)$) and $\mathbf{g}_k$ the $n-1$ vector of $\mathbf{G}$ obtained after removing the $k$ component in the $k$ column of $\mathbf{G}$. It can be proved that by defining the vector:

$$\mathbf{h}_k = \mathbf{A}_k\mathbf{g}_k + \gamma_k\mathbf{a}_k$$

the following relation appears:

$$\left\|\hat{\mathbf{b}}\right\|^2 - \left\|\hat{\mathbf{b}}_k\right\|^2 = \frac{1}{\gamma_k}\left|\mathbf{h}_k'\mathbf{a}_k\right|^2$$

Hence, to minimize the difference $\left\|\hat{\mathbf{b}}\right\| - \left\|\hat{\mathbf{b}}_k\right\|$ it is only necessary to search for:

$$\text{argmin}_h \ \frac{1}{\gamma_k}\left|\mathbf{h}_k'\mathbf{a}_k\right|^2$$

The initial matrix $\mathbf{G}$ can be efficiently obtained from a $qr$ factorization of the matrix $\mathbf{A}$. In the remaining steps, it is possible to use a recursive formula to reflect the removal of columns. If $\mathbf{G}_k$ is the matrix resulting

EBSCOhost - printed on 2/14/2023 2:46 PM via . All use subject to https://www.ebsco.com/terms-of-use

from the elimination of the $k$ row and column of matrix $\mathbf{G}$ , the following equation applies:

$$\left[\mathbf{A}_k^{'}\mathbf{A}_k\right]^{-1} = \mathbf{G}_k - \frac{1}{h_k}\mathbf{g}_k\mathbf{g}_k^{'}$$

This forward selection algorithm can be extended to subset selection for several vectors. The only difference is that in this case, the relations used to determine the column to be removed are:

$$\left\|\mathbf{B}\right\|_F^2 - \left\|\mathbf{B}\right\|_F^2 = \frac{1}{\gamma_k}\left\|\mathbf{h}^{'}_k\mathbf{A}_k\right\|^2$$

## Application to Node Selection in Electrical Networks

The proposed algorithm has been applied to a network of the Spanish TSO REE. The original data described the network for a determined demand situation in the Spanish power system, including data on the different traditional loads connected to the network nodes. Those nodes with nominal voltages of 220 and 400 kV were selected, together with their lines and transformers. With this data, the admittance matrix of the network for each harmonic was calculated by means of a harmonic power flow program, INTAR, commissioned by the Electrical Department of the Polytechnic University of Madrid by REE within the framework of previous R&D projects. The following results were obtained for the 5$^{th}$ harmonic; but this method can be applied to any harmonic.

The network has n = 846 nodes in total. A superficial analysis of the possible loads led to the conclusion that there exists q = 347 nodes where the injection of harmonics will eventually appear (buses connected directly to loads or to distribution networks).

EBSCOhost - printed on 2/14/2023 2:46 PM via . All use subject to https://www.ebsco.com/terms-of-use

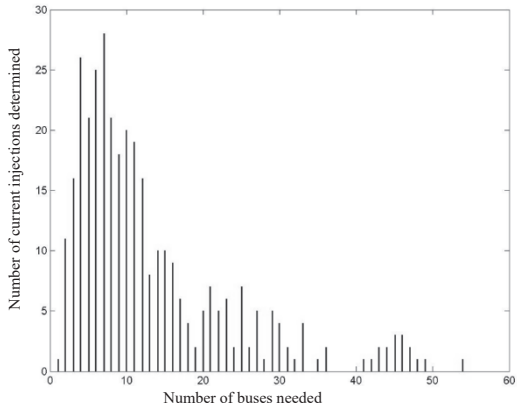



Figure 1: Distribution of voltage measurements needed to estimate a current source.

In a primary analysis of the network, for each of these nodes, and by using the forward greedy algorithm for only one vector, it was possible to obtain the corresponding minimal subset of the nodes where the measurement of voltages allowed the exact determination of the harmonic injection in the node (i.e., buses where harmonic voltage measuring equipment should be present). The histogram in figure 1 gives the distribution of the different number of voltages measured for each injection node.

By combining all the nodes obtained, it was found that there were 590 nodes where the measurement of the voltage was needed to determine the possible injection of harmonics at all of the 347 suspect nodes. It is obvious that the installation of such a large amount of equipment is not an option.

An intermediate option is to choose the buses in which the installation of harmonic voltage measurement devices allows for better estimation of harmonic injection sources. To do this, and to develop some results, a subset of 40 nodes of higher interest were selected from among the 347 suspect nodes. To determine the suboptimal selection of buses for placement of voltage sensors to characterize these nodes, a mixed forward-backward subset selection algorithm was employed. First, an exhaustive greedy forward search was implemented to decide on a set of nodes where the measurement of voltage would determine harmonic injection in the selected nodes. Then a backward iterative process was initiated, where nodes were selected one by one for removal–at each step the least squares errors increments in the numerical solutions were minimized–until the specified number of voltage sensors was obtained.

EBSCOhost - printed on 2/14/2023 2:46 PM via . All use subject to https://www.ebsco.com/terms-of-use

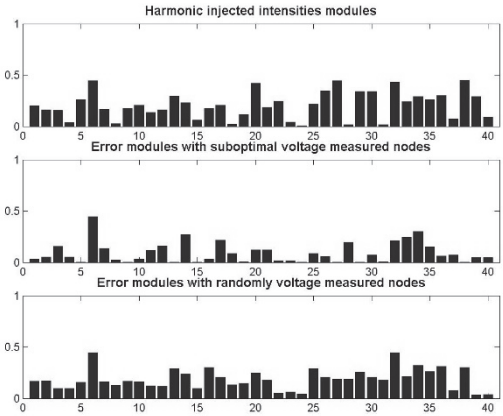



Figure 2: Errors in the determination of harmonic current injection (50 voltage measurements).

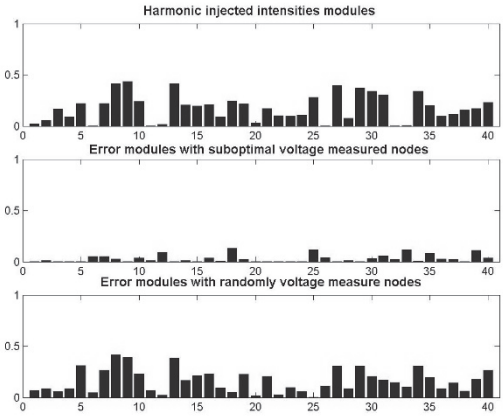



Figure 3: Errors in the determination of harmonic current injection (100 voltage measurements).

In order to validate the results, a simulation of the injection of current sources on an arbitrary selection of buses was made. With these known harmonic currents, a model of harmonic current penetration was developed, and the resultant voltages were calculated. A subset of these harmonic

EBSCOhost - printed on 2/14/2023 2:46 PM via . All use subject to https://www.ebsco.com/terms-of-use

voltages was selected as measurements to inform the estimate. Finally, the estimated current injection values were compared with the actual ones.

The proposed algorithm was implemented in a MATLAB program. Numerical simulations were performed with this program and results are shown for 40 nodes, which were selected at random from the 347 potential sources.

The 5$^{th}$ harmonic injections were done for the 347 potential sources, with random modules of a mean value of 0.2 pu and a variation of 0.5; the phases were also selected randomly. In Figs. 2 and 3, typical results are shown for the 40 selected buses. In both figures, the first graph shows the presence of the 5$^{th}$ harmonic current. The second graph shows the error (differences in absolute values of the obtained modules in pu) between the actual current injection and the estimated ones, when the installation of 50 (Fig. 2) or 100 (Fig. 3) voltage measurement devices was chosen with the proposed suboptimal method. In the third graph of each figure, for comparison, the error when the selection of buses to install the voltage measurement devices was randomly made is shown. It is easy to see that the use of 100 voltage sensors improves the results, particularly when the suboptimal method is used. A random selection masks the advantage of an increased number of devices.

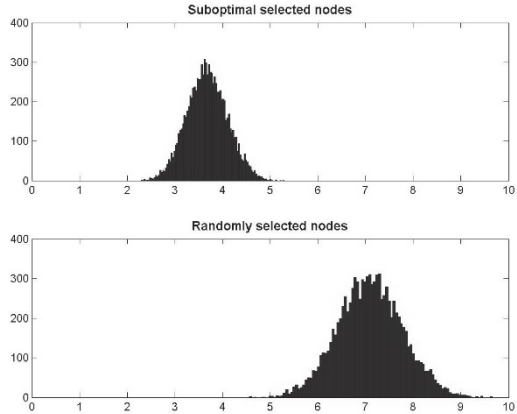



Figure 4: Histograms of the results for 10,000 executions of the algorithm with 50 measurements.

EBSCOhost - printed on 2/14/2023 2:46 PM via . All use subject to https://www.ebsco.com/terms-of-use

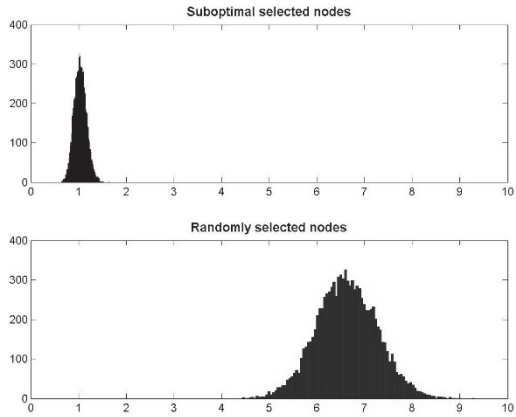



Figure 5: Histograms of the results for 10,000 executions of the algorithm with 100 measurements.

Figs. 2 and 3 show a particular case. The values of the harmonic currents injected are dependent on the load and show a certain amount of random variation. In order to establish the validity of the method, a new simulation was made. Figs. 4 and 5 show the results of a large number of executions with random values for the current injection sources. In all cases, the buses where the current injection existed were the same. The measurement buses were determined only once, in a random way (third graph of each figure), or by means of the suboptimal method described (second graph of each figure). The global errors of the estimated harmonic injection in each of the 40 buses are shown for 50 and 100 voltage measurement devices. These are expressed as the addition of the absolute difference between the estimated and actual values in each of the 40 buses.

## Conclusion

This chapter presents a variation of the problem of choosing the best buses on which to install harmonic voltage measurement devices in a power network. Due to the optimal selection problem, an extension to matrix cases of standard greedy forward-backward algorithms as a basis for subset selection is presented. This method can be applied to real networks, as the obtained results for an actual transmission grid illustrate.

In any network, even when the necessity of a substantial number of measurement systems cannot be avoid, a sub-optimal selection of the buses

EBSCOhost - printed on 2/14/2023 2:46 PM via . All use subject to https://www.ebsco.com/terms-of-use

where installation should be made can reduce the number of devices required.

## Acknowledgement

This investigation is part of the GENINF R&D project funded by REE.

## References

[1] Z.-P. Du, J. Arrillaga and N. Watson, "Continuous harmonic state estimation of power systems," in *Generation, Transmission and Distribution, IEE Proceedings*, 1996.

[2] G. Heydt, "Identification of harmonic sources by a state estimation technique," *Power Delivery, IEEE Transactions on,* vol. 4, no. 1, pp. 569-576, 1989.

[3] R. Hartana and G. Richards, "Harmonic source monitoring and identification using neural networks," *Power Systems, IEEE Transactions on,* vol. 5, no. 4, pp. 1098-1104, 1990.

[4] J. Farach, W. Grady and A. Arapostathis, "An optimal procedure for placing sensors and estimating the locations of harmonic sources in power systems," *Power Delivery, IEEE Transactions on,* vol. 8, no. 3, pp. 1303-1310, 1993.

[5] C. Madtharad, S. Premrudeepreechacharn, N. R. Watson and R. Saeng-Udom, "An optimal measurement placement method for power system harmonic state estimation," *Power Delivery, IEEE Transactions on,* vol. 20, no. 2, pp. 1514-1521, 2005.

[6] C. Almeida and N. Kagan, "Harmonic state estimation through optimal monitoring systems," *Smart Grid, IEEE Transactions on,* vol. 4, no. 1, pp. 467-478, 2013.

[7] J. A. Tropp, "Greed is good: Algorithmic results for sparse approximation," *Information Theory, IEEE Transactions on,* vol. 50, no. 10, pp. 2231-2242, 2004.

[8] S. Reeves, "An efficient implementation of the backward greedy algorithm for sparse signal reconstruction". *IEEE Signal Processing Letters*, vol. 6, pp. 266-268, Oct. 1999

[9] D. Ferreyra, C. Sarmiento and C. Reineri, "Harmonic State Estimation on a Radial Distribution System with Distributed Generation," *Latin America Transactions, IEEE (Revista IEEE America Latina),* vol. 11, no. 1, pp. 499-504, 2013.

[10] M. Farhoodnea, A. Mohamed and H. Shareef, "A new method for determining multiple harmonic source locations in a power distribution

EBSCOhost - printed on 2/14/2023 2:46 PM via . All use subject to https://www.ebsco.com/terms-of-use

system," in *Power and Energy (PECon), 2010 IEEE International Conference on*, 2010.

[11] A. R. Abbasi and A. R. Seifi, "A new coordinated approach to state estimation in integrated power systems," *International Journal of Electrical Power \& Energy Systems,* vol. 45, no. 1, pp. 152-158, 2013.

[12] A. S. Meliopoulos, F. Zhang and S. Zelingher, "Power system harmonic state estimation," *Power Delivery, IEEE Transactions on,* vol. 9, no. 3, pp. 1701-1709, 1994.

EBSCOhost - printed on 2/14/2023 2:46 PM via . All use subject to https://www.ebsco.com/terms-of-use

# CHAPTER THIRTY-SIX

# HARMONIC MODELLING OF ELECTRIC VEHICLE CHARGERS IN THE FREQUENCY DOMAIN

SASCHA MÜLLER, JAN MEYER,
PETER SCHEGNER[1], SASA DJOKIC[2]

## Abstract

In the near future, fully electric cars will be increasingly used in many countries. These are commonly known as electric vehicles (EVs) and typically have on-board power supplies with electronic-based rectifiers for charging their batteries, which may have a significant impact on power quality when using low voltage (LV) and medium voltage (MV) distribution grids. The harmonic emissions of EV chargers (EVCs), which are strongly influenced by distortion of the grid supply voltage, are an important aspect of their large-scale deployment.

This paper presents the results of testing and analysis of the harmonic current emissions of 16 different EVCs, particularly in respect to supply voltage distortion. The analysis is based on extensive measurements performed at a test stand. In order to characterize and classify the voltage dependency of the harmonic emissions, a set of indices was introduced. Furthermore, two different frequency-domain models were developed for each of the EVCs and compared with each other in terms of their harmonic magnitude and phase angle accuracy. Based on the indices, a classification

[1] S. Müller, J. Meyer and P. Schegner are with Technische Universitaet Dresden, Institute of Electrical Power Systems and High Voltage Engineering, Dresden, Germany.
[2] S. Djokic is with the University of Edinburgh, School of Engineering, Edinburgh, Scotland, UK.

EBSCOhost - printed on 2/14/2023 2:46 PM via . All use subject to https://www.ebsco.com/terms-of-use

of the EVCs with respect to their harmonic performance into three groups is proposed.

**Keywords:** Electric vehicles; harmonic analysis; load modelling.

## Introduction

The number of electric vehicles (EVs) in Germany is expected to increase significantly over the next decade due to the anticipated electrification of the road transportation sector. The EV batteries in these vehicles are charged by direct current (DC), which is provided by an on-board controlled rectifier. Due to its topology and control, the electronic circuits of the rectifier will typically cause a distortion of the input AC charging current, which in turn can cause distortion of the grid supply voltage.

To evaluate the impact of the increasing penetration of EVs, appropriate models have to be developed using network simulation software, [1]-[3]. One of the most significant factors that impacts on the harmonic emissions of EVCs is distortion of the grid supply voltage, also known as “background distortion” [4]. In order to develop comprehensive and accurate frequency domain models, the dependency of the harmonic emissions on different supply voltage distortions has to be analysed for a representative set of EVCs.

Another important aspect regarding network simulations is the computational effort required, which increases with the complexity of models. Therefore, the models should preferably be as simple as possible, while still having a good level of accuracy. However, the network studies performed so far have neglected the issue of voltage dependency—we consider this to be a serious omission [5], [6].

This contribution starts with a short review of different modelling approaches and the introduction of two commonly used frequency-domain models, which are then applied. The next section deals with the measurement framework used for detailed characterisation of the 16 tested EVCs. A substantial part of this characterisation involves the introduction of a set of indices to describe the harmonic current emission behaviour of the EVCs. Based on this set of indices, a classification is proposed and the EVCs are divided into three different groups. Finally, both the indices and the accuracy of the models are compared.

EBSCOhost - printed on 2/14/2023 2:46 PM via . All use subject to https://www.ebsco.com/terms-of-use

## Harmonic Emission Models

There are two general modelling methodologies for harmonic studies: the circuit-based approach in the time-domain ("white box" modelling) and the measurement-based approach in the frequency-domain ("black box" modelling). While the circuit-based approach generally requires detailed knowledge of the circuit topology and the control algorithm of the electrical equipment, the measurement-based approach derives the relevant characteristics of the modelled device by matching the parameters of an assumed or postulated model with the measured data [7].

Time-domain models are often developed as circuit-based or component-based models—they allow the establishment of a correlation with the physical characteristics and structure of the modelled equipment [8]. As they can reproduce the instantaneous current waveform for a given supply voltage waveform, they are very flexible to use. They are often used for analysis of connected non-linear loads. Due to their detailed representation of the actual circuits of modelled equipment, time-domain models can be applied without significant changes, or any additional model derivation, to represent relevant load characteristics for different system and load operating conditions. Typically, the results of harmonic analysis with time-domain models are obtained by applying the fast Fourier transform (FFT) on the instantaneous waveforms obtained from the time-domain simulation.

Frequency-domain models, based on measurements, are commonly used to model non-linear loads without knowledge of their exact circuit topology and control algorithms. Depending on the characteristics of the harmonic emissions, different modelling approaches can be applied. However, they are all based on an approximation around a specific operating point. This operating point is defined by the device itself (e.g. operating status, or operating power) and by the network state at the point of connection, which in turn is mainly characterized by the supply voltage and its distortion. The different modelling approaches differ from each other in terms of their degree of approximation. In general, the approximation is performed by applying Taylor's theorem at the operating point. Different levels of accuracy can be achieved by considering different orders of the Taylor polynomial. In the special case where the Taylor polynomial is of the order 1, the resulting function is linear and the approximation is referred to as linearization.

The simplest approach is to use a Taylor polynomial of order 0, which means that the harmonic currents are represented by constant current sources [5]. These are usually parameterised by using the harmonic currents

EBSCOhost - printed on 2/14/2023 2:46 PM via . All use subject to https://www.ebsco.com/terms-of-use

at a pure sinusoidal (i.e., non-distorted) supply voltage. As such, any dependency on the harmonic voltage distortion is neglected. However, for most power electronic devices, including EVCs, harmonic current emissions depend strongly on the distortion of the voltage waveform and, therefore, a constant current source model does not provide accurate results. For this reason, the constant current source model is not considered further here.

In order to account for the voltage dependency, a model based on at least a Taylor polynomial of order 1 is needed, which corresponds to classic linearization. There are several modelling approaches that can be put into this category. Two of them are considered here: the uncoupled and the coupled Norton models.

The uncoupled Norton model extends the constant current source model by adding a passive linear circuit, which is usually represented by a parallel connected admittance. This allows the taking into account of the effect of harmonic voltages on harmonic currents of the same order. In the following equations, the harmonic currents and voltages are expressed as vectors and referred to as $\underline{\boldsymbol{i}}$ and $\underline{\boldsymbol{v}}$. The constant current source is represented by the reference current $\underline{\boldsymbol{i}}_{\mathrm{ref}}$, which is the current at the base/reference operating point and for the sinusoidal supply voltage. If the passive linear circuit is expressed by the admittance vector $\underline{\boldsymbol{y}}$, the uncoupled Norton model takes the form:

$$\underline{\boldsymbol{i}} = \underline{\boldsymbol{i}}_{\mathrm{ref}} + \underline{\boldsymbol{y}} \cdot \underline{\boldsymbol{v}} \tag{1}$$

As such, dependencies between harmonic voltages and currents of different orders ("harmonic couplings") are not included in this model.

In order to account for the impact of harmonic couplings, the original uncoupled Norton model is extended to become a coupled Norton model [9], [10]. It then comprises a frequency coupling matrix, which means that one harmonic current can be affected by all harmonic voltages. The frequency coupling matrix $\underline{\boldsymbol{Y}}$ is also referred to as the harmonic admittance matrix (HAM), as its elements have the dimensions of an admittance. Therefore, the coupled Norton model can be written as:

$$\underline{\boldsymbol{i}} = \underline{\boldsymbol{i}}_{\mathrm{ref}} + \underline{\boldsymbol{Y}} \cdot \underline{\boldsymbol{v}} \tag{2}$$

The HAM has the form

EBSCOhost - printed on 2/14/2023 2:46 PM via . All use subject to https://www.ebsco.com/terms-of-use

$$\underline{\boldsymbol{Y}} = \begin{bmatrix} \underline{Y}^{(11)} & \underline{Y}^{(12)} & \dots & \underline{Y}^{(1\mathrm{N})} \\ \underline{Y}^{(21)} & \underline{Y}^{(22)} & \dots & \underline{Y}^{(2\mathrm{N})} \\ \vdots & \vdots & \ddots & \vdots \\ \underline{Y}^{(\mathrm{M1})} & \underline{Y}^{(\mathrm{M2})} & \dots & \underline{Y}^{(\mathrm{MN})} \end{bmatrix} \tag{3}$$

where $k = 1, 2, \dots, M$ and $l = 1, 2, \dots, N$ being the orders of the harmonic current and the harmonic voltage, respectively. In the following, the HAM is also used for the uncoupled Norton model, but in this case it is a diagonal matrix with all non-diagonal elements being zero. Furthermore, the uncoupled Norton model is denoted as "M1" and the coupled Norton model as "M2". If an equation applies to both models, the general notation "Mx" with $x \in \{1, 2\}$ is used. Based on comprehensive measurements under laboratory test conditions, both models were applied and compared for a set of 16 different EVCs.

## Measurement Framework

The measurements were carried out using a test bed that comprises a three-phase grid simulator. Voltage magnitude and voltage distortion levels of a simulated low voltage (LV) grid can be set in a flexible and automatic way via a control computer (PC). More details about the test bed can be found in [11]. The measurement of voltage and current harmonics is based on the acquisition of 10-cycle waveforms and the subsequent calculation of harmonic magnitudes and phase angles according to IEC 61000-4-7. At each testing point, a trigger signal was generated by the PC, which then opened a new data file. This allowed for a simple match between the predefined testing points and the measurement data files.

In order to characterise the harmonic emissions of an EV charger, measurements with varying supply voltage distortion were carried out. The measuring program contains more than 3,000 testing points, comprising individual harmonics, as well as combinations of various harmonics that were superimposed on the fundamental supply voltage. Analysis of the impact of individual harmonic voltages on the harmonic current emissions was used for model development. Testing points containing combinations of harmonics were intended for model validation.

Only the odd harmonics of the orders 3 to 19 were considered, because these are the most common and therefore the most important harmonics present in public LV grids. When testing an individual harmonic voltage, its magnitude, as well as its phase angle, was varied in 12 steps for each. This method is referred to as "harmonic fingerprint" analysis [12], [13].

EBSCOhost - printed on 2/14/2023 2:46 PM via . All use subject to https://www.ebsco.com/terms-of-use

## Methodology Used for Analysis

Before the harmonic models could be parameterised, a detailed quantification of the EVC behaviour regarding the voltage dependency of its harmonic emission was required. The basis for this was the harmonic fingerprints, which are needed to derive the elements of the HAM. Their quantification can be divided in two steps:

1. Evaluation of the reference current and sensitivity to voltage distortions.
2. Evaluation of the non-linearity of the current-voltage-dependency.

The first step gives an overview of the harmonic emission behaviour of the tested EVCs. By using a so-called sensitivity index, the impact of a distorted voltage can be quantified. The elements of the HAM that have only very little impact, and are therefore negligible, can be sorted out in order to simplify the HAM and to reduce the computational burden in network simulations. In the second step, the non-linearity of the fingerprints was assessed and quantified by a non-linearity index. The number of elements of the HAM with a high non-linearity acts as an indicator of the accuracy of the frequency-domain model. The combined consideration of both the sensitivity and non-linearity was finally used to propose a classification of the EVCs.

In order to quantify the dependency of the harmonic emissions on the voltage distortion, a sensitivity index $S^{(\mathrm{kl})}$ was introduced:

$$S^{(\mathrm{kl})} = \frac{1}{n}\sum_{i=1}^{n}\left|\frac{\underline{I}_{\mathrm{m}\,i}^{(\mathrm{k})} - \underline{I}_{\mathrm{ref}}^{(\mathrm{k})}}{\underline{V}_{\mathrm{m}\,i}^{(\mathrm{l})} - \underline{V}_{\mathrm{ref}}^{(\mathrm{l})}}\right| \tag{4}$$

This is defined as the average ratio of the change of the harmonic current of order $k$, caused by the change of the harmonic voltage of order $l$. Both current change and voltage change are determined with respect to a reference point (denoted by index $ref$), i.e. an undistorted voltage of nominal magnitude. Averaging was performed for all $n$ phase angles at a certain magnitude (denoted by index $m$) of the tested harmonic voltage. Finally, an index was obtained for each element of the HAM, representing the averaged magnitudes of the admittances.

To compare different EVCs, an aggregate sensitivity index was needed. For this purpose, a distinction was made between the diagonal and non-

EBSCOhost - printed on 2/14/2023 2:46 PM via . All use subject to https://www.ebsco.com/terms-of-use

diagonal elements of the HAM. The root mean square (rms) value of the diagonal elements was used to calculate the "total auto-sensitivity" (TAS):

$$\mathrm{TAS} = \sqrt{\frac{1}{N}\sum_{l=1}^{N}\left(S^{(\mathrm{ll})}\right)^{2}} \tag{5}$$

In order to aggregate the non-diagonal elements, the respective sensitivity indices were related to their corresponding diagonal element. Subsequently, the rms value of these percentage sensitivities was calculated as the "total cross-sensitivity" (TCS):

$$\mathrm{TCS} = \sqrt{\frac{1}{N}\sum_{l=1}^{N}\sum_{k\neq l}^{M}\left(\frac{S^{(\mathrm{kl})}}{S^{(\mathrm{ll})}}\cdot 100\ \%\right)^{2}} \tag{6}$$

As the considered Norton models are based on an average harmonic admittance, they inherently assume a linear relationship between current and voltage. However, as this is often not the case, an index indicating the non-linearity of that relationship is required. The basis for its definition was the fingerprint of the respective harmonic current. The non-linearity index can be interpreted as the rms value of the difference between the measured fingerprint ($\underline{I}_i^{(\mathrm{k})}$) and the linearization of that fingerprint ($\underline{I}_{\mathrm{lin}\,i}^{(\mathrm{k})}$). This linearized fingerprint was determined by finding the minimum of the difference to the original fingerprint by the least squares method. Furthermore, all distances between consecutive points within one branch, as well as all phase angle differences between neighbouring branches, were set as equal in the linearized fingerprint. Finally, the rms value of the difference was related to the rms value of the original fingerprint, which was shifted to the centre. In this way, a percentage value was obtained:

$$L^{(\mathrm{kl})} = \sqrt{\frac{\sum_{i=1}^{n}\left(\left|\underline{I}_i^{(\mathrm{k})} - \underline{I}_{\mathrm{lin}\,i}^{(\mathrm{k})}\right|\right)^{2}}{\sum_{i=1}^{n}\left(\left|\underline{I}_i^{(\mathrm{k})} - \underline{I}_{\mathrm{ref}}^{(\mathrm{k})}\right|\right)^{2}}}\cdot 100\ \% \tag{7}$$

EBSCOhost - printed on 2/14/2023 2:46 PM via . All use subject to https://www.ebsco.com/terms-of-use

After the sensitivity and non-linearity indices had been calculated for all elements of the HAM, the characteristics of the considered EVCs could be compared to each other.

## Characterisation of EVCs and Model Comparison

Table 1 gives an overview of the 16 analysed EVCs and summarises the magnitudes of the fundamental, 3rd, 5th, and 7th harmonic currents at the reference point (undistorted voltage), as well as the respective aggregate sensitivity indices (TAS and TCS).

While the charging current was at around 16 A, or slightly below it, for 11 EVCs, for the other 5 EVCs it was higher, with the maximum at 31 A. Regarding the harmonic currents, the highest magnitudes were for the 3rd harmonic, with values of up to 1.8 A. However, the other harmonics were significantly below 1 A. In general, the harmonic emission at an undistorted supply voltage is relatively low.

With respect to sensitivity to voltage distortion, the EVCs exhibited very different characteristics. While the TAS showed a high variation range with

**Table 1: Reference currents and aggregate sensitivity indices**

| EVC | $\left\lvert I_{\mathrm{ref}}^{(1)}\right\rvert$ /A | $\left\lvert I_{\mathrm{ref}}^{(3)}\right\rvert$ /A | $\left\lvert I_{\mathrm{ref}}^{(5)}\right\rvert$ /A | $\left\lvert I_{\mathrm{ref}}^{(7)}\right\rvert$ /A | TAS/mS | TCS/% |
|---|---|---|---|---|---|---|
| **1** | 15.8 | 1.83 | 0.07 | 0.05 | 77.8 | 17.3 |
| **2** | 14.6 | 0.29 | 0.10 | 0.09 | 87.0 | 21.2 |
| **3** | 14.7 | 0.85 | 0.47 | 0.29 | 80.9 | 20.8 |
| **4** | 31.0 | 0.88 | 0.43 | 0.50 | 107.6 | 17.1 |
| **5** | 13.0 | 0.93 | 0.01 | 0.03 | 65.8 | 10.5 |
| **6** | 15.4 | 0.20 | 0.14 | 0.09 | 225.2 | 23.8 |
| **7** | 27.6 | 0.77 | 0.14 | 0.11 | 118.8 | 15.9 |
| **8** | 13.7 | 1.07 | 0.22 | 0.18 | 62.9 | 17.6 |
| **9** | 15.4 | 0.21 | 0.13 | 0.09 | 221.8 | 23.6 |
| **10** | 15.7 | 0.46 | 0.35 | 0.26 | 66.6 | 15.4 |
| **11** | 15.3 | 0.35 | 0.11 | 0.10 | 71.8 | 12.3 |
| **12** | 12.5 | 0.36 | 0.07 | 0.04 | 57.3 | 24.1 |
| **13** | 28.7 | 1.61 | 0.05 | 0.08 | 138.8 | 16.8 |
| **14** | 25.7 | 0.65 | 0.60 | 0.53 | 272.4 | 21.7 |
| **15** | 25.8 | 0.66 | 0.58 | 0.52 | 273.3 | 21.5 |
| **16** | 16.1 | 0.30 | 0.29 | 0.24 | 143.6 | 18.9 |

EBSCOhost - printed on 2/14/2023 2:46 PM via . All use subject to https://www.ebsco.com/terms-of-use

values of between 50 mS and 270 mS, the TCS was limited to values of between 10 % and 25 %. This is illustrated in Figure 1. Due to the considerable differences between the EVCs, each EVC type had to be represented by an individually parameterised model. Using a single HAM for different EVC's was virtually impossible.

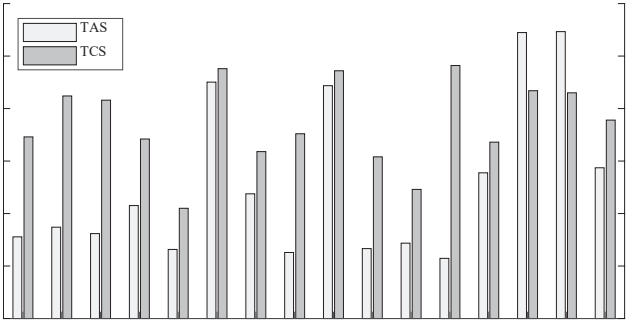



Figure 1: Total auto-sensitivity (TAS) and total cross-sensitivity (TCS) indices

In the following, the accuracy of both the uncoupled (M1) and coupled (M2) Norton models is analysed using the comparison between the corresponding HAM-simulated and actually measured harmonic currents for a set of more than 500 randomly distorted voltage waveforms. Therefore, all elements of the HAM are used, regardless of their sensitivity, or non-linearity. This implementation of the model serves as a reference, as it can be considered to be the most accurate. The HAM of M1 was derived in the same way as for M2, but all non-diagonal elements were set to zero.

The percentage magnitude error was calculated as:

$$\delta I_{\mathrm{Mx}}^{(\mathrm{k})} = \frac{\left|\underline{I}_{\mathrm{Mx}}^{(\mathrm{k})}\right| - \left|\underline{I}_{\mathrm{meas}}^{(\mathrm{k})}\right|}{\left|\underline{I}_{\mathrm{meas}}^{(\mathrm{k})}\right|} \cdot 100\ \% \tag{8}$$

with $\underline{I}_{\mathrm{meas}}^{(\mathrm{k})}$ being the measured harmonic current.

Table 2 lists the 95$^{\mathrm{th}}$ percentiles of the absolute value of the magnitude error. It shows that except for EVC 16, the percentage magnitude errors were mostly below 30 % for model M1 and mostly below 20 % for model M2. It can also be concluded that the improvement of M2 over M1 is greater for higher harmonic orders. While there is often no significant difference

EBSCOhost - printed on 2/14/2023 2:46 PM via . All use subject to https://www.ebsco.com/terms-of-use

for the 3rd harmonic current, the error can be reduced by more than half in some cases for the 7th harmonic current.

**Table 2: The 95th percentiles of percentage magnitude error (values in %)**

| EVC | $\left\|\delta I_{M1}^{(3)}\right\|_{95}$ | $\left\|\delta I_{M2}^{(3)}\right\|_{95}$ | $\left\|\delta I_{M1}^{(5)}\right\|_{95}$ | $\left\|\delta I_{M2}^{(5)}\right\|_{95}$ | $\left\|\delta I_{M1}^{(7)}\right\|_{95}$ | $\left\|\delta I_{M2}^{(7)}\right\|_{95}$ |
|---|---|---|---|---|---|---|
| **1** | 4.3 | 2.6 | 40.8 | 9.6 | 31.9 | 8.9 |
| **2** | 14.5 | 14.3 | 24.7 | 18.5 | 27.2 | 21.3 |
| **3** | 12.4 | 13.4 | 15.5 | 15.9 | 23.3 | 12.6 |
| **4** | 14.4 | 16.0 | 27.6 | 20.2 | 22.4 | 22.9 |
| **5** | 4.2 | 2.8 | 30.5 | 12.6 | 16.7 | 2.8 |
| **6** | 20.6 | 13.0 | 25.5 | 14.0 | 31.6 | 14.7 |
| **7** | 14.4 | 14.8 | 11.9 | 9.0 | 12.2 | 7.6 |
| **8** | 6.4 | 6.1 | 25.6 | 19.2 | 25.1 | 17.8 |
| **9** | 34.1 | 22.3 | 28.3 | 17.9 | 36.9 | 19.4 |
| **10** | 15.2 | 15.4 | 10.9 | 10.4 | 15.6 | 10.8 |
| **11** | 8.4 | 8.2 | 12.2 | 9.9 | 12.1 | 10.2 |
| **12** | 12.8 | 13.8 | 12.2 | 10.9 | 11.1 | 8.9 |
| **13** | 3.6 | 3.4 | 26.7 | 23.7 | 16.8 | 10.9 |
| **14** | 14.4 | 10.2 | 19.2 | 9.7 | 21.9 | 9.7 |
| **15** | 14.5 | 8.9 | 18.9 | 9.2 | 19.8 | 9.6 |
| **16** | 101.0 | 94.7 | 115.5 | 122.9 | 73.8 | 76.3 |

However, the phase angle error is at least as important as the magnitude error. The phase angle difference between simulated and measured currents is calculated as follows:

$$\Delta\varphi_{Mx}^{(k)} = \arg\left(\underline{I}_{Mx}^{(k)}\right) - \arg\left(\underline{I}_{meas}^{(k)}\right) \tag{9}$$

Table 3 summarises the 95th percentiles of the absolute value of the phase angle error. If EVC 16 is again excluded, the phase angle error is for almost all EVCs less than 20° for model M1 and less than 15°, mostly even less than 10°, for model M2. Again, the differences between both models are higher for the 5th and 7th harmonic current than for the 3rd harmonic current. Due to the very high errors in the case of EVC 16, it may be

EBSCOhost - printed on 2/14/2023 2:46 PM via . All use subject to https://www.ebsco.com/terms-of-use

concluded that a linearized frequency-domain model cannot adequately represent this EVC.

**Table 3:** The 95th percentiles of absolute phase angle error (values in °)

| EVC | $\left\lvert\Delta\varphi_{\mathrm{M1}}^{(3)}\right\rvert_{95}$ | $\left\lvert\Delta\varphi_{\mathrm{M2}}^{(3)}\right\rvert_{95}$ | $\left\lvert\Delta\varphi_{\mathrm{M1}}^{(5)}\right\rvert_{95}$ | $\left\lvert\Delta\varphi_{\mathrm{M2}}^{(5)}\right\rvert_{95}$ | $\left\lvert\Delta\varphi_{\mathrm{M1}}^{(7)}\right\rvert_{95}$ | $\left\lvert\Delta\varphi_{\mathrm{M2}}^{(7)}\right\rvert_{95}$ |
|---|---|---|---|---|---|---|
| **1** | 1.6 | 1.1 | 29.6 | 4.8 | 18.8 | 5.0 |
| **2** | 7.5 | 5.7 | 13.2 | 11.0 | 15.1 | 11.0 |
| **3** | 5.9 | 5.0 | 10.2 | 7.3 | 17.4 | 6.6 |
| **4** | 9.2 | 9.3 | 16.0 | 10.6 | 12.1 | 9.9 |
| **5** | 2.0 | 1.2 | 15.0 | 6.6 | 8.6 | 1.6 |
| **6** | 14.0 | 10.6 | 13.0 | 8.1 | 18.2 | 8.4 |
| **7** | 8.1 | 7.6 | 7.3 | 4.6 | 9.4 | 6.8 |
| **8** | 2.8 | 2.1 | 15.4 | 8.0 | 17.0 | 7.7 |
| **9** | 16.7 | 14.1 | 18.4 | 13.6 | 20.5 | 11.0 |
| **10** | 7.8 | 7.1 | 6.9 | 6.3 | 7.8 | 5.9 |
| **11** | 5.1 | 4.8 | 6.0 | 4.6 | 6.1 | 5.0 |
| **12** | 8.5 | 8.3 | 6.9 | 5.6 | 7.5 | 6.2 |
| **13** | 1.5 | 1.3 | 18.2 | 16.8 | 9.2 | 6.8 |
| **14** | 8.2 | 5.4 | 11.8 | 7.5 | 13.2 | 5.8 |
| **15** | 8.1 | 4.7 | 11.3 | 6.4 | 13.4 | 5.9 |
| **16** | 127.6 | 126.5 | 119.4 | 119.3 | 88.6 | 87.6 |

## Classification of EVCs

In order to simplify the model and to improve its performance regarding its implementation in a simulation environment, the elements of the HAM in model M2 that have a negligible impact on the harmonic emissions were identified and removed. For that purpose, a threshold value for sensitivity is required. Whether the impact of a particular element of the HAM is negligible or not, however, depends not only on its absolute value, but also on its value in relation to the other elements of the HAM. Consequently, each EVC had to be analysed individually.

In order to determine a suitable minimal sensitivity, a threshold value was defined and all HAM elements below this value were set to zero. Next, the same accuracy analysis as before was performed and the results were

EBSCOhost - printed on 2/14/2023 2:46 PM via . All use subject to https://www.ebsco.com/terms-of-use

compared with the reference model comprising the full HAM. The starting value of the sensitivity threshold was 1 mS. In each iteration, this was increased by another 1 mS. The final threshold was found when, for any of the harmonic orders considered, either the magnitude error increased by 3 %, or the phase angle error increased by 3 °. In the following, only the 3rd, 5th, and 7th harmonic orders are analysed in more detail. In the case of the other harmonic orders, other limits for their accuracy deviation may be necessary. The procedure applied is illustrated in Figure 2 for EVC 1. In that example, a sensitivity threshold of $S_{\mathrm{thr}} = 6\,\mathrm{mS}$ was found to be an appropriate value.

Following this procedure, the sensitivity thresholds for all 16 EVCs were determined. Subsequently, the HAMs required for the coupled Norton model were reduced accordingly. The number of elements of the resulting HAMs, $n_{\mathrm{thr}}$, was used as a basis for the proposed classification.

In case of the uncoupled Norton model (M1), only the diagonal elements were used. Their number corresponds to the number of considered harmonic orders $N$. The difference to $n_{\mathrm{thr}}$ is thus the number of elements that have an impact on the harmonic emission, but these were not considered. The respective percentage ratio can be defined as:

$$\delta n_{\mathrm{M1}} = \frac{n_{\mathrm{thr}} - N}{n_{\mathrm{thr}}} \cdot 100\ \% \tag{10}$$

Regarding the coupled Norton model, the non-linearity index was applied to the HAM. All elements that had a non-linearity (7) of less than or equal to 25 % were considered to be sufficiently linear. Their number, $n_{\mathrm{lin}}$, was used to calculate a similar ratio as for the uncoupled Norton model:

$$\delta n_{\mathrm{M2}} = \frac{n_{\mathrm{thr}} - n_{\mathrm{lin}}}{n_{\mathrm{thr}}} \cdot 100\ \% \tag{11}$$

However, even if an element had a non-linearity of more than 25 %, it was still included in the model because, in general, it is better to consider it than to neglect it. However, the higher the number of these elements, the higher the chance that they significantly affect accuracy. Figure 3 shows both $\delta n_{\mathrm{M1}}$ and $\delta n_{\mathrm{M2}}$ for all EVCs.

These ratios can be used to divide the EVCs into groups with similar characteristics. As such, the classification shown in Table 4 is proposed. If both $\delta n_{\mathrm{M1}}$ and $\delta n_{\mathrm{M2}}$ are less than 30 %, the HAM can be reduced to a good approximation of a diagonal matrix and can be represented by the uncoupled Norton model. If $\delta n_{\mathrm{M1}}$ is greater than 30 %, but $\delta n_{\mathrm{M2}}$ is still below that value, it is insufficient to consider only the diagonal elements. In that case,

EBSCOhost - printed on 2/14/2023 2:46 PM via . All use subject to https://www.ebsco.com/terms-of-use

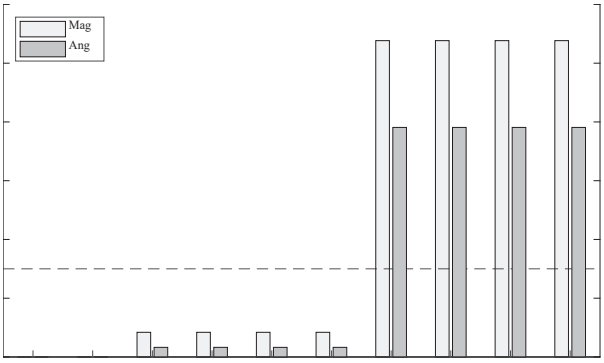



**Figure 2:** Increase of magnitude and phase angle error of the 5th harmonic current depending on the sensitivity threshold $\boldsymbol{S_{\mathrm{thr}}}$ for EVC 1

the coupled Norton model would be expected to have better accuracy. If neither $\delta n_{\mathrm{M1}}$ nor $\delta n_{\mathrm{M2}}$ are less than 30 %, there is a non-negligible number of HAM elements with a high non-linearity, which can considerably affect the accuracy of the coupled Norton model.

Table 5 summarizes the indices required for classification. The three groups of EVCs were marked according to the notation in Table 4. This classification can change depending on the harmonic orders considered. Nevertheless, it is helpful in getting an overview of the possible performance of different modelling approaches.

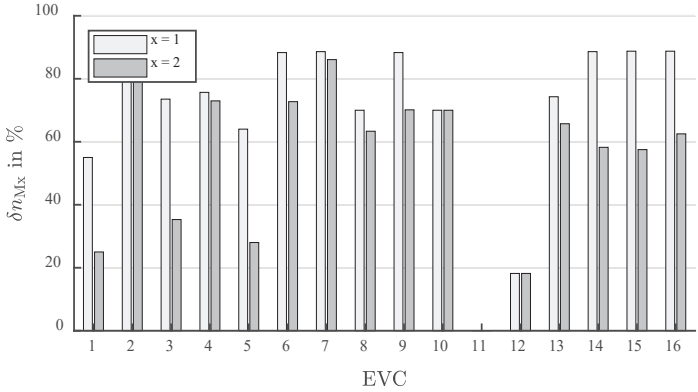



**Figure 3:** Percentage shares of not included couplings (M1) and couplings having high non-linearity (M2)

EBSCOhost - printed on 2/14/2023 2:46 PM via . All use subject to https://www.ebsco.com/terms-of-use

**Table 4:** Proposed classification

| Group | $\delta n_{\mathrm{M1}}$ | $\delta n_{\mathrm{M2}}$ |
|---|---|---|
| **1** | ≤30 % | ≤30 % |
| **2** | >30 % | ≤30 % |
| **3** | >30 % | >30 % |

To determine the actual accuracy of the models, it was crucial to validate them individually for the different EVCs. To exemplify the suitability of the proposed classification, two EVCs from each group have been chosen for the following discussion. The analysis of accuracy was performed in the same way as previously for the assessment of the reference model and the sensitivity analysis.

However, in order to better visualise the magnitude and phase angle accuracy, the deviations are displayed using a modified box plot. While the outer limits indicate the 5th and 95th percentile, the inner limits represent the 25th and 75th percentile, while the median is shown as a horizontal line in

**Table 5:** Classification of EVCs

| Group | EVC | $S_{\mathrm{thr}}$/mA | $n_{\mathrm{thr}}$ | $n_{\mathrm{lin}}$ | $\delta n_{\mathrm{M1}}$/% | $\delta n_{\mathrm{M2}}$/% |
|---|---|---|---|---|---|---|
| **1** | **11** | 10 | 9 | 9 | 0 | 0 |
| **1** | **12** | 10 | 11 | 9 | 18 | 18 |
| **2** | **1** | 6 | 20 | 15 | 55 | 25 |
| **2** | **5** | 3 | 25 | 18 | 64 | 28 |
| **3** | **2** | 3 | 74 | 12 | 88 | 84 |
| **3** | **3** | 6 | 34 | 22 | 74 | 35 |
| **3** | **4** | 7 | 37 | 10 | 76 | 73 |
| **3** | **6** | 4 | 77 | 21 | 88 | 73 |
| **3** | **7** | 3 | 79 | 11 | 89 | 86 |
| **3** | **8** | 4 | 30 | 11 | 70 | 63 |
| **3** | **9** | 4 | 77 | 23 | 88 | 70 |
| **3** | **10** | 4 | 30 | 9 | 70 | 70 |
| **3** | **13** | 4 | 35 | 12 | 74 | 66 |
| **3** | **14** | 7 | 79 | 33 | 89 | 58 |
| **3** | **15** | 7 | 80 | 34 | 89 | 58 |
| **3** | **16** | 3 | 80 | 30 | 89 | 63 |

EBSCOhost - printed on 2/14/2023 2:46 PM via . All use subject to https://www.ebsco.com/terms-of-use

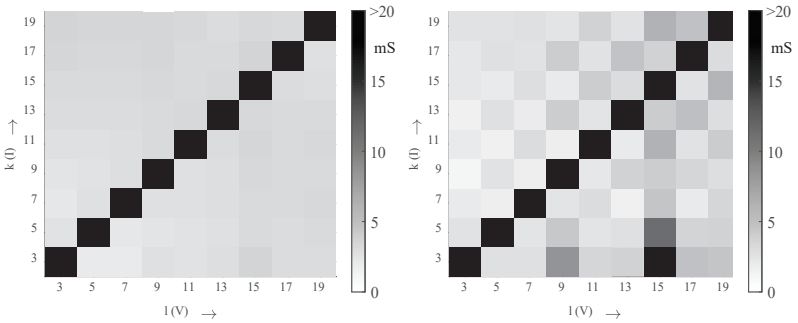
the centre. Additionally, the sensitivity matrices of the chosen EVCs are presented in order to show those HAM elements that can have an impact on harmonic emissions.

Figure 4 shows the respective results for EVCs 11 and 12, which represent Group 1. The sensitivity matrices show that significant sensitivity can mainly be found in the diagonal of their HAMs. In the case of EVC 12, there are a few other elements with significant sensitivity, which have, however, only a small impact on overall accuracy. As such, the uncoupled Norton model is sufficiently accurate, with an approximate magnitude error of between approximately -10 % and +10 % and a rough phase angle error of between -5 ° and +5 °. Compared to these values, the coupled Norton model shows no better accuracy.

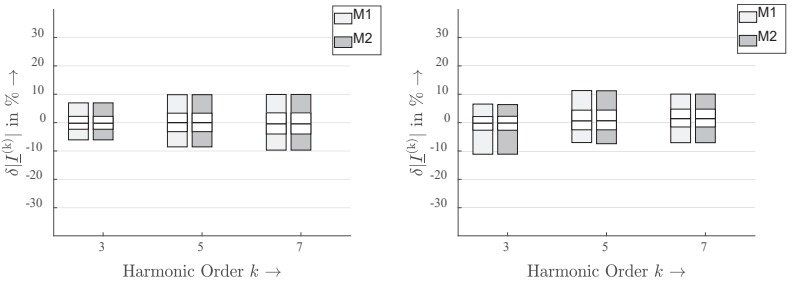
Figure 5 presents the detailed results for EVCs 1 and 5 from Group 2. Analysis of the sensitivity indices suggests that not only the diagonal, but also its adjacent elements have an impact and should not be neglected. Furthermore, these elements mainly show only very little non-linearity. Consequently, the coupled Norton model can represent the harmonic emission behaviour with sufficiently accuracy with an approximate magnitude error of mostly less than ±10 % and a phase angle error of mostly less than ±5 °. In contrast, the uncoupled Norton model exhibits much higher errors.

If an EVC could not be assigned to either Group 1 or Group 2, it was treated as a member of Group 3. This means that there were a significant number of non-negligible HAM elements off the diagonal that were strongly non-linear. Figure 6 shows the examples of EVCs 4 and 9. The magnitude and phase angle error of both models is often clearly higher than ±10 % and ±5 °, respectively, as shown.

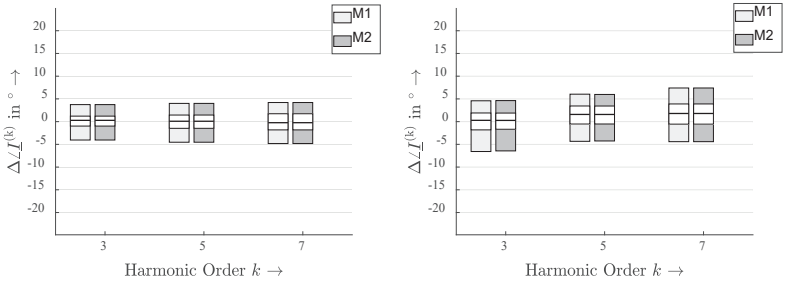
EBSCOhost - printed on 2/14/2023 2:46 PM via . All use subject to https://www.ebsco.com/terms-of-use




(a) Sensitivity matrix (EVC 11) (b) Sensitivity matrix (EVC 12)



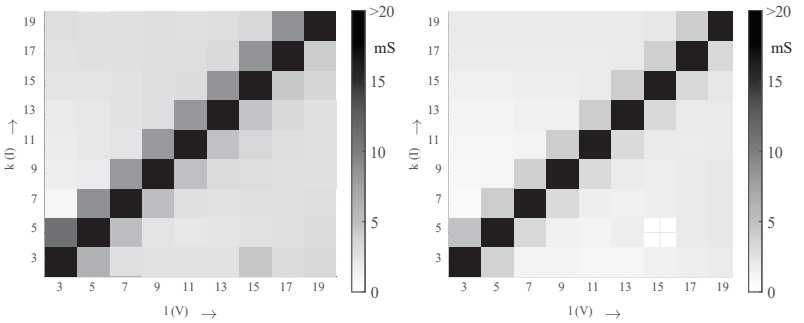

(c) Magnitude error (EVC 11) (d) Magnitude error (EVC 12)




(e) Phase angle error (EVC 11) (f) Phase angle error (EVC 12)

**Figure 4:** Group 1

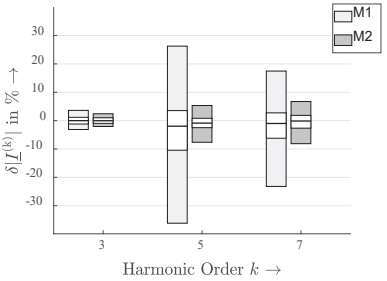
EBSCOhost - printed on 2/14/2023 2:46 PM via . All use subject to https://www.ebsco.com/terms-of-use



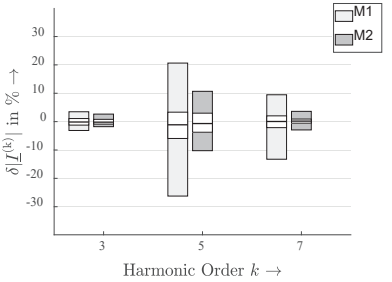

(a) Sensitivity matrix (EVC 1)



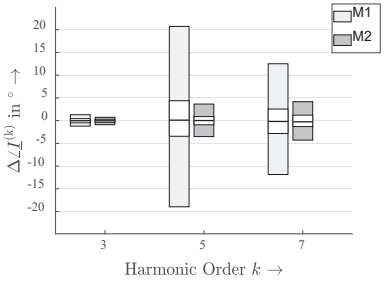

(b) Sensitivity matrix (EVC 5)



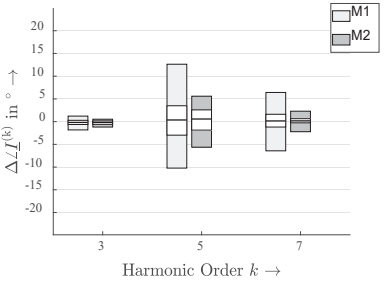

(c) Magnitude error (EVC 1)




(d) Magnitude error (EVC 5)



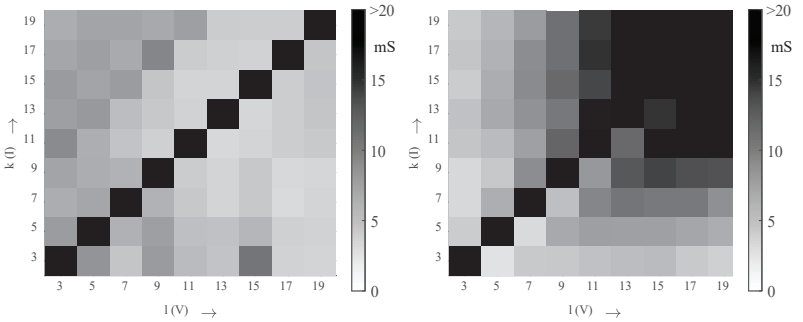

(e) Phase angle error (EVC 1)




(f) Phase angle error (EVC 5)

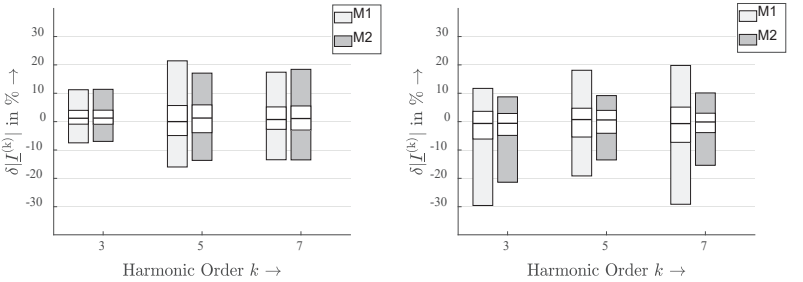
**Figure 5:** Group 2

EBSCOhost - printed on 2/14/2023 2:46 PM via . All use subject to https://www.ebsco.com/terms-of-use



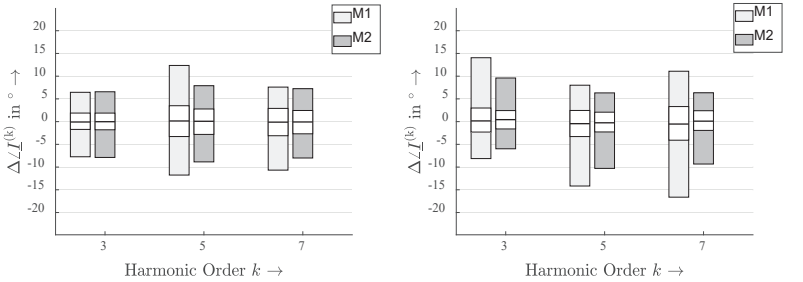

(a) Sensitivity matrix (EVC 4)

(b) Sensitivity matrix (EVC 9)




(c) Magnitude error (EVC 4)

(d) Magnitude error (EVC 9)




(e) Phase angle error (EVC 4)

(f) Phase angle error (EVC 9)

**Figure 6:** Group 3

EBSCOhost - printed on 2/14/2023 2:46 PM via . All use subject to https://www.ebsco.com/terms-of-use

## Conclusions

This paper presents a detailed analysis of the suitability of using coupled and uncoupled Norton models for frequency domain modelling of EVCs. The impact of supply voltage distortion on harmonic current emissions was characterised for 16 different EVCs, which represent the majority share of EVs currently registered in the EU market. Based on extensive measurements, the impact of both individual harmonic voltages and random voltage distortions containing various harmonics was evaluated. While the former measurements were used for model parameterisation, the latter ones were used for model validation.

Indices to quantify the sensitivity and non-linearity of the elements of the harmonic admittance matrices (HAMs) were developed. Furthermore, a sensitivity threshold, to define a limit between negligible and non-negligible HAM elements that takes both magnitude and phase angle accuracy into account, is proposed. This approach allows us to simplify the frequency-domain models available in order to reduce their computational requirements when implemented in network simulations. Moreover, this enables characterisation and classification of the nonlinear behaviour of EVCs.

The results presented show that there is a significant dependency of the EVCs' harmonic current emissions on supply voltage distortion. Even though the technology of different EVCs is similar, they can differ significantly to each other. The 16 different EVCs examined can be divided into three groups on the basis of similar characteristics. The analysis showed that these groups are also connected to the most suitable modelling approach and expected accuracy of the model used. For Group 1, only the dependency between harmonic voltages and currents of the same order need be considered. For Group 2, there are cross-couplings between harmonic voltages and currents of usually adjacent orders that should be taken into account. Finally, there are even more couplings that should be considered for Group 3, which are mostly strongly non-linear.

The set of indices presented can easily be adapted to assess the harmonic emission behaviour of other devices, such as photovoltaic inverters and electronic-based mass-market appliances. Furthermore, they can be used in order to decide what type of frequency domain model is most appropriate for a target application.

EBSCOhost - printed on 2/14/2023 2:46 PM via . All use subject to https://www.ebsco.com/terms-of-use

## Outlook

Future work could include more advanced modelling approaches in order to further improve accuracy, particularly with respect to EVCs in Group 3. Furthermore, the input impedance of EVCs needs to be analysed in order to accurately represent its impact on the network harmonic impedance in real LV networks.

## Acknowledgement

The authors thank the German Federal Ministry for the Environment, Nature Conservation, Building and Nuclear Safety for their financial support (project: ElmoNetQ, FKZ: 16EM1052).

## References

[1] Müller, S.; Meyer, J.; Schegner, P.; Djokic, S.: Harmonic Modelling of Electric Vehicle Chargers in Frequency Domain. In: International Conference on Renewable Energies and Power Quality (ICREPQ'15) (2015), Nr. 13.

[2] Collin, A.J.; Djokic, S.Z.; Thomas, H.F.; Meyer, J.: Modelling of Electric Vehicle Chargers for Power System Analysis. In: Proceeding of the International Conference on Electrical Power Quality and Utilisation, EPQU Bd. 21 (2011), S. 476–481 — ISBN 9781467303798.

[3] Xiao, X.; Molin, H.; Kourtza, P.; Collin, A.; Harrison, G.; Djokic, S.; Meyer, J.; Müller, S.; Möller, F.: Component-Based Modelling of EV Battery Chargers. In: 2015 IEEE Eindhoven PowerTech, PowerTech 2015 (2015) — ISBN 9781479976935.

[4] Meyer, J.; Mueller, S.; Ungethuem, S.; Xiao, X.; Collin, A.; Djokic, S.: Harmonic and Supraharmonic Emission of On-Board Electric Vehicle Chargers. In: 2016 IEEE PES Transmission and Distribution Conference and Exposition-Latin America, PES T and D-LA 2016 (2017) — ISBN 9781509028757.

[5] Jiang, C.; Torquato, R.; Salles, D.; Xu, W.: Method to Assess the Power-Quality Impact of Plug-in Electric Vehicles. In: IEEE Transactions on Power Delivery Bd. 29 (2014), Nr. 2, S. 958–965 — ISBN 9781467364874.

[6] Moses, P.S.; Deilami, S.; Masoum, A.S.; Masoum, M.A.S.: Power Quality of Smart Grids with Plug-in Electric Vehicles Considering Battery Charging Profile. In: IEEE PES Innovative Smart Grid Technologies Conference Europe, ISGT Europe (2010), S. 1–7 — ISBN 9781424485109.

[7] Meyer, J.; Müller, S.; Schegner, P.; Djokic, S.Z.; Collin, A.J.; Xu, X.: Comparison of Methods for Modelling Electric Vehicle Chargers for Harmonic Studies. In: 19th Power Systems Computation Conference, PSCC 2016 (2016) — ISBN 9788894105124.

EBSCOhost - printed on 2/14/2023 2:46 PM via . All use subject to https://www.ebsco.com/terms-of-use

[8] Xiao, X.; Collin, A.J.; Djokic, S.Z.; Yanchenko, S.; Moller, F.; Meyer, J.; Langella, R.; Testa, A.: Analysis and Modelling of Power-Dependent Harmonic Characteristics of Modern PE Devices in LV Networks. In: IEEE Transactions on Power Delivery Bd. 32 (2017), Nr. 2, S. 1014–1023.

[9] Fauri, M.: Harmonic Modelling of Non-linear Load by Means of Crossed Frequency Admittance Matrix. In: IEEE Transactions on Power Systems Bd. 12 (1997), Nr. 4, S. 1632–1638.

[10] Fölting, A.S.; Myrzik, J.M.A.; Wiesner, T.; Jendernalik, L.: Practical Implementation of the Coupled Norton Approach for Nonlinear Harmonic Models. In: Proceedings - 2014 Power Systems Computa-tion Conference, PSCC 2014 Bd. 1 (2014) — ISBN 9788393580132.

[11] Möller, F.; Meyer, J.; Schegner, P.: Load Model of Electric Vehicles Chargers for Load Flow and Unbalance Studies. In: Electric Power Quality and Supply Reliability Conference (PQ). Rakvere, Estonia: IEEE, 2014 — ISBN 9781479950225.

[12] Cobben, S.; Kling, W.; Myrzik, J.: The Making and Purpose of Harmonic Fingerprints. In: 19th International Conference on Electricity Distribution - CIRED (2007), Nr. 0764, S. 1–4.

[13] Müller, S.; Meyer, J.; Schegner, P.: Characterization of Small Photovoltaic Inverters for Harmonic Modelling. In: Proceedings of International Conference on Harmonics and Quality of Power, ICHQP (2014), S. 659–663 — ISBN 9781467364874.

EBSCOhost - printed on 2/14/2023 2:46 PM via . All use subject to https://www.ebsco.com/terms-of-use

# CHAPTER THIRTY-SEVEN

# HARMONIC LIMITS IN CONNECTION AGREEMENTS FOR WIND POWER PLANTS

DAPHNE SCHWANZ[1], MATH BOLLEN[1]

## Abstract

Connection agreements for wind power plants need to be complied with to avoid unacceptable deterioration of grid performance. Such agreements include limits on harmonic emission. The direct aim of those is to ensure an acceptable power quality in the grid, both for voltage and current. The ultimate aim is to ensure a high probability of electromagnetic compatibility. Different limits, different interpretations of those limits and different procedures to follow are in place in different countries. In this chapter, an overview of these will be given, together with a detailed discussion of the advantages and disadvantages.

**Keywords:** Power quality, Power-system harmonics, Grid codes, Wind power plants

## 1. Introduction

### *Background*

Power quality is an important factor in studies that aim to investigate the impact that different energy sources, including wind power plants (WPPs), have through their connection to the public grid. Harmonics are a power quality concern because they can cause excessive heating in motors and generators, increase heating and voltage stress in capacitors, and cause

[1] Luleå University of Technology, Skellefteå, Sweden

EBSCOhost - printed on 2/14/2023 2:46 PM via . All use subject to https://www.ebsco.com/terms-of-use

maloperation in electronic equipment connected to the grid [1][2][3][4][5][6].

## *Harmonic studies*

Harmonic studies are commonly undertaken before the connection of a WPP to the electric power grid. The ultimate reason for performing such a study is to avoid interference between the grid and equipment connected to the grid. That equipment includes equipment in the WPP, as well as equipment connected elsewhere. However, these studies rarely address actual cases of interference; rather after connection harmonic voltages and/or currents are compared with limits provided by the network operator or those set out in standards or regulations. It is these standards and regulations that are the subject of this chapter.

## *Harmonic emission limits*

Different compliance procedures exist in different countries and between different network operators within a country. Some of these limits do not depend on location, while others are related to voltage distortion allocation and fault levels at the point of connection. Due to this diversity of procedures, we present a structured summary of them along with some of their advantages and disadvantages. Those advantages and disadvantages will be discussed from the viewpoint of different stakeholders, especially in terms of the network operator and the owner or operator of the WPP.

## *Disturbances and interference*

In power quality, a very important distinction is made between ‘disturbances’ and ‘interference.’ The term disturbance (power-quality disturbance, disturbance in voltage, etc.) refers to any deviation from the ideal voltage that can be measured and that has a potential impact on equipment (even if very unlikely). Voltage distortion (also known by the term ‘harmonics’) is an example of a power-quality disturbance.

The term interference is used when equipment in the grid or equipment connected to the grid is in any way adversely impacted by a power-quality disturbance. This could be immediate damage to equipment, a reduction in its predicted life-time, a trip, or even, for example, something like a lamp flickering.

Most of the work on power quality concerns disturbances, harmonic limits are for example placed on the level of disturbances. What matters in

EBSCOhost - printed on 2/14/2023 2:46 PM via . All use subject to https://www.ebsco.com/terms-of-use

the end is how to limit the probability of interference. The reason that limits are set is to maintain a sufficiently low probability of interference. Table 1 shows the four possible combinations when considering interference and the exceeding of limits. The setting of limits often involves a difficult balance between reducing both the number of cases in the top left cell (interference, but not exceeding limits) and in the bottom right cell (limits exceeded, but no interference). Power quality, including voltage distortion, is a rather complex phenomenon and it is all but impossible to avoid cases like this. Cases in the top left cell typically call for more strict or more complicated regulation, whereas cases in the bottom right cell result in calls for less strict regulation. This is an important discussion that will go on for a long time, but we will not continue this line any further in this chapter.

**Table 1. Interference and exceeding of limits.**

| | Limits not exceeded | Limits exceeded |
|---|---|---|
| Interference | Investigation triggered by the owner of the equipment that is impacted. | Measures have to be taken by the network operator or by the source of the emission. |
| No interference | Everybody is happy. | Measures are actually not needed, but still often required under regulations or contracts. |

## 2. Location Independent Limits

For mass-produced low-voltage equipment, it is common to have the same emission limits for any device (of a specific type) independently of where it is connected to the grid. Such limits for small equipment are given in IEC 61000-3-2 [7]. A television used in the centre of a city (where the grid is strong) needs to comply with the same harmonic emission limits as a television used in a remote part of the countryside (where the grid is weak). There are good reasons for having the same emission limits for all small equipment: it means that equipment manufacturers and users do not have to consider the impact on the grid of where the equipment is used. That impact is instead considered by teams of experts when setting the emission limits.

The same approach is used for production installations in IEEE 519 [8], where the same emission limits hold for any such installation, no

EBSCOhost - printed on 2/14/2023 2:46 PM via . All use subject to https://www.ebsco.com/terms-of-use

matter how weak or strong the grid is. Under the IEEE 519 recommendations, the limits apply to the complete installation, not to individual turbines. The recommended values in IEEE 519 are based on the fact that some level of voltage distortion is generally acceptable and both system owners/operators and users must work cooperatively to keep voltage distortion below the limits.

Note that for consuming equipment, IEEE 519 recommends limits that are dependent on the local fault level. However, for production equipment, the limits are location independent. The reasons for this go back to the time when production almost exclusively used synchronous machines, which have low levels of harmonic emission. Also, adding a local production unit would not require a strengthening of the grid, thus there would be no additional harmonic hosting capacity made available.

The big advantage of location-independent limits, even for big installations, is that the setting of the limits is simple. No information at all is needed about how strong the grid is at the point of connection. Also, there is no need for any detailed harmonic studies.

A serious disadvantage of location-independent limits is that the limits will be too strict for most locations. The setting of limits aims to avoid interference at the vast majority of locations. For this to be achieved, the limits need to be stricter than required at all but a few locations. A specific concern with IEEE 519 is that the limits for even harmonics are rather strict and several WPPs have shown difficulty in complying with them. Some examples of this are shown in [9]. Even in cases where there is no risk of high harmonic voltage distortion at those frequencies, there is still a need to limit emission to rather low values.

A disadvantage from the network operator viewpoint is that even in the case of high harmonic source impedance at the point of connection, no additional requirements can be placed on the WPP. This could especially be an issue in networks with high-voltage cables and resonance frequencies close to low-order harmonics.

## 3. Voltage Distortion Allocation

### *General principle*

The fundamental idea behind disturbance allocation is that each customer, or group of customers, is allowed to cause a certain level of voltage distortion. The arithmetic sum of all the contributions can be more than the planning level (the total acceptable harmonic voltage during the

EBSCOhost - printed on 2/14/2023 2:46 PM via . All use subject to https://www.ebsco.com/terms-of-use

planning stage), based on the aggregation rule used (see below). Once the allocation is made, it is each customer's responsibility to remain within its allocation, whereas the network operator carries the risk that the allocation rule is too generous towards its customers. Examples of allocation rules are discussed in [10] and [11].

This allocation depends on the existing voltage distortion (the 'background distortion') and assumes certain aggregation rules. In this way, the allocation is strongly location dependent. The current emission limit is determined from the voltage distortion allocation and the local source impedance as a function of frequency. The method gives a good estimation of the actual amount of voltage distortion that the WPP is allowed to cause before acceptable limits are exceeded. The main idea is to ensure that the harmonic voltage level at each bus remains no higher than the planning level. To ensure that the allocation is equitable in some sense, the allocated harmonic emission level should be an increasing function of customer size [12].

## *Aggregation*

The total available emission limit, i.e. the permissible voltage distortion, is shared across all sources of emission. To include all possible sources of emission is obviously not practical, even if it were possible. Instead the available distortion is typically divided between:

- The customer (for example a WPP) that wants to connect;
- Existing customers at the same bus or substation;
- Future customers that may be connected to the same bus or substation;
- All other customer/sources of harmonics in the world.

The second and fourth contributions are often merged into the 'background voltage distortion.' In some allocation schemes, future customers are not given any allocation and they will receive a part of the allocation that is not currently being used by existing customers.

To this point, there is general agreement on the method to be used. Disagreement starts when the contributions from the different sources of emission are added—the so-called 'aggregation rule.' A linear aggregation rule would imply that all emissions are added arithmetically. For example, when the background voltage distortion, at a certain harmonic, is 3% and the limit is 5%, linear aggregation would leave 2% to be allocated to the customer to connect, as well as for future customers.

EBSCOhost - printed on 2/14/2023 2:46 PM via . All use subject to https://www.ebsco.com/terms-of-use

There are a number of reasons why a linear aggregation rule gives an overestimation of the harmonic levels. Using this rule would thus offer unreasonably low allocations to a customer that wants to connect. The reason often mentioned in the literature is the 'phase-angle diversity' between different sources. However, different sources reach their maximum emission at different moments in time and customers rarely use all of their allocation.

The most commonly-used aggregation rules are those recommended in IEC TR 61000-3-6 [13]. This technical report presents a general summation law for each harmonic order ($h$), as presented in (1). The recommended summation exponents are presented at Table 2.

$$U_h = \sqrt[\alpha]{\sum_i U_{hi}^{\alpha}} \quad (1)$$

$U_h$ is the magnitude of the resulting harmonic voltage (order $h$); $U_{hi}$ is the magnitude of the various individual emission levels (order $h$) to be combined; $\alpha$ is an aggregation exponent.

**Table 2 – Aggregation exponent for harmonic aggregation**

| Harmonic Order | α |
|---|---|
| h < 5 | 1 |
| 5 ≤ h ≤ 10 | 1.4 |
| h > 10 | 2 |

The aggregation exponents in Table 2 were selected a long time ago. The kind of equipment connected to modern grids is of a rather different character from the equipment in place when these exponents were selected. Emissions from wind turbines were never considered in the selection of the exponents. Despite this, the aggregation components have remained the same. This issue has been heavily discussed, but no consensus has yet been reached on alternative values.

## *Aggregation for studies*

Another important topic is the aggregation between turbines and the aggregation between existing and future customers. However, these are not always considered in studies on this topic. For the aggregation between the turbines, most of the time, the network operator does not pay attention to this factor. However, due to the different aggregations that can occur

EBSCOhost - printed on 2/14/2023 2:46 PM via . All use subject to https://www.ebsco.com/terms-of-use

inside the WPP, this type should be addressed. The aggregation exponents in Table 2 are also regularly used for this, often because of a lack of better values. Here it should be noted that these exponents were never intended for emission studies, but only as a method for the allocation of voltage distortion. Some studies have been made of the actual aggregation between individual turbines [14][15] and these show that reality is far more complicated than the simple aggregation rule allows.

### *From voltage allocation to current limit*

Once a certain amount of voltage distortion has been allocated to a customer, current emission limits can be set in a number of ways. Most methods are, in one way or another, an application of Ohms' law, calculating a current from a voltage using an impedance. The difference between the methods is the choice of this impedance. Some options include:

- A fixed impedance versus frequency, for all locations.
- An impedance versus frequency dependent only on the fault-level at 50 Hz.
- The actual (or accurately calculated) impedance versus frequency.

The second and third methods need to consider the different operational states of the system. When only normal (strong) operational states are considered, the emission requirements are much lighter than when abnormal (weak) operational states are also considered. Recommendations for the selection of states are given in IEC TR 61000-3-6, where it is, for example, sufficient to consider the most common operational states, totalling 95% of the time. Allowing higher distortion during a small part of the time (i.e. setting 95% or 99%-limits) may at first seem reasonable and fair to wind power plants. This practice, however, may lead to unacceptably high levels of voltage distortion during certain realistic, but rare operational states. As long as the consequences of harmonic voltage distortion are due to thermal impacts or affect only a small number of customers, this is not a serious concern. Depending on the definition used, this may be seen to be a violation of the (N-1)-criterion. This is, however, more a linguistic than a technical matter.

Concern about adverse harmonic control interaction (also known as 'harmonic instability') could make this into a serious issue, whether the language matters or not.

EBSCOhost - printed on 2/14/2023 2:46 PM via . All use subject to https://www.ebsco.com/terms-of-use

Next to the calculation of current emission limits from the voltage emission allocation, there is the method where the actual change in voltage distortion before and after connection is the criterion used. All the other methods only consider primary emission, whereas this last method considers primary and secondary emission [16][17]. See Section 9 for a discussion on primary and secondary emission.

### *Advantages and disadvantages*

The use of this approach is advantageous to both the network operator (limited risk of high voltage distortion) and the WPP owner (no unnecessary severe limits). Detailed studies are needed to obtain the source impedance as a function of frequency, but simplified source impedance models may be used (see above). Allocation is based on certain simplified models for aggregation between customers. It is not clear if those models accurately represent reality, but for the time being they are the best we have.

A disadvantage with this method is that all harmonics are allocated. Even installations that emit very little at a certain frequency (for example harmonic 10) receive their share of the allocation. This is at the expense of those installations that emit at those frequencies. This keeps distortion levels low in the grid, but can create serious challenges in complying with the limits for some installations. As mentioned previously, WPPs emit, more than most classical installations, at even harmonics. Hence, complying with emission limits for those frequencies can actually be a serious challenge for a WPP, even though there is no risk of voltage distortion limits being exceeded.

For the aggregation between existing and future customers (WPPs), as this is a statistical proposition, an ‘uncertain uncertainty’ problem appears. This is especially so in countries where this situation is not considered and the whole allocation is given to the first wind park that wants to connect, which means that it can become impossible or difficult for future installations to connect.

## 4. Limits Depending on Fault Level

### *Basic approach*

A way to diversify between weak and strong grids is to set the emission limits according to the fault level (short-circuit impedance) at the point of connection. This is the approach used in IEEE 519 for the

EBSCOhost - printed on 2/14/2023 2:46 PM via . All use subject to https://www.ebsco.com/terms-of-use

connection of power consuming installations, but not for production installations (see Section 2). The emission requirements in IEC 61000-2-12 [18] also use this approach. What matters in both standards is, strictly speaking, not the actual fault level, but the ratio between the equipment rating and fault level. Small equipment is allowed a higher emission (in percentage of rating) than large equipment. In terms of Section 3, this corresponds to a non-unity aggregation exponent.

A certain profile for source impedance versus frequency should be used to set the limits and this same profile should be assumed for all locations. The system harmonic impedances can be obtained by simulation of various system operating conditions. This impedance may be based on the short-circuit impedance or on the locus of the harmonic impedance. It is necessary to consider the range of variation of harmonic impedance, not just the maximum impedance values, in order to identify possible resonance.

### *IEC 61000-3-6 for small installations*

The current emission limit could be linear with the fault level and the result would be the same harmonic voltage allocation for each location. According to IEC 61000-3-6, this case can be used for the connection of small installations or installations with a limited amount of distorting equipment. For this, a relation between the agreed power of the installation ($S_i$) and the short circuit power at the point of evaluation ($S_{sc}$) are used through (2).

$$\frac{S_i}{S_{sc}} \leq 0.2\% \tag{2}$$

The limit of 0.2% is used assuming that the system is currently operating with a level of distortion sufficiently below the planning level, that amplification due to resonance is not expected to exceed a factor of two, and that there is no risk of interference with system equipment caused by connection of the new installation.

To characterize the amount of distorting equipment within the installation, a ‘weighted distorting power criterion’ can be assumed. The weighted distorting power is calculated using (3). The weighting factors $W_j$ are shown in Table 3.

$$S_{Dwi} = \sum_j S_{Dj} \cdot W_j \tag{3}$$

EBSCOhost - printed on 2/14/2023 2:46 PM via . All use subject to https://www.ebsco.com/terms-of-use

$S_{Dj}$ is the power of each piece of distorting equipment (j) in the installation (*i*). Assuming a conservative criterion, the acceptance of a new installation may be determined by comparing the weighted distorting power with the short-circuit power at the point of evaluation, as shown in (4).

$$\frac{S_{Dwi}}{S_{sc}} \leq 0.2\% \tag{4}$$

**Table 3 – Weighting factors for different types of harmonic producing equipment**

| Typical Equipment Connected to LV, MV or HV | Typical Current THD | Weighting Factor ($W_j$) |
|---|---|---|
| Single phase power supply | 80 % (high 3rd) | 2.5 |
| Semi-converter | High 2nd,3rd, 4th at partial loads | 2.5 |
| 6-pulse converter, capacitive smoothing, no series inductance | 80 % | 2 |
| 6-pulse converter, capacitive smoothing with series inductance > 3%, or d.c. drive | 40 % | 1 |
| 6-pulse converter with large inductor for current smoothing | 28 % | 0.8 |
| AC voltage regulator | Varies with firing angle | 0.7 |
| 12-pulse converter | 15 % | 0.5 |

## *Advantages and disadvantages*

No further study is needed to obtain the emission limits, as the fault level at the connection point will typically be known by the network operator. Even for locations where there is not yet a grid nearby, estimating the fault level is relatively easy.

A disadvantage of this method is that resonances can result in high distortion despite low impedance at power-system frequency. Even if the existing grid would show no serious resonances, the connection of a WPP could result in resonant frequencies close to major harmonic frequencies (such as 5, 7, 11, and 13).

EBSCOhost - printed on 2/14/2023 2:46 PM via . All use subject to https://www.ebsco.com/terms-of-use

## 5. Verification of Limits

Once the limits are set, they need to be verified in one way or another. Different methods are in use, each with their own advantages and disadvantages.

### *Verification of model used*

The network operator may give detailed instructions on how the calculations should proceed. As long as those instructions are followed and the resulting estimated emission is below the set limits, the wind power plant is allowed to connect. However, if excessive harmonic distortion is estimated during the simulation, further analysis and solutions are required. With this verification approach, no verification is done after connection of the WPP.

Preliminary simulations should be performed to identify expected harmonic levels and system response characteristics. These simulations should be performed for different system conditions to identify conditions of potential concern. A complex model is needed to accurately determine frequency response characteristics. Accurate representations for transmission lines, cables, transformers, capacitor banks, loads, and machines are required. The potential impact of the wind power plant should be evaluated at this point. A detailed overview of the state-of-the-art of models to be used for harmonic studies is found in a soon-to-be-released technical brochure by a CIGRE working group [19].

Using this verification approach, the risk of high emissions and high voltage distortion lies with the network operator. But it is also this same network operator that sets the instructions. The instructions are often based on rather extreme operational states and other worst-case scenarios. The risk carried by the network operator is therefore typically not very great.

The advantage of this verification approach for the wind power plant operator is that no detailed knowledge is needed for performing harmonic studies. This information is provided by the network operator in the instructions that go with the connection agreement. Also, there is no risk that the plant cannot be connected once the criteria are complied with according to simulations. Once the design is approved by the network operator, the latter takes over all risks for high harmonic distortion.

EBSCOhost - printed on 2/14/2023 2:46 PM via . All use subject to https://www.ebsco.com/terms-of-use

### *Verification of measured current and/or voltage distortion*

The alternative approach is one where the voltage and/or current distortion of the installation is measured after connection and compared with the set limits.

Either the current emission or the impact of the installation on the voltage distortion can be used as a criterion. In the latter case, the voltage distortion is measured with and without the installation connected. The change in voltage distortion is compared to the allocation. This approach not only considers the impact of current emissions on the voltage distortion (primary emissions), but also the changes in resonant frequency due to the installation, as well as secondary emissions impacting the background voltage distortion. The latter contribution depends on the background voltage distortion and means that the measurement is not fully reproducible.

Verification through measurement of the current has similar challenges. The measurement will capture both primary and secondary emission, whereas emission limits should reasonably only consider primary emission.

The advantage for the network operator of verification through measurement is that the harmonic distortion can be estimated with actual values and for different operational situations. The disadvantage for the installation owner is that there a risk that the plant cannot be connected once the limits are exceeded. This verification approach places strong requirements on simulation to predict emission.

## 6. Voltage distortion limits

Two different sets of voltage distortion limits are in place around the world: those based on IEEE 519 and those based on IEC 61000-2-2 [21]. For historical reasons, these limits are rather different.

### *Limits according to IEEE 519*

This recommended practice was originally published in 1981 to provide direction on dealing with harmonics introduced by static power converters and other nonlinear loads. A review was started in 1984 and published in 1992, incorporating the evolving understanding of the effect of static power converters and other nonlinear loads on electric power systems. In the latest version (2014), a new statistical method for

EBSCOhost - printed on 2/14/2023 2:46 PM via . All use subject to https://www.ebsco.com/terms-of-use

measuring and recording harmonic content is described, revised voltage distortion limits are established, and recommendations for increasing harmonic current limits place active and passive filters on an equal footing with phase shifted multi-pulse drives [20].

Regarding the voltage harmonic limits, at the point of connection, system owners or operators should limit line-to-neutral voltage harmonics as daily 99th percentile very-short-time (3 s) values and they should be less than 1.5 times the values given in Table 4. Also, weekly 95th percentile short-time (10 min) values should be less than the values given in Table 4. Even harmonic limits are one quarter of the odd harmonic limits.

**Table 4 – IEEE 519 voltage distortion limits**

| Bus Voltage at Point of Connection | Individual Harmonic [%] | Total Harmonic Distortion THD [%] |
|---|---|---|
| V ≤ 1kV | 5 | 8 |
| 1kV < V ≤ 69 kV | 3 | 5 |
| 69 kV < V ≤ 161 kV | 1.5 | 2.5 |
| 161 kV < V | 1 | 1.5 |

An important characteristic of the limits in IEEE 519 is that they are independent of frequency. The actual reason for this is lost to history, but the following explanation is a reasonable one considering the situation in the 1960s and 70s when the base for this standard was created:

- The main emission was in the form of inverters for large drives with a large inductance on the DC side; this gives a square-wave for the current with a spectrum decaying as one divided by the frequency.
- Capacitance in the grid was not very common, hence a reactive model for the grid impedance was a good approximation for a wide frequency range. In this model, the source impedance increases linearly with frequency.
- The resulting voltage distortion, being the product of impedance and current, becomes frequency independent.

### *Limits according to IEC 61000-2-2*

The limits used in IEC 61000-2-2 and in the European standard EN 50160 are all based on a 1981 paper presenting measurements for a range of locations in Europe [22]. The lower limits for higher frequency, for

EBSCOhost - printed on 2/14/2023 2:46 PM via . All use subject to https://www.ebsco.com/terms-of-use

even harmonics, and for triplen harmonics are simply a consequence of the lower levels of those harmonics present in European grids around 1980. Some minor changes have been made since then, including a slight rise in the permissible levels for the less common harmonic orders and a large rise for harmonic three. The latter occurred most likely because of the large increase in single-phase distortion equipment. More recently, a similar discussion is on-going about the need for increasing the compatibility levels for harmonics 15 and 21.

The indicative planning levels in IEC TR 61000-3-6, often used in connection agreements, are based on IEC 61000-2-2 as well. Also, the voltage characteristics in EN 50160 can be traced back to IEC 61000-2-2.

## 7. Primary and secondary emission

The terms ‘primary emission’ and ‘secondary emission’ were first introduced in power quality to explain the spread of supraharmonics in lighting installations. Later studies showed that the terms also simplified explanations for the spread of harmonics in the collection grid of wind power plants.

The terms hold for the terminals of an installation connected to the rest of the power grid. This installation can be a single LED lamp, a wind turbine, or even a complete WPP. The primary emission is the harmonic emission driven by what happens inside the installation, typically from power-electronics switching, but it can also, for example, be from transformer saturation. The secondary emission originates outside of the installation.

While it was originally thought that the secondary emission could only be significant at the point of connection of a wind power plant and only for higher frequencies [17], more recent calculations have shown that even between turbines and for lower-order harmonics, the secondary emission should not be neglected [23]. This means that any measurement of harmonic current will potentially contain contributions from both primary and secondary emissions. As shown in [24], the possible presence of both primary and secondary emissions makes it difficult, if not impossible, to determine what the contribution from any one installation to the emission (the ‘primary emission’) actually is. This offers a serious challenge in the verification of emission limits for wind-power installations.

EBSCOhost - printed on 2/14/2023 2:46 PM via . All use subject to https://www.ebsco.com/terms-of-use

## 8. Conclusion

In this chapter, a discussion regarding the procedures and standards used to evaluate the connection of WPPs to the public grid is presented. It can be observed that, depending on the approach used, different results and considerations come into play. Voltage and current limits and assessment procedures can be used depending on the standard. Furthermore, depending on the point of view (network operator or owner/operator of the WPP), one approach may be more advantageous than another. The voltage limits given in IEEE 519 and IEC 61000-2-2 have also been discussed.

Different methods for setting emission limits and for verifying those limits have advantages and disadvantages for different stakeholders. There will be no one method that is perfect for every stakeholder. However, the advantages and disadvantages of the different methods should be considered more transparently in the creation of new connection rules and also, more importantly, in the application of those rules. The rules are just a step in the requirement for the network operator to stay within planning levels and regulatory limits. This in turn is just one tool for ensuring a high probability of electromagnetic compatibility.

## References

[1] Jos Arrillaga, Neville R. Watson, Power system harmonics, Wiley, 2003.
[2] Angelo Baggini (Ed.), Handbook of power quality, Wiley, 2008.
[3] Roger C. Dugan, Mark F. McGranaghan, Surya Santoso, H. Wayne Beaty, Electric power systems quality, McGraw Hill, 2012.
[4] J.C. Das, Power system harmonics and passive filter design, Wiley-IEEE Press, 2015.
[5] Enrique Acha, Manuel Madrigal, Power systems harmonics, Wiley, 2001.
[6] Math H. J. Bollen, Irene Y. H. Gu, Signal processing of power quality disturbances, Wiley-Interscience, IEEE Press, 2006.
[7] IEC 61000-3-2: 2018, Electromagnetic compatibility (EMC) - Part 3-2: Limits - Limits for harmonic current emissions (equipment input current ≤16 A per phase).
[8] IEEE 519-2014 - IEEE Recommended Practice and Requirements for Harmonic Control in Electric Power Systems.
[9] M. Bollen, K. Yang, Harmonics – another aspect of the interaction between wind-power installations and the grid, 22nd Int. Conf. on Electricity Distribution (CIRED), 2013.
[10] M. Bollen, M. Häger, M. Olofsson, Allocation of emission limits for individual emitters at different voltage levels: flicker and harmonics, CIGRE Sessions, Paris, France, August 2010, paper C4-106.

EBSCOhost - printed on 2/14/2023 2:46 PM via . All use subject to https://www.ebsco.com/terms-of-use

[11] Jan Meyer, et al., Survey of international practice of calculating harmonic current emission limits, Int. Conf. Harmonics and Quality of Power, 2016.
[12] T. Hoevenaars, K. LeDoux, M. Colosino "Interpreting IEEE Std 519 and Meeting its Harmonic Limits in VFD Applications", in Proc. IEEE Industry Applications Society 50th Annual Petroleum and Chemical Industry Conference, 2003.
[13] IEC TR 61000-3-6:2008, Electromagnetic compatibility (EMC) - Part 3-6: Limits - Assessment of emission limits for the connection of distorting installations to MV, HV and EHV power systems.
[14] Kai Yang, M. H. J. Bollen, E. O. A. Larsson, Aggregation and amplification of wind-turbine harmonic emission in a wind park, IEEE Transactions on Power Delivery, Vol. 30, April 2015, pp.791-799.
[15] K. van Reusel, S. Bronckers, Summation rule for wind turbines' harmonics challenged by measurements, Int. Conf. Harmonics and Quality of Power, 2016.
[16] M. H. J. Bollen, S.K. Rönnberg, Primary and secondary harmonics emission; harmonic interaction – a set of definitions, Int. Conf. Harmonics and Quality of Power, 2016.
[17] K. Yang, On harmonic emission, propagation and aggregation in wind power plants, Doctoral Thesis, Luleå University of Technology, Sweden, 2015.
[18] IEC 61000-3-12:2011, Electromagnetic compatibility (EMC) - Part 3-12: Limits - Limits for harmonic currents produced by equipment connected to public low-voltage systems with input current >16 A and ≤ 75 A per phase.
[19] JWG C4/B4.38 Network modelling for harmonic Studies.
[20] Eaton Corporation, The effects of changes to IEEE 519-1992 to 2014, 2014.
[21] IEC 61000-2-2:2002, Electromagnetic compatibility (EMC) - Part 2-2: Environment - Compatibility levels for low-frequency conducted disturbances and signalling in public low-voltage power supply systems.
[22] CIGRE Working Group 26-05, Harmonics, characteristic parameters, methods of study, estimates of existing values in the network, Electra, No.77, July 1981, pp. 35-54.
[23] Daphne Schwanz, On Wind Power Plants Harmonic Emission and Single-Phase Photovoltaic Hosting Capacity, half-way report, Luleå University of Technology, Sweden, 2016.
[24] Daphne Schwanz, Math H. J. Bollen, Sarah K. Rönnberg, Anders Larsson, How large wind parks contribute to harmonic waveform distortion, Wind Integration Workshop, Stockholm, 2018.

EBSCOhost - printed on 2/14/2023 2:46 PM via . All use subject to https://www.ebsco.com/terms-of-use

# PART VII:

# VOLTAGE SAGS AND DIPS, POWER QUALITY

EBSCOhost - printed on 2/14/2023 2:46 PM via . All use subject to https://www.ebsco.com/terms-of-use

# CHAPTER THIRTY-EIGHT

# DIPS/SAGS IN POWER QUALITY

MIRCEA BUZDUGAN[1]

## Abstract

The paper is intended to be a brief review of an utmost important power quality events, namely voltage dips/sags that determine annoyances in the normal operation of equipment, especially of the sensitive ones. After the basic definitions of power quality from the introductory section, the main sources of voltage dips, their parameters, the effects they produce, along with a few mitigation measures are addressed. The main indices quantifying the performance of power systems according to the IEEE 1564-2014 guide are consequently presented. The final section is devoted to a short analysis of several measurements performed by the author at the secondary windings of a transformer substation, in terms of time and harmonic analysis.

**Keywords**— voltage dip/sag; voltage dip indices, depth of a dip, reference voltage, phase-angle jump, $THD_V$.

## Introduction

The term power quality is often used as an umbrella term covering many disturbances that occur in electrical systems. In recent decades, the quality of the electricity supply has become a significant concern for utilities, equipment manufacturers, and, not least, for end users.

[1] TUCN – Technical University of Cluj-Napoca - 28, Memorandumului str., 400114, Cluj-Napoca, Romania. Email: mircea.buzdugan@insta.utcluj.ro.

EBSCOhost - printed on 2/14/2023 2:46 PM via . All use subject to https://www.ebsco.com/terms-of-use

The specific literature abounds in power quality definitions, which use several criteria. Regarding this, a utility provider will look at power quality in terms of the continuity and reliability of their power system. Similarly, an equipment manufacturer will look at those features of the power system that make their equipment operate properly or improperly. Ultimately, the end-user of equipment powered by a power grid is the one who needs to be satisfied with the products they use, including both the equipment and electric power. Therefore, from the end user's stand point, power quality issues are represented by any problem that causes variations in current, voltage, and/or frequency that may cause improper operation of equipment.

In many situations, the term electrical power quality is identified with the quality of the supply voltage. This is due to the fact that power supply systems can control the quality of the delivered voltage, while, at the same time, having no control over the currents drawn by the various pieces of equipment connected to the grid. Therefore, regulations contained in power quality standards are dedicated to maintaining the supply voltage within certain limits. In this respect, the International Electrotechnical Commission (IEC) has defined power quality (see IEC/EN 61000-4-30) as the "characteristics of the electricity at a given point on an electrical system, evaluated against a set of reference technical parameters" [1].
IEEE 100:2000, "The Authoritative Dictionary of IEEE Standards Terms" defines power quality as "the concept of powering and grounding electronic equipment in a manner that is suitable to the operation of that equipment and compatible with the premise wiring system and other connected equipment" [2]. The above definition may be considered rather restrictive if one takes into account that, ultimately, any piece of equipment, even if it is not an electronic one, may be more or less sensitive and react in different ways to power quality issues, depending on the severity of the problem.

However, starting from the term power quality and because, generically, electric power represents to the product of voltage and current, power quality should be seen as a combination of voltage quality and current quality. Therefore, any deviation from an ideal voltage and/or ideal current constitutes a problem of power quality.

Without going into complicated analyses, it should be recalled that both ideal voltage and ideal current must have sinusoidal waveforms with constant amplitude and frequency. It is not easy, however, to distinguish between the two categories of disturbances. *Grosso modo*, it may be considered that a voltage disturbance originates in the power supply system, affecting the equipment connected to the grid; a disturbance in the

EBSCOhost - printed on 2/14/2023 2:46 PM via . All use subject to https://www.ebsco.com/terms-of-use

current is generated by the equipment connected to the grid, however, it affects equally the power quality of the grid.

Switching on an important load usually leads to a large current being drawn from the grid, which in turn causes a temporary drop in the supply voltage. From the network's point of view, the utility provider will consider this to be a consumer problem, while a network-connected user will only feel the voltage variation, which, from their point of view, will be the responsibility of the utility provider.

An alternative definition of power quality is one that distinguishes between continuity (reliability) and quality: continuity relates to interruptions in the supply, while quality refers to other perturbations. For instance, short interruptions are sometimes considered to be a component of continuity and sometimes of quality.

Good quality electricity must ensure compatibility between the electrical energy parameters supplied to end-users and the need to be sensitive to disturbances in their receivers.

At international level, standard deviations are set, in order that different disturbances fall within acceptable limits.

In a power system the main voltage quality issues include a large category of perturbations [3, 4, 5]:

- Transients (impulsive and oscillatory).
- Short duration variations: instantaneous (sag/swell); momentary and temporary (interruption, sag/swell).
- Long duration variations: sustained interruptions, under and over voltages (longer than one min.).
- Voltage imbalances.
- Waveform distortion: DC offset, harmonics, interharmonics, notching, noise.
- Voltage fluctuations.
- Power frequency variations.

This paper aims to provide a short outline of the issue of dips/sags—power quality events representing short duration variations. The interest in voltage dips/sags is mainly due to their impact on end-user equipment.

## Voltage Dips/Sags

Voltage sag is an alternative term for the phenomenon of voltage dip. The two terms, dip and sag, are considered interchangeable—dip is used in IEC/EN definitions of this phenomenon, while sag is preferred in the US

EBSCOhost - printed on 2/14/2023 2:46 PM via . All use subject to https://www.ebsco.com/terms-of-use

power quality community. Consequently, in [6] dips are defined as "sudden reductions of the voltage at a point in an electrical system, followed by voltage recovery after a short period of time from a few cycles to a few seconds"; in [5] sags are defined as "a decrease to between 0.1 and 0.9 pu in RMS voltage or current at the power frequency for durations of 0.5 cycle to 1 min. Typical values are 0.1 to 0.9 pu."

Voltage dips/sags are among the most common events in electrical networks.

Conversely, short interruptions represent a "sudden reduction of the voltage on all phases at a particular point on an electricity supply system, below a specified interruption threshold, followed by its restoration after a brief interval" [7].

A series of relevant example of dips, both in single phase and three phase systems can be found in [8].

### *A. Source of Voltage Dips/Sags*

The causes of voltage dips are multiple, but the three main causes are considered to be those highlighted in [8]:

- Short circuits and earth faults, earth-leakage faults, earth short-circuits and short-circuits, occurring at any point on the electricity supply system and stressing the insulation of electrical installations beyond their capacity; as an example, Figs. 1 and 2 depict the RMS values at the occurrence of a single fault (phase B) [9].
- The starting of large induction motors, arc furnaces, welding equipment.
- Energising of transformers.
- Energising of capacitors.

The switching of large loads, the energising of transformers, the starting of large motors, and the fluctuations of great magnitude that are characteristic for some loads, can all produce large changes in current, similar in effect to a short-circuit current. Although the effect is generally less severe at the point of occurrence, the resulting changes in voltage observed at certain locations are most often indistinguishable from those arising during short-circuit phenomena.

It is worth noting that the duration of a voltage dip due to a capacitor energising generally lasts only a few milliseconds and is often classified as a transient [8].

EBSCOhost - printed on 2/14/2023 2:46 PM via . All use subject to https://www.ebsco.com/terms-of-use

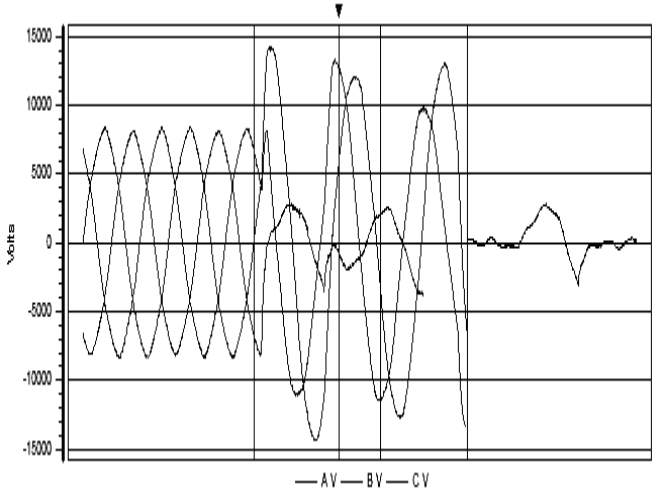



Figure 1. Waveforms at the occurrence of a single fault (phase B).

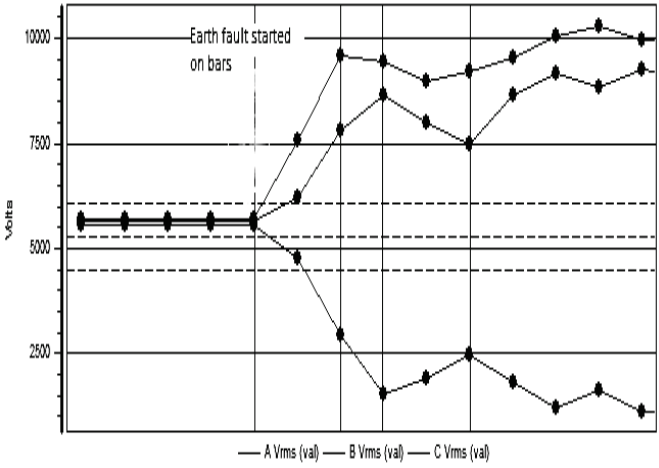



Figure 2. RMS values at the occurrence of a single fault (phase B).

The dielectric breakdown that occurs in short-circuits is either the result of stress due to overvoltage; or it is down to the weakening, damage, or bridging of insulation.

EBSCOhost - printed on 2/14/2023 2:46 PM via . All use subject to https://www.ebsco.com/terms-of-use

Causes of faults that determine these effects are many, the main ones being [7]:

- Atmospheric events: lightning and wind storms; snow, ice, salt deposits or atmospheric pollutants on insulators; debris carried by wind.
- Mechanical interference and damage: collision with vehicles, construction equipment, excavation equipment, animals and birds, tree branches, vandalism, and malicious acts.
- Network failure: deterioration due to aging, corrosion, rotting, and hidden or construction defects.
- Accidents or errors in operation and maintenance.
- Major natural events: floods, landslides, earthquakes, avalanches.

### *B. Voltage Dips/Sags Parameters*

A voltage dip is a two-dimensional electromagnetic disturbance. Its level is determined by (Fig. 3) [7, 8]:

- The reference voltage of a voltage dip—the value specified as the base on which the depth, thresholds, and other values are expressed in per unit or percentage terms.
- The start threshold of the voltage dip—the RMS value of the voltage on an electricity supply system specified for the purpose of defining the start of a voltage dip.
- The end threshold of the voltage dip—the RMS value of the voltage in an electricity supply system specified for the purpose of defining the end of a voltage dip.
- The residual voltage of the voltage dip—the minimum value of RMS voltage recorded during a voltage dip.
- The depth of the voltage dip—the difference between the reference voltage and the residual voltage.
- The duration of the voltage dip—the time interval between the instant at which the voltage at a particular point in an electricity supply system falls below the start threshold and the instant at which it rises to the end threshold.
- The phase angle of the voltage dip—the phase angle of the voltage waveform during an event segment is often different from the phase angle of the voltage waveform prior to the event; this difference is referred to as the “phase shift” or “phase-angle jump”;

EBSCOhost - printed on 2/14/2023 2:46 PM via . All use subject to https://www.ebsco.com/terms-of-use

for dips with multiple in-event segments, the phase shift may be different for each in-event segment.

Note that the term residual voltage is synonymous with other terms also used in the literature, namely retained voltage or remaining voltage.

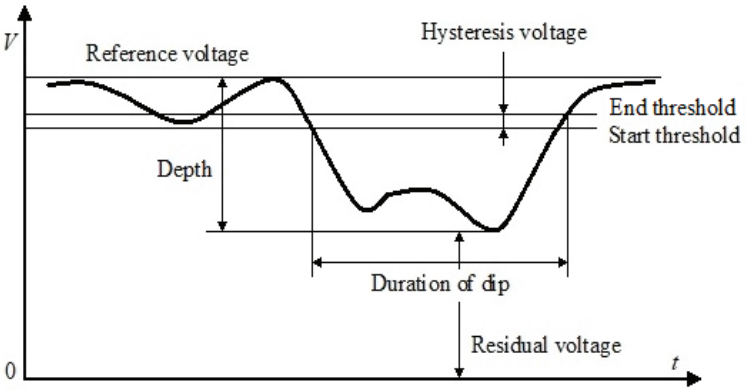



Figure 3. Characteristics of a voltage dip

Two methods are presented in [8] in order to characterize three-phase voltage dips. These are known as “ABC classification” and “symmetrical components classification.” The ABC classification distinguishes between seven types of voltage dips and is used more often due to its simplicity.

Supply systems are provided with protection devices that are able to disconnect short-circuits from energy sources. As soon as such a disconnection takes place, immediate recovery of the voltage, approximating its previous value, follows at every point of the circuit, except in those already disconnected.

There are also self-clearing faults, where short circuits disappear and the voltage recovers before disconnection takes place. Apart from when a self-clearing fault is involved, the duration of voltage dips is governed by the tripping speed of the protection devices.

The magnitude of a voltage dip is determined by the position of the observation point in relation to the short-circuit location and the source(s) of supply. The level to which the voltage dips at a particular observation point, is a random value, depending on its relative position to a short-circuit in the grid [10].

EBSCOhost - printed on 2/14/2023 2:46 PM via . All use subject to https://www.ebsco.com/terms-of-use

In the grid, the protection devices used are either fuses or breakers, controlled by different types of relay. Protective relays are most often designed with an inverse time characteristic—the shorter the short-circuit current, the longer the fault clearance time. Fuses have similar characteristics. The time characteristics and the settings of the fuses and relays are carefully coordinated so that a short-circuit detected by several devices is cleared at the most appropriate point on the circuit.

## *C. Effects of Dips/Sags*

The majority of equipment malfunctions are due to dips caused by faults. As EMC phenomena, voltage dips that lead to short interruptions can cause a piece of equipment connected to the supply network to behave in a manner other than intended. Voltage dips cause a temporary diminution or even stoppage of the energy flow to the equipment, which may lead to a degradation of performance, possibly extending to a complete cessation of operation. When the voltage drops to a too low value, or the duration of the drop exceed certain time limits, the equipment will operate improperly or will be disconnected by the protection system tripping.

As with every phenomenon that disturbs the electricity supply, the severity of the effects of a voltage dip depends not just on the direct effects it has on the equipment in question, but also on how important or critical the functions of the equipment being used are. Modern manufacturing methods often involve complex continuous processes that use multiple devices working together. Therefore, a malfunction or decommissioning of a device in response to a voltage dip may require the shutting down of an entire production process, with damage caused to the equipment. This can be one of the most serious and costly consequences of these events. Such consequential damages or losses may depend also on how precarious the design of the process is.

The economic consequences of voltage dips can be significant, causing loss of production, material losses, costs of restarting technological processes, equipment failure, delays in deliveries, etc. Finally, they may also affect the position of utility companies in the energy market.

Some of the more common effects on certain types of equipment are described in the literature [7, 8, 10]:

- *IT equipment and control systems*

Generally, the main functional units of these sorts of equipment require DC power modules with rectifiers; consequently, the minimum voltage attained during voltage dips (the depth) may affect their operation.

EBSCOhost - printed on 2/14/2023 2:46 PM via . All use subject to https://www.ebsco.com/terms-of-use

- *Relays and contactors*

Relays and contactors trip when the voltage falls below about 80% of the rated value for more than one cycle; the consequences vary with the application, but can sometimes be very severe from a financial or safety standpoint.

- *Induction motors*

During a voltage dip, the torque of the motor, which depends on the voltage square and the mechanical load, starts to decrease, reducing its speed; there may be an increase in the current until a new point of operation is reached.

Induction motors are less sensitive to voltage dips with a residual voltage exceeding 70% of the rated voltage. They determine a current increase of 25% to 35%, while the power absorbed in the grid is fairly constant or decreases slightly. The effects of voltage dips are mainly of a thermal nature. Overcurrent due to voltage recovery is generally limited and, for directly connected motors, does not exceed the usual starting current.

Voltage recovery following a voltage dip can also be a critical phase if there are a large number of motors connected to the same bus. In this case, the high inrush current at voltage recovery may cause a secondary voltage dip, consequently delaying voltage recovery and retarding the re-acceleration of the motors to normal speed. In some cases, re-acceleration is not possible and disconnection followed by a motor restart process is necessary.

- *Synchronous motors*

The operation of a synchronous motor is defined at its output by its torque-speed and at its input by the supply voltage and the active power drawn from the supply system. Magnetic flux, reactive power, and internal rotor angle are variable, depending on the voltage and the torque. A voltage dip can be tolerated as long as new and stable operating conditions are provided. This is generally the case of dips with 75% or 80% residual voltage (direct component). In addition, the excitation circuit may be affected and should be considered.

More severe conditions may create a loss of synchronism with an increase in the rotor angle up to the limit of its stability. Reaching this limit angle depends on the duration of the voltage dip, the mechanical time constant, and the level to which the voltage drops.

- *Power drive systems*

In the case of power drive systems, especially of adjustable power drive systems, which can be sensitive even to minor voltage drops, the

EBSCOhost - printed on 2/14/2023 2:46 PM via . All use subject to https://www.ebsco.com/terms-of-use

effects of voltage dips can be quite complex, and the various components need to be considered both separately and as an ensemble.

The effect on a control element can be critical, because reducing the voltage causes a reduction in the power that can be transferred to the motor and from there to the driven equipment—this can lead to loss of control.

Regenerative converters can be particularly sensitive or require special attention, especially if the voltage dips coincide with a reverse power flow.

Power converters do not have the capacity to store energy, or only in a very limited fashion in certain light conditions.

- *High-pressure discharge lamps*

High-pressure discharge lamps are extinguished by voltage dips that reduce the voltage to less than 90% of the rated value. Their restart may take several minutes due to cooling and loss of pressure.

Lighting systems containing electronic components can also be affected as in the case of LED lighting systems.

In light of the above considerations, international standards provide rules regarding immunity to voltage dips. IEC 61000-4-11 [11] deals with immunity test methods for electrical and electronic equipment with a rated input current not exceeding 16 A per phase; IEC 61000-4-34 [12] applies to the same type of equipment with a rated input current exceeding 16 A per phase.

## *D. Mitigation of Dips/Sags*

The standard approach to electromagnetic compatibility is to apply coordinated emission and immunity limits. Compatibility between equipment or installations and the power supply can be improved in several ways:

- through alterations to the power grid;
- installing mitigation equipment at the interface between sensitive equipment and the grid;
- improving the equipment or the installation [13].

It is well known that a system is electromagnetically compatible with its environment if it satisfies three criteria [14]:

1. It does not cause interference with other systems (emissions).
2. It is not susceptible to emissions from other systems (immunity).
3. It does not cause interference with itself.

EBSCOhost - printed on 2/14/2023 2:46 PM via . All use subject to https://www.ebsco.com/terms-of-use

In the case of voltage dips, which are a normal response of an electric grid to short-circuit or any increase in current, the disturbance level has two dimensions: residual voltage and dip duration.

The residual voltage can vary from zero volts to the normal level of the supply voltage, depending on the relative positions of the short-circuiting locations, the observation point, and the sources of generation.

The duration can be modified, being determined by the speed of the short-circuit clearance time. The clearance time and, consequently, the duration of the voltage dip also depends on the location of the short-circuits.

If the power quality event is other than a short-circuit, its duration depends on the type of event. As such, there is a restrained margin for limiting emissions in terms of the disturbance level, which justifies the necessity of analysing the immunity of equipment exposed to voltage dips and whether it is possible to assure their immunity with respect to these events.

In the case of voltage dips of moderate depth and duration, equipment may have a certain level of inherent immunity determined by its energy storage capacity or inertia. It is important that equipment is designed with this in mind to ensure that it has these features. However, for severe voltage dips, immunity is not a feasible concept. Therefore, immunity to these disturbances tends to be an extrinsic feature. Consequently, one has to provide fast energy restoration through an alternative source or provide mitigation measures, ensuring that the equipment and associated processes can withstand the new conditions of a severe voltage dip.

Several mitigation measures use an energy storage capability to supply the missing energy of the power grid for a limited time. This energy can compensate for a voltage dip's missing energy, regardless of the residual voltage. The ability of the equipment to overcome voltage dips over a certain period of time depends on the relationship between the stored energy and the power demand of the process concerned. In many cases, a certain reaction time (i.e. a few milliseconds) must be considered. Since storing energy is an expensive process, protection needs to be directed to those parts of the process that are particularly sensitive.

Other mitigation measures that do not have energy storage capability cannot cover supply interruptions, but have the ability to compensate for voltage dips with residual voltages of about 50%. Generally, the duration of a voltage dip is not an important parameter in these methods.

Mitigation needs to be approached on the basis of both economic and technical analyses, such those presented in [15].

EBSCOhost - printed on 2/14/2023 2:46 PM via . All use subject to https://www.ebsco.com/terms-of-use

### *E. Measurement of Voltage Dips/Sags [7]*

All voltage values related to voltage dips are RMS values, taken over a minimum of one half period of the voltage at the supply frequency.

An important dimension of voltage dips is their magnitude, quantified by the residual value. This dimension has been expressed both as the value at which the voltage drops during the event and the amount by which that value is less than the pre-existing voltage or other reference value.

Measurement of voltage dips requires the recording of the value of the voltage depth, the duration of the event, and the number of events during a measurement period.

In order to record these values and to allow for comparison of the results, it is necessary to adopt certain rather arbitrary conventions.

During a voltage dip, the fixed reference voltage is used. The residual voltage is usually expressed in relative terms, per cent or per unit. The basis of the relationship is, by convention, the nominal or declared voltage of the grid at the observation point. Thus, the reference voltage for measurements in low and medium voltage grids is usually the nominal voltage or the declared voltage of the network in question.

The sliding reference voltage is another approach, which may be appropriate—measured at different points of the network and operating at different voltages, the subject of the survey includes the comparison of one phase short-circuit voltage dips. This often occurs when measurements are performed on high-voltage networks. In addition, it is useful to analyse to what extent measurements performed on high voltage events correspond to those at a lower voltage, in the knowledge that most equipment is connected to low and medium voltage feeders.

The normal voltage range on high voltage networks may vary freely, which is not the case for low and medium voltage networks. These last ones operate in a regime imposed by the transformer tapping range. An event that causes a certain depth of voltage dips measured on a high voltage network is likely to result in a wide variety of residual voltages at different observation points in lower voltage networks, even if they are situated directly downstream. This is due to the fact that the voltages that precede the voltage dips will vary at different points depending on the taps of the transformers. Under these conditions, the voltage dip can be measured in relation to the voltage that precedes it, in order to allow the change of voltage to be recorded. In this case, to represent the voltage preceding the onset of the voltage dip, the reference voltage is a continuously calculated value over a certain range, generally much longer than the duration of the voltage dip. This reference voltage is referred to as a sliding reference voltage.

EBSCOhost - printed on 2/14/2023 2:46 PM via . All use subject to https://www.ebsco.com/terms-of-use

The choice of voltage thresholds to indicate the start and end of a voltage dip depends on whether the reference voltage is a sliding value representing the immediately preceding voltage or a fixed one, namely the rated or the declared voltage. Note that a fixed reference voltage is considered in the first place.

At any given moment of observation on the supply network, the voltage constantly changes in response to permanent changes and the switching in of loads at different points on the network. Typically, the network is designed to maintain these voltage variations in a specified range, at least under normal supply conditions.

At some observation points, located far enough from the location of the event in question, especially those at which the pre-existing voltage is slightly above the range of the voltage variation, the residual voltage can remain high enough to always remain in this range. In measurements performed at such points, the residual voltage, belonging to the intended range, does not need to be distinguished from voltage variations arising due to normal fluctuations of the local load. By convention, this case is excluded from the dip measurement. For this reason, many voltage dip measurements have been based on a voltage threshold corresponding to the lower limit of the expected range of variation. Only events where the voltage drops to values situated below this threshold are recorded as voltage dips. Each voltage dip is considered from the very moment at which the voltage drops below the set threshold and ends when the voltage recovers to at least the same value.

If at an observation point the voltage at a certain moment of time is very close to the bottom of the intended range of variation, it is possible that normal variations and load switching may cause small voltage oscillations around the lower limit of the range. The number of voltage dips recorded at such an observation point could be considerably inflated by these load-induced oscillations. One method of excluding these variations is to apply another threshold, situated below the normal range of variation.

Another method is the hysteresis method, which uses two thresholds. This last approach classifies only the events in which the voltage falls below a threshold corresponding to the bottom of the range as voltage dips and recovers to a second threshold, situated usually at 1% of the reference voltage above the first threshold.

When the reference voltage is a sliding voltage, calculated continuously to represent the voltage level just before the dip, this process has a smoothing effect that automatically eliminates most of the variations

EBSCOhost - printed on 2/14/2023 2:46 PM via . All use subject to https://www.ebsco.com/terms-of-use

due to local load fluctuations. In this case, the start and end dip thresholds can be chosen at values very close to the sliding reference voltage.

In the case of multi-phase measurements, voltage dips that overlap over time are conventionally considered as a single event. The interval of time between the moment when the first phase or line voltage drops below the start threshold until the moment when the last phase or line voltage exceeds the end threshold is calculated.

Although voltage dips often have complex shapes, in different measurement regimes performed at several sites in order to obtain statistical data, a simplified procedure is adopted. This approach treats voltage dips as if they are all single depth events. Thus, a single data pair is recorded for each dip. The residual voltage is the lowest voltage that occurs during the event. The duration is measured from the moment when the voltage drops below the start threshold until it is equal to or higher than the end threshold.

However, some measured events have been proved to be more complex, their voltage attaining several levels during an event. In this case, the characterization of the voltage dip as having a residual voltage equivalent to the lowest voltage reached and a duration corresponding to the start and end thresholds may be an exaggeration of the importance of the disturbance.

In order to deal with the complexity of non-rectangular dips, it is necessary to indicate several gradations on the voltage scale and to record the duration for which the voltage is equal to or falls below each of the gradations. This results in the recording of several residual voltage-time data pairs to describe each voltage dip.

In collecting or presenting the results of a measurement regime for voltage dips, it is necessary to respect the two-dimensional nature of the phenomenon, which suggests a two-dimensional matrix or a tabular approach—the rows contain the classification of depths or residual voltages, while the columns contain the duration.

Reclosing operations often lead to multiple voltage dips for the same primary event. It is unlikely that repetitive disturbances will repeatedly affect equipment and processes. It is therefore misleading to consider these disturbances as distinct events. In order to take this effect into account, the concept of aggregation can be applied. A set of rules that define how to group events that occur within a limited time frame and characterize the resulting equivalent event in terms of amplitude and duration needs to be used. For example, all events within a one-minute interval could be considered as a single event whose amplitude and duration make it the most severe voltage dip observed during this time interval. It should be

EBSCOhost - printed on 2/14/2023 2:46 PM via . All use subject to https://www.ebsco.com/terms-of-use

noted that using aggregation can have a significant impact on the number and characteristics of recorded events. In addition, the resulting equivalent events do not necessarily accurately reflect impacts on equipment and processes.

In practice, various aggregation procedures are considered, the most extensively used are: voltage-level aggregation; phase aggregation; time aggregation; and space aggregation (for details see [10]).

### *F. Voltage Dips/Sags Indices*

Voltage dip indices allow us to quantify the performance of power systems.

Voltage dips can occur at any location in an electrical system, with a frequency of several times to hundreds of times a year [16-20]. The large variation in a customer's sensitivity to voltage dips makes it difficult to prescribe a specific set of indices.

To evaluate the performance of an electrical system in terms of voltage dips, the IEEE 1564-2014 guide presents a five-step procedure [18]:

- obtain the sampled voltage at a specified sampling rate and resolution;
- calculate the event characteristics as a function of time from the sampled voltages;
- calculate the characteristics of a singular event from the event characteristics;
- calculate site indices from single event indices of all the events measured over a certain time period;
- calculate system indices in location indices for all locations monitored in a particular power system.

In the IEEE guidelines, the term sag is preferred to the IEC/EN term dip. Consequently, in the following considerations, sag will be used.

The IEEE 1564 instructions advocate the calculation of one or more characteristics from the sampled voltages. For single-channel and multi-channel measurements, the RMS voltage is calculated over one cycle, the RMS voltage being estimated á posteriori and calculated using the previous $N$ instantaneous voltage samples. The algorithm used is called a "one cycle window" algorithm.

The RMS values are updated every half-cycle, using only half a cycle of instantaneous values; the algorithm used is called a "half-cycle

EBSCOhost - printed on 2/14/2023 2:46 PM via . All use subject to https://www.ebsco.com/terms-of-use

window" algorithm. This magnitude is defined in IEC 61000-4-30 as $V_{rms(1/2)}$.

For three-phase measurements, either the minimum $V_{rms(1/2)}$ or the "characteristic voltage" (a complex phasor needed to describe a voltage sag) are used to characterize the event. The time functions used to indicate single events are the retained voltage, the depth, and the duration.

The equation of the one cycle window RMS voltage is:

$$V_{rms}(k) = \sqrt{\frac{1}{N}\sum_{i=1+k-N}^{k} v_i^2} \tag{1}$$

where $N$ is the number of samples per cycle, $v_i$ is the sampled voltage waveform, and $k = 1, 2, 3$, etc.

The equation for the half-cycle window RMS is:

$$V_{rms(1/2)}(k) = \sqrt{\frac{2}{N}\sum_{i=k-(N/2)+1}^{k} v_i^2} \tag{2}$$

The half cycle algorithm is more sensitive to changes in the voltage and is faster at detecting an event.

In addition to the two-index method that uses the retained voltage or depth and the duration of the sag, IEEE 1564 introduces two single-indentation methods:

- the energy of the voltage sag and,
- the severity of the voltage sag.

In both cases, the severity of each event is quantified by a single value. The severity of a voltage sag is calculated from the retained voltage $V$ per unit and the duration $d$ of a voltage sag in combination with a reference curve (ITIC curve or the SEMI F47 or other reference curves).

$$S_e = \frac{1-V}{1-V_{ref}(d)} \tag{3}$$

Events with longer duration and a lower magnitude will have higher values of voltage sag severity indices.

EBSCOhost - printed on 2/14/2023 2:46 PM via . All use subject to https://www.ebsco.com/terms-of-use

The total voltage sag severity/the average voltage severity is defined for a single site—these are the sum of voltage sag severities for all qualifying events during a period.

Fig. 4 depicts the ITIC curve (issued by the Information Technology Industry Council), which represents a modified version of the CBEMA (Computer Business Equipment Manufacturers Association) power acceptability curve for power quality evaluation of a survey of the secondary voltage of a transformer substation. The curve reveals six points at which the RMS voltage of line *B* is below the tolerance curve, which means that interval sags occurred [21].

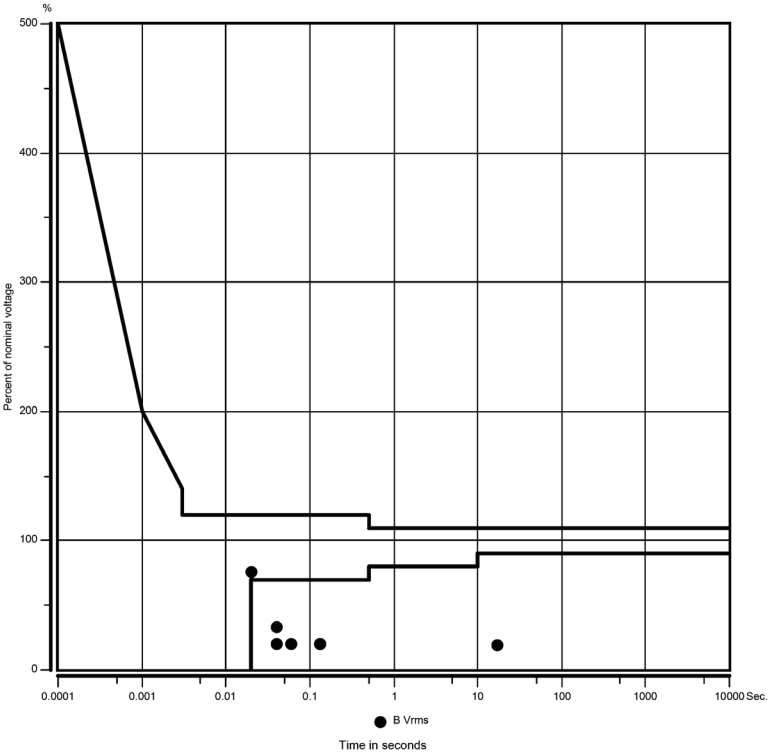



Figure 4. The ITIC curve of the survey

IEEE 1564 also defines the characteristic energy of a voltage sag:

EBSCOhost - printed on 2/14/2023 2:46 PM via . All use subject to https://www.ebsco.com/terms-of-use

$$E_{VS} = \int_0^T \left[ 1 - \left( \frac{V(t)}{V_{nom}} \right)^2 \right] dt \tag{4}$$

which represents the duration of an interruption that would determine the same energy loss for a resistive load.

The energy of the voltage sag can also be defined as the non-delivered energy to a resistive load, divided by the rated power of that load.

For three phase events the voltage sag energy is defined as the sum of the voltage dip energy in the individual channels:

$$E_{VS} = \sum_{k=1}^{3} E_{VSk} \tag{5}$$

It also introduces the 'Sag Energy Index' (SEI), which is the sum of voltage sag energies for all *n* qualified disturbances, at a given site over a given time interval (normally one-month or one-year):

$$SEI = \sum_{k=1}^{n} E_{VS-k} \tag{6}$$

Similarly, the 'Average Sag Energy Index' or ASEI is:

$$ASEI = \frac{1}{n} \sum_{k=1}^{n} E_{VS-k} \tag{7}$$

*SARFIx* index, an acronym that stands for "System Average RMS Variation Frequency Index" is a power quality index, introduced in [20], that provides a count or rate of voltage dips. It can be defined for a single monitor, a single customer service, a feeder, one or more substations, or an entire power delivery system. There are two types of *SARFI* indices: *SARFIx* and *SARFI-Curve* [22]. *SARFIx* is defined with respect to a voltage threshold x, and gives the number of events, with a duration of between a half-cycle and one minute, whose retained voltages deviate from the voltage threshold [23].

EBSCOhost - printed on 2/14/2023 2:46 PM via . All use subject to https://www.ebsco.com/terms-of-use

$$SARFI_X = \frac{\sum_{k=1}^{n_s} N_k}{N_T} \tag{8}$$

where *ns* is the number of events, *Ni* is the number of customers experiencing an event and *NT* is the number of customers served by the section to be assessed.

The index for an entire system can be obtained as follows

$$SARFI = \frac{\sum_{k=1}^{n_s} N_k \cdot SARFI_{(k)}}{N_T} \tag{9}$$

*SARFI-Curve* gives the event rate outside the operating area covered by an acceptability curve. Usually two SARFI-Curves are used:

- SARFI-ITIC: Count or rate of voltage sags and interruptions with retained voltage and duration below the lower portion of the ITI Curve;
- SARFI-SEMI: Count or rate of voltage sags and interruptions with retained voltage and duration below the lower portion of the SEMI F47 Curve.

## Conclusions

Voltage dip/sag events can be of serious concern to utility providers, equipment manufacturers, and end-users, greatly affecting power quality, especially due to their high level of hazard, the variety of their causation, and their high frequency of occurrence.

To improve the performance of a power supply network and get rid of voltage dips can be very expensive, and may be virtually impossible, especially in the case of sensitive loads, which proliferate in modern electric power systems.

Power quality detection and mitigation systems, requiring fast and reliable methods, along with well performing power quality analyzers, are needed

At the same time, for various service quality assessments, the development of variation indices, which provide a means of quantifying

EBSCOhost - printed on 2/14/2023 2:46 PM via . All use subject to https://www.ebsco.com/terms-of-use

power quality events, and the development of common terminology, are necessary.

## References

[1] IEC 61000-4-30:2015 Electromagnetic compatibility (EMC) - Part 4-30: Testing and measurement techniques - Power quality measurement methods.
[2] IEEE 100 - The Authoritative Dictionary of IEEE Standards Terms, Seventh Edition, Published by Standards Information Network IEEE Press, 2000.
[3] Chattopadhyay, S., Mitra, M., Sengupta, S., Electric Power Quality, Springer Science + Business Media B.V., 2011.
[4] Gomatom, K., Short, T., Continuity of Supply, in Handbook of Power Quality, edited by Angelo Baggini, John Wiley & Sons Ltd., 2008.
[5] IEEE Std. 1159-1995, Recommended Practice for Monitoring Electric Power Quality.
[6] IEC 60050-161:1990, International Electrotechnical Vocabulary. Chapter 161: Electromagnetic compatibility.
[7] IEC TR 61000-2-8:2002 Electromagnetic compatibility (EMC) - Part 2-8: Environment - Voltage dips and short interruptions on public electric power supply systems with statistical measurement results.
[8] Bollen, M. H. J., Yu-Hua Gu, I., Signal Processing of Power Quality Disturbances, John Wiley & Sons, Inc., 2006.
[9] Buzdugan, M., Bălan, H., Laslo, H., Electromagnetic Compatibility Issues during Faults in Electric Power Systems, International Conference on Renewable Energies and Power Quality (ICREPQ'18), Salamanca, March 2018.
[10] Hanzelka, Z., Voltage Dips and Short Supply Interruptions, in Handbook of Power Quality, edited by Angelo Baggini, John Wiley & Sons Ltd., 2008.
[11] IEC 61000-4-11: 2004-03 Electromagnetic compatibility (EMC): Testing and measurement techniques - Voltage dips, short interruptions and voltage variations immunity tests.
[12] IEC 61000-4-34:2005 Electromagnetic compatibility (EMC): Testing and measurement techniques - Voltage dips, short interruptions and voltage variations immunity tests for equipment with input current more than 16 A per phase.
[13] CIGRE/CIRED/UIE Joint Working Group C4.110, Voltage Dip Immunity of Equipment and Installations, 2010.
[14] Paul, C. R., Introduction to electromagnetic compatibility, John Wiley & Sons, Inc., 2006.
[15] IEEE 1346-1998 - IEEE Recommended Practice for Evaluating Electric Power System Compatibility with Electronic Process Equipment.
[16] Short, T. A., Electric Power Distribution Handbook, Taylor & Francis Group, LLC, 2014.
[17] Joint WG CIGRE C4.7/CIRED, "Power Quality Indices and Objectives, CIGRE Report, March 2004.

EBSCOhost - printed on 2/14/2023 2:46 PM via . All use subject to https://www.ebsco.com/terms-of-use

[18] IEEE 1564-2014 - IEEE Guide for Voltage Sag Indices.
[19] Sabin, D., Bollen, M., Overview of IEEE Std. 1564-2014 Guide for Voltage Sag Indices CIRED, 23rd International Conference on Electricity Distribution Lyon, June 2015.
[20] Liao, H., Milanović, J. V., Comparative Analysis of Different Voltage Sag Characterisation Indices, CIRED, 23rd International Conference on Electricity Distribution Lyon, June 2015.
[21] Buzdugan, M., Balan, H., About power quality monitoring in residential grids, International Conference on Renewable Energies and Power Quality (ICREPQ'17), Malaga, April 2017.
[22] Brooks, D. L., Dugan, R. C., Waclawiak, M., Sundaram, A., "Indices for assessing utility distribution system RMS variation performance," IEEE Transactions on Power Delivery, vol.13, 2008.
[23] Martinez-Velasco, J. A., Martin-Arnedo, J., Calculation of Voltage Sag Indices for Distribution Networks, International Conference on Power Systems Transients (IPST'05), Montreal, June 2005.

EBSCOhost - printed on 2/14/2023 2:46 PM via . All use subject to https://www.ebsco.com/terms-of-use

# CHAPTER THIRTY-NINE

# THE INFLUENCE OF NETWORK CHARACTERISTICS AND ENVIRONMENTAL CONDITIONS ON VOLTAGE DIPS IN MV NETWORKS

R. CHIUMEO[1], C. GANDOLFI[1], L. TENTI[1]

## Abstract

The number of voltage dips monitored in medium voltage networks, may depend in a number of ways on certain network characteristics (i.e., network configuration, type of neutral operation, geographical area, overhead lines and cable length, etc.), as well as on environmental phenomena (lightning, presence of cell storms). Investigations on these influences have been performed by applying both correlation techniques and multiple linear regression analysis on network and meteorological time series data. Data on voltage dips have been collected over several years of monitoring by the Italian medium voltage network monitoring system QuEEN[2]. As for meteorological factors, data on lightning density and on the occurrence of storm cells have been provided, respectively, by the Italian lightning location system SIRF[3] and by the storm tracking system STAF[4] based on radar reflectivity data. The contribution of each network/environmental factor to the number of voltage dips has been evaluated by time series correlation and/or by multiple linear regression methods. The results of data analysis confirm that overhead line length has

[1] RSE S.p.A. Ricerca sul Sistema Energetico, RSE S.p.A. Via Rubattino 54, 20134, Milano, Italy, e-mail: liliana.tenti@rse-web.it.
[2] QuEEN: **Qu**ality of **E**lectric **En**ergy.
[3] SIRF: **S**istema **I**taliano **R**ilevamento **F**ulmini by CESI S.p.A.
[4] STAF: **S**torm **T**rack **A**lert and **F**orecast is a meteorological application developed by RSE.

EBSCOhost - printed on 2/14/2023 2:46 PM via . All use subject to https://www.ebsco.com/terms-of-use

a significant influence on these disturbances, while cable line length has, as expected, only a negligible effect. The influence of lightning seems to be less important than expected; this is also the case with the neutral type of operation. Voltage dips do, however, appear to relate, in a non-negligible way, to geographical area. The influence of meteorological conditions is more evident when correlating voltage dips with the occurrence of storm cells, rather than with lightning strike density.

**Keywords**: Voltage dip indices, voltage dip origin, multiple regression analysis, correlation, network characteristics, environmental factors, lightning, storm cells

## Introduction

The influence of the principal network parameters and of lightning strike density on voltage dips has been investigated since the beginning of the Italian MV distribution network monitoring. In particular, in 2006 a good correlation (correlation index = 0.93) was found between the average number of voltage dips per week monitored during the spring-summer period and average lightning strike density in Italy, as recorded by the Italian lightning location system SIRF [1]. Besides seasonal limitations, statistics on voltage dips at that time were collected in a limited number of MV bus-bars of HV/MV substations, all characterized by compensated neutral operation. More detailed analysis was then performed on the 2006–2007 events statistic, by applying multiple linear regression analysis (MLR) to evaluate the influence of different network and environmental parameters on the number of voltage dips [2], [3]. MLR allows investigation of the influence of each single network characteristic on an event's frequency, independently of all other parameters[5].

The first regression models implemented considered the *averaged lightning strike density to soil* per week *associated to each Italian Provincia* or district where a measurement unit had been installed as the main environmental factor to be taken into account. According to these models, aerial line length appeared to be able to properly take into account both lightning and other fault-producing factors (occasional contacts with external objects, component defects, insulator pollution).

[5] These results cannot be achieved by analyzing voltage dip performance by simple aggregation of MV networks; this kind of analysis is, however, available at the web site (http://queen.rse-web.it).

EBSCOhost - printed on 2/14/2023 2:46 PM via . All use subject to https://www.ebsco.com/terms-of-use

This chapter deals, in particular, with the results of successive studies. MLR analyses have been applied: i) to *an improved statistical base* (voltage dips monitored at 400 HV/MV primary substations over the three-year period 2009–2011); ii) taking into account of a *more localized measurement of the average lightning strike density* to soil by evaluating this parameter, referring it to 400 circular regions with a 15 km radius centered on QuEEN substation monitored bus-bars; iii) evaluating network voltage dip performance by means of proper indices, depending not only on the number of events, but also on their characteristics (duration and residual voltage) [4]–[8]. MLR analysis only applied to MV-origin events—those caused by faults in MV distribution networks.

Finally, geographic and temporal correlations were made between voltage dip statistics and the storm cells identified by the STAF system using radar reflectivity measurements[6]. The aim was to verify the hypothesis that the frequency of voltage dips may depend less on simple occurrence of lightning strikes and more on atmospheric phenomena considered as a whole, taking into account wind conditions, humidity levels, and the probability of lightning strikes, etc.

## Correlations Between Lightning Activity and Voltage Dip Indices

Lightning activity has been expressed in terms of weekly lightning strike density to soil, where density is referred to the "Total Circular Area Monitored" (TCAM). This corresponds to the sum of 400 circular areas of 15 km[7] radius centered on QuEEN monitored primary substation locations. Voltage dips were evaluated by use of synthetic system indices, $I_i$, summarized in Table 1, and based on proper handling of the event features (residual voltage, or depth and duration).

The investigations, at first, examined the correlation of the weekly time series of lightning strike density Ng to the TCAM, with the corresponding time series of the voltage dip indices, expressed per measured point. This covered the 2009–2011 spring-summer monitoring periods.

[6] Reflectivity means the intensity in dB of the signal received by the radar: the higher the signal, the higher the intensity of the meteorological phenomenon.

[7] In the Italian distribution network, MV lines fed by MV busbars typically have an average length around 15 km.

EBSCOhost - printed on 2/14/2023 2:46 PM via . All use subject to https://www.ebsco.com/terms-of-use

**Table 1. Voltage Dip Indices.**

| Indices $I_i$ | Definition |
|---|---|
| **N** | total number of events occurred in the monitoring period |
| **N2a (N3b)** | total number of events occurred under Class 2 (Class 3) immunity curve |
| **R-DFI** | Regulated Dip Frequency Index [5] |
| **DSI_2a (DSI_3b)** | Discrete Severity Index [6] referred to Class 2 (Class 3) immunity curve |
| **MVTA2 (MVTA3)** | Missing Voltage Time Area [7] referred to Class 2 (Class 3) immunity curve |

The aim of these preliminary analyses was to verify whether the two variables displayed covariance and to quantify the strength of any relationship between them. Table 2 and

Figure **1** confirm the existence of a good correlation between weekly voltage dips and weekly lightning strike density to soil as evaluated per TCAM. In particular, the count indices (N, N2a) and the Regulated Dip Frequency Index (R-DFI)[8] present higher correlation coefficients in comparison to the "energetic" indices (i.e. MVTA2), which show poor performance. In fact, the former indices take into account all the events and their severity, which depends on their relationship to the immunity curves.

**Table 2. Correlation Indices ($I_i$, Ng).**

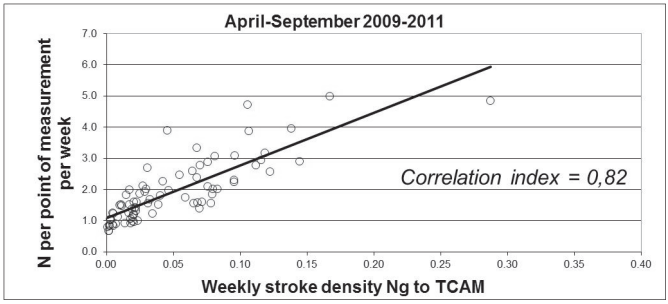
| Monitoring period | N,Ng | N2a,Ng | N3b,Ng | MVTA2,Ng | MVTA3,Ng | R-DFI,Ng | DSI_2a,Ng | DSI_3b,Ng |
|---|---|---|---|---|---|---|---|---|
| AprSep 3 years | 0.82 | 0.74 | 0.62 | 0.54 | 0.34 | 0.72 | 0.79 | 0.78 |
| AprSep 2009 | 0.83 | 0.68 | 0.49 | 0.48 | 0.14 | 0.64 | 0.76 | 0.74 |
| AprSep 2010 | 0.87 | 0.83 | 0.72 | 0.69 | 0.61 | 0.81 | 0.85 | 0.84 |
| AprSep 2011 | 0.80 | 0.84 | 0.76 | 0.51 | 0.43 | 0.83 | 0.85 | 0.83 |

The extension of the monitoring period to autumn and winter makes the correlation index drop to 0.51 for the best correlated voltage dip index (N), and to lower values for the others.

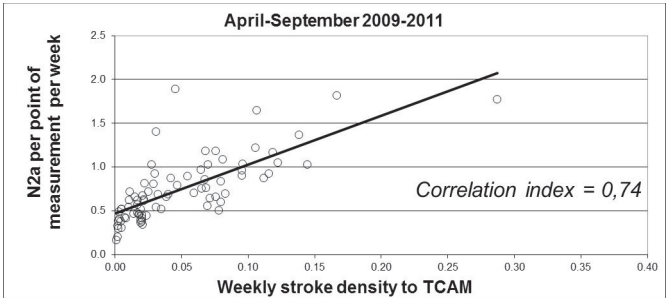
[8] This index is evaluated as a voltage dips weighted sum.

EBSCOhost - printed on 2/14/2023 2:46 PM via . All use subject to https://www.ebsco.com/terms-of-use

Figure **2** clearly shows the reasons for this drop—the October-March period is characterized by a significant monthly number (N) of voltage dips observed (grey curve) and a very low lightning strike density (black curve). This suggests that in autumn and winter, it may be better to consider meteorological perturbations as a whole, including lightning, wind, humidity, ice, etc., as significant environmental factors on events occurring in MV lines.




a)




b)

Figure 1. Correlation between weekly lightning strike density with Total Circular Area Monitored and voltage dip indices: a) N; b) N2a.

EBSCOhost - printed on 2/14/2023 2:46 PM via . All use subject to https://www.ebsco.com/terms-of-use

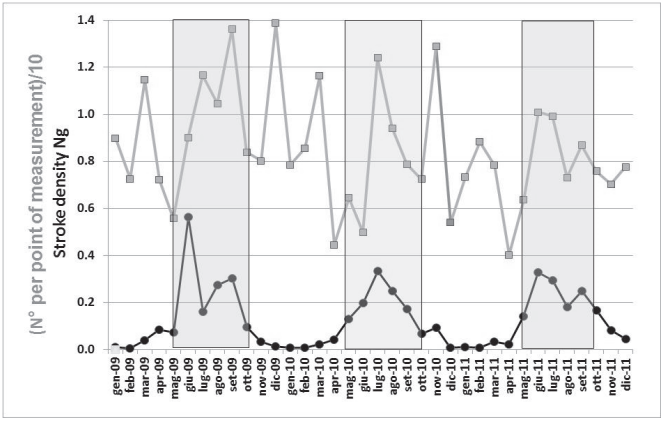



Figure 2. Monthly trend of N (grey curve) and Ng (black curve).

Evaluation of the above mentioned correlation indices at each point of measurement (400 site indices) shows that there is significant variation from year to year. The scatter plot in Figure 3 refers, in particular, to the correlation index of N2a with the lightning strike density Ng evaluated at each point of measurement, respectively, in 2009 and 2010. A high correlation in 2009 (Point A: abscissa = 0.98) may correspond to a lower correlation in 2010 (Point B: abscissa = 0.099).

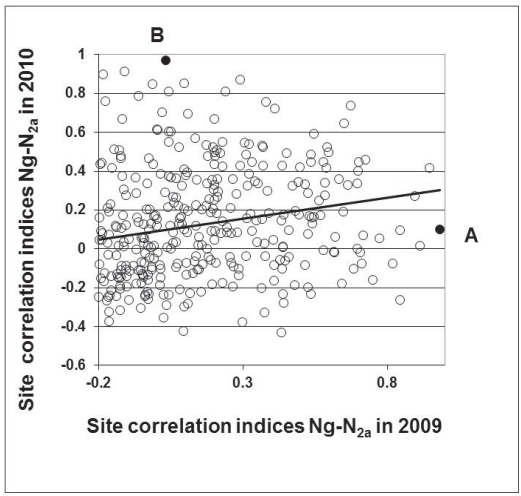



Figure 3. Site correlation indices Ng-N2a in 2009 vs 2010.

EBSCOhost - printed on 2/14/2023 2:46 PM via . All use subject to https://www.ebsco.com/terms-of-use

## Multilinear Regression Models

In order to investigate the relationship between voltage dips indices (*dependent variable or response*) and network/environmental characteristics (*independent or explanatory variables or predictors*) in more depth, multiple linear regression analysis (MLR) was applied to the 2009–2011 data. Usually, MLR is used to identify the relationship between a single explanatory variable and the response of the model when all other explanatory variables in the model are fixed. In this way the following alternatives are evaluated:

- the influence of each predictor irrespective of the others;
- estimation of the expected response for given values of the independent variables for forecasting purposes.

MLR was applied to fulfil the first aim, in order to better investigate the influence of each network characteristic on the number of voltage dips, irrespective of all other parameters.

A typical MLR model can be expressed as:

$$J_i = \beta_1 x_{1i} + \beta_2 x_{2i} + \beta_3 x_{3i} + \cdots + \beta_k x_{ki} + \varepsilon_i \qquad (1)$$

where

| | |
|---|---|
| $i$ | $i^{th}$ observation |
| $J_i$ | model response |
| $x_{2i} \ldots x_{ki}$ | explanatory variables |
| $\beta_2 \ldots \beta_k$ | regression coefficients |
| $\varepsilon_i$ | random error for the $i^{th}$ observation |
| | $\beta_1$ constant, which represents the model response when the explanatory variables are null |
| $x_{1i}$ | unit vector |

As the main objective of this work was to confirm the validity of results from previous analogous analyses, now having a more localized measure of lightning strike density to soil in comparison to the provincial one used in the past, the MLR models implemented were those that had shown promising results in the past and were characterized by the explanatory variables listed in Table 3. Among these, the macro-area [4] and the type of neutral operation are *categorical variables*—they assume

EBSCOhost - printed on 2/14/2023 2:46 PM via . All use subject to https://www.ebsco.com/terms-of-use

only the values 1 or 0 depending on whether they belong or not to a macro-area, or to the compensated or isolated neutral type of operation of the network. All the other explanatory variables are continuous. Two models also take into account the mixed term La*Ng, which is the product of aerial line length and lightning strike density and represents the interaction between these two variables.

**Table 3. MLR Models.**

| MLR models | Model 1 | Model 2 | Model 3 | Model 4 |
|---|---|---|---|---|
| *Response* / Explanatory variables | *All indices (*)* | *All indices (*)* | *All indices (*)* | *All indices (*)* |
| NO (NorthWest) ** | X | X | X | X |
| NE (NorthEast) ** | X | X | X | X |
| CS (Central part + Sardinia)** | X | X | X | X |
| Sud (South) ** | X | X | X | X |
| SN (type of neutral operation) | X | X | X | X |
| Un (rated voltage) | | | | |
| La (aerial line length) | X | X | | X |
| Lc (cable line length) | | | | |
| Ng (stroke density) | X | | | |
| La*Ng (mixed term) | | | X | X |
| (*) N, N2a, N3b, R-DFI, DSI_2a, MVTA2 | (**) macro areas | | | |

The results of the regression models are reported in Table 4 ÷

Table 7. They have been presented for each model in order to point out the percentage contribution of each individual explanatory variable to the total index under examination for the monitoring period (three years).

EBSCOhost - printed on 2/14/2023 2:46 PM via . All use subject to https://www.ebsco.com/terms-of-use

**Table 4. Model 1.**

| Explicative variables | Best Model - Model 1 | | | | | |
|---|---|---|---|---|---|---|
| | N | N2a | N3b | R-DFI | DSI_2a | MVTA2 |
| NO (NorthWest) | 4% | 0% | -2% | -1% | 2% | -4% |
| NE (NorthEast) | 1% | -2% | -5% | -3% | -1% | -9% |
| CS (Central part + Sardinia) | 4% | -2% | -5% | -3% | 1% | -9% |
| Sud (South) | 35% | 39% | 44% | 40% | 37% | 55% |
| SN (type of neutral operation) | 12% | 20% | 22% | 21% | 16% | 9% |
| Un (rated voltage) | | | | | | |
| La (aerial line length) | 26% | 28% | 32% | 29% | 28% | 45% |
| Lc (cable line length) | | | | | | |
| Ng (stroke density) | 18% | 17% | 15% | 17% | 18% | 14% |
| La*Ng (mixed term) | | | | | | |

**Table 5. Model 2.**

| Explicative variables | Model 2 | | | | | |
|---|---|---|---|---|---|---|
| | N | N2a | N3b | R-DFI | DSI_2a | MVTA2 |
| NO (NorthWest) | 9% | 5% | 2% | 4% | 7% | -1% |
| NE (NorthEast) | 5% | 1% | -2% | 0% | 3% | -6% |
| CS (Central part + Sardinia) | 10% | 4% | 0% | 3% | 7% | -4% |
| Sud (South) | 40% | 43% | 47% | 44% | 42% | 58% |
| SN (type of neutral operation) | 12% | 20% | 22% | 21% | 15% | 9% |
| Un (rated voltage) | | | | | | |
| La (aerial line length) | 25% | 27% | 31% | 28% | 26% | 44% |
| Lc (cable line length) | | | | | | |
| Ng (stroke density) | | | | | | |
| La*Ng (mixed term) | | | | | | |

EBSCOhost - printed on 2/14/2023 2:46 PM via . All use subject to https://www.ebsco.com/terms-of-use

**Table 6. Model 3.**

| Explicative variables | Model 3 | | | | | |
|---|---|---|---|---|---|---|
| | N | N2a | N3b | R-DFI | DSI_2a | MVTA2 |
| NO (NorthWest) | 10% | 6% | 3% | 5% | 8% | 2% |
| NE (NorthEast) | 7% | 4% | 2% | 4% | 6% | 0% |
| CS (Central part + Sardinia) | 12% | 7% | 4% | 6% | 10% | 3% |
| Sud (South) | 43% | 47% | 53% | 49% | 46% | 66% |
| SN (type of neutral operation) | 16% | 25% | 29% | 26% | 20% | 19% |
| Un (rated voltage) | | | | | | |
| La (aerial line length) | | | | | | |
| Lc (cable line length) | | | | | | |
| Ng (stroke density) | | | | | | |
| La*Ng (mixed term) | 11% | 11% | 9% | 10% | 11% | 10% |

**Table 7. Model 4.**

| Explicative variables | Model 4 | | | | | |
|---|---|---|---|---|---|---|
| | N | N2a | N3b | R-DFI | DSI_2a | MVTA2 |
| NO (NorthWest) | 9% | 5% | 2% | 4% | 7% | -1% |
| NE (NorthEast) | 5% | 2% | -2% | 1% | 3% | -6% |
| CS (Central part + Sardinia) | 9% | 3% | -1% | 2% | 6% | -5% |
| Sud (South) | 40% | 43% | 47% | 44% | 42% | 58% |
| SN (type of neutral operation) | 12% | 19% | 22% | 20% | 15% | 8% |
| Un (rated voltage) | | | | | | |
| La (aerial line length) | 16% | 18% | 24% | 20% | 18% | 38% |
| Lc (cable line length) | | | | | | |
| Ng (stroke density) | | | | | | |
| La*Ng (mixed term) | 10% | 10% | 8% | 9% | 10% | 8% |

The presentation method adopted for the results of MLR allows us to overcome the limits presented by knowledge of the coefficients β2 … βk, directly supplied by the models. These cannot in fact provide an overall view of the contribution of each individual explanatory variable as they are dimensional coefficients, characterized by different units of measurement, and different from those of the model. The procedure applied, explained in [2], starts from coefficients that have been directly supplied by the MLR models and associated to a period of one week, to point out how each explanatory variable may contribute to the total phenomena observed during the whole monitoring period.

EBSCOhost - printed on 2/14/2023 2:46 PM via . All use subject to https://www.ebsco.com/terms-of-use

Table 8 summarizes the *determination coefficients* R2[9] evaluated for the period 2009–2011 for the different *responses* of the models (N, N2a …) and for the different models.

**Table 8. Determination coefficients.**

| $R^2$ evaluation | | | | | | |
|---|---|---|---|---|---|---|
| $R^2$ | N | N2a | N3b | R-DFI | DSI_2a | MVTA2 |
| model 1 | 0.51 | 0.43 | 0.36 | 0.42 | 0.47 | 0.36 |
| model 2 | 0.49 | 0.42 | 0.36 | 0.41 | 0.46 | 0.36 |
| model 3 | 0.45 | 0.39 | 0.33 | 0.38 | 0.42 | 0.31 |
| model 4 | 0.49 | 0.42 | 0.36 | 0.41 | 0.46 | 0.36 |
| model 5 | 0.51 | 0.44 | 0.37 | 0.43 | 0.48 | 0.37 |

Model 1, which takes into account La and Ng individually, confirms itself to be the best model, characterized as having the highest value of R2, both in terms of the voltage dip index and response in the regression. Model 3 can be considered an alternative to Model 1, being characterized by the presence of the mixed term La*Ng. In particular this model is characterized by an increase in the coefficients associated with the explanatory variable macro-area (Table 4 and Table 6). As for Model 2, it may be considered a reference model in which no environmental factor has been taken into account. Nevertheless, the lack of lightning strike density in this model does not change the contribution of the explanatory variable La to the total estimate. Model 4 does not provide any improvement in R2 evaluation with respect to Model 2, even if Model 4 considers both La and the mixed term La*Ng as explanatory variables.

## MLR Analysis for Events Caused by Faults in MV Networks

Further investigation has been suggested by the following considerations:

[9] Note that R2 is a measurement of the overall quality of the regression — it represents the percentage of the total variation in the model response that is accounted for by the regression model.

EBSCOhost - printed on 2/14/2023 2:46 PM via . All use subject to https://www.ebsco.com/terms-of-use

- MLR analysis, in principle, should refer only to MV-origin events as some explanatory variables (La, Lc, SN) only actually relate to the MV network;
- The frequency of voltage dips may also depend on other atmospheric conditions (wind strength, humidity levels, etc.), as has previously been mentioned;
- environmental factors are likely to have a higher impact on the HV network, which can be characterized by the presence of aerial lines and by a higher extension/interconnection in comparison to MV ones.

As such, MLR analysis was repeated considering only those events related to faults in the MV network[10], adopting the best regression models available and considering only the "pure counting" indices (Table 9).

**Table 9. Model 1 Applied Only to 2010–2011 MV Events**

| Explicative variables | Model 1 | | |
|---|---|---|---|
| | N | N2a | N3b |
| **NO** (NorthWest) | -2% | -4% | -7% |
| **NE** (NorthEast) | -3% | -4% | -11% |
| **CS** (Central part + Sardinia) | 4% | 0% | -7% |
| **Sud** (South) | 33% | 36% | 41% |
| **SN** (type of neutral operation) | 20% | 28% | 33% |
| **Un** (rated voltage) | | | |
| **La** (aerial line length) | **35%** | 31% | 40% |
| **Lc** (cable line length) | | | |
| **Ng** (stroke density) | **13%** | 12% | 10% |
| **La*Ng** (mixed term) | | | |

The principal aim was to improve the estimation of the effect of lightning activity on disturbances. The main results obtained for the index N can be summarized as follows:

- the influence of aerial line length on N increased (35%);
- the high dependence of N on the macro-area variable has been confirmed, especially for the south macro-area;

[10] The method applied by RSE since 2009 to assess the HV origin of events refers to both the signal coming from the distance protection of HV lines and to correlation of the time of occurrence of those events, which are monitored at MV bus bars belonging to different HV/MV primary substations, but underlying a common part of the HV grid [9], [10].

EBSCOhost - printed on 2/14/2023 2:46 PM via . All use subject to https://www.ebsco.com/terms-of-use

- the percentage of MV events due to lightning activity was estimated to be around 13%, a value slightly lower than that related to all the voltage dips monitored independently of their origin (around 18%).

## Regression Analysis Results

Multiple linear regression analyses confirmed that:

- aerial line length has a meaningful effect on voltage dips (percentage contribution in the 25%-30% range), especially when only MV-origin events are concerned (35%);
- cable line length seems, as expected, to have a negligible effect when compared to the influence of other parameters;
- the neutral type of compensation has a positive effect on voltage dips, even if its contribution does not appear as significant as aerial line length, with a range of 12%–19%, or slightly more for MV-origin events;
- lightning activity alone does not seem to have the expected effects on voltage dips in MV networks. It plays a significant role (percentage contribution within the 15%–18% range), but not as much as the line length, even when more localized lightning strike density data is concerned;
- the contribution of lightning activity drops to 13% if only MV-events are considered;
- it is possible to confirm the strong dependence of the different indices of voltage dips as belonging to a particular geographical area. This dependence can be evaluated from the percentage contributions offered by the four macro area constants (a contribution that is revealed to be particularly important for the macro-area of the south).

The results obtained by the best model, based on “pure counting” indices, are summarized in

Figure **4**.

EBSCOhost - printed on 2/14/2023 2:46 PM via . All use subject to https://www.ebsco.com/terms-of-use

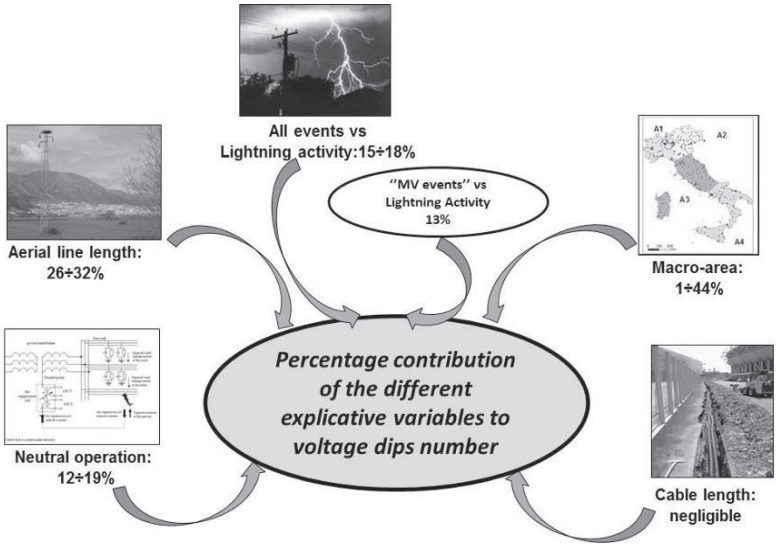



Figure 4. Influence of network and environmental factors on voltage dips "pure counting" indices (Model 1).

This result seems to confirm the hypothesis that voltage dips may be influenced by storm phenomena as a whole, and/or by their effect on HV-origin events. To confirm whether these assessments were correct, radar measurements were used to characterize storm impacts on the electrical networks.

## Correlations Between Storm Cell Occurrence and Voltage Dips

Investigations were carried out in order to identify any possible geographical and temporal correlation between voltage dips and storm cells. The time of occurrence and position of storm cells were provided by the STAF system—a meteorological application [11] that processes radar reflectivity measurements for the alerting to and tracking of severe storms. Radar data were provided by the Monte Lema radar of the MeteoSwiss in Locarno. The area covered by the radar (400 X 400 $km^2$ area in

Figure 5) includes 150 HV/MV substations monitored by QuEEN. The radar reflectivity data processed by STAF covers the 2009 spring-summer

EBSCOhost - printed on 2/14/2023 2:46 PM via . All use subject to https://www.ebsco.com/terms-of-use

period (28 April–20 September)[11] and were characterized by a 5 minute minimum time resolution.

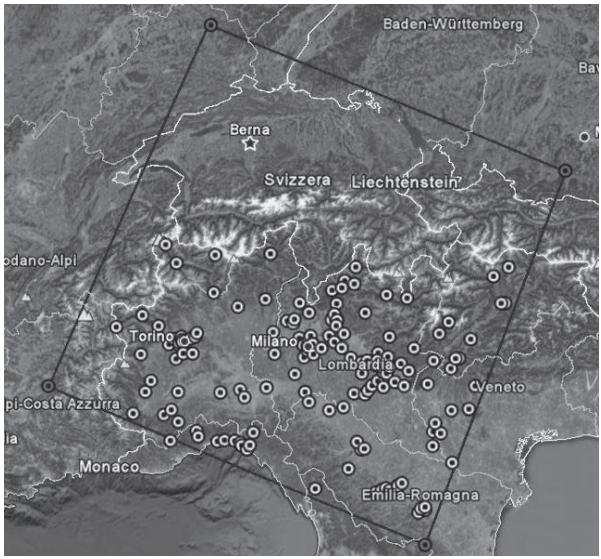



Figure 5. Area covered by the Monte Lema Radar and QuEEN measuring units in the region (bright circles).

The results are summarized in Table 10. Only 2% of events correlated with storm cells occurring in five minutes and within a distance of 4 km of the PQ measurement unit. This percentage increased to 11% when correlation within an hour and a distance of 4 km were taken into account. More detailed analysis revealed that in this last case, a single voltage dip was correlated to the different positions taken in 1 hour by the same storm cell (considering how rapidly storms move) rather than to different storms.

If we consider only time correlations within the minimum time resolution (5 minutes), around 56% of events could be correlated to storm cells. In this case a single storm cell was correlated to more voltage dips monitored by different measurements units located in the same portion of the distribution network—a probable sign that these events had an HV-origin.

[11] Reflectivity measurements in winter and fall are less significant because of the absence of convection currents in the atmosphere in the northern part of Italy.

EBSCOhost - printed on 2/14/2023 2:46 PM via . All use subject to https://www.ebsco.com/terms-of-use

**Table 10. Voltage Dips vs. Storm Cell Correlations.**

| Voltage dips and storm cells correlation within the following: | | Percentage of correlated events |
|---|---|---|
| geographical distance | time unit | |
| 4 km | 5' | 2% |
| 4 km | 1h | 11% |
| any distance | 5' | 56% |

Correlations with storm cells within 5 minutes and irrespective of any distance were applied separately to HV and MV-events. For this purpose, the PQ data used in this work was classified as of HV-origin (43%) or of MV-origin (57%) by the *global method* usually applied to QuEEN data in ex-post analysis [10]. The 67% of events with an origin in the HV network were correlated to storm cells (Figure 6), providing evidence of the significant impact of storms on the HV network because of its particular characteristics (long aerial lines, highly extended and interconnected).

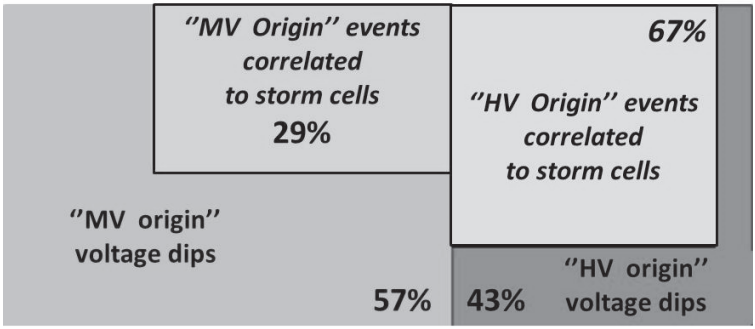



Figure 6. Correlation of storm cells with voltage dips with origin in HV and MV networks respectively.

Regarding MV-origin events, about 29% of these were correlated with storm cells—a value that is significant higher than the 13% of MV-events correlated to lightning strike density. The hypothesis that voltage dips may depend less on simple strike occurrences and more on broader atmospheric phenomena, considered as a whole, seems to be confirmed.

Additionally, more detailed analyses, applied to a few measurement units belonging to an Italian DSO operating in the northern part of Italy, allowed us to verify that the events correlated to storm cells were those

EBSCOhost - printed on 2/14/2023 2:46 PM via . All use subject to https://www.ebsco.com/terms-of-use

monitored by measurement units located in networks characterized by the prevalence of aerial lines on cables [13].

## Conclusions

The influence that some network and environmental parameters may have on the number of voltage dips in MV networks was investigated by both correlation and multiple regression techniques, applied to PQ and lightning data for the three-year period of 2009–2011. Analysis of the correlation between voltage dips and storm cells, supplied by radar reflectivity data, was applied to a subset of PQ data.

The most significant results obtained are summarized in the following:

- there is a good correlation between voltage dips and lightning strike density to earth in the spring-summer period (correlation index = 0.7–0.8), which drops to 0.51 in autumn and winter;
- there were significant variations in the results of the correlations from year to year at each point of measurement.

In terms of multiple linear regression analyses, which allow us *to identify in an independent way* the contribution to voltage dips of different network and environmental factors, the following conclusions can be drawn:

- aerial line length always has a meaningful effect on voltage dips, while cable line length seems, as expected, to have a negligible effect;
- neutral compensation somehow has a positive effect on voltage dip performance;
- the voltage dip statistic depends in a non-negligible way on the geographical area where the monitoring unit has been installed;
- the influence of lightning activity on voltage dip performances does not seem to show the expected results;
- the number of voltage dips depends less on simple occurrences of lightning strikes and more on general storm phenomena. About 29% of voltage dips, having their origin in MV networks, were correlated to storm cells identified by radar reflectivity measurements. This percentage goes up to 67% for events with their origin in the HV network.

EBSCOhost - printed on 2/14/2023 2:46 PM via . All use subject to https://www.ebsco.com/terms-of-use

## Acknowledgements

This work has been financed by the Research Fund for the Italian Electrical System under the Contract Agreement between RSE S.p.A. and the Ministry of Economic Development – General Directorate for Nuclear Energy, Renewable Energy, and Energy Efficiency in compliance with the Decree of March 8, 2006.

## References

[1]. F. Villa, A. Porrino, R. Chiumeo, S. Malgarotti, "The power quality monitoring of the MV network promoted by the Italian regulator," 19th International Conference on Electricity Distribution, CIRED 2007, Vienna, paper 0042.

[2]. Rapporto CESI RICERCA 08005783 "Sistema di monitoraggio della qualità della tensione: evoluzione del sistema a supporto dell'attività regolatoria e delle proposte di revisione della normativa tecnica europea," Febbraio 2009, www.rse-web.it, (in Italian).

[3]. R. Chiumeo and L. Tenti, "The results of MV networks monitoring in Italy," presentation at the "Regulation of voltage quality for the Italian network" Workshop organized by the Italian Regulatory Authority for Electricity and Gas (AEEG, at present ARERA) and by the Politecnico di Milano, Bergamo, Italy - 29th September 2010.

[4]. R. Chiumeo, L. Garbero, L. Tenti, C. Gandolfi, M. de Nigris, "The voltage dip performance assessment of the Italian MV network through global indices," 21st International Conference on Electricity Distribution, CIRED 2011, Frankfurt, paper 0886.

[5]. ARERA - Autorità di Regolazione per Energia Reti e Ambiente, DCO 15/11, "Opzioni e proposte per la regolazione della qualità dei servizi di distribuzione e misura dell'energia elettrica nel periodo di regolazione 2012–2015," https://www.arera.it/it/docs/dc/11/015-11dco.jsp, Aprile 2011 (in Italian).

[6]. R. Chiumeo, L. Garbero, L. Tenti, "Rapporto sintetico sulle prestazioni della rete di distribuzione italiana in media tensione con riferimento ai buchi di tensione," Appendice D al documento di consultazione dell'Autorità per l'energia elettrica ed il Gas DCO 42/10, Novembre 2010 (in Italian).

[7]. G. Carpinelli, P. Caramia, P. Verde, P. Varilone, R. Chiumeo, I. Mastandrea, F. Tarsia, "A Global Index for Discrete Voltage Disturbances," 9th International Conference Electrical Power Quality and Utilization, EPQU 2007, Barcelona.

[8]. A. M. Dan, "Introducing a voltage dip severity index: a proposal," 14th International Conference on Harmonics and Quality of Power, ICHQP 2010, Bergamo, paper 201.

[9]. R. Chiumeo, C. Gandolfi, L. Garbero, F. Malegori, M. Volta, L. Tenti, "The origin of voltage dips monitored in MV network and its effect on the evaluation of MV voltage dips performance indices," 22nd International

EBSCOhost - printed on 2/14/2023 2:46 PM via . All use subject to https://www.ebsco.com/terms-of-use

Conference & Exhibition on Electricity Distribution, Stockholm (2013), paper 0655.

[10]. R. Chiumeo, L. Garbero, F. Malegori, L. Tenti, "Feasible methods to evaluate voltage dips origin," ISN 2172-038X Renewable Energy & Power Quality Journal, No.13, April 2015, Paper 325, 357-361.

[11]. P. Marcacci, G. Stella, "STAF V.2 - Storm Track Alert and Forecast, Ver. 2," Final Technical Report ERSE 09004789, 31st December 2009 (in Italian).

[12]. R. Chiumeo, C. Gandolfi, L. Tenti, "I fenomeni temporaleschi e la numerosità dei buchi di tensione nelle reti MT," AEIT Journal, Milano 2014 (in Italian).

[13]. E. Bionda, R. Chiumeo, D. Della Giustina, D. Pala, G. Proserpio, S. Pugliese, L. Tenti, "A demonstrator tool to provide the network operator with microservices based on big data and semantic web technologies," Rivista on-line ISN 2172-038X Renewable Energy & Power Quality Journal, No.15, Vol.1, April 2017, Paper 250, Pages 137–145.

EBSCOhost - printed on 2/14/2023 2:46 PM via . All use subject to https://www.ebsco.com/terms-of-use

# CHAPTER FORTY

# OPTIMAL VOLTAGE SAG MONITORING IN DISTRIBUTION SYSTEMS THROUGH SIMULTANEOUS ANALYSIS OF SHORT-CIRCUITS AND DIFFERENT LOADING PROFILES[1]

THAIS R. KEMPNER[1],
FABRICIO A. MOURINHO[2],
FERNANDO B. BOTTURA[3],
MÁRIO OLESKOVICZ[3]
AND JOSÉ CARLOS M. VIEIRA JÚNIOR[3]

## Abstract

This study aims to assess the influence of different loading profiles in distribution systems on the optimal placement of power quality (PQ) monitors. It describes a placement methodology that considers different loading profiles of the IEEE 34 node test feeder. The placement methodology is a branch and bound based algorithm, which uses single phase short-circuit simulations with different fault resistances and loading

[1] University of Cuiabá—UNIC Barão, 222 Barão de Melgaço st., Porto, Cuiabá, MT, Brazil. E-mail: thaisrgk@gmail.com
[2] Operator of the National Electricity System (ONS), 251 Júlio do Carmo st., Cidade Nova, Rio de Janeiro, Brazil. E-mail: fabricio.mourinho@ons.org.br
[3] Department of Electrical and Computer Engineering, University of São Paulo, São Carlos School of Engineering, 400 Trabalhador São-carlense Avenue, São Carlos, SP, Brazil. Emails: fernando.bottura@usp.br, olesk@sc.usp.br, and jcarlos@sc.usp.br

EBSCOhost - printed on 2/14/2023 2:46 PM via . All use subject to https://www.ebsco.com/terms-of-use

profiles. An observability index was evaluated and introduced in the optimization process in order to prioritize the placement of monitors at those nodes with the highest sensitivity to voltage sags. Results revealed that the proposed placement methodology was able to provide feasible solutions and identified the same placement nodes regardless of the loading profile. This research provides significant evidence that it is possible to properly optimize the placement of PQ monitors, even when the distribution system is modeled and simulated without loads.

**Keywords:** Distribution systems; power quality; optimal allocation; load profile; voltage sags.

## Introduction

Distribution systems (DS), primarily those with overhead lines, regularly experience disturbances and failures of different kinds. These arise from diverse situations, such as adverse weather conditions, various short-circuits, operational mistakes, and equipment malfunctions.

The occurrence of these disturbances causes a non-ideal power supply condition, which may lead to deterioration in power quality (PQ). Among all possible types of disturbance in DS, short duration voltage variations, especially voltage sags, are the most frequent and easily perceivable to customers [1], [2].

Caused by low impedance short-circuits, or even by the energization of high power loads, severe voltage sags may be propagated throughout the whole system.

Voltage sags are defined as short voltage variations with residual voltage magnitudes of between 0.1 pu and 0.9 pu and lasting less than or equal to one minute [3].

Voltage sags may be considered a major cause of customer complaints, since they may cause malfunctioning of sensitive loads and potentially leading to considerable financial loss if they interrupt industrial processes [4].

Properly predicting DS performance regarding the impact of voltage sags is a complex task, which demands large quantities of measurement, data storage, and computer processing. Moreover, to achieve sufficient monitoring quality, a monitor should be installed at each DS node, significantly increasing financial costs. An extended measurement period would be necessary in order to compile a relevant and reliable database of DS behavior.

EBSCOhost - printed on 2/14/2023 2:46 PM via . All use subject to https://www.ebsco.com/terms-of-use

Recently, some alternatives have been proposed to address the negative impacts of voltage sags and methods for identifying optimal placement of PQ monitors. The proposed techniques aim to reduce the financial costs of purchasing and maintaining PQ monitors [5]-[11].

Despite the efficiency reported in these studies, only a few of them have focused specifically on DS. Moreover, such research has tended only to consider a single DS loading profile when carrying out the monitor placement procedure. As such, it is difficult to determine the effectiveness of these placement solutions, or even infer their potential behavior if different loading conditions were applied in the DS. Because a DS loading profile varies significantly throughout the day, it is necessary to study the influence of distinct loading conditions on the optimal placement of PQ monitors.

Considering the aforementioned context, this research proposes a performance assessment of the optimal placement of PQ monitors, considering different loading scenarios using a branch and bound based optimization methodology. The analyzed scenarios were obtained by considering different loading patterns on the standard IEEE 34 node test feeder [12].

The proposed methodology is expected to provide important information about voltage sag magnitudes and showing the influence and propagation behavior of voltage sages at all nodes of the DS.

The branch and bound based optimization algorithm calculates the optimal number of PQ monitors, as well as the best nodes for their installation, in order to achieve complete monitoring of voltage sags in the DS. Furthermore, this placement solution will ensure that any voltage sag is detected by at least one voltage monitor within the DS.

As the branch and bound based algorithm may provide placement solutions of equal feasibility, and which may suggest different allocation nodes, an observability index was developed. It is therefore possible to prioritize the installation of PQ monitors at those nodes that experience the highest number of voltage sags.

## Methodology

### *DS Modeling Using ATP*

Traditionally, most of the available measurements in a DS are acquired at a DS substation and electrical quantities are not monitored along the feeder itself [13]. Therefore, many disturbances that occur along the DS feeder leading to deterioration in PQ are neither monitored nor assessed by

EBSCOhost - printed on 2/14/2023 2:46 PM via . All use subject to https://www.ebsco.com/terms-of-use

power companies. Additionally, it is known that DS loading varies throughout the day [13]. However, due to a lack of monitors assigned to register the dynamic and random behavior of loads, detailed studies giving an exact characterization of DS loading are hard to find.

As previously mentioned, several studies have suggested procedures for the optimized placement of PQ monitors [5]-[11]. However, they do not consider loading variations of the DS to achieve their final placement solution. As such, in this research four different DS loading profiles were considered in order to demonstrate whether the effectiveness of the PQ monitor placement is directly affected by different loading scenarios or not.

The DS analyzed was the IEEE 34 node test feeder [12], shown in Fig. 1. This DS was modeled using the ATP (Alternative Transients Program) via the ATPDraw interface [14]. In this study, all DS loads were modeled as having constant impedance, which was calculated based on the magnitudes of power and voltage available in [12].

The main feeder of this DS has a nominal voltage of 24.9 kV and is 57.6 km long. The nominal loading was approximately 2.05 MVA.

In order to keep the voltage profile within an acceptable range, this DS contains two voltage regulators and two shunt capacitor banks. Furthermore, there are fixed and distributed unbalanced loads. Additionally, nodes 27 and 28 had nominal voltages of 4.16 kV.

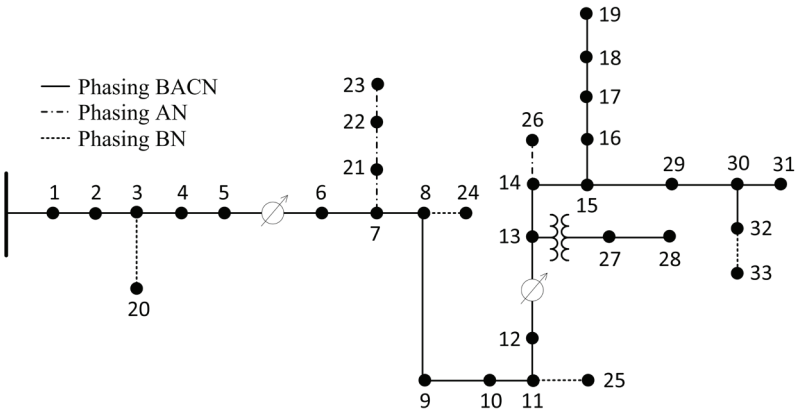



Figure 1. IEEE 34 node distribution test feeder.

The four loading profiles are briefly described in the following.

EBSCOhost - printed on 2/14/2023 2:46 PM via . All use subject to https://www.ebsco.com/terms-of-use

The first profile considered was Regular Loading, which consisted of a normal loading as described in [12]. The second profile was Heavy Loading. This saw a 20 % increase of both active and reactive power for each load of the system with respect to the regular condition, totaling 2.5 MVA. The third scenario considered was Light Loading. This saw a 20 % reduction of both active and reactive power for each load of the system with respect to the regular condition, totaling 1.65 MVA.

For the three loading scenarios, the taps of the voltage regulators were fixed.

Finally, the fourth scenario was No Loading and consisted the classical approach for short-circuits studies, i.e., the loads, capacitor banks, and voltage regulators are neglected in the simulation analysis [13]. This loading scenario offers an alternative approximation for short-circuit simulations when precise information about the DS is unknown.

The phase A voltages for each node of the DS, corresponding to the four loading profiles, are shown in Fig. 2. Accordingly, it is possible to observe that the Light Loading scenario had the highest pre-fault voltages, since smaller loading causes fewer voltage drops along the feeder. The opposite situation can be observed in the Heavy Loading scenario, which had the lowest steady-state pre-fault voltages, as the loading magnitude was higher.

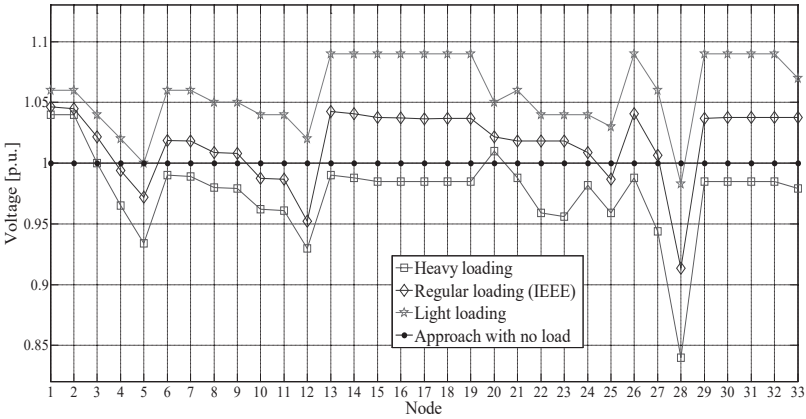



Figure 2. Phase A voltage profiles for all loading scenarios.

Because it would be technically difficult and impractical to represent all possible loading combinations of the DS, the extreme loading conditions (heavy and light) were analyzed together with Regular Loading.

EBSCOhost - printed on 2/14/2023 2:46 PM via . All use subject to https://www.ebsco.com/terms-of-use

This approach aims to cover all other intermediary operation points of the DS, i.e., other loading combinations should be adequately represented within the range of heavy to light loading.

## *Assessment of Voltage Sag Magnitudes*

The proposed methodology consists of applying single phase short-circuits at all nodes of the test DS. Single phase short-circuits in phase A were studied and the measured residual voltages during the short-circuit simulations were used to build a 'during fault voltage matrix' (DFVM) [11].

Fig. 3 illustrates the voltage sag matrix derived from the occurrence of single phase short-circuits in the IEEE 34 node DS (Fig. 1), after a phase aggregation procedure, in order to present the DFVM and show the residual voltages in the network for all the analyzed nodes [11]. In this figure, only solid single-phase short-circuits were considered under regular loading conditions.

The matrix in Fig. 3 correlates the intensity of voltage sags at each node with an appropriate grayscale color. The column numbers relate to short-circuited nodes and the row numbers to those nodes affected by the voltage variations caused by the fault. For example, line 5 and column 11 means that node 5 sensed a residual voltage of about 0.4 pu caused by a single phase short-circuit at node 11.

Single phase short-circuits were used in this study because they are a relatively common occurrence in overhead DS [13].

Single phase short-circuits in phase B were simulated at nodes 20, 24, 25, and 33 of the test DS, as they do not involve phase A of the system. In these cases, the phase B voltages of all the other nodes in the DS were monitored.

This research analyzes single phase short-circuits with fault resistances equal to 0 (zero) and 40 Ω. As such, for each of the four loading scenarios, 33 short-circuit simulations were carried out including the two fault resistances, totaling 264 short-circuit simulations within the DS.

The DFVM was calculated for the three phases of the system, storing all remaining voltages at each node due to the aforementioned short-circuit simulations. Thus, 24 DFVM were obtained and after a phase aggregation procedure were used to build eight voltage sag matrices. These voltage sag matrices were later used as inputs of the optimal placement algorithm, as described in the following.

EBSCOhost - printed on 2/14/2023 2:46 PM via . All use subject to https://www.ebsco.com/terms-of-use

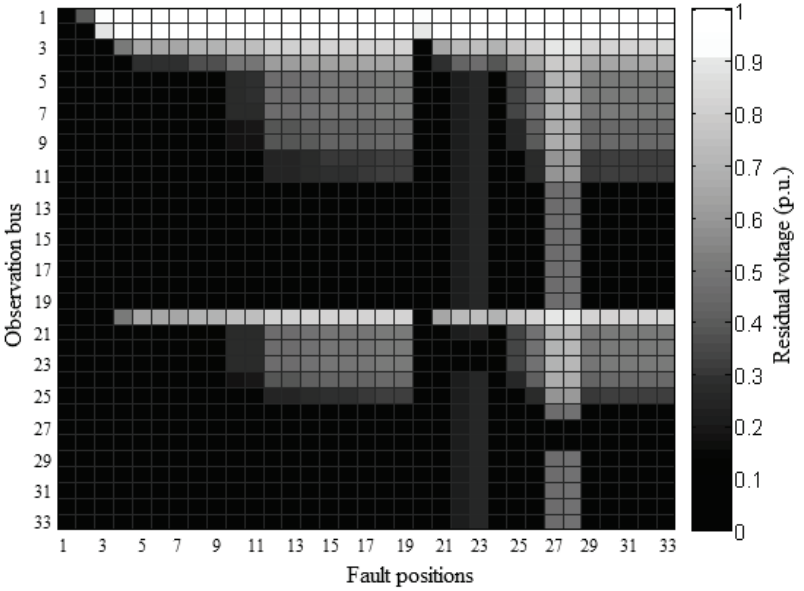



Figure 3. DFVM during the occurrence of single phase short-circuits at all nodes in the 34-node DS.

## *Optimization Problem*

It is known from a practical standpoint that complete monitoring of a DS may require the purchase and maintenance of a large number of PQ monitors, making investment in monitoring and planning expensive. Therefore, the optimization problem aims to determine the minimal number of PQ monitors necessary to monitor voltage sags. Furthermore, the optimization process provides an allocation solution, describing at which nodes the PQ monitors should be installed in order to maximize the detection coverage of voltage sags within the DS.

In order to quantify the monitoring reach of one PQ monitor installed at a certain node in the DS, a voltage threshold value ($\tau$) was set after the DFVM calculation. This voltage threshold remained at between 0.9 pu and 0.1 pu. This defined the range for detectable voltage sags, i.e., remaining voltages varying between 0.9 pu (less severe voltage sags) and 0.1 pu (more severe voltage sags).

The combination of the DFVM and $\tau$ allowed the construction of a binary observability matrix (BOM): the elements of the BOM are filled

EBSCOhost - printed on 2/14/2023 2:46 PM via . All use subject to https://www.ebsco.com/terms-of-use

with 0 (zero) if the magnitude of the measured remaining voltage is greater than τ, and filled with 1 (one) if it is smaller or equal to τ. Referring to Fig. 3, Fig. 4 illustrates the resulting BOM for $\tau \leq 0.3$ pu.

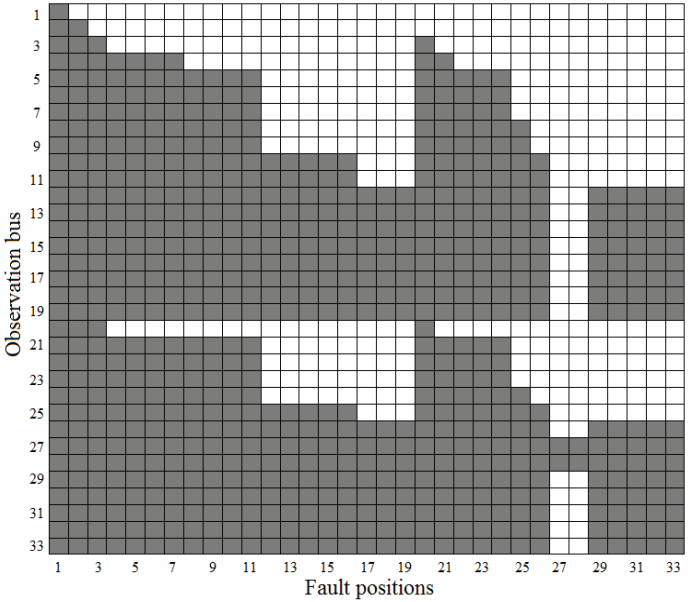



Figure 4. Binary observability matrix for voltage threshold ≤ 0.3 pu: 1 ≤ 0.3 pu and 0 > 0.3 pu.

The branch and bound algorithm was used in order to determine the best nodes for installation of the PQ monitors to ensure maximum observability across the DS. This is an exact algorithm for implicit enumeration and its structure is based on building a linear programming tree that explores possible solutions in the search space [15].

The objective function is a minimization function (1) that aims to minimize the sum of the elements of the monitoring vector ($X$), associating the priority of installation ($P$) of the PQ monitors to ensure maximum voltage sag observability.

$$\min f(x) = \sum_{i=1}^{n} x_i p_i = X \cdot P^t \tag{1}$$

The number of nodes ($n$) in the DS defines the dimension of the monitoring vector $X$ ($n$×1), which is a binary vector that provides the

EBSCOhost - printed on 2/14/2023 2:46 PM via . All use subject to https://www.ebsco.com/terms-of-use

solution for the optimized placement of the PQ monitors. This binary vector contains the minimal number of monitoring devices that are needed to detect possible voltage sags due to faults within the DS, as well as the nodes on which one should install them. Therefore, during the optimization process the binary vector $X$ is either 0 (zero) or 1 (one), respectively representing whether the monitor is installed or not.

In (1), the priority vector $P$ is a coefficient vector of $X$, which has $1 \times n$ dimensions. A priority coefficient is assigned to all elements of $P$, representing monitor installation priority in the optimization process. Thus, $P$ is determined by an observability index (OI), which is calculated for each candidate node to receive a PQ monitor. The OI provides the average number of the monitored voltage sags at each node, as shown in (2).

$$OI = \frac{\sum_{i=1,j=1}^{n} bom_{ij} \cdot x_i}{n} \qquad x_i = \begin{cases} 1, & \text{if } i = j \\ 0, & \text{otherwise} \end{cases} \tag{2}$$

Once the OI is obtained for all available PQ monitor allocation points, it is possible to define the nodes that must be prioritized in the optimization process. This prioritization is done by assigning the lower priority coefficient (with respect to the other elements of vector $P$) to those nodes with the highest observability. Thus, the positions of the element of vector $P$ (priority coefficients) are sorted from highest to lowest observability.

The lowest integer coefficients are prioritized in the search for an optimal solution. Therefore, if there is one feasible solution that contains the penalized variable, the algorithm will calculate the optimal solution, prioritizing monitor allocation at those nodes with the lowest coefficients, i.e., those nodes that possess the highest observability.

After assigning a weight to each element of $P$, it is possible to completely observe the DS by employing an optimal allocation solution to the PQ monitors.

Despite the use of the branch and bound algorithm in this research, it is possible to easily adapt the proposed methodology if the computational complexity of the problem increases. Alternatively, heuristic methods suitable for the binary logic described can be used in the optimization process.

The problem constraints were formulated in order to ensure the detection of any voltage sag within the DS by at least one of the installed PQ monitors. This condition is set when the vector product between the

EBSCOhost - printed on 2/14/2023 2:46 PM via . All use subject to https://www.ebsco.com/terms-of-use

transposed BOM and vector $X$ is greater than or equal to 1 (one), as shown in (3).

$$Subject\ to: \sum_{i=1}^{n} bom_{ij} x_i \geq 1 \tag{3}$$

Thereby, for each loading profile and respective fault resistances, the placement algorithm calculates an optimal solution, considering each chosen voltage threshold, and prioritizing the installation of PQ monitors at those nodes with the highest observability.

## Results

The branch and bound algorithm was applied to the 34-bus testing system and the optimal allocation results were obtained. The results showed the minimum number of meters and their location for each threshold analyzed for each fault type.

As previously stated, in order to assess the performance of the proposed methodology, the IEEE 34 node test feeder was modeled considering four loading profiles (Fig. 2) and two fault resistances (0 Ω and 40 Ω) for the short-circuit simulations.

For each fault resistance, four voltage sag matrices were obtained, i.e., one matrix for each loading scenario with the respective fault resistances. Then, as described above, it was necessary to define the voltage threshold. Usually, this definition is not an easy task because there is a tradeoff between monitor sensitivity and the redundancy of the measurements needed. The higher the voltage threshold is, the more voltage sags are detected by the PQ. However, high threshold values will reduce the redundancy of the measurements, since a lower number of PQ monitors is then required. This may compromise the reliability of the monitoring system and possibly even overload the storage capacity of the PQ monitor.

In this context, the threshold setting was based on the probability of the occurrence of voltage sags in [16]. This study reported that almost 90 % of voltage sags have a remaining RMS voltage of between 50 % and 85 %. Therefore, in this research the thresholds τ considered were 0.4, 0.5, 0.6, 0.7, 0.8, and 0.9 pu, resulting in 6 BOM for each voltage sag matrix. After computing the 8 voltage sags matrices in the short-circuit simulations using the ATP, 48 BOM were built.

For each one of the 48 BOM, the branch and bound algorithm was executed in order to calculate the minimal number and correct location of PQ monitors. However, each run of the algorithm produced a different

EBSCOhost - printed on 2/14/2023 2:46 PM via . All use subject to https://www.ebsco.com/terms-of-use

feasible allocation solution. This is because there was more than one solution available, resulting in different allocation points. As such, it was not possible to perform an adequate comparison between the different allocation solutions when considering distinct loading scenarios.

To overcome this drawback, the OI was calculated, as previously described, in order to obtain a solution that could cover all considered loading profiles, as well as both fault resistances (0 Ω and 40 Ω).

Tables I and II show the OI calculated by (2), for all loading profiles and a fault resistance of 0 Ω.

**Table I: OI for No Loading and Regular Loading profiles with 0 Ω fault resistance.**

| Node | No Loading | Regular Loading | Node | No Loading | Regular Loading |
|---|---|---|---|---|---|
| **1** | 2.2727 | 2.0000 | **18** | 8.4242 | 8.3939 |
| **2** | 2.4242 | 2.0303 | **19** | 8.4242 | 8.3939 |
| **3** | 4.1515 | 3.6667 | **20** | 4.1818 | 3.6970 |
| **4** | 5.5758 | 5.3636 | **21** | 6.5152 | 6.4545 |
| **5** | 6.5152 | 6.5758 | **22** | 6.7273 | 6.6970 |
| **6** | 6.5152 | 6.4545 | **23** | 6.7273 | 6.6970 |
| **7** | 6.5152 | 6.4545 | **24** | 7.0000 | 6.9091 |
| **8** | 7.0000 | 6.9091 | **25** | 7.6061 | 7.5455 |
| **9** | 7.0000 | 6.9091 | **26** | 8.4242 | 8.3939 |
| **10** | 7.5152 | 7.5152 | **27** | 8.5758 | 8.5455 |
| **11** | 7.5758 | 7.5152 | **28** | 8.7273 | 8.6667 |
| **12** | 8.3939 | 8.4242 | **29** | 8.4242 | 8.3939 |
| **13** | 8.4242 | 8.3636 | **30** | 8.4242 | 8.3939 |
| **14** | 8.4242 | 8.3939 | **31** | 8.4242 | 8.3939 |
| **15** | 8.4242 | 8.3939 | **32** | 8.4242 | 8.3939 |
| **16** | 8.4242 | 8.3939 | **33** | 8.4242 | 8.3939 |
| **17** | 8.4242 | 8.3939 | | | |

As previously detailed, the allocation algorithm prioritizes the installation of PQ monitors at those nodes with the highest OI, assigning to them a lower index of the respective *P* element when compared to nodes that are less sensitive to voltage sags. The OI in Tables I and II uses the priority vector *P* calculated as shown in Table III.

EBSCOhost - printed on 2/14/2023 2:46 PM via . All use subject to https://www.ebsco.com/terms-of-use

**Table II. OI for Light Loading and Heavy Loading profiles with 0 Ω fault resistance.**

| Node | Light Loading | Heavy Loading | Node | Light Loading | Heavy Loading |
|---|---|---|---|---|---|
| **1** | 2.0000 | 2.0000 | **18** | 8.3939 | 8.3939 |
| **2** | 2.0303 | 2.0303 | **19** | 8.3939 | 8.3939 |
| **3** | 3.6364 | 3.6970 | **20** | 3.6667 | 3.7273 |
| **4** | 5.3333 | 5.3636 | **21** | 6.4545 | 6.4545 |
| **5** | 6.5455 | 6.6061 | **22** | 6.6667 | 6.7576 |
| **6** | 6.4545 | 6.4545 | **23** | 6.6970 | 6.7576 |
| **7** | 6.4545 | 6.4545 | **24** | 6.9091 | 6.9091 |
| **8** | 6.9091 | 6.9091 | **25** | 7.5455 | 7.5455 |
| **9** | 6.9091 | 6.9394 | **26** | 8.3939 | 8.3939 |
| **10** | 7.5152 | 7.5152 | **27** | 8.5758 | 8.5758 |
| **11** | 7.5152 | 7.5152 | **28** | 8.6970 | 8.6970 |
| **12** | 8.3939 | 8.4545 | **29** | 8.3939 | 8.3939 |
| **13** | 8.3636 | 8.3636 | **30** | 8.3939 | 8.3939 |
| **14** | 8.3939 | 8.3939 | **31** | 8.3939 | 8.3939 |
| **15** | 8.3939 | 8.3939 | **32** | 8.3939 | 8.3939 |
| **16** | 8.3939 | 8.3939 | **33** | 8.3939 | 8.3939 |
| **17** | 8.3939 | 8.3939 | | | |

**Table III. PQ monitor installation priority for all loading profiles with 0 Ω fault resistance.**

| | **Installation Priority** | | | | | | | | |
|---|---|---|---|---|---|---|---|---|---|
| **Load** | **(1)** | **(2)** | **(3) ... (12)** | **(13)** | **(14) ... (22)** | **(23) ... (26)** | **(27)** | **(28)** | **(29) ... (33)** |
| **No load** | 15 | 14 | 13 ... 4 | 3 | 3 ... 9 | 9 ... 3 | 2 | 1 | 3 ... 3 |
| **Light** | 16 | 15 | 14 ... 3 | 4 | 3 ... 9 | 8 ... 3 | 2 | 1 | 3 ... 3 |
| **Regular** | 17 | 16 | 15 ... 3 | 5 | 4 ... 9 | 10 ... 4 | 2 | 1 | 4 ... 4 |
| **Heavy** | 17 | 16 | 15 ... 3 | 5 | 4 ... 10 | 10 ... 4 | 2 | 1 | 4 ... 4 |

As verified in Table III, node 28 has the highest priority for all the loading scenarios considered. This node was the most affected by voltage sags for all four of the analyzed loading scenarios. This does not necessarily mean that node 28 is the optimal point for monitor installation. This decision is made by the branch and bound algorithm, i.e., if node 28 is included in the possible solution set it will be chosen as one of the best places to install a PQ monitor.

EBSCOhost - printed on 2/14/2023 2:46 PM via . All use subject to https://www.ebsco.com/terms-of-use

After the definition of vector *P*, the branch and bound algorithm was executed. The nodes where the monitors should be installed and the number of monitors required to monitor each threshold voltage are shown in Tables IV and V. As node 28 was found to be present in the solution for all the analyzed scenarios, this node was prioritized for PQ monitor installation. These results provided an adequate comparison of the allocation solutions calculated by the optimization algorithm. It is possible to state that even if the loading of the DS by ±20 % with respect to Regular Loading was changed, the number of PQ monitors would remain the same for the voltage threshold from 0.9 pu to 0.5 pu.

For the 0.4 pu threshold and the Light Loading scenario, the algorithm suggested placement of a PQ monitor at node 23 instead of node 22, node 23 being prioritized in the allocation solution (Table III). However, node 22 or node 23 are both part of optimal solutions for all loading profiles, as can be seen in Table VI.

Also in Table IV, one may observe that considering the Heavy Loading scenario with a 0.4 pu threshold, only one monitor was needed to detect any voltage sag within the DS, whereas at least two monitors were needed for all other scenarios. This is because Heavy Loading contains the lowest pre-fault voltage values (Fig. 2) and therefore it sees the most severe voltage sags after short-circuits are applied.

**Table IV. Optimal placement of PQ monitors for single phase short-circuits (0 Ω fault resistance).**

| τ (pu) | Required monitors / { Monitoring node } | | | |
|---|---|---|---|---|
| | No Loading | Light Loading | Regular Loading | Heavy Loading |
| ≤ 0.9 | 1 / {28} | 1 / {28} | 1 / {28} | 1 / {28} |
| ≤ 0.8 | 1 / {28} | 1 / {28} | 1 / {28} | 1 / {28} |
| ≤ 0.7 | 1 / {28} | 1 / {28} | 1 / {28} | 1 / {28} |
| ≤ 0.6 | 1 / {28} | 1 / {28} | 1 / {28} | 1 / {28} |
| ≤ 0.5 | 1 / {28} | 1 / {28} | 1 / {28} | 1 / {28} |
| ≤ 0.4 | 2 /{22;28} | 2 /{23;28} | 2 /{22;28} | 1 / {28} |

Table V gives the results for all loading scenarios of single phase short-circuits with a 40 Ω fault resistance. Despite the algorithm being executed for all voltage thresholds, it was observed that the higher the fault resistance, the less severe the voltage sag was. As such, allocation solutions were only obtained for the highest voltage thresholds.

EBSCOhost - printed on 2/14/2023 2:46 PM via . All use subject to https://www.ebsco.com/terms-of-use

**Table V. Optimal placement of PQ monitors for single phase short-circuits (40 Ω fault resistance).**

| τ (pu) | Required monitors / { Monitoring node } | | | |
|---|---|---|---|---|
| | No Loading | Light Loading | Regular Loading | Heavy Loading |
| ≤ 0.9 | 1 / {28} | 1/ {28} | 1 / {28} | 1 / {28} |
| ≤ 0.8 | - | 1/ {28} | 1 / {28} | 1 / {28} |
| ≤ 0.7 | - | - | - | 1 / {28} |

The placement of PQ monitors (M1 and M2) for the 34 node DS is depicted in Fig. 5. This figure shows that a single PQ monitor installed at node 28 would be enough to monitor any voltage sag caused by a single phase short-circuit. Moreover, it is possible to state that this allocation solution would be sufficient even for different loading variations. This demonstrates that even if load information is neglected when modeling the DS, usually as a result of a lack of precise data, DS monitoring will not be affected.

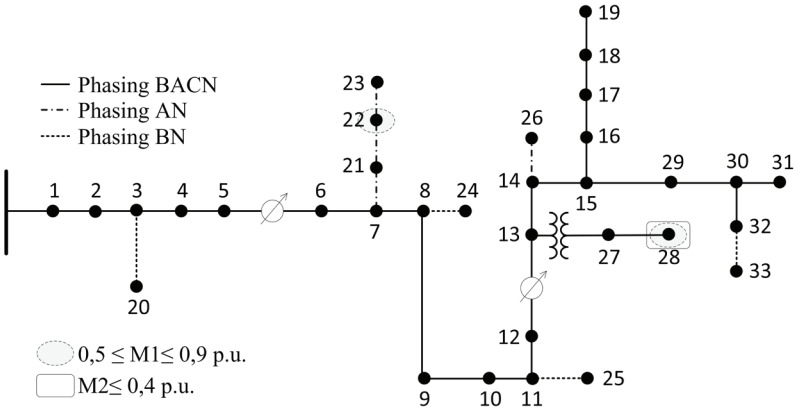



Figure 5. Optimal placement of PQ monitors M1 and M2 on IEEE 34 node test feeder considering different loading profiles.

As shown in Fig. 5, reducing the voltage threshold gives more options for the installation of PQ monitors, offering higher redundancy. Therefore, if more PQ monitors are available, or if the power company budget is sufficient and new monitors can be purchased, monitoring efficiency and reliability can be increased.

EBSCOhost - printed on 2/14/2023 2:46 PM via . All use subject to https://www.ebsco.com/terms-of-use

Solutions should be presented in such a way that allows the DS operator to decide on the best allocation pattern. Tables VI and VII contain other possible solutions that are suitable for all the loading profiles studied. Results are displayed following the prioritized order of installation of the PQ monitors, so that is possible to verify which nodes possess better monitoring capabilities for voltage sags. The total number of possible solutions for each voltage threshold is also shown in Table VI and VII.

**Table VI. Other possible solutions suitable for all loading profiles following the order of installation priority (0 Ω fault resistance).**

| τ (pu) | Solutions number | Nodes for monitor installation |
|---|---|---|
| ≤ **0.9** | 29 | {28},{27},{12},{14},{17},{19},{26},<br>{29},{31},{33},{13},{25},...,{4} |
| ≤ **0.8** | 19 | {28},{27},{12},{14},{17},{19},{26},<br>{29},{31},{33},{13},{25},...,{10} |
| ≤ **0.7** | 2 | {28},{27} |
| ≤ **0.6** | 2 | {28},{27} |
| ≤ **0.5** | 1 | {28} |
| ≤ **0.4** | 2 | {22; 28}, {23; 28} |

## Conclusion

The methodology for placement of PQ monitors presented in this paper has shown the best nodes for the installation of PQ monitors, ensuring voltage sag detection for as wide an operation range as the DS may experience.

The allocation solutions given by this methodology cover distinct short-circuit simulations evaluated for all DS nodes, including variations of the fault resistance (0 Ω and 40 Ω). Furthermore, short-circuit simulations were carried out using four different loading levels of the test DS. This was done in order assess whether the effectiveness of PQ monitor placement was directly affected or not.

The results show that, based on the calculation of the OI, the allocation algorithm was able to prioritize the installation of the PQ monitors at those nodes that were most affected by voltage sags. Using this approach, it is possible to state that the installation of only one PQ monitor at node 28 of the test DS would be enough to detect voltage sags caused by single phase short-circuits. Furthermore, this allocation solution is suitable even when the DS loading changes (±20 % from the regular loading), as shown when

EBSCOhost - printed on 2/14/2023 2:46 PM via . All use subject to https://www.ebsco.com/terms-of-use

the voltage threshold was set from 0.5 pu to 0.9 pu.

**Table VII. Other possible solutions suitable for all loading profiles following the order of installation priority (40 Ω fault resistance).**

| τ (pu) | Nodes for monitor installation | | | |
|---|---|---|---|---|
| | No Loading | Light Loading | Regular Loading | Heavy Loading |
| ≤ **0.7** | - | - | - | {28} |
| ≤ **0.8** | - | {28} | {28},{12},{5} | {28},{27},{12},{25} {10},{11},{22},{23},{5} |
| ≤ **0.9** | {28},{27},{12},{14},{15},{16},{17},{18},{19},{26},{29},{30}, {31},{32},{33},{13},{25},{11},{10},{5},{9},{8},{24}, {23},{22},{21},{6},{7},{4} | | | |

The results also demonstrated that if the voltage threshold was set to be equal to or lower than 0.4 pu, more than one possible allocation solution including node 28 was available. Setting $\tau \leq 0.4$ pu would increase redundancy, but this would also require a greater number of PQ monitors.

It is important to highlight that the convergence of the allocation solutions calculated by the proposed methodology, considering all the studied loading scenarios, shows that is possible to execute the placement of PQ monitors by considering the DS modeled without loads (the No Loading profile). Indeed, there are several drawbacks in obtaining precise information about all the loads of a real DS in order to do the necessary computer modeling and the No Loading scenario is a viable alternative through which to carry out further studies on the optimal placement of PQ monitors in a DS.

## Acknowledgement

The authors gratefully acknowledge the support of the Department of Electrical and Computer Engineering, São Carlos School of Engineering, University of São Paulo (Brazil), and financial support provided by FAPESP (São Paulo Research Foundation - 2011/22151-5) and Eletrobrás Distribuição Piauí - EDPI (PD-0042/2014-ANEEL).

EBSCOhost - printed on 2/14/2023 2:46 PM via . All use subject to https://www.ebsco.com/terms-of-use

## References

[1] M. F. Mcranaghan, D. R. Mueller and M. J. Samotyj, “Voltage Sags in Industrial Systems,” Industry Applications, IEEE Transactions on, vol.29, no.2, pp.397-403, Mar/Apr 1993.

[2] M. H. J. Bollen, M. R. Qader and R. N. Allan, “Stochastical and statistical assessment of voltage dips,” Tools and Techniques for Dealing with Uncertainty (Digest No. 1998/200), IEEE Colloquium on, pp.5/1-5/4, 27 Jan 1998.

[3] IEEE Recommended Practice for Monitoring Electric Power Quality, IEEE Standard 1159 – 1995, Nov. 1995.

[4] M. H. J. Bollen, “Voltage sag: Effects, Mitigation and Prediction,” Power Engineering Journal, vol.10, no.3, pp.129-135, June 1996.

[5] G. Olguin, F. Vuinovich and M. H. J. Bollen, “An optimal monitoring program for obtaining Voltage sag system indexes,” Power Systems, IEEE Transactions on, vol.21, no.1, pp. 378- 384, Feb. 2006.

[6] D. C. S. Reis, P. R. C. Villela, C. A. Duque and P. F. Ribeiro, “Transmission Systems Power Quality Monitors Allocation,” Power and Energy Society General Meeting - Conversion and Delivery of Electrical Energy in the 21st Century, 2008 IEEE, pp.1-7, 20-24, July 2008.

[7] E. Espinosa-Juárez, A. Hernandes and G. Olguin, “An Approach Based on Analytical Expressions for Optimal Location of Voltage Sags Monitors,” Power Delivery, IEEE Transactions on, vol.24, no.4, pp.2034-2042, Oct. 2009.

[8] C. F. M. Almeida and N. Kagan, “Allocation of Power Quality Monitors by Genetic Algorithms and Fuzzy Sets Theory,” Intelligent System Applications to Power Systems, 2009. ISAP '09. 15th International Conference on, pp.1, 6, 8-12, Nov. 2009.

[9] F. Salim and K. M. Nor, “Voltage sags observation through optimal monitor locations,” In Harmonics and Quality of Power (ICHQP), 14th International Conference on, 2010.

[10] M. Oleskovicz, H. M. G. C. Branco, R. P. M. da Silva, D.V. Coury and A. C. B. Delbem, “A Compact Genetic Algorithm structure used for the optimum allocation of power quality monitors based on electrical circuit topology,” in Harmonics and Quality of Power (ICHQP), 2012 IEEE 15th International Conference on, pp.34-39, 17-20, June 2012.

[11] T. R. Kempner, A. Q. Santos and M. Oleskovicz, “Optimized monitoring of voltage sags in distribution systems caused by balanced and unbalanced short-circuits,” in PES General Meeting | Conference & Exposition, 2014 IEEE, pp.1-5, 27-31, July 2014.

[12] IEEE PES Test Feeders, “Distribution System Analysis Subcommittee,” IEEE Power Engineering Society, Available: http://www.ewh.ieee.org/soc/pes/dsacom/testfeeders.html

[13] W. H. Kersting, *Distribution System Modeling and Analysis*. 2nd ed. Boca Raton, Florida USA. CRC Press LLC. 421p., 2007.

EBSCOhost - printed on 2/14/2023 2:46 PM via . All use subject to https://www.ebsco.com/terms-of-use

[14] ATPDraw, “Help and about ATPDraw,” Avaliable: http://www.atpdraw.net/help.php.
[15] L. A. Wolsey, *Integer Programming*, John Wiley & Sons, ISBN: 9780471283669, 1998.
[16] EPRI – Electric Power Research Institute. Distribution System Power Quality Assessment: Phase II. Voltage Sag and Interruption Analysis. Project Manager A. Sundaram, pp. 5-17, 2003.

EBSCOhost - printed on 2/14/2023 2:46 PM via . All use subject to https://www.ebsco.com/terms-of-use

# CHAPTER FORTY-ONE

# A POWER QUALITY INSTRUMENT FOR SMART GRID MONITORING BASED ON HIGHER ORDER STATISTICS

OLIVIA FLORENCIAS-OLIVEROS, JUAN-JOSÉ GONZÁLEZ-DE-LA-ROSA, AGUSTÍN AGÜERA-PÉREZ, JOSÉ-CARLOS PALOMARES-SALAS, JOSÉ-MARÍA SIERRA-FERNÁNDEZ[1]

## Abstract

This paper proposes a virtual instrument for PQ assessment based on higher-order statistics. Accompanied by a new global index, the instrument implements a monitoring strategy that triggers a measurement procedure when an electrical fault is present and a local predefined threshold is surpassed. The method helps to classify events and continuous disturbances by tracking deviations in statistical parameters from their ideal steady-state values. Designed in LabVIEW™, the user interface includes online graphs showing variance, skewness, and kurtosis, along with hybrid representations of variance versus the cited higher-order statistics. Based on a 50 Hz 100-signal battery, which gathers different types of electrical disturbances, the instrument was validated during online measurement sessions. Using stat-vs.-stat graphs that implement cycle-to-cycle surveillance, results are depicted in 2D. The graphs show that

[1] Research Group PAIDI-TIC-168 in Computational Instrumentation and Industrial Electronics (ICEI)
Department of. Automation Engineering, Electronics, Architecture and Computers Networks. University of Cádiz. Spain

EBSCOhost - printed on 2/14/2023 2:46 PM via . All use subject to https://www.ebsco.com/terms-of-use

voltage sags and transients can be classified within different clusters, with a low level of uncertainty. These visualization features allow the operator to view the relevant data objectively during an online monitoring session and, if needed, enhance the report with additional data, for example if they need to claim for economic losses and potential breaches of contract.

**Keywords**: power quality index, electronic instrumentation, higher-order statistics, virtual instrument, real-time monitoring.

## Nomenclature

| | |
|---|---|
| HOS | Higher-order statistics |
| N samples | Number of data cycles |
| j+N samples | Sequence of data cycles |
| $PQ_j$ | Power quality indicator cycle-to-cycle |
| abs | Absolute value |
| var | Variance |
| skew | Skewness |
| kurt | Kurtosis |
| SG | Smart Grid |

## Introduction

Currently, smart grids (SG) are incorporating more and more distributed generation (DG) systems, like wind turbines, photovoltaic modules (PV), and fuel cells, along with the conventional loads, with the goal of configuring more energy-efficient systems. The effects of DG systems, along with the deregulation of SGs, is increasing concerns about power quality (PQ), as they have direct impacts on utilities and customers, as well as effects on the quality of the sinusoidal signal of the power line.

The unknown features of distributed energy resources (DER) introduce non-linear behaviours in loads associated with a variety of PQ disturbances, such as voltage sags, swells, interruptions, transients, harmonics, and flicker, etc. These anomalies can affect highly sensitive equipment, cause resets in industrial control systems, and produce failures in motors and equipment, with consequent process perturbation and economic losses [1], [2], [3]. Several studies have focused attention on the necessity of improving effective detection and prevention of these system irregularities and mitigating their effects in the electrical configurations used by

EBSCOhost - printed on 2/14/2023 2:46 PM via . All use subject to https://www.ebsco.com/terms-of-use

customers. They aim to develop a new strategic standard for PQ criteria that allows designers to optimize future networks [4].

Many techniques and instruments for PQ monitoring have been developed. In recent years, artificial intelligence and online smart meters have become the main trends in PQ monitoring [5], [6], [7], [8]. These methods should serve both SG conventional users and prosumers [9].

Traditional methods for PQ monitoring have been based on the evolution of the spectral component (FFT), frequency change in the time domain (e.g., wavelets transforms), and the total harmonic distortion (THD) index [10], [11].

These methods have limitations when it comes to real-time identification and characterization of all the complex perturbations that are produced in SGs.

The conventional procedure, which considers the RMS values of the signal components, is not enough. The introduction of new tools and methods of analysis has introduced and defined new factors and coefficients to characterize the quality of the shape of the signal and complete signal processing. There is also a balance to maintain in computational cost, data storage, and performance of detection methods [4].

Changes in the fundamental frequency and harmonic distortion have been revealed as one of the most important PQ phenomena within the SG context [12], [13], [26].

Traditional techniques, such as FFT and THD, are based primarily in the static spectrum and cannot be applied to non-stationary signals, like transients. In addition, noise degrades the effectiveness of these second-order techniques. Recent studies have concluded that better characterization of symmetry and shape of the waveform is possible by using 3$^{rd}$ and 4$^{th}$ higher-order statistics (HOS), which can also account for nonlinear assessment of the signals [14], [15].

Some studies have developed cluster analysis of 4th-order estimates to examine the duration and intensity of PQ transients. They have used higher-order cumulants as the parameters [16], [17], and quadratic classifiers as the classification method [17]. This technique can be applied to data generated by the sensors in a SG [18].

The implementation of HOS algorithms in intuitive graphical user interfaces is not easy, as the user must have a significant amount of scientific knowledge to use them well. Traditional displays and graphs have been improved through the integration of additional information, e.g. phasors and energy-related parameters. It would be useful to develop a new PQ index that includes additional information (beyond Gaussian statistics) of PQ events [19].

EBSCOhost - printed on 2/14/2023 2:46 PM via . All use subject to https://www.ebsco.com/terms-of-use

This study introduces a new HOS-based PQ index that triggers a PQ measurement session when an electrical disturbance alters the steady-state ideal power supply. It then enables subsequent signal analysis. The system has been designed around a rack-mounted connector block for mounting measurement modules from National Instruments. It has been designed according to the European Standard EN50160:2015[20] and the testing and measurement techniques are based on the Spanish Standard for PQ measurement methods [21]. The quality of the voltage range allows ± 10% in voltage variation depending on the voltage supply measuring point, the instant at which the signal is disturbed, the type of disturbance, the internal configuration of the user's network, and the equipment connected to it.

The recorded data were all real disturbances obtained from the electrical network at the University of Cadiz.

## Description of the Power Quality Index

The instrument was implemented in the virtual platform LabVIEW™, in order to monitor the supply voltage in real-time. The instrument measures the signal stability through the PQ index. If a disturbance surpasses the PQ threshold, it triggers the storage unit and a classification analysis takes place within a visual frame (the HOS space), in order to quantify the degree of the event and its deviation from the ideal contractual power supply.

The signals studied through the index were acquired from the power line at a sampling frequency of 20 kHz. The index was built from data about a 50 Hz sinusoidal voltage signal, sampled using a sliding window that, cycle-to-cycle, computes the HOS estimators. Each cycle comprises 400 time-domain data in a single point in HOS 2D tracking, which is a time-compression strategy to save data storage space and enables coherent organization of the information about the modern SG [26].

In this case, each cycle was characterized by three higher-order statistics, each one accounting for different features of the tested signal. The analytical procedure was based on surveillance of the values of variance (var), skewness (skew), and kurtosis (kurt) in each cycle, compared to the theoretical 'healthy' values of an ideal 50 Hz voltage signal (an ideal sinusoidal signal) where variance, skewness, and kurtosis are a triplet (0,5; 0; 1,5).

In order to reduce the computational demands, the 400-point sliding window sweeps the signal cycle-to-cycle without overlapping (Fig. 1). More information related to the sliding window technique is addressed in [8] and [15].

EBSCOhost - printed on 2/14/2023 2:46 PM via . All use subject to https://www.ebsco.com/terms-of-use

The HOS space presents the PQ data in an intuitive way. It reports the quality of the signal in terms of its shape and its deviation from the ideal state of the voltage signal. The HOS space represents these deviations and the PQ index helps quantify them in a single indicator.

Accordingly, an effective comparison is based on the cycle-oriented PQ index. The PQ values estimated from the sampled signal are absolute values. Thus, given the *N*-point segment (data time-series), $x_j^N = (X_j,...X_{j+N})$, associated with the *jth*-cycle, the proposed PQ index for the *jth*-cycle can be defined using the following expression:

$$PQ_j^N = \left|0{,}5 - \mathrm{var}\left(x_j^N\right)\right| + \left|0 - skew\left(x_j^N\right)\right| + \left|1{,}5 - kurt\left(x_j^N\right)\right| \quad (1)$$

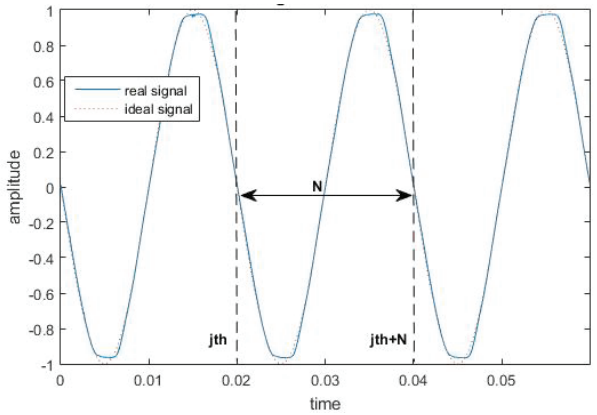



Figure 1. Representation of the sliding window in a 50 Hz power signal recorded at a sampling frequency of 20 kHz (400 samples per cycle). The number of data-cycles is represented by *N* samples and *j+N* samples the sequence. The amplitude is relative to the maximum.

The final goal of this technique is to improve the representation of the information on reported power quality.

## Experimental Strategy for Power Quality Monitoring

The experimental strategy followed the analysis steps given in the organigram in Fig. 2 (Data Acquisition—PQ Evaluation—Classification Analysis). First, in the data acquisition session the voltage signal was acquired through the virtual instrument. The HOS analysis was based on HOS measurements and the PQ evaluation according to a voltage ideal

EBSCOhost - printed on 2/14/2023 2:46 PM via . All use subject to https://www.ebsco.com/terms-of-use

signal of 50–60 Hz. An ideal signal would obtain a PQ index of 0. This is an ideal case and all real-life signals contain a certain level of perturbation, thereby producing PQ indices higher than 0,0. Secondly, in order to detect relevant behaviour in the tested signal, a threshold was established by the operator according to the point-area being tested and the needs of the monitoring session. The classification analysis was triggered once the PQ index surpassed the specified threshold, indicating unusual signal behaviour. The detection procedure helped generate a database of deviations related to the previously selected threshold. The classification analysis was performed in three steps: HOS representation, cluster analysis, and trajectory analysis (point-to-point) (Fig. 2). The main objective was to classify the recorded deviations as either events or continuous disturbances, so as to indicate the norm and represent them in a more intuitive way.

Previous studies have proposed the use of cluster analysis. In an earlier study using the instrument [22], the authors focused on the HOS average. The approach used with the current instrument follows the point-to-point behaviour of the recorded deviations and aggregates more relevant information in real time.

The authors detected that point-to-point tracking allows the discrimination of new zones in the HOS space related to sag and swell, as demonstrated in [23]. These new zones can be associated with signal disturbances, such as sags and transients. Also, the phase in which the event occurs influences the cycle-to-cycle position in the HOS space and the trajectory that follows the whole disturbance. These transition zones are addressed in [22]. The new cluster zones and their detection can be indicative of the advent of an event or change in the state of a signal suffering a continuous disturbance, such as in the case of sags [22].

A battery of data on real-life signals, sags, and transients were analysed from a building node at the University of Cadiz. The deviations were of different durations, however, the HOS space represented them in the same graphical manner (Figs. 3–5). In the analysed graphs, the authors found the most representative results when comparing 2nd-order vs. 3rd-order estimates (var. vs. skew) and 2nd-order vs. 4th-order estimates (var. vs. kurt.). Figures 3 and 4 show a trend in the data from which data clusters could be created. The HOS trends can be used to group data points that show a characteristic closeness, such as in the case of sag clusters (figs. 3–4). In Fig. 5, the 3rd vs. 4th-order representation shows an intersecting area that makes it difficult to discriminate different events. Nevertheless, transients are less accurate in the 3rd and 4th-order than sags because of their natural instability. Thus, the study of statistical clusters of transient

EBSCOhost - printed on 2/14/2023 2:46 PM via . All use subject to https://www.ebsco.com/terms-of-use

events cannot be conclusive without there being some previous information with which to compare the data. It would be useful to have data from a previous monitoring campaign with which to make such comparisons.

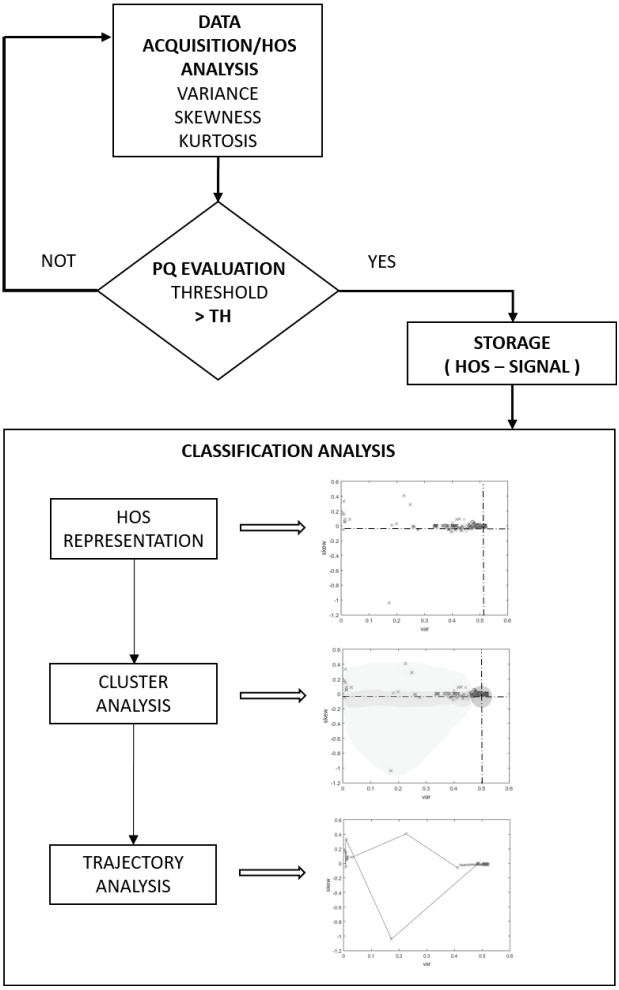



Figure 2. Experimental strategy of the PQ procedure based on HOS acquisition, the implementation of a threshold based on the PQ index, and classification analysis of the two different strategies: cluster analysis and trajectory analysis of events.

EBSCOhost - printed on 2/14/2023 2:46 PM via . All use subject to https://www.ebsco.com/terms-of-use

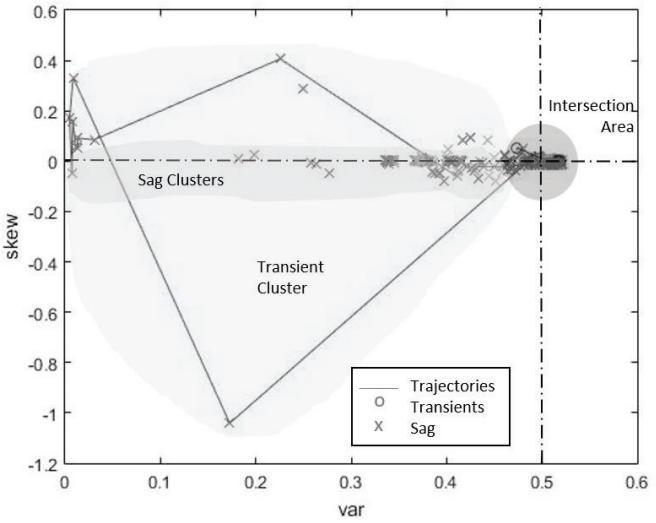



Figure 3. Sag and transient cluster tendency (point-to-point variance vs. skewness), from the PQ instrument panel.

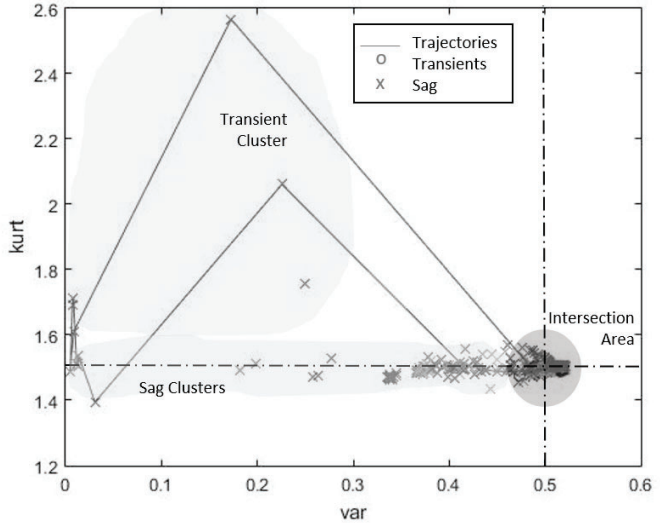



Figure 4. Sag and transient cluster tendency (point-to-point variance vs. kurtosis), from the PQ instrument panel.

EBSCOhost - printed on 2/14/2023 2:46 PM via . All use subject to https://www.ebsco.com/terms-of-use

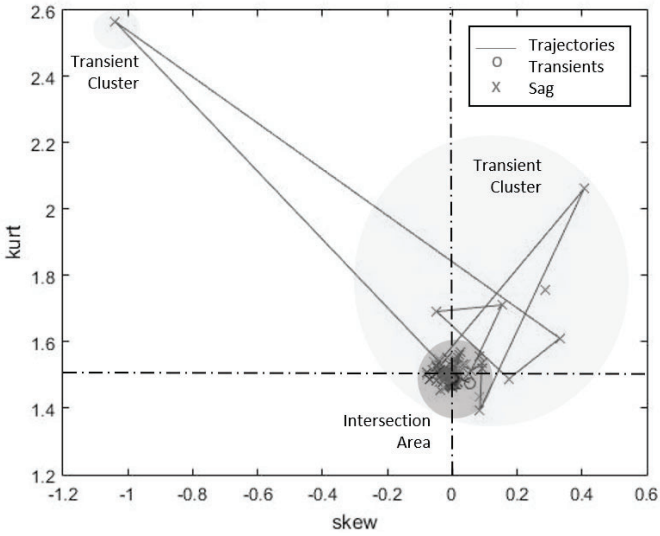



Figure 5. Intersecting area: point-to-point skewness vs. kurtosis values, from the PQ instrument's panel.

The experimental strategy was validated through a comparative analysis with a storage database. This validation was done to help outline improvements to the virtual instrument for monitoring the network. The results of comparative analysis show similar conclusions to the offline analysis and the virtual instrument procedure. Sag and transient events have been classified into different clusters.

## The PQ Index in Real-time Monitoring

As described in the previous section, in order to evaluate HOS space detection, a group of real-life signals were detected and analysed (100 signals: 50 sags and 50 transients) at a sampling frequency of 20 kHz (400 samples per cycle). 51% showed a RMS voltage variation of 70%, while 43% showed a RMS voltage variation of 90%.

Several data acquisition strategies were used based on the threshold of the PQ index. Real-time analysis commonly gave PQ values of 0.026, indicating that the monitored signal was highly deviant (an ideal signal would be PQ = 0). Transient disturbances were detected when the PQ value was superior to 0.02. Sags were detected when the PQ value reached 0.05. The characteristic PQ of the monitoring point was established

EBSCOhost - printed on 2/14/2023 2:46 PM via . All use subject to https://www.ebsco.com/terms-of-use

according to the behaviour of the quality of the voltage during the monitoring period. The aim of this was to calibrate the PQ value under normal conditions and set a PQ 'floor.' The test point was set as an average PQ floor value of 0.02. An empirical PQ threshold was derived from analysis, (more than twice the value of the previous PQ floor) PQ ≥ 0.05, in order to detect relevant events and study their behaviour in the HOS space.

It is important to emphasize that these PQ thresholds derived from the instrument are characteristic of the measurement locations being tested. Several testing sessions were carried out prior to using the instrument in an experimental monitoring session, in order to derive suitable thresholds in accordance with the test objectives.

Fig. 6 gives a graphical presentation of the real-time analysis of two different registers: sag and transient events. The experimental strategy followed the procedure previously described in order to show the final representation of events in the HOS space. The first step, acquisition of data, tracked cycle-to-cycle HOS measurements facilitating the tracking of signal perturbations in the time domain. The second step, PQ evaluation, shows how the index computes the three HOS deviations in a single indicator (PQ vs. data index). The index helped to detect the most relevant disturbances using an indicator that displays the average of the temporary deviations of the HOS. In the third step, classification analysis was undertaken. The disturbances were recorded and their behaviour was used to establish a preliminary cluster space for HOS (Figs. 3–5).

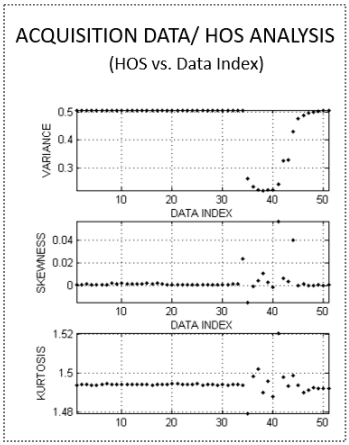
As we have previously seen, the graphs of variance vs. kurtosis and variance vs. skewness discriminate between types of events, as well as allowing us to investigate the cycle-to-cycle behaviour of deviations.

The methodology of the instrument can be used both for analysis of the signal in real time and, in the case of an offline session, in the analysis of a battery of recorded signals.

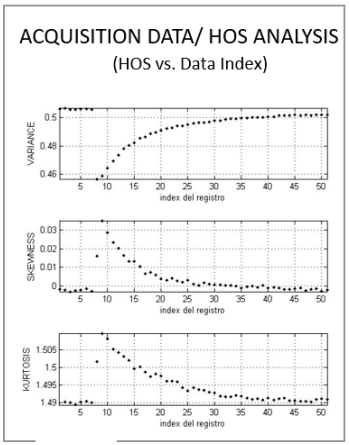
Figure 6 (next page). Representation of the PQ experimental strategy in the real-time analysis of two- disturbed signals, 50 Hz, sampling frequency of 20 kHz (400 samples per cycle): the first, a sag of 60–70% and the second, a transient disturbance. The different analytical steps of the methodology have the objective of classifying the behaviour of these disturbances. According to the samples the signal has a PQ index of 50. When a sag occurs, the PQ index helps to determine the subsequent behaviour of the signal. Using this we can see that the signal shows a tendency to stabilize. Transients are instantaneous events making them more difficult to characterize and classify.

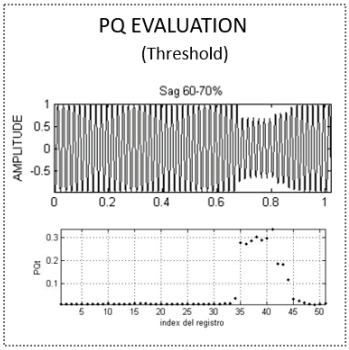
EBSCOhost - printed on 2/14/2023 2:46 PM via . All use subject to https://www.ebsco.com/terms-of-use

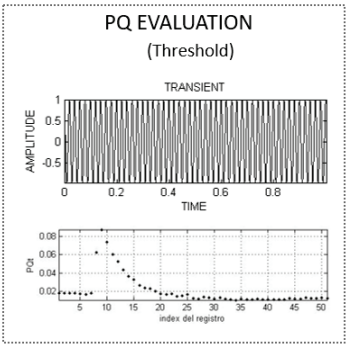
SAG 60-70%

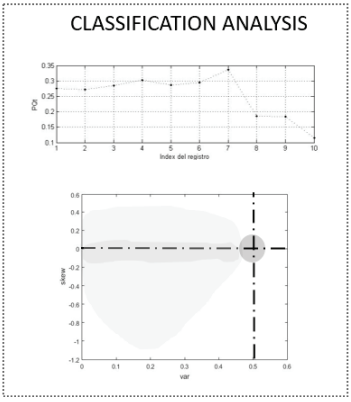


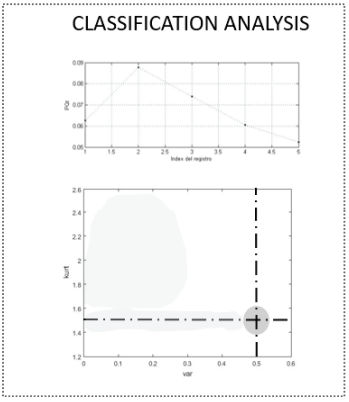

TRANSIENT




EBSCOhost - printed on 2/14/2023 2:46 PM via . All use subject to https://www.ebsco.com/terms-of-use

## Configuration of the Virtual Instrument

The instrument configuration follows the organigram and measurement methodology proposed by UNE-EN-61000-4-30 (Fig. 7). The main objective was to design an instrument (class S) for statistical applications, such as measurement and evaluation of power supply quality.

The hardware used was from National Instruments, with an Ethernet connection and the NIcDAQ$^{TM}$ 9188 chassis. The analogue input module was the NI-9225 model from the C series. In an earlier version of the instrument, the authors used a Hameg HZ 115 Differential probe, in order to amplify the signal from the consumer power line (measuring transducer) [22]. The authors decided that the NI9225 module would give better accuracy when testing the signal.

All operator level management of monitoring was made possible through a portable computer ASUS X554L via Ethernet connection. The virtual interface was designed in the LabVIEW$^{TM}$ (2014) environment so that it could be evaluated before further development and the introduction of improvements related to new quality parameters of the power supply.

The instrument interface used different panels that worked primarily in two PQ control modes, see figs. 8–9.

1. Mode 1. Characterization of the power line. This mode was aligned with the standard [UNE-EN 61000-4-30]. It was used for real-time monitoring of the voltage, harmonics, inter-harmonics, and network imbalances. The measurement procedure continuously analysed windows of 10 cycles ($10T_{signal}$), with a critical time interval measurement of 15 blocks of $10T_{signal}$ ($150T_{signal}$).
2. Mode 2. Detection of transients. This mode used an alternative procedure to the measurement requirements of the standard. It used a sliding window method (Fig. 1). The main objective was to reduce the measurement resolution to each cycle and to obtain greater measurement precision.

The main difference between the two mode settings, characterization and detection, is related to the measurement resolution (basic window) and their PQ index results. The transient detection mode (Fig. 8) shows the PQ index in real time, while the characterization mode averages the measurement window data (PQ values of 10 cycles; 150 cycles) reducing the possibility of detecting PQ events of less than 0,2s (20 kHz one cycle 0,02s).

EBSCOhost - printed on 2/14/2023 2:46 PM via . All use subject to https://www.ebsco.com/terms-of-use

The user interface was managed from a main panel, PQ control (Fig. 8), so that the operator could configure information related to the working session, including: the network analysed; the operator; the session number; and the file path for signal data storage. This data was used to identify the header of each of the files generated in the database. Additionally, it was possible to track the signal acquisition, the PQ index trend, the PQ characterization, and the PQ in real time. The operator also had the ability to abort the session at any time and the PQ threshold panel (Fig. 9) could be used to choose a predefined threshold, or for the operator could set a threshold manually, according to session behaviour. The main variables shown in this panel were the PQ value, the HOS disturbance trend, PQ floor and the PQ threshold alarm.

The input of the instrument automatically computed the state of the signal from the power line, establishing PQ behaviour. The virtual instrument (implemented in LabVIEW$^{TM}$) helped to monitor the network and its configuration added flexibility to the working session.

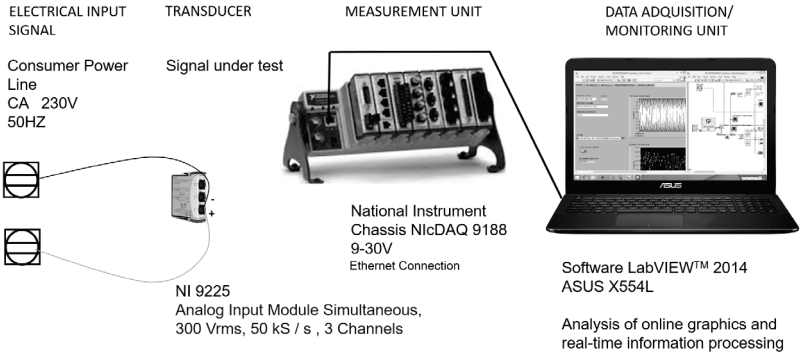



Figure 7. The configuration of the virtual instrument guarantees measurement tracking of the devices. The hardware consists of certificated instruments, such as those by National Instruments. The interface can bring up on-line graphs for analysis, processes signals in real time, and report incidents.

EBSCOhost - printed on 2/14/2023 2:46 PM via . All use subject to https://www.ebsco.com/terms-of-use

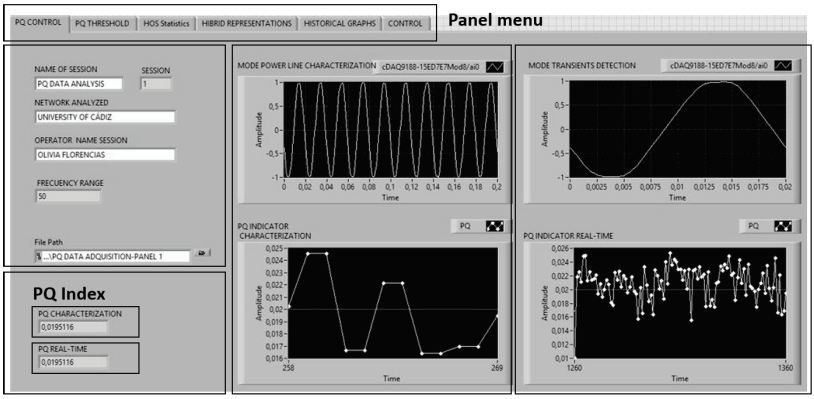



Figure 8. PQ control panel. The left side allows the operator to configure the session and save the information. The rest of the panel presents the different operating modes: characterization of the power line (left) and detection of transients (right), following PQ index trends in both modes. The horizontal line in the PQ panels (grey) represents the PQ floor = 0,02.

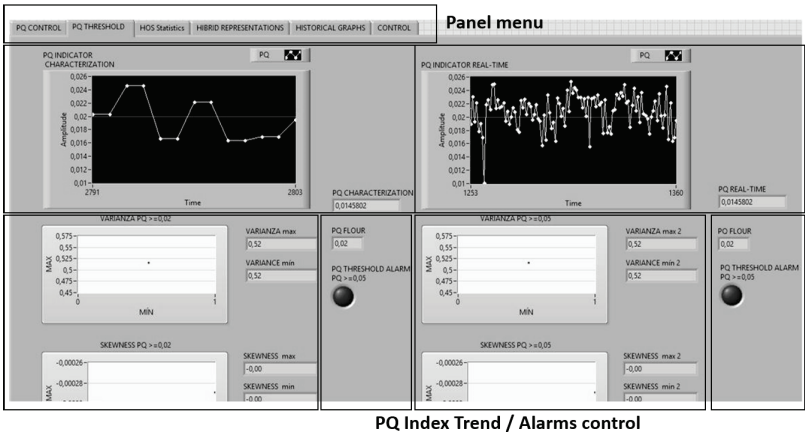



Figure 9. The PQ threshold panel allows monitoring of PQ behaviour in both modes for the power line and transients. The operator can select a conventional configuration or a specific one depending on the variables to be monitored, the thresholds desired, and the data needed to be saved. The transient detection mode is more effective at detecting PQ events and more accurately measures PQ values. This includes when the PQ floor threshold (PQ = 0,02) and the PQ alarm threshold (PQ ≥ 0,05) are passed.

EBSCOhost - printed on 2/14/2023 2:46 PM via . All use subject to https://www.ebsco.com/terms-of-use

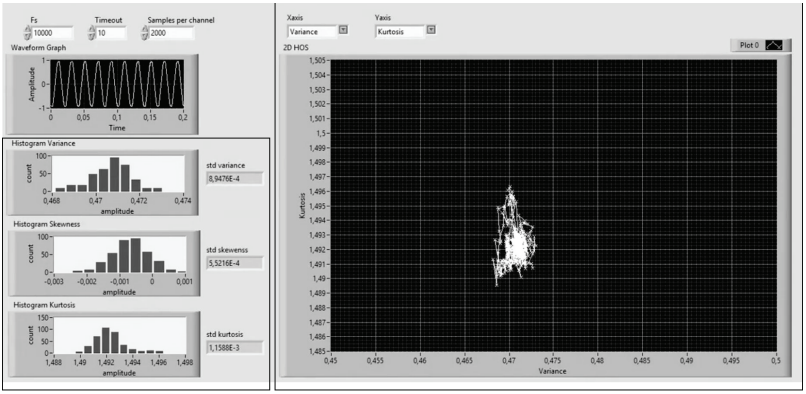



Figure 10. The PQ HOS statistics panel. Surveillance of HOS with standard deviation and histograms are on the left. On the right, the operator can observe the analytical trajectory of HOS space events.

## Results

PQ evaluation using the PQ index helped with the classification analysis. This classification allowed the configuration of two IEEE database (IEEE DataPort): real-life PQ sags [24] and real-life PQ transients [25].

The selection of desired limits depends on the behaviour of the signal at the monitoring point. Improved knowledge of this allows for better setting of thresholds according to the needs of the operator. LabVIEW™ offer multiples possibilities, including: saving graphical representations of PQ behaviour; saving a cluster analysis or the trajectory of a relevant event; and updating the online session and other available options shown in the panels (figs. 8–10). In order to reduce the uncertainty of measurements made by the instrument, instrument design is a key issue. HOS surveillance can be presented through real-time histograms and the standard deviation of individual HOS (Fig. 10). Also, the statistical range of the monitored variables, and max and min values, can be controlled.

An additional innovation to the virtual instrument is cluster analysis or ‘hybrid representations’ [23]. In this case, the hybrid representation corresponds to a theoretical XY graph using individual statistical values vs. other statistics of the signal: variance vs. skewness; variance vs. kurtosis; and kurtosis vs. variance (See figs. 3–5). The cluster method includes other graphs in the virtual instrument including diverse maximum and minimum graphs corresponding to the real value of individual statistics and depending on the behaviour of a number of data cycles

EBSCOhost - printed on 2/14/2023 2:46 PM via . All use subject to https://www.ebsco.com/terms-of-use

(limits) or a predefined interval -*th* of analysis: variance (max vs. min); skewness (max vs. min); and kurtosis (max vs. min). Analysis of the limits set offers the possibility of modifying a real session according to empirical experience, and the introduction of alternative measurement procedures.

The dynamics of events can be characterized in the HOS space according to the trajectories of events. Cycle-to-cycle surveillance helps improve our understanding of the behaviour of events in HOS space. More information related to conventional power quality events, such as sag, swell, and transients, can be divined from this new space of representation, analysis, and classification (HOS space).

The quantification of HOS aligned to the events characterized, adds more information allowing us to identify different zones in HOS space.

## Conclusions

This work has described a virtual instrument that implements a HOS-based global, scalable PQ index, associated to a specific location in the tested network. It was tested and validated using a battery of real-life signals. The index has a twofold purpose: to set a threshold for the power supply signal and to trigger a PQ analysis once a threshold has been breached. The experimental strategy used real-life signals to demonstrate the validity of the procedure, which assessed the stability of the signal in the time domain through cycle-to-cycle tracking of the time-series of the index.

This HOS-based approach helps in monitoring the PQ dynamics and tracks voltage supply stability in 2D. This also allows us to infer the type of disturbance according to the trajectory displayed in the HOS graphs.

Another concept that emerges from this work is the PQ floor, from which it is possible to fix a PQ threshold associated with a measurement location during a measurement interval. The threshold should be modified according to customer and system requirements. During a monitoring session, the index dynamics enables reporting of PQ trends and help discrimination by network type and detected deviations, as well as allowing forecasting analysis.

The classification analysis streamlines the capture process and reduces the storage space required for the data—fewer samples are needed to monitor the voltage signal. It obtains effective results when compared to traditional methods of analysis.

The instrument has different operation procedures that can be adapted for users depending on their knowledge of power quality. Transient detection mode measures power line disturbances with greater specificity.

EBSCOhost - printed on 2/14/2023 2:46 PM via . All use subject to https://www.ebsco.com/terms-of-use

This information is useful in predicting issues for all classes of equipment, which is one of the main research topics in the power quality research community.

Outcomes of the online monitoring sessions confirmed the theoretical approach of clustering found in the different graphs analysed. Different clusters (sags and transients) were depicted, as well as an intersecting area. Additionally, graphing the trajectory of events helped analyse cluster behaviour better. The authors are currently in the process of improving the clustering and trajectory strategies so as to better characterize other PQ events in HOS space.

Finally, the solution provided in this research is relevant, at a professional level as an enterprise technical solution for the power instrumentation market and other potential clients, and as a means of indexing equipment control and monitoring the quality of the power delivered to final consumers. HOS measurement solutions can be implemented in new smart meters with PQ capabilities in order to reduce computational costs.

PQ representation through the HOS method can be a tool for visualization and plotting data so that consumers can more easily understand what is happening.

Accurate measurement are necessary for the taking of decisions, diagnostic purposes, and reliability analysis. The aim is to add new perspectives to the management of SGs, the DER, and improve the standard TC-39—Measurements in Power Systems.

## References

[1] M. H. J. Bollen, S. Bahramirad, and A. Khodaei, “Is there a place for power quality in the smart grid?,” *Proc. Int. Conf. Harmon. Qual. Power, ICHQP*, pp. 713–717, 2014.

[2] C. Muscas, “Power quality monitoring in modern electric distribution systems,” *IEEE Instrum. Meas. Mag.*, vol. 13, no. 5, pp. 19–27, 2010.

[3] F. Martzloff and T. M. Gruzs, “Power Quality Site Surveys: Facts, Fiction, and Fallacies,” *IEEE Trans. Ind. Appl.*, vol. 24, no. 6, pp. 1005–1018, 1988.

[4] C. Cired, C. Jwg, F. Zavoda, R. Langella, G. C. Lazaroiu, M. Bollen, S. K. Rönnberg, J. Meyer, and P. Ciufo, “Power Quality in the Future Grid – Results from CIGRE/CIRED JWG C4.24,” pp. 404–409.

[5] B. Alsayyed Ahmad, H. H. ElSheikh, and A. Fadoun, “Review of power quality monitoring systems,” *2015 Int. Conf. Ind. Eng. Oper. Manag.*, pp. 1–8, 2015.

[6] I. Monedero, C. Leon, J. Ropero, A. García, J. M. Elena, and J. C. Montaño, “Classification of Electrical Disturbances in Real Time Using Neural Networks,” *IEEE Trans. Power Deliv.*, pp. 1–9, 2007.

EBSCOhost - printed on 2/14/2023 2:46 PM via . All use subject to https://www.ebsco.com/terms-of-use

[7] S. S. S. R. Depuru, L. Wang, and V. Devabhaktuni, "Smart meters for power grid: Challenges, issues, advantages and status," *Renew. Sustain. Energy Rev.*, vol. 15, no. 6, pp. 2736–2742, 2011.

[8] J. J. G. De La Rosa, A. Agüera-Pérez, J. C. Palomares-Salas, J. M. Sierra-Fernández, and A. Moreno-Muñoz, "A novel virtual instrument for power quality surveillance based in higher-order statistics and case-based reasoning," *Meas. J. Int. Meas. Confed.*, vol. 45, no. 7, pp. 1824–1835, 2012.

[9] O. Florencias-Oliveros, J.-J. González-de-la-Rosa, A. Agüera-Pérez, and J.-C. Palomares-Salas, "Discussion on Reliability and Power Quality in the Smart Grid : a prosumer approach of a time scalable index," no. 16, 2018.

[10] M. H. J. Bollen, I. Y. H. Gu, P. G. V Axelberg, and E. Styvaktakis, "Classification of underlying causes of power quality disturbances: Deterministic versus statistical methods," *EURASIP J. Adv. Signal Process.*, vol. 2007, 2007.

[11] L. Angrisani, P. Daponte, and M. D'Apuzzo, "Wavelet network-based detection and classification of transients," *IEEE Trans. Instrum. Meas.*, vol. 50, no. 5, pp. 1425–1435, 2001.

[12] A. M. Blanco, M. Gupta, A. G. De Castro, S. Rönnberg, and J. Meyer, "Impact of flat-top voltage waveform distortion on harmonic current emission and summation of electronic household appliances," vol. 1, no. 16, pp. 698–703, 2018.

[13] S. Yanchenko and J. Meyer, "Harmonic emission of household devices in presence of typical voltage distortions," *2015 IEEE Eindhoven PowerTech, PowerTech 2015*, 2015.

[14] M. V. Ribeiro, C. A. G. Marques, C. A. Duque, A. S. Cerqueira, and J. L. R. Pereira, "Detection of disturbances in voltage signals for power quality analysis using HOS," *EURASIP J. Adv. Signal Process.*, vol. 2007, 2007.

[15] A. Agüera-Pérez, J. J. Palomares-Salas, J.-J. González-de-la-Rosa, J. M. Sierra-Fernández, D. Ayora-Sedeño, and A. Moreno-Muñoz, "Characterization of electrical sags and swells using higher-order statistical estimators," *Measurement*, vol. 44, pp. 1453–1460, 2011.

[16] J. J. González-de-La-Rosa, A. Moreno, and C. G. Puntonet, "A practical review on higher-order statistics interpretation. Application to electrical transients characterization," *ISPA 2007 - Proc. 5th Int. Symp. Image Signal Process. Anal.*, pp. 224–229, 2007.

[17] Ö.¨ N. Gerek and D. G. Ece, "Power-quality event analysis using higher order cumulants and quadratic classifiers," *IEEE Trans. Power Deliv.*, vol. 21, no. 2, pp. 883–889, 2006.

[18] K. Zhou, C. Fu, and S. Yang, "Big data driven smart energy management: From big data to big insights," *Renew. Sustain. Energy Rev.*, vol. 56, pp. 215–225, 2016.

[19] IEEE, *IEEE Std 1159 - IEEE Recommended Practice for Monitoring Electric Power Quality.*, vol. 2009, no. June. 2009.

[20] UNE-EN, "UNE EN 50160 2011/A1 : 2015.Voltage characteristics of electricity supplied by public electricity networks." 2015.

EBSCOhost - printed on 2/14/2023 2:46 PM via . All use subject to https://www.ebsco.com/terms-of-use

[21] UNE-EN, “UNE-EN 61000-4-30:2015. Electromagnetic compatibility (EMC).Part 4-30: Testing and measurement techniques. Power quality measurement methods.” 2015.

[22] O. Florencias-Oliveros, A. Agüera-Pérez, J.-J. González-de-la-Rosa, J. C. Palomares-salas, and J. M. Sierra-Fernández, “A novel instrument for power quality monitoring based in higher-order statistics : a dynamic triggering index for the smart grid,” *Int. Conf. Renew. Energies Power Qual.*, no. 15, 2016.

[23] O. Florencias-Oliveros, J.-J. González-de-la-Rosa, A. Agüera-Pérez, and J.-C. Palomares-Salas, “Power quality event dynamics characterization via 2D trajectories using deviations of higher-order statistics,” *Meas. J. Int. Meas. Confed.*, vol. 125, 2018.

[24] Olivia Florencias-Oliveros, M. J. Espinosa-Gavira, Juan-José González de la Rosa, A. Agüera-Pérez, José Carlos Palomares-Salas, J. M. Sierra-Fernández, "Real-life Power Quality Sags ", IEEE Dataport, 2017. [Online]. Available: http://dx.doi.org/10.21227/H2K88D. Accessed: Sep. 13, 2018.

[25] Olivia Florencias-Oliveros, M. J. Espinosa-Gavira, J. J. González-de-la-Rosa, A. Agüera-Pérez, J. C. P. Salas, J. M. Sierra-Fernández, "Real-life Power Quality Transients ", IEEE Dataport, 2017. [Online]. Available: http://dx.doi.org/10.21227/H2Q30W. Accessed: Sep. 13, 2018.

EBSCOhost - printed on 2/14/2023 2:46 PM via . All use subject to https://www.ebsco.com/terms-of-use

# CHAPTER FORTY-TWO

# A POWER INDEX-BASED DIAGNOSTIC FOR SYSTEMS WITH ACTIVE POWER LOAD CONDITIONING

JAIME PRIETO, PATRICIO SALMERÓN, ALEJANDRO PÉREZ, SALVADOR P. LITRÁN[1]

## Abstract

This paper presents an enhanced diagnostic method for the improvement of electrical power quality using compensation equipment with active power filters (APF). Using an enhanced procedure, indicators of power quality allow the identification of the contribution to unbalance made by the harmonics and interharmonics of voltages and currents. From this set of power terms, unbalanced fundamental, balanced harmonic, and unbalanced harmonic indices can been derived that allow us to evaluate separately distortion and unbalance. These indicators were applied to a system with unbalance and distortion in the supply and the load, before and after the connection of a parallel active compensator and with the connection of a series-parallel active compensator. The results obtained, using a dedicated experimental platform, have allowed us to verify the validity of the proposed procedure, and to clarify the interpretation of unbalance and harmonic distortions with these kinds of compensation.

**Keywords**: Power quality, harmonics, unbalance, active power filters.

[1] Authors are with the Department of Electrical Engineering, Huelva University, Spain.

EBSCOhost - printed on 2/14/2023 2:46 PM via . All use subject to https://www.ebsco.com/terms-of-use

## Introduction

The IEEE Std. 1459 presents the most extended model for the decomposition of apparent power terms under conditions of asymmetry and distortion, [1]. However, this model does not present an adequate assessment of unbalance produced by the load, [2]. This is especially significant in terms of the contribution made to such an unbalance by the set of harmonics that differ from the fundamental frequency. This problem is further accentuated when modern compensation equipment is used. It is possible to dispose of compensation systems by using active power filters (APFs) connected in parallel; and a combined system of series-parallel compensation with the use of APFs in series and shunt connection [3–7]. In this second case, it is possible to eliminate the harmonics and unbalance in the current, as well as to obtain a conditioned voltage at the load terminals through the use of an appropriate control strategy. The use of active compensation equipment based on power inverters gives rise to the appearance of time-variant waveforms of voltage and current. Analysis of these waveforms in the frequency domain shows the presence of harmonics and inter-harmonics. Std IEC 61000-4-7 establishes the measurement periods of various fundamental cycles for the spectral analysis of voltage and current. Thus, Fourier analysis of the waveforms identifies harmonic and interharmonic components. The need to provide the power terms and associated indices to characterize the resulting mitigation require a model of the decomposition of the apparent power that makes explicit the contribution of harmonics to unbalance [8–10]. Proposals in [8] and [9] established a new model of the decomposition of apparent power, which can be separated into four components. From there, they defined three indices that characterize the unbalance and distortion. However, this model does not include the contribution of interharmonics to each power component. In [10], a transformation matrix was introduced, which can identify the balanced, first-unbalanced, and second-unbalanced components of waveforms that include inter-harmonics. This work relies on these previous proposals to develop an efficient method of computing the balanced and unbalanced components in the measured waveforms of voltage and current in systems with active conditioners, [11–12].

This new procedure was applied to an unbalanced and distorted system, before and after compensation with a shunt active filter and with combined series-parallel compensation. A description of a practical case and the results obtained are presented here to evaluate the performance of

EBSCOhost - printed on 2/14/2023 2:46 PM via . All use subject to https://www.ebsco.com/terms-of-use

the proposed procedure and to characterize the values of power quality indicators with this kind of compensation.

## Power Components and Power Quality Indices in Unbalanced and Non-sinusoidal Conditions

In balanced non-sinusoidal three-phase systems, where the waveforms are repeated every third of a cycle in the corresponding phase, the voltage and current harmonics can be divided into three groups with different phase sequences: the harmonic set of order 3h+1 (for h = 0, 1, 2, …), which has a positive sequence of phases; the set of order 3h+2, which has a negative phase sequence; and the set of order 3h+3, where the harmonics are in phase with each other (zero sequence). However, in unbalanced and non-sinusoidal systems, this is no longer the case. Determining balanced and unbalanced harmonic components is important because some solutions to counter harmonic distortion are based on the previous assumption. For instance, the Δ connection of transformer windings to block 3rd order harmonics, or the change in behaviour of nonlinear loads against unbalance all rely on this model.

A recent proposal to set the balanced and unbalanced components of each signal was laid out in [10]. This model calculates a balanced component and two unbalanced components, defined through the following relation:

$$\begin{bmatrix} X_{br} \\ X_{u'r} \\ X_{u''r} \end{bmatrix} = T_r \cdot \begin{bmatrix} X_{Ar} \\ X_{Br} \\ X_{Cr} \end{bmatrix} = \frac{1}{3} \begin{bmatrix} 1 & \alpha_k & \alpha_{2k} \\ 1 & \alpha_{k+1} & \alpha_{2k+2} \\ 1 & \alpha_{k+2} & \alpha_{2k+1} \end{bmatrix} \cdot \begin{bmatrix} X_{Ar} \\ X_{Br} \\ X_{Cr} \end{bmatrix} \quad (1)$$

where $X_{Ar}$, $X_{Br}$, and $X_{Cr}$ are the phasors of the voltages or currents of each phase, at the angular frequency $r \cdot \omega_F$, obtained from the Fourier transform of the instantaneous values in a measuring window of period $T_F = 2\pi/\omega_F$; and $X_{br}$, $X_{u'r}$, $X_{u''r}$ are the corresponding balanced, first-unbalanced, and second-unbalanced components. The transformation matrix $T_r$ is defined using the complex exponential expressions $\alpha(\cdot) = e^{j(\cdot)\,2\pi/3}$, with $k = r\,\omega_F/\omega_1$, where $r = 1, 2, \ldots N$ is the harmonic order in relation to the fundamental frequency in the measurement period. $k$ is the relative harmonic order, referring to the fundamental frequency of the system $\omega_1$. It takes integer values for the harmonics of $\omega_1$ and non-integer values for the remaining inter-harmonics. The transformation matrix $T_r$ is orthogonal for all possible values of $k$. This property allows us to establish the

EBSCOhost - printed on 2/14/2023 2:46 PM via . All use subject to https://www.ebsco.com/terms-of-use

following relation between the magnitudes of the phasors of the phase values and those of the phasors of the balance/unbalance components:

$$X_{Ar}^2 + X_{Br}^2 + X_{Cr}^2 = 3\left(X_{br}^2 + X_{u'r}^2 + X_{u''r}^2\right) \tag{2}$$

This relation is very useful in defining balanced and unbalanced components of voltages and currents, because the definitions of the effective values $V_e$ and $I_e$ in the IEEE Standard 1459 [1] are based on the summations of quadratic expressions of the magnitudes.

However, before addressing the development of the different terms, let us explain the relation between the balanced/unbalanced components and the Fortescue symmetrical components. Firstly, the symmetrical components of the harmonic spectrum can be obtained more efficiently using the FFT Transform than the Park vector of the three-phase signals [11–12], which reduces computational cost. Secondly, the explicit relationship helps us understand how symmetrical components are transformed into balanced or unbalanced components. When the inverse Fortescue transform is used to substitute the phase components with the symmetrical components in (1), the resultant relationship is:

$$\begin{bmatrix} X_{br} \\ X_{u'r} \\ X_{u''r} \end{bmatrix} = \frac{1}{3}\begin{bmatrix} b_1 & b_2 & b_3 \\ b_3 & b_1 & b_2 \\ b_2 & b_3 & b_1 \end{bmatrix} \cdot \begin{bmatrix} X_{\mathrm{Pr}} \\ X_{Nr} \\ X_{Zr} \end{bmatrix} \tag{3}$$

where $X_{Pr}$, $X_{Nr}$, and $X_{Zr}$ are the positive, negative, and zero sequence phasors at this frequency. The coefficients $b_1$, $b_2$, and $b_3$ have the expressions:

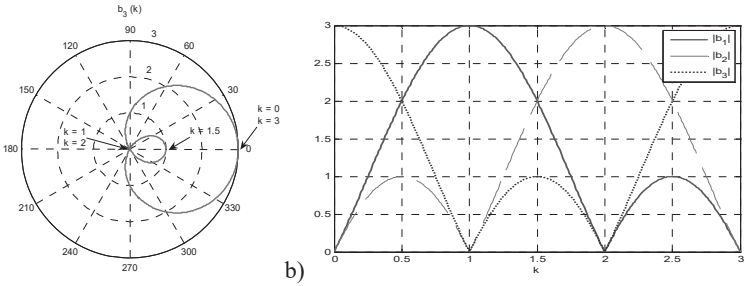
$$\begin{aligned} b_1 &= 1 + \alpha_{k+2} + \alpha_{2(k+2)} \\ b_2 &= 1 + \alpha_{k+1} + \alpha_{2(k+1)} \\ b_3 &= 1 + \alpha_k + \alpha_{2k} \end{aligned} \tag{4}$$

The three coefficients have the same functional structure and are periodic for variable $k$ (period 3). For instance, the expression for $b_3$ can be expressed as:

$$b_3 = 1 + \alpha_k + \alpha_{2k} = \left(1 + 2\cos\frac{2\pi k}{3}\right) e^{j\frac{2\pi k}{3}} \tag{5}$$

EBSCOhost - printed on 2/14/2023 2:46 PM via . All use subject to https://www.ebsco.com/terms-of-use

Fig. 1a shows the polar plot of eq. (5), while Fig. 1b presents the magnitudes of the complex coefficients $b_1$, $b_2$, *and* $b$ as a function of $k$. The three values evolve cyclically, changing the position of the symmetrical components into balanced/unbalanced components. For instance, when $k = 1$, the transformation (3) is the identity matrix: the positive-sequence component, $X_{Pr}$, is identified with the balanced component, $X_{br}$: and the negative and zero sequence components with the first and second-unbalanced components, respectively. When $k = 2$ the balanced component is the negative-sequence component, $X_{Nr}$; and when $k = 3$ the balanced component is the zero-sequence component, $X_{Zr}$. These figures allow us to estimate the weight of each symmetrical component as balanced/unbalanced components when $k$ has non-integer values. For instance, for inter-harmonics very near the fundamental frequency, the major contribution to the balanced component $X_{br}$ comes from the positive-sequence $X_{Pr}$.




a) b)

Figure 1. Coefficients $b_i$ as a function of k: a) Polar plot of $b_3$, b) Magnitudes $|b_1|$, $|b_2|$, $|b_3|$.

On the other side, calculation of the equivalent voltages and currents according to IEEE Std. 1459 can be formulated with the Fortescue symmetrical components [1]:

$$V_e^2 = \sum_{\forall r} V_{er}^2 = \sum_{\forall r} \left[ V_{\mathrm{Pr}}^2 + V_{Nr}^2 + \frac{V_{Zr}^2}{1+\xi} \right]$$
$$I_e^2 = \sum_{\forall r} I_{er}^2 = \sum_{\forall r} \left[ I_{\mathrm{Pr}}^2 + I_{Nr}^2 + (1+3\rho) I_{Zr}^2 \right] \quad (6)$$

EBSCOhost - printed on 2/14/2023 2:46 PM via . All use subject to https://www.ebsco.com/terms-of-use

where $\xi$ is the ratio between the Y and $\Delta$ equivalent load active powers, considered to be 1.0 as the general case; $\rho$ is the ratio between the resistance of the neutral conductor and the phase conductors, also usually considered to have a value of 1.0 [1]. If the symmetrical component magnitudes are formulated into balanced and unbalanced components, the values of the equivalent voltages and currents can be separated in both components at each frequency:

$$V_{er}^2 = \left[ V_{Pbr}^2 + V_{Pur}^2 + V_{Nbr}^2 + V_{Nur}^2 + \frac{V_{Zbr}^2 + V_{Zur}^2}{1+\xi} \right]$$
$$V_{er}^2 = V_{ebr}^2 + V_{eur}^2 \tag{7}$$

$$I_{er}^2 = I_{Pbr}^2 + I_{Pur}^2 + I_{Nbr}^2 + I_{Nur}^2 + (1+3\rho)(I_{Zbr}^2 + I_{Zur}^2)$$
$$I_{er}^2 = I_{ebr}^2 + I_{eur}^2 \tag{8}$$

Combining all the harmonics and taking the fundamental components separately allows us to formulate the equivalent voltage as:

$$V_e^2 = V_{b1}^2 + V_{u1}^2 + V_{bh}^2 + V_{uh}^2 \tag{9}$$

where $V_{b1}$ is the balanced fundamental component of the equivalent voltage, identified with the positive-sequence component; $V_{u1}$ is the unbalanced fundamental component, related to the negative and zero sequence components; and $V_{bh}$ and $V_{uh}$ are the balanced and unbalanced harmonic components, respectively. A similar partition is performed with the currents:

$$I_e^2 = I_{b1}^2 + I_{u1}^2 + I_{bh}^2 + I_{uh}^2 \tag{10}$$

This new procedure highlights the relation between the symmetrical components and the balanced/unbalanced components. Eq. (7) and (8) explicitly show the relative weight of the zero sequence components in the definition of the balanced and unbalanced components. The decomposition established in (9) and (10) with the effective values of voltages and currents allows us to formulate a partition of the effective apparent power that fulfils the relation:

EBSCOhost - printed on 2/14/2023 2:46 PM via . All use subject to https://www.ebsco.com/terms-of-use

$$S_e^2 = \left(3V_e I_e\right)^2 = S_{b1}^2 + S_{u1}^2 + S_{bh}^2 + S_{uh}^2 \tag{11}$$

which identifies the following four power components:

$$S_{b1}^2 = 9V_{b1}^2 I_{b1}^2 \tag{12}$$

$$S_{u1}^2 = 9\left(V_{b1}^2 I_{u1}^2 + V_{u1}^2 I_{b1}^2 + V_{u1}^2 I_{u1}^2\right) \tag{13}$$

$$S_{bH}^2 = 9\left(V_{b1}^2 I_{bH}^2 + V_{bH}^2 I_{b1}^2 + V_{bH}^2 I_{bH}^2\right) \tag{14}$$

$$S_{uH}^2 = S_e^2 - S_{b1}^2 - S_{u1}^2 - S_{bH}^2 \tag{15}$$

The power component $S_{b1}$ is the balanced fundamental apparent power; $S_{u1}$ is the unbalanced fundamental apparent power; $S_{bH}$ is the balanced harmonic apparent power; and $S_{uH}$ is the unbalanced harmonic apparent power. If $S_{b1}$ is taken as the base value, it is possible to define indicators related to unbalance and harmonic distortions like:

$$SUF = \frac{S_{u1}}{S_{b1}}, \quad SBH = \frac{S_{bH}}{S_{b1}}, \quad SUH = \frac{S_{uH}}{S_{b1}} \tag{16}$$

*SUF*, *SBH*, and *SUH* are the unbalanced fundamental, balanced harmonic, and unbalanced harmonic factors of the system, respectively. Similarly, it is possible to define global indicators to assess the total unbalance and total harmonic distortion of the system according to the previous definitions:

$$STHD = \sqrt{\frac{SBH^2 + SUH^2}{1 + SUF^2}}, STUD = \sqrt{\frac{SUF^2 + SUH^2}{1 + SBH^2}} \tag{17}$$

where *STHD* and *STUD* are the total harmonic distortion and total unbalance of the system. Besides, to analyse the obtained results of practical cases, it is also convenient to use unitary indices of unbalance and distortion of the voltage and current magnitudes, defined with expressions similar to (16) and (17):

EBSCOhost - printed on 2/14/2023 2:46 PM via . All use subject to https://www.ebsco.com/terms-of-use

$$VUF = \frac{V_{u1}}{V_{b1}}, \quad VBH = \frac{V_{bH}}{V_{b1}}, \quad VUH = \frac{V_{uH}}{V_{b1}} \tag{18}$$

$$IUF = \frac{I_{u1}}{I_{b1}}, \quad IBH = \frac{I_{bH}}{I_{b1}}, \quad IUH = \frac{I_{uH}}{I_{b1}} \tag{19}$$

$$VTHD = \sqrt{\frac{VBH^2 + VUH^2}{1 + VUF^2}}, VTUD = \sqrt{\frac{VUF^2 + VUH^2}{1 + VBH^2}} \tag{20}$$

$$ITHD = \sqrt{\frac{IBH^2 + IUH^2}{1 + IUF^2}}, ITUD = \sqrt{\frac{IUF^2 + IUH^2}{1 + IBH^2}} \tag{21}$$

The following section describes how these indices and power components were addressed in a system with unbalance and harmonic distortions. This unbalanced and distorted system was compensated with two forms of active power conditioning: parallel and series-parallel. From this experiment, we can estimate the relative contribution of the different magnitudes seen in the power indices, and how they respond when different forms of active compensation are applied.

## Experimental Results

An experimental platform was designed on which to perform the validation of the proposals and verify the behaviour of the indices. Parallel and series-parallel compensation were applied to an unbalanced, nonlinear load supplied by an unbalanced set of voltages. Figure 2 shows the power circuit per phase of the series-parallel conditioner with corresponding matching transformers and passive elements for the filtering of high frequency components. The series and shunt three-phase IGBT converters (Semikron SKM50GB123D) were connected back-to-back, with a common DC link composed of two electrolytic capacitors, $C_{DC+}$ and $C_{DC-}$ of 2200 μF, each one having a rating of 400 V [4, 5]. The middle point of the DC link was connected to the neutral wire of the three-phase line. The turn ratio of the matching transformers $T_P$ and $T_S$ was 1:2 and 2:1 respectively, to achieve reasonable voltage values in the DC link and to set the maximum series compensating voltage at 25% of the output voltage of the shunt converter. The filtering inductances, $L_P$ and $L_S$, were rated for 50 mH each, and the values of the parallel filtering capacitor $C_P$ and

EBSCOhost - printed on 2/14/2023 2:46 PM via . All use subject to https://www.ebsco.com/terms-of-use

resistance $R_P$ were 30 μF and 2.5 Ω, respectively. A panel selector switch allowed the bypassing of the series converter to undertake tests using parallel active compensation only.

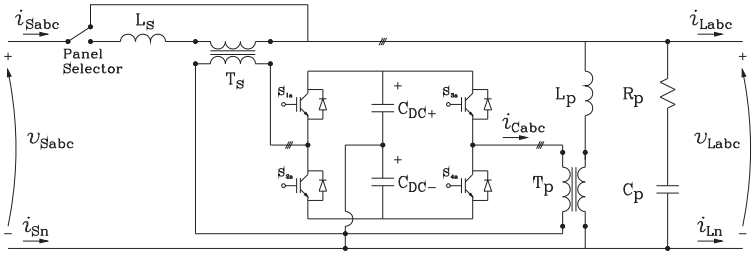



Figure 2. Power circuit of the active conditioners.

The switching control of the active converters and the calculation of the compensation references used a data acquisition and control system (dSPACE-DS1103). The sampling time of the main processor was set to 50 μs in the case of parallel compensation and 80 μs for series-parallel compensation. The target references for the compensation were set at the fundamental positive sequence components of the load currents $i_L$ and supply voltages $v_S$, in order to achieve the smallest unbalance and harmonic components in the compensated system. When performing parallel compensation, the reference for the compensating current $i_C$ was:

$$i_C^* = i_L - i_S^* \tag{22}$$

where $i_S^*$ is a set of balanced currents in phase with the fundamental direct sequence component of the supply voltage, which transports the average active power of the load and the losses of the conditioner [4]. As such, the unbalanced and harmonic components of the load current are compensated for.

When series-parallel compensation was performed, the references for the series compensating voltage $v_C$ and the shunt compensating current $i_C$ were [4]:

$$v_C^* = (v_L^* - v_S) + R\,(i_S^* - i_S) \tag{23}$$

$$i_C^* = (i_L - i_S^*) + G\,(v_L^* - v_L) \tag{24}$$

EBSCOhost - printed on 2/14/2023 2:46 PM via . All use subject to https://www.ebsco.com/terms-of-use

where $v_L^*$ is the reference for the load voltage: the fundamental positive sequence component of the supply voltage, with its amplitude regulated to its nominal value [4]. The second terms of (23) and (24) are crossed correcting signals proportional to the deviation of the target magnitudes to the reference values, which damp system behaviour with strong transients and with different kinds of loads. With this kind of compensation, the load voltage $v_L$ and the supply current $i_S$ should be free of unbalance and harmonic components.

The compensating voltage of the series converter, $v_C$, was built with a 20 kHz PWM generator (DS1103 slave), using the calculated reference $v_C^*$. The compensating current of the shunt converters was built with periodic sampling control at 20 kHz in an external circuit, using the deviation of the compensating current $i_C$ in respect of its reference $i_C^*$.

An independent measurement system [11–12] to calculate the indices was implemented in another data acquisition card (dSPACE-DS1005), with a signal conditioning system formed by six voltage sensors (LEM-LV25-P) and eight current sensors (LEM LA35-NP). These signals were acquired simultaneously to avoid phase differences between the measurements so as to enhance the accuracy of the results. The configuration of the virtual instrument was made following the recommendations of EN 61000-4-7 and EN 61000-4-30, using a sampling window equal to various cycles of the fundamental component and a sampling frequency of 6400 Hz, avoiding problems of aliasing and leakage errors.

Finally, the load was composed of three different single phase loads. Phase 1 used a single phase diode rectifier with a high capacitor, a resistive load on the DC side, and a smoothing reactor on the AC side. Phase 2 used a single phase diode rectifier with a series RL load on the DC side. A resistor was used for phase 3. This load was fed with an unbalanced set of voltages through a variable auto-transformer (95,100,110 V), with a nominal value of 100 $V_{rms}$ and a small distortion similar to the pre-existing one in the supply network of the laboratory. Fig. 3 shows the voltage and current waveforms of the load fed with this power supply.

EBSCOhost - printed on 2/14/2023 2:46 PM via . All use subject to https://www.ebsco.com/terms-of-use

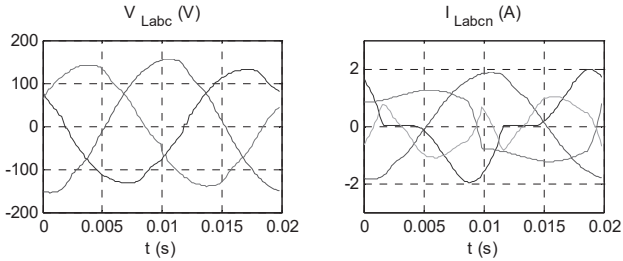



Figure 3. Voltage and current waveforms of the load without compensation.

Figures 4 and 5 show the resulting voltage and current waveforms with parallel compensation of the load currents, in the load and supply side respectively. The supply currents, $i_{Sabcn}$, are practically balanced, sinusoidal and in phase with the fundamental positive sequence component of the supply voltage, despite its distortion and unbalance.

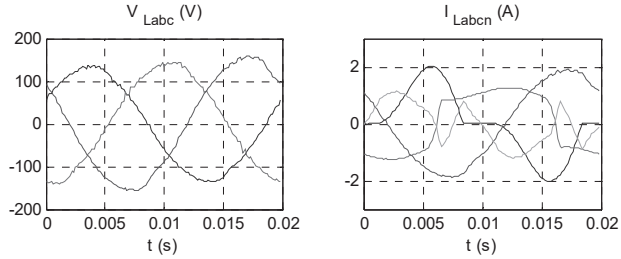



Figure 4. Voltage and current waveforms of the load side with active parallel compensation.

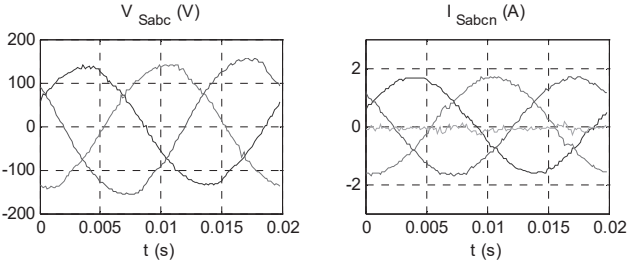



Figure 5. Voltage and current waveforms of the supply side with active parallel compensation.

EBSCOhost - printed on 2/14/2023 2:46 PM via . All use subject to https://www.ebsco.com/terms-of-use

Figures 6 and 7 show the resulting voltage and current waveforms with series-parallel compensation of the supply voltages and load currents. The supply currents were practically balanced, sinusoidal, and in-phase with the fundamental positive sequence component of the supply voltage. The load voltage was also enhanced, compensating for the distortion and unbalance present in the supply voltage.

Table I presents the calculations obtained with the virtual instrument, corresponding to the effective value of the three-phase voltages, currents, and apparent power for the different cases and measuring points. The data of the first column corresponds to the load before compensation; the second and third columns correspond to the use of shunt compensation, PC, with the measurements obtained at the load side $v_L$, $i_L$ (PC_l), and at the supply side $v_S$, $i_S$, (PC_s). The last two columns show the measurements at the load side and supply side with series-parallel compensation (SPC_l, SPC_s). Table I also includes the resultant voltage, current, and power components; as well as the corresponding power quality indices. At first glance, it appears that the unbalanced and harmonic components of the load current are almost compensated by both kinds of compensation; and that series-parallel compensation produces a regulated load voltage with small unbalance and harmonic components.

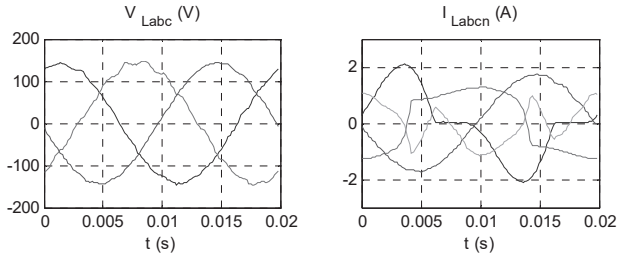



Figure 6. Voltage and current waveforms of the load side with active series-parallel compensation.

EBSCOhost - printed on 2/14/2023 2:46 PM via . All use subject to https://www.ebsco.com/terms-of-use

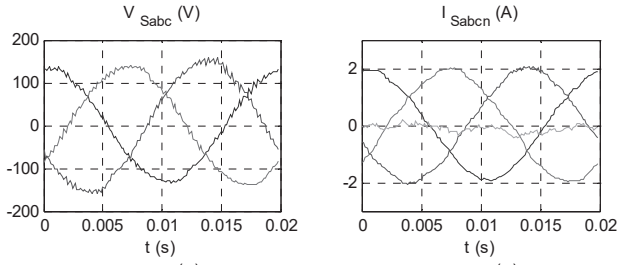



Figure 7. Voltage and current waveforms of the supply side with active series-parallel compensation.

**Table I: Values of the voltages, currents, and apparent power components, with related indices.**

| | Load | PC_l | PC_s | SPC_l | SPC_s |
|---|---|---|---|---|---|
| | *Effective values* | | | | |
| $V_e$ (V) | 101.2 | 101.4 | 101.4 | 100.7 | 99.81 |
| $I_e$ (A) | 1.206 | 1.227 | 1.166 | 1.201 | 1.375 |
| $S_e$ (VA) | 366.1 | 373.3 | 354.9 | 362.9 | 411.6 |
| | *Voltage components* | | | | |
| $V_{bl}$ (V) | 101.0 | 101.2 | 101.3 | 100.7 | 99.60 |
| $V_{ul}$ (V) | 5.34 | 5.28 | 5.19 | 0.88 | 5.24 |
| $V_{bh}$ (V) | 2.23 | 2.44 | 2.46 | 1.53 | 3.18 |
| $V_{uh}$ (V) | 2.11 | 1.69 | 1.68 | 2.08 | 3.22 |
| | *Current components* | | | | |
| $I_{bl}$ (A) | 1.075 | 1.082 | 1.164 | 1.066 | 1.371 |
| $I_{ul}$ (A) | 0.399 | 0.419 | 0.020 | 0.380 | 0.059 |
| $I_{bh}$ (A) | 0.257 | 0.280 | 0.034 | 0.282 | 0.057 |
| $I_{uh}$ (A) | 0.271 | 0.284 | 0.052 | 0.287 | 0.050 |
| | *Apparent power components* | | | | |
| $S_{bl}$ (VA) | 325.7 | 328.5 | 353.8 | 321.9 | 409.6 |
| $S_{ul}$ (VA) | 122.3 | 128.6 | 19.10 | 114.7 | 27.91 |
| $S_{bh}$ (VA) | 78.26 | 85.50 | 13.51 | 85.43 | 21.42 |
| $S_{uh}$ (VA) | 82.89 | 86.81 | 16.94 | 87.12 | 20.15 |
| | *Voltage indices (%)* | | | | |
| VUF | 5.29 | 5.22 | 5.12 | 0.87 | 5.26 |
| VBH | 2.21 | 2.41 | 2.43 | 1.52 | 3.19 |
| VUH | 2.09 | 1.67 | 1.66 | 2.07 | 3.23 |
| VTHD | 3.04 | 2.93 | 2.94 | 2.56 | 4.54 |
| VTUD | 5.68 | 5.48 | 5.38 | 2.24 | 6.17 |

EBSCOhost - printed on 2/14/2023 2:46 PM via . All use subject to https://www.ebsco.com/terms-of-use

| | *Current indices (%)* | | | | |
|---|---|---|---|---|---|
| IUF | 37.12 | 38.72 | 1.72 | 36.65 | 4.30 |
| IBH | 23.91 | 25.88 | 2.92 | 26.45 | 4.16 |
| IUH | 25.21 | 26.25 | 4.47 | 26.92 | 3.65 |
| ITHD | 32.57 | 34.37 | 5.34 | 35.55 | 5.53 |
| ITUD | 43.54 | 45.29 | 4.78 | 43.19 | 5.64 |
| | *Apparent power indices (%)* | | | | |
| SUF | 37.55 | 39.15 | 5.40 | 35.63 | 6.81 |
| SBH | 24.03 | 26.03 | 3.82 | 26.54 | 5.23 |
| SUH | 25.45 | 26.43 | 4.79 | 27.06 | 4.92 |
| STHD | 32.77 | 34.54 | 6.12 | 35.71 | 7.16 |
| STUD | 44.11 | 45.71 | 7.21 | 43.25 | 8.39 |

Looking at the indices of the first column of Table I, corresponding to the load without compensation, we can appreciate that the current values are much higher than those of the voltages. This indicates a kind of load with a strong fundamental unbalance and a significant source of harmonic distortion. The values in the power indices are similar to those of the currents. Taking into consideration the relation between the different indices (see eq. 9–21), it appears that the main contribution to the fundamental unbalance (SUF = 37.55 %) is that of the current fundamental unbalance, IUF. The value of the total harmonic distortion index (STHD = 32.77 %) is due to a similar contribution of balanced and unbalanced current harmonics, IBH, IUH. Furthermore, the total unbalance distortion index STUD reaches a value of 44.11 %, with similar contributions by the unbalanced fundamental power $S_{u1}$ and the unbalanced harmonic power $S_{uh}$.

The shunt active compensation case shows a significant reduction of the unbalance and harmonic components of the supply currents, with a corresponding enhancement of the apparent power components. Additionally, in this case, the current fundamental unbalance, IUF, reaches much lower values than that of the voltage fundamental unbalance, VUF, imposed on the supply. Therefore, the VUF value becomes dominant in the expression of the fundamental unbalance power index SUF. On the other side, voltage and current harmonic distortion have similar values and produce higher results in the corresponding power indices. In the ideal case, where the supply currents are perfectly compensated, the power indices will correspond only to the supply network conditions.

The power indices on the load side with parallel compensation shows a small increase, because parallel compensation can lead to a reduction in the filtering effect of the supply impedance [7]. This is also in line with the slight enhancement in the voltage indices due to a better supply current.

EBSCOhost - printed on 2/14/2023 2:46 PM via . All use subject to https://www.ebsco.com/terms-of-use

With series-parallel compensation, the unbalance and harmonic power components at the supply side also see a significant reduction, similar to shunt compensation. At the load side voltage indices, a significant reduction is seen, with a smaller unbalance and harmonic content in the load and regulation of the balanced fundamental component of the load voltages. Nevertheless, the power indices are similar to those seen in parallel compensation, because the main source of unbalance and distortion are their own load currents. For instance, a small reduction can be observed in the fundamental unbalance power component, SUF and in the current index SUF. At this level of fundamental unbalance, there may have been some masking effects produced between the unbalance of the applied voltages and the unbalance of the load impedances. Only when the unbalance of the supply voltages is greatly reduced, do the unbalance indices of the load reach their own level.

## Conclusions

The procedure used to calculate unbalanced components enhances the implementation of FFT and clarifies the relationship between the Fortescue sequence components and unbalanced components for all frequencies. This partition is based on a rigorous separation of the phase sequence components of the system harmonics, which allows a partition of the apparent power into four categories: balanced fundamental; unbalanced fundamental; balanced harmonic; and unbalanced harmonic. Using the above categories, three indicators of measurements for the system EPQ can be defined: Unbalanced Fundamental; Balanced Harmonic; and Unbalanced Harmonic. Using these it is possible to evaluate unbalanced non-sinusoidal situations, considering the physical effects of the phenomenon of unbalance in the system. In the same way, these latter indicators can be used to introduce two additional indices to assess the total distortion and the total unbalance. Finally, an experimental platform was developed to test the procedure and the categorization of the power and its indicators. The application of apparent power decomposition and its indices to various practical cases with active power compensation, allowed us to assess any expected improvements in these components, establishing theoretical and practical limits to their values. Interpretation of the results through the power rates has also us allowed to characterize the behaviour of supply and load sides when interaction between them has been reduced with the operation of active compensators.

EBSCOhost - printed on 2/14/2023 2:46 PM via . All use subject to https://www.ebsco.com/terms-of-use

## References

[1] "Definitions for the measurement of electric power quantities under sinusoidal, nonsinusoidal, balanced, or unbalanced conditions, IEEE Std. 1459–2000, January 2000.

[2] T. E. Seiphetlho and A. P. J. Rens, "On the assessment of voltage unbalance," 14th International Conference on Harmonics and Quality of Power (ICHQP), 2010, pp. 1–6.

[3] H. Akagi, "Active Harmonic Filters," Proc. IEEE, Vol. 93 (12), Dec. 2005, pp. 2128–2141.

[4] J. Prieto, P. Salmerón, J. R. Vázquez, F. J. Alcántara. "A Series-Parallel Configuration of Active Power Filters for VAR and Harmonic Compensation." Proc. of IECON'02, Sevilla, November 2002, Paper FILTQ.4 pp. 1–6.

[5] J. Prieto, P. Salmerón, R. S. Herrera. "A unified power quality conditioner for wide load range: practical design and experimental results." Proc. of IEEE St. Petersburg PowerTech Conference, 2005, Russia. pp. 429.1–429.7.

[6] V. Khadkikar, "Enhancing Electric Power Quality Using UPQC: A Comprehensive Overview," IEEE Trans. Power Electronics, vol. 27, No. 5, May 2012.

[7] L. Sainz, J. Balcells. "Harmonic Interaction Influence Due to Current Source Shunt Filters in Networks Supplying Nonlinear Loads," IEEE Trans. on Power Delivery, Vol. 27, No. 3, July 2012, pp. 1385–1393.

[8] T. Zheng, E.B. Makram, A.A. Girgis, "Evaluating power system unbalance in the presence of harmonic distortion". IEEE Trans. on Power Delivery, Vol. 18, No. 2, April 2003, pp. 393–397.

[9] G. Chicco, P. Postolache, and C. Toader, "Analysis of three-phase systems with neutral under distorted and unbalanced conditions in the symmetrical component-based framework" IEEE Trans. on Power Delivery, Vol. 22, No. 1, January 2007, pp. 674–683.

[10] R. Langella, A. Testa, and A. E. Emanuel, "Unbalance Definition for Electrical Power Systems in the Presence of Harmonics and Inter-harmonics," IEEE Trans. on Instrumentation and Measurement, vol. 61, No. 10, pp. 2622-2631, Oct. 2012.

[11] P. Salmerón, A. Pérez, S. P. Litrán, "New Approach to Assess Unbalance and Harmonic Distortion in Power Systems." Proc. of International Conference on Renewable Energies and Power Quality (ICREPQ'13), Bilbao (Spain), March, 2013, pp. 1–4.

[12] J. Prieto; P. Salmerón; A. Pérez; S. P. Litrán, "Practical evaluation of unbalance and harmonic distortion in power conditioning." Electric Power Systems Research, Vol. 141, pp. 487–499. 2016.

EBSCOhost - printed on 2/14/2023 2:46 PM via . All use subject to https://www.ebsco.com/terms-of-use

# CHAPTER FORTY-THREE

# A CASE STUDY ON A HIGH POWER COMPENSATOR OF POWER GRID IRREGULARITIES FOR INDUSTRIAL APPLIANCES[1]

JAN IWASZKIEWICZ[1]
LESZEK WOLSKI[1]
MANUEL PEREZ DONISÓN[2]

## Abstract

This paper presents a case study on the development of a high power compensator for power grid irregularities. The compensator is dedicated to the protection of sensitive industrial installations against dips, sags, and short duration interruptions in public power networks. The energy for compensation is stored in a bank of high voltage stacked supercapacitors. The development of this new high power medium voltage compensator will draw on experience gained during the realisation in the Gdansk branch of the Electrotechnical Institute a similar medium power low voltage device. This study includes: main power converter topology considerations with some preliminary simulation results, including a discussion of harmonic components; a solution to the problem of fast identification of grid voltage disturbances; a solution to the problem of synchronizing compensator waveforms with the grid; and a description of the main operational algorithm of the compensator.

[1] The Electrotechnical Institute, Poland
[2] Electrical Engineering Department, Vigo University, Spain

EBSCOhost - printed on 2/14/2023 2:46 PM via . All use subject to https://www.ebsco.com/terms-of-use

**Keywords:** power quality; voltage interruptions; voltage dips and sags; power converter.

## Introduction

The increasing number of non-linear devices connected to public grids, as well as an increasing share of unstable renewable energy sources, has led to a deterioration in energy system reliability. To cope with this situation, it is necessary to increase the number of switchover operations, generating voltage disturbances of short duration. These disturbances can be identified as: surges (1); flickers (2); voltage deviations (3); dips (4); interruptions (5); and wave-shape disturbances (5). The typical disturbances in a public supply grid are presented in Fig. 1.

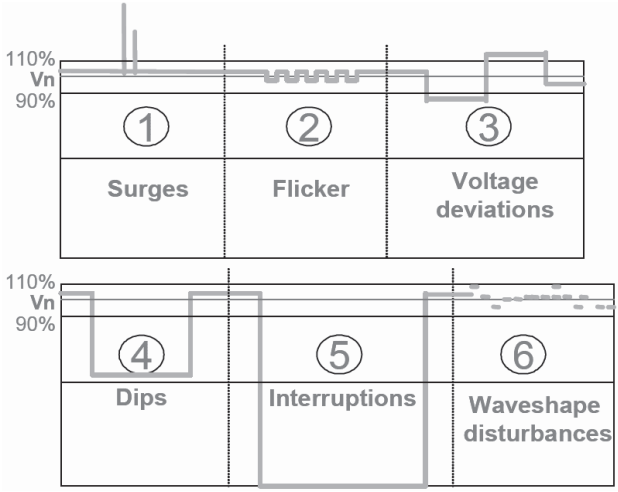



Figure 1. The typical disturbances in a public grid.

Even brief supply interruptions may cause the malfunctioning of sensitive industrial installations, and the need therefore arises for devices that are able to protect such receivers against power outages. For low power, one phase devices like computers, there is already the established practice of using uninterruptible power supplies (UPS) with chemical batteries as energy sources. The standard computer type UPS device allows the maintenance of power for an interval of several minutes to

EBSCOhost - printed on 2/14/2023 2:46 PM via . All use subject to https://www.ebsco.com/terms-of-use

several hours. This kind of solution is not suitable for high power, three-phase industrial installations.

Because more than 90% of public grid failures are short-term disturbances, in the shape of voltage dips and short interruptions, it is reasonable to concentrate on compensating only for these kinds of irregularities, without setting-up a huge energy storage for long term supply. The idea of a short duration disturbance industrial compensator was developed at the Gdansk branch of the Electrotechnical Institute under the framework of COST Action 542: High Performance Energy Storages for Mobile and Stationary Applications. The energy storage for the proposed compensator is based around high voltage supercapacitors. This kind of energy storage does not need any regular service applied, as is usually the case with energy storage devices based on batteries. The supercapacitors also have a large number of charge/discharge cycles; a high level of charge and discharge current; and a broad working temperature range.

Based on this idea, a prototype for a medium power (100 kW), low voltage (400 V) three-phase compensator was developed and tested at the Gdansk branch of the Electrotechnical Institute as part of the special research project COST/255/2006 [1]. The experience gathered during the designing and testing of this prototype will now be used to design a high power (1 MW), medium voltage (6 kV) three-phase compensator.

## Identification of Voltage Disturbances

In order to compensate grid voltage disturbances effectively, they must be detected immediately, and perhaps even anticipated. Instant diagnosis of a failure state is the elementary condition of effective compensator performance, allowing for a rapid rebuilding of the necessary voltage level and shape. However, methods faster than those in [11] were not used because of the independent controllers in each phase. If detection of lower voltage states (dips) occurs when the network voltage and the time base generated by the control circuit are synchronized, then it is possible to determine the current voltage amplitude of the first harmonic, $A_1$, of the signal $u_s(t)$. The amplitude $A_1$ is given by:

$$A_1 = \left| 2 \cdot \sum_{n=0}^{N-1} u_s(n) \cdot \sin(2\pi n / N) \right| \tag{1}$$

where:

$u_s(n)$—$n$-th sample of the input signal,

EBSCOhost - printed on 2/14/2023 2:46 PM via . All use subject to https://www.ebsco.com/terms-of-use

*n*—input sample index,
*N*—number of input samples or frequency components of the discrete Fourier transform (DFT).

The idea of the actual and reference voltage comparison ('prediction') during an interval, T, is illustrated in Fig. 2. The reference voltage signal is created as a predictive, alternating voltage synchronized with the fundamental harmonic of the mains voltage. The comparison process occurs only in selected intervals of the period T. Comparison results during short zero crossing intervals are not taken into consideration. These intervals have been adopted experimentally and set to the value of ± 1,25 ms. Analyzing deviations of the instantaneous voltage outside zero crossing intervals results, in the worst case scenario, in a delay of the compensator response to a dip that will be of maximum length $t_{opmax}$ = 2.5 ms (2 • 0,125 • T/2, T = 20 ms). Nevertheless, the likelihood of such events during the process of comparison is small and the delay will be relatively comparable with the assumed cycle of sampling (e.g. Tp = 80 μs typically). A parameter that better describes the possible delay in dip detections is the expected value. In the presented method, this value may be estimated at approximately 0.7 ms as the average delay time of variability shown in Fig. 2b.

In the case of strong deformation of the voltage waveform in the network, the above-described method may result in detection of dips even though the root-mean-square (rms) voltage is acceptable. In such a case, the predicted signal should take into account the most likely form of the forecast. The inclusion of an appropriate reference signal distortion can be obtained by taking into account the higher harmonic components. The amplitudes of these components can be calculated using the conversion formula in (1).

Effective dip detection that is fast and immune to noise, requires the use of specialized algorithms, including the synchronization mechanism (described below), which uses the fast Fourier transform (FFT) or wavelet transform. The main difference between the wavelet transform described in [8] and the DFT is that the first one operates in the time domain, while the FFT operates in the frequency domain and uses variable window sizes to capture voltage changes. Practical implementation of the detection process, however, is still difficult [11]. In [5], the dip detection mechanism was performed in two ways: by exploring patterns of instantaneous value deviation and using the rms value of the measured waveform.

EBSCOhost - printed on 2/14/2023 2:46 PM via . All use subject to https://www.ebsco.com/terms-of-use

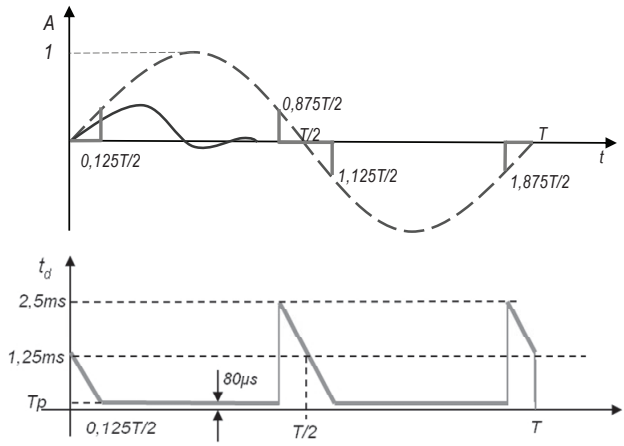



Figure 2. The detection mechanism: comparison of the real and predicted signals in the interval T (one period) and marked zones of measurement insensitivities; a way to estimate the average delay of the dip detection.

## Synchronization with the Mains Voltage

In order to minimize transients after a power outage in the main supply, a replacement supply source (loss-compensated) must have an amplitude and voltage phase compatible with the pre-distortion waveform. The compensator controller provides synchronization of the internal reference voltage signal generator with the voltage occurring during proper operation of the main power supply by means of a phase-locked loop (PLL). The applied software method of synchronization with the mains voltage is based on the use of the DFT signal, *us(t)*, into two orthogonal components of the formula:

$$Us(m) = \sum_{n=0}^{N-1} u_s(n) \cdot [\cos(2\pi nm / N) - j\sin(2\pi nm / N)] = \mathrm{Re}\, Us(m) + j\,\mathrm{Im}\, Us(m) \quad (2)$$

where: $U_s(m)$—$m$-th component of the DFT,
$m$—output component index in frequency domain,
$u_s(n)$—$n$-th sample of the input signal,
$n$—input sample index,
$N$—number of input samples or frequency components in the DFT.

EBSCOhost - printed on 2/14/2023 2:46 PM via . All use subject to https://www.ebsco.com/terms-of-use

If the signal $u_s(t)$ is an odd function of time and the period of the input signal is T = Tp • N (Tp—sampling period; N—constant) then the real components of the DFT will all be zeroes:

$$Us\,(m) = -j\sum_{n=0}^{N-1} u_s\,(n)\cdot \sin(\,2\pi nm\,/\,N\,) \tag{3}$$

In the case of no synchronization, when T ≠ Tp • N, where T is the period of the signal $u_s(t)$, the real component Re($U_s$ ($m$)) and imaginary component Im($U_s$ ($m$)) will have non-zero values. The equation in (3) describes the synchronization state of the odd components of the signal $u_s(t)$ within the sampling system.

The compensator should synchronize the sampling system with the first harmonic of the grid voltage for $m$ = 1. The angle between the vector $us(1)$ and the real axis is described by the formula:

$$\varphi\,(1) = \arctan\ \frac{\text{Im}\ Us\ (1)}{\text{Re}\ Us\ (1)} \tag{4}$$

The output signal $S(t)$ is a synchronized time-base common to all signal processing blocks in the digital controller.

The synchronization state can be obtained by changing the sampling period Tp in such a way that (T – Tp • N) → 0. Then the angle defined by formula (4) tends toward π/2. A simplified angle control system is shown in Fig. 3. Only the real component of the DFT is calculated and in this way the time-consuming calculation of the function arctan(φ) is omitted.

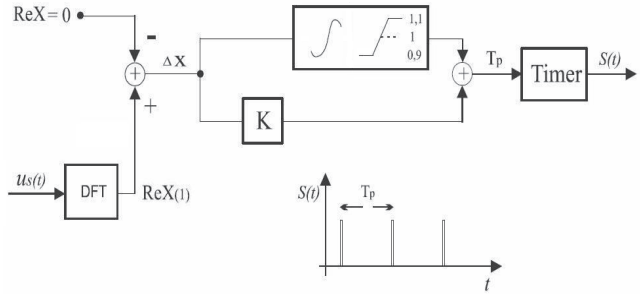



Figure 3. A simplified synchronization circuit.

EBSCOhost - printed on 2/14/2023 2:46 PM via . All use subject to https://www.ebsco.com/terms-of-use

## Power Converter Topology

The already built prototype compensator consists of three independent one-phase multilevel cascaded inverters; and its energy storage is based on high voltage stacked supercapacitors. There are three identical single phase compensators connected in a star as shown in Fig. 4.

Each single phase compensator is formed as a cascaded multilevel inverter built from two H-bridge units, which are independently supplied. A simplified diagram of a single phase circuit is shown in Fig. 5.

The energy exchange between the network and the supercapacitor is accomplished by the cascade inverter, consisting of two H-bridge inverters connected in series and supplied by two DC/DC intermediary circuit converters (P1 and P2). The key, K, denotes a very fast switch placed between the phase line and the protected network. The switch is able to disconnect the load from the mains. Symbols C and RL denote parameters of the load. Most of time, the switch K is closed allowing energy flow from the mains to load and to the compensator. It must be disconnected at the specific instant of voltage interruption or dip when the compensator takes over to power sensitive loads.

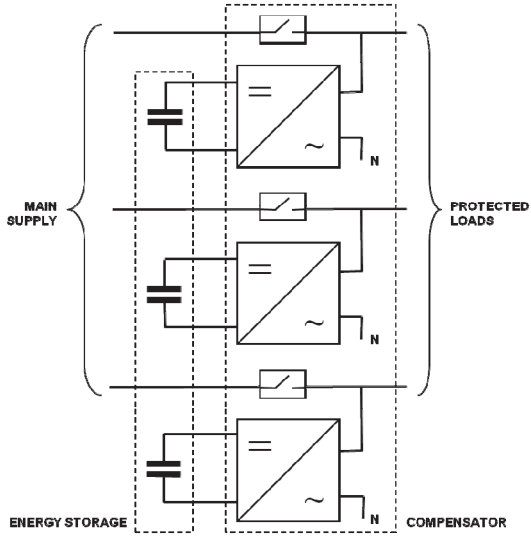



Figure 4. Block diagram of the three-phase voltage outages compensator.

EBSCOhost - printed on 2/14/2023 2:46 PM via . All use subject to https://www.ebsco.com/terms-of-use

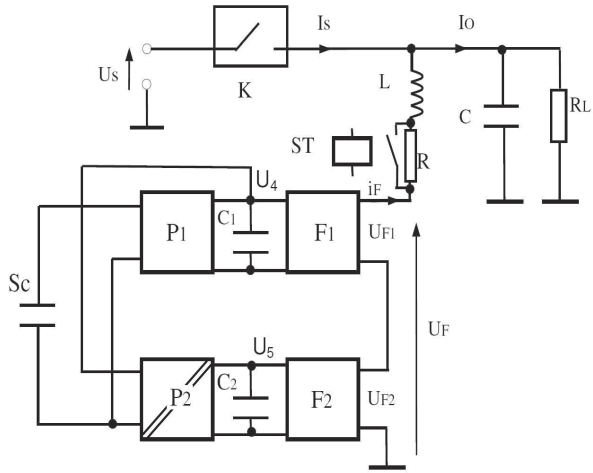



Figure 5. A simplified diagram of one phase of the three-phase voltage outages compensator.

The cascaded multilevel converter allows for a low level THD factor in the generated waveforms. When the supplying voltages ratio is $U_1/U_2 = 1/3$, the available step voltage levels are as follows:

$$\begin{cases} U = U_1 = \dfrac{1}{4} \\ U = U_2 - U_1 = \dfrac{1}{2} \\ U = U_2 = \dfrac{3}{4} \\ U = U_2 + U_1 = 1 \end{cases} \tag{5}$$

The output waveforms (phase and line-to-line) and their harmonic spectra are presented in Fig. 6.

EBSCOhost - printed on 2/14/2023 2:46 PM via . All use subject to https://www.ebsco.com/terms-of-use

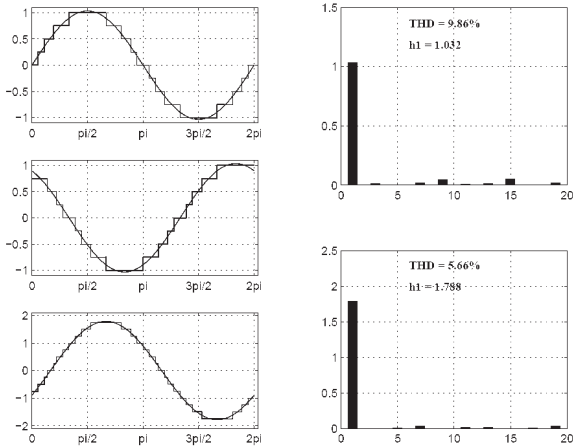



Figure 6. Phase and line-to-line voltages and their spectral analysis.

The experimental results, presented in figs. 7 and 8 are in agreement with the predicted properties of the multilevel cascade converter used.

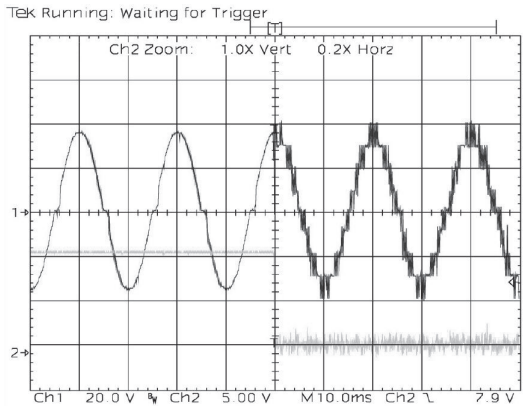



Figure 7. Experimental waveforms showing the start of voltage generation by the cascade inverter.

EBSCOhost - printed on 2/14/2023 2:46 PM via . All use subject to https://www.ebsco.com/terms-of-use

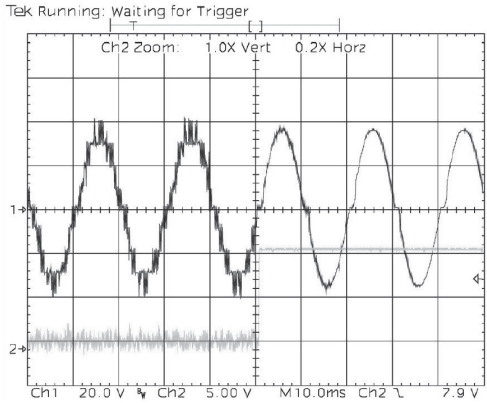



Figure 8. Experimental waveforms showing the end of voltage generation by the cascade inverter.

The above figures show the operation of the compensator in response to grid voltage disturbances. Fast switching from network to supercapacitor storage supply is shown in Fig. 7 and back switching after restoring the network voltage is shown in Fig. 8. The slight deformation of the obtained voltage around zero crossing points is caused by the properties of the thyristor switch K at low voltage.

The multilevel cascade architecture used in the medium power compensator is not an optimal topology for the developed high power compensator, due to the high price of the power switching components. As such, it is necessary to consider a somewhat simpler converter topology with fewer active switching components. At this power level, there are serious limitations on the switching frequency for the switching components and output waveforms of a typical two-level PWM converter, which inevitably include a high level of harmonic components, as shown in Fig. 9.

Much better results can be obtained using a three-level converter. For this kind of converter, the harmonic distortion is approximately two times lower. The simulation results are presented in Fig. 10.

The three-level PWM converter can be considered to be the most suitable solution for a high power compensator from a technical, as well as an economic, point of view. It consists of 12 switching transistors and 6 clamping diodes, while the H-bridges of the previously used two-stage cascade converter consisted of 24 switching transistors.

EBSCOhost - printed on 2/14/2023 2:46 PM via . All use subject to https://www.ebsco.com/terms-of-use

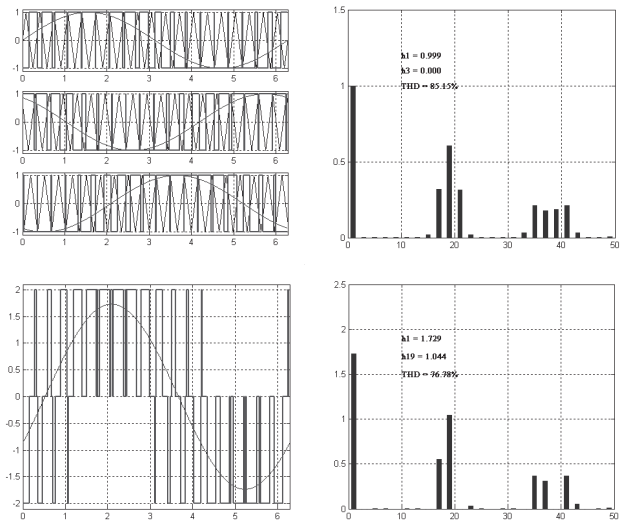



Figure 9. Phase and line-to-line voltages and their spectral analysis for a two-level PWM converter with a 1 kHz switching frequency.

The number of switching components is in between those of a simple two-level converter (6 transistors) and a two-stage cascade one (24 transistors).

An additional disadvantage of the considered solution with a three-level converter is that in this topology, even if the voltage interruption appears in only one phase, it is necessary to generate all three phase voltages. There is no possibility of operate the phases independently—as is possible when using the cascade converter.

Two different configurations were considered for the new compensator. In the first version, shown in Fig. 11, there are two additional DC/DC converters stabilizing the DC link voltages of the converter when the supercapacitors' voltage decreases during discharge in the active state of the compensator.

The second configuration, without stabilizing converters, is presented in Fig. 12. In this version, the appropriate level of the generated voltage is obtained using PWM modulation.

EBSCOhost - printed on 2/14/2023 2:46 PM via . All use subject to https://www.ebsco.com/terms-of-use

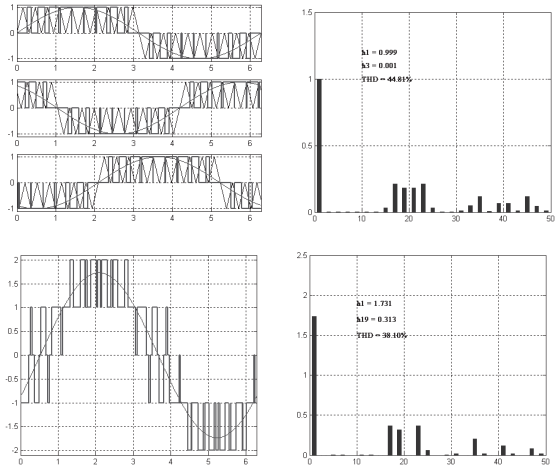



Figure 10. Phase and line-to-line voltages and their spectral analysis for a three-level PWM converter with a 1 kHz switching frequency.

Simulations using a PWM technique for first harmonic stabilization were carried out with very promising results, if we assume that the allowed discharge of the supercapacitors is in the range of nominal voltage to 0.5 of the nominal value. This discharge level equates to usage of 75 % of the stored energy:

$$E_{full} = \frac{U^2}{2} \tag{6}$$

and

$$E_{usable} = \frac{U^2 - \left(\frac{U}{2}\right)^2}{2} = \frac{\frac{3U^2}{4}}{2} \tag{7}$$

We should also not that full discharge of the supercapacitors is not recommended by their manufacturers because it reduces their life span.

The tests proved that for modulation changing the amplitude of the first harmonic in the range of 0.4 to 1.25, the level of the higher harmonic components was at a similar level. This means that a properly adjusted low-pass filter could cope with the output waveform quality within this range of the PWM.

EBSCOhost - printed on 2/14/2023 2:46 PM via . All use subject to https://www.ebsco.com/terms-of-use

The version without additional DC/DC stabilizing converters is interesting both economically and in terms of energy conversion efficiency.

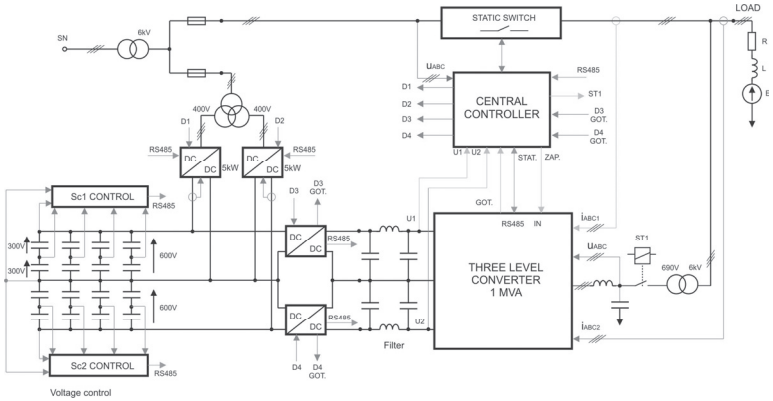



Figure 11. Proposed structure of the high power compensator—version with stabilizing DC/DC converters.

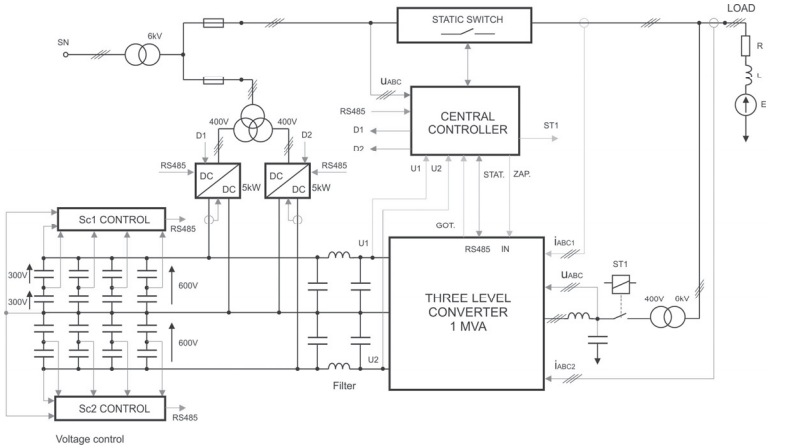



Figure 12. Proposed structure of the high power compensator—version without stabilizing DC/DC converters.

The resulting output phase and line-to-line waveforms and their spectral analysis for $U = 0.8\ U_n$ are presented in Fig.13.

EBSCOhost - printed on 2/14/2023 2:46 PM via . All use subject to https://www.ebsco.com/terms-of-use

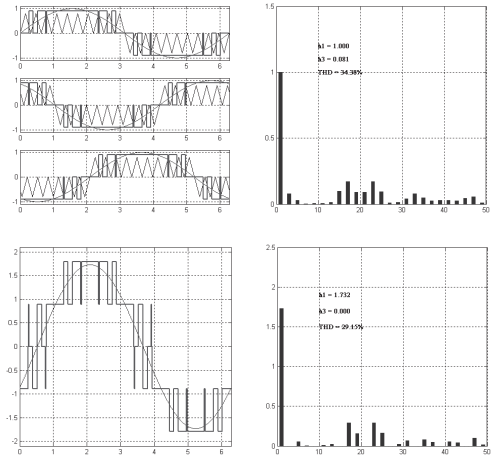



Figure 13. Phase and line-to-line voltages and their spectral analysis for U = 0,8 $U_n$.

The resulting output phase and line-to-line waveforms and their spectral analysis for U = 2.5 $U_n$ are presented in Fig.14. The final choice of which version to use should be made on the basis of experimental results.

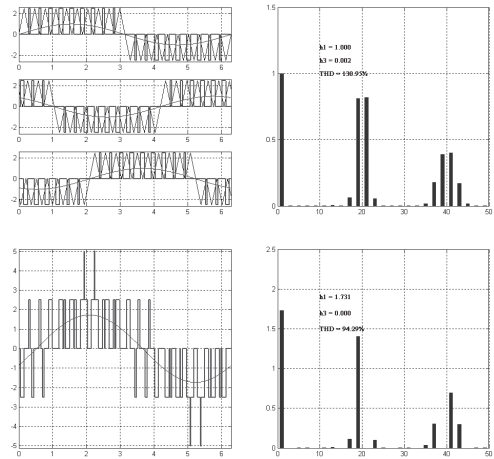



Figure 14. Phase and line-to-line voltages and their spectral analysis for U = 2,5 $U_n$.

EBSCOhost - printed on 2/14/2023 2:46 PM via . All use subject to https://www.ebsco.com/terms-of-use

## Operational Algorithm of the Compensator

The operation of the compensator requires realization of multiple concurrent real-time control tasks. In order to solve the complexity of these issues, a finite-state machine (called a finite automaton) was created in the controller of the compensator.

Six basic states of operation were distinguished in the control algorithm:

STOP: off—no mains power.

CHARGE C2: device is powered and supply voltage (Us) is normal. Capacitor $C_2$ is charged to the nominal voltage.

CHARGE C1: device is powered and supply voltage (Us) is normal. Capacitor $C_1$ is charged to the nominal voltage.

WAIT: standby—waiting for dip or voltage outage

CHARGE Sc: charging the supercapacitor Sc in a given compensator's phase. The charger raises and maintains the level of the supercapacitor voltage at $U_{sc}$ = 300 V.

INVERTER: based on the energy stored in the supercapacitor, Sc phase voltage is generated using the cascade inverter. The device enters this state after the identification of a voltage dip or power failure.

A simplified operating graph for the created finite-state machine with the conditions for transitions between states is presented in Fig. 15.

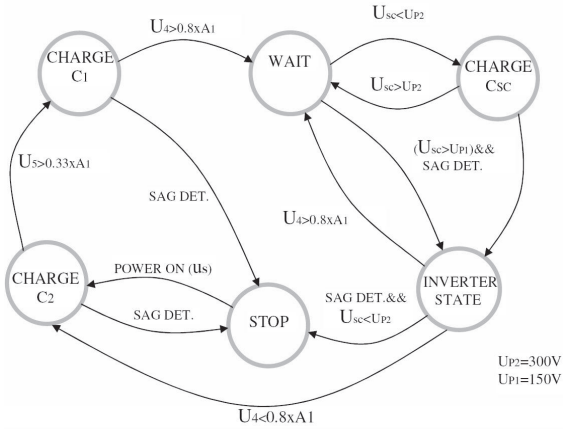



Figure 15. A simplified graph of the operating states of the voltage compensator.

EBSCOhost - printed on 2/14/2023 2:46 PM via . All use subject to https://www.ebsco.com/terms-of-use

These conditions are discrete variables (logical states 0 or 1), obtained through simple comparison or as the result of more complex calculations (dip detection—SAG_DET). Threshold values UP1 and UP2 determine the supercapacitor working voltage range. In addition to measuring the grid voltage; managing waveform synchronization; compensating voltage generation; and regulating energy flows between the grid, energy storage, and load, the controller also supports communication with a higher level control system using a local or wide area network.

## Medium Voltage Compensator Operationality Tests

The operational tests of the compensator required a real medium voltage supply system with a high power transformer, fast circuit breaker, and a dedicated protected part of the medium voltage grid with load. The test circuit schema is presented in Fig. 16.

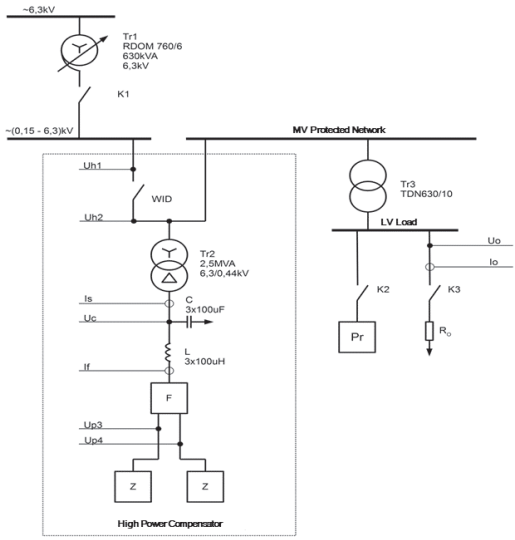



Figure 16. Experimental stand of the MV voltage compensator.

where: Tr1—autotransformer regulating mains voltage; WID—inductive, dynamic switch; L, C, Tr2—elements of the coupling circuit; F—compensator inverter; Z—DC power supply; Tr3—transformer supplying low-voltage receivers; Pr—three-phase rectifier; Ro—load resistance.

EBSCOhost - printed on 2/14/2023 2:46 PM via . All use subject to https://www.ebsco.com/terms-of-use

Voltage faults were caused by switching the K1 contactor from its on-state to off. The test started with the network operation mode, in which the WID switch and contactor K1 are shorted. The experimental results were recorded using the Tektronix DPO 3034B digital scope with a TCP0150 current probe, and a voltage transformer with a 1:10 000 V/V ratio as a high voltage probe. The voltage on the protected circuit was gradually increased and the voltage and current waveforms recorded. The test for the rated voltage was carried out under the following conditions:

| | |
|---|---|
| Voltage Supply: | 6,3 kV |
| Load Power: | 16,6 kW |
| Tr2 transformer ratio: | 6,3/0,44 kV |
| Reference of reactive current of compensator: | 0 A |
| Reference of intermediate voltage of compensator: | 500 V |

The experimental compensator's output waveforms for supply voltage and current are presented in Fig. 17 and magnified waveforms of the start and stop operations are presented in Fig. 18.

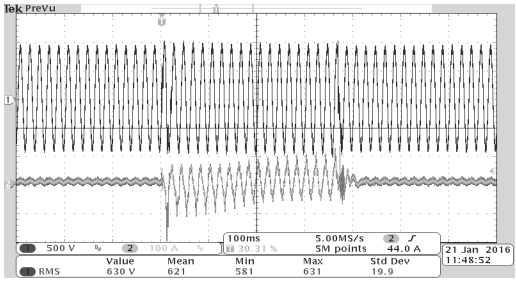



Figure 17. Supply voltage [1 ] and output current [2] of the compensator.

EBSCOhost - printed on 2/14/2023 2:46 PM via . All use subject to https://www.ebsco.com/terms-of-use

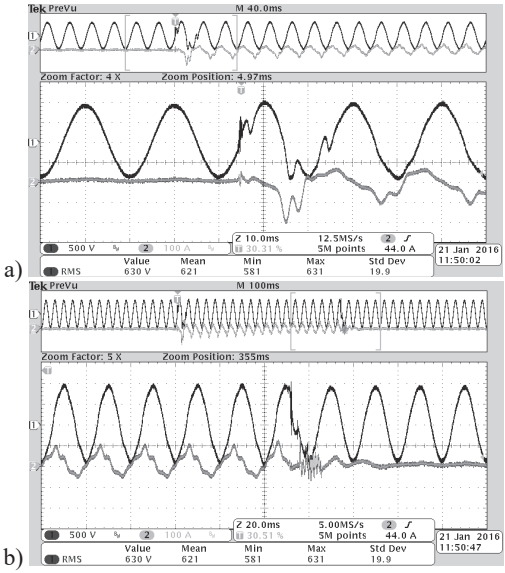



Figure 18. Zoomed supply voltage [1] and output current [2] of the compensator in start [a] and stop [b] of load supplying by the compensator.

Experimental waveforms of the protected grid load voltage and current are presented in Fig. 19; magnified waveforms of start and stop operation are presented in Fig. 20.

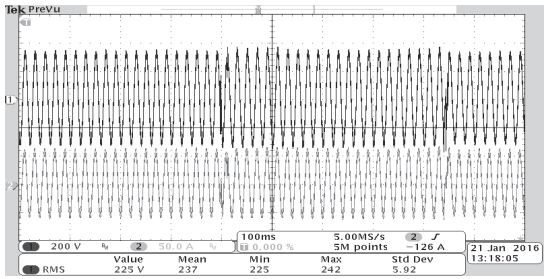



Figure 19. Protected output voltage [1] and load current [2].

EBSCOhost - printed on 2/14/2023 2:46 PM via . All use subject to https://www.ebsco.com/terms-of-use

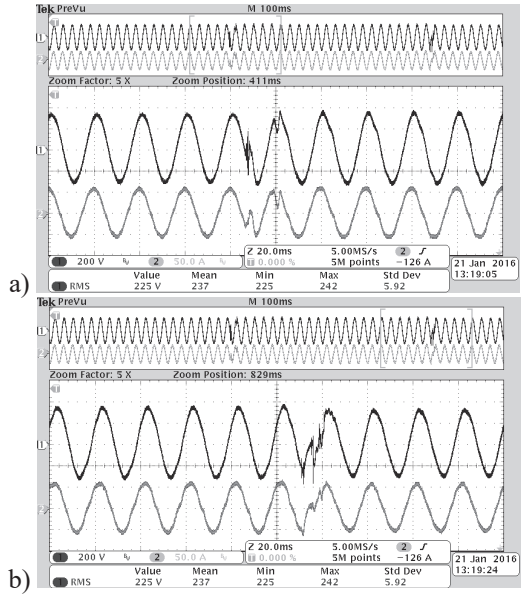



Figure 20. Protected output voltage [1] and load output current [2] in start [a] and stop [b] of load supply by the compensator.

## Conclusions

The voltage disturbances on the load occurring during changeover of the compensator (after detection of voltage decay and its re-occurrence) are less than 10ms, meeting the condition for continuity of the power supply. Voltage disturbances during the switch to island operation cause significant currents, which magnetize the transformer Tr2. These currents decay, but they must be taken into account when designing the inverter. The rated power of the Tr2 transformer should correspond to the rated power of the converter or converters from which it is powered by the load.

The method developed, tested, and experimentally confirmed on sag detection can be used in the target system. The model of the device requires additional checking in real industrial conditions. The set installation for testing in medium voltage power supply conditions offered limited possibilities for generating network disturbances. The construction of a specialist supply station can meet all the necessary requirements.

A large, and still increasing, number of non-linear loads and a growing share of energy from distributed resources has resulted in a decrease in the

EBSCOhost - printed on 2/14/2023 2:46 PM via . All use subject to https://www.ebsco.com/terms-of-use

reliability of public power grids. Therefore, issues relating to the improvement of the quality and reliability of the electrical energy supply are particularly important.

The high power compensator proposal presented here compensates for dips and short-term interruptions in a medium voltage three-phase four-wire grid. A three-level three-phase converter with PWM modulation is considered to be the most suitable power converter topology for the compensator. Using this technique, it is probably possible to eliminate the additional DC/DC converters stabilizing the DC-link voltages in the main converter. Further experimental testing needs to be carried out to prove this idea. Compensator energy storage is achieved through the use of high voltage stacked supercapacitors. Their use as energy storage devices in such an application has many advantages. Up until now, they have not been practically implemented in energy supply systems, mainly because this technology is not yet widely known and because high voltage supercapacitors are still very expensive.

The rapid development observed in supercapacitor technology will undoubtedly lead to mass production of these components with better parameters and a much lower price in the near future. This will allow wider use of supercapacitor-based compensators for the protection of sensitive processes and devices against interruptions or voltage dips in supply networks and the suppression of disturbances in networks with disruptive sources.

## Acknowledgement

The work was carried out under the Project
INNOTECH-K1/IN1/56/158978/NCBR/12.

## References

[1] Special Research Project Report COST/255/2006, IEl/OG 2009.
[2] Łowiec E., Bogusławski P., Rysztowski M.: “One phase voltage interruptions kompensator with supercapacitor energy storage,” Conference Materials, SENE 2007 Conference.
[3] Hashad M., Iwaszkiewicz J.: “A Novel Orthogonal-Vectors-Based Topology of Multilevel Inverters,” IEEE Transactions on Industrial Electronics, Vol. 49, No. 4, 2002.
[4] Casadei D., Grandi G., Rossi C.: “A Supercapacitor-Based Power Conditioning System for Power Quality Improvement and Uninterruptible Power Supply,” Proceedings of the 2002 IEEE International Symposium on Industrial Electronics, ISIE 2002.

EBSCOhost - printed on 2/14/2023 2:46 PM via . All use subject to https://www.ebsco.com/terms-of-use

[5] Bae B., Jeong J., Lee J., Han B.: "Novel Sag Detection Method for Line-Interactive Dynamic, Voltage Restorer," Power Engineering Letters, IEEE Transactions on Power Delivery, Vol. 25, No. 2, 2010.
[6] Iwaszkiewicz J.: "Mathematical models of the power electronic multilevel converters," monograph, Proceedings of the Electrotechnical Institute, Vol. 227, 2006.
[7] Iwaszkiewicz J., Perz J.: "Mathematical Approach to THD Optimization in Multilevel Convertors," International Conference on Renewable Energy and Power Quality ICREPQ '06, Palma de Mallorca, Spain, 2006.
[8] Iwaszkiewicz J., Perz J.: "A Novel Approach to Sine-wave Approximation in Multilevel Converters," The IEEE Industry Applications Society Workshop on Renewable Energy Based Units and Systems (REBUS), St. Petersburg, Russia, 2006.
[9] Maharjan L., Inoue S., Akagi H.: "A Transformerless Energy Storage System Based on a Cascade Multilevel PWM Converter with Star Configuration," IEEE Transactions on Industry Applications, Vol. 44, No. 5, September/October 2008.
[10] Newman M., Holmes D., Nielsen J., Blaabjerg F., "A Dynamic Voltage Restorer (DVR) With Selective Harmonic Compensation at Medium Voltage Level," IEEE Transaction on Industry Applications, Vol. 41, No. 6, November/December 2005.
[11] Fitzer C., Barnes M., Green P., "Voltage Sag Detection Technique for a Dynamic Voltage Restorer," IEEE Transaction on Industry Applications, Vol. 40, No. 1, January/February 2004.
[12] Silva L., Pimentel S., Pomilio J., "Analysis and Proposal of Capacitor Voltage Control for an Asymmetric Cascaded Inverter," Conference Publications, PESC '05 IEEE 36th Power Electronics Specialists Conference, 2005.

EBSCOhost - printed on 2/14/2023 2:46 PM via . All use subject to https://www.ebsco.com/terms-of-use

# CHAPTER FORTY-FOUR

# POWER QUALITY VERSUS ELECTROMAGNETIC COMPATIBILITY IN ADJUSTABLE SPEED DRIVES

MIRCEA BUZDUGAN[1] AND HORIA BALAN[1]

## Abstract

The approach presented here is intended to reveal a tighter physical relationship between power quality and electromagnetic interference in electric drives.

It is the opinion of the authors that harmonics—low frequency perturbations—are widely covered in the literature on power quality, while higher frequency perturbations, which are inherent and mostly due to power electronic equipment, are generally neglected.

The core idea is that a bijection occurs in issues of power quality between low frequency phenomena and electromagnetic emissions, which are high frequency phenomena. There is a close relationship between the two categories of phenomena and they determine each other. As such, it is important that both these issues are mitigated concurrently and, if possible, using a single technical solution in order to minimize costs.

In this paper the harmonic content of the electric current is analysed together with the conducted electromagnetic interference. Finally, proper countermeasures for mitigation are proposed and applied.

The concept is developed here for the adjustable speed drives of wellhead induction motors in a large oil onshore extraction field.

[1] TUCN – Technical University of Cluj-Napoca - 28, Memorandumului str., 400114, Cluj-Napoca, Romania. Email: mircea.buzdugan@insta.utcluj.ro, horia.balan@eps.utcluj.ro

EBSCOhost - printed on 2/14/2023 2:46 PM via . All use subject to https://www.ebsco.com/terms-of-use

This chapter is based on a revised version of a paper presented at the International Conference on Renewable Energies and Power Quality (ICREPQ'13), Bilbao, March 2013.

**Keywords:** Harmonics, conducted interference, ASD - adjustable speed drives, six-pulse inverters, passive filters.

# 1. Introduction

In recent years, attention to power quality has become more and more important for suppliers, manufacturers, and customers of power electronic equipment.

Suppliers are interested in the quality of their service; manufacturers have to build equipment compliant with standards and regulations concerning power quality; and, finally, customers in their turn want to enjoy modern comfort and technology using electrically powered products.

High speed semiconductor devices with fast switching capabilities, along with the emerging digital era, have only increased control and signal processing issues. Unfortunately, such issues have become the main enemies of electrical power quality.

Such equipment needs a good level of power quality, being relatively intolerant of voltage and current disturbances; however, it also constitutes the main source of electromagnetic perturbations in electric distribution grids.

In the literature, one can find plenty of, often conflicting, definitions of power quality, related more or less to the performance of equipment or to the possibility of measuring and quantifying the performance of an electric power system (see IEEE, IEC, and EN Standards).

For instance, the Council of European Energy Regulators - Working Group on the Quality of the Electricity Supply speaks about voltage quality, including the following disturbances: "frequency and voltage magnitude variations, voltage dips, temporary and transient overvoltage and harmonic distortion," without explicitly mentioning "current quality," which is probably considered only when it affects voltage quality [1]. The view taken is that current quality represents a concern only if it affects voltage quality. This difficulty of distinguishing between voltage and current disturbances is one of the reasons the term power quality is generally used. The term voltage quality is reserved for cases where only the voltage at a certain location is considered. The term current quality is generally used to describe the performance of power electronic equipment connected to low voltage distribution grids [2].

EBSCOhost - printed on 2/14/2023 2:46 PM via . All use subject to https://www.ebsco.com/terms-of-use

In the authors' opinion, there is no power quality in the presence of electromagnetic interference, i.e. the process by which disruptive electromagnetic energy is transmitted from one piece of electronic equipment to another via radiated and/or conducted paths [3]. In this respect, any electromagnetic disturbance is a power quality issue, even if the IEC and EN standards make a clear distinction between a (electromagnetic) disturbance and an (electromagnetic) interference. The standard states that "a disturbance is a phenomenon which may degrade the performance of a device, equipment and system, or adversely affect living or inert matter" [4]. In terms of power quality, any deviation from the ideal voltage or current can be considered a disturbance. On the other hand, interference is much more strictly defined, interference being the actual degradation of a device, equipment, or system caused by electromagnetic disturbance.

Along with a large variety of nonlinear loads (e.g. discharge lamps, uninterruptible power supplies, electronic power supplies, electronic converters, etc.), adjustable-speed drives represent an important source of power quality disturbances and waveform distortions; additionally, they are sensitive to certain types of power quality disturbances.

It is well-known that power electronics offers plenty of advantages in terms of efficiency and controllability of the power system. However, power electronic devices draw non-sinusoidal currents from AC power systems, reacting to the impedances of the system. Consequently, they determine voltage harmonics and, in some cases, resonances in distribution feeders.

In the literature, power quality, in relation to variable/adjustable-speed drives, mainly deals with voltage dips, supply interruptions, and harmonic distortion—these have negative impacts on almost all the components of an electrical system and cause supplementary dielectric, thermal, and/or mechanical stresses [5-9].

Harmonic components can significantly impact motors, especially by voltage distortion directly related to the harmonic fluxes within motors. Harmonic fluxes do not contribute to a motor's torque, as they rotate at different frequencies. The high-frequency induced currents in the rotors are similar to those of positive or negative-sequence currents at the fundamental frequency. A well-known effect of this is overheating of the motor, especially when the voltage distortion (THDU) exceeds the limit of 8% set by standard EN 61000-4-7. Overheating, though, is far from being the single or the most important effect. Another important drawback due to the presence of harmonics, is the phenomenon of torsional oscillation.

EBSCOhost - printed on 2/14/2023 2:46 PM via . All use subject to https://www.ebsco.com/terms-of-use

The 5th harmonic component acts like a negative sequence, its resulting magnetic field revolving in a direction opposite to that of the fundamental field and at a speed five times higher than the speed of the fundamental field. The resultant effect is a magnetic field revolving at a relative speed of four times the speed of the rotor.

The 7th harmonic component acts like a positive sequence, with a resulting magnetic field revolving in the same direction as the fundamental field at a speed seven times higher than the speed of the fundamental field. The resultant effect is a magnetic field revolving at a relative speed of six times the speed of the rotor.

The interaction between these magnetic fields and the currents induced in the rotors produces torsional oscillations in the motor.

Clearly, severe damage to the motor may occur if the frequency of the oscillation matches the natural frequency of the motor.

Harmonic currents affect all the components of a power system and contribute significantly to its inefficiency.

When the operating frequency increases, harmonic currents cause other damaging effects. For instance:

- undersized conductors and cables present a more pronounced “skin effect”;
- capacitors can be affected by the rise in temperature, due to power loss, and consequently have a reduced lifetime of operation;
- fuses and circuit breakers can cause false or spurious operations and trips;
- transformers and generators may have increased iron and copper losses or eddy currents, due to stray flux losses that cause excessive overheating in their windings;
- high frequencies in the switching and transient spikes are also induced in the rotor, building up a voltage potential between the rotor and stator, which is dissipated by arcing through the ball bearings—over time this will ruin the finish in the bearing races and causing premature failure;
- electric drives can be affected by harmonic currents by misoperation due to multiple zero crossings and failure of the commutation circuits.

Today, both low and high-power equipment is almost exclusively powered by power electronic converters, which generate a broad spectrum of distortion if frequencies increase. However, high-frequency transients do occasionally receive attention as causes of equipment malfunction,

EBSCOhost - printed on 2/14/2023 2:46 PM via . All use subject to https://www.ebsco.com/terms-of-use

although they are generally insufficiently covered in the literature on power quality. For example, the European standard EN 50160 [10] gives useful information for variations (voltage fluctuations, dips, interruptions, etc.), which are regulated disturbances, but nothing is mentioned about events (fast transients).

The approach presented here is intended to widen the investigation of power quality for power converters, considering power quality to be part of the larger concept of electromagnetic compatibility. The concept will be illustrated by the following case study, undertaken by the authors, in an onshore oil field.

## 2. Measurements and Discussions

The oil field is quite a large one having its own power supply system consisting of: two medium voltage overhead lines of 20 kV; sixteen transformer substations at 20/0.5 kV; and a low voltage distribution grid supplying the wellheads, the water injection pumps, the gas injection compressors, and the crude pumps. In addition, low voltage distribution is necessary for utilities (HVAC with cogeneration, firefighting systems, potable water, lighting, etc.). The complexity of the power system supplying the oil field is obvious and an energy audit intended to draw up technical and organizational measures increasing energy efficiency was more than necessary.

The power quality and problems of conducted electromagnetic interferences detected in the adjustable-speed drives (ASD) of the wellhead induction motors, together with some mitigation countermeasures, are also described.

The wellhead induction motors are supplied by six-pulse, pulse-width modulation (PWM) drives with insulated gate bipolar transistors (IGBTs), which is the most common type used in such an environment (Fig. 1) [11-13].

EBSCOhost - printed on 2/14/2023 2:46 PM via . All use subject to https://www.ebsco.com/terms-of-use

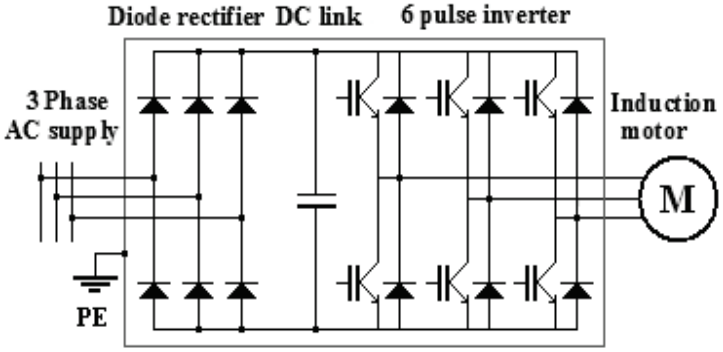



Figure 1. The six-pulse converter

The converter in the ASDs dominates the interaction of the drives with their supply system. Therefore, their operation determines the quantum of the harmonics introduced into the electrical distribution system to which they are connected.

Measurements were performed using a Power & Quality Analyser, Qualistar Plus C.A. 8335 (Chauvin Arnoux)—a recorder and analyser for measurements on electrical power networks, which has all the necessary functions to a level of specification usually reserved for top-of-the-range laboratory instruments [14].

The instrument has all the functions of an electrical network analyser in a portable, battery-powered instrument. Its features include:

- Real-time display of wave forms (4 voltages and 4 currents).
- RMS voltage and currents per half-period.
- Automatic recognition of the different types of current sensors.
- Integration of all the DC components.
- Measurement, calculation, and display of the harmonics up to the 50th order, along with the phase information.
- Calculation of total harmonic distortion (THD).
- Capture of transients per sample (1/256th of a period).
- Display of phasor diagram (in practice the use of phasor diagrams is an effective way of ensuring that the right connections are set up for reliable measurement).
- Measurement of VA, W and VAr power values (total and per phase).
- Measurement of VAh, Wh and VArh energy values (total and per phase).

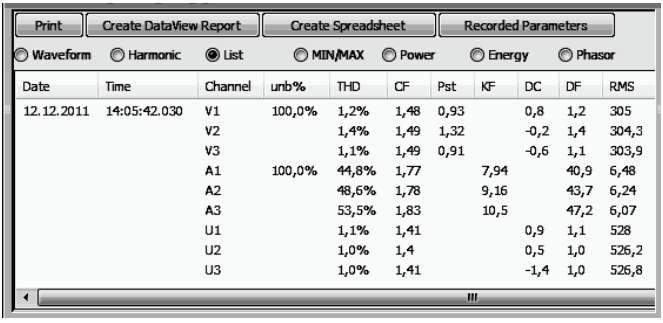
EBSCOhost - printed on 2/14/2023 2:46 PM via . All use subject to https://www.ebsco.com/terms-of-use

- Calculation of the K-Factor (indicates the amount of heat produced by sinusoidal currents compared to the same rms value of a pure sine current—a K-Factor of 1.0 corresponds to a linear load with no harmonics)
- Calculation of the cosφ displacement power factor (DPF) and the power factor (PF).
- Capture of up to 300 transients.
- Flicker calculation.
- Imbalance calculation (current and voltage).
- Monitoring of the electrical network with setting of alarms.
- Back-up and recording of screenshots (image and data).
- Software for data recovery and real-time communication with a PC.
- Recording and export onto PC.

A set of recorded values concerning the main electrical parameters of the supply grid is presented in Fig. 2.

In Fig. 3, it can be seen that the THDs of the three phase supply voltages are around 1.0%, which justifies the almost sinusoidal shape of the voltage waveforms depicted. The almost pure sine form is affected only by the PWM frequency, as one can see from the shape of the wave.

The high value of the K-Factor in the supply lines, associated with the excessive THDs of the currents drawn from the lines and a poor displacement power factor, indicates a power quality issue regarding current distortions and harmonic content. Pst (the short-term flicker) determined by the supply voltage is of less importance for this type of environment.




| Date | Time | Channel | unb% | THD | CF | Pst | KF | DC | DF | RMS |
|---|---|---|---|---|---|---|---|---|---|---|
| 12.12.2011 | 14:05:42.030 | V1 | 100,0% | 1,2% | 1,48 | 0,93 | | 0,8 | 1,2 | 305 |
| | | V2 | | 1,4% | 1,49 | 1,32 | | -0,2 | 1,4 | 304,3 |
| | | V3 | | 1,1% | 1,49 | 0,91 | | -0,6 | 1,1 | 303,9 |
| | | A1 | 100,0% | 44,8% | 1,77 | | 7,94 | | 40,9 | 6,48 |
| | | A2 | | 48,6% | 1,78 | | 9,16 | | 43,7 | 6,24 |
| | | A3 | | 53,5% | 1,83 | | 10,5 | | 47,2 | 6,07 |
| | | U1 | | 1,1% | 1,41 | | | 0,9 | 1,1 | 528 |
| | | U2 | | 1,0% | 1,4 | | | 0,5 | 1,0 | 526,2 |
| | | U3 | | 1,0% | 1,41 | | | -1,4 | 1,0 | 526,8 |

Figure 2. Main electrical parameters recorded by the power analyser

EBSCOhost - printed on 2/14/2023 2:46 PM via . All use subject to https://www.ebsco.com/terms-of-use

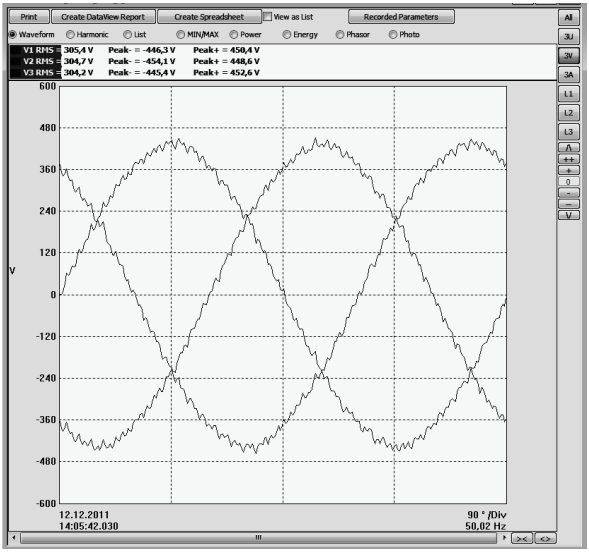



Figure 3. Supply voltages of the ASD

The distorted waveforms of the current drawn from line 2 are presented in Fig. 4. Its highly distorted waveform and the lagging phase angle of 67$^{O}$ can be observed.

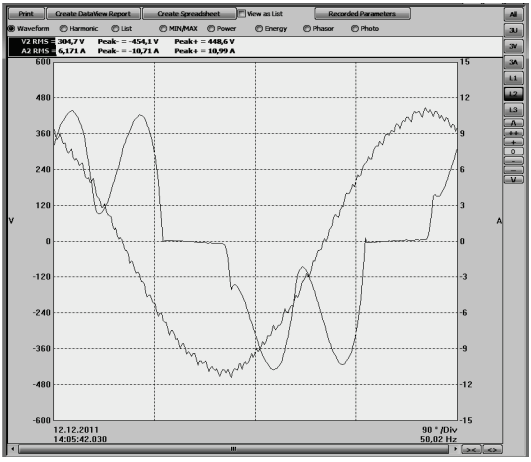



Figure 4. Voltage supply and current value drawn by line 2 of the ASD

EBSCOhost - printed on 2/14/2023 2:46 PM via . All use subject to https://www.ebsco.com/terms-of-use

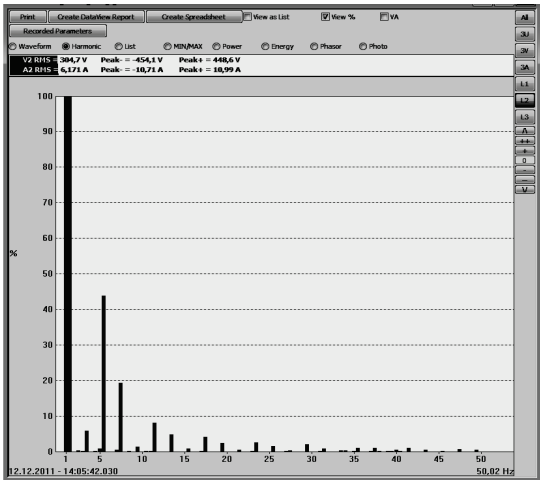



Figure 5. THVD and THDI in line 2 of the ASD

Fig. 5 depicts the FFT chart of the supply voltage and current drawn by line 2. One can easily notice that the harmonic content of the supply voltage is negligible. The supply voltage is represented only by the dark spectrum line of 50 Hz; the content of the rest of the harmonics is quite insignificant.

The mathematical representation of harmonics has been widely covered in the literature [6-9]. Consequently, leaving aside the mathematical aspects and looking only at the graph depicted in Fig. 5, a noteworthy fact is that such an AC drive does not produce a third harmonic component: the $5^{th}$, $7^{th}$, and somehow the $11^{th}$ and $13^{th}$ order harmonic components are significant.

Starting from these preliminary observations, one may conclude that the system faces a simple issue of harmonic filtering. However, due to high frequency transients, determined especially by the PWM frequency, parasitic capacitance to the ground plane, and the coupling of adjacent cables, the AC drive creates a certain level of electromagnetic interference in the radio frequency spectrum of 150 kHz–30 MHz in the mains power grid. This interference affects the surrounding electrical devices as well.

Conducted interferences were measured using a spectrum analyser (HM5014-Hameg Instruments) [15], an instrument based on high frequency characteristics.

The most important features of the spectrum analyser are: the usable frequency range, from 150 kHz to above 30 MHz; the available resolution

EBSCOhost - printed on 2/14/2023 2:46 PM via . All use subject to https://www.ebsco.com/terms-of-use

bandwidths of 9 kHz, 120 kHz, and 400 kHz; processor-controlled operation; and a digital signal display, which works in real-time and is resolved with up to 4,000 points over the entire screen.

The quasi-peak value of the conducted perturbation spectrum, ranging from 100 kHz to 30 MHz in a linear scale, is depicted in Fig. 6. It can be seen that in the frequency range of 100 kHz to 10 MHz, the recorded values exceeded the limits of the standard EN 61800-3:2004/A1 [16]. The situation is better revealed, with the same characteristics, when depicted in a logarithmic scale (Fig. 7).

The limits set by the standard are represented on the graph: the lower limit represents the average value limit and the higher one represents the quasi-peak value.

One can easily see that the quasi-peak values of the conducted electromagnetic emissions exceeded the average and the quasi-peak limits set by the standard (the peak value being nearly 20 dBμV higher than the standard limit).

In order to improve energy efficiency, it was obvious that a few power quality countermeasures with respect to harmonics and conducted interferences were necessary. It is well-known that in such cases filtering methods represent the best solution.

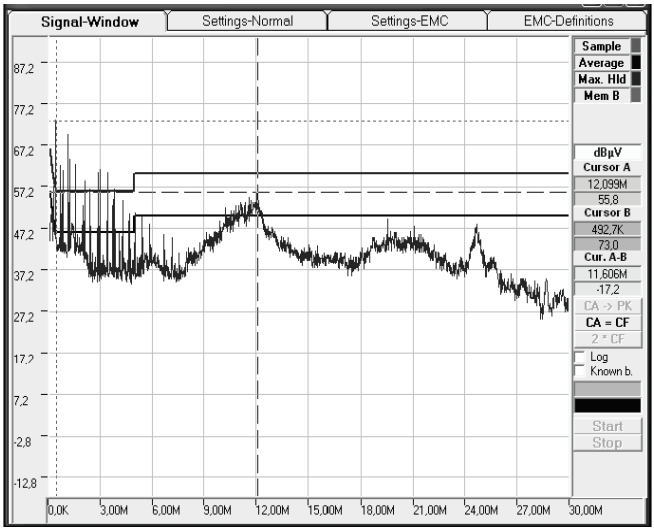



Figure 6. Conducted interference generated by the ASD

EBSCOhost - printed on 2/14/2023 2:46 PM via . All use subject to https://www.ebsco.com/terms-of-use

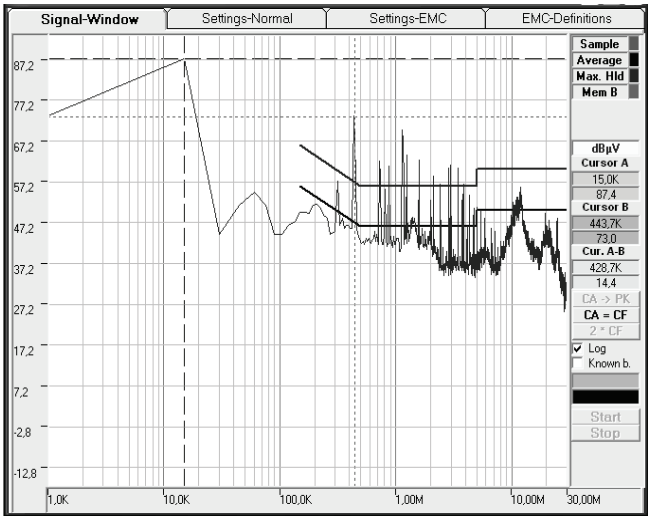



Figure 7. Conducted interference generated by the ASD (logarithmic scale)

## 3. Harmonics and Conducted Interference Mitigation

Active filters are superior in terms of filtering performance, smaller in physical size, and more flexible in application, compared to traditional passive filters using capacitors, inductors, and/or resistors. However, active filters are slightly inferior in terms of cost and operating loss compared to passive filters [17]. In the case studied here, while only the $5^{th}$, $7^{th}$, and $11^{th}$ order harmonic components matter, together with the wide conducted interference spectrum, from 1 kHz to 12 MHz, a three-phase filter F.LL. D3 series AN/HN type, suitable for industrial environments and available in 440Vac and 520Vac models was the proper option (Fig. 8.) [18].

This high performance, high voltage, three phase filter has high attenuation characteristics, being especially designed for industrial frequency inverters and motor drives.

In the graph in Fig. 9, one can observe the differential (dotted line) and the common mode (solid line) insertion loss in the frequency range from DC to 100 MHz.

The 60-80 dBs value of the insertion loss in the frequency ranges from 100 kHz to 30 MHz, which is of interest in the standard EN 50011 [19].

EBSCOhost - printed on 2/14/2023 2:46 PM via . All use subject to https://www.ebsco.com/terms-of-use

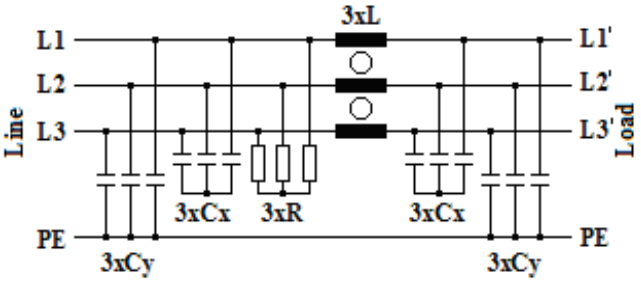



Figure 8. The three-phase passive EMI filter

The essential part of an electromagnetic interference passive filter is represented by the common mode choke, which allows high inductance values, typically 1–10 mH, in a small volume without fear of a choke saturation caused by the mains frequency supply current. This is because the common mode inductor is wound on ferrite cores having high $A_L$ values.

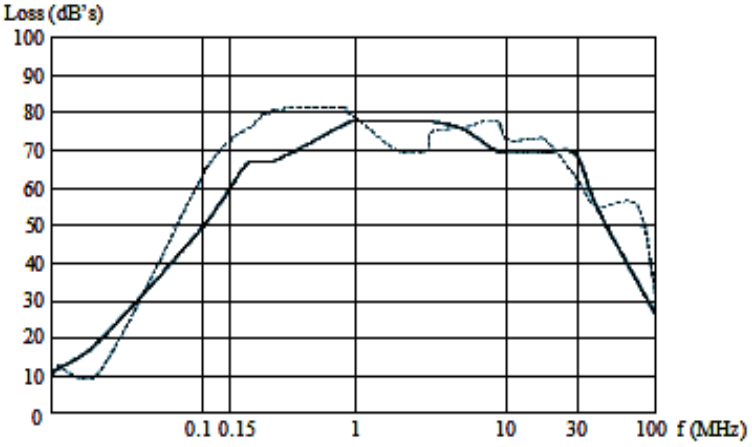



Figure 9. The insertion loss of the passive filter

Generally, common mode chokes are manufactured using ferrites—low-density ceramic materials with the composition $Fe_2O_3XO$—where X is a type of metal (cobalt, nickel, zinc, manganese, etc.), which has reduced electrical conductivity and therefore very low eddy currents.

EBSCOhost - printed on 2/14/2023 2:46 PM via . All use subject to https://www.ebsco.com/terms-of-use

The concept of complex magnetic permeability permits the formal separation of the cores into two components: $\underline{\mu} = \mu' - j \cdot \mu''$.

Its real part, denoted by $\mu'$, is related to the ability of the material to concentrate magnetic flux, an ideal inductive component (without losses) $X = \omega \cdot L_0 \cdot \mu'$, where $L_0$ represents the air coil inductance (without magnetic core). The imaginary part, $\mu''$, is related to the dissipation of magnetic energy, as it flows through the material, a resistive component, which is frequency dependent and quantifies the losses in the material of the magnetic core $R = \omega \cdot L_0 \cdot \mu''$. The impedance $|\underline{Z}| = \sqrt{R^2 + X^2}$ and the loss tangent angle $(\tan \delta = \mu'' / \mu')$ are both functions of frequency.

This formal approach seeks to represent a basic characteristic that allows for efficient discrimination between inductors and ferrites.

Figs. 10 and 11 represent the reactive and resistive part of the impedance of ferrites.

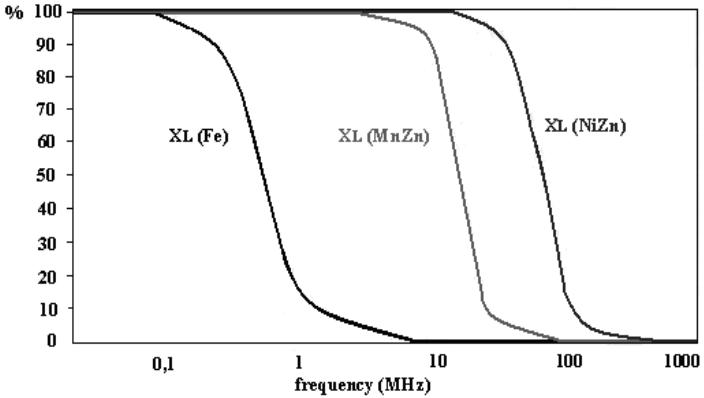



Figure 10. The reactive part of different ferrites impedance versus frequency

EBSCOhost - printed on 2/14/2023 2:46 PM via . All use subject to https://www.ebsco.com/terms-of-use

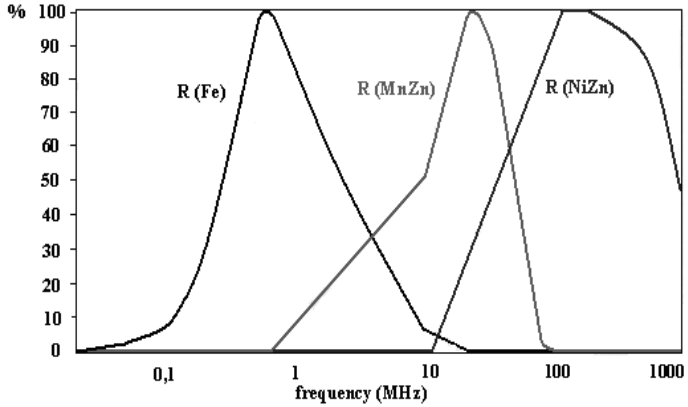



Figure 11. The resistive part of different ferrites impedance versus frequency

They show, beyond any doubt, that only Ni Zn material is effective for frequencies higher than 100MHz, where the common mode choke becomes dissipative. The other ferrite materials present zero impedance beyond 100 MHz [20], [21].

Tests were performed with a 50 Ω source and load impedances, matched to the characteristic impedance of most RF test equipment. However, in practical situations, a 50 Ω source and load impedances are complex and, in general, unknown, thus the predicted attenuation is likely optimistic. As such, one must take into account the prescriptions set out by the standard EN 61800-3:2004/A1 [16], concerning EMC requirements and specific test methods for adjustable-speed electrical power drive systems.

The chosen filter has the following rated values: $I_R$=16 A; $\Delta I_L$=18 mA; $C_X$=3x4.4+3x2.2 μF (which attenuates mostly the differential mode interference); $C_Y$=3x10+3x47 nF (which attenuates mostly the common mode interference); $L$=3x5.2 mH (the common mode choke $L$ is built in a symmetrical configuration, which allows high inductance values in a small volume; the common mode choke is wound on a ferrite core having a high $A_L$ value, which enhances the magnetic properties of the core and improves insertion loss characteristics); $R$=3x1 MΩ; temperature range: -25°C to +85°C;

Measurements were repeated after retrofitting the filter, the results are shown in Figs. 12 - 16.

EBSCOhost - printed on 2/14/2023 2:46 PM via . All use subject to https://www.ebsco.com/terms-of-use

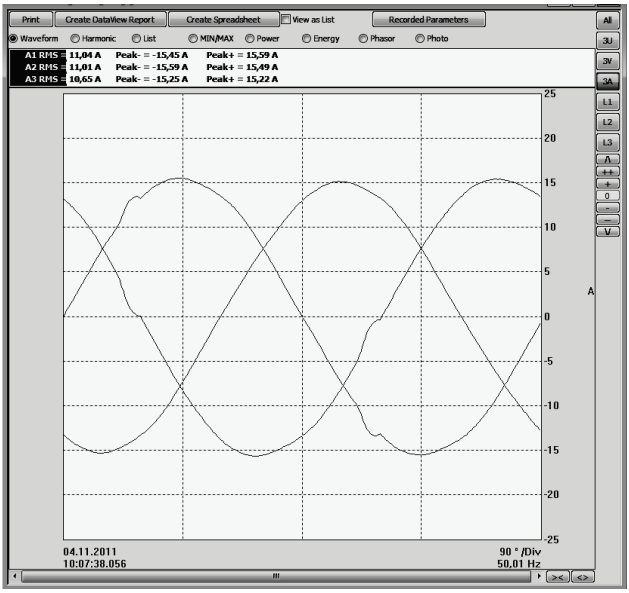



Figure 12. Three phase supply voltages of the ASD after EMI filtering

Current distortions greatly improved, their harmonic content being almost negligible, and the level of conducted interferences decreased below the limits set by the standards. However, a problem remains, namely the poor displacement power factor, determined by the lagging phase of the current due to the high inductive character of the motors.

EBSCOhost - printed on 2/14/2023 2:46 PM via . All use subject to https://www.ebsco.com/terms-of-use

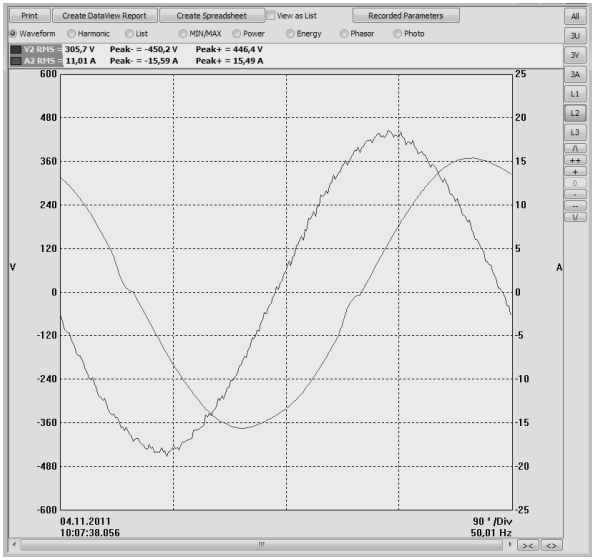



Figure 13. Voltage supply and current drawn by line 2 of the ASD after EMI filtering

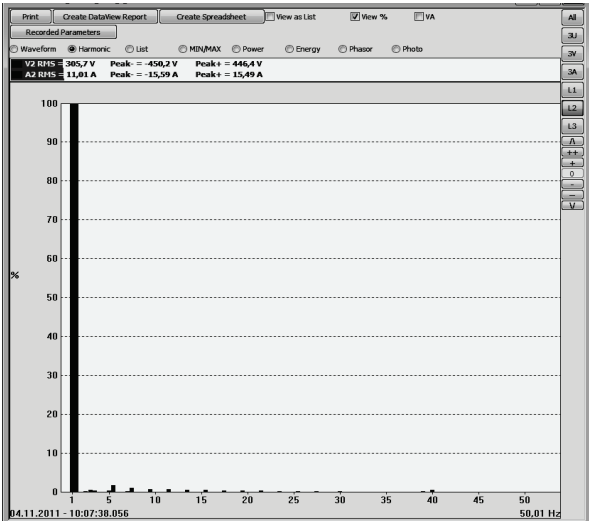



Figure 14. THVD and TDID in line 2 of the ASD after EMI filtering

EBSCOhost - printed on 2/14/2023 2:46 PM via . All use subject to https://www.ebsco.com/terms-of-use

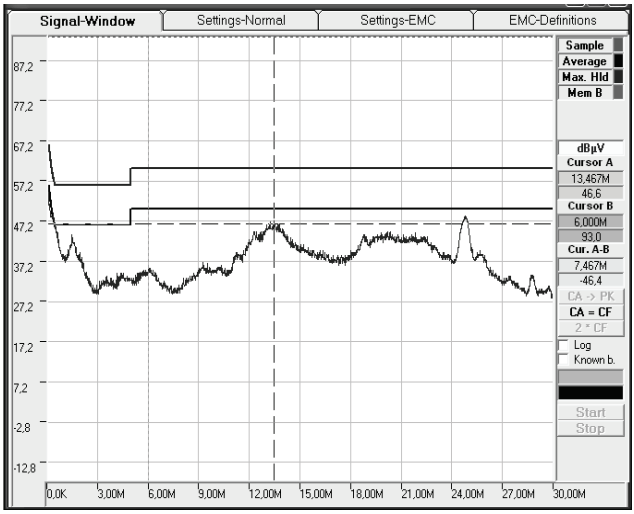



Figure 15. Conducted interference generated by the ASD (linear scale)

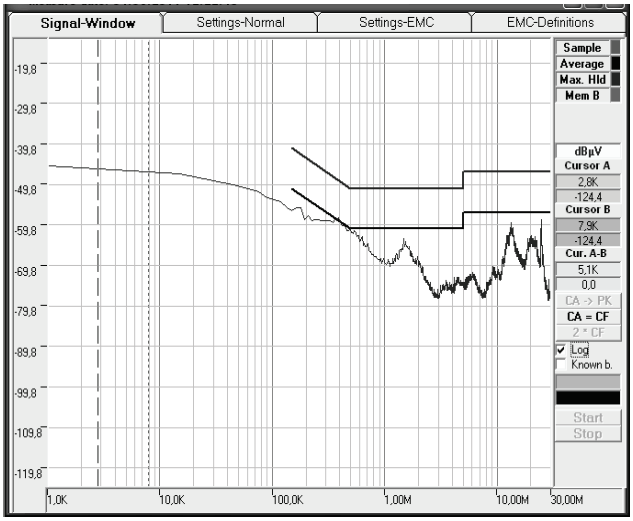



Figure 16. Conducted interference generated by the ASD (logarithmic scale)

Consequently, in this situation it is more cost effective to use a centralized solution in order to improve the displacement power factor, for instance, by use of dynamic capacitor banks placed in the point of power

EBSCOhost - printed on 2/14/2023 2:46 PM via . All use subject to https://www.ebsco.com/terms-of-use

coupling (PCC) in the immediate vicinity of the secondaries of the transformer substations.

## 4. Conclusions

In the above case study, since a large number of wells were driving heavy and high variable loads, mitigating harmonics was absolutely necessary to improve energy efficiency. At the same time, due to the environmental conditions, electromagnetic noise and perturbations were inherent.

One simple, single, straightforward solution was chosen to solve both problems: the use of a passive filtering method, which is much more cost effective than active filtering. Additionally, it is well-known that active filtering introduces supplementary electromagnetic interferences, which in their turn also have to be cancelled out by the use of a passive electromagnetic interference filter.

Looking at the measurements performed in the oil field, one can conclude that the best method for improving the displacement power factor issue, which still persists, is to provide dynamic capacitor banks in the vicinity of the output feeders of the transformer substations.

An alternative method could be the use of tuned harmonic filters on every ASD, in order to obtain the necessary reactive power, but the resonances that might occur in the distribution feeders due to the large number of ASDs connected to a PCC and the variability of the loads represent a major drawback of this kind of solution.

## References

[1] Council of European Energy Regulators—Working Group on Quality of Electricity Supply (2001), Quality of electricity supply: Initial benchmarking on actual levels, standards and regulatory strategies.
[2] Math H. J. Bollen, Irene Yu-Hua Gu. Signal Processing Of Power Quality Disturbances, John Wiley & Sons, Inc., 2006
[3] Montrose, M. I., Nakauchi, E. M. Testing for EMC Compliance -Approaches and Techniques, John Wiley & Sons, Inc., 2004
[4] IEC/TR 61000-1-1(1992), Electromagnetic compatibility (EMC) - Part 1: General - Section 1: Application and interpretation of fundamental definitions and terms
[5] Sankaran, C. Power Quality, CRC Press LLC 2002
[6] Kusko, A., Thompson M.T. Power Quality in Electrical Systems, McGraw-Hill Companies, Inc., 2007

EBSCOhost - printed on 2/14/2023 2:46 PM via . All use subject to https://www.ebsco.com/terms-of-use

[7] Chattopadhyay, S., Mitra, M., Sengupta, S. Electric Power Quality, Springer Science+Business Media B.V. 2011
[8] Dugan, R. C., et al. Electrical Power Systems Quality, McGraw-Hill, 2004
[9] Arrillaga, J., Watson, N. R. Power System Harmonics, John Wiley & Sons, Ltd, 2003
[10] European standard EN 50160, Voltage characteristics of electricity supplied by public distribution systems, CENELEC TC 8X, 2006
[11] Shepherd, W, Zhang, Li. Power Converter Circuits, Marcel Dekker, Inc., 2004
[12] Wilamowski, B. M., Irwin, J. D. Power Electronics and Motor Drives, Taylor and Francis Group, LLC, 2011
[13] Mohan, N., Undeland, T.M., Robbins, W. P. Power Electronics Converters, Applications and Design, John Wiley & Sons, Inc., 2003.
[14] http://www.chauvin-arnoux.com/produit/Famille_detail.asp?idFam=2058&idPole=1
[15] http://www.hameg.com/datasheets.0.html?&no_cache=1
[16] EN 61800-3:2004/A1:2012 Adjustable speed electrical power drive systems - Part 3: EMC requirements and specific test methods
[17] H. Akagi. "Modern active filters and traditional passive filters" Bulletin of the Polish Academy of Sciences Technical Sciences, 2006, Vol. 54, No. 3, pp. 255-269
[18] http://www.kemet.com/kemet/web/homepage/kechome.nsf/file/F.LL.D3%20Series%20AN,%20HN%20Type/$file/F9000_F.LL.D3_ AN_HN.pdf
[19] EN 55011:2007 Industrial, scientific and medical (ISM) radio-frequency equipment - Electromagnetic disturbance characteristics - Limits and methods of measurement
[20] Gerfer, A., Ralf, B., Zenker, H. Trilogy of Inductors, Swiridoff Verlag, 2002.
[21] Buzdugan, M. I., Simion, E., Bălan, H., Baru, E. Electromagnetic Compatibility at the Mains Ports for Medical Equipment, International Conference on Renewable Energies and Power Quality (ICREPQ'09), Valencia, April 2009.
[22] Buzdugan, M. I., Bălan, H. Power Quality versus Electromagnetic Compatibility in Adjustable Speed Drives, International Conference on Renewable Energies and Power Quality (ICREPQ'13), Bilbao, March 2013.

EBSCOhost - printed on 2/14/2023 2:46 PM via . All use subject to https://www.ebsco.com/terms-of-use

# CHAPTER FORTY-FIVE

# APPLICATION OF GENERALIZED NON-ACTIVE POWER THEORY FOR PARALLEL HYBRID COMPENSATION OF PERIODIC AND NON-PERIODIC DISTURBANCES

ZDENĚK MULLER[1], JOSEF TLUSTÝ[1], AND VIKTOR VALOUCH[1]

## Abstract

A strategy for the decomposition of detrimental current components in an electric power systems is presented here. This method is based on the non-active power theory, with different averaging time intervals. These individual current components can be used as reference signals for devices compensating for periodic, as well as non-periodic and stochastic currents, generated by nonlinear unbalanced loads connected to an unsymmetrical non-sinusoidal voltage power source. The use of an appropriate set of parallel compensation devices for mitigating individual detrimental load current components with different dynamics can lead to a substantial reduction of the power rating and cost of such a hybrid compensator. The effectiveness of the generalized non-active power theory in contributing to mitigation of non-periodic current disturbances is demonstrated in the frequency domain, as well as by simulation.

**Keywords:** Generalized non-active power theory; detrimental current components; simulation; electric power system; parallel hybrid compensation.

[1] Department of Electrical Power Engineering, Faculty of Electrical Engineering, CTU in Prague Prague, Czech Republic, E-mail: zdenek.muller@fel.cvut.cz, tlusty@fel.cvut.cz, viktor.valouch@fel.cvut.cz

EBSCOhost - printed on 2/14/2023 2:46 PM via . All use subject to https://www.ebsco.com/terms-of-use

## Introduction

Although electric power is produced with almost ideal parameters, the shape of the voltage may be influenced considerably by large, dynamic, and nonlinear loads, which can produce unbalanced, non-periodic, and even stochastic currents. Equipment that displays issues with these loads include: electric arc furnaces (EAF), big drives, welding machines, and traction drives, etc. [1]. As such, the compensation of concurrent undesirable phenomena represents a great challenge for engineers from both the theoretical and the practical points of view [2]-[7]. The extension of existing power theories, and perhaps the development of some new ones, has the potential to establish a theoretical background for the compensation of such disturbances and is of great importance.

The relevant power theories have mostly been discussed, classified, and compared in terms of their capabilities in compensating for unwanted instantaneous power components in three-phase asymmetrical systems with non-sinusoidal voltages and currents.

The compensation of subharmonic, non-periodic, and stochastic disturbances in electric power systems has emerged as a very serious problem that requires a solution. The diversity of the features of these disturbances makes their compensation quite difficult.

The original theory of Fryze on non-active current may be extended using a general averaging time interval $T_C$ that can be either one-half of a fundamental cycle, one full fundamental cycle $T$—as in Fryze's theory—or multiple fundamental cycles, depending on the character of the load current, the objectives of compensation, and the energy storage capacity of a powered electronics-based compensator.

If the current $\boldsymbol{i}(t)$ is the current of an unbalanced load, which may contain, harmonic and also non-periodic or stochastic components, and the active current $\boldsymbol{i}_a(t)$ is the required source current, then $\boldsymbol{i}_n(t) = \boldsymbol{i}(t)-\boldsymbol{i}_a(t)$ is the non-active current, which should be injected by a parallel compensator connected to the PCC (point of common coupling).

By choosing $T_C \rightarrow 0$, the GNP (generalized non-active power) theory gives the same results as those obtained by using the well-known IRP (instantaneous reactive power) theory. If $T_C \rightarrow \infty$, the non-active component in the non-periodic load current is completely eliminated, leaving only the source current active.

A principal of usage of the generalized non-active power theory [10]-[17] for the parallel hybrid compensation of periodic and non-periodic disturbances is presented in this paper. A non-linear unbalanced load generating periodic, as well as non-periodic and stochastic currents,

EBSCOhost - printed on 2/14/2023 2:46 PM via . All use subject to https://www.ebsco.com/terms-of-use

connected to an unsymmetrical non-sinusoidal voltage source is considered. Based on the so-called running quantities [9], [10] with different integration intervals, the non-active current of the non-linear load is separated into several characteristic components that can represent reference signals for different parts of the compensation system. According to the different characters of the reference currents, compensators with slow dynamics or active devices based on fast electronic power converters can be used as appropriate. The applied approach and presented formulas have been verified by simulation in the Matlab/Simulink environment.

This chapter is the based on a revised version of a paper presented at the International Conference on Renewable Energies and Power Quality (ICREPQ'16) [19].

## Overview of Generalized Non-Active Power Theory

In Fryze's theory, the active power $P$ is calculated as the average value of $p = v\ i$ over one fundamental cycle $T = 1/f$. A serious limitation is that the calculation of $i_a$ is characterized by the time delay $T$.

The original version of Fryze's theory of non-active current is extended in [10] by using a general averaging time interval $T_C$ that can be either one-half fundamental cycle, one full fundamental cycle $T$—the same as in Fryze's theory—or multiple fundamental cycles, depending on the character of the load current, the objectives of compensation, and the energy storage capacity of the power electronics-based compensator. For the three-phase system, the voltage and current vectors may be expressed as follows:

$$\begin{aligned} \boldsymbol{v} &= \left[v_a, v_b, v_c\right]^T \\ \boldsymbol{i} &= \left[i_a, i_b, i_c\right]^T \end{aligned} \tag{1}$$

The active current is defined in this generalized non-active power (GNP) theory by:

$$\boldsymbol{i}_a(t) = \frac{P(t)}{V_P^2(t)} \boldsymbol{v}_P(t) = Y(t)\boldsymbol{v}_P(t) \tag{2}$$

EBSCOhost - printed on 2/14/2023 2:46 PM via . All use subject to https://www.ebsco.com/terms-of-use

$$P(t) = \frac{1}{T_C} \int_{t-T_C}^{t} \boldsymbol{v}^T(\tau)\boldsymbol{i}(\tau)\,\mathrm{d}\tau \tag{3}$$

$$V_P^2(t) = \frac{1}{T_C} \int_{t-T_C}^{t} \boldsymbol{v}_P^T(\tau)\boldsymbol{v}_P(\tau)\,\mathrm{d}\tau \tag{4}$$

where $\boldsymbol{v}_P\,(t)$ is the reference voltage vector—this can be the voltage at the PCC (point of common coupling), the fundamental positive sequence component of this voltage, or something else, depending again on the type of compensator and/or compensation objectives.

The non-active current is the remaining part of the current vector:

$$\boldsymbol{i}_n(t) = \boldsymbol{i}(t) - \boldsymbol{i}_a(t) \tag{5}$$

If the current $\boldsymbol{i}\,(t)$ is the current of an unbalanced non-linear load, which may contain harmonic and also non-periodic stochastic components, and the current $\boldsymbol{i}_a\,(t)$ is the required source current, then $\boldsymbol{i}_n\,(t)$ is the current that should be injected by a parallel compensator connected to the PCC, as in Fig. 1.

Non-periodic current means here a current whose frequency is not an integer multiple of the fundamental frequency. As such, it may contain subharmonic, interharmonic, and stochastic components.

The GNP theory has already been used for the compensation of non-periodic disturbances using parallel active filters [10]-[14]; a STATCOM [15]; a voltage and current parallel compensator [16]; and a UPQC (unified power quality conditioner) [17].

## Principle of Decomposition of Detrimental Currents

The parallel hybrid compensation system shown in Fig. 1 can be composed of several parts.

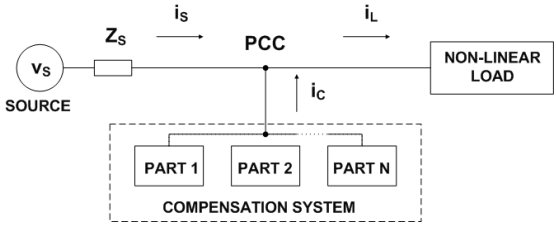



Figure 1. Configuration of parallel hybrid compensation

EBSCOhost - printed on 2/14/2023 2:46 PM via . All use subject to https://www.ebsco.com/terms-of-use

One part of the system can be a parallel APF (active power filter)—an electronic power converter-based compensator with high dynamics—while the other compensators need only be passive compensators or electronic power converters, but with a lower switching frequency than the first one. This configuration has advantages over a conventional universal electronic power compensator consisting of only one converter covering all compensation and filtration functions with respect to the necessary power rating and cost of the complete compensation device.

The active load current is:

$$\boldsymbol{i}_{\mathrm{La}}(t) = \frac{P_{\mathrm{L}}(t)}{V_{\mathrm{LP}}^2(t)} \boldsymbol{v}_{\mathrm{LP}}(t) \tag{6}$$

where:

$$P_{\mathrm{L}}(t) = \frac{1}{T_{\mathrm{C}}} \int_{t-T_{\mathrm{C}}}^{t} \boldsymbol{v}_{\mathrm{L}}^{\mathrm{T}}(\tau)\, \boldsymbol{i}_{\mathrm{L}}(\tau)\, \mathrm{d}\tau \tag{7}$$

$$V_{\mathrm{LP}}^2(t) = \frac{1}{T_{\mathrm{C}}} \int_{t-T_{\mathrm{C}}}^{t} \boldsymbol{v}_{\mathrm{LP}}^{\mathrm{T}}(\tau)\, \boldsymbol{v}_{\mathrm{LP}}(\tau)\, \mathrm{d}\tau \tag{8}$$

and $\boldsymbol{v}_{\mathrm{LP}}$ is the reference voltage vector. Let us take for this reference voltage the fundamental positive sequence component $\boldsymbol{v}^{+}_{\mathrm{L1}}$ of the load voltage $\boldsymbol{v}_{\mathrm{L}}$. The current $\boldsymbol{i}_{\mathrm{La}}$ is then balanced and purely sinusoidal without any harmonics, regardless of the distorted and unbalanced voltage $\boldsymbol{v}_{\mathrm{L}}$ of the power system and the reactive and unbalanced load current $\boldsymbol{i}_{\mathrm{L}}$ with harmonic components. Even for the non-periodic load current $\boldsymbol{i}_{\mathrm{L}}$ the active current component $\boldsymbol{i}_{\mathrm{La}}$ then approaches a pure sine wave if the time averaging interval $T_{\mathrm{C}}$ is properly chosen. The non-active load current $\boldsymbol{i}_{\mathrm{Ln}}$ is then:

$$\boldsymbol{i}_{\mathrm{Ln}}(t) = \boldsymbol{i}_{\mathrm{L}}(t) - \boldsymbol{i}_{\mathrm{La}}(t) \tag{9}$$

The current $\boldsymbol{i}_{\mathrm{Ln}}$ is the current that should be generated by the parallel compensator so that the source current is only active $\boldsymbol{i}_{\mathrm{S}}(t) = \boldsymbol{i}_{\mathrm{La}}(t)$.

The so-called CRMS (complex RMS) value $\boldsymbol{I}_{\mathrm{L1}}$ of the fundamental harmonic of the load current $\boldsymbol{i}_{\mathrm{L}}$ is:

$$\boldsymbol{I}_{\mathrm{L1}}(t) = \frac{\sqrt{2}}{T} \int_{t-T}^{t} \boldsymbol{i}_{\mathrm{L}} e^{-\mathrm{j}\omega\tau}\, \mathrm{d}\tau \tag{10}$$

EBSCOhost - printed on 2/14/2023 2:46 PM via . All use subject to https://www.ebsco.com/terms-of-use

The CRMS value $\boldsymbol{I}_{L1}$ is the quasi-instantaneous variable calculated over averaging the interval $T = 1/f$, $f$ is the fundamental frequency, $\omega = 2\pi f$.

The time response $\boldsymbol{i}_{L1}$ can be calculated as:

$$\boldsymbol{i}_{L1}(t) = \sqrt{2}\,\mathrm{Re}\left\{\boldsymbol{I}_{L1}e^{j\omega t}\right\} \tag{11}$$

This current vector $\boldsymbol{i}_{L1}$ is harmonic free, but generally not balanced, and may contain reactive and non-periodic parts (in the sense of the previous paragraph) if such components are present in $\boldsymbol{i}_L$.

By applying equations (10) and (11) on only the positive sequence components in the load current $\boldsymbol{i}_L$, the current vectors $\boldsymbol{I}^+_{L1}$ and $\boldsymbol{i}^+_{L1}$ (t) are obtained. To eliminate the negative sequence components from the load current $\boldsymbol{i}_L$, a proper positive/negative sequence detector, based for example on a type of PLL (phase lock loop) circuit, must be used.

In [8], the current $\boldsymbol{i}_L$ of a non-linear load or a load with periodically variant parameters was decomposed into five mutually orthogonal components: the generalized active current; scattered current; reactive current; unbalanced current; and current generated by a load with harmonics not present in the non-sinusoidal voltage source. We will not consider the scattered current appearing in systems with a changing equivalent conductance, e.g. due to the skin effect on transmission lines. However, we will suppose that the generated current also contains non-periodic components, in the sense mentioned previously, produced, for example, by an EAF (electric arc furnace), which can be separated. The GNP theory is formulated in the time domain thanks to this and in opposition to the CPC theory [9].

Let us suppose that the load current in unbalanced non-sinusoidal systems with non-periodic load current disturbances can be decomposed into the following components:

$$\begin{aligned}\boldsymbol{i}_L(t) &= \boldsymbol{i}_{La}(t) + \boldsymbol{i}_{Ln}(t) = \boldsymbol{i}_{La}(t) + \boldsymbol{i}_{L1r}(t) \\ &\quad + \boldsymbol{i}_{L1u}(t) + \boldsymbol{i}_{Lh}(t) + \boldsymbol{i}_{Lnp}(t)\end{aligned} \tag{12}$$

where $\boldsymbol{i}_{L1r}$ is the reactive current associated with the fundamental harmonic only; $\boldsymbol{i}_{L1u}$ is the fundamental harmonic unbalanced current; $\boldsymbol{i}_{Lh}$ is the harmonic current; and $\boldsymbol{i}_{Lnp}$ is the non-periodic current containing all remaining non-active disturbances (subharmonics, interharmonics, stochastic).

EBSCOhost - printed on 2/14/2023 2:46 PM via . All use subject to https://www.ebsco.com/terms-of-use

The question is whether the non-periodic load current components can be detected with reasonable accuracy by using the GNP theory.

It has been theoretically, and to some extent experimentally, proved [12]-[17] that the precision of the calculation of the currents $\boldsymbol{i}_{\mathrm{La}}$, $\boldsymbol{i}_{\mathrm{Ln}}$ by using (6), (9) in unbalanced non-sinusoidal systems with non-periodic load currents is sufficient if $T_{\mathrm{C}}$ is chosen to be 5–10 times the fundamental period. Contrary to this, where $T_{\mathrm{C}}$ decreases to under 5 times the fundamental period ($T_{\mathrm{c}}$=$T$/2 is the lowest possible value), the non-periodic component of the load current becomes more and more pronounced in the current $\boldsymbol{i}_{\mathrm{La}}$.

Let us introduce:

$$\boldsymbol{i}_{\mathrm{Lnp}}(t) = \boldsymbol{i}_{\mathrm{La}}(t)\Big|_{T_{\mathrm{C}}=T} - \boldsymbol{i}_{\mathrm{La}}(t)\Big|_{T_{\mathrm{Cnp}}=T_{\mathrm{C}}>>T} \tag{13}$$

where $\boldsymbol{i}_{\mathrm{La}}(t)$, $T_{\mathrm{Cnp}}$>>$T$ will be calculated by (6) with $T_{\mathrm{Cnp}}$ = (5–10)$T$ in the following analysis.

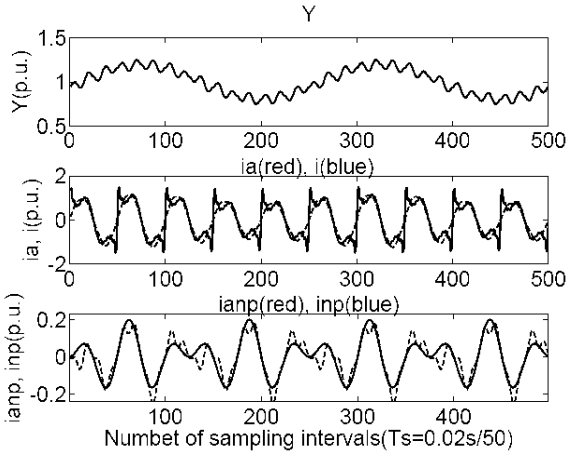



Figure 2. Waveforms of admittance $Y$ and phase current responses $i$, $i_{\mathrm{a}}$ (dashed), $i_{\mathrm{np}}$, $i_{\mathrm{anp}}$ (dashed) in the time domain for $T_{\mathrm{C}} = T/2$, $T_{\mathrm{Cnp}} = 5T$

Fig. 2 shows the waveforms of the admittance $Y$, and the current responses $i$, $i_{\mathrm{a}}$, $i_{\mathrm{np}}$, $i_{\mathrm{anp}}$ in the time domain for $T_C = T/2$; $i$ is the load current in any phase; $i_{\mathrm{a}}$ is the calculated active current; and $i_{\mathrm{np}}$, $i_{\mathrm{anp}}$ are the non-periodic currents in the same phase where the superscript “a” denotes the non-periodic current calculated using (13). The subharmonic component

EBSCOhost - printed on 2/14/2023 2:46 PM via . All use subject to https://www.ebsco.com/terms-of-use

of the frequency 10 Hz and the set of the most important twelve harmonic components ($h$=2-13, with the amplitude law $I_h$=1/$h$ p.u.) are present in the current $i$. Due to the high content of even harmonics, especially the second one, the current $i$ is highly distorted and very different from a sinusoidal waveform. We can see that the estimated current $i_{anp}$ follows its actual waveform $i_{np}$ well, but some small residual harmonic components in the current $i_{anp}$ still remain.

In general, we can say that the choices $T_C = T/2$, $T_C = T$ provide us with similar results in estimating the non-periodic current component $i_{anp}$ by using (13). Nevertheless, for currents $i$ with a high content of harmonics, we could give a preference to the option $T_C = T$ where all harmonics are eliminated, which is not the case in Fig. 2.

The remaining three non-active current components in (12) can be determined as follows:

$$\boldsymbol{i}_{L1r}(t) = \boldsymbol{i}^{+}_{L1}(t) - \boldsymbol{i}_{La}(t) - \boldsymbol{i}_{Lnp}(t) \tag{14}$$

$$\boldsymbol{i}_{L1u}(t) = \boldsymbol{i}_{L1}(t) - \boldsymbol{i}^{+}_{L1}(t) \tag{15}$$

$$\boldsymbol{i}_{Lh}(t) = \boldsymbol{i}_{L}(t) - \boldsymbol{i}_{L1}(t) \tag{16}$$

By summing these three components we obtain:

$$\boldsymbol{i}_{L1r}(t) + \boldsymbol{i}_{L1u}(t) + \boldsymbol{i}_{Lh}(t) = \boldsymbol{i}_{L}(t) - \boldsymbol{i}_{La}(t) - \boldsymbol{i}_{Lnp}(t) \tag{17}$$

which is in agreement with (12).

So, all the load current components can be determined by calculating $\boldsymbol{i}_{La}$, $\boldsymbol{i}_{L1}$, $\boldsymbol{i}^{+}_{L1}$, and $\boldsymbol{i}_{Lnp}$ (6), (11), (11) for $\boldsymbol{I}^{+}_{L1}$, (13). However, it should be emphasized that the calculation of $\boldsymbol{i}_{Lnp}$ using (13) is only an approximation whose accuracy depends on the character of the non-periodic current disturbances and the respective choice of the averaging interval $T_{Cnp}$>>$T$.

If the non-active load current $i_{Ln}$ (9) is completely compensated for by a parallel hybrid compensator, only the active load current $\boldsymbol{i}_{La}$ (6) is provided by the source, i.e. $\boldsymbol{i}_S = \boldsymbol{i}_{La}$. We can see that the four components (13)-(16) of the non-active current $\boldsymbol{i}_{Ln}$ require different dynamics for their compensation. The compensation of the harmonic component $\boldsymbol{i}_{Lh}$ requires a higher switching frequency of the respective PWM (pulse width modulated) converter than the compensation of the remaining three components. Sometimes, the reactive $\boldsymbol{i}_{Lr}$ and unbalanced $\boldsymbol{i}_{Lu}$ current can be

EBSCOhost - printed on 2/14/2023 2:46 PM via . All use subject to https://www.ebsco.com/terms-of-use

extremely detrimental to the load. A SVC (static VAR compensator) based on three thyristor-controlled susceptances, whose parameters are updated only twice per fundamental voltage cycle, is the proper device for the compensation of these two components. Furthermore, some selected harmonics can be compensated for by using PFs (passive filter) tuned to some orders or a range of harmonics.

As can be seen, it is evident that for different concrete situations, the compensation objectives are different too and the use of an appropriate set of compensation devices for mitigating individual detrimental current components can lead to a substantial reduction of the power rating and cost of such a hybrid compensator.

## Analysis of GNP Theory

It was shown in [1]-[3] that the precision of the calculation of the currents $\boldsymbol{i}_{\mathrm{a}}$, $\boldsymbol{i}_{\mathrm{n}}$ using (2), (5) in unbalanced non-sinusoidal systems with non-periodic load currents is sufficient if $T_{\mathrm{C}}$ is chosen to be 5–10 times that of the fundamental period. Let us demonstrate some basic attributes of the GNP theory on an example of one phase voltage and current:

$$v = \sqrt{2}\,V \sin \omega t \tag{18}$$

$$i = \sqrt{2}\,I\left(1 + \Delta \sin \Delta\omega t\right)\sin \omega t + \sqrt{2}\,I_{\mathrm{h}} \sin \omega_{\mathrm{h}} t = \left(\sqrt{2}\,I + \sqrt{2}\,\Delta I \sin \Delta\omega t\right)\sin \omega t + \sqrt{2}\,I_{\mathrm{h}} \sin \omega_{\mathrm{h}} t = \sqrt{2}\,I \sin \omega t + i_{\mathrm{np}} + i_{\mathrm{h}} \tag{19}$$

The current contains three components: the fundamental; the non-periodic (specifically subharmonic here); and the harmonic.

By using the concept of the GNP theory (2)-(4), the calculated active current can be expressed as follows:

$$i_{\mathrm{a}} = Yv = \sqrt{2}\,I \sin \omega t + i_2 + i_{\mathrm{anp}} + i_{\mathrm{ah}} \tag{20}$$

where:

$$i_2 = \frac{\sqrt{2}}{T_{\mathrm{C}}}\left[-\frac{I}{2\omega}\sin 2\omega\tau\right]_{t-T_{\mathrm{C}}}^{t} \sin \omega t \tag{21}$$

$$i_{\mathrm{anp}} \approx \sqrt{2}\Delta I G_{\mathrm{D}} \sin\left(\Delta\omega t - \phi_{\mathrm{D}}\right)\sin \omega t \quad (\text{for } \Delta\omega << 2\omega) \tag{22}$$

$$G_{\mathrm{D}} = \sin \phi_{\mathrm{D}} / \phi_{\mathrm{D}}, \;\; \phi_{\mathrm{D}} = \Delta\omega T_C / 2 \tag{23}$$

EBSCOhost - printed on 2/14/2023 2:46 PM via . All use subject to https://www.ebsco.com/terms-of-use

$$i_{\mathrm{ah}} = \frac{\sqrt{2}I_{\mathrm{h}}}{2}\begin{bmatrix} G_{\mathrm{h}}{}^{+}\sin\left(\omega_{\mathrm{h}}t-\phi_{\mathrm{h}}{}^{+}\right)+G_{\mathrm{h}}{}^{-}\sin\left(\omega_{\mathrm{h}}t-\phi_{\mathrm{h}}{}^{-}\right)- \\ -G_{\mathrm{h}}{}^{+}\sin\left((\omega_{\mathrm{h}}+2\omega)t-\phi_{\mathrm{h}}{}^{+}\right)- \\ -G_{\mathrm{h}}{}^{-}\sin\left((\omega_{\mathrm{h}}-2\omega)t-\phi_{\mathrm{h}}{}^{-}\right) \end{bmatrix} \tag{24}$$

$$G_{\mathrm{h}}{}^{+} = \sin\phi_{\mathrm{h}}{}^{+}/\phi_{\mathrm{h}}{}^{+},\ \ \phi_{\mathrm{h}}{}^{+} = (\omega_{\mathrm{h}}+\omega)T_C/2$$

$$G_{\mathrm{h}}{}^{-} = \sin\phi_{\mathrm{h}}{}^{-}/\phi_{\mathrm{h}}{}^{-},\ \ \phi_{\mathrm{h}}{}^{-} = (\omega_{\mathrm{h}}-\omega)T_C/2 \tag{25}$$

The components $i_2$, $i_{\mathrm{anp}}$, $i_{\mathrm{ah}}$ are more or less excluded from the active current component $i_{\mathrm{a}}$ depending on the value of the general averaging time interval $T_{\mathrm{C}}$ and the frequencies $\Delta\omega$, $\omega_{\mathrm{h}}$.

If $T_{\mathrm{C}} = kT/2$, $k$=1, 2, 3…, the current component $i_2$ is equal to zero. By changing the value of $T_{\mathrm{C}}$ we can evaluate how the components $i_{\mathrm{anp}}$, $i_{\mathrm{ah}}$ are more or less excluded from the active current component $i_{\mathrm{a}}$.

By using formulas (24)-(25), we can analyze how the current component with the frequency $\omega_{\mathrm{h}}$, which is present in the load current $i_{\mathrm{L}}$, will appear in the active current $i_{\mathrm{La}}$ when the GNP theory is applied. Let us suppose here that the frequency $\omega_{\mathrm{h}}$ is not only an integer multiple of the fundamental frequency $\omega$ (harmonic component), but generally any other one: subharmonic <2π1, 2π49 Hz>; harmonic (2π$h$50 Hz, $h$=1, 2, 3,…); or interharmonic higher than 2π50 Hz.

Fig. 3 shows the impact of the value of $T_{\mathrm{C}}$ on the rate $I_{\mathrm{La}}/I_{\mathrm{L}}$ for different frequencies, where $I_{\mathrm{La}}$, $I_{\mathrm{L}}$ are the respective magnitudes of the current components presented in $i_{\mathrm{La}}(t)$, $i_{\mathrm{L}}(t)$ (for $i_{\mathrm{La}}$ given by the first two terms in (24)). We can see that all harmonics presented in $i_{\mathrm{L}}(t)$ are completely suppressed for $T_{\mathrm{C}}$ being one full fundamental cycle $T$ or any multiple fundamental cycles. We see that the components of interharmonic frequencies are substantially suppressed as well.

EBSCOhost - printed on 2/14/2023 2:46 PM via . All use subject to https://www.ebsco.com/terms-of-use

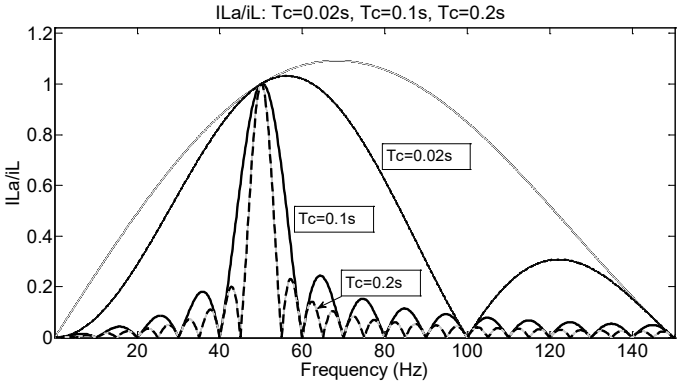



Figure 3. Impact of value of $T_C$ on rate $I_{La}/I_L$ for frequencies in range <0, 150 Hz>

Now, let us continue with the load current component $i_{np}$ induced by modulation of the subharmonic magnitude. By using formulas (22)-(23), we can analyze how the current component with the magnitude modulation frequency $\Delta\omega$, which is present in the load current $i_L$, will appear in the active current $i_{La}$ when the GNP theory is applied.

Fig. 4 demonstrates how the dominating gain $G_D$ depends on the subharmonic frequency $\Delta f$ for different values $T_C$ =0.02, 0.1, 0.2 s. We can see that for the frequencies $\Delta f = k / T_C,\ k = 1,2,3,\ldots$ the subharmonic components are nullified and for other frequencies the gain $G_D$ decreases as $\Delta f$ gets higher.

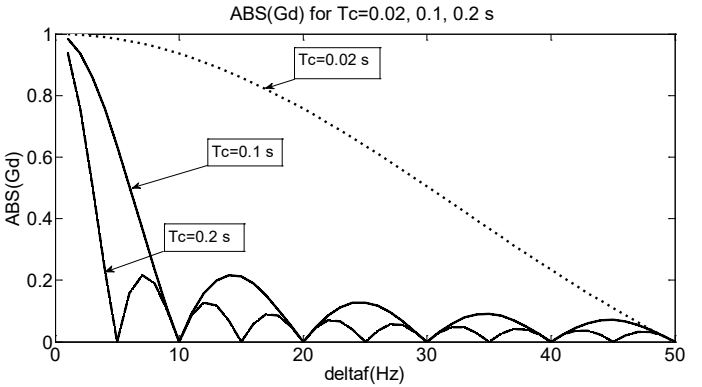



Figure 4. Dominating gain $G_D$ in (22) versus subharmonic frequency $\Delta f$ for different values $T_C$ =0.02, 0.1, 0.2 s

EBSCOhost - printed on 2/14/2023 2:46 PM via . All use subject to https://www.ebsco.com/terms-of-use

## Simulation of Decomposition of Detrimental Load Current Components

Let us demonstrate the strategy presented above on the example of a three phase unbalanced non-sinusoidal system with the load current $\boldsymbol{i}_L$. This contains, in addition to the active current $\boldsymbol{i}_{La}$, the reactive current $\boldsymbol{i}_{L1r}$, which is only associated with the fundamental harmonic; the fundamental harmonic unbalanced current $\boldsymbol{i}_{L1u}$; the harmonic current $\boldsymbol{i}_{Lh}$; and the non-periodic current containing all remaining non-active disturbances $\boldsymbol{i}_{Lnp}$.

Figs. 5-7 show the results of the simulation of a model based on (6)-(11), (13)-(16) with $\boldsymbol{v}_{LP}= \boldsymbol{v}^{+}_{L1}$ ($\boldsymbol{v}_{LP}$ is selected as the fundamental positive sequence component), $T_{Cnp} = 5T$, and with the parameters of the fundamental positive sequence components $\boldsymbol{v}^{+}_{L1}$, $\boldsymbol{i}^{+}_{L1}$, fundamental negative sequence component $\boldsymbol{i}^{-}_{L1}$, and the fifth harmonic current $\boldsymbol{i}_{L5}$, as shown in Tab. I.

**Table I. Parameters of the three phase load voltage and current used in simulation**

| Variable | Magnitude (p.u.) | Phase |
|---|---|---|
| $\boldsymbol{v}_L= \boldsymbol{v}_{L1}= \boldsymbol{v}^{+}_{L1}= \boldsymbol{v}_{LP}$ | 1 | 0 |
| $\boldsymbol{i}^{+}_{L1}$ | 1 | $-\pi/2$ |
| $\boldsymbol{i}^{-}_{L1}$ | 0.5 | 0 |
| $\boldsymbol{i}_{L5}$ | 0.2 | 0 |

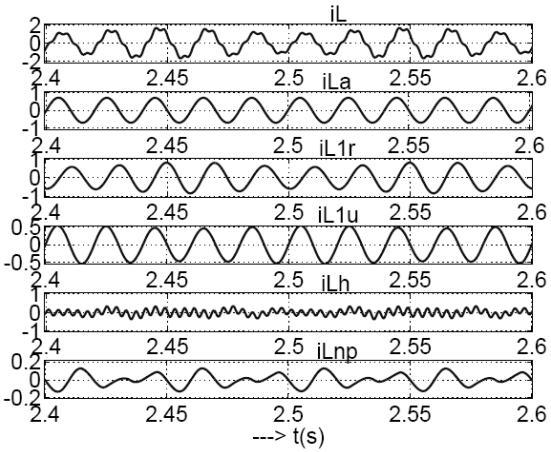



Figure 5. Decomposition of load current $\boldsymbol{i}_L$ modulated by the subharmonic signal

EBSCOhost - printed on 2/14/2023 2:46 PM via . All use subject to https://www.ebsco.com/terms-of-use

In Fig. 5 we can see the decomposition of the load current $\boldsymbol{i}_{\mathrm{L}}$ in one phase into the components $\boldsymbol{i}_{\mathrm{La}}$, $\boldsymbol{i}_{\mathrm{L1r}}$, $\boldsymbol{i}_{\mathrm{L1u}}$, $\boldsymbol{i}_{\mathrm{Lh}}$, $\boldsymbol{i}_{\mathrm{Lnp}}$, when the magnitude of the load current $\boldsymbol{i}_{\mathrm{L}}$ specified by Tab. I is modulated by the subharmonic signal with a magnitude $\Delta I_{\mathrm{L}}$=0.2 p.u. and frequency 10 Hz. Due to the phase shift $-\pi/2$ between $\boldsymbol{v}_{\mathrm{L1}}$ and $\boldsymbol{i}^{+}_{\mathrm{L1}}$, the current components $\boldsymbol{i}_{\mathrm{La}}$, $\boldsymbol{i}_{\mathrm{L1r}}$ should ideally have the magnitudes $\sqrt{2}$ p.u. (without subharmonic modulation of the load current) and the current $\boldsymbol{i}_{\mathrm{L1u}}$ should replicate $\boldsymbol{i}^{-}_{\mathrm{L1}}$. We can see in Fig. 5 that the waveforms of the separated current components $\boldsymbol{i}_{\mathrm{L1r}}$, $\boldsymbol{i}_{\mathrm{L1u}}$ are only partially influenced by the subharmonic modulation, but exhibit the expected responses. The same is true for the component $\boldsymbol{i}_{\mathrm{Lh}}$. It is evident as well that the maximum amplitudes of the components $\boldsymbol{i}_{\mathrm{Lh}}$, $\boldsymbol{i}_{\mathrm{Lnp}}$ are somewhat lower than those of these components originally contained in the load current $\boldsymbol{i}_{\mathrm{L}}$, namely 0.2.

In Fig. 6 we can see the decomposition of the load current $\boldsymbol{i}_{\mathrm{L}}$ in one phase into the components $\boldsymbol{i}_{\mathrm{La}}$, $\boldsymbol{i}_{\mathrm{L1r}}$, $\boldsymbol{i}_{\mathrm{L1u}}$, $\boldsymbol{i}_{\mathrm{Lh}}$, $\boldsymbol{i}_{\mathrm{Lnp}}$ when the magnitude of the load current $\boldsymbol{i}_{\mathrm{L}}$ is modulated by the white noise signal. We can see that the load current imitates fairly well a waveform with a non-periodic stochastic character, like that produced by an EAF, for example.

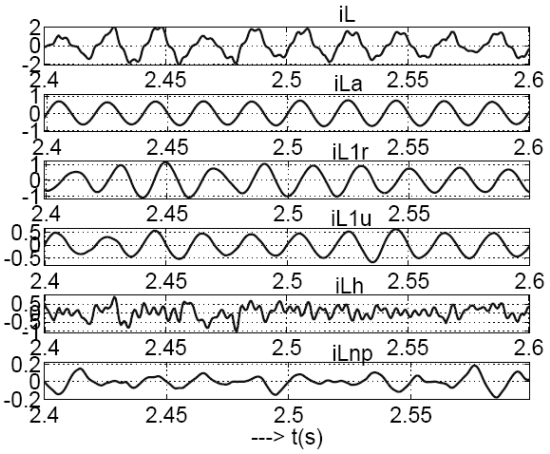



Figure 6. Decomposition of load current $\boldsymbol{i}_{\mathrm{L}}$ modulated by white noise signal

EBSCOhost - printed on 2/14/2023 2:46 PM via . All use subject to https://www.ebsco.com/terms-of-use

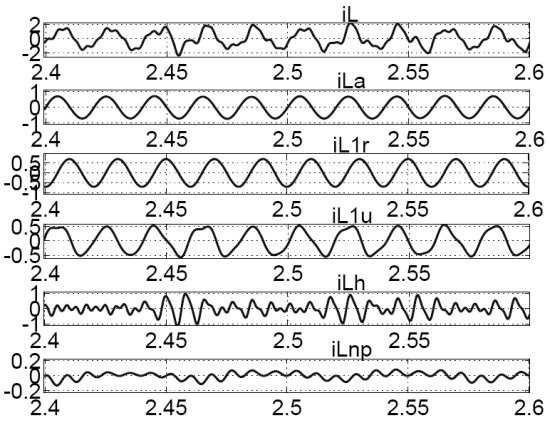



Figure 7. Decomposition of load current $\boldsymbol{i}_{\mathrm{L}}$ with superimposed interharmonics

The separated current components $\boldsymbol{i}_{\mathrm{L1r}}$, $\boldsymbol{i}_{\mathrm{L1u}}$ are again partially influenced by the non-periodic stochastic modulation of the load current. The component $\boldsymbol{i}_{\mathrm{Lh}}$ contains not only the fifth harmonic, but also some of the disturbances introduced into the load current by the white noise signal.

Figs. 5, 6 show the results of the decomposition of the load current $\boldsymbol{i}_{\mathrm{L}}$ into its components under the sinusoidal voltage $\boldsymbol{v}_{\mathrm{L}}= \boldsymbol{v}^{+}_{\mathrm{L1}}$ (Tab. I). When the voltage also includes a negative sequence component $\boldsymbol{v}^{-}_{\mathrm{L1}}$ and the fifth harmonic $\boldsymbol{v}_{\mathrm{L5}}$, both of the magnitude of 0.2 p.u., we cannot recognize any important difference. As can be seen, the method presented is not significantly affected by load voltage distortions.

Finally, Fig. 7 presents the results of the decomposition of the load current $i_{\mathrm{L}}$ into its components when the additional current interharmonics (104, 117, 134, and 147 Hz) specified by [18] and used in [17] are added. Again, this stochastic non-periodic current $i_{\mathrm{L}}$ imitates a current waveform produced, for example, by an EAF. We can see that the current components $i_{\mathrm{L1u}}$, $i_{\mathrm{Lnp}}$ are partially influenced by the imposed interharmonics, while Fourier analysis of the current ($i_{\mathrm{Lh}}+i_{\mathrm{Lnp}}$) confirms that this current contains the interharmonic (104, 117, 134, and 147 Hz) and harmonic (250 Hz) components with very similar magnitudes as those injected into the load current $i_{\mathrm{L}}$.

EBSCOhost - printed on 2/14/2023 2:46 PM via . All use subject to https://www.ebsco.com/terms-of-use

## Parallel Active Power Filter Compensation

A three phase power system was simulated in the Matlab/Simulink™ environment. The parallel APF (active power filter) was based on a PWM (pulse width modulated) converter. The converter was modeled as a 4-level capacitor clamped inverter (CCI) working with the sampling frequency 1600 Hz (due to supposed use of IGCT switching elements). The converter reference current was $i_{CCI}^{*} = i_L - i_{La}$.

The nominal line-to-line voltage of the grid was 10 $kV_{RMS}$, without any disturbances. The parameters of the 400 kVA load, modeled as the three phase system of current sources, are in Tab. II.

**Table II. Parameters of non-linear load**

| Current component | Value in phase | Current vector phase shift |
|---|---|---|
| $i^{+}_{L1}$ | $I_N$ = 23.1 $A_{RMS}$ | $-\pi/2$ |
| $i^{-}_{L1}$ | 0.5 $I_N$ | 0 |
| $i_{L5}$ | 0.2 $I_N$ | 0 |
| $i_{L7}$ | 0.15 $I_N$ | 0 |

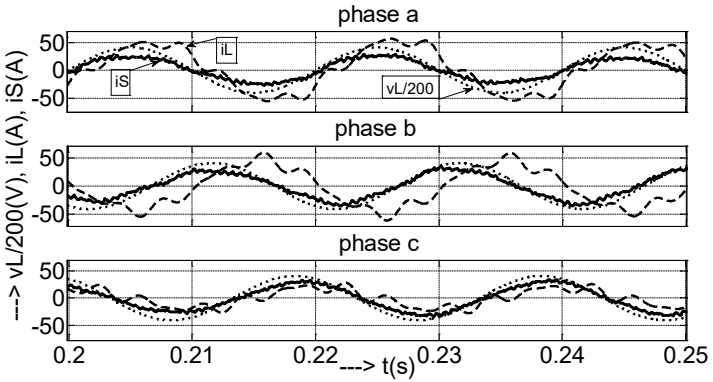



Figure 8. Waveforms of grid voltage $\boldsymbol{v}_L$, load current $\boldsymbol{i}_L$, and grid current $\boldsymbol{i}_S$ after compensation in all three phases. The magnitude of load current $\boldsymbol{i}_L$ with components declared in Tab. II was additionally modulated by a subharmonic signal with magnitude $\Delta I_L = 0.2 I_N$ and frequency 5 Hz

EBSCOhost - printed on 2/14/2023 2:46 PM via . All use subject to https://www.ebsco.com/terms-of-use

In Fig. 8, we can see the waveforms of the grid voltage $v_L$, load current $i_L$, and grid current $i_S$ after compensation in all three phases. The magnitude of the load current $\boldsymbol{i}_L$ with components shown in Tab. II was additionally modulated by a subharmonic signal with the magnitude $\Delta I_L$=0.2$I_N$ and frequency 5 Hz. We can see that there is a phase shift between the grid voltage and the load current, which is not the case for the grid current. In addition, the magnitudes of the grid currents in all three phases are approximately the same, although the load current is, due to the presence of the negative component $\dot{\boldsymbol{I}}_{L1}$, highly unbalanced. But, due to the choice $T_C = 5T$, a part of the subharmonic component with the frequency 5 Hz is still present in the grid current in accordance with the results presented before. This is why the magnitudes of the three phase grid currents are not exactly the same in the time window shown. The full compensation of this subharmonic component could be obtained by setting $T_C = 10T$.

## Conclusion

The presented method of decomposition of the three phase current with non-periodic components is based on the generalized non-active power theory working with different averaging time intervals $T_C$. The current can be decomposed into active current; reactive current associated only with the fundamental harmonic; fundamental harmonic unbalanced current; harmonic current; and non-periodic current containing all remaining non-active disturbances (subharmonics, interharmonics, and stochastic).

The injected non-periodic current component has been decomposed from the load current with a good level of precision for all the analyzed examples (subharmonic, stochastic, and interharmonic disturbances). The impact of the value of $T_C$ on the rate $I_{La}/I_L$ for different frequencies has been studied in the frequency domain ($I_{La}$ is a residuum of the magnitude $I_L$ of the load current component remaining in the active current after applying the GNP strategy). It was found that interharmonic current components above 100 Hz are sufficiently suppressed for $T_C = (5 – 10)T$. As for subharmonics, the lower their frequency, the higher the value of $T_C$ that should be used to achieve sufficient compensation. On the other hand, the compensation dynamics in the case of transient processes becomes worse as $T_C$ increases.

The individual decomposed current components can be used as the reference signals for devices compensating periodic, as well as non-periodic, stochastic current components generated by nonlinear unbalanced loads connected to an unsymmetrical non-sinusoidal voltage

EBSCOhost - printed on 2/14/2023 2:46 PM via . All use subject to https://www.ebsco.com/terms-of-use

power source. The use of an appropriate set of compensation devices to mitigate individual detrimental current components with different dynamics can lead to a substantial reduction of the power rating and cost of such a hybrid compensator.

## Acknowledgement

Financial support from the project Analysis of transmission and distribution systems with FACTS elements (SGS17/181/OHK3/3T/13) is gratefully acknowledged.

## References

[1] H. Akagi, Y. Kazanawa, A. Nabae: Instantaneous reactive power compensators comprising switching devices without energy storage components. IEEE Trans. Ind. Appl., Vol. IA-20, No. 3, pp. 625–630, May/June 1984.

[2] W. le Roux, J. D. van Wyk: Evaluation of Residual Network Distortion during Compensation According to the "Instantaneous Power Theory". ETEP, Vol. 8, No. 5, pp. 337–344, September/October 1998.

[3] L. S. Czarnecki: On some misinterpretations of the instantaneous reactive power p-q theory. IEEE Trans. on Power Electronics, Vol. 19, No. 3, pp. 828–836, 2004.

[4] L. S. Czarnecki: Effect of Supply Voltage Asymmetry on IRP p-q – Based Switching Compensator Control. IET on Power Electronics, Vol. 3, No. 1, pp. 11–17, 2010.

[5] Horn, L. A. Pittorino, and J. H. R. Enslin: Evaluation of active power filter control algorithms under non-sinusoidal and unbalanced conditions. Proc.7th Int. Conf. Harmonics and Quality Power, Oct. 16-18, 1996, pp. 217-224.

[6] H. Kim, F. Blaabjerg, B. Bak-Jensen, J. Choi: Instantaneous Power Compensation in Three-Phase Systems by Using p-q-r Theory. IEEE Trans. on Power Electronics, Vol. 17, No. 5, pp. 701–710, September 2002.

[7] F. Z. Peng, J.-S. Lai: Generalized instantaneous reactive power theory for three-phase power systems. IEEE Trans. Instrum. Meas., Vol. 45, No. 1, pp. 293–297, February 1996.

[8] L. S. Czarnecki: Orthogonal Decomposition of the Currents in a 3-phase Nonlinear Asymmetrical Circuit with a Nonsinusoidal Voltage Source. IEEE Trans. on Instrument and Measure, Vol. 37, No. 1, March, 1988.

[9] L. S. Czarnecki: Comparison in Instantaneous Reactive Power p-q Theory with Theory of the Current´s Physical Components. Electrical Engineering, Vol. 85 (2003), pp. 21–28, Springer-Verlag 2002.

[10] F. Z. Peng, L. M. Tolbert: Compensation of Non-Active Current in Power Systems-Definitions from Compensation Standpoint-. IEEE Power Eng. Society, Summer Meeting, July 15–20, Seattle, USA, 2000, pp. 983–987.

EBSCOhost - printed on 2/14/2023 2:46 PM via . All use subject to https://www.ebsco.com/terms-of-use

[11] L. M. Tolbert, T. G. Habetler: Comparison of Time-Based Non-Acive Power Definitions for Active Filtering. IEEE Int. Power Electronics Congress (CIEP 2000), Acapulco, Mexico, pp. 73–79, 15–19 October 2000.
[12] L. M. Tolbert, Y. Xu, J. Chen, F. Z. Peng, J. N. Chiasson: Application of Compensators for Non-Periodic Currents. IEEE PES Conference (PESC), Acapulco, Mexico, 2003.
[13] Y. Xu, L. M. Tolbert, F. Z. Peng, J. N. Chiasson, J. Chen: Compensation-Based Non-Active Power Definition. IEEE POWER ELECTRONICS LETTERS, Vol. 1, No. 2, pp. 45–50, June 2003.
[14] Y. Xu, L. M. Tolbert, J. N. Chiasson, J. B. Campbell, F. Z. Peng: Active Filter Implementation Using a Generalized Nonactive Power Theory. IEEE IAS Conf., 2006, pp. 153–160.
[15] Y. Xu, L. M. Tolbert, J. N. Chiasson, J. B. Campbell, F. Z. Peng: A Generalised Instantaneous Non-Active Power Theory for STATCOM. IET Elect. Power Appl. 1., (2007), pp. 853–861.
[16] Y. Xu, L. M. Tolbert, J. D. Kueck, D. T. Rizy: Voltage and Current Unbalance Compensation Using a Parallel Active Filter. IEEE PESC, Orlando, USA, 2007, pp. 2919–2925
[17] M. Ucar, S. Ozdemir, E. Ozdemir: A four-leg unified series-parallel active filter system for periodic and non-periodic disturbance compensation. Electric Power Systems Research (2011), doi: 10.1016/j.epsr.2011.01.001.
[18] IEEE Interharmonic Task Force, Cigré 36.05/CIRED 2 CC02 Voltage Quality Working Group, Interharmonics in power systems, 1997.
[19] Muller, Z., Švec, J., Tlustý, J., Valouch, V.: Application of generalized non-active power theory for parallel hybrid compensation of periodic and non-periodic disturbances. ICREPQ 16 – Inter. Conference on Renewable Energies and Power Quality, Madrid, Spain, May 4–6, pp. 1–5, 2016, ISSN: 2172-038 X

EBSCOhost - printed on 2/14/2023 2:46 PM via . All use subject to https://www.ebsco.com/terms-of-use